5th GRACM International Congress on Computational Mechanics

GRACM 05

29 June - 1 July 2005, Limassol, Cyprus

Dedicated to the Memory of Professor John H. Argyris

PROCEEDINGS
Volume 1

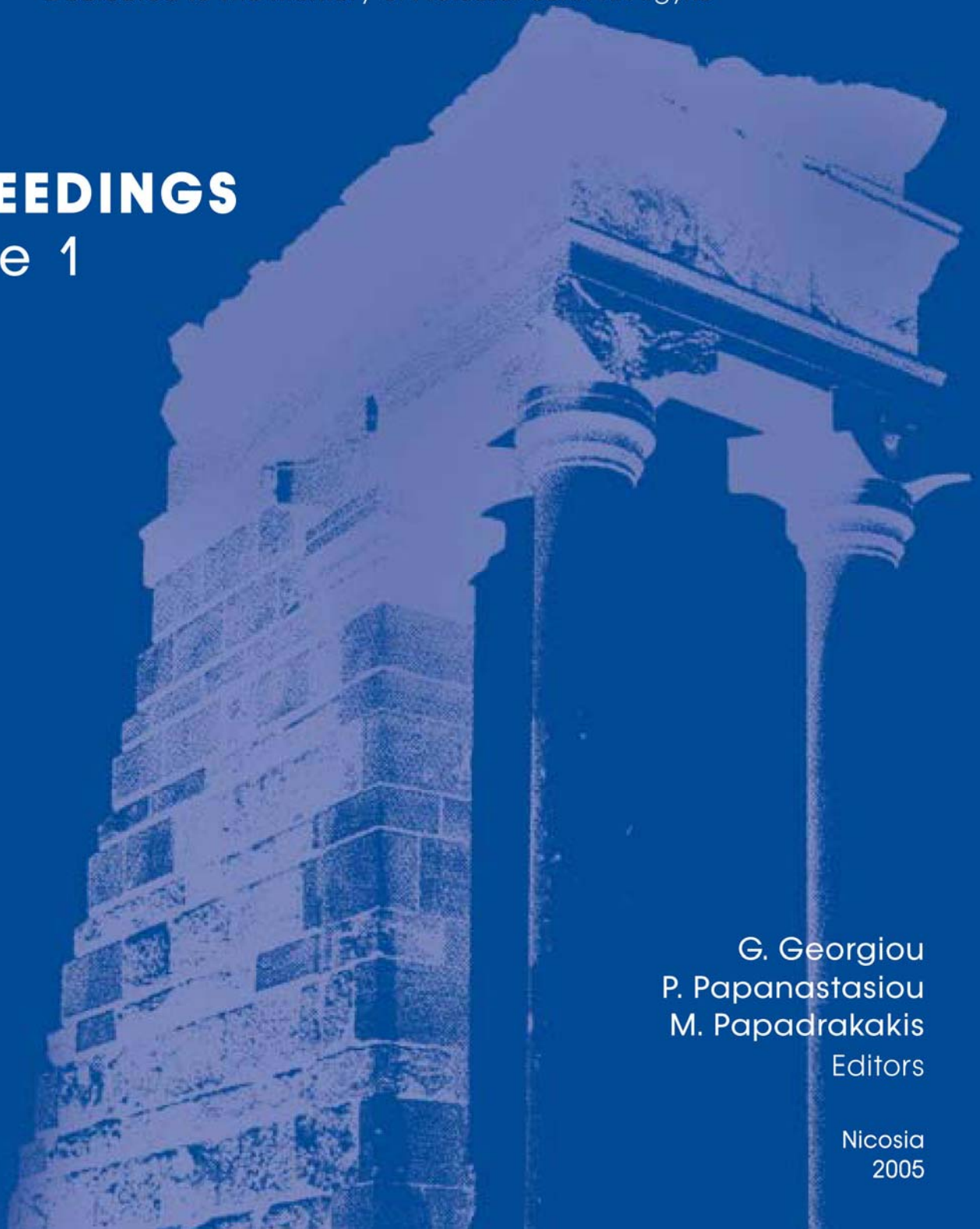

G. Georgiou
P. Papanastasiou
M. Papadrakakis
Editors

Nicosia
2005

Proceedings of GRACM 05

VOLUME 1

5th GRACM International Congress
on Computational Mechanics
Limassol, Cyprus, 29 June – 1 July 2005

Dedicated to the Memory
of Professor John H. Argyris

Edited by
G. Georgiou, P. Papanastasiou and M. Papadrakakis

Nicosia
2005

ISBN set 9963 – 644 – 50 - 3
ISBN v.1 9963 – 644 – 51 – 1
Kantzilaris Publications
Nicosia
June 2005

Preface

The 5th International Congress of the Greek Association of Computational Mechanics (GRACM) will be held in Limassol, Cyprus during 29 June - 1 July 2005. The previous conferences in the series were held in Athens, 1992; Chania, 1996; Volos, 1999; and Patras, 2002.

Since their inception, the conferences have grown in size and scope covering more and wider areas of Computational Mechanics. In addition to the 8 invited plenary papers, 107 contributed papers from 12 countries have been accepted for presentation in GRACM05. These papers covered a wide range of topics: Solid and Structural Mechanics, Mechanics of Materials, Structural Dynamics and Earthquake Engineering, Stability and Chaos, Fracture Mechanics, Fluid Mechanics and Hydraulics, Aerodynamics, Transport phenomena, Electromagnetism, Biomechanics, Inverse Problems in Mechanics, Structural Control and Optimization, Artificial Intelligence and Expert Systems, System Identification, Numerical Methods and Algorithms, Finite Elements, Boundary Elements and Finite Differences.

The fifth Congress heralds new and innovative activities in a number of areas of Computational Mechanics and addresses the important issue of where the developments stand today and what the future will be in the applications of research developments for the solution of complex problems of modern technology.

The aims of the Congress are to encourage graduate student participation as well as to become a forum for critical discussion so as to lead to an assessment of past developments and future application and research needs. The outcome is expected to help researchers and engineers to shoulder important responsibilities toward the use of computational methods and mathematical models for the solution of a wide range of Engineering problems, and to pursue advanced research for the understanding and definition of the issues that remain to be addressed.

We thank the authors of the plenary and contributed papers for timely submission and participation in the Congress, the reviewers of the papers, the members of the Scientific Committee and the members of the Organizing Committee for their support and guidance. We also express our appreciation to the technical and financial cosponsors, including the Department of Civil & Environmental Engineering and the Department of Mathematics & Statistics of the University of Cyprus, the Hyperion Systems Engineering, the Cyprus Tourism Organization and the Department of Antiquities, Cyprus. Thanks are also due to the vice-president of GRACM, professor A. Boudouvis, and to all members of the Executive Board of GRACM for their continuous support and close cooperation.

An electronic color version of these Proceedings can be found at

http://www.ucy.ac.cy/~gracm05/e-Proceedings.htm

Georgios Georgiou
Panos Papanastasiou
Manolis Papadrakakis

June 2005

Author Statistics

The origin of a paper is assumed to be that of the presenting author. The numbers in parentheses include the affiliations of all co-authors.

Greece		**79** (83)
Athens	**46** (48)	
Crete	**8** (9)	
Ioannina	**3**	
Patras	**10**	
Thessaly	**3**	
Thessaloniki	**9** (10)	
Cyprus		**14**
USA		**8** (13)
UK		**5** (8)
Germany		**2** (6)
Canada		**1**
Israel		**1** (2)
Italy		**1** (2)
Japan		**1**
The Netherlands		**1** (2)
Poland		**1**
Taiwan		**1**
Bulgaria		(3)
Austria		(1)
Belgium		(1)
Hungary		(1)
Spain		(1)
Sweden		(1)
Total:		**115**

GRACM 05 Committees

Scientific Committee

M. Papadrakakis, Athens (Chair)
A. Alexandrou, Nicosia
N. Aravas, Volos
D. Beskos, Patras
A. Boudouvis, Athens
G. Georgiou, Nicosia (Co-chair)
A. Karageorghis, Nicosia
S. Karamanos, Volos
J. Katsikadelis, Athens
N. Makris, Patras
P. Papanastasiou, Nicosia (Co-chair)
G. Provatidis, Athens
K. Spiliopoulos, Athens
S. Theotokoglou, Athens

Organizing Committee

G. Georgiou (Co-Chair)
P. Papanastasiou (Co-Chair)
A. Alexandrou
C. Doumanides
S. Kassinos
P. Komodromos
Y. Smyrlis
C. Xenophontos

Invited Speakers

Nenad Bicanic, University of Glaskow (UK)
George Karniadakis, Brown University (USA)
Chris Kleijn, Delft University of Technology (The Netherlands)
Costas Pantelides, Imperial College (UK)
Glaucio Paulino, University of Illinois, Urbana (USA)
Ekkerard Ramm, University of Stuttgart (Germany)
Matasaka Tanaka, Shinshu University (Japan)
Zohar Yosibash, Ben-Gurion University (Israel)

Reviewers

A. Alexandrou
A. Boudouvis
S. Christodoulou
G. Georgiou
I. Ioannou
S. Karamanos
P. Komodromos
E. Mitsoulis
M. Papadrakakis
P. Papanastasiou
M. Phocas
G. Provatidis
K. Spiliopoulos
S. Theotokoglou
C. Xenophontos

Session Chairs

Z. Agioutantis
A. Alexandrou
D. Beskos
A. Boudouvis
J. Ekaterinaris
S. Karamanos
J. Katsikadelis
P. Komodromos
N. Makris
E. Mitsoulis
M. Neophytou
C.P. Pantelides
M. Papadrakakis
G. Provatidis
E. Sapountzakis
K. Spiliopoulos
G.E. Stavroulakis
L. Stavridis
D. Talaslidis
J. Tassoulas
E. Theotokoglou
G. Tsamasphyros
C. Xenophontos

GRACM 05 Sponsors

University of Cyprus
Department of Civil & Environmental Engineering, University of Cyprus
Department of Mathematics and Statistics, University of Cyprus
Hyperion Systems Engineering
Cyprus Tourism Organization
Department of Antiquities, Cyprus

Table of Contents

Volume 1

Plenary papers

SOME ASPECTS OF COMPUTATIONAL MODELLING OF SAFETY CRITICAL CONCRETE STRUCTURES

Nenad Bićanić[*], Chris Pearce[*], Colin Davie[†], Dimitrios Kourepinis[*]

[*] [*]Department of Civil Engineering
University of Glasgow
Glasgow, G12 8LT
e-mail: bicanic@civil.gla.ac.uk, web page: http://people.civil.gla.ac.uk/~bicanic/

[‡]School of Civil Engineering and Geosciences,University of Newcastle upon Tyne

Keywords: concrete cracking, numerical manifold method in modelling discontinuities, thermo-hygro-mechanical modelling of concrete at high temperature

Abstract. *Aspects of computational modelling of safety critical concrete structures are considered. The Numerical Manifold Method is discussed as one of the representatives of novel discontinuous modelling strategies. The need for multiphysics modelling frameworks is argued through the development of a comprehensive thermo-hygro-mechanical coupling (T-H-M), in order to account for the development of spallation pressures at exposures to high temperatures. Finally, a simulation of ageing process in prestressed concrete pressure vessels is considered.*

1 INTRODUCTION

Computational modelling of structural concrete (plain, reinforced and/or prestressed) and concrete structures with nonlinear finite elements has been a subject of research, development and practical industrial relevance for nearly forty years. Despite such a long 'track record' it has often been argued that the impact on engineering practice of extensive research in constitutive modelling of concrete as well as in nonlinear solution algorithms has been relatively moderate – the difficulties lay mainly in translating the continuous field quantities from nonlinear finite element analyses into the design code related data, like crack widths, crack spacing, residual section capacities, damage levels etc. Nonlinear analyses are almost exclusively applied in a safety assessment of non standard and/or safety critical structures.

On this occasion, it is perhaps fitting to revisit the introduction to the seminal paper by John Argyris et al[1] from the second SMIRT conference in 1973 and reflect on how much has changed over the many years in between

> *"This paper describes recent developments in the nonlinear deformation and ultimate load analysis of prestressed concrete reactor vessels using finite elements. First, a number of finite element models are called into attention for the idealization of composite structures such as reinforced and prestressed concrete components. Then different inelastic constitutive models are proposed for the behaviour of concrete in the pre- and post-failure regime. Subsequently various numerical techniques are examined for the solution of nonlinear problems, especially with regard to their distortion of the constitutive model. In conclusion these modelling techniques are applied to the analysis of four typical examples, the nonlinear deformation analysis of a concrete specimen subjected to biaxial compression, the crack analysis of a thick-walled concrete cylinder, the overload analysis of the THTR 1 : 5 scale model, and the ultimate load analysis of a concrete top closure model"*

It is interesting – to say the least – to note that the current issues remain surprisingly similar, despite the fact that many advances have indeed happened in the meantime. The early, often intuitive developments to account for the most significant nonlinear effects – associated with concrete cracking – have gradually been replaced with complex concepts which have brought together various modelling formulations and theoretical frameworks, and where strict boundaries between the traditional concepts like plasticity, damage mechanics or fracture mechanics no longer apply. Recent developments comprise various novel constitutive models which are cast in a more rigorous thermodynamic setting and these developments, associated with more robust and stable

algorithms, have increased confidence and helped to narrow the gap between the research and practice, as demands for complex and sophisticated nonlinear analyses of concrete structures grow.

An increased demand for reliable, robust and - above all - industry relevant analyses has identified marked differences in numerical predictions emanating from different constitutive models and have highlighted an apparent lack of experimental data to fully support capabilities of sophisticated analyses. This has in turn led to a whole series of well documented comparative studies[2,3] and more complex benchmark model problems - on the material point level (Fig 1), on the component level, as well on the full scale structures (Fig 2) [4,5].

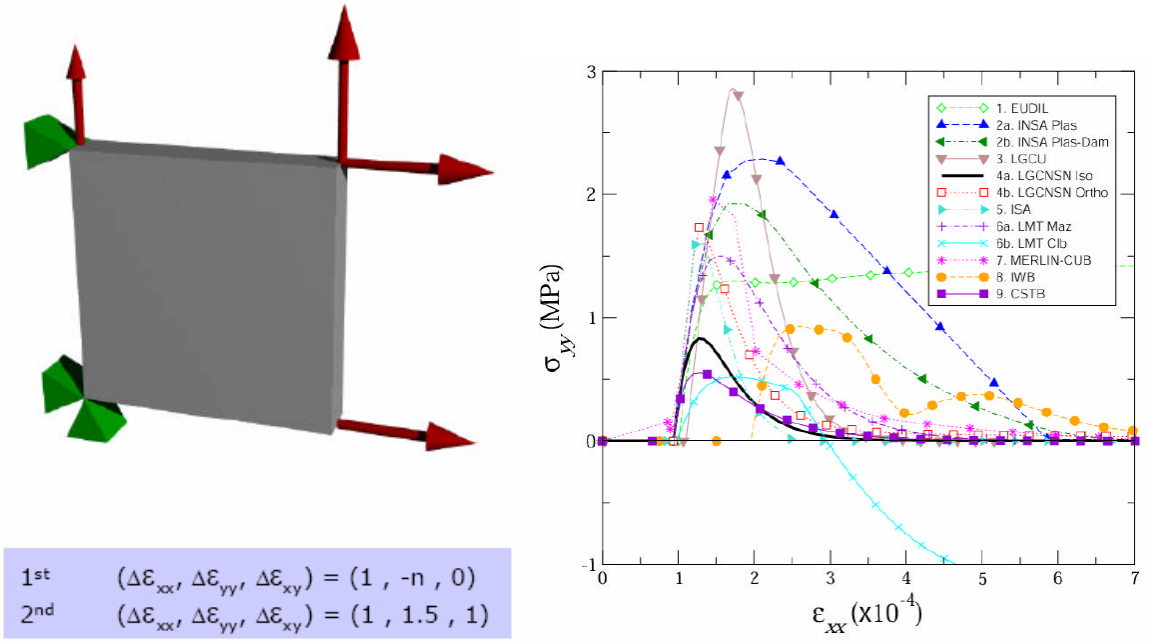

Figure 1. Wide range and marked differences in predictions, Willam's Material Point Test (from Ghavaminan et al 2004)

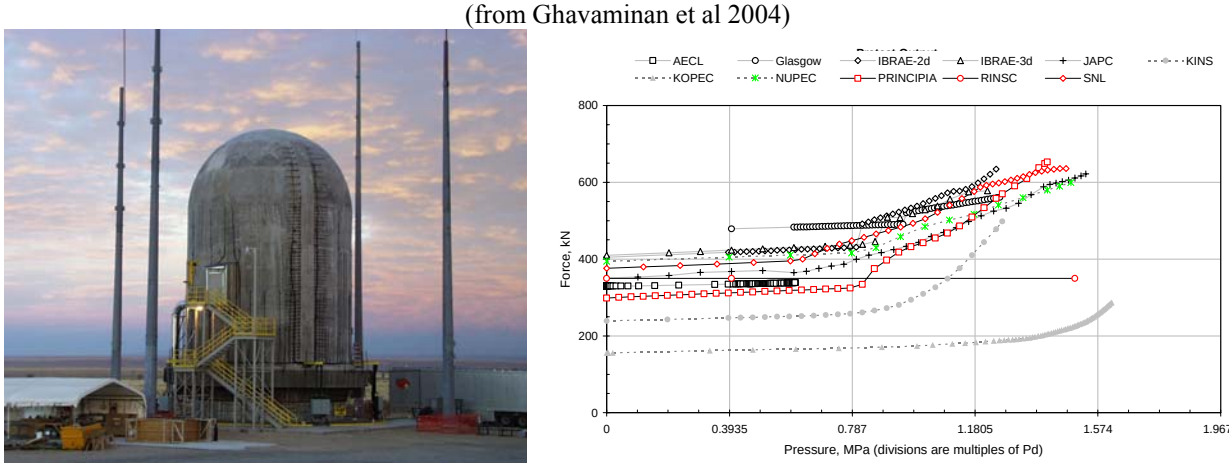

Figure 2. Sandia National Laboratories, Robin Analysis of a 1:4 Scaled Pre-stressed Concrete Containment Vessel Model, 2000

In the overall context of continuing advancement in computational modelling of safety critical structures (e.g. series of regular specialist conferences EURO-C, FRAMCOS and CONCREEP), there are two broad aspects that have recently attracted considerable research attention

(a) a more direct modelling of the *discontinuous nature* of concrete cracking and an increased mathematical rigour in both capturing and kinematically resolving emerging discontinuities (strain localisation, cracks, embedded discontinuities) through non standard discretisation strategies, and

(b) an inceased importance and potential of *multiphysics (multifield)* and *multiscale* modelling frameworks, as it transpires that some crucial macroscopic manifestations cannot always be adequately described by considering only the macro level, especially in consideration of exceptional and/or extreme conditions or degradation processes.

Many exciting development can be cited in both of the two above mentioned areas of interest – however, in the following, some apects associated with research conducted at Glasgow will be briefly considered.

2 MODELLING DISCONTINUITIES AND THE NUMERICAL MANIFOLD METHOD

The Numerical Manifold Method (NMM) [6,7], a relatively recent Partition of Unity method[8], casts a potentially powerful unified continuous-discontinuous modelling framework by integrating aspects of traditional, hierarchical and Extended Finite Element methods, with which there are strong parallels. To date, the original NMM has been extended in order to exploit its potential to improve the level of approximation up to any theoretical level[7,9,1013], either globally or locally and without remeshing, while preserving the ability to undertake integration of the discretised system of equations explicitly.

One of the particularly interesting aspects of NMM with respect to its potential in computational failure lies in its ability to deal with displacement discontinuities naturally, without the need for remeshing, while preserving the ability to undertake integration explicitly. Arbitrary displacement discontinuities can be implemented in the NMM using discontinuous partitions of unity in a computationally efficient manner, without the need for remeshing or interface elements.

2.1 NMM Discretisation

The essence of NMM lies in constructing the finite space as an assemblage of sub-domains of overlapping covers (or supports). Similar to meshless methods, a cover is a nodal domain of influence. The common area of an arbitrary number of overlapping covers constitutes an element. In R^2, the approximation to the unknown function, say displacements, within an element (defined by *n* nodes *i*) is given as:

$$u = \sum_{i=1}^{n} w_i(\boldsymbol{x})\, a_i(\boldsymbol{x}) \tag{1}$$

where w_i is the cover weighting function associated with node *i*, a_i is the cover function and *n* is the number of overlapping covers. The cover weighting functions w_i form a partition of unity; hence, they must satisfy the following conditions

$$\begin{aligned} &\sum_{i=1}^{n} w_i(\boldsymbol{x}) = 1 \quad && \forall\ \boldsymbol{x} \in \Omega \\ &0 \le w_i(\boldsymbol{x}) \le 1 \quad && \forall\ \boldsymbol{x} \in \Omega_i \\ &w_i(\boldsymbol{x}) = 0 && \forall\ \boldsymbol{x} \notin \Omega_i \end{aligned} \tag{2}$$

where $\Omega_i \in R^2$ is a cover, which may not necessarily be a sub-set of $\Omega \in R^2$.

In general, a_i are polynomials of any order and therefore (1) can be rewritten as:

$$u = \sum_{i=1}^{n} T_i(\boldsymbol{x})\, d_i \tag{3}$$

where d_i contains only the coefficients of the polynomial function a_i and therefore represent the fundamental unknowns.

The element stiffness matrix can be written as

$$\begin{aligned} \boldsymbol{K}_e &= \iint_A \boldsymbol{B}^T \boldsymbol{C}\boldsymbol{B}\, dxdy \\ &= \sum_{i=1}^{(N+1)(N+2)} \sum_{j=1}^{(N+1)(N+2)} \sum_{n_1=0}^{2N} \sum_{n_2=0}^{2N} \boldsymbol{K}_e^*(i,j,n_1,n_2) S_{n_1 n_2} \end{aligned} \tag{4}$$

where $K^*_{,e}$ is a 4th order coefficient array and it is assumed in this case that all nodes are associated with the same order N of the cover displacement function.

The term S_{n1n2} represents a simplex integral[9]

$$S_{n_1 n_2} = \iint_A x^{n_1} y^{n_2}\, dxdy$$

$$= |J| \sum_{k_1=0}^{n_1} \sum_{k_2=0}^{n_2} \eta(n_1, n_2, k_1, k_2) x_1^{n_1-k_1} x_2^{k_1} y_1^{n_2-k_2} y_2^{k_2}$$

$$\eta(n_1, n_2, k_1, k_2) = \frac{n_1! n_2!}{(n_1 + n_2 + 2)!} \cdot \frac{(n_1 + n_2 - k_1 - k_2)!(k_1 + k_2)!}{k_1! k_2! (n_1 - k_1)! (n_2 - k_2)!} \tag{7}$$

2.2 Crack Modelling

Where the cover (or support) of a node is completely cut by a discontinuity, that node is duplicated by an additional node that is unconnected to its parent. For example, consider the element in Figure 3(a), where the covers of nodes 1 and 2 are deemed to have been cut by the discontinuity. These nodes are highlighted by a double circle. Node 1 lies to the 'left' of the discontinuity and thus is renamed 1^+ and is duplicated by an additional node 1^-. Node 2 lies to the 'right' of the discontinuity and therefore is renamed 2^- and duplicated by an additional node 2^+.

The displacement fields to the 'left' and to the 'right' are now described by separate displacement functions

$$\boldsymbol{u} = \boldsymbol{u}^+ + \boldsymbol{u}^-, \quad \text{where } \boldsymbol{u}^+ = \boldsymbol{M}^+ \boldsymbol{a}^+ \quad \& \quad \boldsymbol{u}^- = \boldsymbol{M}^- \boldsymbol{a}^- \tag{8}$$

$\boldsymbol{a}^+$ and $\boldsymbol{a}^-$ denote the cover displacement functions which, in the case that the cover functions are constant, represent two alternative sets of nodal displacements. $\boldsymbol{M}^+$ and $\boldsymbol{M}^-$ represent the standard cover weighting functions modified by the Heaviside function (H)

$$M_i^+ = HM_i; \quad M_i^- = (1-H) M_i \tag{9}$$

Clearly, M_1^+ is equal to the original cover weighting function M_1 on the left of the discontinuity and equal to zero on the right of the discontinuity. Conversely, M_1^- is equal to zero on the left of the discontinuity and M_1 on the right of the discontinuity (Figures 3b, 3c). Therefore, the condition that the weighting functions must form a partition of unity is still satisfied. In the case that the cover of a node has not been cut $M_i^+ = M_i^- = M_i$.

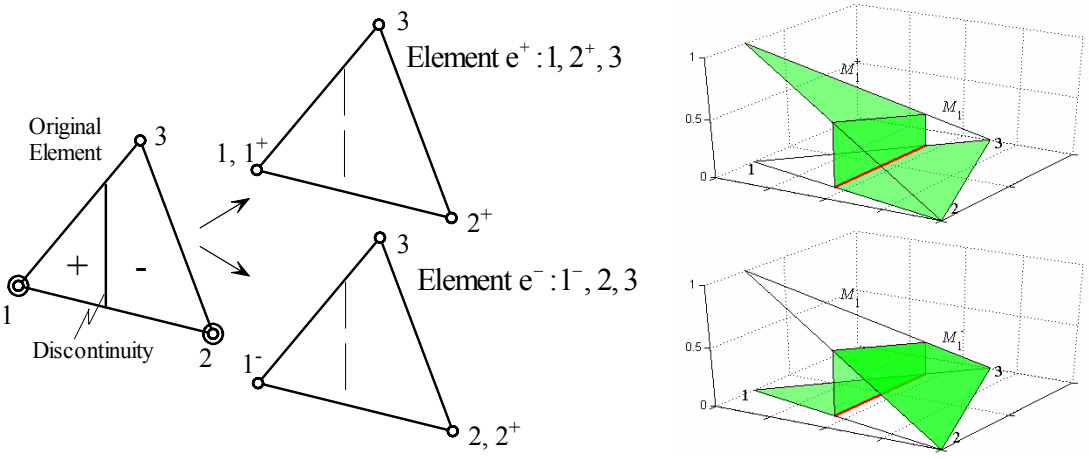

Figure 3. (a) Element cut by discontinuity. (b) Cover weighting function associated with node 1^+, (c) Cover weighting function associated with node 1^-.

It is computationally convenient to consider that the two displacement fields $\boldsymbol{u}^+ \,\&\, \boldsymbol{u}^-$ are associated with separate but identical overlapping elements, denoted as e^+ and e^- (Figure 3a). Note that in Figure 3(a) node 1^+ is identical to node 1 and has only been renamed for notational convenience. Thus, element e^+ comprises nodes 1 and 3 of the original mesh and the additional node 2^+, which is unconnected to the original mesh. Essentially, the displacement discontinuity has been introduced arbitrarily into the body of the element via an enhancement of the nodal degrees of freedom.

An example problem presented by Jirasek[11] has been considered here as an illustration. Although the introduction of arbitrary displacement discontinuities in NMM has been suggested in the relevant specialist literature, it has rarely been undertaken in practice. The problem in Figure 4 illustrates a crack with a curved trajectory that would be introduced into the model based on some criterion (here arbitrarily). Figure 4(a) illustrates not only the discontinuity but also those nodes whose cover or support has been cut by the discontinuity. Figure 4(b) shows how the structure would behave without a discontinuity and Figure 4(c) with the discontinuity. In Figure 4(c) the duplicate elements are shown to illustrate how two separate elements are required to capture the displacement jump across the discontinuity. If those parts of each element which correspond to the zero weighting function (Figures 4b, 4c) are removed, a more realistic representation of the fracture is revealed – Figure 4(d). Figure 4(e) shows displacement contours which again illustrate the displacement discontinuity. Furthermore, the above formulation also allows crack closure and therefore contact between crack surfaces can be modelled using a variety of standard contact techniques.

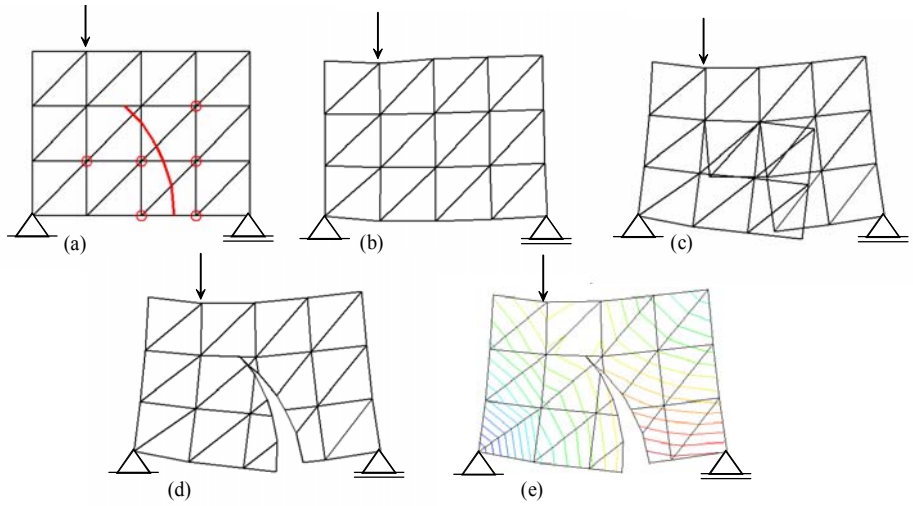

Figure 4.

a) NMM mesh plus location of discontinuity. Nodes with cut covers are highlighted.

b) Deformed mesh without fracture.

c) Deformed mesh with fracture. No clipping of elements.

d) Deformed mesh with fracture. Elements clipped.

e) Displacement contours

The strong parallels between NMM and XFEM[12] refer to the manner of how the displacement discontinuities are introduced. In essence, the NMM captures the jump in the displacement field using discontinuous displacement functions to the 'left' and to the 'right' of the discontinuity in order to restore the partition of unity requirement. The XFEM technique, on the other hand, introduces an additional degree of freedom at each node by directly enriching the trial function **Error! Reference source not found.**. In both methods the resulting stiffness matrix can be symmetric and there is a bandwidth increase due to the introduction of discontinuities.

$$u(\boldsymbol{x}) = \sum_{i=1}^{n} N_i(\boldsymbol{x}) \left(d_i + \sum_{j=1}^{m} G_j(\boldsymbol{x}) \overline{d_i^j} \right) \tag{10}$$

where n is the total number of nodes, N_i the standard finite element shape functions, d_i the nodal degrees of freedom, m the number of enriched nodes, G_j the enrichment functions containing the Heaviside function and $\overline{d_i^j}$ the additional degrees of freedom associated with node i and enrichment function j.

A distinctive difference between the two methods stems from the requirement in XFEM to partition the elements affected by the crack, yet without introducing any additional degrees of freedom other than $\overline{d_i^j}$, so that numerical integration of the weak form can account for the discontinuities on either side of the cracked surface. In the NMM, no additional steps need to be taken for integration purposes due to the the multivariate polynomial form of the cover displacement functions and the inherent ability to undertake integration explicitly, even for higher-order elements, using simplexes.

However, if the effects of partial or branched cracking are to be captured in NMM, the trial function needs to be modified directly, leading to an approach identical to XFEM. Nevertheless, the effect of partial cracking may also be potentially accounted by a reasonably fine mesh. While additional crack tip functions in XFEM are meant to negate this requirement, the enhanced degrees of freedom will not be activated in the first place if the mesh is not fine enough i.e. if a support is too large to be completely cut by a crack.

As shown by Jirasek[11], XFEM can be recast in a format very similar to that described here. This means that the substantial amount of research that has been carried out with regard to XFEM (such as tracking discontinuities and resolving crack branching in 2D and 3D) can be utilised in further developments of the NMM in providing a rational prediction of actual crack widths.

3 MULTI-PHYSICS FORMULATIONS FOR CONCRETE AT HIGH TEMPERATURES

Consideration of multiphysics is clearly needed when the behaviour of concrete at high temperature needs to be considered.

Despite it's low tech image, concrete is a complex, multi-phase material, consisting of aggregates bound by a highly porous, hygroscopic solid cement paste skeleton, which can be up to 68% pore space by volume (~28% gel pores ≤ 2.6nm in diameter and up to 40% capillary pores in the range of 1μm in diameter). Under normal environmental conditions the pore space is filled with fluids, typically including dry air and water. The water is characteristically present in the form of vapour, liquid and adsorbed water, which is physically bound onto the surface of the solid skeleton.

Concrete can experience high temperatures through a number of accidental or deliberate scenarios, e.g. fire or high temperature industrial applications. In all these scenarios the concrete and the fluids within it will, to some degree, undergo the processes described above and damage may occur. The severity of the damage will depend on numerous factors including the intensity of heating, the material and physical properties of the concrete and the environmental conditions to which the concrete is exposed over its lifetime.

The behaviour of concrete under exposure to high temperatures is greatly dependent on its composite structure and in particular, on the physical and chemical composition of the cement paste, which is a highly porous, hygroscopic material. At room temperature, the pores in the paste may be fully or partially filled with fluids typically including free (evaporable) water, water vapour and dry air. On the surfaces of the pores the free water exists as adsorbed water, physically bound to the solid, and as such does not behave as a liquid. The solid skeleton of the paste itself is composed of various chemical compounds and chemically bound water.

When exposed to high temperature, heat is transported through the material, resulting in changes in the chemical composition, physical structure and fluid content of the cement paste which in turn result in changes to the overall mechanical properties (strength, stiffness, fracture energy, etc.) and physical properties (thermal conductivity, permeability, porosity, etc.) of the concrete. When exposed to high temperatures, heat is conducted and convected through the material, leading to various changes in the fluids, including phase changes (both evaporation and condensation) and transportation, through several mechanisms including pressure driven flow and diffusion. Furthermore, the fluid content may be affected by temperature dependent changes in the structure of the concrete. These may be chemical changes such as (de)hydration, or physical changes, for example to the porosity and permeability of the concrete, all of which have a direct effect on the fluid transport behaviour.

As these processes act on the pore fluids, they result in changes to the pore pressures. These pressures have a direct mechanical affect on the concrete in that they modify the effective stress state. Through this mechanism, pore pressures are generally thought to be a major contributing factor to the development of damage, and spalling.

3.1 Mathematical Formulation - Governing Equations

A computational model for concrete subject to thermal loading needs to consider as many of the above (mostly non-linear) phenomena and their coupled interactions, as possible[14,15]. The governing mass conservation equations to describe heat and moisture transport in concrete containing free (evaporable) water, water vapour and dry air can be defined by (11-13). Furthermore, the energy conservation for the system can be defined by (14).

$$\frac{\partial\left(\varepsilon_L \rho_L\right)}{\partial t} = -\nabla \cdot \mathbf{J}_L - \dot{E}_L + \frac{\partial\left(\varepsilon_D \rho_L\right)}{\partial t} \tag{11}$$

$$\frac{\partial\left(\varepsilon_G \widetilde{\rho}_V\right)}{\partial t} = -\nabla \cdot \mathbf{J}_V + \dot{E}_L \tag{12}$$

$$\frac{\partial\left(\varepsilon_G \widetilde{\rho}_A\right)}{\partial t} = -\nabla \cdot \mathbf{J}_A \tag{13}$$

$$\left(\underline{\rho C}\right)\frac{\partial T}{\partial t} = -\nabla \cdot \left(-k\nabla T\right) - \left(\underline{\rho C \mathbf{v}}\right)\cdot \nabla T - \lambda_E \dot{E}_L - \lambda_D \frac{\partial\left(\varepsilon_D \rho_L\right)}{\partial t} \tag{14}$$

From equations (11-14), a system of coupled differential equations can be derived in terms of the chosen primary variables; e.g. temperature, T, gas pressure, P_G, and the vapour content, $\widetilde{\rho}_V$. It may be noted that the convection term, $\left(\underline{\rho C \mathrm{v}}\right)\cdot\nabla T$ in equation (14), is ignored on the assumption that the transfer of energy by convection is accounted for within the empirical relationship for the thermal conductivity, $k(T)$.

The mass fluxes of dry air, water vapour and free water can be expressed in terms of pressure and concentration gradients (re Darcy's Law and Fick's Law) (15-18). The water flux equation is affected by the capillary pressure and the model adopted for the diffusion of adsorbed water

$$\mathbf{J}_V = \varepsilon_G \widetilde{\rho}_V \mathbf{v}_G - \varepsilon_G \widetilde{\rho}_G D_{VA} \nabla\left(\frac{\widetilde{\rho}_V}{\widetilde{\rho}_G}\right) \tag{15}$$

$$\mathbf{J}_A = \varepsilon_G \widetilde{\rho}_A \mathbf{v}_G - \varepsilon_G \widetilde{\rho}_G D_{AV} \nabla\left(\frac{\widetilde{\rho}_A}{\widetilde{\rho}_G}\right) \tag{16}$$

$$\mathbf{J}_L = \left(1 - \frac{S_B}{S}\right)\varepsilon_L \rho_L \mathbf{v}_L + \left(\frac{S_B}{S}\right)\varepsilon_L \rho_L \mathbf{v}_B \tag{17}$$

where

$$\mathbf{v}_G = -\frac{KK_G}{\mu_G}\nabla P_G \quad \mathbf{v}_L = -\frac{KK_L}{\mu_L}\nabla P_L \tag{18}$$

$$\mathbf{v}_B = -D_B \nabla S_B \qquad \phi = \varepsilon_L + \varepsilon_G \qquad S = \frac{\varepsilon_L}{\phi} \qquad S_B = \begin{cases} S & \textbf{for } S \le S_{SSP} \\ S_{SSP} & \textbf{for } S > S_{SSP} \end{cases} \tag{19}$$

The free water content in the concrete is determined from sorption isotherms, as defined by Bažant and Kaplan[16], which are a function of the concrete cement content and the relative humidity (P_V /P_{Sat}) and temperature in the pores (16). The gas volume fraction can then be determined from equation (19b):

$$\varepsilon_L = \frac{\varepsilon_{Cem}\rho_{Cem}}{\rho_L} \cdot f\left(\frac{P_V}{P_{Sat}}, T\right) \tag{20}$$

The dry air and water vapour are assumed to behave as ideal gases and their pressures and partial densities are considered to be additive (re Dalton's law) (21-22):

$$\widetilde{\rho}_G = \widetilde{\rho}_A + \widetilde{\rho}_V \qquad P_G = P_A + P_V \tag{21}$$

$$P_V = R_V \widetilde{\rho}_V T \qquad P_A = R_A \widetilde{\rho}_A T \tag{22}$$

The liquid pressure is the difference between the gas pressure and the capillary pressure (23). The two remaining variables, fundamental to this modified formulation, are the coefficient of bound water diffusion, D_B, given[17] by the empirical relationship (24), and the capillary pressure, P_C, which is calculated via the Kelvin-Laplace Equation (25).

$$P_L = P_G - P_C \tag{23}$$

$$D_B = D_B^0 \exp\left(-2.08 \frac{S}{S_{SSP}} \frac{T}{T_{Ref}} \right) \textbf{ for } S \le S_{SSP} \tag{24}$$

$$P_C = -R_V T \rho_L \ln\left(\frac{P_V}{P_{Sat}} \right) \tag{25}$$

From the governing equations (11-14) a system of coupled differential equations can be developed, with reference to an appropriate set of primary variables, such that, in matrix-vector form (26)

$$\mathbf{C}\dot{\mathbf{u}} - \nabla \cdot \left(\mathbf{K} \nabla \mathbf{u} \right) = 0 \tag{26}$$

where $\mathbf{u} = \left(T \quad P_G \quad \tilde{\rho}_V \right)^{\mathrm{T}}$

After algebraic manipulation, the system of governing differential equations can be written in the form below (27).

$$\begin{aligned}
C_{TT} \frac{\partial T}{\partial t} + C_{TP} \frac{\partial P_G}{\partial t} + C_{TV} \frac{\partial \tilde{\rho}_V}{\partial t} &= \nabla \cdot \left(K_{TT} \nabla T + K_{TP} \nabla P_G + K_{TV} \nabla \tilde{\rho}_V \right) \\
C_{AT} \frac{\partial T}{\partial t} + C_{AP} \frac{\partial P_G}{\partial t} + C_{AV} \frac{\partial \tilde{\rho}_V}{\partial t} &= \nabla \cdot \left(K_{AT} \nabla T + K_{AP} \nabla P_G + K_{AV} \nabla \tilde{\rho}_V \right) \\
C_{MT} \frac{\partial T}{\partial t} + C_{MP} \frac{\partial P_G}{\partial t} + C_{MV} \frac{\partial \tilde{\rho}_V}{\partial t} &= \nabla \cdot \left(K_{MT} \nabla T + K_{MP} \nabla P_G + K_{MV} \nabla \tilde{\rho}_V \right)
\end{aligned} \tag{27}$$

with the LHS matrices

$$\begin{aligned}
C_{TT} &= \left(\underline{\rho C} \right) + \left(\lambda_D + \lambda_E \right) \left(\varepsilon_D \frac{\partial \rho_L}{\partial T} + \rho_L \frac{\partial \varepsilon_D}{\partial T} \right) - \lambda_E \left(\varepsilon_L \frac{\partial \rho_L}{\partial T} + \rho_L \frac{\partial \varepsilon_L}{\partial T} \right) \\
C_{TP} &= 0 \\
C_{TV} &= -\lambda_E \rho_L \frac{\partial \varepsilon_L}{\partial \tilde{\rho}_V} \\
C_{AP} &= \frac{\varepsilon_G}{R_A T} \\
C_{AV} &= -\frac{\varepsilon_G R_V}{R_A} - \tilde{\rho}_A \frac{\partial \varepsilon_L}{\partial \tilde{\rho}_V} \\
C_{AT} &= \tilde{\rho}_A \left(\frac{\partial \phi}{\partial T} - \frac{\partial \varepsilon_L}{\partial T} \right) - \frac{\varepsilon_G P_G}{R_A T^2} \\
C_{MV} &= \varepsilon_G + \left(\rho_L - \tilde{\rho}_V \right) \frac{\partial \varepsilon_L}{\partial \tilde{\rho}_V} \\
C_{MP} &= 0 \\
C_{MT} &= \tilde{\rho}_V \frac{\partial \phi}{\partial T} + \left(\varepsilon_L - \varepsilon_D \right) \frac{\partial \rho_L}{\partial T} + \left(\rho_L - \tilde{\rho}_V \right) \frac{\partial \varepsilon_L}{\partial T} - \rho_L \frac{\partial \varepsilon_D}{\partial T}
\end{aligned} \tag{28}$$

and the RHS matrices

$$K_{TT} = k - \lambda_E \varepsilon_L \rho_L \left(\frac{S_B D_B}{S\phi} \left(\frac{\partial \varepsilon_L}{\partial T} - \frac{\varepsilon_L}{\phi} \frac{\partial \phi}{\partial T} \right) - \left(1 - \frac{S_B}{S} \right) \frac{KK_L R_V \rho_L}{\mu_L} \left(\frac{T}{P_{Sat}} \frac{\partial P_{Sat}}{\partial T} - \left(1 + \frac{T}{\rho_L} \frac{\partial \rho_L}{\partial T} \right) \ln \left(\frac{\tilde{\rho}_V R_V T}{P_{Sat}} \right) - 1 \right) \right)$$

$$K_{TP} = -\lambda_E \left(1 - \frac{S_B}{S} \right) \varepsilon_L \rho_L \frac{KK_L}{\mu_L}$$

$$K_{TV} = -\lambda_E \varepsilon_L \rho_L \left(\left(1 - \frac{S_B}{S} \right) \frac{KK_L}{\mu_L} \frac{R_V T \rho_L}{\tilde{\rho}_V} + \frac{S_B D_B}{S\phi} \frac{\partial \varepsilon_L}{\partial \tilde{\rho}_V} \right)$$

$$K_{AT} = -\frac{\varepsilon_G D_{AV} \tilde{\rho}_V P_G}{\tilde{\rho}_G R_A T^2}, \; K_{AP} = \frac{KK_G}{\mu_G} \varepsilon_G \tilde{\rho}_A + \frac{\varepsilon_G D_{AV} \tilde{\rho}_V}{\tilde{\rho}_G R_A T}, \; K_{AV} = -\frac{\varepsilon_G D_{AV}}{\tilde{\rho}_G} \left(\tilde{\rho}_A + \frac{R_V}{R_A} \tilde{\rho}_V \right) \tag{29}$$

$$K_{MT} = \frac{\varepsilon_G D_{AV} \tilde{\rho}_V P_G}{\tilde{\rho}_G R_A T^2} + \varepsilon_L \rho_L \left(\frac{S_B D_B}{S\phi} \left(\frac{\partial \varepsilon_L}{\partial T} - \frac{\varepsilon_L}{\phi} \frac{\partial \phi}{\partial T} \right) - \left(1 - \frac{S_B}{S} \right) \frac{KK_L R_V \rho_L}{\mu_L} \left(\frac{T}{P_{Sat}} \frac{\partial P_{Sat}}{\partial T} - \left(1 + \frac{T}{\rho_L} \frac{\partial \rho_L}{\partial T} \right) \ln \left(\frac{\tilde{\rho}_V R_V T}{P_{Sat}} \right) - 1 \right) \right)$$

$$K_{MP} = \frac{KK_G}{\mu_G} \varepsilon_G \tilde{\rho}_V - \frac{\varepsilon_G D_{AV} \tilde{\rho}_V}{\tilde{\rho}_G R_A T} + \left(1 - \frac{S_B}{S} \right) \varepsilon_L \rho_L \frac{KK_L}{\mu_L}$$

$$K_{MV} = \frac{\varepsilon_G D_{AV}}{\tilde{\rho}_G} \left(\tilde{\rho}_A + \frac{R_V}{R_A} \tilde{\rho}_V \right) + \varepsilon_L \rho_L \left(\left(1 - \frac{S_B}{S} \right) \frac{KK_L}{\mu_L} \frac{R_V T \rho_L}{\tilde{\rho}_V} + \frac{S_B D_B}{S\phi} \frac{\partial \varepsilon_L}{\partial \tilde{\rho}_V} \right)$$

3.2 Simulation of Ageing in Concrete Pressure Vessels

Ageing of concrete nuclear reactor pressure vessels (Figure 5) is a subject of renewed interest. During their normal working life the internal chambers of these vessels are exposed to temperatures up to ~80°C, with an ambient temperature on the outside.. Some of these vessels have currently been in operation for more than 30 years Another consideration for these vessels is the possibility of accidental and unplanned excursions of exposure to higher temperatures (up to ~400°C), as may be experienced due to a loss of cooling water.

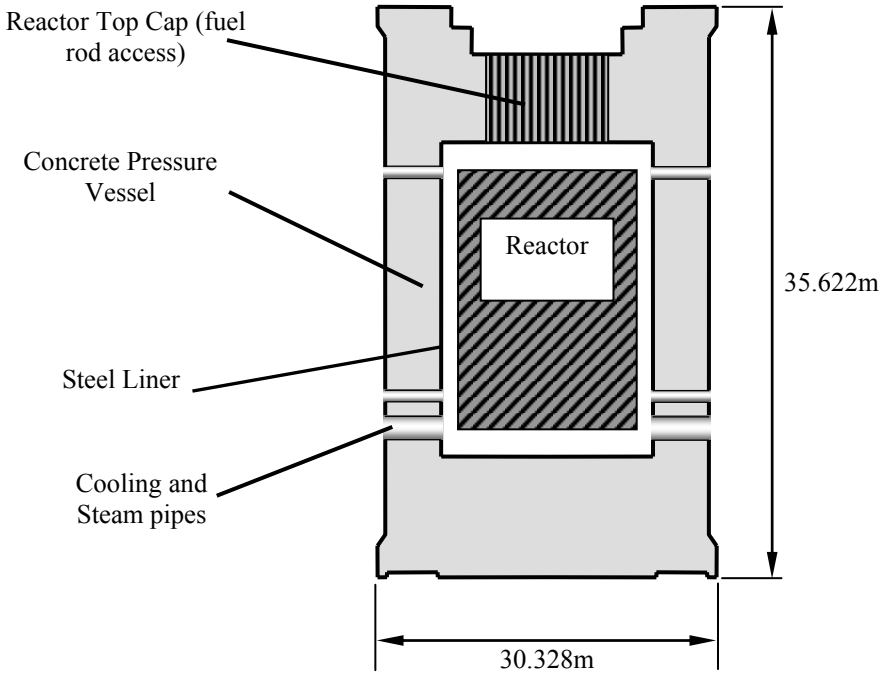

Figure 5. Section through Cylindrical Concrete Nuclear Reactor Pressure Vessel

Simulations to follow focus on the heat and moisture transport in concrete nuclear pressure vessels and the direct effect that this could have on their structural integrity, both under normal operating conditions and under temperature excursions. The investigation was carried out using the fully coupled hygro-thermal-mechanical numerical model developed during the MAECENAS[18] project and described in detail in Davie et al[19]. Although reference is made to the mechanical consequences of the transport behaviour, mechanical behaviour is not fully considered here.

Detailed 3D and Axisymmetric finite element meshes, representative of a specific type of nuclear pressure vessel were developed for use during the MAECENAS project (Figures 6a, 6b). However, an initial coupled hygro-thermal-mechanical model presented here was conducted on a smaller mesh, equivalent to a slice through the full axi-symmetric mesh (Figure 6c).

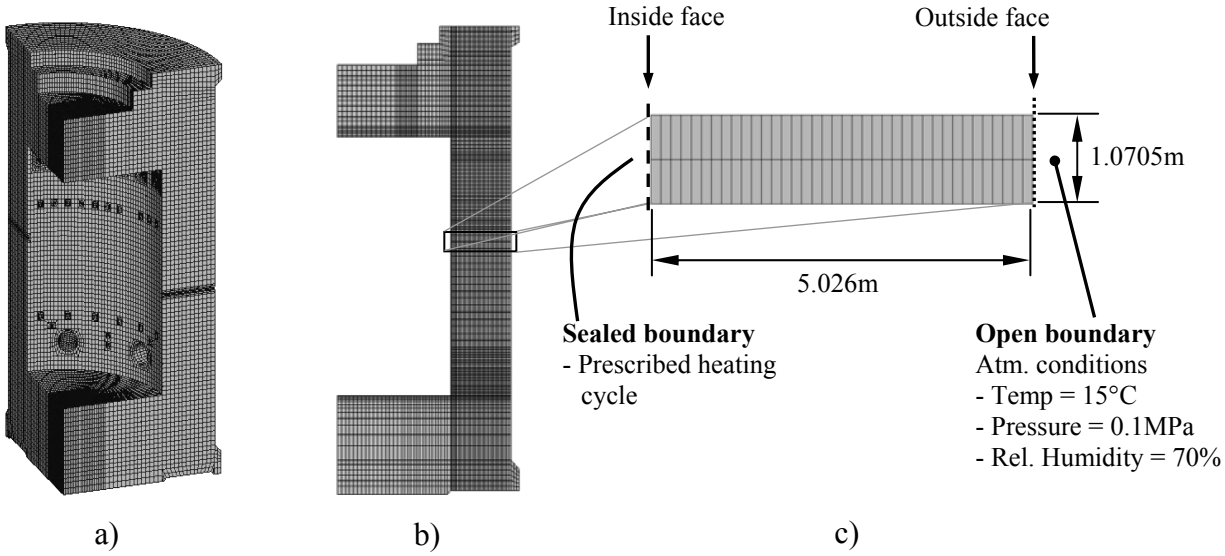

Figure 6. MAECENAS Pressure Vessel FE meshes a) One Quarter 3D Mesh (20 noded elements), b) Axi-symmetric Mesh (8 noded elements), c) Axi-symmetric 'Slice' Mesh (8 noded elements)

In order to reproduce the external conditions experienced by a nuclear pressure vessel, Cauchy type boundary conditions to simulate the free exchange of heat and fluid with the atmosphere were applied at the outside face of the mesh, while for the inside face, only a prescribed (Dirichlet type) temperature boundary was defined. Boundary conditions were not defined for the fluid phases in order to represent the sealed conditions imposed by the steel liner on the inside of the vessel. The top and bottom sides of the mesh were considered as symmetric boundaries to represent the large, continuous structure above and below the 'slice'.

The first of the two parametric series comprised 5 analyses in which a 33 year heating cycle (from data recorded for an existing pressure vessel) (Figure 7a) was applied to the inside face and the resulting fluid transport behaviour monitored.

The parameters investigated were the initial permeability K_0, and the initial porosity ϕ_0, of the concrete. It should also be noted that both permeability K, and porosity, ϕ_0, increase irreversibly with increasing temperature. The second study involved two further analyses in which heating cycles representative of typical temperature excursions were applied (Figures 7b, 7c) and again the resulting fluid transport behaviour was monitored. All other parameters were kept constant and a summary of all the analyses can be found in Tables 1 and 2.

Series	Analysis	Initial Permeability, K_0	Initial Porosity, ϕ_0	Temperature Profile
1	1	5.0×10^{-17} m^2	0.099	Standard
1	2	1.0×10^{-21} m^2	0.099	Standard
1	3	2.0×10^{-18} m^2	0.099	Standard
1	4	2.0×10^{-18} m^2	0.090	Standard
1	5	2.0×10^{-18} m^2	0.120	Standard

Table 1 - Summary of Analyses for Parametric Series for Standard Temperature Profile (Figure 7a)

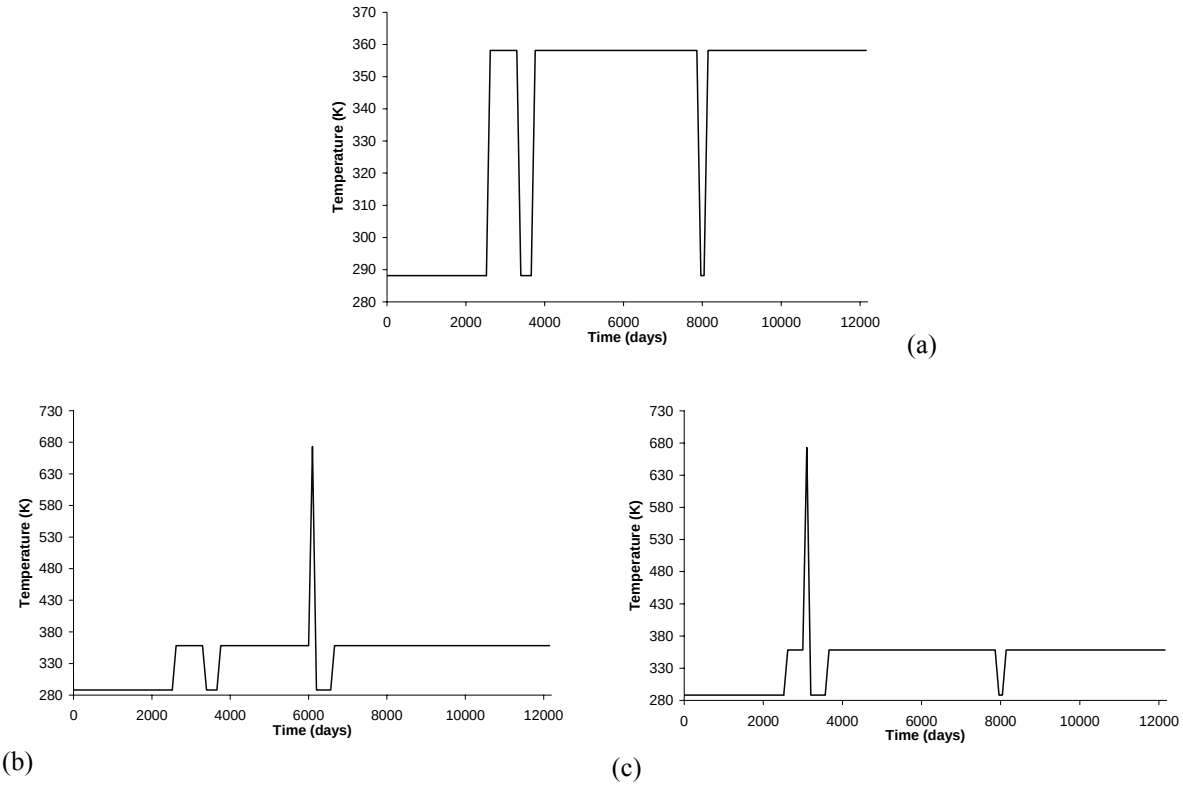

Figure 7. (a) Standard Heating Cycle, (b) Excursion 1 Heating Cycle, c) Excursion 2 Heating Cycle

Series	Analysis	Initial Permeability, K_0	Initial Porosity, ϕ_0	Temperature Profile
2	1	2.0×10^{-18} m^2	0.099	Excursion Scenario 1
2	2	2.0×10^{-18} m^2	0.099	Excursion Scenario 2

Table 2 - Summary of Analyses for Parametric Series for Exceptional Temperature Scenarios (Figure 7a)

As discussed previously, the development and the level of pore pressures in the concrete were of particular interest. However, for simplicity only gas pressures, which can be shown to be largely analogous with the overall pore pressure behaviour, are reported here.

PARAMETRIC SERIES 1 - As can be seen from the results shown in Figures 8 and 9 the gas pressures predicted at the inside face of the pressure vessel over its 33 year life, vary considerably depending on the initial values of both permeability and porosity. As it would be expected, both higher permeabilities and higher porosities lead to lower maximum predicted pressures as fluids can move more easily away from the hot face, towards the atmosphere.

Despite the variations, the magnitudes of the gas pressures (~0.2-0.8MPa) are generally not high enough to exceed the tensile strength of the concrete and cause structural damage on their own. However, in conjunction with mechanical stresses produced during operation of the reactor, these pressures may become significant and should be taken into account.

Of more immediate concern is the gas pressure predicted with the lowest permeability (1.0×10^{-21}m^2). After 33 years this has reached ~1.4MPa and continues to rise. While not enough to cause fracture of the concrete on its own, this pressure may threaten the structural integrity of the steel liner in the vessel. If this liner is ruptured, radioactive gases will escape into the concrete and eventually into the atmosphere.

While both parameters can be seen to have a significant effect, the porosity can often be related to the design mix of the concrete and is therefore readily known and accounted for. However, values for permeability are less easily estimated and vary considerably (over about 4 orders of magnitude) in the literature [2, 3]. This uncertainty is clearly a concern when its potential effects are considered.

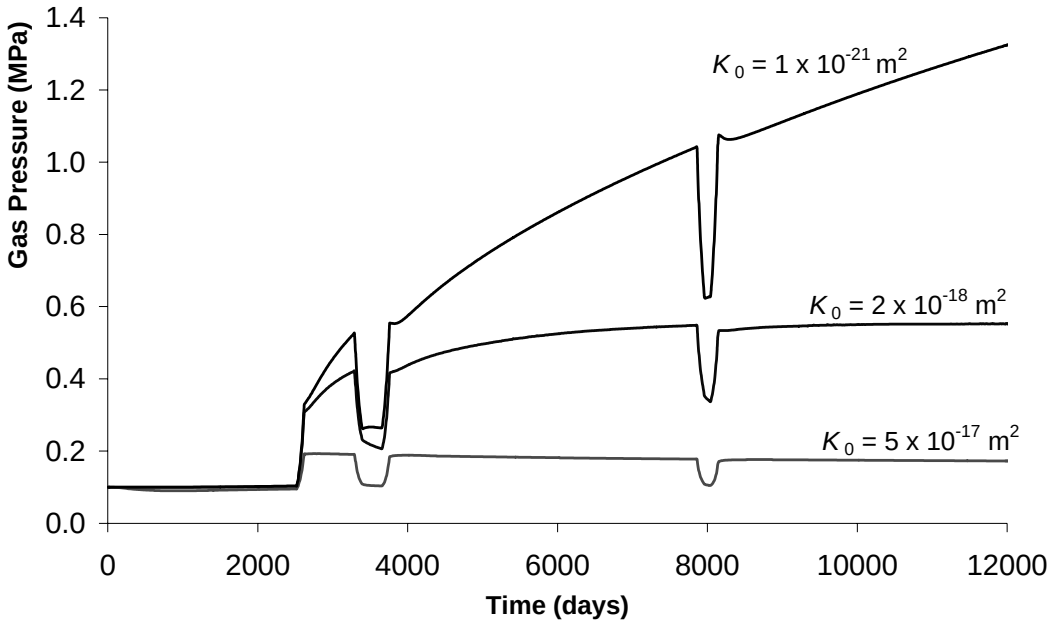

Figure 8. Gas Pressure Histories for the 33 years cycles. Standard temperature profile. Influence of changing permeability for constant initial porosity

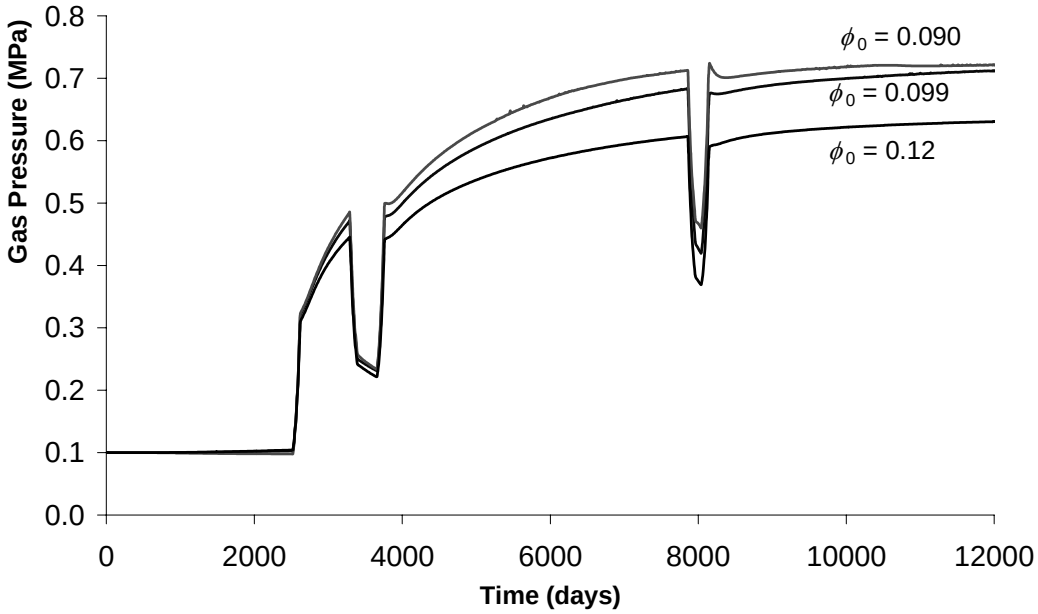

Figure 9. Gas Pressure Histories for the 33 years cycles. Standard temperature profile. Influence of changing initial porosity for constant permeability

PARAMETRIC SERIES 2 - As can be seen from Figure 10, the two transient temperature excursions have a significant effect on the predicted gas pressures. During both excursions, pressures of ~10MPa were predicted. If these values were realistic they would potentially compromise the structural integrity of the pressure vessel both by causing fracturing, since the pressure will exceed the tensile strength of most concretes, and by rupturing the steel liner.

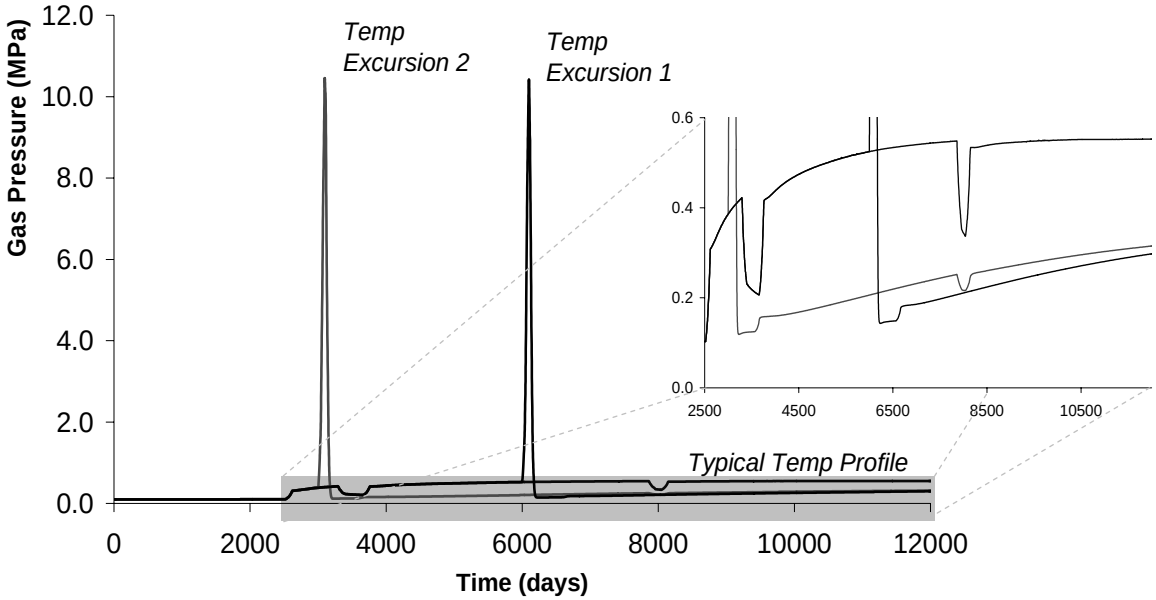

Figure 10. Gas Pressure Histories for the 33 years cycles. Two representative exceptional transient temperature profiles

A further point of note is that in both cases the gas pressures predicted after the temperature excursion are considerably lower than those predicted under the normal operating heat cycle (Figure 10 inset). This is because the permeability and porosity of the concrete have been increased significantly by the irreversible damage caused by the temperature excursion and the fluids can more easily flow away from the inside face of the pressure vessel. It should also be noted, however that, although the temperature excursions reached the same temperatures and therefore caused the same permeability and porosity increases, the gas pressures predicted after the two incidents were different. This highlights the importance of considering the full heat and fluid transport history of a concrete structure when predicting the potential effects on its structural integrity.

4. CONCLUSIONS

Two aspects of computational modelling of safety critical concrete structures are considered. The Numerical Manifold Method is discussed as one of the representatives of novel discontinuous modelling strategies where the discretisation space is enhanced by discontinuous partition of unity functions without the need to modify the form of the original trial function. This results in an ability to undertake explicit integration for any level of the approximation, together with the ability to enhance the level of approximation locally or globally, up to an arbitrary order. The multiphysics modelling framework is argued through the development of a comprehensive thermo-hygro-mechanical coupling (T-H-M), in order to account for the development of spallation pressures at exposures to high temperatures. Capillary pressure and adsorbed water diffusion are incorporated into a computational model in order to investigate their influence on the finite element analysis of heat and moisture transfer in concrete exposed to high temperatures. Comparative studies were carried out by a simulation of ageing process in prestressed concrete pressure vessels.

REFERENCES

[1] J. H. Argyris, G. Faust, J. Szimmat, E. P. Warnke and K. J. Willam, Recent developments in the finite element analysis of prestressed concrete reactor vessels, Nuclear Engineering and Design, Volume 28, Issue 1 , July 1974, Pages 42-75

[2] S. Ghavamian et al, Civil engineering structures of nuclear power plants - Modelling issues, NAFEMS Awareness Seminar, Modelling Concrete Structures with Finite Elements, London, June 2003

[3] Sandia National Laboratories, Pre-test Round Robin Analysis of a Pre-stressed Concrete Containment Vessel Model, NUREG/CR-6678, SAND 00-1535, Aug 2000.

[4] R.A. Dameron et al, Posttest Analysis of the NUPEC/NRC 1:4 Scale Prestressed Concrete Containment Vessel Model, (NUREG/CR-6809), June 2003
http://www.nrc.gov/reading-rm/doc-collections/nuregs/contract/cr6809/

[5] N. K. Prinja, D. Shepherd, Simulating Structural Collapse of a PWR Containment, Paper # H04-6, Transactions of the 17th International Conference on Structural Mechanics in Reactor Technology (SMiRT 17), Prague, Czech Republic, August 17 –22, 2003

[6] Shi, G. Numerical manifold method. Ohnishi, Y. 1-35. 1997. Proceedings of ICADD-2.

[7] Lu, M. Numerical Manifold Method with complete N-order cover function. STF22-F02121 to STF22-F02124. 2002. SINTEF.

[8] Babuška, I. & Melenk, J.M. 1996. The partition of unity finite element method: Basic theory and applications. In Computer methods in applied mechanics and engineering, 139: 289-314, 1996

[9] Chen, G., Ohnishi, Y., Ito, T. 1998. Development of high-order manifold method. In International Journal of Numerical Methods in Engineering, 43: 685-712, 1998

[10] Chen, G. & Ohnishi, Y. 1999. Practical Computing Formulas of Simplex Integration. In Proceedings of 3rd International Conference on Analysis of Discontinuous Deformation: 75-84, June 1999

[11] Jirasek, M. and Belytschko, T. Computational resolution of strong discontinuities. 2002. WCCM V - Fifth World Congress on Computational Mechanics. Mang, H., Rammerstorfer, F. G., and Eberhardsteiner, J.

[12] Belytschko T, Moes N, Usui S, Parimi C. Arbitrary discontinuities in finite elements. International Journal for Numerical Methods in Engineering 2001; 50:993-1013.

[13] Kourepinis, D., Bicanic, N., and Pearce, C. J. A Higher-Order Variational Numerical Manifold Method Formulation and Simplex Integration strategy. 145-152. 2003. SINTEF. The 6th International Conference on Analysis of Discontinuous Deformation. Lu, M.

[14] Tenchev, R. T., Li, L. Y. & Purkiss, J. A., Finite Element Analysis of Coupled Heat and Moisture Transfer in Concrete Subjected to Fire, Numerical Heat Transfer, Part A, 2001; 39: pp 685 - 710.

[15] Baroghel-Bouny, V., Mainguy, M. Lassabatere, T. & Coussy, O., Characterization and Identification of Equilibrium and Transfer Moisture Properties for Ordinary and High-Performance Cementitious Materials, Cement and Concrete Research, 1999; 29: pp 1225 – 1238.

[16] Bažant, Z. P. & Kaplan, M. F., Concrete at High Temperatures: Material Properties and Mathematical Models; Longman: Harlow, 1996, ISBN 0 582 08626 4.

[17] Gawin, D., Majorana, C. E. & Schrefler, B. A., Numerical Analysis of Hygro-Thermal Behaviour and Damage of Concrete at High Temperature, Mechanics of Cohesive-Frictional Materials, 1999; 4: pp 37 – 74.

[18] "Modelling of ageing in concrete nuclear power plants" (MAECENAS Consortium), European Community EURATOM programme (Contract no. FIKS-CT-2001-00186)

[19] Davie, C. T., Pearce, C. J. and Bićanić, N., Influence of Capillary Pressure and Adsorbed Water Diffusion on Heat and Moisture Transport in Concrete at High Temperatures, Proc. of 12th Ann. Conf. of the Assoc. for Comp. Mech. Eng. - UK, University of Cardiff, Cardiff, 2004.

SPECTRAL/HP ELEMENT METHOD IN RANDOM SPACE

Xiaoliang Wan, George Em Karniadakis†

† Division of Applied Mathematics
Brown University
182 George St, Providence, Rhode Island, USA
e-mail: gk@dam.brown.edu, web page: http://www.cfm.brown.edu/crunch

Keywords: Uncertainty, Polynomial chaos, Finite elements.

Abstract. *In this paper we present a multi-element generalized polynomial chaos (ME-gPC) method, which can achieve hp convergence in random space. ME-gPC is based on the decomposition of random space and generalized polynomial chaos (gPC). Using proper numerical schemes to maintain local orthogonality on-the-fly, we perform gPC locally and adaptively. The key idea is to combine the polynomial chaos method of h version and p version. ME-gPC shows good performance in dealing with problems related to long-term integration, large perturbation and discontinuities. Benchmarks and applications of ME-gPC in fluid dynamics are presented..*

1 INTRODUCTION

In past decades, spectral/*hp* element methods for deterministic problems have been greatly advanced; orthogonal polynomials are used as a powerful tool for high accuracy and efficiency. Recently, orthogonal polynomials have received great attention in *uncertainty quantification* (UQ) in the context of *polynomial chaos* (PC). Polynomial chaos originated from *homogenous chaos* first defined by Wiener as the span of Hermite polynomial functionals of a Gaussian process. Ghanem and Spanos first combined Wiener-chaos with a finite element method to model uncertainty in solid mechanics[1,2,3], A more general framework, termed *generalized polynomial chaos* (gPC), was proposed in [4] by Xiu and Karniadakis based on the correspondence between the PDFs of certain random variables and the weight functions of orthogonal polynomials of the Askey scheme. The family of gPC includes Wiener-chaos as a subset and supplies optimal bases for stochastic processes represented by random variables of commonly used distributions, such as uniform distribution, Beta distribution, etc. In [5] and [6], polynomial chaos was combined with wavelets to deal with discontinuities for uniform random inputs for which standard PC or gPC fail to converge. Due to the polynomial chaos basis, fast (exponential) convergence is achieved as in the deterministic case, which is referred to as *p* convergence.

The decomposition of random space into elements is another technique to model uncertainty; it was first proposed by Deb, Babuska and Oden[7, 8] within the framework of deterministic finite element method. This method is based on the discretization of random space and employs the finite element basis to approximate the random field, whose accuracy relies on the *h* refinement in random space. Based on gPC and the decomposition of random space, multi-element generalized polynomial chaos (ME-gPC) was propose in [15, 12], which can achieve *hp* convergence in random space for arbitrary PDFs. ME-gPC implements the decomposition of random space in the context of probability theory and maintains local orthogonality numerically on-the-fly, which yields a simple and effective way to perform gPC locally and adaptively. The adaptive ME-gPC has been used to deal with stochastic problems related to long-term integration and discontinuities[12,15].

In the next section of this paper we overview the essential properties and procedure of gPC. Subsequently, we present the ME-gPC procedure, including the decomposition of random space, construction of orthogonal polynomials and an adaptive criterion. Lastly, benchmarks and applications of ME-gPC in fluid dynamics are discussed.

2 MULTI-ELEMENT GENERALIZED POLYNOMIAL CHAOS

2.1 Overview of generalized polynomial chaos (gPC)

The original polynomial chaos was first proposed by N. Wiener[9]. It employs the Hermite polynomials in terms of Gaussian random variables as the trial basis to expand stochastic processes in the random space. According to the theorem by Cameron and Martin[10] such expansion converges for any second-order processes in the L_2 sense; gPC employs more types of orthogonal polynomials from the Askey family. It is a

generalization of the original Wiener's Hermite-chaos and can deal with non-Gaussian random inputs more efficiently.

Let $(\Omega, \mathcal{F}, P)$ be a probability space, where Ω is the sample space, $\mathcal{F}$ is the σ-algebra of subsets of Ω and P is a probability measure. Let $\boldsymbol{\xi}$ be a $\mathbb{R}^d$-valued random variable defined on such a probability space. A general *second-order* random process $R(\omega) \in L_2(\Omega, \mathcal{F}, P)$ can be expressed by gPC as

$$R(\omega) = \sum_{i=0}^{\infty} \hat{a}_i \Phi_i(\boldsymbol{\xi}(\omega)) \tag{1}$$

where ω is the random event and $\Phi_i(\boldsymbol{\xi})$ denotes the gPC basis of degree p in terms of the random variable $\boldsymbol{\xi}$. The family $\{\Phi_l\}$ is an orthogonal basis in $L_2(\Omega, \mathcal{F}, P)$ with an orthogonality relation

$$\langle \Phi_i \Phi_j \rangle = \langle \Phi_i^2 \rangle \delta_{ij} \tag{2}$$

where δ_{ij} is the Kronecker delta, and $\langle \cdot, \cdot \rangle$ denote the ensemble average. Here, the ensemble average can be defined as the inner product in the Hibert space in terms of the random vector $\boldsymbol{\xi}$

$$\langle g_1(\boldsymbol{\xi}) g_2(\boldsymbol{\xi}) \rangle = \int g_1(\boldsymbol{\xi}) g_2(\boldsymbol{\xi}) w(\boldsymbol{\xi}) \mathrm{d}\boldsymbol{\xi} \tag{3}$$

or

$$\langle g_1(\boldsymbol{\xi}) g_2(\boldsymbol{\xi}) \rangle = \sum_{\boldsymbol{\xi}} g_1(\boldsymbol{\xi}) g_2(\boldsymbol{\xi}) w(\boldsymbol{\xi}) \tag{4}$$

for the continuous and discrete case, respectively, where $w(\boldsymbol{\xi})$ denotes the weight function, which corresponds to a probability measure.

For a certain random vector $\boldsymbol{\xi}$, the gPC basis $\{\Phi_i\}$ can be chosen in such a way that its weight function has the same form as the probability distribution function $f(\boldsymbol{\xi})$ of $\boldsymbol{\xi}$. The corresponding types[4] of classical orthogonal polynomials $\{\Phi_i\}$ and their associated random variable $\boldsymbol{\xi}$ are listed in Table 1. Given sufficient regularity of the solution, gPC leads to fast (exponential) convergence to the statistics, such as mean and variance[4].

	Random variables $\boldsymbol{\xi}$	Wiener–Askey chaos $\{\Phi_i\}$	Support
Continuous	Gaussian	Hermite-chaos	$(-\infty, \infty)$
	Gamma	Laguerre-chaos	$[0, \infty)$
	Beta	Jacobi-chaos	$[a, b]$
	Uniform	Legendre-chaos	$[a, b]$
Discrete	Poisson	Charlier-chaos	$\{0,1,2,\cdots\}$
	Binomia	Krawtchouk-chaos	$\{0,1,\cdots,N\}$
	Negative binomial	Meixner-chaos	$\{0,1,2,\cdots\}$
	Hypergeometric	Hahn-chaos	$\{0,1,\cdots,N\}$

Table 1: Correspondence of the types of Wiener–Askey polynomial chaos and their underlying random variables ($N \geq 0$ is a finite integer)

2.2 GPC Procedure

We now present the gPC method using the following general PDE system

$$\begin{aligned} &\frac{\partial \mathbf{u}(t,\mathbf{x};\xi(\omega))}{\partial t} + \mathrm{L}(\mathbf{u}) = \mathbf{f}(t,\mathbf{x};\xi(\omega)) \\ &\mathrm{B}(\mathbf{u}) = g(t,\mathbf{x};\xi(\omega)) \qquad \text{on } \partial \mathrm{D} \quad , \\ &\mathbf{u}(0,\mathbf{x};\xi(\omega)) = h(\mathbf{x};\xi(\omega)) \qquad \text{at } t=0 \end{aligned} \tag{5}$$

where $\xi(\omega)$ indicates a random vector, L is an operator in the physical space and B is an operator on the boundary of physical domain D.

To employ gPC, we first project $\mathbf{u}$ and the force term $\mathbf{f}$ onto the polynomial basis $\{\Phi_i\}$ in the following form

$$\mathbf{u} = \sum_{i=0}^{N_p} \mathbf{u}_i \Phi_i, \quad \mathbf{f} = \sum_{i=0}^{N_p} \mathbf{f}_i \Phi_i, \tag{6}$$

where N_p indicates the number of basis modes given by

$$N_p = (p+d)!/(p!d!) - 1 \tag{7}$$

with d being the dimension of random vector ξ. Then we substitute eqn. (6) into eqn. (5) and obtain

$$\sum_{i=0}^{N_p} \frac{\partial \mathbf{u}_i}{\partial t} \Phi_i + \mathrm{L}\left(\sum_{i=0}^{N_p} \mathbf{u}_i \Phi_i \right) = \sum_{i=0}^{N_p} \mathbf{f}_i \Phi_i \,. \tag{8}$$

By performing a Galerkin projection and taking into account the orthogonality of polynomial chaos basis, we obtain

$$\frac{\partial u_k}{\partial t} + \left\langle L\left(\sum_{i=0}^{N_p} u_i \Phi_i\right), \Phi_k \right\rangle \Big/ \left\langle \Phi_k^2 \right\rangle = \mathbf{f}_k, \quad k = 0,1,\cdots,N_p, \tag{9}$$

which is a deterministic system of PDEs. Any classical numerical schemes, e.g., finite difference and finite element method, can be employed to solve such a system. A similar procedure can be applied to the boundary and initial conditions to complete eqn. (9).

2.3 Decomposition of random space

gPC is efficient for many problems. However, by simply increasing the polynomial order may not be the most efficient way to improve accuracy, e.g., problems related to random frequencies. For such cases, we need to discretize the random space as the deterministic spectral/*hp* element method does in the physical space. We assume that ξ is defined on $B = \times_{i=1}^{d} [a_i, b_i]$, where a_i and b_i are finite or infinite in $\mathbb{R}$ and the components of ξ are identical independent distributed (IID) random variables. We define a decomposition $\mathbf{D}$ of B as

$$D = \begin{cases} B_k = [a_{k,1}, b_{k,1}] \times [a_{k,2}, b_{k,2}) \times \cdots \times [a_{k,d}, b_{k,d}], \\ B = \bigcup_{i=1}^{N} B_k, \\ B_i \bigcap B_j = \varnothing, \quad \text{if} \quad i \neq j \end{cases} \tag{10}$$

where $k, i, j = 1,2,\cdots,N$. Based on the decomposition $\mathbf{D}$, we define the following indicator random variables

$$I_{B_k} = \begin{cases} 1 & \text{if } \xi \in B_k, \\ 0 & \text{otherwise.} \end{cases} \tag{11}$$

It is obvious that

$$\Pr\left(I_{B_k}=1\right)=\int_{B_k} f(\xi)\mathrm{d}\xi, \tag{12}$$

where $f(\xi)$ is the PDF of ξ. In each random element B_k we define a new random variable ξ_k subject to a conditional PDF

$$\hat{f}_k\left(\xi_k \middle| I_{B_k}=1\right)=\frac{f(\xi)}{\Pr\left(I_{B_k}=1\right)}. \tag{13}$$

Instead of considering ξ in the whole random space by gPC, we can first approximate the random filed locally with respect to ξ_k within each random element B_k, then reconstruct the original random field. Once we obtain the localized random field, we can compute any statistics using the Bayes' theorem

$$\int_B g(u(\xi))f(\xi)d\xi \approx \sum_{i=1}^{N}\Pr\left(I_{B_k}=1\right)\int_{B_k} g\left(\hat{u}(\xi_k)\right)\hat{f}\left(\xi_k \middle| I_{B_k}=1\right)\mathrm{d}\xi, \tag{14}$$

where $g(\cdot)\in L_2(\Omega,\mathcal{F},P)$ is any function of random field $u(\xi)$, and $\hat{u}_k(\xi_k)$ denotes the approximated local random field in element B_k.

To avoid overflow[12] in numerical implementation we usually re-scale the random elements with *finite* boundaries by the following transformation

$$\xi_{k,i}=\frac{b_{k,i}-a_{k,i}}{2}Y_{k,i}+\frac{b_{k,i}+a_{k,i}}{2}, \tag{15}$$

where we map the random variable ξ_k defined in element k to a random variable $\mathbf{Y}_k$ defined in $[-1,1]^d$. The PDF of $\mathbf{Y}_k$ can be obtained as

$$\bar{f}(\mathbf{y}_k)=\det\left|\frac{\partial\xi_k}{\partial\mathbf{y}_k}\right|\hat{f}(\xi_k(\mathbf{y}_k))=\frac{f(\xi_k(\mathbf{y}_k))}{\Pr\left(I_{B_k}=1\right)}\prod_{i=0}^{d}\frac{b_{k,i}-a_{k,i}}{2}, \tag{16}$$

After such a transformation is employed, we can perform gPC locally with respect to $\mathbf{Y}_k$. Compared to the original random inputs ξ, the degree of perturbation related to the local random inputs $\mathbf{Y}_k$ has been decreased effectively by the factor $(b_{k,i}-a_{k,i})/2$ in each random dimension. Note that such a mapping is usually unnecessary for random elements with at least one *infinite* boundary since these elements are related to a very small factor $\Pr\left(I_{B_k}=1\right)$.

2.4 Construction of orthogonal polynomials

The orthogonal gPC basis on the entire random space will, in general, lose local orthogonality with respect to the local PDF $\bar{f}(\mathbf{y}_k)$. The only exception is Legendre-chaos due to the nice properties of uniform distribution. Thus, we have to perform numerical construction to maintain the local orthogonality. For simplicity, here we only discuss the construction of one-dimensional orthogonal polynomials, since the high-dimensional basis can be obtained using tensor products of one-dimensional basis.

It is a distinctive feature of orthogonal polynomials, compared to other orthogonal systems, that they satisfy a three-term recurrence relation,

$$\begin{aligned}&\pi_{i+1}(t)=(t-\alpha_i)\pi_i(t)-\beta_i\pi_{i-1}(t), \qquad i=0,1,\cdots\\ &\pi_0(t)=1,\ \ \pi_{-1}(t)=0,\end{aligned} \tag{17}$$

where $\{\pi_i(t)\}$ is a set of (monic) orthogonal polynomials,

$$\pi_i(t) = t^i + \text{ lower - degree term}, \qquad i = 0,1,\cdots \tag{18}$$

and the coefficients α_i and β_i are uniquely determined by a positive measure $\sigma(t)$, which corresponds to a probability measure in the construction we propose herein.

For a continuous measure $\sigma(t)$ there are two classical methods to compute the recurrence coefficients α_i and β_i: the Stieltjes procedure and the modified Chebyshev algorithm[13]. For a discrete measure

$$\mathrm{d}\sigma_M(t) = \sum_{i=1}^{M} w_i \delta(t - x_i)\mathrm{d}t, \qquad i = 0,1,\cdots,M \tag{19}$$

with δ being the Dirac delta function, we have another choice: the Lanczos algorithm[14, 13].

Using the above procedures, the recurrence coefficients α_i and β_i can be computed iteratively using the following stopping criterion[13]

$$\left|\beta_i^s - \beta_i^{s-1}\right| \le \varepsilon \beta_i^s, \qquad i = 0,1,\cdots,n-1, \tag{20}$$

where s indicates the iteration step and ε the relative error. To show the efficiency of such a numerical re-construction, we decompose the PDF of Beta distribution $B(1,4)$ and Gaussian distribution $N(0,1)$ into equidistant elements, construct orthogonal polynomials in each element and project $g(x) = x^{10} + 1$ onto these local basis. We record the time cost and the normalized L_∞ error on quadrature points, which are shown in Table. 2. It can be seen that the numerical re-construction is fast and accurate. Compared to the cost of gPC solver, such cost is negligible in practice.

	Beta distribution: $B(1,4)$		Gaussian Distribution: $N(0,1)$	
N	**Error**	**time (sec)**	**Error**	**time (sec)**
1	7.98e-11	<0.01	1.50e-10	<0.01
2	2.58e-12	<0.01	4.94e-11	<0.01
4	2.38e-13	<0.01	1.53e-11	<0.01
6	4.58e-13	<0.01	4.66e-13	<0.01
8	3.53e-13	<0.01	3.60e-13	<0.01
10	7.45e-13	0.01	1.10e-12	0.01
10^2	9.45e-13	0.08	8.28e-13	0.08
10^3	1.00e-12	0.79	9.37e-13	0.84
10^4	3.69e-12	7.92	4.51e-13	7.87
10^5	9.28e-13	76.43	4.09e-13	78.74

Table 2: Normalized L_∞ errors on quadrature points and time cost for a uniform mesh with N elements. The relative error for the recurrence coefficients was set to be 10^{-13}. Only the middle element $[-6,6]$ was decomposed for Gaussian distribution. The computations were performed on a 1.5GHz AMD CPU

2.5 Adaptive criterion

For many problems, such as long-term integration and discontinuities, adaptivity is a necessary technique to obtain good result with less effort. It is well known that in deterministic methods the co-continuity between two elements should be kept for second-order differential operators. However, such a continuity is not required in the decomposition of random space because most of the statistics we are interested in, e.g., mean and variance, are defined as integrations with respect to a probability measure and the probability measure of the interface between two random elements is zero. Based on such observations, we here construct a criterion for *h*-type refinement using the properties of orthogonal polynomials.

We assume that the gPC expansion of a random field in element k is

$$\hat{u}_k(\xi_k) = \sum_{j=1}^{N_p} \hat{u}_{k,j} \Phi_j(\xi_k) \tag{21}$$

where p is the highest order of polynomial chaos. From the orthogonality of gPC we can obtain the approximate local variance given by polynomial chaos with order p

$$\sigma_{k,p}^2 = \sum_{j=1}^{N_p} \hat{u}_{k,j}^2 \left\langle \Phi_j^2 \right\rangle . \tag{22}$$

The approximate global mean $\bar{u}$ and variance $\bar{\sigma}^2$ can be expressed as

$$\bar{u} = \sum_{k=1}^{N} \hat{u}_{k,0} \Pr(I_{B_k} = 1), \qquad \bar{\sigma}^2 = \sum_{k=1}^{N} \left[\sigma_{k,p}^2 + (\hat{u}_{k,0} - \bar{u})^2 \right] \Pr(I_{B_k} = 1). \tag{23}$$

By noting that the error of mean is usually much smaller than that of variance, we neglect the error contribution from $\hat{u}_{k,0}$ and express the exact global variance as

$$\sigma^2 \approx \bar{\sigma}^2 + \sum_{i=1}^{N} \gamma_k \Pr(I_{B_k} = 1), \tag{24}$$

where γ_k is the error of local variance. We define the decay rate of relative error of polynomial chaos in each element as follows

$$\eta_k = \frac{\sum_{i=N_{p-1}+1}^{N_p} \hat{u}_{k,i}^2 \left\langle \Phi_i^2 \right\rangle}{\sigma_{k,p}^2} . \tag{25}$$

Based on η_k and the scaled parameter $\Pr(I_{B_k} = 1)$, we implement *h-type refinement* if the following criterion[15,12]

$$\eta_k^{\gamma} \Pr(I_{B_k} = 1) \geq \theta_1, \quad 0 < \gamma < 1 \tag{26}$$

is satisfied, where γ and θ_1 are prescribed constants. For high-dimensional random inputs, we can choose the most sensitive random dimensions for refinement. We define the sensitivity for each random dimension as

$$r_i = \frac{\hat{u}_{i,p}^2 \left\langle \Phi_i^2 \right\rangle}{\sum_{j=N_{p-1}+1}^{N_p} \hat{u}_{k,j}^2 \left\langle \Phi_j^2 \right\rangle}, \qquad i = 1,2,\cdots,d \ , \tag{27}$$

where we neglect the subscript k for clarity, and the subscript $*_{i,p}$ denotes the mode consisting only of the random dimension ξ_i with polynomial order p. All random dimensions which satisfy

$$r_i \geq \theta_2 \max_{j=1,2,\cdots,d} r_j, \qquad 0 < \theta_2 < 1, \quad d = 1,2,\cdots,d \tag{28}$$

will be split into two *equal* random elements in the next time step while all other random dimensions will remain unchanged. By implementing decomposition selectively we can reduce the total element number while gaining efficiency.

3 NUMERICAL RESULTS

In this section, we first demonstrate the *hp* convergence of ME-gPC by a benchmark problem, then apply ME-gPC to stochastic flow past a stationary cylinder.

3.1 Benchmark (Stochastic ODE)

We consider the performance of the ME-gPC method for the following simple ODE equation[4,12,15]

$$\frac{\mathrm{d}u}{\mathrm{d}t} = -\kappa(\omega)u, \quad u(0;\omega) = u_0, \tag{29}$$

where $\kappa(\omega)$ is a random variable. The exact solution can be easily found as

$$u(t;\omega) = u_0 e^{-\kappa(\omega)t}. \tag{30}$$

Using ME-gPC with uniform meshes, we study the following two cases:

(1) κ is a uniform random variable defined in $[-1,1]$.

(2) κ is a Beta random variable $B(1,4)$ defined in $[-1,1]$.

For case (1), we employ Legendre-chaos in each random element; for case (2), the local orthogonal basis is constructed numerically. In Fig. 1, we show the convergence of ME-gPC at $t = 5$ for case (1) with *p*-convergence on the left and h-convergence on the right. It can be seen that ME-gPC exhibits exponential convergence while the index of algebraic convergence reaches asymptotically a constant. The convergence of the ME-gPC method at $t = 5$ for case (2) is shown in Fig. 2. For both case (1) and case (2) the index of algebraic convergence for the variance goes asymptomatically to $2(p+1)$, which means that the error $\varepsilon \propto N^{-2(p+1)}$. This is consistent with the error estimate given in [7]. From the theory of deterministic finite element method[7], it can be shown that the index of algebraic convergence is $2(p+1)$ for any PDF. Furthermore, such an index is also valid for the h-convergence of mean of any PDF, which is not shown here. When computing the recurrence coefficients α_i and β_i iteratively, a relative error 10^{-13} is imposed for case (2). From the plot of p-convergence in Fig. 2, it can be seen that the maximum accuracy ME-gPC can achieve is $O(10^{-13})$, which implies that the constructed orthogonal polynomials are very accurate.

3.2 Application of ME-gPC in Fluid Dynamics: Flow Past Cylinder with Random Inflow

ME-gPC method is applied to a random two-dimensional flow past a stationary cylinder. The mesh of the physical space is shown in Fig. 3. We employ deterministic spectral/*hp* element method[16,11] to solve the system of deterministic PDEs introduced by the Galerkin projection in ME-gPC. Periodic conditions are specified in the crossflow direction and tenth-order Jacobi polynomials are employed in each element to provide a high accuracy in physical space.

The inflow velocity is $u = \bar{u} + \sigma\xi$ and cross-flow velocity $v = 0$, where σ is a constant and ξ is a random variable with zero mean and unit variance. The Reynolds number Re is based on the mean value $\bar{u}$ of the inflow velocity and the diameter of the cylinder. In this work, we set $\mathrm{Re} = 100$, $\bar{u} = 1.0$ and $\sigma = 0.1$ and assume that ξ is of uniform distribution in $[-\sqrt{3}, \sqrt{3}]$.

We first simulate the deterministic flow past the cylinder with $u = \bar{u}$ and $v = 0$ up to $t = 1000$, then impose the aforementioned random boundary conditions. In Fig. 4 and 5, we show the mean and variance of the drag coefficients given by gPC and ME-gPC, respectively. The solutions are periodic with decreasing amplitude. Since the inflow velocity is uniformly distributed in $[1-0.1\sqrt{3}, 1+0.1\sqrt{3}]$, the Reynolds number will be correspondingly uniform in $[100-10\sqrt{3}, 100+10\sqrt{3}]$. Thus the frequencies of the solutions should also be random and depend on the random inputs. Compared to the results given by ME-gPC with $N = 20, p = 8$, gPC with $p = 8$ begins to diverge at $t \approx 1012$ and gPC with $p = 15$ begin to diverge at $t \approx 1020$. Thus, to obtain the convergence of gPC, we have to increase the polynomial order quickly. More specifically, if the

variation of random frequencies is large (from a finite value to infinity), gPC usually begin to diverge after a short-term integration[15] and increasing the polynomial order can help little for the convergence. Thus, increasing the polynomial order is not the most efficient way to obtain accuracy for a long-term integration. For such cases, ME-gPC can extend the performance of gPC effectively by the decomposition of random space.

4 CONCLUSIONS

In this work we present a multi-element generalized polynomial chaos (ME-gPC) method to deal with differential equations with random inputs. ME-gPC can achieve hp convergence in random space and improve the performance of gPC by the decomposition of random space, which is shown by a benchmark problem and an application of ME-gPC in fluid dynamics.

ACKNOWLEDGEMENT

This work was supported by AFOSR, ONR and NSF.

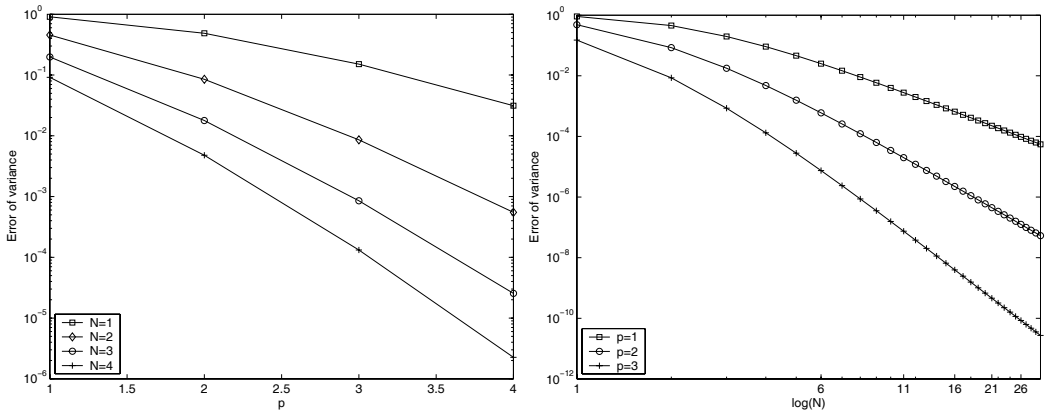

Figure 1: Convergence of ME-gPC for the simple ODE with κ being a uniform random variable. Left: p-convergence; Right: h-convergence.

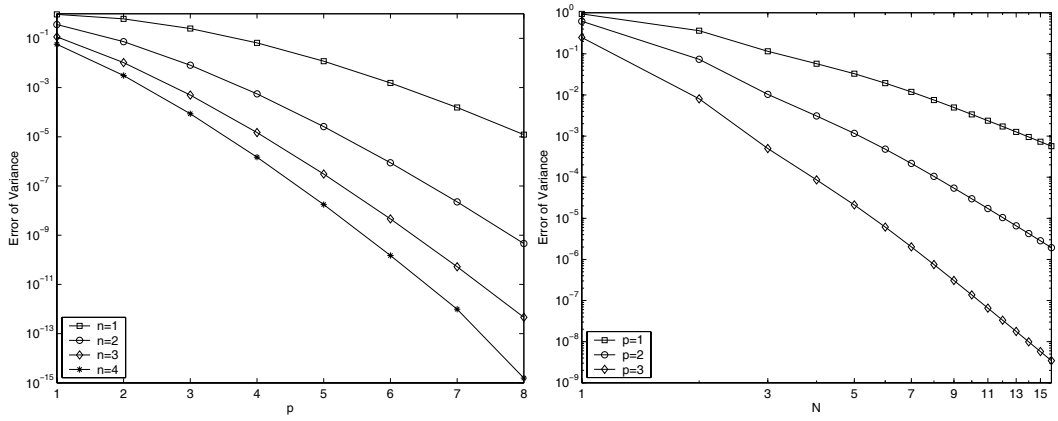

Figure 2: Convergence of ME-gPC for the simple ODE with κ being a Beta random variable. Left: p-convergence; Right: h-convergence.

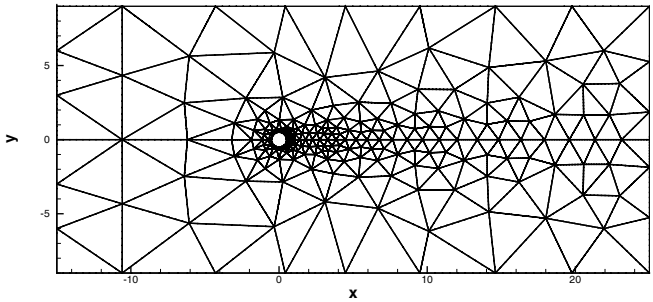

Figure 3: The size of the computational domain is $[-15D,25D]\times[-9D,9D]$ and the cylinder is at the origin $(0,0)$ with diameter $D=1$. The mesh consists of 412 triangular elements.

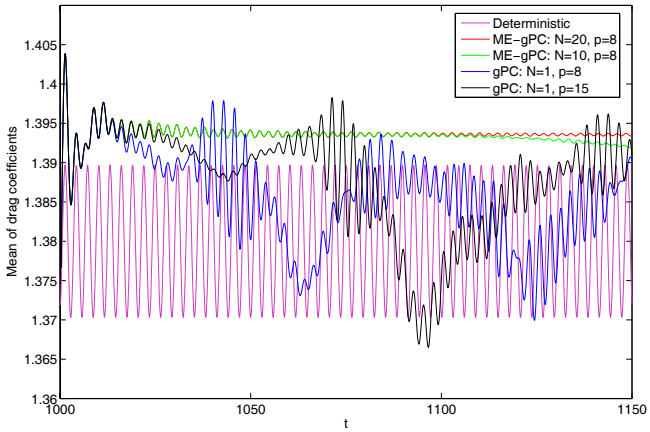

Figure 4: Mean of drag coefficients given by gPC and ME-gPC. The deterministic (time averaged) drag coefficient is about 1.38 with $\sigma=0$.

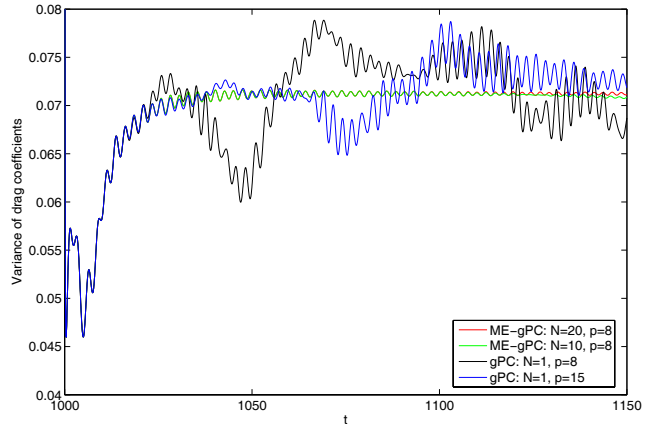

Figure 5: Variance of drag coefficients given by gPC and ME-gPC.

REFERENCES

[1] Ghanem, R.G. and Spanos P. (1991), "Stochastic Finite Elements: A Spectral Approach", Springer-Verlag, New York, 1991

[2] Ghanem, R.G. (1999), "Ingredients for a general purpose stochastic finite element formulation," Comput. Methods Appl. Mech. Engrg., 168, pp. 19–34.

[3] Ghanem, R.G. (1999), "Stochastic finite elements for heterogeneous media with multiple random non-gaussian properties," ASCE J. Engrg. Mech., 125(1), pp. 26–40.

[4] Xiu D. and Karniadakis G.E. (2002), "The Wiener-Askey polynomial chaos for stochastic differential equations," SIAM J. Sci. Comput., 24(2), pp. 619–644.

[5] Le Maitre O.P., Njam H.N., Ghanem R.G. and Knio O.M. (2004), "Uncertainty propagation using Wiener-Haar expansions," J. Comput. Phys., 197, pp. 28–57.

[6] Le Maitre O.P., Njam H.N., Ghanem R.G. and Knio O.M. (2004), "Multi-resolution analysis of Wiener-type uncertainty propagation schemes," J. Comput. Phys., 197, pp. 502–531.

[7] Deb M.K., Babus, ̆ka I. and Oden J.T. (2001), "Solution of stochastic partial differential equations using Galerkin finite element techniques," Comput. Methods Appl. Mech. Engrg., 190, pp. 6359–6372.

[8] Babus, ̆ka I., Tempone R. and Zouraris G.E. (2004), "Galerkin finite element approximations of stochastic elliptic differential equations," Technical Report 2.

[9] Wiener N. (1938), "The homogeneous chaos," Amer. J. Math., 60, pp. 897–936.

[10] Cameron R.H. and Martin W.T. (1947), "The orthogonal development of nonlinear functionals in series of Fourier-Hermite functionals," Ann. Math., 48, pp. 385.

[11] Xiu D. and Karniadakis G.E. (2003), "Modeling uncertainty in flow simulations via generalized polynomial chaos," J. Comput. Phys., 187, pp. 137–167.

[12] Wan X. and Karniadakis G.E. (2005) "Multi-element polynomial chaos for arbitrary probability measures," Submitted to SIAM J. Sci. Comput.

[13] Gautschi W. (1982), "On generating orthogonal polynomials," SIAM J. Sci. Stat. Comput., 3(3), pp. 289–317.

[14] Boley D. and Golub G.H. (1987), "A survey of matrix inverse eigenvalue problems," Inverse Problems, 3(4), pp. 595–622.

[15] Wan X. and Karniadakis G.E. (2004) "An adaptive multi-element generalized polynomial chaos method for stochastic differential equations," J. Comput. Phys. (to appear).

[16] Karniadakis G.E. and Sherwin S.J. (1999) "Spectral/*hp* Element Methods for CFD," Oxford University Press, Oxford.

MULTI-SCALE COMPUTATIONAL MODELING OF FLUID MECHANICS IN THIN FILM PROCESSING

Chris R. Kleijn

Delft University of Technology
Faculty of Applied Sciences
Department Multi Scale Physics
Prins Bernhardlaan 6, 2628 BW Delft, The Netherlands
e-mail C.R.Kleijn@TNW.TUDelft.NL

keywords: computational fluid dynamics, mixed convection, rarefied gas flow, LES, radiation, multi scale modeling.

Abstract *Thin film processing plays a key role in many technologies. The processes through which thin films are being manufactured bring together various aspects of fluid flow engineering. In this paper, the focus is on Chemical Vapor Deposition (CVD) processes for thin film deposition from gaseous precursors. After a short introduction into the role of fluid flow, heat and mass transfer in CVD processing, the paper addresses several challenges for computational fluid mechanics and heat transfer engineering in thin film processing. These challenges relate to* (i) *laminar and transitional mixed convection flow;* (ii) *rarefied gas flow;* (iii) *wall-to-wall thermal radiation; and* (iv) *multi-scale phenomena.*

1. INTRODUCTION

Thin film processing constitutes an important technology for the manufacturing of *e.g.* thin films on wafers in the IC-industry, anti-reflection and spectrally selective coatings on optical components, and anti-corrosion and anti-wear layers on mechanical tools and equipment [1]. In virtually all thin film processes, the objects to be treated are placed inside a reactor chamber and exposed to a (reactive) fluid (gas or liquid) flow. Inside the reactor chamber, large temperature differences are often present, with the temperature of the treated objects differing from that of the reactor walls and the fluid flow.

The design of thin film processing equipment such that the surface processes take place selectively on the desired surfaces only, at a high rate, with a high spatial uniformity and an efficient use of resources is a thermal fluid flow optimization problem with many complicating factors. In this paper, several challenges for computational fluid flow and heat transfer engineering related to the design and optimization of thin film processes and equipment will be discussed. The focus will be on Chemical Vapor Deposition (CVD) processes for the deposition of thin solid films through chemical reactions from gaseous precursors. However, many of the issues discussed here apply to many other surface treatment processes as well.

Section 2 provides a short introduction into the basics of Chemical vapor Deposition and the role of hydrodynamics, heat and mass transfer and chemistry in these processes. Section 3 discusses the use of numerical simulation techniques for modeling CVD processes and equipment. In section 4, some challenges for computational fluid flow and heat transfer modeling with respect to CVD process and equipment design and simulation are discussed.

2. CHEMICAL VAPOR DEPOSITION

2.1 Principles of CVD

In CVD processes a thin solid film is deposited from gaseous precursors through chemical reactions at the surface. Reactive gases are introduced into the controlled environment of a reactor chamber in which the substrates on which deposition takes place are positioned. Depending on the process conditions, homogeneous reactions may lead to the creation of gaseous intermediates. The precursors and reactive intermediates diffuse to and adsorb on the surface, were heterogeneous reactions lead to film growth.

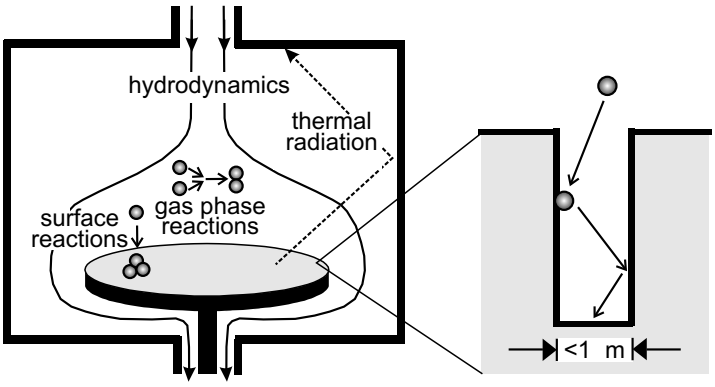

Figure 1: CVD for the coating and manufacturing of sub-micron structures.

The energy required to drive the chemical reactions is usually supplied thermally, by heating the surfaces/objects to be coated.

Typical operating temperatures are between 500 K and 1500 K. Reactant gases can be diluted in an inert carrier gas, or used undilutedly. Typical operating pressures are from 10 Pa to 1 atm. CVD processes have been reviewed in *e.g.* refs. [2]-[5].

Usually, the quality demands on deposited thin films are quite stringent, particularly regarding the uniformity of film thickness and composition as well as its morphology. Perhaps the most important advantage of CVD over other deposition techniques is its capability of conformal deposition, *i.e.* the capability of depositing films of uniform thickness on highly irregularly shaped and patterned surfaces. This makes CVD techniques particularly suited for the manufacturing, coating and modification of small (nano to sub micron scale) structures (See Fig. 1). Today, CVD is even developing to be the most important technique for the manufacture of carbon nano-tubes and nano-wires ([6]-[8]).

2.2 Hydrodynamics, transport phenomena and chemistry in CVD processes

CVD processes are essentially *chemical* surface processes. With a high degree of simplification the rate R of these processes is described by

$$R = k_s C_s \tag{1}$$

with k_s the reaction rate constant which strongly depends on the surface temperature T_S and C_s the reactant concentration close to the surface. In order to achieve a uniform deposition rate R, both T_s and C_s should be uniform along the surfaces. Local surface temperatures and near-the-surface reactant concentrations are related to set inlet process conditions through *reactor dependent* interactions between gas flow, (radiative) heat and mass transfer, and chemical reactions. Therefore, identical process conditions will lead to different film deposition characteristics in different reactors designs. This makes the design and optimization of CVD equipment a task for thermal and fluid flow engineers.

As a simple example illustrating the interaction between hydrodynamics, transport phenomena and chemistry in CVD, consider the highly simplified stagnation flow CVD reactor configuration in Fig. 2. The reactant gas, diluted in an inert carrier gas, is fed into the reactor through a porous plate. This leads to a uniform gas velocity perpendicular to the substrate surface, which is kept at a uniform temperature T_s. The reactant gas reacts at the substrate surface to form a solid film. Homogeneous gas-phase reactions are assumed to be negligible. The situation is one-dimensional, axial coordinate only.

A highly simplified description of the hydrodynamics and transport in this CVD reactor leads to the following picture: Above the substrate, a boundary layer with thickness δ is formed, where the axial velocity rapidly decreases. At the substrate, the axial velocity is zero. As a result, the reactant supply through the boundary layer is mainly due to diffusion, with diffusivity D. Outside the boundary layer, the bulk reactant concentration equals C_∞. Thus, the reactant supply flux J through the boundary layer equals

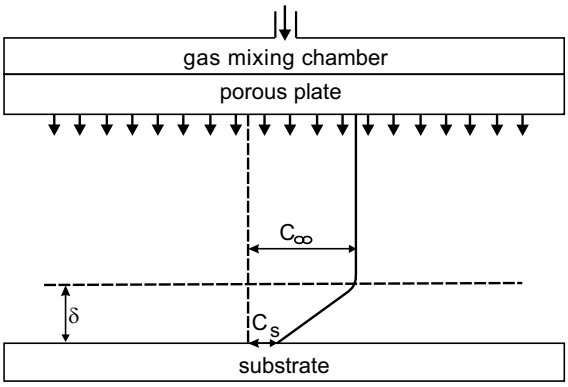

Figure 2: A simplified representation of a stagnation flow CVD reactor.

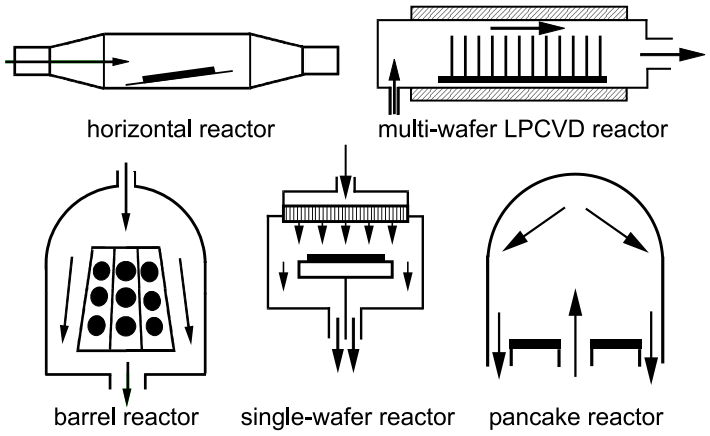

Figure 3: A few examples of different CVD reactor designs.

$$J = \frac{D\,(C_\infty - C_s)}{\delta} \tag{2}$$

In steady state, the this flux must be equal to the deposition rate R from Eqn. 1. This leads to

$$R = \left(\frac{k_s \delta}{D} + 1\right)^{-1} k_s C_\infty \tag{3}$$

with $k_s\delta/D$ is the surface Damköhler number Da_s. For large Da_s, deposition is limited by the maximum rate at which the reactant can be transported to the surface (*transport limited* regime). For small Da_s, deposition is limited by the surface reaction rate (*kinetically limited* regime). In practice, CVD process operation is performed at an intermediate regime, in which both transport and reaction kinetics play a role.

In realistic multi-dimensional CVD reactors, thermal and hydrodynamic non-idealities will lead to variations in the bulk reactant concentration C_∞, in the boundary layer thickness δ, and in T_s leading to variations in k_s. As a result, the deposition rate will be non-uniform. Moreover, in processes in which homogeneous gas phase reactions in the heated boundary layer lead to the formation of reactive intermediates, a non-uniform boundary layer thickness and surface temperature will lead to variations in the amounts of reactive intermediates formed.

The key issue in designing CVD reactors is to optimize their thermal and hydrodynamic behavior in such as way, that the deposition rate is high and spatially uniform, and that the film is of good quality.

Dimensionless group	Typical magnitude
Reynolds	$10^{-2} - 10^{2}$
Grashof	$0 - 10^{7}$
Reactor Scale Knudsen	$10^{-6} - 10^{-1}$
Micro Scale Knudsen	$10^{-1} - 10^{4}$

Table 1: Dimensionless numbers in CVD.

Depending on the process characteristics, the nature and geometry of the objects to be coated, and the required film properties, this leads to various designs. A few examples from the semi-conductor industry are shown in Fig. 3.

3. MODELING OF CVD PROCESSES AND EQUIPMENT

3.1 Principles of CVD simulation

The application of new materials, the wish to reinforce new ceramic and fibrous materials, the tremendous miniaturization and increase in complexity of semiconductor products, the manufacture of nano-sized and nano-structured objects and materials, etc. lead to a continuous need for new CVD processes, and ever increasing demands on the performance of CVD equipment.

It has been recognized in a early stage [9], that simulation models based on computational fluid dynamics can be of great help in the optimization of CVD equipment and processes. Besides, CVD simulation models may provide fundamental insights in the underlying physico-chemical processes, and can be used in the interpretation of experimental data and in relating local operating conditions to film properties.

Ideally, a computational fluid dynamics model for CVD model describes all relevant physicochemical processes in the reactor, and relates these phenomena to the properties of the deposited films. Such a model will generally include: *(i)* A *gas phase chemistry model*, which gives the reaction paths and rate constants for the homogeneous reactions, which influence the species concentration distribution near the deposition surface through the production/destruction of chemical species. *(ii)* A *surface chemistry model*, which describes how reactions between these species and free sites and adsorbed species on the surface lead to the growth of a solid film. In order to model these chemical processes, the macroscopic distribution of the gas flow and temperatures in the reactor must be known. Therefore, the core of a CVD model is formed by *(iii)* a *gas flow and transport phenomena model*, complemented by *(iv)* a *thermal (wall-to-wall) radiation model*, describing the gas flow and the transport of energy and species in the reactor and setting the thermal boundary conditions.

Together, the above model components describe the macroscopic behavior of the process. Apart from macroscopic process characteristics, in thin film processing the interest is mostly in microscopic film properties. Also, the surfaces to be coated are often non-uniform on microscopic length scales. To model these small scale phenomena, *microscopic models* are added to the macroscopic models. Obviously, microscopic models will generally be of a molecular nature, in contrast the the continuum based macroscopic models. The coupling of models at different scales is a topic of recent interest and a challenge that is further discussed in section 4.4.

3.2 CVD simulations models: a literature review

Early CVD models aimed at predicting growth rate and uniformity through simplified analytical descriptions of transport phenomena and chemistry in the reactor [12, 13].

In the late 70's and early 80's, the papers by Wahl [14], Jensen and Graves [15] and Coltrin and coworkers [16] marked the beginning of the computational era in computational CVD equipment modeling, allowing for a much more realistic description of hydrodynamics, transport phenomena and chemistry. Following these landmark publications, many computational CVD studies have been performed in the 80's and early 90's, which can roughly be categorized as: *(i) Hydrodynamic models*, aiming at simulating multi-dimensional flow and transport phenomena in relation to process operation and equipment design, in combination with simple models for the CVD chemistry. Most of these studies addressed classical

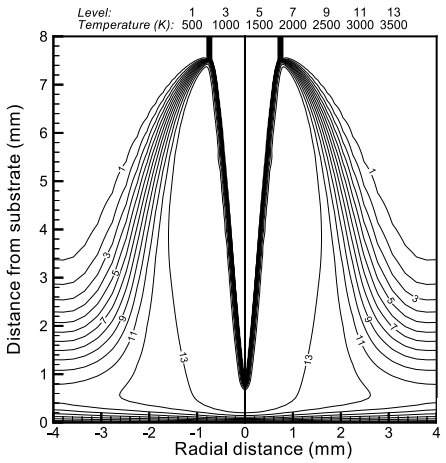

Figure 4: Computed isotherms in the oxy-acetylene torch reactor.

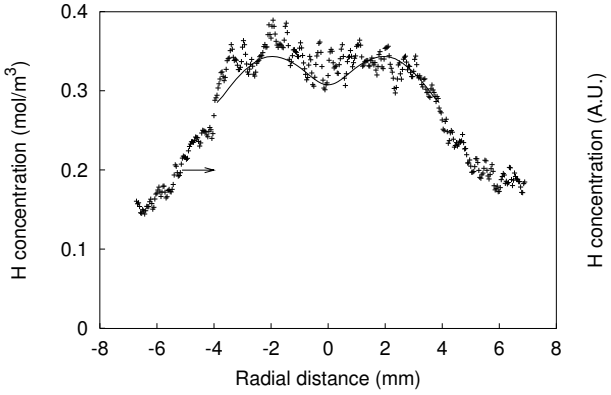

Figure 5: $2-D$ simulations and LIF-measurements [10] of radial H profiles directly above the surface.

reactor configurations (see Fig. 3), such as horizontal rectangular duct reactors (*e.g.* [17]-[21], vertical impinging jet and rotating disk reactors (*e.g.* [22]-[26]), pancake reactors (*e.g.* [27]-[28]), barrel reactors (*e.g.* [29]-[30]), planetary reactors (*e.g.* [31]-[32]), and hot-wall multi-wafer LPCVD reactors (*e.g.* [15], [33]-[35]). Many studies were devoted to low pressure single wafer reactors of the stagnation flow type (*e.g.* [36]-[40]). Studied CVD processes included atmospheric pressure CVD of epitaxial Si and of B, SiC and $CdTe$, MOVPE of $GaAs$ and InP, and low pressure deposition of doped and un-doped poly-Si, tungsten, silicon-dioxide and silicon-nitride. *(ii) Chemistry models*, aiming at unraveling homogeneous and heterogeneous reaction mechanisms, in combination with simple zero or 1-dimensional reactor models. Such models have been made for CVD of *e.g.* epitaxial silicon [25], B-doped silicon [41], silicon-dioxide [42], silicon-carbide [43], cadmium-telluride [44], gallium-arsenide [45, 46], silicon-germanium [47], $TiSi_2$ [48], tungsten [49, 50], and diamond [51, 11]. *(iii) Microscopic models*, describing the interaction between (molecular) transport phenomena and deposition within sub-micron trenches and contact holes on wafers for semiconductor manufacturing ([52]-[56]).

Since the late 90's, enabled by the ever increasing computer performance, it has become possible to combine detailed descriptions of transport phenomena and reaction chemistry into a single computational model (*e.g.* [40], [46], [57]-[60]). To an increasing extent, theoretical and computational chemistry tools are being used to determine reaction pathways and kinetics, both in the gas and at the surface (*e.g.* [41],[61]-[65]). Also, significant efforts have been made to integrate equipment scale and feature scale models into multi-scale CVD models (*e.g.* [66]-[70]). More detailed overviews of the development of CVD

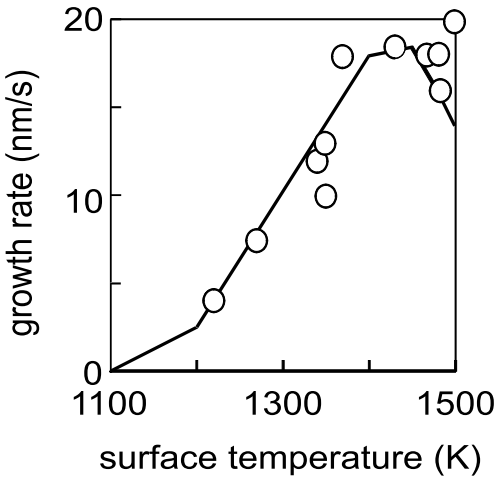

Figure 6: Diamond growth rate as a function of surface temperature as predicted by the model (line) and measured [11] (symbols).

simulation models in the past decades can be found in [71] and [72].

In recent years, successful attempts have been made in using simulation not only to optimize hydrodynamic reactor design and eliminate flow recirculations [19, 24] and to predict and optimize deposition rate and uniformity [15, 20, 73, 74], but also to optimize temperature uniformity [75, 76], to predict and control formation and transport of particles [77, 78], to scale-up existing reactors to larger wafer diameters [79, 80], to optimize processing conditions with respect to deposition conformality [53], to predict the influence of process conditions on doping rates [81], to evaluate loading effects on selective deposition rates [82], to study the influence of operating conditions on selectivity loss [58], *etc.* Today, CVD simulation models are being used routinely by process engineers and equipment manufacturers.

3.3 Example: Modeling CVD of crystalline diamond films

Crystalline diamond possesses many superior physical properties, *e.g.*, hardness, optical transparency, large electronic band-gap and high carrier mobilities (doped), wear and chemical resistance and thermal conductivity, which can be exploited in various technological applications [83]. With oxy-acetylene combustion CVD, mono-crystalline diamond layers can be grown [84] at high growth rates and low costs. The reactor consists of an ordinary welding torch, fed with a slight super-saturation of acetylene. The torch is pointed towards a cooled substrate, on which diamond is deposited. The main drawback of diamond growth by means of this technique is that the growth area is as yet limited to $\sim 20mm^2$. Scale-up is not trivial, and requires a detailed knowledge of the interaction between hydrodynamics, temperatures and chemistry. Computational modeling may be of aid in obtaining such knowledge, and in designing and optimizing reactor geometries.

Okkerse and coworkers [11, 85, 86] constructed a $2-D$ model of the reactor, based on the simultaneous simulation of *(i)* the multi-reaction combustion chemistry in the flame, *(ii)* the multi-reaction deposition chemistry, and *(iii)* the multicomponent transport phenomena,

The gas-phase chemistry mechanism used was based on that of Miller and coworkers [87]. Through sensitivity analysis, it was reduced to a 27 species, 119 reactions mechanism [11]. Based on quantum-mechanical calculations by Skokov and coworkers [88, 89, 90] a surface reaction mechanism was developed consisting of 67 elementary reactions between 41 adsorbed species [11]. These two chemistry models were combined with a $2-D$ hydrodynamics model.

Figure 4 gives an example of the calculated temperature profiles. The $2-D$ flame simulations were compared to qualitative *in situ* gas species concentration measurements by Klein-Douwel and coworkers [10], obtained with the aid of Laser Induced Fluorescence (LIF). In Fig. 5 the radial distribution of atomic hydrogen just above the substrate as computed with the $2-D$ model is compared to LIF measurements. Fig. 6 shows a comparison between model predictions and experimental data for the film growth as a

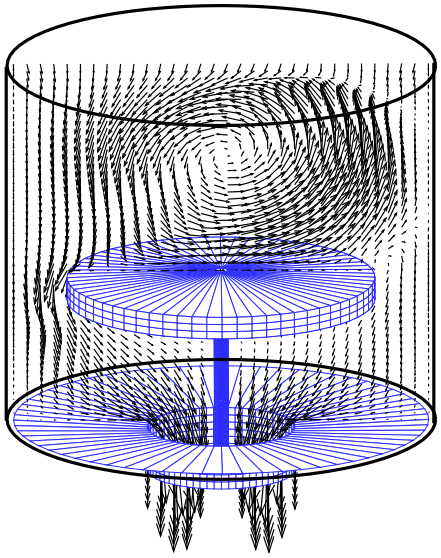

Figure 7: Symmetry breaking in a stagnation flow CVD reactor (from [91]).

function of surface temperature.

4. CHALLENGES FOR COMPUTATIONAL MODELING IN CVD PROCESS AND EQUIPMENT DESIGN

4.1 Laminar and transitional mixed convection gas flows

Reynolds numbers in Chemical Vapor Deposition reactors are usually quite low (see table 1), and as a consequence the gas flow is usually laminar. These low Reynolds numbers in combination with quite large temperature differences can lead to significant interactions between forced an free convection in CVD equipment. Especially at higher pressures, mixed convection can be an important factor influencing gas flow, chemistry, heat and mass transfer.

A general picture of the relevant dimensionless group(s) that determine the mixed convection behavior in CVD equipment is still lacking. This is mostly due to the large variety in geometries and configurations being used. Roughly, three gas flow directions can be distinguished: horizontal, vertically upward and vertically downward. Often, the substrates to be coated are rotated to improve deposition uniformity. This creates additional gas flow patterns. Each gas flow configuration can be combined with horizontal, vertically upward and vertically downward temperature gradients. In addition, horizontal and vertical density differences may be present due to concentration gradients, especially when a heavy reactant gas, diluted in a light carrier gas, is depleted at a reaction surface [92]. So at least four dimensionless groups play a role: the forced flow Reynolds number Re, the rotational Reynolds number Re_ω, the thermal Grashof number Gr and the solutal Grashof number Gr_C.

In horizontal CVD reactors (see fig. 3) heated from below, a combination of transversal and longitudinal rolls is observed [19, 20]. The occurrence of longitudinal rolls seems to depend on Gr only, but the entrance length for these rolls to develop depends on Re. Also, the sidewall temperatures have a large influence. The occurrence of transversal rolls or recirculation flows at the upstream edge of the heated bottom was found to depend on Gr/Re for low Re and on Gr/Re^2 for larger Re ([19, 93]). In rotating disk reactors, with a cold gas flow being sucked vertically downward towards a horizontally spinning heated susceptor, the relevant mixed convection parameter was found to be $Gr/Re_\omega^{3/2}$ [94]. When in such a configuration a forced vertically downward gas flow is combined with a spinning induced gas flow, the mixed convection parameter is reported to be $Gr/ReRe_\omega$ [95]. For radially outward gas flows between two heated horizontal disks, it is difficult to define a characteristic velocity scale and Reynolds number, as it is still a matter of debate whether the observed longitudinal rolls are determined by Gr and Re, or by Gr only [96, 97]. It is clear that a complete picture is still missing.

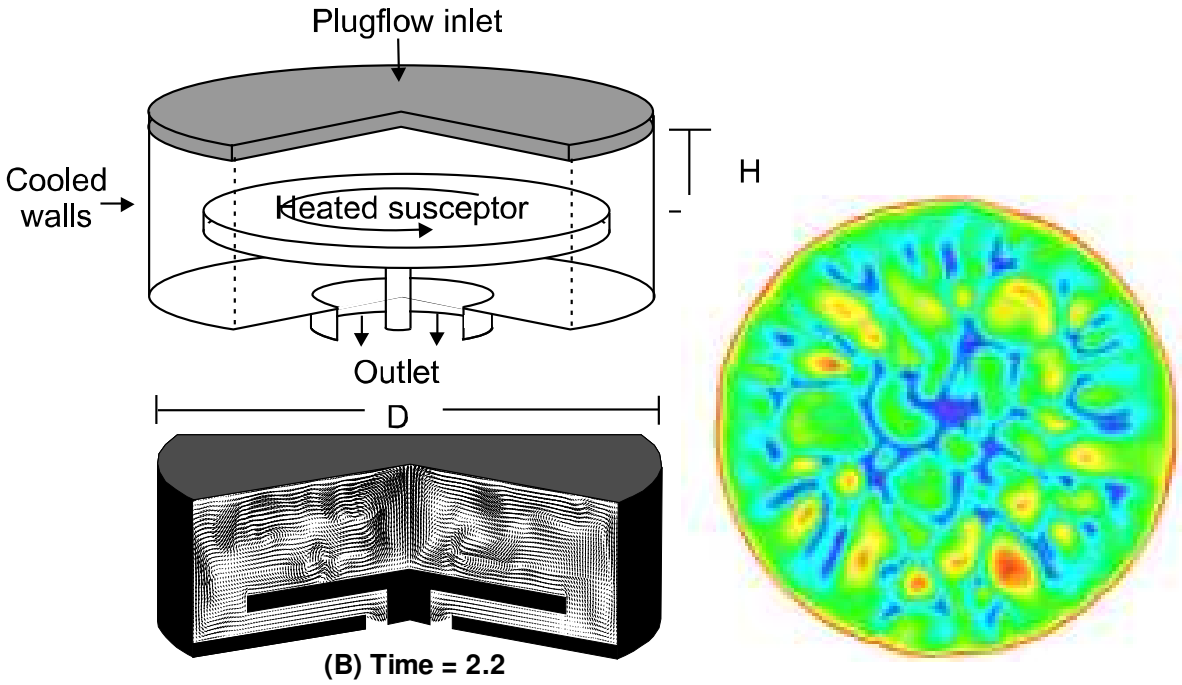

Figure 8: Reactor geometry (upper left), instantaneous rz velocities (lower left), and instantaneous heat transfer (right) in a stagnation flow CVD reactor operated under buoyancy driven turbulent flow conditions (From [100]).

Mixed convection at the relatively low Re and Gr numbers as encountered in CVD reactors may lead to surprising flow phenomena that are only partly understood and that may have a large impact on the process characteristics. One such phenomenon is that of multiple stability of mixed convection flows: At one specific combination of Re and Gr, both a buoyancy dominated and a forced flow dominated solution of the flow equations may be stable. A small change in either of these parameters may cause a bifurcation to the other solution branch [98, 99]. Another example is the existence of stable, non-symmetric flow solutions in axi-symmetric geometries with axi-symmetric boundary conditions [91], see Figure 7. It has been shown that the symmetry breaking is due to buoyancy alone, and does not result from an interaction between forced and free convection.

Although the gas flow in Chemical Vapor Deposition reactors is usually laminar, there are various good reasons for studying transitional and turbulent mixed convection flows in CVD equipment, and their interaction with chemistry, heat and mass transfer.

Firstly, in large scale, cold-wall CVD reactors turbulence may be caused - unintentionally - by buoyancy effects. In the IC industry, wafer diameters and reactor dimensions are increasing, and there is a tendency to use higher operating pressures, not only for the purpose of increasing the deposition rate, but also to enhance film conformality. Since the Rayleigh number increases quadratically in the pressure, and cubically in the reactor dimensions, buoyancy induced turbulence can be expected to become of increasing importance. In a single-wafer cold-wall reactor (see Fig. 3), for example, with a cold gas flow impinging vertically on a horizontally placed heated susceptor, the Rayleigh number may easily exceed 10^5 when nitrogen at atmospheric pressure is used as a carrier gas. In a barrel reactor (see Fig. 3), operated at atmospheric pressure with a nitrogen carrier gas, the Rayleigh number for the vertical annulus between the wafer holder and the reactor wall may easily exceed 10^8. For large scale atmospheric CVD equipment used to coat large numbers of *e.g.* machine parts and tools, the Rayleigh number may even be much higher. Secondly, there may be interesting opportunities in employing turbulent flow properties for efficient and uniform deposition of unstable chemical species.

By means of large Eddy Simulations, Van Santen and coworkers [100] studied mixed convection turbulence and heat transfer in cold-wall Chemical Vapor Deposition reactors of the rotating disk/stagnation flow type (see upper left part of Fig. 8) for inlet Reynolds numbers from 60 to 300, rotational Reynolds

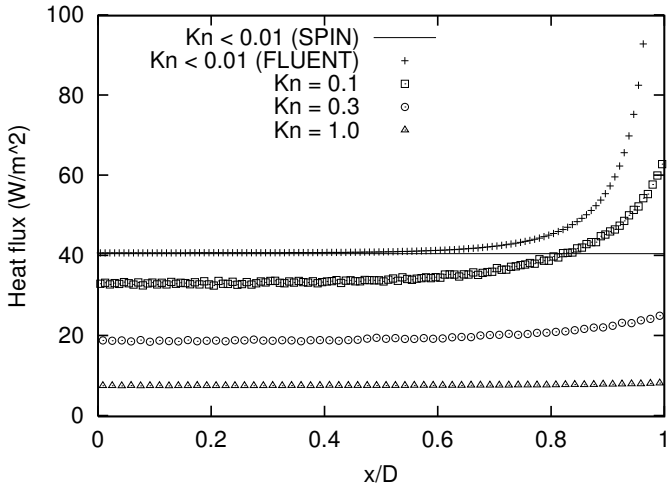

Figure 9: Heat flux to the susceptor surface in an stagnation flow CVD reactor; Included are 1-D (SPIN) and 2-D (Fluent) continuum simulations (Kn $\rightarrow$ 0), and simulations in the rarefied regime by means of DSMC at $Kn = 0.1 - 1.0$. (From [101])

numbers from 0 to 24×10^3, Rayleigh numbers from 2×10^5 to 10^6, and H/D aspect ratios from 1/6 to 1. In Fig. 8 (lower left part), a snapshot of the projection of the $rz-$velocity field at a specific instant in time has been plotted for $H/D = 0.2$, $Re = 10$, and $Ra = 10^6$. A turbulent chaotic flow is found between the wafer and the reactor inlet, that resembles plain turbulent Rayleigh-Bénard convection. In CVD, the heat transfer to the susceptor surface, that conditionally can be related to the deposition rate, is an important quantity. The instantaneous heat transfer at the susceptor surface, of which an example has been plotted in Fig. 8 (right), is highly non-uniform, due to the turbulent flow conditions. However, The time averaged Nusselt number was found to be reasonably uniform and about a factor five higher than would be the case in the absence of buoyancy induced turbulence.

From the above it may be clear that the low Re, low Gr mixed convection gas flows encountered in gas phase materials processing equipment are as yet only partly understood and still hold many challenges for thermo fluids science and engineering.

4.2 Rarefied gas flow modeling

Many film materials manufacturing processes are operated at reduced pressures. The main reasons for this are to increase diffusion and to suppress gas phase reactions (and thus improve process control and uniformity and conformality of the film thickness). At a pressure of $\sim 100Pa$, the mean free path length l of gas molecules is of the order of $0.1mm$, as compared to $0.1\mu m$ at atmospheric pressure. In order to be able to describe the gas as a continuum, the mean free path length should be ~ 100 times smaller than the characteristic dimensions L of the reactors, *i.e.* the Knudsen number $Kn = l/L$ should be smaller than 0.01. When the distances between closely stacked objects and surfaces in CVD reactors are of the order of millimeters, this criterion is easily violated under low pressure conditions (see Table 1). But even under atmospheric pressure conditions, the continuum approach does not hold inside sub-micrometer structures in and on the coated surfaces. In addition, there is a tendency to operate CVD processes at even lower pressures of $1 - 10Pa$. At these pressures, the molecular nature of the gas must be accounted for even at the scale of the entire reactor chamber.

For the modeling of gas flows in the continuum regime ($Kn < 0.01$), models based on the Navier-Stokes equations for continuum fluid dynamics are applicable. Free molecular flows at ultra-high-vacuum conditions ($Kn > 10$) can be modeled through line-of-sight-type models. For the intermediate pressure ($Kn = 0.01 - 10$) ranges, neither of the approaches is suitable. These are the regimes that are important at the sub-micron structures scale in atmospheric pressure CVD, and at the reactor scale in (very) low pressure CVD. Models for this regime should be based on the Boltzmann equation. Its mathematical intractability however necessitates rather rigorous simplifications, even when numerical solutions to the

discretized Boltzmann equation are sought. Alternative techniques are based on Monte-Carlo computer simulations on the molecular level. The most well-known method is the Direct Simulation Monte Carlo Method by Bird [102]. Figure 9 shows the influence of the Knudsen number on the heat flux to the susceptor in a stagnation flow CVD reactor in the transition regime, as compared to the heat flux for continuum conditions [101]. The heat flux decreases with increasing Kn. At the same time, the heat flux uniformity is improved.

The simulation of flow, chemistry, heat and mass transfer in rarefied reacting gas flows as encountered in materials processing equipment is a task with many challenges for the application and extension of DSMC methods. These include: *(i)* the modeling of surface and gas phase reactions with large, complex reactant molecules; *(ii)* the accurate modeling of trace species concentrations, which play an important role in *e.g.* doping and contamination; *(iii)* collection of experimental data and development of theoretical models for (thermal) accommodation coefficients of the various gas molecules and the solid services encountered in materials processing equipment; and *(iv)* the development of hybrid continuum/rarefied flow solvers capable of simulating gas flow with large variations in local Kn numbers.

The computational expenses of Monte-Carlo rarefied gas simulations increase rapidly with decreasing Knudsen number ($\sim Kn^{-3}$), limiting the practical applicability of the method to the transition and Knudsen regimes. With the arrival of powerful parallel computer architectures, these limits are now being pushed into the near-hydrodynamic regime. On the other hand, the range of validity of continuum models can be extended to higher Knudsen numbers through the use of modified (slip and temperature jump boundary conditions and modified transport properties [103, 104]. This is attractive, since continuum models are considerably less computationally demanding than Monte-Carlo simulations. For simple geometries, the necessary modifications of the boundary conditions in continuum models are known, but a more generic approach is still lacking.

4.3 Wall-to-wall radiation heat transfer modeling

Most Chemical Vapor Deposition processes are thermally activated and therefore the temperature distribution in the reactor is a key parameter. Temperature distributions play a role in three different ways: *(i)* Gas temperatures determine the chemical reaction rates in the gas phase. *(ii)* Surface temperatures determine the reaction rates of heterogeneous chemical reactions at the surface. *(iii)* The temperatures of the walls in a CVD reactor determine the gas flow pattern in the reactor.

The three main heat transfer mechanisms in CVD reactors are wall-to-wall thermal radiation, convective heat transfer and solid conduction. The most challenging part for computational modeling is the wall-to-wall radiation heat transfer. Materials on which thin films are being deposited generally exhibit a complex optical behavior. Emissivities strongly depend on film thickness (which varies during the deposition process) and surface temperature and exhibit a large spectral variation. Although reasonable results have been obtained by assuming diffuse reflection [105], in fact many materials used in CVD exhibit a partly diffuse, partly specular reflection behavior. Thus, thermal radiation modeling in CVD involves the modeling of wall-to-wall radiation in complex geometries, with partly diffuse-specular walls, the optical properties of which are a strong function of wavelength, temperature and deposited film thickness.

Clearly, Monte-Carlo ray tracing methods are the obvious choice for such type of modeling [76, 106, 107]. Theoretical models to compute the optical properties of bulk materials and thin films from the so-called complex refractive index of the materials are known and the spectral dependence of this refractive index of many materials can be found in *e.g.* [108, 109]. For many materials, however, data are lacking. Particularly difficult is the temperature dependence, which is especially important for semiconductors. The full implementation of wall-to-wall radiation models, taking into account all the temporal and spatial variations in optical properties mentioned above, and their coupling to fluid flow solvers is not a trivial task. The computations are computationally demanding, especially for transient simulations. The use of lamp heating, necessitating the modeling of radiation within and from the lamps and the lamp houses, further complicates matters significantly.

In many CVD and other thin film processes, the surfaces to be treated are patterned or structured on various length scales. In *e.g.* IC fabrication, the average optical properties of the centimeter sized dyes on a wafer are clearly distinct from those of the surrounding material. Within the dyes, the microscopic structure of the IC introduces variations in optical properties at a sub-micrometer scale, whereas clustering of these structures leads to variations at the scale of $\sim 10 - 100\mu m$. Modern nano-structured materials exhibit spatial property variations the scale of a few nanometers. With optical and thermal radiation wavelength between ~ 0.5 and $\sim 5\mu m$, the modeling of wall-to-wall radiation to and from such patterned

surfaces is a quite challenging task for micro-scale heat transfer science and engineering.

4.4 Multi scale modeling

In CVD, and in thin film surface processing in general, physical and chemical processes take place at largely differing length scales. Important properties of the films such as adhesion, morphology and purity, are determined by processes at molecular (*i.e.* nanometer) scale, such as molecular adsorption, chemical reactions, nucleations and island growth. At the *macroscopic* (*i.e.* reactor) scale, gas flow, (radiative) heat transfer and species diffusion determine process characteristics such as overall film uniformity and reactant consumption. In between these two extremes, additional length scales are often introduced due the close packing of large numbers of objects to be coated, the complex shape of surface geometries, patterning and structuring of surfaces, and small scale variations in optical, thermal and chemical properties of surfaces. This is *e.g.* most obviously the case in IC manufacturing, where the average surface properties of the centimeter sized dyes (*i.e.* the IC's to be) on a wafer are clearly distinct from those of the surrounding material. Within the dyes, the microscopic structures of the IC (the so called *features*) introduce variations in surface properties at a sub-micrometer scale. It is at this sub-micron scale that the quality of the products is determined. With the continuous increase in wafer diameters and the continuous decrease in pattern line widths in semiconductor manufacturing, the ratio between equipment scales and product scales continues to increase, see Fig. 10. Currently, it is of the order of 10^6. This ratio is increased to $10^7 - 10^8$ when molecular scales are also included.

Clearly, such differences in scales cannot be resolved within a single simulation model. As an example, the maximum ratio between domain size and (uniform) grid cell sizes in 3-dimensional CFD simulations for fluid flows with heat and mass transfer currently is about 500. This ratio approximately doubles every 5 years, leading to a ratio of 10^6 around the year 2060! Therefore, a hierarchy of different models for different scales must be used. This is not a trivial task, since models at different scales will be of a very different nature and communication between the models is not straightforward. One example of the problems encountered is the coupling between micro scale molecular models and macro scale continuum models. Also, the typical time scales for the two types of modeling lay far apart. The coupling between the smaller and the larger scales is bi-directional. The larger scales determine the local supply of heat and mass to the surface. But consumption rates of reactants and optical and thermal surface properties are determined by phenomena and structures at the smallest scales, thus setting the boundary conditions for the larger scale phenomena. Ideally, a full dynamic coupling between models for all different scales should be established.

The first approach towards full integration of macroscopic reactor scale and microscopic feature scale models was presented in [66]. In an iterative approach, pseudo steady state species concentrations at the reactor scale were given as input to a micro scale simulator, which then returned a homogenized net flux of each species back to the reactor scale. Also, mesoscopic scales were introduced in between the reactor and the feature scale, to provide information regarding spatial variations of species concentrations and fluxes at the scale of individual dies and clusters of features. In [68, 69] this approach was extended to transient cases. Another approach has been the effective reactivity function formulation described in [70, 110]. Here, the reactor and feature scale simulations are linked together using an effective reactivity ϵ, calculated from a molecular Monte Carlo simulation, which includes effects of both surface variations and molecular transport inside sub-micron features. The reactivity of each set of features is then linearly superimposed to obtain ϵ. Whereas the above studies addressed the coupling between the reactor scale, the (cm) die scale and the (μm) feature scale, in [111, 112, 113] the focus was on coupling reactor scale simulations to molecular scale simulations.

Clearly, promising results have been obtained in coupling models for the different scales in CVD. However, a fully integrated dynamic coupling between models for all relevant scales is still a terrific challenge. Also, the attempts so far have mainly addressed the coupling between mass fluxes and deposition at the various scales. There is a clear need for an extension of these types of approaches towards thermal modeling at different scales, integrating macroscopic conjugate and radiative heat transfer models to micro-heat transfer models, with optical and thermal properties varying in time and at length scales comparable to thermal radiation wavelengths and molecular free paths lengths.

5. CONCLUSIONS AND OUTLOOK

In Chemical Vapor Deposition and other surface treatment processes for the manufacturing of thin films and small structures, the product quality is primarily determined by chemistry. However, in order to

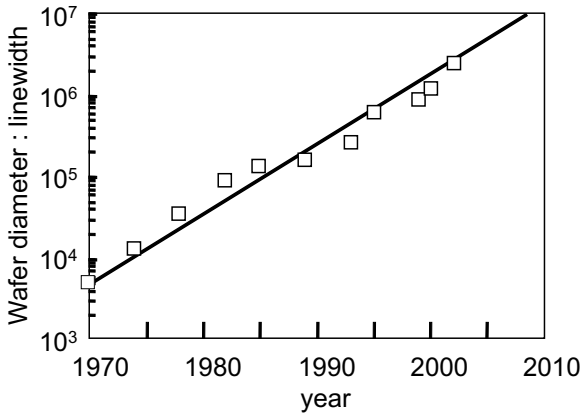

Figure 10: Ratio between the diameter of wafers and the typical line-widths in IC manufacturing.

make chemical processes proceed in a uniform manner and to control them on the widely varying length scales that play a role, sophisticated thermal and fluid flow equipment engineering is needed. Reactants and heat must be transported to the treated objects and surfaces in such a way, that surface temperatures and near-surface species concentrations are uniform and well controlled. Modeling and simulation are important tools to help in the complex design and optimization of equipment and processes.

In the last two decades thermal and fluid flow modeling has had a large impact on the field of CVD, especially when combined with chemistry modeling: Not only on the way in which processes are developed and operated, but possibly even more on the way in which CVD researchers conceptualize the various processes in a CVD reactor.

This paper has discussed examples of challenges yet to be tackled by the heat transfer and fluid flow community in order to resolve technological and modeling problems in designing equipment for the manufacture of smaller and smaller structures. In order to be really successful, these efforts should be conducted in close multi-disciplinary collaboration with chemists, materials scientists and chemical reactor engineers.

References

[1] J.L. Vossen and W. Kern, editors. *Thin Film Processes II.* Acad. Press, Boston, 1991.

[2] M.L. Hitchman and K.F. Jensen, editors. *Chemical Vapor Deposition - Principles and Applications.* Acad. Press, London, 1993.

[3] T. Kodas and M. Hampden-Smith. *The chemistry of metal CVD.* VCH, Weinheim, Germany, 1994.

[4] W.S. Rees jr. (ed.). *CVD of nonmetals.* VCH, Weinheim, Germany, 1996.

[5] A.C. Jones and P. O'Brien. *CVD of compound semiconductors.* VCH, Weinheim, Germany, 1997.

[6] M. Meyyappan, L. Delzeit, A. Cassell, and D. Hash. Carbon nanotube growth by PECVD: a review. *Plasma Sources Science and Technology*, 12(2):205–216, 2003.

[7] L. Zambov, A. Zambova, M. Cabassi, and T.S. Mayer. Template-directed CVD of dielectric nanotubes. *Chem. Vap. Dep.*, 9(1):26–33, 2003.

[8] R. Seidel, G.S. Duesberg, E. Unger, A.P. Graham, M. Liebau, and F. Kreupl. Chemical vapor deposition of single-walled carbon nanotubes at 600 degrees C and a simple growth model. *J. Phys. Chem. B*, 108(6):1888–1893, 2004.

[9] K.F. Jensen. Micro-reaction engineering applications of reaction engineering to processing of electronic and photonic materials. *Chem. Engng. Sci.*, 42 (5):923–958, 1987.

[10] R.J. Klein-Douwel and J.J. ter Meulen. Spatial distributions of atomic hydrogen and C_2 in an oxyacetylene flame in relation to diamond growth. *J. Appl. Phys.*, 83(9):4734, 1998.

[11] M. Okkerse, M.H.J.M. de Croon, C.R. Kleijn, G.B. Marin, and H.E.A. van den Akker. A surface and gas-phase mechanism for the description of growth on the diamond(100) surface in an oxy-acetylene torch reactor. *J. Appl. Phys.*, 84(11):6387–6398, 1998.

[12] F.C. Eversteijn, P.J.W. Severin, C.H.J. van den Brekel, and H.L. Peek. A stagnant layer model for the epitaxial growth of silicon from silane in a horizontal reactor. *J. Electrochem. Soc.*, 117 (7):925–931, 1970.

[13] A.E.T. Kuiper, C.H.J. van den Brekel, J. de Groot, and F.W. Veltkamp. Modelling of low pressure CVD processes. *J. Electrochem. Soc.*, 129 (10):2288–2291, 1982.

[14] G. Wahl. Hydrodynamic description of CVD processes. *Thin Solid Films*, 40:13–26, 1977.

[15] K.F. Jensen and D.B. Graves. Modeling and analysis of low pressure CVD reactors. *J. Electrochem. Soc.*, 130 (9):1950–1957, 1983.

[16] M.E. Coltrin, R.J. Kee, and J.A Miller. A mathematical model of the coupled fluid mechanics and chemical kinetics in a Chemical Vapor Deposition reactor. *J. Electrochem. Soc.*, 131 (2):425–434, 1984.

[17] J. van de Ven, G.J.M. Rutten, M.J. Raaymakers, and L.J. Giling. Gas phase depletion and flow dynamics in horizontal MOCVD reactors. *J. Cryst. Growth*, 76:352–372, 1986.

[18] H.K. Moffat and K.F. Jensen. Three-dimensional flow effects in silicon CVD in horizontal reactors. *J. Electrochem. Soc.*, 135 (2):459–471, 1988.

[19] E.P. Visser, C.R. Kleijn, C.A.M. Govers, C.J. Hoogendoorn, and L.J. Giling. Return flows in horizontal MOCVD reactors studied with the use of TiO particle injection and numerical calculations. *J. Cryst. Growth*, 94:929–946, 1989. Err vol. 96, pp. 732-735.

[20] C.R. Kleijn and C.J. Hoogendoorn. A study of 2- and 3-D transport phenomena in horizontal Chemical Vapor Deposition reactors. *Chem. Engng. Sci.*, 46 (1):321–334, 1991.

[21] S. Kommu, G.M. Wilson, and B. Khomami. A theoretical/experimental study of silicon epitaxy in horizontal single-wafer chemical vapor deposition reactors. *J. Electrochem. Soc.*, 147(4):1538–1550, 2000.

[22] R. Pollard and J. Newman. Silicon deposition on a rotating disk. *J. Electrochem. Soc.*, 127 (3):744–752, 1980.

[23] D.I. Fotiadis, A.M. Kremer, D.R. McKenna, and K.F. Jensen. Complex flow phenomena in vertical MOCVD reactors: effects on deposition uniformity and interface abruptness. *J. Cryst. Growth*, 85:154–164, 1987.

[24] G. Evans and R. Greif. A numerical model of the flow and heat transfer in a rotating disk chemical vapor deposition reactor. *J. Heat Transfer*, 109:928–935, 1987.

[25] M.E. Coltrin, R.J. Kee, and G.H. Evans. A mathematical model of the fluid mechanics and gas-phase chemistry in a rotating disk chemical vapor deposition reactor. *J. Electrochem. Soc.*, 136 (3):819–829, 1989.

[26] Y.B. Wang, C. Chaussavoine, and F. Teyssandier. 2D modelling of a non-confined circular impinging jet reactor; Si Chemical Vapour Deposition. *J. Cryst. Growth*, 126:373–395, 1993.

[27] I-H Oh, C.G. Takoudis, and G.W. Neudeck. Mathematical modeling of epitaxial silicon growth in pancake Chemical Vapor Deposition reactors. *J. Electrochem. Soc.*, 138 (2):554–567, 1991.

[28] A.P. Peskin. Gallium arsenide growth in a pancake MOCVD reactor. *J. Cryst. Growth*, 186(4):494–510, 1998.

[29] L. Yang, B. Farouk, and R.L. Mahajan. Three-dimensional predictions of silicon deposition in a barrel type CVD reactor. *J. Electrochem. Soc.*, 139 (9):2666–2673, 1992.

[30] E. De Paola and P. Duverneuil. Simulation of silicon deposition from $SiHCl_3$ in a CVD barrel reactor at atmospheric pressure. *Computers Chem. Engng.*, 22 (Suppl):S683–S686, 1998.

[31] C. Werner, M. Ilg, and K. Uram. Three-dimensional equipment modeling for Chemical Vapor Deposition. *J. Vac. Sci Technol A*, 14(3):1147–1151, 1996.

[32] T. Bergunde, M. Dauelsberg, Yu.N. Makarov L. Kadinski, M. Weyers, D. Schmitz, G. Strauch, and H. Jürgensen. Heat transfer and mass transport modeling in a multiwafer MOVPE reactor: modelling and experimental studies. *J. Cryst. Growth*, 170(1-4):66–71, 1997.

[33] Ch. Hopfmann, Ch. Werner, and J.I. Ulacia. Numerical analysis of fluid flow and non-uniformities in a polysilicon LPCVD batch reactor. *Appl. Surf. Sci.*, 52:169–187, 1991.

[34] W.G. Houf, J.F. Grcar, and W.G. Breiland. A model for low pressure Chemical Vapor Deposition in a hot-wall tubular reactor. *Mat. Sci. Eng. B*, 17(1-3):163–171, 1993.

[35] G.J. Schoof, C.R. Kleijn, H.E.A. Van den Akker, Oosterlaken T.G.M., Terhorst H.J.C.M., and F. Huussen. Simulation and Validation of SiO_2 LPCVD from TEOS in a vertical 300mm multi-wafer reactor. *J. de Phys. IV*, 12(PR4):51–61, 2002.

[36] C.R. Kleijn. A mathematical model of the hydrodynamics and gas-phase reactions in silicon LPCVD in a single-wafer reactor. *J. Electrochem. Soc.*, 138 (7):2190–2200, 1991.

[37] C.R. Kleijn, C.J. Hoogendoorn, A. Hasper, J. Holleman, and J. Middelhoek. Transport phenomena in tungsten LPCVD in a single-wafer reactor. *J. Electrochem. Soc.*, 138:509–517, 1991.

[38] Ch. Werner, J.I. Ulacia, C. Hopfmann, and P. Flynn. Equipment simulation of selective tungsten deposition. *J. Electrochem. Soc.*, 139 (2):566–574, 1992.

[39] H. Habuka, T. Nagoya, M. Katayama, M. Shimada, and K. Okuyama. Modeling of epitaxial silicon thin-film growth on a rotating substrate in a horizontal single-wafer reactor. *J. Electrochem. Soc.*, 142(12):4272–4278, 1995.

[40] C.R. Kleijn. Computational modeling of transport phenomena and detailed chemistry in chemical vapor deposition - a benchmark solution. *Thin Solid Films*, 365:294–306, 2000.

[41] I. Lengyel and K.F. Jensen. A chemical mechanism for in situ boron doping during silicon chemical vapor deposition. *Thin Solid Films*, 365:231–241, 2000.

[42] M.E. Coltrin, P. Ho, H.K. Moffat, and R.J. Buss. Chemical kinetics in chemical vapor deposition: growth of silicon dioxide from tetraethoxysilane (TEOS). *Thin Solid Films*, 365:251–263, 2000.

[43] M.D. Allendorf and R.J. Kee. A model of silicon carbide chemical vapor deposition. *J. Electrochem. Soc.*, 138 (3):841–852, 1991.

[44] B. Liu, R.F. Hicks, and J.J. Zinck. Chemistry of photo-assisted organometallic vapor-phase epitaxy of cadmium telluride. *J. Cryst. Growth*, 123:500–518, 1992.

[45] M. Tirtowidjojo and R. Pollard. Elementary processes and rate-limiting factors in MOVPE of GaAs. *J. Cryst. Growth*, 77:108–114, 1988.

[46] T.J. Mountziaris, S Kalyanasundaram, and N.K. Ingle. A reaction-transport model of GaAs growth by metalorganic Chemical Vapor Deposition using trimethyl-gallium and tertiary-butyl-arsine. *J. Cryst. Growth*, 131:283–299, 1993.

[47] E.J. Kim and W.N. Gill. Modeling of CVD of silicon dioxide using TEOS and ozone in a single-wafer reactor. *J. Electrochem. Soc.*, 141(12):3462–3472, 1994.

[48] R.P. Southwell and E.G. Seebauer. A Predictive Kinetic Model for the Chemical Vapor Deposition of $TiSi_2$. *J. Electrochem. Soc.*, 143(5):1726–1736, 1996.

[49] R. Arora and R. Pollard. A mathematical model for chemical vapor deposition influenced by surface reaction kinetics: Application to low pressure deposition of tungsten. *J. Electrochem. Soc.*, 138 (5):1523–1537, 1991.

[50] Y.-F. Wang and R. Pollard. A method for predicting the adsorption energetics of diatomic molecules on metal surfaces. *Surf. Sci.*, 302:223–234, 1994.

[51] E. Meeks, R.J. Kee, D.S. Dandy, and M.E. Coltrin. Computational simulation of diamond chemical vapor deposition in premixed $C_2H_2/O_2/H_2$ and CH_4/O_2-strained flames. *Comb. Flame*, 92:144–160, 1993.

[52] G.B. Raupp and T.S. Cale. Step coverage prediction in low-pressure chemical vapor deposition. *Chem. Mater.*, 1(2):207–214, 1989.

[53] A. Hasper, C.R. Kleijn, J. Holleman, J. Middelhoek, and C.J. Hoogendoorn. Modeling and optimization of the step coverage of tungsten LPCVD in trenches and contact holes. *J. Electrochem. Soc.*, 138:1728–1738, 1991.

[54] T.S. Cale and G.B. Raupp. Free molecular transport and deposition in cylindrical features. *J. Vac. Sci. Technol. B*, 8(4):649–655, 1990.

[55] D.G. Coronell and K.F. Jensen. Simulation of Rarefied Gas Transport and Profile evaluation in Nonplanar Substrate Chemical Vapor Deposition. *J. Electrochem. Soc.*, 141(9):2545–2551, 1994.

[56] Y. Akiyama and N. Imaishi. Applicability of one-dimensional diffusion model for step coverage analysis - Comparison with a simple Monte Carlo method. *Appl. Phys. Lett.*, 67 (5):620–622, 1995.

[57] Y.A. Mankelevich, A.T. Rakhimov, and N.V. Suetin. Two-dimensional simulation of a hot-filament Chemical Vapor Deposition reactor. *Diamond Rel. Mat.*, 5(9):888–894, 1996.

[58] K.J. Kuijlaars, C.R. Kleijn, and H.E.A. van den Akker. Simulation of selective tungsten Chemical Vapour Deposition. *Solid State Electronics*, 42(5):A43–A54, 1998.

[59] N.K. Ingle, C. Theodoropoulos, T.J. Mountziaris, R.M. Wexler, and F.T.J. Smith. Reaction kinetics and transport phenomena underlying the low-pressure metalorganic Chemical Vapor Deposition of $GaAs$. *J. Cryst. Growth*, 167 (3-4):543–556, 1996.

[60] A. Ern, V. Giovangigli, and M.D. Smooke. Detailed modeling of three-dimensional Chemical Vapor Deposition. *J. Cryst. Growth*, 180(3-4):670–679, 1997.

[61] H. Simka, M. Hierlemann, M. Utz, and K.F. Jensen. Computational chemistry predictions of kinetics and major reaction pathways for germane gas-phase reactions. *J. Electrochem. Soc.*, 143(8):2646–2654, 1996.

[62] K. Sato, H. Haruta, and Y. Kumashiro. *Ab initio* molecular-orbital study on the surface reactions of methane and silane plasma chemical vapor deposition. *Phys. Rev. B*, 55 (213):15467–15470, 1997.

[63] M. Frenklach. Simulation of surface reactions. *Pure & Appl. Chem.*, 70(2):477–484, 1998.

[64] R. Metzger, C. Werner, and A. Spitzer. Adsorption of precursor molecules in the CVD process of (Ba;Sr)titanate simulated by ab-initio calculations. *Thin Solid Films*, 365:242–250, 2000.

[65] S. Maruno, T. Furukawa, T. Nakahata, and Y. Abe. A chemical mechanism for determining the influence of boron on silicon epitaxial growth. *Jap. J. Appl. Phys. - Part I*, 40(11):6202–6207, 2001.

[66] M.K. Gobbert, C.A. Ringhofer, and T.S. Cale. Mesoscopic Scale Modeling of Microloading during Low Pressure Chemical Vapor Deposition. *J. Electrochem. Soc.*, 143(8):2624–2631, 1996.

[67] K.F. Jensen, S.T. Rodgers, and R. Venkataramani. Multiscale modeling of thin film growths. *Curr. Opin. Solid State Mat.*, 3(6):562–569, 1998.

[68] T.P. Merchant, M.K. Gobbert, T.S. Cale, and L.J. Borucki. Multiple scale integrated modeling of deposition processes. *Thin Solid Films*, 365:368–375, 2000.

[69] T.S. Cale, M.O. Bloomfield, D.F. Richards, K.E. Jansen, and M.K. Gobbert. Integrated multiscale process simulation. *Comp. Mat. Sci.*, 23(1-4):3–14, 2002.

[70] C. Cavalotti, M. Nemirovskaya, and K.F. Jensen. A multiscale study of the selective movpe of $al_xga_{1-x}as$ in the presence of *hcl*. *J. Cryst. Growth*, 248:411–416, 2003.

[71] C.R. Kleijn. Chemical Vapor Deposition Processes. In M. Meyyappan, editor, *Computational Modeling in Semiconductor Processing*, chapter 4, pages 97–229. Artech House, Boston, 1995.

[72] C.R. Kleijn, K.J. Kuijlaars, M. Okkerse, H. Van Santen, and H.E.A. van den Akker. Some recent developments in Chemical Vapor Deposition process and equipment modeling. *J. Phys. IV*, 9:Pr8–117–132, 1999.

[73] Y.K. Chae, Y. Egashira, Y. Shimogaki, K. Sugawara, and H. Komiyama. Chemical Vapor Deposition Reactor Design Usining Small-Scale Diagnostic Experiments Combined with Computational Fluid Dynamics Simulations. *J. Electrochem. Soc.*, 146(5):1780–1788, 1999.

[74] W.K. Cho and D.H. Choi. Optimization of a horizontal MOCVD reactor for uniform epitaxila layer growth. *Int. J. Heat Mass Trans.*, 43(10):1851–1858, 2000.

[75] T.A. Badgwell, I. Trachtenberg, and T.F. Edgar. Modeling the wafer temperature profile in a multiwafer LPCVD furnace. *J. Electrochem. Soc.*, 141 (1):161–171, 1994.

[76] A. Kersch and T. Schafbauer. Thermal modelling of rtp and rtcvd processes. *Thn Solid Films*, 365:307–321, 2000.

[77] H. Setyawan, M. Shimada, K. Ohtsuka, and K. Okuyama. Visualization and numerical simulation of fine particle transport in low-pressure parallel plate Chemical Vapor Deposition Reactor. *Chem. Eng. Sci.*, 57(3):497–506, 2002.

[78] S. Kommu, B. Khomami, and P. Biswas. Simulation of aerosol dynamics and transport in chemically reacting particulate laeden flows. part II: Application to CVD reactors. *Chem. Eng. Sci.*, 59(2):359–371, 2004.

[79] T.A. Badgwell, T.F. Edgar, and I. Trachtenberg. Modeling and scale-up of multiwafer LPCVD reactors. *AIChE Journal*, 138 (6):926–938, 1992.

[80] C.R. Kleijn, K.J. Kuijlaars, and H.E.A. Van den Akker. Design and scale-up of Chemical Vapour Deposition reactors for semiconductor processing. *Chem. Eng. Science*, 51 (10):2119–2128, 1996.

[81] M. Masi, H. Simka, K.F. Jensen, T.F. Kuech, and R. Potemski. Simulation of carbon doping of GaAs during MOVPE. *J. Cryst. Growth*, 124:483–492, 1992.

[82] J. Holleman, A. Hasper, and C.R. Kleijn. Loading effects on kinetical and electrical aspects of silane-reduced low-pressure chemical vapor deposited selective tungsten. *J. Electrochem. Soc.*, 140(3):818–825, 1993.

[83] K.E. Spear and J.P Dismukes. *Synthetic diamond, Emerging CVD science and technology.* J. Wiley and Sons, USA, 1994.

[84] J.J. Schermer, W.J.P. van Enckevort, and L.J. Giling. Flame deposition and characterization of large type IIA diamond single crystals. *Diamond Rel. Mater.*, 3:408–416, 1994.

[85] M. Okkerse, C.R. Kleijn, H.E.A. van den Akker, M.H.J.M. de Croon, and G.B. Marin. Two-dimensional simulation of an oxy-acetylene torch diamond reactor with a detailed gas-phase and surface mechanism. *J. Appl. Phys.*, 88(7):4417–4428, 2000.

[86] M. Okkerse, C.R. Kleijn, H.E.A. van den Akker, M.H.J.M. de Croon, and G.B. Marin. The influence of nitrogen on diamind growth in oxyacetylene combustion chemical vapor deposition. *J. Appl. Phys.*, 92(7):4095–4102, 2002.

[87] J. Miller and C. Melius. Kinetic and thermodynamic issues in the formation of aromatic compounds in flames of aliphatic fuels. *Comb. Flame*, 91:21–39, 1992.

[88] S. Skokov, B. Weiner, and M. Frenklach. Elementary reaction mechanism for growth of diamond (100) surfaces from methyl radicals. *J. Phys. Chem.*, 98:7073–7082, 1994.

[89] S. Skokov, B. Weiner, and M. Frenklach. Chemistry of acetylene on diamond (100) surfaces. *J. Phys. Chem.*, 99:5616–5625, 1995.

[90] S. Skokov, B. Weiner, M. Frenklach, Th. Frauenheim, and M. Sternberg. Dimer row pattern formation in diamond (100) growth. *Phys. Rev. B*, 52:5426–5432, 1995.

[91] H. van Santen, C.R. Kleijn, and H.E.A. van den Akker. Symmetry breaking in a stagnation-flow cvd reactor. *J. Cryst. Growth*, 212:311–323, 2000.

[92] S. Patnaik, R.A. Brown, and C.A. Wang. Hydrodynamic dispersion in rotating-disk OMVPE reactors: Numerical simulation and experimental measurements. *J. Cryst. Growth*, 96:153–174, 1989.

[93] T.M. Makhviladze and A.V. Martjushenko. Several aspects of return flows formation in horizontal CVD reactors. *Int. J. Heat Mass Trans.*, 41(16):2529–2536, 1998.

[94] G. Evans and R. Greif. Effects of boundary conditions on the flow and heat transfer in a rotating disk chemical vapor deposition reactor. *Numererical Heat Transfer*, 12:243–252, 1987.

[95] C.R. Biber, C.A. Wang, and S. Motakef. Flow regime map and deposition rate uniformity in vertical rotating-disk omvpe reactors. *J. Cryst. Growth*, 123:545–554, 1992.

[96] H. Van Santen, C.R. Kleijn, and H.E.A. Van Den Akker. Mixed convection in radial flow between horizontal plates−I. Numerical Simulations. *Int. J. Heat Mass Trans.*, 43:1523–1535, 2000.

[97] H. Van Santen, C.R. Kleijn, and H.E.A. Van Den Akker. Mixed convection in radial flow between horizontal plates−II. Experiments. *Int. J. Heat Mass Trans.*, 43:1537–1546, 2000.

[98] D.I. Fotiadis, S. Kieda, and K.F. Jensen. Transport phenomena in vertical reactors for metalorganic vapor phase epitaxy: I. effects of heat transfer characteristics, reactor geometry, and operating conditions. *J. Cryst. Growth*, 102:441–470, 1990.

[99] H. van Santen, C.R. Kleijn, and H.E.A. van den Akker. On multiple stability of mixed-convection flows in a chemical vapor deposition reactor. *Int. J. Heat Mass Transf.*, 44:659–672, 2001.

[100] H. Van Santen. *Mixed-Convection Instabilities in Chemical Vapor Deposition Reactors*. PhD thesis, Delft University of Technology, Delft, The Netherlands, 1999 (copies can be requested from the author).

[101] R. Dorsman and C.R. Kleijn. Heat transfer in very low pressure stagnation flow CVD reactors. In M. Allendorf, F. Maury, and F. Teyssandier, editors, *Chemical Vapor Deposition XVI and EuroCVD 14*, pages 171–178, Pennington, NJ, USA, 2003. The Electrochemical Society.

[102] G.A. Bird. *Molecular Gas dynamics*. Oxford University Press, Oxford, 1976.

[103] A. Kersch and W.J. Morokoff. *Transport Simulation in Microelectronics*. Birkhäuser, Basel, 1995.

[104] T.L. Hu and N.G. Glumac. The effect of temperature jump on CVD modeling. *Chem. Vapor Depos.*, 8(5):205–212, 2002.

[105] I.K. Kim and W.S. Kim. Theoretical analysis of wafer temperature dynamics in a low pressure chemical vapor deposition reactor. *Int. J. Heat Mass Trans.*, 42(22):4131–4142, 1999.

[106] T.P. Merchant, J.V. Cole, K.L. Knutson, J.P. Hebb, and K.F. Jensen. A Systematic Approach to Simulating Rapid Thermal Processing Systems. *J. Electrochem. Soc.*, 143(6):2035–2043, 1996.

[107] P.M. Lofgren, C. Hallin, C.Y. Gu, and W. Ji. 3-D thermal and flow modeling of hot wall epitaxial chemical vapor deposition reactors, heated by induction. *Silicon Carbide and Related Materials - 1999 PTS, 1 & 2 - Materials Science Forum*, 338(3):153–156, 2000.

[108] E.D. Palik. *Handbook of optical constants of solids*. Acad. Press, New York, 1985.

[109] M.A. Ordal, R.J. Bell, R.W. Alexander, L.L. Long, and M.R. Querry. Optical properties of fourteen metals in the infrared and far infrared. *Applied Optics*, 24 (24):4493, 1985.

[110] S.T. Rodgers and K.F. Jensen. Multiscale modeling of Chemical Vapor Deposition. *J. Appl. Phys.*, 83(1):524–530, 1998.

[111] Grujicic M. and S.G. Lai. Multi-length scale modeling of CVD of diamond - Part I - A combined reactor-scale/atomic-scale analysis. *J. Mat. Sci.*, 35(21):5359–5369, 2000.

[112] Grujicic M. and S.G. Lai. Multi-length scale modeling of CVD of diamond - Part II - A combined atomic-scale/grain-scale analysis. *J. Mat. Sci.*, 35(21):5371–5381, 2000.

[113] Grujicic M. and S.G. Lai. Multi-length scale modeling of Chemical Vapor Deposition of titanium nitride coatings. *J. Mat. Sci.*, 36(12):2937–2953, 2001.

PROCESS SYSTEMS ENGINEERING – PROBLEMS, MODELS AND TECHNIQUES

C. Pantelides

Centre for Process Systems Engineering
Department of Chemical Engineering and Chemical Technology
Imperial College London
London SW7 2AZ, United Kingdom
E-mail: c.pantelides@psenterprise.com

Keywords: Process systems engineering.

Abstract: *Process systems engineering is concerned with general-purpose model-based methodologies and tools for the design, operation and control of processes in a wide range of industries, from oil exploration and basic petrochemicals and chemicals to pharmaceuticals, foods and consumer goods. It also operates on a vast range of scales of space and time, from electrons and atoms to molecules, particles and process equipment, all the way to global supply chains.*

The aim of this talk is to provide a short overview of process systems engineering, before focusing on a small number of topics that pervade the entire field. These include the use of multiscale modelling techniques, formal techniques for model validation, and the management of risk arising from uncertainty in process design.

COHESIVE ZONE MODELING OF DYNAMIC CRACK PROPAGATION IN FUNCTIONALLY GRADED MATERIALS

Glaucio H. Paulino* **and Zhengyu Zhang**

Department of Civil and Environmental Engineering, University of Illinois at Urbana-Champaign, Newmark Laboratory, 205 North Mathews Avenue, Urbana, IL 61801, U.S.A.

*e-mail:paulino@uiuc.edu, web page: http://www.cee.uiuc.edu/paulino

Keywords: Finite element method, functionally graded material (FGM), cohesive zone model (CZM), dynamics, crack, fracture.

Abstract. *This paper presents a Cohesive Zone Model (CZM) approach for investigating dynamic crack propagation in homogeneous and Functionally Graded Materials (FGMs). The failure criterion is incorporated in the CZM using both a finite cohesive strength and work to fracture in the material description. A novel CZM for FGMs is explored and incorporated into a finite element framework. The material gradation is approximated at the element level using a graded element formulation. A numerical example is provided to demonstrate the efficacy of the CZM approach, in which the influence of the material gradation on the crack branching pattern is studied.*

1 INTRODUCTION

Functionally graded materials or FGMs are a new generation of engineered composites characterized by spatially varied microstructures and smooth variation of mechanical/thermal/electromagnetic properties. This new concept of engineering the material microstructure and recent advances in material processing science allows one to fully integrate the desirable properties of individual material phases and acquire optimized structural performance[1].

Fracture mechanics of FGMs has been an active area of research during recent years[2]. Compared to the classical linear elastic fracture mechanics (LEFM) and some other existing fracture models, Cohesive Zone Models (CZMs) provide advantages of allowing spontaneous crack nucleation, crack branching and fragmentation, as well as crack propagation without an external fracture criterion[3, 4].

CZMs incorporate a cohesive strength and finite work to fracture in the description of material behavior, and allow simulation of near-tip behavior and crack propagation. The concept of "cohesive failure" is illustrated in Figure 1, in which a *cohesive zone*, along the plane of potential crack propagation, is present in front of the crack tip. Within the extent of the cohesive zone, the material points which were identical when the material was intact, separate to a distance Δ due to influence of high stress state at the crack tip vicinity. The cohesive zone surface sustains a distribution of tractions T which are function of the displacement jump across the surface Δ, and the relationship between the traction T and separation Δ is defined as the constitutive law for the cohesive zone surface.

CZMs can be categorized into two major groups: intrinsic and extrinsic. In the intrinsic CZM (as employed in the numerical example), the traction T first increases with increasing interfacial separation Δ, reaches a maximum value δ, then decreases and finally vanishes at a characteristic separation value δ_c, where complete decohesion is assumed to occur. In contrast, the extrinsic CZM does not display the initial ascending branch of the curve. A brief discussion on the characteristics of each model is presented in Section 3.

The CZM approach has the promise of simulating fracture process where cracking occurs spontaneously. The fracture path and speed become natural outcome of the simulation rather than being specified *ad hoc* or *a priori*. In this paper, a novel cohesive zone model developed for FGMs[6] is adopted to simulate dynamic crack growth in FGMs.

2 NUMERICAL SCHEME

This section briefly outlines the essential components of the numerical scheme, namely, the FEM framework incorporating CZM, the dynamic updating scheme and the material gradation.

To incorporate a CZM into the numerical scheme for dynamic fracture, the *cohesive element* is developed and positioned along the potential path or region of crack propagation, and attached to the

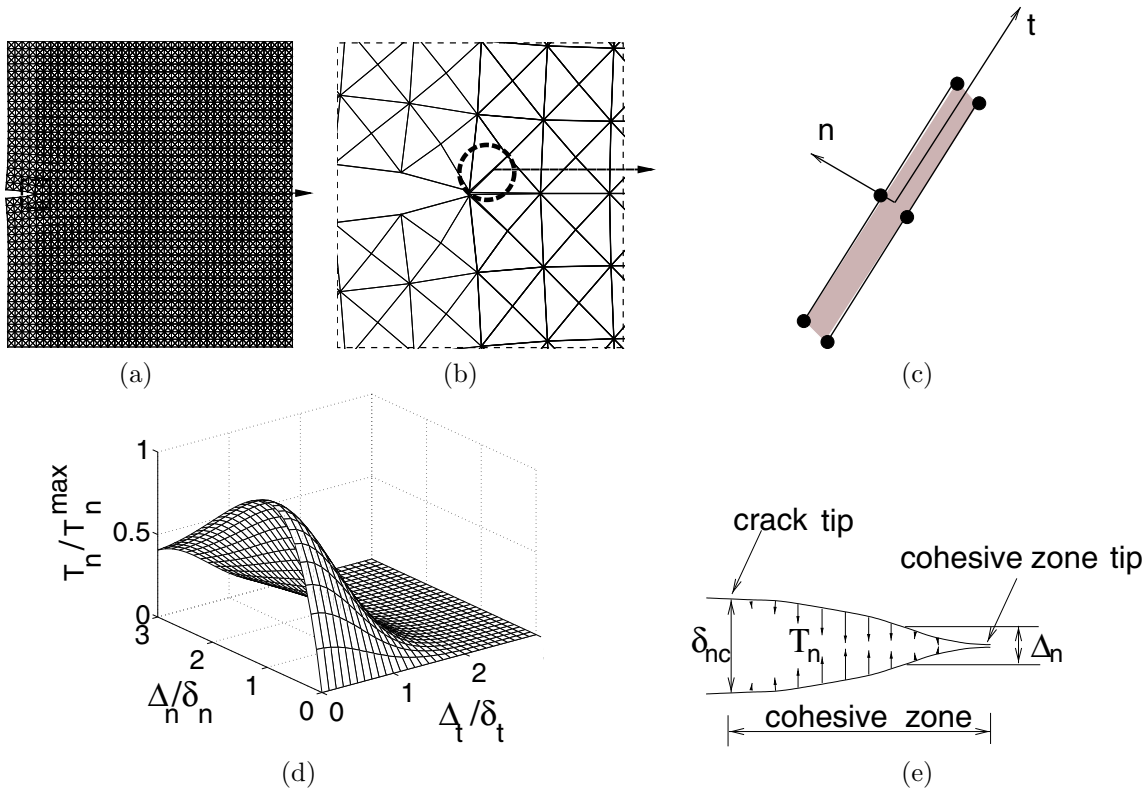

Fig. 1: Schematic representation of cohesive zone model concept; (a) A plate containing crack; At potential crack propagation path *e.g.*, as circled in (b), cohesive element is inserted, as shown in (c), which follows the specified cohesive zone model shown in (d) for normal traction; (e) cohesive zone in Mode I case.

volumetric elements, which follows a cohesive *traction-separation* relationship as shown in Figure 1. In contrast, the conventional finite element, which is now called "*bulk* element", follows conventional *stress-strain* relationships (continuum description). The constitutive law of cohesive elements is inherently embedded in the finite element model, so that the presence of cohesive elements allows spontaneous crack propagation.

The FEM formulation incorporating cohesive elements is derived from the principle of virtual work, and discretized using the explicit central difference time stepping scheme to update displacements $\mathbf{u}$, accelerations $\ddot{\mathbf{u}}$ and velocities $\dot{\mathbf{u}}$ as follows:

$$\mathbf{u}_{n+1} = \mathbf{u}_n + \Delta t \dot{\mathbf{u}}_n + \frac{1}{2}(\Delta t)^2 \ddot{\mathbf{u}}_n \tag{1}$$

$$\ddot{\mathbf{u}}_{n+1} = \mathbf{M}^{-1}(\mathbf{F} - \mathbf{R}_{int_{(n+1)}} + \mathbf{R}_{coh_{(n+1)}}) \tag{2}$$

$$\dot{\mathbf{u}}_{n+1} = \dot{\mathbf{u}}_n + \frac{\Delta t}{2}(\ddot{\mathbf{u}}_n + \ddot{\mathbf{u}}_{n+1}) \tag{3}$$

where Δt denotes the time step, $\mathbf{M}$ is the lumped mass matrix, $\mathbf{F}$ is the external force vector, $\mathbf{R}_{int}$ and $\mathbf{R}_{coh}$ are the global internal and cohesive force vectors, which are obtained from the contribution of *bulk* and *cohesive* elements, respectively. Large deformation formulation is employed[6].

To treat the material nonhomogeneity inherent in the problem, *graded elements*, which incorporate the material property gradient at the element level, are introduced. In this investigation, the scheme proposed by Kim and Paulino[7] is adopted. The same shape functions are used to interpolate the unknown displacements, the geometry, and the material parameters, and thus the interpolations for material properties (E, ν, ρ) are given by

$$E = \sum_{i=1}^{m} N_i \; E_i, \qquad \nu = \sum_{i=1}^{m} N_i \; \nu_i, \qquad \rho = \sum_{i=1}^{m} N_i \; \rho_i \tag{4}$$

where N_i are the standard shape functions.

3 INTRINSIC VERSUS EXTRINSIC COHESIVE ZONE MODELS

The distinction between intrinsic and extrinsic CZMs is the presence of initial elastic curve, as shown in Fig. 3. Intrinsic CZMs assume that, *e.g.* in pure tension case, traction T_n first increases with increasing interfacial separation Δ_n, reaches a maximum value T_n^{max}, then decreases and finally vanishes at a characteristic separation value δ_n, where complete decohesion is assumed to occur. On the other hand, extrinsic CZMs assume that separation only occurs when interfacial traction reaches the finite strength T_n^{max}, and once the separation occurs, the interfacial cohesion force monotonically decreases as separation increases.

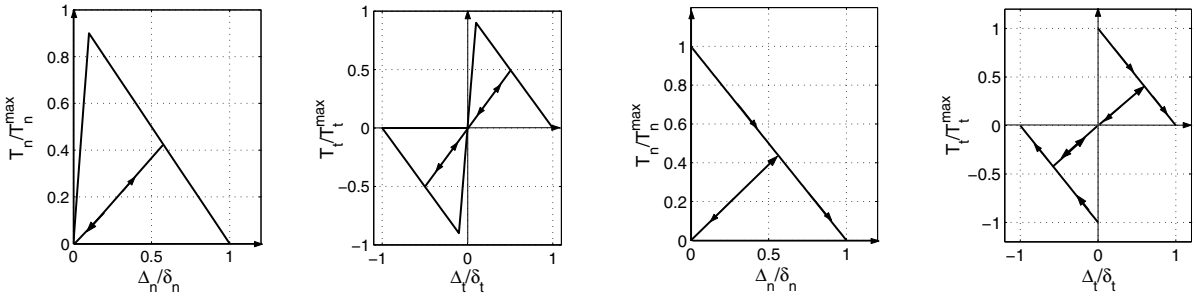

(a) (b)

Fig. 2: Comparison of two typical intrinsic and extrinsic CZMs: (a) bilinear intrinsic cohesive zone model[5] in pure tension and pure shear, respectively; (b) initially-rigid extrinsic cohesive zone model[4] in pure tension and pure shear, respectively.

A brief comparison of the two types of CZMs (intrinsic and extrinsic) is summarized as follows:

- The *Intrinsic* model requires that all cohesive elements be embedded in the discretized structure at the beginning of simulation, and the mesh connectivity remains unchanged during the whole simulation process.
- The *Intrinsic* model allows easy implementation, however, it introduces artificial compliance depending on the area of cohesive element surfaces introduced and the cohesive element property. If the crack grows along a pre-defined path, the adverse effect is relatively minor, while for simulations involving cohesive element inserted in a large area, the result can be (highly) non-convergent for different mesh discretizations. Moreover, this approach usually necessitates adoption of very high cohesive strength, e.g., $T_n^{max} = E/10$ (which is not physical for macroscopic, *i.e.* engineering-scale, applications).
- For *extrinsic* models, cohesive elements are adaptively inserted into the mesh. This usually requires complicated mesh updating schemes for the modified mesh by renumbering nodes and elements.
- *Extrinsic* models avoid the artificial compliance effect, which is present in intrinsic models. The critical fracture stress adopted is usually much lower than that used in intrinsic models. For example, in their work, Camacho and Ortiz[4] used a value around $T_n^{max} = E/600$.

The above observations are made in general regarding the *intrinsic* and *extrinsic* models (not confined to the two models illustrated in Fig 3). Different types of CZMs within each group are developed based on various considerations, and one may have certain advantage over the other for specific problems. For example, the above bilinear CZM has an adjustable initial slope, which provides the user more control on the artificial compliance than a model with fixed initial slope. Some of these issues were addressed in more detail in the work by the authors[6], where mesh convergence studies were carried out for both cracks along pre-defined path and cracks along arbitrary path.

4 COHESIVE ZONE MODEL FOR FGMS

We propose a new FGM cohesive zone model [6], which is a combination of the models by Xu and Needleman[3] and Jin *et al.*[8]. It avoids effective quantities and thus uses the actual quantities to describe the relationship between normal traction-separation and tangential traction-separation.

Assume that the energy potential of each individual material phase takes the exponential form[3]:

$$\phi_i(\boldsymbol{\Delta}) = \phi_{ni} + \phi_{ni}\exp\left(-\frac{\Delta_n}{\delta_{ni}}\right)\left\{\left[1 - r_i + \frac{\Delta_n}{\delta_{ni}}\right]\frac{(1-q_i)}{(r_i-1)} - \left[q_i + \frac{(r_i-q_i)}{(r_i-1)}\frac{\Delta_n}{\delta_{ni}}\right]\exp(-\frac{\Delta_t^2}{\delta_{ti}^2})\right\} \quad (5)$$

in which superscripts i ($i = 1, 2$) denote the two individual material phases (*e.g.*, metal and ceramic respectively), and parameters $\boldsymbol{\Delta} = [\Delta_n, \Delta_t]$ denote the displacement jump across the cohesive surface in normal and tangential directions. Other parameters in the expressions that respectively refer to material phase i are explained hereby without subscript notation: parameters ϕ_n and ϕ_t are the energies required for pure normal and tangential separation, respectively; δ_n and δ_t are the critical opening displacement for normal and tangential separation, which are related to the cohesive normal strength $T_n^{\max}$ and tangential strength $T_t^{\max}$ as

$$\phi_n = eT_n^{\max}\delta_n, \qquad \phi_t = \sqrt{e/2}T_t^{\max}\delta_t, \quad (6)$$

where $q = \phi_t/\phi_n$, and r is defined as the value of Δ_n/δ_n after complete shear separation with $T_n = 0$.

The cohesive traction force vectors associated with material phases 1 and 2 in the 2-D case comprise traction in normal and tangential directions as $\mathbf{T}_1 = [T_{n1}, T_{t1}]$, $\mathbf{T}_2 = [T_{n2}, T_{t2}]$, and can be derived directly from the energy potentials as

$$\mathbf{T}_1 = -\partial\phi_1/\partial\boldsymbol{\Delta}, \qquad \mathbf{T}_2 = -\partial\phi_2/\partial\boldsymbol{\Delta}. \quad (7)$$

The resulting normal and shear traction components are illustrated in Figure 3 (a).

Let $\mathbf{T}_{\mathrm{FGM}} = \left[T_n^{\mathrm{FGM}}, T_t^{\mathrm{FGM}}\right]$ denote the traction force vector across the cohesive surfaces of a two-phase FGM, which comprises normal and tangential traction force components. The cohesive traction $\mathbf{T}_{\mathrm{FGM}}$ is approximated by the following volume fraction based formula

$$\mathbf{T}_{\mathrm{FGM}}(\mathbf{x}) = \frac{V_1(\mathbf{x})}{V_1(\mathbf{x}) + \beta_1[1 - V_1(\mathbf{x})]}\mathbf{T}_1 + \frac{1 - V_1(\mathbf{x})}{1 - V_1(\mathbf{x}) + \beta_2 V_1(\mathbf{x})}\mathbf{T}_2 \quad (8)$$

where the parameter $V_1(\mathbf{x})$ denotes volume fraction of the material phase 1, while β_1 and β_2 are two cohesive gradation parameters that describe the transition of failure mechanisms from pure material phase 1 to pure material phase 2, and should be calibrated with experimental data. Figure 3 (b) compares the normal traction-separation laws for two material constituents.

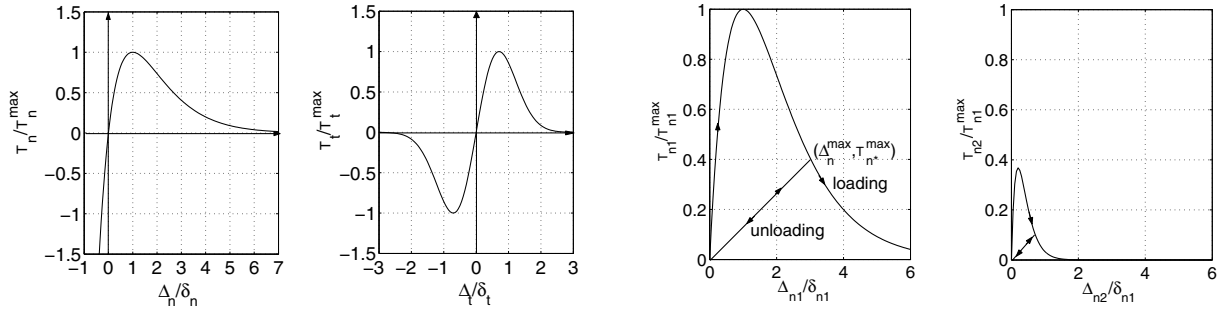

Fig. 3: (a) Exponential cohesive zone model[3] in pure tension and pure shear; (b) cohesive zone model in pure tension case, for two material phases with strength ratio $T_{n2}^{max}/T_{n1}^{max} = 0.35$, and critical displacement ratio $\delta_{n2}/\delta_{n1} = 0.15$, where δ_{ni} denotes normal separation at peak normal traction for material i.

5 NUMERICAL EXAMPLE

In this section, a test example is provided to illustrate the application of the cohesive model introduced above to both homogeneous and FGM systems through investigation of dynamic crack branching phenomenon for a plane strain plate containing an initial central crack subjected to tensile velocity loading.

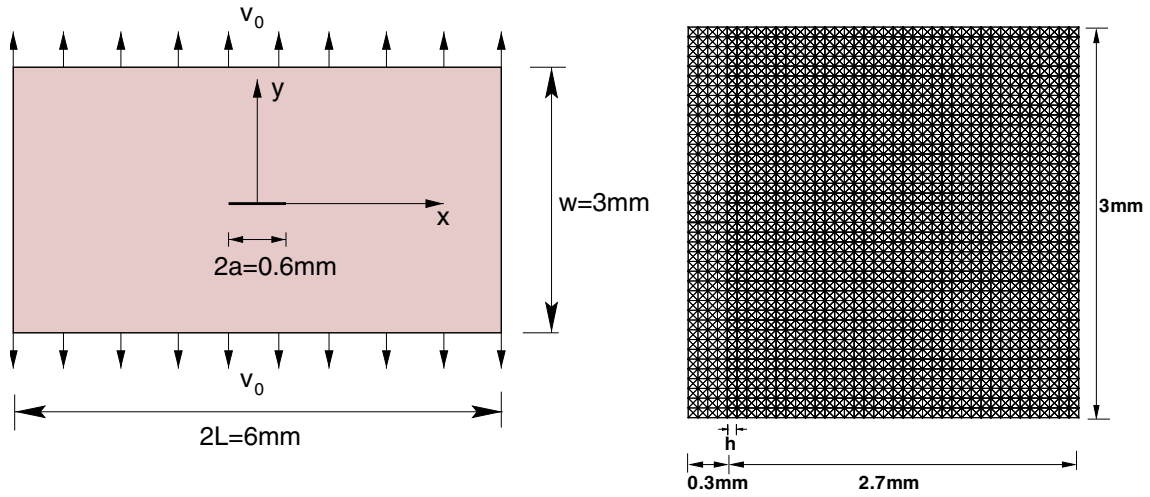

(a) (b)

Fig. 4: Branching problem; (a) geometry and boundary conditions of a plate containing a central crack subjected to velocity loading; (b) Mesh descretization of the dynamic branching problem with half of the original geometry modelled due to symmetry along the y axis.

5.1 Problem Description

The computation is carried out for a center cracked rectangular plate as shown in Figure 4 (a). Symmetric velocity loading $v_0 = 5m/s$ is applied along the upper and lower surfaces. To explore the influence of material gradation on crack branching patterns, three material gradation profiles are studied, as listed in Table 1: *case 1*: both the bulk and cohesive properties are considered for homogeneous materials; *case 2*: hypothetical "FGM", with homogeneous bulk material and linearly graded cohesive properties along y direction. *case 3*: FGM with both the bulk and cohesive properties linearly graded in y direction.

Due to symmetry of the geometry, material gradation and loading condition with respect to y axis, only the right half of the geometry is modelled for the numerical simulation, along with proper boundary condition to account for the symmetry at $x = 0$. The domain is discretized with 40 by 40 quads each divided into 4 T3 elements, as depicted in Figure 4 (b). Cohesive elements are inserted inside a rectangular region right to the initial crack, as shown with the thicker lines. The other material parameters for the CZM are: $q = 1, r = 0, and\ \beta_1 = \beta_2 = 1$.

Table 1: Three material gradation profiles for plate containing central crack.

	y position	E (GPa)	ν	ρ (kg/m^3)	G_{Ic} (N/m)	$T_{\max}$ (MPa)	δ_c (μm)
case 1: homog.	$-1/2W$ to $1/2W$	3.24	0.35	1190	352.3	324	0.4
case 2: graded T_{max}	$1/2W$	3.24	0.35	1190	528.4	486	0.4
	$-1/2W$	3.24	0.35	1190	176.1	162	0.4
case 3: graded E & T_{max}	$1/2W$	4.86	0.35	1190	528.4	486	0.4
	$-1/2W$	1.62	0.35	1190	176.1	162	0.4

5.2 Results for Various Material Gradation Profiles

Case 1: homogeneous PMMA material. Symmetric branch pattern is obtained (Figure 5 (a)). The crack begins to branch at $a_{branch} = 1.05mm$, and further branches occur when the cracks approach the edge. Although crack branching can only take place either parallel to the coordinate axes or at $\pm 45°$, the overall branching angle is less than $45°$ from the x axis. In the example, the overall branching angle is about $29°$, calculated by approximating the main branch as a straight line.

Case 2: Variation of cohesive strength. In this example, the cohesive strength T_{max} is lower at the bottom surface and higher at the top surface, which means weaker fracture resistance at the lower region. Therefore, the crack branching is expected to be more significant at the lower part of the plate,

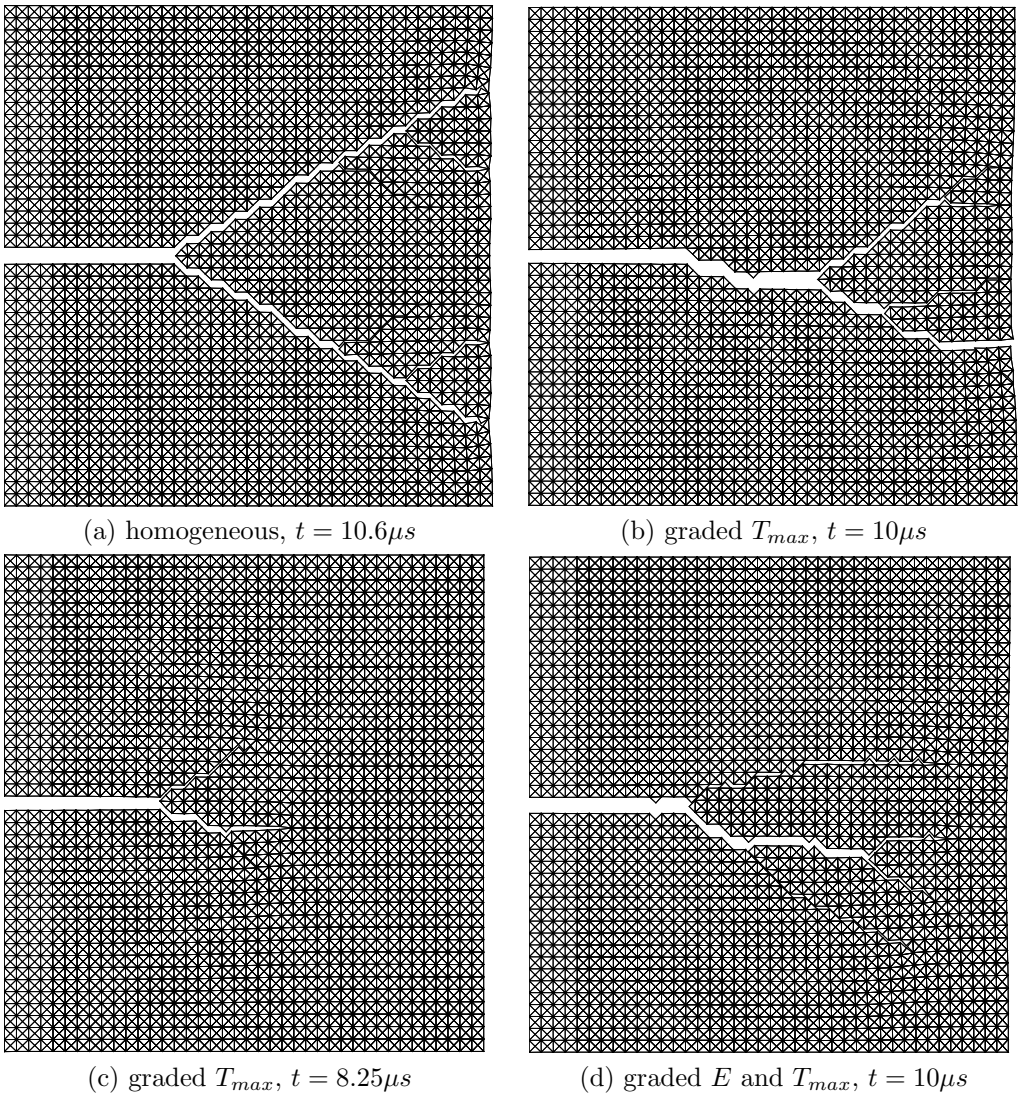

(a) homogeneous, $t = 10.6\mu s$ (b) graded T_{max}, $t = 10\mu s$

(c) graded T_{max}, $t = 8.25\mu s$ (d) graded E and T_{max}, $t = 10\mu s$

Fig. 5: Crack branch pattern for various material gradation profiles; loading velocity at $v_0 = 5m/s$; (a) final crack pattern at $t = 10.6\mu s$ for homogeneous plate (case 1); (b) final crack pattern at $t = 10\mu s$ for graded plate (case 2); (c) attempted crack branching at $t = 8.25\mu s$ for graded plate (case 2); (d) final crack pattern at $t = 10\mu s$ for graded plate (case 3).

as shown in Figure 5(b). The initial crack branching location is roughly the same as the homogeneous case (*cf* Figure 5(c)). As the lower region of the plate is weaker in resisting fracture, the crack branch towards the lower region dominates, and shields the upward one from developing further.

Case 3: Graded bulk and cohesive properties. In this example, both bulk and cohesive properties vary linearly in y direction. On one hand, the weaker cohesive resistance favors the crack branching into the $y < 0$ region. On the other hand, stress developed in the stiffer region ($y > 0$) is higher than that at the compliant region, which may promote the crack branching into the $y > 0$ region. These two mechanisms compete with each other in influencing crack branching pattern. The final crack pattern is plotted in Figure 5 (d).

6 CONCLUSIONS

This paper presents a numerical scheme incorporating CZM to investigate dynamic fracture behavior of homogeneous and FGMs under dynamic loading. Two basic types of elements are employed in the present investigation: *graded* elements in the bulk material, and *graded intrinsic cohesive* elements to model fracture. Discussion on the *pros* and *cons* of the *intrinsic* and *extrinsic* CZMs are also presented.

Xu and Needleman[3] model was extended to treat FGMs, which eliminates the dependence upon effective quantities, and may provide certain advantages when mixed-mode effect is prominent.

As illustrated in the study, the cohesive element approach is promising for modeling generalized fracture without predefined external fracture criteria. Further numerical issues, including the artificial compliance introduced in the system by incorporating cohesive elements, were studied and related results reported in a recent publication by the authors[6].

REFERENCES

[1] Paulino, G.H., Jin, Z.-H., Dodds Jr., R.H. (2003), *Failure of Functionally Graded Materials", Encyclopedia of Comprehensive Structural Integrity*, Ed Karihaloo, B. et al. Elsevier, Amsterdam, 2, pp. 607-644.

[2] Erdogan, F. (1995), "Fracture mechanics of functionally graded materials", Composites Engineering 5, pp.753-770.

[3] Xu, X. and Needleman, A. (1995), "Numerical simulations of dynamic crack growth along an interface", International Journal of Fracture 74, pp. 289-324.

[4] Camacho, G. T. and Ortiz, M. (1996), "Computational modeling of impact damage in brittle materials", International Journal of Solids and Structures 33, pp. 2899-2938.

[5] Geubelle, P.H. and Baylor, J. (1998), "Impact-induced delamination of laminated composites: a 2D simulation", Composites Part B Engineering 29, pp. 589-602.

[6] Zhang, Z. and Paulino, G. H. (2005), "Cohesive zone modeling of dynamic failure in homogeneous and functionally graded materials", International Journal of Plasticity 21, pp. 1195-1254.

[7] Kim, J.H. and Paulino, G. H. (2002), "Isoparametric graded finite elements for nonhomogeneous isotropic and orthotropic materials" ASME Journal of Applied Mechanics, 69, pp. 502-514.

[8] Jin, Z.-H., Paulino, G.H. and Dodds Jr., R.H. (2002), "Finite element investigation of quasi-static crack growth in functionally graded materials using a novel cohesive zone fracture model". ASME Journal of Applied Mechanics, 69, pp. 370-379.

A PARTICLE MODEL FOR COHESIVE FRICTIONAL MATERIALS

Gian Antonio D'Addetta & Ekkehard Ramm
Institute of Structural Mechanics
University of Stuttgart
70550 Stuttgart, Germany
email: eramm@statik.uni-stuttgart.de, web page: http://www.uni-stuttgart.de/ibs/members/ramm

Keywords: Discrete Element Method, Geomaterials, Homogenization, Gradient Model, Micropolar Model, Continuum with Microstructure

Abstract. *Different discrete element models (DEM) for the simulation of cohesive geomaterials like concrete, ceramics or marl will be presented. Starting from a basic polygonal two-dimensional DEM model for non-cohesive granular materials, more complex models for cohesive materials are obtained by inclusion of beam or interface elements between corresponding particles. The last step in the series of increasing complexity is the realization of a microstructure-based simulation environment which utilizes the enhanced DEM models. With growing model complexity a wide variety of failure features of geomaterials can be represented. A validation of these discrete models with regard to qualitative and quantitative aspects enriches the plan of the paper. Thereby, extracts of the extensive simulation program are reported in order to clarify the respective subject matter.*

1 INTRODUCTION

A steadily increasing interest in a preferably exact description of geomaterials demonstrates in a formidable manner that the modeling of these materials still poses a challenge to the research community, as it was since ancient times. The research is driven, on one hand, by the natural endeavor to find an optimal exploitation of the load capacity of engineering structures and, on other hand, to advance the design of new artificial geomaterial-based materials. The last point parallels the developments in neighboring engineering disciplines like aeronautical- and space technology or mechanical engineering. These artificial materials combine the advantages of their constituents, while compensating their disadvantages. Two examples are high strength and textile reinforced concrete. From a physical point of view geomaterials like concrete, ceramics or marl can be considered as cemented granulates forming a heterogeneous macroscopic solid. In order to predict the remaining load capacity after reaching the ultimate load a substantiated knowledge of the underlying failure mechanisms is essential. For example, this knowledge may be based on micromechanical observations.

The failure mechanisms of geomaterials are characterized by complex failure modes and, furthermore, they show a highly anisotropic bias due to their inhomogeneous microstructure. The growth and coalescence of microcracks in cohesive geomaterials lead to the formation of macroscopic crack patterns. Finally, this results in a fragmentation into separate particle clusters forming a solid-granulates mix. Behaving quasi-brittle under load these materials are characterized by a localization of deformations in narrow zones, as shown for concrete in tension in figure 1 (a) or the biaxial failure of marl according to (Marcher 2002) in figure 1 (b). Since localization phenomena like cracks or shear bands occur, the material cannot be treated as continuous in the usual manner. If fracture and fragmentation of the solid occurs, the creation and continuous motion of the evolving crack surfaces apparently represent discontinuous phenomena and are difficult to handle. Therefore, most continuum models, and in particular those ones based on continuum damage mechanics, cannot account for the discrete nature of material failure in a natural way and need some extension, confer (Kuhl 2000). Alternatively, discrete particle models like discrete element methods (DEM) have been developed. As the name DEM suggests, a solid is replaced by a discontinuous particle composite which allows for a detachment of bonds between particles (if initially present) and a re-contact of open surfaces. In order to simulate and quantify the full range of geomaterials from non-cohesive ones like sand to cohesive ones like concrete, ceramics or rock, starting from the pioneering work by (Cundall and Strack 1979) different types of discrete element models have been elaborated, see (Cundall 2001) for a recent review. Starting with a basic polygonal two-dimensional DEM model for non-cohesive granular materials, more complex models for cohesive materials are obtained by inclusion of beam or interface elements between corresponding particles. As the quantification of previously presented beam enhanced DEM models is an arduous task, see (Kun and Herrmann 1996a; Kun and Herrmann 1996b; Kun et al. 1999; D'Addetta et al. 2001; D'Addetta

(a)  (b) 

Figure 1: (a) Failure mechanism of concrete in tension and (b) marl under biaxial loading (courtesy of (Marcher 2002)).

et al. 2002), the standard (non-cohesive) version of the DEM model, see (Tillemans and Herrmann 1995), is augmented by interface elements between the particle edges. The formulation and numerical implementation of this interface enhanced DEM model is presented in detail. Tension and compression simulations of cohesive quadratic particle composites are utilized to validate the model. The next step is the realization of a microstructure-based simulation environment which utilizes the foregoing enhanced DEM models, confer (D'Addetta 2004). The microstructure can be included, if different properties of the cohesive components (beam or interface) are assigned with respect to their position, i. e. inside the matrix, inside the aggregate and between aggregate and matrix. With growing model complexity a wide variety of failure features of geomaterials can be represented. Furthermore, the inclusion of an artificial microstructure which regards for stiffer aggregates embedded in a less stiffer matrix enables a coherent quantification of the model.

In a parallel line, homogenization techniques have been introduced which allow to relate microscopic quantities, like the contact forces and displacements, to corresponding macroscopic quantities, like stresses and strains, confer (D'Addetta 2004; D'Addetta et al. 2002; D'Addetta et al. 2004; Ehlers et al. 2003). The development and numerical implementation of adequate homogenization approaches by means of a micro to macro transition from the particle to the macro level supplements the formal definition of the DEM models. Homogenization procedures have been developed which allow for a transfer from a simple Boltzmann continuum based particle model to a more complex continuum with microstructure, see (D'Addetta 2004) for a detailed overview. The numerical realization of the transitions towards enhanced continuum theories like micropolar, see (D'Addetta et al. 2002; D'Addetta et al. 2004; Ehlers et al. 2003), and gradient models, see (D'Addetta 2004), is verified from a micromechanical viewpoint. The quantities of the micro or particle scale are linked to comparable continuum mechanical quantities on the macro scale and, thus, average dynamic and kinematic quantities are derived. Starting point of these homogenization approaches is the argument of scale separation between the characteristic scales of a particle assembly, namely that of a macroscopic body, a representative volume and an individual particle. Use of these arguments yields simplified equilibrium conditions for a representative volume element (RVE) on an intermediate scale. For brevity, no details concerning this topic are given here. Interested readers are referred to the noted literature.

The paper is organized as follows: Section 2 provides a brief outline of the theoretical background of a standard (non-cohesive) form of the DEM model supplemented by a discussion on the modeling of cohesion within particle models. In section 3 the extension to an interface enhanced DEM model along with some representative simulation results is sketched. Afterwards, section 4 presents the formulation of a microstructure-based DEM environment which utilizes the interface enhanced model according to section 3. Again, simulation results are used to validate the proposed method. We conclude with a summary of the attained insights and an outlook on future perspectives.

2 STANDARD DEM MODEL

The starting point of our DEM model development is a two-dimensional DEM code with convex polygonal particles based on the work of (Kun and Herrmann 1996a; Kun and Herrmann 1996b) and (Tillemans and Herrmann 1995). As this standard DEM model has been presented elsewhere in more detail, see the references above or (D'Addetta et al. 2001; D'Addetta et al. 2002; D'Addetta 2004), the model is only briefly outlined here.

2.1 Outline of the Model

The individual particles can be considered as rigid bodies. They are not breakable and not deformable, but they can overlap when pressed against each other. Three degrees of freedom, two translational and one rotational

one, are assigned to each particle center, confer figure 2 (a). The local deformational behavior of the particles is approximated by an elastic repulsive force related to the overlapping area of contacting particles, grey shaded in figure 2 (a). The contact force is decomposed with respect to the local coordinate system of the contact zone

$$\mathbf{f}^c = f_n^c\,\mathbf{n} + f_t^c\,\mathbf{t}\,. \tag{1}$$

The normal and tangential components of the contact force vector $\mathbf{f}^c$ are defined by

$$f_n^c = -\frac{E_p A_p}{d^c} - m_{eff}\gamma_n v_{rel,n}\,, \qquad\qquad f_t^c = -\min\left(m_{eff}\gamma_t\,|v_{rel,t}|\,,\mu\,|f_n^c|\right)\,. \tag{2}$$

The coefficients γ_N and γ_T refer to the viscous dissipative damping and μ is chosen according to Coulomb's friction law. Thereby, for $\mu > 0$ the present scheme allows for a non associated plasticity law, as schematically shown in figure 2 (b) for three characteristic situations. If the grey shaded flow surface is left as for force point ③, the force state is reflected back in vertical direction onto the surface confined by the Coulomb criterion μf_n^c. E_p denotes the elastic modulus of the particles and A_p the overlapping area of two contacting polygons. This overlap represents up to some extent the local deformation of the polygons, comparable with the Hertzian contact law for spherical particles. The relative velocity at the contact zone, the effective mass and the characteristic length of the contact region of two contacting particles i and j are given by

$$\mathbf{v}_{rel} = \mathbf{v}_j - \mathbf{v}_i\,, \qquad\qquad m_{eff} = \frac{m_i m_j}{m_i + m_j}\,, \qquad\qquad \frac{1}{d^c} = \frac{1}{d_i} + \frac{1}{d_j}\,. \tag{3}$$

d_i and d_j define the diameters of circles of equivalent areas as the polygons i and j. The forces and resulting moments are inserted into the equations of motion, which are solved numerically for each particle with the aid of the Gear-Predictor-Corrector time integration scheme, confer (Allen and Tildesley 1987). The dynamical basis of the DEM implies the solution of the equation of motion at discrete time steps $t + \Delta t$ for each particle i of all particles N within the sample. For each individual particle i one obtains

$$\mathbf{M}_i\,\ddot{\mathbf{x}}_i = \mathbf{f}_i + \mathbf{g}_i\,, \qquad \text{with} \qquad \mathbf{M}_i = \begin{bmatrix} m_i & 0 & 0 \\ 0 & m_i & 0 \\ 0 & 0 & \theta_i \end{bmatrix} \qquad \text{and} \qquad \mathbf{f}_i = \sum_{j=1}^{n_p} \mathbf{f}_{ij}^p\,. \tag{4}$$

$\mathbf{M}_i$ represents the diagonal generalized mass matrix and $\ddot{\mathbf{x}}_i$ the generalized acceleration of particle i. m_i describes the mass of polygon i (translational degrees of freedom) and θ_i describes the mass moment of inertia of polygon i (rotational degree of freedom). $\mathbf{f}_i$ in equation (4) stands for all interaction forces between two contacting particles and $\mathbf{g}_i$ specifies the gravitational forces of the same particle. In the case of a simple (non-cohesive) particle contact $\mathbf{f}_i$ is expressed by equation $(4)_3$, i. e. this generalized force vector contains solely contact forces. Thereby, n_p denotes the number of particle contacts of a particle i. Cohesive forces, as introduced in the coming sections will be simply added on the right hand side of equation (4).

The application of this basic (non-cohesive) DEM model has proven to be capable to qualitatively picture the behavior of cohesionless granular materials like sand. The localization of shear bands along with the formation of complex failure pattern was studied by means of dense and porous samples and reflected experimental observations in an astonishing manner. More information on the applied model can be found in (D'Addetta et al. 2001; D'Addetta et al. 2002) and descriptive simulation results on cohesionless particle samples can be found in (D'Addetta 2004; D'Addetta et al. 2004; Ehlers et al. 2003).

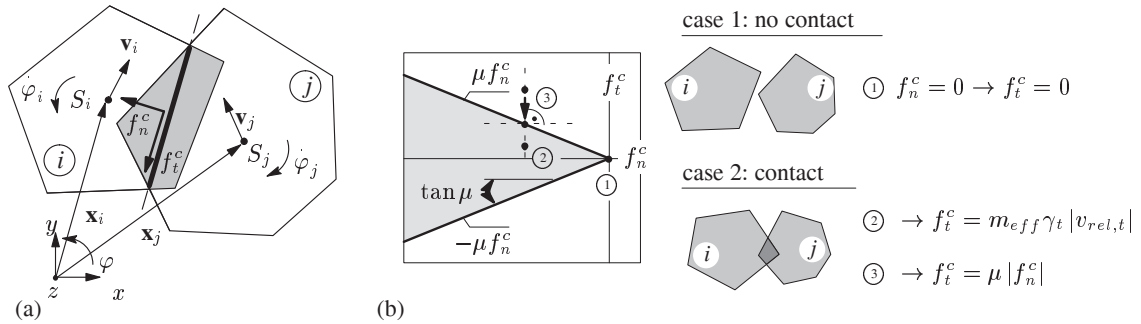

Figure 2: (a) Geometry of the contact and (b) interpretation of contact force logic in terms of plasticity law.

2.2 Discussion of Cohesion Modeling

The model presented so far allows for the application to non-cohesive granular materials like sand, stone or rock heaps, but also vegetables. Admittedly, most geomaterials are more or less cohesive. Therefore, a model is demanded which is capable to describe this kind of materials and represent cohesion. In other words, attractive forces between particles are necessary to bond these particles together to some extent. Usually, the physical effect of cohesion is limited for tension.

Several ways of incorporating cohesion into particle models are feasible. The implementation strongly depends on the chosen particle shape and problem class: The easiest way in the case of circular particles is the introduction of attractive potentials like in molecular dynamics (MD). In this regard, the most prominent law that accounts for attractive action between particles is the Lennard-Jones potential adopted from physical chemistry, see among others the description in (Allen and Tildesley 1987). Another way, only reasonable for circular particles, is based on an extension of the Hertz contact law for "negative" overlaps. An implementation is rather straightforward as the primary geometric variable defining the contact of circles is the distance between the particle centroids, see e. g. (Donzé and Magnier 1995). In contrast to circles, the geometric definition of polygonal particles in contact is by far more complex. This is the case since more than one geometric variable describing the contact and the position of the individual bonded edges is involved. The distinction between a point contact (circles) and line contact (polygons) must be drawn. Therefore, alternative options have to be considered. Two different approaches that account for cohesive bonds between two polygon edges have been implemented in the present DEM model: In the first approach beam elements between the centers of mass of neighboring particles are introduced and constitute a beam enhanced DEM model. This approach will not be given in detail here as it was extensively discussed in the past, see (Kun and Herrmann 1996a; Kun and Herrmann 1996b; Kun et al. 1999; D'Addetta et al. 2001; D'Addetta et al. 2002). The simulation results with a beam enhanced DEM model show that the general failure behavior of cohesive frictional materials like concrete is qualitatively very well represented. In particular, the beam enhanced DEM model is capable of simulating typical inherent failure mechanisms of cohesive geomaterials. Furthermore, it has proven to be very well suited for a visualization of these mechanisms which are technically difficult to observe in experiments. Admittedly, a realistic softening behavior cannot be obtained in the simulations, due to the included breaking law of the beam elements, i. e. the failure appears mostly brittle in the context of normalized load-displacement diagrams. So far the qualitative picture of the beam enhanced model is satisfactory, but the quantification remains still a demanding task. As an alternative, we introduce an interface enhanced DEM model where continuous interfaces along common particle edges represent the bonding component. The next section will be dedicated to this topic.

3 INTERFACE ENHANCED DEM MODEL

In order to represent the cohesion between particles in a DEM model, an approach borrowed from FE-technology is adopted, see (D'Addetta 2004) for more details. It makes use of so-called interface elements that are directly defined at the particle edges. In that, the model is made more complex: Instead of simple elastic beams with an oversimplified brittle failure law as in earlier versions of this DEM model, see the references in the previous section, more elaborate interface elements with a popular constitutive law on the basis of the plasticity theory are used here. The realization of this interface enhanced model is influenced by a former work of (Vonk 1992) and follows the plasticity formulation introduced therein. The motivation to use this material law in the context of the DEM follows the principle that a proven and established macroscopic material law may be at least much that successful in modeling the failure on a smaller scale as in a continuum model. Apparently, this approach pictures the real physics involved in the debonding process of bonded granulates far better than the beam enhancing approach.

A variety of models for the representation of the interaction between the constituents of two- and more-phase particle composites via interface elements have been proposed since the late 1960's. The works by (Goodman et al. 1968) and (Ngo and Scordelis 1967) have been pioneering as they were among the first ones to introduce discontinuities into numerical models in the context of the FEM either as continuous or lumped interface elements. On the one hand, lumped interface elements evaluate a force-relative-displacement constitutive relation at a nodal point. Insofar, to a certain extent they exert a similar behavior as simple springs. No further assumptions with regard to tractions and relative displacement distributions across the interfaces are made. On the other hand, the formulation of continuous interface elements (line, plane or shell type) implies a continuous relative displacement field and a traction-relative displacement constitutive relation. Following these lines interface elements have been the focus of intensive studies in the context of FEM.

3.1 Basic Idea

The interface layer is regarded as infinitely thin in the initial stage. Since the particles are undeformable by definition, use is made of the key assumption that the deformation of the interface is constrained to be linear. In

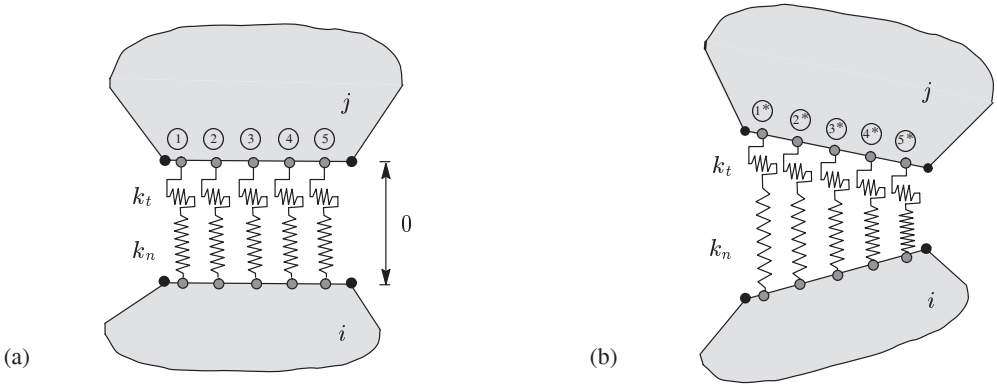

Figure 3: Idealization of interface in (a) undeformed stage and in (b) deformed stage.

analogy to the previously introduced beam model this fact represents the Bernoulli-hypothesis of a planar cross-section to some extent. The interface can be discretized and is represented in a lumped sense by a fixed number of normal and tangential spring sets with stiffnesses k_n and k_t. These springs are attached along the common edge of two initially bonded particles i and j, as shown in figure 3 (a). The current location of start and end points of the springs relative to the bond are initially fixed and evaluated after each time step. It is important to note that the interface shown in figure 3 (a) has a visible initial thickness for visualization reasons only. Ongoing relative motion of the particles leads to a finite value of relative deformation for each spring, i. e. overlapping of particles and, thus, contraction of springs (negative relative deformation) is also allowed. The relative deformation of the bonds is represented by the extension and contraction of the springs, as indicated in figure 3 (b). As further assumption the numerical integration of the constitutive law of the spring sets, which are noted integration points in the sequel, yields an approximated stepwise constant stress distribution over the edge. This procedure compares that for the computation of stress resultants in beams. The constitutive law used throughout this chapter is a non-associated Mohr-Coulomb type softening plasticity model defined by two yield surfaces according to (Vonk 1992) and is discussed in more detail in section 3.2. A failure, or more precisely detachment, of the bonds is achieved, if all integration points of the interface layer are completely softened. It should be kept in mind that no extra contact force according to equation (1) is created, as long as a bond between two particles exists. This means that once the bond is completely detached, a "standard contact" according to section 2 is assumed to control the interaction between two particles. The forces evaluated in the integration points can be combined to a bond force vector and transferred to the mass centers of the involved particles, thus, giving rise to a moment. The bond force vector then takes the form $\mathbf{f}^{bond} = [f_x^{bond} \quad f_y^{bond} \quad m^{bond}]^T$ and enters the equation of motion. Therefore, the generalized interaction force vector in equation (4) is reformulated

$$\mathbf{f}_i = \sum_{j=1}^{n_p} \mathbf{f}_{ij}^{p} + \sum_{k=1}^{n_{bond}} \mathbf{f}_{ik}^{bond}. \tag{5}$$

Additionally to n_p, noting the number of particle contacts of a particle i, n_{bond} denotes the overall number of existing bonds of a particle i.

3.2 Mohr-Coulomb plasticity model

The principal ingredients of a plasticity formulation are the yield condition, the flow rule and the hardening law (if needed), compare (Jirásek and Bažant 2001). In the present context the basic idea of a strain-driven formulation from classical plasticity is straightforwardly transferred to a "relative displacement-driven" formulation. The actual state of the spring set is determined by the total relative displacement $\mathbf{u}$, the plastic relative displacement $\mathbf{u}^p$ and the softening variable κ. Here, the range of validity is restricted to small strains and, following the above logic, small relative displacements. Hence, an additive elastic-plastic split of the relative deformation $\mathbf{u}$ of one spring set is admissible

$$\mathbf{u} = \mathbf{u}^e + \mathbf{u}^p \qquad \text{with} \qquad \mathbf{u} = \begin{bmatrix} u_n \\ u_t \end{bmatrix}. \tag{6}$$

The stress-relative deformation law for the elastic part yields

$$\boldsymbol{\sigma}^{tr} = \boldsymbol{\sigma}^0 + \mathbf{K}^{bond} \cdot \mathbf{u} \qquad \text{with} \qquad \mathbf{K}^{bond} = \begin{bmatrix} k_n & 0 \\ 0 & k_t \end{bmatrix}, \tag{7}$$

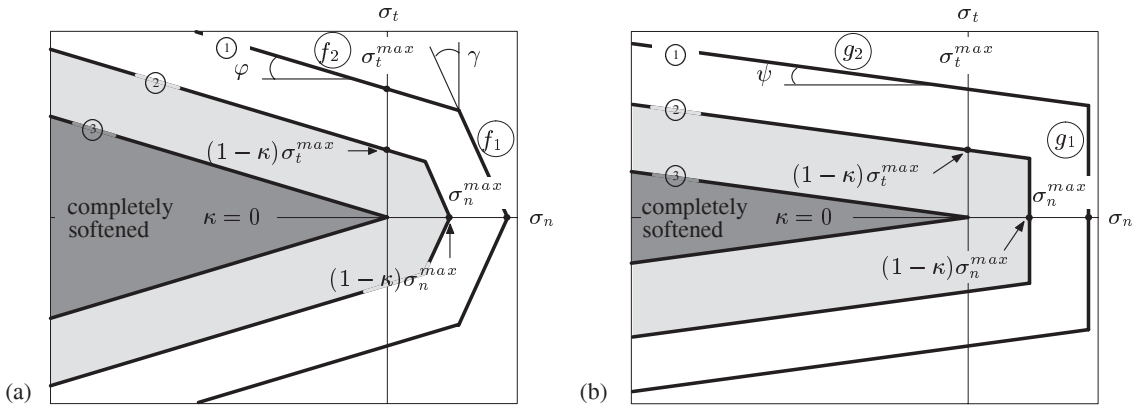

Figure 4: (a) Failure surface and (b) plastic potential of interface constitutive law in biaxial stress plane.

where $\boldsymbol{\sigma}^{tr}$ is the trial stress state, that may lie outside the flow surface f. k_n and k_t represent the normal and tangential spring stiffnesses. The flow rule is denoted by

$$\dot{\mathbf{u}}^p = \dot{\lambda}\,\mathbf{g}(\boldsymbol{\sigma}, \kappa) \tag{8}$$

with the plastic multiplier $\dot{\lambda}$. $\mathbf{g}(\boldsymbol{\sigma}, \kappa)$ represents the direction of the plastic flow and depends upon the fact whether an associated or non-associated flow rule is included. Since associated flow rules for pressure-sensitive materials like geomaterials are often unrealistic a non-associated one is used, i. e. the direction of plastic flow is prescribed by the gradient of the plastic potential g in the form $\mathbf{g}(\boldsymbol{\sigma}, \kappa) = \partial g / \partial \boldsymbol{\sigma}$. In general, plastic flow occurs if the yield function $f(\boldsymbol{\sigma}, \kappa)$ and its derivative both vanish: $f = 0$ and $\dot{f} = 0$. The consistency condition $\dot{f} = 0$ then yields

$$\left[\frac{\partial f}{\partial \boldsymbol{\sigma}}\right] \dot{\boldsymbol{\sigma}} - h\dot{\lambda} = 0 \qquad \text{with} \qquad h = -\left[\frac{\partial f}{\partial \kappa}\right] \left[\frac{\partial \kappa}{\partial \mathbf{u}^p}\right] \cdot \left[\frac{\partial g}{\partial \boldsymbol{\sigma}}\right], \tag{9}$$

where h expresses the hardening parameter. Further elaboration, including a combination of equations (6) to (9) results in a relation between stress and relative displacement rates and, finally, in the corrected stress state $\boldsymbol{\sigma}$ along with the plastic multiplier $\dot{\lambda}$

$$\boldsymbol{\sigma} = \boldsymbol{\sigma}^{tr} - \underbrace{\frac{f(\boldsymbol{\sigma}^{tr}, \kappa)}{-\left[\frac{\partial f}{\partial \kappa}\right] \left[\frac{\partial \kappa}{\partial \mathbf{u}^p}\right] \cdot \left[\frac{\partial g}{\partial \boldsymbol{\sigma}}\right] + \left[\frac{\partial f}{\partial \boldsymbol{\sigma}}\right] \cdot \mathbf{K}^{bond} \cdot \left[\frac{\partial g}{\partial \boldsymbol{\sigma}}\right]}}_{\dot{\lambda}} \mathbf{K}^{bond} \cdot \left[\frac{\partial g}{\partial \boldsymbol{\sigma}}\right]. \tag{10}$$

The procedure in equation (10) operates as a one-step return mapping algorithm, so that no iteration is needed. However, a simple one-step algorithm that yields an explicit solution for the corrected stress state is only possible if linear yield surfaces, linear plastic potentials and linear softening evolution laws are chosen. The bracket terms in equation (10) are either of scalar or vectorial order.

The initial behavior of the spring sets is assumed to be linear elastic and to depend on the spring constants k_n and k_t. Therefore, no coupling of the springs in the elastic regime is assumed. The softening of a spring set starts when the stress state $\boldsymbol{\sigma} = [\sigma_n \;\; \sigma_t]^T$ reaches the yield surface that in the present context could be viewed as a failure surface. The initial failure surface in the biaxial stress plane is given in figure 4 (a) by graph ① and is symmetric with respect to the normal stress. Since the failure mechanisms dominated by shear and tension differ substantially in geomaterials, it is advisable to model them separately. This implies the bounding of the elastic domain by two distinct failure surfaces, usually termed two- or in the general case multi-surface plasticity. Indeed, this does not substantially change the treatment presented above for one single surface, except the singularities in the failure surface at the segue of different failure surface segments, i. e. a unique flow direction cannot be specified. The solution of this problem has been treated by (Koiter 1953) or (de Borst 1987), confer (D'Addetta 2004) for more details. In short, in analogy to equation (8) the flow rule

$$\dot{\mathbf{u}}^p = \dot{\lambda}_1 \frac{\partial g_1}{\partial \boldsymbol{\sigma}} + \dot{\lambda}_2 \frac{\partial g_2}{\partial \boldsymbol{\sigma}} \tag{11}$$

is adapted to capture the flow directions defined by the two plastic potentials along with the essential constraints $\dot{\lambda}_1 \geq 0$ and $\dot{\lambda}_2 \geq 0$.

In the present case the failure surface resembles a two-surface Mohr-Coulomb type plasticity criterion. The tensile failure is governed by $\sigma_n^{max} > 0$ and an angle γ which define the yield surface f_1. Whereas the shear failure is

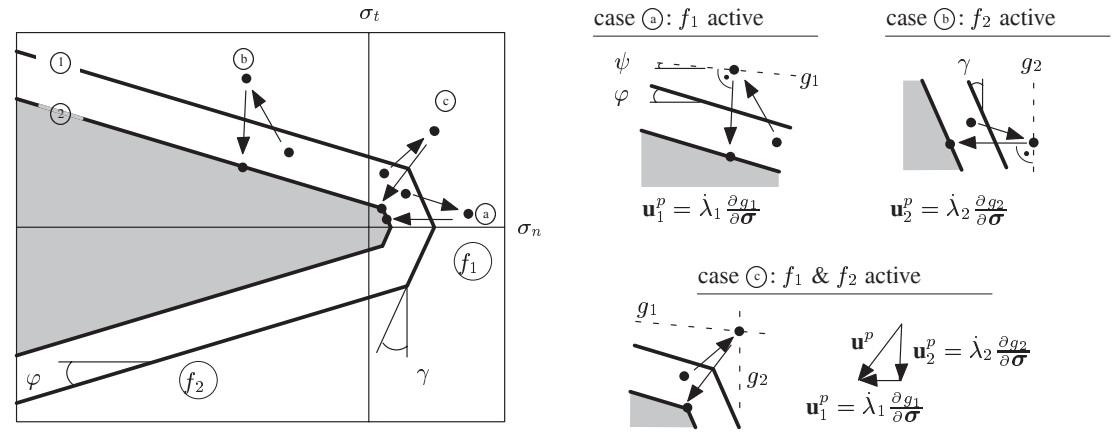

Figure 5: Representation of return mapping algorithm.

controlled by a classical Mohr-Coulomb failure envelope with cohesion $\sigma_t^{max} > 0$ and friction angle $\varphi > 0$ which define the yield surface f_2. In the compressive regime (for negative σ_n) the trapezoidal or triangle (in the final state) formed by the flow surfaces is open, as no failure is possible in pure compression. With ongoing softening the failure surface shrinks to an intermediate stage (② in figure 4 (a)) and ends up on the classical Mohr-Coulomb failure surface without any cohesion $\sigma_t = 0$ and tension limit $\sigma_n = 0$, expressed by ③ in figure 4 (a). The functional representation of the failure surfaces is given by

$$f_1 = \sigma_n + \sigma_t \tan\gamma - (1-\kappa)\sigma_n^{max} \leq 0\,, \qquad f_2 = \sigma_n \tan\varphi + \sigma_t - (1-\kappa)\sigma_t^{max} \leq 0\,. \tag{12}$$

In order to describe a non-associated plasticity along the lines of the two-surface formulation, two plastic potential surfaces are introduced:

$$g_1 = \sigma_n - (1-\kappa)\sigma_n^{max} = 0\,, \qquad g_2 = \sigma_n \tan\psi + \sigma_t - (1-\kappa)\sigma_t^{max} = 0\,. \tag{13}$$

The plastic potential surfaces are also symmetric with respect to the normal stress, as visualized in figure 4 (b). Figure 5 represents the one-step return mapping algorithm based on equation (10) in more detail for the following three different cases: Yield surface f_1 active (case ⓐ), yield surface f_2 active (case ⓑ) and combined activation of yield surfaces f_1 & f_2 (case ⓒ). Starting from an elastic or plastic stress state $\boldsymbol{\sigma}^0$, an elastic predictor step yields a non valid trial stress state outside of the yield surface $\boldsymbol{\sigma}^{tr}$. The following plastic corrector step towards the yield surface in direction of the perpendicular to the plastic potential results in a valid stress state on the yield surface $\boldsymbol{\sigma}$. As explained above, the special case of a projection in the influence area of the corner (case ⓒ) is treated by a linear combination of both directions. Graph ① in figure 5 denotes the yield surface at the start of the step and graph ② that one at the end of the step. The representation includes a shrinking of the yield surface from ① to ② due to softening.

The softening of the spring set is described by the parameter κ which represents the actual state of damage: κ ranges from 0 in the undamaged state to 1 in the fully damaged state. The softening behavior is driven by the plastic deformation u_n^p and u_t^p of the spring sets in form of predefined fracture energies $G_{f,n}$ and $G_{f,t}$. In the case of a two-surface plasticity this involves two different softening evolutions for tension and shear either, see figure 6 (a) and (b). Pure tensile softening ends after a fracture energy $G_{f,n}$ has been released and pure shear softening ends after a fracture energy $G_{f,t}$ has been released. In the decoupled case, i. e. if only one mechanism is active, the softening variable for the tensile and shear loading is defined by

$$\kappa = \frac{1}{u_n^{max} - u_n^*} u_n^p\,, \qquad \kappa = \frac{1}{u_t^{max} - u_t^*} u_t^p\,, \tag{14}$$

with $u_n^* = \sigma_n^{max}/k_n$ and $u_t^* = \sigma_t^{max}/k_t$, see figure 6. The plastic part of the deformation starts at u_n^* and u_t^*. These evolutions are coupled in that, both tensile strength σ_n^{max} and cohesion σ_t^{max} decrease at the same time and at the same rate. This yields an isotropic shrinkage of the failure surfaces, as shown in figure 4 (a). A simultaneous tensile and shear softening is treated as linear combination of both, as depicted in figure 6 (c). Therefore, the definitions in equation (14) are formally coupled

$$\kappa = \frac{1}{u_n^{max} - u_n^*} u_n^p + \frac{1}{u_t^{max} - u_t^*} u_t^p \leq 1\,. \tag{15}$$

By definition, in combined softening u_n^p is solely determined by the plastic deformation due to tensile loading (surface 1 - f_1 & g_1) and not by the normal part of the plastic shear deformation. For this reason, the dilatant

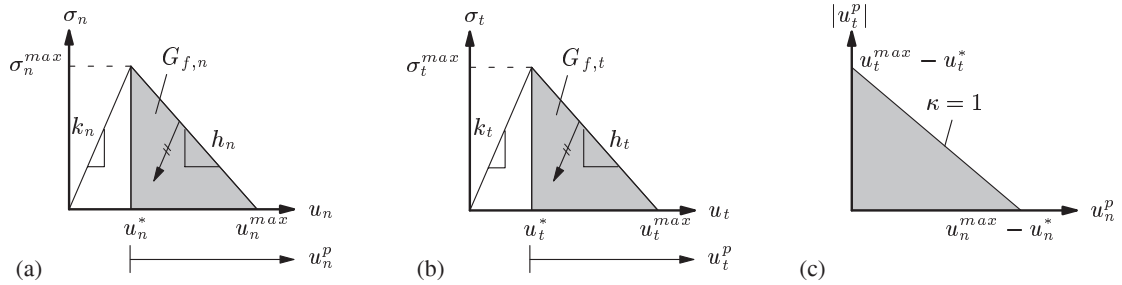

Figure 6: (a) Evolution law for tensile, (b) shear and (c) combined softening.

behavior with shear loading does not influence the softening since it is physically not justified in combined softening. The predefined fracture energies for mode I and II softening enter the above equations through the integral expression of the graphs in figure 6 (a) and (b). This formalism may be interpreted in the sense of the cohesive crack concept, see e. g. (van Mier 1997), where the crack opening is replaced by the components of the plastic relative displacement. The evolution laws of the normal and tangential stresses

$$\sigma_n(u_n^p) = \sigma_n^{max}\left(1 - \frac{u_n^p}{u_n^{max} - u_n^*}\right), \qquad \sigma_t(u_t^p) = \sigma_t^{max}\left(1 - \frac{u_t^p}{u_t^{max} - u_t^*}\right), \tag{16}$$

are inserted into the conditional equations of the fracture energies

$$G_{f,n} = \int_0^{u_n^{max}-u_n^*} \sigma_n(u_n^p)\,\mathrm{d}u_n^p = \frac{1}{2}\,(u_n^{max} - u_n^*)\,\sigma_n^{max}\,,$$

$$G_{f,t} = \int_0^{u_t^{max}-u_t^*} \sigma_t(u_t^p)\,\mathrm{d}u_t^p = \frac{1}{2}\,(u_t^{max} - u_t^*)\,\sigma_t^{max}\,.$$

3.3 Numerical realization

The numerical realization of the plastic interface model in the context of the DEM model is a straightforward task. Each spring set is described by the material law and along each common edge a fixed number of spring sets, termed integration points, are chosen. From there, it is important to define a reference edge where the corresponding relative displacement-force law is evaluated. Different possibilities are feasible: One way is the definition of the reference line in between the bonded edges by connecting the midpoints of the deformation vectors of the bond, as shown in figure 7 (a). Admittedly, the length of the reference line is generally smaller than the bond width h and induces a more demanding numerical treatment as the alternative approach which is followed here and shown in figure 7 (b): One bond is chosen as reference edge and the local coordinate system with the normal vector $\mathbf{n}$ is fixed along this bond. Particle i can be considered as the master and the other one as the slave particle. For this case, the relative deformation of the start and end point of the reference edge are split up into a normal and tangential part. The normal and tangential relative deformation distribution between the start and end point of the reference edge are linearly approximated. The actual complete relative deformation $\mathbf{u}$ is evaluated at each integration point and is processed in an incremental format $\Delta\mathbf{u}$ by subtracting the complete relative deformations of two successive time steps. The straightforward implementation of the elastic predictor step for the calculation of the trial stress state in equation (7) implies the determination of the spring forces at

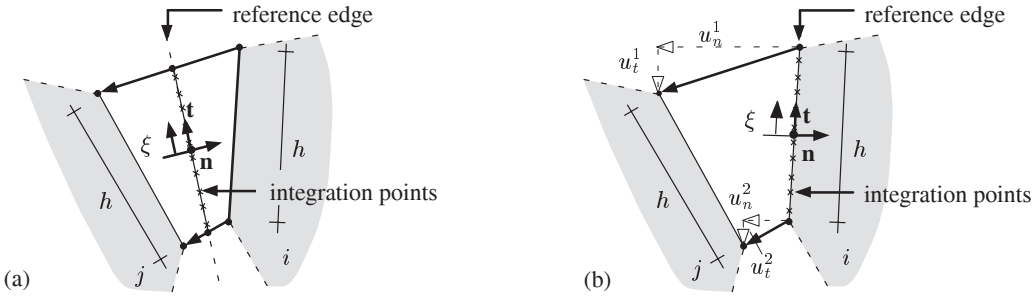

Figure 7: Numerical integration - Two different possibilities of definition of reference edge.

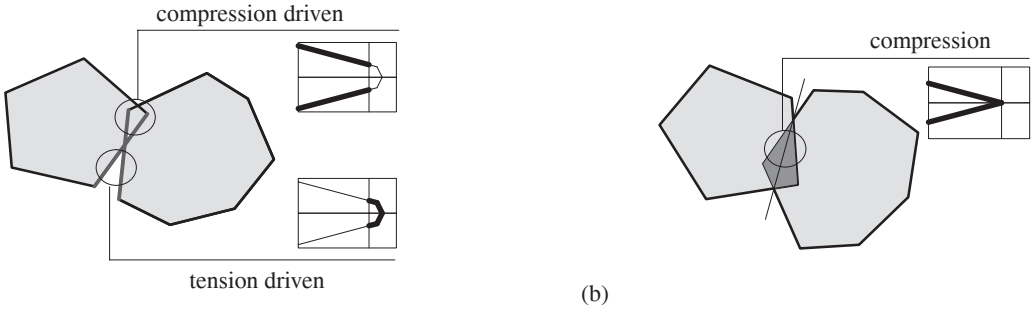

Figure 8: Difference between interface and particle contact: (a) Deformed situation (interface activated) and (b) after complete interface failure (activation of contact).

each integration point k of the bond

$$f_{n,k}^{tr}(\xi) = \frac{1}{n_{ip}} \left[f_{n,k}^{old}(\xi) + k_n \Delta u_{n,k}(\xi) \right] , \qquad f_{t,k}^{tr}(\xi) = \frac{1}{n_{ip}} \left[f_{t,k}^{old}(\xi) + k_t \Delta u_{t,k}(\xi) \right] . \tag{17}$$

n_{ip} denotes the number of integration points along the reference edge and is fixed for all polygon's bonds. The position of the integration point k is determined in the local coordinate system by the normalized coordinate ξ ranging from $[-1, 1]$. In order to evaluate the yield conditions $f_{1/2}(\boldsymbol{\sigma}^{tr}(\xi), \kappa^{old}(\xi)) \leq 0$ in equation (12) the local stresses at each integration point are computed

$$\sigma_n^{tr}(\xi) = \frac{f_n^{tr}(\xi)}{h/n_{ip}} , \qquad \sigma_t^{tr}(\xi) = \frac{f_t^{tr}(\xi)}{h/n_{ip}} . \tag{18}$$

If the yield surfaces $f_{1/2}$ are left, a plastic corrector step is necessary. Therefore, the type of back projection mode (determination which yield surface/s is/are active) has to be evaluated. Equation (10) yields the corrected stress state at the integration point. Afterwards, an a-posteriori check is performed, because it cannot completely be excluded that erroneously a corner regime is predicted, although this is actually not the case. This behavior may appear, as the final position of the yield surface is not known a-priori, see (de Borst 1987). In particular, for stress states in the influence region of the corner a transition from a tensile to a shear state may be obtained. Thereafter, the corresponding forces at the integration points are calculated via an inversion of equation (18). The new forces, the actual relative deformation and the state of softening are saved as history variables for the next time step. All forces along a bond are summed up and transferred to the center of the master particle giving rise to a moment. A force and moment with the same absolute values are applied to the slave particle. An interface is detached or eliminated, if at all integration points of this interface the softening is completed, i. e. $\langle \kappa \rangle = 1$ according to

$$\langle \kappa \rangle = \frac{1}{h} \int_{-1}^{1} \kappa(\xi) \, \mathrm{d}\xi = \frac{1}{n_{ip}} \sum_{k=1}^{n_{ip}} \kappa(\xi_k) . \tag{19}$$

When the softening at all integration points has reached its limit, the bond is detached. A standard contact as described in section 2.1 is assumed whenever two initially bonded particles with broken bond come again into contact, see the schematic figure 8, i. e. no re-introduction of interfaces is applied.

3.4 Numerical results

The interface enhanced DEM model is involved in the simulation of standard loading setups. The structured validation of this model, first, on the integration point level and, second, by simple loading setups of quadratic rows with a thickness of one particle are presented elsewhere, see (Vonk 1992) and (D'Addetta 2004). As these preliminary test programs have been successful, larger samples with variable particle shapes are simulated in uniaxial tension and compression.

Tension simulations

As mentioned earlier, a parameter identification of the beam enhanced DEM model parameters with respect to a quantification of the load-displacement behavior of geomaterials is not convincing at all. The following examples will highlight that the bond description via interfaces is capable to represent the softening not only in very simple tests, as shown before, but also in the context of standard experiments. The softening behavior is investigated by means of a comparative study of rectangular plates with the width 40 cm and a variable height of 10 cm ①, 20 cm ②, 30 cm ③, 40 cm ④, 64 cm ⑤ and 72 cm ⑥. Thus, the amount of included particles ranges from 400 to 2880. First, the results of a uniaxial tension simulation are presented. The specimens are vertically loaded under

constant strain rate conditions by applying the load in a strain driven format via a constant increase of the velocity of the particles at the top and bottom of the plate. Thereby, we follow the procedure firstly described in (Potapov et al. 1995), as it ensures that disturbing initial dynamic effects are reduced to a tolerable level, see the discussion by (Kun et al. 1999). The parameters and material properties of the model have been chosen in order to obtain results that are as close as possible to experimental results obtained from the literature. However, only limited information on the "real" values of the bond strength and the corresponding softening behavior is available in the literature. Therefore, no attempt was undertaken to fit the material parameters more closely than needed.

Uniaxial tension experiments by (Evans and Marathe 1968) as well as (van Mier 1997) are considered for a quantitative comparison. The normal and tangential stiffness of the interfaces are chosen as $k_n = 1200$ kN/cm^2 and $k_t = 360$ kN/cm^2. Moreover, the density was chosen as $\rho = 2.5$ g/cm^3 and the time step as $\Delta t = 5 \cdot 10^{-7}$ s. The shape parameters of the plasticity model are $\varphi = 26.6°$, $\gamma = 10°$ and $\psi = 0°$, except the maximum yield stress $\sigma_n^{max} = \sigma_t^{max} = 0.12$ kN/cm^2 and the softening parameters $G_{f,n} = 5.94 \cdot 10^{-4}$ kN/cm^2 and $G_{f,t} = 2.98 \cdot 10^{-3}$ kN/cm^2. The yield stresses for each interface are statistically distributed around ± 10 % the average value defined above. Parameters of the contact model according to section 2 like those concerning the viscous damping and friction are set to zero ($\gamma_N = 0$, $\gamma_T = 0$, $\mu = 0$) and the contact stiffness to $E_p = 100$ kN/cm^2. The stress-strain curves for the six simulations ① to ⑥ are plotted in figure 9 (a) along with the experimental results by (Evans and Marathe 1968), which are included as a grey shaded band. It becomes clear that the stress-strain relation is a non-objective measure of the softening, i. e. the longer the specimen the steeper is the post-peak behavior. Nevertheless, the normalized load-displacement relations in figure 9 (a) generally elucidate the transition from a linear relation to a horizontal tangent up to a complete overall softening of the sample. The stresses are measured in the form of a normalized load as ratio of the reaction force of the boundary particles and the specimen width. The strain is measured via a determination of the ratio of the actual length and the initial length of the specimen. The mesh/length dependence of the strain is one of the main reasons why data of tension tests (of experimental as well as simulation nature) is typically displayed by a stress or load vs. crack width diagram in the literature. The axial deformation is evaluated in a comparable format as in experiments by a measuring device of fixed length $l_{me} = 5$ cm for all simulations. This means that not the elongation of the complete specimen, but the extension of a fixed area of the specimen containing the macroscopic crack is evaluated. The extension of this fixed area compares to the crack width Δw, see the inset of figure 9 (b). Thus, if a stress-Δw diagram is plotted, all curves coincide and the softening effect is the same regardless of the height of the sample, compare figure 9 (b). Moreover, these results have been compared with experimental results in the form of the stress-average-crack opening diagram of a concrete with a maximum aggregate size $d_{max} = 1.6$ cm according to figure 3.49 of (van Mier 1997). The numerical results fit qualitatively as well as quantitatively well the experimental ones. However, the height of the tail in the softening region could not completely be recast, as the stress drops below the experimental value in the later simulation stages. In the experiments still a considerable stress transfer is obtained in the later softening regime. The reason for this is quite conceivable and can be traced back to the maximum size of aggregates contained within a sample. Moreover, following the discussion in (van Mier 1997) this behavior is an indirect effect of crack face bridging which provides a crack toughening mechanism. In order to enclose the feature of crack face bridging and a corresponding stress transfer even in a later softening stage, one may include a distinct microstructure which for example regards for stiffer aggregates embedded in a less stiffer matrix. This path will be followed in the next section. An alternative concept takes into account a higher dispersion of bond stiffness and/or yield stresses.

A cutout of the deformed sample ④ in figure 10 at four different time steps ⓐ, ⓑ, ⓒ and ⓓ according to the

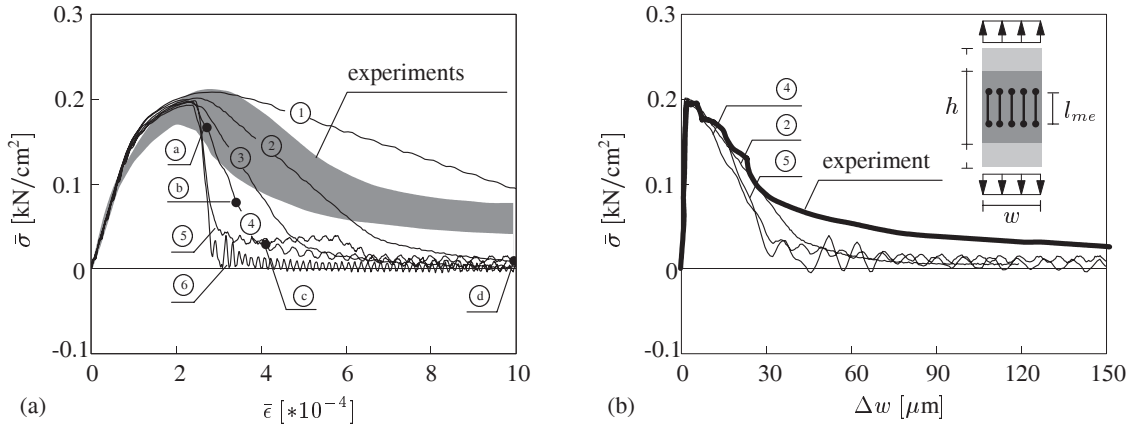

Figure 9: (a) Stress-strain and (b) stress-displacement diagram of tension test.

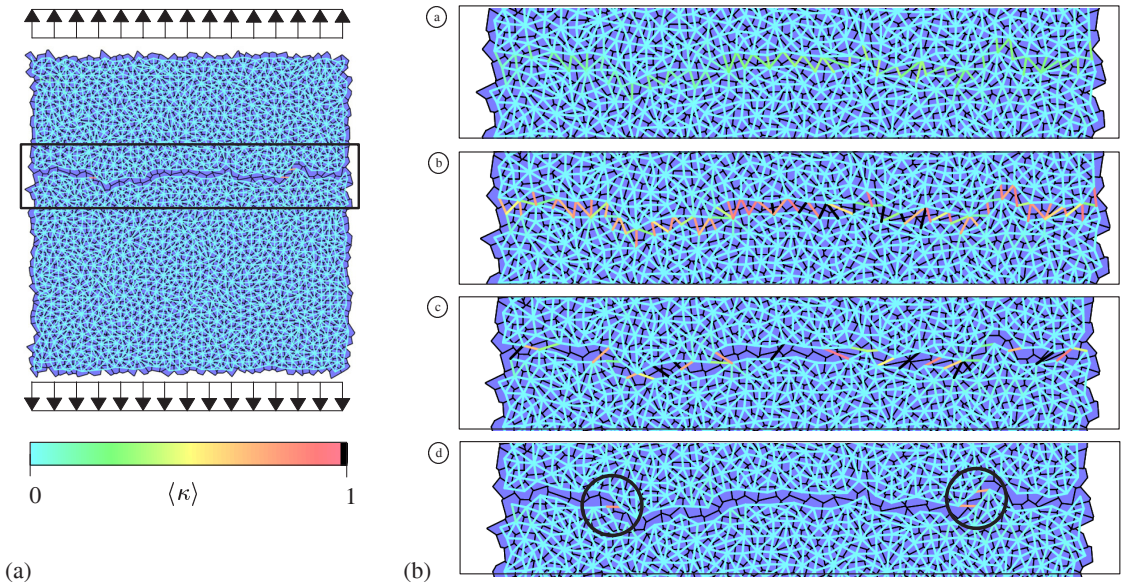

Figure 10: Simulation output in the post-peak regime: (a) Final stage ⓓ and (b) detail of macroscopic crack of stages ⓐ to ⓓ.

stress-strain curve in figure 9 (a) emphasizes the distinct macroscopic crack opening as well as the evolution of softening. The bonds are represented by a line between the respective particles. The scale defines the transition from a non-softening stage to a fully softened stage just before elimination of the bond (black). The state of softening of the bonds $\langle\kappa\rangle$ in figure 10 (b) is computed based on equation (19) as the average of the softening of all springs (i. e. integration points) representing this bond. One can see that at stage ⓓ the macroscopic crack has completely formed. However, three interfaces positioned perpendicular to the primary load transfer direction (marked by circles) sustain the load and yield a non-vanishing stress of curve ④.

Compression simulations

Next, uniaxial compression tests of plates with different geometries using the same parameter set as for the tension simulation are carried out. Therefore, a similar load setup as discussed before for the tension case but with interchanged loading direction is applied. Different boundary conditions are studied. Here, we will discuss the result of a specimen with an unrestricted boundary which represents a situation with very low friction at the boundary. Therefore, the particles forming the upper and lower boundary of the specimen are completely free to move, e. g. like a loading by teflon platens or platens with brushes. For brevity, the stress-strain diagram and a comparison with experimental result is not given, compare (D'Addetta 2004) for more details. The failure evolution of the unrestricted compression simulation is visualized by means of the output at two time stages ① and ② in figure 11, which capture the situation around peak load. Once again, the bonds between the particles are represented by a line between them. Time stage ① refers to a situation just before the peak and stage ② to a situation after formation of a failure pattern. The gradual development of inclined localization zones, as shown in figure 11 (b) has started long before the peak value is reached and yields a sudden breakdown of the particle composite. This result agrees quite well with the experimental results on cubical specimens by (Vonk 1989; Vonk 1992). However, the softening behavior is less pronounced in compression with respect to the experimental results by Vonk. The simulation output of a restricted sample (high friction case, not given here) resembles the same hourglass failure mode coupled with en-enchelon cracks as observed in simulations with the beam enhanced DEM model in (D'Addetta et al. 2001; D'Addetta et al. 2002; D'Addetta 2004) as well as in experiments.

Note that the additional complexity of the bond description compared to the beam one is accompanied by a higher sensitivity of the parameter choice with respect to the post-peak failure. This implies that the more or less "controlled" failure in compression as obtained with the beam enhanced DEM model, e. g. compare the results in (D'Addetta et al. 2001; D'Addetta et al. 2002; D'Addetta 2004), is not reproducible with the interface enhanced DEM model in the present form. For example, a continuation of the loading after formation of a failure pattern like that presented in figure 11 yields a complete disintegration of the initially bonded particle assembly. Thus, no conical rest pieces as in the experiments, e. g. in the form of fragments composed by bonded particles, remain after complete cracking. In the context of this destabilizing effect the following two points are worth to be further investigated: First, the formulation of the interface model has to be enhanced. For example an inclusion of a physical coherent damping or comparable stabilizing contribution to the interface forces may provide for a stable simulation path in the later post-peak regime. Furthermore, a second, probable reason for

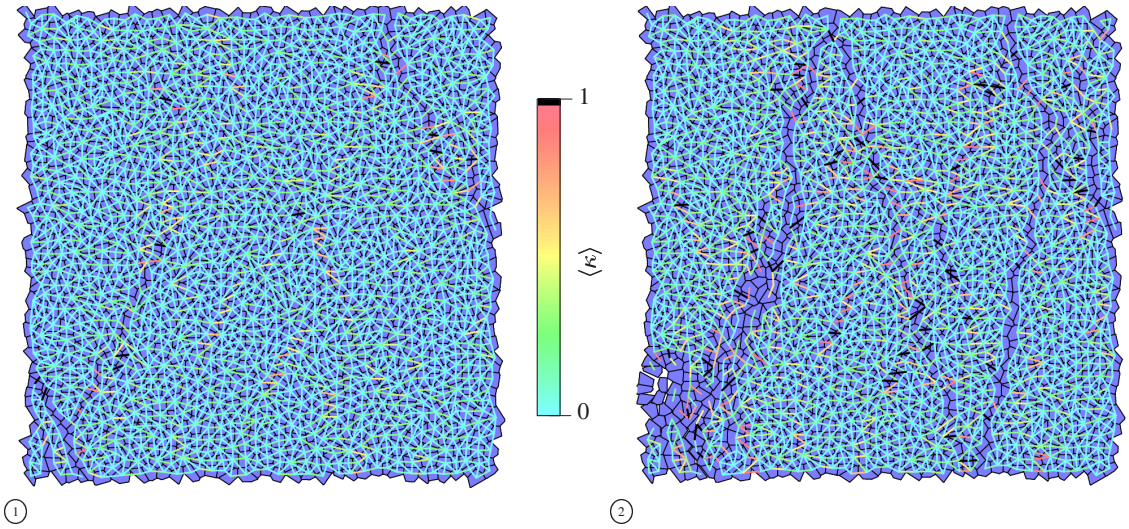

Figure 11: Failure evolution of compression simulation.

the found behavior is the missing rotational resistance of two bonded granulates in the interface enhanced model compared to a consideration of it in the beam enhanced model. There, the rotational resistance is considered via the corresponding stiffness entry in the Timoshenko stiffness matrix and the corresponding rotational breaking parameter. The effect of the rotational resistance inherent within the beam enhanced DEM model has already been emphasized as a basic microdeformation mechanism for the simulation of geomaterials by (Oda and Kazama 1998).

3.5 Discussion of cohesion modeling

Two approaches that account for cohesion between two polygon edges have been implemented in the context of the DEM model according to section 2.1. In the first, rather simplistic approach (not presented in detail here) beam elements between the centers of mass of neighboring particles have been introduced, confer (Kun and Herrmann 1996a; Kun and Herrmann 1996b; Kun et al. 1999; D'Addetta et al. 2001; D'Addetta et al. 2002). As an alternative, a model based on continuous interfaces along common particle edges was proposed in the past section.

The approach based on the introduction of beam elements has shown to be capable to represent most inherent fracture mechanisms of cohesive frictional materials, see the simulation results in (D'Addetta et al. 2001; D'Addetta et al. 2002; D'Addetta 2004). The simulations fit qualitatively well experimental observations. However, the quantification of the corresponding parameters with respect to the output of experiments like stress-strain curves is still unsatisfactory, confer the discussion in (D'Addetta 2004). This is primary due to the choice of the two beam breaking parameters. Although physically plausible from the micromechanical point of view, these parameters cannot be identified with any known (micro) material parameters of geomaterials. Hence, at the present stage, a pure parameter search would end up in a curve fitting without winning any new knowledge on the physics behind it. Anyhow, it should be kept in mind that this model is very well suited for a visualization of typical failure mechanisms appearing in the testing of cohesive geomaterials. The interface enhanced DEM model shows the advantage to picture the real physics involved in the debonding process of bonded granulates far better than the beam enhanced one. However, this is only possible at the expense of a higher computational cost which is required due to the increased complexity of the model and a higher sensitivity of the simulation results with respect to the chosen parameters. The inclusion of the more complex bond representation favors the quantification of the model to experimental results, i. e. the post-peak softening is better reproducible and quantifiable than in the case of the beam enhanced DEM model. Though, still some features like the softening behavior at a later simulation stage in tension as well as a less pronounced softening in compression are to be clarified. Therefore, the complexity of the enhanced DEM model is further enhanced by defining a microstructure-based simulation environment.

4 MICROSTRUCTURE-BASED DEM MODEL

The inclusion of a microstructure is thought to remedy the mentioned "problem" points. This chapter comprises simulations with the interface enhanced DEM model where the particle mesh represents an artificial microstructure. Therefore, stiff macro particles that are composed by an agglomeration of a finite number of particles are embedded in a soft matrix, which is also represented by a composition of particles. In order to include a "real"

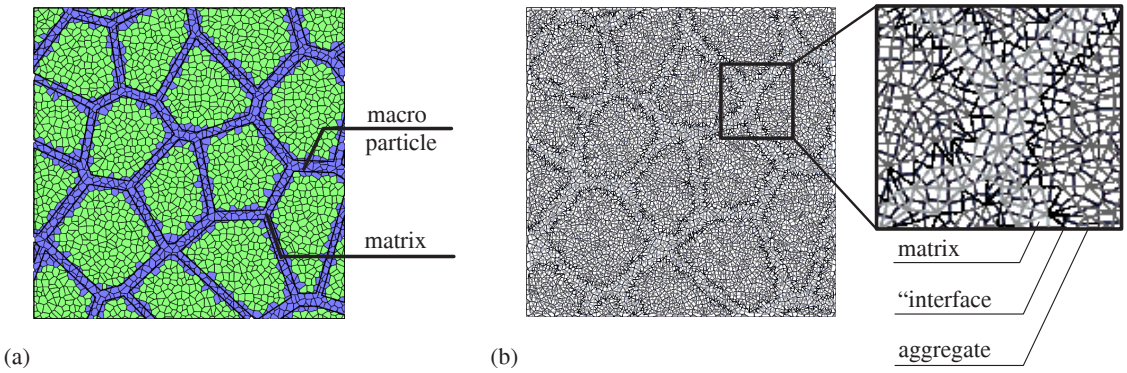

Figure 12: (a) Definition of particle properties (cohesive components suppressed) and (b) definition of properties of cohesive component.

microstructure corresponding digital image processing software has to be connected to the mesh generation module of the DEM program. Since at the present stage an easily realizable implementation is sought, this way is not followed here. Instead, an alternative, approximative implementation is carried out by creating an "artificial" microstructure, see (D'Addetta 2004) for more details. In that, the procedures proposed in in the framework of the FEM by (Carol et al. 1997; Stankowski 1990; Vonk 1992) are principally paralleled, as these publications concern the creation of artificial two-phase materials using polygonal aggregate shapes. Furthermore, the present approach is related to that of (Schlangen and van Mier 1992), see also (van Mier 1997), where circular aggregate particles are generated based on a statistical distribution which is related to grading curves of concrete. Thus, the composition of a real microstructure of concrete-type materials as shown in figures 1 (a) is treated in an approximate and artificial way here. It is not thought that the simulation results based on a "real" and an "artificial" two-phase microstructure differ that much though. First, the procedure applied for the creation of an artificial microstructure is given. Afterwards, we will present simulation results of uniaxial compression and tension load setups and a concluding discussion of the attained insights.

4.1 Generation of a microstructure

The generation of an artificial microstructure is based on the formulation of macro particles, i. e. one macro particle is composed by an accumulation of a finite number of polygonal particles which are denoted as micro particles. An initially created polygon mesh is overlaid by a mesh composed of larger particles. Certainly, as mentioned before, the geometry of a known microstructure, e. g. by means of electron microscopy images, could be included as an overlaying mesh. This option is not considered here, however, is in the realm of possibility in future implementations. Several possibilities to create an overlaying mesh that ought to represent this virtual microstructure are conceivable, see (D'Addetta 2004). After generating a corresponding particle assembly (dense or porous), the particles are scaled down and rotated in a statistical fashion. The scaling down of these (macro) particles by a variable factor is controlled by the desired proportion of aggregate to matrix volume. In order to obtain the overlaying mesh of larger particles the afore mentioned mesh is scaled up. This scaling up depends on the favored size of aggregates. Finally, this mesh is laid over the (underlying) dense particle mesh and represents the pattern for the definition of the macro particles. Based on this information the (micro) particles of the underlying mesh are flagged as being inside or outside the macro particles. The macro particles represent the stiff aggregates and the remaining particles define the matrix. As example the contiguous particles colored in light grey in figure 12 (a) are identified as the macro particles and the particles colored in dark grey as the matrix material. The corresponding cohesive components are classified as follows, compare also the sketch in figure 12 (b): Inside the aggregate (a) (middle grey), inside the matrix (m) (light grey) and defining the "interface layer" between aggregate and matrix (i) (black). This "interface layer" should not be confused with the interface elements used within the interface enhanced DEM model. The first one describes a real material interface layer (between aggregate and matrix), while the last one represents a model interface in form of a component of the enhanced DEM model. Finally, the values of the stiffnesses of the interface element (k_n, k_t), the corresponding fracture law $(\sigma_n^{max}, \sigma_t^{max})$ or both stiffness and fracture law parameters, are chosen accordingly. In order to consider the microstructural properties of a concrete-type material like concrete as best as possible, benefit was made from the extensive knowledge of the group of van Mier. This knowledge comprises the simulation of microstructures via pure beam lattice models starting from the first publication by (Schlangen and van Mier 1992), compare also (van Mier 1997). The respective parameter ratios between (a), (m) and (i) are estimated based on the corresponding ratios introduced in the context of lattice models. In that, an analogous approach of calibrating the stiffnesses and fracture law parameters noted in (van Mier et al. 1995) is partially followed. In order to prevent aggregate (i. e.

macro particle) cracking at the present stage the ratios noted in (van Mier et al. 1995) are partly adopted. The following choices were made:

$$\begin{aligned} \frac{k_n^{(i)}}{k_n^{(m)}} &= 0.1\,, & \frac{k_t^{(i)}}{k_t^{(m)}} &= 0.4\,, & \frac{\sigma_{n,t}^{max,(i)}}{\sigma_{n,t}^{max,(m)}} &= 0.25\,, \\ \frac{k_n^{(a)}}{k_n^{(m)}} &= 2.8\,, & \frac{k_t^{(a)}}{k_t^{(m)}} &= 2.8\,, & \frac{\sigma_{n,t}^{max,(a)}}{\sigma_{n,t}^{max,(m)}} &= 100\,. \end{aligned} \tag{20}$$

The matrix values $(\cdot)^m$ are used as input values and the other values, $(\cdot)^a$ and $(\cdot)^i$, result from equation (20). Keep in mind that the choice of parameters is only influenced by the fitting of the softening behavior and without consideration of a detailed, because unknown, knowledge of the "real" micromechanical parameters. Despite the advanced measuring devices and setups available in laboratories, the "real" parameters of the phases (a), (m) and (i) actually remain in the dark, i. e. no precise and experimentally verified values of the phases' stiffness, yield strength and softening law are available. In order to fit experimental results of concrete-type materials these parameters may be estimated on the basis of a macroscopic view of the problem: One supposes that the known macroscopic parameters of concrete are identical to the microscopic ones. For example, the fracture energy of the interface elements is identified as the experimentally measured, macroscopic one and so forth. An alternative and, in the authors opinion, more promising way is the estimation of these parameters on the basis of the insights of section 3 and utilizing the experience of the group of van Mier in the context of the micromechanical simulations of concrete-type materials.

4.2 Numerical results

It is a moot point whether the inclusion of a material description based on an artificial microstructure as introduced in the previous section instead of the "model" material may help to overcome the deficiencies of the beam and interface enhanced DEM models. Recall that the "model" material in section 3 included nearly identical stiffnesses and failure laws of the cohesive components. Compression and tension simulations of an artificial microstructure based on the interface enhanced DEM model presented in section 3 have been carried out. The model parameters have been fit to the compression experiments by (Vonk 1989) under consideration of equation (20).

Compression simulations

The load setup and measuring procedure was already discussed in the context of the tension simulation in section 3.4. Note that the parameter choice is the result of a parameter fitting to experimental results on concrete in absence of more detailed information on the micromechanical parameters. The following matrix parameters have been used: The normal and tangential stiffnesses are chosen as ${k_n}^{(m)} = 2000$ kN/cm^2, ${k_t}^{(m)} = 600$ kN/cm^2 and the fracture energies as ${G_{f,n}}^{(m)} = 4.996 \cdot 10^{-4}$ kN/cm^2, ${G_{f,t}}^{(m)} = 5.988 \cdot 10^{-3}$ kN/cm^2. The yield stresses are statistically distributed for each interface about ± 10 % the average value. On average one gets ${\sigma_n}^{max,(m)} = 0.04$ kN/cm^2, ${\sigma_t}^{max,(m)} = 0.12$ kN/cm^2. Corresponding values for the aggregate and the interface layer between aggregate and matrix are obtained via equation (20). The shape parameters are unaltered with respect to the choice in section 3 and are noted $\varphi = 26.6°$, $\gamma = 10°$ and $\psi = 0°$. The general parameters of the DEM model are also unchanged: The density was chosen as $\rho = 2.5$ g/cm^3, the time step as $\Delta t = 5 \cdot 10^{-7}$ s, the viscous damping and friction are set to zero ($\gamma_N = 0$, $\gamma_T = 0$, $\mu = 0$) and the contact stiffness amounts to $E_p = 100$ kN/cm^2.
Seven compression simulations with the same amount of aggregates and almost identical aggregate/matrix ratios

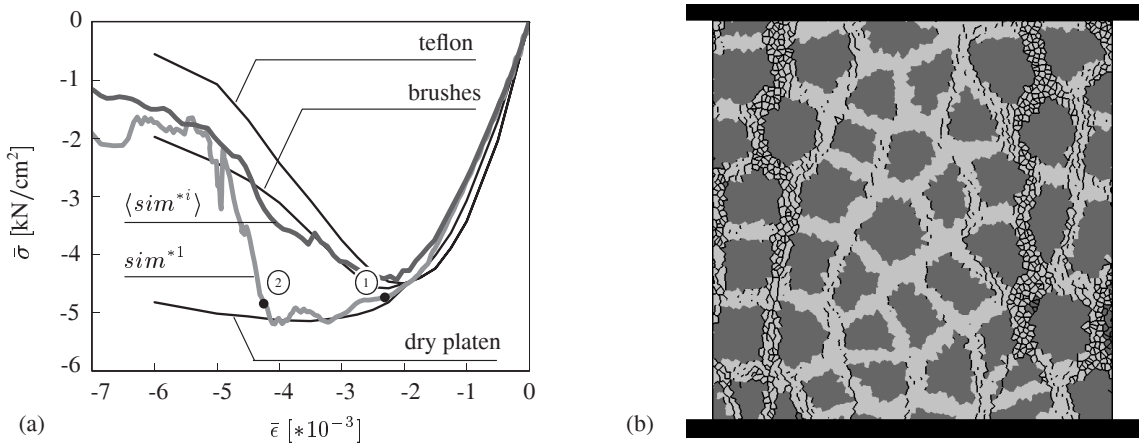

Figure 13: (a) Stress-strain diagram of simulations and Vonks's experiments and (b) eliminated bonds at stage ②.

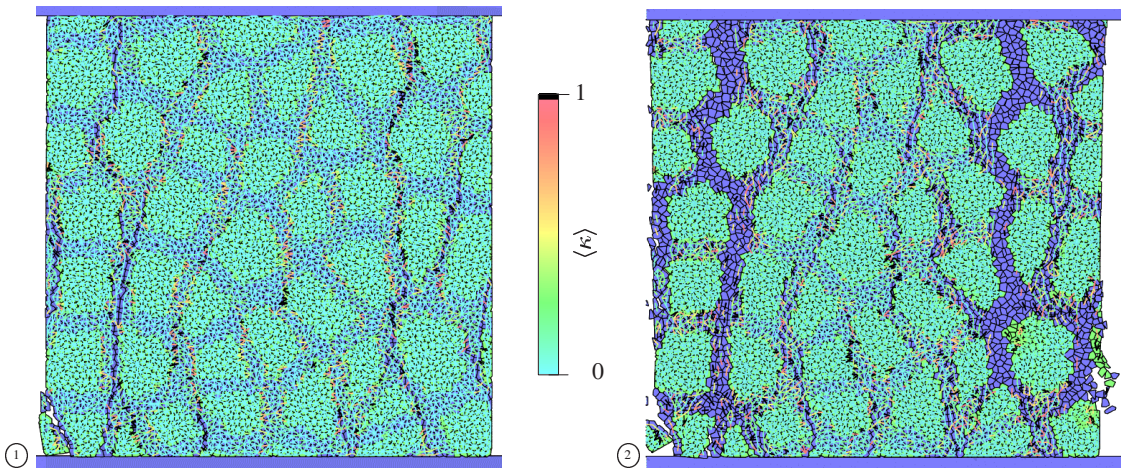

Figure 14: Graphical output of compression simulation.

have been carried out. The only difference between these simulation sets is the starting number of the random number generator for the generation of the underlying particle mesh. The quadratic 75 cm $\times$ 75 cm sample used in simulation series sim^{*1} is composed by 5501 particles and a total of 16489 interface elements between all particles within the sample. The microstructure is created by use of 46 macro particles. The composition of the sample includes a total of 2896 particles representing the aggregates and a total of 2605 particles representing the matrix. Thus, the fraction of aggregate volume to complete volume is 0.525.

The simulations are confronted with the experiments of (Vonk 1989; Vonk 1992) by means of the nominal stress vs. nominal strain diagram and, in particular, the associated softening branch. The stress-strain curves of all simulation series sim^{*i} with $i = 1...7$ are averaged via a superposition of the corresponding data files. This average curve is symbolically denoted by $\langle sim^{*i} \rangle$. In figure 13 (a) the comparison of $\langle sim^{*i} \rangle$, simulation series sim^{*1} and (Vonk 1989)'s tests on concrete with different boundary conditions is presented. After linearly increasing in the first part of the loading program the average stress-strain curve $\langle sim^{*i} \rangle$ turns into a nonlinear regime up to the peak. Afterwards, in contrast to the simulation results presented in the previous chapters the softening regime is less pronounced, i. e. it follows the predicted experimental results quite well. The continuous failure of interface elements yields a decrease of the stresses with increasing strains. The average simulation result $\langle sim^{*i} \rangle$ lies near the limit curves of the low friction boundary cases (teflon/brushes) in the post-peak regime. In summary, the inclusion of artificial microstructures has proven to be an important feature for a realistic representation of the post-peak softening behavior in terms of the stress-strain relation.

In order to give a detailed view of the failure within the specimen snapshots of simulation series sim^{*1} are considered. The softening stadium of the interface elements is monitored at two time steps ① and ② in figure 14. These simulation stages document the course of the nonlinear and softening branch of curve sim^{*1} in figure 13 (a). The simplified picture of the composite structure of the sample in figure 13 (b) highlights the crack propagation through the specimen shortly after peak load. The dark grey color denotes the aggregate particles and light grey the surrounding matrix. Bear in mind that the aggregates are represented by a finite amount of (macro) particles. For this reason, the shape of the aggregates is irregular. The black lines represent the real geometry of the interface elements that have been eliminated in the course of the simulation, i. e. $\langle \kappa \rangle = 1$. These lines connect the start and end point of an eliminated interface element and represent the corresponding particle edges. The tensile splitting type failure, mostly along the boundaries of the aggregates, is obvious. Two crack zones in the left and right part of the specimen initiate the macroscopic failure of the particle sample. In figure 14 the brighter background area represents the aggregates, while the darker background displays the matrix. The scale included in this figure refers only to the softening of the interface elements marked by the line connections between bonded particles. Please note that if an interface element reaches a stage $\langle \kappa \rangle > 1$, the corresponding line connection in figure 14 is eliminated. Thus, the dark grey colored matrix particles become visible in regions where the failure localizes, i. e. the overlaying interface element mesh has been partially dissolved in these zones. In the course of simulation at stage ① two macroscopically failure zones form, see figure 14 (a). The continuous debonding results in the final failure mechanism in form of a complete disintegration of the matrix material in these zones, compare stage ②, see figure 14 (b). The final failure at stage ② pictures the reality quite well, compare the fractured samples by (Vonk 1992).

Tension simulations

The load setup and strain measurement of the tension simulation is accommodated according to section 3.4. Irrespective of the different material parameters of the target concretes to be compared with, the same DEM

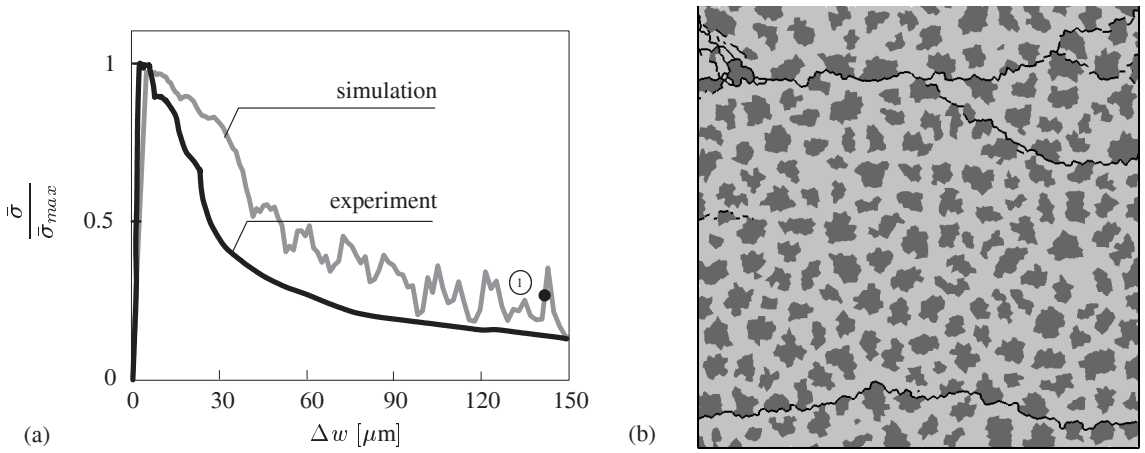

Figure 15: (a) Stress-displacement diagram of simulations and experiments by van Mier and (b) eliminated bonds at stage ①.

parameters as used in the compression simulations are considered in the tension simulations. In tension the experiments by (van Mier 1997) with a concrete with a maximum aggregate size d_{max} = 1.6 cm are considered, compare also figure 9 (b). Simulations with different aggregate sizes and varying dispersions of the yield stresses have been performed. The yield stresses have been statistically distributed for each interface element around ± 10 %, ± 50 % and ± 90 % the average values. The exemplary results detailed below are concerned with a simulation series with a dispersion of the yield stresses of ± 50 % and inclusion of 220 aggregates. Thus, the aggregate size is smaller compared to the compression simulations. Smaller aggregate sizes have been considered to accommodate the smaller maximum aggregate size of the target material in mind. In the context of the realized implementation, the higher the amount of aggregates is chosen, the smaller is the corresponding aggregate size. This yields a higher volume fraction of matrix particles and, finally, a smaller effective stiffness of the composite sample. The 75 cm $\times$ 75 cm test sample was composed by 2145 particles representing the aggregates and 3354 particles representing the matrix. The fraction of aggregate volume to the complete volume amounts to 38.4 % and the ratio of aggregate to matrix volume to 0.623.

Figure 15 (a) compares the described simulation series and experimental results of a concrete with a maximum aggregate size d_{max} = 1.6 cm according to (van Mier 1997). The crack width Δw is measured as difference between the top and bottom particles, since two macroscopically observable cracks appear, see figure 15 (b). The sample height is assumed as a representary crack zone with a finite width. The simulated peak stress is less than the experimental one by a factor of 2, if the parameter set of the compression simulation is used. One reason for this difference is the uncertainty of the parameter choice, since the extraction of "real" parameters from laboratory tests for a definition of the model parameters is not straightforward. Another reason concerns the different target concretes used for the comparisons in the compression and tension simulations. Therefore, the corresponding curves are given in a normalized format by scaling the stresses by the respective maximum stress. Anyhow, the course of the simulated and experimental curves agree qualitatively well. The post-peak behavior is more ductile than predicted by the experiments. Probably, the fracture energy choice was slightly to high. This is not astonishing at all, as the parameters have been pre-optimized for the compression simulations and the corresponding material parameters. As the concrete tested by Vonk differs from that used by van Mier with regard to the different key material parameters, this behavior is quite comprehensible. The snapshot in form of the simplified picture of eliminated interface elements in figure 15 (b) highlights the crack propagation through the specimen. As expected, only cracks in the horizontal direction and, thus, perpendicular to the loading direction are obtained. The cracks appear mostly at the "interface layer" between aggregate and matrix and fit quite well to the cracking in concrete, compare figure 1 (a).

5 CONCLUSION

The advancement and implementation of a polygonal two-dimensional discrete element model (DEM) has been carried out in a structured form. Starting from a basic DEM model for non-cohesive polygonal particles, the complexity of the model was successively increased in order to include a coherent representation of cohesive particle assemblies. This coherent representation implied a qualitative as well as quantitative reproduction of characteristic features of cohesive geomaterials. As a quantification of beam enhanced DEM models represents an arduous task, interface elements between the particles have been inserted in order to form a cohesive bond. The last step in the series of increasing complexity was the realization of a microstructure-based simulation environment which utilizes the foregoing enhanced DEM models. With growing intricacy and, therewith, freedom

of the models a wide variety of features typically observed in cohesive frictional materials could be represented in a satisfactory manner. In detail, it was shown that microstructure-based interface enhanced DEM simulations are an effective approach to remedy the deficiencies of non-microstructure simulations. The inclusion of an artificial microstructure via the definition of corresponding stiffnesses and yield stresses has shown up to be an important feature for a realistic representation of the post-peak softening behavior in terms of the stress-strain relation. With increasing complexity and, therewith, freedom of the model all characteristics of a cohesive frictional material can be represented. However, the increasing complexity is at the expense of the choice and definition of material and model parameters. Starting from the standard DEM model with a total number of 6 parameters and the beam enhanced DEM model with 9 parameters over the interface enhanced DEM model with 13 parameters, the microstructure-based interface enhanced DEM model includes the definition of 18 independent parameters. This fact may be seen as a disadvantage of the procedure, as typically material parameters should be physically coherent and directly determined by experiments. Indeed, alternative models which account for a simplified form of the microstructure and enable a reduction of the number of parameters, but still allow for a quantification of the softening regime are also conceivable: for example, by a physically coherent distribution of yield strengths and stiffnesses of the interface elements.

As future perspective, the procedures for a quantification of the parameters should be advanced. In this sense, the relation between the micromechanical properties of geomaterials and the corresponding model parameters has to be further elaborated. This implies a consideration of special experimental setups to gain more knowledge on parameters like the micromechanical yield strength or the corresponding ratios for the aggregate, matrix and "interface layer" components. In order to achieve this, very simple composite (model) materials should be created, e. g. regular polygonal particles embedded in a soft matrix with glue between matrix and particles. Due to the clear knowledge of all micromechanical material and, therewith, model parameters, a comparison of simulation and experiment should get much easier. If this point is satisfactorily solved, a real microstructure-based DEM environment may be considered. Then, an interface module between a digital image processing tool that is capable to handle electron microscopy images and the mesh generation module of the DEM program may be incorporated.

Acknowledgement The authors are indebted for the financial support of the German Research Foundation (DFG) within the research group FOR 326 *Modellierung kohäsiver Reibungsmaterialien* under grant no. RA 218/20 . The authors are grateful for the useful discussions with H. J. Herrmann from the University of Stuttgart, Germany, F. Kun from the University of Debrecen, Hungary and S. Luding from Delft University, The Netherlands.

References

Allen, M. P. and D. J. Tildesley (1987). *Computer Simulation of Liquids*. Oxford, England, UK: Oxford University Press.

Carol, I., P. C. Prat, and C. M. Lopez (1997). Normal/shear cracking model: Application to discrete crack analysis. *J. Engng. Mech. 123*, 765–773.

Cundall, P. A. (2001). A discontinuous future for numerical modelling in geomechanics. *Geotech. Engng. 149*, 41–47.

Cundall, P. A. and O. D. L. Strack (1979). A discrete numerical model for granular assemblages. *Géotechnique 29*, 47–65.

D'Addetta, G. A. (2004). *Discrete models for cohesive frictional materials*. Ph. D. thesis, Bericht Nr. 42, Institut für Baustatik, Universität Stuttgart, Germany.

D'Addetta, G. A., F. Kun, H. J. Herrmann, and E. Ramm (2001). From solids to granulates - discrete element simulations of fracture and fragmentation processes in geomaterials. In P. A. Vermeer, S. Diebels, W. Ehlers, H. J. Herrmann, S. Luding, and E. Ramm (Eds.), *Continuous and Discontinuous Modelling of Cohesive Frictional Materials, Lecture Notes in Physics 586*, pp. 231–258. Springer-Verlag, Berlin, Germany.

D'Addetta, G. A., F. Kun, and E. Ramm (2002). On the application of a discrete model to the fracture process of cohesive granular materials. *Granular Matter 4*, 77–90.

D'Addetta, G. A., E. Ramm, S. Diebels, and W. Ehlers (2002). Homogenization for particle assemblies. In B. K. Cook and R. P. Jensen (Eds.), *Discrete Element Methods - Numerical Modeling of Discontinua - Proc. 3rd Int. Conf. on DEM, Santa Fe, NM, USA, Geotechnical Special Publication No. 117*, pp. 259–264. ASCE, Reston, VI, USA.

D'Addetta, G. A., E. Ramm, S. Diebels, and W. Ehlers (2004). A particle center based homogenization strategy for particle assemblies. *Engng. Comp. 21*, 360–383.

de Borst, R. (1987). Integration of plasticity equations for singular yield functions. *Comp. & Struct. 26*, 823–829.

Donzé, F. V. and S.-A. Magnier (1995). Formulation of a 3-D numerical model of brittle behaviour. *Geophys. J. Int. 122*, 790–802.

Ehlers, W., E. Ramm, S. Diebels, and G. A. D'Addetta (2003). From particle ensembles to Cosserat continua: Homogenization of contact forces towards stresses and couple stresses. *Int. J. Solids & Structures 40*, 6681–6702.

Evans, R. H. and H. S. Marathe (1968). Microcracking and stress-strain curves for concrete in tension. *Materiaux et constructions 1*, 61–65.

Goodman, R. E., R. L. Taylor, and T. L. Brekke (1968). A model for the mechanics of jointed rock. *ASCE J. Soil Mech. Found. Div. 94*, 637–659.

Jirásek, M. and Z. P. Bažant (2001). *Inelastic Analysis of Structures*. John Wiley & Sons, Chichester, England, UK.

Koiter, W. T. (1953). Stress-strain relations, uniqueness and variational theorems for elastic-plastic materials with a singular yield surface. *Quart. Appl. Math. 11*, 350–354.

Kuhl, E. (2000). *Numerische Modelle für kohäsive Reibungsmaterialien*. Ph. D. thesis, Bericht Nr. 32, Institut für Baustatik, Universität Stuttgart, Germany.

Kun, F., G. A. D'Addetta, E. Ramm, and H. J. Herrmann (1999). Two-dimensional dynamic simulation of fracture and fragmentation of solids. *Comp. Ass. Mech. Engng. 6*, 385–402.

Kun, F. and H. J. Herrmann (1996a). Fragmentation of colliding discs. *Int. J. Mod. Phys. C 7*, 837–855.

Kun, F. and H. J. Herrmann (1996b). A study of fragmentation processes using a discrete element method. *Comp. Meth. Appl. Mech. Engng. 138*, 3–18.

Marcher, T. (2002). *Resultate eines Versuchsprogramms an Beaucaire Mergel*. Bericht Nr. 49, Institut für Geotechnik, Universität Stuttgart, Germany.

Ngo, D. and A. C. Scordelis (1967). Finite element analysis of reinforced concrete beams. *ACI Mat. J. 64*, 152–163.

Oda, M. and H. Kazama (1998). Microstructure of shear bands and its relation to the mechanisms of dilatancy and failure of dense granular soils. *Géotechnique 48*, 465–481.

Potapov, A. V., M. A. Hopkins, and C. S. Campbell (1995). A two-dimensional dynamic simulation of solid fracture - part II: Examples. *Int. J. Mod. Phy. C 6*, 399–425.

Schlangen, E. and J. G. M. van Mier (1992). Experimental and numerical analysis of micromechanisms of fracture of cement-based composites. *Cem. Concr. Res. 14*, 105–118.

Stankowski, T. (1990). *Numerical simulation of progressive failure in particle composites*. Ph. D. thesis, University of Colorado, Boulder, CO, USA.

Tillemans, H.-J. and H. J. Herrmann (1995). Simulating deformations of granular solids under shear. *Physica A 217*, 261–288.

van Mier, J. G. M. (1997). *Fracture Processes of Concrete*. Boca Raton, FL, USA: CRC Press.

van Mier, J. G. M., E. Schlangen, A. Vervuurt, and M. R. A. van Vliet (1995). Damage analysis of brittle disordered materials: Concrete and rock. In A. Bakker (Ed.), *Mechanical Behaviour of Materials - Proc. of the ICM 7*, pp. 101–126. Delft University Press, Delft, The Netherlands.

Vonk, R. (1989). *Influence of boundary conditions on softening of concrete loaded in compression*. Report TUE/BKO 89.14, Faculteit Bouwkunde, Technische Universiteit Eindhoven, The Netherlands.

Vonk, R. (1992). *Softening of concrete loaded in compression*. Ph. D. thesis, Technische Universiteit Eindhoven, The Netherlands.

RECENT APPLICATIONS OF THE BOUNDARY ELEMENT METHOD TO SOME INVERSE PROBLEMS IN ENGINEERING

Masataka Tanaka

Department of Mechanical Systems Engineering
Shinshu University
4-17-1 Wakasato, Nagano City, 380-8553 Japan
e-mail: dtanaka@gipwc.shinshu-u.ac.jp, web page: http://homer.shinshu-u.ac.jp/caesyslab/index.html

Keywords: Boundary Element Method, Computational Mechanics, Inverse Problem, Numerical Simulation

Abstract. *This paper is concerned with the fundamental aspects of the computational approach to the solution of inverse problems using the methods of analysis for the direct problems. After some brief review on current work on computational approach to the inverse problems, it presents several investigations on the inverse problems in engineering mechanics with emphasis on work by author's group using the boundary element method as a basic technique.*

1 INTRODUCTION

Computational methods of analysis based on the finite difference, finite element, and boundary element methods have been so well developed that we can easily solve the initial- and boundary-value problems, which are to be called the direct problems. It has been increasingly attracting the attention of scientists and engineers to apply the computer analysis software well established for the direct problems to the corresponding inverse problems [e.g., 1-4].

There are many inverse problems around the world, in which we should estimate the reasons from the observed results. However, from the engineering point of view, the inverse problem can be stated such that some information on the initial and/or boundary conditions, domain shapes, material constants, etc. are not entirely known, and this lacking information should be identified by using additional information which is usually given as measured data.

If we consider a system which is mathematically modeled as an initial- and boundary-value problem, we may classify the corresponding inverse problems into the following:

1. Estimation of the initial and/or boundary conditions
2. Determination of domain shapes
3. Estimation of sources
4. Estimation of material constants
5. Estimation of governing differential equations

In this paper, we shall first explain fundamentals of the computational approach to the solution of inverse problems using the methods of analysis for the direct problems, and then show several investigations on the inverse problems by author's group. Finally, the paper is concluded by some remarks toward more fruitful and more

successful analysis of the inverse problems.

2 METHODS OF INVERSE ANALYSIS

The inverse problem under consideration is modeled as a parameter identification problem. In a computational approach to this inverse problem, we first assume the values of parameters in an appropriate manner and then carry out analysis of the direct problem. The results obtained are compared with the measured data given as additional information, and the parameter values are then modified so that an appropriate cost function is minimized in an iterative manner. The cost function is usually defined as a square sum of differences between the measured and computed data. We may express the cost function as follows:

$$W = W(\mathbf{z}) \tag{1}$$

where $\mathbf{z}$ is a vector of parameters, and denoting by M the number of parameters we have

$$\mathbf{z} = \{z_1 \; z_2 \; \cdots \; z_M\}^{\mathrm{T}} \tag{2}$$

where the superscript T denotes the transpose of a matrix. We can apply the standard procedures of optimization [5] for the solution of the above-modeled inverse problems of parameters identification. The filter theory can also be implemented for the solution of the optimization problems.

In the inverse problems of estimating defects, e.g. cracks or cavities, which is the main subject of NDT (non-destructive testing), we may select as the parameters to be detected the quantities which are related to the locations and shapes of the defects. If the defect is modeled as an ellipse or a sphere, the number of parameters can be reduced and then inverse analysis can be easily carried out[6]. Although we may choose all the nodes located on the defect surface as the parameters, it would usually lead us to a large amount of computation time for inverse analysis and to unstable computation which yields less successful results. Hence, such inverse analysis could not be recommended. It is true that the smaller the number of parameters is, the more effective the performance of inverse analysis is.

The finite element methods have been best developed as computational software for direct problems, and naturally there are many of such investigations on the inverse problems [1-4]. In optimal shape design, however, we have to search the shape in an iterative manner, and careful attention should be paid to re-meshing at each iterative step of inverse analysis so that accuracy of computational results is not reduced. The boundary element methods [e.g., 7,8] can provide a more convenient tool for the problems of shape optimization design, because discretization by the method is confined within the boundary surface. In addition, it is reported that the BEM can give more accurate numerical results than the finite element or finite difference methods, if appropriate care is taken for singular integrals. This advantage is very important and makes the BEM more attractive than other methods, because in inverse analysis only a limited number of measurements are available and hence the computational results should be kept to be accurate at each iterative step. From these reasons the boundary element methods have been employed for inverse analyses, and many successful results have been reported in Refs.[1-4].

3 PARAMETERS IDENTIFICATION WITH TWO-STEP INVERSE ANALYSIS

3.1 Two-Step Inverse Analysis

There are many investigations in which computational software so far developed for direct analysis is successfully applied to the solution of inverse problems. We now show a boundary element analysis of some

inverse problems on an elastic plate subjected to dynamic loadings. In another paper[9] attempt has been made to use the measured data of bending displacement for the same inverse analysis. Instead of using the displacement measurements, we shall use to identify the parameter values of the elastic plate using the measured data of strains on the plate surfaces. The extended Kalman filter[10] is applied to improve the assumed parameter values in an iterative manner. The square sum of differences between the measured strain and the calculated one at some selected points on the plate surfaces is defined as a cost function to evaluate convergence. The strain responses are calculated by use of the boundary element method.

Successful identification of the parameters by an inverse analysis based on sensitivity analysis depends on assumption of the parameter values as close as possible to the target values to be estimated. Careful attention is paid to first assumption of the parameter values. Roughly approximate values of the parameters are first estimated by finding a minimum cost function for a finite number of combinations in the parameter space without sensitivity analysis, and then a sensitivity-based procedure is applied. This process is repeated until a successful estimation can be made.

The usefulness of the two-step inverse analysis mentioned above is demonstrated through calculation of some inverse problems of the circular plate subjected to a dynamic load[11]. It is interesting to note that the proposed method of inverse analysis can be equally applied to elastic plates with arbitrary shapes, dynamic loads and boundary conditions.

Numerical procedures available for optimization and inverse analysis can be applied to the present inverse problem. To obtain an accurate solution of the inverse problem, we shall use in the following an inverse analysis based on the extended Kalman filter[10]. Success in this approach would deeply depend on how the initial values of parameters are assumed as closely as possible to those to be identified: A successful solution can be expected if the values of parameters are appropriately assumed at the beginning of iterative computations. Otherwise, however, the solution procedure would fall in a local minimum of the cost function or no successful solution would be obtained. It is extremely difficult or almost impossible to assign appropriately the initial values of parameters for a successful identification.

To circumvent the above difficulty, we shall employ in this study a two-step inverse analysis: First, we estimate an approximate set of parameter values by searching an optimal combination in an appropriate range in the parameter space. Then, we carry out inverse analysis based on the Kalman filter, using the parameter values found in the first-step inverse analysis mentioned above. A more detailed explanation of the proposed two-step inverse analysis will be given in the following.

First, several values of each parameter to be identified are selected due to a priori information and depict a map of finite number of parameter combinations. We next compute the cost function for the discrete number of parameter combinations, and then find the optimal combination which gives the minimum value of the cost function. With these values of parameters thus roughly estimated, we then proceed to the next step of inverse analysis using the extended Kalman filter. In the second step of inverse analysis, the parameter values estimated in the above manner are used as the their initial values. If the inverse analysis can be carried out successfully in the second step, no return to the first step is required. However, unless the inverse analysis indicates any convergence toward an expected minimum value of the cost function, return to the first step is required. In this case, we try to find an optimal combination of parameters within a narrower range compared with the first trial. After a few trials of this process, a successful estimation could be expected almost always.

3.2 Application to Material Parameters Identification

To demonstrate the usefulness of the proposed solution procedure for the inverse problems under consideration, we shall apply it to identification of material constants (Yong's modulus and density of mass) of the elastic plate[11]. We shall consider the circular plate of radius a=0.5[m] and thickness h=0.01[m] with the whole edge clamped. For numerical simulation's sake, we first compute via the BEM software the dynamic responses of the elastic plate under the given dynamic load, $P(t) = 100H(t)[\mathrm{N}]$ at the center of plate, assuming that Young's modulus $E = 2.0\times10^{11}[\mathrm{Pa}]$, Poisson's ratio $\nu = 0.3$ and the density of mass $\rho = 7.8\times10^{3}[\mathrm{kg/m^3}]$.

The boundary and the circular domain are discretized as shown in Fig.1, where the circular boundary is divided uniformly into 8 quadratic boundary elements of an equal size and the inner circular domain is divided into 16 internal cells with quadratic interpolation functions. For the numerical Laplace inverse transform, we place 20 sampling points in the time axis with an equal interval.

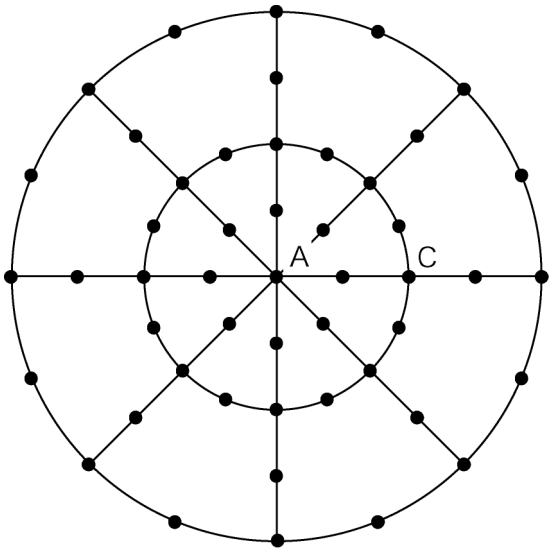

Figure 1. Discretization of circular plate

The computational results thus obtained are used as the averaged values of measured data. It is assumed that in the example under consideration the normal strain ε_x in the axis x is measured at the center point A and the mid-point of radius C, and that these measured data include the errors with variance $\sigma^2 = 10^{-20}$. In this numerical example, the exact values of the material constants are known as E_0 and ρ_0, and hence we assume that the non-dimensional material constants defined as E/E_0 and ρ/ρ_0 fall within an appropriate square rigion, for example, 9×9 in the parameter space. The cost function is calculated for the non-dimensional material constants at a finite number of nots, say 4×4, from which we can colclude that the non-dimensional material constants $E/E_0 = 2.25, \rho/\rho_0 = 2.25$ can provide the minimum value of the cost function. Then, we try to do inverse analysis of the second step based on the extended Kalman filter and BEM, using the above values of material constants. The results obtained are summarized in Table 1. Unfortunately, inverse analysis fails to estimate the material constants even after 15 iterations under the above rough estimation of parameter values. In the above case, we have to again go back to the first step of inverse analysis. We now assume a narrow region of search aound the first trial, and repeat the first step analysis. Through this computation, the material constants ($E/E_0 = 1.125, \rho/\rho_0 = 1.125$) are estimated. Using these material constants, we repeat precise inverse analysis of the second step. Then, we can eventually arrive at the target values of material constants as summarized in Table 2 after 11 iterations. It is interesting to note that the present two-step inverse analysis is also successful for the cases with larger measurement errors. To decide an appropriate search region of the parameter values for the first step of inverse analysis, we can make use of a priori information as much as possible. Such a priori information can be used for reduction of the range of parameter values to be searched in the first step.

Rough Estimation of initial values		Final estimation by extended Kalman filter		
E/E_0	ρ/ρ_0	E/E_0	ρ/ρ_0	Iterations
2.25	2.25	-8447	-8421	15

Table 1. Estimated results of material constants (1st trial)

Finer estimation of initial values		Final estimation by extended Kalman filter		
E/E_0	ρ/ρ_0	E/E_0	ρ/ρ_0	Iterations
1.125	1.125	1.0000	1.0000	11

Table 2. Estimated results of material constants (2nd trial)

4 AN APPLICATION OF CELLULAR AUTOMATA

4.1 Approximate Estimation of Parameter Values

It is true that if the initial guess of parameter values is appropriate, the extended Kalman filter or other techniques available for optimization problems can be successfully applied to a wide variety of the inverse problems. Therefore, it is essentially important to assess approximate values of the parameters. At this end, we may apply a two-step inverse analysis in which first a rough estimation of the parameters is made, and then based on this estimation a second step of inverse analysis is carried out to improve the solution of the inverse problem under consideration. There are several approaches for the first step of inverse analysis. We may use for this purpose the method of designed experiments, cellular automata, GA, etc. If a rough estimation of the parameters is sufficient, we can use this estimation as the final solution and there is no need for the second step of inverse analysis. In this article, we show an application of the cellular automata to estimating the part of the boundary shape by the measured temperatures. This is an extension of the similar procedure proposed for optimization of an acoustic field[12].

In the cellular automaton (CA), the domain of interest is discretized into a number of uniform cells. Some quantity which represents the cell state is assigned to each cell, and then is modified by a transition rule under the condition that a local rule for cells is satisfied. An optimal solution can thus be found in an iterative manner. A concrete procedure of the CA will be briefly explained in the following application.

In general, triangular or rectangular cells can be used for a two-dimensional region. In the following application, rectangular cells are employed and the domain of investigation is discretized into cells of a uniform size. The Moore neighbor cells are defined so that the target cell is surrounded by the neighbor eight cells. Then, we introduce a local rule determining a mutual relation between the neighbor cells for the current state of iterative computation. The most favorite shape of the boundary is selected through a transition rule and this shape is used for the next iterative computation to search a more suitable shape for the transition rule. Eventually, the optimal shape of the boundary can be estimated through such an iterative computation.

4.2 Estimation of Erosion Line of Refractory Brick in Blast Furnace Hearth

It is assumed that the blast furnace is axi-symmetric and the refractory brick of the furnace is in a steady heat conduction state. The temperature field can be estimated through the boundary element method for solving the

steady-state heat conduction problem of axi-symmetric body[13]. Attention is paid to finding the erosion line of the refractory brick in the blast furnace hearth. The meridional cross-section of blast furnace is divided into a series of square cells as shown in Fig. 2. The meshed region is composed of three kinds of cells: "Alive", "Remaining" and "Dead" in which the remaining cells are not changed and always remain as "Alive". Assuming the alive cells we may produce s shape of the internal line of the refractory brick. For this computation we now introduce a local rule as shown in Fig. 3. When the local rule holds for the current target cell, we change the state of the target cell from "Alive" to "Dead" or "Dead" to "Alive" and then boundary element analysis is carried out. If the target cell is "Alive", we apply the rule 1 to add a cell; If the target cell is "Dead", we apply the rule 2 to delete it. In addition, an empirical rule is also applied to avoid an unacceptable shape of the erosion line.

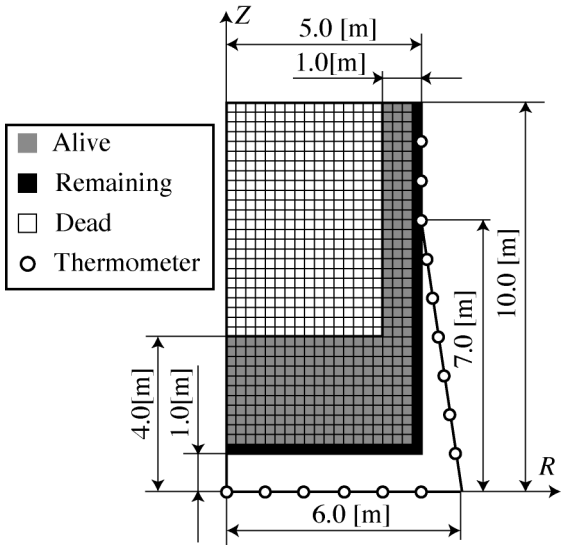

Fig. 2 Analysis model and cell division

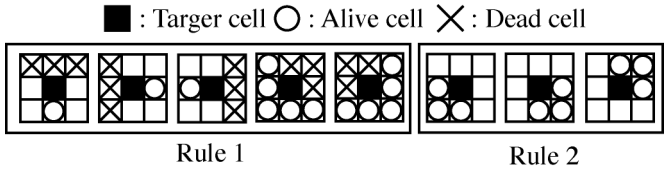

Fig. 3 Local rules

It is assumed that the temperature is measured at selected points on the outer boundary of the blast furnace hearth as shown in Fig. 2 by small circles. In numerical simulation, such measured temperatures are created from the computed temperature by BEM analysis for the target shape of erosion line. The cost function for evaluating the optimal shapes of the erosion line is defined in this study as the square sum of differences between the measured and computed temperatures as mentioned above. Namely, the non-dimensional expression of the cost function is written as follows:

$$W = \sum_{i=1}^{N} \left(\frac{u_i - \hat{u}_i}{\hat{u}_i} \right)^2 \tag{9}$$

where u_i is the computed temperature, $\hat{u}_i$ the measured and N the number of measuring points. The outline of inverse analysis is summarized in the following:

1. Carry out BE analysis for the assumed initial shape of erosion line, and calculate the cost function.
2. When the target cell is "Alive" and not "Remaining", change the cell state from "Alive" to "Dead according to the Rule 1. Carry out BE analysis and compute the new cost function.
3. If the new cost function is smaller than the previous one, save the cell state.
4. Do the same check as above for all the cells for the initial shape of erosion line, and save the state of cells corresponding to the least cost function as the next "initial" shape of erosion line.
5. Repeat the steps (2) to (4) until the variation of the cost function falls within a given tolerance.
6. Change the local rule to the Rule 2 and repeat the steps (2) to (5), applying the rule only when the target cell is "Dead" and not "Remaining".
7. The shape of internal boundary corresponding to the least cost function is regarded as the final results on the estimated shape of erosion line.

We now show some of the numerical results. Five initial shapes with a different height of bottom line of the refractory are assumed for the erosion line as shown in Fig. 5. Inverse analysis is carried out for each initial shape, and the final estimated shape is determined so that the converged value of the const function is minimum.

Figure 6 shows the convergence properties for the five initial shapes of erosion line, while Fig. 7 does the final estimated shape and the initial one. It is interesting to note that the present estimation can be easily improved if a more sophisticated inverse analysis, such as the one based on the extended Kalman filter theory[14], is applied to further inverse analysis using the present estimation as the initial shape of erosion line.

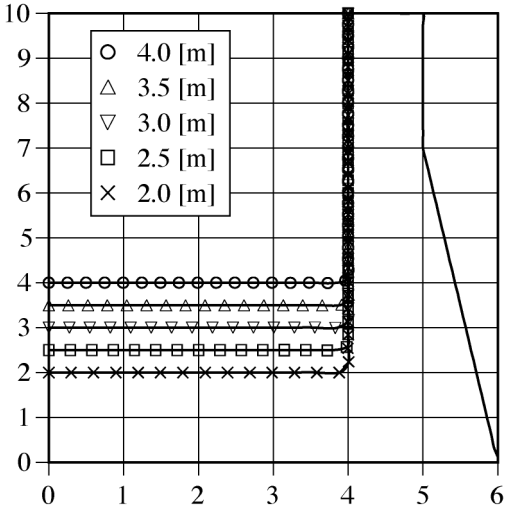

Fig. 5 Five initial shapes with different bottom heights

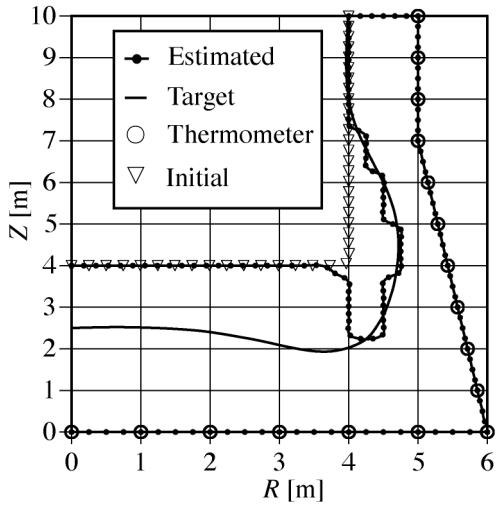

Fig. 6 Less successful estimation

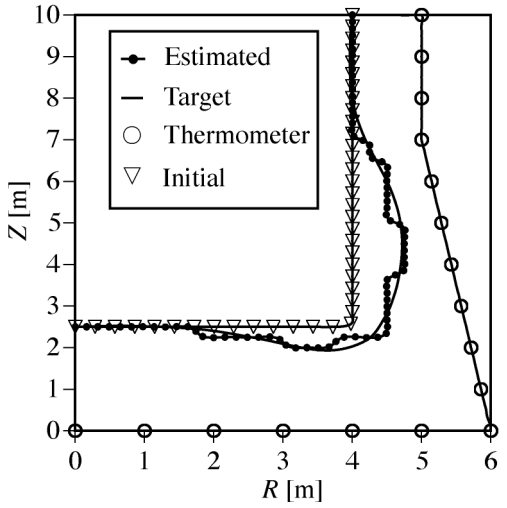

Fig. 7 Successful estimation

Figure 6 shows a less successful estimation, whereas Fig.7 does a fairly good estimation from the initial shape with 2m bottom line. It is also confirmed that through the above five initial shapes a wide range of erosion lines can be successfully estimated.

5 CONCLUDING REMARKS

This paper has briefly reviewed the current research on the inverse problems with emphasis on the boundary element method, and introduced some of the topical investigations along this line. It is shown that the optimization methods without sensitivity analysis are robust so that they can provide almost always an approximate solution of the inverse problem. To improve the thus obtained solution, we may successfully apply the optimization procedures based on sensitivity analysis. It can be concluded that the two-step inverse analysis mentioned above is applicable to a wide range of the inverse problems.

Due to space limitation the present paper has introduced only a limited number of investigations in current research on the inverse problems. The interested reader can refer to the proceedings of recent international conferences on the inverse problems.

REFERENCES

1. Tanaka, M. and Dulikravich, G.S. (Eds.) (1998), *Inverse Problems in Engineering Mechanics*, Elsevier Science, Amsterdam.
2. Tanaka, M. and Dulikravich, G.S. (Eds.) (2000), *Inverse Problems in Engineering Mechanics II*, Elsevier Science, Amsterdam.
3. Tanaka, M. and Dulikravich, G.S. (Eds.) (2001), *Inverse Problems in Engineering Mechanics III*, Elsevier Science, Amsterdam.
4. Tanaka, M. (Ed.) (2003), *Inverse Problems in Engineering Mechanics IV*, Elsevier Science, Amsterdam.
5. Papalambros, P.Y. and Wilde, D.J. (1988), *Principles of Optimal Design*, Cambridge University Press, Cambridge/UK.
6. Tanaka, M., Nakamura, M. and Nakano, T. (1991), In *Boundary Integral Methods - Theory and Applications*, L. Morino and R. Piva (Eds.), Springer-Verlag, pp.470-479.
7. Brebbia, C.A., Telles, J.C.F. and Wrobel, L.C. (1984), *Boundary Element Techniques - Theory and Applications in Engineering*, Springer-Verlag, Berlin.
8. Katsikadelis, J.T. (2002), *Boundary Elements - Theory and Applications*, Elsevier Science, Amsterdam.
9. Tanaka, M., Matsumoto, T. and Yamamura, H. (2003), In *Recent Developmennt in Theories and Numerics*, Yiu-Chung Hon Y.C., Yamamoto, M., Cheng, J. and Lee, J. Y. World Scientific, Hong Kong, pp.384-393.
10. Tosaka, N. (1994), In *Inverse Problems in Engineering Mechanics*, Bui, H.D., Tanaka, M., et al. (Eds.), A.A. Balkema, Rotterdam, pp.453-460.
11. Tanaka, M., Matsumoto, T. and Wang, Y.B. (2004), In *Computational Mechanics,* Z.H. Yao, M.W. Yuan, W.X. Zhong (Eds.), Tsinghua University Press, Springer, pp.673-677.
12. Tanaka, M., Matsumoto, T. and Arai, Y. (2003), In *Ref.*[4], pp.363-373.
13. Yoshikawa, F. and Tanaka, M. (1982), "Boundary elements in axisymmetric potential problems", In *Proc. 4th Int. Conf. on BEM in Eng.*, C.A. Brebbia (Ed.), Springer-Verlag, pp.101-111.
14. Tanaka, M., Matsumoto, T. and Oida, S. (1998), in *Ref.*[3], pp.121-130.

P-FEM ANALYSIS OF SINGULARITIES: THEORY AND APPLICATIONS

Zohar Yosibash

Dept. Mech. Eng. Ben-Gurion Univ. of the Negev, Beer-Sheva, Israel
e-mail: zohary@bgu.ac.il - web page: http://www.bgu.ac.il/~zohary

Key words: Failure initiation, Generalized stress intensity factors, V-notch

Abstract. *A three-part study composed of analytical, numerical and experimental investigation is described for investigating failures in micro-electronic devices. The point of departure is the exact solution of the elasticity system in the vicinity of 2-D singular points, characterized by an asymptotic expansion composed of eigenpairs and their coefficients called generalized stress intensity factors (GSIFs). High-order finite element methods for computing them for 2-D singular points, including anisotropic and multi-material interfaces is presented. These methods are being utilized for validating a simple proposed failure criterion for micro-electronic devices by experimental observations.*

In the second part of the paper we extend the knowledge on 2-D singular points to edge singularities in 3-D elastic domains where asymptotic expansions are somewhat different compared to the 2-D singularities. Because the known Cherepanov-Rice J-Integral ceases to be path independent in 3-D domain, a new extraction technique (Quasi-Dual Extraction Method (QDEM)) for edge stress intensity functions is presented.

1 Introduction

Predicting and preventing failure initiation at V-notch tips and delaminations in anisotropic composites, is of increasing importance in such seemingly different areas as structural mechanics and electronic packaging. The common link is the displacements in linear elastostatics in *two dimensions* in the vicinity of any singular point, which are expanded in a series having coefficients used in engineering practice to predict failure initiation [1]:

$$\boldsymbol{u} = \sum_{\ell=1}^{L} A_\ell \; r^{\alpha_\ell} \begin{Bmatrix} u_1^{(\ell)}(\theta) \\ u_2^{(\ell)}(\theta) \end{Bmatrix} + \boldsymbol{u}_{reg} = \sum_{\ell=1}^{L} A_\ell \; r^{\alpha_\ell} \boldsymbol{u}^{(\ell)}(\theta) + \boldsymbol{u}_{reg} \tag{1}$$

The associated stress field is singular as $r \to 0$ for $\alpha_\ell < 1$:

$$\boldsymbol{\sigma} = \sum_{\ell=1}^{L} A_\ell \; r^{\alpha_\ell - 1} \begin{Bmatrix} \sigma_{11}^{(\ell)}(\theta) \\ \sigma_{22}^{(\ell)}(\theta) \\ \sigma_{12}^{(\ell)}(\theta) \end{Bmatrix} + \boldsymbol{\sigma}_{reg} = \sum_{\ell=1}^{L} A_\ell \; r^{\alpha_\ell - 1} \boldsymbol{\sigma}^{(\ell)}(\theta) + \boldsymbol{\sigma}_{reg} \tag{2}$$

where (r, θ) are cylindrical coordinates of a system located in the crack tip, A_ℓ are the coefficients of the asymptotic expansion (called the generalized stress intensity factors - GSIFs), α_ℓ and $\boldsymbol{u}^{(\ell)}(\theta)$ are eigenpairs which depend on the material properties, the geometry, and the boundary conditions in the vicinity of the singular point. The first two exponents α_1 and α_2 are equal to $1/2$ for crack tips. L may be taken as large as required, and the remainder $\boldsymbol{u}_{reg}$ is a vector of smooth functions. Usually "mode I" stress intensity factor, $K_I = A_1 * \sqrt{2\pi}$ associated with the "symmetric crack mode", determines the onset of failure in fracture mechanics. Under special circumstances, power-logarithmic stress singularity may exist [2], however these are not addressed herein.

The key to a successful failure analysis is to develop methods to compute reliably the characteristics of the solution near singular points, i.e., to determine the eigenpairs and the GSIFs. This is because failure theories directly or indirectly involve them. For general singular points in elastostatics, neither the eigenpairs nor the GSIFs are known explicitly.

Nowadays most of the available methods for the computation of eigen-pairs and GSIFs are applicable to crack singularities in isotropic materials, do not provide any desired number of stress intensity

factors, and fail when the eigenpairs are complex. They are difficult or even impossible to incorporate into standard finite element programs. A high-order FE method which combines the computation of the eigenpairs and the extraction of the coefficients of the asymptotic expansion for singular points in anisotropic inhomogeneous 2-D domains (which may have multi-material interfaces) with any opening angle is presented. A short description of the methods followed by a numerical example demonstrates its efficiency and accuracy is given in Section 2.

Failure laws are associated with the elastostatic solution in the vicinity of the V-notches and multi-material interfaces. We utilize the ability to compute eigen-pairs and GSIFs for predicting and eventually preventing mechanical failures that may occur in the passivation layer of micro-electronic devices during the fabrication process in Section 3. A sufficiently simple and reliable failure law, named strain energy density SED criterion, for predicting failure initiation (crack formation) in the above mentioned cases is provided and validated by experimental observation.

We have also validated the SED criterion by performing experiments on specimens at the macro level as reported in [3, 4]. The validity of the SED criterion has been compared to several known failure initiation criteria at reentrant corners in brittle elastic materials, and documented in Section 4.

Finally, in Section 5 we discuss 3-D domains where we show that the asymptotic expansion of the elasticity system in the vicinity of an edge contains more than the 2-D eigenpairs, and therefore special methods for the computation of the quantities of interest are formulated.

2 Singularities in two-dimensional domains

The departing point is the elastic solution in the vicinity of a singular point which is detailed in the following two subsections.

2.1 Determination of eigenpairs by the modified Steklov method

First, the modified Steklov method for determining the eigenpairs in the neighborhood of the singular point is described. For a detailed discussion we refer to [5].

We denote the two displacements in the x_1 and x_2 directions by u_1 and u_2 respectively. The normal and tangential tractions (resp. displacements) on a boundary, will be denoted by T_n and T_t (resp. u_n and u_t).

Let us consider a domain Ω_R^* shown in Figure 1, where r, θ are the coordinates of a cylindrical coordinate system located in the singular point. In Ω_R^* the solution is regular such that high-order

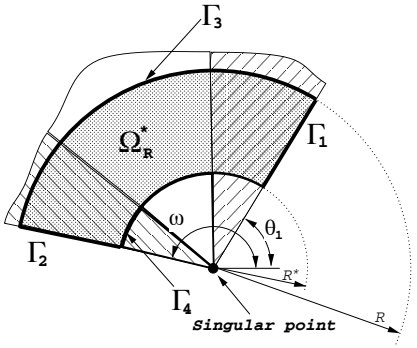

Figure 1: Domain and notations for modified Steklov formulation.

finite elements are expected to attain a superconvergent rate. On the boundaries Γ_1 and Γ_2 we consider homogeneous boundary conditions which can represent zero tractions, or zero displacements:

$$\left.\begin{array}{llll} u_n = 0 & or & T_n = 0 \\ u_t = 0 & or & T_t = 0 \end{array}\right\} \quad on \quad \Gamma_i \quad , \quad i = 1, 2, \tag{3}$$

In Ω_R^*, u_1 and u_2 may be represented as follows:

$$\boldsymbol{u} \stackrel{\Delta}{=} \begin{Bmatrix} u_1 \\ u_2 \end{Bmatrix} = r^{\alpha} \begin{Bmatrix} s_1(\theta) \\ s_2(\theta) \end{Bmatrix}. \tag{4}$$

Under special (exceptional) circumstances, $\boldsymbol{u}$ may also have additional terms as:

$$r^{\alpha} ln(r) \begin{Bmatrix} s_1(\theta) \\ s_2(\theta) \end{Bmatrix}.$$

These cases occur when a special combination of the material properties and the geometry occur and are not treated herein. Details on these cases can be found for bi-material corners and interface cracks in [2].

Using (4), on Γ_3 we have:

$$(\partial \boldsymbol{u}/\partial \nu) = (\alpha/R)\boldsymbol{u} \quad , \quad on\ \Gamma_3, \tag{5}$$

and a similar condition on Γ_4. The boundary conditions on Γ_3 and Γ_4 are Steklov boundary conditions, so that the obtained problem is an eigen-value problem.

The weak formulation of the elasticity system, after substituting (5) for the boundary conditions is called the modified Steklov weak form (see detailed derivation in [5]):

$$\begin{gathered} \textbf{Seek} \qquad \alpha \in \mathcal{C} \ , \ \mathbf{0} \neq \boldsymbol{u} \in H^1(\Omega_R^*) \times H^1(\Omega_R^*), \\ \mathcal{B}(\boldsymbol{u},\boldsymbol{v}) - (\mathcal{N}_R(\boldsymbol{u},\boldsymbol{v}) + \mathcal{N}_{R^*}(\boldsymbol{u},\boldsymbol{v})) = \alpha \left(\mathcal{M}_R(\boldsymbol{u},\boldsymbol{v}) + \mathcal{M}_{R^*}(\boldsymbol{u},\boldsymbol{v})\right), \quad \forall \boldsymbol{v} \in H^1(\Omega_R^*) \times H^1(\Omega_R^*) \end{gathered} \tag{6}$$

where $H^1(\Omega_R^*)$ is the usual Sobolev space, and is restricted to $H_0^1(\Omega_R^*)$ if homogeneous displacements boundary conditions are prescribed,

$$\mathcal{B}(\boldsymbol{u},\boldsymbol{v}) \stackrel{\text{def}}{=} \int\int_{\Omega_R^*} ([D]\boldsymbol{v})^T [E][D]\boldsymbol{u} d\Omega, \qquad \mathcal{M}_R(\boldsymbol{u},\boldsymbol{v}) = \int\limits_{\theta} \left[\boldsymbol{v}^T [A_1]^T [A_3][E][A_5]\boldsymbol{u}\right]_{r=R} d\theta, \tag{7}$$

$$\mathcal{N}_R(\boldsymbol{u},\boldsymbol{v}) = \int\limits_{\theta} \left[\boldsymbol{v}^T [A_1]^T [A_3][E][D^{(\theta)}]\boldsymbol{u}\right]_{r=R} d\theta \ , \tag{8}$$

and $[A_1]$, $[D]$, $[A_3]$, $[A_5]$, $[D^{(\theta)}]$ are given as follows:

$$[A_1] = \begin{bmatrix} \cos\theta & \sin\theta \\ -\sin\theta & \cos\theta \end{bmatrix}, \quad [D] = \begin{bmatrix} \frac{\partial}{\partial x_1} & 0 \\ 0 & \frac{\partial}{\partial x_2} \\ \frac{\partial}{\partial x_2} & \frac{\partial}{\partial x_1} \end{bmatrix}, \quad [A_3] = \begin{bmatrix} \cos^2\theta & \sin^2\theta & \sin 2\theta \\ -\frac{1}{2}\sin 2\theta & \frac{1}{2}\sin 2\theta & \cos 2\theta \end{bmatrix},$$

$$[A_5] = \begin{bmatrix} \cos\theta & 0 \\ 0 & \sin\theta \\ \sin\theta & \cos\theta \end{bmatrix}, \quad [D^{(\theta)}] = \begin{bmatrix} -\sin\theta \frac{\partial}{\partial\theta} & 0 \\ 0 & \cos\theta \frac{\partial}{\partial\theta} \\ \cos\theta \frac{\partial}{\partial\theta} & -\sin\frac{\partial}{\partial\theta} \end{bmatrix},$$

and $[E]$ is the material matrix. $\mathcal{M}_{R^*}(\boldsymbol{u},\boldsymbol{v})$ and $\mathcal{N}_{R^*}(\boldsymbol{u},\boldsymbol{v})$ are the same as in (7) and (8) except that the integrand is evaluated on $r = R^*$.

Remark 1 *The domain Ω_R^* does not include singular points, hence no special refinements are required if the finite element method is used.*

Remark 2 *Negative eigen-values and their associated eigen-functions (the dual eigen-pairs) are obtained because the domain Ω_R^* does not include singular points. These are necessary for extracting the stress-intensity functions by the dual singular function method [6, 7].*

Remark 3 *The formulation of the weak form was not based on the assumption that the material is isotropic, and in fact can be applied to multi-material anisotropic interface.*

The domain Ω_R^* is divided into finite elements through a meshing process. Denoting the set of all coefficients by $\{u_{tot}\}$, and the set of coefficients associated with Γ_3 and Γ_4 by $\{u_R\}$, we obtain the following matrix eigenproblem:

$$([K] - [N_R] - [N_{R^*}])\{u_{tot}\} = \alpha([M_R] + [M_{R^*}])\{u_R\} = \alpha[M]\{u_R\}. \tag{9}$$

The vector which represents the total number of nodal values in Ω_R^* can be divided into two vectors such that one contains the coefficients $\{u_R\}$, the other contains the remaining coefficients: $\{u_{tot}\}^T = \{\ \{u_R\}^T\ ,\ \{u_{in}\}^T\ \}$. Eliminating $\{u_{in}\}$ using static condensation we obtain a reduced eigenproblem:

$$[K_S]\{u_R\} = \alpha[M]\{u_R\}. \tag{10}$$

Solution of the eigenproblem (10) yields excellent approximations for eigenpairs with high accuracy, efficiency and robustness (see also [5]).

2.2 Extraction of GSIFs by the Complementary Energy Method (CEM)

Once eigenpairs have been computed, they are used for extracting GSIFs from the finite element solution (full details are provided in SzYo94b). The procedure is as follows: First one solves the elastostatic problem over the entire domain Ω by means of finite element method thus obtaining $\boldsymbol{u}_{FE}$. Second, a sub-domain around the singular point is considered. Define S_R as the set of interior points of a circle of radius R, centered on the point P. Ω_R is defined by $\Omega \cap S_R$ and Γ_R is the *circular* part of its boundary, see Figure 2. The *complementary variational principle* over Ω_R can be stated as:

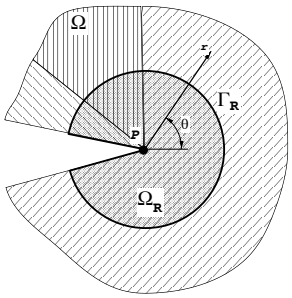

Figure 2: Typical singular point P.

Seek $\boldsymbol{\sigma_0} \in E_c(\Omega_R)$, such that

$$\mathcal{B}_c\ (\boldsymbol{\sigma_0},\boldsymbol{\sigma_1}) = \mathcal{F}_c\ (\boldsymbol{\sigma_1}) \qquad \forall\ \boldsymbol{\sigma_1} \in E_c(\Omega_R), \tag{11}$$

$E_c(\Omega_R)$ being the statically admissible space (see detailed definition in [26]), and $\mathcal{B}_c$ and $\mathcal{F}_c$ are given by:

$$\mathcal{B}_c(\boldsymbol{\sigma_0},\boldsymbol{\sigma_1}) = \int\int_{\Omega_R} \boldsymbol{\sigma_0}^T [E]^{-1}\ \boldsymbol{\sigma_1} d\Omega \tag{12}$$

$$\mathcal{F}_c\ (\boldsymbol{\sigma_1}) = \int_{\partial\Omega_R^{(u)}} \hat{\boldsymbol{u}}^T [A_5]^T\ \boldsymbol{\sigma_1}\ ds, \tag{13}$$

where $\partial\Omega_R^{(u)}$ is that part of the boundary where the displacement vector $\hat{\boldsymbol{u}}$ is prescribed. For the complementary weak form the trial and test spaces are chosen to be linear combinations of the eigenstresses, which are computed from the eigenpairs, using the stress-strain relationship and Hooke's law. The unknowns are the series coefficients.

The ij-th term of the compliance matrix which corresponds to the bilinear form in (12) is generated using the i-th and j-th eigen-pairs.

The eigenstress tensor, being derived from the eigenpairs, automatically satisfies the boundary conditions on all boundaries except Γ_R, so that the linear form (13) degenerates to an integral over the circular boundary Γ_R alone.

The vector $\hat{\boldsymbol{u}}$ in (13) is replaced by the approximated finite element solution on Γ_R, $\boldsymbol{u}_{FE}$. Solving (11), one obtains an approximation for the coefficients of the asymptotic expansion, the GSIFs. Numerical examples provided in the following demonstrate that the rate of convergence of the GSIFs is as fast as the convergence of the strain energy, therefore the method is "superconvergent".

2.3 A Numerical Example

Consider the edge-cracked panel in an isotropic material under plane strain situation with Poisson's ratio of 0.3. In [7] the first and second GSIFs were computed by the contour integral method (CIM) and the cutoff function method (CFM) and it was demonstrated that the rate of convergence using these methods is as fast as the rate of convergence of the strain energy. It should be noted that the exact eigenpairs were used in [7].

In our computations the approximated eigenpairs obtained by the modified Steklov method were used. These approximated eigenpairs are computed using a 4-element mesh (not shown) at p=6. The two eigenvalues obtained are $\alpha_1 = 0.49999967$, $\alpha_2 = 0.50000051$ (the exact values are 1/2).

The tractions that exactly correspond to the stresses of Mode 1 and Mode 2 stress fields are applied on the sides of the solution domain, see Figure 3. We select the first two GSIFs to be A (A is arbitrary) and defined the normalized stress intensity factors $\tilde{A}_1$ and $\tilde{A}_2$ as follows:

$$\tilde{A}_i \stackrel{\text{def}}{=} (A_i)_{FE}/A. \qquad i = 1, 2. \tag{14}$$

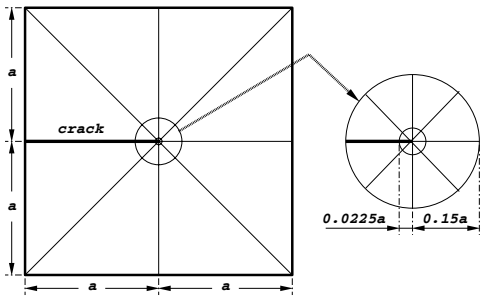

Figure 3: Solution domain and mesh design for a crack in an isotropic material.

In this way both normalized GSIFs have to converge to 1 as the number of degrees of freedom is increased.

The first two normalized GSIFs are computed with $R = 0.5a$, where $2a$ is the length of the side of the square. The number of degrees of freedom, the error in energy norm, and the computed values of the normalized GSIFs are listed in Table 1. The relative error in energy norm, the relative error in strain

Table 1: First two GSIFs for a crack in an isotropic material computed by CEM.

	p=1	p=2	p=3	p=4	p=5	p=6	p=7	p=8
DOF	53	155	273	439	653	915	1225	1583
$\|e\|_E(\%)$	29.92	11.07	5.52	3.15	2.24	1.78	1.48	1.26
$\tilde{A}_1$	0.8144	0.9548	0.9912	0.99783	0.99795	0.99825	0.99862	0.99882
$\tilde{A}_2$	0.8317	0.9641	0.9946	0.99942	0.99888	0.99898	0.99926	0.99943

energy, and the absolute value of the relative error in GSIFs, computed by the CEM and by the CIM, are plotted against the number of degrees of freedom on a log-log scale in Figure 4.

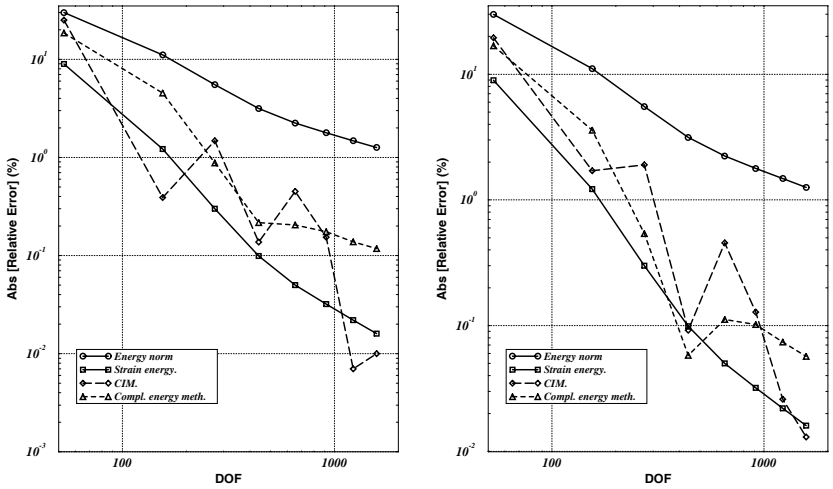

Figure 4: Convergence of $\|e\|_E$, the strain energy ($\|e\|_E^2$), A_1 (left) and A_2 (right) for the crack in an isotropic material.

It is seen that the rate of convergence of the GSIFs is faster than the rate of convergence in the energy norm and both the CEM and CIM have similar convergence patterns. Note that as the error in energy norm decreases the CIM (based on the exact eigenpairs) performs better as compared with the CEM (based on the approximated eigenpairs). However, up to the relative error of approximately 0.1 percent the performance of both methods is virtually the same. Example problems for anisotropic materials, multi-material interfaces, and nearly incompressible materials reported in [9–11] demonstrate the efficiency of the proposed extraction method.

3 Failure criterion at the micron scale in electronic devices

The eigen-pairs and GSIFs are being utilized for predicting, and eventually preventing mechanical failures that may occur in the passivation layer of micro-electronic devices during the fabrication process. These are in form of cracks which initiate at keyhole corners. A failure criterion is presented, based on the strain energy density (SED), which is an average value of the elastic strain energy in the vicinity of a reentrant corner of any angle. The failure criterion is validated by a test including 24 full size wafers which have been fabricated with different parameters: the interconnects (metal lines) height, the passivation thickness, and the passivating plasma power which was shown to correlate with the mechanical properties of the passivation layer. For each wafer, a FE model has been constructed, and the SED computed. It has been clearly shown, that above the critical value of $SED_{cr}[R = 0.15\mu m] \approx 1000\ [J/m^3]$, all wafers manufactured were cracked. The SED criterion seems to correlate well with the empirical observations, and may be used as a standard tool for the mechanical design of failure free micro-electronic devices. Herein a short description is provided whereas the full details are given in [12].

Description of the problem:

The fabrication of micro-electronic devices (chips) is a multi-step process aimed at creating a layered structure made of semiconductors, metals and insulators. Thin aluminum interconnect lines are fabricated by sputtering technology on top of which the passivation is deposited by PECVD (Plasma Enhanced Chemical Vapor Deposition). At this last step of the fabrication process, the wafer is heated to approximately 400^{o}C, and the passivation Si_3N_4 layer is deposited to cover the metalic lines. Then, the wafer is cooled to room temperature, at which stage mechanical failures in the form of cracks are sometimes encountered. The cracks are often detected on "test chips" placed on the silicon wafer (typically of diameter of 12 inches) among the many chips fabricated on same wafer. The "test chips" are manufactured so to represent the worst possible configurations which increase their affinity to failure. I.e. if failure does not initiate in them (mechanical, functional, etc.), all other chips on the wafer are fail safe (see Figure 5). Previous work indicated that these cracks, emanating in the passivation layer

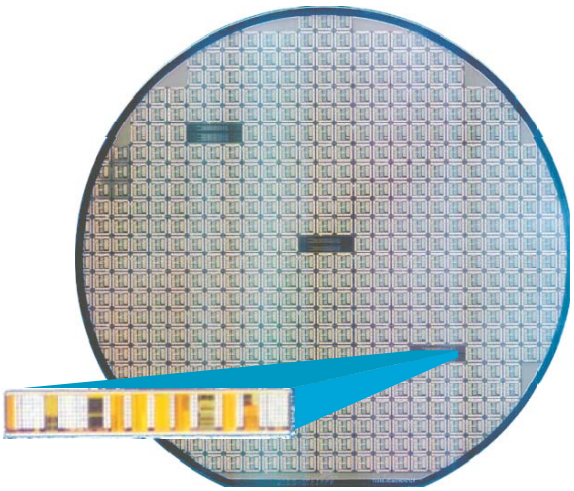

Figure 5: The silicon wafer patterned with hundreds of square dies. The unpatterned areas are the scribes. The 3 wide rectangles dies are the test chip arrays seen in the blowup.

at reentrant corners are due to the thermal loading caused when cooling the wafer in the last step of fabrication. The cause for the cracks is identified as a mismatch of the elastic constants and thermal expansion coefficients between the metal lines and the passivation layer. Typical cracks can be observed by sectioning the wafer at the test chip followed by a scanning electron microscope (SEM) inspection, as shown in Figure 6. Zoom-in figures of a typical top view and cross section of failed components show that the failure initiates at the vertex of a reentrant V-notch (keyhole corner) - as shown in Figure 7, and a plane-strain situation can be assumed. The typical feature dimension of the studied electronic devices are 0.1 to 1 μm where the assumptions of linear elasticity still hold, see e.g. Brandt et al. [13]. It is conceivable to assume that failure initiates when the average elastic strain energy contained in a sector of radius $R << 1$ around the singular point, over the volume of this sector, SED, reaches a critical value.

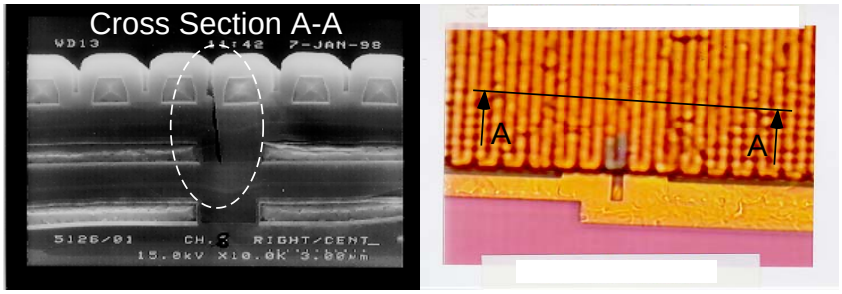

Figure 6: Cracks in the passivation layer: on the right a top view of the wafer, on the left a Scanning Electron Microscope image of the cross-section.

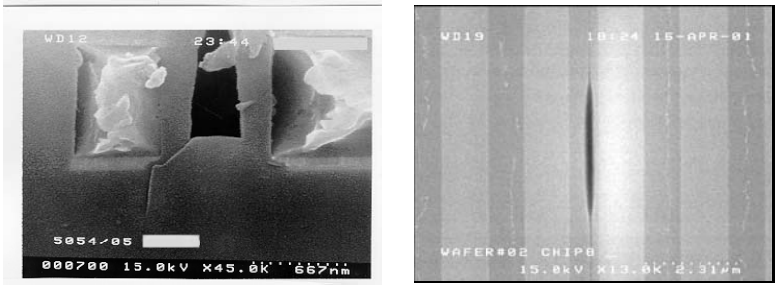

Figure 7: Top view of a crack (right) and a zoom-in at a cross-section (left) of typical failure initiation sites in the passivation layer (SEM image).

See also [14, 15]. This SED is computed once GSIFs and eigenfunctions have been computed:

$$SED[R] \approx \frac{A_1^2}{R^{2(1-\alpha_1)}(\pi - \frac{\omega}{2})} \int_{\theta_0}^{\theta_1} \left[\sigma_{11}^{(1)} u_1^{(1)} \cos\theta + \sigma_{12}^{(1)} \left(u_1^{(1)} \sin\theta + u_2^{(1)} \cos\theta\right) + \sigma_{22}^{(1)} u_2^{(1)} \sin\theta\right] d\theta \quad (15)$$

The $SED[R]$ depends of course on a characteristic length size R. It should be chosen small enough so that Ω_R is within the K-dominance region, ensuring that the singular terms do represent the exact solution. Given the value of $SED[R_1]$, one can easily determine the value of SED for a domain having a different radius R_2 by the simple equation derived from (15):

$$SED[R_2] = SED[R_1] \left(R_1/R_2\right)^{2-2\alpha_1} \quad (16)$$

A characteristic material dependent R can be determined for macroscopic domains, which is a function of the ultimate stress and the critical stress intensity factor, but for microscopic domains considered in this paper, these parameters are unavailable. We chose R as a characteristic dimension of 0.15μm and report all results for this value.

The electronic device in the neighborhood of the failures (Figure 8) is a layered structure made of the passivation layer (Si_3N_4 green colour in the Figure), the metal lines under the passivation and in the dielectric (made of aluminum, blue colour in the Figure) and the SiO_2 dielectric shown in red. It has been observed that failures if occur, initiate at one of the reentrant corners above the gap in the wide metal lines. Simulating of a small portion as shown in the right part of Figure 8 does not mimic important details and there is a need to simulate a larger portion as shown in the left part of Figure 8. There are several parameters which may contribute to the failure initiation, however, the design rules allow to change three during the fabrication process, namely: (a) the thickness of the passivation layer (denoted by h), (b) the height of the metal lines (denoted by H), (c) plasma power (W in Watts) applied during the chemical vapor deposition of the passivation layer, which indirectly influences the material properties (Young modulus and thermal expansion coefficient) according to the equation:

$$E(W) = 0.682 \exp\left(0.0097W\right) \quad [\text{GPa}], \qquad \alpha(W) = 0.000122 \exp\left(-0.0224W\right) \quad [1/C^o] \quad (17)$$

Passivation thickness has two effects. First, the deposition PECVD process has a relatively poor step coverage, and therefore tends to form overhangs resulting in "keyholes" (e.g. [16][p. 95]) and singular points. Second, the reentrant angle tends to zero as the passivation thickness increases until a given

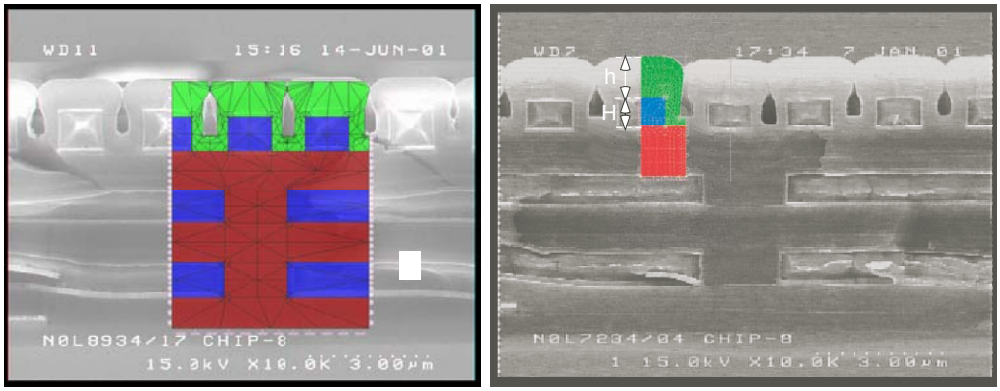

Figure 8: Finite element models superimposed in color on the SEM cross section of the test chip device. Blue-Aluminum, Red-SiO_2 dielectric and Green-Si_3N_4 passivation.

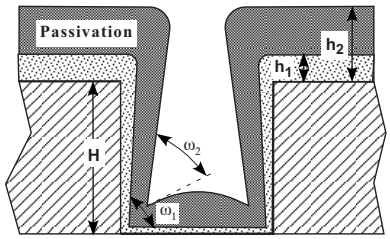

Figure 9: Nonconformal step coverage of deposited passivation film

thickness, and the strength of the singularity is more severe (see Figure 9), then, beyond $h \approx 6500\mathring{A}$, the angle slightly increases again.

Experimental validation of the failure criterion:

Validation of the failure criterion requires the same critical value of the SED be obtained for different configurations of the device. A set of experiments have been designed to test the hypothesis, and herby to determine the failure envelope. Past experience showed that the failure envelope resides within the following extreme limits:

1. Al lines of height $7000\ \mathring{A} \le H \le 11000\ \mathring{A}$ with the standard being $H = 9000\ \mathring{A}$.
2. Si_3N_4 thickness of $5000\mathring{A} \le h \le 8000\mathring{A}$ with the standard being $h = 6500 \pm 300\ \mathring{A}$.
3. Plasma power of 305 $Watts \le p \le 485\ Watts$ with the standard being $395 Watts$ (E and α for Si_3N_4 computed by (17)).

Twenty four wafers were fabricated with different manufacturing parameters in a form of a "test-cube" as shown in Figure 11, so that in some a crack was detected in the passivation layer after fabrication.

In order to correlate the experimental observations with the proposed failure criterion, we computed the SED associated with each tested wafer by p-FEM. The precise dimensions and the geometry in the neighborhood of the singular points has been measured for each of the tested wafers, and a p-version parametric finite element model has been constructed. The p-FEM commercial code StressCheck[1] has been used in our computations. Figure 10 presents several of the finite element models. To visualize the failure envelope, all wafers are shown on the test-cube together with the SED values in Figure 11. A semi-cylindrical failure envelope is observed, assessing the proposed criterion. A single value of the SED distinguishes between the cracked and intact wafers - under a threshold value of $SED_{cr}[R = 0.15\mu m] \approx 1000\ [J/m^3]$, all wafers manufactured are intact.

[1]StressCheck is trademark of Engineering Software Research and Development, Inc, St. Louis, MO, USA

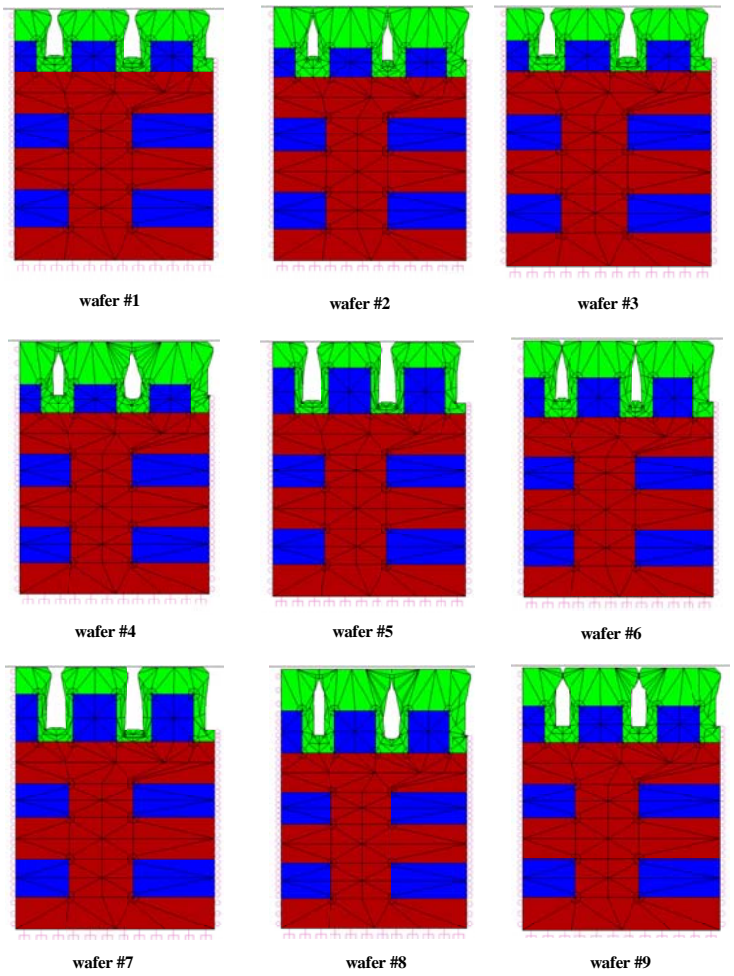

Figure 10: Finite element models simulating phase 1 wafers.

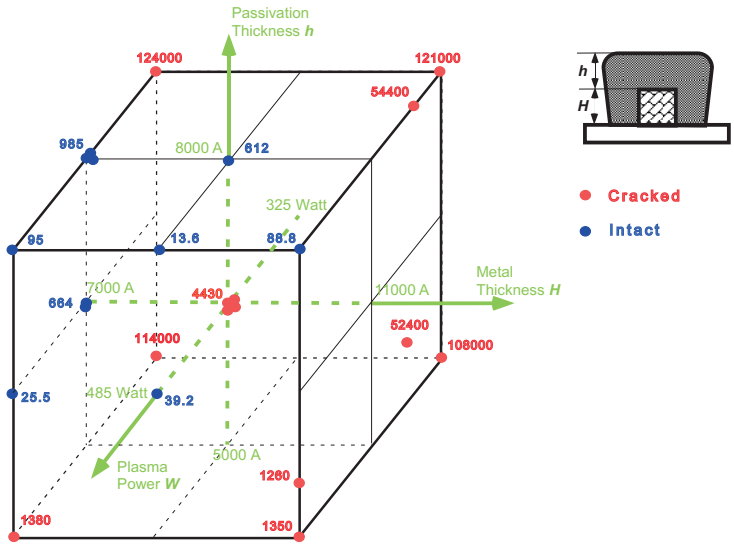

Figure 11: Mapping of SEDs on the "test-cube" (Units are J/m^3). The variation of the SED appears to reflect the mechanical status of the devices.

4 Failure criterion for V-notched specimens

We have also validated the SED criterion by performing experiments on specimens at the macro level as reported in [3, 4]. The validity of the SED criterion has been compared to several known failure initiation criteria at reentrant corners in brittle elastic materials. Their predictions, under mode I stress field, are compared to experimental observations carried out on PMMA (polymer) and Alumina-7%Zirconia (ceramic) V-notched specimens of varying opening angle as shown in Figure 12. These materials have been chosen due to their brittle elastic properties. Three different failure criteria, all

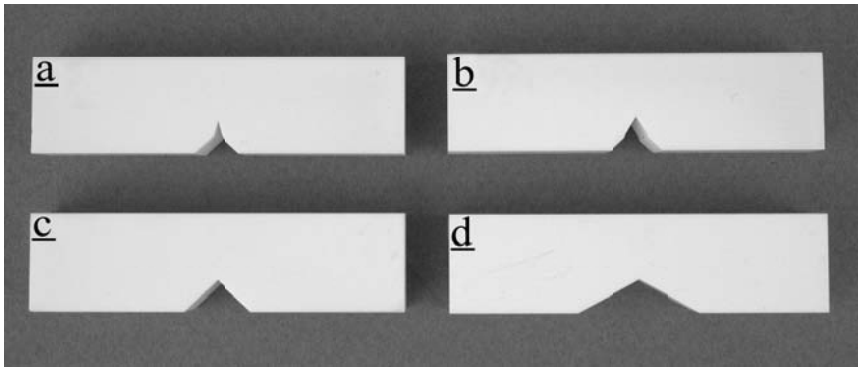

Figure 12: Alumina-7%Zirconia specimens with various radii and notch angles; (a) 0.06mm, 30° (b) 0.1mm, 60° (c) 0.1mm, 90° (d) 0.1mm, 120°.

requiring the GSIFs and eigen-pairs, have been compared: the SED defined in (15), Leguillon's criterion and Novoshilov's criterion defined below. Leguillon criterion [17], predicts failure if the first GSIF and eigen-pair equal a *critical material dependent parameter* k_c:

$$A_1\sigma_{11}^{(1)}(\theta=90^o)=k_c \stackrel{\text{def}}{=} \left(\frac{G_c}{K(\omega)}\right)^{1-\alpha_1}\sigma_c^{2\alpha_1-1} \tag{18}$$

where G_c is the fracture energy per a unit surface (also denoted by *toughness*) and σ_c is the 1-D stress at brittle failure (*strength*), both being material properties. The parameter $K(\omega)$ depends on the local geometry and boundary conditions in the neighborhood of the V-notch tip, the eigen-value α and its corresponding eigen-function, and the material properties (E and ν in isotropic materials).

Novozhilov [18] proposed the following failure criterion, investigated by Seweryn [19]:

$$A_1\sigma_{11}^{(1)}(\theta=90^o)=\alpha_1\sigma_c\left(\frac{2}{\sqrt{2\pi}}\frac{K_{I_c}}{\sigma_c}\right)^{2-2\alpha_1} \tag{19}$$

We performed experiments on over 70 V-notched specimens with four opening angles $\omega=30^o,60^o,90^o$ and 120^o, each having three different tip radii $\rho=0.03,0.06$ and 0.1 mm. The specimens were loaded so to produce pure "symmetric mode" stress field in the vicinity of the V-notch tip. The experimental set-up including the AE sensor is illustrated in Figure 13. We constructed finite element models of the various specimens tested, and loaded these by the load that caused the fracture. The p-FEM commercial code StressCheck has been used in our computations for the extraction of $A_1\times\sigma_{11}^{(1)}(\theta=90^o)$ at fracture. The predicted values by the various failure criteria and the experimental observations are plotted in Figure 14. Both the Novoshilov-Seweryn and Leguillon criteria seem to predict well the observed failures, however, as the opening angle increases, their validity deteriorates. This may be attributed to the non-exact measurement of σ_c, and the blunt tip radius. Leguillon criterion outperforms the Novoshilov-Seweryn criterion, and it has been refined to include ρ dependency so to match better the experimental observations - see [3].

Using the eigen-pairs, A_1 and the integration radius $R_{mat}=0.062mm$, we computed the SED at the instance of failure (denoted by $SED_{cr}[0.062mm]$) for the Alumina-7%Zirconia specimens, whereas or the PMMA, the integration radius used in our computations is $R_{mat}=0.0158mm$ (the determination of R_{mat} is detailed in [4]). Because the SED is proportional to the square of A_1, the sensitivity of the results to changes in this parameter is more pronounced. We have seen that the predicted SED_{cr} is a

Figure 13: Four-point-bending test fixture with acoustic emission transducer and crack opening displacement gage (PMMA specimen).

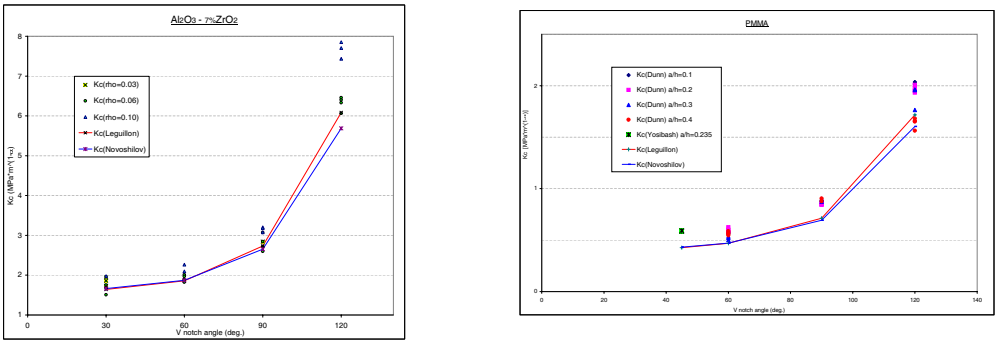

Figure 14: Predicted GSIFs (k_c) at failure by using Novoshilov and Leguillon's criteria, and GSIFs. Left - Alumina-7%Zirconia, Right - PMMA.

lower estimate of the experimental observations, and the scattering in SED_{cr} is wide. These two effects can be reduced by using the square root of the SED as the failure criterion, and taking into account the V-notch radius tip ρ.

5 Some remarks on edge singularities in 3-D domains

Although most of the research work on singularities in the past concentrated on 2-D domains under plane-stress/strain assumptions, in reality 3-D domains containing singular edges are of interest (we don't address herein vertex singularities). In this last section we show that the asymptotic expansion of the elasticity system in the vicinity of an edge contains more than the 2-D eigenpairs, and therefore special methods for the computation of the quantities of interest are formulated. Consider a 3-D domain Ω with a solid angle ω, created by the intersection of two flat surfaces, as shown in Figure 16. We denote the flat surfaces by Γ_1 and Γ_2. For simplicity of presentation assume that Ω contains only one straight edge $\mathcal{E}$, and is generated by the product $\Omega = G \times I$ where I is an interval $[-x_3, x_3]$, and G is a plane bounded sector of opening ω. The coordinate system is chosen so that G coincides with the (x_1, x_2) plane and I is along x_3. The *edge* $\mathcal{E}$ of interest is the set $\{\boldsymbol{x} \in \mathbb{R}^3 \mid r = 0,\ x_3 \in I\}$. The displacements vector in polar coordinates is denoted by $\tilde{\boldsymbol{u}} = \{u_r, u_\theta, u_{x_3}\}^T$. The Navier-Lamè (N-L) equations, in the neighborhood of the edge $\mathcal{E}$ is obtained by splitting the operator into three parts (see [20]):

$$\mathcal{L} = [M_0(\partial_r, \partial_\theta)] + [M_1(\partial_r, \partial_\theta)]\partial_3 + [M_2]\partial_3^2 \tag{20}$$

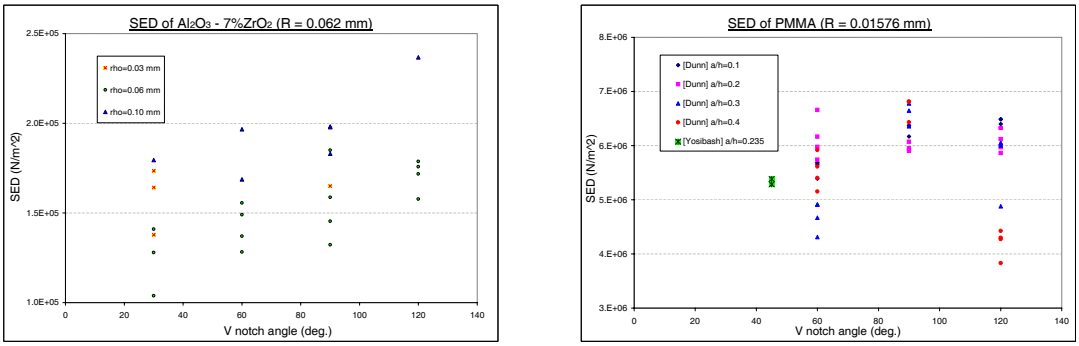

Figure 15: $SED_{cr}[0.062mm]$ in Alumina-7%Zirconia specimens and $SED_{cr}[0.0158mm]$ in PMMA specimens.

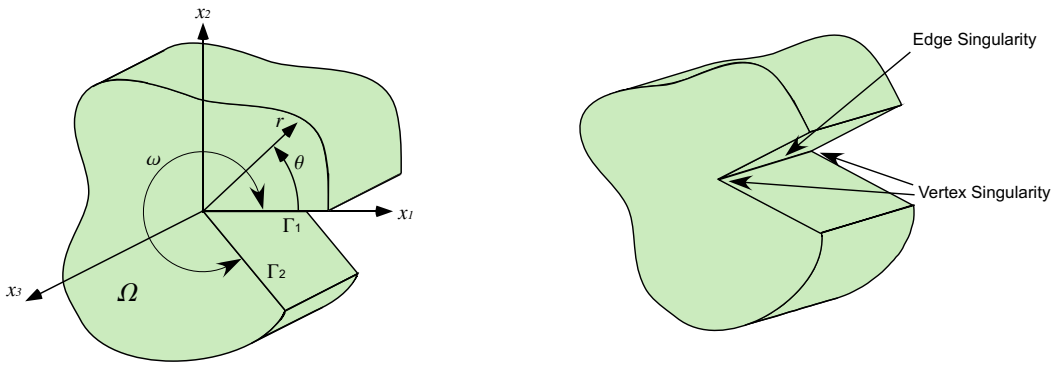

Figure 16: *(Left): Schematic 3-D domain, Ω. (Right): Edge and vertex singularities in 3-D domain.*

where $[M_i]$ are given for an isotropic elastic material by:

$$[M_0] = \begin{pmatrix} (\lambda+2\mu)\left(\partial_r^2 + \frac{1}{r}\partial_r - \frac{1}{r^2}\right) + \mu\frac{1}{r^2}\partial_\theta^2 & -(\lambda+3\mu)\frac{1}{r^2}\partial_\theta + (\lambda+\mu)\frac{1}{r}\partial_r\partial_\theta & 0 \\ (\lambda+\mu)\frac{1}{r}\partial_r\partial_\theta + (\lambda+3\mu)\frac{1}{r^2}\partial_\theta & (\lambda+2\mu)\frac{1}{r^2}\partial_\theta^2 + \mu\left(\partial_r^2 + \frac{1}{r}\partial_r - \frac{1}{r^2}\right) & 0 \\ 0 & 0 & \mu\left(\partial_r^2 + \frac{1}{r}\partial_r + \frac{1}{r^2}\partial_\theta^2\right) \end{pmatrix} \tag{21}$$

$$[M_1] = \begin{pmatrix} 0 & 0 & (\lambda+\mu)\partial_r \\ 0 & 0 & (\lambda+\mu)\frac{1}{r}\partial_\theta \\ (\lambda+\mu)\left(\partial_r + \frac{1}{r}\right) & (\lambda+\mu)\frac{1}{r}\partial_\theta & 0 \end{pmatrix}, \qquad [M_2] = \begin{pmatrix} \mu & 0 & 0 \\ 0 & \mu & 0 \\ 0 & 0 & (\lambda+2\mu) \end{pmatrix} \tag{22}$$

The splitting allows the consideration of a solution $\tilde{\boldsymbol{u}}$ of the form:

$$\tilde{\boldsymbol{u}} = \sum_{j\geq 0} \partial_3^j A(x_3)\boldsymbol{\Phi}_j(r,\theta) \tag{23}$$

Substituting (23) into (20), and collecting terms of same order of r, the functions $\boldsymbol{\Phi}_j$ must satisfy the three equations below, each defined on a two-dimensional domain G:

$$\begin{cases} [M_0]\boldsymbol{\Phi}_0 = 0 \\ [M_0]\boldsymbol{\Phi}_1 + [M_1]\boldsymbol{\Phi}_0 = 0 \\ [M_0]\boldsymbol{\Phi}_{j+2} + [M_1]\boldsymbol{\Phi}_{j+1} + [M_2]\boldsymbol{\Phi}_j = 0, \quad j \geq 0 \end{cases} \qquad (r,\theta) \in G \tag{24}$$

accompanied by traction free boundary conditions on the two surfaces Γ_1 and Γ_2.

The first partial differential equation in (24) generates the solution $\boldsymbol{\Phi}_0$, denoted *primal singular function*, which is the well known two-dimensional eigen-function of the form:

$$\boldsymbol{\Phi}_0 = r^\alpha \boldsymbol{\varphi}_0(\theta) \tag{25}$$

$\boldsymbol{\Phi}_0$ is the eigen-function associated with the eigen-value α of the degenerate boundary value problem over the 2-D domain G. The second PDE in (24) generates the function $\boldsymbol{\Phi}_1$ which depends on $\boldsymbol{\Phi}_0$ and is of the form:

$$\boldsymbol{\Phi}_1 = r^{\alpha+1}\boldsymbol{\varphi}_1(\theta) \tag{26}$$

The sequence $\boldsymbol{\Phi}_j$ (where $j \geq 2$) are the solutions of the third equation of (24). These are of the form:

$$\boldsymbol{\Phi}_j = r^{\alpha+j}\boldsymbol{\varphi}_j(\theta) \tag{27}$$

The $\boldsymbol{\Phi}_j$, where $j > 1$ are called *shadow functions* associated with the primal function $\boldsymbol{\Phi}_0$. There are an infinite number of shadow functions $\boldsymbol{\Phi}_j$ associated with any positive eigen-value α_i, and therefore:

$$\boldsymbol{\Phi}_j^{(\alpha_i)} = r^{\alpha_i+j}\boldsymbol{\varphi}_j^{(\alpha_i)}(\theta) \quad j = 0, 1, \cdots \tag{28}$$

Thus, for each eigen-value α_i, the 3-D solution, in the vicinity of an edge is:

$$\tilde{\boldsymbol{u}}^{(\alpha_i)} = \sum_{j\geq 0} \partial_3^j A_i(x_3) r^{\alpha_i+j}\boldsymbol{\varphi}_j^{(\alpha_i)}(\theta) \tag{29}$$

and the overall solution $\tilde{\boldsymbol{u}}$ is:

$$\tilde{\boldsymbol{u}} = \sum_{i\geq 1}\sum_{j\geq 0} \partial_3^j A_i(x_3) r^{\alpha_i+j}\boldsymbol{\varphi}_j^{(\alpha_i)}(\theta) \tag{30}$$

where $A_i(x_3)$ is the Edge Stress Intensity Function (ESIF) associated with the i^{th} eigen-value. For each positive eigen-value α_i and its primal and shadow eigen-functions, there exist a negative eigen-value and the associated *dual* and *dual − shadow* eigen-functions, denoted by $\boldsymbol{\Psi}_j^{(\alpha_i)}$. These, although not physically plausible, are used for extraction of the ESIFs (see for details [21, 22]).

5.1 The Quasidual Function Method for ESIFs extraction

The ESIF is a function along the edge, and therefore, it is our aim to compute its functional representation, and not only its value at specific points. If one is interested in $A_i(x_3)$ for example, a *quasidual-singular functions* is constructed:

$$\mathbf{K}_m^{(\alpha_i)}[B] \stackrel{\text{def}}{=} \sum_{j=0}^{m} \partial_3^j B(x_3)\, \boldsymbol{\Psi}_j^{(\alpha_i)}. \tag{31}$$

where m is a natural integer called the *order* of the quasidual function, and $B(x_3)$ is a constructed function called *extraction polynomial*. Each $\mathbf{K}_m^{(\alpha_i)}[B]$ is characterized by the number of dual singular functions m chosen.

By using the quasidual functions, one can extract a scalar product of $A_i(x_3)$ with $B(x_3)$ on $\mathcal{E}$. This is accomplished with the help of the surface integral $J[R]$, over the a cylindrical surface of radius R denoted by Γ_R. Define:

$$J[R](\mathbf{f}, \mathbf{v}) \stackrel{\text{def}}{=} \int_{\Gamma_R} \left([T]|_{\Gamma_R}\mathbf{f}\cdot\mathbf{v} - \mathbf{f}\cdot[T]|_{\Gamma_R}\mathbf{v}\right) dS = \int_I \int_0^w \left([T]|_{\Gamma_R}\mathbf{f}\cdot\mathbf{v} - \mathbf{f}\cdot[T]|_{\Gamma_R}\mathbf{v}\right)|_{r=R}\, R\, d\theta\, dx_3 \tag{32}$$

where $I \equiv \mathcal{E}$ (the edge) along x_3 and $[T]|_{\Gamma_R}$ is the radial Neumann trace operator:

$$[T]|_{\Gamma_R}\tilde{\boldsymbol{u}} \stackrel{\text{def}}{=} \begin{pmatrix}\sigma_{rr}\\ \sigma_{r\theta}\\ \sigma_{r3}\end{pmatrix} = \begin{pmatrix}(\lambda+2\mu)\partial_r + \lambda\frac{1}{r} & \lambda\frac{1}{r}\partial_\theta & \lambda\partial_3\\ \mu\frac{1}{r}\partial_\theta & -\mu\frac{1}{r} + \mu\partial_r & 0\\ \mu\partial_3 & 0 & \mu\partial_r\end{pmatrix}\begin{pmatrix}u_r\\ u_\theta\\ u_3\end{pmatrix} \tag{33}$$

With the above definitions we have the following theorem [21]:

Theorem 1 *Take $B(x_3)$ such that*

$$\partial_3^j B(x_3) = 0 \quad \textit{for} \quad j = 0, ..., m-1 \quad \textit{on } \partial I \tag{34}$$

then, if the ESIFs A_i in the expansion (30) *are smooth enough:*

$$J[R](\tilde{\boldsymbol{u}}, \mathbf{K}_m^{(\alpha_i)}[B]) = \int_I A_i(x_3)\, B(x_3)\, dx_3 + \mathcal{O}(R^{\alpha_1-\alpha_i+m+1}), \quad \textit{as} \quad R \to 0. \tag{35}$$

Here α_1 is the smallest of the eigen-values α_i, $i \in \mathbb{N}$.

Theorem 1 allows a precise determination of $\int_I A_i(x_3)\,B(x_3)\,dx_3$ by computing (35) for two or three R values and using Richardson's extrapolation as $R \to 0$.

Because $A_i(x_3)$'s functional representation is unknown, we seek its polynomial approximation using the orthonormal Jacobi-polynomials with a given weight $w(x_3) = (1-x_3^2)^n$, and similarly for constructing $B_n(x_3)$. Thus, the N-th order polynomial approximation of $A_i(x_3)$ is:

$$A_i(x_3) = \tilde{a}_0 J_n^{(0)} + \tilde{a}_1 J_n^{(1)}(x_3) + \cdots + \tilde{a}_N J_n^{(N)}(x_3) \tag{36}$$

where $J_n^{(k)}$ is the Jacobi polynomial of degree k and order n, i.e. associated with the weight $w(x_3) = (1-x_3^2)^n$. Due to the orthogonality property:

$$\int_{-1}^{1} (1-x_3^2)^n J_n^{(p)}(x_3) J_n^{(k)}(x_3)\,dx_3 = \delta_{pk} h_k \tag{37}$$

with some real coefficients h_k (depending on n), we choose the specific extraction polynomials denoted in the sequel by JB as:

$$JB_n^{(k)}(x_3) = (1-x_3^2)^n\,\frac{J_n^{(k)}(x_3)}{h_k}\,, \tag{38}$$

so that, according to (37), we retrieve the coefficients $\tilde{a}_k$ in (36) as a simple scalar product:

$$\int_{-1}^{1} A_i(x_3) JB_n^{(k)}(x_3)\,dx_3 = \tilde{a}_k \qquad k = 0, 1, \ldots, N. \tag{39}$$

Thus, by virtue of Theorem 1, the $J[R]$ integral evaluated for the quasi-dual functions $K_m^{(\alpha_i)}[JB]$ with the extraction polynomials $B = JB_n^{(k)}$, $k = 0, 1, \ldots, N$ provide approximations of the coefficients $\tilde{a}_k$.

5.2 Numerical Example - CTS

Consider the classical compact tension specimen (CTS) shown in Figure 17 under a bearing load of $100[N]$ in the x_2 direction and constant in x_3 direction, as presented in Figure 18. The thickness of the specimen is 2 ranging from $-1 < x_3 < 1$. Although the loading is independent of x_3, because of the Poisson's ratio effect and the vertex singularities at $x_3 = \pm 1$, we anticipate to see a variation in A_1 as the vertices are approached. The domain is discretized by using a p-FEM coarse mesh, with geometrical progression towards the singular edge with a factor of 0.15 (the smallest layer in the vicinity of the edge is at $r = 0.15$). In x_3 direction a geometrical progression of the mesh was adopted due to the vertex singularity at $x_3 = \pm 1$. Smallest layer in the vicinity of the vertex singular is $-1 < x_3 < -1 + 0.15^2$, $1 < x_3 < 1 - 0.15^2$. We perform a p-FEM analysis using the trunk space up to $p = 7$ (125,442 DOF). We

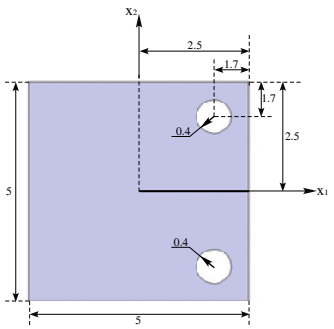

Figure 17: The CTS dimensions. The thickness of the specimen is 2 ranging from $-1 < x_3 < 1$.

extract the ESIF A_1, A_2 and A_3 as polynomials of degree 4 and 5. A_2 and A_3 are of order of 10^{-3} (the exact value is zero except maybe at the vertices), which is negligible compared to A_1, and therefore not plotted herein. The difference between the approximation of 4^{th} and 5^{th} order polynomial is negligible, demonstrating that a polynomial of order 5 approximates the ESIF well. The computed function A_1 by the QFM and pointwise values of K_I using the contour integral method (extracted at several points along the edge) at $R = 0.5$, $R = 0.3$, $R = 0.2$, and the Richardson's extrapolation for A_1, are shown in

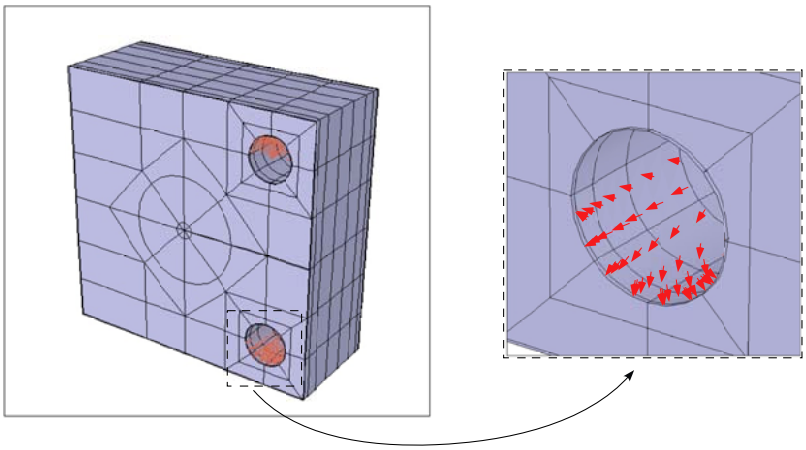

Figure 18: The p-FEM model of the CTS with a constant loading in x_3 direction.

Figure 19. One may notice the good convergence of the ESIF as $R \to 0$, as well as the better accuracy compared to the point-wise SIFs.

Although the loading is constant in x_3, the vertex singularities influence the the ESIF, and as seen usually in practice the crack propagation in the middle of the specimen is usually faster than at the outer surfaces. One may also notice the faster convergence of the ESIF compared to K_I values as $R \to 0$. The results obtained using ESIF extraction method are generated faster than point-wise extraction methods (K_I extraction), produce more accurate results and do not require plane stress or plane strain assumptions.

Moreover, we can see that by using Richardson extrapolation using $R = 0.5$, $R = 0.3$ and $R = 0.2$ we obtain better results than the extracted K_I at $R = 0.05$, thus we may use a much coarser mesh in the vicinity of the singular edge.

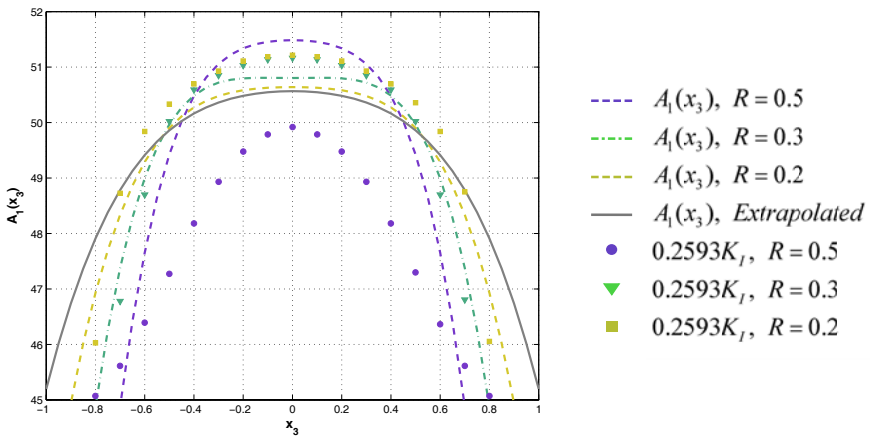

Figure 19: $A_1(x_3)$ and K_I extracted using different R's for the compact test specimen using coarse grid with 125442 DOF.

ACKNOWLEDGEMENTS: The author gratefully acknowledges the partial support of this work by the VATAT-VEE (grant number 84154201-86/02).

REFERENCES

[1] M. L. Williams. Stress singularities resulting from various boundary conditions in angular corners of plates in extension. *Trans. ASME, Jour. Appl. Mech.*, 19:526–528, 1952.

[2] J. P. Dempsey. Power-logarithmic stress singularities at bi-material corners and interface cracks. *Jour. Adhesion Sci. Technol.*, 9(2):253–265, 1995.

[3] D. Leguillon and Z. Yosibash. Crack onset at a v-notch. Influence of the notch tip radius. *Int. Jour. Fracture*, (122):1–21, 2003.

[4] Z. Yosibash, A. Bussiba, and I. Gilad. Failure criteria for brittle elastic materials. *Int. Jour. Fracture*, 125(3-4):307–333, 2004.

[5] Z. Yosibash and B. A. Szabó. Numerical analysis of singularities in two-dimensions. Part 1: Computation of eigenpairs. *Int. Jour. Numer. Meth. Engrg.*, 38(12):2055–2082, 1995.

[6] H. Blum and M. Dobrowolski. On finite element methods for elliptic equations on domains with corners. *Computing*, 28:53–63, 1982.

[7] B. A. Szabó and I. Babuška. Computation of the amplitude of stress singular terms for cracks and reentrant corners. In Cruse T. A., editor, *Fracture Mechanics: Nineteenth Symposium*, pages 101–124. ASTM STP 969, ASTM, Philadelphia, 1988.

[8] B. A. Szabó and Z. Yosibash. Numerical analysis of singularities in two-dimensions. Part 2: Computation of the generalized flux/stress intensity factors. *Int. Jour. Numer. Meth. Engrg.*, 39(3):409–434, 1996.

[9] Z. Yosibash and B. A. Szabó. Generalized stress intensity factors in linear elastostatics. *Int. Jour. Fracture*, 72(3):223–240, 1995.

[10] Z. Yosibash. On solutions of two-dimensional linear elastostatic and heat-transfer problems in the vicinity of singular points. *Int. Jour. Solids and Structures*, 34(2):243–274, 1997.

[11] Z. Yosibash. Computing edge singularities in elastic anisotropic three-dimensional domains. *Int. Jour. Fracture*, 86(3):221–245, 1997.

[12] Z. Yosibash, O. Adan, R. Shneck, and H. Atlas. Thermo-mechanical failure criterion at the micron scale in electronic devices. *Int. Jour. Fracture*, 122:47–64, 2003.

[13] O. Brandt, K. Ploog, Bierwolf R., and M. Hohenstein. Breakdown of continuum elasticity theory in the limit of monoatomic films. *Physical Review Letters*, 68(9):1339–1342, 1992.

[14] G. Amar and Z. Yosibash. p-FEM for formulating an elastic criterion for predicting mechanical failures at 2-D singular points. In *p-FEM2000, May 31 - June 2: Summaries of Papers.*, page 15, St. Louis, MO, USA, 2000. Washington Univ.

[15] P. Lazzarin and R. Zmabardi. A finite-volume-energy based approach to predict the static and fatigue behavior of components with sharp v-shaped notches. *Int. Jour. Fracture*, 112:275–298, 2001.

[16] S.M. Sze. *VLSI Technology.* McGraw-Hill, 1983.

[17] D. Leguillon. A critetion for crack nucleation at a notch in homogeneous materials. *C.R. Acad. Sci. Paris, Ser IIb*, 329:97–102, 2001.

[18] V.V. Novozhilov. On a necessary and sufficient criterion for brittle strength. *Jour. Appl. Math. Mech. (Translation of PMM)*, 33(2):212–222, 1969.

[19] A. Seweryn. Brittle fracture criterion for structures with sharp notches. *Eng. Frac. Mech.*, 47(5):673–681, 1994.

[20] M. Costabel and M. Dauge. General edge asymptotics of solution of second order elliptic boundary value problems I & II. *Proc. Royal Soc. Edinburgh*, 123A:109–184, 1993.

[21] M. Costabel, M. Dauge, and Z. Yosibash. A quasidual function method for extracting edge stress intensity functions. *SIAM Jour. Math. Anal.*, 35(5):1177–1202, 2004.

[22] Z. Yosibash, N. Omer, M. Costabel, and M. Dauge. Edge stress intensity functions in polyhedral domains and their extraction by a quasidual function method. Submitted for publication.

Solid and Structural Mechanics

JOHN ARGYRIS AND HIS DECISIVE CONTRIBUTION IN THE DEVELOPMENT OF LIGHT-WEIGHT STRUCTURES. FORM FOLLOWS FORCE

Marios C. Phocas
Department of Civil and Environmental Engineering,
Faculty of Engineering, University of Cyprus,
75 Kallipoleos Str., B.O.Box 20537, 1678 Nicosia, Cyprus
e-mail: mcphocas@ucy.ac.cy

Keywords: John Argyris, Finite Elements, Light-Weight Cable-Net Structures, Computer Applications

Abstract. *This presentation contains an introductory outline of the biography and major achievements of John H. Argyris in the area of computational mechanics, emphasizing their influences on the development of light-weight structures. His contribution to the development of the Finite Element Analysis and his subsequent influential work at the University of Stuttgart are also addressed herein. The main areas of interest are the numerical methods of analysis initiated by John Argyris on the design of long-span net structures, since their origin, in the early 70ies. The design methodology applied for the first time at the University of Stuttgart at that time, based on computer applications of analysis is briefly documented. Most important, reference throughout the presentation is made to the cable-net structure for the roof of Munich 1972 Olympics-Arenas. The particular project, the first of its kind worldwide, represents historically the first architectural-engineering, holistic design approach of long-span cable-net structures, attaining the borders of structural engineering of its time. The structural requirements demanded equilibrium between the architectural form concept and the structural analysis; the latter is based on the concept of form finding as an interactive result of defined loading case, and led to the first large-scale computer applications. Further developments from John Argyris and his research team are highlighted herein in the respective interdisciplinary research, which followed at the University of Stuttgart in the time range of the subsequent 15 years, ever since being invaluable in structural engineering and the development of high-technology architecture.*

1 INTRODUCTION

The 5th international congress on computational mechanics is dedicated to the memory of Professor John H. Argyris, the most outstanding pioneer in the area, been an exceptional specialist in the field of computers, aeronautics and fluid mechanics and one of the inventors and creators of the Finite Element method that revolutionised engineering sciences. The finite element method was expanded and applied for the first time internationally for the design, development and analysis of the long-span cable-net structure of the Olympic Stadium in Munich 1972, making the realisation of the original “architectural vision” feasible.

The historical evolution of the project is representative in broader context of the fact, that light-weight structures revolutionised on their turn architectural technology and engineering in the early 70´s, while having established new frame conditions and methodologies regarding cooperation between architects and structural engineers in practise and research. Cable-nets as architectural and at the same time structural elements enable a wide variety of forms with no similarity, precisely because their form finding obeys strict physical laws as to the geometry of the structure and the prestress of the elements. On this line the directly derived architectural advantages of lightness, transparency, open and yet protected free spaces, as well as optimal integration in the urban context, are made possible due to the respective engineering advancements in structural analysis, initiated mainly by John Argyris.

2 THE PERSON, JOHN H. ARGYRIS; HIS EARLY ACHIEVEMENTS

John Argyris, Professor Emeritus of the University of Stuttgart and the University of London, died on the 2nd April 2004 in Stuttgart at the age of 91. Born on 19th August 1913 in Volos, Greece, he was educated in Civil Engineering at the Technical Universities of Athens and Munich, where he completed in 1936 his Diploma in Engineering with distinction. He was then employed by a private consulting organisation (J. Gollnow & Son, Stettin, Germany) working on the technical design of highly complex steel and light alloy structures, including the design of a 320 m high radio transmitter mast with a heavy mass concentrated at the top – at that time an irresolvable problem. Following post-graduate studies in Aeronautics and Mathematics at the Technical University of Berlin and at the Technical University of Zurich he became director of the research department of the Royal Aeronautical Society from 1943 to 1949, and joined the University of London, Imperial College of Science and Technology, as Senior Lecturer in 1949, Reader in the Theory of Aeronautical Structures from 1950 to 1955 and Professor of Aeronautical Structures between 1955 and 1975. He was appointed Professor at the

University of Stuttgart in 1959, Director of the Institute of Statics and Dynamics of Aerospace Structures between 1959 and 1984, and subsequently Director of the Institute of Computer Applications from 1984 to 1994, which became one of the most renowned of its kind in the world.

The comprehensive analytical research work performed by Argyris at the Royal Aeronautical Society on elements of the elastic aircraft was included as part of the Handbook of Aeronautics No. 1 in the early 50ies[1]. The work on energy theorems and structural analysis undertaken at Imperial College, originally published in a series of articles in Aircraft Engineering between October 1954 and May 1955, appeared as a book in 1960, been followed by four further editions until 1977[3]. As stated by Argyris himself, the purpose of the work achieved in this frame was two-folded: "Firstly, to generalise and extend but at the same time also to unify the fundamental energy principles of analysis of elastic structures. Secondly, to develop in considerable detail practical methods of analysis of complex structures, in particular for aeronautical engineering applications". The most important contributions are the matrix methods of analysis, whereas Argyris believed that "the matrix formulation besides providing an elegant and concise expression of the theory of such structures, is ideally suited for modern automatic computation because of the systematic ordering of numerical operations which the matrix calculus affords". As developed in this context, the matrix methods of analysis follow particular forms of the two fundamental energy principles applicable to structures made up as an assembly of discrete elements. The first principle leads to an analysis in terms of displacements as unknowns (displacement method), while the second leads to an analysis in terms of forces (force method). But in stressing the advantages of a unified approach to these diverse problems, Argyris pointed even at this time out, that "the ability to tackle successfully problems in which the numbers of unknowns is measured in hundreds carries with it the necessity of rethinking one's practical approach, if maximum advantage is to be gained from modern computational techniques, (…) in order to reduce the manual preparation of data to a minimum, and reduce the probability of errors". This respectable background, along with the appealing presentation in matrix notation of the dual force and displacement methods, raised indeed the active interest in the scientific circles and formed his major contribution in the creation of the revolutionary finite elements analysis method.

Recognizing the significance from the very beginning of an effective utilization of the digital computer in structural analysis, Argyris with his Institute of Statics and Dynamics at the University of Stuttgart was mainly devoted to the research and development of computer methods for structural analysis. With the development of the regional Computing Centre at the University of Stuttgart, stress analysis and the restricted capacity of digital computer had favoured the elaboration of the force method first. However further developments as regards the computer capacity played an important role in advancing the displacement method, enabling this way the complete automation in the computer. The development of automatic system for kinematic analysis (ASKA) provided the unifying frame for diverse research activities in the areas of finite elements, solution techniques and software. At this time, in the second half of the 60´s intensive research on and with finite elements began, replacing by now the term matrix methods. Apart from linear elasticity, geometrical non-linearity and plasticity were touched upon at an early stage.

3 LIGHT-WEIGHT STRUCTURES

Long-span cable-net or membrane structures possess in architectural context several advantages: Column free roofing of large areas, the possibility of translucent covering, fast and easy erection, dismantlement, recycle ability and intensive space experience. These can be supplemented with the definition of "usage", expanded on its term, a) through the recognition of persistent values´ assessments determining the contemporary beliefs of usage or usefulness, b) through the decision of planning and constructing buildings based on presently set usage necessities or on more conditional flexibility for further usages to plan with and c) through the construction of buildings allowing for future changes in their disposition. Light-weight structures in architecture should thus imply the development of an optimal structural form, having at the same time the identity of a "sculptural element", whose image and effectiveness correspond to the task formulation of space delimitation, related to the usage and urban context. The analogies towards the forms of nature are easily perceived visually, although these buildings are in their construction and development of high technology.

Light-weight structures stand in the process of design, or better of the form-finding, closer to the applied sciences than the design and arts, although they look like they were designed freely. Both, cable-net and membrane structures are stressed only in tension while flexible in bending, and stabilised through prestress. Cable-nets usually consist of two intercrossing cable meshes with opposite curvature to each other, leading to primarily anticlastic shapes. The cable meshes are prestressed against each other and connected to flexible edge cables in bending, in order to carry their loads to singular anchoring points (fig. 1). Due to manufacture reasons, in the regular inner areas almost equally meshed nets are selected. For the creation of the double curvature high and low points – masts and anchorage points on foundations – are developed, having a fixed spatial location in space. Support conditions, members stiffness and axial properties are main factors affecting the final form. For these structures, form, construction and stress distribution are conditioned reciprocally, i. e. the structural form cannot be geometrically determined and then analysed in its static behaviour, the way this is practised for

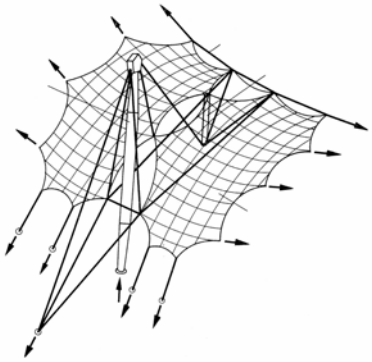

Figure 1. Principle of force transition in two cable-net elements

conventional buildings. Instead, the design geometry is revised in an iterative process of form finding, so long until the equilibrium form under the imposed requirements and edge conditions has been reached. Furthermore, alterations of the structural form have direct consequences in the construction and montage of all elements. Form finding means the search for a form, which initiating from the design idea, satisfies to the best the static forces and material specific conditions, in the sense of an optimization. In this context, the subjective selection of the architectural form is rather replaced by the objective determination of the structural form.

3.1 The Olympic Stadium of Munich

When the architectural competition on Friday 13.10.1967 for the sporting premises of the 20th Olympic Games in 1972 in Munich was won by the Stuttgart architects Behnisch & Partner with Juergen Joedicke, the advantages of the design were obvious, arising from the main architectural idea for a transparent, unusual and innovative tent roof (fig. 2). Nevertheless no one from the jury actually believed that the proposed design of the light-weight structure, covering an area of 75.000 m², could be realised. Frei Otto and Fritz Leonhardt, both Professors at the Faculty of Civil Engineering at the University of Stuttgart, while not having participated in the design, insisted on the contrary. The competition results were documented in the German architectural press as follows[7]: “The realisation and conviction are important, that not the tent roof structure à la Montréal was awarded, as a fashion of architecture, but it was the overall concept of the work of Behnisch that convinced the jury. (…) The built form is not the primary, but the aim conception for a task, which exactly is not derived from a formal aspect but from the nature of the problem. And for this the technological construction possibilities ought to be found”.

Figure 2. Aerial view of the Olympic Stadium in Munich 1972

On the 1.3.1968 Behnisch & Partner were commissioned with the construction of the sport premises on the southern area of the Olympic park. The prestressed cable-net roof was set to further planning. A timber and a perlite concrete covering of the net were abandoned, as well as a timber shell solution. All systems were too stiff for the selected roof form. The preliminary construction solution was then found by Frei Otto and his team through model studies. Owing to the lack of other possibilities, initially tulle models were measured photogrammetrically to ascertain the exact cutting pattern. At that time, only model techniques, geometrical

expedients and idealised calculation methods, that were adequate for relatively simple forms, were used. To that, construction possibilities would compensate the insufficiencies of the design, the construction planning and the finishing on site. Nevertheless, such traditional methods of design, practiced already by Frei Otto with Rolf Gutbrod and Fritz Leonhardt for the preceded German pavilion of the Expo 67 in Montréal could not satisfy any more the requirements for precision, safety and calculability of the particular structure; in detail, the requirements with respect to the geometrical precision, as well as the cutting pattern, meaning the determination of the exact length of all cables under the planned prestress, material related issues, as for example cable anchorages and fittings and the prefabrication demanded totally new solutions. As a matter of fact the light-weight structure of Munich showed that to that point there was no experience with the scale and measures of the particular project. With the task of its construction the breakthrough into a different, new quantitative dimension was needed, as this project went to the borders of structural engineering of its time in many fields: Structural design, computer application, material science and technology, structural detailing, prefabrication, welding technology, erection.

The costs of the project increased from an originally estimated amount of 17 millions DM to 190 millions DM, not only due to the necessary high-technology construction but also due to lack of practical experience with this new technology from the planners. The words of the German politician Hans-Jochen Vogel are remarkable in this context[6]: “I have voted from the beginning for this project and I would have given an unconditional yes even today (1972), in knowledge of all facts. (…) A society should also once bring the strength and the courage to spend a large amount for an aim-free project, in narrow sense, for an architectural work of art. Without this a lot of buildings would not have originated, that we count today with pride to the unrenounceable components of human culture”. In this frame the planned expenditure should remain manageable; otherwise the reaction at a misfortunate effort would fall socially destructive. All decisions taken for the project complied with the aims set in correspondence to the state of technology and science to select progressive but sufficiently secure solutions.

3.2 Analytical form finding

Form finding implies a procedure for the investigation of the geometry of the structure. The principle of form finding relates to the fact that under given loads a favourable geometry of the structure is adjusted. Favourable flow of forces and form are interdependent. The form and the respective stress situation, that is also dependent on the material properties lead to the equilibrium state. Analytical form finding is, contrary to the experimental methods, based on physical models. In dependence to the position of the outer guyed points – fixed points –, the connection of the net in its knots and the size of the tension forces of the individual cables, an endless variety of equilibrium forms can be developed. The final solution is a compromise between function and aesthetics on one side, and allowable forces, uniformity in their distribution, material properties and deformations under the loading on the other side.

In prestressed cable-nets the geometric form and the prestress, which develops through elastic alteration of the length of all individual elements, are unified with each other. Modification of the double curvature and the prestress are the most important ways for influencing and optimising the strains. But influencing the curvature relations in the net means always alteration of the fixed points, i. e. alteration of the height and location of the guyed points and with this, a sensible encroachment in the overall design concept. This particular property of prestressed cable-nets concentrates in influencing the stiffness and overall structural behaviour under different loadings only through global modifications of the curvature, through modification of the location of the fixed points and the prestress in the entire net. On this line, aim of the form finding is the calculation of the structure with defined geometric edge conditions in obtaining a concrete stress situation.

Computer oriented calculation methods that were developed at the Institute of Statics and Dynamics for Aerospace Structures and were at that point for long time applied with success offered the decisive momentum. In correspondence to the requirements of computer applications in structural engineering there is the aim at foreground of investigating analytically each individual structure with a unified calculation process. The method of analysis through finite elements includes the following main steps:

- Fictive division of the structure in small individual elements (finite elements)
- Mathematical description of the behaviour manner of every fictive element according to a behaviour pattern
- Join of individual elements to a discrete mathematical model for the entire structure
- Numerical investigation of the displacements and stresses in the discretised structure according to a predefined loading.

A direct application to the stated problem formulation for long-span net structures was nevertheless not possible. New developments regarding the theory and calculation programs with appropriate formulation and design of the second and fourth analysis step became necessary and had to be worked out in very limited time. Within six weeks a new safe calculation of the structure was to be set up at the Institute of Statics and Dynamics of Aerospace Structures. The Institute was once again required to perform pioneer work and succeeded to manage the given tasks, while achieving a breakthrough with the calculation of nonlinear problems with more than 11.000 unknowns (fig. 3). The success of the new computer designs was confirmed by the problem free

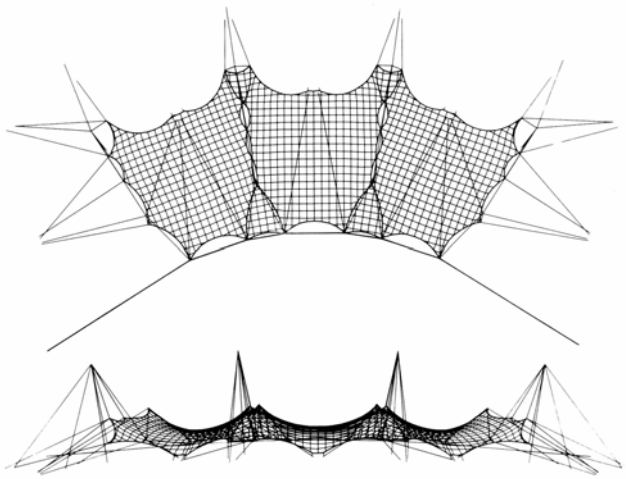

Figure 3. Analytical form finding of the east tribune with finite elements[5]

mounting and the stability of the structure. The affordance of the first large scale computers CD6600 in Germany showed repeatedly, what kind of revolution was initiated in the engineering sciences.

In the applied method of finite elements, the static equilibrium of the prestressed net was investigated through a geometrical nonlinear elastostatic analysis. The investigated form of the structure was at first approximated and then numerically improved interactively, until equilibrium at the required prestress level was achieved (fig. 4). In general the origin can even be a flat net, which is prestressed between fixed points in plane. The fixed points are then shifted vertically for bringing the net in a spatial curved shape. The calculation is nonlinear due to significant modifications in the net geometry. The prescribed displacements destroy the equilibrium state of the cable forces. Therefore, for every displacement state of the supports the related equilibrium form of the prestressed net is investigated. The procedure can also be described as the numerical simulation for a stepwise hanging of the net from the origin plane. The method is not restricted only to cable-nets, but it can also be applied at equal level to membrane structures and structures with cable and membrane components.

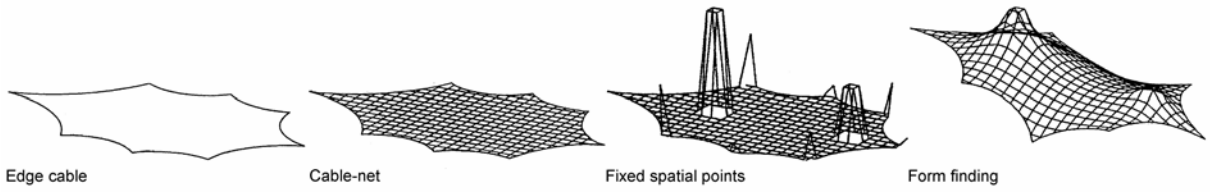

Figure 4. Typical procedure for analytical form finding of light-weight structures

3.3 Construction

The developed cable-net structure consisted of a number of almost regular saddle-shaped surfaces framed by edge cables (fig. 5). In the case of the stadium roof, a huge massive edge cable curving around the boundary of the playing field provides the tension for the roof to project over the stands. By contrast, for example the swimming hall was given a freeform geometry, point-suspended from an overhanging mast on the outside. Following the design phase, in the choice of cables and the construction design, a modular principle was adopted in order to achieve clarity in design and a sense of calmness and tranquillity through structural order, as well as for rationalisation by means of serial production. This ensured that the building would be completed on time. For this reason, the edge, ridge and valley cables in the nets consist all of an identical locked coil cable with diameter of 80 mm, meaning that according to requirements, one, two or more of these cables were linked one after the other. In this way all the clamps, devitative grooves in the cast saddles, and cable anchors could be standardised. The large edge cable for the stadium was treated in a similar manner, as were in principle, the bundles of prestressed strands for the stay cables.

Designed as the first permanent cable net construction, minimum corroding tendencies, minimum sensitivity to transverse forces on the clamps and devitative points or to bends during erection, as well as controlled expansion were all deciding factors in the choice of cables made of 19 thick wire strands. In addition, rotating clamps with a single-screw pivot were used, resulting in double strands. In this way rotating nodes were realised,

Figure 5. Detail views of the cable-nets

so that no deformation restrictions of the meshes would result in unacceptable falsification in cutting the nets to size. At the factory stage, aluminium clamps with a centered hole were pressed on for ensuring that no additional measurements would be needed at the site.

The 75 x 75 cm mesh width of the double layer cable-net was meant to be as large as possible in order to minimise the number of clamps and nodes, but small enough for the net and its covering to be accessed directly, thus enabling it to be erected without scaffolding. Following long consultations with specialists it was decided, that the roof should be covered with translucent, quadratic brown toned acryl-glass plates with dimensions in plane of 3 m, connected to flexible rubber supports.

4 COMPUTER APPLICATIONS

In the short time available between the architectural competition and the construction of the project it was not possible to achieve an entirely harmonic composition between form, construction and function. Even so the result in Munich was a great success internationally. The phase of in-depth study for evaluation of the gained experience, integration and consolidation succeeded. The instrumentation was enlarged and at high level optimised. That was the time of initiation of the special interdisciplinary research area 64 on Long-Span Net Structures. The research was undertaken based on a multidisciplinary composition of 12 Institutes of the University of Stuttgart, covering the related areas of architectural analysis, historical development, structural analysis, construction and computational mechanics.

The pioneer spirit of the first time phase continued in the following years. Fundamental considerations on the natural methodology conceived earlier by Argyris were consistently extended from structural mechanics to the mechanics of solid continua, heat flow and fluid dynamics up to the mid 80ies. With the form finding for the suspended cable roof of the Olympic Stadium in Munich, a period was initiated which was dedicated to an automatic form generation, including pronouncedly nonlinear problems in statics, dynamics, finite strains in elasticity and plasticity. In nonlinear elastic structures, progress was achieved regarding issues of static and dynamic stability under non-conservative loading. The conclusion of the research on the form finding, the statics and dynamics of long-span net structures formed the basis for the subsequent development of a modern program system for nonlinear analysis of such structures. The treatment of the tasks in the frame of the special research area demanded the development of a corresponding project group at the Institute, which was in its interdisciplinary composition unique. Involved herein were the disciplines of statics and dynamics, numerical analysis and programming, subsequently joined by the material mechanics. The developed calculation procedures could be expanded and applied for further studies, as for example for the stadium of Niedersachsen in Hanover and the Olympic Stadium of Montréal.

Following emeritation from the Institute of Statics and Dynamics of Aerospace Structures at the University of Stuttgart, Argyris founded the Institute of Computer Applications, which soon became one of the most renowned of its kind in the world for research and development in engineering and science. At that time, from 1986 until 1988, Argyris published the material on the finite element method in three volumes that had been the subject of work at the Institute in Stuttgart[4]. Interdisciplinary research on an international level was characteristic, the projects ranging from the micro-mechanics of materials to re-entry aerodynamics within the European Hermes Programme and the utilization of novel computer architectures such as multiprocessor ones. Further primary area of interest was on chaotic phenomena, which fascinated Argyris for years and concluded with the publication of a textbook in 1994[2]. But ever devoted to the academia, Professor Argyris stayed in close relation with his office even after the Institute of Computer Applications was restructured in 1994.

5 CONCLUSIONS

The continuous, creative work of John H. Argyris has left its mark on science, his personality influenced generations of engineers, scientists and researchers, who studied his thorough accomplishments in the fields of

computational mechanics. More than 400 paper publications documenting his work, his founding in 1972 of the Journal "Computer Methods in Applied Mechanics and Engineering", as well as his distinguished memberships, among others to the Royal Society (F.R.S.), 1986, and to the Royal Aeronautical Society (F.R.Ae.S.), from 1955 onward, 18 honorary doctoral titles, Professorships and more than 25 awards, prizes and medals from 16 industrialized nations of the world, among others the Einstein award, the von Kármán Medal in 1975, the Timoshenko Medal in 1981 and the Prince Philip Medal in 1997, are all indicative for his achievements in the engineering sciences.

If one makes the question of the relation of aims and means, it seams that the answer is clear: Aims should not always be set according to means. The historical importance of the Olympic Stadium in Munich and since then, its every day usage is today subject to no disagreement. When presently it is realised with high certainty that the construction type of long-span structures is entirely commanded and a series of design and analysis methods is available, this is the outcome of the interdisciplinary work during and after the period of Munich 1972 Olympics-Arenas. The subject area will still occupy for many years architects and engineers while bearing further on fruits. The first light-weight structures in Munich secured international influence and recognition, and light-weight structures are built according to these ideas and the method of analysis developed. Elsewhere independent further developments have arisen. New materials support these developments. What remains the same is the methodology of design and the tools of analysis that enabled the breakthrough for implementation at the first place.

REFERENCES

[1] Argyris, J., Dunne, P.C. (1952), "Structural Analysis, Structural Principles and Data, Part 2", *Handbook of Aeronautics No. 1*, The New Eva Publ. Co. Ltd, London.
[2] Argyris, J., Faust G., Haase, M. (1994), *An Exploration of Chaos*, Elsevier, Amsterdam.
[3] Argyris, J., Kelsey, S. (1960), *Energy Theorems and Structural Analysis*, Butterworths, London.
[4] Argyris, J., Mlejnek, H.-P. (1986, 1987, 1988), *Die Methode der Finiten Elemente*, Vol. I, II, III, Vieweg, Braunschweig.
[5] Doltsinis, I. (1990), "Computermethoden der Tragwerksberechnung", *Leicht und Weit. Zur Konstruktion weitgespannter Flächentragwerke; Ergebnisse aus dem Sonderforschungsbereich 64 "Weitgespannte Flächentragwerke" der Universität Stuttgart*, pp. 170-189, VCH Verlagsgesellschaft mbH, Weinheim.
[6] *Olympia in München*. Offizielle Sonderhefte (1969-1972), Münchener Leben Verlag, Munich.
[7] Wallenborn, J.K. (1967), "Für die XX. Olympischen Spiele 1972 in München…, Ergebnisse des Städtebau- und Bauwettbewerbs", deutsche bauzeitung 11, Stuttgart.

LIMIT LOAD OF A MASONRY ARCH BRIDGE BASED ON FINITE ELEMENT FRICTIONAL CONTACT ANALYSIS

G.A. Drosopoulos[I], G.E. Stavroulakis[II], C.V. Massalas[III]

[I]Department of Material Science and Technology, University of Ioannina, Ioannina, Greece
[II]Department of Mathematics, University of Ioannina, Ioannina, Greece and
Depatment of Civil Engineering, Technical University of Braunschweig, Germany
[III]Department of Material Science and Technology, University of Ioannina, Ioannina, Greece
Emails: {me01122}{gestavr}{cmasalas}@cc.uoi.gr

Keywords: masonry arch, limit load, unilateral contact

Abstract. *The limit load of a stone arch bridge can be identified by the lack of solvability of a finite element analysis including contact interfaces that simulate potential cracks. Opening or sliding at some of them indicates crack initiation. The ultimate load has been calculated by using a path - following (load incrementation) technique. The method is applied on the Strathmashie stone bridge and the results are comparable with the ultimate failure load prediction of the collapse mechanism method and with experimental data published in the literature.*

1 INTRODUCTION

The limit load of a masonry arch is mainly attributed to the interaction of unilateral (no-tension) effects and the structural form. In the present work the limit load of such a bridge is calculated by exploiting the solvability of the arising unilateral structural analysis problem. The finite element of the bridge includes a number of interfaces obeying unilateral contact with friction. The loading conditions of the bridge include the self weight and a concentrated load at the middle of the span or at the quarter-span. A parametric investigation demonstrates the influence of the location of the concentrated load, of stick or stick-slip conditions and of the number of interfaces on the limit load. The results are compared with the ultimate failure load of the traditional collapse mechanism method[10] and with the results of the experimental work reported in[9].

2 UNILATERAL CONTACT FINITE ELEMENT ANALYSIS AND ESTIMATION OF THE LIMIT LOAD

The structural analysis problem for an elastic structure with unilateral contact interfaces takes the form:

$$\mathbf{Ku} + \mathbf{N}^T\mathbf{r} = \mathbf{P}_O + \lambda\mathbf{P} \tag{1}$$

$$\mathbf{Nu - g} \le 0 \tag{2}$$

$$\mathbf{r} \ge 0 \tag{3}$$

$$\mathbf{(Nu - g)}^T\mathbf{r} = 0 \tag{4}$$

In the above equations, **K** is the stiffness matrix, **u** is the displacement vector, **r** represents the Lagrange multipliers and is equal to the normal pressure $-\mathbf{t}^n$, $\mathbf{P}_O$ is the self - weight and P is the live (applied) load of the structure. The problem described by equations (1) - (4) is a linear complementarity problem (LCP) [5].

For the theoretical study and the solution of the unilateral contact problem, the arising variational inequalities

and the available numerical techniques, the reader may consult [1], [2], [4], [5], [6], [8]. By considering a loading path with a scalar load parameter λ, the structural analysis problem is transformed to a parametric linear complementarity problem. The maximum value of λ for which problem (1)-(4) has a solution is related with the limit load.

A path - following method is applied here, thus λ is a scalar loading factor which will be used in the sequel for the determination of the limit load; $0 \le \lambda \le \lambda_{failure}$ 0, where $\lambda_{failure}$ represents the value of the loading factor in which the unilateral contact problem does not have a solution. For more information on the solvability conditions for unilateral contact problems the reader is refered to[3].

The behavior in the tangential direction is defined by a static version of the Coulomb friction model which takes into account stick - slip effects and, in analogy to the deformation theory of plasticity, is suitable for holonomic loading. This means that two contacting surfaces start sliding when the shear stress in the interface reaches a maximum critical equal to:

$$\tau_{cr} = \mu t^n, \tag{5}$$

where t^n is the contact pressure and μ is the friction coefficient.

The variational inequality problem is transformed into a system of nonlinear equations by means of a suitable Lagrangian method. Finally, a set of nonlinear equations is solved by the Newton-Raphson incremental iterative procedure[4], [5], [6], [7].

3 THE BRIDGE WITH FRICTIONAL CONTACT INTERFACES

Quadrilateral, four - node, bilinear, plain strain elements are used for the finite element model of the bridge. The model has 3302 nodes and 3036 elements. Large displacement effects are neglected.

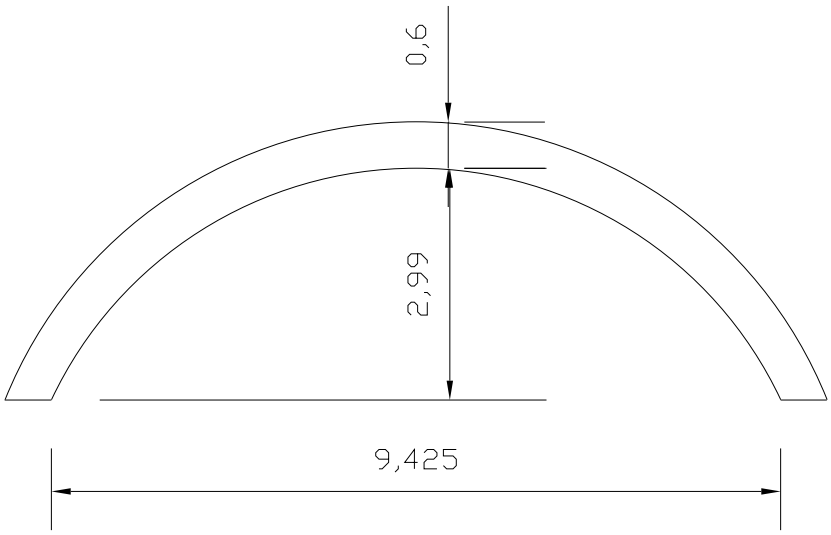

Figure 1. Geometry of Strathmashie bridge

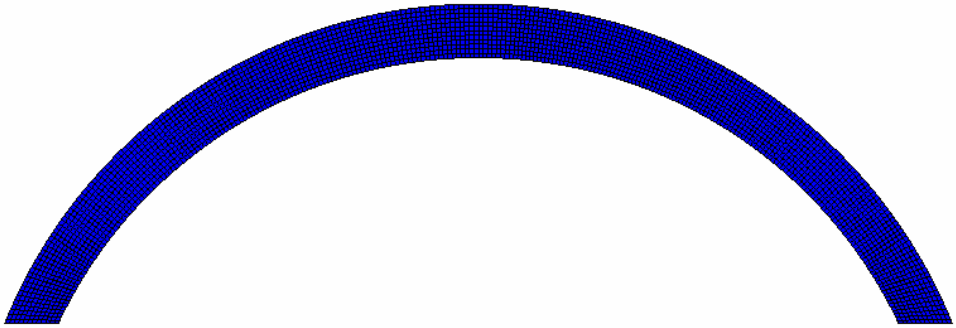

Figure 2. Mesh of the finite element model

The load is applied in small steps. Termination of the analysis is caused from numerical singularity due to negative eigenvalues of the stiffness matrix at the onset of failure. In figure 3 the failure load is given for various number of unilateral contact interfaces equidistantly distributed along the bridge. The load is reduced for higher number of interfaces. If the force is applied in the middle span, the failure load is greater than if it is applied in the quarter span. In the model with 26 interfaces the failure load is approximately equal with that received from the experimental work[9], if a quarter span force is applied as it is shown in figure 4. If the friction coefficient is assumed to be equal to 0,4 instead of 0,3, the failure load is increased.

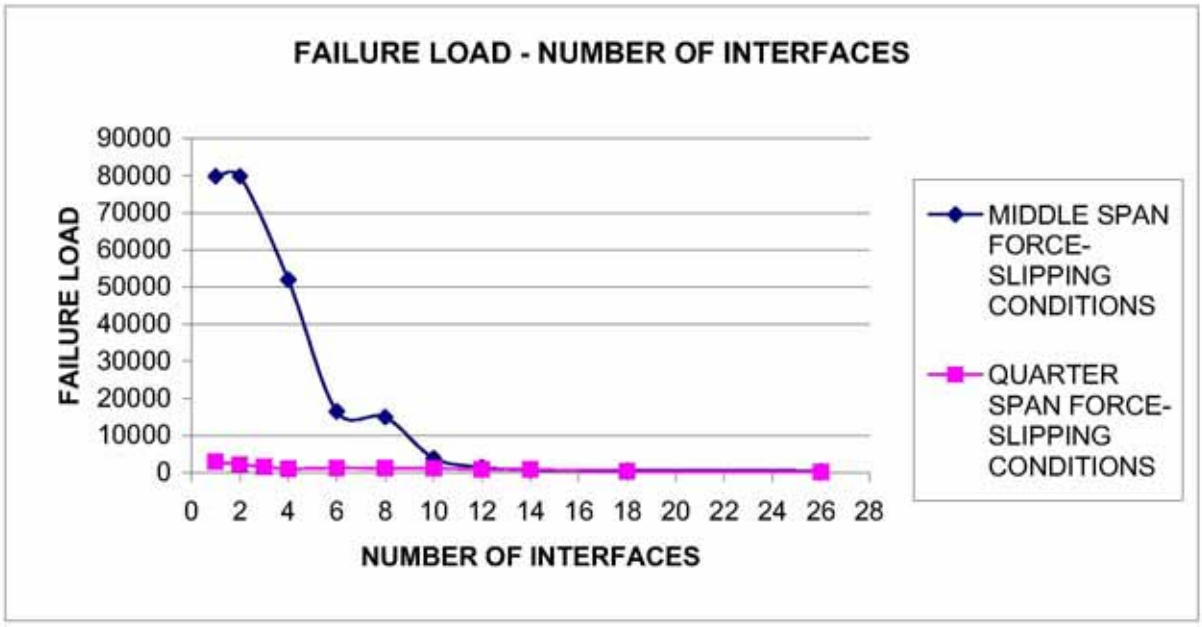

Figure 3. Failure load - Number of interfaces

	FAILURE LOAD
EXPERIMENT	228KN
THIS STUDY	250KN

Figure 4. Failure load

4 MECHANISM OF COLLAPSE

A comparison between the results received from the collapse mechanism method[10] and the finite element method is presented. The program Archie-m has been used for the implementation of the collapse mechanism method. The failure load is found by solving the equilibrium equations of the arch; this is achieved by creating the thrust line of the arch[10]. When the thrust line in a cross section is adjacent to the ring of the arch, a hinge is opened in that point. According to the upper bound theorem from the theory of plasticity, the maximum load corresponding to some collapse mechanism is greater or equal to the maximum load corresponding to the real collapse mechanism. This theorem implies that when the thrust line is adjacent to the ring of the arch in four points then the arch is not safe. Friction is high enough between stones and sliding failure cannot occur. The masonry has an infinite compressive strength.

A finite element model without sliding, equivalently with infinite friction coefficient is developed and used for the comparison. The failure load of this model with 26 interfaces and the quarter span load is four times greater than the experimental one. The deformation of the model at the onset of collapse is shown in figure 5. The load is applied at the quarter span of the bridge. Four hinges are opened. The comparison with the results of the collapse mechanism method given in figure 6, is satisfactory.

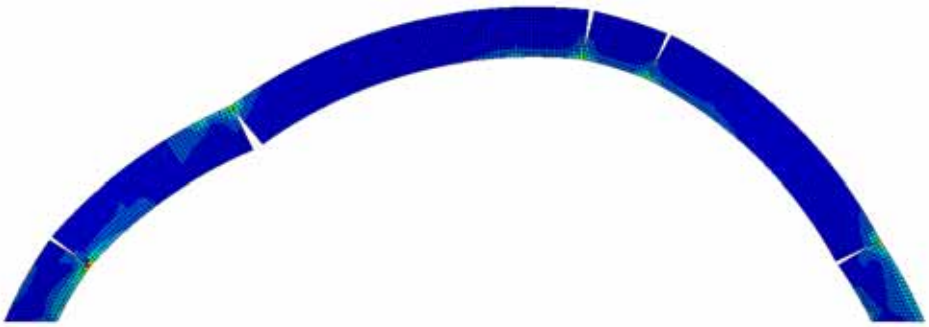

Figure 5. Failure mode of the 26 interfaces contact model - Quarter span load

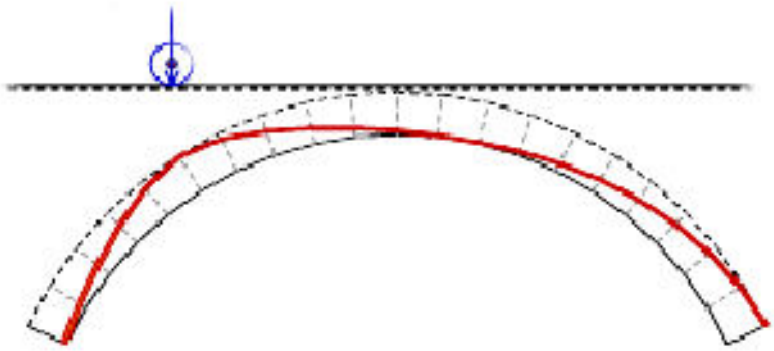

Figure 6. Failure mode calculated by the collapse mechanism method - Quarter span load

5 CONCLUSIONS

A model of unilateral contact with friction integrated into a finite element analysis can be used for the determination of the ultimate failure load of a masonry bridge. For a quite large number of potential interfaces, the computational ultimate load calculated by the model with friction with a quarter span load is equal with the experimental one. The model without frictional sliding, which is more compatible with the collapse mechanism method, led to higher values. The four hinge mechanism when failure occurs is confirmed both by the usage of the contact model and of the collapse mechanism method.

One advantage of the proposed method is that it can be numerically implemented within every modern, general purpose, nonlinear finite element program (Abaqus has been used here), provided that no failure due to numerical instabilities arise before the activation of the failure mechanism. Otherwise a limit load problem must be formulated and solved, a task which would have required the use of specialized software.

REFERENCES

[1] Panagiotopoulos, P. D. (1985), *Inequality problems in mechanics and applications. Convex and Nonconvex Energy Functions*, Birkhauser, Boston, Basel, Stuttgart.

[2] Stavroulaki, M. E., Stavroulakis, G. E. (2002), "Unilateral contact applications using FEM software," Int. J. Appl. Comput. Sci., Vol.12, No.1, pp. 101-111.

[3] Stavroulakis G. E., Panagiotopoulos P. D. and Al-Fahed A. M. (1991) "On the rigid body displacements and rotations in unilateral contact problems and applications," Computers and Structures Vol. 40, No 3, pp. 599-614.

[4] Bathe K. J. (1996), *Finite Element Procedures*, Prentice-Hall, New Jersey.

[5] Mistakidis E. S. and Stavroulakis G. E. (1998), *Nonconvex optimization in mechanics. Smooth and nonsmooth algorithms, heuristics and engineering applications*, Kluwer Academic Publishers, Dordrecht.

[6] Stavroulakis G. E and Antes H. (2000) "Nonlinear equation approach for inequality elastostatics. A 2-D BEM implementation," Computers and Structures 75(6), pp. 631-646.

[7] Zhowy H. W., He S. Y., Li X. S., Wriggers P. (2004) "A new algorithm for numerical solution of 3-D elastoplastic contact problems with orthotropic friction law," Computational Mechanics, 34(1), pp. 1-14.

[8] Hlavacek I., Haslinger J., Necas J., Lovisck J. (1988), *Solution of variational inequalities in mechanics*, Springer Verlay.

[9] Page J. (1993), *Masonry arch bridges - TRL state of the art review*, HMSO, London.

[10] Heyman J. (1980), *The masonry arch*, Ellis Horwood Series In Engineering Science.

SIZING AND SHAPE OPTIMIZATION OF 3D STEEL STRUCTURES WITH WEB OPENINGS

L. D. Psarras, N. D. Lagaros, M. Papadrakakis

Institute of Structural Analysis & Seismic Research
National Technical University of Athens
Zografou Campus, Athens 15780, Greece

Keywords: Web openings, Shell discretization, Optimization.

Abstract. *The objective of this work is to obtain the optimum design of 3D steel framed buildings with perforated I-sections beams. The optimization problem is considered as a combined sizing, shape and topology optimization problem. The size of the columns and the beams of the structure of each storey constitute the sizing design variables, while the number and the size of the web openings of the beams constitute the topology and shape design variables, respectively. Two distinctive formulations of the optimization problem are considered depending on the Finite Element (FE) simulation used, with beam and shell discretization. The two formulations are compared in terms of the optimum design achieved. The test examples studied, showed that a reduction in the structural weight of the building is achieved by incorporating web openings into the beams of the structure. A mixed-discrete Evolutionary Algorithm specially tailored, for this type of structural optimization problems is implemented in this work. Additionally a mesh generator has been developed, to be coupled with the optimization procedure, when the discretization with shell element is used.*

1 INTRODUCTION

The Steel I-sections are nowadays widely used in the design of steel framed structures. There are three major reasons for considering web openings: (i) for incorporating services within the floor-ceiling zone of the building, (ii) for cost efficiency and (iii) in order to protect the beam column connections from high stresses. Moreover, the provision of multiple circular openings in the beams also became a popular architectural feature of these structures. For the above mentioned reasons a number of studies have been carried out in the past dealing with the behavior of I-section beams with web openings [1], while design codes have incorporated guidelines into the design rules [2]. In the authors' knowledge, no studies have been reported on the optimum design of steel framed structures with I-sections having web openings.

In most of sizing optimization problems of 3D steel frames the beam element simulation is adopted [3]. However many phenomena, like local buckling, non conventional geometries, like I-section beams with web openings, among other, that affect significantly the behavior of the structure, is not possible to be taken into account with the beam element simulation. Furthermore, in the framework of an optimization procedure, additional features like shape and topology optimization cannot be dealt adequately with conventional finite element simulation. For this reason a more detailed discretization, using triangular shell elements, is proposed in this work.

During the last three decades many numerical methods have been developed to meet the demands of structural design optimization. The great improvements in the optimization methods and the advancements in computer technology have made optimization an important part in the design of structures. Optimization algorithmic methods can be classified in two categories, the deterministic and the probabilistic ones. Mathematical programming methods are the most popular methods of the first category, while evolutionary algorithms are the most widely used class of methods of the second category. In this work an evolution based algorithm is considered for the solution of the optimization problem at hand [4].

The design optimization of 3D steel framed structures is examined in this study using a triangular shell element discretization which is compared, in terms of the optimum design achieved, with the beam element discretization. In the formulation of the optimization problem with the beam element discretization only sizing design variables are used. In the formulation with the shell element discretization three types of design variables are considered: sizing, shape and topology. The sizing design variables are referred to the dimensions of the cross sections of the beams and the columns. The shape design variables are referred to the size of the openings at the webs of the beams, while the topology design variables are referred to the number of the web openings along the beam length. According to past studies on the subject of reduced webs, the openings may be

rectangular or circular and must be in the form of discrete openings or a series of identical openings along the beam. In this study circular openings are considered and the case of a series of identical openings is adopted.

2. REDUCED WEB - DESIGN CRITERIA

In order to understand the effects of both the shapes and the sizes of web openings to the structural performance of perforated sections, it is important to relate the global shear force and bending moment acting on the perforated sections to the local co-existing forces and moment, acting on the tee-sections above and below the web openings. It should be noted that any increase in the opening depth always reduces both the shear and the moment resistances of the perforated sections while it has no effect on the applied forces, i.e. the global shear force and bending moment at the perforated sections. Thus, both shear and flexural failures of the perforated sections are primarily controlled by the size of the opening.

However, while the opening length has no effect on the local shear and moment resistances of the tee-sections above and below the web openings, any increase in the opening length will increase the local Vierendeel moment acting at the tee-sections significantly. Thus, the Vierendeel mechanism of the perforated sections is essentially controlled by the opening length. In practice, both the opening depth and the opening length are geometrically related, and thus any increase in sizes in web openings of given shapes will reduce not only the global shear and the global moment resistances of the perforated sections, but also the local axial, shear and moment resistances of the tee-sections. Furthermore, the Vierendeel moment is also increased at the same time.

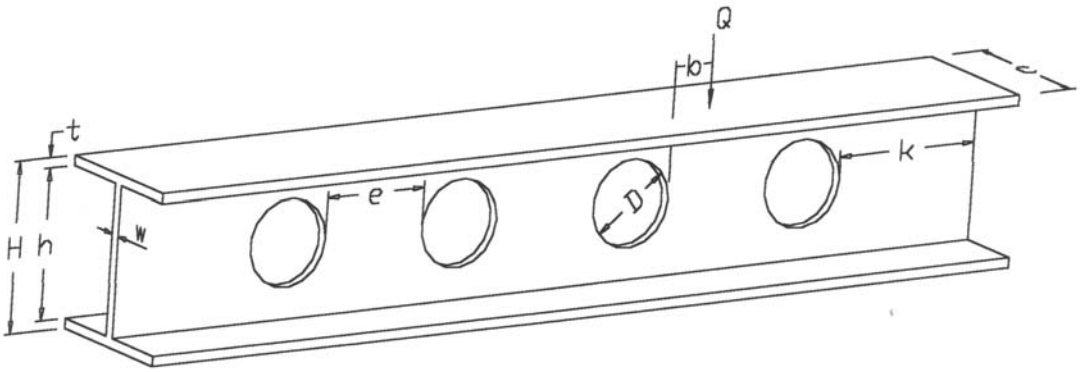

Figure 1. I-section with web openings

In the studies reported so far and in the design codes related to beams with circular openings the following restrictions in the design of steel beams with large openings should be followed [1].

- All web openings should be located along the centerline of the web.
- The maximum diameter of a circular opening should be 0.75 times the total height of the beam H ($D \leq 0.75 \times H$), see figure 1.
- The distance between the edges of adjacent openings should not be less than the total height of the beam H ($e \geq H$), see figure 1.
- The distance between the edge of a web opening and an adjacent point load should exceed D ($b > D$), see figure 1.
- The distance between the edge of the web opening that is closer to the beam's edge should exceed D ($k > D$), see figure 1.
- The center of the web opening should be located away from restrains, point loads or supports by a distance of at least the overall section height of the steel beam H.

3. THE OPTIMIZATION PROBLEM

Structural optimization problems are characterized by various objective and constraint functions that are generally non-linear functions of the design variables. These functions are usually implicit, discontinuous and non-convex. The mathematical formulation of structural optimization problems with respect to the design variables, the objective and constraint functions depend on the type of the application. However, most optimization problems can be expressed in standard mathematical terms as a non-linear programming problem. A mixed-discrete structural optimization problem can be formulated in the following form:

$$
\begin{aligned}
&F(\mathbf{s}) \rightarrow \min \\
&\mathbf{s}_{\mathrm{d}}=[\mathrm{s}_{\mathrm{l}_{\mathrm{d}}},\ldots,\mathrm{s}_{\mathrm{n}_{\mathrm{d}}}]^{T},\mathbf{s}_{\mathrm{c}}=[\mathrm{s}_{\mathrm{l}_{\mathrm{c}}},\ldots,\mathrm{s}_{\mathrm{n}_{\mathrm{c}}}]^{T} \\
&\mathbf{s}_{\mathrm{d}} \in D^{n_d},\mathbf{s}_{\mathrm{c}} \in C^{n_c} \\
&g_j(\mathbf{s}) \leq 0,\ \mathrm{j}=1,2,\ldots,\mathrm{m}
\end{aligned}
\tag{1}
$$

Where $\mathbf{s} = (\mathbf{s}_d,\mathbf{s}_c)$, $\mathbf{s}_d$ and $\mathbf{s}_c$ are the vectors of discrete and continues design variables respectively, while D and C are the discrete and continuous design sets of size nd and nc, respectively.

There are three main classes of structural optimization problems depending on the type of the design variables employed: sizing, shape and topology. In sizing optimization problems the aim is usually to minimize the weight of the structure under certain behavioral constraints on stresses and displacements. The design variables are most frequently chosen to be dimensions of the cross-sectional areas of the members of the structure. In structural shape optimization problems the aim is to improve the performance of the structure by modifying its shape. The design variables are either some of the coordinates of the key points in the boundary of the structure or some other parameters that influence the shape of the structure. Structural topology optimization assists the designer to define the type of structure, which is best suited to satisfy the operating conditions for the problem at hand. In the current study the task of topology optimization is to define the number of the web openings in each group of the beams.

Two distinctive formulations of the optimization problem are employed in this study and assessed in terms of the optimum design achieved. The difference of the two formulations stems from the type of FE discretization used. In the fist one the conventional beam element discretization is used while in the second one a detailed shell element discretization is applied. For each formulation separate behavioral checks are considered. These behavioral checks are performed following a structural analysis where stresses and displacements are calculated.

3.1 Beam element discretization

The first formulation corresponds to a discrete optimization problem ($n_c = 0$) with sizing design variables only, corresponding to the size of the groups of the beams and the columns of the structure. The constraint functions for beams subjected to biaxial bending under compression are given by the following formula of Eurocode 3 (EC3) [5]:

$$
\frac{\mathrm{N_{sd}}}{\mathrm{Af_y}/\gamma_{\mathrm{M1}}}+\frac{\mathrm{M_{sd,y}}}{\mathrm{W_{pl,y}f_y}/\gamma_{\mathrm{M1}}}+\frac{\mathrm{M_{sd,z}}}{\mathrm{W_{pl,z}f_y}/\gamma_{\mathrm{M1}}} \leq 1.0 \tag{2}
$$

where $\mathrm{N_{sd}}$, $\mathrm{M_{sd,y}}$, $\mathrm{M_{sd,z}}$ are the computed stress resultants, $\mathrm{W_{pl,y}}$, $\mathrm{W_{pl,z}}$ are the plastic first moment of inertia, $\mathrm{f_y}$ is the yield stress and γ_{M1} is a safety factor equal to 1.10. The interstorey drift constraint employed in a frame structure can be written as:

$$
\frac{\mathrm{d_r}}{\nu} \leq 0.004 \times \mathrm{h} \tag{3}
$$

where v is a reduction factor (taken equal to 2.0 for the test examples considered in this study) and d_r is the relative drift between two consecutive stories.

3.2 Shell element discretization

In the second formulation the detailed FE discretization makes possible the consideration of web openings on the beams and for this reason additional shape and topology design variables are considered. The optimization problem is a mixed-discrete optimization problem where the sizing (referred to the dimensions of the beams and the columns) and topology (referred to the number of web openings) are discrete design variables while the shape design variables (referred to the size of the web openings) are continuous. The von Mises yield criterion is employed in order to assess the value of an equivalent stress that will be compared with the yield stress *fy*. Therefore the following expression has to be satisfied for each triangular shell element:

$$
\sqrt{\sigma_1^2+\sigma_2^2-3\sigma_1\sigma_2+3\tau^2} \leq \mathrm{f_y}/\gamma_{\mathrm{M0}} \tag{4}
$$

where σ_1,σ_2,τ are the stresses in the middle surface x-y of the triangle and γ_{M0} is a safety factor equal to 1.10. The interstorey drift constraint is also employed expressed as in the case of beam element discretization.

4. MESH GENERATION

In the second formulation of the optimization problem, where a shell element discretization of the FE model is used, a mesh generator for creating the FE mesh for every new candidate optimum design needs to be implemented. For this reason a mesh generator specially tailored for generating a shell element mesh in 3D framed buildings with I-sections having web openings has been developed. The mesh generator is fully parameterized regarding the geometric data with respect to the beam and column dimensions, the number and the dimensions of the circular web openings.

The geometric data that is required by the mesh generator is the following: (i) the coordinates of the joints of the elements of the building (hypernodes which define the FE model for the case of the beam element discretization), (ii) the dimensions of the I-sections of the beams and columns and (iii) the number and the size of the circular web openings. Special care should be given in creating a good quality mesh around the openings and near the joints as shown in Figure 2. The mesh nodes of the beams should be compatible with either the mesh nodes of the web of the flanges of the columns that the beams meet to the joint in question.

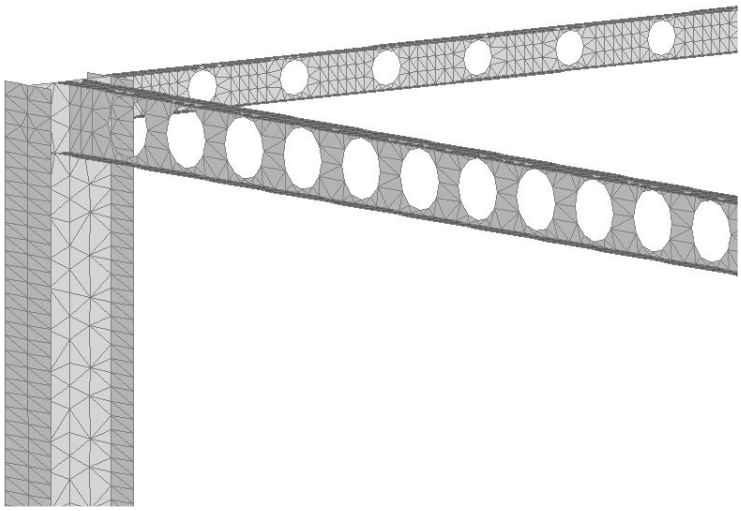

Figure 2. Detail of the generated mesh

An attempt to derive an efficient and robust shell finite element led Argyris and co-workers to the formulation of the TRIC (TRIangular Composite) shell element [6]. The formulation is based on the natural mode method. TRIC is a shear-deformable facet shell element suitable for linear and nonlinear analysis of thin and moderately thick isotropic as well as of composite plate and shell structures, while due to its natural formulation it does not suffer from the various locking phenomena [7]. The TRIC element is considered reliable, accurate and cost-effective as has been shown in previously published work [8,9].

5. EVOLUTIONARY ALGORITHMS

Evolutionary Algorithms (EA) were proposed for parameter optimization problems in the seventies with continuous variables. In engineering practice the design variables are not continuous because usually the structural parts are constructed with certain variation of their dimensions. Thus design variables can only take values from a predefined discrete set. In this work a new mixed-discrete EA optimizer is proposed. Each individual, in the proposed mixed discrete EA, is equipped with a set of parameters

$$\begin{aligned} &\mathbf{a} = [(\mathbf{s}_d, \boldsymbol{\gamma}), (\mathbf{s}_c, \boldsymbol{\sigma}, \boldsymbol{\alpha})] \in (I_d, I_c) \\ &I_d = D^{n_d} \times R_+^{n_\gamma} \\ &I_c = R^{n_c} \times R_+^{n_\sigma} \times [-\pi, \pi]^{n_a} \end{aligned} \tag{5}$$

where $\mathbf{s}_d$ and $\mathbf{s}_c$ are the vectors of discrete and continuous design variables, respectively. Vector $\boldsymbol{\gamma}$ corresponds to the variances of the Poisson distribution. Vector $\boldsymbol{\sigma} \in R_+^{n_\sigma}$ corresponds to the standard deviations ($1 \le n_\sigma \le n_c$) of the normal distribution while vector $\boldsymbol{\alpha} \in [-\pi, \pi]^{n_a}$ corresponds to the inclination angles ($n_\alpha = (n_c - n_\sigma/2)(n_\sigma - 1)$), defining linearly correlated mutations of the continuous design variables $\mathbf{s}_c$. Vectors $\boldsymbol{\gamma}$, $\boldsymbol{\sigma}$ and $\boldsymbol{\alpha}$ are the distribution parameter vectors.

Let $P^{(t)} = \{\mathbf{a}1, \ldots, \mathbf{a}\mu\}$ denotes a population of individuals at the t-th generation. The genetic operators used in

the EA method are denoted by the following mappings:

$$\begin{aligned} &\text{rec} : (I_d, I_c)^{\mu} \rightarrow (I_d, I_c) \text{ recombination} \\ &\text{mut} : (I_d, I_c) \rightarrow (I_d, I_c) \text{ mutation} \\ &\text{sel}_{\mu}^{k} : (I_d, I_c)^{k} \rightarrow (I_d, I_c)^{\mu} \text{ selection, } k \in \{\lambda, \mu+\lambda\} \end{aligned} \tag{6}$$

A single iteration of the EA, which is a step from the population $P^{(t)}$ to the next parent population $P^{(t+1)}$ is modeled by the mapping

$$\text{opt}_{EA} : (I_d, I_c)^{\mu} \rightarrow (I_d, I_c)^{\mu} \tag{7}$$

Combining the recombination, mutation and selection operators the main loop for the case of (μ,λ)-EA is formulated as follows:

$$\text{opt}_{(\mu,\lambda)-EA}(P^{(g)}) = \text{sel}_{\mu}^{\lambda}\left(\cup_{i=1}^{\lambda}\{\text{mut}(\text{rec}(P^{(g)}))\}\right) \tag{8}$$

While for the case of the (μ+λ)-EA scheme the main loop is formulated as follows:

$$\text{opt}_{(\mu+\lambda)-EA}(P^{(g)}) = \text{sel}_{\mu}^{\mu+\lambda}\left(\cup_{i=1}^{\lambda}\{\text{mut}(\text{rec}(P^{(g)}))\} \cup P^{(g)}\right) \tag{9}$$

The optimization procedure terminates when the following termination criterion is satisfied: the ratio μ_b/μ has reached a given value ε_d (=0.8 in the current study) where μ_b is the number of the parent vectors in the current generation with the best objective function value.

6. TEST EXAMPLE

For the purposes of this study a two storey 3D frame, with fixed supports at its ground nodes has been considered for the evaluation of the proposed methodology. The following material properties have been considered: steel with modulus of elasticity E_s=210GPa and yield stress $f_{yk,s}$=350MPa. Three groups of columns and six groups of beams are considered as shown in Figure 3, in total 21 design variables, n_d = 15 and n_c = 6. In this work the (5+5)-EA scheme has been used for solving the optimization problem.

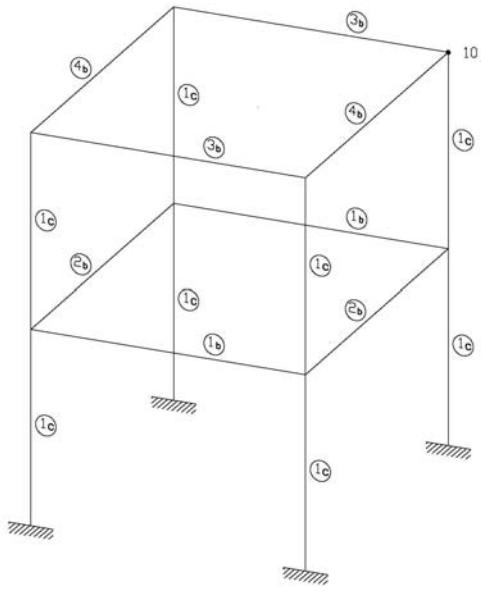

Figure 3. The two storey space frame

6.1 Efficiency of the shell element discretization

In the first part of the numerical investigation, a parametric study is performed. In order to find the best combination between accuracy and computational efficiency, a parametric study has been carried out for the test

example considered before accomplishing the optimization procedure. The purpose of this parametric study was to define the most efficient shell discretization in terms of accuracy and computational efficiency in order to be used during the optimization procedure. In Table 1 the results of this parametric study are shown. The TRIC element proved to be very efficient since it can be seen that even a coarse mesh can predict with acceptable accuracy the response of the structure. For the optimization procedure the 3 and 4 aspect ratios have been selected for the columns and the beams respectively. (The aspect ratio of a shell element is considered the length over width).

Table 1. Parametric study

Column aspect Ratio	Beams aspect Ratio	u_x (cm)	Nodes	Elements
5	5	9.5	2384	4096
4	5	9.8	2552	4384
4	4	9.9	2864	4920
3	4	10.4	3132	5384
3	3	10.7	3708	6392
2	3	10.8	4196	7224
2	2	10.9	5300	9152
1	2	10.5	6812	11744
1	1	10.7	10100	17472
0.5	1	10.7	15068	26544

6.2 Optimization results

In the second part of this study the advantages of the design with web openings are demonstrated through a comparison with the formulation based on the beam element discretization. For this test example the optimum designs achieved by the two formulations are shown in Table 2. As it can be see in Table 2 the optimum design achieved with the beam element simulation corresponds to a weight 15% higher compared to the optimum weight achieved using the shell element simulation. The shell element simulation allows the consideration of openings on the webs of the beams, and this is the main reason for the reduction of the weight of the structure.

Table 2. The optimum designs

Design Variable	Beam	Shell (n_{open},D)
1c	HEB500	HEB450
1b	IPE400	IPE400(10,D37.3)
2b	IPE200	IPE200(11,D15.9)
3b	IPE400	IPE300(12,D25.7)
4b	IPE200	IPE180(13,D14.6)
Weight (kN)	69.7	59.9

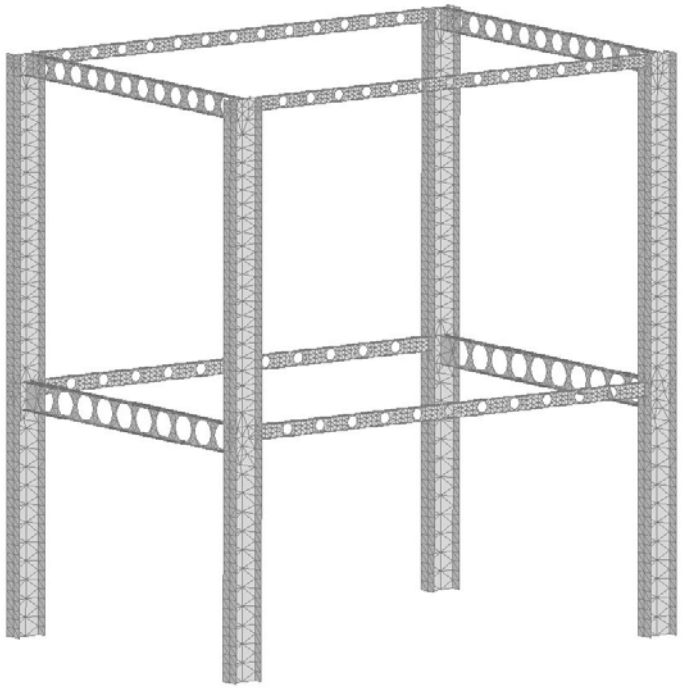

Figure 4. Optimum design

7. CONCLUSIONS

In this study a mixed discrete Evolutionary Algorithm has been implemented for the optimization problems encountered. Two distinctive design formulations are examined depending on the type of the FE simulation, with beams and shell elements. The beneficial effect of the detailed FE simulation with the TRIC shell element combined with the consideration of web openings is demonstrated. An improvement of 15% on the optimum weight has been achieved compared to the optimum design achieved with the beam element simulation. Evolutionary Algorithms have proved to be a robust and efficient tool for economically design optimization of steel 3D framed buildings with web openings.

REFERENCES

1. Chung, K.F., Lawson, R.M. (2001), "Simplified design of composite beams with large web openings to Eurocode 4", Journal of Constructional Steel Research 57, pp 135-163.
2. Building Seismic Safety Council. NEHRP Recommended Seismic Design Criteria for New Steel Momentframe Buildings, FEMA-350, Federal Emergency Management Agency, Washington, DC, 2000.
3. Charmpis, D.C., Lagaros, N.D. and Papadrakakis, M. (2005), "Multi-database exploration of large design spaces in the framework of cascade evolutionary structural sizing optimization", Comput. Methods Appl. Mech. Engrg.
4. Papadrakakis, M., Lagaros, N.D. and Fragakis, Y. (2003), "Parallel computational strategies for structural optimization", International Journal for Numerical Methods in Engineering 58(9), pp. 1347-1380.
5. Eurocode 3: Design of steel structures, Part 1.1: General rules; Part 1.5: Strength and stability of planar plated structures without transverse loading, European Committee for Standardization, Jan 1993.
6. Argyris, J. H., Tenek, L., and Olofsson, L. (1997), "TRIC: a simple but sophisticated 3-node triangular element based on 6 rigid body and 12 straining modes for fast computational simulations of arbitrary isotropic and laminated composite shells", Computer Methods in Applied Mechanics and Engineering 145, pp. 11-85.
7. Argyris, J. H., Papadrakakis, M., Apostolopoulou, C., and Koutsourelakis, S. (2000), "The TRIC shell element: theoretical and numerical investigation", Computer Methods in Applied Mechanics and Engineering 182, Issues 1-2, pp. 217-245.

8. Argyris, J., Tenek, L., Papadrakakis, M., and Apostolopoulou, C. (1999), "Post-bucking Performance of the TRIC Natural Mode Triangular Element for Isotropic and Laminated Composite Shells," Computer Methods in Applied Mechanics and Engineering 166, pp. 211-231.
9. Gisakis, A.G., Papadrakakis, M. and Karapitta, L. (2005) "Improving the performance of the TRIC shell element", Proceedings of the 5th International Congress on Computational Mechanics (GRACM 05), Limassol, Cyprus, 29 June – 1 July.

STATIC RESPONSE OF A SUSPENSION BRIDGE SYSTEM UNDER LIVE LOAD

Leonidas T. Stavridis

Structural Engineering Department
National Technical University of Athens
Iroon Polytexneiou 9, 15780 Zografou, Greece
email : stavrel@central.ntua.gr

Keywords : Cable force, stiffening girder, main cable, suspended beam

Abstract. *As the initial geometry and response of a suspension bridge under permanent load can be easily established in construction phase, the problem of finding the cable forces, the deformed geometry and the resulting bending response of the stiffening girder for the prescribed live load has been treated under the necessary consideration of the second order theory effects. The problem is reduced to that one of a beam subjected to an accordingly determined transverse and axial tensile load and is solved in a way which is directly applicable for preliminary design purposes. A dimensionless formulation of the problem is included in the paper, which may lead through a parametric study to the influence of the geometric data, the cable section and the girder inertia properties on the examined response.*

INTRODUCTION

The suspension bridges is the structural system which is adequate for bridging very long spans and as such has been established over many years in the engineering history of mankind, achieving nowadays a high level of performance in all the technologically advanced countries.
As can be seen in Fig.1 the basic structural components of a suspension bridge system consist of the stiffening girder or truss, the main cables, the main towers and the anchorages.

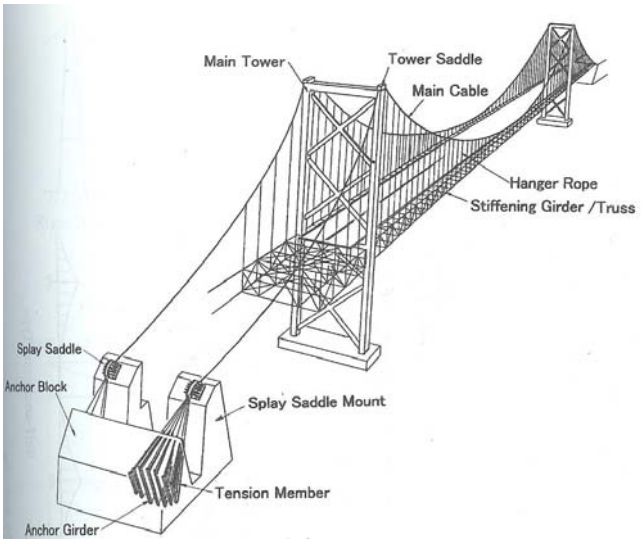

Figure 1. Suspension bridge layout

The purpose of the present paper is to give a very simple tool to estimate the increase in structural response regarding the cable force and the bending of the girder, due to the action of the live load for which the suspended system has to be designed. Although there are also other design criteria regarding e.g. dynamic actions, the examined static response is of essential importance. The analysis handles essentially with a single simply supported beam suspended on a cable with fixed supports. In that way the influence of the side spans as well as the deformability of the main towers of the bridge are ignored. Although the approach is approximate and directed to preliminary design purposes, the influence of the deformed geometry is appropriately taken into account (second order theory)

ANALYSIS

The cable tensile force H_g is appropriately calibrated with respect to the desired sag f so that for the existing dead load (cable self weight included) g, the deck takes an absolutely horizontal position or even exhibits some light concave upwards curvature. It will be :

$$H_g = g*L^2/8*f \tag{1}$$

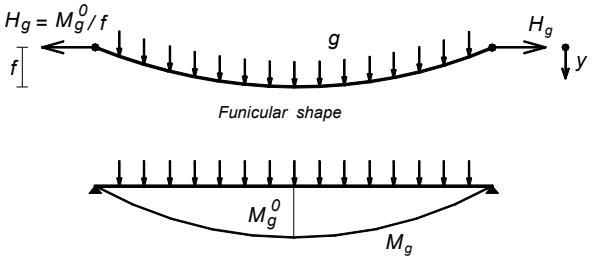

Figure 2. Funicular form of the cable under dead load

In this way the bending of the girder is kept to a negligible level, given the small distance of the hangers. Nevertheless the action of an additional live load p on the girder tends to deform the cable and this additional cable deflection η , due to the assumed relative inextensibility of the hangers, will be imposed exactly the same on the stiffening girder.
The girder should be able on one side to restrict the cable deformation resulting from the live load and on the other to resist the bending imposed to it by this very same deflection as previously mentioned.
However, as can be seen later, the influence of the girder stiffness on the cable deflection decreases for very long spans , because the increasing cable weight plays then an important role.

In the present work, the additional cable force represented by its horizontal component H_p will be dealt together with the determination of the additional deflection η, as well as of the implied bending of the girder. Though the approach will be approximate and appropriate rather for preliminiray design purposes, the consideration of the equilibrium of the system takes into account the deformed geometry (second order theory).

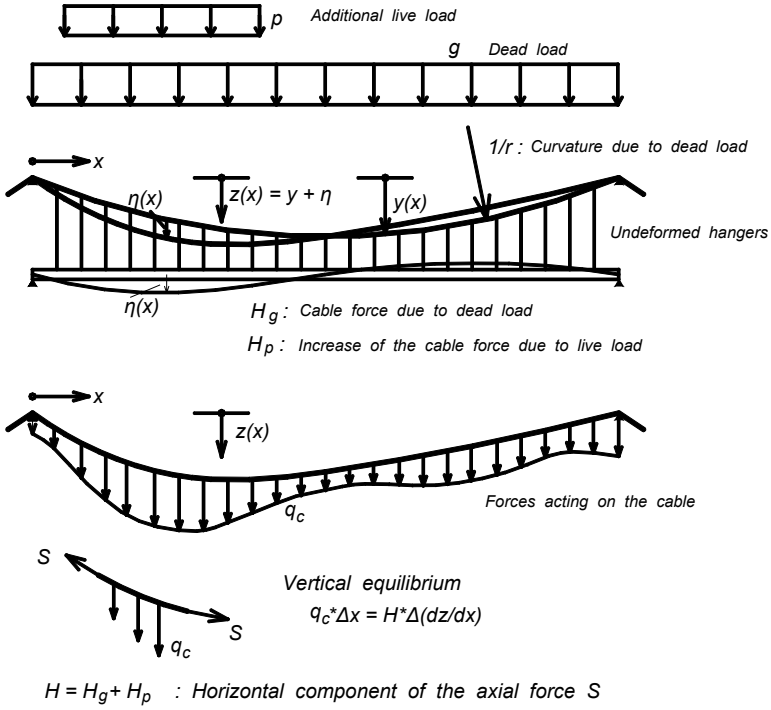

Figure 3. Cable deformation and acting forces

The girder is in equilibrium under the following loadings :
1) Self weight *g*
2) Live load *p* acting on a specified length
3) The actions $q_c(x)$ of the hangers directed upwards which, due to the small distances of the hangers can be considered as continuously distributed.

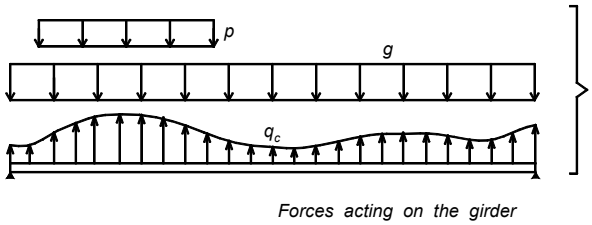

Figure 4 . Acting forces on the girder

The loadings *g* and *p* can be considered uniform but the loading $q_c(x)$ changes along the girder length. As this loading is applied also to the cable the latter will assume correspondingly a new funicular shape different from the former parabolic one due to the uniform load g.
If $z(x)$ represents the new cable geometry and *H* is the horizontal component of its axial force, from the equilibrium of an elementary cable segment and according to the well known "funicular" relation $q = H*(1/r)$ it is obtained

$$q_c(x) = -\frac{d^2 z}{dx^2} H \tag{2}$$

In this relation $q_c(x)$ represents a downward action, whereas the term $-dz^2/dx^2$ stands for the cable curvature.

According to Fig.3 :

$$z(x) = y(x) + \eta(x) \tag{3}$$

and

$$H = H_g + H_p \tag{4}$$

The girder is in equilibrium under a total load $q(x)$, which, taken downwards as positive, is :

$$q(x) = -q_c(x) + g + p \tag{5}$$

and is related to the bending response *M* of the girder, according the equilibrium relation

$$d^2M/dx^2 = -q(x) \tag{6}$$

Then, according to the basic constitutive relation for the girder bending

$$M = -E * I \frac{d\eta^2}{dx^2} \tag{7}$$

it is obtained :

$$EI \frac{d\eta^4}{dx^4} = q(x) \tag{8}$$

Replacing in the above expression of *q(x)* and taking into account that

$$\frac{d^2 y}{dx^2} \cdot H_g + g = 0 \tag{9}$$

it is obtained :

$$q(x) = \left(\frac{d^2 y}{dx^2} + \frac{d^2 \eta}{dx^2} \right)(H_g + H_p) + g + p = \frac{d\eta^2}{dx^2}(H_g + H_p) + H_p \frac{d^2 y}{dx^2} + p \tag{10}$$

As the term d^2y/dx^2 equals the negative cable curvature under the load *g* - i.e. ($-8*f/L^2$) - , the above differential equation of the suspended beam takes the form :

$$EI\frac{d^4\eta}{dx^4} - \frac{d^2\eta}{dx^2}(H_g + H_p) = p - \frac{H_p}{r} \tag{11}$$

This result is recognized according to the second order theory, as the equation of a simple beam having a transverse load ($p - H_p/r$) and being subjected to an axial tensile load ($H_g + H_p$).

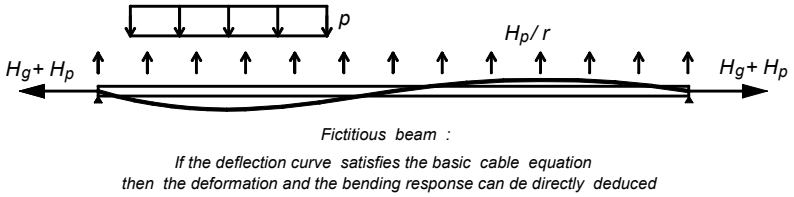

Figure 5 . Acting forces on the fictitious beam

According to a well known result of the second order theory of beams, $\eta(x)$ can be determined (of course as function of H_p) from the relation

$$\eta = W_1 \cdot \frac{1}{1+\xi} \tag{12}$$

where W_1 represents the deflection line of the classical simply supported beam under the load ($p - H_p/r$) and

$$\xi = (H_g + H_p)/P_{cr} \tag{13}$$

with P_{cr} its buckling load, equal to ($\pi^2 EI/L^2$).
Now, the increase H_p of the cable force H_g is related to the additional deflection η through the established relation [1] :

$$\frac{H_p}{A_c E_c} * L_s = \frac{g}{H_g}\int_0^L \eta dx - \frac{1}{2}\int_0^L \frac{d^2\eta}{dx^2} * \eta * dx \tag{14}$$

where, for ratios f/L between 1/10 and 1/12 , the length L_s is given with good approximation from the expression :

$$L_s = L * \left[1 + 8 * \left(\frac{f}{L}\right)^2\right] \tag{15}$$

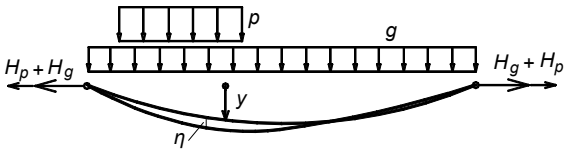

Figure 6. Cable deformation under direct action of live load

It has been found that the omission of the second integral term in the right side of the above equation affects very little the overall accuracy, so it can be written more simply :

$$\frac{H_p}{A_c E_c} * L_s = \frac{g}{H_g} \int_0^L \eta dx \tag{16}$$

According now to the usual design practice, two loading configurations for the live load p have to be taken into account, namely one acting on the left half of the girder length and the second one extending over the whole span. The first loading leads to the most unfavorable girder bending, whereas the second one leads to the maximum developed value of cable force.

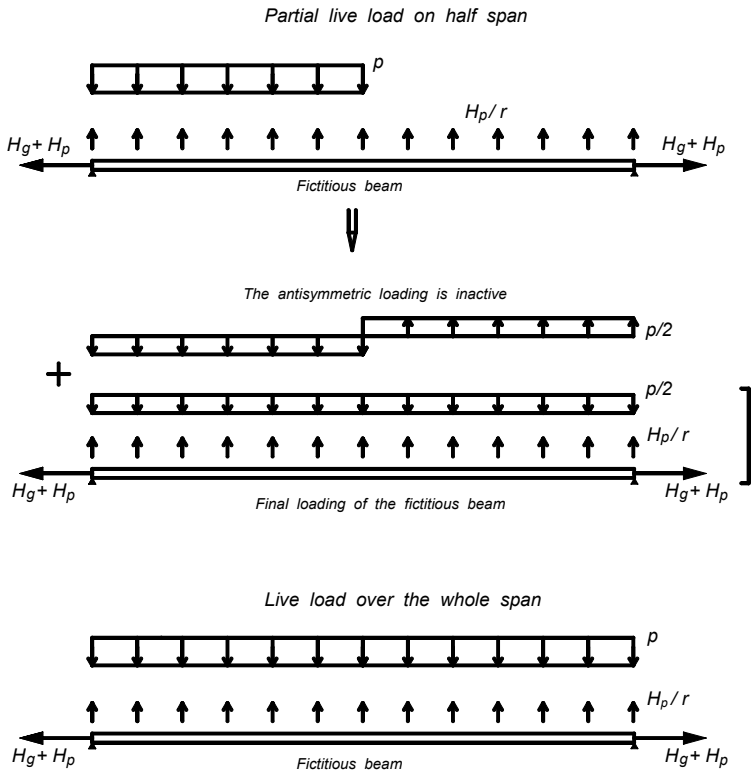

Figure 7. Characteristic positions of live load on the fictitious beam

In the first case the load p is equivalent to the action of a symmetrical load ($p/2$) over the whole span and an antisymmetric one ($p/2$), as shown in Fig.7. The deflection line $\eta(x)$ of the fictitious beam can be equally evaluated from the superposition of the deflection η_{sym} due to symmetric loading ($p/2 - H_p/r$) over the whole length and of the deflection η_{ant} due to the antisymmetric loading ($p/2$) according to Fig.7. It is noted that this superposition is possible, given the constant axial load of the beam. After these considerations the last equation is written :

$$\frac{H_p}{A_c E_c} * L_s = \frac{g}{H_g} \left(\int_0^L \eta_{sym} dx + \int_0^L \eta_{ant} dx \right) \tag{17}$$

As η_{ant} represents an antisymmetric function, the second integral in the right hand side of this equation vanishes, so it is obtained finally

$$\frac{H_p}{A_c E_c} * L_s = \frac{g}{H_g} \left(\int_0^L \eta_{sym} dx \right) \tag{18}$$

It is obvious that this relation is valid also for the second case where the fictitious beam is loaded with ($p - H_p/r$) over its whole length.

As it has been previously noted, η_{sym} can be determined with satisfactory accuracy from the expression

$$\eta_{sym} = W_1 \cdot \frac{1}{1+\xi} \tag{19}$$

where W_1 represents the deflection line of the simple beam with the transverse load ($p^* - H_p/r$) and p^* equals either $p/2$ for the partial loading of the left half of the span, or p for the loading of the whole span.

The deflection line W_1 of the beam results as the bending diagram of the simple beam under the load (M_1^0/EI) , where M_1^0 is the function of the bending moment of the beam due to the loading ($p^* - H_p/r$).
It is obtained :

$$W_1(x) = \frac{(p^* - H_p/r) * L^4}{24 * EI}\left[\left(\frac{x}{L}\right)^4 - 2*\left(\frac{x}{L}\right)^3 + \left(\frac{x}{L}\right)\right] \tag{20}$$

Replacing in the above expressions gives :

$$\int_0^L \eta_{sym} dx \;=\; \frac{(p^* - H_p/r) * L^5}{120 * EI} \frac{1}{1+\dfrac{H_g + H_p}{P_{cr}}} \tag{21}$$

Replacement and rearrangement of the last equation leads to the following algebraic equation of second order for the unknown H_p :

$$\frac{H_p}{A_c E_c} * L_s = \frac{g}{H_g}\left[\frac{(p^* - H_p/r) * L^5}{120 * EI} \frac{1}{1+\dfrac{H_g + H_p}{P_{cr}}}\right] \tag{22}$$

which is written in the final dimensionless form :

$$\left(\frac{H_p}{P_{cr}}\right)^2 + (1 + k + G)\left(\frac{H_p}{P_{cr}}\right) - k * G * \left(\frac{p^*}{g}\right) = 0 \tag{23}$$

where :

$$k = \frac{8}{15} \cdot \frac{\lambda^2}{1 + 8 \cdot \lambda^2} \cdot \frac{E_c}{E} \cdot \frac{A_c * L^2}{I} \quad , \quad G = \frac{g \cdot L^2}{8} \cdot \frac{L}{\lambda \cdot \pi^2 \cdot EI} \quad \text{and} \quad \lambda = \frac{f}{L} \tag{24}$$

After the determination of H_p the bending response of the stiffening girder can be directly established.
From the previous examination it can be concluded that the bending responses of the suspended and of the fictitious beam are identical. Partial loading with the live load results in maximum bending moment M_{max} about at the quarter of the span, whereas loading over the whole length results in maximum increase in cable force.

For the case of partial loading it is :

$$M_{\max} = M_{sym} + M_{ant} \tag{25}$$

where :

$$M_{sym} = M_{sym}{}^0 - (H_g + H_p) * \eta_{sym} \tag{26}$$

or

$$M_{sym} = 0.75 * \frac{(p/2 - H_p/r) * L^2}{8} - 0.2227 * \frac{(p/2 - H_p/r) * L^4}{24 * EI} \frac{H_g + H_p}{1 + \xi} \quad (27)$$

and

$$M_{ant} = \frac{(p/2) * (L/2)^2}{8} - 0.3125 * \frac{(p/2) * (L/2)^4}{24 * EI} \frac{H_g + H_p}{1 + \xi/4} \quad (28)$$

The term $\xi/4$ is due to the fact that in the middle of the fictitious beam the deflection curve exhibits an inflection point and as a result its buckling load is multiplied by four.
The above quadratic equation could be studied parametrically to give the influence of the above introduced parameters to the final results

NUMERICAL EXAMPLE

For a numerical application the example of Bosporus bridge is taken with the following data according to [2] and following the introduced notations in this paper.

L = 1074 m f = 91 m
E = 2.1*10^8 kN/m^2 E_c = 1.9*10^8 kN/m^2
I = 1.88 m^4 A_c = 0.40 m^2

The permanent weight g is 150 kN/m^2 and the live load p is taken equal to 24 kN/m^2

The initial cable force H_g is determined according to Eq.1 as $H_g = \frac{g * L^2}{8 * f}$ = 237700 kN

For the determination of the additional cable force H_p the dimensionless parameters are established according to Eqs 24 :
λ = 0.08473 k = 804.016 G = 70.36

The buckling load of the beam is : $P_{cr} = \frac{\pi^2 * EI}{L^2}$ = 3377.9 kN

For the partial loading with the live load, according to Eq.23, the following quadratic equation has to be solved :

$$\left(\frac{H_p}{P_{cr}}\right)^2 + (1 + k + G)\left(\frac{H_p}{P_{cr}}\right) - k * G * \left(\frac{(p/2)}{g}\right) = 0$$

It is obtained : H_p/P_{cr} = 5.14 so that H_p = 5.14*3377.9 = 17362 kN

This positioning of the live load gives rise to the maximum bending response of the girder. According to the above expressions it is :
M_{sym} = 4052 kNm and M_{ant} = 10224 kNm and consequently :
M_{max} = 4052 + 10224 = 14276 kNm

Loading now the whole span with the live load results in the maximum cable force through the solution of the quadratic equation, according to Eq.23 :

$$\left(\frac{H_p}{P_{cr}}\right)^2 + (1 + k + G)\left(\frac{H_p}{P_{cr}}\right) - k * G * \left(\frac{p}{g}\right) = 0$$

It is obtained : H_p/P_{cr} = 10.22 so that H_p = 10.22*3377.9 = 34522 kN

CONCLUSIONS

A simple procedure for the estimation of the increase in cable force and of the bending moment in stiffening girder of a suspension bridge due to the imposed live load is proposed. The procedure is preferable a detailed finite element analysis especially for preliminary design purposes, including second order effects. It is presented

in a dimensionless form appropriate to assess the influence of the geometric data of the system on the overall response.

REFERENCES

1. S.Timoshenko (1941), "Suspension bridges", Franklin Inst. Vol.235, no. 3 March and no. 4 April.
2. Brown W.C., Parsons M.F. (1975): "Bosporus bridge" *Proceedings of ICE* 58, pp. 505 – 532
3. Wai-Fah-Chen , Lian Duan (editors) (1999), *Bridge Engineering* , CRC Press, Florida U.S.A..
4. Stuessi F. (1936): „Zur Berechnung verankerter Hängebrücken" , IVBH Abhandlungen 4 , pp. 531-542
5. Steinman D.B. (1935) : "A generalized deflection theory for suspension bridges", Transactions of ASCE, 100

ANALYSIS OF STEEL FRAMES WITH PITCHED ROOF EXPOSED TO FIRE BY A TRUSS MODEL

Panagis G. Papadopoulos*, Anastassia K. Papadopoulou*, Kyriakos K. Papaioannou*

*Department of Civil Engineering
Aristotle University of Thessaloniki
541 24 Thessaloniki, Greece

Keywords: Steel portal frame, Pitched roof, Fire, Snap-through, Plastic hinges, Truss model.

Abstract. *Plane steel portal frames, with pitched roof, exposed to fire, are examined. Yield stress and Young modulus of steel are assumed constant up to 300°C and then linearly decreasing to zero for 900°C. First, a determinate frame, with a single vertical load at the apex, is analysed by hand. For flexible columns and shallow roof, snap-through occurs before plastic hinges mechanism is formed. Then, an indeterminate frame, with stiffer columns, taller roof and vertical loads at the middles of rafters, is examined. This frame is first analysed by hand for the static loads and a gradual temperature increase. Also, a limit plastic analysis of the frame is performed by hand. In order to take into account geometric non-linearities due to large displacements and material non-linearities due to plastic yielding, the frame is simulated by a truss, which has a simple stiffness matrix, updated within each step of the temperature increase. The bars obey non-linear uniaxial stress-strain laws. The temperature increase rises the roof, which initially strengthens the frame, but a further increase of temperature, and subsequent reduction of Young modulus and yield stress of steel, leads finally to collapse of frame.*

1 INTRODUCTION

A fire, occurring in a multi-bay, multi-storey frame, is usually confined in one compartment only, thus a local collapse is possible. Whereas, in a portal frame exposed to fire, a global collapse may happen, as a portal frame consists of one compartment only. This is a reason that the fire analysis of portal frames have attracted a particular interest[3,8].

In a portal frame with pitched roof, if the beams are flexible and the roof shallow, a snap-through of roof apex is possible. The circumstances, under which a snap-through occurs in such a frame, are investigated in the literature[6,7]. Recently, for the relevant problem of large deflections of plane frames, a simple formulation has been proposed based on position description[2]. This concept is used in the present work.

If an early snap-through does not occur in a portal frame with pitched roof, the frame may finally fail by the formation of a plastic collapse mechanism[3,8].

Aim of present work is to investigate the behavior of plane steel portal frames with pitched roof, exposed to fire. Wherever this is possible, simple analyses, by a hand calculator, are performed. For a more accurate nonlinear analysis of a frame, the Finite Element Method can be used [1]. Here, a frame is alternatively simulated by a truss model[3-5], which has a simple stiffness matrix and can simply describe material non-linearities by the nonlinear uniaxial stress-strain laws of bars, as well as geometric non-linearities by writing the equilibrium conditions with respect to deformed structure, within each step of the gradual temperature increase.

2 DETERMINATE FRAME ANALYSED BY HAND

2.1 Given data

The plane determinate symmetric steel portal frame of fig. 1a, with a pitched roof and a vertical load at the apex, is considered. Fig. 1b shows the shape and dimensions of the beam cross-section, fig. 1c the primary elastoplastic stress-strain σ-ε curve of steel for 20°C. Fig. 1d presents the assumption that yield stress σ_y and Young modulus E_o of steel remain constant up to 300°C and then linearly decrease to zero for 900°C. And fig. 1e the temperature-time T– t history of ISO fire, approximated by a trilinear curve. The coefficient of thermal expansion is $\alpha_T = 10^{-5}/°C$.

Because of the fast heat conduction in steel, which is counteracted only by the external cold surrounding, it is assumed that the steel frame immediately attains the fire gases temperature, and the temperature distribution over beam cross-sections is uniform.

2.2 Snap-through analysis

The geometric non-linearity is taken into account by using the concept of position for the apex, no the concept of displacement[2]. The position of the apex is defined by its ordinate y above the head of column as shown in fig. 2a in the half of the symmetric frame. For a given value of y we can write the accurate nonlinear geometric equation, according to Pythagoras theorem:

$$\begin{aligned} &y^2+(L+u)^2=L_o^2, \text{ or} \\ &y^2+(16.0+u)^2=16.0^2+3.0^2=265.0, \end{aligned} \tag{1}$$

where u horizontal displacement of eave, and the reasonable assumption of constant length L_o of the rafter is adopted. From the above equation, we can easily, for a given y, find the corresponding u. The inertia moment of the beam cross-section is (fig. 1b):

$$J = 2\times1.6\times20\times24.2^2 +1.02\times46.8^3/12 +2\times20\times1.6^3/12 = 46208\text{cm}^4$$

Thus, the lateral stiffness of the column is

$$K=\frac{3EJ}{H^3}=\frac{3\times2\times10^4\times46208}{1000^3}=2.772\,\text{kN/cm}$$

The horizontal thrust of the column is $F_x = Ku$, the inclination of the rafter tga = y/(L+u) and the corresponding load at the apex $P = 2F_x$ tga.

For values of y ranging from +6.0m up to –6.0m (with a step $\Delta y = 0.1$m), by applying the above equations, the diagram of fig. 2b has been drawn which shows the variation of the load P at the apex with respect to the ordinate y of the apex, for room temperature 20°C. We observe in fig. 2b, that, for a vertical load P = 11.1kN, directing downwards, for a roof ordinate y = +1.70m, a snap-through of the apex occurs, which suddenly jumps to a new position y = –3.45m.

All the above happen for room temperature 20°C. For an increase of temperature to T = 300°C, the rafter expands to $1.003L_o$, thus the unloaded roof height increases to y = 3.255m>3.0m. By following the previous procedure, we find that the critical snap-through load increases now to P_s = 13.9kN for a roof height y = 1.875m. That is, for T = 300°C, the frame is strengthened against snap-through. However, for further increase of temperature with values T > 300°C, the reduction of Young modulus E leads to a reduction of column lateral stiffness, thus of critical snap-through load P_s, too.

For values of temperature T ranging from 20°C up to 900°C, the critical snap-through loads P_s and the corresponding roof heights y_s have been found and the diagrams of fig. 3 have been drawn showing the variations $P_s – T$ and $y_s – T$.

2.3 Limit plastic analysis

In fig. 4a is calculated the ultimate plastic bending moment of the beam cross-section for T = 20°C which is M_p = 842.9kNm. As M_p depends on yield stress of steel σ_y, it remains constant up to 300°C and then linearly decreases to zero for 900°C. In fig. 4b, the plastic hinge collapse mechanism of the frame is presented, for which we write the virtual works principle and find the ultimate plastic load P_p:

$$\frac{P}{2}\upsilon=M_p\vartheta=M_p\frac{u}{H}=M_p\frac{y}{LH}\upsilon \qquad \rightarrow \qquad P_p=2M_p\frac{y}{LH}$$

Because of the significant variation of M_p with T and the slight variation of y, H with T, the P_p varies with T as shown in fig. 3. We observe that, in the specific frame under consideration, for every value of temperature T, the ultimate plastic load P_p is larger than the corresponding critical snap-through load P_s. That is, the snap-through always happens before the plastic hinge collapse mechanism is formed. Thus, the snap-through determines the load that the frame can receive, and we find in fig. 3 that, for the given external load P = 10kN, the snap-through happens for a temperature T = 530°C.

3 INDETERMINATE FRAME

3.1 Given data

The indeterminate portal frame of fig. 5 is examined. The columns are shorter, thus stiffer and the roof taller than in previous example. Two vertical loads P = 80kN are applied at the middles of the rafters. All the other given data are the same as in the first application.

Obviously, this second frame is stronger than the first one, that is, it can receive heavier loads. Also, it will be shown that this frame finally fails by formation of a plastic collapse mechanism, not by a snap-through effect.

3.2 Static loading and thermal expansion analysis by hand

For T = 20°C, the linear analysis of the frame is performed, for the static loading, by a hand calculator. The results are shown in fig. 6a.

As the Young modulus E varies with T, it can be shown that the stresses of the frame due to static loading remain constant, whereas the deformations due to static loading are constant up to 300°C and then they increase being multiplied by the ratio 600/(900 – T).

For T = 300°C, the linear analysis of the frame is performed, for thermal expansion only, without static loading. The results are shown in fig. 6b.

It can be shown that the thermal deformations are proportional to temperature T, whereas the thermal stresses, up to T = 300°C, are proportional to T and then they vary by the ratio $(10^{-4}/18)\cdot T(900–T)$, having as reference state that for 300°C, and they present a maximum value for T = 450°C, for which this ratio becomes 1.125.

For T ranging from 20°C to 900°C, we find the vertical apex displacement, due to static loads on one hand and to thermal expansion on the other, as well as the total displacement υ. The results are shown in fig. 7a. Also for T ranging from 20°C to 900°C, we find the bending moment at the base of column, due to static loads on one hand and to thermal expansion on the other, as well as the total moment M_c (fig. 7b), which is compared with the curve showing the variation of ultimate plastic bending moment M_u of beam cross-section with T. In the intersection of the two curves M_c – T and M_u – T, we find that the first plastic yield occurs at the base of column for T = 635°C and M_c = 375kNm.

3.3 Limit plastic analysis by hand

We consider a collapse mechanism of the frame with three plastic hinges, at the sections where the bending moments with the maximum absolute values appear, as shown in fig. 8a. We write the virtual work principle for this collapse mechanism

$$P\upsilon = 2M_u\vartheta_r + 2M_u\vartheta_c = 2M_u\left(\frac{\upsilon}{L/2}+\frac{u}{H}\right) = 2M_u\left(\frac{2\upsilon}{L}+\frac{y\upsilon}{LH}\right) \quad \rightarrow \quad P_p = \frac{2M_u}{L}\left(2.0+\frac{y}{H}\right)$$

As the M_u significantly varies with T, whereas y, H slightly varies, we determine the variation of the ultimate plastic load P_p with T, which is shown in fig. 8b. We observe that, for the external load P = 80kN, the plastic collapse mechanism is formed for T = 726.5°C.

3.4 The proposed truss model

In order to perform a more accurate nonlinear analysis of the frame under consideration, by taking into account in detail the material non-linearities i.e. the gradual formation of plastic hinges, and the geometric non-linearities i.e. the significant N – M (axial force-bending moment) interaction, due to large displacements, we can use the Finite Element Method[1]. However, the usual Finite Elements have complicated stiffness matrices and present difficulties particularly in handling nonlinear problems. A bar of a truss is the Finite Element with the simplest possible stiffness matrix. And a truss model can be used as an alternative of a usual finite element discretization. A truss model can simply take into account material non-linearities by the nonlinear uniaxial stress-strain laws of the bars and geometric non-linearities by writing the equilibrium conditions with respect to the deformed structure and updating the stiffness matrix within each step of an incremental loading procedure.

Numerical results by truss models have been compared with published experimental data[5] and Codes requirements[4] and a satisfactory agreement between them has been observed.

The local stiffness matrix of a bar, in 2D, is written:

$$\mathbf{K}_\ell = \mathbf{K}_E + \mathbf{K}_G = \frac{EA}{\ell_o}\bar{c}\,\bar{c}^{+} + \frac{N}{\ell}I_2 = \frac{EA}{\ell_o}\begin{pmatrix} c_x^2 & c_xc_y \\ c_xc_y & c_y^2 \end{pmatrix} + \frac{N}{\ell}\begin{pmatrix} 1 & 0 \\ 0 & 1 \end{pmatrix}, \tag{2}$$

where $\mathbf{K}_E$ elastic stiffness, $\mathbf{K}_G$ geometric stiffness, E Young (elasticity) modulus, A cross-section area, ℓ_o undeformed length of the bar, $\bar{c} = \{c_x \;\; c_y\}$ direction cosines of bar axis, N axial force, ℓ present length of the bar.

The global stiffness matrix of the truss is written:

$$\mathbf{K}_g = \mathbf{B}\;\mathrm{diag}\,(\mathbf{K}_{\ell I})\;\mathbf{B}^t \qquad i = 1 \ldots n_b\,, \tag{3}$$

where $\mathbf{B} = (B_{ik})$, i = 1 … n_n, k = 1 … n_b, the Boolean (linkage) matrix of the truss, n_n number of nodes, n_b number of bars, B_{ik} =–1 if node i is left end of bar k, B_{ik} =+1 if node i is right end of bar k and B_{ik} =0 if there is no connection between node i and bar k.

If we have to simulate a usual steel beam element with a double-tau cross-section, by a rectangular plane truss element, first the flanges are, in a simple and obvious way simulated by bars (fig. 9a). Then, by considering

the correspondence between the elasticity equations of a plate element, which is the web of the steel beam element:

$$\begin{pmatrix}\sigma_x\\ \sigma_y\end{pmatrix}=\frac{E}{1-\nu^2}\begin{pmatrix}1 & \nu\\ \nu & 1\end{pmatrix}\begin{pmatrix}\varepsilon_x\\ \varepsilon_y\end{pmatrix}, \tag{4}$$

and the force-deformation equations of the rectangular plane truss element, we determine the sections of bars of the truss element (fig. 9b), where a Poisson ratio $\nu = 1/3$ is assumed, by the following formulas:

$$\begin{aligned}&\frac{A_3\cos^2\vartheta\sin\vartheta}{(9/8)(td/2)}=\frac{1}{3} && \rightarrow A_3\\ &A_3\cos^3\vartheta+A_1=\frac{9}{8}\frac{td}{2} && \rightarrow A_1\\ &A_3\sin^3\vartheta+A_2=\frac{9}{8}\frac{t\ell}{2} && \rightarrow A_2\end{aligned} \tag{5}$$

If the angle of the web element in fig. 9b is $a < 21°$, the above formulae cannot be used because negative bar sections A_1 result, which is inadmissible. In this case of a long web element with $\ell >> d$ and $a < 21°$, the following simplified formulae can be used for the determination of bar sections of the truss element simulating the web of the beam element (fig. 9b):

$$\begin{aligned}A_1&=A_3=td/4\\ A_2&=t\ell/2\end{aligned} \tag{6}$$

A short, thus transparent, computer program, with less than 200 Fortran instructions, has been developed for the analysis of a plane truss model by an incremental loading (temperature increase) procedure, by taking into account material and geometric non-linearities.

3.5 Discretization of the frame

The column of the frame under consideration is discretized to four truss elements (fig. 10). The rafter to eight elements. And there is one more element for the column-rafter joint. That is, there are totally, 8 + 4 + 1 = 13 elements, thus 28 nodes, which means that an algebraic system 56×56 of equilibrium equations is solved within each step of the incremental loading algorithm. There are 13×5 = 65 bars. The two nodes at the base of column have both DOFs restricted. The two nodes of rafter, at symmetry axis, have the horizontal DOFs restricted. For the determination of bar sections, all the elements are approximately considered as rectangular. The column and rafter elements are long with $\ell \approx 4d$ and $a \approx 14° < 21°$, thus the simplified formulae (6) are used for the determination of bar sections. Only the rafter-column joint element is short with $\ell \approx d$, thus $a \approx 45° > 21°$, so here the formulae (5) are used for the determination of bar sections.

3.6 Results of truss model

The results of the analysis of the second application (indeterminate frame) by the truss model are presented in fig. 11, for the following characteristic temperatures: 1) T = 300°C, up to which yield stress σ_y and Young modulus E_o of steel are assumed constant, 2) T = 600°C, for which σ_y, E_o are reduced to half of their initial values, 3) T = 669°C, for which the first plastic yield appears at the base of column, and 4) T = 729°C, for which the final plastic collapse mechanism is formed. For every one of the above four characteristic temperatures, the deformed configuration of the frame has been drawn, with a large scale for displacements, along with the free body diagram of the frame. In each case, a satisfactory agreement of displacements and reactions is observed with those previously found by a hand calculator. The first yield appeared at the base of column, where predicted by hand, for T = 669°C slightly different from T = 635°C of hand prediction. The final plastic collapse mechanism is formed for T = 729°C, very close to hand prediction T = 725°C. However, a slightly different failure mode is revealed by the truss model: The yielding at column base is not rotational but translational. In other words, the diagonals of web yield, which is a shear yielding.

Also, in figs. 7a,b, the variations with T of total vertical apex displacement υ, and total bending moment M_c at base of column, respectively, obtained by the truss model, are compared with the corresponding ones, obtained previously by a hand calculator, and a satisfactory approximation between them is observed.

Up to the first plastic yield of a bar, as the above approximation holds, a linear analysis by the truss model, for comparison, seems not necessary. On the other hand, from the first plastic yield until the final collapse of the frame, the nonlinear analysis, by the truss model, is necessary.

4 CONCLUSIONS

1. In a determinate portal frame with pitched roof, with a single vertical load at the apex, a simple analysis by hand can be performed, in order to investigate the snap-through effect.
2. If the columns of the frame are flexible and the pitched roof shallow, snap-through may occur before the formation of a plastic collapse mechanism.
3. For a temperature increase up to 300°C, for which yield stress and Young modulus of steel are assumed remaining constant, the roof rises, which implies a strengthening of the frame against snap-through.
4. In an indeterminate frame analysed first for static loading only, it is observed that stresses remain constant for any temperature T, whereas the deformations are constant up to T = 300°C and then, as Young modulus decreases, they increase by the ratio 600/(900 – T).
5. In an indeterminate frame analysed for thermal expansion only, it is observed that the deformations increase proportionally with the temperature T, whereas the stresses increase proportionally with T up to 300°C and then they vary by the ratio $(10^{-4}/18)\cdot T(900–T)$, which takes a maximum value 1.125 for T = 450°C and then decreases to zero for 900°C.
6. For a more accurate nonlinear analysis, a frame can be simulated by a truss model, which has a simple stiffness matrix and takes simply into account material non-linearities by the nonlinear uniaxial stress-strain laws of the bars and geometric non-linearities by writing the equilibrium conditions with respect to deformed structure and updating the stiffness matrix within each step of the gradual increase of temperature.
7. Numerical results of a steel frame exposed to fire, obtained by a truss model, are found in a satisfactory agreement with corresponding results obtained by a hand calculator, as regards deformations and reactions for various values of temperature, as well as the temperature and position of first yield and the temperature of the final plastic collapse mechanism of the frame.
8. A shear type of yield failure, at the base of column, has been revealed by the truss model. That is, a yield of both diagonal bars of web was observed.

REFERENCES

[1] Argyris, J.H. Editor. (I. 1978, II. 1981, III. 1984), Fe.No.Mech. (Finite Elements in Nonlinear Mechanics), International Conferences, Institut für Statik und Dynamik, Stuttgart, Germany.
[2] Coda, H.B., Greco, M.A. (2004), "A simple FEM formulation for large deflection 2D frame analysis, based on position description", Computer Methods in Applied Mechanics and Engineering, Vol. 193, pp. 3451-3557.
[3] Papadopoulos, P.G., Mathiopoulou, A.K. (2004), "Analysis of portal steel frame exposed to fire by use of a truss model", *Proceedings of the 8th Int. Conf. on Adv. Comp. Meth. in Heat Transfer*, Lisbon, 24-26 March, pp. 495-505.
[4] Papadopoulos, P.G., Xenidis, H.C. (1999 II), "A truss model with structural instability for the confinement of concrete columns", Journal of European Earthquake Engineering, pp. 57-80.
[5] Papadopoulos, P.G., Karayannis, C.G. (1988), "Seismic analysis of RC frames by network models", Computers and Structures, Vol. 28, pp. 481-494.
[6] Scholz, H. (1991), "Stability control of pitched roof frames by allowable member depth", J. Constr. Steel Research, Vol. 18, pp. 253-267.
[7] Scholz, H. (1988), "A new solution to the snap-through of pitched-roof steel frames", J. Constr. Steel Research, Vol. 9, pp. 265-285.
[8] Wong, M.B. (2001), "Elastic and plastic methods for numerical modeling of steel structures subject to fire", J. Constr. Steel Research, Vol. 57, pp. 1-14.

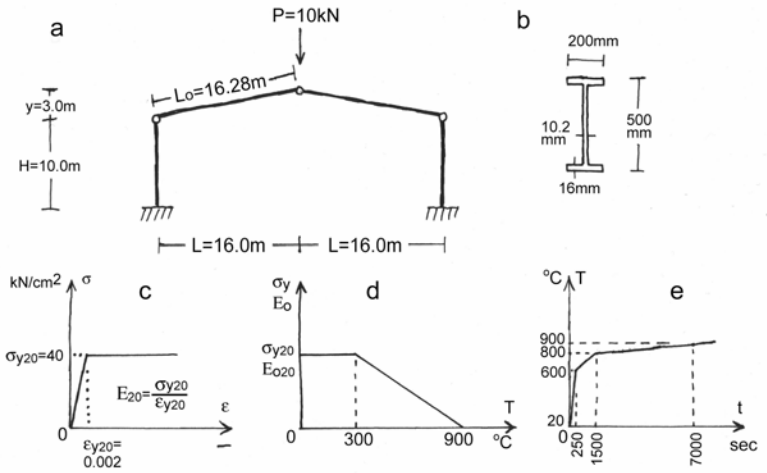

Figure 1. Given data of the determinate portal frame

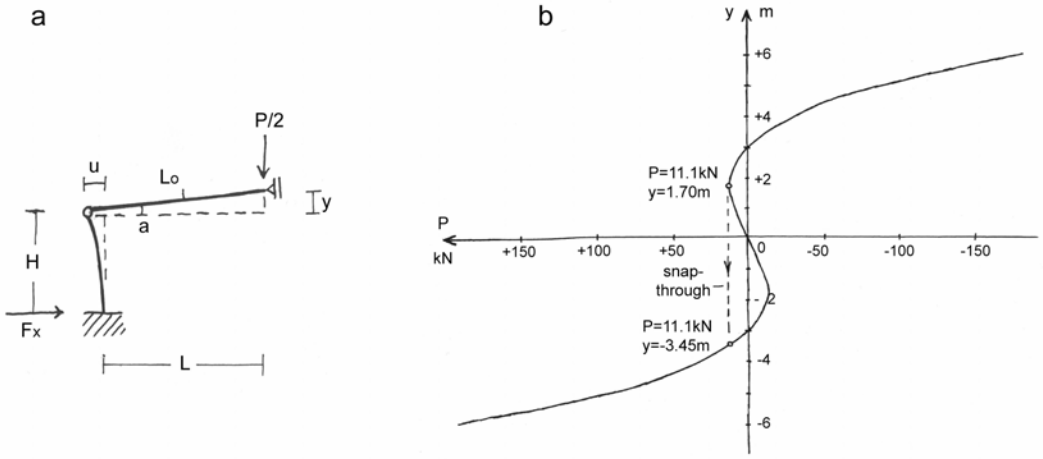

Figure 2. a. Position description of half frame, b. Variation of load P with respect to apex ordinate y for T=20°C

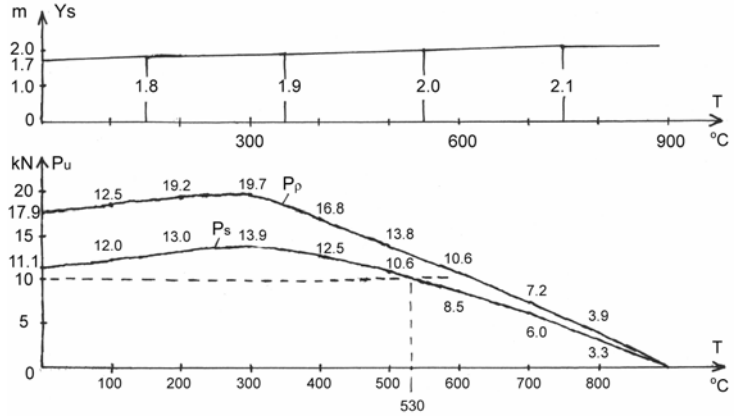

Figure 3. Variation with respect to temperature T of the snap-through critical load P_s, the corresponding apex ordinate y_s and the ultimate plastic load P_p

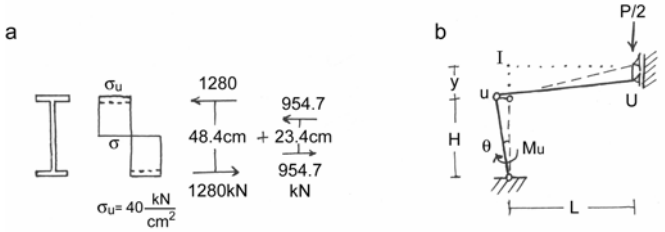

Figure 4. a. Ultimate plastic bending moment of beam cross-section for T = 20°C, b. Plastic hinge collapse mechanism of the frame

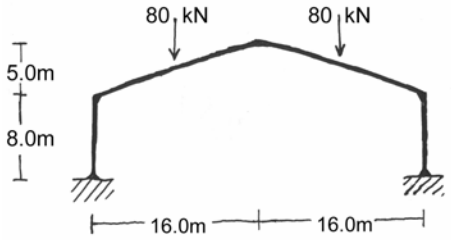

Figure 5. Given data of the undeterminate portal frame

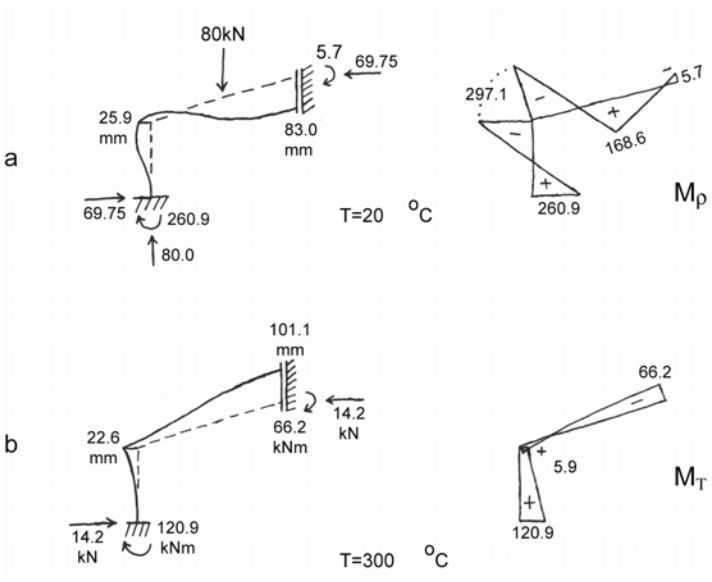

Figure 6. Linear analysis of the frame. a. Static loading for T = 20°C, b. Thermal expansion for T = 300°C

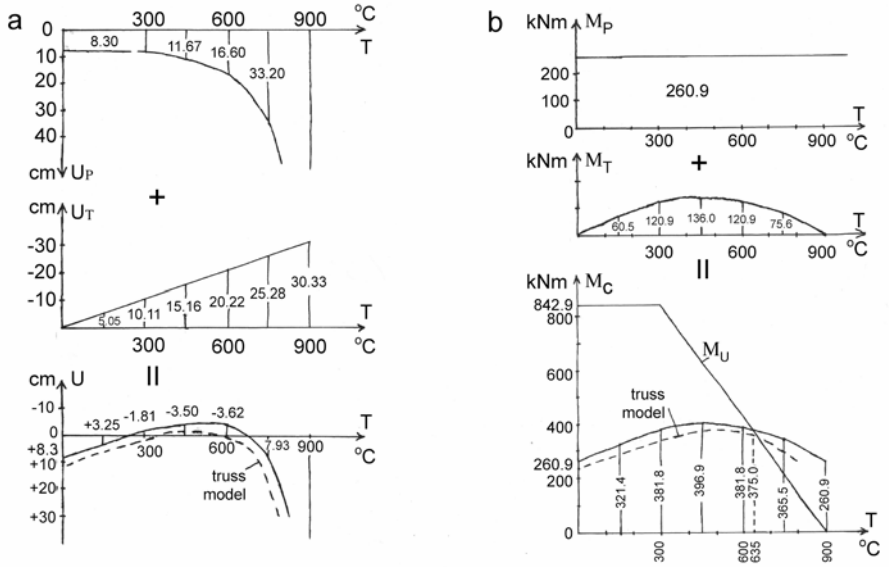

Figure 7. Variation with respect to temperature T of: a. Vertical displacement υ of apex, b. Bending moment M_c at base of column. Both due first to static loading, then to thermal expansion and total values

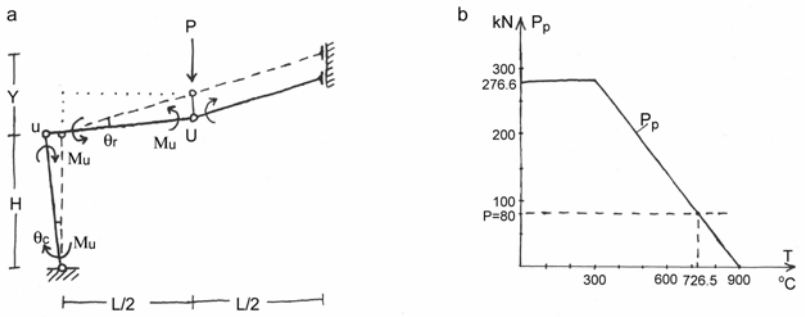

Figure 8. a. Plastic collapse mechanism of the frame, b. Variation of ultimate plastic load P_p with temperature T

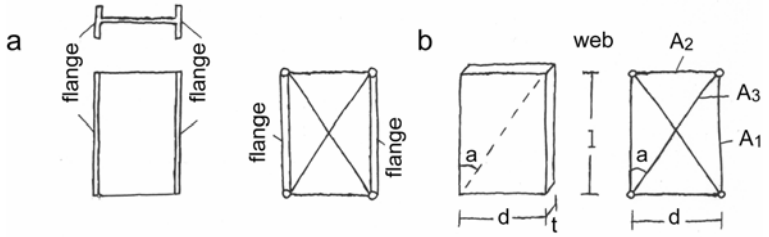

Figure 9. Simulation of a steel beam element by a truss element

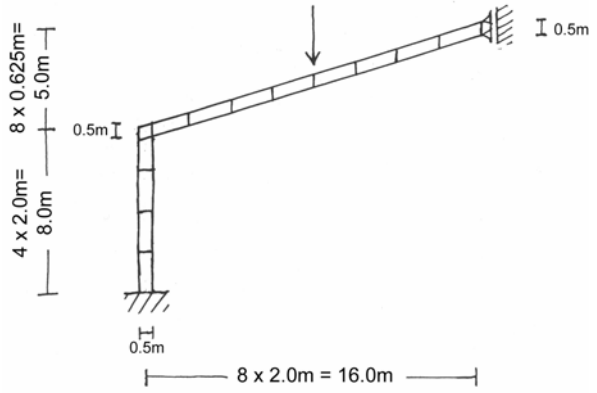

Figure 10. Discretization of the frame

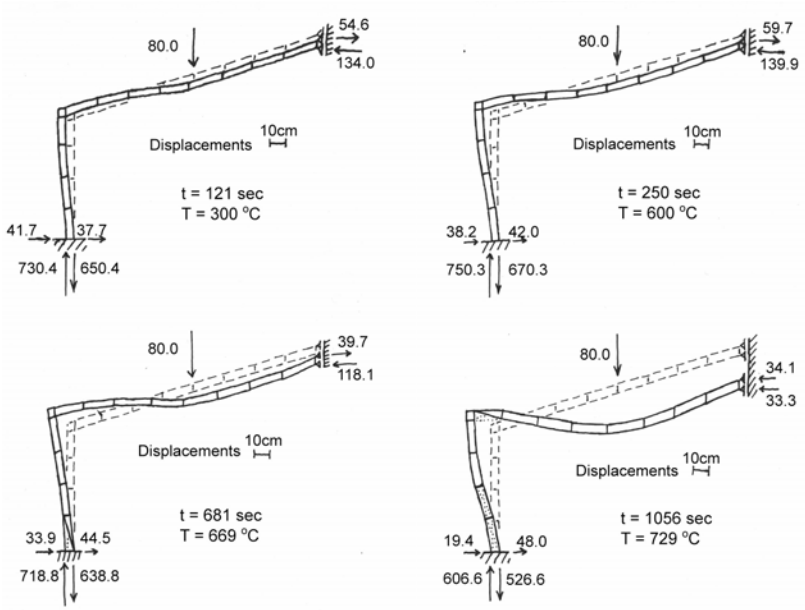

Figure 11. Results of truss model for characteristic temperatures

SHEAR DEFORMATION COEFFICIENTS IN COMPOSITE BEAMS BY BEM

V.G. Mokos and E.J. Sapountzakis[†]

School of Civil Engineering, National Technical University,
Zografou Campus, GR-157 73 Athens, Greece
e-mail: cvsapoun@central.ntua.gr

[†]Greek Association of Computational Mechanics

Key words: Shear center, Shear deformation coefficients, Composite, Beam, Boundary element method.

Abstract: *In this paper a boundary element method is developed for the evaluation of the shear deformation coefficients in composite beams of arbitrary constant cross section subjected in transverse shear loading. The composite beam consists of materials in contact, each of which can surround a finite number of inclusions. The materials have different elasticity and shear moduli with same Poisson's ratio and are firmly bonded together. The analysis of the beam is accomplished with respect to a coordinate system that has its origin at the centroid of the cross section, while its axes are not necessarily the principal ones. The transverse shear loading is applied at the shear centre of the cross section, avoiding in this way the induction of a twisting moment. Two boundary value problems that take into account the effect of Poisson's ratio are formulated with respect to stress functions and solved employing a pure BEM approach, that is only boundary discretization is used. The shear deformation coefficients are obtained from these functions using only boundary integration.*

1 INTRODUCTION

The problem of a homogeneous prismatic beam subjected in shear torsionless loading has been widely studied from both the analytical and numerical point of view. Both theoretical discussions and text books analyzing ways of estimation of shear deformation coefficients are mentioned among the extended analytical studies. Numerical methods have also been used for the analysis of the aforementioned problem. Among these methods the majority of researchers have employed the finite element method based on assumptions for the displacement field or introducing a stress function that fulfils the equilibrium equations. The boundary element method has also been employed for the solution of the aforementioned problem only in homogeneous cross sections, neglecting Poisson ratio v or presenting an analysis with respect only to the principal bending axes of the cross section restricting in this way its generality.

In this paper a boundary element method is developed for the evaluation of the shear deformation coefficients in composite beams of arbitrary constant cross section subjected in transverse shear loading. The essential features and novel aspects of the present formulation are summarized as follows.

i. All basic equations are formulated with respect to an arbitrary coordinate system, which is not restricted to the principal axes.
ii. The boundary conditions at the interfaces between different material regions have been considered.
iii. There is no need of splitting the stress function into the sum of two alternate cross section functions leading to resolved shear stresses. A stress function is introduced, which fulfils the equilibrium and compatibility equations.
iv. Finite element methods require the whole cross section to be discretized into area elements and are also limited with respect to the shape (distortion) of the elements. BEM solutions require only boundary discretization resulting in line or parabolic elements instead of area elements of the FEM solutions, while a small number of line elements are required to achieve high accuracy.
v. The effect of the material's Poisson ratio v is taken into account.

Numerical examples with great practical interest are worked out to illustrate the efficiency, the accuracy and the range of applications of the developed method. The accuracy of the proposed shear deformation coefficients compared with those obtained from a 3-D FEM solution of the 'exact' elastic beam theory is remarkable.

2 STATEMENT OF THE PROBLEM

Consider a prismatic beam of length L with an arbitrarily shaped composite cross section consisting of materials in contact, each of which can surround a finite number of inclusions, with modulus of elasticity E_j, shear modulus G_j and common Poisson's ratio v, occupying the regions Ω_j $(j=1,2,...,K)$ of the y,z plane (Fig.1). The materials of these regions are firmly bonded together and are assumed homogeneous, isotropic and linearly elastic. Let also the boundaries of the nonintersecting regions Ω_j be denoted by Γ_j $(j=1,2,...,K.)$.

These boundary curves are piecewise smooth, i.e. they may have a finite number of corners. Without loss of generality, it may be assumed that the beam end with centroid at point C is fixed, while the $x-$axis of the coordinate system is the line joining the centroids of the cross sections.

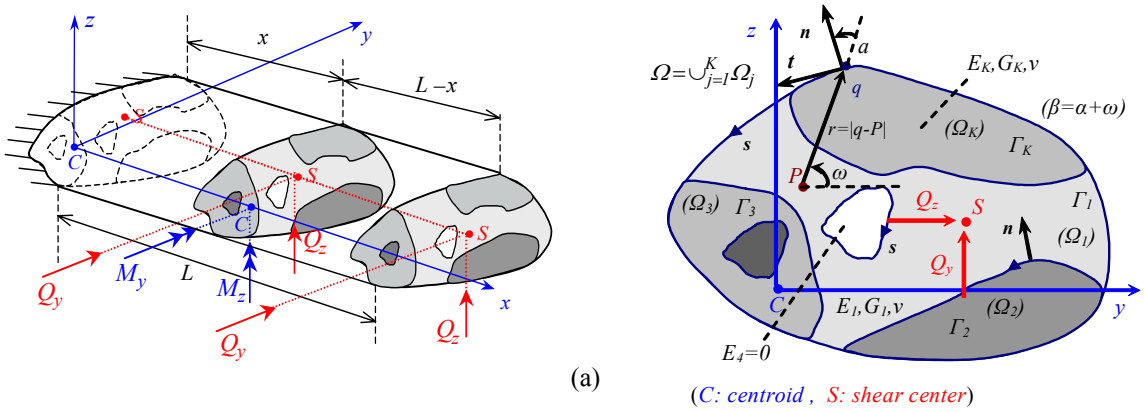

Figure 1. Prismatic beam subjected to torsionless bending (a) and two dimensional region Ω occupied by the composite cross–section (b)

When the beam is subjected to torsionless bending arising from a concentrated load Q applied at the shear center S of its free end composite cross section, at a distance x from the fixed end, the internal forces are the shear forces Q_y, Q_z being the components of the concentrated load Q along y and z axes, respectively and the bending moments M_y, M_z given as

$$M_y = -Q_z\left(L-x\right) \qquad M_z = Q_y\left(L-x\right) \tag{1a,b}$$

Following the procedure presented in[1] and assuming a stress function $\left(\Phi\left(y,z\right)\right)_j$ having continuous partial derivatives up to the third order such that the compatibility conditions to be identically satisfied, the transverse shear stress components $\left(\tau_{xy}\right)_j$, $\left(\tau_{xz}\right)_j$ and the resultant shear stress $\left(\tau_{\Omega}\right)_j$ in the regions Ω_j $(j=1,2,...,K)$ are expressed as

$$\left(\tau_{xy}\right)_j = E_j\frac{Q_z}{B}\left[\left(\frac{\partial\Phi}{\partial y}\right)_j - d_y\right] \qquad \left(\tau_{xz}\right)_j = E_j\frac{Q_z}{B}\left[\left(\frac{\partial\Phi}{\partial z}\right)_j - d_z\right] \qquad \left(\tau_{\Omega}\right)_j = \left[\left(\tau_{xy}\right)_j^2 + \left(\tau_{xz}\right)_j^2\right]^{1/2} \tag{2a,b,c}$$

where d_y, d_z are the y,z components of the vector $\boldsymbol{d}$ defined by

$$\boldsymbol{d} = d_y\boldsymbol{i}_y + d_z\boldsymbol{i}_z = \left[\nu\left(I_{zz}yz - I_{yz}\frac{y^2-z^2}{2}\right)\right]\boldsymbol{i}_y + \left[-\nu\left(I_{zz}\frac{y^2-z^2}{2} + I_{yz}yz\right)\right]\boldsymbol{i}_z \tag{3}$$

in which $\boldsymbol{i}_y, \boldsymbol{i}_z$ denote the unit vectors along the y and z axes and B is defined as

$$B = E_1\Delta = E_1 2\left(1+\nu\right)\left(I_{yy}I_{zz} - I_{yz}^2\right) \tag{4}$$

depending on the moduli of elasticity, the Poisson's ratio and the cross section geometry. Substituting eqns.(2a,b) in the first equation of equilibrium of the three-dimensional elasticity, the partial Poisson type differential equation governing the stress function $\left(\Phi\left(y,z\right)\right)_j$ is obtained as

$$\left(\nabla^2\Phi\right)_j = 2\left(I_{yz}y - I_{zz}z\right) \qquad \text{in } \Omega_j \quad (j=1,2,...,K) \tag{5}$$

where $\left(\nabla^2\right)_j \equiv \left(\partial^2/\partial y^2\right)_j + \left(\partial^2/\partial z^2\right)_j$ is the Laplace operator and $\Omega = \cup_{j=1}^{K} \Omega_j$ denotes the whole region of the composite cross section.

The boundary conditions of the aforementioned stress function will be derived from the following physical considerations:

- The traction vector in the direction of the normal vector $\boldsymbol{n}$ vanishes on the free surface of the beam, that is

$$\left(\tau_{xn}\right)_j = \left(\tau_{xy}\right)_j n_y + \left(\tau_{xz}\right)_j n_z = 0 \tag{6a}$$

- The traction vectors in the direction of the normal vector $\boldsymbol{n}$ on the interfaces separating the j and i different materials are equal in magnitude and opposite in direction, that is

$$\left(\tau_{xn}\right)_j = \left(\tau_{xn}\right)_i \quad \text{or} \quad \left(\tau_{xy}\right)_j n_y + \left(\tau_{xz}\right)_j n_z = \left(\tau_{xy}\right)_i n_y + \left(\tau_{xz}\right)_i n_z \tag{6b}$$

- The displacement components remain continuous across the interfaces, since it is assumed that the materials are firmly bonded together

where $n_y = cos\,\beta$, $n_z = sin\,\beta$ are the direction cosines of the normal vector $\boldsymbol{n}$ to the boundaries Γ_j *(j=1,2,...,K)*, with $\beta = \hat{y\boldsymbol{n}}$ (see Fig.1). It is worth noting that on both sides of the equality of (6b) the normal vector **n** points in one and the same direction, while the third physical consideration ensures the continuity of the stress function $\left(\Phi\left(y,z\right)\right)_j$ inside the region Ω_j *(j=1,2,...,K)* as well as across the boundaries separating different materials $\left(\left(\Phi\right)_j = \left(\Phi\right)_i\right)$.

Substituting eqns.(2a,b) in eqns.(6a,b), the Neumann type boundary condition of the stress function can be written as

$$E_j\left(\frac{\partial \Phi}{\partial n}\right)_j - E_i\left(\frac{\partial \Phi}{\partial n}\right)_i = \left(E_j - E_i\right)\boldsymbol{n}\cdot\boldsymbol{d} \qquad \text{on } \Gamma_j \ (j=1,2,...,K) \tag{7}$$

where E_i is the modulus of elasticity of the Ω_i region at the common part of the boundaries of Ω_j and Ω_i regions, or $E_i = 0$ at the free part of the boundary of Ω_j region, while $\left(\partial/\partial n\right)_j \equiv n_y\left(\partial/\partial y\right)_j + n_z\left(\partial/\partial z\right)_j$ denotes the directional derivative normal to the boundary Γ_j. The vector **n** normal to the boundary Γ_j is positive if it points to the exterior of the Ω_j region. It is worth here noting that the normal derivatives across the interior boundaries vary discontinuously.

Similarly, considering the beam subjected only to Q_y shear force and assuming the stress function $\left(\Theta\left(y,z\right)\right)_j$ having continuous partial derivatives up to the third order such that all the compatibility conditions to be identically satisfied, the transverse shear stress components τ_{xy}, τ_{xz} are expressed as

$$\left(\tau_{xy}\right)_j = E_j\frac{Q_y}{B}\left[\left(\frac{\partial \Theta}{\partial y}\right)_j - e_y\right] \qquad \left(\tau_{xz}\right)_j = E_j\frac{Q_y}{B}\left[\left(\frac{\partial \Theta}{\partial z}\right)_j - e_z\right] \tag{8a,b}$$

where e_y, e_z are the y,z components of the vector $\boldsymbol{e}$ defined by

$$\boldsymbol{e} = e_y\boldsymbol{i_y} + e_z\boldsymbol{i_z} = \left[\nu\left(I_{yy}\frac{y^2 - z^2}{2} - I_{yz}yz\right)\right]\boldsymbol{i_y} + \left[\nu\left(I_{yy}yz + I_{yz}\frac{y^2 - z^2}{2}\right)\right]\boldsymbol{i_z} \tag{9}$$

Substituting eqns.(8a,b) in the first equation of equilibrium of the three-dimensional elasticity and in the boundary condition (6a,b) the following Neumann problem for the stress function $\left(\Theta\left(y,z\right)\right)_j$ is obtained as

$$\left(\nabla^2\Theta\right)_j = 2\left(I_{yz}z - I_{yy}y\right) \qquad \text{in } \Omega_j \quad (j=1,2,...,K) \tag{10}$$

$$E_j\left(\frac{\partial \Theta}{\partial n}\right)_j - E_i\left(\frac{\partial \Theta}{\partial n}\right)_i = \left(E_j - E_i\right)\boldsymbol{n}\cdot\boldsymbol{e} \qquad \text{on } \Gamma_j \ (j=1,2,\ldots,K) \tag{11}$$

Furthermore, the shear deformation coefficients a_y, a_z and $a_{yz} = a_{zy}$ which are introduced from the approximate formula for the evaluation of the shear strain energy per unit length

$$U_{appr.} = \frac{a_y Q_y^2}{2AG_1} + \frac{a_z Q_z^2}{2AG_1} + \frac{a_{yz} Q_y Q_z}{2AG_1} \tag{12}$$

are evaluated equating this approximate energy with the exact one given from

$$U_{exact} = \sum_{j=1}^{K} \frac{E_1}{E_j} \int_{\Omega_j} \frac{\left(\tau_{xz}\right)_j^2 + \left(\tau_{xy}\right)_j^2}{2G_1} d\Omega_j \tag{13}$$

and are obtained for the cases $\left\{Q_y \neq 0,\ Q_z = 0\right\}$, $\left\{Q_y = 0,\ Q_z \neq 0\right\}$ and $\left\{Q_y \neq 0,\ Q_z \neq 0\right\}$, respectively, as

$$a_y = \frac{1}{\kappa_y} = \frac{A}{E_1 \Delta^2} \sum_{j=1}^{K} \int_{\Omega_j} E_j \left(\left(\nabla\Theta\right)_j - \boldsymbol{e}\right)\cdot\left(\left(\nabla\Theta\right)_j - \boldsymbol{e}\right) d\Omega_j \tag{14a}$$

$$a_z = \frac{1}{\kappa_z} = \frac{A}{E_1 \Delta^2} \sum_{j=1}^{K} \int_{\Omega_j} E_j \left(\left(\nabla\Phi\right)_j - \boldsymbol{d}\right)\cdot\left(\left(\nabla\Phi\right)_j - \boldsymbol{d}\right) d\Omega_j \tag{14b}$$

$$a_{yz} = \frac{1}{\kappa_{yz}} = \frac{A}{E_1 \Delta^2} \sum_{j=1}^{K} \int_{\Omega_j} E_j \left(\left(\nabla\Phi\right)_j - \boldsymbol{d}\right)\cdot\left(\left(\nabla\Theta\right)_j - \boldsymbol{e}\right) d\Omega_j \tag{14c}$$

where

$$A = \sum_{j=1}^{K} \frac{G_j}{G_1} \int_{\Omega_j} d\Omega_j \tag{15}$$

is the area of the composite cross–section, κ_y, κ_z and $\kappa_{yz} = \kappa_{zy}$ are the shear correction factors, Δ is defined from eqn.(4), while $\left(\nabla\right)_j \equiv \boldsymbol{i}_y\left(\partial/\partial y\right)_j + \boldsymbol{i}_z\left(\partial/\partial z\right)_j$ is a symbolic vector. Employing the shear deformation coefficients a_y, a_z, a_{yz} using eqns (14a,b,c) we can define the cross section shear rigidities of the Timoshenko's beam theory as

$$GA_{sy} = GA/a_y \qquad GA_{sz} = GA/a_z \qquad GA_{syz} = GA/a_{yz} \tag{16a,b,c}$$

In the case of an asymmetric cross section the principal shear axes, defined as

$$tan\,2\varphi^S = \frac{2a_{yz}}{a_{yy} - a_{zz}} \tag{17}$$

do not coincide with the principal bending ones, defined by the engineering beam theory. Due to this difference, the deflection components in the *y* and *z* directions are in general coupled, even if the system of axes of the cross section coincides with the principal bending one. If the cross section is symmetric about an axis, the principal shear axes system coincides with the principal bending one. In this case, the deflection components with respect to the principal directions are not coupled any more ($a_{yz} = a_{zy} = 0$ and $I_{yz} = I_{zy} = 0$).

3 INTEGRAL REPRESENTATIONS – NUMERICAL SOLUTION

According to the precedent analysis, the evaluation of the shear deformation coefficients in a composite beam reduces in establishing the stress functions $\left(\Phi\left(y,z\right)\right)_j$ and $\left(\Theta\left(y,z\right)\right)_j$ having continuous partial derivatives up to the third order, satisfying the governing equations (5), (10) inside the regions Ω_j *(j=1,2,...,K)* of the y, z plane and the boundary conditions (7), (11) on the corresponding boundary Γ_j, respectively. The numerical

evaluation of these functions is accomplished using the procedure presented in Mokos and Sapountzakis[1], while the shear deformation coefficients a_y, a_z, $a_{yz} = a_{zy}$ are obtained from the relations

$$a_y = \frac{A}{E_1 \Delta^2}\left((4\nu+2)\left(I_{yy} I_{\Theta y} - I_{yz} I_{\Theta z}\right) + \frac{1}{4}\nu^2 \left(I_{yy}^2 + I_{yz}^2\right) I_{ed} - I_{\Theta e} \right) \tag{18a}$$

$$a_z = \frac{A}{E_1 \Delta^2}\left((4\nu+2)\left(I_{zz} I_{\Phi z} - I_{yz} I_{\Phi y}\right) + \frac{1}{4}\nu^2 \left(I_{zz}^2 + I_{yz}^2\right) I_{ed} - I_{\Phi d} \right) \tag{18b}$$

$$a_{yz} = \frac{A}{E_1 \Delta^2}\left((2\nu+2)\left(I_{zz} I_{\Theta z} - I_{yz} I_{\Theta y}\right) + 2\nu\left(I_{yy} I_{\Phi y} - I_{yz} I_{\Phi z}\right) - \frac{1}{4}\nu^2 \left(I_{yy} + I_{zz}\right) I_{yz} I_{ed} - I_{\Phi e} \right) \tag{18c}$$

where

$$I_{\Theta e} = \sum_{j=1}^{K} \int_{\Gamma_j} \left(E_j - E_i\right) (\Theta)_j \, (\boldsymbol{n}\cdot\boldsymbol{e}) ds \tag{19a}$$

$$I_{\Phi e} = \sum_{j=1}^{K} \int_{\Gamma_j} \left(E_j - E_i\right) (\Phi)_j \, (\boldsymbol{n}\cdot\boldsymbol{e}) ds \tag{19b}$$

$$I_{\Phi d} = \sum_{j=1}^{K} \int_{\Gamma_j} \left(E_j - E_i\right) (\Phi)_j \, (\boldsymbol{n}\cdot\boldsymbol{d}) ds \tag{19c}$$

$$I_{ed} = \sum_{j=1}^{K} \int_{\Gamma_j} \left(E_j - E_i\right) \left(y^4 z \sin\beta + z^4 y \cos\beta + \frac{2}{3} y^2 z^3 \sin\beta \right) ds \tag{19d}$$

$$I_{\Theta y} = \frac{1}{6} \sum_{j=1}^{K} \int_{\Gamma_j} \left(E_j - E_i\right) \left[\left(I_{yz} y^3 z^2 - 2 I_{yy} y^4 z\right) \sin\beta + \left(3(\Theta)_j \cos\beta - y(\boldsymbol{n}\cdot\boldsymbol{e})\right) y^2 \right] ds \tag{19e}$$

$$I_{\Theta z} = \frac{1}{6} \sum_{j=1}^{K} \int_{\Gamma_j} \left(E_j - E_i\right) \left[\left(2 I_{yz} z^4 y - I_{yy} z^3 y^2\right) \cos\beta + \left(3(\Theta)_j \sin\beta - z(\boldsymbol{n}\cdot\boldsymbol{e})\right) z^2 \right] ds \tag{19f}$$

$$I_{\Phi y} = \frac{1}{6} \sum_{j=1}^{K} \int_{\Gamma_j} \left(E_j - E_i\right) \left[\left(2 I_{yz} y^4 z - I_{zz} y^3 z^2\right) \sin\beta + \left(3(\Phi)_j \cos\beta - y(\boldsymbol{n}\cdot\boldsymbol{d})\right) y^2 \right] ds \tag{19g}$$

$$I_{\Phi z} = \frac{1}{6} \sum_{j=1}^{K} \int_{\Gamma_j} \left(E_j - E_i\right) \left[\left(I_{yz} z^3 y^2 - 2 I_{zz} z^4 y\right) \cos\beta + \left(3(\Phi)_j \sin\beta - z(\boldsymbol{n}\cdot\boldsymbol{d})\right) z^2 \right] ds \tag{19h}$$

4 NUMERICAL EXAMPLES

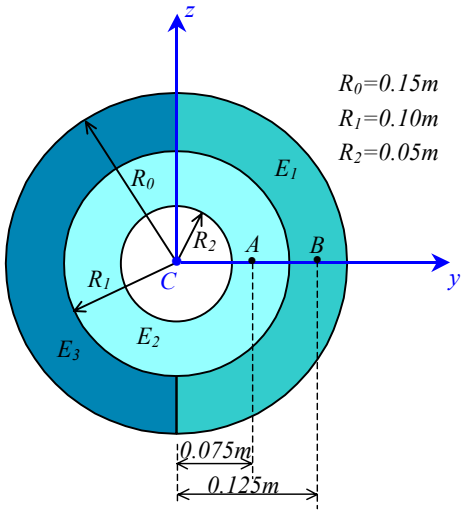

Figure 2.Composite circular tube cross section of the cantilever beam of Example 1.

Example 1

A cantilever beam of a composite circular tube cross section (Fig.2) has been studied. In Table 1 the shear correction factors κ_y, κ_z (values in parentheses come from Cowper's[2] definition) for various values of the Poisson's ratio are presented.

E_1/E_2	E_3/E_2	κ_y	κ_z
		$v = 0$	
1	1	0.681859 (0.681818) [2]	0.681859 (0.681818) [2]
	2	0.640786	0.657460
2	2	0.641179	0.641179
	3	0.619113	0.626847
3	3	0.616298	0.616298
	4	0.602910	0.607428
4	4	0.600434	0.600434
	5	0.591500	0.594473
5	5	0.589558	0.589558
	6	0.583187	0.585294
		$v = 0.3$	
1	1	0.679233 (0.714024) [2]	0.679233 (0.714024) [2]
	2	0.638623	0.655198
2	2	0.639397	0.639397
	3	0.617548	0.625189
3	3	0.614919	0.614919
	4	0.601652	0.606107
4	4	0.599284	0.599284
	5	0.590427	0.593355
5	5	0.588554	0.588554
	6	0.582234	0.584310

Table 1 : Shear Correction Factors of the composite cross section of Example 1.

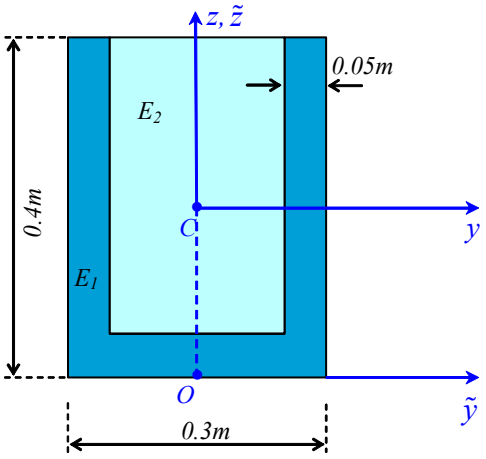

Figure 3. Composite cross section of the cantilever beam of Example 2.

Example 2

A cantilever beam having the cross section shown in Fig.3 has also been studied. In Table 2 the shear correction factors κ_y, κ_z for the Poisson's ratios $\nu = 0$ and $\nu = 0.33$ are presented, respectively, as compared wherever possible with those obtained from a 3-D FEM solution[3] of the 'exact' elastic beam theory. The minor alteration of the shear correction factors with the Poisson's ratio variation is verified.

E_1/E_2	κ_y		κ_z	
	$\nu = 0$	$\nu = 0.33$	$\nu = 0$	$\nu = 0.33$
1	0.833427	0.817572	0.833412	0.831403
2	0.709248	0.701529	0.800961	0.799247
3	0.615573	0.611080	0.776744	0.775299
4	0.547215	0.544287	0.759048	0.757802
5	0.495951	0.493891	0.745721	0.744624
6.837	0.429505	0.428269	0.728338	0.727431
		(0.428) [3]		(0.727) [3]

Table 2 : Shear correction factors of the composite cross section of Example 2.

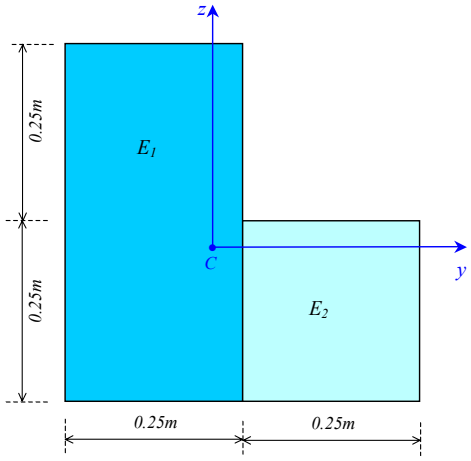

Figure 4. L-shaped composite cross section of the cantilever beam of Example 3.

Example 3

A cantilever beam having the L-shaped composite cross section shown in Fig.4 has also been studied. In Table 3 the shear correction factors κ_y, κ_z and κ_{yz} for various Poisson's ratios of the composite cross section are presented.

Example 4

A cantilever beam of the composite cross section consisting of a HEB-300 totally encased in a circular matrix, as shown in Fig.5, has been studied. In Table 4 the shear correction factors are presented, for various E_1/E_2 ratios.

E_1/E_2	$\nu = 0$			$\nu = 0.3$		
	κ_y	κ_z	κ_{yz}	κ_y	κ_z	κ_{yz}
1	6.94797	6.94797	-9.39352	6.89009	6.89008	-10.4203
2	6.31971	7.48088	-9.96204	6.26030	7.43914	-10.8879
3	5.88818	7.69788	-9.47095	5.82538	7.66498	-10.2073
4	5.63135	7.81607	-9.13537	5.56410	7.78885	-9.75711
5	5.47999	7.89124	-8.97955	5.40770	7.86797	-9.53309
6	5.39318	7.94390	-8.95006	5.31554	7.92352	-9.46158
7	5.34746	7.98327	-9.00643	5.26430	7.96509	-9.49145
8	5.32882	8.01410	-9.12245	5.24006	7.99765	-9.59073
9	5.32849	8.03910	-9.28115	5.23411	8.02402	-9.73916
10	5.34079	8.05989	-9.47129	5.24081	8.04595	-9.92353

Table 3 : Shear correction factors of the composite cross section of Example 3.

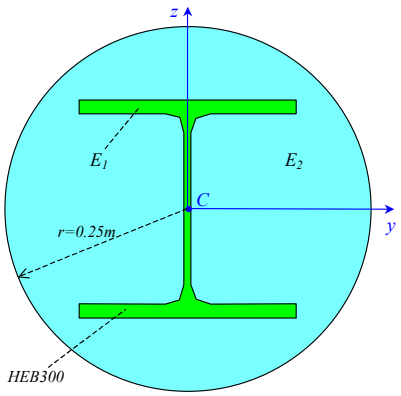

Figure 5. Composite cross section of the cantilever beam of Example 4.

E_1/E_2	κ_y	κ_z
5	0.838187	0.708029
6	0.830843	0.677910
7	0.823672	0.650976
8	0.816794	0.626828
9	0.810262	0.605101
10	0.804093	0.585472

Table 4 : Shear correction factors κ_y , κ_z for $\nu = 0.3$ of the composite cross section of Example 4.

5 CONCLUDING REMARKS

a. The numerical technique presented in this investigation is well suited for computer aided analysis for beams of arbitrary composite cross section, while the analysis is performed with respect to an arbitrary system of axes and not necessarily the principal one.
b. The convergence of the obtained results employing the proposed numerical procedure with those obtained from a 3-D FEM solution applied to the 'exact' elastic beam theory is easily verified.
c. The alteration of the shear deformation coefficients with the Poisson's ratio variation is not significant.
d. The accuracy of the results is remarkable.
e. The developed procedure retains the advantages of a BEM solution over a pure domain discretization method since it requires only boundary discretization.

ACKNOWLEDGMENTS

Financial support for this work provided by the "*Iraklitos Research Fellowships with Priority to Basic Research*", an EU funded project in the special managing authority of the Operational Program in Education and Initial Vocational Training.

REFERENCES

[1] Mokos, V. and Sapountzakis E. (2005), "A BEM Solution to Transverse Shear Stresses in Composite Steel – Concrete Beams", *4th European Conference on Steel and Composite Structures*, Eurosteel (2005).
[2] Cowper, G.R. (1966), "The Shear Coefficient in Timoshenko's Beam Theory", Journal of Applied Mechanics, ASME, 33(2), pp. 335-340.
[3] Fatmi, R.E. and Zenzri, H. (2004), "A Numerical Method for the Exact Elastic Beam Theory. Applications to Homogeneous and Composite Beams", International Journal of Solids and Structures, 41, pp. 2521–2537.

5th GRACM International Congress on Computational Mechanics
Limassol, 29 June – 1 July, 2005

ANALYTICAL MODELING OF ELASTOMERIC LEAD-RUBBER BEARINGS WITH THE USE OF FINITE ELEMENT MICROMODELS

I.N. Doudoumis*, F. Gravalas*, N.I. Doudoumis*

* Department of Civil Engineering
Aristotle University of Thessaloniki (A.U.Th.)
54006 Thessaloniki, GREECE,
e-mail: doud@civil.auth.gr

Keywords: Lead Rubber Bearings, Finite element micromodels, Analytical modeling, Base isolation.

Abstract. *The simplified models used for the simulation of the mechanical behavior of the Lead-Rubber Bearings (LRBs) are not always sufficiently accurate. The current paper attempts to certify the accuracy of the simplified models by comparing their mechanical behavior with the behavior of proper finite-element micromodels. The LRBs consist of two mounting steel plates located at the top and bottom of the bearing, several alternating layers of elastomer and steel shims and a central lead core. In the paper, the geometric shape of these bearings is modeled analytically with sufficient accuracy by taking into account detailed fabrication drawings of a standard LRB, while several thousands of solid finite elements are used for the modeling of the rubber layers, the steel plates, the steel shims and also the lead core. Two alternative micro-models are formed and investigated, in an attempt to define the bounds of the effects of the lead core's confinement to the behavior of the bearing. The models are tested for vertical static loading followed by a horizontal cyclic loading and the distribution of strains, stresses and plastic zones within the bearing is studied. Also the lateral force-displacement curves obtained from the analytical study are compared to the respective simplified bilinear elastoplastic curve suggested by the manufacturer of the LRB.*

1 INTRODUCTION

The elastomeric Lead-Rubber Bearings (LRB), which are used for the base isolation of structures, generally consist of two fixing steel plates located at the top and bottom of the bearing, several alternating layers of elastomer and steel shims and a central lead core (Figure 1a). The elastomeric material provides the isolation component with lateral flexibility, the lead core provides the energy dissipation or damping component, while the internal steel shims provide the vertical load capacity of the bearing. The steel shims, together with the top and bottom steel fixing plates, also confine the central lead core. During the seismic excitation of the structure, the rubber layers deform laterally by shear deformation, allowing the structure to translate horizontally and absorbing energy when the lead core yields [1].

For the deformation and strength capacity control of each bearing part (rubber layers, lead core and steel shims) and for the different load conditions (vertical load, cyclic lateral loading, buckling control, etc.) that must be taken into account according to the Code Provisions [2], simple analytical formulas are used. These formulas are referred to a simplified model of the bearing, not necessarily the same for each design check.

Even for a more detailed description of the bearing's response to lateral loading, simple analytical models are also used, usually with one finite element and bilinear elastoplastic law with hardenind [3], or with two finite elements (one perfectly plastic and one unlimited elastic) in parallel conection [4]. In these models, the bearing's parameters that describe the lateral force–displacement bilinear law are the initial elastic stiffness K_u, the yielded stiffness K_d, the characteristic strength Q_d and the lateral design displacement D_d. Values for these parameters are acquired from the manufacturer of the bearing, so as to be in accordance with the elaborated results from a series of experimental tests, where the basic matching criterion is the equivalence of the hysteresis loop area between the experimental and the analytical model. They can also be predicted with remarkable accuracy by using simple analytical formulas, except from the initial elastic stiffness K_u value which is mainly a function of the fabrication details of the bearing and especially of the confinement of the lead core. It should be noted that limited only attempts of using finite element micromodels for the analysis of the LRBs are known to date and they mainly focus on determining the lateral force-displacement curves of the bearings [5].

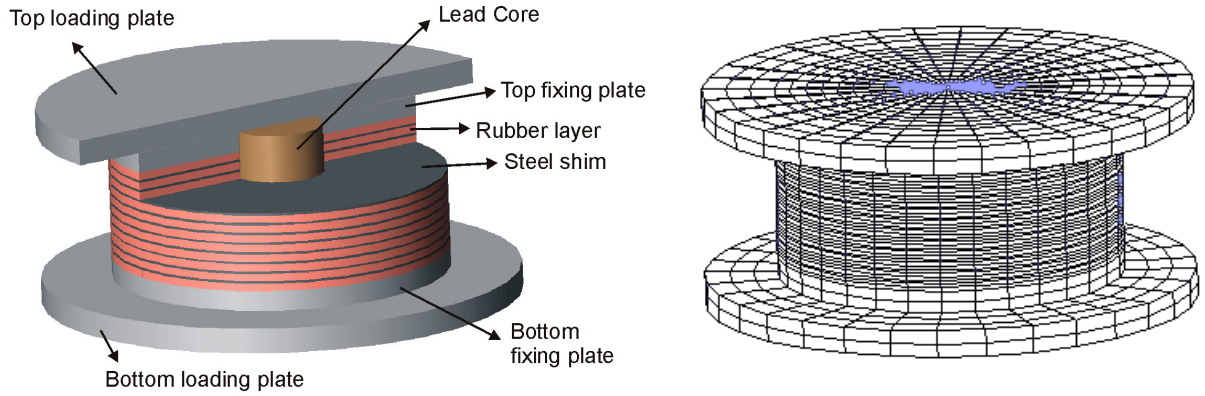

Figure 1. (a) Examined LRB, (b) Finite element micromodel

In this paper, the geometric shape of these bearings is modeled analytically by taking into account detailed fabrication drawings of a standard lead-rubber bearing, while several thousands of solid finite elements are used for the modeling of the rubber layers, the steel plates and shims and also the lead core. Two alternative micro-models are formed and investigated, in an attempt to define the bounds of the effects of the lead core's confinement. The models are tested for vertical static loading together with horizontal cyclic loading and the distribution of stresses and plastic strains within the bearing is studied. Also the lateral force-displacement curves obtained from the analytical study are compared to the respective simplified bilinear elastoplastic curve suggested by the manufacturer of the isolation bearing.

2 ANALYTICAL MODELING

The LRB under consideration is the Skellerup150 isolator, made by the Skellerup Industries[1] and shown in Figure 1a. The isolator consists of:

- 2 loading steel plates (top and bottom) with a 601 mm diameter and a 31,8 mm thickness,
- 2 fixing steel plates (top and bottom) with a 431 mm diameter and a 25,4 mm thickness,
- 11 rubber layers with a 431 mm diameter and a 9,5 mm thickness,
- 10 steel shims with a 431 mm diameter and a 3,0 mm thickness,
- a central lead core with a 116,8 mm diameter and a 185 mm height.

The basic technical specifications given by the manufacturer are as follows:

- design compressive load DCL=667 kN (150 kip),
- lateral design displacement D_d=0,1524 m,
- yielded stiffness K_d=858 kN/m,
- elastic stiffness K_u=11050 kN/m,
- lateral force (at D_d)= 251,3 kN.

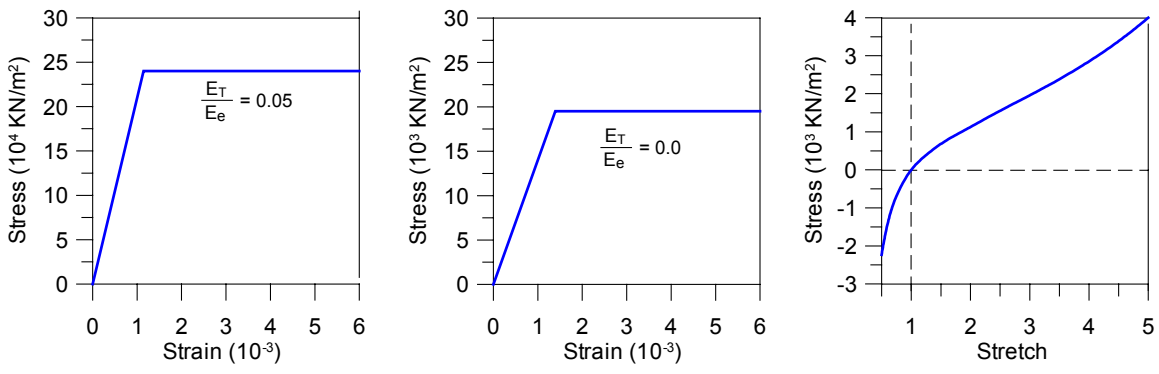

Figure 2. Stress-strain laws of the LRB materials

The proposed finite element model of the bearing (model-1) is shown in Figure 1b and includes 5632 solid hexaedron 8-node elements for the rubber layers, 2560 elements for the steel shims and 1440 elements for the lead core, to a total of 12448 elements and 14326 nodes. In model-1, full bond was assumed between the steel and rubber material. Also the lead core was assumed to be tightly fitted in the bearing [6], thus considering fixed boundary conditions to hold between the lead core and the steel shims and rubber layers. However, since the confinement of the core depends on the manufacturing details, a second alternative model (model-2) was formed, without any interaction between the lead core and the steel shims and rubber layers, in order to define the bounds of the effects of the core's confinement to the deformation and stress state of the bearing. In the later model the lead core was firmly connected only with the top and bottom fixing plates of the bearing.

The steel material of the top and bottom plates and the shims was assumed to be a mild steel with a Young modulus $E=21\times10^7$ kN/m, Poisson's ratio $\nu=0,30$, bilinear elastoplastic constitutive law (Figure 2a) with 5% strain hardening ratio and a Von Mises yield criterion with $\sigma_y=240\times10^3$ kN/m^2 (uniaxial). The lead core was assumed to have a Young modulus $E=18\times10^6$ kN/m, Poisson's ratio $\nu=0,43$, bilinear elastoplastic constitutive law (Figure 2b) and a Von Mises yield criterion with $\sigma_y=19,5\times10^3$ kN/m^2 (uniaxial). For the rubber layers an hyper-elastic material law was considered (Figure 2c), according to the Arruda-Boyce constitutive model [7] which was properly modified in order to take into consideration the finite compressibility of the rubber. This model requires two material constants, the initial shear modulus G_o and the locking stretch λ_m. The material constants of the rubber were estimated according to AASHTO 1999 Guide Specifications [2] for natural rubber with hardness 50, taking the values G=620 kN/m^2 for the shear modulus and $K=15\times10^5$ kN/m^2 for the bulk modulus. In fact, an attempt was made to fairly estimate all the material constants related to this bearing, since they could not been found from the manufacturer of the bearing.

The examined models were subjected to 2 quasi-static loading sequences, corresponding to the design compressive load and the design lateral displacement suggested by the manufacturer. That is, a vertical compressive load with a maximum value of P=667 kN (150 kips) was applied in 10 steps, followed by a cycling imposed horizontal displacement with an amplitude of 0,1524 m (6 inches) applied in 120 steps, which results in a rubber's maximum shear strain of about 145%. The quasi-static analysis was performed by the computer code ADINA [8], taking into consideration the large strain and large displacement effects.

3 RESPONSE RESULTS TO QUASI-STATIC LOADING

In the following, some characteristic results of the system's response are presented and evaluated, beginning with the first stage of the loading process.

3.1 Vertical compressive loading

Figure 3 shows the distribution of the effective stresses within the lead core of the examined models, when applying 100% of the total vertical load. The stress state in both models is quite similar, while in the most of the core the effective stress has already reached the yielding stress of the lead, even before any additional lateral load was applied to the bearing. It should be noted that the first yielding took place at about 60% of the total vertical load, an event that is not yet sufficiently known, neither is taken into consideration by the simplified analytical models which are used for the LRBs.

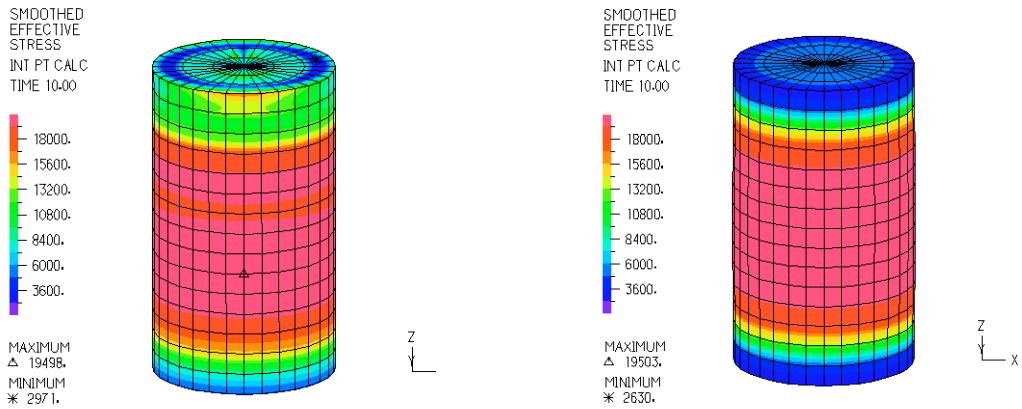

(a) model-1 (b) model-2

Figure 3. Effective stress within lead core for the maximum value of the vertical load.

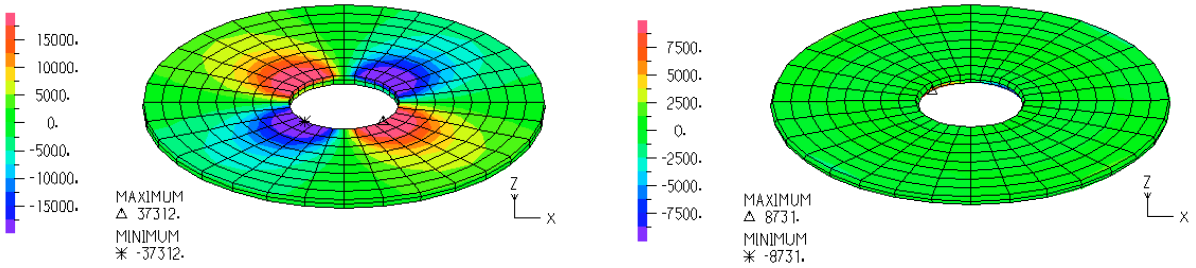

(a) model-1 (b) model-2

Figure 4. Horizontal shear stresses S_{xy} within the bottom rubber layer

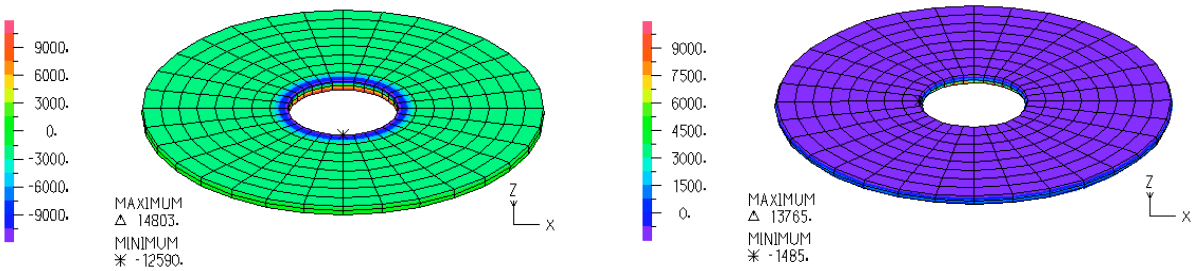

(a) model-1 (b) model-2

Figure 5. Hydrostatic pressure S_o within the bottom rubber layer

Figure 4 shows the distribution of horizontal shear stresses S_{xy} within the top face of the bottom rubber layer, corresponding to the 100% application of the total vertical load. It is observed that in model-1 the extreme shear stresses are about 4 times greater than in model-2, which means that the tight fitting of the lead core in model-1 causes a high concentration of rubber shear stresses around the hole of the layer.

Figure 5 shows the distribution of hydrostatic pressure S_o within the top face of the bottom rubber layer, for the 100% application of the total vertical load. The maximum positive pressure (compression) is quite similar in both models and is located around the central hole at the bottom face of the layer. However, in model-1 the minimum negative pressure (tension) is many times greater than in model-2 and is located at an area around the central hole at the top face of the layer. This area is critical for the control of the bond strength between the rubber layers and the steel shims. This stress concentration, shown in Figures 4a and 5a, cannot be predicted by the simplified analytical models which are used for the LRBs.

3.2 Horizontal cycling loading

After the application of the vertical commpressive load, a cycling imposed horizontal displacement with an amplitude of ±0,1524 m (6 inches) was applied into 120 steps. In Figure 6 the deformed shape of the compared models is shown when the horizontal displacement takes its maximum value U_{xmax}=0,1524 m. The deformed shape of the compared models is very similar, except from the left corner of the top rubber layer, where the deformation of model-2 is considerably greater than that of model-1. The largest deformation of the rubber develops at the right corner of the bottom rubber layer.

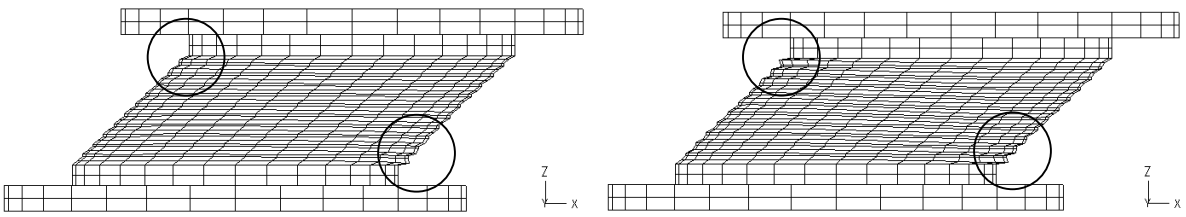

(a) model-1 (b) model-2

Figure 6. Deformed shapes of examined models for max imposed horizontal displacement

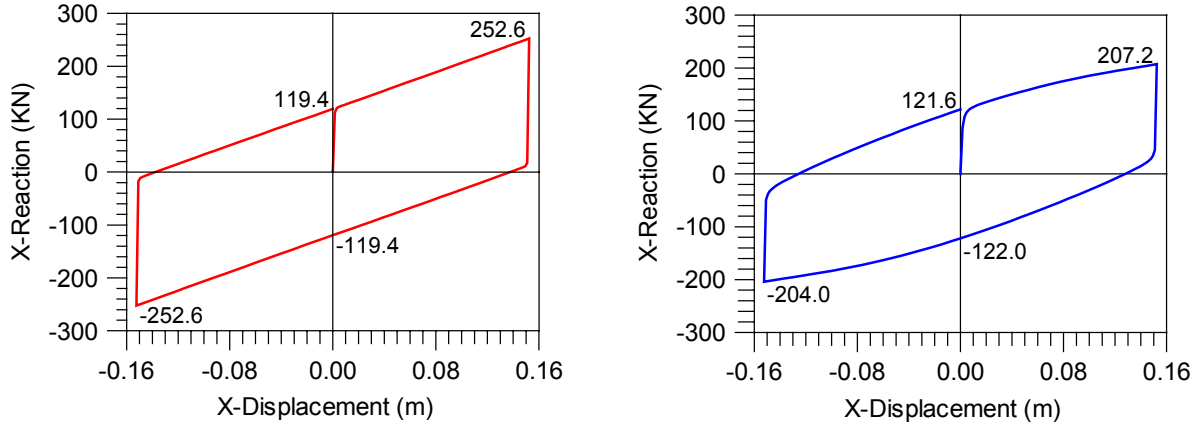

(a) model-1 (b) model-2

Figure 7. Force-displacement diagrams of the examined models

Figure 7 shows the horizontal force-displacement curves of the examined models during the entire loading cycle. It is observed that the characteristic strength of model-1 (119,4 kN) is about equal to the strength of model-2 (121,8 kN), which means that the confinement of the lead core very little affected the characteristic strength of the compared models. It is also observed that the maximum horizontal force of model-2 is about 20% less than the respective force of model-1 and the area of hysteresis loop of model-2 (indicating the energy loss per cycle) is about 8,0% less than the area of model-1. These observations denote that the confinement of the lead core affects significantly the size of the maximum horizontal force, but affects less the energy dissipation properties of the bearing. In conclusion, the bilinear form of the force-displacement curve resulted from model-1 indicates the perfect confinement of the lead core.

In Figure 8 the deformed shape of the lead core, as well as the distribution of the effective stresses within the core is shown, due to the maximum value of the imposed horizontal displacement. In both models a significant stretching of the lead core is observed, not only in shear but in elongation too. It is noted that this elongation cannot be accurately described without considering large displacement effects in the finite element analysis. It is also noted that the deformed shape of the lead core of model-2 is highly incompatible to the deformed shape of the rubber layers and steel shims, thus concluding that model-2 is suitable only for comparison purposes with the more precise model-1. Regarding the distribution of the effective stresses, it is very similar in both models. Namely, the effective stresses have reached the yielding stress over the whole height of the core, except from the top and bottom ends which are firmly connected with the respective steel fixing plates.

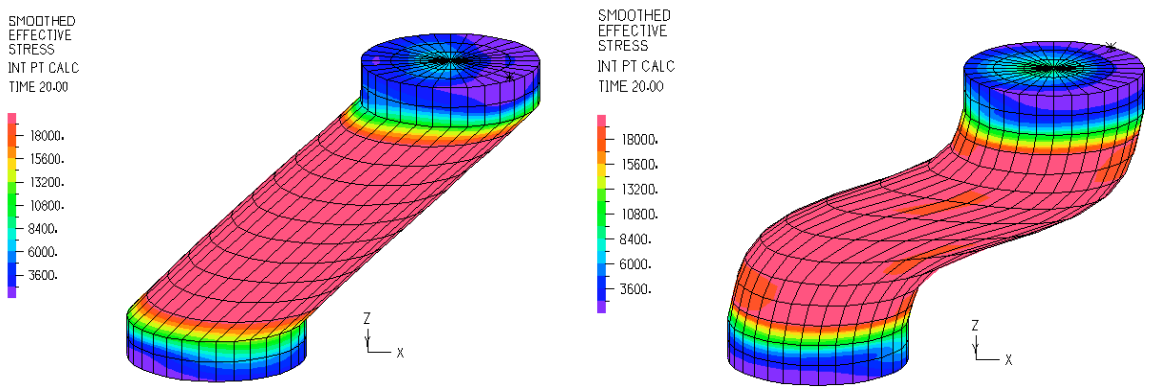

(a) model-1 (b) model-2

Figure 8. Deformed shape and effective stresses in lead core due to max imposed horizontal displacement

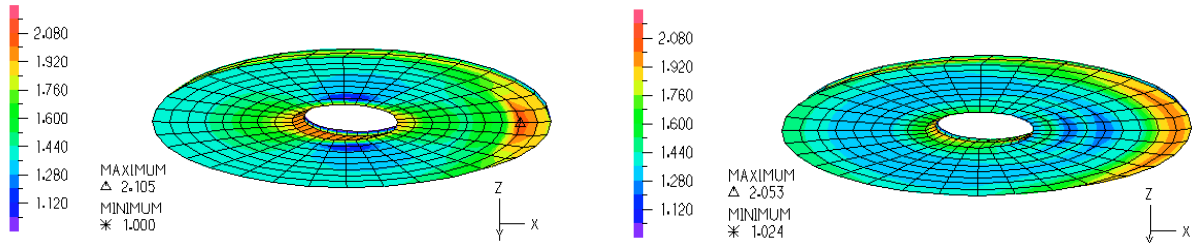

(a) model-1 (b) model-2

Figure 9. Maximum principal strains at the bottom rubber layer

Figures 9, 10 and 11 are related to the deformation and stress state in the bottom rubber layer, due to the maximum value (+0,1524 m) of the imposed horizontal displacement. In particular, Figure 9 shows the distribution of the maximum principal strains at the bottom face of this layer. It can be seen that the largest values of the strains are about 40% higher than the mean shear strains of the bearing's rubber layers (which have been previously estimated to 145%) and are located around the central hole and near the right boundary of the layer.

Figure 10 shows the distribution of the horizontal shear stresses S_{xz} within the rubber layer. It is observed that in model-2 the stress distribution is fairly smooth, while in model-1 the stress distribution contains large positive and negative peak values. The maximum values in model-1 are about 4 times greater than the maximum values in model-2 and the minimum values in model-1 are more than 20 times greater than in model-2. This non-smooth distribution of shear stresses S_{xz} within the rubber layer of model-1 is obviously due to the tight fitting of the lead core in this model.

Figure 11 shows the distribution of hydrostatic pressure S_o within the rubber layer. It is observed that the pressure distribution is significantly different within the compared models, as well as the location of the maximum (compressive) pressure values. In conclusion, the confinement of the lead core significantly affects the distribution and the size of the stresses within the rubber layers. Moreover, the non-smooth stress distribution in model-1, as shown in Figures 10a and 11a, cannot be predicted by the simplified analytical models which are used for the LRBs.

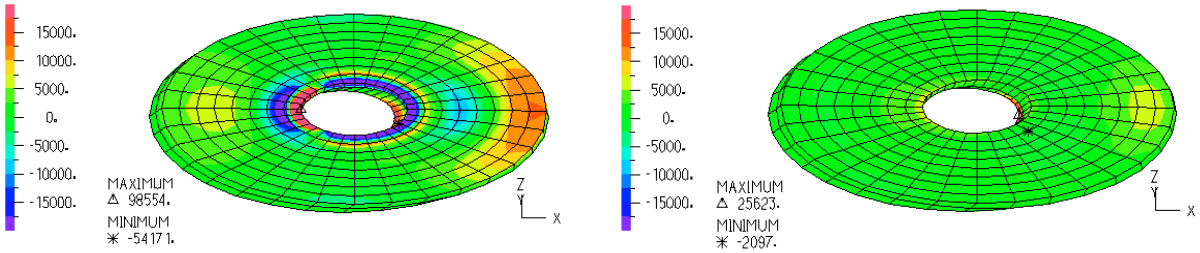

(a) model-1 (b) model-2

Figure 10. Horizontal shear stresses S_{xz} within bottom rubber layer

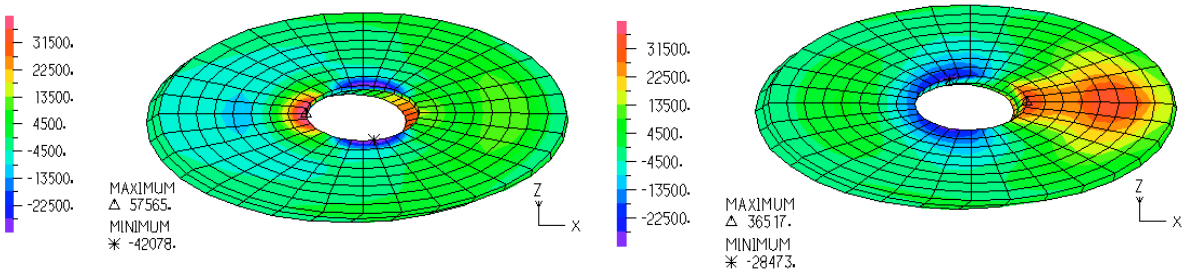

(a) model-1 (b) model-2

Figure 11. Hydrostatic pressure within bottom rubber layer

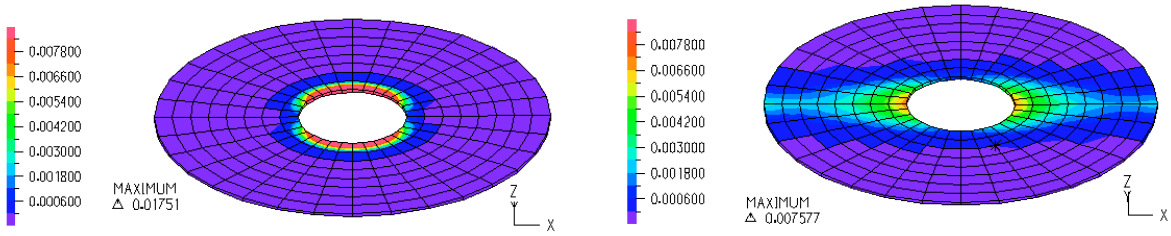

(a) (b)

Figure 12. Total accumulated effective plastic strains within the middle steel shim

Figure 12 shows the distribution of the accumulated effective plastic strains within the middle steel shim of the bearing, at the end of the cycling loading process. The plastic strains in model-1 take values more than twice larger than those in model-2 and are strictly located around the central hole of the shim, while in model-2 they are distributed in a strip along the x-x diameter of the shim. The development of plastic strains in model-2 is due to the low yield strength of the mild steel. However, the development of plastic strains in model-1 is mainly due to the lateral strong interaction between the steel shims and the lead core. This conclusion has been assured by analyzing a model similar to model-1, but with a twice higher strength in the steel shims.

Figure 13 shows the vertical distribution of plastic zones within the steel shims, as well as the lateral interaction between the shims and the core of the model-1, due to the maximum value (+0,1524 m) of the imposed horizontal displacement. When reversing the imposed horizontal displacement (–0,1524 m), the shape of the core-shims' interaction also changes and finally, at the end of the cyclic loading process, accumulative plastic strains have developed in all the steel shims of the LRB.

The horizontal force-displacement curves of the examined models during the entire loading cycle, are comparatively shown in Figure 14a, together with the respective simplified bilinear elastoplastic curve suggested by the manufacturer of the isolation bearing (model-3). It is evident that the characteristic strengths of the compared three models, as well as the entire curves of model-1 and model-3, practically coincide, except from their unloading parts, where the unloading stiffness of model-3 is considerably less than the unloading stiffness of model-1 and model-2. Consequently, the area of hysteresis loop of model-1 is about 7,0% more than the area of model-3, while the area of hysteresis loop of model-2 is about 1,0% less than the area of model-3. It must be noted that the unloading stiffness (which is equal to the initial elastic stiffness K_u) suggested by the manufacturer, has not been established directly by the experimental tests of this bearing (Figure 14b). The unloading stiffness obtained by these tests is quite similar to the unloading stiffness obtained by the examined model-1 and model-2.

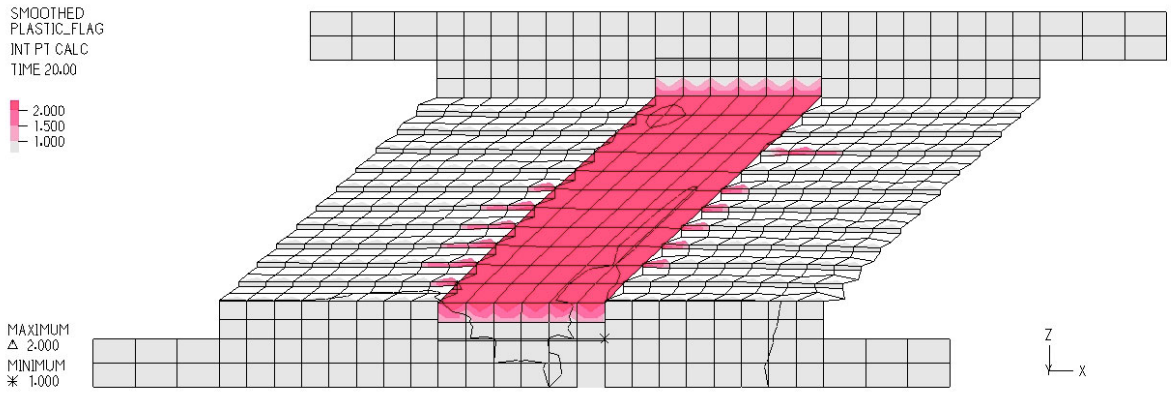

Figure 13. Distribution of plastic zones (red color) in a meridian x-x section.

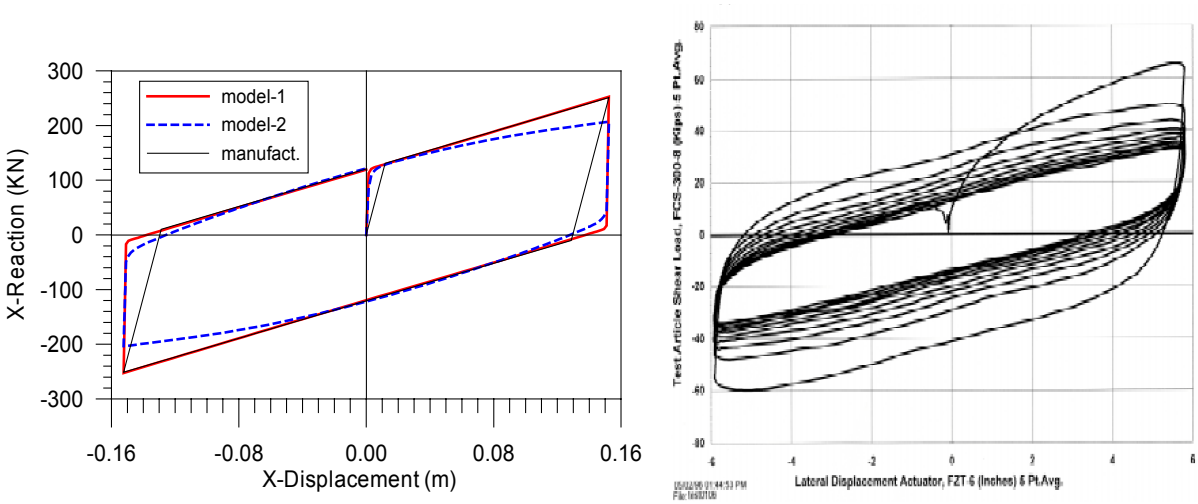

(a) Analytical models (kN, m) (b) Experimental results (kip, in)

Figure 14. Force-displacement curves' comparison between analytical and experimental results

4 CONCLUSIONS

The finite element micromodels provide increased possibilities for a more detailed study of the stress, strain and available strength of LRBs. In this way, a better understanding of their mechanical behavior is possible, by detecting their critical areas and thus contributing to the improvement of their design.

Concerning the examined structural system, it must be noted that the existence of the lead core causes a significant disturbance on the smooth distribution of the stresses and strains in the interior of the bearings, so the use of micromodels in the study of LRBs would be advisable.

It must be noted also that for the validity of the quantitative conclusions obtained for the examined LRB, it is necessary to verify the basic assumptions that have been made, which concern its material properties and fabrication details.

ACKNOWLEDGEMENTS

A part of this report is based on research sponsored by the European Commission and the Ministry of National Education and Religions Affairs of Greece (within the framework of the Operational Programme of Education and Initial Vocational Training – Ε.Π.Ε.Α.Ε.Κ.).

REFERENCES

[1] "Evaluation findings for skellerup base isolation elastomeric bearings" (1998), Technical evaluation report, (CERF report: HITEC 98-12), prepared by the Highway Innovative Technology Evaluation Center.

[2] AASHTO, American Association of State Highway Transportation Officials (1999), "Guide Specifications for Seismic Isolation Design" , Washington D.C.

[3] SAP2000: "Integrated Finite Element Analysis and Design of Structures" (1999), Computers and Structures, Inc., Berkeley, USA.

[4] Kelly T. E. (2001), "Base isolation of Structures- Design Guidelines", Holmes Consulting Group Ltd, Wellington, New Zealand.

[5] Ali, H. M. and Abdel-Ghaffar, A. M. (1995), "Modeling of rubber and lead passive-control bearings for seismic analysis", J. Struct. Engrg., ASCE, Vol. 121 (7), 1134-1144.

[6] Naeim F, Kelly J. (1999), "Design of seismic isolated structures". John Wiley & Sons, Inc.

[7] Arruda E. M. and Boyce M. C. (1993), "A three-dimensional constitutive model for the large stretch behavior of rubber elastic materials", J. Mech. Phys. Solids, Vol. 41 (2), 389-412.

[8] ADINA: "Automatic Dynamic Incremental Nonlinear Analysis" (2003), Adina R&D, Inc., Watertown, USA.

ON THE NUMERICAL MODELING OF THE BOLT PULL-OUT PHENOMENON FROM A STEEL PLATE IN A BOLTED STEEL CONNECTION

P. Iványi[#], M. Zygomalas[+] and C. C. Baniotopoulos[+]

[#]Research Group on Dynamics of Machines and Vehicles,
Hungarian Academy of Sciences – Budapest University of Technology and Economics
H-1111 Budapest, Hungary
e-mail: peteri@morpheus.pte.hu

[+]Institute of Steel Structures, Department of Civil Engineering,
Aristotle University of Thessaloniki, GR-54124 Thessaloniki, Greece

Keywords: Pull-out test, numerical simulation, failure analysis, plasticity, energy balance.

Abstract. *Recent laboratory and numerical experiments have been carried out to investigate the pull out phenomenon of a bolt from a steel plate. The experiments have shown two distinctly different failure modes and a transition failure mode; the failure modes mainly depend on the thickness of the steel plate. The obtained numerical results are compared with those obtained by the laboratory testing program.*

1 INTRODUCTION

One of the most critical and in the mean time, dangerous damage mechanism in connections in structural steelwork is the one that corresponds to the pull-out of bolts from steel plates [1] . Due to the great significance of this problem laboratory test have been recently carried out to investigate this phenomenon. In addition, another important reason for this investigation is that very limited literature about this phenomenon has been found.

2 EXPERIMENTS

In this section the main experimental results are presented which are in a second step simulated by applying the finite element method. The major parts of the experiments have been carried out at the Thessaloniki University, while some further experiments have been performed at the Budapest University of Technology and Economics.

2.1 Experimental setup

The geometric arrangement of the experiment is shown in Figure 1a, while Figure 1b shows the geometry of the steel plate. All measurements in Figure 1b are expressed in millimeter. The experimental model has symmetry along the X and the Y axes. In different experiments the thickness of the plate is 1, 2, 3, 4 or 5 millimeters. The plate is fixed to a rigid frame by M6 bolts. The diameter of the bolt hole at the center of the plate is one millimeter larger than the diameter of the shaft of the bolt, which is a requirement by the Eurocode 3 standard for steel structures. Finally a bolt is placed in the center hole. When an M12 bolt is used in the experiments, the diameter of the hole is 13 mm and in the case of M14 bolt the diameter is 14 mm. No bolt nut or washer is used. Since the bolt is not hold in place by the nut, it was very important to ensure that the bolt is centered at the hole at the beginning of the experiment.

The experiment force is applied increasingly to the M12 (or M14) bolt until the bolt is pulled-out of the plate. *Pulling-out of the plate* means, that the material of the plate will at the end fail and the bolt will become free. The duration of each experiment lasted approximately half an hour and therefore, it is assumed that the loading is static and not dynamic. Furthermore, it can be interesting that the machine is constructed in such a way that it was possible to follow the behaviour of the structure even after the failure of the plate, for example when only the friction between the bolt and the plate restricts the movement of the bolt.

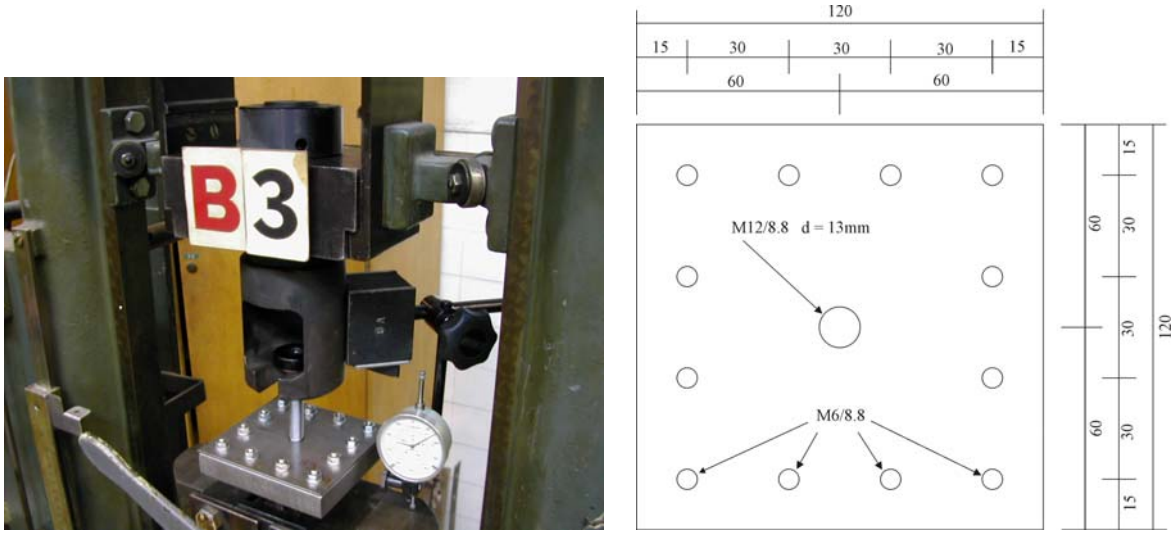

(a) (b)

Figure 1: (a) Experimental setup and (b) geometric arrangement of the plate

2.2 Experimental results

The results of the experimental testing suggests that there are two distinctive failure modes for bolt pull-out from a steel plate. When the steel plate is thin, for example 1 mm, then the corner of the bolt penetrates the plate through the thickness. Later the failure of the elements propagates towards the center, which means that the corner of the bolt basically cuts up the plate. This phenomenon can be seen in Figure 2a. The other failure mode occurs when the plate is thick, for example the thickness is 5mm. At the final failure stage, a ring separates from the plate as it is shown in Figure 2c. It is also important to note, that in this case at the corners of the bolt a pool of plastified material forms. On the other hand, along the sides of the bolt sudden fracture occurs. These two phenomena can be seen in Figure 3. Figure 2b shows the transition failure mode where there is plastification at the corner of the bolts and fracture along the side of the bolt occurs. However in this case no closed ring is formed.

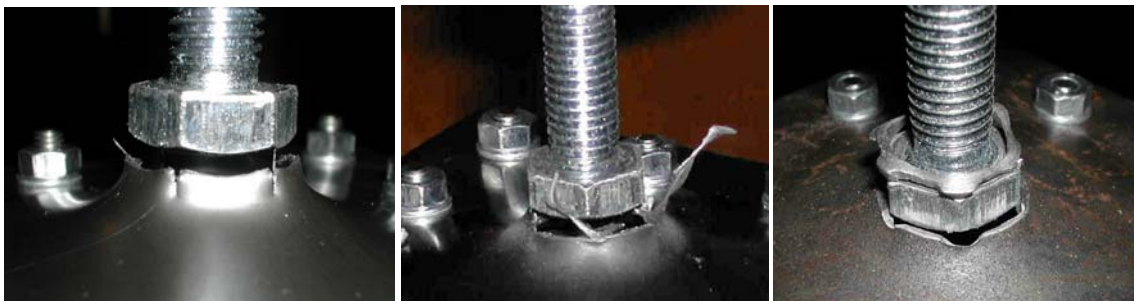

(a) (b) (c)

Figure 2: Failure modes for different plate thicknesses; (a) 1 mm, (b) 3 mm and (c) 5mm

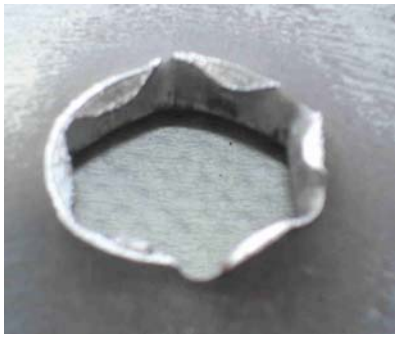

Figure 3: Plastification at the corner of the bolt and sudden fracture along the side of the bolt

Apart from observing the failure modes, two other properties have been measured in the experiments, the applied force on the bolt and the displacement of the bolt. Figure 4 depicts the measured displacement-applied load curves for the 1 mm and 5 mm plate thicknesses. Figure 5 shows the relation between the thickness of the plate and the ultimate applied load. The ultimate load is calculated as an average of the maximum load of the same type of experiments.

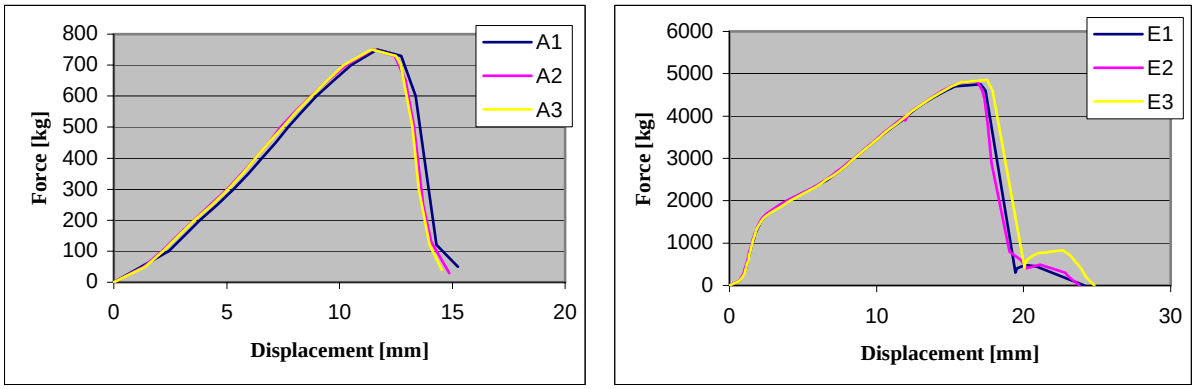

(a) 1mm (b) 5mm

Figure 4: Displacement-load curve for different plate thicknesses

Figure 5: Relation between the plate thickness and the ultimate applied load

3 NUMERICAL ANALYSIS

Although the problem may seem a very simple one, it is not a traditional engineering analysis problem. Usually the structures or the components of the structures are designed by elastic or elasto-plastic theory. However, even in the case of plastic theory only limited plastic capability is considered. In this paper a problem is discussed where the experiment or numerical simulation is carried out up to a “full” material failure. Considering the material and geometric non-linearities several difficulties had to be solved. For the numerical analysis the LS-DYNA[2] software was used because of its capabilities, for example handling of contact and material failure.

3.1 Geometric model

The geometry have two symmetry axes and therefore, it is sufficient to model only one quarter of the structure for the numerical simulation. Due to this modeling, a large number of finite elements can be used at important places. Figure 6 clearly indicates the part which is modeled for this paper. The figure also shows that another simplification has been introduced. It is assumed that the M6 bolts provide fixity not only at the bolt points but along the line of the bolts. This means that the middle points marked in Figure 6 are restricted, although in reality these points can move vertically.

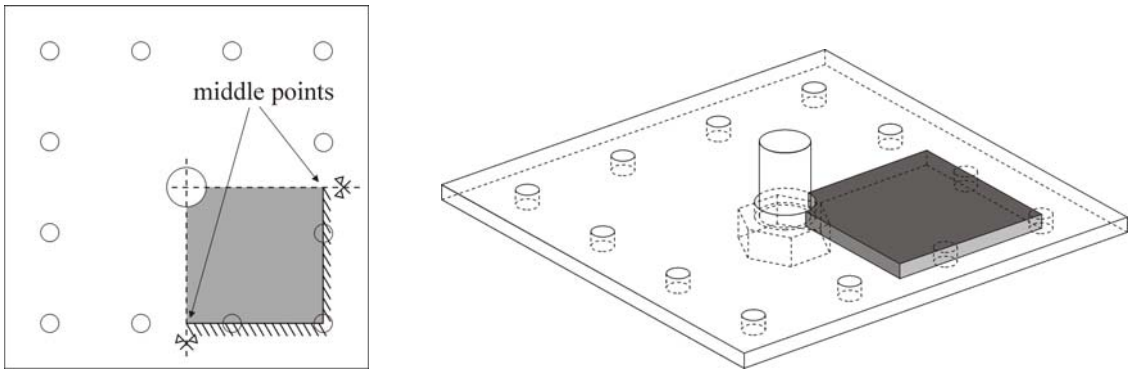

Figure 6: Part of the modeled plate, 2D and 3D view

3.2 Boundary conditions

The boundary conditions are applied to all points of the surfaces across the thickness. The boundary condition along the line of the fixing bolts is that the displacements are restricted in all directions. The boundary condition along the symmetry axes is that no movement is allowed perpendicularly to the symmetry planes. These boundary conditions can also be seen in Figure 6.

3.3 Material definition

Two types of material are used in the analyses: a rigid and an elasto-plastic material. The rigid material is used for the bolt for two reasons: The first is that the material of the bolt has higher strength in comparison to the material of the plate. Moreover, the size effect can be considered, as the bolt head is much smaller compared to the plate and therefore, it will be more rigid than the plate.

The material of the plate is an elasto-plastic material with failure strain. Unfortunately, at the time of writing this paper no material measurements are available; therefore, for the numerical analyses in this paper the following typical steel material properties have been assumed: the elastic modulus is 210000 N/mm^2, the density is 0.786 kg/mm^3, the Poisson's ratio is 0.292, the yield stress is 210 N/mm^2, the tangent modulus is 1010 N/mm^2 and the failure strain is set as 0.3 percent. It is important to note how the LS-DYNA software handles the material failure. When the strain in a finite element reaches the 0.3 percent then the element is **deleted** from the mesh. This behaviour will hopefully simulate the fracture in the plate.

It may be noticed that the density is actually not correct. The valid value is 7860 kg/m^3 which does not correspond to 0.786 kg/mm^3. The reason for this discrepancy is that usually time-dependent problems are analyzed by LS-DYNA, but the problem at hand is a static one. To speed up the analysis, the problem is solved as a quasi-static problem with mass scaling which is applied by increasing the density.

3.4 Load and contact definition

The load is applied on the bolt and it is transmitted to the plate through contact. As it is mentioned in the previous section, the problem must be analyzed as a quasi-static problem and therefore, the load is applied in such a way that the maximum force and the maximum analysis time is defined, while all intermediate values are linearly interpolated.

The contact between the bolt and the plate is defined as an eroding contact, since the surface is continuously changing as finite elements are removed from the mesh when material failure occurs. LS-DYNA is one of the programs that is capable to handle eroding contact. This was one of the main reasons to choose the LS-DYNA software for the analysis.

3.5 Element type selection

Since even 5 mm thick plate has been investigated in the experiments, solid and not shell elements have been used for meshing. For this reason SOLID164 hexahedron element is used from the element library of the LS-DYNA[1] program. This element is generally used for the 3D modeling of solid structures. The hexahedron element is defined by eight nodes, where the degrees of freedom at each node are translations, velocities, and accelerations in the nodal x, y, and z directions. The element uses reduced, one point integration plus viscous, hourglass control.

3.6 Finite element meshing

The finite element mesh is built up of hexahedron elements. To ensure good quality results and considering the eroding behaviour of the elements it was decided that a large number of elements are required in the plate around the edges and the corner of the bolt but in other parts of the plate coarser meshing is enough. For this reason, an area around the bolt points in the plate is defined where a large number of finite elements are generated as shown in Figure 7. This fine mesh area can also help to reduce hourglassing. Hourglassing occurs due to the one-point, reduced integration of the solid elements and it refers to the zero-energy mode of the elements. These zero energy modes are oscillatory and their period is so short that the elements form a zigzag shape. Hourglassing can invalidate the results and therefore, it must be avoided if possible. However in the current setup the point loads from the bolt cannot be avoided therefore it was chosen that as fine meshes must be defined as it is possible around the contact regions. Furthermore to help the initial contact analysis, the finite element meshes have matching nodes and elements at the contact surfaces.

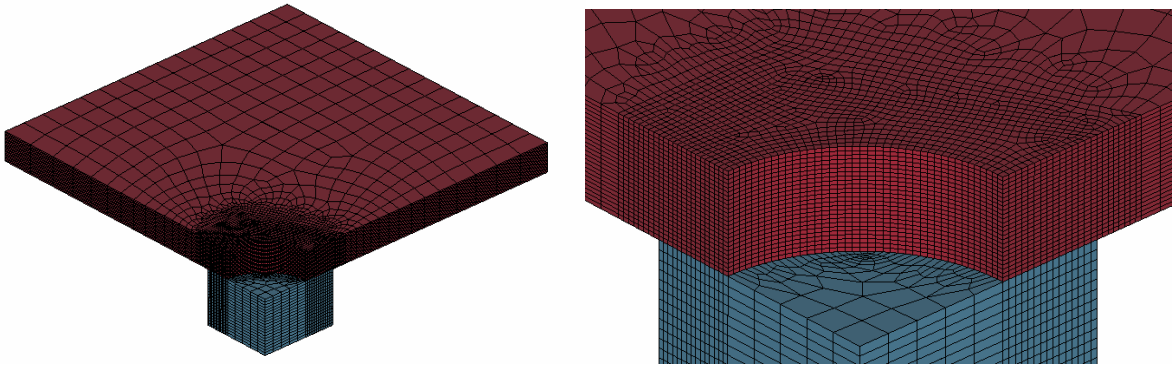

Figure 7: Finite element meshing of the plate and the bolt for 4 mm plate thickness

4. ANALYSIS RESULTS

The main aim of this paper was to numerically simulate the bolt pull-out experiments and therefore, this section aims to present and compare the analysis results with the experimental ones.

4.1 Failure mechanism

Figure 8 shows the failure mechanism for 1 mm plate thickness. In this case the corner of the bolt first penetrates the plate (Figure 8a) and then this fracture spreads radially towards the centre of the plate (Figure 8b). Once the fracture reaches the edge of the plate, the plate opens up and let the bolt through (Figure 8c). Figure 8d shows the final stage of the pull-out of the bolt. These figures show that along the fracture line the plate of the material is plastified, since some of the elements are removed around that area.

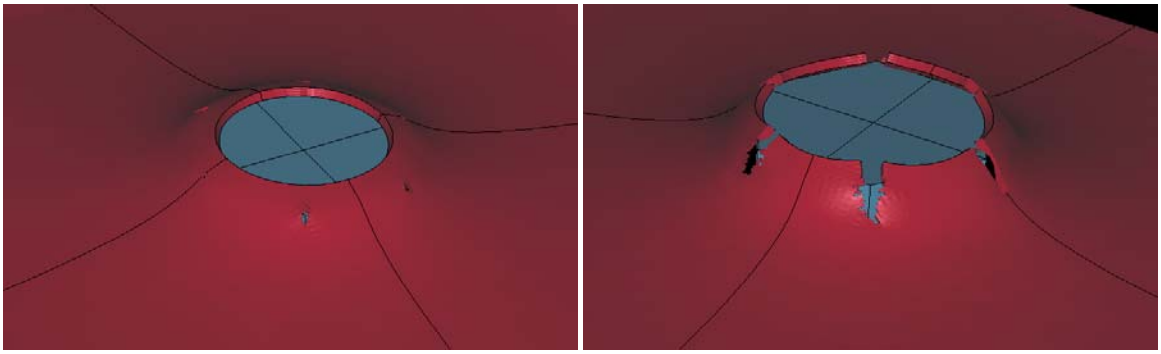

(a) (b)

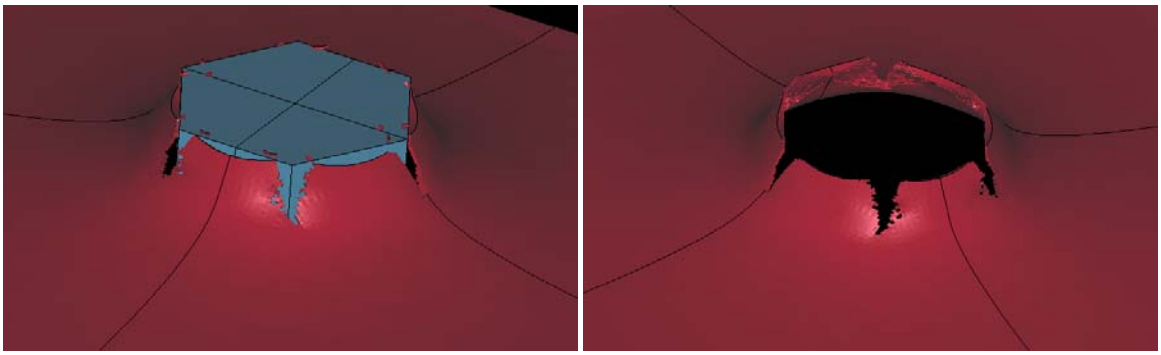

(c) (d)

Figure 8: The failure mechanism for 1 mm plate thickness

Figure 9 shows the failure mechanism for 4 mm plate thickness. The failure mechanism in Figure 9 is a kind of ring, which corresponds to the experiment results. However one of the major differences in the failure mechanism is that the ring is not continuous and there is no “drop” of plastified material in the ring above the corner of the bolt. Obviously the reason is that in the current analysis all finite elements with fully plastified, failed material are removed from the mesh.

Figure 10, showing how many elements are removed at a given moment, supports the observation of the experiments that at the final moments of the analysis a large number of elements are removed and a sudden “fracture” occurs. However by comparing Figure 9 to Figure 3, another difference is apparent that in the analysis (in Figure 9) it is not possible to identify plastified regions and sudden fracture regions in the plate after the bolt is pulled out.

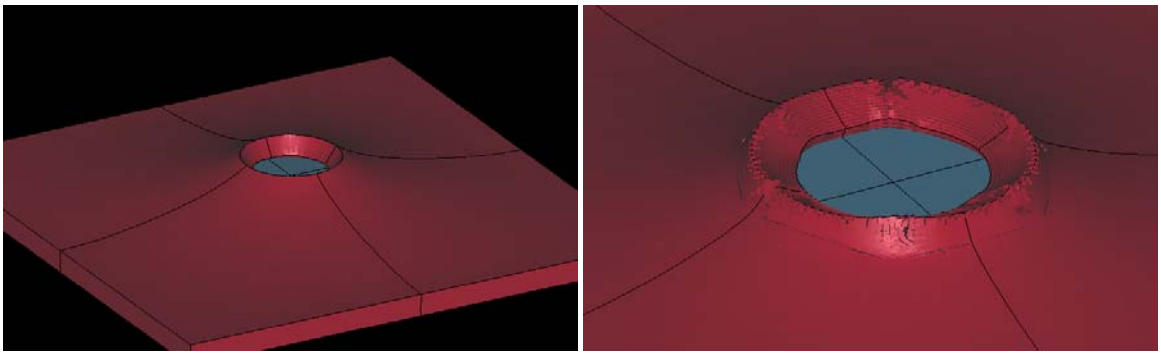

(a) (b)

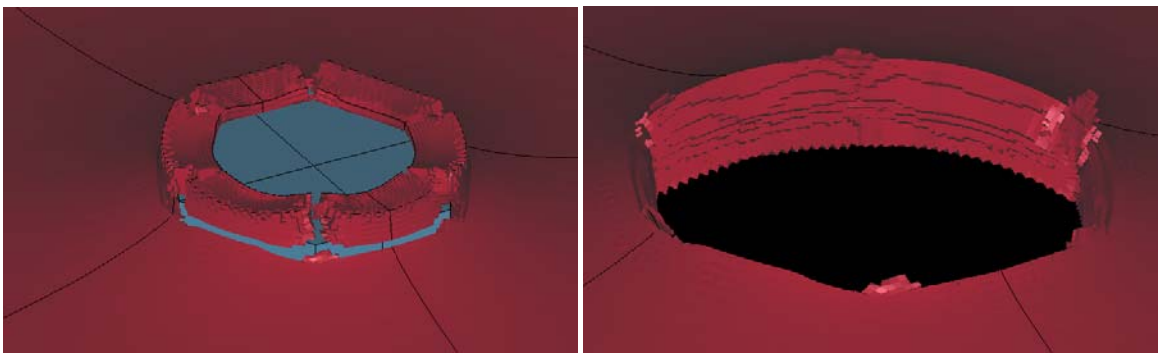

(c) (d)

Figure 9: The failure mechanism for 4 mm plate thickness

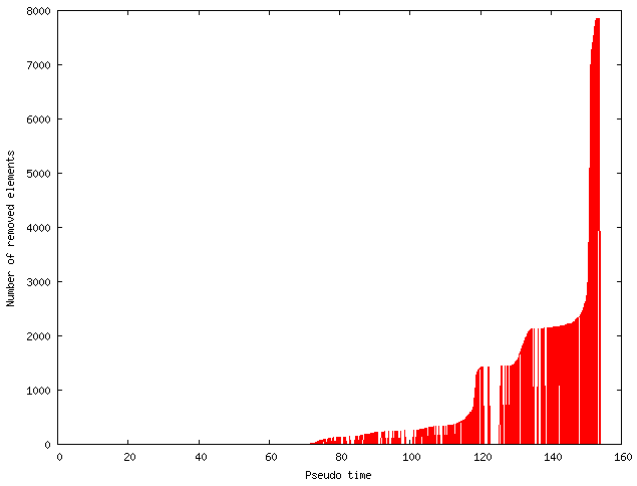

Figure 10: Number of removed elements at a given time

4.2 Load-displacement curves

As in the experiments, beside observing the failure mechanism two main properties have been measured: the applied load on the bolt and the displacement of the bolt. Figure 11 shows one quarter of the ultimate load that is required to pull-out the bolt from the plate determined by the experiments and the analysis. It can be seen that the analysis results are relatively good for 1 and 2 mm plate thicknesses, but for larger plate thicknesses the ultimate forces determined by the analysis are much smaller compared to the experiment results. The explanation for this discrepancy is related to the material plastification and element failure mechanism. Although the element failure mechanism accurately simulates the radially developing fracture, the element failure does become a problem for large plate thicknesses, since in that case a large number of elements are removed from the mesh.

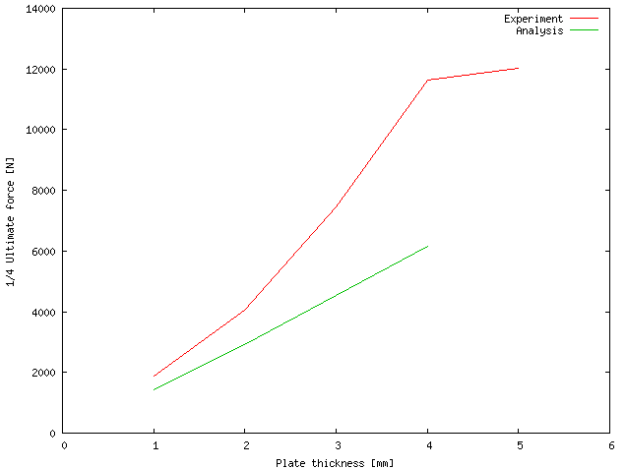

Figure 11: Ultimate load for different plate thicknesses

The load-displacement curve for the 1 mm plate thickness is shown in Figure 12a. The analysis results are adjusted by 0.6 mm which is accounted for the initial slack in the experimental setup. The analysis curve is very similar to the experimental curve except the ultimate value. Figure 12b displays the load-displacement curve for the 4 mm plate thickness. In this case it is obvious that the two curves do not match, although they show similar behaviour with two branches: a steeper, initial line and a second, less steep, non-linear line.

It is also important to observe the energy of the whole system shown in Figure 13a. The figure shows the internal, the kinetic, the hourglass, the eroded internal and the kinetic energy, where the eroded internal and kinetic energies are related to the removed elements. During the analysis the internal energy increases continuously while there is a sudden jump in the kinetic energy when the bolt comes free of the plate. Another observation is that although the hourglass energy stays relatively low but it causes visible discrepancy in the analysis as it can be seen in Figure 9d at the bottom edge of the hole, where the contour of the elements forms a zigzag shape. Finally, the eroded internal energy should be examined considering Figure 13b shows the relation

between the eroded internal energy and the internal energy in percentage. The figure can be related to Figure 10 where the number of removed elements is shown. It can be seen that the removal of elements disturbs the energy balance of the system quite substantially and probably this is one of the main reasons why the values measured in the experiment and in the analysis do not match.

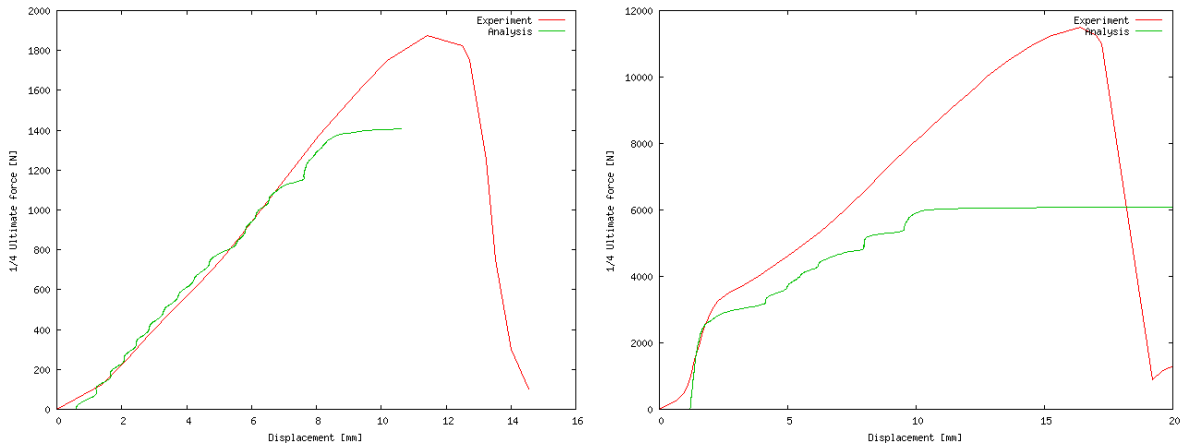

(a) (b)

Figure 12: Load-displacement curve for (a) 1 mm and (b) 4 mm plate thickness

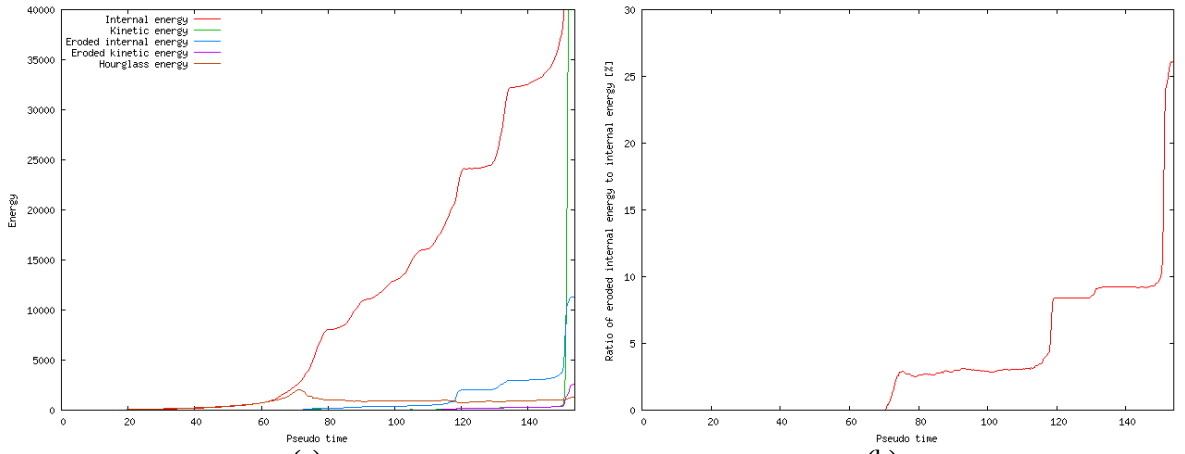

(a) (b)

Figure 13: Energy balance of the system and the ratio of the eroded internal energy to the internal energy for 4mm plate thickness

5. CONCLUSIONS

A finite element simulation of the pull-out experiment has been presented in this paper. Although some promising results have been achieved (cf. e.g. the failure mechanism is properly simulated), the load-displacement values do not correspond to the values measured in the experiments. These results show that some further considerations are necessary to simulate this phenomenon properly. Probably the two of the most important features of any further analysis have to be a correct model for material and material plastification and a better method for fraction simulation.

ACKNOWLEDGEMENT

The project has been sponsored by the European Commission project entitled ”New Materials, Adaptive Systems and their Nonlinearities. Modelling, Control and Numerical Simulation”, contract number: HPRN-CT-2002-00.

REFERENCES

[1] Baniotopoulos, C.C. (2003) (ed.), *Connections in Metal Structures*, Ziti Editions, Thessaloniki.
[2] LS-DYNA user manual, Livermore Software Technology Corporation, 2003

INTRODUCING THE ROTATIONAL FIELD DECOMPOSTION IN THE ANALYSIS OF THE BEHAVIOUR OF SHELL PROBLEMS

Demetres Briassoulis

Department of Agricultural Engineering
Agricultural University of Athens
Iera Odos 75, Athens, 11855, Greece
e-mail: briassou@aua.gr, web page: http://www.aua.gr

Keywords: Shell Elements, Finite Elements, Asymptotic Behaviour, Benchmark Tests.

Abstract. *An innovative numerical approach is developed in the present paper for the analysis of the asymptotic shell behaviour based on the physical decomposition of the finite element rotational field, allowing for an insight to be gained into the mechanisms underlying the asymptotic behaviour of shell problems. The way a finite shell element model, and so a shell structure, activates the various load carrying mechanisms in membrane-dominated, bending-dominated and mixed mode shell problems may be investigated and understood in this way. The asymptotic behaviour of selected bending and membrane dominated classical benchmark shell problems is analysed by means of the rotational field decomposition approach.*

1 INTRODUCTION

Research work on the asymptotic behaviour of shell elements has been rather limited and it is only very recently that research work has been directed and focused systematically on this question. D.Chapelle and K.J.Bathe [1,2] brought forward fundamental considerations regarding the finite element analysis of shell structures. A strict 'dual set' of two alternative analytically derived limiting cases describing the asymptotic behaviour of a typical shell problem with respect to its characterisation as been either a bending inhibited or a non-inhibited problem was derived [1]. A set of limit tests, considered to be 'clean' with respect to the identification of the asymptotic behaviour of shell elements as been either bending inhibited or non inhibited test problems, complying in that way with the dual asymptotic behaviour of shell elements presumption of [1], were proposed [1,3,4]. Following the fundamental considerations raised in the above-mentioned works, the asymptotic behaviour of several benchmark shell problems was investigated in [,5,6]. Analytical solutions based on Flugge's theory [7] were derived [5,6] to investigate the asymptotic behaviour of selected classical benchmark shell problems and some of the new limit benchmark shell problems proposed in [4]. The so derived analytical solutions were confirmed with extensive finite element analyses and in the case of the new limit tests, with the corresponding theoretical solutions obtained symbolically earlier [8] using the Reissner-Mindlin shell model. The Reformulated Four-Node Shell element (acronym: RFNS element) [9] was employed in the corresponding numerical analyses. The work of [5] and [6] has shown that the shell problems do not exclusively fall in either one of the two distinct categories, that is of a bending inhibited or a bending non-inhibited category. The asymptotic behaviour of shell problems may very well span the whole range between the bending inhibited and the non-inhibited limit problems by developing the mixed-mode behaviour, in various forms.

In a recent work [10], a simple analytical approach for defining the asymptotic behaviour of shell elements was proposed. The proposed approach was implemented in defining the asymptotic deformation modes of selected benchmark problems suitable for the evaluation of the asymptotic behaviour of shell elements. It was shown that the various modes encountered with the asymptotic analysis of these shell problems are clearly defined in a very simple way leading to explicit expressions for the corresponding characteristic asymptotes, which may be used as benchmark characteristic asymptotes of the corresponding benchmark shell problems.

An innovative numerical approach is developed in the present paper for the analysis of the asymptotic behaviour of shells based on the physical decomposition of the finite element rotational field.

2 THE RFNS ELEMENT

The formulation of the reformulated C^o shell element, presented in detail in ref [9], is briefly reviewed in this section. The performance of the RFNS element in linear elastic analysis of shell problems has been already examined in depth and its excellent behaviour has been verified against a wide range of the most well known severe benchmark tests for shell elements [9] as well as against several critical benchmark asymptotic problems [2,,5,10]. An analogous high performance-nonlinear formulation of the RFNS element was developed in [11].

The linear elastic formulation of [9] for the reformulated C° plate/shell element, built at the finite element

assembly level, is based on partitioning the finite element assembly equations of equilibrium as follows:

$$\left\{\begin{bmatrix}\mathbf{0} & \mathbf{0}\\ \mathbf{0} & \mathbf{Kb}_{aa}\end{bmatrix}+\begin{bmatrix}\mathbf{Ks}_{uu} & \mathbf{Ks}_{ua}\\ \mathbf{Ks}_{ua}^{T} & \mathbf{Ks}_{aa}\end{bmatrix}\right\}\begin{pmatrix}\mathbf{u}\\ \mathbf{a}\end{pmatrix}=\begin{pmatrix}\mathbf{f}\\ \mathbf{m}\end{pmatrix} \tag{1}$$

In this formulation, the deformations vector $\mathbf{v}=(\mathbf{u},\mathbf{a})^T$ is expressed in terms of the transverse and membrane displacements $\mathbf{u}=(\mathbf{u}_i)T$ and the rotations $\mathbf{a}=(\boldsymbol{\alpha},\boldsymbol{\beta})^T$. The load vector $\mathbf{P}=(\mathbf{f},\mathbf{m})^T$ is expressed in terms of the transverse/in-plane load vector **f** and the moments vector **m** whereas the finite element assembly bending and shear/membrane stiffness matrices **Kb** and **Ks** are partitioned accordingly. The finite element assembly solution can be obtained by solving this system in two steps for the corresponding equilibrium equations:

$$\begin{aligned}&\mathbf{Ks}_{uu}\mathbf{u}=\mathbf{f}-\mathbf{Ks}_{ua}\mathbf{a}\\ &\mathbf{Kb}_{aa}\mathbf{a}+\underline{(\mathbf{Ks}_{aa}-\mathbf{Ks}_{ua}^{T}\mathbf{Ks}_{uu}^{-1}\mathbf{Ks}_{ua})\mathbf{a}}=\underline{\mathbf{m}-\mathbf{Ks}_{ua}^{T}\mathbf{Ks}_{uu}^{-1}\mathbf{f}}\end{aligned} \tag{2}$$

or, rewriting the underlined terms of the second equation of the system of Eqs. (2) in a compact form:

$$\mathbf{Kb}_{aa}\mathbf{a}+\mathbf{Kbs}\,\mathbf{a}=\mathbf{mm} \tag{3}$$

Where **mm** stands for an equivalent applied moment vector, in accordance with the static moment equilibrium requirements of the system. Of special importance in the course of the formulation of [9], but also of the present analysis, is the term **Kbs a** . As it is apparent from Eq (3) this term stands for the potential contribution of shear-membrane strain to the total flexural strain energy of the system. As shown in detail in [9] any potential shear locking mechanism would come from the **Kbs** transverse shear/membrane stiffness matrices-assemblage. However, for a locking-free shell or plate element the **Kbs** transverse shear/membrane stiffness matrices-assemblage offers essential non-spurious contribution to the bending mode of deformation. According to the analysis of ref. [12] the non-spurious contribution of the finite element assembly transverse shear/membrane stiffness **Kbs** to the flexural strain energy of the shell system is vital and includes, in general, the contribution of the tangential shear strain components γ^{sk} and the complementary participation of the membrane strain components ε_{ij} of **Kbs** to the activation of an internal moment redistribution mechanism.

The translations-bending coupling effect, which is very important for warped element configurations, is taken care of in the formulation of [9], through appropriate augmentation of the **Ks** stiffness submatrices. Then, the RFNS formulation based on the special construction of the non-spurious **Kbs** stiffness matrix enables, as a first step, the calculation of a "spurious strain and kinematic mechanisms free" rotations field **a** for the finite element assembly solution by solving the second equation of the set of Eqs. (2) [9]. The bending ($\mathbf{u}^b$) and the shear/membrane ($\mathbf{u}^s$) displacement vectors may be calculated subsequently through the first equation of the system Eqs. (2). Accordingly, the system equations (2) of the linear formulation of the RFNS element become:

$$\begin{aligned}&\mathbf{a}=[\mathbf{Kb}_{aa}(e_{ij}^{b})+\mathbf{Kbs}(e_{ij}^{m},\gamma_s^{k},\zeta)]^{-1}\ (\mathbf{m}-\mathbf{Ks}_{ua}(e_{ij}^{m},\gamma_s^{k},\zeta)^{T}\ \mathbf{Ks}_{uu}(e_{ij}^{m},\gamma_s^{k},\zeta)^{-1}\ \mathbf{f})\\ &\mathbf{u}=\mathbf{Ks}_{uu}(e_{ij}^{m},\gamma_{ij})^{-1}\ \mathbf{f}-\mathbf{Ks}_{uu}(e_{ij}^{m},\gamma_s^{k},\zeta)^{-1}\ \mathbf{Ks}_{ua}(e_{ij}^{m},\gamma_s^{k},\zeta)\ \mathbf{a}=\mathbf{u}^s+\mathbf{u}^b\\ &\mathbf{v}_s=(\mathbf{u}^s,\mathbf{0})^T,\qquad \mathbf{v}_b=(\mathbf{u}^b,\mathbf{a})^T\end{aligned} \tag{4}$$

Where all $\mathbf{Ks}_{kl}(e_{ij}^{m},\gamma_s^{k},\zeta)$ submatrices of the finite element assembly shear/membrane stiffness matrix **Ks** are composed of a) the corresponding $\mathbf{Ks}_{kl}(e_{ij}^{m},\gamma_s^{k})$ submatrices (built with the participation of the membrane strain components e_{xx}, e_{yy} and γ_{xy} calculated at the full integration points and the tangential edge shear strain components γ_s^{k} calculated at the element mid sides) and b) augmented with the corresponding thickness dependent membrane-bending coupling $\mathbf{Ks}_{kl}(\zeta)$ stiffness submatrices (notation ζ in the parenthesis refers to the augmentation of the corresponding matrices with the thickness dependent membrane strain-deformation terms part of the membrane strain-deformation matrix [9]).The displacement vector $\mathbf{u}^s$ contributes to the shear/extensional deformation field $\mathbf{v}_s=(\mathbf{u}^s,\mathbf{0})^T$ while the displacement vector $\mathbf{u}^b$ and the rotations vector **a** constitute the bending deformation field $\mathbf{v}_b=(\mathbf{u}^b,\mathbf{a})^T$. The remaining sub-matrix of the finite element assembly transverse shear/membrane stiffness matrix $\mathbf{Ks}_{uu}$ participating in Eqs. (4), that is $\mathbf{u}_s=\mathbf{Ks}_{uu}^{-1}\mathbf{f}$ is simply associated with the pure shear/extensional deformation field $\mathbf{v}_s=(\mathbf{u}^s,\mathbf{0})^T$. This particular $\mathbf{Ks}_{uu}$ stiffness sub-matrix may be either composed of the conventional transverse shear strain components calculated at the full integration points or, in order to render the formulation simpler, the $\mathbf{Ks}_{uu}(e_{ij}^{m},\gamma_s^{k},\zeta)$ submatrix can be used.

3 THE ROTATIONS COMPONENTS

In the present work, it is proposed that the rotations field $\mathbf{a}=(\boldsymbol{\alpha},\boldsymbol{\beta})T$ in Eq. (3) is decomposed into two physical components as follows:

$$\mathbf{a}=\mathbf{a}_b+\mathbf{a}_s \tag{5}$$

a) the component $\mathbf{a}_b$ represents the pure bending behaviour of the shell, resulting from the activation of the bending stiffness term $\mathbf{Kb}_{aa}$ of Eq (3) in directly carrying part of the equivalent applied static moment vector **mm** (a part that may be significant or not, depending on the problem)**;**

b) the rotations field component $\mathbf{a}_s$ representing the membrane-flexural behaviour of the shell, in-plate twist and beam-plate on elastic foundation actions, resulting from the activation of the **Kbs** transverse shear/membrane stiffness in directly carrying the remaining part of the equivalent applied moment vector **mm**.

The proposed decomposition of the rotations field is based on two requirements:

A. The two components of the rotations field should satisfy the external static equilibrium condition under the equivalent applied moment vector **mm** according to Eq (3) as follows:

$$\mathbf{Kb}_{aa}\mathbf{a}_b + \mathbf{Kbs}\,\mathbf{a}_s = \mathbf{mm} \tag{6}$$

This relation represents an internal moment redistribution mechanism where the two stiffness components $\mathbf{Kb}_{aa}$ and **Kbs** contributing to the bending equilibrium of the system take their own share in directly carrying the external equivalent moment vector **mm**, in a proportion that is defined internally through the principle of minimisation of the total energy of the system and depends on the shell problem under consideration. In a few cases (e.g. beam problems) characterised by an inactive internal moment redistribution mechanism, the load is assumed totally by the pure bending mechanism with the rotations field component, $\mathbf{a}_s$, being zero. In cases characterised by the activation of the internal moment redistribution mechanism (typical shell problems), this internal moment redistribution mechanism is triggered mainly by the membrane flexural behaviour of the shell and/or other mechanisms like the beam-plate on elastic foundation action. In such cases, the rotations field component $\mathbf{a}_s$ is nonzero and its contribution to the moment equilibrium system is vital even if $\mathbf{a}_s$ is of a relative low magnitude compared to the magnitude of the rotations component $\mathbf{a}_b$. In a typical shell problem, the pure bending rotations component $\mathbf{a}_b$, when interacting with the $\mathbf{Kb}_{aa}$ bending stiffness matrix, activates the pure bending load carrying mechanism to carry part of the applied load; likewise, the rotations field component $\mathbf{a}_s$ when interacting with the **Kbs** transverse shear/membrane stiffness matrix activates the membrane flexural and/or other membrane/transverse shear strain related mechanisms in carrying another part of the applied load.

B. In satisfying Eq. (6), the two components of the rotational filed $\mathbf{a}_b$ and $\mathbf{a}_s$ should also satisfy Eqs. (5) and (3). The simultaneous satisfaction of Eqs. (5) and (3) requires that the two components of the rotations field $\mathbf{a}_b$ and $\mathbf{a}_s$ should also satisfy an internal moment coupling condition. The internal moment coupling mechanism is activated in specific problems where the cross-interaction of the two components of the rotational filed $\mathbf{a}_b$ and $\mathbf{a}_s$ with the two stiffness components **Kbs** and $\mathbf{Kb}_{aa}$, respectively, is non-zero (e.g. development of boundary layer effects). The part of the moment load transferred under this coupling mechanism from one load carrying mechanism to the other one, through the interactions of the corresponding moment vectors of the internal moment redistribution mechanism **Kbs** $\mathbf{a}_b$ and $\mathbf{Kb}_{aa}$ $\mathbf{a}_s$, should be balanced. This requirement is met by imposing the condition that the internal moment coupling mechanism yields always a zero moment vector:

$$\mathbf{Kbs}\,\mathbf{a}_b + \mathbf{Kb}_{aa}\mathbf{a}_s = \mathbf{0} \tag{7}$$

Thus, the pure bending rotations component $\mathbf{a}_b$ when interacting with the **Kbs** transverse shear/membrane stiffness matrices-assemblage may produce either: a) a zero internal coupling moment vector or b) a non-zero coupling internal moment vector **Kbs** $\mathbf{a}_b$ that is counter-balanced by an equal and opposite internal coupling moment vector developed by the rotations component as interacting respectively with the bending stiffness $\mathbf{Kb}_{aa}$ (e.g. through the transfer-coupling of the so-generated moment vector from the membrane-flexural to the bending load carrying mechanism and vice-versa: **Kbs** $\mathbf{a}_b$=-$\mathbf{Kb}_{aa}$ $\mathbf{a}_s$). In that way, the static moment equilibrium system described by Eq. (6) is not affected, as the resulting external moment vector of Eq. (7) is zero.

These two conditions can be combined in the following linear system that can be solved for the two components of the rotations field:

$$\begin{bmatrix} \mathbf{Kb}_{aa} & \mathbf{Kbs} \\ \mathbf{Kbs} & \mathbf{Kb}_{aa} \end{bmatrix} \begin{pmatrix} \mathbf{a}_b \\ \mathbf{a}_s \end{pmatrix} = \begin{pmatrix} \mathbf{mm} \\ \mathbf{0} \end{pmatrix} \tag{8}$$

The decomposition of the rotations field **a** into the two physically defined discrete rotational entities $\mathbf{a}_b$ and $\mathbf{a}_s$ can be shown to be important for the analysis of the behaviour of finite element shell models in general, but it is especially important for the asymptotic analysis of a shell model in the limit of the shell thickness going to zero. The nature of the load carrying mechanisms, the way a bending or a membrane mode of deformation develops or a mixed deformation mode dominates in various shell problems can be identified and analysed by means of the rotational field decomposition of some typical benchmark shell problems. The characteristic categories of bending and membrane dominated shell problems are investigated in the following sections.

3 ROTATIONAL DECOMPOSITION OF CLASSICAL BENCHMARK SHELL PROBLEMS

3.1 Bending dominated problems

Pure bending dominated problem with internal moment redistributions: The simplest case, a pure bending mode of deformation can be identified by the fact that the Euclidean vector norm of the component $\mathbf{a}_s$ is of a relatively insignificant magnitude, as compared to the magnitude of the Euclidean vector norm of the component $\mathbf{a}_b$, tending to zero in the limit of the thickness going to zero. This is also reflected in the limit of the Euclidean vector norms of the internal coupling moments $\mathbf{Kb}_{aa}\ \mathbf{a}_s$ and $\mathbf{Kbs}\ \mathbf{a}_b$ developed under the $\mathbf{a}_s$ and $\mathbf{a}_b$ fields respectively, and tending to zero. The pure bending dominated problems may be described by the fact that the bending stiffness matrix $\mathbf{Kb}_{aa}$ is responsible for carrying the applied equivalent moment **mm**:

$$\begin{aligned} &\lim_{t\to 0}\left\|\mathbf{a_s}\right\|_2 = \mathbf{0} \\ &\lim_{t\to 0}\left\|\mathbf{Kb}_{aa}\ \mathbf{a_s}\right\|_2 = \lim_{t\to 0}\left\|\mathbf{Kbs\ a_b}\right\|_2 = \lim_{t\to 0}\left\|\mathbf{Kbs\ a_s}\right\|_2 = \mathbf{0} \\ &\mathbf{Kb}_{aa}\mathbf{a_b} = \mathbf{mm} \end{aligned} \tag{9}$$

A typical example of pure bending dominated problems is the beam bending behaviour. As an illustrative example, a cantilever beam under end load is analysed, with the beam being simulated by RFNS shell elements. The rotations components suggest that in this case $\lim_{t\to 0}\left\|\mathbf{a}\right\|_2 - \lim_{t\to 0}\left\|\mathbf{a_b}\right\|_2 = \mathbf{0}$. The displacements and stress resultants subsequently develop under the rotational field $\mathbf{a} = \mathbf{a}_b$ following Eqs. (4).

Bending dominated problems with internal moment redistribution due to in-plane twisting stiffness: In the vast majority of plate and shell problems, both rotational components contribute to the moment equilibrium of the system described by Eq. (8). However, the relative magnitude of the two rotations components may not reflect in an analogous way their corresponding contributions to the external moment equilibrium and the internal bending moments redistribution mechanisms. The contribution of the in-plane twisting stiffness of the plate/shell through the activation of the moment redistribution mechanism (triggered by the tangential edge shear strain components γ_s^k of the **Kbs** stiffness), results in the following moment equilibrium system:

$$\begin{aligned} &\lim_{t\to 0}\left\|\mathbf{a_s}\right\|_2 \neq \mathbf{0}\ , \quad \lim_{t\to 0}\frac{\left\|\mathbf{a_s}\right\|_2}{\left\|\mathbf{a_b}\right\|_2} = \mathbf{0} \\ &\lim_{t\to 0}\left\|\mathbf{Kbs\ a_s}\right\|_2 \neq \mathbf{0}\ , \quad \mathbf{Kb}_{aa}\mathbf{a_b} = \mathbf{mm\text{-}Kbs\ a_s} \Rightarrow \text{moment redistribution} \\ &\mathbf{Kbs\ a_b} = -\mathbf{Kb}_{aa}\ \mathbf{a_s}\ ,\ \lim_{t\to 0}\left\|\mathbf{Kbs\ a_b}\right\|_2 = \lim_{t\to 0}\left\|\mathbf{Kb}_{aa}\ \mathbf{a_s}\right\|_2 = \mathbf{0} \\ &\begin{bmatrix} \mathbf{Kb}_{aa} & \mathbf{Kbs} \\ \mathbf{Kbs} & \mathbf{Kb}_{aa} \end{bmatrix}\begin{pmatrix} \mathbf{a}_b \\ \mathbf{a}_s \end{pmatrix} = \begin{pmatrix} \mathbf{Kb}_{aa}\mathbf{a_b} + \mathbf{Kbs\ a_s} \\ \mathbf{Kbs\ a_b} + \mathbf{Kb}_{aa}\ \mathbf{a_s} \end{pmatrix} = \begin{pmatrix} \mathbf{mm} \\ \mathbf{0} \end{pmatrix} \end{aligned} \tag{10}$$

Typical examples of bending dominated problems with internal moment redistribution due to the activation of the in-plane twisting stiffness are plate-bending problems. In the following illustrative example a fixed square plate under uniform load is analysed by an 8x8 RFNS shell elements model. The rotations components suggest that the dominant deformation mode is due to the rotational field component $\mathbf{a}_b$. In this case, despite the low magnitude of the rotational component $\mathbf{a}_s$, the internal moment $\mathbf{Kbs}\ \mathbf{a}_s$ is shown to remain thickness independent and be of the same order of magnitude as that of the equivalent applied moment vector **mm**. This behaviour may be explained by calculating the best-fit power functions of the curves of the Euclidean vector norms of $\mathbf{a}_s$ and $\mathbf{a}_b$. Then, the Euclidean vector norms of the rotational components $\mathbf{a}_s$ and $\mathbf{a}_b$ are found to be power functions of $(t/L)^{-1}$ and $(t/L)^{-3}$ respectively:

$$\left\|\mathbf{a}_s\right\|_2 = 2\text{E-}09(t/L)^{-1}, \qquad \left\|\mathbf{a}_b\right\|_2 = 2\text{E-}10(t/L)^{-3} \tag{11}$$

As a result of this differentiation in the rate of the thickness dependence of the relative magnitudes of the rotational field components, and given that the stiffness sub-matrices $\mathbf{Kb}_{aa}$ and **Kbs** are known to be functions of $(t/L)^3$ and $(t/L)^1$ respectively, the moment redistribution vector $\mathbf{Kbs\ a}_s$ remains constant as the plate thickness is reduced. The moment redistribution vector $\mathbf{Kbs\ a}_s$ assumes part of the equivalent moment load **mm** while it redistributes the equivalent applied moment to be assumed by the bending sub-stiffness $\mathbf{Kb}_{aa}$ of the system from **mm** to $\mathbf{mm\text{-}\ Kbs\ a}_s$. The Euclidean vector norms of the equal in magnitude and opposite (cancel each other) internal moment coupling vectors $\mathbf{Kb}_{aa}\ \mathbf{a}_s$ and $\mathbf{Kbs\ a}_b$, developed under the $\mathbf{a}_s$ and $\mathbf{a}_b$ fields respectively, tend to zero as power functions of $(t/L)^2$ in the limit of the thickness ratio going to zero.

Bending dominated problems with internal moment redistribution due to the activation of the beam-on-elastic foundation mechanism: In most cases of shell problems, both rotational components contribute to the moment equilibrium of the system described by Eq. (8) mainly as a result of the activation of the 'membrane-

flexural' and the 'beam on elastic foundation' mechanisms [5,6,**Error! Bookmark not defined.**,9]. The cylindrical shell with free ends under various loading conditions represents a typical bending dominating shell problem. As shown analytically in [5,6], the equivalent ring bending behaviour dominates the cylindrical shell behaviour in the circumferential direction, while the beam on elastic foundation action simulates adequately the free boundary layer effects on the rotations field. The ring-bending load carrying mechanism is activated through the equivalent moment vector due to the bending stiffness sub-matrix $\mathbf{Kb}_{aa}\ \mathbf{a}_b$. On the other hand, the equivalent beam on elastic foundation mechanism (responsible for the boundary layer effects in these cases) is activated through a strong interaction between the $\mathbf{Kbs}\ \mathbf{a}_s$ and the $\mathbf{Kb}_{aa}\ \mathbf{a}_b$ equivalent moment vectors, along with the participation of the $\mathbf{Kb}_{aa}\ \mathbf{a}_s$ and $\mathbf{Kbs}\ \mathbf{a}_b$ internal coupling moment vectors within the boundary zone. In such cases, the strong boundary layer effects are associated with non-zero individual contributions of the internal coupling moment vectors $\mathbf{Kb}_{aa}\ \mathbf{a}_s$ and $\mathbf{Kbs}\ \mathbf{a}_b$. These two vectors remain equal and opposite in sign, cancelling each other and not directly contributing to the load carrying mechanism, but rather to an internal coupling moment redistribution mechanism. As a result of the activation of the beam on elastic foundation mechanism (e.g. associated with strong boundary layer effects) and the active involvement of all equivalent moment vectors of Eq. (8), the thickness ratio dependence of the rotations components is not simple. Accordingly, the shell bending dominated problem may be described in terms of the rotational field as follows:

$$
\begin{aligned}
&\lim_{t\to 0}\left\|\mathbf{a_s}\right\|_2 \neq \mathbf{0}\ , \quad \lim_{t\to 0}\frac{\left\|\mathbf{a_s}\right\|_2}{\left\|\mathbf{a_b}\right\|_2} = \mathbf{0}\\
&\lim_{t\to 0}\left\|\mathbf{Kbs}\,\mathbf{a_s}\right\|_2 \neq \mathbf{0}\ , \quad \mathbf{Kb}_{aa}\mathbf{a_b} = \mathbf{mm}\text{-}\mathbf{Kbs}\,\mathbf{a_s} \Rightarrow \text{moment redistribution}\\
&\mathbf{Kbs}\,\mathbf{a_b} = -\mathbf{Kb}_{aa}\ \mathbf{a_s}\ ,\ \lim_{t\to 0}\left\|\mathbf{Kbs}\,\mathbf{a_b}\right\|_2 = \lim_{t\to 0}\left\|\mathbf{Kb}_{aa}\ \mathbf{a_s}\right\|_2 \neq \mathbf{0}\\
&\begin{bmatrix}\mathbf{Kb}_{aa} & \mathbf{Kbs}\\ \mathbf{Kbs} & \mathbf{Kb}_{aa}\end{bmatrix}\begin{pmatrix}\mathbf{a}_b\\ \mathbf{a}_s\end{pmatrix} = \begin{pmatrix}\mathbf{Kb}_{aa}\mathbf{a_b} + \mathbf{Kbs}\,\mathbf{a_s}\\ \mathbf{Kbs}\,\mathbf{a_b} + \mathbf{Kb}_{aa}\ \mathbf{a_s}\end{pmatrix} = \begin{pmatrix}\mathbf{mm}\\ \mathbf{0}\end{pmatrix}
\end{aligned}
\qquad (12)
$$

Three critical, in terms of boundary conditions, cases of a cylindrical shell were proposed [4] and analysed [4,6] as representing three distinct benchmark limit tests for shell elements, for bending dominated, membrane dominated and mixed mode problems. The cylindrical shell with a half-length L/2 equal to the radius r (measured to the middle surface) and a varying thickness ratio t/r, is loaded by a normal periodic pressure distribution that acts on the outer surface of the shell, and varies angularly as:

$$p = p_o \cos 2\theta \qquad (13)$$

The case of the cylindrical shell being free along its boundaries under the load of Eq. (13) represents a strong bending-dominated test problem. A 25x35 RFNS shell elements model was used to analyse a symmetric-antisymmetric 1/16 part the cylinder. The rotations components in the circumferential direction, plotted in Figure 1, suggest a dominant bending effect described by the rotational field component $\mathbf{a}_b$. In the meridional direction, both components, being of a much lower magnitude, contribute to the free end effects Figure 2). The rotational components a_b and a_s developing within the boundary zone are strongly dependent on the thickness ratio and they interact strongly with each other in composing the strong boundary layer effects for the rotational filed a Figure 2). Referring to the system of Eq. (12), the ring-type shell bending behaviour is reflected in the relative magnitude of the $\mathbf{Kb}_{aa}\ \mathbf{a}_b$ Euclidean vector norm. However, the free boundary layer effects, represented by the rotational component $\mathbf{a}_s$, also result in a rather significant internal moment redistribution vector $\mathbf{Kbs}\ \mathbf{a}_s$ shown to be of the same order of magnitude as that of the equivalent applied moment vector **mm**.

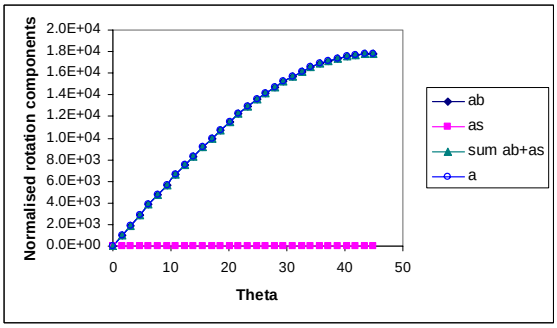

Figure 1: Rotations components plotted in the circumferential direction along the middle line of the shell, directed normal to the corresponding line; normalised with respect to $p_o/E(t/r)^2$ in the case of a cylindrical shell; free ends under the load of Eq. (13) (t/L= 0.0001)

The best-fit power functions of the curves of the Euclidean vector norms of $\mathbf{a}_s$ and $\mathbf{a}_b$ suggest that the

Euclidean vector norms of the rotational components $\mathbf{a}_s$ and $\mathbf{a}_b$ are power functions of $(t/L)^{-2.5}$ and $(t/L)^{-3}$:

$$\|\mathbf{a}_s\|_2 = 2E\text{-}06(t/L)^{-2.5}, \qquad \|\mathbf{a}_b\|_2 = 3E\text{-}05(t/L)^{-3.0} \tag{14}$$

The behaviour of the $\mathbf{a}_s$ rotational component in this case (i.e. $\mathbf{a}_s$ is not a function of t/L^{-1}) is explained by the boundary layer effects. The boundary layer effects develop in this case as a result of the imposition of the free boundary conditions, requiring that the stress resultants related to the Poison's effect are cancelled out (e.g. imposition of a moment equal to $-\nu\mathbf{M}_x$ to counterbalance the corresponding moment $\nu\mathbf{M}_x$; refer to the analysis of [6]). This activates the beam-on-elastic foundation dominant load carrying mechanism in the meridional direction within the free boundary zone (refer to Figure 3), responsible for the corresponding moment redistribution mechanism **Kbs** $\mathbf{a}_s$. The beam-on-elastic foundation mechanism is also reflected in the variation of the bending moment acting perpendicular to the meridional direction. This mechanism triggers the hoop strain of the **Kbs**$(e_{ij}^m, \gamma_s^k, \zeta)$ stiffness sub-matrix contribution, acting as elastic foundation [**Error! Bookmark not defined.**,6].

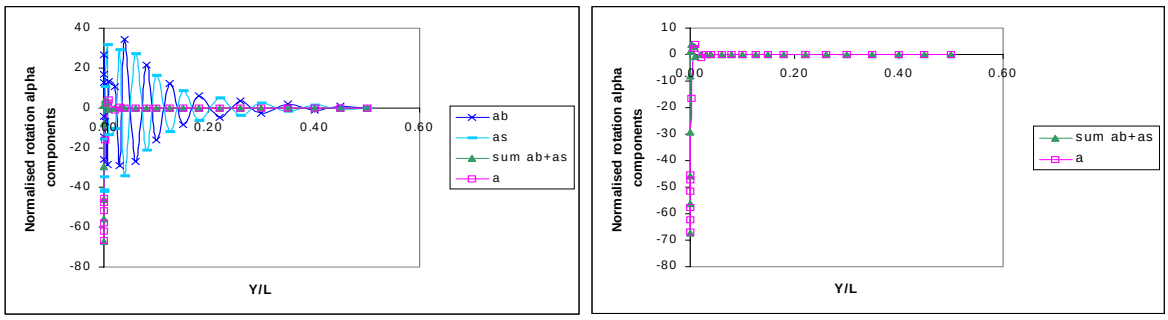

(a) (b)

Figure 2: Rotations components plotted along the crown line of the shell, directed normal to the corresponding line; normalised with respect to $p_o/E(t/r)^2$ in the case of a cylindrical shell with free ends under the load of Eq. (13) (t/L= 0.0001)

The Euclidean norm of the moment redistribution vector **Kbs** $\mathbf{a}_s$ remains practically constant as the shell thickness is reduced. In general terms, the **Kbs** $\mathbf{a}_s$ vector length over the model domain does not change significantly with the shell thickness, resulting in an analogous moment redistribution of the equivalent applied moment **mm.** In addition, the interaction of some of the higher order components of the rotational field $\mathbf{a}_s$ and of the lower order components of the rotational field $\mathbf{a}_b$ with the stiffness sub-matrices $\mathbf{Kb}_{aa}$ and **Kbs**, respectively, are responsible for retaining the Euclidean vector norms of $\mathbf{Kb}_{aa}$ $\mathbf{a}_s$ and **Kbs** $\mathbf{a}_b$ constant (slightly depending on the shell thickness, in a way analogous to that of the **Kbs** $\mathbf{a}_s$ vector, as shown in , as the two norms also depend on the boundary layer effects and the mesh refinement). The internal coupling moment vectors $\mathbf{Kb}_{aa}$ $\mathbf{a}_s$ and **Kbs** $\mathbf{a}_b$ are equal and opposite (they cancel each other) developing within the boundary layer zone were the boundary layers effects of the rotational fields a_s and a_b develop Figure 2).

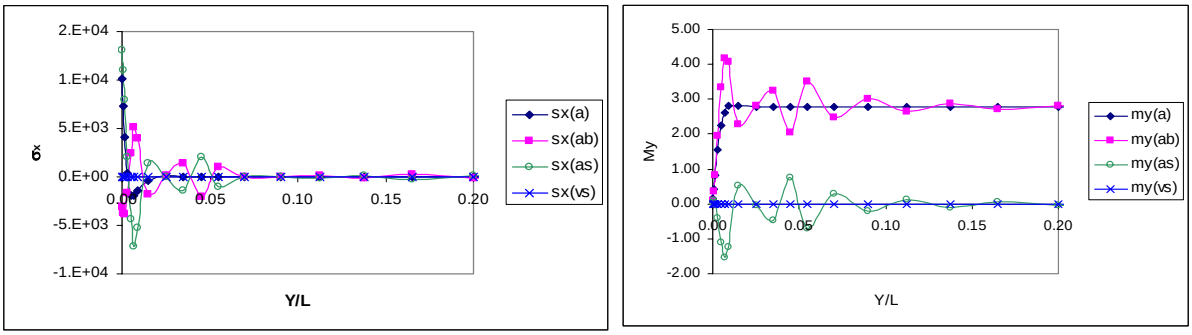

Figure 3: Hoop stress resultants and bending moment perpendicular to the meridional direction developing along the crown line within the boundary zone of the cylindrical shell with free ends under the load of Eq. (13).

3.2 Membrane dominated problems

Membrane dominated problems with internal moment redistribution due to the activation of flexural membrane mechanism: The case of the cylindrical shell being fixed along its boundaries under the load of Eq. (13) represents a clear membrane-dominated test problem. An analytical solution of the asymptotic behaviour of this problem was derived in [6], confirmed with a detailed numerical analysis. A 25X35 RFNS shell elements model was used to simulate 1/16 part of the cylinder. In the case of membrane dominated shell problems the contribution of the rotational field $\mathbf{a}_s$ to the moment equilibrium of the system described by Eq. (8) is significant, as a result of the activation of the membrane flexural load carrying mechanism [5,6,**Error! Bookmark not defined.**,9,**Error!**

Bookmark not defined.]. In these cases the membrane flexural mechanism is activated through a constant equivalent moment vector **Kbs** $\mathbf{a}_s$ that counterbalances almost completely the equivalent applied moment vector **mm** while the Euclidean norms of the equivalent moment vectors **Kb**$_{aa}$ $\mathbf{a}_b$, **Kb**$_{aa}$ $\mathbf{a}_s$ and **Kbs** $\mathbf{a}_b$ remain insignificant and tend to zero in the limit of the shell thickness going to zero. The presence of strong boundary layer effects implies that the rotational field components $\mathbf{a}_b$ and $\mathbf{a}_s$ may be significant within the boundary zone and their thickness ratio dependence be rather complicated. The membrane dominated shell problem may be described as follows:

$$\lim_{t\to 0}\|\mathbf{a_s}\|_2 \neq \mathbf{0}\ , \quad \lim_{t\to 0}\|\mathbf{a_b}\|_2 \neq \mathbf{0}$$
$$\lim_{t\to 0}\|\mathbf{Kbs\,a_s}\|_2 = \mathbf{mm} \neq \mathbf{0}\ , \quad \lim_{t\to 0}\|\mathbf{Kb_{aa}a_b}\|_2 = \mathbf{0} \Rightarrow \text{moment redistribution}$$
$$\mathbf{Kbs\,a_b} = -\mathbf{Kb_{aa}\,a_s}\ , \ \lim_{t\to 0}\|\mathbf{Kbs\,a_b}\|_2 = \lim_{t\to 0}\|\mathbf{Kb_{aa}\,a_s}\|_2 = \mathbf{0} \qquad (15)$$
$$\begin{bmatrix}\mathbf{Kb_{aa}} & \mathbf{Kbs}\\ \mathbf{Kbs} & \mathbf{Kb_{aa}}\end{bmatrix}\begin{pmatrix}\mathbf{a}_b\\ \mathbf{a}_s\end{pmatrix} = \begin{pmatrix}\mathbf{Kb_{aa}a_b} + \mathbf{Kbs\,a_s}\\ \mathbf{Kbs\,a_b} + \mathbf{Kb_{aa}\,a_s}\end{pmatrix} = \begin{pmatrix}\mathbf{mm}\\ \mathbf{0}\end{pmatrix}$$

The rotations components plotted in along the crown line of the shell suggest the development of strong interacting boundary layer effects between the two rotational field components $\mathbf{a}_b$ and $\mathbf{a}_s$. The algebraic sum of the two components, in turn, cancels out their oscillatory coupling interactions and leads to a lower in magnitude total rotational field **a**, the distribution of which clearly reveals the strong boundary layer effects within a narrow boundary zone [6]. The Euclidean vector norms of the rotational components $\mathbf{a}_s$ and $\mathbf{a}_b$ are both found to be power functions of approximately $(t/L^{-1.4})$, strongly affected by the boundary layer effects:

$$\|\mathbf{a}_s\|_2 = 5\text{E-}05(t/L)^{-1.37}, \qquad \|\mathbf{a}_b\|_2 = 2\text{E-}05(t/L)^{-1.44} \qquad (16)$$

However, the function of the rotational components described above mainly reflects the strong boundary layer effects that develop within a zone that becomes extremely narrow as the shell thickness is reduced. As a result, the relative significance of the two rotational components in terms of contributing to the load carrying mechanisms is not analogous to their magnitude (this is because the magnitude of a rotational component may reflect strong boundary layer effects rather than a prevailing load carrying mechanism). The dominance of the membrane flexural shell mechanism on the load carrying mechanism is reflected in the relative magnitude of the **Kbs** $\mathbf{a}_s$ Euclidean vector norm as compared to the norms of the other vectors. The Euclidean vector norm of the **Kbs** $\mathbf{a}_s$ membrane flexural equivalent moment vector remains rather thickness independent and it is equal to the applied moment vector **mm.**

$$\|\mathbf{Kbs\,a_s}\|_2 = \mathbf{mm}, \quad \|\mathbf{Kb_{aa}\,a_b}\|_2 = \|\mathbf{Kbs\,a_b}\|_2 = \|\mathbf{Kb_{aa}\,a_s}\|_2 = 6.18(t/L)^{1.0} \qquad (17)$$

It is interesting to notice that even though the relative magnitude of the rotational field component $\mathbf{a}_b$ is comparable to that of the $\mathbf{a}_s$ component, its contribution to the equivalent moment vectors **Kb**$_{aa}$ $\mathbf{a}_b$ and **Kbs** $\mathbf{a}_b$ is insignificant. The Euclidean vector norms of both vectors tend to zero as linear functions of the shell thickness in the limit of shell thickness going to zero (Eq. (17)). As the corresponding internal moment vectors **Kb**$_{aa}$ $\mathbf{a}_s$ and **Kbs** $\mathbf{a}_b$ are equal and opposite in sign, the Euclidean vector norm of **Kb**$_{aa}$ $\mathbf{a}_s$ also tends to zero as the shell thickness decreases. This behaviour is related to the gradual 'shrinkage' of the corresponding boundary layer zone with the decrease of the shell thickness while the load carrying mechanism remains stable and dominant.

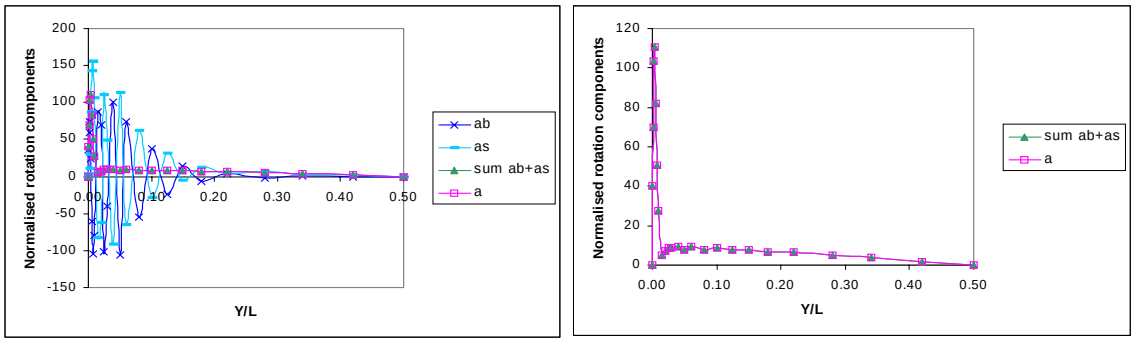

(a) (b)

Figure 4. Rotations components a_s and a_b (a) and total rotational field a (b) plotted along the crown line of the shell, directed normal to the corresponding lines, normalised with respect to $p_o/E(t/r)$ in the case of a cylindrical shell with fixed ends under the load of Eq. (13) (t/L= 0.0001)

The membrane flexural mechanism triggers the meridional strain of the **Kbs**(e_{ij}^{m},γ_s^{k}, ζ) stiffness sub-matrix, acting as beam fibre strain developing along the corresponding shell strip. The membrane flexural mechanism is depicted in the variation of the meridional stress resultants along the meridional direction of the shell and dominated by the stress components due to $\mathbf{a}_s$ (Figure 5). This variation follows the variation of the equivalent bending moment fibre stress developing along the shell strips. The shell strips simulate the beam fibres of the cylindrical shell-beam fixed at the two ends, under the corresponding uniform load (in the meridional direction). The hoop stress resultants due to the rotational field components $\mathbf{a}_s$ and $\mathbf{a}_b$ developing within the narrow boundary zone are responsible for the strong boundary layer effects as shown in Figure 5.

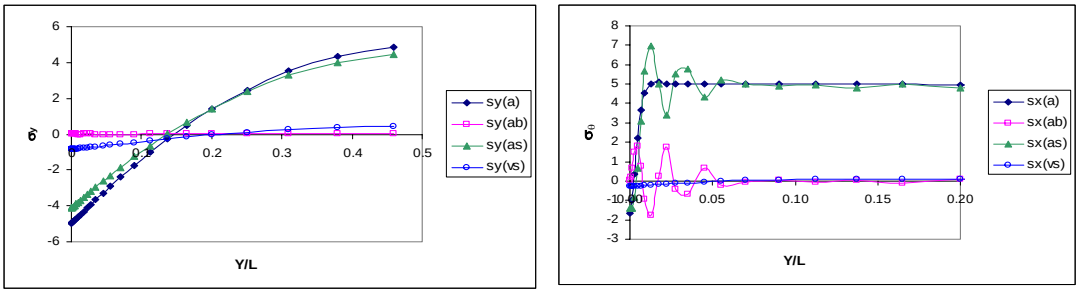

(a) (b)

Figure 5. Meridional and hoop stress resultants developing along the crown line (a) and within the boundary zone (b), respectively, of the cylindrical shell with fixed ends (t=0.0005) under the load of Eq. (13).

4 CONCLUSIONS

An innovative numerical approach is developed for the analysis of the asymptotic shell behaviour based on the physical decomposition of the finite element rotational field, allowing for an insight to be gained into the mechanisms underlying the asymptotic behaviour of shell problems. The way a finite shell element model, and so a shell structure, activates the various load carrying mechanisms in membrane-dominated, bending-dominated and mixed membrane-bending mode shell problems may be investigated and understood in this way.

The asymptotic behaviour of selected classical benchmark shell problems analysed by means of the rotational field decomposition approach identifies clearly distinct load carrying mechanisms in each case.

REFERENCES

[1] Chapelle D. and Bathe K.J. (1998) Fundamental Considerations for the Finite Element Analysis of Shell Structures, Computers and Structures, 66(1) pp. 19-36.
[2] Chapelle D. and Bathe K.J. (1993) The inf-sup Test, Computers and Structures, 47(4/5) 537-545.
[3] K. J. Bathe, A. Iosilevich and D. Chapelle (2000) An inf-sup test for shell finite elements, Computers and Structures, 75, pp. 439-456.
[4] Bathe, K. J. Iosilevich A. and Chapelle D. (2000) An evaluation of the MITC shell elements, Computers and Structures, 75, pp. 1-30.
[5] Briassoulis D. (2002) Testing the Asymptotic Behaviour of Shell Elements, Part I. The Classical Benchmark Tests, Int. J. Numer. Meth. Eng, 54(3), pp. 421-452.
[6] Briassoulis D. (2000) Testing the Asymptotic Behaviour of Shell Elements, Part II. New limit tests: Analytical Solutions and the RFNS Element Case, Int. J. Numer. Meth. Eng., 54, pp. 631-670.
[7] Flugge W. (1973) Stresses in Shells (Springer-Verlag, Berlin, Second Edition.
[8] Pitkaranta, J. Leino, Y. Ovaskainen O. and Piila J. (1995) Shell deformation states and the finite element method: A benchmark study of cylindrical shells, Computer Methods in Applied Mechanics and Engineering, 128, pp. 81-121.
[9] Briassoulis D. (1996) The Four-node C° Shell Element Reformulated, Int. J. Numer. Meth. Eng., 39, pp. 2417-2455.
[10] Briassoulis, D. (2005) Asymptotic Deformation Modes of Benchmark Problems Suitable for Evaluating Shell Elements, Computer Methods in Applied Mechanics and Engineering, to be published
[11] Briassoulis D. (2003) Nonlinear behaviour of the RFNS element – large displacements and rotations', Computer Methods in Applied Mechanics and Engineering, 192 (26-27), pp. 2909-2924.
[12] Briassoulis D. (1991) The moment redistribution effect of the C° structural elements formulation ", Int. J. Numer. Meth. Eng., 32, pp. 541-557.

5th GRACM International Congress on Computational Mechanics
Limassol, 29 June – 1 July, 2005

ANALYSIS AND CONTROL OF SMART VISCOELASTIC BEAMS

Georgia Foutsitzi [*], Evangelos Hadjigeorgiou [*], Daniela Marinova [†] and Georgios Stavroulakis [†]

[*] Department of Material Science and Technology
University of Ioannina
P.O.BOX 1186, 45110 Ioannina, Greece
e-mail: gfoutsi@cc.uoi.gr, ehadjig@cc.uoi.gr

[†] Department of Applied Mathematics and Informatics
Technical University of Sofia
8 Kl. Ohridski Str., 1756 Sofia, Bulgaria
email: dmarinova@dir.bg

[†] Department of Mathematics, Institute of Mechanics,
University of Ioannina, GR-45110 Ioannina, Greece
And Institute of Applied Mechanics, Technical University of Braunschweig, Germany
e-mail: gestavr@cc.uoi.gr

Keywords: Smart Beams, Active Control, Viscoelastic Material, Piezoelectric Material.

Abstract. *A finite element formulation for modelling the dynamic response of laminate composite beams with bonded viscoelastic and piezoelectric layers is presented. The formulation is based on the Euler-Bernoulli beam theory and Hamilton's principle. The active control of the beam is designed using either the optimal linear quadratic regulator strategy or the robust H_∞ control theory. The behavior of the smart structure in the presence of damage in the viscous layer is investigated. The implemented numerical simulation shows the dynamical response of the uncontrolled beam as well as the suppression of the vibrations of the controlled beam.*

1 INTRODUCTION

Smart structures generally consist of a host structure or structural component with bonded or embedded sensors and actuators, which are used for the vibration control. Piezoelectric materials can be used as sensor or actuator elements in smart structures. A vast number of analytical and computational models for smart piezoelectric structures using various mechanical theories have been reported, among others, in the recent review by Sunar and Rao [1].

In this work, the active vibration control of a composite beam sandwiched between viscoelastic and piezoelectric layers is studied. The upper piezoelectric layer acts as an actuator, while the bottom one as a sensor. The purpose of the viscoelastic layers is to model the adhesive that possible exists between the piezoelectric layers and the host beam. A finite element formulation of the model is presented.

The problem of active control is studied using classical optimal linear quadratic regulator (LQR) to obtain the optimal control gains and to investigate the behavior of the beam in the presence of possible damages which are reflected in the properties of the viscous layer. In order to take into account our incomplete information about the damages and of the external disturbances the theory robust H_∞ feedback controller is also used. The H_∞ optimal control technique uses as performance measure the H_∞ norm of the transfer matrix from external disturbances to regulated outputs defined in the frequency domain. In this way disturbances are rejected in an optimal way by the robust control.

The proposed models are investigated numerically. Simulations show the effectiveness and the good quality of the proposed model and the control strategies.

2 THEORETICAL FORMULATION

A composite beam made of laminate faces, with viscoelastic and piezoelectric sub-layers, and an elastic core is considered (see Fig 1). The whole beam is modelled using classical laminate theory. Euler-Bernoulli assumptions are considered for the beam. The piezoelectric layers are assumed to be transversely polarized and subjected to transverse electrical fields. Elastic and viscoelastic layers are assumed to be insulated. All layers are assumed to be perfectly bonded and in uniaxial stress state. The length, width and thickness of the beam are denoted by L, b and h, respectively. The mid-plane of the core is set to coincide with the origin of the z-axis. The superscripts p, v and b refer to the piezoelectric layer, the viscoelastic layer and the elastic core beam, respectively.

2.1 Kinematics

By using the kinematical assumptions of the Euler-Bernoulli theory, the axial displacement u and the transverse deflection w of every point cross-section x and every time instance t, can be written as

$$\begin{aligned} u(x,y,z,t) &= -z\frac{\partial w(x,t)}{\partial x} \\ w(x,y,z,t) &= w(x,t) \end{aligned} \tag{1}$$

Notice that the same displacement fields u and w are considered for all sub-layers.

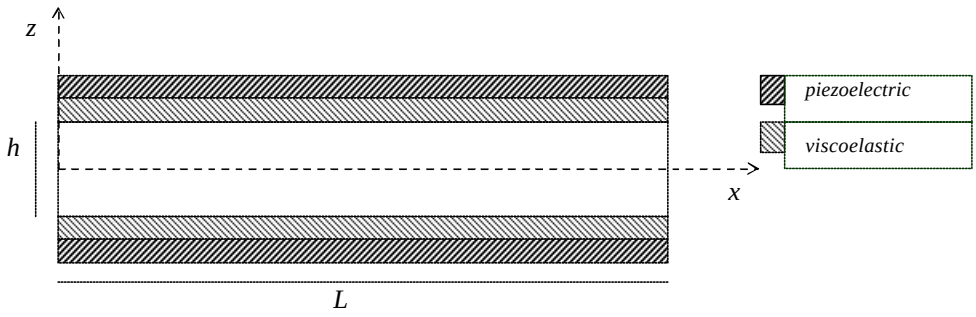

Figure 1. A laminate composite beam

By using the usual strain-displacement relations, the axial strain can be written as

$$e_x = \frac{\partial u}{\partial x} = -z\frac{\partial^2 w}{\partial x^2} \tag{2}$$

A constant transverse electrical field is assumed for the piezoelectric layers and the remaining in-plane components are supposed to vanish. Consequently the electric field intensity E_z can be expressed as

$$E_z = \frac{V}{h_p} \tag{3}$$

where h_p is the thickness of the piezoelectric layer and V is the applied voltage across the piezoelectric layer.

2.2 Constitutive Equations

Using the linear theory of elasticity the constitutive equation for the axial extensional strain s_x^b is given by

$$s_x^b = Q_{11}^b e_x = -zQ_{11}^b \frac{\partial^2 w}{\partial x^2} \tag{4}$$

where Q_{11}^b is the Young modulus of the beam core material.

The properties of the piezoelectric layer are considered to be orthotropic and homogeneous, and those of viscoelastic layer are considered to be of rate-type, isotropic and homogeneous. When only the independent variables e_x and E_z are not equal to zero, the one-dimensional constitutive equations can be expressed as

$$s_x^p = Q_{11}^p e_x - e_{31}^p E_z, \qquad D_z = e_{31}^p e_x + x_{33}^p E_z, \tag{5}$$

$$s_x^v = Q_{11}^v e_x + F_{11}^v \dot{e}_x, \tag{6}$$

where s_x^p, s_x^v denote the axial stress of the piezoelectric and the viscoelastic layers, respectively. Furthermore, D_z is the electric displacement in the *z*-direction, Q_{11}^p, Q_{11}^v is the Young modulus of the piezoelectric and the viscoelastic layers, respectively, F_{11}^v is the coefficient of the shear viscosity of the viscoelastic layers, e_{31}^p is the piezoelectric constant and x_{33}^p is the dielectric constant.

Notice that electromechanical coupling in the piezoelectric layers is between axial strain and transverse electrical field. This is the conventional piezoelectric extension actuation mechanism.

2.3 Energy Expressions

Based on the above constitutive equations, the contributions to the potential energy due to the elastic beam, the piezoelectric layers and the viscoelastic layers are given by

$$U^b = \frac{1}{2}\int_V s_x^b e_x dV = \frac{1}{2}\int_0^L (EI)^b \left(\frac{\partial^2 w}{\partial x^2}\right)^2 dx \tag{7}$$

$$U^p = \frac{1}{2}\int_V s_x^p e_x dV = \frac{1}{2}\int_0^L (EI)^p \left(\frac{\partial^2 w}{\partial x^2}\right)^2 dx - \frac{1}{2}\int_0^L M^p \frac{\partial^2 w}{\partial x^2} dx \tag{8}$$

$$U^v = \frac{1}{2}\int_V s_x^v e_x dV = \frac{1}{2}\int_0^L (EI)^v \left(\frac{\partial^2 w}{\partial x^2}\right)^2 dx + \frac{1}{2}\int_0^L G^v \left(\frac{\partial^2 \dot{w}}{\partial x^2}\right)\left(\frac{\partial^2 w}{\partial x^2}\right) dx \tag{9}$$

where

$$(EI)^k = \int_{S_k} Q_{11}^k z^2 dS, \qquad M^p = \int_{S_p} z e_{31}^p E_z dS, \qquad G^v = \int_{S_v} F_{11}^v z^2 dS,$$

and S_k, $k = b, p, v$ is the cross area of the *k*-th layer.

The kinetic energy of the the *k*-th layer, *k*=*b*, *p*, *v*, is represented as

$$T^k = \frac{1}{2}\int_V r^k \left[(\dot{u})^2 + (\dot{w})^2\right] dV = \frac{1}{2}\int_0^L I_3^k \left(\frac{\partial \dot{w}}{\partial x}\right)^2 dx + \frac{1}{2}\int_0^L I_1^k (\dot{w})^2 dx \tag{10}$$

where

$$I_1^k = \int_{S_k} r^k z dS, \qquad I_3^k = \int_{S_k} r^k z^2 dS.$$

2.4 Virtual Work

The virtual work done by the electrical forces is given by

$$W^p = \frac{1}{2}\int_V D_z E_z dV = \frac{1}{2}\int_0^L M^p \frac{\partial^2 w}{\partial x^2} dx + \frac{1}{2}\int_0^L \int_{S_p} x_{33}^b \left(E_z\right)^2 dS dx\,, \tag{11}$$

while the virtual work done by the mechanical forces is written as

$$W^{ext} = \frac{1}{2}\int_0^L f(x,t) w(x,t) dx\,. \tag{12}$$

2.5 Finite Element Formulation

For the approximation of the transverse deflections w Hermite interpolation functions are considered. Beam elements are constructed with a length equal to L_e, and two nodes, each one with two degrees of freedom: the deflection w and its slope $\partial w / \partial x$. Using Hamilton's principle, one can construct automatically the equilibrium equations

$$\int_0^T \left(dT^b + dT^v + dT^p - dU^b - dU^v - dU^p + dW^p + dW^{ext} \right) dt = 0 \tag{13}$$

By this approach, a finite element discretized model for the beam bonded with viscous layers and piezoelectric sensors and actuators is derived

$$M\ddot{q} + C\dot{q} + Kq = F_{ext} + F_c\,, \tag{14}$$

where $q, \dot{q}$ and $\ddot{q}$ are vectors of nodal displacement, velocity and acceleration. M, C and K are the mass, damping and stiffness matrices. In addition, F_{ext} is the external mechanical force and F_c is the control force coming from the actuator layer. In should be noted that the damping matrix C in this paper corresponds to the behaviour of the viscous layer. Additional structural damping of the beam may be added, if necessary.

Equation (14) represents a linear, time-invariant, finite dimensional dynamical system that can be placed in standard state space form

$$\dot{x} = Ax + Bu + F \qquad y = Dx\,, \tag{15}$$

where $x = [q, \dot{q}]$ is the state vector, $A = \begin{bmatrix} 0 & I \\ -M^{-1}K & -M^{-1}C \end{bmatrix}$ is the system matrix, $B = \begin{bmatrix} 0 \\ M^{-1}F_c \end{bmatrix}$ is the control collocated matrix and $F = \begin{bmatrix} 0 \\ M^{-1}F_{ext} \end{bmatrix}$ is the state distribution of the external mechanical loads F_{ext}. The control input u is a column vector formed by the voltages applied to the actuators. The output vector y consists of measures formed from the state vector x by the output matrix D.

The model of the smart composite beam used by the authors in the Ref. [2] can be obtained by removing the viscoelastic layer from the model of this paper.

3 STATEMENT OF THE ROBUST CONTROL PROBLEM

The optimal control problem is initially studied for the nominal system, i.e., the beam with known elastic, piezoelectric and viscous properties. A more realistic question concerning the robustness of the control in the presence of defects is also addressed. In particular, we are interested in damages at the interfaces between the host beam and the piezoelectric patches. The viscous layer models the glue between the host material and the sensors or actuators. The assumption that the piezoelectric patches are bonded perfectly corresponds to viscous glue with predetermined properties. The bonding layer may include manufacturing imperfections or service-induced damage, like fatigue, debonding or delamination. Several of these defects can be modelled as changes of the parameters of the viscous layer. A first investigation of the influence of damage on the mechanical response of the smart composite beam is done with the help of the proposed model.

Further, two control laws for the composite beam are designed in order to suppress the vibrations. Because of its linearity and easy implementation, the linear quadratic regulator (LQR) is presented first. The response of the controlled nominal and damaged beams is investigated. In order to take into account the incompleteness of the information about the eventual damages and external additional influences a robust H_∞ controller is designed. For practical applications both algorithms need several trial-and-error design iterations in order to provide appropriate control voltages, since the piezoelectric actuators can be depoled by high oscillating voltages. The effectiveness of the proposed control strategies is investigated with the help of numerical simulations.

4 CONTROL DESIGN

We solve a regulator problem for the smart beam with viscous layer. The objective in this section is to determine the optimal vector of active control forces $u(t)$ subjected to performance criteria and satisfying the dynamical equations of the system, such that to reduce in an optimal way the external excitations. We consider the steady state (infinite time) case, i.e. the optimization horizon is allowed to extend to infinity. We seek a linear state feedback

$$u = -Kx\,, \tag{16}$$

with constant gain K.

4.1 LQR optimal control strategy

Consider the first equation of the system (15) and the quadratic cost function

$$J = \frac{1}{2}\int_0^\infty (x^T Q x + u^T R u)dt\,. \tag{17}$$

The problem consists of minimizing the functional J with respect of the control input u subject to the linear system constraints (17). Here the matrix Q is positive semi-definite $(Q \geq 0)$ and the matrix R is strictly positive definite *(R>0)*. The first requirement implies that some of the states may be irrelevant for the problem. The latter requirement emphasizes that the control energy must be finite. This is known as the linear quadratic regulator (LQR) problem [3]. It leads to the Algebraic Riccati Equation (ARE)

$$A^T P + PA + Q - PBR^{-1}B^T P = 0\,. \tag{18}$$

The equation (18) has a positive definite solution P if and only if the pair (A,B) is stabilizable, $R>0$ and Q can be expressed as $Q = C_q^T C_q$, such that the pair (C_q, A) is detectable. These are the necessary and sufficient conditions for existence and uniqueness of an optimal controller with constant gain K, which realizes an asymptotically stable closed loop system. The main design parameters for the controller are the weight matrices Q and R. They are chosen iteratively in order to guarantee a stable optimal system with limited value of maximum control.
The solution of the problem is the constant matrix K in the form

$$K = R^{-1}B^T P\,, \tag{19}$$

where P is the symmetric positive definite solution of the ARE (18). LQR requires that the whole state of the dynamical system is available.

4.2 Robust H_∞ optimal control strategy

Let the plant representation in state space form is the following

$$\begin{aligned} \dot{x} &= Ax + B_1\tilde{w} + B_2u \\ z &= C_1x \quad\quad + D_{12}u \\ y &= C_2x + D_{21}\tilde{w} \end{aligned}, \tag{20}$$

where $\tilde{w}$ denotes the external forces and some unknown disturbances that the controller cannot manipulate. The output signals are divided by two groups: y are signals that are measured and fed back to the controller and z are regulated outputs.

The following assumptions are made for the output feedback H_∞ problem [4]:

(i) (A, B_2) is stabilizable and (C_2, A) is detectable;

(ii) $D_{12}^*D_{12} > 0$ and $D_{21}D_{21}^* > 0$;

(iii) $\begin{bmatrix} A - jwI & B_2 \\ C_1 & D_{12} \end{bmatrix}$ has full column rank for all frequencies w;

(iv) $\begin{bmatrix} A - jwI & B_1 \\ C_2 & D_{21} \end{bmatrix}$ has full row rank for all frequencies w.

Let us denote by T_{zw} the transfer matrix from exogenous inputs $\tilde{w}$ to controlled outputs z. The H_∞ control problem is to find a proper, real rational controller K that stabilizes the system (20) and minimizes the H_∞ norm of the transfer matrix T_{zw}. The following is the objective function we wish to minimize

$$\min \|T_{zw}\|_\infty = \min_K \left\{ \max_{w(t)\neq 0} \frac{\|z(t)\|_2}{\|\tilde{w}(t)\|_2} \right\}, \quad \text{where } \|z(t)\|_2 = \sqrt{\int_0^\infty |z_i(t)|^2 dt}. \tag{19}$$

In the frequency domain the minimization of the H_∞ norm minimizes the maximal value of the maximal singular value of T_{zw}. In the time domain, minimizing this norm can be interpreted as a worst case minimization with respect to the induced 2-norm.

5 NUMERICAL SIMULATIONS

For the numerical simulations a cantilevered composite beam with viscous and piezoelectric layers bonded on its top and bottom and discretized with four finite elements is used. A finer finite element discretization, which certainly is required for the approximation of higher frequency behavior, does not change the trend of the results. The parameters of the beam are similar to that used in the Ref. [5]. Our aim is to study the response of the composite beam in the presence of defects and damages, which can be expressed as changes of the main parameters of the viscous layer.

Let us first investigate the response of the free and LQR-controlled composite beam with piezoelectric and viscous layers for various parameters of the glue layer, namely, its density, its thickness and its viscous coefficient. A vertical impulsive load is applied at the free-end of the beam.

Figure 2 shows the free displacement response at the tip of the excited beam for three different amounts of density $r = 250kg/m^3$ - dot line, $r = 1250kg/m^3$ - solid line, $r = 6250kg/m^3$ - dash line. Decreasing density of the viscous layer slightly changes the behavior of the composite beam. Increasing the density of the adhesive

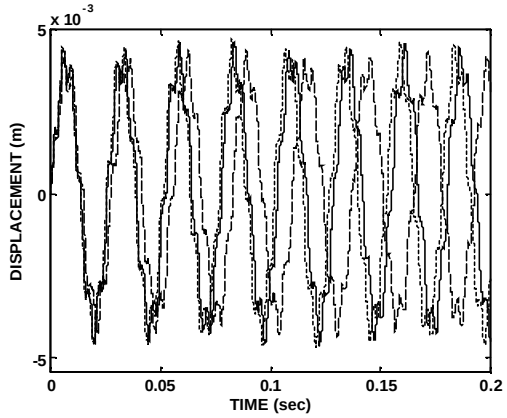

Figure 2. Displacement of the free vibrating beam tip for different densities.

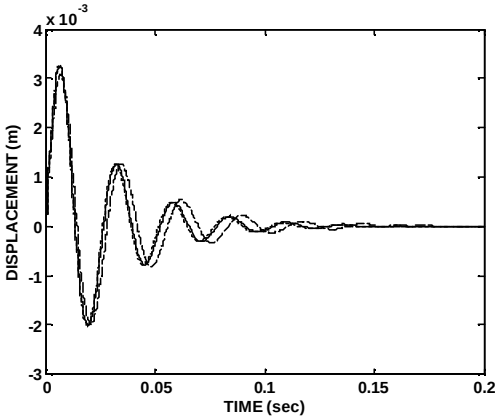

Figure 3. Displacements of the controlled by LQR beam tip for different densities.

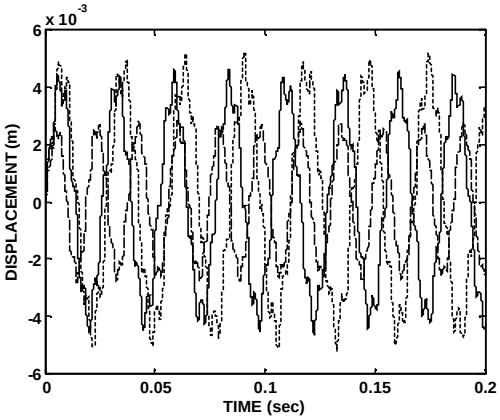

Figure 4. Displacements of the free vibrating tip for different thickness.

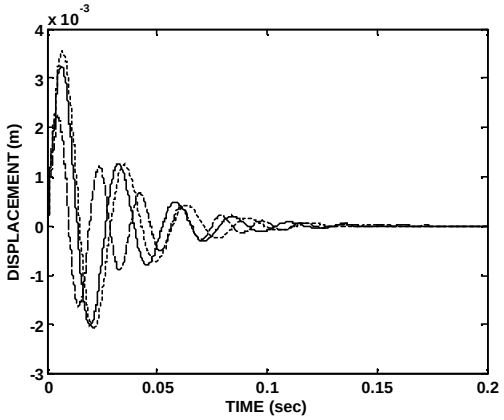

Figure 5. Displacements of the controlled by LQR beam tip for different thickness.

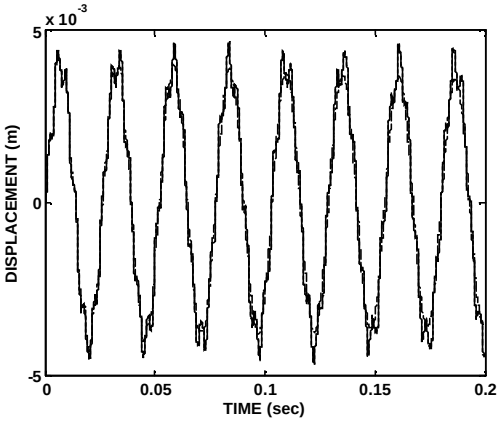

Figure 6. Displacements of the free vibrating beam for different viscous coefficients F_{11}^{v}

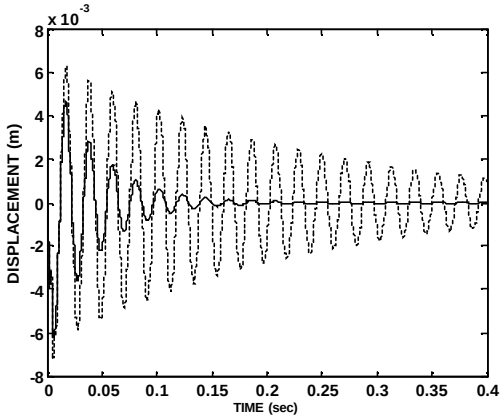

Figure 7. Displacements of the free and controlled by H_{∞} vibrating not damaged beam tip.

leads to some delay of the free vibration response and at the same time slightly improves the vibration suppression. In Figure 3 one can see the corresponding displacements of the controlled response of the beam-tip for the same three different amounts of density. The changes of the density lead to changes in the controlled beam behavior. However, practically, they neither improve nor deteriorate the vibration suppression of the controlled beam.

The displacements at the tip of the uncontrolled beam for different thicknesses of the viscoelastic layer are shown in Figure 4. Three different thicknesses are used: *h=0.000125 m* - dot line, *h=0.00025 m* - solid line, *h=0.0005 m* - dash line. It can be observed that for decreasing thicknesses of the viscous layer the amplitude of the free vibrating beam increases. The response of the controlled beam-tip for the same three different values of the thickness is exhibited in Figure 5. The simulations show that lower thicknesses of the adhesive layer give worse suppressions of the first peak in the vibrations, while higher thicknesses lead to better suppression. However, the settling time for a sufficiently large range of different thicknesses is practically the same.

Figure 6 displaces the free response of the exited beam tip for different viscous coefficients $F_{11}^{v} = 0.105.10^{5}$ - dot line, $F_{11}^{v} = 1.05.10^{5}$ - solid line, $F_{11}^{v} = 10.5.10^{5}$ - dash line. The numerical investigation shows that the viscous coefficient F_{11}^{v} slightly influences the response of the composite beam. Only very big amounts of this parameter lead to slight reduction in the peaks of vibrations of the uncontrolled beam that can be seen in the Figure 5. Practically this circumstance leads to stable behavior of the controlled beam. Hence, defects expressed by changes in the viscous coefficient F_{11}^{v} do not influence the controlled response of the beam.

Figure 7 shows the response of the uncontrolled and controlled beam using the H_{∞} control strategy for the nominal beam without defects. Numerical investigations show that the suppressions of vibrations of the exited smart beam in this case are weaker but the structure remains stable for larger changes in the viscous parameters.

6 CONCLUSIONS

A mathematical formulation and finite element model for the vibration suppression of a cantilever beam with piezoelectric laminated surface and viscous layers and elastic core is considered in this paper. The design of the piezoelectric active control using LQR strategy and H_{∞} control theory for the nominal and damaged sandwich beam has been studied. The numerical results show that the proposed model and method are effective and the control behavior of the beam achieves the predicted characteristics.

REFERENCES

[1] Sunar M and Rao S (1999) “Recent advances in sensing and control of flexible structures via piezoelectric materials technology”, Appl. Mech. Rev. 52, pp.1-16.

[2] Foutsitzi G, Marinova D, Hadjigeorgiou E and Stavroulakis G (2003) “Robust H-2 vibration control of beams with piezoelectric sensors and actuators”, *Proceedings of Physics and Control Conference (PhyCon03),* St. Petersburg, Russia, 20-22 August, Vol. I, pp. 158-163.

[3] Preumont A., (1997), *Vibration Control of Active Structures. An Introduction*, Kruwer Academic Publishers.

[4] Zhou K., (1998), *Essentials of robust control*, Upper Saddle River, New Jersey: Prentice-Hall.

[5] Liao W. H. and Wang K. W. (1997), “On the analysis of viscoelastic materials for active constrained layer damping treatment”, J. Sound and Vibration 207, pp. 319-334

STRUCTURAL-CONCRETE BEHAVIOUR: SEPARATING MYTHS FROM REALITY

Michael D. Kotsovos[*], Milija N. Pavlović[†], and Demetrios M. Cotsovos[†]

[*]Civil Engineering Department, National Technical University of Athens
email: mkotsov@central.ntua.gr

[†]Civil Engineering Department, Imperial College, London

Keywords: finite element nonlinear analysis; static and dynamic loading; structural concrete behaviour.

Abstract. *Most finite-element models of reinforced-concrete structures attribute to concrete material characteristics which are in conflict with true behaviour established from valid experimental information. As a result the constitutive models adopted are case-study dependent. The present work summarizes already published work which shows that the use of realistic concrete properties coupled with well-tried numerical techniques can yield a finite-element model characterised by both generality and objectivity.*

1 INTRODUCTION

Most finite-element (FE) models of structural concrete rely on constitutive relationships which place emphasis on the description of post-peak concrete characteristics such as, for example, strain softening, tension stiffening, shear-retention ability, etc, coupled with stress- and/or strain-rate sensitivity when blast or impulsive types of loading are considered. However, the application of these models in practical structural analysis has shown that such constitutive relationships are case-study dependent, since the solutions obtained are realistic only for particular problems; in order to extend, therefore, the applicability of the models to a different set of problems requires modifications, sometimes significant, of the constitutive relationships.

The cause of the above apparent lack of generality is considered to relate on the one hand with the misinterpretation of the observed material behaviour and, on the other, with the use of experimental data of questionable validity for the calibration of the constitutive relationships. To this end, the work presented in the paper is intended to show that the use of valid experimental data can lead to the development of a model of concrete behaviour which enables FE analysis to yield realistic solutions for a wide range of practical problems covering both static and dynamic loading conditions. The fundamental material characteristics which underlie the development of such a model are first discussed and the FE results obtained from various already published case studies are presented as additional evidence of the validity of the material characteristics adopted.

2 FUNDAMENTAL CONCRETE CHARACTERISTICS

2.1 Brittle post-peak behaviour

The experimental data on concrete behaviour used for the development of constitutive laws are obtained from tests on specimens such as, for example, cylinders, prisms, cubes, etc. Such specimens are subjected to various load combinations, usually applied (at least in one of the three principal directions) through rigid steel platens; the resulting data are expressed in the form of stress-strain curves comprising a strain hardening branch followed by a strain softening one, widely considered to be essential in ultimate limit-state analysis and design.

And yet, it has been known since the early 80's[11,21], and confirmed in the late 90's[22], that only strain hardening may describe material behaviour under a definable state of stress; strain softening merely reflects the interaction between specimen and loading platens, which is effected through the development of indefinable frictional stresses at the end faces of the specimen. In fact, it has been shown that the rate of reduction of the residual concrete strength with increasing strain increases rapidly as the means to reduce the above frictional stresses becomes more effective (see Fig. 1)[11]. Such behaviour indicates that were the frictional stresses completely eliminated, concrete would be characterised by a complete and immediate loss of load-carrying capacity, as soon as the peak load level is attained. Therefore, attributing strain softening characteristics to the post-peak behaviour of concrete is in conflict with this material's brittle nature.

2.2 Stress path independency

Decomposing the stress-strain behaviour of concrete under any state of stress into hydrostatic and deviatoric components yields stress-strain curves, which can be expressed in the form of normal and shear octahedral stresses (σ_o and τ_o) and strains (γ_o and ε_o). Such curves show that, while σ_o yields only ε_o, τ_o yields both γ_o and ε_o[12]. More importantly, however, it has been shown experimentally that the curves exhibit a statistically insignificant deviation from those obtained from tests on specimens subjected to either σ_o or τ_o [12]. Such a small deviation indicates that concrete behaviour is essentially stress-path independent[15].

A similar conclusion has also been drawn from experimental data on concrete strength. Such data form an open surface in stress space characterised by six-fold symmetry with respect to the space diagonal, with most of them having been obtained from tests on specimens under axisymmetric states of stress, and hence defining the meridians of the strength surface corresponding at $\sigma_1 = \sigma_2 \geq \sigma_3$ and $\sigma_1 \geq \sigma_2 = \sigma_3$. It is such experimental data that have also been found to be stress-path independent[7].

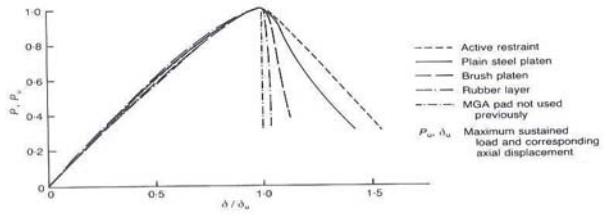

Figure 1. Load-displacement curves of concrete in uniaxial compression tests on cylinders using various methods to reduce friction.

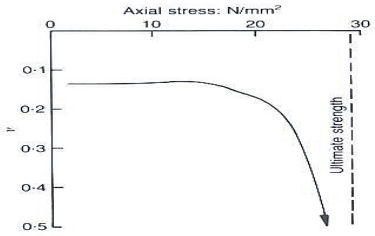

Figure 2. Typical variation of Poisson's ratio with increasing stress established from tests on cylinders in uniaxial compression.

2.3 "Poisson's ratio" effect

The development of most constitutive relations of concrete behaviour published to date has been directly or indirectly based on the assumption of a constant value of the Poisson's ratio (PR). However, such an assumption is in conflict with experimental data which show that the variation of PR with the applied load exhibits a trend similar to that indicated in Fig. 2.[16] From the figure, it can be seen that PR is essentially constant up to a value of the applied load equal to between approximately 30% and 50% of the peak load level; beyond this load level, PR increases at an increasing rate and attains a value that becomes significantly larger than 0.5 when the peak load level is reached. Such behaviour clearly indicates that concrete ceases to be a continuum beyond a load level close to, but not beyond, the peak one, a fact consistent with the material's brittle nature.

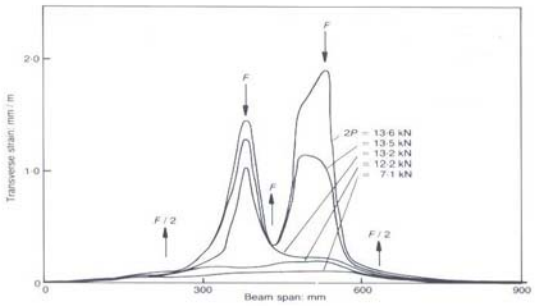

Figure 3. Transverse deformation profile of an RC beam under two-point loading.

The above rapid increase of PR with increasing stress has a very significant, but rarely recognized effect on structural-concrete behaviour, since it has been shown to underlie the ultimate limit-state behaviour of structural members such as, for example, beams, columns, slabs, etc[16]. A typical such example is indicated in Fig. 3 which shows the transverse (lateral and vertical) deformation profile of the upper face of a reinforced-concrete (RC) beam designed to fail in flexure under two-point loading (2P in Fig. 3)[10].

From the figure, it is interesting to note the large transverse expansion which the beam (at its ultimate-limit state) undergoes within localised regions of its middle portion between the load points. This is because the above localised regions include primary flexural cracks which reduce the depth of the compressive zone and, hence, increase the intensity of the compressive stress field (developing due to the bending action) to a level significantly higher than that in adjacent regions where the depth of the compressive zone is larger. It is this difference in the intensity of the compressive stress field that causes the large variations in the transverse expansion profile of the upper face of the specimen (see Fig. 3), with the larger transverse expansion corresponding to the locations of peak stresses where, as indicated in Fig. 2, PR attains its largest value.

However, the regions exhibiting different degrees of transverse expansion interact, with the regions with the small expansion imposing a restrain to the large expansion of the adjacent regions; on the other hand, the latter regions tend to impose their rate of expansion to the former. Such an interaction leads to the development of transverse compressive-stress resultants (F in Fig. 3) in the regions exhibiting large transverse expansion and transverse tensile-stress resultants (F and F/2 in Fig. 3) in the adjacent regions where the transverse expansion is small (see Fig. 3). In fact, flexural failure eventually occurs due to horizontal cracking of the compressive zone in the regions where longitudinal compression is combined with transverse tension, rather than due to "crushing" of concrete at its post-peak state in the compressive zone of cross sections including a deep flexural crack as widely believed[10].

2.4 Cracking

An element of concrete in an RC structure cracks in order to relieve tensile stresses when the material strength in tension is attained. The crack faces coincide with the plane of the maximum and intermediate principal stresses (assuming compression as positive) and opens in the orthogonal direction (i.e. in the direction of the minimum principal compressive stress or maximum principal tensile stress), whereas its extension occurs in the direction of the maximum principal compressive stress[8,13]. Such a cracking mechanism precludes any shearing movement of the crack faces and, therefore, contrasts widely adopted mechanisms of shear resistance such as, for example, aggregate interlock and dowel action, which can only be effected through the "shearing" movement of the crack faces.

The cracking mechanism described above implies that an RC structural member suffers loss of load-carrying capacity before failure of concrete in compression anywhere within the member[15]. In fact, loss of load-carrying capacity is preceded by the initiation of cracking in regions where the state of stress is predominantly tensile with propagation into regions under a compressive state of stress occurring after one of the principal stress components of this state of stress becomes tensile. Eventually, failure occurs due to crack formation in regions where large transverse expansion causes transverse tension as described in the preceding section.

2.5 Loading-rate independency

The vast majority of existing constitutive models used for describing the behaviour of concrete under high rates of loading are based on the assumption that there is a link between the mechanical properties of concrete and the rate at which the loading is imposed. However, such a "loading-rate sensitivity" is based on an uncritical interpretation of the available experimental data, the validity of which has recently been questioned[3]. In the present work, the mechanical properties of concrete are considered to be independent of the loading rate, with the effect of the latter on the specimen behaviour being primarily attributed to the inertia effect of the specimen mass: this simple (and, arguably, obvious – though, at present, unorthodox) postulate was the subject of a numerical investigation which proved capable of reproducing the experimental data available from past tests[3]. Moreover, this numerical investigation confirmed the importance of the role that inertia plays in the specimen's response when subjected to high rates of loading.

3. USE IN FINITE-ELEMENT ANALYSIS

3.1 Constitutive law of concrete behaviour

An analytical description of concrete behaviour may be based on an analysis of experimental stress-strain data expressed in the form of octahedral stress-strain curves. The variations of the secant and tangent values of the bulk (K_S ,K_T)) and shear (G_S,,G_T) modulae may easily be expressed as functions of σ_o and τ_o from the σ_o-ε_o and τ_o-γ_o curves, respectively, as fully described elsewhere[14]. The values of K_T and G_T at the origin of the normal and shear octahedral stress-strain curves have been shown to adequately describe material behaviour during unloading[12,15]. In order to allow for the coupling between the hydrostatic and deviatoric components of stress and strain expressed by the variation of ε_o with τ_o for a given σ_o, the latter variation has been transformed into the variation of an *internal hydrostatic stress* σ_{int} with τ_o for a given σ_o[12,14]. Having expressed K_S (K_T) and G_S (G_T) as functions of σ_o and τ_o, respectively, and σ_{int} as a function of σ_o and τ_o, the strains corresponding to a given state of stress is easily obtained from Hook's law by adding σ_{int} to σ_o[15].

As for the case of the deformational properties, the analytical description of the strength surface may also be based on an analysis of experimental data expressed in the form of σ_o, τ_o and θ (defining the direction of τ_o on the deviatoric plane (plane normal to the space diagonal)). Such data were used for the analytical description of the strength-surface meridians corresponding to $\theta=0^o$ ($\sigma_1 = \sigma_2 \geq \sigma_3$) and $\theta=60^o$ ($\sigma_1 \geq \sigma_2 = \sigma_3$.)[9]. For meridians corresponding to $0^o \leq \theta \leq 60^o$ an interpolation function derived elsewhere[23] is used.

3.2 Constitutive law for steel bars

The constitutive model used to describe the behaviour of steel reinforcement is essentially an analytical description of the stress-strain curve of steel in compression or tension describing material behaviour under both monotonic and cyclic loading. Full details are provided elsewhere[3].

3.3 Concrete-steel interaction

It is considered that the concrete-steel interaction is adequately described by the assumption of perfect bond. Three arguments may be adduced for such an approach: First, the notion of perfect bond is compatible with the thinking behind the smeared-crack model – in the sense the detailed description of localised effects is avoided – which spreads the effect of cracking to such an extent that integration points in bar elements represent, generally, bar lengths usually exceeding the localised regions where bond slip occurs, thus precluding a minute account of the local concrete-steel interaction. Secondly, experiments attempting to determine bond-stress against slip-displacement curves exhibit a large scatter of data, which precludes any refinement implicit in the departure from the perfect-bond condition. Thirdly, and most importantly, there are the actual values of the bond stress and

corresponding slip themselves. From the experimental data, an order of magnitude for the maximum bond stress and corresponding slip of around 5 MPa and 0.005 cm, respectively, appears to be relevant. These values are larger that the values of 1 MPa and 0.0006 of the tensile strength and corresponding displacement resulting from the failure criterion incorporated in the FE model, by an order of magnitude. It is evident therefore that concrete in the vicinity of concrete-steel interface will usually have cracked before the maximum bond stress could be developed.

3.4 Finite-element solution technique

The implementation in structural analysis of a constitutive law of concrete behaviour with the above characteristics was achieved through the development of a finite-element (FE) package that is fully described elsewhere[3,15,17,18] and therefore will only briefly presented in the following.

The package is capable of performing not only static[15,17,18], but also dynamic[3] analysis, the latter being effected through the unconditionally stable average acceleration method of the implicit Newmark integration scheme[1,4,5]. Moreover, it uses three dimensional (3D) nonlinear (NL) analysis in order to allow for (a) the nonlinear behaviour of concrete under the triaxial stress conditions, which invariably develop prior to local failure (i.e. cracking), and (b) the introduction of non-homogeneity and stress redistribution after the occurrence of cracking. Concrete is modelled by using 27-node brick Lagrangian elements, whereas truss 3-node isoparametric elements are used to model the steel reinforcement.

The nonlinear analysis is based on an iterative procedure, known as the modified Newton-Raphson[15] which is used to calculate stresses, strains and residual forces. Every Gauss point is checked, at first, in order to determine whether loading or unloading takes place, and then in order to establish whether any crack closes or forms. Depending on the results of the previous checks, changes are introduced to the stress-strain matrices of the individual FE's and, consequently, to the stiffness matrix of the structure. Based on these modified matrices, deformation, strain and stress corrections are evaluated. Convergence is accomplished once the above corrections become very small. It should be pointed out that the formation and closure of cracking is checked separately during each load step.

3.5 Crack formation and closure procedure

During the crack-closure procedure only Gauss points with cracks formed in previous load steps are checked. For a crack to close, the criterion that must be satisfied is that the strains normal to the plane of the crack be compressive. In the course of each iteration, the program singles out the crack with the largest compressive strain and closes it, as it has been observed that, after the closure of one crack, there is usually a drastic drop in the number of cracks that need to close next. The crack-closing procedure is repeated until all cracks that fulfil the crack-closure criterion close.

The crack-formation procedure commences after the completion of the crack-closure procedure. During each iteration of this procedure all Gauss points are checked in order to determine if any new cracks form. This is achieved by using the failure criterion since the opening of a crack corresponds to localized failure of the material. In order to avoid numerical instabilities during the solution of the problem, only a limited number of cracks (no more than three) are allowed to form per iteration. Should the number of cracks that need to open exceed this predefined number, then only the most critical cracks will be allowed to form. As for the case of crack closure, after the formation of the most critical cracks the number of cracks that need to form in the next iteration reduces rapidly due to the redistribution of stress achieved during this process.

Crack formation is modelled by using the smeared-crack approach and may occur up to three times at any given point. Failure is followed by immediate loss of load-carrying capacity in the direction normal to the plane of the crack. Concurrently, the shear stiffness is also considered to reduce drastically to a small percentage of its previous value (during the uncracked state). However, it is not set to zero in order to minimize the risk of numerical instabilities during the execution of the solution procedure, as explained elsewhere[15].

4. FINITE-ELEMENT PREDICTIONS OF STRUCTURAL-CONCRETE BEHAVIOUR

The validity of the above NLFE package has been verified by comparing the numerical predictions with experimental data obtained from tests on a wide range of structural members subjected to various regimes of static and dynamic loading. Full details of these comparative studies are given elsewhere[3,6,15,17,18]. An indication of the predictive capabilities of the package is provided in the following in the form of load-displacement curves of typical RC structural members under loading regimes varying from static to dynamic and static to periodic.

4.1 Simply-supported beam with overhang under sequential static loading

The case discussed in the present section has been extracted from a research programme concerned with the study of the performance of RC beams exhibiting points of inflection[6]. All beams were simply supported with a span of 1600 mm and an overhang of 400 mm. Their total length was 2200 mm, with a rectangular cross-section of 230 mm (depth)x100 mm (width). The loading arrangement is shown in Fig. 4. The beams were under-reinforced using two 16 mm diameter high-yield deformed bars as both top and bottom reinforcement. The

transverse reinforcement provided was in the form of 8 mm plain mild-steel bars. The average test values of yield and ultimate stresses were, respectively, 536 MPa and 626 MPa (16 mm bars) and 368 MPa and 480 MPa (8mm bars). The average concrete strength of all beams was around 30 MPa and the same mix was used throughout. Full details on the specimens and their production are reported in Ref. 6. Information on the test rig, instrumentation, loading and deflection measurement is also contained there.

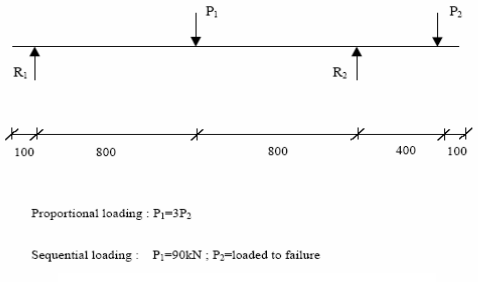

Figure 4: Loading arrangement.

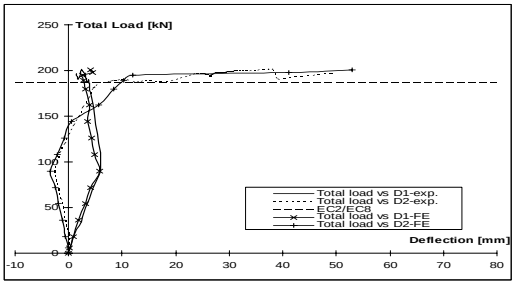

Figure 5: Predicted and experimental load-deflection curves.

The analytical load-deflection characteristics for a typical beam designed to the "compressive-force path" method[16] and subjected to sequential loading are compared with the experimental behaviour in Fig. 5. In the figure, the total load is plotted against the deflections corresponding to the locations of the two concentrated loads, namely the middle of the main span (deflection D1) and the end of the overhang (deflection D2). It can be seen that the analytical prediction of the peak load agrees well with its experimental counterpart. Similarly, the maximum deflection at both the main span and the overhang is realistically estimated by the NLFE analysis.

4.2 Structural-concrete wall under cyclic loading

The structural wall investigated is one of the structural walls (specimen SW33), taken from the set of experiments conducted by Lefas[19]. The wall was 650mm wide, 1300mm high and 70mm thick. The uniaxial cylinder compressive strength (f_c) of the concrete used was around 50 MPa, whereas the yield stress (f_y) and ultimate strength (f_u) of the reinforcement was 420 MPa and 480 MPa for the 4 mm bars, 520 MPa and 610 MPa for the 6.25 mm bars, and 470 MPa and 560 MPa for the 8 mm bars. The reinforcement arrangement is shown in Fig. 6. From the figure, it can be seen that the wall was monolithically connected to a rigid RC prism at both top and bottom. The bottom prism was firmly bolted to the laboratory strong floor in order to resemble a rigid type of foundation, while at the end faces of the top prism the external loading was imposed through two 50-ton jacks. The prisms were designed so as to remain undamaged throughout the course of the experiment. Each wall was subjected to different cyclic loading conditions. After a prescribed number of load cycles, the load increased monotonically up to the full loss of load-carrying capacity.

Initially, the behaviour of the RC walls is investigated when subjected to monotonic loading conditions in order to determine numerically their load-carrying capacity, nonlinear behaviour and mode of failure. Typical results obtained in the form of external load-displacement curves representing the relation between external load and the horizontal displacement of the top prism of the wall are presented in Fig. 7. Following, the monotonic-loading case studies, the specimens were analysed under cyclic loadings equivalent to those imposed in the experimental investigation. The results obtained are also presented in Fig. 7 in the form of external load-displacement curves.

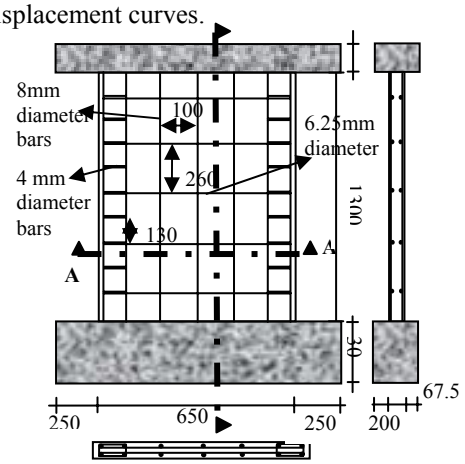

Figure 6. Arrangement of the reinforcement for the RC walls tested (dimensions in mm).

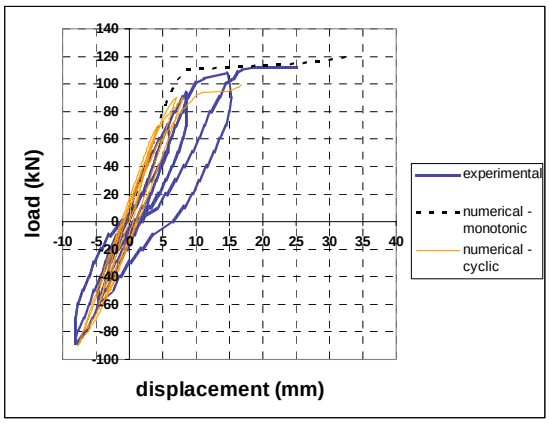

Figure 7. Load-displacement curves for the wall of Fig. 6 under static loading.

A comparison between the numerical predictions (cyclic and monotonic case studies) and experimental data is presented also in Fig. 7. From the figure, it can be seen that the value of the predicted load deviated from its experimental counterpart by around 20%. Such a deviation is comparable with the variability of the experimental data used for the derivation of the constitutive law of concrete and, hence, it is considered acceptable. On the other hand, the predicted deflections were similar to their experimental counterparts up to maximum load of the last load cycle (load cycle 5) when the specimen failed.

4.3 Three-storey structural wall under seismic excitation

Full details of the specimen and the test arrangement are provided elsewhere[20]. The RC wall had a cross-section of 900mm x 100mm and a height of 3 m. The wall corresponds to a three-story building and along its height three 12 ton masses were attached to it at approximately 1 m intervals as schematically shown in Fig. 8. Each mass (corresponding to the mass of a floor in the equivalent three-story building) was supported by a separate rigid steel three-story frame and was able to move only in the horizontal direction (so that the inertia of the masses affects only the horizontal motion of the structure). The wall was also subjected to uniaxial compressive loading, at approximately 30% of the axial compressive strength.

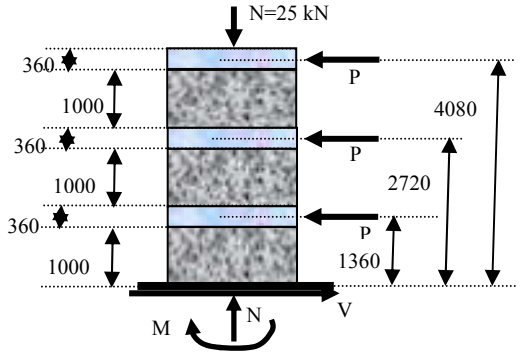

Figure 8. External loading and reactions on RC wall (dimensions in mm).

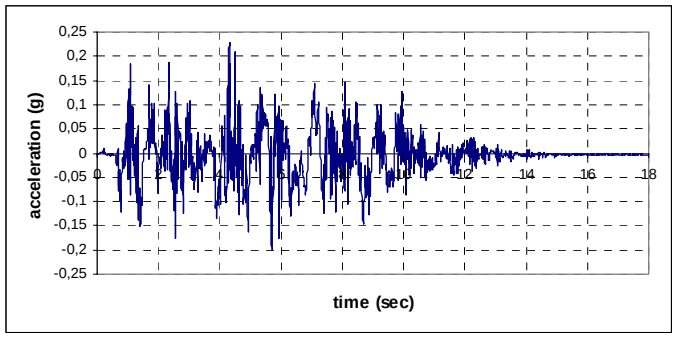

Figure 9. Acceleration record used for the analysis

Full details of the FE modelling and numerical predictions are given elsewhere[3]. Only the main results are presented herewith in a graphical form. The dynamic load was applied in the form of an acceleration record, which is presented in Fig. 9. The full response of the specimen during the experimental investigation is presented in Figs 10 and 11 in the form of displacement-time, shear-time and base moment-time curves, respectively. It can be seen from the figures that the correlation between numerical predictions and measured values is very close in all cases.

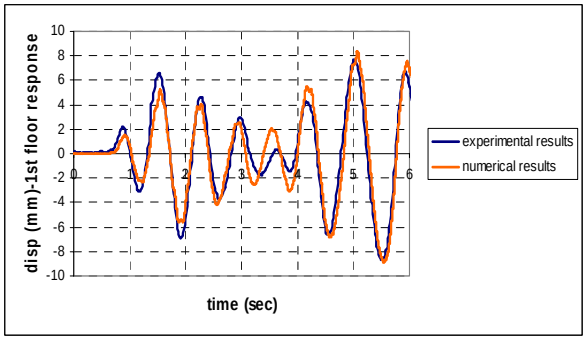

(a)

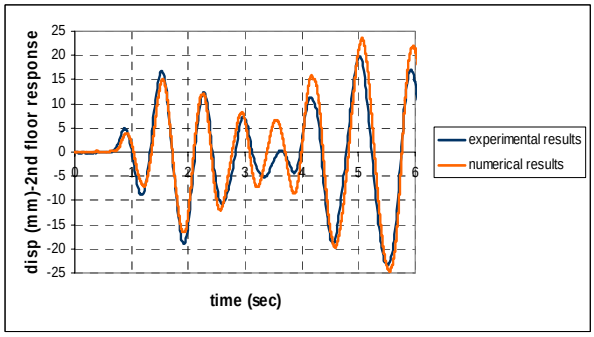

(b)

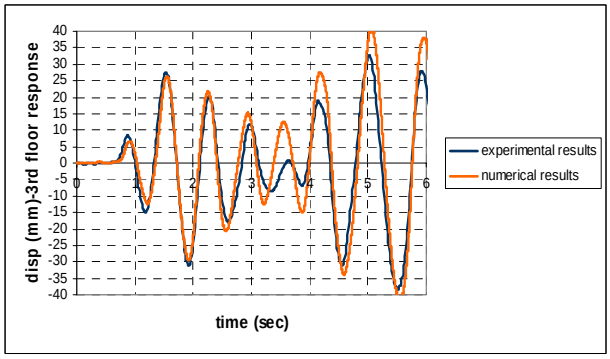

(c)

Figure 10. Numerical and experimental displacement response of (a) the first floor (b) the second floor and (c) the third floor of the RC wall under seismic excitation.

4.4 Concrete behaviour under high rates of compressive loading

The structural form which provides the basis of this investigation is a concrete prism, similar to the concrete specimens used in various experimental investigations carried out to date on this subject[2]. The prism is assumed to be fixed at its bottom face, and to be subjected to an axial load applied at its upper face through a rigid plate element with the same cross-section (see Fig. 12) imposing a uniform displacement on the upper face of the concrete prism. It is assumed that concrete and the rigid plate on the top are fully bonded at their interface. The prism height is 253mm and its cross-section forms a square with a side of 100mm, whereas the rigid plate has a height of 200mm. The uniaxial compressive strength of concrete f_c is assumed to be 30 MPa a fairly typical value in practice.

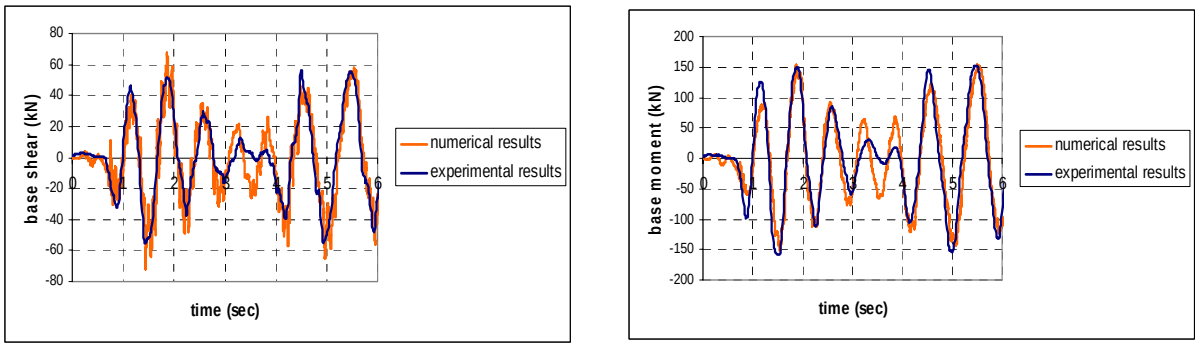

(a) (b)

Figure 11. Numerical (for C = 5 kN·m/sec) and experimental (a) base shear and (b) base moment of the RC wall under seismic excitation.

Both the concrete prism and the rigid plate are modelled by using the 27-node Lagrangian brick element. Meshes consisting of 3 (vertically)x1x1 (horizontally) and a 1x1x1 elements are adopted in order to model the concrete prism and the rigid plate, respectively. The mass of the specimen is modelled as concentrated masses either located on the FE nodes situated along the longitudinal axis of symmetry of the specimen (model A) or distributed to all FE nodes (model B). In the case of model A, only mass displacement in the direction of the applied load (i.e. along the axis of symmetry) is allowed, whereas in the case of model B, the mass is allowed all three degrees-of-freedom of the nodes. The external load is imposed as a force incrementally at the beginning of each time step. In order to vary the rate of loading, the load increments are kept constant and the time step is varied. The numerical investigation consists of two case studies. Case study 1 adopts model A whereas case study 2 relies on model B.

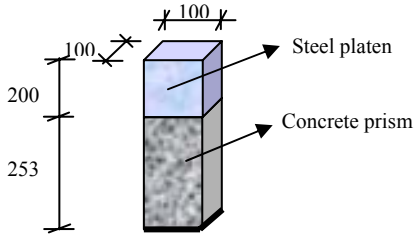

Figure 12. The specimen used for the investigation.

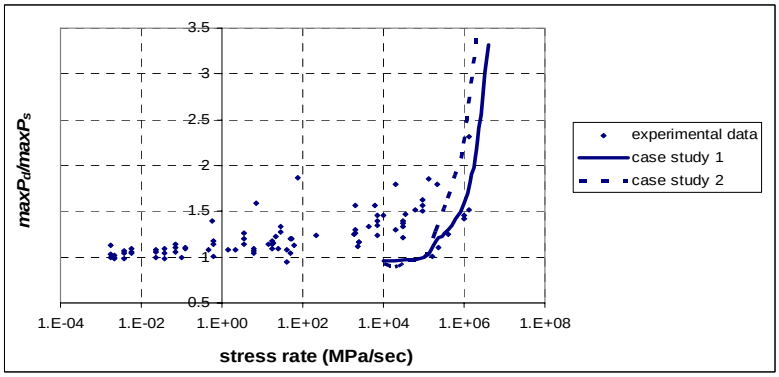

Figure 13. Variation of load-carrying capacity with the applied stress rate for concrete in uniaxial compression.

The results obtained from case studies 1 and 2 show that the behaviour of the concrete specimen under high rates of uniaxial compressive loading differs considerably compared to that exhibited under static loading. A typical indication of such difference in behaviour is shown in Fig. R13, in which it can be seen that the specimen load-carrying capacity increases as the rate of loading becomes higher. What is important to note is that he above increase in load-carrying capacity is die to the development of inertia forces the magnitude of which increases with the rate of loading and not, as widely assumed, due to the loading-rate dependence of the properties of concrete.

5. CONCLUSIONS

It appears from the above that NLFEA incorporating a brittle, triaxial model of concrete behaviour, load-path and loading rate independent is capable of yielding realistic predictions for a wide range of structural-concrete configurations subjected to any type of static and dynamic loading.

6. REFERENCES

1. Bathe K. J. (1996) *Finite Element Procedures*, Prentice Hall, Upper Saddle River, New Jersey.
2. Bischoff P. H. & Perry S. H. (1995), "Impact behaviour of plain concrete loaded in uniaxial compression". J. Eng. Mechanics 24, 425-450.
3. Cotsovos D. M. (2004), "Numerical Investigation of Structural Concrete under Dynamic (Earthquake and Impact) Loading". *PhD thesis,* University of London, UK
4. Cook, R. D., Malkus, D. S. & Plesha, M. E. (1989), *Concepts and applications of finite element analysis*, J. Wiley, New York, 2nd edition.
5. Hinton E. & Owen D. R. J. (1980), *Finite elements in plasticity: Theory and application*, Pineridge Press, Swansea.
6. Jelic I., Pavlovic M.N., and Kotsovos M.D. (2004) "Performance of structural-concrete members under sequential loading and exhibiting points of inflection". Computers and Concrete, vol. 1, no. 1, February, pp. 99-113.
7. Kotsovos M.D. (1979a), "Effect of Stress Path on the Behaviour of Concrete under Triaxial Stress States," ACI Journal, Proceedings Vol. 76, No. 2, February, pp. 213-223.
8. Kotsovos M.D. (1979b), "Fracture Processes of Concrete under Generalised Stress States," Materials & Structures, RILEM, Vol. 12, No. 72, pp. 431-437.
9. Kotsovos M.D. (1979c), "Mathematical Description of the Strength Properties of Concrete under Generalised Stress," Magazine of Concrete Research, Vol. 31, No. 108, September, pp. 151-158.
10. Kotsovos M.D. (1982), "A Fundamental Explanation of the Behaviour of Reinforced Concrete Beams in Flexure Based on the Properties of Concrete under Multiaxial Stress," Materials & Structures, RILEM, Vol. 15, No. 90, pp. 529-537.
11. Kotsovos M. D. (1983), "Effect of Testing Techniques on the Post-Ultimate Behaviour of Concrete in Compression", Materials & Structures, RILEM, Vol. 16, No. 91, pp. 3-12.
12. Kotsovos M.D. (1984), "Concrete - A Brittle Fracturing Material," Materials & Structures, RILEM, Vol. 17, No. 98, pp. 107-115.
13. Kotsovos M.D. and Newman J.B. (1977), "Behaviour of Concrete under Multiaxial Stress," ACI Journal, Proceedings Vol. 74, No. 9, pp. 453-456.
14. Kotsovos M.D. and Newman J.B. (1978), "Generalised Stress-Strain Relations for Concrete," Journal of the Engineering Mechanics Division, ASCE, Vol. 104, No. EM4, August, pp. 845-856.
15. Kotsovos M. D. and Pavlovic M. N. (1995), *Structural concrete: Finite-element analysis for limit-state design.* Thomas Telford, 550pp.
16. Kotsovos M. D. and Pavlovic M. N. (1999), *Ultimate limit-state design of concrete structures: A new approach*. Thomas Telford, 164pp.
17. Kotsovos M.D. and Spiliopoulos K.V. (1998a), "Modelling of crack closure for finite-element analysis of structural concrete." Computers and Structures, Vol. 69, pp. 383-398.
18. Kotsovos M.D. and Spiliopoulos K.V. (1998b), "Evaluation of structural-concrete design-concepts based on finite-element analysis." Computational Mechanics, Vol. 21, pp. 330-338.
19. Lefas I. (1988), "Behaviour of reinforced concrete walls and its implementation for ultimate limit state design", *Ph.D. Thesis*, University of London.
20. Lestuzzi P., Wenk T. and Bachmann H. (1999) "Dynamic Tests of RC Structural Walls on the ETH Earthquake Simulator". IBK Report No. 240, Institüt für Baustatik und Konstruktion: ETH, Zurich.
21. van Mier J. G. M. (1986), "Multiaxial strain-softening of concrete", Materials & Structures, RILEM. Vol. 19, No. 111, pp. 179-200.
22. van Mier J.G.M; Shah S.P.; Arnaud M.; Balayssac J.P.; Bassoul A.; Choi S.; Dasenbrock D.; Ferrara G.; French C.; Gobbi M.E.; Karihaloo B.L.; Konig G.; Kotsovos M.D.; Labnz J.; Lange-Kornbak D.; Markeset G.; Pavlovic M.N.; Simsch G.; Thienel K-C.; Turatsinze A.; Ulmer M.; van Vliet M.R.A.; and Zissopoulos D. (1997), (TC 148-SSC: Test methods for the strain-softening of concrete). "Strain-softening of concrete in uniaxial compression". Materials & Structures RILEM, Vol. 30, No. 198, pp. 195-20.
23. Willam K. J. and Warnke E. P. (1974) "Constitutive model for the triaxial behaviour of concrete". *Seminar on Concrete Structures Subjected to Triaxial Stresses.*Instituto Sperimentale Modeli e Strutture, Bergamo, May, Paper III-1.
24. Zienkiewicz O. C. (1971), *The Finite Element Method in Engineering Science*, McGraw-Hill, London, 2nd edition.

MODELING OF THE BEHAVIOR OF ULTRA-HIGH STRENGTH FIBER REINFORCED CONCRETE BY MEANS OF NONCONVEX ENERGY SUPERPOTENTIALS

E.S. Mistakidis*, O.K. Panagouli

* Laboratory of Structural Analysis and Design, Department of Civil Engineering,
University of Thessaly
Pedion Areos, 383 34 Volos, Greece
e-mail: emistaki@uth.gr

Keywords: High performance concrete, composite materials, nonconvex optimization.

Abstract. *In this paper, the bending behavior of ultra-high strength fiber reinforced concrete is studied within a nonsmooth mechanics framework. The material, which has properties that classify it in the range of ultra-high strength concretes, is a composite one, consisting of a cementitious matrix reinforced by steel fibers. The scope of the paper is to model the nonlinear bending response of the composite material by means of a nonconvex energy mininization approach. For this reason, the response of each one of the constituent materials is modeled by means of monotone or nonmonotone, possibly multivalued constitutive laws. The numerical investigations presented in the paper, shed light into the complex behavior of the composite structural elements.*

1 INTRODUCTION

The ability to design structural elements with greater strength and ductility to resist seismic loads is an increasingly important civil engineering need. For this reason, several approaches have been followed during the past decades leading to materials with exceptional properties, as e.g. high strength steels and ultra high strength concretes. In Greece, it is of major interest the application of materials with exceptional properties for seismic applications, particularly for retrofitting of existing structures. Using for example ultra high strength concrete (compressive strength greater than 100 Mpa) for the construction of additional elements (walls, frames etc.) that undertake the seismic forces in rather weak existing buildings, the design engineer can avoid the massive structural elements that reduce the floor space and cause, in some cases, excessive increase of the total mass of the building.

Recognizing the above need, the Greek cement company ΑΓΕΤ, decided to fund the development of a new material with exceptional properties that will be used primarily for retrofitting of existing structures. The project is co-funded by the General Secretariat of Research and Technology within the ΕΠΑΝ framework and is supervised by the first author.

Till now, the result of the project is a fiber reinforced composite material, which has a cementitious base. Specimens of the new material have been tested experimentally with very promising results. The compressive strength is of the order of 110 Mpa, while the bending strength is more than 6 Mpa. This bending strength has its nature to the tensile strength of the cementitious matrix, however, the fracture of the matrix is brittle, giving rise to a stress-strain law of the type shown in Figure 1. On the other hand, the ductility that was observed even from the first tests has its nature to the presence of the steel fibers which either break or pull-off from the matrix. Both mechanisms are ductile.

The type of laws appearing in the composite material developed for the needs of the project are a special case of a more general family of mechanical laws, called nonmonotone, multivalued laws. In [1], [2], [3], [4], [5], it is shown that this type of laws gives rise to a new type of variational forms expressed by inequalities, called hemivariational inequalities. Hemivariational inequalities express the ``principle'' of virtual or complementary virtual work in inequality form. The theory of hemivariational inequalities leads to the conclusion that local minima of the potential or the complementary energy functional represent equilibrium positions of the structure. However, it is possible, that certain solutions of the problem may not be local minima but another more general type of points which make the potential or the complementary energy ``substationary'' [4], [6].

Although the formulation of a nonmonotone problem as a hemivariational inequality has many advantages concerning its mathematical study that makes possible significant progress in this area [4], [7], [8] this progress has not yet been matched by similar developments of the numerical approximation methods. Indeed, the numerical determination of all local minima of a nonconvex function is still an open problem in numerical

optimization [9].

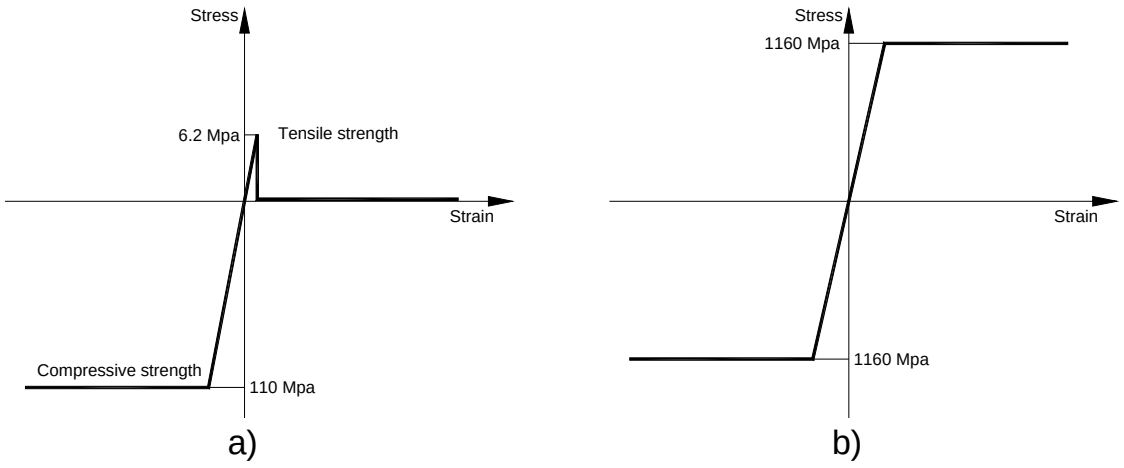

Figure 1. Stress-strain laws for a) the cementitious matrix and b) the steel fibers

The objective of the paper is to model the nonlinear bending response of the composite material by means of a nonconvex energy mininization approach. For this reason, the response of each one of the constituent materials is modeled by means of monotone or nonmonotone, possibly multivalued constitutive laws. The properties of each one of the constituent materials are determined by means of experimental testing. Then, a non-differentiable and nonconvex (due to degradation effects) potential energy is formulated for the whole mechanical system. For the structural analysis problem the potential energy minimization problem is considered. The arising variational or hemivariational (in the case of nonmonotone laws) inequality problems are solved by appropriate nonconvex-nonsmooth computational mechanics techniques developed by the first author [6].

The results obtained by the above numerical model are compared against those obtained by bending tests of specimens of the composite material. The numerical investigations presented in the paper, shed light into the complex behavior of the composite structural elements.

2 THEORETICAL FORMULATION

An elastic structure with both classical, linearly elastic and degrading elements is considered. The static analysis problem is described by the following relations:

- *Stress equilibrium equations*:

$$\overline{\mathbf{G}}\overline{\mathbf{s}} = \begin{bmatrix}\mathbf{G} & \mathbf{G}_n\end{bmatrix}\begin{bmatrix}\mathbf{s}\\ \mathbf{s}_n\end{bmatrix} = \mathbf{p} \tag{1}$$

where $\overline{\mathbf{G}}$ is the equilibrium matrix of the discretized structure which takes into account the stress contribution of the linear $\mathbf{s}$ and nonlinear $\mathbf{s}_n$ elements and $\mathbf{p}$ is the loading vector.

- *Strain–displacements compatibility equations:*

$$\bar{\mathbf{e}} = \overline{\mathbf{G}}^T\mathbf{u} \text{ or explicitly} \begin{bmatrix}\mathbf{e}\\ \mathbf{e}_n\end{bmatrix} = \begin{bmatrix}\mathbf{G}^T\\ \mathbf{G}_n^T\end{bmatrix}\mathbf{u} \tag{2}$$

where e, u are the deformation and displacement vectors respectively.

- *Linear material constitutive law* for the structure :

$$\mathbf{s} = \mathbf{K}_0(\mathbf{e} - \mathbf{e}_0), \tag{3}$$

where $\mathbf{K}_0$ is the natural and stiffness flexibility matrix and $\mathbf{e}_0$ is the initial deformation vector.

- *Monotone and nonmonotone, superpotential constitutive laws* for the nonlinear elements:

$$\mathbf{s}_n \in \partial \phi_n(\mathbf{e}_n). \tag{4}$$

Here $\phi_n(.)$ is a general nonconvex and nondifferentiable potential which produces the law (4) by means of an appropriate generalized differential, set–valued operator ∂ (see, e.g., [1]). Summation over all nonlinear elements gives the total strain energy contribution of them as:

$$\Phi_n(\mathbf{e}_n) = \sum_{i=1}^{q} \phi_n^{(i)}(\mathbf{e}_n). \tag{5}$$

- Classical support *boundary conditions* (b.c's.).

For the variational formulations of the problem the *virtual work* equation is first formulated in a discretized form:

$$\mathbf{s}_T(\mathbf{e}^* - \mathbf{e}) + \mathbf{s}_n^T(\mathbf{e}_n^* - \mathbf{e}_n) = \mathbf{p}^T(\mathbf{u}^* - \mathbf{u}), \forall \mathbf{e}^*, \mathbf{u}^*, \mathbf{e}_n^* \quad \text{s.t. (2) b.c's.} \tag{6}$$

Entering the elasticity law (3) into the virtual work equation (6), and using (2) we get:

$$\mathbf{u}^{\mathrm{T}}\mathbf{G}\mathbf{K}_0^{\mathrm{T}}\mathbf{G}^{\mathrm{T}}(\mathbf{u}^* - \mathbf{u}) - (\mathbf{p} + \mathbf{G}\mathbf{K}_0\mathbf{e}_0)^{\mathrm{T}}(\mathbf{u}^* - \mathbf{u}) + \mathbf{s}_{\mathrm{n}}^{\mathrm{T}}(\mathbf{e}_{\mathrm{n}}^* - \mathbf{e}_{\mathrm{n}}) = 0, \forall \mathbf{u}^* \in \mathrm{V}_{\mathrm{ad}} = \{\mathbf{v} \in \mathbb{R}^{\mathrm{n}} \mid (2)\ \mathrm{b.c's.\ hold}\}, \tag{7}$$

Where $\mathbf{K} = \mathbf{G}^{\mathrm{T}}\mathbf{K}_0^{\mathrm{T}}\mathbf{G}$ denotes the stiffness matrix of the structure and $\bar{\mathbf{p}} = \mathbf{p} + \mathbf{G}\mathbf{K}_0\mathbf{e}_0$ denotes the nodal equivalent loading vector.

At this point we use the weak form of the nonlinear law (4), i.e.

$$\mathbf{s}_n^T(\mathbf{e}_n^* - \mathbf{e}_n) \le \Phi_n^o(\mathbf{e}_n^* - \mathbf{e}_n), \forall \mathbf{e}_n^* \tag{8}$$

where $\Phi_n^o(\mathbf{e}_n^* - \mathbf{e}_n)$ is the directional derivative of the potential Φ_n or, in terms of mechanics the virtual work of the nonlinear structural elements for a small deformation equal to $\mathbf{e}_n^* - \mathbf{e}_n$. Thus the following *hemivariational inequality* is obtained:

Find kinematically admissible displacements $\mathbf{u} \in V_{ad}$ such that

$$\mathbf{u}^T\mathbf{K}(\mathbf{u}^* - \mathbf{u}) - \bar{\mathbf{p}}^T(\mathbf{u}^* - \mathbf{u}) + \Phi_n^o(\mathbf{u}_n^* - \mathbf{u}_n) \ge 0, \forall \mathbf{u}^* \in V_{ad}. \tag{9}$$

Equivalently the potential energy should be stationary at equilibrium, i.e. the structural analysis problem reads:

Find $\mathbf{u} \in V_{ad}$ such that:

$$\Pi(\mathbf{u}) = \underset{\mathbf{v} \in V_{ad}}{\mathrm{stat}} \left\{ \Pi(\mathbf{v}) = \frac{1}{2}\mathbf{v}^T\mathbf{K}\mathbf{v} - \bar{\mathbf{p}}^T\mathbf{v} + \Phi_n(\mathbf{v}) \right\}. \tag{10}$$

3 ALGORITHMIC APPROXIMATION OF THE NONCONVEX- NONSMOOTH OPTIMIZATION PROBLEM

The aim of this section is to bypass the nonconvex substationarity problem (10) by minimizing a sequence of appropriately defined convex functions in which the nonconvex potential $\Phi_n(\mathbf{v})$ has been substituted with the convex potential $p(\mathbf{v})$. We consider first the following minimization problems

$$\min\{\frac{1}{2}\mathbf{v}^T\mathbf{K}\mathbf{v} - \bar{\mathbf{p}}^T\mathbf{v} + p^{(i)}(\mathbf{v})\} \tag{11}$$

where in each step the convex potential $p^{(i)}(\mathbf{v})$ is selected such as the following relation is fulfilled:

$$\partial p^{(i)}(\mathbf{v}^{(i-1)}) = \bar{\partial}\Phi_n(\mathbf{v}^{(i-1)}). \tag{12}$$

If the nonconvex minimization problem is written in the form

$$\min\{\Pi(\mathbf{v})\} = \min\left\{\frac{1}{2}\mathbf{v}^T\mathbf{K}\mathbf{v} - \bar{\mathbf{p}}^T\mathbf{v} + p(\mathbf{v}) + [\Phi_n(\mathbf{v}) - p(\mathbf{v})]\right\} \tag{13}$$

then we can write the following minimization problems

$$\begin{aligned}
\min\{\Pi^{(1)}(\mathbf{v})\} &= \min\left\{\frac{1}{2}\mathbf{v}^T\mathbf{K}\mathbf{v} - \bar{\mathbf{p}}^T\mathbf{v} + p^{(1)}(\mathbf{v}) + [\Phi_n(\mathbf{v}^{(0)}) - p^{(1)}(\mathbf{v}^{(0)})]\right\} \\
&\vdots \\
\min\{\Pi^{(i)}(\mathbf{v})\} &= \min\left\{\frac{1}{2}\mathbf{v}^T\mathbf{K}\mathbf{v} - \bar{\mathbf{p}}^T\mathbf{v} + p^{(i)}(\mathbf{v}) + [\Phi_n(\mathbf{v}^{(i-1)}) - p^{(i)}(\mathbf{v}^{(i-1)})]\right\} \\
&\vdots \\
\min\{\Pi^{(n)}(\mathbf{v})\} &= \min\left\{\frac{1}{2}\mathbf{v}^T\mathbf{K}\mathbf{v} - \bar{\mathbf{p}}^T\mathbf{v} + p^{(n)}(\mathbf{v}) + [\Phi_n(\mathbf{v}^{(n-1)}) - p^{(n)}(\mathbf{v}^{(n-1)})]\right\}
\end{aligned} \tag{14}$$

If we suppose that in the last case we have the convergence of the iterative scheme then we have that $|\mathbf{v}^{(n)} - \mathbf{v}^{(n-1)}| \leq \varepsilon$. Due to (12) the variation of the last term of (14) with respect to $\mathbf{v}$ becomes very small and finally we can write

$$\operatorname{argmin}\{\Pi(\mathbf{v})\} = \operatorname{argmin}\left\{\frac{1}{2}\mathbf{v}^T\mathbf{K}\mathbf{v} - \bar{\mathbf{p}}^T\mathbf{v} + p^{(n)}(\mathbf{v})\right\} \tag{15}$$

where in the left hand side we mean the local minimum sought. By means of the previous relations it is easily verified that a solution of the initial minimization problem of $\Pi(\mathbf{v})$ is obtained using the proposed iterative scheme but the full proof of convergence remains still an open problem. However, in the various numerical experiments we have performed, convergence was always achieved. Therefore, the following heuristic algorithm is formulated:

1. Select a starting point $\mathbf{v}^{(0)}$ and initialize i to 1.
2. For the point $\mathbf{v}^{(i)}$ select a convex superpotential $p^{(i)}$ such that relation (12) is fulfilled.
3. Find the minimum $\mathbf{v}^{(\mathbf{i})}$ of the convex superpotential
   $\frac{1}{2}\mathbf{v}^T\mathbf{K}\mathbf{v} - \bar{\mathbf{p}}^T\mathbf{v} + p^{(i)}(\mathbf{v})$
4. If $|\mathbf{v}^{(i)} - \mathbf{v}^{(i-1)}| \leq \varepsilon$ where ε is an appropriate small number then a substationarity point of (10) has been determined and terminate the algorithm, else set $i = i + 1$ and repeat Step 2.

In an engineering problem where a one-dimensional nonmonotone stress-strain law $h(\mathbf{v})$ is involved, the process in Step 2 of the above algorithm is an easy task since one has to select a monotone law $g(\mathbf{v})$ such that $g(\mathbf{v}^{(i)}) = h(\mathbf{v}^{(i-1)})$. In general, the convex superpotentials that approximate the nonconvex superpotentials are selected in such a way that the computational effort is minimum. This task depends on the particular nonmonotone potentials to be approximated. Notice also that different starting points for the above algorithm may lead to different substationarity points of the nonconvex superpotential.
More general types of algorithms and the relation with other nonsmooth computational mechanics methods are discussed in [6].

4 EXPERIMENTAL TESTING

The main objective of the experimental tests performed until now is to determine the load-deflection behaviour of specimens with dimensions 10x10x50cm. The specimens are submitted in the so-called four-point bending test. The distance between the supports is 30cm. The specimen is loaded in two points dividing the length between the supports in three equal parts, as shown in Figure 2.

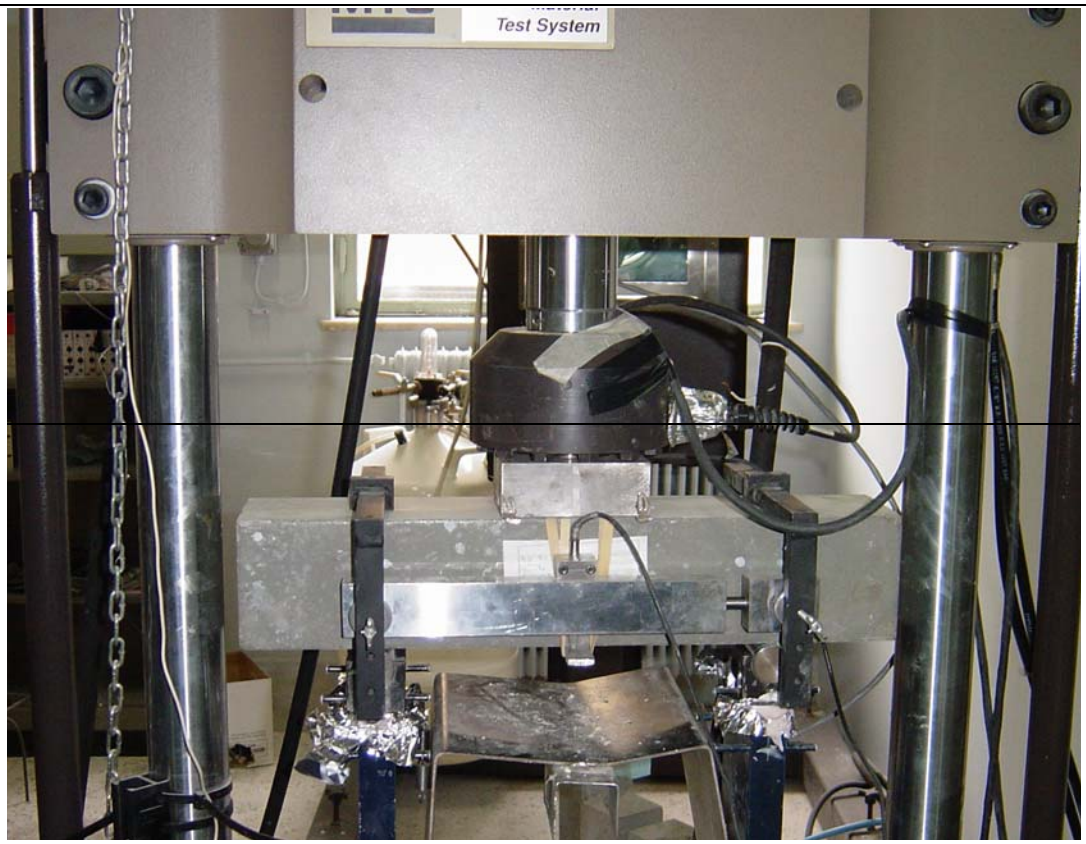

Figure 2. The setup of the four-point bending tests

The applied load and the maximum displacement in the middle of the specimen are recorded electronically. All the experimentally obtained load-deflection curves have a similar shape as the one shown in Figure 3. It is interesting to notice in this figure the vertical branches that have their nature in the sudden loss of the tensile strength of the cementitious matrix and the transfer of the corresponding load to the steel fibers.

It is also interesting to notice the great deformation capacity of the specimen which is the result of the use of the steel fibers. Similar tests in specimens made from the cementitious matrix alone (without steel fibers) show a brittle behavior just after the tensile strength of the concrete is exhausted (see Figure 4).

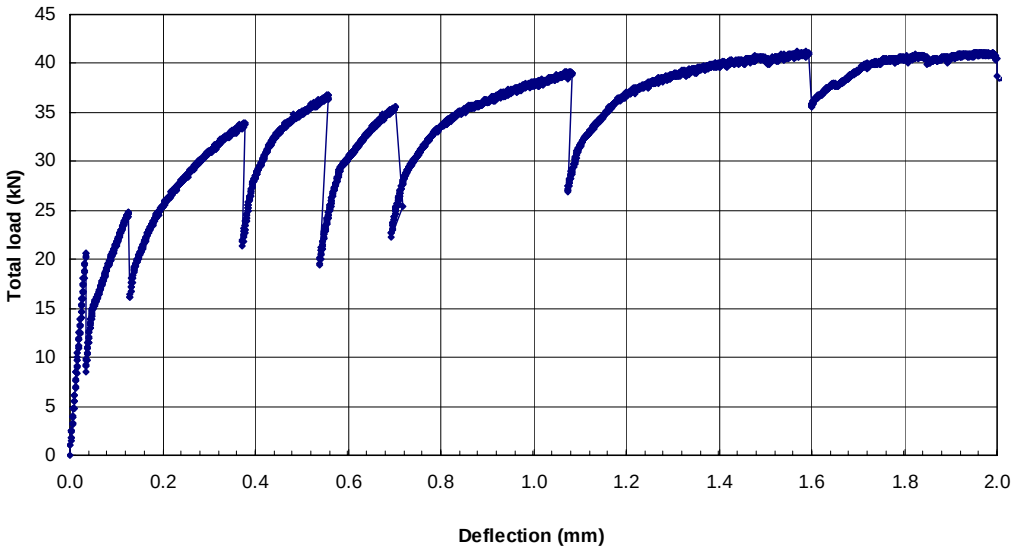

Figure 3. Load-deflection curve obtained experimentally in fiber-reinforced specimens

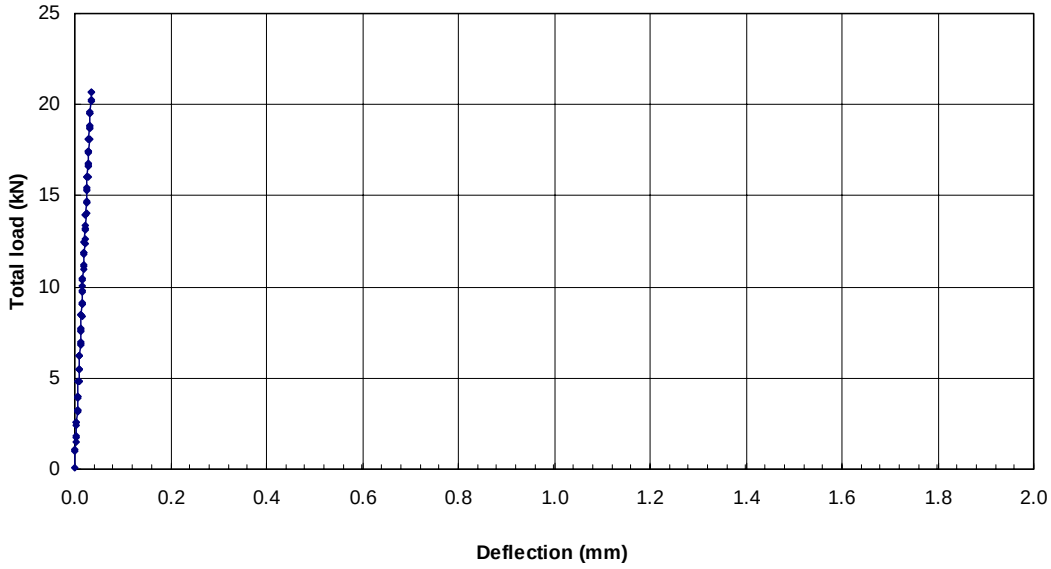

Figure 4. Load-deflection curve obtained experimentally in specimens without fibres

5 NUMERICAL SIMULATION USING NONCONVEX OPTIMIZATION

In order to simulate the four-point bending tests, the model of Figure 5 was used. In this model, only half of the real specimen is modeled, by realizing appropriate symmetry conditions at the right edge. The model is simulated by truss elements (parallel to the x-axis) which actually consist of two coupled elements, one representing the cementitious matrix and one representing the steel fibers. Ten (10) parallel layers are used for the modeling, which provide sufficient accuracy for the simulation of the bending behavior. The parallel truss elements are connected regularly with rigid bars which enforce the Bernoulli beam conditions (deformed cross section remains plane). Moreover, diagonal elements are used in order to take into account the shear mechanism.

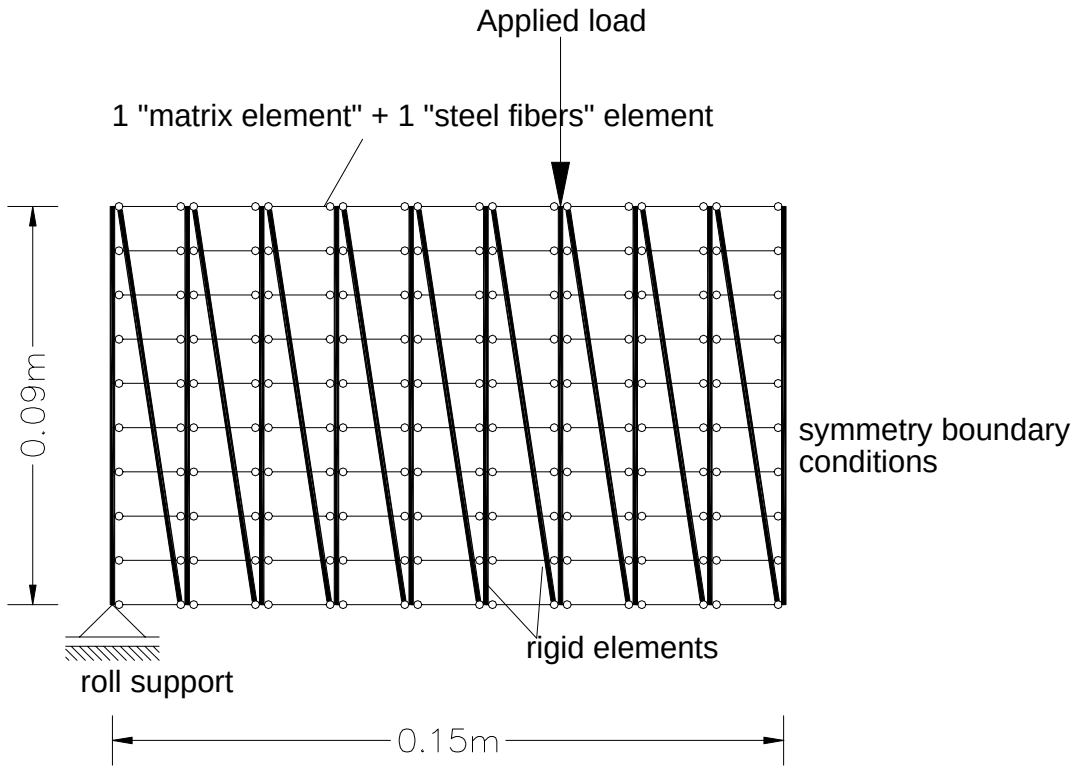

Figure 5. The model used for the simulation of the experiments

The elements representing the cementitious matrix have a constant rectangular cross-sectional area equal to 0.1x0.01m. The compressive strength of the matrix is equal to 110Mpa, while the tensile strength of the matrix was calculated from the bending strength of the unreinforced specimens and was equal to 6.2 Mpa. Therefore, the elements representing the cementitious matrix are assumed to obey to the simplified law of Figure 1a. The elasticity modulus was calculated experimentally and set to $E_c = 3.35 \times 10^7 \, kN/m^2$.

The cross sectional area of elements representing the steel fibers is calculated from the fiber content of the composite material which is 63.1g/l. This leads to a geometrical percentage of 0.8%. Moreover, due to the fact that the fibers are randomly oriented in three directions, an efficiency factor of 0.5 is used according to [10]. Therefore, the elements representing the steel fibres that exist in the 0.1x0.01m cross section of the cementitious matrix, have a cross-sectional area of $0.1 \times 0.01 \times 0.008 \times 0.5 = 4 \times 10^{-6}$ m^2. The yield strength of the steel fibers is 1400 Mpa, however, it is assumed that the fibers cannot attained their ultimate stress due to the onset of slippage between the steel fiber and the matrix. An efficiency factor equal to 0.83 is used giving rise to the simplified material law shown in Figure 1b. The elasticity modulus was taken equal to $E_s = 2.1 \times 10^8 \, kN/m^2$.

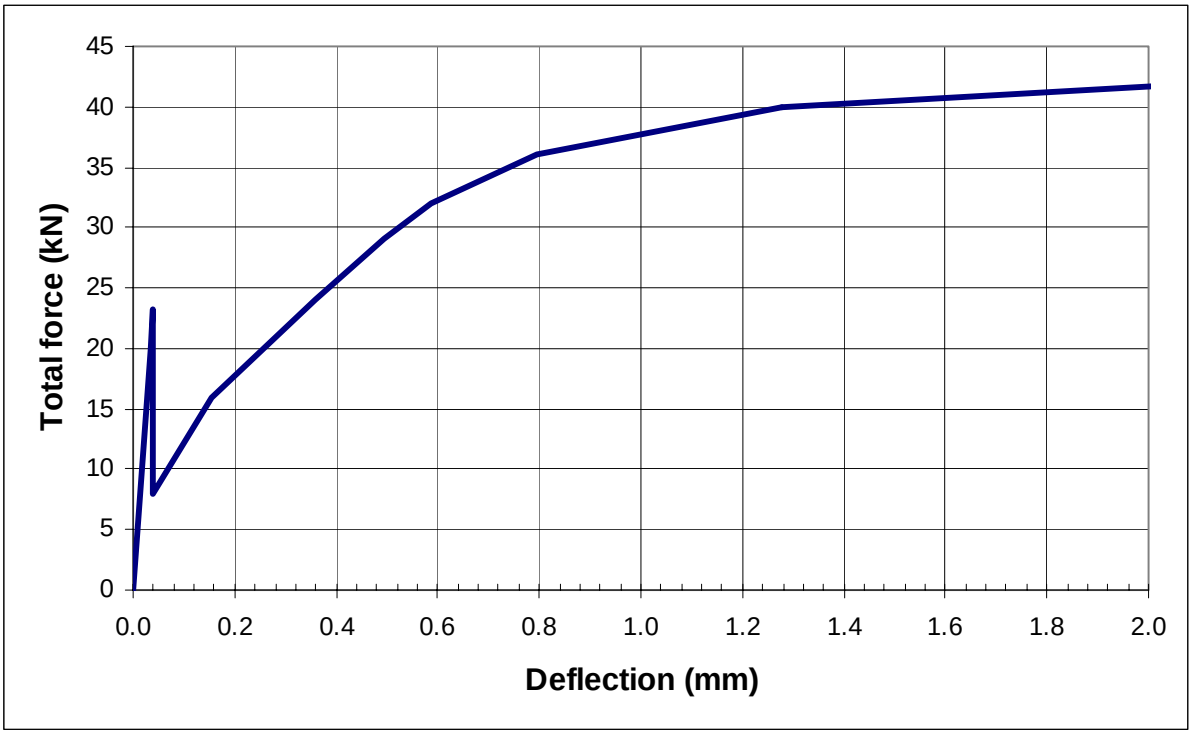

Figure 6. Load-deflection curve obtained numerically

The above model was analyzed using the algorithm outlined in the previous Section. Due to the particular characteristics of the problem (multiple minima for the same load level), different starting points had to be defined in order to obtain the points beyond the breaking of the cementitious matrix. The obtained load-deflection curve is depicted in Figure 6 and resembles closely the load-deflection curve obtained experimentally (Figure 3). The basic difference between the two curves is that the curve obtained numerically can capture accurately only the position of the first crack, as the numerical model used here cannot take into account multiple crack openings. However, the predicted first crack load and the predicted ultimate load match closely the experimentally obtained values.

Concerning the efficiency of the proposed numerical schemes, the algorithm converged quickly to the solution of the problem. All the load cases were solved within 2-3 steps of the iterative algorithms presented in the previous section with a relative accuracy of 10^{-4} with respect to a second order norm of the displacements, i.e. the algorithms are assumed to converge when $\dfrac{\mathbf{v}^{(i)} - \mathbf{v}^{(i-1)}}{\mathbf{v}^{(i)}} < 10^{-4}$

ACKNOWLEDGEMENTS

The authors acknowledge with thanks the financial support from the General Secretariat of Research and Technology in the framework of the project “Development, pilot production and trial application of new generation composite materials based upon cement for the improvement of the seismic structural behavior”.

REFERENCES

[1] Panagiotopoulos, P.D. (1985), *Inequality problems in mechanics and applications. Convex and nonconvex energy functions*, Birkhauser, Basel - Boston - Stuttgart,1985. Russian translation, MIR Publ., Moscow 1988.

[2] Panagiotopoulos, P.D. (1993), *Hemivariational inequalities. Applications in mechanics and engineering*, Springer, Berlin - Heidelberg - New York.

[3] Panagiotopoulos, P.D. (1983), "Nonconvex energy functions. Hemivariational inequalities and substationary principles", Acta Mechanica, 42, pp. 160-183.

[4] Panagiotopoulos, P.D. (1991), "Coercive and semicoercive hemivariational inequalities", Nonlin. Anal. Theo. Meth. Appl., 16, pp. 209-231.

[5] Panagiotopoulos, P.D. (1988), Nonconvex superpotentials and hemivariational inequalities. Quasi-diferentiability in mechanics, In Moreau, J.J. and Panagiotopoulos, P.D. editors, *Nonsmooth Mechanics and Applications*, volume 302 of CISM Lecture Notes, pp. 83--176. Springer, Wien - New York.

[6] Mistakidis, E.S. and Stavroulakis, G.E. (1997), *Nonconvex optimization in Mechanics. Algorithms, heuristics and engineering application by the F.E.M.*, Kluwer, Boston.

[7] Moreau, J.J., Panagiotopoulos, P.D. and Strang, G. (editors), (1988), *Topics in nonsmooth mechanics* Birkhauser, Basel-Boston.

[8] Naniewicz, Z. (1989), "On some nonconvex variational problems related to hemivariational inequalities", Nonlin. Anal., 13, pp. 87-100.

[9] Fletcher, R. (1990), *Practical methods of optimization*, J. Wiley, Chichester.

[10] J.M. Illston (editor) (1990), *Construction materials. Their nature and behaviour*. E&FN Spon, London and New York.

ABSORBING BOUNDARY CONDITIONS AND PERFECT MATCHED LAYER MODELS FOR PLANE SOIL-STRUCTURE INTERACTION PROBLEMS

Fotini E. Michou and Vlasis K. Koumousis

Institute of Structural Analysis and Aseismic Research
National Technical University of Athens
NTUA, Zografou Campus GR-15773, Athens, Greece
e-mail: vkoum@central.ntua.gr, web page: http://users.ntua.gr/vkoum

Keywords: wave propagation, absorbing boundary conditions, reflected waves, dashpot.

Abstract. *Solution of the wave equation over unbounded domains is of interest in various fields of both science and engineering. In particular, solution of the elastodynamic wave equation on an unbounded domain finds applications in soil-structure interaction analysis and in the simulation of earthquake ground motion, considering the ground as an unbounded elastic domain. In complex configurations usually a Finite Element solution of the problem requires the use of a bounded domain, along with an absorbing boundary that imposes the radiation condition i.e. no incoming waves at infinity. Among the various methods of imposing the Absorbing Boundary Condition (ABC) the simplest one is the use of dashpots in both directions according to the suggestion of Lysmer & Kuhlemeyer. A more efficient approach is to employ the notion of Perfect Matched Layer (PML) consisting of the same material, but having attenuation characteristics that damp the outgoing and reflected wave within the layer thickness. Thus, wave propagation in an unbounded domain can be modeled through a bounded domain surrounded by a suitably defined PML capable to absorb the incoming waves. A comparative study of both methods is performed on a number of simple problems to reveal their special features and characteristics.*

1 INTRODUCTION

Solution of a wave equation in an unbounded domain requires the enforcement of a radiation condition in any unbounded direction. Irregularities in the geometry of the domain, or in the material, often compel a numerical solution of the problem using FEM, thus requiring the use of a bounded domain, along with an artificial boundary, that absorbs outgoing waves.

A perfectly matched layer (PML) is an absorbing boundary layer for linear wave equations that absorbs, almost perfectly, propagating waves of all non-tangential angles of incidence and of all non-zero frequencies. The concept of a PML was introduced in the context of electromagnetic waves by Berenger [1]. Since its introduction, extensive research has been done on various aspects of PMLs for electromagnetic waves.

The simple problem of propagation of longitudinal waves in a restrained elastic rod, is first introduced to demonstrate all relevant concepts and features of both the ABC and PML methods. Then, the concept of a PML is developed in the field of time-harmonic elastodynamics in Cartesian coordinates [2-4], and the effect of various parameters on the accuracy of dynamic stiffness is examined. Finally, the response of the PML at complex conditions is verified through a FEM implementation, using Abaqus code. The PML concept is illustrated through the one-dimensional example of a rod on elastic foundation, which studied through analytical results for the dynamic stiffness. The PML for plane-strain is also demonstrated. Numerical results are presented for the soil-structure interaction problems in the plane of a rigid strip-footing on a half-plane.

2 ABSORBING BOUNDARY CONDITIONS

2.1 Longitudinal waves in an elastically restrained rod

For the rod as shown in Fig. 1, it is assumed that the longitudinal displacement of each section is given by $u(x,t)$. Moreover, the rod is subjected to a dynamically varying stress field $\sigma(x,t)$. The rod is restrained by linear springs and visco-elastic dampers characterized by the material constants k_e and e, respectively [5]. The equation of motion is the following:

$$-\sigma A + (\sigma + \frac{\partial \sigma}{\partial x} dx)A - k_e u dx - e\frac{\partial u}{\partial t} dx - \rho A \frac{\partial^2 u}{\partial t^2} dx = 0 \qquad (1)$$

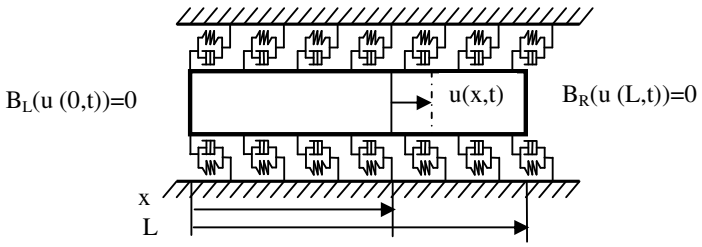

Figure 1. Model of an elastically restrained rod

For a linear elastic material Hooke's law is given by the equation $\sigma = \mathrm{E}u_{,x}$, and the equation of motion becomes:

$$AE\frac{\partial^2 u}{\partial x^2} = \rho A\frac{\partial^2 u}{\partial t^2} + k_e u + e\frac{\partial u}{\partial t} \quad or \quad \frac{\partial^2 u}{\partial x^2} = \frac{1}{c^2}\frac{\partial^2 u}{\partial t^2} + \kappa^2 u + 2\frac{\varepsilon}{c}\frac{\partial u}{\partial t} \tag{2}$$

where the parameters c, κ and ε are defined as $c = \sqrt{E/\rho}$, $\kappa = \sqrt{k_e/EA}$ and $\varepsilon = ec/2EA$, respectively. For the outgoing waves the solution is of the following form:

$$u(x,t) = u_o e^{-ikx+i\omega t} \tag{3}$$

where ω is the circular frequency and k is the wave number. Substitution of relation (3) in relation (2) gives which the dispersion relation which associates the wave number with circular frequency ω.

$$k = \pm\frac{1}{c}\sqrt{\omega^2 - \kappa^2 c^2 - 2i\varepsilon\omega c} \tag{4}$$

The dispersion relation expresses the equation of motion in the frequency domain and can be used to analyze the propagation of wavetrains within the medium. The wave number is a complex number and is given by $k = k_R + ik_I$, where k_R represents the real part and k_I the imaginary part.

$$\begin{aligned} k_I &= -\frac{1}{\sqrt{2}c}\sqrt{\kappa^2 c^2 - \omega^2 + \sqrt{\kappa^4 c^4 - 2\kappa^2 c^2\omega^2 + \omega^4 + 4c^2\varepsilon^2\omega^2}} \\ k_R &= \frac{\varepsilon\omega\sqrt{2}}{\sqrt{\kappa^2 c^2 - \omega^2 + \sqrt{\kappa^4 c^4 - 2\kappa^2 c^2\omega^2 + \omega^4 + 4c^2\varepsilon^2\omega^2}}} \end{aligned} \tag{5}$$

The general solution of the wave equation (2) consists of two parts, a wavetrain traveling in the positive and another traveling in the negative direction. These are associated with the two roots of the dispersion relation (4). The graphs of $k_R(\omega)$ and $k_I(\omega)$ are shown in Figure 2 as function of ω. For $\omega \to \infty$ the imaginary part converges *to* $k_I(\omega) = -\varepsilon$. At $\omega_c = \kappa c$ the wave number $k(\omega)$ changes from a purely imaginary to a purely real function. In the frequency domain for $\omega > \kappa c$, $k_I = 0$ the harmonic wave is propagating. In the frequency domain where $\omega < \kappa c$, $k_R = 0$ and there is no wave propagation or evanescent mode, because the amplitude of the oscillation decays with increasing x.

2.2 Reflection of Waves at the Boundary and Exact Absorbing Boundary Conditions

For a finite rod of length L, there exists a solution in the form:

$$u(x,t) = A_1 e^{i\omega t - ikx} + A_2 e^{i\omega t + ikx} \tag{6}$$

The coefficients A_1 and A_2 are determined from the boundary conditions which are:

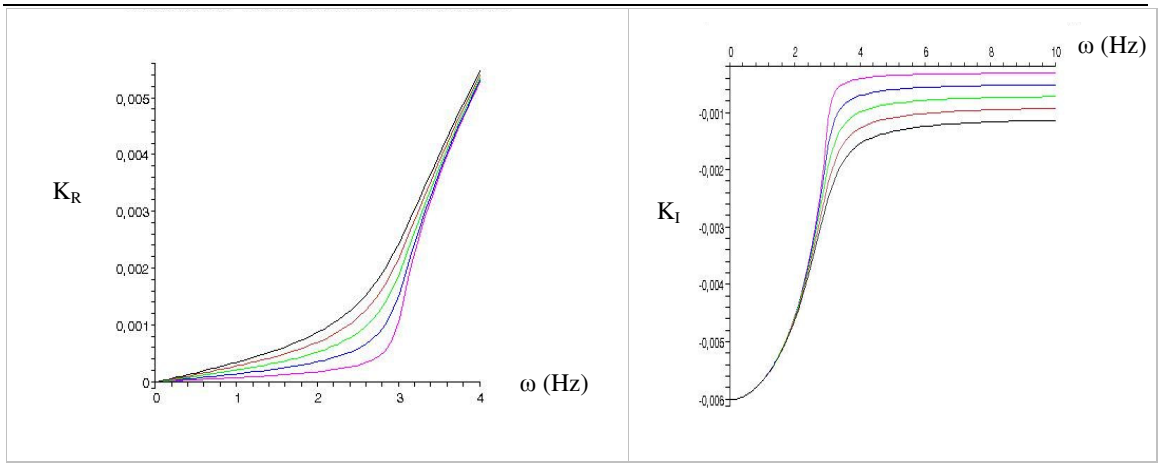

Figure 2. Real and imaginary part of the positive root of the dispersion relation (c=500 and κ=0.006)

$$u(0) = u_o \tag{7}$$

$$\sigma(L,t) = Eu_{,x}(L,t) = \frac{F(t)}{A} = f(t) \tag{8}$$

where equation (8) expresses the Neumann boundary condition at x=L. Considering the function *f(t)* as $f(t) = -\int_{-\infty}^{t} G(t-\tau)u(L,t)dt = \frac{F(t)}{AE} = u_{,x}(L,t)$, the boundary condition (8) becomes:

$$\left[\frac{\partial u}{\partial x}\right]_{x=L} + g(\omega)u(L) = 0 \tag{9}$$

where the function $g(\omega)$ is the Fourier-transform of $G(t)$. Combining relations (6) with (7) and (9) the following expressions are obtained:

$$A_1 = u_o - \frac{u_o(ik - g(\omega))e^{i\omega t - ikL}}{ike^{i\omega t - ikL} + ike^{i\omega t + ikL} - g(\omega)e^{i\omega t - ikL} + g(\omega)e^{i\omega t + ikL}}$$
$$A2 = \frac{u_o(ik - g(\omega))e^{i\omega t - ikL}}{ike^{i\omega t - ikL} + ike^{i\omega t + ikL} - g(\omega)e^{i\omega t - ikL} + g(\omega)e^{i\omega t + ikL}} \tag{10}$$

As a result the negative traveling wave is multiplied by the factor $q(\omega)$, which is the reflection coefficient given by:

$$q(\omega) = \frac{\left(ik - g(\omega)\right)e^{-2ikL}}{ik + g(\omega)} \tag{11}$$

The exponent e^{-2ikL} in (11) does not depend on $g(\omega)$ and expresses the decay of the amplitude of the non-propagating mode and the dissipation of energy in the rod. The graphs in Fig. 3 show the solution of the equation of motion of a rod of length *L*. The function $g(\omega)$, which gives no reflection at the right boundary, is $g(\omega)=ik(\omega)$ and is unique. All other values stimulate a reflection at the boundary. In Fig. 4 the complex function $u(x,t)$ in 2d and 3d graphs are presented.

3 PERFECT MATCHED LAYER (PML)

3.1 One dimensional systems

A semi-infinite rod on elastic foundation, Figure 5, subjected to an imposed displacement $u_o \exp(i\omega t)$ at the left end (x = 0), and a radiation condition for $x \to \infty$, with ω the frequency of excitation, in the absence of any body

forces. The above excitation causes time-harmonic displacements $u(x)\exp(i\omega t)$, which are governed by the following equation is considered:

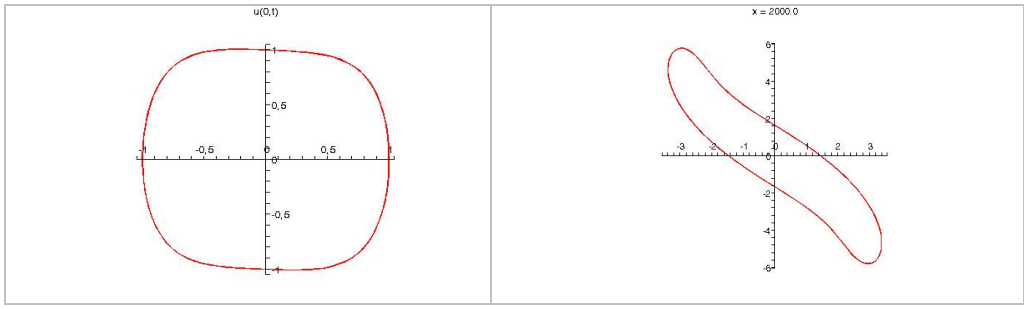

Figure 3. The complex solution u(x,t) = u_R(x,t) +i u_I(x,t) for x=0 and x=2000

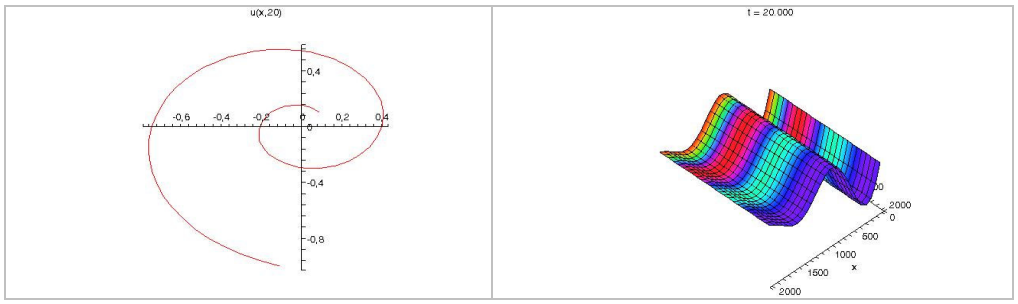

Figure 4. The complex value of u(x,t) with absorbing boundary condition at the right edge in 2d and 3d plot.

$$\frac{d\sigma}{dx} - \frac{k_g}{A}u = -\omega^2 \rho u \tag{12}$$

where σ is the axial stress of the rod, A its cross-sectional area, ρ the mass density, and k_g the static stiffness per unit length of the foundation.

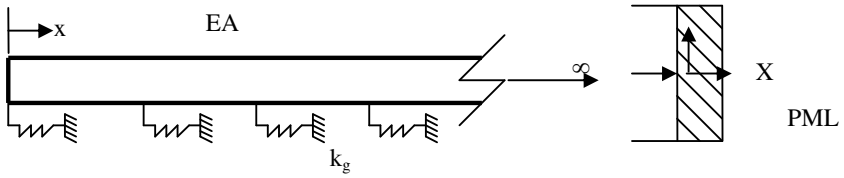

Figure 5. Homogeneous elastic semi-infinite rod on elastic foundation and the PML model

To express the frequency-response of this system in terms of non-dimensionalized parameters the following expressions are introduced, $a_o = \omega r_o / c_1$, where $r_o = \sqrt{EA/k_g}$ is a characteristic length and $c_1 = \sqrt{E/\rho}$ is the wave velocity in the rod.

For the wave propagation within the PML the same equation holds [Eq. (12)] with x replaced by a stretched coordinate X. The solution of that equation for $a_o \geq 1$, with $a_o = 1$ being the cut-off frequency of the system, is given by the positive and negative propagating waves, and has the following form :

$$u(x,t) = \left[A\sin\left(\frac{\sqrt{k_g}\sqrt{a_o^2 - 1}}{\sqrt{EA}} X \right) + B\cos\left(\frac{\sqrt{k_g}\sqrt{a_o^2 - 1}}{\sqrt{EA}} X \right) \right] e^{ia_o\sqrt{\frac{k_g}{A\rho}}t} \tag{13}$$

The stretched coordinate X, is defined as $X = \int_0^x \lambda(s)ds$, where λ is a nowhere zero, continuous, complex-valued coordinate stretching function [6-7]. A special property of PMLs is that if λ matches at the interface of the two layers, then a wave-type motion will pass through the interface without generating any reflected wave (this is

the perfect matching property of the PML). Another special property of the PMLs is that for suitable choices of λ, the solutions within the PML take the form of the corresponding elastic-medium solution, but with an imposed spatial attenuation. For $a_o>1$, X is given as:

$$X=\begin{cases} x & if \quad x\in[0,L] \\ x-i\dfrac{r_o}{\sqrt{a_o^2-1}}F(x/r_o) & if \quad x\in(L,L+L_p] \end{cases} \tag{14}$$

The solution of the same equation for $a_o<1$, that contains the positive and negative evanescent wave motion, is defined as:

$$u(x,t)=\left[Ae^{-\sqrt{1-a_o^2}\frac{X}{r_o}}+Be^{+\sqrt{1-a_o^2}\frac{X}{r_o}}\right]e^{ia_o\sqrt{\frac{k_g}{Ap}}t} \tag{15}$$

In that case, X is defined as:

$$X=\begin{cases} x & if \quad x\in[0,L] \\ x+\dfrac{r_o}{\sqrt{1-a_o^2}}F(x/r_o) & if \quad x\in(L,L+L_p] \end{cases} \tag{16}$$

where the attenuation function $f(x)$ can be of the form $f(x)=f_o\left(\dfrac{x}{L_p}\right)^m$ and $F(x)=\int_0^x f(q)dq$.

Table1 indicates the steps of evaluating an accurate depth of PML. In according to these steps, an example for $a_o=2$ is presented for which Lp must be selected equal to 17m (Fig. 6).

Given E, A, k_g, p and ω:

(1) Calculate the dimensionless parameters a_o, r_o and c_1.
(2) Select f_o and m to establish the function $f(x)$ and evaluate the stretching coordinate X, using either Eq. (14) for $a_o \geq 1$, or Eq. (16) for $a_o<1$, respectively.
(3) Calculate the displacement using the Eq.(13) or (15) for $a_o \geq 1$ and $a_o < 1$, respectively.
(4) For a specific dimension L, plot the amplitude of the wave with the L_p.
(5) Find a suitable value of L_p for which the displacement is approximately zero at the interface of two layers.

Table 1. Computing the min depth of PML.

The effect of PML can be studied thoroughly by calculating the amplitude of waves that are reflected from the fixed boundary and examining the influence of L, L_p, f and a_o on the dynamic stiffness $S(a_o)$. The dynamic stiffness is computed as:

$$S(a_o)=S^{\infty}(a_o)\frac{1+|R|e^{-2\sqrt{1-a_o^2}\frac{L+L_p}{r_o}}}{1-|R|e^{-2\sqrt{1-a_o^2}\frac{L+L_p}{r_o}}} \tag{17}$$

where $S^{\infty}(a_o)=\sqrt{1-a_o^2}$ and $|R|=e^{-2F\left(\frac{L_p}{r_o}\right)}$. To facilitate the study of the influence of the parameters Lp, L

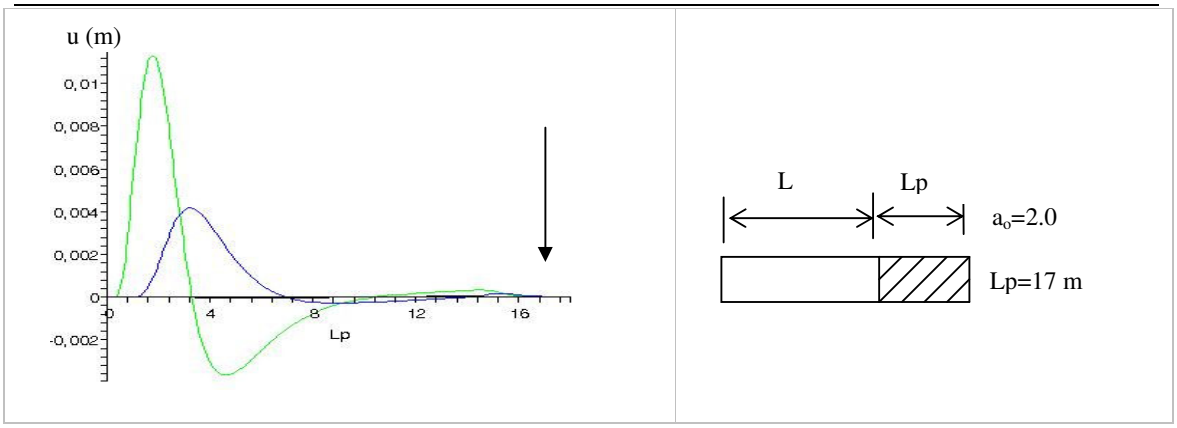

Figure 6 Displacement u at the interface (blue) and at x=3m (green) for different values of L_p, for a_o=2.

and f on the dynamic stiffness, it is preferable to split Eq. (17) into the real and imaginary part, as: $S(a_o) = K(a_o) + ia_oC(a_o)$, where $K(a_o)$ and $C(a_o)$ are the stiffness and damping coefficients, respectively. Using the attenuation function f(x), the reflection coefficient $|R|$ is given by the following relation:

$$|R| = e^{-\frac{2f_o\left(\frac{1}{Lp}\right)^m\left(\frac{L_p}{r_o}\right)^{m+1}}{m+1}} \tag{18}$$

Thus, the reflection coefficient depends on the maximum value of the attenuation function, f_o, the depth of the PML, the ratio L_p/r_o, and the degree of the polynomial attenuation function m. The reflection coefficient indicates that the accuracy is proportional to f_o and to L_p/r_o, but inversely proportional to m. In Fig. 7 the variation of dynamic stiffness is presented with L_p. It is evident that for small values of L_p/r_o the depth of the PML and/or the static stiffness of foundation are both small, while if in addition L/r_o, is large, the results become inaccurate. Moreover, for large values L_p/r_o the dimensions of the bounded domain do not affect the accuracy of the results as compared to the exact solution.

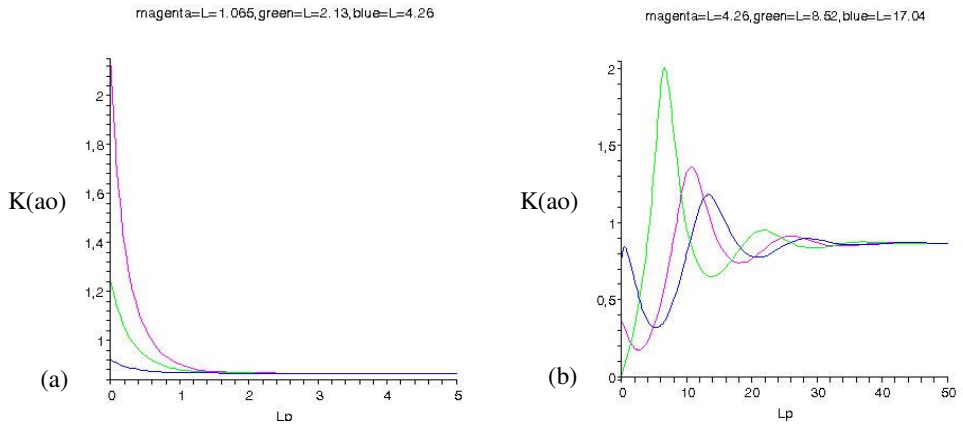

Figure 7. The real part of dynamic stiffness for different L in case of (1) a_o=0.5, and (b) a_o=3.

3.2 Plane-strain soil-structure interaction problem

A PML for plane-strain motion is a layer in which body-wave solutions are admitted in the form of P waves:

$$u(x) = q\exp[-ik_p x \cdot p] \tag{19}$$

where $k_p = \omega/c_p$, with $c_p = \sqrt{(\kappa+4\mu/3)/p}$ the P-wave speed, p is a unit vector denoting the propagation direction, and $q = \pm p$ the direction of particle motion, and in the form of S waves:

$$u(x) = q\exp[-ik_s x\cdot p] \tag{20}$$

where $k_s = \omega/c_s$, with $c_s = \sqrt{\mu/p}$ the S-wave speed, and $q\cdot p = 0$. Furthermore, it can be argued that for appropriately defined λ and appropriate boundary conditions, Rayleigh waves are propagated along a free surface with exponentially-decreasing amplitude in the direction normal to and away from the surface. The absorptive capability of such a layer can be analyzed by studying the reflection of plane waves from the fixed boundary. The incident wave will be reflected from the boundary as a P-type wave and a S-type wave, with the total wave motion represented as [6-7]:

$$u(x) = q_p^I e^{-ik_p X\cdot p_p^I} + R_{pp} q_p^R e^{-ik_p X\cdot p_p^R} + R_{sp} q_s^R e^{-ik_s X\cdot p_s^R} \tag{21}$$

where the s and p subscripts refer to S-type and P-type waves, respectively, and superscripts I and R refer to incident and reflected waves, respectively. Imposing $u(x)=0$ for $x_1=L_p$, and expressing the directions of propagation and of particle motion in terms of θ, gives:

$$\left|R_{pp}\right| = \frac{\cos\left(\theta+\arcsin\left(\frac{c_s\sin\theta}{c_p}\right)\right)}{\cos\left(-\theta+\arcsin\left(\frac{c_s\sin\theta}{c_p}\right)\right)}\exp\left[-2\frac{c_s}{c_p}F\left(L_p\right)\cos\theta\right] \tag{22}$$

$$\left|R_{sp}\right| = \frac{\sin(2\theta)}{\cos\left(-\theta+\arcsin\left(\frac{c_s\sin\theta}{c_p}\right)\right)}\exp\left[-F\left(L_p\right)\left(\frac{c_s\cos\theta}{c_p}+\sqrt{1-\frac{c_s^2\sin\theta^2}{c_p^2}}\right)\right] \tag{23}$$

Numerical results are presented for the plane-strain soil-structure interaction problem of a rigid strip-footing on a half plane. For comparison, the half-space is also modeled using a viscous dashpot boundary model [8], wherein the entire domain is considered (visco) elastic and viscous dashpot elements are placed at the fixed outer boundary. The mesh used for both models is the same and the results were obtained using Abaqus code.

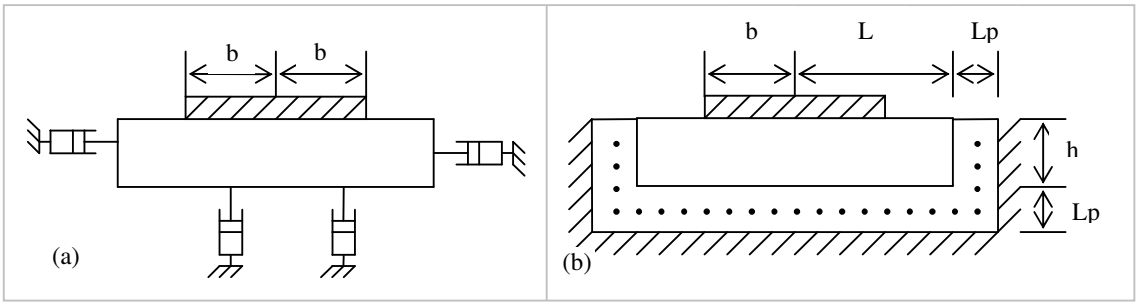

Figure 8. Cross-section of a rigid strip of half-width b on a half-plane (a) the dashpot and (b) the PML model.

Studying the results of the soil-structure interaction for the case of half-plane it is notable that using a small domain, the results obtained from the PML model are quite accurate, while the dashpot model is not reliable for the selected small dimensions of the layer. The computational cost of the PML model is similar to that of the dashpot model. Numerical investigations of the effect of mesh density on the accuracy of results suggest that the mesh density in the PML should be chosen to be similar to that in the bounded domain [6-7].

4 CONCLUSIONS

A PML model that absorbs the incoming waves reflected at its boundary is investigated for 1D and 2D simple problems. Solutions admitted by the PML are of the same form as that admitted by the elastic medium, but with

the stretched coordinates replacing the real coordinates. Termination of the layer by a fixed boundary causes reflection of the waves back towards the bounded domain, with the amplitude of reflected waves being independent of the size of the bounded domain and controllable by the depth of the layer and the attenuation profile. Thus, wave propagation in an unbounded domain can be modeled through a bounded domain that is restricted to the region of interest for the analysis, and a suitably-defined PML.

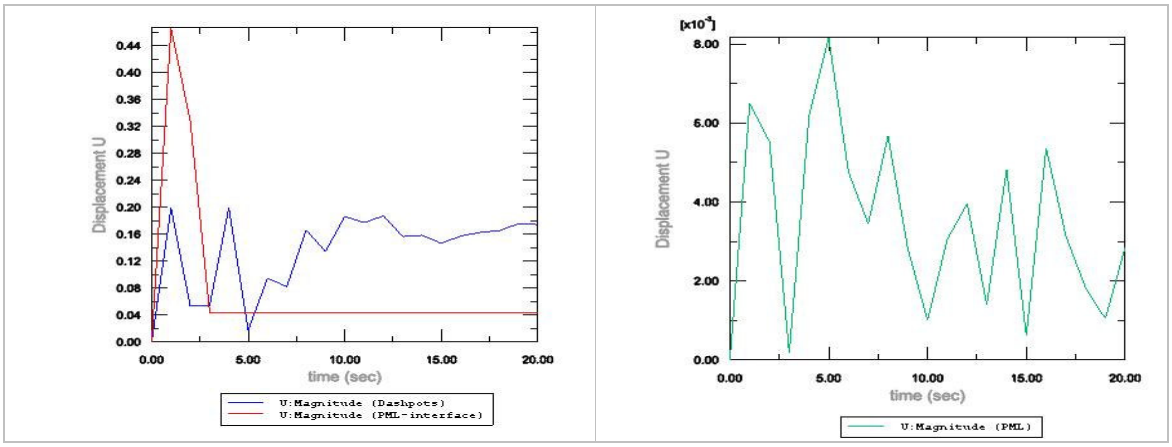

Figure 9. (a) Displacements at the interface, (b) displacements in the PML

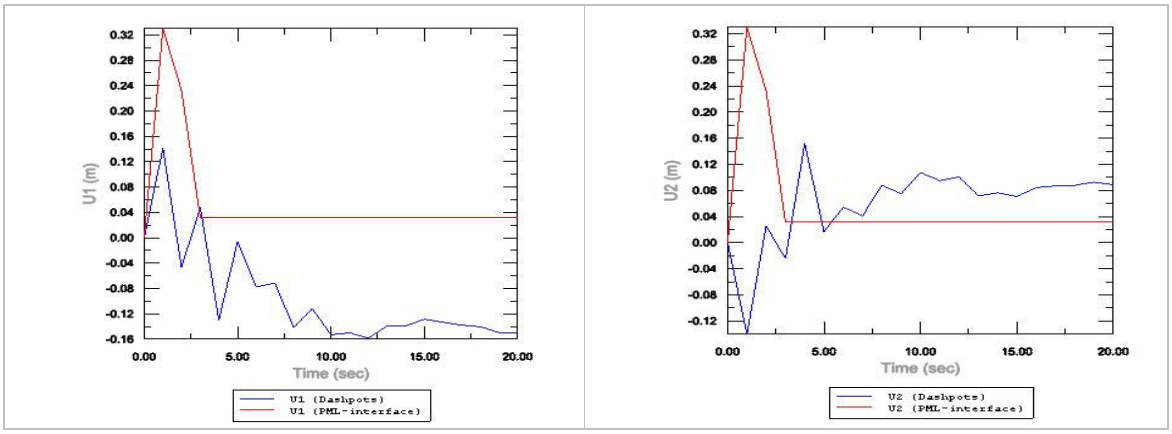

Figure 10. (a) U_1(m) at ABC (dashpots) and the PML model, (b) U_2(m) at ABC (dashpots) and the PML model.

REFERENCES

[1] J. –P. Berenger, A perfectly matched layer for the absorption of electromagnetics waves, J. Computat. Phys. 114(2)(1994) 185-200

[2] W.C. Chew, J.M. Jin, E. Michielssen, Complex coordinate stretching as a generalized absorbing boundary condition, Microw. Opt.Technol. Lett. 15 (6) (1197) 363-369.

[3] F.L. Teixeira, W.C. Chew, Unified analysis of perfectly matched layers using differential forms, Microw. Opt. Technol. Lett. 20 (2) (1999) 124-126.

[4] F.L. Teixeira, W.C. Chew, A general approach to extend Berenger's absorbing boundary condition to anisotropic and dispersive media, IEEE Trans. Antenn. Propag. 46 (9) (1998) 1386-13687.

[5] Glauco Feltrin, Absorbing boundaries for the time-domain analysis of dam-reservoir-foundation systems (thesis), Institute of Structural Engineering, Swiss Federal Institute of Technology Zurich, November 1997.

[6] Ushnish Basu, Anil K. Chopra, Perfectly matched layers for time-harmonic elastodynamics of unbounded domains: theory and finite-element implementation, Comput. Methods Appl. Mech. Engrg. 192 (2003) 1337-1375.

[7] Ushnish Basu, Anil K. Chopra, Perfectly matched layers for transient elastodynamics of unbounded domains, Int. J. Numer. Meth. Engng 2004; 59: 1039-1074

[8] J. Lysmer, R.L. Kuhlemeyer, Finite dynamic model for infinite media, J. Engrg. Mech. Div., ASCE 95 (EM4) (1969) 859-877.

BLAST BEHAVIOR OF PLATES WITH SACRIFICIAL CLADDING

C. Kotzialis, C. Derdas, and V. Kostopoulos
Applied Mechanics Laboratory, Department of Mechanical Engineering & Aeronautics, University of Patras and ICE-HT/FORTH
Patras University Campus, GR 265 00 Patras, Greece
e-mail: kostopoulos@mech.upatras.gr

Keywords: blast, sacrificial cladding, explicit finite element

Abstract:
The use of sacrificial armor against blast loading has become an important issue in the design of protective structures. A small amount of work has been published in what concerns sacrificial armor clads and all mainly concerns metals as clad materials.
This paper addresses the problem of the non-linear transient behaviour of sacrificial cladding protection structures under time-dependent blast loads. The expendable armors analyzed are made of aluminum, while the main structure is made of aluminium too.
The main structure and the sacrificial cladding are considered fixed together and special care is taken in order to correctly model the interface between them via contact elements.
The sacrificial cladding is comprised of webs of ellipsoidal cross-sections, fixed to a plate. The case which is studied in the present work is consisted by aluminum webs with an aluminum sacrificial plate. The system protects an aluminium panel.
In what concerns material modeling, special care is given, in order to accurately simulate the inelastic behavior of aluminum due to high strain rate loading.
A unit cell of the armor is analyzed in order to allow for the extrapolation of the results to any size of armor.
Comparisons are made in terms of displacement, force and deformation energy observed on the main structure.
The analysis has been conducted with the hydrodynamic code LS-DYNA 3D.

INTRODUCTION

Structures undergoing impact by a solid body or by loading them by a blast wave absorb energy through plastic deformations. During the deformation process the elastic response of the system has to be taken into consideration, as well as the strain hardening of the material and strain rate effects.
The design of a structure tolerant to blast loading is a difficult task and it requires systematic test validation for an acceptable design to be achieved.
A structure undergoing blast loading absorbs energy through plastic deformation processes, however since in the most of the cases the structure is required to operate after its blast loading, then armoring of the structure must be applied on by the use of a sacrificial cladding [1, 2]. Armor will deform plastically and in that way will transfer the minimum energy of the blast load to the main structure.
The sacrificial cladding must operate in a predictable way for all the spectrum of loads that is being designed for. The important characteristics of such armor are: the deformation pattern, the transferred Impulse, the energy absorption during its plastic deformations and the collapse space efficiency.

The deformation pattern is very important since many of the above parameters depend on it. For many structural configurations the deformation pattern changes as a function of the pressure and the velocity profile of the blast loading. Thus, for given blast loading ranges it is necessary to choose carefully geometrical configurations for the armoring that deform in a consistent manner with the structure they have been designed to protect. Furthermore, since plastic deformation is introduced as design criterion, the ability of the plastically deformed armor to absorb energy and the collapse space efficiency, depend on the distribution of plastic hinges and plastic zones.
In the literature of shock loaded structures most theoretical and experimental studies are carried out on simple structures as plates, beams and shells. There isn't great discrepancy in the results among researchers, but most of the theoretical studies barely agree with the experiments. Both metallic and composite materials are considered. In [3, 4] an excellent review work that covers the theoretical investigation of the blast loading of metallic structures is presented. It stresses the fact that accurate modelling of the blast load is necessary and also that the non – linearity of the material response and the effect of boundary conditions must be modelled accurately. In addition, in [3] the results concluded by the analysis are in excellent agreement with the experimental data presented.
Galiev in [4] mentions a phenomenon known as counterintuitive behaviour. This phenomenon is the final deflection of plates or shallow shells in direction contrary to the direction of loading by the blast wave. It has

been observed both in air and underwater explosions experimentally and it has a great significance for explosive forming applications.
Studies concerning the prediction of the behaviour and the failure of composite and metallic structures under blast loading can be found in the literature. Nurick in [5] and [6] has conducted a series of experiments on metallic plates and the results are in good agreement with the theoretical results for the onset of tearing and the effect of boundary conditions. Turkmen in [7] and [8] conducted experiments were the load was modelled with the Friedlander equation and showed that although the modelling of the loading was accurate, the finite element models were not so elaborated to provide good agreement with the experimental results.

GENERIC STRUCTURAL CONFIGURATIONS FOR ABSORBING ENERGY

Two general types of response under shock loading are shown in Figure 1, [1, 2].

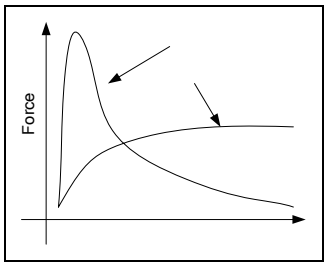

Figure 1: Two general types of response under shock loading

The deformation of structures that belong in type 1 is more sensitive in the velocity of loading than that of type 2. Moreover, for the structures belonging in type 1 response configuration, inertia is the critical parameter that controls the response of the system and also elastic behavior and strain rate effects play also an important role. It has been proved that the combined effect of inertia and strain rate produce much higher peak forces and less permanent deformations. This means that the elastic perfectly plastic material model is insufficient for this type of structures, because elasticity and strain rate are closely connected. Thus, more sophisticate material models are required for the material response in cases of shock loading.

Collapse space efficiency [1, 2], in case of impact of a solid body, is defined by the equation:

$$n = \frac{U_e}{m \cdot d} \tag{1}$$

where U_e is the absorbed energy, m is the mass of the impactor and d the collapse distance.
In the present analysis a modified version of equation (1) is proposed by the authors for blast loading, where instead of the mass of a solid body, the ratio of impulse of the blast wave to the initial velocity is used. So, equation (1) becomes:

$$n = \frac{U_e \cdot c_w}{I_w \cdot d} \tag{2}$$

where the impulse of the blast wave is given by:

$$I_w = \int_{t_1}^{t_2} \int_{A_t} p dA_t dt$$

In the equation above, p is the pressure profile of the wave, A_t the area of the surface where pressure p is acting upon.
For achieving an optimum value for n, the stiffness and the shape of the armor must be chosen on the basis of the protecting structure. The plastic deformations must be under control from the very beginning of the process and in such a pattern that does not affect and interact with the main structure much. This requires the prediction in advance of the spread of plastic zones and the formation of plastic hinges. One way this can be done is by predetermining the position they appear by curving specific elements of the armor. It is also important for the

protection of the main structure that the plastic deformations must distributed in time and occur during the whole deformation process or to cover as much as possible so that the transfer of impulsive loading to be minimal.
During blast loading, the imparted kinetic energy must be absorbed by the plastic deformations within the armor. In the case where not enough energy is absorbed, then the remaining part of the kinetic energy will lead to a large transfer of impulse through the armor to the main structure. In the case of stiff main structure, it will not absorb energy during the transfer phase of impulse and high accelerations will be developed. In the case where the stiffness of the main structure is not high enough, it will absorb part of the remaining energy and significant deformations will appear exposing to great risk the whole system.
A well designed sacrificial cladding armor must minimize as much as possible the peak force and increase the deformation time as much as possible, so that energy absorption and low impulse transfer to be achived.

MODELLING ASPECTS

Numerical simulations of the inelastic response of structures under blast loading are carried out usually with many simplifications in their response. The theories applied ranges from the elementary linear bending theory and extend to methods where the membrane forces are taken into consideration. This is carried out by shell theory which includes levels of geometrical non linearity.
However, shell theory is used when deformations are large, so that membrane forces have a significant effect on the response of the structure. The current research in the field of blast loading of metallic structures agrees [3] that the following phenomena must be considered:

1. The continuous change of curvature of the structure during deformation.
2. The coupled action of membrane forces and bending moments.

According to Shmidt [3], the elastic perfectly plastic material model gives acceptable result only when the plastic work or the plastic deformation is quite large. Also the same researcher mentions that when the ratio of the kinetic energy that is given to the system to the elastic energy that can be stored in the system is grater that 2 – 3 for beams and 4 for plates made of steel or aluminum, then the elastic perfectly plastic model will provide good results. However, this rule of thump becomes truth only because beams and plates are simple geometrical structures that do not belong to type 1 response profile.
Another very important issue in the modeling of blast loaded structures is the description of the transient loads. This is very difficult to be done analytically, because the complexity of the interaction of the fluid with the structure does not give paths to analytically find solutions for practical applications. On the other hand for plane blast waves in air the equation of Friedlander can be used to give the overpressure profile on the structure.

$$P_s(t) = P_s \cdot \left(1 - \frac{t - t_a}{t_d}\right) \cdot \exp\left(-a\frac{t - t_a}{t_d}\right) \tag{3}$$

In equation (3) P_s is the intense of the blast wave, t is time, t_d is the time interval for which the overpressure is positive and a is a dimensionless constant for calibration of the pressure profile. This equation can model accurately the overpressure when a wave impinges on a solid plate. The most general case needs the solution of the dynamic aeroelastic problem.

OPTIMAL PERFORMANCE OF A SACRIFICIAL CLADDING

A sacrificial cladding is defined as the mechanical structure which through its deformation or even failure has to protect another structure. It has to be replaceable and easy to transfer so the need for light materials is obvious. Also, the materials of this armor have to be very ductile in order to yield quickly and sustain large plastic deformations.

The optimum performance of a sacrificial cladding is achieved when the force between the main structure and the armor is close to zero, which means that the collapse space efficiency should satisfy the following relation:

$$n \approx \frac{m_c \cdot c_w}{I_w} \cdot n_c \tag{4}$$

where n_c is the mean acceleration developed inside the armor and m_c is the armor mass. n is the deceleration that the sacrificial cladding gives to the load by the blast wave.

GEOMETRY OF A SECTION

The proposed geometry for the section of a sacrificial cladding is given in Figure 2.

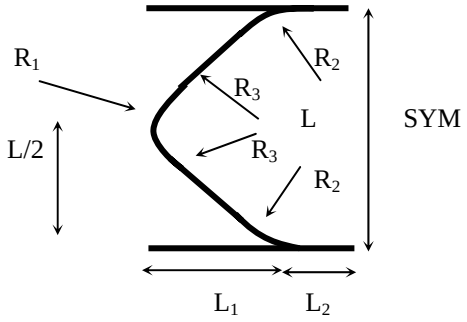

Figure 2: The proposed geometry for the section of a sacrificial cladding

with $L_1 + L_2 = L$, and $L_1 = \frac{2}{3}L$, $L_2 = \frac{1}{3}L$.

This specific geometry provides the same deformation pattern for every type of loading. It forms a plastic hinge at the center of the section. R_2 and R_3 contribute to the resistance of the section in transverse deformation. The plates above and below the curved web are bonded to it and the whole system is also bonded to the main structure.

ANALYSIS

For the purposed of the present analysis a section the following dimensions have been used:

L = 50 mm, R_1 =5 mm, R_2 =15 mm and R_3 = 50 mm

The thickness of the plates and of the web is equal to 1.5 mm and the length of the structure is equal to 1 m. Damping forces are not included.

The finite element model is presented in Figure 3, and shows a plate of 1x1 m and 1.5 mm thick which is protected by a sacrificial cladding of this type:

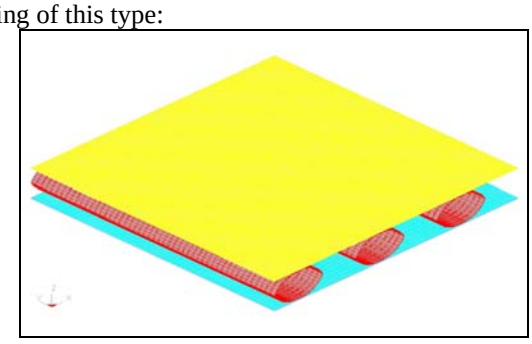

Fig. 3: Geometrical configuration of the section of a sacrificial cladding

Model Description

The structure simulated was a 1m x 1m x 0.0015m aluminum plate, clamped on its edges and protected by a sacrificial cladding armor comprised of a aluminum webs and plates made from aluminum sheets of the same thickness (0.0015 m).

The analysed model is comprised of 4 main parts: The main plate, which is the structure intended to be protected against blast-loading, the upper plate, the webs and the lower plate, which comprise the sacrificial cladding structure. After consecutive runs of an increasingly larger number of elements, in order to verify convergence, the following number for each part has been used, leading to a total of 68400 elements.

Part	Number of Elements
Upper Plate	10000
Webs	38400
Lower Plate	10000
Main Structure	10000

Table 1: Components of the model and number of elements

The element formulation used was that proposed by Belytcsko-Leviathan [5]. Five integrations points through the thickness were used because the problem is bending dominated and also because plastic deformations commence due to shear stress.

Material Model

The implementation of strain-rate dependent plastic behaviour on the plastic-kinematic hardening material model used in this analysis is implemented by the use of the Cowper-Symonds yield stress scaling factor which scales yield stress in the following way:

$$\sigma_y = \left[1 + \left(\frac{\dot{\varepsilon}}{C}\right)^{1/p}\right] \times \left(\sigma_0 + \beta E_p \varepsilon_{eff}^p\right) \tag{5}$$

where C and p are the Cowper-Symonds material dependent parameters, $\dot{\varepsilon}$ is the strain rate of the loading, E^p is the plastic hardening modulus, ε_{eff}^p is the effective plastic strain and β *is a* parameter that determines the plasticity behavior between isotropic and kinematic hardening [5] . Element failure is implemented by a failure strain criterion. The materials used in the simulation were AL-1015-0 for the cladding and AL-1015-H18 for the non-sacrificial structure. The constants used are shown in Table 1.

	AL 1050-O	**AL 1050-H18**
E_x^T [GPa]	69	69
E_x^C [GPa]	70.4	70.4
G [GPa]	26	26
v_{xy}	0.33	0.33
σ_y [MPa]	28	145
σ_f [MPa]	76	160
τ_f [MPa]	51	83
ε_f^T	39 %	7 %
ρ [Kg/m^3]	2705	2705

Table 2: Engineering constants of the materials used

AL 1050-0 was used for the sacrificial cladding webs, because it allows for the quick development of plastic deformations due low yield stress and moreover it is characterised by high failure strain, while AL 1050-H18 was used for every other part of thestructure.

Contact Interfaces

In order to accurately predict the deformation behaviour of the cladding, special care has been applied on ensuring proper contact conditions between the parts of the simulated structure.

At first, tie-break contact has been considered between the sacrificial cladding plates and webs. Tie-break contact has also been used between the lower sacrificial plate and the main structure, so as to simulate the attachment of parts between them. The failure stresses for the tie-break interfaces that were assumed are: 100 MPa and 50 MPa for normal and shear failure respectively. The failure stresses came from the failure stresses of a moderate strength aerospace glue, since the different parts of the cladding are considered glued together.

Additionally, surface-to surface contact interfaces have been introduced between each part of the cladding so as to simulate the interaction of those parts during the plastic deformation and subsequent wrapping of the free sides of the upper and lower plates along the web structures.

Loading & Boundary Conditions

The model was loaded by a time varying pressure profile representing the pressure pulse that would occur in the case of a Mach 1.0 blast wave impacting the structure. The wave was considered as plane, simulating the blast loading of an explosion far from the target. Figure 4 presents the pressure against time profile applied on the structure.

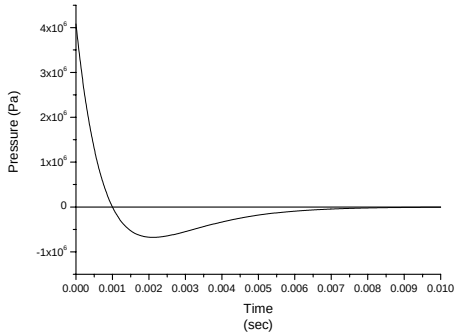

Figure 4: Pressure profile against time for a blast wave of Mach =1.0

Only ¼ of the structure was analysed since appropriate symmetry conditions have been applied, in order to reduce computational costs. Additionally, the pressure applied was on the model for a time of 0.8 msec. The simulation time is such since this was the time for complete crushing of a unit cell of the cladding as outlined in [10]. The Mach number for the plane wave was chosen as such since it was the lowest Mach number blast wave that under preliminary analysis has proven to rupture the unprotected main structure.

RESULTS& DISCUSSION

Even at half the simulation time, deformation of both the webs and the upper plate has occurred, and the upper plate has approached the main structure. Additionally, wrapping of the upper structure along the webs in conjunction with web buckling can be observed at figure 5c.. When the run time has reached 0.8 msec , one can notice the total crushing of the sacrificial cladding and also some deformations of the main structure.
Plastic Hinges on the webs have already begun to format t=7.76x10^{-6} sec, as shown in figure 6, proving that the design of the proposed cladding is successful in terms of fast plastic deformation. At the end of the simulated the cladding has totally collapsed.

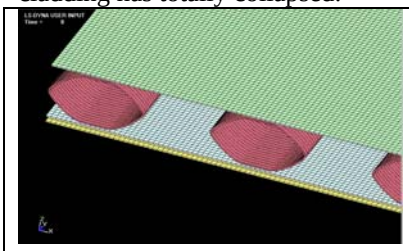	t=0	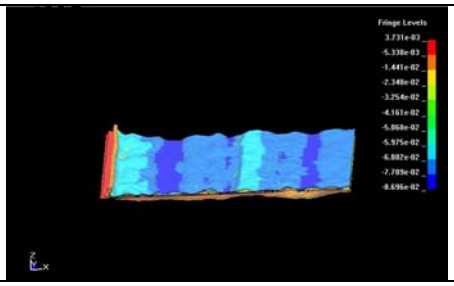	t=8x10^{-4}sec
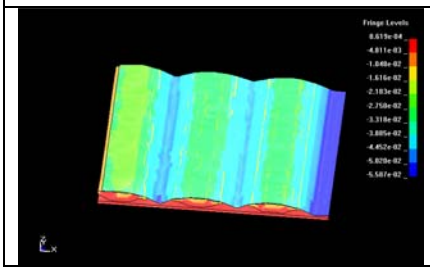	t=4x10^{-4}sec		

Figures 5a, 5b, 5c: Displacement Contours of the sacrificial cladding at different times points

Correlating the center node displacement against time profile in Figure 6, and Figure 4, one can draw the conclusion that during the time the blast pulse has commenced to act on the sacrificial cladding, the main structure remains intact and not obvious center of mass displacement occurs. Only after half the simulation time does the mass center of the main structure center begin to move, demonstrating the effectiveness of the sacrificial cladding.

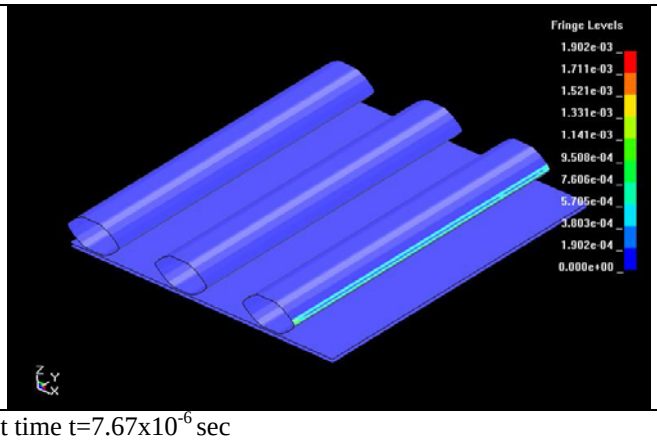

Figure 6: Plastic strains at time t=7.67x10^{-6} sec

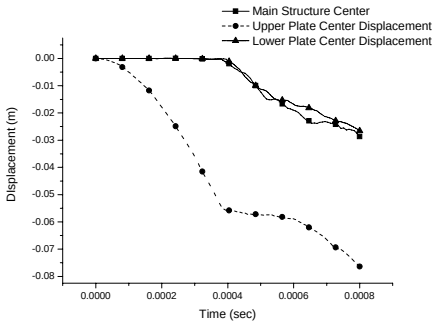

Figure 7: Time Profile of the displacement of the center node of the upper clad plate, the lower clad plate and the main (un-sacrificial) structure

The energy time-history plots in Figure 8 present the total energy (sum of kinetic and deformation) absorbed by each part of the structure. The blast energy pulse is mainly absorbed by the sacrificial cladding and not the main structure. The displacement profile is further collaborated by Figure 8 since only after t=0.004sec does the main structure begin to have an increase in total energy. At that time, the upper plate total energy reaches a maximum in terms of energy, while the webs continue to demonstrate an energy increase.

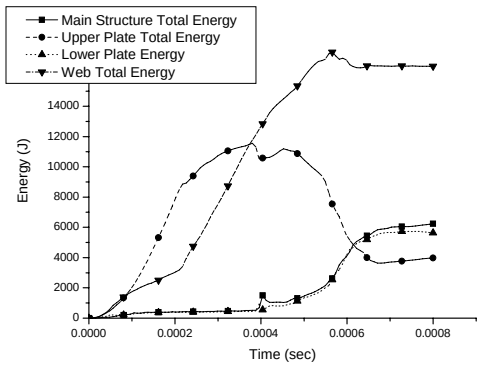

Figure 8: Total Energy Plots (Sum of kinetic and deformation) of the four components of the model

As a proof of the effectiveness of the sacrificial cladding armor, time-history plots of the deformation energy for each different component of the simulated model (Figure 9a) and the percentage of the deformation energy at the t=0.8 msec of the points of the simulation (Figure 9b) are shown. Throughout the simulated time, the webs seem to absorb more energy than the plates and main structure. This fact is apparent in Figure 8b where the cladding seems to have taken up to the 87.34% of the deformation energy of the system.

Additionally, the webs seem to be able to resist the threat excessively well, even if they are surrounded by more brittle materials, providing an insight on their importance in the design of collapsible claddings. Should there have been chosen more ductile armor plates, the energy dissipated would have been more, through the increased

plastic deformation of the lower and upper cladding plates. The fact that brittle materials with higher yield stresses are used on the upper and lower plates ensures the protection of the main structure from direct force transmission by the contact of the upper plate with it, since only small deformations can be undertaken by it and additionally makes the simulation more demanding for the webs.

CONCLUSIONS

A sacrificial cladding against pressure threats taking into advantage the ductility of certain aluminum material types and careful design of plastic hinges that will commence to deform immediately, has been designed. Its behavior has been simulated using the hydrocode DYNA 3D and the most important conclusion would be that even if the upper and lower plates are not ductile enough to absorb high amounts of blast energy, the careful and efficient design of the webs can provide protection for the main structure.

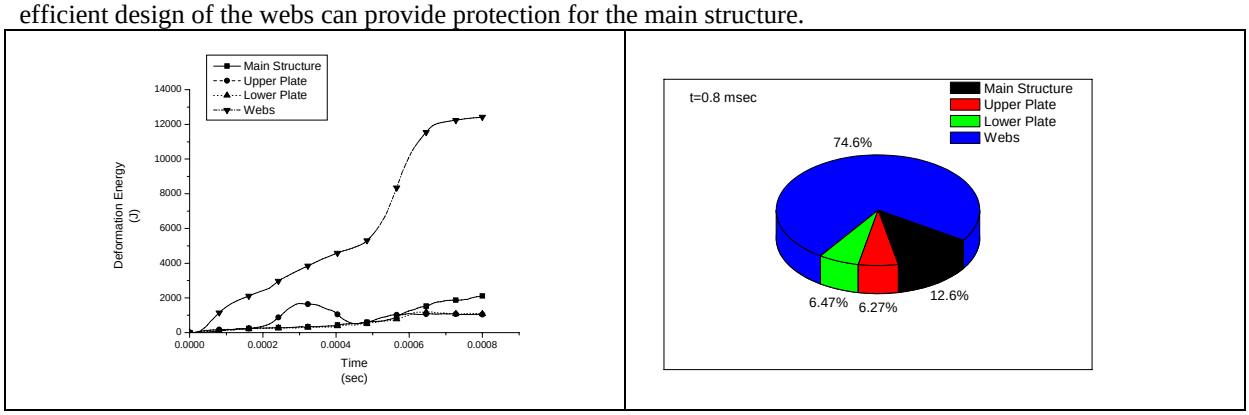

Figures 9a, 9b: Deformation Energy time history for the different components of the model (a) and percentages of deformation energy at t=0.8 msec (b)

While ballistic impact requires high stiffness in order to "beat" the projectile, blast protection requires compliance and high energy dissipation via material failure modes (like plasticity) in order to reduce the amount of forces and energies acting on the structure to be protected.

ACKNOWLEDGEMENTS

Part of this work has been funded by the EKVAN/4.5/DP6 Research project funded by the General Secretariat for Research and Technology of Greece.

REFERENCES

[1] Guruprasad. S, Abhijit Muckerjee ''Layered sacrificial claddings under blast loading Part I – analytical studies.'', Int. J. of Impact Engineering 24, pp. 957 – 973
[2] Guruprasad. S, Abhijit Muckerjee ''Layered sacrificial claddings under blast loading Part I – experimental studies.'', Int. J. of Impact Engineering 24, pp. 975 – 984
[3] Stoffel M., Schmidt R., Weichert D. (2001) ''Shock wave loaded plates'', Int. Jr. of Solids and Structures 38, pp 7659 – 7680
[4] Galiev Sh. U. (1996) ''Experimental observations and discussion of counterintuitive behavior plates and shallow shells subjected to blast loading'', Int. J. of Impact Engineering 18, pp. 783 – 802
[5] Wierzbicki T., Nurick G. N. (1996) ''Large deformation of thin plates under localized impulsive loading'', Int. J. of Impact Engineering 18, pp. 899 – 918
[6] Nurick G. N., Gelman M. E., Marshall N. S. (1996) ''Tearing of blast loaded plates with clamped boundary conditions'', Int. J. of Impact Engineering 18, pp. 803 – 827
[5] John O. Halquist (1998) *Ls – Dyna Theoretical Manual* LSTC, California
[6] Ted Belytschko, Wing Kam Liu, Brian Moran (2001) *Nonlinear finite elements for continua and structures*, Wiley,UK
[7] Turkmen H. S., Mecitoglu Z. (1999) ''Dynamic response of a stiffened laminated composite plate subjected to blast load'', Jr. of Sound and Vibration 3, pp 371 – 389
[8] Turkmen H. S. (2002) ''Structural response of laminated composite shells subjected to blast loading: Comparison of experimental and theoretical methods'', Jr. of Sound and Vibration 4, pp. 663 – 678
[9] Pan Y.G, Watson A.J., Hobbs B. (2001) ''Transfer of impulsive loading on cladding panels to the fixing assemblies.'', Int. Jr. of Impact Engineering, 25, pp 949 – 964
[10] Kotzialis K., ''Study of The Transient Response of Basic Structural Elements and Protection of Structures from Blast Waves'', Diploma Thessis, AML, MEAD, University of Patras, 2004.

5th GRACM International Congress on Computational Mechanics
Limassol, 29 June – 1 July, 2005

ANALYTICAL MODELING OF MASONRY-INFILLED TIMBER TRUSS-WORKS

I.N. Doudoumis*, J. Deligiannidou *, A. Kelesi *

* Department of Civil Engineering
Aristotle University of Thessaloniki (A.U.Th.)
54006 Thessaloniki, GREECE,
e-mail: doud@civil.auth.gr

Keywords: Infilled truss-works, Infilled trusses, Timber and masonry, Analytical modeling.

Abstract. *Masonry infilled timber truss-works is a kind of wall that has been used for the load bearing system of many residential buildings all over the world during the last centuries. In this structural system the walls are composed by a wooden skeleton, with vertical, diagonal and horizontal beam-like elements, that is filled with brick-masonry or stone-masonry with (or without) mortar, or just mortar alone. The static behavior of the wooden skeleton is characterized by the development of axial forces and bending moments, while the contribution of the infilling material in the system's stiffness, strength, and stress distribution is remarkable.*
In the present paper a detailed analytical finite-element model of this structural system is formed and studied. The wooden elements are modeled with beam-column elements, the infilling material with plane-stress elements, while the boundary conditions between the infilling material and the wooden elements are modeled with proper contact bonds. Elastic or inelastic constitutive laws can be used for the materials and the joint connections of the wooden elements. Numerical applications of the proposed model, with comparisons to other models, are presented for several cases of simple walls without openings, as well as for the case of a complex wall with openings, representing the entire face of a building storey.

1 INTRODUCTION

Masonry infilled timber truss-works is a kind of wall that has been used for the load bearing (structural) system of many residential buildings all over the world during the last centuries. It has been used in Portugal and Italy as an earthquake-resistant structural system. It has also been used with the name "tsatmades", in several old traditional and preservable buildings that are yet met in many regions of Greece, Turkey and other Balkan countries (Figure 1).

In this structural system the walls are composed by a wooden skeleton in the form of a usual braced-frame or truss structure, with vertical, diagonal and horizontal beam-like elements, that is filled with brick-masonry or stone-masonry with (or without) mortar, or just mortar alone. The joint connections of the wooden elements are rarely implemented with steel plates and mortises, and more often with solitary nails or rows of nails. A detailed description of this structural system is done in [1], but there isn't any other analysis suggested that could be helpful for the calculation of their stress state and bearing capacity. It is evident that static behavior of the truss-work is characterized by the development of axial forces (mainly), as well as bending moments, while the contribution of the infilling material in the system's stiffness, strength, and stress distribution is remarkable in general.

The static activation of the infilled truss-works is not always completely straightforward and a priori obvious. The tensile bond strength of the mortar at the interface between infill and truss-work is low and unreliable in general, thus allowing only compressive (normal) and limited frictional contact stresses to develop, while penetration is prohibited and separation or slipping along any parts of this interface may occur. The actual contact area varies during the seismic loading of the structure, thus resulting in a nonlinear response, even in the case of linearly elastic material laws. Furthermore, additional non-linearities may be presented due to inelastic material behavior. Due to the complexity of this structural system, some researchers [2] have fully ignored the presence of the infilling material in the structural analysis of the system, while some others [3] have considered the contribution of the infilling material by assuming a full bond at the interface between infill and truss-work. So, although there are plenty of studies concerning the static behavior of infilled frames ([4], [5], etc.), we have no knowledge of research works or codes that refer to a more precise structural analysis of the masonry infilled timber truss-works.

Figure 1. Old traditional buildings with load bearing walls made by "tsatmades"

In the present paper a proper detailed analytical finite element model (micromodel) for this structural system is formed and studied, which can describe with sufficient accuracy the static and dynamic (seismic) behavior of these walls, taking into account the aforementioned contact interface conditions. Numerical applications of the proposed model with comparisons to other suggested and often-used models are presented too.

2 ANALYTICAL MODELING

2.1 Description of the proposed model

A fine discretization mesh of finite elements is applied to the structural system under consideration, and a typical mesh of such a kind is shown in Figure 2 [6], which concerns the face wall of an existing old building.

In particular, the wooden elements of the truss-work are modeled with frame (beam-column) elements, the infilling masonry is modeled with plane-stress or shell elements, while for the joint connections of the frame elements, rigid or flexible link elements (springs) with finite size can be used.

The discontinuities along the length of the wooden parts and within their joint connections are modeled by using proper release-end conditions in the respective frame elements. For the proper consideration of the finite size of the frame elements' sections, rigid offsets between the neutral axis of the frame elements and the contact interface must be introduced.

The boundary conditions between the infilling masonry and the wooden elements are modeled with proper contact-friction bonds with Coulomb's law of dry friction [4]. Furthermore, elastic or inelastic constitutive laws can be used for the respective materials ([5]), as well as for the joint connections of the frame elements [2]. At this point, the significant role of the flexural stiffness of the frame elements must be emphasized; this means that the flexural stiffness must not be neglected, so that the contact interaction between the infilling masonry and the timber truss-work can be activated with certainty.

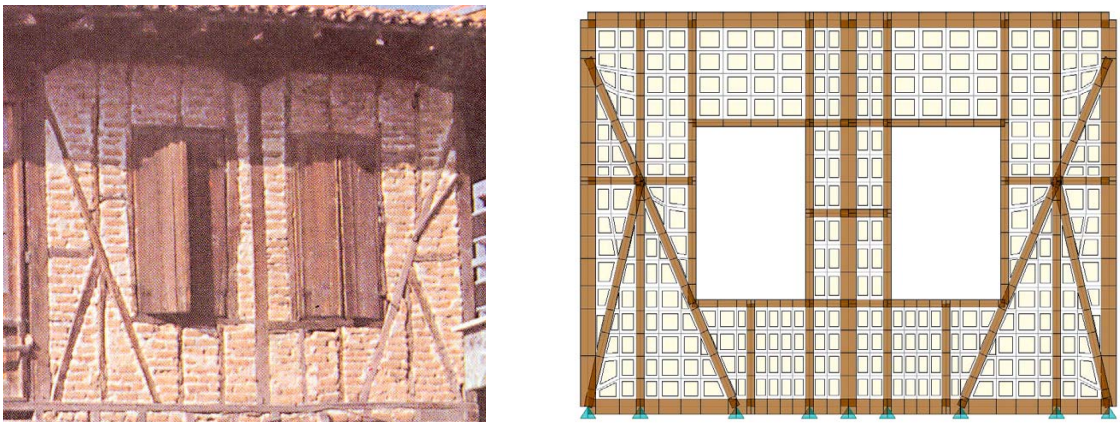

(a) (b)

Figure 2. (a) Face wall of an old building, (b) Respective analytical micromodel with finite elements

2.2 Contac interface conditions and solution procedure

If S_N and S_T are the normal and tangential (shear) force of the contact bond (tension positive), U_N and U_T are the corresponding relative end displacements (extension positive), δS_N, δS_T, δU_N, δU_T are their incremental values and μ is the friction coefficient, these incremental values are subjected to the following constraints (2-D formulation [3]):

a. For initial conditions of separation $(U_N > 0)$, the incremental contact state is also separation, that is:

$$\delta S_N = 0, \quad \delta S_T = 0, \quad \delta U_N + U_N > 0 \tag{1}$$

b. For initial conditions of sticking contact $(U_N > 0, \quad \mu \cdot S_N + |S_T| < 0)$, the incremental contact state is also sticking contact:

$$\delta U_N = 0, \quad \delta U_T = 0, \quad \mu(S_N + \delta S_N) + |S_T + \delta S_T| < 0 \tag{2}$$

c. For initial conditions of slipping contact $(U_N > 0, \quad \mu \cdot S_N + |S_T| = 0)$:
If $S_N < 0$, the incremental contact state may be either sticking contact (3a), or slipping contact (3b):

$$\delta U_N = 0, \quad \delta U_T = 0, \quad \mu(S_N + \delta S_N) + |S_T + \delta S_T| < 0 \tag{3a}$$
$$\delta U_N = 0, \quad \delta U_T \cdot S_T \le 0, \quad \mu(S_N + \delta S_N) + |S_T + \delta S_T| = 0 \tag{3b}$$

If $S_N = 0$, the incremental contact state may be either sticking or slipping contact (relations 3a, 3b), or separation, that is:

$$\delta S_N = 0, \quad \delta S_T = 0, \quad \delta U_N \ge 0 \tag{3c}$$

It is noted that the tangential relative displacements U_T are reversible for the separation state and irreversible for the slipping contact state. In certain existing computer programs for non-linear structural analysis, the above mentioned contact incremental constraints can be modeled approximately by using proper gap elements.

For the solution of the resulting mathematical problem with all the aforementioned non-linearities, standard nonlinear time-history methods of static or dynamic analysis can be applied (combination of the step-by-step and iterative methods). Within the framework of the present study, the analysis and solution capabilities of the computer programs SAP2000 [8] and ADINA [9] have been used.

3 APPLICATIONS TO SIMPLE WALLS WITHOUT OPENINGS

In the applications that follow, a proportionally increasing quasi-static horizontal load with a maximum amplitude of P=100 kN is applied at the top corners of the examined walls and the response values of the system are calculated. For each application the following 3 alternative models are formed and compared:

- model1: the proposed micromodel with contact interface conditions between truss-work and infilling
- model2: the respective bare truss-work model (without infilling)
- model3: a micromodel similar to model1, but with full bond at the interface of truss-work and infilling.

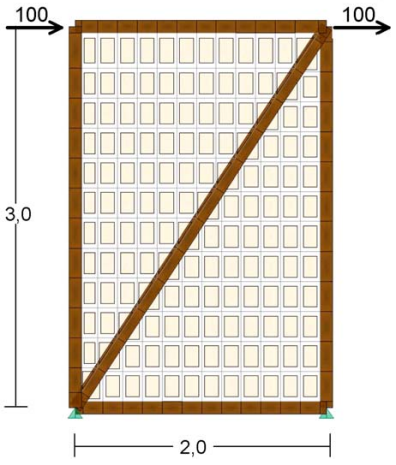

Wood: $E=12\times10^6$ kN/m^2
$G=5\times10^6$ kN/m^2
Column sections: 10×10 cm
Beam sections: 10×10 cm
Diagonal section: 10×10 cm

Infilling: Isotropic
$E=3\times10^6$ kN/m^2
$G=1{,}2\times10^6$ kN/m^2
Thickness: t=10 cm

Interface: Friction coefficient μ=0,50

Figure 3. Micromodel of a rectangular (1×1)–span infilled truss-work with single diagonal bracing

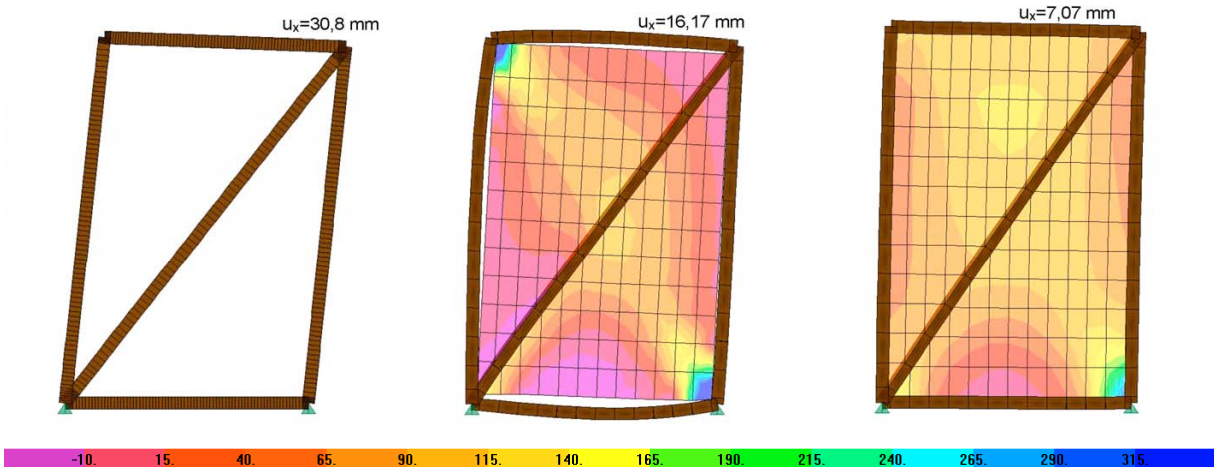

(a) model2 (b) model1 (c) model3

Figure 4. Deformed shape of the wall shown in Figure 3 and distribution of shear forces within infilling.

3.1 Rectangular 1×1–span truss-work with single diagonal bracing

The examined wall [7] and the respective discretized model are shown in Figure 3, together with the material and section properties of the structural members. For a more consistent comparison with the results of model2 (bare truss-work) the assumption of linear elastic behavior of all the materials is made, although this assumption is realistic only for small values of the applied horizontal load. Zero-size joints (without link elements or springs) are considered at the nodal connections of the frame elements, with release-end conditions (for zero bending moments) at the ends of these elements. The proposed model1 includes 72 frame elements, 156 shell elements and 78 gap elements.

Figure 3 shows the deformed shape of the wall and the distribution of shear forces within the infilling masonry. In the proposed model1 the separation areas between the infilling and the truss-work are clearly shown. The horizontal displacement at the top-right corner of the simplified model2 is 90% larger than in model1, while in the simplified model3 is 56% smaller than in model1. Regarding the distribution of shear forces, in model1 there is a high concentration at the compressive top-left and bottom-right corners of the infilling, and a formation of a respective diagonal zone with high shear forces which can be related to the well-known compressive diagonal strut of the infilled frames. In model2 the shear forces are substantially smaller and the formation of a diagonal zone with high shear forces is not so distinct.

Figure 4 shows the axial force diagrams of the truss-works of the examined models. The divergence of the extreme axial forces, with respect to model1, range from 86% to 100% in the case of model2 and from -46% to 50% in the case of model3. It is obvious that all the results of both simplified models are very different than those of the proposed model1.

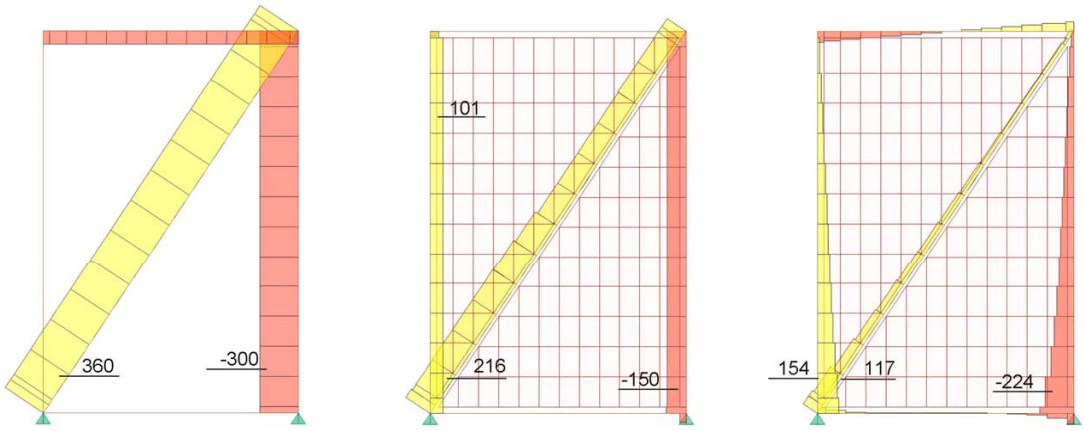

(a) model2 (b) model1 (c) model3

Figure 5. Axial force diagram in the truss-work of the wall shown in Figure 3.

3.2 Rectangular 1×2–span truss-work with double diagonal X-bracing

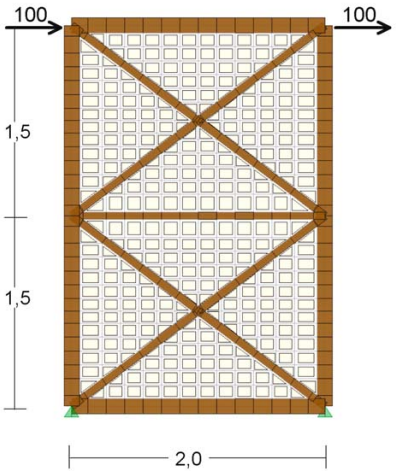

Wood: $E=12\times10^6$ kN/m^2
$G=4{,}61\times10^6$ kN/m^2
Column sections: 12×12 cm
Beam sections: 12×12 cm (top-bottom)
Beam sections: 12×6 cm (middle)
Diagonal sections: 12×6 cm

Infilling: Isotropic
$E=6\times10^6$ kN/m^2
$G=2{,}4\times10^6$ kN/m^2
Thickness: t=12 cm

Interface: Friction coefficient μ=0,50

Figure 6. Micromodel of a rectangular (1×2)–span truss-work with double diagonal bracing

The proposed micromodel of the examined wall [6] is shown in Figure 6, together with the material and section properties of the structural members. In this model the diagonals have half the section height (12×6) than the other elements (12×12), while the values of the Young modulus E and the shear modulus G of the infilling masonry are twice larger than those in the previous application. As before, the assumption of linear elastic behavior of all the materials is made, and zero-size joints (without link elements) are considered at the nodal connections of the frame elements. Release-end conditions (for zero bending moments) are considered at the ends of the beams and diagonals, while the continuity of the columns in the middle of their height is retained. The proposed model1 includes 178 frame elements, 336 shell elements and 216 gap elements.

Figure 7 shows the deformed shape of the wall and the distribution of shear forces within the infilling masonry. With respect to the proposed model1, the horizontal displacement at the top-right corner of the simplified model2 is 25% larger, while in the simplified model3 is 60% smaller. In Figure 7b a concentration zone of the shear forces is observed along the two shortened diagonals (from up-left to down-right) of model1, which take their maximum values near the ends of these diagonals. Also the separation areas between the infilling and the truss-work are clearly shown. In Figure 7c the shear forces of model3 have a smoother distribution than in model1, while any diagonal zone with shear concentration cannot be observed.

Figure 8 shows the axial force diagrams of the truss-works of the examined models. The divergence of the axial forces of model2, with respect to model1, ranges from –3% to 26% for the columns, is about 15% for the tensile diagonals and about 44% for the compressive diagonals. The respective divergence of model3 ranges from –16% to 9% for the columns, is up to –84% for the tensile diagonals and up to 80% for the compressive diagonals. In conclusion, the simplified model2 provides a better estimation of axial forces than model3.

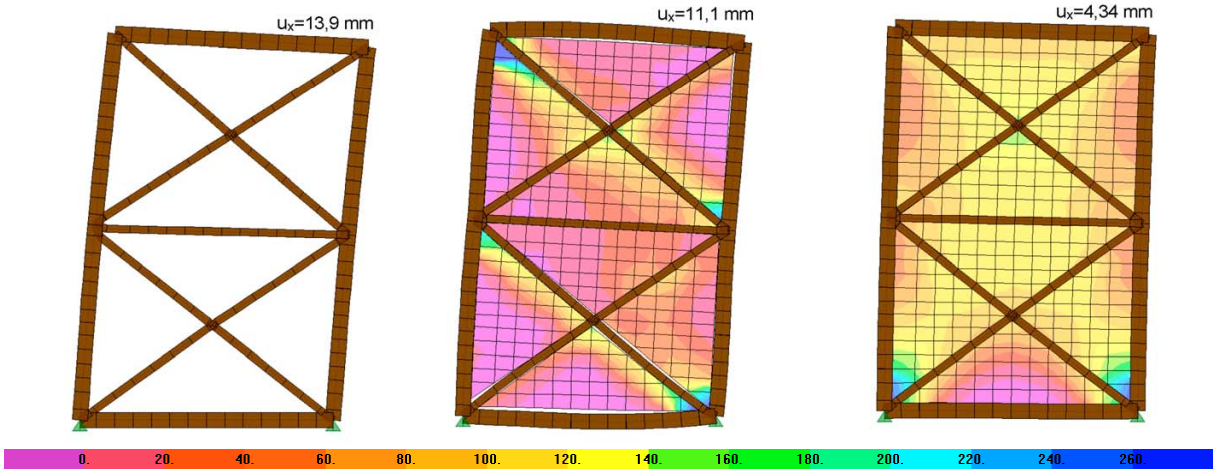

(a) model2 (b) model1 (c) model3

Figure 7. Deformed shape of the wall shown in Figure 6 and distribution of shear forces within infilling.

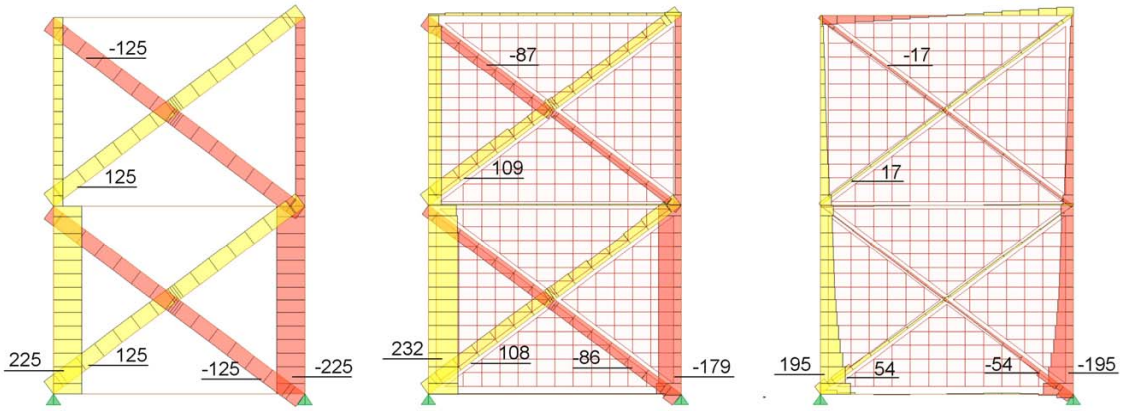

(a) model2 (b) model1 (c) model3

Figure 8. Axial force diagram in the truss-work of the wall shown in Figure 6.

4 APPLICATION TO A COMPLEX WALL WITH OPENINGS

The examined wall [7] in this application represents the entire face of a small building's storey. The proposed model1 is shown in Figure 9a, and the material and section properties of the structural members are shown in Table1. As previously, two additional simplified models (model2 and model3) are formed and compared.

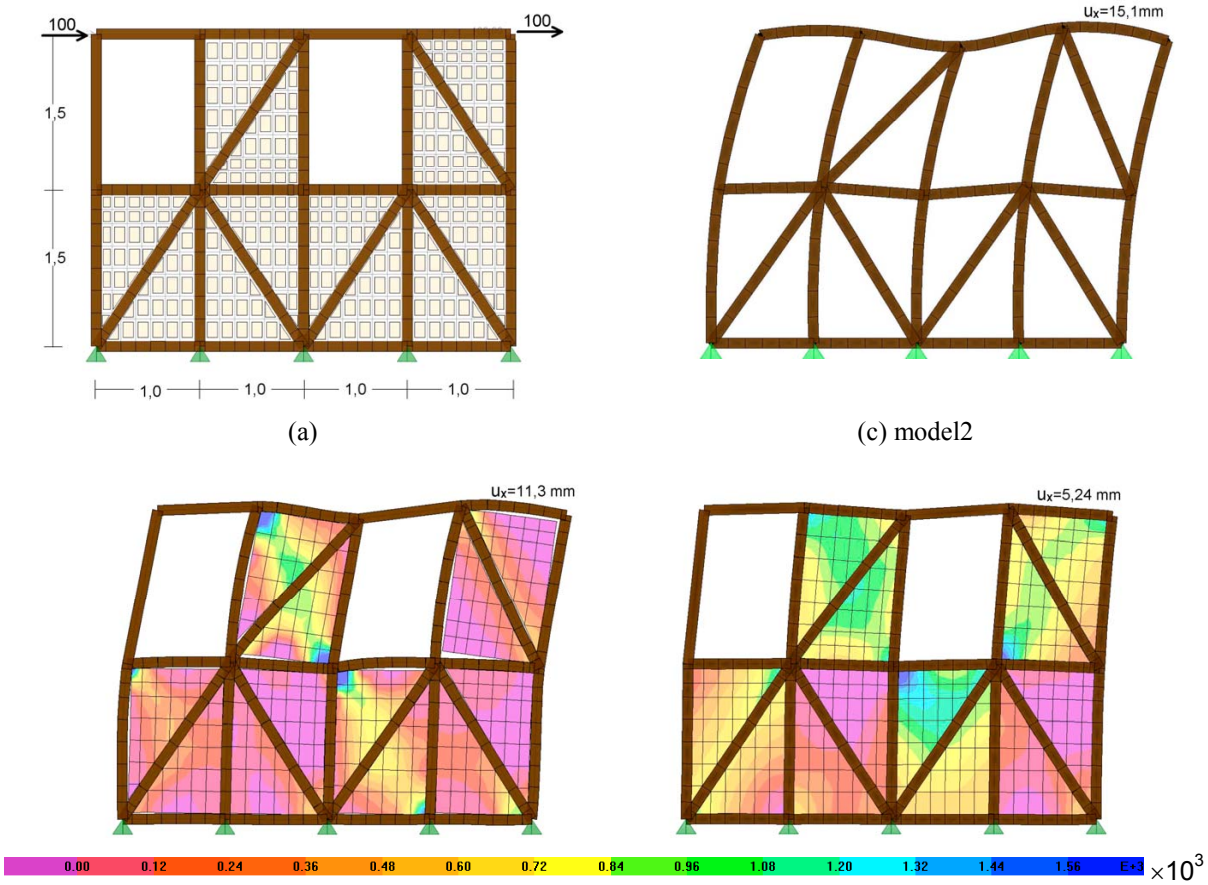

(a) (c) model2

(b) model1 (d) model3

Figure 9 (a): Discretization of the examided wall, (b) (c) (d): Deformed shape and distribution of shear streses within infilling of the wall shown in (a).

Wood	Infilling masonry	Interface
$E = 12\times10^6$ kN/m^2 $G = 5\times10^6$ kN/m^2 Column sections: 10×10 cm Beam sections: 10×10 cm Diagonal sections: 10×10 cm	Isotropic $E = 3\times10^6$ kN/m^2 $G = 1{,}2\times10^6$ kN/m^2 Thickness: t=10 cm	Friction coefficient: μ=0,50

Table 1. Material and section properties of the examined wall with openings.

The assumption of linear elastic behavior is made for all the materials, and zero-size joints are considered at the nodal connections of the frame elements. All the columns have a 3,0 m continuous length, the top and bottom beams have a 4,0 m continuous length, while release-end conditions (for zero bending moments) are considered at the ends of the 6 diagonals and the 5 beams in the middle of the storey's height. The proposed model1 includes 234 frame elements, 294 shell elements and 266 gap elements.

Figures 9b, 9c and 9d show the deformed shape of the examined models and the distribution of shear stresses within the infilling masonry. In the proposed model1 the separation areas between infilling and truss-work are clearly shown. With respect to the proposed model1, the horizontal displacement at the top-right corner of the simplified model2 is 34% larger, while in the simplified model3 it is 54% smaller.

In Figure 9c diagonal zones with shear concentration can be observed in all the 3 shortened diagonals of model1, where truss elements do no exist. In Figure 9d the shear forces of model3 have a smoother distribution than in model1, while less distinct diagonal zones with shear concentration can be observed at the upper level of the wall along the shortened diagonal (on the left), as well as along the lengthened diagonal (on the right).

Figures 10b, 10c and 10d show the axial force diagrams of the truss-works of the examined models. The divergence of the axial forces of model2, with respect to model1, is up to 26% for the most tensile elements and up to 49% for the most compressive elements. The respective divergence of model3 is up to -51% for the most tensile elements and up to -64% for the most compressive elements. In conclusion, the simplified model2 provides a better estimation for the axial forces than model3, especially for the most tensile elements.

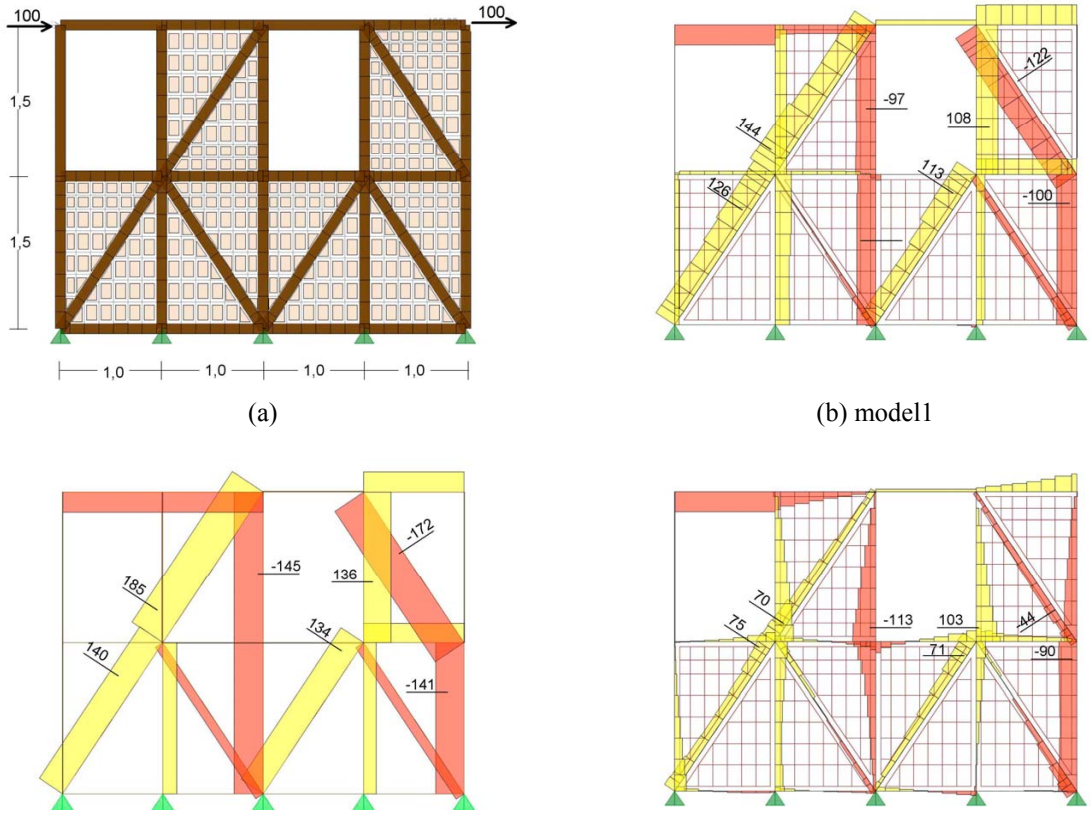

(a) (b) model1

(c) model2 (d) model3

Figure 10 (a): Discretization of the examided wall, (b) (c) (d): Axial force diagram in the truss-work of the wall shown in (a).

5 CONLUSIONS

The methodology of the micromodels with contact interface conditions provides increased analysis capabilies for a more detailed and accurate study of the stress, strain and available strength of the masonry-infilled timber truss-works. In the writers opinion, the uncertainties of the material laws, the joint connections and the construction details of these walls in general, affect much more the results of the system's response than the inevidable imperfections of the proposed micromodels. However it is not yet efficiently applicable in large structural systems like an entire building.

Regarding the examined simplified models, it must be noted that, depending on the form of the diagonal bracing, these models may give very inaccurate results. It must be noted also that the simplified model of the bare truss-work without infilling provided better results than the simplified model with full-bond interface conditions.

REFERENCES

[1] Gulkan P., Langenbach R. (2004), "The earthquake resistance of traditional timber and masonry dwellings in Turkey", Proceedings of the 13th World Conference on Earthquake Engineering, Vancouver, Canada, August 1-6, CD-ROM.

[2] Hatzitrifon N.K. (2004), "Bearing capability of historical timber timber framed walls, infilled or lattice covered", Proceedings of the 2nd National Congress on Appropriate Interventions for the Safeguarding of Monuments and Historical Buildings, Thessaloniki, Greece, 14-16 October, Vol II, pp. 15-25.

[3] Makarios T, Demosthenous M. (2004), "Seismic response of traditional buildings of Lefkas", Proceedings of the 2nd National Congress on Appropriate Interventions for the Safeguarding of Monuments and Historical Buildings, Thessaloniki, Greece, 14-16 October, Vol II, pp. 26-35.

[4] Doudoumis I.N., Mitsopoulou E.N., Nikolaidis G.N. (1994), "A macroelement for the simulation of the infill panels in multistorey frames under horizontal seismic actions", Proceedings of the 10th European Conference on Earthquake Engineering., Vienna, Austria, pp.1371-1376

[5] Doudoumis I.N., Mitsopoulou E.N. (1998), "Analytical modelling of infill panels using inelastic macroelements with contact interface conditions", Proceedings of the 11th European Conference on Earthquake Engineering, Paris, France, CD-ROM.

[6] Deligiannidou J. (2004), "Analytical study of rectangular infilled trusses with double diagonal bracing and contact interface conditions", Dipl. thesis in postgraduate studies: Protection, Conservation and Restoration of Architectural Monuments, School of Technology, Aristotle University of Thessaloniki, Greece.

[7] Kelesi A. (2004), "Analytical study of rectangular infilled trusses with simple diagonal bracing and contact interface conditions", Dipl. thesis in postgraduate studies: Protection, Conservation and Restoration of Architectural Monuments, School of Technology, Aristotle University of Thessaloniki, Greece.

[8] SAP2000: "Integrated Finite Element Analysis and Design of Structures" (1999), Computers and Structures, Inc., Berkeley, USA.

[9] ADINA: "Automatic Dynamic Incremental Nonlinear Analysis" (2003), Adina R&D, Inc., Watertown, USA.

STRUCTURAL ANALYSIS OF E.S.A YOUNG ENGINEERS SATELLITE 2 EJECTION SYSTEM

Antonios I. Vavouliotis[1], Dimitrios Lamprou[1], Vassilis Kostopoulos[1], Jens Carlevi[2], Erik Van de Heide[3]

[1]Applied Mechanics Laboratory, Department of Mechanical Engineering & Aeronautics,
University of Patras
Patras University Campus, GR 265 00 Patras, Greece
E-mail: kostopoulos@mech.upatras.gr
[2]Division of Machine Elements, Lulea University of Technology, Sweden
[3]Delta-Utec SRC, the Netherlands

Keywords: structural analysis

Abstract:
This work addresses the structural analysis of the ejection system of Young Engineers Satellite 2 (YES2). The YES2 ejection system is a redesigned system based on the low mass separation system for micro satellites in order to meet the requirements of the YES2 mission. The goal of the structural analysis was to give confidence to the resized mechanical design.
The YES2 satellite consists of 2 parts, connected by a tether: the FLOYD module (Foton Located YES2 Deployer), and the capsule, build up from FOTINO module (A low mass Re-entry capsule) and MASS module (Mechanical and data Acquisition Support System). The YES2 Ejection System is a spring based mechanical subsystem that connects mechanically the FLOYD and MASS & FOTINO modules, which sustains the loads during launch phase and gives to MASS & FOTINO the desired relative velocity (2 m/sec) with the expansion of 3 constrained linear springs after the explosive cut of a steel wire that holds 3 freely rotating hooks that anchor the MASS & FOTINO in its initial position.
The structural analysis procedure followed can be divided in two steps. Firstly the forces acting on the ejection mechanism due to the random vibration and transient loads during the launch phase were derived from a modal analysis of FE model of MASS & FOTINO satellite part. The second step covers the FE modeling of the complex ejection mechanism and then the calculation of the developing stresses on the each components of the mechanism under the action of those forces that were calculated during the first step. Finally the safety margins were calculated.
In addition special attention has been given in the modeling of the sliding contact interface of the rotating hooks.

INTRODUCTION

In May 2002 the European Space Agency kicked off a hands-on educational project called Young Engineers Satellite 2, managed by Delta-Utec in Leiden, Holland. The YES2 is building on the experience and success of YES & TEAMSAT, launched on Ariane 502 in 1997. The objective of the project further from the educational perspective of giving the European students a motivating technological experience is to demonstrate the "SpaceMail" application of returning a low mass Re-entry capsule (FOTINO) from space to Earth, using a 30 km 5 kg wire (tether) rather than a rocket engine. The YES2 mission is planned to be launched late 2006 on the Russian spacecraft Foton M3 mission.
The first phase of YES2 (2002-2003) focused on the conceptual design of the Re-entry vehicle and the building and testing of a tether deployment mechanism. Phase I ended with the Preliminary Design Review (PDR) taking place at ESA/ESTEC on December 2003. After PDR, the YES2 project entered phase II which focused on a detailed design of the different subsystems, leading up to the building and testing of the actual space hardware. The second phase of YES2 project is being developed at Delta-Utec (NL) and at 4 Centres of YES2 Expertise (CoE) located at 4 different universities in Europe and Russia. CoE Patras (Applied Mechanics Laboratory/University of Patras, Greece), CoE Krefeld (Fachhochschule RheinAhrCampus Remagen/Krefeld, Germany), CoE Reggio (University of Modena & Reggio Emilia, Italy) and CoE Samara (Samara State Aerospace University, Russia).
The YES2 satellite consists of 2 parts, connected by a tether: the FLOYD module (Foton Located YES2 Deployer), and the capsule, build up from FOTINO module (A low mass Re-entry capsule) and MASS module (Mechanical and data Acquisition Support System). The YES2 Ejection System is a spring based mechanical subsystem that connects mechanically the FLOYD and the capsule, which sustains the loads during launch phase and gives to MASS & FOTINO the desired relative velocity (2 m/sec) with the expansion of 3 constrained linear springs after the explosive cut of a steel wire that holds together 3 freely rotating hooks that anchor the MASS & FOTINO in its initial position.

PROBLEM DEFINITION

The YES2 Ejection System is a subsystem of the FLOYD module of the YES2 satellite. It is the subsystem that makes the mechanical interface between FLOYD and MASS module and gives the desired initial velocity to MASS and FOTINO assembly during the first stage of the tether deployment. The desired initial velocity is defined to be 2.1 m/sec normal to the ejection system and the current mass estimation of the ejected assembly is 20 kilograms.

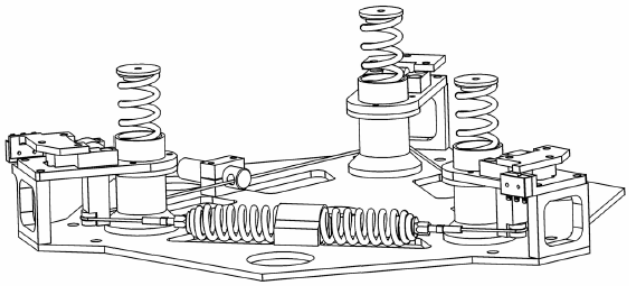

Figure 1: The YES2 Ejection System

The separation system consists of:
1. Base plate
2. Three ejection assemblies
3. A pretension steel wire
4. Pretension spring
5. Wire cutter
6. Two micro switches for status of ejection monitoring.

Function

When the wire cutter cuts the steel cable the three hooks in the ejection assemblies are released. The ejection springs then pushes the MASS assembly and forces the hooks to rotate. After a rotation of the three hooks of about 60 degrees the MASS assembly is completely free and the separation is completed. The energy stored in the ejection springs is transformed into kinetic energy in the MASS elements. The separation velocity between Foton and the MASS and FOTINO assembly will be 2.1 m/s. The pretension cable is attached to the pretension spring, which is kept in place on the base plate by a bracket. The ejection springs are kept in place inside the canisters all the time. No other parts than the MASS elements will separate. The energy stored in the pretension cable is low enough for not causing any damage to the surrounding systems when cut.

Objectives

The YES2 Ejection System mechanical design is based on a low mass separation system for micro satellites that had been designed by the Swedish Space Corporation and successfully tested in different configurations on MASER-5(1992), Astrid-1 (1992), Astrid-2 (1998) and DLR-TUBSAT (1999). The SSC has licensed the use of the design within the frame the YES2 project. The adaptation from the SSC initial system involves scaling of the ejection system to be used on the YES2 platform and some design modifications in order to meet the new requirements. The needed energy output from the ejection system is approx 2-5 times higher for the YES2 project compared to the previous systems depending on configuration. This work addresses the structural analysis of the redesigned ejection system of Young Engineers Satellite 2. The goal of the structural analysis is to give confidence to the resized mechanical design before the manufacturing of the functional prototype.

This work introduces an innovative F.E analysis procedure of the structural validation of this kind of mechanical systems since until now the preferred procedure covered mainly structural validation by testing. After a extensive bibliography research no relative work has been fund.

PROCEDURE

The objective of the YES2 Ejection System structural analysis is to extract the safety margins of the developing stresses on each part during the mission and to conclude for the acceptance of those margins. The critical parts of the sub-system from structural point of view are those of the Ejection Assemblies. In order to perform the stress analysis of them the applied forces acting on the ejection assemblies are calculated first. These forces are created by the stored spring and by the reaction of the interface between MASS and Ejection System on the mechanical loading during each stage of the mission. Those reaction forces are calculated with a series of static analyses under loading conditions indicated from a combination of the mechanical behavior of the assembly during the random vibrating loads and the linear acceleration loads [1]. Having calculated the acting forces the procedure continues with the detailed FE modeling of the Ejection Assembly giving special attention in the modeling of the sliding contact interface of the rotating hooks. Finally the static forces are applied together with

the appropriate boundary constraints on the FE model and the Von Misses stresses for each part were calculated. Having those results the safety margins and the appropriate safety factors can be provided and the integrity of the parts can be evaluated completely.

CALCULATION OF THE REACTION FORCES

Model description

For the computation of the Random Vibration Load Factor (RVLF) as it is described in Design Load Requirements[1] for the YES2 Ejection System it is needed to be studied the dynamic behavior of the YES2 Ejection System together with the structure that is mounted on top. The mounting structure includes the MASS and FOTINO modules. Approximately the mass of this structure is 20 kilograms. Because the mass of the Ejection System is considerable small, less than 1 kilogram compared to the mass of the MASS and FOTINO modules it can be assumed that the dynamic characteristics of the MASS and FOTINO modules control the RVLF and omit the modeling of the Ejection System at this stage. This step can be done only if the appropriate constraints will be applied in order to model the interaction of the two parts.

The CAD model that will be used as the reference for the building up of the FE model is a simplified version of the full model. Thus a simplified model that will correctly provide the system behavior was conducted. In that sense only the primary structure was modeled. The secondary parts like electronics and FOTINO module that is mounted on top of the MASS module will be introduced as lumped masses. Also as it was noted earlier ejection system was omitted and its interface with the MASS module was modeled by constraining all Degrees of Freedom (D.O.F) in the nodes where the Ejection System connects with MASS. In order to connect the lumped masses with the primary structure RBE3 elements were used. The RBE3 element distributes the force/moment applied at the master node to a set of slave nodes, taking into account the geometry of the slave nodes as well as weighting factors.

The primary structure of YES2 MASS module consists of four parts: the Base plate (1), the Inner Cylinder (2), the Cone (3) and the Outer Cylinder (4).

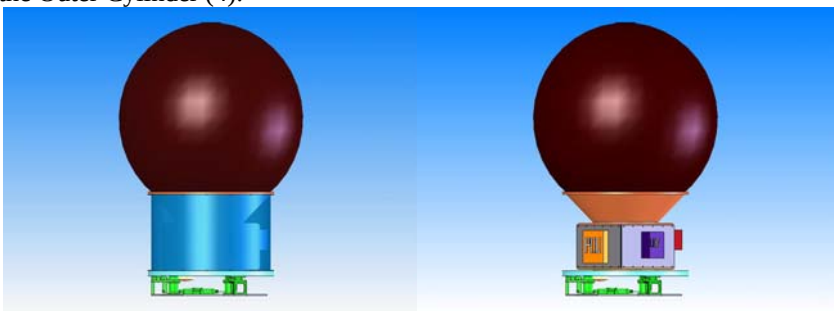

Figure 2: The assembly of Ejection System with MASS module and FOTINO module on top and the detailed view of the internal structure of the MASS module where the secondary structures are shown (electronics, and support structures for electronics)

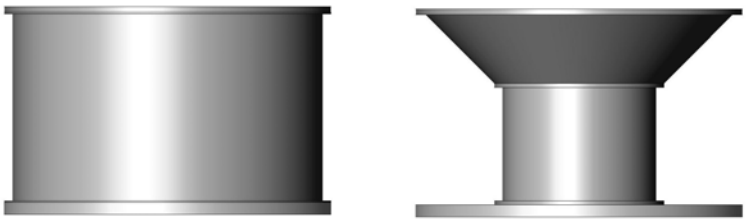

Figure 3: View of the simplified CAD model that shows the parts of the primary structure

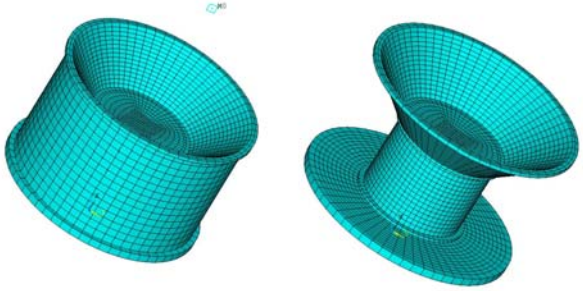

Figure 4: The FE model of the primary structures of YES2 MASS module. On the left the outer cylinder is shown which is modeled with shell elements. Also the lumped mass element is shown that models the YES2 FOTINO capsule. On the right the base plate, the inner cylinder and the cone are presented where 8 node brick solid elements were used

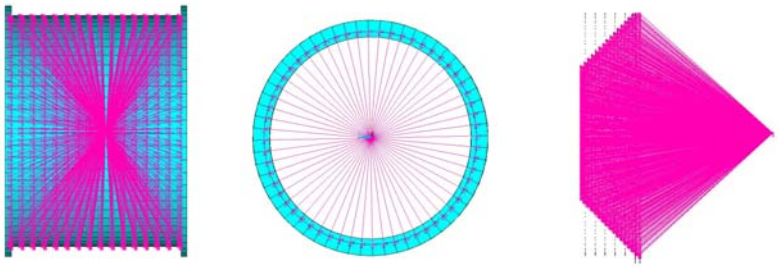

Figure 5: View of the RBE3 elements used for the modeling of the connection of the lumped mass elements.

For the electronics mounted symmetrically around the inner cylinder of MASS, a lumped mass element in the center of the inner cylinder is used. RBE3 elements connect this element with the internal nodes of the cylindrical structure. Since we are not interested for stress calculation and the main focus is in the approximate modeling of the mass distribution of the structure no further modeling consideration is taken for the electronics.

All the structure is made of Aluminium 7075 T651. The material characteristics used in this analysis is presented below:

Material Type	Density [kg.m^{-3}]	Young's Modulus [GPa]	Poisson's Ratio
Aluminum 7075 T7351	2810	72	0.33

In order to check the integrity of the model an unconstrained (free-free) modal analysis is conducted. The first six eigen-frequencies must be near zero. The check was passed.

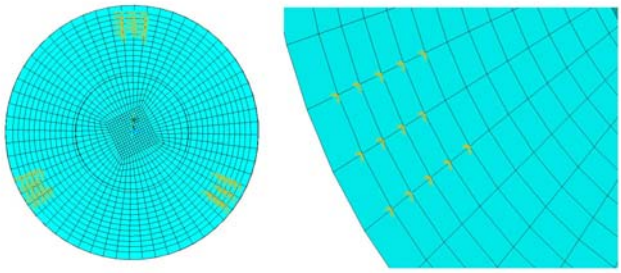

Figure 6 The DOF constraints in the nodes of bottom side of the base plate where the ejection system is connected.

The modal analysis

An eigen-frequency analysis (modal analysis) is performed including a calculation of effective modal masses to identify the importance of each mode. The quantity of eigen-frequencies to be calculated has to be large enough in order the sum of modal masses for each direction is greater than 80% of the equipment mass. In this analysis 36 mode shapes were calculated in the frequency range of 0 to 2000 Hz. The first eigen-frequency is 322.507 Hz and the last one is 1922.62 Hz.

Approximation of random vibration response load factors (RVLF)

The results of the modal analysis will be used in order to evaluate the overall random vibration response for each axis by using the following formula:

$$G_{RMS}^2 = \sum \left(m_i \sqrt{\frac{1}{2} \times \pi \times Q \times f_i \times W_i} \right)^2$$

Were:

Mi: the mass fraction that takes part in the specified resonant frequency

Q: amplification factors assumed 10 for those applications

Fi: the resonant frequency

Wi: the Power Spectral Density value for fi that is given by the chapter 2 named "Operational Requirements" of the "Scientific Hardware Design Specifications for PHOTON Spacecraft" [2]

For this evaluation only modes with an effective mass contribution >0.01% were considered.

Frequency Sub-range, Hz						
20	50	100	200	500	1000	2000
Power Spectral Density (g^2/Hz)						
0.02	0.02	0.02	0.05	0.05	0.02	0.02

Table 1: Power Spectral Density values for launch phase

From this procedure one value (Ri) is calculated for each axis.

Random Vibration Load Factor	Axis	Value	Unit
R1	X	14.143016	[g]
R2	Y	7.3815847	[g]
R3	Z	7.3815847	[g]

Combination of RVLF with Low Frequency Transient Load Factors (linear accelerations), extraction of load sets

The RVLF [R1, R2, R3] will be combined with Low Frequency TLF (linear accelerations) [T1, T2, T3] using a NASA procedure (chapter 1,page 4)[1]

Load Set	X-axis [g]	Y-axis [g]	Z-axis [g]
1.1-1.8	$+/- (T1^2+R1^2)^{0.5}$	+/- T2	+/- T3
2.1-2.8	+/- T1	$+/- (T2^2+R2^2)^{0.5}$	+/- T3
3.1-3.8	+/- T1	+/- T2	$+/- (T3^2+R3^2)^{0.5}$

The Low Frequency Transient Load Factors are given by the chapter 2 named "Operational Requirements" of the "Scientific Hardware Design Specifications for PHOTON Spacecraft" and they can be summarized

Transient Load Factor	Axis	Value	Unit
T1	X	10	[g]
T2	Y	10	[g]
T3	Z	10	[g]

The result of the combination is the production of 24 load sets presented in the following table:

Load Sets	X AXIS	Y AXIS	Z AXIS	Unit
Lift off 1	±17.321	±10.000	±10.000	[g]
Lift off 2	±10.000	±12.429	±10.000	[g]
Lift off 3	±10.000	±10.000	±12.429	[g]

The static analysis

Static Analysis for each load set is performed applying to the MASS module FE model (with the constraints for the ejection system) inertial gravitational acceleration loads. The Reaction Forces at the nodes that are constrained in order to model the ejection system were extracted and summarized for each mechanism. The maximum force was identified for each axis that is applying on to the Ejection Mechanism. This maximum force is the load case scenario that is requested for the second part of the structural analysis.

Axis	Reaction Force Calculated (N)	Ejection Spring Force (N)	Total forces acting (N)	Final Value (N)
X	2759.8	667	3427	4000
Y	920.42	0	920	1074
Z	925.81	0	926	1081

STRESS ANALYSIS OF THE EJECTION ASSEMBLY

Model Description

As it is presented in the following figure each Ejection Assembly consists of the following parts:
The vertical plate (1), the horizontal plate (2), the shaft brackets (3), the shaft (4), the hook (5), the interface (6), the steel cable (7), the spring tube (8), the spring cup (9), the base plate (10)

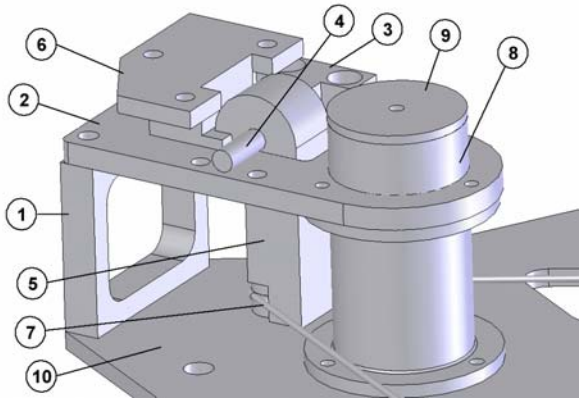

Figure 7: The Ejection Mechanism (the second shaft bracket is not shown)

In order to conduct the detail stress analysis a precise FE model was built including only the key structural components. The final FE model involves: The horizontal plate that the main ejection mechanism is mounted (1), the shaft brackets mounted on the horizontal plate (2), the shaft (3), the hook (4), the satellite interface (5), the steel cable (6) .

The reason of the decision of those parts as critical is that these parts constitute the main load paths. In addition, the satellite interface part will be modeled in a second step since a detailed contact interface must be introduced between the hook and the satellite interface part. This hierarchical approach is conservative since concerning the loading conditions of the hook it is assumed that the satellite interface part is un-deformed and the force acting on the top surface of the satellite interface part is directly transferred to the hook.

All components which are involved into the FE model are meshed with a full Mapped Mesh, and 8noded brick elements was used for the meshing of the solids and 2noded link elements was used for the modeling of the wire.

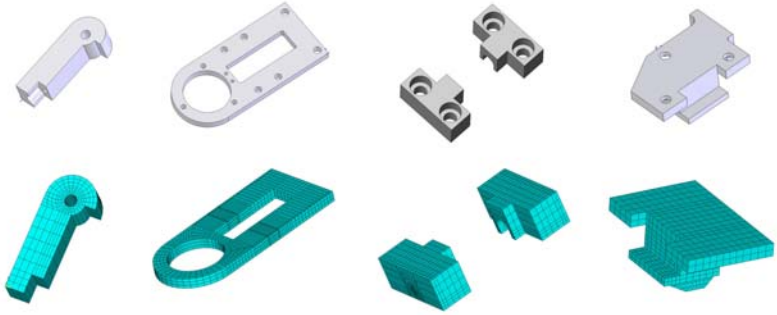

Figure 8: View of the FE modeling with 8-node brick solid elements of the hook, the horizontal plate, the brackets and the satellite interface

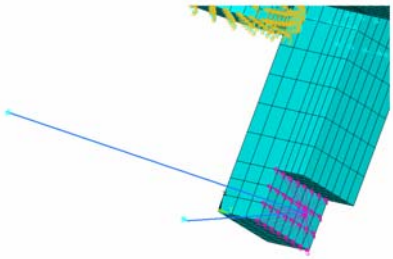

Figure 9: View of the link element used for the modeling of the steel cable. Also the RBE3 elements used to model the attachment of the cable on the hook are shown.

Since the modeling of the vertical plate and the spring tube is omitted, corresponding boundary conditions was applied in the form of nodal constraints of all degrees of freedom on certain nodes of the horizontal plate, as it is shown in the next Figure. In the same Figure, the modeling of the tight fit between the hook and the shaft with merging the coincident nodes is also presented.

For the separate model of the satellite interface part also corresponding boundary conditions were introduced in the form of nodal constraints of all degrees of freedom on certain nodes. In this FE model the loading environment is reversed and the force is applied in the contact surface with the hook and the top surface is fully constrained.

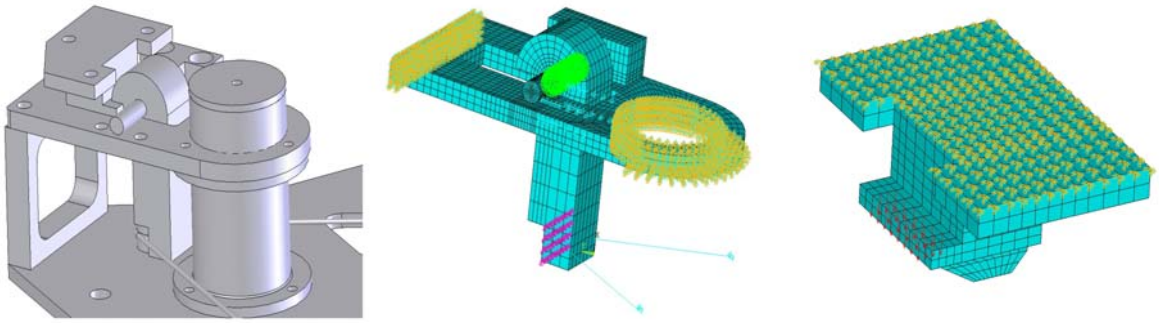

Figure 10: An overall view of the DOF constraints used

For the Shaft-Bracket contact, Contact Elements was used and a Friction Coefficient of 0.2 was assumed.

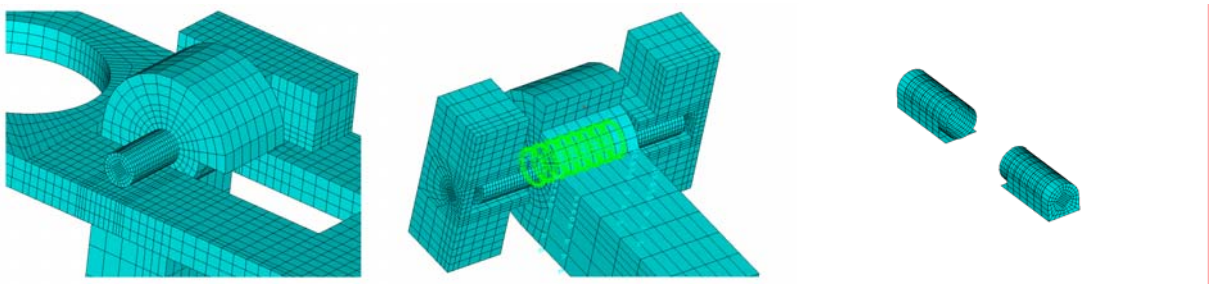

Figure 11: View of the contact elements used for the Shaft-bracket mechanical interface

In the Table 2 the material used for each part of the structure is presented and afterward the material properties are given in Table 3.

Part Name	Material
Horizontal Plate	Al7075 T7351
Shaft brackets	Al7075 T7351
Shaft	Steel A286
Hook	Al7075 T7351
Satellite Interface	Al7075 T7351
Cable	Steel AISI 316

Table 2

Material	Density [kg.m^3]	Young's Modulus [Pa]	Yield Strength [MPa]	Ultimate strength [MPa]	Poisson Ratio
Aluminum 7075 T7351	2810	72 x10^9	435	505	0.33
Steel AISI 316	7872	200 x10^9			
Steel A286	7872	200 x10^9	827	1100	0.29

Table 3

In order to check the integrity of the model a free-free modal analysis is conducted. The check was passed successfully.

The Stress analysis and calculation of Safety Margins

The analysis performed is a static analysis of the Hook-Shaft-Brackets-Horizontal Plate assembly, and a static analysis of the MASS Hook. The load applied in both cases was a 4000N force in the X axis (the ejection axis), in a pressure form on the contact surface between Hook and satellite interface parts.

In the case of the satellite interface part the load was applied as distributed force on the nodes (24 nodes x 166.6 Nt). In the model of the rest ejection assembly the loading is applied in a pressure form (76.95 10^6 Pa) at the area (4 x 13 mm^2) of the hook where the connection with the satellite interface part locates.

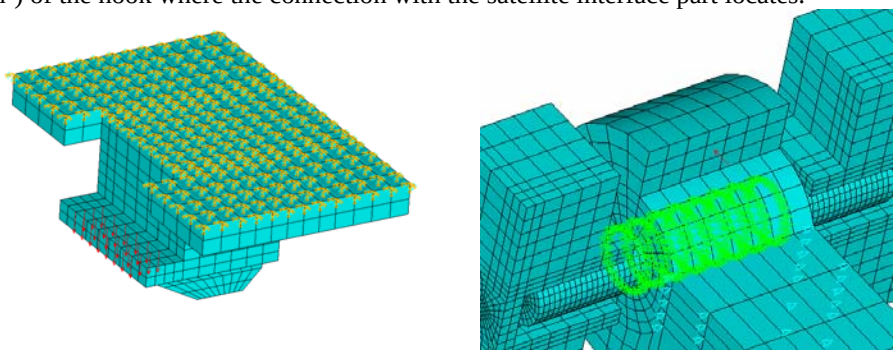

Figure 12

For calculation of safety margins the following safety factors will be applied:

For the yield stresses safety Factor = 1.0, for the ultimate stresses safety factor= 1.4. These values are considered for metallic structures (tested Shuttle, analysis and test) from TABLE 5.1.2–1 MINIMUM SAFETY FACTORS FOR PAYLOAD FLIGHT STRUCTURES MOUNTED TO PRIMARY AND SECONDARY STRUCTURE of [1].

The Safety Margins (MoS) are calculated by:

$$MoS_y = \left[\frac{\sigma_{yield}}{SF_{yield} \times stress^{VonMises}_{\max}} - 1 \right] \text{ And } MoS_u = \left[\frac{\sigma_{ultimate}}{SF_{ultimate} \times stress^{VonMises}_{\max}} - 1 \right] \text{ paragraph 5.2 of [1]}$$

RESULTS AND DISCUSSION

The required Safety Margins are: (a) MoSy > 0.0 and (b) MoSu > 0.0

The calculated Von Misses stresses are summarized in the following table 4 where the Safety Margins are also given.

Part	**SFy**	**SFu**	**Von-Misses [MPa]**	**MoSy**	**MoSu**
Hook	1	1.4	272	0.60	0.33
Shaft	1	1.4	769	0.08	0.02
Brackets (max)	1	1.4	400	0.09	-0.10
Brackets (real)	*1*	*1.4*	*311*	*0.40*	*0.16*
Horizontal Plate	1	1.4	246	0.77	0.47
MASS Hook	1	1.4	324	0.34	0.11

Table 4

It is observed (Figure 13) that for the Brackets, the maximum Von-Misses stress value is associated with only one node hence this value does not correspond to reality since singularity effects were arisen by the contact modeling. In order to have a more realistic value the Von Misses stress on the neighboring nodes are taken into account.
In the following Figure the Von-Misses contours are presented:

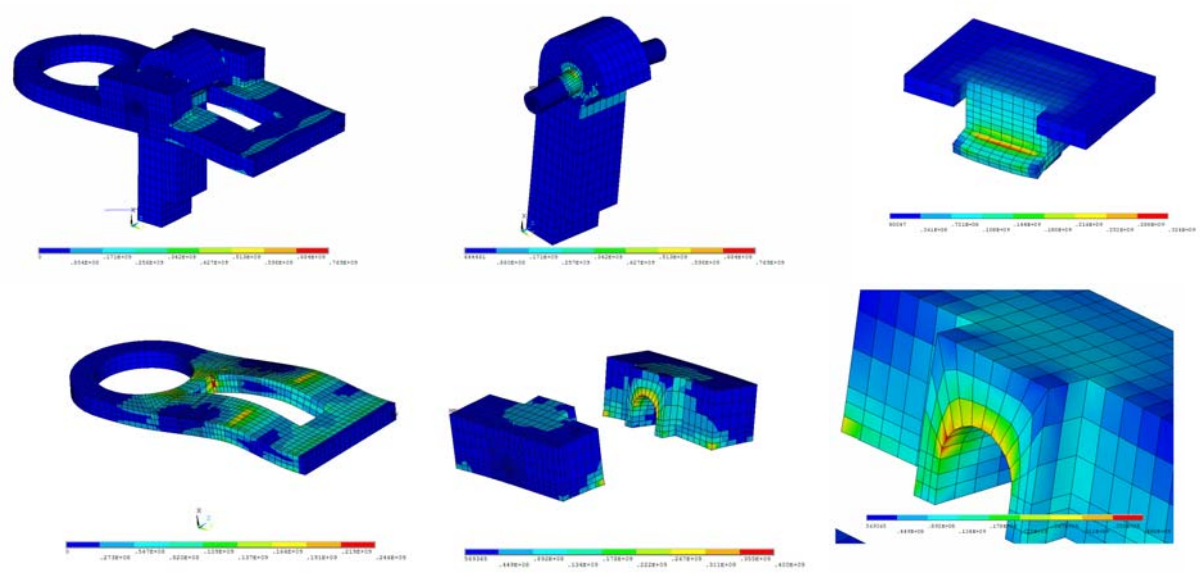

Figure 13

The deformed model is shown in Figure 14 together with the tensioning of the steel cable.

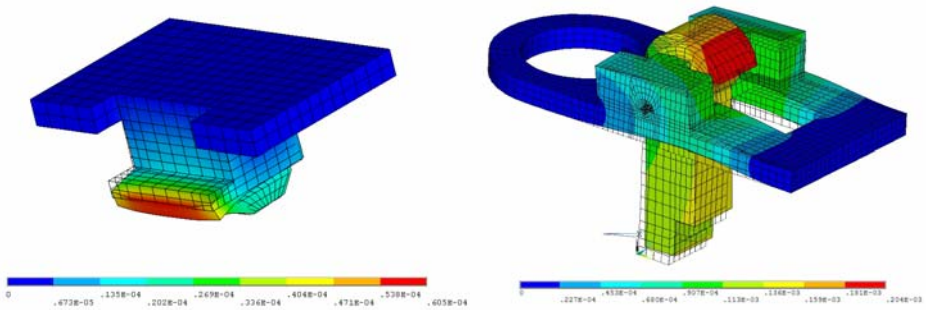

Figure 14

From the reaction solution of the link element constraints the reaction force is calculated to be of 837.5 N. This value is crosschecked with the result of an analytical static analysis of the hook.
The analytic static solution gives a value of 890 N. The results of the FE analysis have a difference of 5.80 %. This small deviation serves as a verification index of the FE model.

CONCLUSIONS

With this work the resized Ejection System of YES2 system gained the required confidence before the prototype manufacturing. Further work includes the comparison of the results of this FE analysis with the experimental ones during the mechanical testing campaign of the YES2 system.

ACKNOWLEDGMENTS

The manufacture of the YES2 Ejection system prototype was made by Bradford Engineering, The Netherlands
The FEA software package used was ANSYS, Inc.

REFERENCES

[1] (December 10, 1998), NASA SSP5200B, Payload Flight Equipment Requirements and Guidelines for Safety Critical Structures, International Space Station Program.
[2] (1990), PHOTON Design Bureau, Scientific Hardware Design Specifications for PHOTON Spacecraft

ROBUST DESIGN OPTIMIZATION OF STEEL STRUCTURES

Vagelis Plevris, Nikos D. Lagaros, and Manolis Papadrakakis

Institute of Structural Analysis & Seismic Research
National Technical University of Athens
Zografou Campus, Athens 15780, Greece
e-mail: {vplevris, nlagaros, mpapadra @central.ntua.gr}

Keywords: Multi-objective, Optimization, Robust design, Monte Carlo, Latin Hypercube, Cascade evolutionary algorithms.

Abstract. *In real world engineering applications, the uncertainties are inherent and the scatter of structural parameters from their nominal ideal values is unavoidable. In deterministic based structural sizing optimization problems the aim is to minimize the weight or the cost of the structure, taking into account certain behavioral constraints on stresses and displacements, as imposed in a deterministic manner by the design codes. On the other hand, stochastic performance measures that involve various reliability requirements are being taken into consideration in many contemporary engineering applications. Reliability is defined as the probability of the system to meet the design demands during its life time. In structural optimization, stochastic performance measures can be taken into account using two distinguished formulations, Robust Design Optimization (RDO) and Reliability-Based Design Optimization (RBDO).*

In the case of a RDO problem, the uncertainties play a dominant role. Compared to the basic Deterministic Based Optimization (DBO) formulation, a RDO formulation yields a design with a state of robustness, so that its performance is the least sensitive to the variability of the uncertain parameters. In this work, the optimum design achieved based on a deterministic formulation is compared with the ones obtained employing a robust design formulation, with reference to the structural weight, the variance of the response and the probability of violation of the constraints.

1 INTRODUCTION

Although a great deal of studies has been proposed during the last three decades for structural optimization, those devoted to RDO are rather limited. In the present work, the non-dominant Cascade Evolutionary Algorithm (CEA)-based multi-objective optimization scheme is proposed for the solution of structural RDO problems, together with an improved handling of the multi-objective optimization problem, and is compared to the Linear Weighting Sum (LWS) method. The stochastic finite element problem is solved using the Monte Carlo simulation method combined with the Latin Hypercube Sampling (LHS) technique in order to reduce the number of simulations needed for the calculation of the required statistical quantities. Up to one hundred LHS simulations proved to be sufficient, for the test cases considered for calculating the statistical quantities. Furthermore, the advantages of the proposed cascade multi-objective optimization methodology over the classical LWS method and the importance of considering the variance of the structural response as a criterion are demonstrated. A real-scale truss structure has been examined subject to constraints imposed by the Eurocode 3 [7].

2 STOCHASTIC FINITE ELEMENT ANALYSIS

During the last two decades much progress has been achieved on stochastic finite element methods [18, 19]. However, comparatively few studies have been performed in structural optimization taking into account uncertain parameters. For the solution of stochastic finite element analysis problems, a number of methods have been proposed that can be classified into statistical and non-statistical ones. In this work, a statistical method and in particular Monte Carlo Simulation combined with the Latin Hypercube Sampling is employed.

2.1 Monte Carlo Simulation (MCS) Method

The MCS method is particularly applicable for the stochastic analysis of structures when an analytical solution is not attainable. This is mainly the case in problems of complex nature with a large number of uncertain variables, where all other stochastic analysis methods are inapplicable. Despite the fact that the mathematical formulation of the MCS is simple, the method has the capability of handling practically every possible case regardless of its complexity and the variation of the uncertain variables. The MCS method has

proven to be efficient [16] for the calculation of the statistical quantities in the framework of a RBDO problem.

For the structural stochastic analysis problems examined in this study, the probability of violation of the behavioral constraints and the probability of failure are calculated along with the mean value and the variance of a characteristic nodal displacement that represents the response of the structure.

2.2 Latin Hypercube Sampling

The Latin Hypercube Sampling (LHS) method was introduced by MacKay et al. [13] in an effort to reduce the required computational cost of purely random sampling methodologies. Latin hypercube sampling is a strategy for generating random sample points ensuring that all portions of the random space in question are properly represented. LHS is generally recognized as one of the most efficient size reduction techniques. The basis of LHS is a full stratification of the sampled distribution with a random selection inside each stratum. In consequence, sample values are randomly shuffled among different variables. A Latin hypercube sample is constructed by dividing the range of each of the n_r uncertain variables into N non-overlapping segments of equal marginal probability. Thus, the whole parameter space, consisting of N parameters, is partitioned into N^{n_r} cells. A single value is selected randomly from each interval, producing N sample values for each input variable. The values are randomly matched to create N sets from the N^{n_r} space with respect to the density of each interval for the N simulation runs. The advantage of the LHS approach is that the random samples are generated from all the ranges of possible values.

3. MULTI-OBJECTIVE OPTIMIZATION

In many practical applications a single criterion rarely gives a representative measure of the actual structural performance, as several conflicting and usually incommensurable criteria have to be taken into account simultaneously. The optimization problem with more than one objective is called as multi-criteria, multi-objective or vector optimization problem [4].

3.1 Formulation of the multi-objective optimization problem

In general, the mathematical formulation of a multi-objective problem that includes a set of n design variables, a set of m objective functions and a set of k constraint functions can be defined as follows

$$\begin{aligned} \min_{\mathbf{s}\in F} \quad & [f_1(\mathbf{s}), f_2(\mathbf{s}), \ldots, f_m(\mathbf{s})]^T \\ \text{subject to} \quad & g_j(\mathbf{s}) \le 0 \quad j=1,\ldots,k \\ & s_i \in R^d, \quad i=1,\ldots,n \end{aligned} \tag{1}$$

where the vector $\mathbf{s} = [s_1\, s_2 \ldots s_n]^T$ represents a design variable vector and F is the feasible region, a subspace of the design space R^n for which the constraint functions $g(\mathbf{s})$ are satisfied

3.2 Domination and non-domination

In single objective optimization problems the feasible set F can be ordered univocally according to the value of the objective function. For example, in the case of the minimization problem of $f(\mathbf{s})$, two solutions $\mathbf{s}_a$ and $\mathbf{s}_b \in$ F can be classified using the condition $f(\mathbf{s}_a) < f(\mathbf{s}_b)$. In a multi-objective optimization problem two solutions $\mathbf{s}_a$ and $\mathbf{s}_b \in$ F cannot be classified in a univocal manner. The concept of the Pareto dominance is used for assessing the two solutions, which for a minimization problem can be defined as follows

$$\begin{aligned} &\mathbf{s}_a \text{ dominates } \mathbf{s}_b \text{ if } f_i(\mathbf{s}_a) < f_i(\mathbf{s}_b)\ \forall i=1,\ldots,m \\ &\mathbf{s}_a \text{ weakly dominates } \mathbf{s}_b \text{ if } f_i(\mathbf{s}_a) \le f_i(\mathbf{s}_b)\ \forall i=1,\ldots,m \\ &\mathbf{s}_a \text{ is indifferent to } \mathbf{s}_b \text{ otherwise} \end{aligned} \tag{2}$$

Using the definition of Eq. (2), the Pareto optimality can be stated as follows: A solution $\mathbf{s}^* \in$ F is Pareto optimal if it is not dominated by any other feasible design.

3.3 Solving the multi-objective optimization problem

Several methods have been proposed for treating structural multi-objective optimization problems [3, 9, 11]. According to Marler and Arora [12] these methods can be divided into: (i) methods with a priori articulation of preferences, (ii) methods with a posteriori articulation of preferences and (iii) methods with no articulation of

preferences. The proposed Cascade Evolutionary Algorithm-based (CEA) multi-objective optimization scheme belongs to the first category. This algorithm is compared to the Linear Weighting Sum method (LWS), also belonging to the a priori articulation of preferences. The LWS method, due to its simplicity, is the most widely implemented method for solving such problems. In both methods employed, the problem in finding the Pareto front curve is reduced into a sequence of parameterized single-objective optimization *subproblems*, using scalarizing functions.

In general, by using scalarizing functions, locally Pareto optimal solutions are obtained. Global Pareto optimality can be guaranteed only when the objective functions and the feasible region are both convex or quasi-convex and convex, respectively. For non-convex cases, such as the majority of structural multi-objective optimization problems, a global single objective optimizer must be implemented. Evolutionary Algorithms (EA) are considered as global optimizers since they are not prone to being trapped in local optima and therefore can be considered as the most reliable methods in approaching the global optimum for non-convex constrained optimization problems. For this reason an evolutionary algorithm has been considered in this study for the solution of the sequence of the parameterized single objective optimization problems.

3.4 Non-dominant multi-objective search using the Tchebycheff metric

The proposed Cascade Evolutionary Algorithm (CEA)-based optimization scheme combines the CEA methodology with a non-dominance search and the Tchebycheff metric.

3.4.1 Augmented weighted Tchebycheff problem

The augmented weighted Tchebycheff method belongs to the methods with a priori articulation of the preferences for treating the multi-objective optimization problem and unlike the LWS method, can be applied effectively to convex as well as non-convex problems [15]. The weighted Tchebycheff metric can generate any optimal solution, to any type of optimization problem [20]. In order to overcome weakly Pareto optimal solutions, the Tchebycheff method formulates the distance minimization problem as a weighted Tchebycheff problem

$$\min_{\mathbf{s}\in F} \max_{i=1,\ldots,m} \left[w_i \frac{\left| f_i(\mathbf{s}) - z_i^* \right|}{f_i(\mathbf{s})} + \rho \sum_{i=1}^{m} \frac{\left| f_i(\mathbf{s}) - z_i^* \right|}{f_i(\mathbf{s})} \right] \tag{3}$$

where ρ is a sufficiently small positive scalar (in this work $\rho = 0.1$). The weight parameters w_i are random numbers, uniformly distributed between 0 and 1. The weight parameters have to make a sum of 1, if not, they are updated according to the following expression:

$$w_i = \begin{cases} w_i + \dfrac{1 - \sum_i^m w_i}{\sum_i^m w_i} w_i, & \text{if } \sum_i^m w_i \neq 1 \\ w_i, & \text{if } \sum_i^m w_i = 1 \end{cases} \tag{4}$$

3.4.2 CEA-based multi-objective optimization scheme

It is generally accepted that there is still no unique optimization algorithm capable of handling all optimization problems efficiently. Cascade optimization attempts to alleviate this deficiency by applying a multi-stage procedure in which various optimizers are implemented successively. In the present work the idea of cascading is implemented in the EA-context (CEA) for solving multi-objective structural optimization problems. In particular, the CEA method is employed for the solution of the sequence of parameterized single objective optimization problems. The resulting cascade evolutionary procedure consists of a number of optimization stages (*csteps*), each of which employs the same EA optimizer. In order to diversify the search paths followed by the same optimization algorithm during the cascade stages, the initial conditions of the individual optimization runs are suitably controlled by using a different initial design at each stage (each stage initiates from the end point of the previous stage) and a different seed for the random number generator of the EA procedure [1].

A non-dominant search is performed in the context of the CEA and the Tchebycheff metric in the sense that all non-dominated solutions attained so far are kept in a set called temporary Pareto set. The multi-objective optimization problems are decomposed into *subproblems* which are solved with independent runs (*nruns* in total) of the CEA methodology. Each subproblem is independent from the others and therefore all subproblems can be dealt with simultaneously. Furthermore, in every global generation a non-dominant search is applied for updating the temporary Pareto set. The global generation is achieved when all local generations of the

independent CEA runs are completed. According to this procedure in every global generation a local Pareto front is produced which approaches the global one.

The optimization algorithm proposed in this study is denoted as: Non-dominant $CEATm(\mu+\lambda)_{nruns,csteps}$ where μ, λ are the number of the parent and offspring vectors used in the ES optimization strategy, *nruns* is the number of independent CEA runs and *csteps* is the number of cascade stages employed. The proposed optimization scheme can be easily applied in two parallel computing levels, an external and an internal one. The multi-objective optimization problem is converted into a series of single objective optimization problems. The solution of each subproblem can be performed concurrently constituting the *external parallel computing level*. On the other hand, the utilization of the natural parallelization capabilities of the CEA methodology within each independent run defines the *internal parallel computing level*.

4. ROBUST DESIGN OPTIMIZATION

In the present study the robust design versus the deterministic-based design optimization of large-scale 3D truss structures is investigated. The random variables chosen are the cross-sectional dimensions of structural members, the modulus of elasticity E, the yield stress σ_y, as well as the applied loading.

4.1 Deterministic-based optimization

In a Deterministic-Based Optimization (DBO) problem the aim is to minimize the weight of the structure under certain deterministic behavioral constraints. In this study three types of constraints are imposed to the sizing optimization problem considered: (i) Stress, (ii) Compression force (for buckling) and (iii) Displacement constraints. The stress constraint can be written as follows

$$\sigma_{max} \le \sigma_a, \quad \sigma_a = \frac{\sigma_y}{1.10} \tag{5}$$

where σ_y is the yield stress, σ_{max} is the maximum axial stress in each element group for all loading cases and σ_a is the allowable axial stress, all taken according to the Eurocode 3 [7] for design of steel structures. For members under compression an additional constraint is used

$$\left|P_{c,max}\right| \le P_{cc}, \quad P_{cc} = \frac{P_e}{1.05}, \quad P_e = \frac{\pi^2 EI}{L_{eff}^2} \tag{6}$$

where $P_{c,max}$ is the maximum axial compression force for all loading cases, P_e is the critical Euler buckling force in compression, taken as the first buckling mode of a pin-connected member, and L_{eff} is the effective length. The effective length is taken equal to the actual length. Similarly, the displacement constraints can be written as

$$\left|d\right| \le d_a \tag{7}$$

where d_a is the limit value of the displacement at a certain node or at the maximum nodal displacement.

4.2 Formulation of the robust design optimization problem

In a robust design sizing optimization problem an additional objective function is considered which is related to the influence of the random nature of some structural parameters on the response of the structure. In the present study the aim is to minimize both the weight and the variance of the response of the structure due to the uncertainty of the random parameters. This problem is treated as a two-objective optimization problem using the weighted Tchebycheff metric. The mathematical formulation of the RDO problem implemented in this study is as follows

$$\begin{aligned} &\min && \Phi(\mathbf{s}) \\ &\text{subject to} && g_j(\mathbf{s}) \le 0 \quad j = 1,...,k \\ & && s_i \in R^d, \quad i = 1,...,n \end{aligned} \tag{8}$$

where $\Phi(\mathbf{s})$ is the multi-objective function, which is expressed as

$$\Phi(\mathbf{s}) = \max\left[w_1 \frac{\left|f(\mathbf{s}) - z_1^*\right|}{f(\mathbf{s})} + \rho \sum_{i=1}^{m} \frac{\left|f(\mathbf{s}) - z_1^*\right|}{f(\mathbf{s})}, w_2 \frac{\left|\sigma_{u_i}(\mathbf{s}) - z_2^*\right|}{\sigma_{u_i}(\mathbf{s})} + \rho \sum_{i=1}^{m} \frac{\left|\sigma_{u_i}(\mathbf{s}) - z_2^*\right|}{\sigma_{u_i}(\mathbf{s})} \right] \tag{9}$$

where $f(\mathbf{s})$ is the weight of the structure and $\sigma_{u_i}(\mathbf{s})$ is the standard deviation of the response of the structure.

5. NUMERICAL TESTS

The numerical tests examined are performed in three stages. In the first stage the statistical methods used for the stochastic analysis are verified. The number of LHS simulations required for the calculation of the mean value and the standard deviation of the characteristic displacement that represents the structural response is compared with the corresponding number required by the basic MCS. In the second stage the advantages of the proposed non-dominant CEATm method over the LWS method are demonstrated through the comparison of the Pareto front curves obtained. In the third stage, the differences between DBO and RDO optimum designs, in terms of the final structural weight, the variance of response, the probability of violation of the constraints and the probability of failure, are illustrated.

The test example considered is a transmission tower, depicted in Figure 1. The design variables are the dimensions of the structural members, divided into seven groups, taken from the Equal Angle Section (EAS) table of the Eurocode. For each design variable, two stochastic variables are assigned: The length L and the width t of the legs of the section. The following loading vectors [Fx, Fy, Fz] in kN are applied to the structure: node A [-8.51, 0.00, -4.82], node B [-9.77, 0.00, -5.36], node C [-9.77, 0.00, -5.36], node D [-10.70, 0.00, -5.36] and node E [-10.70, 0.00, -5.36], while the type of probability density function, the mean value, and the variance of the random parameters are given in Table 1. A constraint maximum deflection of 200 mm is imposed.

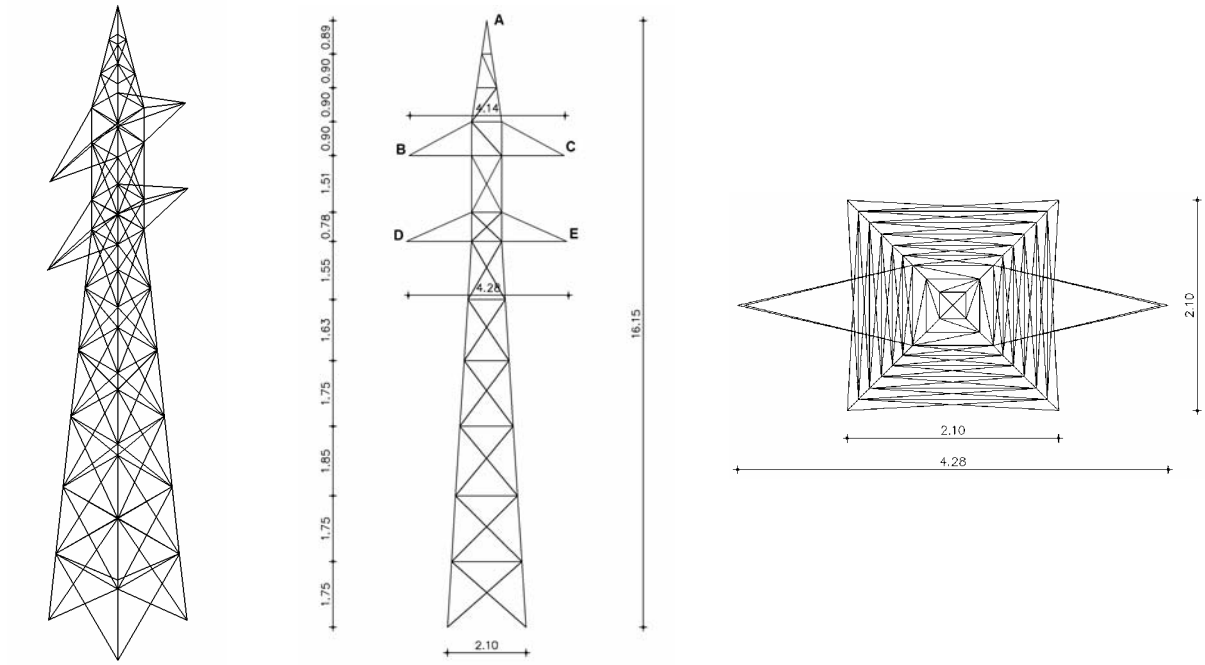

(a) (b) (c)

Figure 1. Transmission tower: (a) 3D view, (b) Side view, (c) Top view

		PDF	Mean μ	St. Dev. σ	σ/μ	95% of values within
E (kN/m^2)	Young's Modulus	Normal	2.10E+08	1.50E+07	7.14%	(1.81E+08, 2.39E+08)
σ_y (kN/m^2)	Allowable stress	Normal	355000	35500	10.00%	(2.85E+05, 4.25E+05)
F (kN)	Nodal loading	Normal	μ_F	0.05 μ_F	5%	(0.902 μ_F, 1.098 μ_F)
L	Legs length	Normal	L_i *	0.02 L_i	2%	(0.961 L_i, 1.039 L_i)
t	Legs width	Normal	t_i *	0.02 t_i	2%	(0.961 t_i, 1.039 t_i)

* Taken from the Equal Angle Section (EAS) table of the Eurocode for every design

Table 1. Characteristics of the random variables

5.1 Efficiency of the stochastic analysis method

In the first stage of the numerical study, the performance of the LHS procedure in calculating the statistical parameters required during the RDO procedure compared to the basic MCS is examined, by measuring the influence of the number of simulations on the computed value of the variance of the characteristic displacement. The results, for randomly selected designs, shown in Figure 2 demonstrate the efficiency of the implemented LHS procedure. It can be observed from Figure 2 that 100 LHS compared to 500 MCS simulations are required in order to calculate the standard deviation of the structural response. It has to be stated that the number of

simulations required may vary depending on the type of the structure, the loading conditions and the statistical characteristics of the structural parameters.

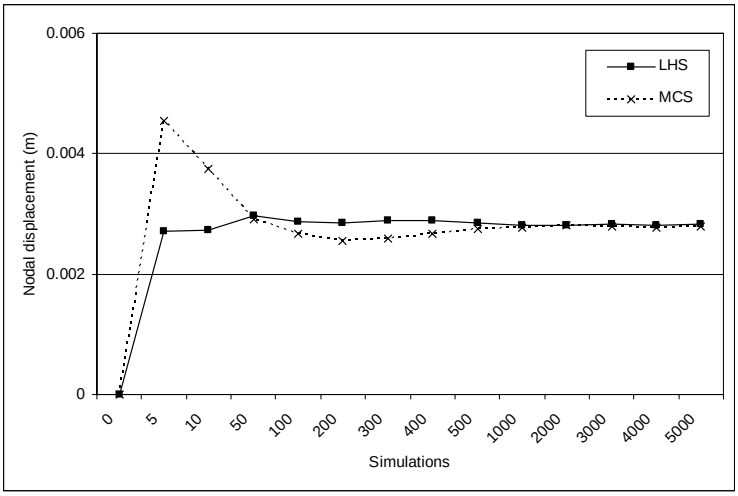

Figure 2. Efficiency of the LHS compared to the MCS in calculating the st. deviation of the structural response

5.2 Comparison between LWS and CEATm

In the second stage of this study the advantages of the cascade evolutionary multi-objective optimization scheme using the Tchebycheff metric are demonstrated over the linear weighing sum method. The quality of the Pareto front curve can be assessed by the number of Pareto optimum solutions obtained and their distribution along the front curve. Well distributed solutions along the curve provide an indication of the efficiency of the multi-objective optimization method employed. The main drawback of the multi-objective optimization methods using scalarizing functions, such as the LWS, is the difficulty to fulfil these two requirements.

For the comparative study performed in this study the robust design optimization problem considered has been solved with the LWS method and the proposed non-dominant *CEATm* multi-objective optimization scheme. The LWS method has been implemented through two different runs with 10 and 30 points using the ES(μ+λ) optimization algorithm where $\mu = \lambda = 5$ are the number of parents and offsprings, respectively. For the non-dominant CEATm$(\mu+\lambda)_{nrun,csteps}$ optimization scheme the corresponding parameters are $\mu = \lambda = 5$, nrun = 10 and csteps = 3. The resultant Pareto front curves are depicted in Figure 3 (a) and (b) for the LWS and the CEATm, respectively. The horizontal axis corresponds to the structural weight while the vertical axis corresponds to the standard deviation of the characteristic node displacement.

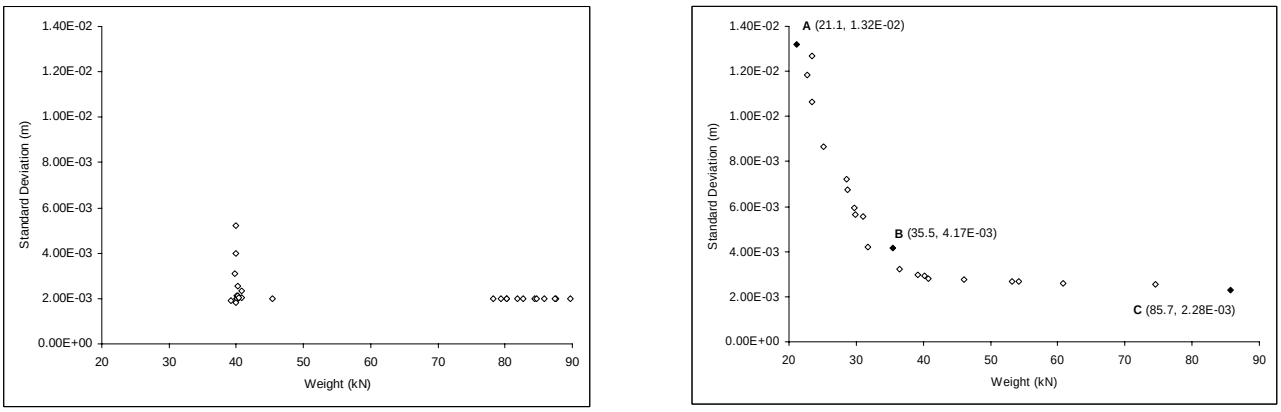

(a) (b)

Figure 3. The Pareto front curve obtained with (a) LWS - 30 points, (b) the non-dominant CEATm

The RDO multi-objective optimization problem is non-convex and the weakness of the LWS is obvious from the front curves of figure 3(a). Well distributed pairs of weighting coefficients do not correspond to equally well distributed Pareto optimum solutions along the front curve. On the other hand, the proposed CEATm optimization scheme manages to generate the Pareto front curve having a good distribution of the Pareto solutions along the front curve, seen in Figure 3(b).

5.3 Comparison between DBO and RDO solutions

In the third stage of this study the difference between DBO and RDO optimum designs is demonstrated in terms of the structural weight, the variance of the response and the probability of violation of the constraints. The resultant Pareto front curve, when the proposed optimization scheme is used, is shown in Figure 3(b). The two ends of the Pareto front curve represent two extreme designs. Point A corresponds to the deterministic-based optimum where the weight of the structure is the dominant criterion. Point C is the optimum when the standard deviation of the response is considered as the dominant criterion. The intermediate Pareto optimal solutions are compromise solutions between these two extreme optimum designs under conflicting criteria.

In Table 2 comparisons are performed for the three optimum designs A, B and C of Figure 3(b). The RDO(B) optimum design is achieved considering a compromise between the weight and the standard deviation. An important outcome of this investigation is that the DBO optimum design violates the constraints with probability equal to 1.1% and probability of failure equal to 0.6%. On the other hand, the probability of violation and the probability of failure, in the case of the compromise optimum design B, are computed one to two orders of magnitude lower compared to those corresponding to DBO designs. As a consequence of this reduced probability of violation and failure, an increase of 70% and 30% on the optimum weights achieved is observed in the case of RDO compared to the DBO. The value of the probability of violation is significantly lower in the case of optimum design C where the corresponding probability is 0.002%. However, the optimum weights achieved are 4 and 2 times more than the one obtained with the DBO formulations.

	DBO (A)	**RDO (B)**	**RDO (C)**
Weight (kN)	21.1	35.5	85.7
Standard Deviation (m)	$1.32\ 10^{-02}$	$4.17\ 10^{-03}$	$2.28\ 10^{-03}$
P_{viol} (%)	$1.1\ 10^{0}$	$7.0\ 10^{-2}$	$2.0\ 10^{-3}$
P_f (%)	$0.6\ 10^{0}$	$1.0\ 10^{-2}$	$0.8\ 10^{-3}$

Table 2. Characteristic optimal solutions

The hardware platform that was used in this work for the parallel computing implementation consists of a PC cluster with 25 nodes Pentium III in 500 MHz interconnected through Fast Ethernet, with every node in a separate 100Mbit/sec switch port. Message passing is performed with the programming platforms PVM working over FastEthernet. Two parallel processing schemes have been considered: *Parallel 1* corresponding to the exploitation of the parallel implementation of the optimization scheme and *Parallel 2* corresponding to the parallel implementation of the stochastic analysis involved in the optimization procedure. The computational performance for obtaining the multi-objective RDO Pareto front curve is compared in Table 3. The solution of the single-objective DBO(A) and RDO(C) problems, in sequential and parallel computing environments is examined. It can be seen that the computational time required for obtaining the RDO(C) optimum solutions is two orders of magnitude more than the corresponding time required to obtain the DBO(A) optimum solutions in sequential computing environment. This difference is reduced to one order of magnitude in parallel computing environment.

Formulation	**Optim. Scheme**	**Generations**	**FE analyses**	**Time (s)**		
				Sequential	**Parallel 1***	**Parallel 2***
DBO (A)	CEA(5+5)	103	627	63	19	-
DBO (C)	$CEATm(5+5)_{1,3}$	109	576	5214	349	229
RDO Par. F. C.	$CEATm(5+5)_{10,3}$	947	5528	51092	3127	2259

* In 25 processors

Table 3. Computational perfrormance

6. CONCLUSIONS

With the proposed multi-objective optimization scheme a uniform distribution of the Pareto optimum solutions along the front curve is achieved that is an indication of the efficiency of the optimization procedure. For the robust design optimization problem considered the proposed non-dominant *CEATm* multi-objective optimization methodology manages to generate the Pareto front curve with a good distribution of the Pareto solutions along the front curve.

The results obtained with the deterministic and the robust design optimization formulation underline the importance of minimizing the variance of the structural response when uncertain parameters are taken into account. For the test examples considered in this study, the probability of constraint violation of the DBO designs is computed two orders of magnitude greater than the corresponding probabilities for the RDO designs when the standard deviation of the response is considered as the dominant criterion to be minimized. On the

other hand, the computational cost required for obtaining the DBO designs is two orders of magnitude in sequential and one order of magnitude in parallel computing environment less than the corresponding computing cost required for obtaining the RDO optimum solutions.

In the computational framework of robust design optimization of real-scale structures, the efficiency of the Latin hypercube sampling is also shown, requiring about a hundred of samples, in calculating the necessary statistical parameters. This part of the optimization procedure is very crucial since the computational cost of the RDO procedure is dependent directly on the number of simulations, while the reliability of the results obtained from the RDO procedure is influenced by the accuracy on the calculation of the statistical parameters.

REFERENCES

[1] D.C. Charmpis, N.D. Lagaros and M. Papadrakakis, Multi-database exploration of large design spaces in the framework of cascade evolutionary structural sizing optimization, Comput. Methods Appl. Mech. Engrg., In this Issue, 2005.

[2] W. Chen and K. Lewis, A robust design approach for achieving flexibility in multidisciplinary design, *AIAA Journal*, 37(8), 1999, 982-990.

[3] R.F. Coelho, H. Bersini and Ph. Bouillard, Parametrical mechanical design with constraints and preferences: application to a purge valve, Comput. Methods Appl. Mech. Engrg., 192(39-40), 2003, 4355-4378.

[4] C.A. Coello Coello, An updated survey of GA-based multi-objective optimization techniques, *ACM Computing Surveys*, 32(2), 2000, 109-143.

[5] I. Doltsinis and Z. Kang, Robust design of structures using optimization methods, Comput. Methods Appl. Mech. Engrg., 193, 2004, 2221-2237.

[6] Eurocode 1, Basis of design and actions on structures - Part 2-4: Actions on Structures - Wind actions, CEN, ENV 1991-2-4, 1995.

[7] Eurocode 3, Design of steel structures, Part1.1: General rules for buildings, CEN, ENV 1993-1-1, 1993.

[8] D.M. Frangopol and C.G. Soares (eds.), Reliability-oriented optimal structural design, Special Issue, Reliability Engineering & System Safety, 73(3), 2001, 195-306.

[9] D. Greiner, J.M. Emperador and G. Winter, Single and multiobjective frame optimization by evolutionary algorithms and the auto-adaptive rebirth operator, Comput. Methods Appl. Mech. Engrg., 193(33-35), 2004, 3711-3743.

[10] K.-H. Lee and G.-J. Park, Robust optimization considering tolerances of design variables, Computers and Structures, 79, 2001, 77-86.

[11] G.-C. Luh and C.-H. Chueh, Multi-modal topological optimization of structure using immune algorithm, Comput. Methods Appl. Mech. Engrg., 193(36-38), 2004, 4035-4055.

[12] R.T. Marler and J.S. Arora, Survey of multi-objective optimization methods for engineering, Structural and Multidisciplinary Optimization, 26(6), 2004, 369-395.

[13] M.D. McKay, R.J. Beckman and W.J. Conover, A comparison of three methods for selecting values of input variables in the analysis of output from a computer code, *Technometrics*, 21(2), 1979, 239-245.

[14] A. Messac and A. Ismail-Yahaya, Multi-objective robust design using physical programming, Struct. Multidisc Optim, 23, 2002, 357-371.

[15] K. Miettinen, Non linear multi-objective optimization, Kluwer Academic Publishers, 2002.

[16] M. Papadrakakis and N.D. Lagaros, Reliability-based structural optimization using neural networks and Monte Carlo simulation, Comput. Methods Appl. Mech. Engrg., 191(32), 2002, 3491-3507.

[17] M. Papadrakakis, V. Plevris, N.D. Lagaros and V. Papadopoulos, Robust design optimization of 3D truss structures using evolutionary computation, 6th WCCM in conjuction with APCOM'04, Beijing, China, Sept., 5-10, 2004.

[18] H. J. Pradlwarter, G. I. Schuëller and C. A. Schenk, A computational procedure to estimate the stochastic dynamic response of large non-linear FE-models, Comput. Methods Appl. Mech. Engrg., 192(7-8), 2003, 777-801.

[19] G.I. Schuëller (ed.), Computational stochastic structural mechanics and analysis as well as structural reliability, Special Issue, Comput. Methods Appl. Mech. Engrg., 2005.

[20] R.E. Steuer, Multiple criteria optimization: Theory computation and applications, John Wiley & Sons, 1986.

INELASTIC ANALYSIS OF FRAMED STRUCTURES USING THE FIBER APPROACH

Iason Papaioannou, Michalis Fragiadakis and Manolis Papadrakakis

Institute of Structural Analysis & Seismic Research
National Technical University of Athens
Zografou Campus, Athens 15780, Greece

Keywords: Fiber approach, Numerical Integration, Stiffness-Flexibility Formulation, Localization effects

Abstract. *The efficiency of different formulations for the inelastic analysis with beam-column elements using the fiber approach is investigated in this study. Two versions of the fiber approach are examined based in, the stiffness and the flexibility method. Both methods are implemented on a natural mode type beam-column element. The first method is the commonly used formulation, while the flexibility-based formulation, also known as force-based formulation, relies on iterations in the element level in order to improve the nodal forces and thus lead to increased accuracy and convergence rate. Three methods for the integration of the stiffness matrix are examined for both formulations and the performance of each method in terms of the FE mesh required is investigated.*

1 INTRODUCTION

Inelastic analysis of frames has many practical applications in the simulation of structures. In order to perform the nonlinear static or dynamic analysis of frame structures, the use of a model that combines accuracy and simplicity is necessary. The models used for the inelastic analysis of frames can be classified into two categories: lumped and distributed plasticity models. When a lumped plasticity model is adopted, the inelastic behavior is concentrated at the ends of otherwise linear-elastic beam elements. This approach is also known as the plastic hinge approach. On the other hand in the distributed plasticity models the plasticity is evaluated in a number of sections along the element which in turn are divided to a number of monitoring points which correspond to the fibers of the section. The distributed plasticity model is also known as the fiber-approach. The use of fibers allows the accurate representation of the stress level across the sections, while using a number of sections along the element allows nonlinearities to develop along the element. The yield criteria adopted for the plastic hinge approach are expressed in moment-rotation terms for each plastic hinge, while in the fiber approach uniaxial stress-strain laws for each fiber are adopted. Fiber-based elements offer increased accuracy compared to plastic hinge models at the expense of increased computational cost. This paper presents two alternative formulations of the fiber approach.

The two versions of the fiber approach implemented are based on the stiffness and the flexibility method. The former is the common method used, where the strain field is obtained by means of appropriate interpolation techniques from the nodal displacements. Displacement-based elements ensure that the compatibility between deformations will be satisfied. However, the equilibrium of forces along the member is satisfied only when an efficient number of elements per member is used. In order to circumvent this problem a denser mesh of beam elements is required at the locations where inelastic deformations are expected to be high. On the other hand, in the flexibility formulation, interpolation is performed in order to reach equilibrium, the forces at each section are calculated with respect to the nodal forces[1]. Force interpolation functions are adopted where the bending moments are distributed linearly and the axial force remains constant along the element. As a result of this handling element equilibrium is always satisfied, while compatibility of deformations is satisfied by integrating the section deformations to obtain the element deformations and the nodal displacements.

Both formulations are implemented on a beam-column element based on the natural approach[2]. According to the natural mode method the displacement field is decomposed to twelve natural modes, six rigid body modes, that leave the element unstrained, and six natural straining modes. Based on this concept we can compute the natural stiffness matrix, using only the natural modes that produce strain. The adoption of the natural mode method leads to a reduction of the computational cost.

In order to compute the natural stiffness matrix three integration methods were examined. In the simplest version of the displacement-based natural element, the integrals that form the natural stiffness matrix are computed analytically[3]. Analytical integration requires the stress-strain relationship to be evaluated at a single section of the element. In this study the middle section of the element is used. Numerical integration schemes, such as Gauss quadrature or Gauss-Lobatto quadrature, allow a more detailed description of the inelastic

behavior of the element, since the strain field is monitored on several sections along the element. Theoretically, both quadrature schemes can be combined with either displacement or force based elements.

2 DISPLACEMENT-BASED FORMULATION

Both versions of the fiber approach are implemented on the natural mode beam-column[3]. According to the natural mode method, the displacement field is decomposed to six rigid body modes ρ_0 and six straining modes ρ_N, grouped in the vector:

$$\underset{(12x1)}{\rho_e^T} = \begin{bmatrix} \underset{(6x1)}{\rho_0} \\ \underset{(6x1)}{\rho_N} \end{bmatrix} \tag{1}$$

In particular the vector of the natural staining modes ρ_N consists of the following entries

$$\rho_N = \begin{bmatrix} \rho_{N1} & \rho_{N2} & \rho_{N3} & \rho_{N4} & \rho_{N5} & \rho_{N6} \end{bmatrix}^T \tag{2}$$

where ρ_{N1} is a unit extension, while ρ_{N2} and ρ_{N4} are symmetric unit rotations along the principal and the secondary axis, respectively. The third mode ρ_{N3} is the sum of a unit antisymmetrical bending rotation and a couple of shear forces employed in order to satisfy equilibrium. In a similar fashion ρ_{N5} represents a unit antisymmetrical bending rotation along the secondary axis and finally, ρ_{N6} is the torsional mode. The correlation between the natural straining modes and the displacements in the element local system is achieved with simple algebraic expressions:

$$\underset{(6x1)}{\rho_N} = \underset{(6x12)}{\overline{\alpha}_N} \underset{(12x1)}{\overline{\rho}} \tag{3}$$

where,

$$\underset{(6x12)}{\overline{\alpha}_N} = \begin{bmatrix} -1 & . & . & . & . & . & 1 & . & . & . & . & . \\ . & . & . & . & . & -1 & . & . & . & . & . & 1 \\ . & -\frac{2}{L} & . & . & . & -1 & . & \frac{2}{L} & . & . & . & -1 \\ . & . & . & . & 1 & . & . & . & . & . & -1 & . \\ . & . & \frac{2}{L} & . & 1 & . & . & . & -\frac{2}{L} & . & 1 & . \\ . & . & . & -1 & . & . & . & . & . & 1 & . & . \end{bmatrix} \tag{4}$$

The relationship between the vector of strains and the natural displacement is $\gamma = B_N \rho_N$, or analytically

$$\begin{bmatrix} \gamma_x \\ 2\gamma_{yx} \\ 2\gamma_{xz} \end{bmatrix} = \frac{1}{L} \begin{bmatrix} 1 & y & -3y\zeta & z & -3z\zeta & 0 \\ 0 & 0 & 0 & 0 & 0 & \left(\frac{\partial \Psi(y,z)}{\partial y} - z \right) \\ 0 & 0 & 0 & 0 & 0 & \left(\frac{\partial \Psi(y,z)}{\partial z} - y \right) \end{bmatrix} \begin{bmatrix} \rho_{N1} \\ \rho_{N2} \\ \rho_{N3} \\ \rho_{N4} \\ \rho_{N5} \\ \rho_{N6} \end{bmatrix} \tag{5}$$

where ζ is the non-dimensional natural coordinate along the element ($\zeta \in [-1,1]$) and $\Psi(y, z)$ is the warping function that describes the behavior under torsion. If κ is the constitutive matrix, the natural stiffness matrix is obtained as:

$$K_N = \int_{V_e} B_N{}^T \cdot \kappa \cdot B_N dV_e \tag{6}$$

or equivalently

$$K_N = \frac{1}{L^2}\int_{V_e}\begin{bmatrix} E & yE & -3y\xi E & zE & -3z\xi E & . \\ . & y^2E & -3y^2\xi E & zyE & -3zy\xi E & . \\ . & . & 9y^2\xi^2E & -3zy\xi E & 9zy\xi^2E & . \\ . & symmetrical & . & z^2E & -3z^2\xi E & . \\ . & . & . & . & 9z^2\xi^2E & . \\ . & . & . & . & . & G(\Psi_{,y}-z)^2 - G(\Psi_{,z}-y)^2 \end{bmatrix} dV_e \tag{7}$$

The integral of equation (7) can be calculated analytically or numerically. Depending on the integration scheme adopted different FE meshes are required. Among the three integration schemes adopted, the Gauss-Lobatto scheme has been proved to behave unreliably when implemented for the displacement element.

3 FORCE-BASED FORMULATION

The vector of internal forces, which are the forces at the sections along the element (Figure 1), are obtained by interpolating the natural nodal forces. Therefore the forces of section i, $D^i = [N \quad M_y \quad M_z]$, are obtained as

$$D^i = b(\zeta^i)\cdot P_N^i \tag{8}$$

where P_N^i is the vector of the natural forces of section i that correspond to the natural straining modes of equation (2) and $b(\zeta^i)$ is a interpolation function matrix, expressed in the natural coordinate system as:

$$b(\zeta) = \begin{bmatrix} 1 & 0 & 0 & 0 & 0 \\ 0 & -1 & \zeta & 0 & 0 \\ 0 & 0 & 0 & -1 & \zeta \end{bmatrix} \tag{9}$$

The adopted section force-deformation relationship that always satisfies element equilibrium is obtained using the section flexibility matrix:

$$d^i = f(\zeta^i)\cdot D^i \tag{10}$$

where d^i is the section deformation vector that consists of the axial strain and the curvatures about the two orthogonal axis, and $f(\zeta^i) = \left(k(\zeta^i)\right)^{-1}$ is the section flexibility matrix.

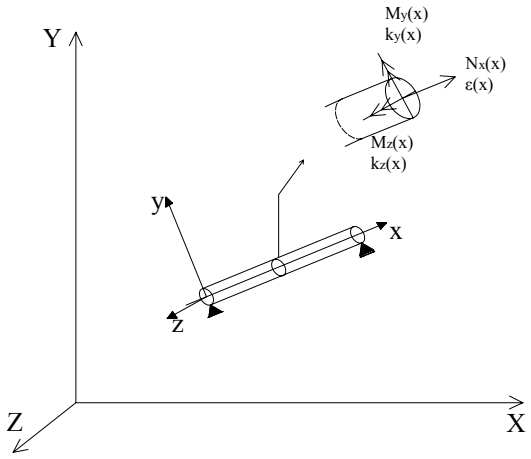

Figure 1. Section generalized forces and deformations

Following the hypothesis that plane sections remain plane and normal to the longitudinal axis, the section stiffness matrix is computed by integrating the area of the cross section and thus taking into consideration the

influence of the stiffness of each fiber. In addition, the deformation compatibility condition is satisfied as follows:

$$\rho_N = \int_0^L b(\zeta^i)^T d(\zeta^i) dx \tag{11}$$

In the flexibility-based formulation the natural stiffness matrix is derived from the inversion of the element natural flexibility matrix, which is constructed as follows:

$$F_N = \int_0^L b^T(\zeta) \cdot \left(k(\zeta)\right)^{-1} \cdot b(\zeta) dx \tag{12}$$

The integrals of equations (11) and (12) have to be computed numerically. It is apparent, according the case studies examined, that the Gauss quadrature scheme is not as effective as the Gauss-Lobatto scheme, since more integration points are required in order to produce accurate results.

In a flexibility-based element the determination of the natural element forces is performed iteratively for each element. The first step of the iterative procedure is to determine the vector of natural forces. Then using force interpolation functions the section forces are obtained, and subsequently the section forces are corrected according to the constitutive law. From the corrected forces the section deformations are obtained (eq. (10)) which are then integrated according to eq. (11) to obtain the residual natural straining modes. The iterative process is terminated when an energy convergence criterion that combines element residual natural modes and natural forces is satisfied[4].

4 FINITE ELEMENT MESH

In order to compute the stiffness matrix, three integration methods were examined. In the original formulation of the displacement-based natural element, the integrals that form the natural stiffness matrix can be computed analytically. When this is the case the inelastic behavior of the element is derived directly from the behavior of the middle section. For this reason, a fine mesh must be used in order to capture accurately the inelastic behavior. This approach offers a significant reduction of computations required per element compared to numerical integration methods, where the required computation cost and memory storage per element is increased since more integration points are necessary.

Numerical integration schemes, such as Gauss or Gauss-Lobatto quadrature, allow a more detailed description of the inelastic behavior of the element, since the element state is derived from the weighted summation of the state of several integration sections along the element. The main difference between the two numerical procedures is that the Gauss-Lobatto scheme uses as integration points the end sections of the beam. This is important since these sections are the locations of possible plastic hinges. Both integration schemes are based on the expression:

$$\int_{-1}^{1} f(\zeta) d\xi = \frac{1}{2} \sum_{h=1}^{m} w_i \cdot f(\zeta_i) \tag{13}$$

where i denotes the monitored section and w_i is the corresponding weight factor. The weight factors for different number of integration points are shown in Figure 2, for both schemes. It can be seen that smaller weights are assigned at the sections near the ends of the beam compared to the middle sections. The distribution of weights is responsible for the majority of numerical problems that may arise during analysis.

The number of integration points used affects the assumed length of plastic hinge[5]. When the plastic moment is reached at the first integration point (element end), the displacement continues to increase. As the bending moment cannot increase furthermore, the adjacent integration points remain elastic and the inelastic curvature localizes at the integration point at the beam end. If an inefficient number of integration points is used, the length of the plastic hinge and thus the curvature that corresponds to the yield strength, are not evaluated correctly. These effects are known in the literature as localization effects. This localization effect is alleviated when hardening is present. However, for softening structures or elastic-perfectly plastic cases, the localization effects may cause numerical problems and require special attention. Furthermore, these effects are more pronounced when the Gauss-Lobatto flexibility-based element is used. Strain localizations also affect stiffness-based frame elements with analytical integration, but in that case the localization effects are related to the length of the element. In displacement-based elements with numerical integration the localization effects depend on both the element length, which is usually small, and also on the number of integration points, which usually is less than those used for force-based elements.

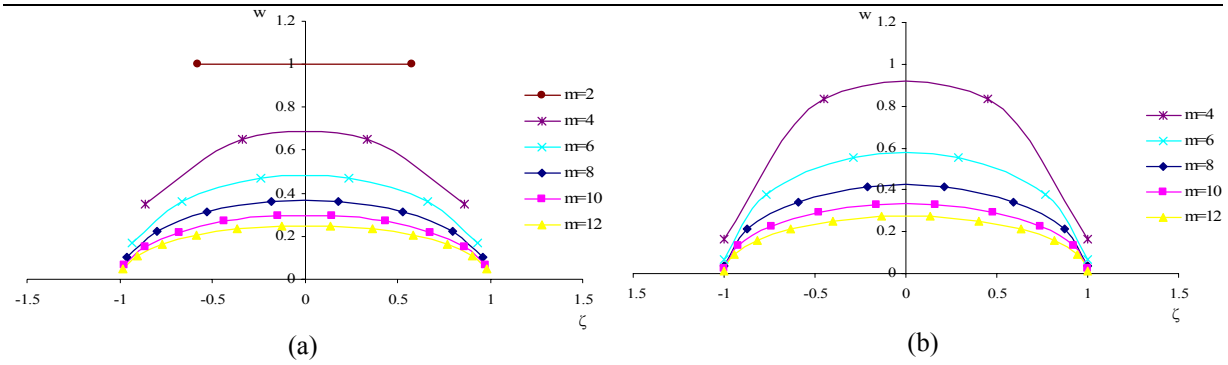

Figure 2. Distribution of weight factors for the (a) Gauss and (b) Gauss-Lobatto quadrature

5 CASE STUDIES

5.1 Simple I-beam with fixed ends

The purpose of the first example is to investigate the efficiency of both fiber formulations for the analysis of the I-beam of Figure 3 when subjected to a concentrated load in its middle. The section behavior is assumed elastic-perfectly plastic. Three meshes, shown in Figure 4 were considered.

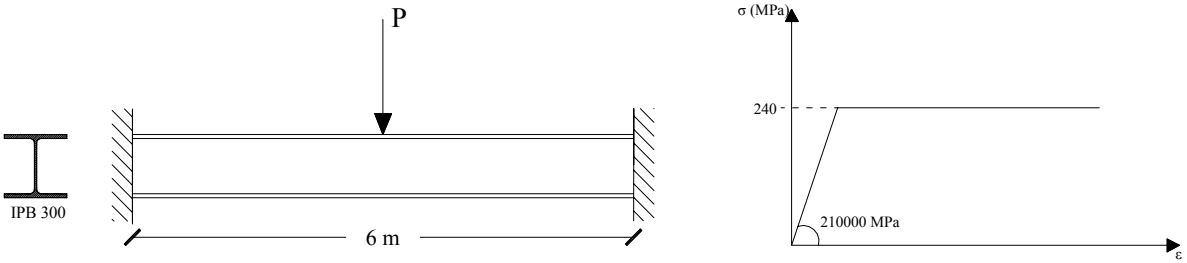

Figure 3. Simple I-beam under concentrated load

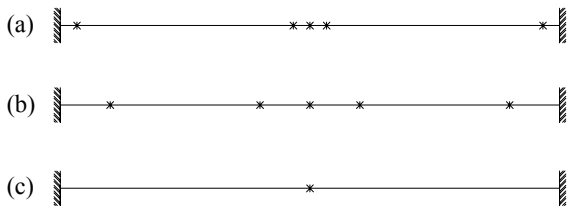

Figure 4. Discretization of I-beam. Three alternative finite element

In Figure 5 it is shown that only the denser mesh (a) is capable to provide an accurate estimation of the collapse load (P_c = 598kN) when the flexibility element with analytical integration is used. Figure 6 proves the efficiency of the two Gauss point integration scheme against the Gauss schemes with more integration points. It is also shown that when the Gauss-Lobatto scheme is used the collapse load is overestimated regardless of the number of integration points. Furthermore, it can be seen that the solution provided by the force-based element, when mesh (c) was used, is the best among all solutions provided by the displacement based elements.

Figure 7 shows the response of the I-beam obtained when the flexibility-based element and Gauss-Lobatto quadrature is used. The prediction of the element inelastic response is accurate, although the localization effects affect the smoothness of the response. Furthermore, it is shown that Gauss quadrature failed to produce accurate results when implemented in a force-base element. Finally, the displacement based element failed to determine the collapse load when mesh (c) is used for both integration schemes.

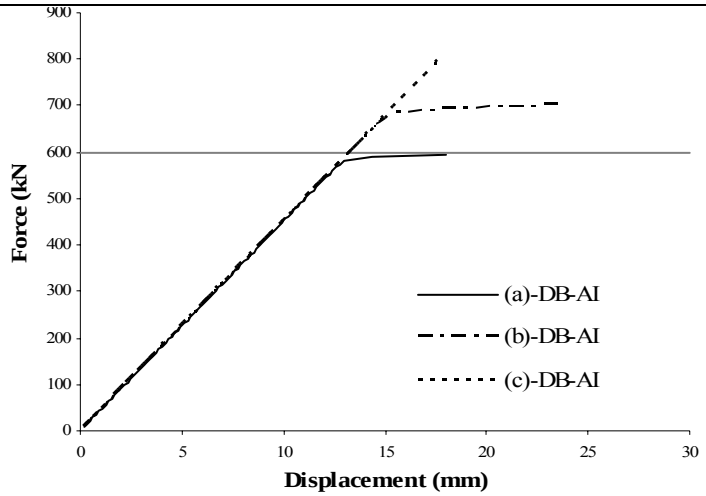

Figure 5. Inelastic response of I-beam using the displacement-based (DB) element with analytical integration (AI)

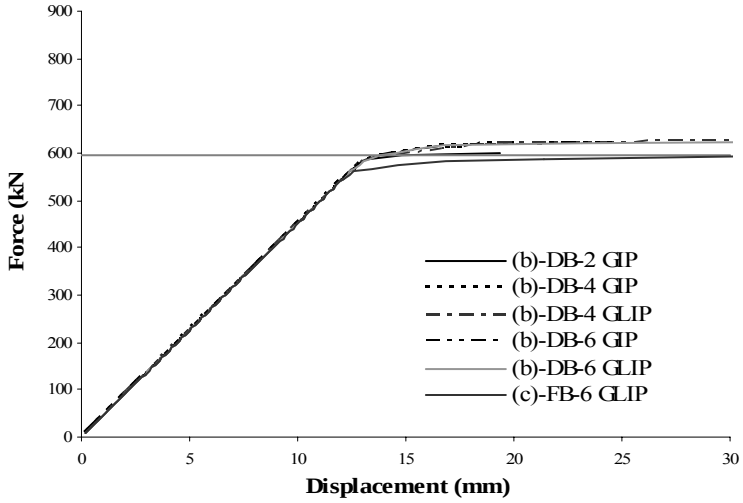

Figure 6. Inelastic response of I-beam using the displacement-based (DB) element with a different number of Gauss (GIP) or Gauss-Lobatto (GLIP) integration points

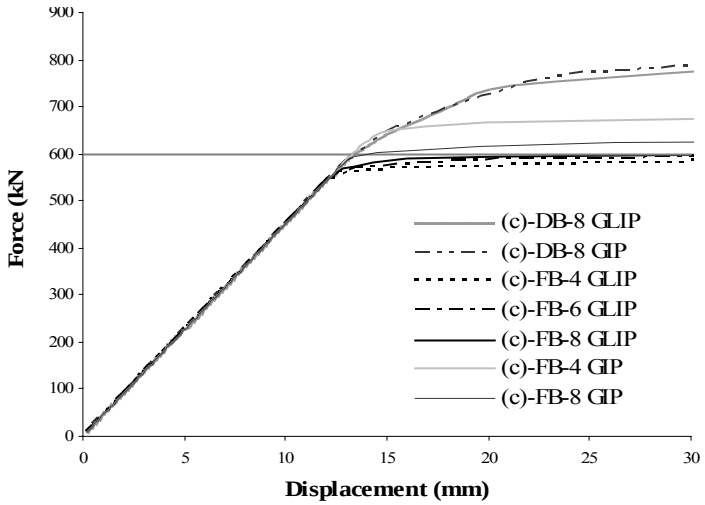

Figure 7. Inelastic response of I-beam using the force-based (FB) element with a different number of Gauss (GIP) or Gauss-Lobatto (GLIP) integration points

5.2 Reinforced concrete column

The second example is the reinforced concrete column[6], shown in Figure 8. At the top of the column a constant axial load is applied while the horizontal tip displacement is increased incrementally. The constitutive model used to describe the nonlinear behavior of the concrete fibers is the modified Kent-Park model[7], shown also in Figure 8, while a bilinear model with a Young's modulus of E=29000ksi, a yield stress of f_y=64.9ksi and a kinematic strain hardening ratio of 0.67% are used for the reinforcing steel bars. A single force-based element is used for the entire member, and the numerical integration is performed with the Gauss-Lobatto scheme. The purpose of this example is to demonstrate the ability of the flexibility-based element to capture the inelastic response of a reinforced concrete member and, at the same time, to illustrate the localization effects developed.

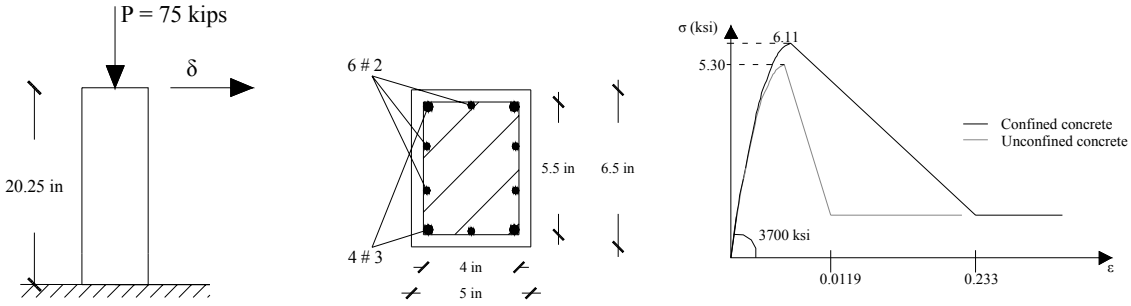

Figure 8. RC cantilever beam-column with strain-softening section response and material properties

Figure 9 shows the tip displacement response of the cantilever beam, when the axial load is not present. It can be seen that the influence of the number of integration points is small since mild strain hardening is present. Figure 10 shows the effect of the strong axial compression at the inelastic response of the member. Softening takes place as soon as the ultimate capacity of the column is reached. The column softening is described well with at least four integration points, although considerable differences are observed when a different number of integration points is used due to localization effects[5].

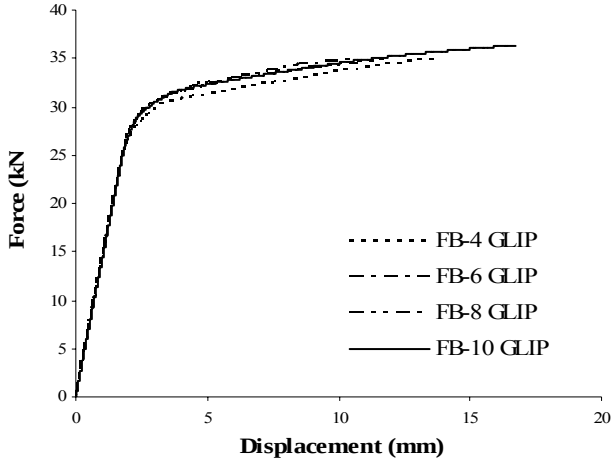

Figure 9. Inelastic response of RC beam-column without the axial dead load

6 CONCLUSIONS

It would seem fair to say that both nonlinear elements examined have the ability to capture the inelastic behavior of framed structures, although they conceal important numerical problems that must be thoroughly considered in order obtain accurate results. Most importantly, the appropriate finite element mesh for the displacement-based element, or the necessary number of integration points for the force-based element requires the knowledge of the plastic hinge length prior to the analysis in order to obtain accurate results. The conclusions of the study, with respect to the first case study examined, can be summarized as follows:

- When the displacement-based natural element is used, adopting analytical integration, for the stiffness matrix is proved to be more efficient than implementing a numerical integration scheme. The mesh required in that case is three elements per member, where the length of the two end elements coincides with the plastic hinge length.

- When the Gauss scheme is combined with the displacement-based element the required mesh is similar to that of the analytical integration, although the length of the end elements should coincide be increased slightly. However, as the increase of the CPU time and memory storage required is disproportionate to the gain in terms of FE mesh, this approach is considered ineffective.
- When Gauss-Lobatto quadrature is used to implement the force-based natural element, the results obtained seem to be accurate with a FE mesh of a single element per member and four integration points. Nevertheless, if section softening is expected in order to ensure the smoothness of the response, the number of integration points must be adjusted, so that the length that corresponds to the first point is close to the length of the plastic hinge.

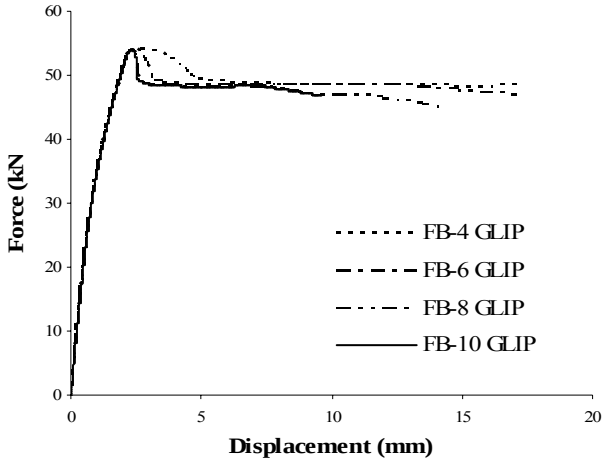

Figure 10. Inelastic response of softening RC beam-column

REFERENCES

[1] Taucer, F.F., Spacone, E., Filippou, F.C. (1991), *A fiber beam-column element for seismic response analysis of reinforced concrete structures,* Report No. UCB/EERC-91/17, University of California, Berkeley.

[2] Argyris, J., Tenek, L., Mattsson, A. (1988), *BEC: A 2-node fast converging shear-deformable isotropic and composite beam element based on 6 rigid-body and 6 straining modes*, Comput. Methods Appl. Mech. Engrg, 152, pp. 281-336.

[3] Fragiadakis, M. (2000), *Inelastic analysis with the natural beam finite element (BEC)*, Diploma Thesis, National Technical University of Athens, Athens, Greece (in Greek).

[4] Spacone, E, Filippou, F.C., Taucer, F.F. (1996), Fibre beam-column model for non-linear analysis of R/C frames: Part I. Formulation. Earthquake Engineering and Structural Dynamics, 25, pp. 711-725.

[5] Coleman, J., Spacone, E. (2001), "Localization issues in force-based frame elements", Journal of Structural Engineering, 127, pp. 1257-1265.

[6] Low, S.S., Moehle, J.P. (1987), *Experimental study of reinforced concrete columns subjected to multi-axial cyclic loading*, Report No. EERC-87-14, University of California, Berkeley.

[7] Kent, D. C. (1969), *Inelastic behavior of reinforced concrete members with cyclic loading*, Ph.D. Thesis, University of Canterbury, Christchurch, New Zealand.

Structural Dynamics and Earthquake Engineering

VARIATIONAL SOLUTIONS OF LIQUID SLOSHING IN HALF-FULL HORIZONTAL CYLINDERS

Lazaros A. Patkas, Spyros A. Karamanos and Manolis A. Platyrrachos

Department of Mechanical & Industrial Engineering
University of Thessaly, GR-38334, Volos, Greece
e-mail: skara@mie.uth.gr, web page: http://www.mie.uth.gr/karamanos.htm

Keywords: liquid container, sloshing, variational methods, earthquake analysis.

Abstract. *The paper examines sloshing in partially-filled containers of horizontal-cylindrical shape. A semi-analytical variational formulation is adopted, and the unknown sloshing potential is expressed through a series of harmonic spatial functions. Thus, the boundary-value problem reduces to a system of ODEs with explicit expressions for the elements of the coefficient matrices, and solutions of high accuracy for the sloshing frequencies are obtained. Finally, sloshing forces can be calculated through either a direct integration of the equations of motion or a modal analysis.*

1 INTRODUCTION

The oscillations of the liquid surface in a partially-filled container, referred to as "liquid sloshing", are generally caused by external excitation, and may have a significant influence on the dynamic response of the container. The linearized sloshing problem can be treated as an eigenvalue problem, representing free fluid vibrations inside a stationary container (sloshing frequencies and modes), whereas under a specific external excitation, the problem becomes transient, representing fluid motion within the moving container.

The sloshing solution depends strongly on the container shape. For non-deformable rectangular and vertical-cylindrical containers the sloshing problem for ideal fluids can be solved analytically, using separation of variables[1], resulting in a set of uncoupled equations, one for each sloshing mode. The case of vertical cylindrical vessels has been extensively investigated since the late 50's, mainly motivated by space vehicle applications[2], and the seismic design of liquid storage tanks[3,4,5]. The recent publication of Ibrahim et al.[6] offers a broad overview of sloshing dynamics with emphasis on vertical cylinders and rectangles.

Containers in other geometries, such as horizontal cylinders or spheres have received much less attention. In these configurations exact analytical solutions may not exist, and the use of numerical methods becomes necessary. Most of the work in horizontal cylinders and spheres has focused on the calculation of sloshing frequencies (eigenvalue problem). The have been computed through semi-analytical approaches or on numerical methods[7-11]. The corresponding transient problem of externally-induced sloshing has been studied numerically in an early work by Budiansky[12], using space transformations to map the initial circular or spherical region to a more convenient plane region. The flow field was described by a set of integral equations, which was solved using a Galerkin-type solution. Budiansky's method was further refined by Chu[13] to compute more accurately sloshing frequencies and forces in spherical containers.

For the particular case of half-full horizontal cylinders, Evans & Linton[14] presented a elegant semi-analytical solution for the sloshing frequencies, expanding the velocity potential in terms of non-orthogonal bounded spatial functions. This solution was extended in the recent work of Papaspyrou et al.[15], for externally-induced sloshing in half-full containers, with particular emphasis on seismic response.

The present work is aimed at calculating the dynamic response in half-full horizontal-cylindrical containers under external excitation in the transverse horizontal direction, using a variational formulation. In particular, the paper examines externally-induced liquid sloshing in those vessels under any form of excitation. A semi-analytical variational formulation is developed, where the velocity potential is expressed through series of non-orthogonal spatial functions. The boundary-value problem reduces to a system of ordinary linear differential equations, with explicit expressions of the coefficient matrices, which allow for semi-analytical solutions of benchmark quality. Under zero external excitation and assuming harmonic solution, sloshing frequencies and modes are computed. In addition, hydrodynamic forces are computed using either a direct integration of the equations of motion, or a modal analysis. The semi-numerical results are characterized by the rapid convergence of the sloshing frequencies, masses and forces.

2 VARIATIONAL FORMULATION

Assuming ideal fluid conditions, the liquid motion in a undeformed (rigid) two-dimensional container under horizontal excitation $X(t)$ in the x direction (Figure 1) is described by the flow potential $\Phi(x,y,t)$, so that the liquid velocity is the gradient of Φ ($\mathbf{u} = \nabla\Phi$), which satisfies the Laplace equation,

$$\nabla^2\Phi = \frac{\partial^2\Phi}{\partial x^2} + \frac{\partial^2\Phi}{\partial y^2} + \frac{\partial^2\Phi}{\partial z^2} = 0 \qquad \text{in the fluid domain } \Omega \tag{1}$$

subjected to the following boundary conditions

$$\frac{\partial\Phi}{\partial n} = \dot{X}\left(\mathbf{e}_x \cdot \mathbf{n}\right) \qquad \text{at the "wet" surface of the vessel wall } \mathrm{B}_1 \tag{2}$$

$$\frac{\partial^2\Phi}{\partial t^2} + g\frac{\partial\Phi}{\partial y} = 0 \qquad \text{at the free surface } \mathrm{B}_2 \tag{3}$$

where $\mathbf{e}_x$ is the unit vector in the x direction and $\mathbf{n}$ is the outward normal vector at B_1. The unknown potential can be decomposed in two parts, the "sloshing" potential Φ_S, and the "uniform motion" potential Φ_U, where

$$\Phi_U = \dot{X}(t)x \tag{4}$$

Therefore, the sloshing potential should satisfy the Laplace equation

$$\nabla^2\Phi_S = 0 \qquad \text{in } \Omega \tag{5}$$

and the following boundary conditions

$$\frac{\partial\Phi_S}{\partial n} = 0 \qquad \text{at } \mathrm{B}_1 \tag{6}$$

$$\frac{\partial^2\Phi_S}{\partial t^2} + g\frac{\partial\Phi_S}{\partial y} = -\frac{\partial^2\Phi_U}{\partial t^2} \text{ on } \mathrm{B}_2 \tag{7}$$

Herein, solution of the above problem is conducted using the weak statement of problem (5) - (7) considering an admissible function $\varphi^*(x,y)$:

$$\int_\Omega \left(\nabla^2\Phi_S\right)\varphi^* d\Omega = 0 \tag{8}$$

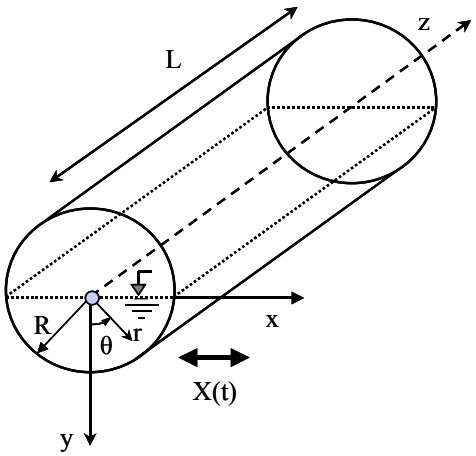

Figure 1: Configuration of a half-full horizontal cylinder under external excitation in the transverse direction.

Using Green's theorem and boundary conditions (6) and (7), the above expression is written as follows:

$$\int_{\Omega} \left(\nabla \Phi_S\right)\left(\nabla \varphi^*\right) d\Omega + \frac{1}{g}\int_{B_2} \frac{\partial^2 \Phi_S}{\partial t^2}\varphi^* dB_2 = -\frac{1}{g}\int_{B_2} \frac{\partial^2 \Phi_U}{\partial t^2}\varphi^* dB_2 \tag{9}$$

where B_2 is the "free-surface" line of the fluid domain depicted in Figure 1. Subsequently, Galerkin's discretization is considered:

$$\Phi_S = \sum_{n=1}^{\tilde{N}} q_n(t)\, N_n(x,y) = \left[\mathbf{N}\right]\dot{\mathbf{q}} \tag{10}$$

$$\varphi^* = \sum_{n=1}^{\tilde{N}} q_n^*\, N_n(x,y) = \left[\mathbf{N}\right]\mathbf{q}^* \tag{11}$$

where $N_n(x,y)$ are known spatial functions, [**N**] is a row-matrix containing functions $N_n(x,y)$, $\dot{\mathbf{q}}$ is a column vector with the unknown functions $\dot{q}_n(t)$ to be determined, the dot denotes time derivative, $\mathbf{q}^*$ is an arbitrary vector and $\tilde{N}$ is the truncation size. Differentiation of the above equations gives

$$\nabla\Phi = \left[\mathbf{B}\right]\dot{\mathbf{q}} \tag{12}$$

$$\nabla\varphi^* = \left[\mathbf{B}\right]\mathbf{q}^* \tag{13}$$

Substituting Equations (10) - (13) into Equation (9), and considering arbitrary $\mathbf{q}^*$, one results in the following system of second-order linear ordinary differential equations:

$$[\mathbf{M}]\,\ddot{\mathbf{q}} + [\mathbf{K}]\,\mathbf{q} = -\boldsymbol{\gamma}\,\ddot{X} \tag{14}$$

where

$$[\mathbf{M}] = \frac{1}{g}\int_{B_2} [\mathbf{N}]^T [\mathbf{N}]\, dB_2 \tag{15}$$

$$[\mathbf{K}] = \int_{\Omega} [\mathbf{B}]^T [\mathbf{B}] d\Omega \tag{16}$$

$$\boldsymbol{\gamma} = \frac{1}{g}\int_{B_2} x[\mathbf{N}]^{\mathrm{T}}\, \mathrm{dB}_2 \tag{17}$$

The system of Equations (14) can be integrated directly to provide the unknown functions $q_n(t)$ and their derivatives, so that the sloshing potential Φ_S is determined.

The sloshing frequencies and the corresponding eigen-vectors are computed from the solution of the corresponding free-vibration eigenvalue problem

$$\left([\mathbf{K}] - \omega_k^2[\mathbf{M}]\right)\boldsymbol{\Psi}_k = 0 \qquad\qquad k = 1,2,3,\ldots\tilde{N} \tag{18}$$

where ω_k is the sloshing frequency of the k^{th} mode $\boldsymbol{\Psi}_k$.

Hydrodynamic pressures $p(x,y,z,t)$ associated with liquid motion are calculated directly from Φ through the Bernoulli equation ($p = -\rho\dot{\Phi}$) and the total hydrodynamic force at the container wall is obtained through an appropriate integration of those pressures on the "wet" surface of the container in the direction of the earthquake excitation.

$$F = -\rho\int_{B_1}\left(\frac{\partial\Phi_U}{\partial t} + \frac{\partial\Phi_S}{\partial t}\right)\left(\mathbf{e}_x \cdot \mathbf{n}\right) dB_1 \tag{19}$$

Equation (19) indicates that the force can be expressed as a summation of the "uniform motion" force

$$F_U = -\rho \int_{B_1} \frac{\partial \Phi_U}{\partial t} \left(\mathbf{e}_x \cdot \mathbf{n} \right) dB_1 = -\mathsf{M}_L \ddot{X} \tag{20}$$

where M_L is the total liquid mass, and the force associated with sloshing:

$$F_S = -\rho \int_{B_1} \frac{\partial \Phi_S}{\partial t} \left(\mathbf{e}_x \cdot \mathbf{n} \right) dB_1 = -\rho \boldsymbol{\beta}^T \ddot{\mathbf{q}} \tag{21}$$

where

$$\boldsymbol{\beta} = \int_{B_1} [\mathbf{N}]^T \, n_x \, dB_1 \tag{22}$$

and $\ddot{\mathbf{q}}$ are calculated from the direct integration of Equations (14).

If modal analysis is used instead of a direct integration of Equations (14), the equations of motion are transformed in the following set of uncoupled ordinary differential equations

$$M_k \ddot{Y}_k + \omega_k^2 M_k Y_k = -\gamma_k \ddot{X} \qquad k = 1,2,3,...NM \tag{23}$$

where NM is the number of modes considered ($NM \le \tilde{N}$),

$$\mathbf{q} = \sum_{k=1}^{NM} Y_k \boldsymbol{\Psi}_k \tag{24}$$

$$M_k = \boldsymbol{\Psi}_k^T [\mathbf{M}] \boldsymbol{\Psi}_k \qquad k = 1,2,3,...NM \tag{25}$$

$$\gamma_k = \boldsymbol{\Psi}_k^T \mathbf{P} \qquad k = 1,2,3,...NM \tag{26}$$

Therefore, the sloshing force can be also written as follows:

$$F_S = -\rho \int_{B_1} \frac{\partial \Phi_S}{\partial t} \left(\mathbf{e}_x \cdot \mathbf{n} \right) dB_1 = -\sum_{k=1}^{NM} \mathcal{L}_k \ddot{Y}_k \tag{27}$$

where

$$\mathcal{L}_k = \rho \, \boldsymbol{\Psi}_k^{\mathrm{T}} \, \boldsymbol{\beta} \qquad k = 1,2,3,...NM \tag{28}$$

Thus, the total hydrodymanic force on the container's wall is

$$F = -\sum_{k=1}^{NM} \mathcal{L}_k \ddot{Y}_k - \mathsf{M}_L \ddot{X} \tag{29}$$

Using the following change of variables

$$a_k = Y_k \frac{M_k}{\gamma_k} \qquad \text{and} \qquad u_k = a_k + X \qquad k = 1,2,3,...NM \tag{30}$$

the liquid motion equations (including damping) become

$$\ddot{a}_k + 2\xi_k \omega_k \dot{a}_k + \omega_k^2 a_k = -\ddot{X} \qquad k = 1,2,3,...NM \tag{31}$$

or equivalently,

$$\ddot{u}_k + 2\xi_k \omega_k \left(\dot{u}_k - \dot{X} \right) + \omega_k^2 \left(u_k - X \right) = 0 \qquad k = 1,2,3,...NM \tag{32}$$

Equations (31) express the liquid motion with respect to the container, and Equation (32), express the total liquid motion (including the motion of the container). Furthermore, the hydrodynamic force in Equation (29) becomes

$$F = -\sum_{k=1}^{NM} \mathsf{M}_{kC} \, \ddot{a}_k - \mathsf{M}_L \ddot{X} \tag{33}$$

or equivalently,

$$F = -\sum_{k=1}^{NM} \mathbf{M}_{kC}\ \ddot{u}_k - \mathbf{M}_I \ddot{X} \tag{34}$$

where

$$\mathbf{M}_{kC} = \frac{\gamma_k \mathcal{L}_k}{M_k} \qquad k = 1,2,3,...NM \tag{35}$$

are the so-called "sloshing" or "convective" masses. The above equation shows that the total hydrodynamic force F consists of two components, an "impulsive" force F_I and a "convective" force F_C,

$$F_I = -\mathbf{M}_I\ \ddot{X} \tag{36}$$

$$F_C = -\sum_{k=1}^{NM} \mathbf{M}_{kC}\ \ddot{u}_k \tag{37}$$

where

$$\mathbf{M}_I = \mathbf{M}_L - \sum_{k=1}^{NM} \mathbf{M}_{kC}\ , \tag{38}$$

In addition, the total liquid mass $\mathbf{M}_L$ is the sum of

- the "sloshing" or "convective" masses $\mathbf{M}_{kC}$ (k=1,2,3,…), which correspond to the sloshing modes, and refer to the liquid motion due to free-surface elevation (convective motion).
- the "impulsive" mass $\mathbf{M}_I$, which refers to the mass that "follows" the container motion $X(t)$.

In rectangular and vertical-cylindrical liquid storage tanks, the sloshing potential can be written in terms of orthogonal shape functions N_n, analytically calculated. In such a case, the formulation results in a set of uncoupled equations of motion (i.e. matrices [**M**] and [**K**] are diagonal), and the functions N_n are the eigenmodes or sloshing modes (e.g. Abramson[2]). On the other hand, in horizontal-cylindrical and spherical vessels, analytical expressions for orthogonal functions do not exist, and the use of numerical methods becomes necessary. In the present work, the sloshing problem in half-full horizontal cylinders is formulated in a semi-analytical manner, expressing the sloshing potential in equation (10) in terms of non-orthogonal harmonic functions. All calculations in the present paper are performed in a Matlab programming environment

3 SOLUTION FOR HALF-FULL HORIZONTAL CYLINDER

Using the formulation described in the previous cross-section, the case of cylindrical container of semi-circular cross-section is examined, in terms of its sloshing frequencies and its dynamic behaviour under horizontal external excitation (Figure 1) in the transverse direction. The results are compared with numerical and semi-analytical results from previous publications. Finally, assuming only the first two terms of the series, an elegant analytical solution of fairly-good accuracy is obtained.

The fluid with density ρ is inside a non-deformable horizontal cylindrical half-full container of internal radius and length equal to R and L respectively. The origin of the Cartesian axes x, y, z is the centroid of the circular cross-section, axis y is downward, and the geometry of the cylinder is described by the cylindrical (polar) coordinates r, θ, z ($x = r\sin\theta$, $y = r\cos\theta$). The vessel is subjected to arbitrary external excitation in the direction of the x axis, with displacement $X(t)$. Due to the vessel geometry and the direction of the external excitation, the problem is two-dimensional in terms of r, θ, and the following harmonic functions are used to describe the sloshing potential:

$$N_n(r,\theta) = r^n \sin n\theta \qquad n = 1,2,3,\ldots \tilde{N} \tag{39}$$

and the elements of the $2\times\tilde{N}$ matrix [**B**] are:

$$B_{1n} = \frac{\partial N_n}{\partial r} = n\, r^{n-1}\, sin\left(n\theta\right) \qquad n = 1,2,3,\ldots \tilde{N} \tag{40}$$

$$B_{2n} = \frac{1}{r}\frac{\partial N_n}{\partial \theta} = n\, r^{n-1}\, cos\left(n\theta\right) \qquad n = 1,2,3,\ldots \tilde{N} \tag{41}$$

Substituting (39), (40), (41) into Equations (15), (16) and (17), and conducting the appropriate integrations, the elements of symmetric matrices [**M**], [**K**], and vector **γ** are obtained:

$$M_{mn} = \frac{2L\,R^{m+n+1}}{g\left(m+n+1\right)} \cdot \sin\left(\frac{m\pi}{2}\right) \cdot \sin\left(\frac{n\pi}{2}\right) \qquad m,n = 1,2,3,\ldots \tilde{N} \tag{42}$$

$$K_{mn} = \begin{cases} \dfrac{2nm\,L\,R^{n+m} \sin\left[\dfrac{\left(m-n\right)}{2}\pi\right]}{\left(m-n\right)\cdot\left(m+n\right)} & ,\, m \neq n \\ \dfrac{m\pi}{2} L\,R^{2\cdot m} & ,\, m = n \end{cases} \qquad m,n = 1,2,3,\ldots \tilde{N} \tag{43}$$

$$\gamma_m = \frac{2L\,R^{m+2}}{g\left(m+2\right)} \cdot sin\left(\frac{m\pi}{2}\right) \qquad m = 1,2,3,\ldots \tilde{N} \tag{44}$$

In Table 1, the sloshing frequencies of the half-full horizontal cylinder are shown in terms of the truncation size. The convergence is monotonic and rather fast, taking into account that a truncation size equal to 20 is necessary to achieve convergence up to 5 significant digits for the first four sloshing frequencies. This table shows that sloshing frequencies are in very good agreement with the corresponding values reported in previous publications[10],[15]. Also note the good comparison between the present results and those reported in the early work of Budiansky[12].

$\tilde{N}$	$n=1$	$n=2$	$n=3$	$n=4$
2	1.5074			
4	1.3569	10.592		
6	1.3558	4.9917	67.632	
8	1.3557	4.6660	11.451	558.89
10	1.3557	4.6514	8.2250	31.564
12	1.3557	4.6511	7.8578	13.550
14	1.3557	4.6511	7.8221	11.431
16	1.3557	4.6511	7.8199	11.035
18	1.3557	4.6511	7.8199	10.977
20	1.3557	4.6511	7.8199	10.972
30	1.3557	4.6511	7.8199	10.972
McIver[10]	1.3557	4.6511	7.8199	10.972
Evans &Linton[15]	1.3557	4.6511	7.8199	10.972
Budiansky[12]	1.36	4.70	7.96	*

Table 1: Normalized values of sloshing frequencies $\lambda_n = \omega_n^2 R/g$ for hemi-circular two-dimensional container.

M_{1C}/M_L	M_{2C}/M_L	M_{3C}/M_L	M_{4C}/M_L	$\left(\sum M_{nC}\right)/M_L$	M_I/M_L
0.5692	0.0178	0.0041	0.0015	0.5956	0.4054

Table 2: Converged values of mass ratios for convective and impulsive forces for hemi-circular two-dimensional container.

An important observation regarding matrix [**M**], and vector **γ** is that

$$M_{mn} = 0 \qquad \text{if } m = 2,4,6,\ldots \text{ or } n = 2,4,6,\ldots \tag{45}$$

$$\gamma_m = 0 \qquad \text{if } m = 2,4,6,\ldots \tag{46}$$

Therefore, separating odd and even equations, the ODE system of the equations of motion (14) can be written as follows,

$$\begin{Bmatrix} [\mathbf{M}_{aa}] & [\mathbf{0}] \\ [\mathbf{0}] & [\mathbf{0}] \end{Bmatrix} \begin{pmatrix} \ddot{\mathbf{q}}_a \\ \ddot{\mathbf{q}}_b \end{pmatrix} + \begin{Bmatrix} [\mathbf{K}_{aa}] & [\mathbf{K}_{ab}] \\ [\mathbf{K}_{ba}] & [\mathbf{K}_{bb}] \end{Bmatrix} \begin{pmatrix} \ddot{\mathbf{q}}_a \\ \ddot{\mathbf{q}}_b \end{pmatrix} = -\begin{pmatrix} \boldsymbol{\gamma}_a \\ \mathbf{0} \end{pmatrix} \ddot{X} \tag{47}$$

where

$$\mathbf{q}_a = \begin{bmatrix} q_1 & q_3 & q_5 & \ldots \end{bmatrix}^T$$
$$\mathbf{q}_b = \begin{bmatrix} q_2 & q_4 & q_6 & \ldots \end{bmatrix}^T$$

and using typical static condensation, Equations (47) can be written equivalently as follows:

$$\mathbf{q}_b = -[\mathbf{K}_{bb}]^{-1}[\mathbf{K}_{ba}]\mathbf{q}_a \tag{48}$$

$$[\mathbf{M}_{aa}]\ddot{\mathbf{q}}_a + [\mathbf{K}']\mathbf{q}_a = -\boldsymbol{\gamma}_a \ddot{X} \tag{49}$$

where $[\mathbf{M}_{aa}]$ and $[\mathbf{K}']$ are square symmetric matrices with dimension $\tilde{N}/2$, and

$$[\mathbf{K}'] = [\mathbf{K}_{aa}] - [\mathbf{K}_{ab}][\mathbf{K}_{bb}]^{-1}[\mathbf{K}_{ba}] \tag{50}$$

Equations (49) can be directly integrated in a straightforward manner, to compute the generalized coordinates $q_n(t)$ for an arbitrary excitation $X(t)$. Upon direct integration, the sloshing force F_S is calculated from Equation (21), where $n_x = \sin\theta$, and the elements of vector $\boldsymbol{\beta}$ are

$$\beta_m = \begin{cases} \pi L R^{m+1}/2 & , m = 1 \\ L R^{m+1}\left[\dfrac{\sin\dfrac{(m-1)\pi}{2}}{(m-1)} - \dfrac{\sin\dfrac{(m+1)\pi}{2}}{(m+1)} \right] & , m = 3,5,7,.... \\ 0 & , m = 2,4,6,.... \end{cases} \tag{51}$$

Note that only odd-number coefficients $q_n(t)$ contribute to the sloshing force. The time history of F_S with for different values of truncation size $\tilde{N}$, for a horizontal vessel with radius *R* equal to 1 meter and length *L* equal to 6 meters, and for the earthquake motion shown in Figure 2, is plotted in Figures 3a, 3b. The results show that convergence of the results is obtained for relatively few terms on the truncation size ($\tilde{N} \simeq 10$). Furthermore, the sloshing force is in very good agreement with the results reported by Papaspyrou et al.[16].

Using a modal analysis approach, coefficients $\mathcal{L}_n$ are obtained by Equation (28), where the elements of vector $\boldsymbol{\beta}$ are defined in Equation (51). The sloshing mass ratios over the entire liquid mass M_L are tabulated in Table 2.

REFERENCES

[1] Lamb, H. (1945), *Hydrodynamics*, Dover, New York.

[2] Abramson, H. N. (1966), The Dynamic Behavior of Liquids in Moving Containers, *Southwest Research Institute*, NASA SP-106, Washington, DC.

[3] Housner, G. W. (1957), "Dynamic Pressures on Accelerated Fluid Containers", *Bulletin Seismological Society of America*, Vol. 47, pp. 15-35.

[4] Veletsos, A. S. and Yang, J. Y. (1977), "Earthquake Response of Liquid Storage Tanks", *2nd Engineering Mechanics Conference*, ASCE, Raleigh, NC, pp. 1-24.

[5] Rammerstorfer, F. G., Fisher, F. D. and Scharf, K. (1990), "Storage Tanks Under Earthquake Loading", *Applied Mechanics Reviews,* ASME, Vol. 43, No. 11, pp. 261-283.

[6] Ibrahim, R. A., Pilipchuk, V. N. and Ikeda, T. (2001), "Recent Advances in Liquid Sloshing Dynamics", *Applied Mechanics Reviews,* ASME, Vol. 54, No. 2, pp. 133-177.

[7] Moiseev, N. N. and Petrov, A. A. (1966), "The Calculation of Free Oscillations of a Liquid in a Motionless Container", *Advances in Applied Mechanics*, Vol. 9, pp. 91-154.

[8] Fox, D. W. and Kutler, J. R. (1981), "Upper and Lower Bounds for Sloshing Frequencies by Intermediate Problems", *Journal of Applied Mathematics and Physics*, Vol. 32, pp. 667-682.

[9] Fox, D. W. and Kutler, J. R. (1983), "Sloshing Frequencies", *Journal of Applied Mathematics and Physics*, Vol. 34, pp. 669-696.
[10] McIver, P. (1989), "Sloshing Frequencies for Cylindrical and Spherical Containers Filled to an Arbitrary Depth", *Journal of Fluid Mechanics*, Vol. 201, pp. 243-257.
[11] McIver, P. and McIver, M. (1993), "Sloshing Frequencies of Longitudinal Modes for a Liquid Contained in a Trough", *Journal of Fluid Mechanics*, Vol. 252, pp. 525-541.
[12] Budiansky B. (1960), "Sloshing of liquids in circular canals and spherical tanks", *Journal of Aero/Space Sciences*, Vol. 27, No. 3, pp. 161-173.
[13] Chu, W.-H. (1964), "Fuel Sloshing in a Spherical tank Filled to an Arbitrary Depth", *AIAA Journal*, Vol. 2, No. 11, pp. 1972-1979.
[14] Kobayashi, N., Mieda, T., Shibata, H. and Shinozaki, Y. (1989), "A Study of the Liquid Slosh Response in Horizontal Cylindrical Tanks", *J. Press. Vessel Tech.*, ASME, Vol. 111, No. 1, pp. 32-38.
[15] Evans, D. V. and Linton, C. M. (1993), "Sloshing Frequencies", *Quarterly Journal of Mechanics and Applied Mathematics*, Vol. 46, pp. 71-87.
[16] Papaspyrou S., Karamanos, S. A. and Valougeorgis D. (2004), "Response of Half-Full Horizontal Cylinders under Transverse Excitation", *Journal of Fluids and Structures*, Vol. 19, No. 7, pp. 985-1003.

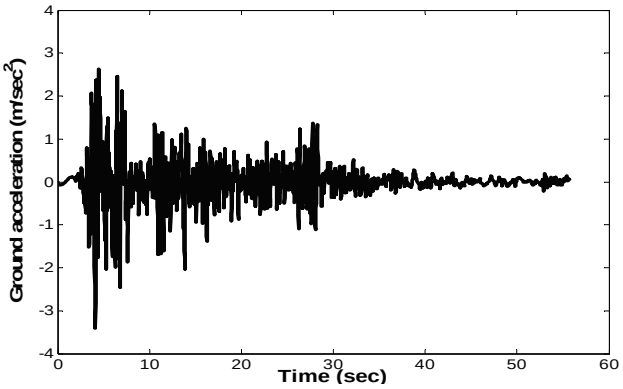

Figure 2: Ground acceleration (El Centro, 1940), source www.vibrationdata.com/elcentro.htm.

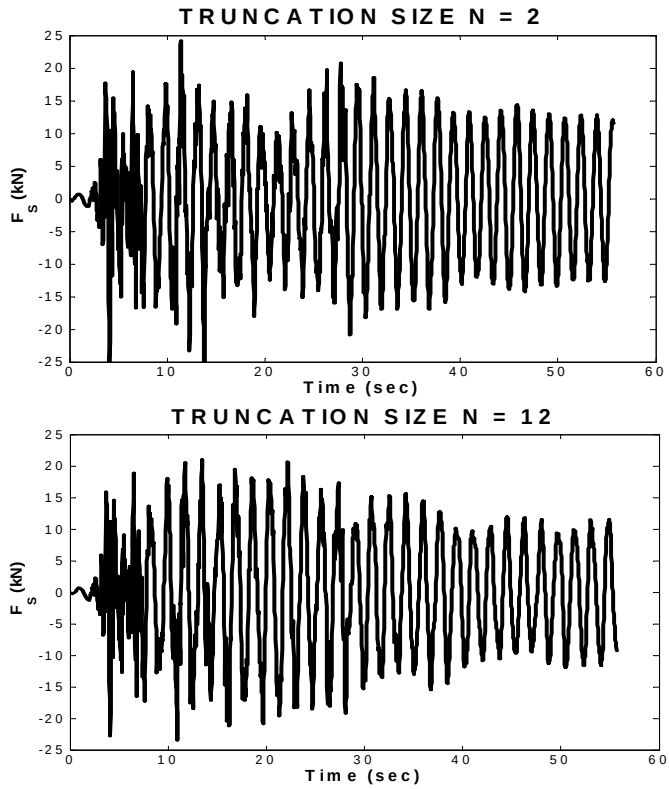

Figure 3: Sloshing force with respect to the truncation size $\tilde{N}$.

COMPUTING NATURAL PERIODS OF PLANE STEEL FRAMES BY APPROXIMATE FORMULAE

Costas Chrysanthakopoulos, Nikitas Bazeos and Dimitri E. Beskos

Department of Civil Engineering
University of Patras
GR-26500 Patras, Greece
e-mail: n.bazeos@upatras.gr

Keywords: Natural periods; Plane steel frames; Braced frames; Unbraced frames; Multi-storey-bay frames; Equivalent flexural-shear beam.

Abstract. *Approximate formulae for determining by hand with a high enough accuracy the first three natural periods of vibration of plane steel unbraced and braced frames are provided. These formulae are based on the modeling of a steel plane frame as an equivalent cantilever beam for which analytical expressions for the natural periods are available. Extensive parametric studies involving the finite element computation of the first three natural periods of 110 plane steel unbraced and braced frames are employed to establish correction factors for the equivalent beam modeling formulae which are functions of the number of stories and bays of the frame. The resulting corrected formulae permit a highly accurate determination of the first three natural periods of plane steel frames.*

1 INTRODUCTION

Seismic building codes, such as UBC [1] or EC8 [2], provide analytical expressions for the computation of the design seismic acceleration in terms of the natural period of vibration of the structure for the first mode or the first few modes. These codes [1, 2] require the participation in the response of so many modes as to have at least a participation of the 90% of the total structural mass and provide very simple but crude empirical formulae for the fundamental period of structures in terms of their material, structural type and height.

In this work approximate formulae for determining by hand the first three natural periods of vibration of plane steel frames are presented. These high enough accuracy formulae for both unbraced and braced frames are based on their modeling as equivalent cantilever beams in accordance with the approach of Stafford Smith and Crowe [4] for which analytic expressions for natural periods are available. These formulae are modified by some correction factors, functions of the number of frame stories and bays, which are constructed with the aid of extensive parametric studies involving finite element computation of the first three natural periods of 110 plane steel unbraced and braced frames. In this work frames of up to 15 stories are considered and thus the first three modes are enough to satisfy the 90% vibrating mass criterion of seismic codes [1, 2].

2 FREE VIBRATIONS OF A FLEXURAL-SHEAR BEAM

The free vibrations of a flexural-shear prismatic beam of length H are governed by the equation [4]

$$E\,I\,\frac{\partial^4 v}{\partial x^4} - E\,I\,(\alpha\,k)^2\,\frac{\partial^2 v}{\partial x^2} + m\frac{\partial^2 v}{\partial t^2} = 0 \qquad (1)$$

where EI and m are the flexural rigidity and mass per unit length, respectively, of the beam, v = v (x, t) is the lateral deflection of the beam, x and t denote axial coordinate and time, respectively and αk expresses a shear rigidity to be defined explicitly later on.

According to Rutenberg [3] one can finally obtain the natural periods T of free vibrations governed by Eq. (1) in the form

$$T = \left(2\,\pi / \lambda^2\right)\sqrt{m / E\,I} \qquad (2)$$

where

$$\frac{1}{\lambda^4} \approx \left(\frac{k^2 - 1}{k^2} \right) \frac{1}{\lambda_f^4} + \left(\frac{1}{k^2} \right) \frac{1}{\lambda_{sf}^4} \tag{3}$$

In the above λ_f and λ_{sf} can be computed from the following relations [4]

$$\begin{aligned} &\left(\lambda_f H\right)_1 = 1.875, \qquad \left(\lambda_f H\right)_2 = 4.694 \\ &\left(\lambda_f H\right)_n \cong (n - 0.5)\pi, \quad n = 3, 4 \ldots \end{aligned} \tag{4}$$

$$\left(\lambda_{sf} H\right)^2 \cong (n - 0.5)\pi \left(1 + k \alpha H\right) \tag{5}$$

3 PLANE FRAME STRUCTURES AS EQUIVALENT BEAMS

Plane orthogonal, braced or unbraced frames, shear walls or coupled frame-wall systems fixed on the ground can be modeled as equivalent flexural-shear cantilever beams. This equivalence can be established by expressing EI and αk of Eq. (1) in terms of the geometrical and material parameters of the frame or the frame-wall system. Following [4] one has that for

$$\alpha = \left[G A / E I \right]^{1/2}, \qquad k = \left[1 + \left(E I / E A c^2 \right) \right]^{1/2} \tag{6}$$

the equivalent flexural-shear beam can be established provided the three parameters EI, EAc^2 and GA can be expressed in terms of the properties of the frame or the frame-wall system.

Thus, for an unbraced bay of a frame, EI and EAc^2 of the equivalent beam can be expressed as [4]

$$E I = \sum_{j=1}^{n} \left(E I \right)_j, \qquad E A c^2 = \sum_{j=1}^{n} \left(E A c^2 \right)_j \tag{7}$$

where $(EI)_j$ is the flexural rigidity of the j_{th} vertical member (column or wall) of the system, $(EA)_j$ the axial rigidity of the j_{th} vertical member, $(c)_j$ the distance of the j_{th} column to the center of the area of the vertical members of the lateral load resisting frame and n is the total number of vertical members of the frame. On the other hand, GA of the equivalent beam can be computed from [4]

$$G A = 12 E / H \left[\frac{1}{\sum_{j=1}^{n} \left(I_c / H \right)_j} + \frac{1}{\sum_{i=1}^{m} \left(I_b / L \right)_i} \right] \tag{8}$$

where H is the floor height, L the bay length, I_b and I_c are beam and column moments of inertia, respectively and n and m denote the total number of columns and beams, respectively.

For a braced bay of a frame, EAc^2 is given again by $(7)_2$, while EI by [5]

$$E I = E A_f h^2 / 2 \tag{9}$$

where A_f is the cross-sectional area of the column and h the distance between the centroids of the two columns. On the other hand, GA receives different expressions for different types of bracing. Thus, e.g., for x or double-diagonal (n=2) and single-diagonal (n=1) bracing one has that

$$G A = n E A_d s h^2 / d^3 \tag{10}$$

Expressions for K and knee types of bracing can be found elsewhere [9].

In the above expressions, s and h are the dimensions of the composite brace elements and A_d the sectional area of the bracing element.

For a framed structure consisting of b braced and u unbraced bays, the parameters EI, EAc^2 and GA of the equivalent flexural-shear beam are obtained by

$$E I = \sum_{i=1}^{u} \left(E I \right)_i + \sum_{j=1}^{b} \left(E I \right)_j \tag{11}$$

$$G\,A = \left(G\,A\right)_u + \sum_{j=1}^{b} \left(G\,A\right)_j \tag{12}$$

4 PARAMETRIC STUDIES AND COMPARISONS

In order to check the validity of the simple approximate formulae for natural period determination of steel frames presented in the previous section, the natural periods of a large number of steel plane frames were computed by these formulae and compared against those obtained by a finite element analysis considered to be the "exact" values. In addition, the same periods were also compared against those obtained by the crude approximate formulae of codes.

4.1 Frame properties and methods of analysis

The analyzed plane steel frames are divided in two major categories. Those that retain their member properties constant along the height of the building and those that do not. Furthermore, there are five subcategories depending on the type of brace that each frame incorporates. As a result there are unbraced frames and frames with single, double, K or knee bracing. In each subcategory, there are frames composed of 1 to 3 bays and 4 to 15 stories. The total number of steel plane frames analyzed is one hundred and ten (110).

The length of one bay is 4m and the story height is 3m, while the diagonal brace in every case is of the tubular cross section D127x4.

Young modulus of Elasticity E is 200GPa, Poisson ratio v equals 0,3 and mass per unit volume is 795 Kg/m^3. The mass of each frame comes from the G+0.3Q combination, where the dead load G=36KN/m and the live load Q=10KN/m.

Geometric configurations and members properties of these frames can be found in Chrysanthakopoulos et al [9].

All the plane steel frames are analyzed by the finite element method. Once the finite element model of every frame is created, a modal analysis is performed using SAP2000 [6] and the first three natural periods are calculated. The calculated natural periods are considered to be the exact and correct values, so they serve as control variables to check the periods obtained from the equivalent cantilever formulae, as well as the formulae of the various codes.

The equivalent cantilever modeling considers the entire structure as a single cantilever (Fig. 1). The properties EI, EAc^2 and GA of the equivalent cantilever are derived from the equations of section 3. For the calculation of λ_{sf}, Eq. (5) is used because preliminary results showed that it is more accurate compared to Eq. (13) in predicting the first periods.

For reasons of completeness, the first natural periods of vibration of the considered plane steel frames are compared against those obtained by the very simple but crude formulae of some codes. Thus, according to UBC [1], EC8 [2] and E.A.K. [7] codes.

4.2 Comparison of results and error study

The values of the first three natural periods of the 110 plane steel frames considered here as obtained by the equivalent cantilever formulae and the finite element method together with the values of the fundamental periods as obtained by the seismic codes formulae were tabulated and compared. The relative % errors were computed on the basis of the relation

$$\varepsilon\left(\%\right) = \left(T_{FEM} - T\right) 100 / T_{FEM} \tag{13}$$

where T_{FEM} is the "exact" value of the period as computed by the finite element code of SAP 2000 [6] and T is the corresponding value as obtained by any other method.

Tables 3 and 4 present results for unbraced and x-braced frames, respectively with constant cross-sections along the height, while Tables 5 and 6 corresponding results for the case of cross-sections varying with height. Additional results for other three types of bracing for both constant and variable cross-sections with height can be found in Chrysanthakopoulos [8].

It is observed that for unbraced frames the error is quite low. The prediction of the first period is very good and its error ranges between 10 and 20%. Similar are the results for the second and third natural periods.

On the contrary, for braced frames the relative error for the first period increases drastically up to 50% (double diagonal and K bracing) and 60% (single diagonal and knee bracing). Minimum errors stay above 20% in all cases. The estimation of the second and third periods is even worse, with deviations reaching 90%.

Generally speaking, the relative error increases as frame height decreases for the same type of diagonal bracing. An increase in the number of bays slightly improves the estimated periods for a given plane frame.

5 CORRECTION FACTORS

From the error analysis of the previous section, becomes necessary to improve the prediction of natural periods by the equivalent cantilever method with the appropriate introduction of correction factors in order to bring the error down to acceptable levels. The fact that for the braced frames the error increases significantly in comparison with the unbraced frames, leads to the conclusion that the flexural-shear component of the equivalent cantilever response requires adjustment. The correction in the form of a correction factor is applied to the obtained eigenvalues λ or λ_{sf} of the equivalent cantilever.

The correction factor must be applicable to all frames. Thus, it must depend on some characteristic parameters of the frame. Parameters like these are the number of floors, bays, section properties and even α and k of the equivalent cantilever. The following general linear form for the correction factor (C) is adopted

$$C = c_1 + n \cdot c_2 + (m-1) \cdot c_3 \tag{14}$$

where c_1, c_2, c_3 are constants, n is the number of floors and m is the number of bays. The determination of the constants c_1, c_2, c_3 has been made so that

i) Correction factor C depends only on the number of natural period and not on the type of the brace
ii) Constants c_2, c_3 are independent of the bracing and of the number of bays
iii) Equation (14) can be used in every case of frame, brace type and natural period

Thus, Eq. (14) for braced frames becomes

$$C_{BR} = c_1 + 0.02 \cdot n + 0.03 \cdot (m-1) \leq C_{\max} \tag{15}$$

with

$$C_{\max} = \alpha_1 + \alpha_2 \cdot (m-1) \leq 1,0 \tag{16}$$

while for unbraced frames reduces to a single constant

$$C_{UBR} = c_1 \tag{17}$$

The corrected eigenvalue, is given by

$$\lambda_c = \lambda \cdot C_i \tag{18}$$

or

$$\lambda_{sf,c} = \lambda_{sf} \cdot C_i \tag{19}$$

where C_i is the appropriate correction factor.

The coefficients α_1, α_2 and c_1 of the above equations are given for various frame cases in Table 5.

After applying the correction factors, a recalculation of the deviations between the exact periods (SAP2000) and the predicted ones (equivalent cantilever with corrections) was performed. Equation (13) was used in this occasion as well.

In general, great improvement is achieved in all periods and in all frames when correction factors are applied. The first natural period is best estimated in every case (error below 15%). The second natural period displays deviations ranging from –5% to 15% while for the third natural period the deviation remains under 20%. Only for braced frames with 1 bay and 4 stories the error ranges between 30 and 40%.

6 EXAMPLES OF USING CORRECTED FORMULAE

Consider the steel plane frame of Fig. 1 with and without the x-bracing system and with constant and variable sections along its height. Story heights and bay lengths are 3,0 m and 4,0 m, respectively. Columns are HEB 280, beams IPE 360 and braces TUBO D 127x4. The following three cases are presented to illustrate the method in a detailed manner for the convenience of the reader or the user.

6.1 Frame without bracing

Due to the symmetry of the frame the center of the area of the vertical members is easily found to be at the center of the frame, that is at x=6m. The terms EAc^2 and EI are computed with the aid of Eqs (7) and the term GA is calculated through Eq. (8) and yields

$$EAc^2 = 1{,}0480\,E\,,\ EI = 154160\,KNm^2 \text{ and } GA = 66186{,}3\,KN \tag{20}$$

Parameters α and k can be calculated with the aid of Eq. (6). Thus $k\alpha H_{o\lambda}$ equals to 7,8655.
The total mass of the frame per meter of height is m = 1686 kg/m. Equation (4) provides directly the values of $\lambda_f H$ for the first three modes. Equation (5) is then used to calculate λ_{sf}. Having determined λ_{sf} and λ_f for the first three natural periods, Eq. (3) is finally used to obtain the eigenvalues λ as

$$\lambda_1 = 0{,}3101,\quad \lambda_2 = 0{,}5385,\quad \lambda_3 = 0{,}6955 \tag{21}$$

Thus, the initial natural periods according to Eq. (2) are

$$T_1 = 0{,}6765\,s,\quad T_2 = 0{,}2245,\quad T_3 = 0{,}1346 \tag{22}$$

The above values of periods should be corrected through appropriate correction factors. Using Table 5 for the case of a frame without bracing and constant sections, one can obtain the coefficient c_1. Then Eq. (17) yields

$$C_{UBR,1} = 0{,}94 \qquad C_{UBR,2} = 0{,}94 \qquad C_{UBR,3} = 0{,}99 \tag{23}$$

Use of Eq. (18) enables one to compute the corrected eigenvalues λ of the shear-flexure cantilever, which read

$$\lambda_1 = 0{,}2902,\quad \lambda_2 = 0{,}5062,\quad \lambda_3 = 0{,}6885 \tag{24}$$

Thus, the corrected natural periods on account of Eq. (2) are

$$T_1 = 0{,}7728s,\quad T_2 = 0{,}2540\,s,\quad T_3 = 0{,}1373\,s \tag{25}$$

For comparison purposes the "exact" values of these periods as obtained by finite elements read

$$T_1 = 0{,}8325s,\quad T_2 = 0{,}2621,\quad T_3 = 0{,}1465 \tag{26}$$

and the values of the first period as determined by the codes read

$$UBC: T_1 = 0{,}5501\,s,\quad EC8: T_1 = 0{,}5481\,s,\ EAK: T_1 = 0{,}3118\,s$$

6.2 Frame with bracing

Following similar procedures as in the previous example, the initial natural periods according to Eq. (2) can be computed as

$$T_1 = 0.2106\,\text{sec},\quad T_2 = 0.0669\,\text{sec},\quad T_3 = 0.0398\,\text{sec} \tag{27}$$

The above values of periods should be corrected through appropriate correction factors. Using Table 5 for the case of a frame with more than one bay and double diagonal bracing, one can obtain the coefficients α_1, α_2 and c_1. Then, Eqs (15), (16), (18) and (2) yield the corrected natural periods

$$T_1 = 0.4216\,\text{sec},\quad T_2 = 0.1350\,\text{sec},\quad T_3 = 0.0764\,\text{sec} \tag{28}$$

For comparison purposes the "exact" values of these periods as obtained by finite elements read

$$T_1 = 0{,}4397s,\quad T_2 = 0{,}1441\,s,\quad T_3 = 0{,}0855\,s$$

and the values of the first period as determined by the codes read

$$UBC: T_1 = 0{,}5501\,s,\quad EC8: T_1 = 0{,}4836\,s,\ EAK: T_1 = 0{,}2357\,s$$

6.3 Frame with bracing and variable sections

Following similar procedures, as in example 6.2, one can compute the initial natural periods according to Eq. (2) as

$$T_1 = 0{,}2139\,s,\quad T_2 = 0{,}0679\,s,\quad T_3 = 0{,}0404\,s \tag{29}$$

The above values of periods should be corrected through appropriate correction factors. Using Table 5 for the case of a frame with more than one bay and double diagonal bracing the coefficients α_1, α_2 and c_1 are obtained. Then, Eqs (15), (16), (18) and (2) yield

$$T_1 = 0{,}4279\,s, \quad T_2 = 0{,}1370\,s, \quad T_3 = 0{,}0775\,s \tag{30}$$

For comparison purposes the "exact" values of the periods as obtained by finite elements are

$$T_1 = 0{,}4442\,s, \quad T_2 = 0{,}1475\,s, \quad T_3 = 0{,}08723\,s \tag{31}$$

and the values of the first period as determined by the codes are

$$UBC: T_1 = 0{,}5501\,s, \quad EC8: T_1 = 0{,}4836\,s, \quad EAK: T_1 = 0{,}2357\,s \tag{32}$$

7 CONCLUSIONS

On the basis of the preceding discussion, one can draw the following conclusions:

1) The proposed method of modeling a plane steel frame (braced or unbraced) as an equivalent cantilever in conjunction with the use of certain correction factors constitutes a simple, conservative enough and accurate enough way of predicting by hand calculations the first three natural periods of that frame.
2) First and second periods are determined with a relative error below 15%, while the third period is determined with a relative error below 20%.
3) The method is limited to braced frames with only one braced bay. Further studies and some modifications on the correction factors should be made if a frame consists of more than one braced bay.
4) The height of the story and the span of the bay play a little role on the accuracy of the prediction provided one is kept away from extreme cases.

REFERENCES

[1] UBC (Uniform Building Code) (1997), *International Conference of Building Officials,* Whittier, California.

[2] EC 8 (Eurocode 8) (1994), *Design Provisions for Earthquake Resistance of Structures, Part 1,* CEN (European Committee for Standardization), Brussels.

[3] Rutenberg, A (1975), "Approximate natural frequencies for coupled shear walls", Earthquake Engineering and Structural Dynamics 4, pp. 95-100.

[4] Stafford Smith, B. and Crowe, E. (1986), "Estimating periods of vibration of tall buildings", Journal of Structural Engineering, ASCE, 112, pp. 1005-1019.

[5] EC 3 (Eurocode 3) (1992), *Design of Steel Structures, Part 1.1,* CEN (European Committee for Standardization), Brussels.

[6] SAP 2000 (May 2000), *Three Dimensional Static and Dynamic Finite Element Analysis and Design of Structures*, *Basic Analysis Reference*, Computers and Structures Inc., Berkeley, California.

[7] E.A.K. (September 1999) *Greek Earthquake Resistant Design Code*, Earthquake Design and Protection Organization (Ο.Α.Σ.Π.), Athens.

[8] Chrysanthakopoulos, C. (2004), *Approximate Formulae for Computing Natural Periods of Steel Frames and Simple Bridges*. M.S. Thesis, Department of Civil Engineering, University of Patras, Patras, Greece, (in Greek).

[9] Chrysanthakopoulos, C., Bazeos, N. and Beskos, D.E. (2004), "Approximate Formulae for Natural Periods of Plane Steel Frames", Journal of Constructional Steel Research, submitted.

UNBRACED FRAMES			Equivalent cantilever			Relative error (%)					
			T1	T2	T3	Equivalent cantilever			EAK	UBC	EC8
1 BAY	1	4 storey	0,6405	0,2099	0,1255	16,19	9,78	-0,76	29,34	28,02	28,29
	2	7 storey	1,0286	0,3255	0,1933	12,82	11,71	2,79	19,91	29,06	29,33
	3	10 storey	1,4054	0,4169	0,2437	11,36	15,77	8,58	14,85	31,02	31,28
2 BAY	4	4 storey	0,6647	0,2199	0,1317	18,78	13,30	5,98	53,34	32,78	33,03
	5	7 storey	0,8717	0,2816	0,1679	15,87	14,85	8,70	35,51	19,23	19,53
	6	10 storey	1,2664	0,3982	0,2360	13,22	14,54	8,44	34,59	25,05	25,34
	7	15 storey	2,0114	0,5990	0,3506	10,54	15,53	9,20	36,32	34,07	34,32
3 BAY	8	4 storey	0,6765	0,2245	0,1346	18,74	14,21	8,13	62,55	33,93	34,18
	9	7 storey	0,8735	0,2858	0,1709	16,54	15,06	9,82	47,87	20,03	20,33
	10	10 storey	1,2468	0,4012	0,2390	14,13	14,31	9,22	46,32	24,67	24,95
	11	15 storey	1,9215	0,5967	0,3527	11,84	14,82	9,67	46,36	31,98	32,24

Table 1: Comparison of the first three natural periods of unbraced frames with constant sections per height

BRACED FRAMES			Equivalent cantilever			Relative error (%)					
			T1	T2	T3	Equivalent cantilever			EAK	UBC	EC8
1 BAY	12	4 storey	0,1333	0,0213	0,0076	54,58	77,47	86,16	-84,05	-87,49	-64,81
	13	7 storey	0,3701	0,0591	0,0211	35,90	64,83	76,06	-63,66	-44,96	-27,42
	14	10 storey	0,7348	0,1173	0,0419	24,24	53,77	66,76	-39,18	-12,75	0,89
2 BAY	15	4 storey	0,1729	0,0527	0,031	54,94	58,03	58,56	0,49	-43,37	-26,02
	16	7 storey	0,3684	0,1063	0,0617	43,13	47,24	44,01	-3,14	-29,18	-13,56
	17	10 storey	0,6233	0,1694	0,0966	37,05	42,70	37,94	3,60	-10,45	2,91
	18	15 storey	1,1618	0,2883	0,1591	30,85	39,06	33,60	14,77	11,77	22,44
3 BAY	19	4 storey	0,2106	0,0669	0,0398	52,11	53,56	53,49	29,10	-25,11	-9,97
	20	7 storey	0,4263	0,1308	0,0771	38,66	41,11	38,07	21,50	-20,43	-5,86
	21	10 storey	0,6951	0,2047	0,1194	31,78	35,94	31,55	23,50	-7,34	5,64
	22	15 storey	1,2328	0,3383	0,1935	24,52	32,01	26,78	28,42	9,24	20,22

Table 2: Comparison of the first three natural periods of braced frames with constant sections per height

UNBRACED FRAMES			Equivalent cantilever			Relative error (%)					
			T1	T2	T3	Equivalent cantilever			EAK	UBC	EC8
1 BAY	1	4 storey	0,6856	0,2251	0,1346	13,17	10,66	-1,30	31,60	30,32	30,59
	2	7 storey	1,1574	0,3687	0,2192	7,60	13,44	6,66	24,56	33,18	33,43
	3	10 storey	1,6380	0,4976	0,2927	4,69	14,86	10,36	21,45	36,36	36,60
2 BAY	4	4 storey	0,7118	0,2356	0,1412	15,33	14,32	5,57	54,58	34,57	34,81
	5	7 storey	0,9788	0,3180	0,1898	9,90	14,69	8,13	38,49	22,96	23,25
	6	10 storey	1,3953	0,4417	0,2622	7,85	15,20	10,20	36,96	27,77	28,04
	7	15 storey	2,1452	0,6418	0,3760	6,82	16,44	13,41	37,81	35,61	35,85
3 BAY	8	4 storey	0,7246	0,2406	0,1442	15,75	15,27	7,73	63,75	36,04	36,28
	9	7 storey	0,9824	0,3225	0,1929	10,48	15,08	9,38	50,28	23,72	24,01
	10	10 storey	1,3796	0,4458	0,2659	8,68	15,24	11,03	48,41	27,61	27,88
	11	15 storey	2,0582	0,6413	0,3794	8,14	16,15	13,97	47,82	33,84	34,09

Table 3: Comparison of the first three natural periods of unbraced frames with variable sections per height

BRACED FRAMES			Equivalent cantilever			Relative error (%)					
			T1	T2	T3	Equivalent cantilever			EAK	UBC	EC8
1 BAY	12	4 storey	0,1365	0,0218	0,0078	53,50	77,09	85,96	-83,92	-87,36	-64,70
	13	7 storey	0,3952	0,0631	0,0225	31,78	63,25	75,03	-63,13	-44,48	-27,01
	14	10 storey	0,7826	0,1249	0,0446	19,56	51,80	65,77	-38,76	-12,42	1,18
2 BAY	15	4 storey	0,1742	0,0529	0,0311	54,90	58,56	59,14	1,13	-42,44	-25,21
	16	7 storey	0,3700	0,1061	0,0615	44,18	49,20	46,01	-0,82	-26,28	-11,01
	17	10 storey	0,6339	0,1699	0,0964	37,57	44,94	40,44	5,98	-7,72	5,31
	18	15 storey	1,1953	0,2895	0,1581	30,18	41,30	36,93	16,36	13,41	23,88
3 BAY	19	4 storey	0,2121	0,0673	0,0400	52,26	54,39	54,17	29,81	-23,84	-8,86
	20	7 storey	0,4295	0,1314	0,0774	40,03	43,86	40,45	23,82	-16,86	-2,73
	21	10 storey	0,7065	0,2063	0,1201	32,66	39,04	34,61	25,71	-4,25	8,36
	22	15 storey	1,2622	0,3403	0,1936	24,30	35,00	30,77	29,88	11,10	21,85

Table 4: Comparison of the first three natural periods of braced frames with variable sections per height

		BRACING	T_1			T_2			T_3			Apply to
			c_1	a_1	a_2	c_1	a_1	a_2	c_1	a_1	a_2	
CONSTANT SECTIONS		NO	0.94	-	-	0.94	-	-	0.99	-	-	λ_{sf}
VARIABLE SECTIONS		NO	0.98	-	-	0.95	-	-	1.00	-	-	λ_{sf}
1 BAY	CONSTANT SECTIONS	DOUBLE	0.67	1.00	-	0.48	0.90	-	0.39	0.85	-	Λ
		SINGLE	0.62	1.00	-	0.43	0.85	-	0.34	0.80	-	Λ
		K	0.67	1.00	-	0.44	0.65	-	0.35	0.55	-	Λ
		KNEE	0.62	0.85	-	0.40	0.60	-	0.30	0.50	-	Λ
	VARIABLE SECTIONS	DOUBLE	0.71	1.00	-	0.51	0.90	-	0.39	0.85	-	Λ
		SINGLE	0.65	1.00	-	0.43	0.85	-	0.39	0.80	-	Λ
		K	0.70	1.00	-	0.46	0.65	-	0.35	0.55	-	Λ
		KNEE	0.66	0.90	-	0.41	0.65	-	0.30	0.50	-	Λ
MORE THAN 1 BAY		DOUBLE	0.55	0.75	0.10	0.56	0.75	0.05	0.58	0.80	0.05	λ_{sf}
		SINGLE		0.75	0.10		0.75	0.05		0.80	0.05	λ_{sf}
		K		0.80	0.05		0.75	0.10		0.80	0.05	λ_{sf}
		KNEE		0.80	0.05		0.75	0.05		0.80	0.05	λ_{sf}

Table 5: Parameters a_1, a_2 and c_1 for correction factor equations

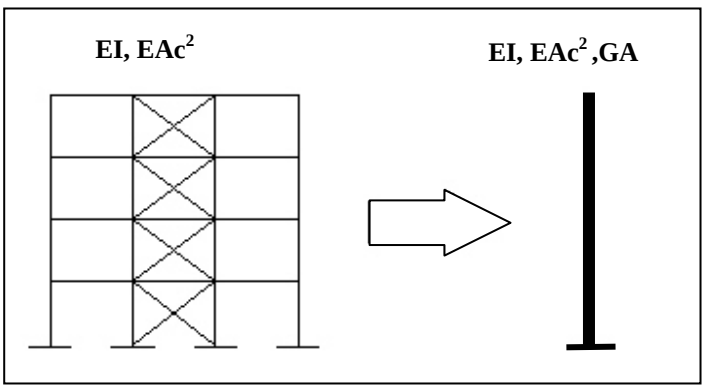

Figure 1. Modeling of a frame structure as an equivalent cantilever

ROOFTOP TUNED MASS DAMPER FRAME

Jerod G. Johnson, Lawrence D. Reaveley, and Chris P. Pantelides

Department of Civil & Environmental Engineering
University of Utah
122 South Central Campus Drive, Salt Lake City, Utah 84112, USA
e-mail: chris@civil.utah.edu

Keywords: Dampers, Nonlinear, Reduction, Response, Rooftop, Seismic, Tuning.

Abstract. *A feasibility study is presented for placing a tuned mass damper in the form of a steel moment resisting frame on the roof of relatively stiff structures to reduce seismic acceleration response. Six existing structures ranging from three to nine stories, originally designed to meet UBC Seismic Zone 3 lateral force requirements, were studied using various earthquake records. The analyses indicate that adding mass in conjunction with a steel moment resisting frame on the roof results in the elongation of the fundamental period of the structures. For most cases seismic acceleration response reduction was achieved, although the response could increase if the rooftop frame was not tuned to accommodate the structure's behavior, specific earthquake characteristics, and local soil conditions. Non-linear analysis methods were used to evaluate the stability of the rooftop tuned mass damper frame. Appropriate design of the rooftop tuned mass damper frame could result in reduction of the seismic acceleration response, which translates to safer structures when used as a retrofit measure, or a more economical design if used in new construction.*

1 INTRODUCTION

Engineers have long understood that flexible structures with relatively long fundamental periods respond with a lower level of internal forces due to seismic activity than stiff structures with short fundamental periods. To reduce the seismic acceleration response in stiff structures, innovations such as base isolation have been developed which make stiff structures behave as flexible structures while maintaining the inherent advantages of a rigid system[1, 2]. The effectiveness of base isolation stems from its ability to lengthen the fundamental period of a structure so that it responds less dramatically to lateral seismic acceleration. If the fundamental period of a structure could be lengthened in another way, the effect would be similar to that provided by seismic base isolation.

For the Single Degree of Freedom (SDOF) system shown in Figure 1(a), which represents the structural system of Figure 1(b), the fundamental period is obtained from the characteristic equation as:

$$T_1 = 2\pi\sqrt{\frac{m}{k}} \tag{1}$$

where k is the stiffness of the system, and m is its mass. Equation (1) demonstrates that the factors that establish the period of the structure are stiffness and mass. Although altering the stiffness and/or mass of a structure may be beyond practical or economical feasibility in many cases, the fundamental period of a structure could be increased by adding a flexible frame coupled with a specific mass at the roof level. Since many structures use the roof to house mechanical equipment, the Rooftop Tuned Mass Damper Frame (RTMDF) could be altered, tuned and used as a passive tuned mass damper.

Figure 1(c) represents the modification to the SDOF system model shown in Figure 1(a). Figure 1(d) represents the modification of the structural system of Figure 1(b). These figures represent the alteration of the original primary structure by adding a flexible frame coupled with a specific mass at the roof level. Addition of the RTMDF at the roof level modifies the structure's dynamic properties and its response. For example, if the added mass is represented by a fraction of the total mass of the structure (m/20) and if the stiffness of the RTMDF is represented by a fraction of the total stiffness (k/20), the mass and stiffness matrices become:

$$\boldsymbol{m} = \begin{bmatrix} m & 0 \\ 0 & m/20 \end{bmatrix}; \qquad \boldsymbol{k} = \begin{bmatrix} 21k/20 & -k/20 \\ -k/20 & k/20 \end{bmatrix} \tag{2}$$

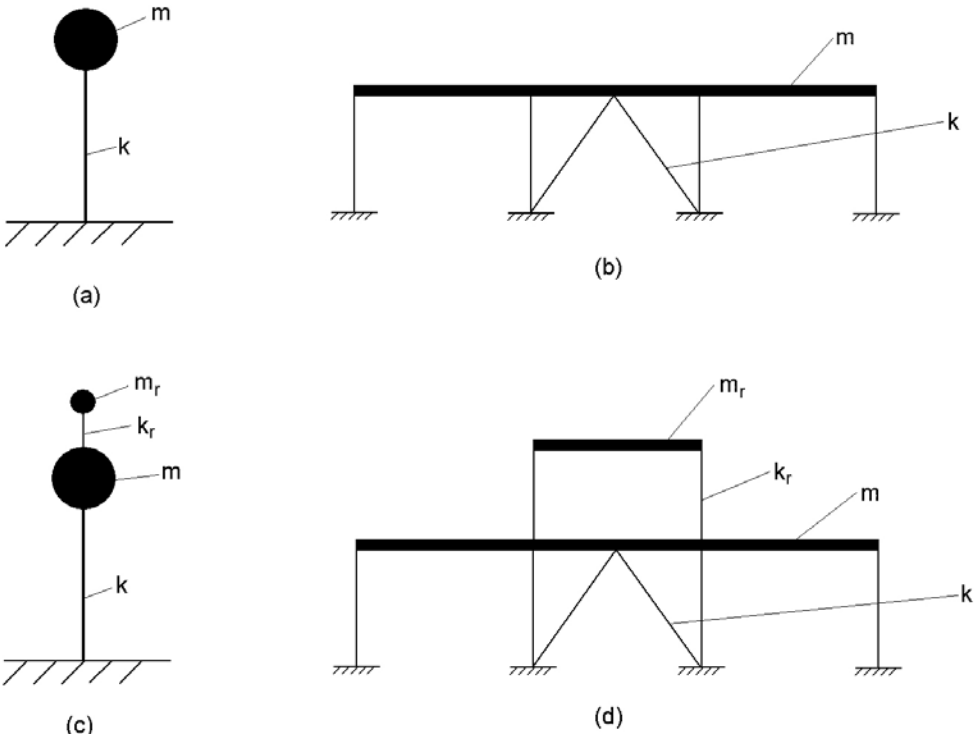

Figure 1. Idealized lumped mass systems: (a) SDOF system, (b) structure, (c) SDOF system with RTMDF, (d) structure with RTMDF.

Solving the characteristic equation yields the modal periods as:

$$T_1 = \frac{2\pi}{0.894}\sqrt{\frac{m}{k}} \quad ; \qquad T_2 = \frac{2\pi}{1.120}\sqrt{\frac{m}{k}} \tag{3}$$

The fundamental period of the idealized structural system is increased by a factor of 1/0.894 or 12% thus demonstrating that lengthening of the fundamental period, and therefore a decrease in seismic response, can be achieved by adding a RTMDF on the roof of the primary structure.

To analyze the effectiveness of a rooftop frame as a passive tuned mass damper six existing structures were analytically modeled using SAP2000 Nonlinear[3]. The structures were evaluated for the as-is (undamped) condition and the modified (damped) condition using a suite of ground motions. Time history and response spectra analyses were performed using historical earthquakes. In addition, the structures were evaluated using a design response spectrum from the 1997 Uniform Building Code[4] for Zone 4, soil type S_D. To scale the analysis of each structure to an appropriate value, the FEMA 356 Guidelines for the Seismic Rehabilitation of Buildings[5] were employed.

Past research has yielded mixed results with respect to the effectiveness of passive tuned mass dampers (TMD) for controlling seismic response. Kaynia, Veneziano, and Biggs investigated the effectiveness of passive TMD for seismic applications in a study conducted in 1981[6]; based on the statistical results of their model, they concluded that tuned mass dampers might not be as effective as once thought for reducing seismic response of structures. In 1983 Sladek and Klingner studied the effect of a TMD addressing both linear and nonlinear behavior of a prototype structure subjected to the N-S component of the El Centro 1940 ground motion[7]; their results suggest that tuned mass dampers do not appear to be an effective method of reducing seismic response. These results appear contrary to other studies that indicate tuned mass dampers are an effective passive control device to suppress steady state structural vibrations[8]. Villaverde studied the possibility and effectiveness of using a rooftop structure as mass for a passive TMD[9]. The analytical model consisted of an isolated rooftop structure that rests upon laminated rubber bearings; viscous dampers were also used in addition to the laminated rubber bearings to create a highly damped vibration absorbing mechanism at the roof level. Reductions in peak seismic response parameters as high as 84 percent for the damped structure were reported; this result suggests that a significant reduction in seismic response is possible using a tuned mass damper at the roof level of a structure. The difference between the proposed system and the TMD systems studied in the past is that the proposed RTMDF system yields and participates in the response in the nonlinear range.

2 DESCRIPTION OF STRUCTURES AND SEISMIC EXCITATIONS

The structures used in this research are actual buildings, originally designed to meet UBC Seismic Zone 3 lateral force requirements. Table 1 lists the characteristics of each structure used in the study; each has a relatively short fundamental period thus requiring design lateral forces corresponding to the peak of the typical design spectrum. The earthquake records used for the study were selected to encompass a broad range of seismic response and are summarized in Table 1. For each of the accelerograms listed in Table 1 the acceleration response spectra are given in Figure 2. For certain earthquakes, the acceleration response spectra are significantly higher than the UBC Seismic Zone 4 spectrum within specific period ranges. In general, the peak acceleration response occurs for structures with periods between 0.2 s and 0.5 s; the Kobe record is the exception with the peak response occurring at 0.75 s and is attributable to a combination of near field effects and unusually soft soils.

3 RTMDF DESIGN PROCEDURE

Preliminary analyses per AISC guidelines[10, 11] indicated that allowable stresses in the steel members of the RTMDFs were exceeded; for the RTMDF to be effective its members must yield and respond in the nonlinear range. To evaluate the overall stability of the RTMDFs as moment resisting steel frames, the procedures for Nonlinear Static Pushover Analysis set forth in FEMA 356[5] were implemented; a structure is analyzed by determining the maximum nonlinear target displacement and comparing it to the allowable nonlinear displacement as calculated through analysis. The target displacement is a function of the fundamental period and the design spectral acceleration of the stand-alone RTMDF. The spectral acceleration used in calculating the target displacement was derived from the rooftop acceleration time-history for each structure and seismic record. The spectral acceleration was determined using the rooftop acceleration time-history results in combination with linear interpolation methods. The maximum allowable nonlinear target displacement for the RTMDFs was based on the nonlinear static pushover curves that were developed for each RTMDF per FEMA 356 guidelines.

Designation	No. Stories	Lateral System	Use	Period (s)
BF-1	3	Braced Frame	Office Building	0.47
BF-2	4	Braced Frame	Office Building	0.70
BF-3	9	Braced Frame	Office Building	1.06
EBF-1	4	Ecc. Braced Frame	Computation Facility	0.75
SW-1	6	Concrete Shear Wall	Office Building	0.35
SW-2	6	Concrete Shear Wall	Research Facility	0.53

Record (station/year)	Earthq. Magnitude	Distance to Epicenter (km)	Duration (s)	PGA (g)
Imperial Valley (El Centro 1940)	6.9	10	31.14	0.32
Loma Prieta (Gilroy 1989)	7.0	12	39.98	0.54
Kobe (1995)	6.9	3.4	59.98	0.84
Northridge (Rinaldi 1994)	6.7	7.5	14.95	0.68
San Fernando (Pacoima 1971)	6.4	7.2	41.82	1.17

Table 1: Summary of structures and time history records

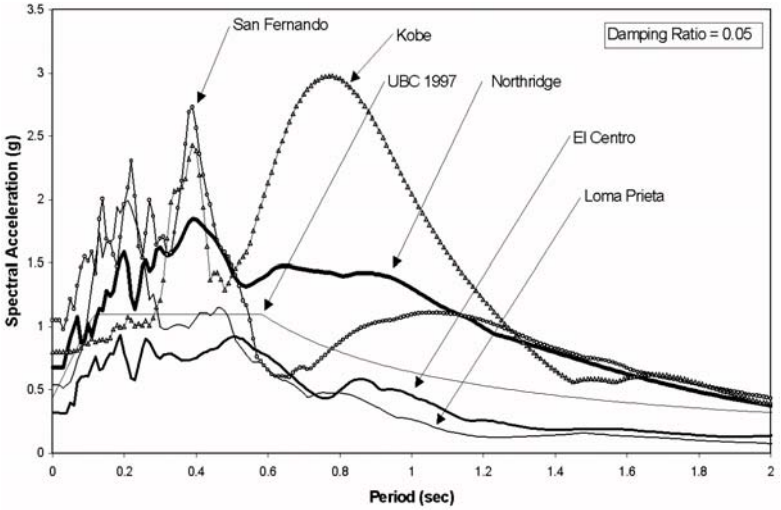

Figure 2. Acceleration response spectra

3.1 Refining the Analyses

The stability analyses of the RTMDFs in conjunction with the analyses of the damped structures to which they were added required an iterative design approach. Upon designing a RTMDF for each structure that appeared to perform at a Collapse Prevention level or better, according to the nonlinear static pushover curve, the damper was added to the original undamped structure, thus making it the damped structure, and the analyses were re-run. The results of the analyses indicated whether the addition of the RTMDF had increased or decreased the overall seismic response for the structure. In addition, the resulting rooftop acceleration histories were used to create rooftop response spectra to determine spectral accelerations and other parameters needed to assess the overall stability of the RTMDF. In some cases, the addition of the RTMDF resulted in an increase in the seismic acceleration response; in other cases, the resulting accelerations at the rooftop level caused the RTMDF to displace to a point of instability. In each case, the frame and/or mass of the RTMDF was revised and the analyses were repeated until an acceptable or final design was reached. For some structures and earthquakes, particularly the Kobe record, the RTMDF often resulted in an increase in the seismic acceleration response or instability of the RTMDF frame or both. For most structures and seismic records, a reduction in seismic response was achieved with a stable RTMDF.

3.2 RTMDF Design Considerations

In the development of the design process for the RTMDFs, it was found that using at least three columns on each side of the RTMDF frame for each direction resulted in a frame that could withstand much greater nonlinear displacements than a frame with just two columns on each side; this reinforces the design concept of redundancy, which is a consideration for design in building codes. The use of heavier columns and lighter beams appeared to increase the maximum allowable displacement in the nonlinear static pushover; this relates to the strong column-weak beam requirement of current building codes in the design of special moment frames. Overall safety is enhanced by having beams rather than columns yield and form plastic hinges at the beam ends. The amount of allowable displacement typically increased for steel with higher yield strengths; however, higher yield strengths sometimes led to strength degradation over the nonlinear range of the pushover curve. For the RTMDF frames studied for the present set of buildings, it appeared that a stand-alone target period for design of at least 0.6 seconds, for the RTMDF resulted most often in a stable design coupled with an overall reduction in seismic acceleration response. For a RTMDF with stand-alone period greater than 1.2 seconds, the damper appeared to be too flexible to effectively alter the dynamics of the structure. For the RTMDF to be effective, the cladding or skin system cannot increase its stiffness or significantly alter its mass. To accomplish this, alternative skin systems such as those used for base isolation must be employed for enclosing the RTMDF.

The steps for designing an effective RTMDF are: (1) Determine the primary modes of vibration and structural response of the structure; (2) Perform a geotechnical investigation and develop site-specific accelerograms or scale previously recorded accelerograms. Develop a site-specific response spectrum to determine the magnitude of fundamental period shift required for effective seismic response reduction. Verify that a longer fundamental period does not place the structure at a region of higher response on the site-specific spectrum. Perform time-history and response spectrum analyses of the as-is structure; (3) Develop the model for a stand-alone rooftop frame that will eventually become the RTMDF; (4) Apply gravity loads to the RTMDF and perform modal dynamic and nonlinear static pushover analyses of the RTMDF; (5) Depending on the shape of the nonlinear static pushover curve and the maximum displacement indicated for Collapse Prevention (CP), redesign the RTMDF until an acceptable nonlinear static pushover curve is achieved; (6) Add the RTMDF frame at the roof level of the undamped structure, making it the damped structure, and re-run the time-history and response spectrum analyses. If the RTMDF does not reduce the response, return to step 3 and alter the mass or framing of the RTMDF to change the fundamental period and overall dynamic properties of the stand alone RTMDF; (7) Repeat steps 3 and 4 until a final RTMDF design with seismic acceleration response reduction is achieved; (8) Record the rooftop acceleration time histories for each seismic record used; (9) Develop rooftop response spectra for the acceleration time-histories; (10) Use the rooftop response spectra and the effective period of the stand-alone RTMDF to determine the coefficients used for calculation of target displacements per FEMA 356; (11) Verify that calculated target displacements are less than those corresponding to the Collapse Prevention (CP) level on the nonlinear static pushover curve developed in steps 2 and 3. The RTMDF design procedure may begin with step 6 provided that the stability of the frame of the RTMDF is verified by subsequently completing steps 3, 4, and 5.

3.3 Analysis and Design of RTMDF for BF-2

Braced Frame 2 (BF-2) is a 4-story braced frame office building as shown in Figure 3. Based on modal analysis, the fundamental period of the as-is structure is approximately 0.70 s. For this example the RTMDF mass is considered as approximately 11.6% of the mass of the original building. Increasing the mass could yield an increased response reduction, but must be carefully weighed against the system's ability to support the added gravity load. Elastic analysis of the as-is structure yields peak base shears and rooftop displacements as shown in Table 2 for both response spectra and time-history analyses.

Figure 4 shows the configuration, dimensions, member sizes, and nonlinear deformation of the RTMDF for BF-2, whereas Figure 5 shows the mass of the RTMDF and the deformation of the combination of the RTMDF frame with the original structure. Pushover analysis of the RTMDF, shown in Figure 6, indicates that the frame has the capacity to be laterally displaced approximately 335 mm before passing a Collapse Prevention level of performance as defined by FEMA 356. In addition, modal analysis indicates that the fundamental mode of vibration for the stand-alone frame of the RTMDF is approximately 1.05 s.

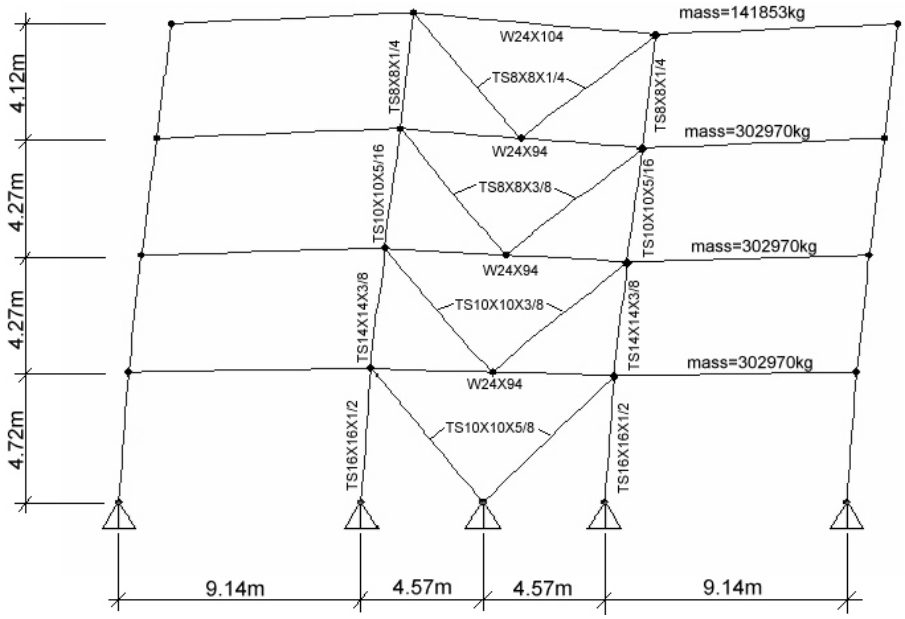

Figure 3. Mode shape of undamped structure BF-2 corresponding to a fundamental period of 0.70 s

	Response Spectrum Analyses		Time-History Analyses	
Record	Roof Displ. (mm)	Base Shear (kN)	Roof Displ. (mm)	Base Shear (kN)
El Centro	90	4212	94	4261
Loma Prieta	84	4897	84	4924
Kobe	248	11302	246	12099
Northridge	105	4831	106	4878
San Fernando	47	2553	50	2967

Table 2. Peak roof displacements and peak base shears for undamped building BF-2

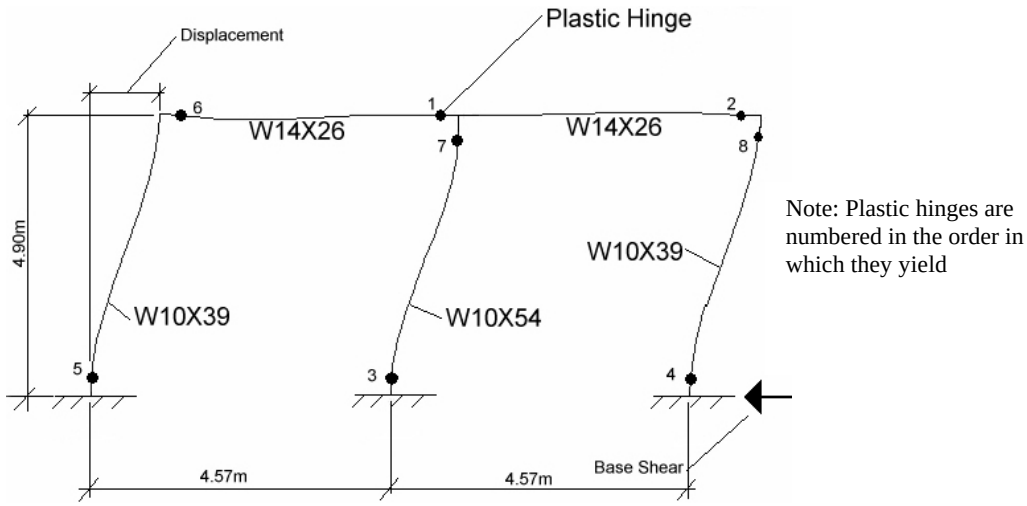

Figure 4. RTMDF during application of load at a period of 1.05 s

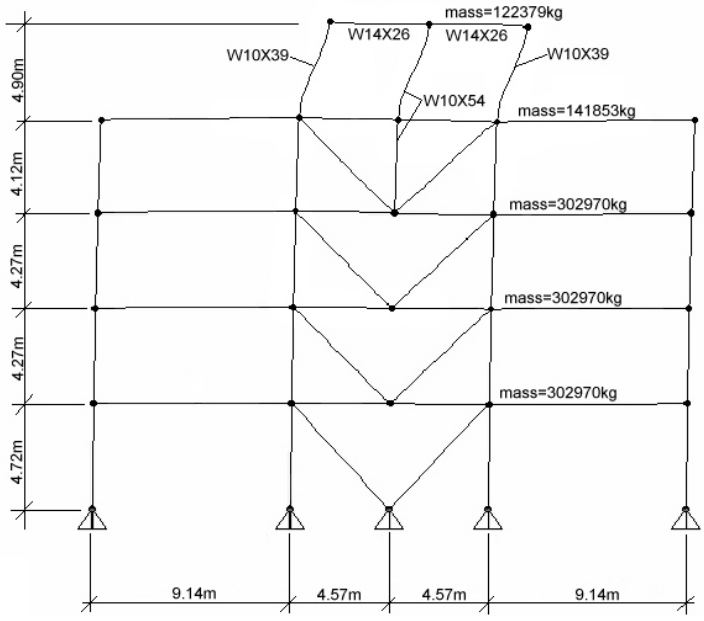

Figure 5. Mode shape of damped structure BF-2 corresponding to a fundamental period of 1.24 s

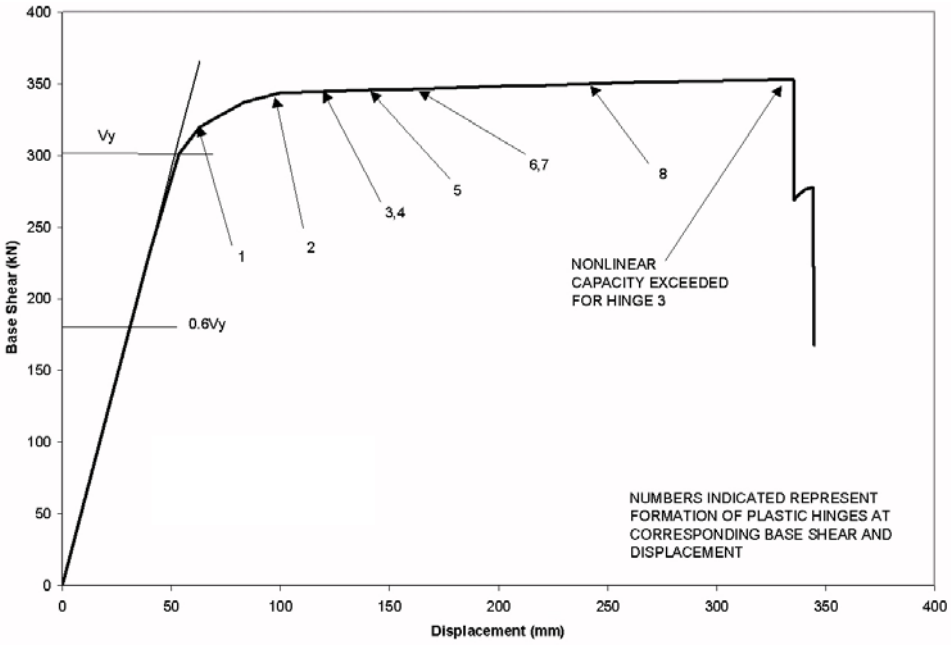

Figure 6. Nonlinear static pushover curve for RTMDF

Placing the RTMDF frame on the roof of the building of Figure 5 provides the results needed to perform the stability analysis of the RTMDF; thus, the response spectra at the rooftop level of the structure are obtained. Analysis of the damped structure produced the spectral acceleration response spectra shown in Figure 7. Using the spectral accelerations in conjunction with the effective period of the RTMDF of 1.05 s enables calculation of the target displacement (δ_t) for the RTMDF based on the following equation (Eq. 3-15 from FEMA 356):

$$\delta_t = C_0 C_1 C_2 C_3 S_a T_e^2 g/(4\pi^2) \tag{4}$$

where T_e = effective fundamental period based on the initial elastic period multiplied by the square root of the ratio of initial slope of the nonlinear static pushover curve over the secant stiffness; S_a = spectral acceleration at effective fundamental period; C_0 = modification factor to relate spectral displacement of an equivalent SDOF system to the roof displacement of the building; C_1 = modification factor to relate expected maximum inelastic displacements to displacements calculated for linear elastic response; C_2 = modification factor to represent the effect of stiffness degradation and strength deterioration on maximum displacement response; C_3 = modification factor to represent increased displacements due to dynamic P-delta effects.

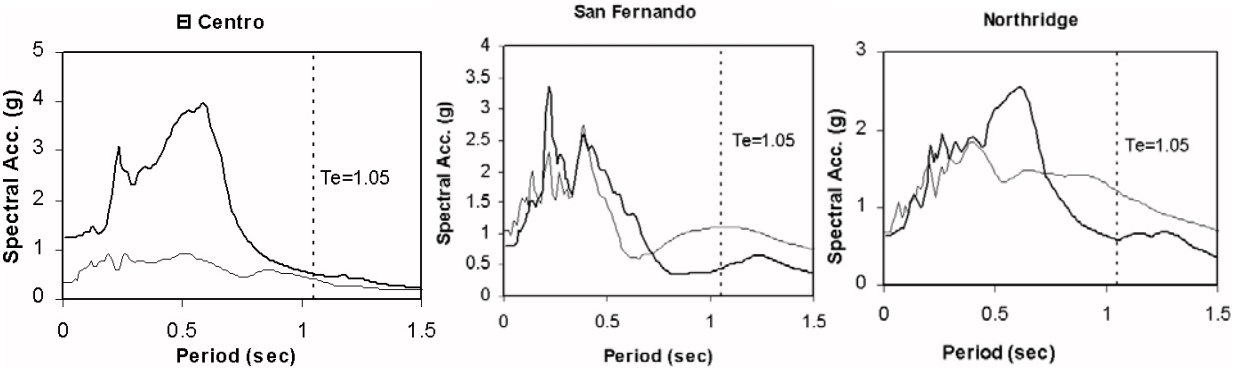

Figure 7. Rooftop acceleration response spectra compared to ground level spectra for building BF-2

Table 3 summarizes the results of the nonlinear static pushover stability analysis of the RTMDF frame for building BF-2. The target displacements of the RTMDF corresponding to each seismic record indicate that the configuration has the capacity to perform to at least a Collapse Prevention level of performance (maximum allowable target displacement of 335 mm) and is therefore deemed adequate. The resulting damped configuration for BF-2 has a fundamental period of 1.24 s, which is considerably longer than the 0.70 s period of the original undamped structure. As a result, the response of the structure to seismic excitation is altered. Table 4 provides a summary of the analysis for building BF-2 and compares the undamped and damped structures. The results show that a reduction in seismic response can be achieved with a stable RTMDF, with the exception of the peak rooftop displacement for the San Fernando earthquake. The same RTMDF was used in all of the seismic records and this is the cause of the amplification observed in Table 4; therefore a single RTMDF cannot reduce the seismic response of a specific building for all possible ground accelerations. Similar results were obtained for the other five buildings described in Table 1. Ground accelerations are highly dependent on soil type; this narrows the range of likely ground motions and enables the design of a RTMDF that would correspond to a specific site. To design a stable RTMDF that can effectively reduce overall seismic response, the engineer must be familiar with the characteristics of lateral ground accelerations that are likely to occur.

4 CONCLUSIONS

The results of the analyses performed in this study indicate that utilizing and modifying the structure and mass of a building's rooftop enclosure as a passive Rooftop Tuned Mass Damper Frame (RTMDF) can be an effective method for reducing the overall seismic response of the primary structure. The period shift produced by the RTMDF results in decreased acceleration and displacement response of the primary structure for most of the buildings and earthquakes studied. It should be noted that the RTMDF is allowed to yield and behave nonlinearly as opposed to the traditional tuned mass damper (TMD). Although the results show that a reduction in seismic response can be achieved for most buildings, there are certain soil conditions, building types, and ground motions for which the use of the RTMDF results in amplification of the seismic response. For this study, amplification typically resulted for structures with low fundamental periods of less than 0.5 s that are supported on soft soils. The cause of this amplification is that one RTMDF was designed for each structure with the intent of reducing the seismic response for all five earthquakes, even though they occurred at various sites. The results indicate that one RTMDF design for a structure may not reduce the structural response for all possible unrelated ground motions. However, the results show that one RTMDF design can effectively reduce the structural response corresponding to a group of similar, specific ground motions. RTMDF frames proposed in this study are therefore deemed an effective prospect for reducing structural response due to a site specific seismic ground motion.

Benefits of using RTMDFs for reducing structural response include; (a) cost of the system is less than other methods; (b) the proposed system does not require use of specialized materials or methods of construction; (c) for rehabilitation, installation of the proposed system would cause minimal impact on the occupants or contents of a structure; (d) the proposed system is passive and does not require a power source; (e) the system does not require additional space within the structure; (f) the system could significantly improve the expected performance of a structure during seismic activity; (g) for new construction, the proposed system would reduce seismic response by inducing lower stresses resulting in reduced structural costs.

The limitations of the proposed RTMDFs include: (a) the RTMDF may not be effective for all structures and soil types; (b) the system can cause amplification of seismic response if not designed correctly or if earthquakes occur unlike those anticipated; (c) for rehabilitation, reinforcement of existing structural members at the roof level would be required; (d) the system may not be self restoring, depending on the severity of ground motion; (e) the RTMDF frame requires a rooftop enclosure cladding system that does not increase the stiffness of the rooftop enclosure, that is capable of significant displacement, and does not alter the mass of the RTMDF.

Record	$C0$	$C1$	$C2$	δi (mm)	$C3$	Spectral Acceleration (g)	Target Displacement, δt (mm)
El Centro	1.00	1.00	1.20	192	1.00	0.50	166
Loma Prieta	1.00	1.00	1.20	157	1.00	0.41	137
Kobe	1.00	1.00	1.20	323	1.00	0.85	280
Northridge	1.00	1.00	1.20	220	1.00	0.58	192
San Fernando	1.00	1.00	1.20	170	1.00	0.45	148

Table 3. Summary of target displacement calculations for RTMDF for building BF-2

Response Spectrum Analyses						
	Peak Rooftop Displacement (mm)			Peak Base Shear (kN)		
Record	Undamped	Damped w/RTMDF	% Change	Undamped	Damped w/RTMDF	% Change
El Centro	90	80	-11%	4212	4266	1%
Loma Prieta	84	67	-19%	4897	4684	-4%
Kobe	248	140	-44%	11302	6961	-38%
Northridge	105	80	-24%	4831	3825	-21%
San Fernando	47	56	19%	2553	2442	-4%
Time History Analyses						
	Peak Rooftop Displacement (mm)			Peak Base Shear (kN)		
Record	Undamped	Damped w/RTMDF	% Change	Undamped	Damped w/RTMDF	% Change
El Centro	94	71	-25%	4261	4026	-6%
Loma Prieta	84	68	-20%	4924	4132	-16%
Kobe	246	132	-46%	12099	6334	-48%
Northridge	106	80	-24%	4878	4533	-7%
San Fernando	50	58	16%	2967	2576	-13%

Table 4. Peak displacements and base shears for undamped and damped building BF-2

REFERENCES

[1] Skinner, R.I., Robinson, W.H., McVerry, G.H. (1993), *An Introduction to Seismic Isolation*, John Wiley & Sons, New York.
[2] Naeim, F., Kelley, J.M. (1999), *Design of Seismic Isolated Structures*, John Wiley & Sons, New York.
[3] Computers and Structures Inc. (1999), *SAP 2000 Nonlinear Version 7*, CSI, Berkeley, California.
[4] International Conference of Building Officials (1997), *Uniform Building Code UBC-97*, Whittier, California.
[5] Federal Emergency Management Agency (2000), *Prestandard and Commentary for the Seismic Rehabilitation of Buildings*, Publication No. FEMA 356, Washington, D.C.
[6] Kaynia, A.M., Veneziano, D., Biggs, J.M. (1981), "Seismic effectiveness of tuned mass dampers," J. of the Structural Division, ASCE 107, pp. 1465-1484.
[7] Sladek, J.R., Klingner, R.E. (1983), "Effect of tuned mass dampers on seismic response," J. of Structural Engineering, ASCE 109, pp. 2004-2009.
[8] Den Hartog, J.P. (1956), *Mechanical Vibrations*, 4th Edition, McGraw-Hill, New York.
[9] Villaverde, R. (1998), "Roof isolation system to reduce seismic response of buildings: a preliminary assessment," Earthquake Spectra 14, No. 3, pp. 521-532.
[10] American Institute of Steel Construction Inc. (1989), *Manual of Steel Construction: ASD*, 9th Edition, Chicago, Illinois.
[11] American Institute of Steel Construction Inc. (1994), *Manual of Steel Construction: LRFD*, 2nd Edition, Chicago, Illinois.

DESIGN PROCEDURE FOR STRUCTURES EQUIPPED WITH A CONTROL SYSTEM AND SUBJECTED TO EARTHQUAKE LOADING

Nikos G. Pnevmatikos, Charis J. Gantes

Metal Structures Laboratory, School of Civil Engineering,
National Technical University of Athens,
9 Heroon Polytechneiou, GR-15780 Zografou, Greece
Tel: +302107723440, Fax: +302107723442, Email: chgantes@central.ntua.gr

Keywords: Seismic design, Response spectrum, Acceleration control, Pole placement, Saturated control, Time delay.

Abstract. *An alternative direction of designing a new structure is to design a light economical structure capable of resisting the permanent loads and small earthquakes, and install a control system which will provide the reservoir of strength, stiffness or damping, necessary for resisting potential severe earthquakes that will occur only a few times during the structure's life. The main challenge of structural control is to determine a control strategy that uses the measured structural response and the excitation signal to calculate appropriate control forces, which will be applied indirectly to the structure through specific devices, and will enhance the structural safety and serviceability against extreme dynamic excitation. In this paper a procedure for the design of new structures equipped with control systems is proposed. The main idea is to achieve a cost effective design, based on a reduced response spectrum, as one portion of the earthquake energy will be taken by the control system. The savings from the design of the conventional structural system will be utilized to install the control system. To do that, a scale factor α that reduces the design response spectrum is calculated. Then, a dynamic control analysis with acceleration feedback and with or without saturation control is performed. If the response satisfies the design criteria, then the scale factor a is accepted, otherwise it is increased and the procedure is repeated. The simulation results indicate that an adequate reduction of the design response spectrum can be achieved by means of the proposed approach.*

1 INTRODUCTION

Over the past few decades various control algorithms and control devices have been developed, modified and investigated by various groups of researchers. The work of Yao, Housner et al., Kobori et al., Spenser et al., Yang, Caughey, Masri, Renzi, Skelton and Soong is representative[1-10]. While many of these structural control strategies have been successfully applied, challenges pertaining to cost, reliance on external power and mechanical intricacy during the life of the structure have delayed their widespread use. In the work of Kurata et al.[11] the reliability from the point of view of health monitoring and fail safe function is discussed. There have been some attempts to connect the control forces with the design codes. Yang et al.[12] suggest the maximum control force to be a percentage of the building weight, while Cai et al.[13] give this force as a portion of the seismic force. Lee et al.[14] determine the upper limit of control force based on the response spectrum of the external earthquake.

As far as cost is concerned, it is possible to achieve substantial savings by designing a new structure based on a reduced response spectrum and utilize these savings to install a control system. A systematic procedure to achieve the above objective is proposed in this paper.

2 DESIGN PROCEDURE FOR STRUCTURES EQUIPPED WITH A CONTROL SYSTEM

Initially the structure is designed based on a response spectrum provided by the pertinent code. From the seismic forces and the maximum capacity of the control device a scale factor α is obtained and applied on the response spectrum. The structure is redesigned based on this reduced spectrum. Then, dynamic control analysis is performed for a range of high and low frequency earthquakes, with acceleration feedback, with or without saturation of control forces. If the response satisfies the design criteria, then the value of α is accepted, otherwise it is slightly increased and the above procedure is repeated. The flow chart of this procedure is shown in figure1.

Knowing the mass and initial stiffness of the structure the eigenmodes Φ_i, eigenperiods T_i or eigenfrequencies f_i and the corresponding damping ratios ξ_i of the uncontrolled system are obtained from the solution of the following eigenvalue problem (Chopra[15]):

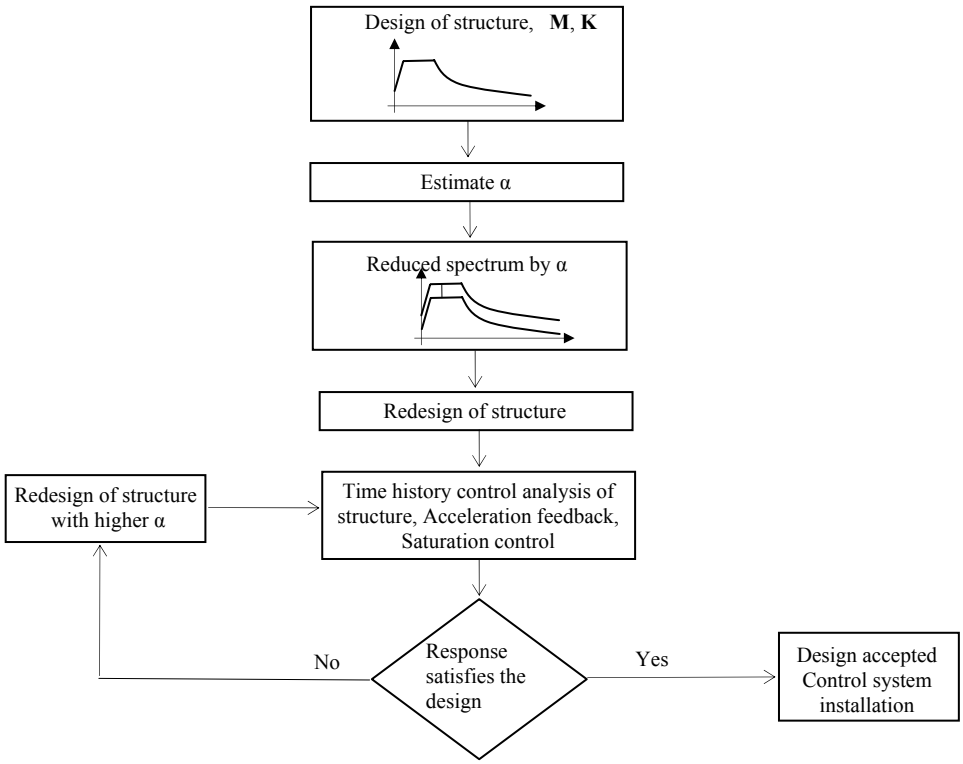

Figure 1. The flow chart of the proposed design procedure

$$\left[\mathbf{K}-\omega^2\mathbf{M}\right]_{nxn}\boldsymbol{\Phi}=0 \Rightarrow \left|\mathbf{K}-\omega^2\mathbf{M}\right|=0 \Rightarrow \begin{cases}\boldsymbol{\Phi}_1,\boldsymbol{\Phi}_2,...,\boldsymbol{\Phi}_n \Rightarrow \\ \omega_1,\omega_2,...\omega_n\end{cases}$$
$$T_i=\frac{2\pi}{\omega_i}, \quad f_i=\frac{\omega_i}{2\pi}, \quad i=0,...,n\text{-}1 \tag{1}$$

$$\begin{aligned}\mathbf{C}_n &= \boldsymbol{\Phi}_n^T\mathbf{C}\boldsymbol{\Phi}_n \\ \mathbf{M}_n &= \boldsymbol{\Phi}_n^T\mathbf{M}\boldsymbol{\Phi}_n \\ \xi_i &= 2\mathbf{C}_n\mathbf{M}_n\omega_n\end{aligned} \tag{2}$$

The participation factor ψ_i, and seismic forces $\mathbf{F}_{q,i}$ for the i^{th} eigenmode are given as:

$$\psi_i=\frac{\boldsymbol{\Phi}_i^T\mathbf{M}\mathbf{E}}{\boldsymbol{\Phi}_i^T\mathbf{M}\boldsymbol{\Phi}_i}, \quad i=1,...,n \tag{3}$$

$$\mathbf{F}_{q,i}=\mathbf{M}\boldsymbol{\Phi}_i\psi_i\Phi_{d,i}(T_i,\xi_i), \quad i=1,...,n \tag{4}$$

where $\mathbf{E}$ is the direction matrix for the earthquake and $\Phi_{d,i}(T_i, \xi_i)$ is the spectral acceleration. The maximum seismic forces $\mathbf{F}_q$ for each degree of freedom are obtained combining the seismic forces from each eigenmode with the corresponding participation factor, thus:

$$\mathbf{F}_q=\sum_i^n\psi_i\mathbf{F}_{q,i} \tag{5}$$

If $F_{d,max}$ is the maximum control device capacity (maximum possible control force), then the maximum control force that can be applied on the system is:

$$\mathbf{F}_{d,max}=\mathbf{E}_f F_{d,max} \tag{6}$$

where $\mathbf{E}_f$ is the location matrix for the control devices on the structure. The remaining maximum seismic forces

which are applied to the structure equipped by control devices are:

$$\mathbf{F}_{q,\,new}=\begin{cases}\mathbf{F}_q-\text{sign}(\mathbf{F}_q)\mathbf{F}_{d,max} & \text{if} \quad |\mathbf{F}_q|>\mathbf{F}_{d,max}\\ 0 & \text{if} \quad |\mathbf{F}_q|>\mathbf{F}_{d,max}\end{cases} \tag{7}$$

These forces correspond to a reduced spectral acceleration. From equation (4) this new spectral acceleration $\Phi_{d,i,new}(T_i, \xi_i)$, corresponding to new seismic forces, can be obtained:

$$\Phi_{d,i,new}(T_i,\xi_i)=\frac{\left(\mathbf{M}\boldsymbol{\Phi}_i\right)^{-1}\mathbf{F}_{q,new,i}}{\psi_i}, \qquad i=1,...,n \tag{8}$$

The reduction factor α can be obtained by dividing the new spectral acceleration $\Phi_{d,i,new}(T_i, \xi_i)$ by the corresponding initial one:

$$\alpha_i=\frac{\Phi_{d,i,new}(T_i,\xi_i)}{\Phi_{d,i}(T_i,\xi_i)}, \qquad i=1,...,n \tag{9}$$

and using the maximum α_i value to scale the response spectrum:

$$\alpha=\max(\alpha_i) \tag{10}$$

Based on the reduced response spectrum the conventional structure is redesigned and time history analysis of the controlled system for a representative range of earthquake accelerograms is performed. The equation of motion of a controlled structural system with n degrees of freedom subjected to an earthquake excitation a_g is:

$$\mathbf{M}\ddot{\mathbf{U}}+\mathbf{C}\dot{\mathbf{U}}+\mathbf{K}_{new}\mathbf{U}=-\mathbf{M}\mathbf{E}a_g+\mathbf{E}_f\mathbf{F} \tag{11}$$

where **M**, **C** denote the mass and damping matrices of the structure, respectively , $\mathbf{K}_{new}$ is the new stiffness matrix of the redesigned structure, and **F** is the control force matrix. In the state space approach the above equation (11) can be written as follows:

$$\dot{\mathbf{X}}=\mathbf{A}\mathbf{X}+\mathbf{B}_g a_g+\mathbf{B}_f\mathbf{F} \tag{12}$$

The matrixes **X**, **A**, $\mathbf{B_g}$, $\mathbf{B_f}$ are given by

$$\mathbf{X}=\begin{bmatrix}\mathbf{U}\\ \dot{\mathbf{U}}\end{bmatrix}_{2nx1}, \quad \mathbf{A}=\begin{bmatrix}\mathbf{0} & \mathbf{I}\\ -\mathbf{M}^{-1}\mathbf{K}_{new} & -\mathbf{M}^{-1}\mathbf{C}\end{bmatrix}_{2nx2n}, \quad \mathbf{B}_g=\begin{bmatrix}\mathbf{0}\\ -\mathbf{E}\end{bmatrix}_{2nx1}, \quad \mathbf{B}_f=\begin{bmatrix}\mathbf{0}\\ \mathbf{M}^{-1}\mathbf{E}_f\end{bmatrix}_{2nx1} \tag{13}$$

The control forces **F** are determined by saturated acceleration feedback. This is so because at the beginning of the procedure, calculation of the reduction factor α was based on the assumption that the control forces resist seismic forces, which are proportional to the mass and acceleration of the corresponding degree of freedom. However, other control algorithms such as linear quadratic regulator, pole assignment or sliding mode control can be used.

$$\mathbf{F}=\begin{cases}-\mathbf{G}\left(\dot{\mathbf{X}}+\mathbf{E}_g a_g\right) & \text{if} \quad \left|\mathbf{G}\left(\dot{\mathbf{X}}+\mathbf{E}_g a_g\right)\right|<\mathbf{F}_{d,max}\\ -\text{sign}(\dot{\mathbf{X}}+\mathbf{E}_g a_g)\mathbf{F}_{d,max} & \text{if} \quad \left|\mathbf{G}\left(\dot{\mathbf{X}}+\mathbf{E}_g a_g\right)\right|\geq\mathbf{F}_{d,max}\end{cases}, \quad \mathbf{G}=\begin{bmatrix}\mathbf{0} & \mathbf{M}\end{bmatrix}, \ \mathbf{E}_g=\begin{bmatrix}\mathbf{0} & \mathbf{E}\end{bmatrix} \tag{14}$$

If the response obtained for the controlled system satisfies the design criteria, then the scale factor α is accepted. In this work a representative design criterion was used, that the story drift does not exceed h/300 (where h is the story height). In a similar way, additional design criteria concerning the strength of structural members can be used. This can also be implemented by limiting story drift below values that cause member yielding. The above procedure was tested for a number of numerical simulations, and some representative examples are presented next.

3 EXAMPLES AND NUMERICAL EXPERIMENTS

The proposed approach is demonstrated by means of numerical examples where an eight-story building,

shown in figure 2a and described in [16], is analyzed. Initially the design spectrum is calculated based on the Greek seismic code[17], with parameters shown in figure 3. Based on that spectrum and on the dynamic characteristics of the building the seismic forces $F_{q,i}$ for each eigenmode and their combination are calculated and are shown in figure 4. Assuming that the control devices are installed at each floor as shown in figure 2b (cs1) and the maximum capacity is 300kN the scale factor α is calculated to be equal to 0.85. The reduced seismic forces due to control devices and the reduced spectrum by 15% for which the structure will be redesigned are illustrated in figure 5a and 5b, respectively. The structure is redesigned by reducing the stiffness by a factor equal to or lower than the reduction factor of the spectrum. In the example the stiffness matrix was reduced by 15% with respect to the initial stiffness. After redesigning the structure, dynamic time history control analyses for a wide range of earthquakes were performed with acceleration feedback. The earthquakes were scaled so that their spectrum is an envelop of the initial design spectrum. The numerical simulations were performed in Simulink toolbox of Matlab software[18].

The numerical simulation of the control scheme is described in figure 6. The maximum and the root mean square (rms) values from the response of the system subjected to El Centro 1940 are shown in table 1. The rms values were calculated in order to see to what extent the system performs near the maximum values. The earthquake was scaled at 0.23g, in order to have a response spectrum comparable to the design spectrum. From table 1 it is seen that for unsaturated control full compensation of the displacements was achieved. This is due to the fact that for each degree of freedom there exists one control force with unlimited capacity. The acceleration is equal to the external signal and the building is like executing a rigid body motion. The control forces are all the same, with maximum value at 817 kN and rms value at 104 kN, because the mass of each story is the same. For saturated control at 300 kN, the limit value h/300=10 mm was exceeded at the 8th floor, and reduction in acceleration up to three times compared to the uncontrolled one was also observed. The rms values of the control forces range from 113 kN to 180 kN. For saturation at 600 kN the limit value was not exceeded at any floor and further reduction in acceleration could also be observed. The rms control forces of the devices range from 103 kN to 112kN.

In table 2 the results are from the system subjected to the Athens 1999 earthquake signal scaled at 0.35g. For unsaturated control full compensation of the displacements was achieved again. The acceleration is equal to the external signal. The control forces are all the same, with maximum value at 1224 kN and rms value at 107 kN. For saturated control at 300 kN, the limit value h/300=10 mm was exceeded at the 5th, 6th, 7th and 8th floor, but reduction in acceleration could be observed. The rms values of the control forces range from 113 to 180 kN. For saturation at 800 kN the limit value was not exceeded at any floor and further reduction in acceleration could also be observed. The rms control forces of the devices range from 111 kN to 118kN.

The results for the control with five control devices, placed at the locations shown in figure 2c (cs2) subjected to the Athens 1999 earthquake signal scaled at 0.35g, are shown in table 3. In this case from the beginning (unsaturated control) the displacements at the 4th, 5th, 6th,7th and 8th floor exceed the limit value. Thus, it has no meaning to continue with saturation control since the response will be worse. This control scheme (five control devices) is not capable to keep the displacements of the structure under the design limit.

m_i=345.6 t, k_i=9.8 10^5 kN/m
Eigenperiods:
{ 0. 63, 0.21, 0.13, 0.09 0.07,
0.069, 0.063, 0.06 } sec
Eigenfrequencies f_i:
{1.56, 4.63, 7.55, 10.21, 12.52,
14.41, 15.80, 16.66 }sec^{-1}

$F_{d,max}$=300kN

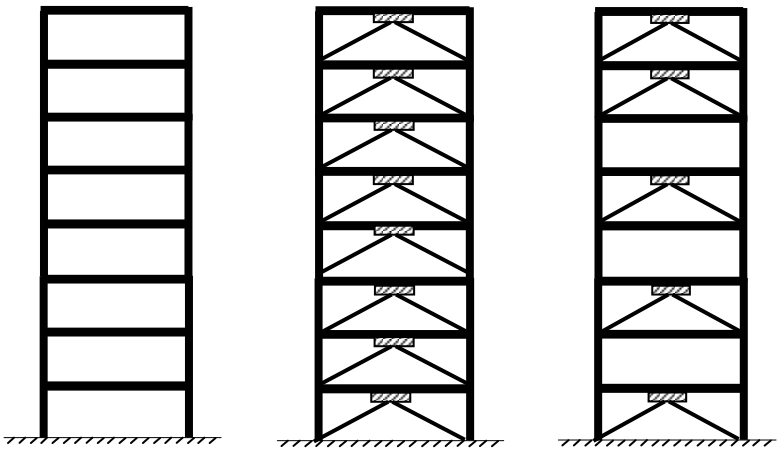

(a) uncontrolled (b) controlled with cs.1 (c) controlled with cs.2

Figure 2. The dynamic characteristic and the control scheme of building

Max ground acceleration (A)=0.24g
Importance factor γ_1=1
Behavior factor q=1
Correction coefficient for damping ≠5%, n=1 for ζ=0.05
Spectrum amplification factor β_o=2.5
Soil category B, T_1=0.15, T_2=0.6,
Foundation coefficient Θ=1

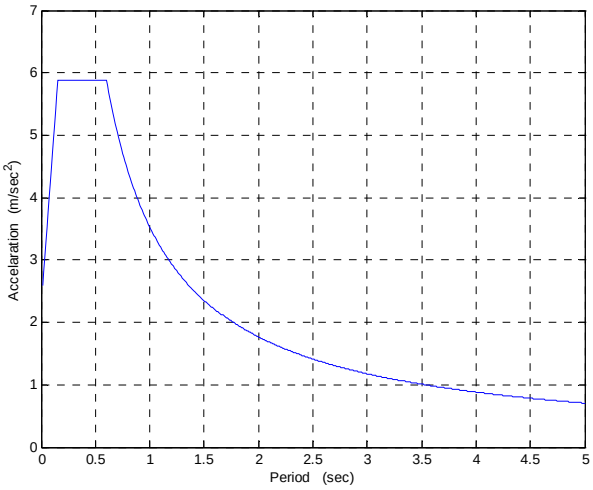

Figure 3. Code parameters and the design spectrum

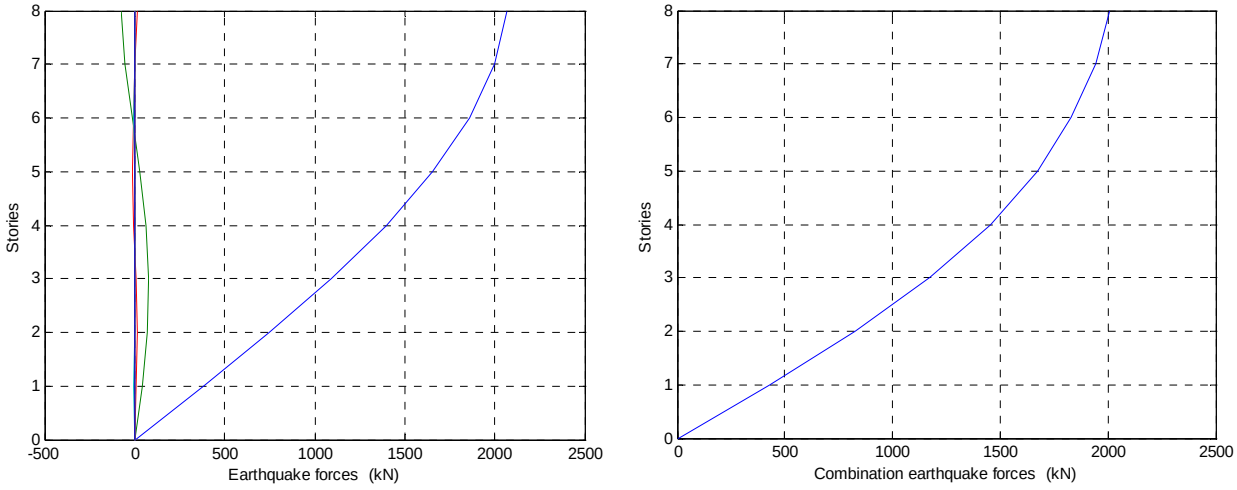

Figure 4. Seismic forces for each eigenmode (a), and their combinations (b)

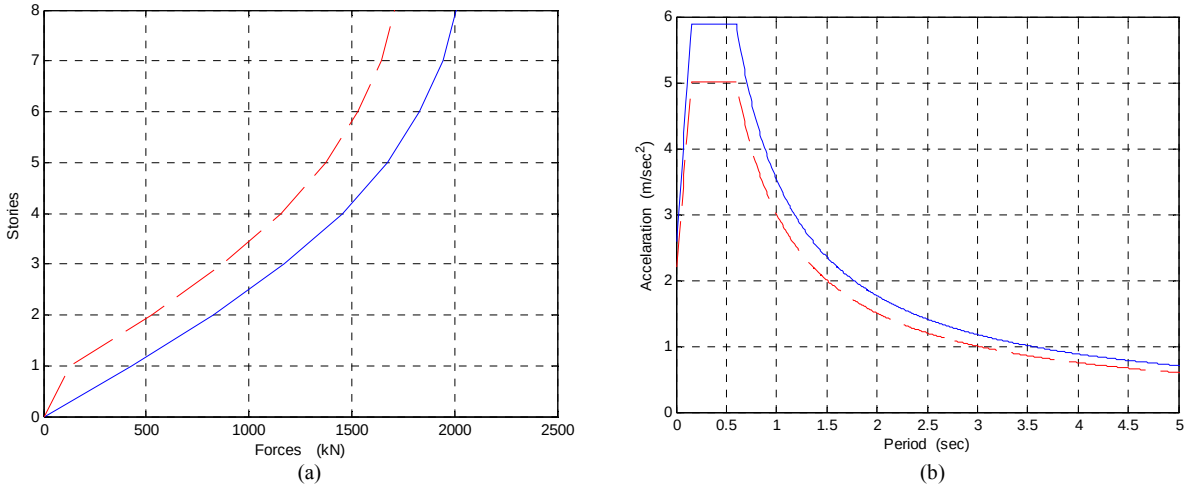

Figure 5. Seismic forces with (dashed line) and without control devices (continuous line) (a) and the design spectrum with and without control devises (b)

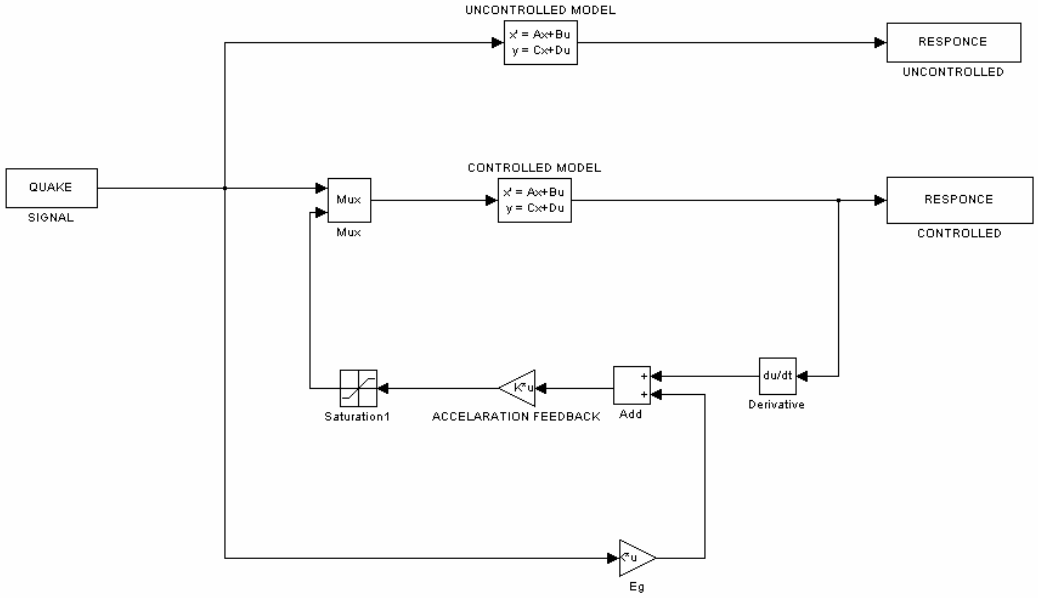

Figure 6. Model and control scheme in Simuling toolbox

			u_1	u_8	$\ddot{u}_1$	$\ddot{u}_8$	F_1	F_2	F_3	F_4	F_5	F_6	F_7	F_8
			(mm)		(m/sec^2)		(kN)							
Controlled	Unsaturated	max	0.00	0.00	2.36	2.36	817	817	817	817	817	817	817	817
		rms	0.00	0.00	0.30	0.30	104	104	104	104	104	104	104	104
	Saturated (300kN)	max	9.00	46.4	3.57	4.77	300	300	300	300	300	300	300	300
		rms	2.09	15.60	0.39	0.95	113	132	145	156	167	174	179	181
	Saturated (600kN)	max	1.10	6.90	2.49	2.99	600	600	600	600	600	600	600	600
		rms	0.52	2.8	0.30	0.33	103	105	107	108	110	111	111	112
Uncontrolled		max	29.50	162.70	3.89	14.73								
		rms	12.60	69.90	1.20	6.05								

Table 1: Response and control forces of the system subjected to El Centro 1940 earthquake

4. SUMMARY AND CONCLUSIONS

A procedure to design a new structure equipped with control devices is proposed. The cost of installation of the control system can be counterbalanced by designing a more economical structure based on a reduced design spectrum. A scale factor α which reduces the design response spectrum is obtained. The numerical results indicate that reduction of the spectrum can be achieved using control devices. The cost of repairing the post earthquake damages of an uncontrolled structure can be considered as a motivation to install a control system which will keep the structure under its yield limit.

			u_1	u_8	$\ddot{u}_1$	$\ddot{u}_8$	F_1	F_2	F_3	F_4	F_5	F_6	F_7	F_8
			(mm)		(m/sec^2)		(kN)							
Controlled	Unsaturated	max	0.00	0.00	3.54	3.54	1224	1224	1224	1224	1224	1224	1224	1224
		rms	0.00	0.00	0.31	0.31	107	107	107	107	107	107	107	107
	Saturated (300kN)	max	12.30	66.30	6.17	10.09	300	300	300	300	300	300	300	300
		rms	3.70	19.40	0.66	1.47	113	133	149	166	182	192	200	201
	Saturated (800kN)	max	2.30	9.90	4.46	5.58	800	800	800	800	800	800	800	800
		rms	0.97	4.20	0.34	0.39	111	110	113	115	114	115	116	118
Uncontrolled		max	22.00	116.30	6.77	13.84								
		rms	7.20	38.70	0.91	3.52								

Table 2: Response and control forces of the system controlled with control devices at every degree of freedom subjected to Athens 1999 earthquake

			u_1	u_8	$\ddot{u}_1$	$\ddot{u}_8$	F_1	F_2	F_3	F_4	F_5	F_6	F_7	F_8
			(mm)		(m/sec^2)		(kN)							
Controlled	Unsaturated	max	3.60	15.00	4.55	5.03	1562		1696		2132		1658	1738
		rms	1.20	6.80	0.44	0.57	153		214		205		193	199
Uncontrolled		max	22.00	116.30	6.77	13.84								
		rms	7.20	38.70	0.91	3.52								

Table 3: Response and control forces of the system controlled with five control devices subjected to Athens 1999 earthquake

If control devices with unlimited capacity are installed at every degree of freedom, then full complete compensation of the displacements can be achieved. But the market devices have a maximum capacity and therefore, saturation control should be considered. The control system is accepted if for the unsaturated control the resulting control forces are lower than the capacity of the control devices. Also, the control system is accepted if the saturated control keeps the structure under the limit values of the design criteria. Such design criteria could be the interstory drift which shouldn't exceed a specific value that causes yielding of the structural member or moments or shears forces higher than the moment and shear capacity of the member. Another design criterion could be that the relative displacements of each story do not exceed a value which would cause serviceability problems.

The control system helps the structure not only to reduce the maximum response (displacements and accelerations), but also to perform at much lower level than the maximum response values. This is proved by comparison of the root mean square (rms) values to the maximum response and control force values.

REFERENCES

[1] Yao JTP. (1972), "Concepts of structural control," Journal of structural engineering ASCE, 98(7), pp.1567-1574.

[2] Housner G.W., Marsi S.F., Chassiakos A.G. (1994), *Proc. 1st World Conf. on Structural Control*, California, 3-5 August 1994, pp.223-235.

[3] Kobori T., Inoue Y., Seto K., Iemura H. Nishitani A. (1998), *Proc. 2nd World Conf. on Structural Control*, Kyoto, Japan June 27-30 1998. Vol. II, pp. 171-188.

[4] Spencer B.F., Dyke S.J., Deoskar H.S. (1997), "Benchmark problem in structural control Part I: Active Mass Driver System," *Proc. ASCE Structures Congress*, Portland 1997.

[5] Spencer, B.F., Dyke, S.J., Deoskar, H.S. (1997), "Benchmark problem in structural control Part II: Active Tendon System," *Proc. ASCE Structures Congress*, Portland 1997.

[6] Yang J.N., (1975), "Application of optimal control theory to civil engineering structures," Journal of Engineering Mechanics Division ASCE, pp.819-838.

[7] Soong T.T., (1990) *Active structural control: Theory and practice,* Longman Scientific &Technical/Wiley London/New York.

[8] Lu J., Skelton R. (1998) "Covariance control using closed-loop modeling for structures" Earthquake Engineering and Structural Dynamics, 27 pp. 1367–1383.

[9] Housner, G. W., Bergman, L. A., Caughey, T. K., Chassiakos, A. G., Claus, R. O., Masri, S. F., Skelton, R. E., Soong, T. T., Spencer, Jr., B. F., and Yao, J. T. P. (1997) "Structural control: Past, present and future" Journal of Engineering Mechanics, 123(9) pp. 897–971.

[10] Renzi E. Serino G. (2004) "Testing and modeling a semi-actively controlled steel frame structure equipped with MR dampers" Structural Control Health Monitoring, 11 pp.189–221.

[11] Kurata N. and Kobori T. (2003), "Reliability of applied semiactive structural control system," Journal of Structural Engineering, 129(7), pp.914-921.

[12] Yang J.N., Wu J.C., Agrawal A.K., Hsu S.Y., (1995), "Sliding mode control of seismically excited linear structures,". Journal of Engineering Mechanics, ASCE; 121, pp.1386-1390.

[13] Cai GP, Huang JZ, Sun F, Wang C. (1997), "Modified sliding mode bang-bang control for seismically excited linear structure," Earthquake Engineering and Structural Dynamic 29, pp.1647-1657.

[14] Lee S.H., Min K.W., Lee Y.C., Chung L. (2004), "Improved design of sliding mode control for civil structures with saturation problem," Earthquake Engineering and Structural Dynamics 33, pp.1147-1164.

[15] Chopra A.K., (1990), *Dynamics of Structures: Theory and Applications to Earthquake Engineering*, Prentice Hall, Upper Saddle River, New Jersey.

[16] Yang J.N., Wu J.C., Agrawal A.K., Hsu S.Y., (1995), "Sliding mode control for non linear and hysteretic structures," Journal of Engineering Mechanics ASCE, 121, pp.1330-1339.

[17] OASP (2000), *Greek seismic design code,*

[18] MATLAB. The Math Works Inc. Natick, Massachusetts, 1994.

DYNAMIC ANALYSIS OF TAPERED COMPOSITE POLES WITH FLEXIBLE CONNECTIONS USING THE FINITE ELEMENT METHOD

Ioannis G. Raftoyiannis*, and Dimos J. Polyzois**

* Laboratory of Metal Structures, Department of Civil Engineering
National Technical University of Athens
9 Iroon Polytechneiou St., Zografou Campus, Athens 15780, Greece
e-mail: rafto@central.ntua.gr

** Department of Civil Engineering, University of Manitoba, Winnipeg, Manitoba, R3T 5V6, Canada

Keywords: FRP poles, filament winding, tapered columns, modal analysis, flexible connections

Abstract. *This paper presents a simple finite element formulation for the dynamic analysis of tapered composite poles with hollow circular cross-section and flexible connections, which are designed for use in power transmission lines. These poles, made from Vinylester reinforced with E-glass fibers, are produced using the filament winding technique. Transmission poles are mainly subjected to cantilever bending, since loading due to the wires and wind gusts is applied laterally. In the present analysis, the poles are modelled with tapered beam elements. It is assumed that the behavior is linearly elastic and the material is orthotropic. Shear effects are accounted for in the analysis because of their significant role. A simple model for flexible connections is established and incorporated into the tapered finite element presented herein. Modal analysis is performed to obtain the natural frequency and period of poles with various geometrical characteristics and material lay-up, as well as the effect of connection flexibility. The analytical results presented in this work are based on typical composite poles produced by filament winding, and are compared to commercially available finite element codes.*

1 INTRODUCTION

Many studies have been conducted on the dynamic behavior of thin-walled sections made from steel as well as composite materials, but only a few on tapered sections [1]. In fact, the vast majority of relative studies are concerned with the static and dynamic behavior of steel members where the material is homogeneous and isotropic. Composite cross-sections are usually thin-walled and the wall is treated in this study as a laminated plate that can be specially orthotropic or generally orthotropic.

Various manufacturers produce on an industrial basis composite structural members with a variety of cross-sectional shapes and dimensions (e.g. I-beams, wide flange I-beams, box-beams, angle-beams, tubes, etc.). These products are made from polymer matrix with fiber reinforcement. Polyester, vinylester or epoxy, are mainly used as a matrix to hold together E-glass, S-glass, aramid or carbon fibers used as reinforcement. Fibers and polymer are joined through a suitable process such as filament winding to form the desired cross section [2].

A scientific project involving construction and testing of FRP poles is under way at the University of Manitoba in Canada. The main goal of this program is to produce FRP poles for power transmission lines as a replacement of poles made of conventional materials. These poles are made of vinylester reinforced with E-glass fibers and are produced by the filament winding technique. The cross-sections of composite poles have hollow circular shape and are thin-walled; thus, the final product is considerably lighter compared to current poles, while requirements regarding stiffness and strength are being preserved. Transmission poles are mainly subjected to cantilever bending since lateral loads due to the wires and wind are applied. Their dynamic behavior, though, is significantly different from that of poles made from conventional materials. The relatively low elasticity modulus of the E-glass-vinylester material results in lower natural frequencies. On the other hand, the pole itself consists from two parts (tapered cylindrical shells) jointed together with resin applied on a reasonable joint length, thus, forming a semi-rigid connection. The presence of such an elastic connection may affect the dynamic behavior of the pole.

In this work, the dynamic characteristics of tapered composite poles with one semi-rigid joint are investigated. A simple finite element formulation for the dynamic analysis of tapered poles with semi-rigid joints is presented. Shear effects are accounted for in the analysis because of their significant role. A modal analysis is carried out for various cases of material properties, cross-sectional dimensions and joint characteristics. The results obtained in this study are compared to numerical results obtained from commercially available finite element codes and correspond to actually produced composite poles via filament winding.

2 MATERIAL PROPERTIES

Composite cross-sections are usually thin-walled and are produced with various cross-sectional dimensions. In the present case, the filament winding technique is employed to produce a tapered pole with circular hollow cross-section. A typical geometry of such a pole is shown in Fig. l. The wall consists of an even number of layers with ±β orientation angle with respect to the longitudinal direction forming an antisymmetric angle-ply laminate. Each layer has a thickness 0.22 mm while a constant volume fraction v_f = 65% applies. The stacking sequence of a 6-layered laminate is also shown in Fig. 1. The properties of the material under study, as computed from information provided by the material suppliers, are E_1 = 48 GPa, E_2 = 13.30 GPa, ν_{12} = 0.235 and G_{12} = 5.17 GPa, where 1 denotes the fiber direction and 2 the transverse direction. Using the classical lamination theory [3], the stiffness components of a generally orthotropic plate can be determined. The constitutive equation for the laminate is

$$\begin{Bmatrix} N_x \\ N_y \\ N_{xy} \end{Bmatrix} = \begin{bmatrix} A_{11} & A_{12} & A_{16} \\ A_{12} & A_{22} & A_{26} \\ A_{16} & A_{26} & A_{66} \end{bmatrix} \begin{Bmatrix} \varepsilon_x \\ \varepsilon_y \\ \gamma_{xy} \end{Bmatrix} \tag{1}$$

where {N} are the membrane forces (also called stress resultants) and { ε } are the corresponding strains. The membrane stiffness coefficients A_{ij} can be determined from the following relation

$$A_{ij} = \int_{-t/2}^{t/2} \overline{Q}_{ij}\, dz \tag{2}$$

where t is the laminate thickness and $\overline{Q}_{ij}$ are the transformed layer stiffness components. The terms $\overline{Q}_{ij}$ for various values of lamination angle β are listed in Table 1. Inverting eqn (1) we obtain

$$\begin{Bmatrix} \varepsilon_x \\ \varepsilon_y \\ \gamma_{xy} \end{Bmatrix} = \begin{bmatrix} a_{11} & a_{12} & a_{16} \\ a_{12} & a_{22} & a_{26} \\ a_{16} & a_{26} & a_{66} \end{bmatrix} \begin{Bmatrix} N_x \\ N_y \\ N_{xy} \end{Bmatrix} \tag{3}$$

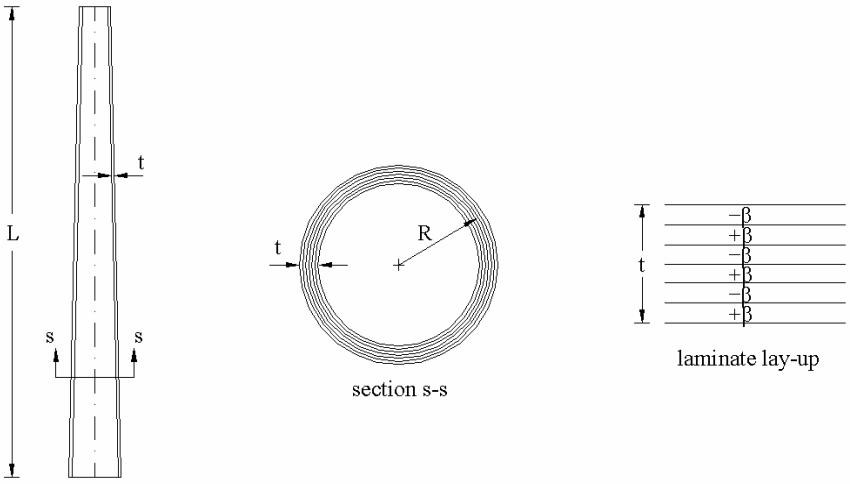

Figure 1. Geometry and lay-up of a tapered composite pole

Notice that although the shear-extension coupling terms A_{16} and A_{26} in eqn (1) vanish in antisymmetric laminates, the term a_{11} in eqn (3) includes the shear effect due to layer stiffness transformation. The terms a_{16} and a_{26} are also zero in this case. The effective longitudinal modulus E_x can be calculated from eqn (3) as

$$E_x = \frac{1}{a_{11} t} \tag{4}$$

It must be noted at this point that the values of E_x obtained from eqn (4) are approximate since bending-extensional coupling exists in antisymmetric laminates. This effect though becomes negligible as the number of layers increases [3] and for 10 or more layered laminates eqn (4) provides accurate values for the effective longitudinal modulus E_x. Since the cross-section is thin-walled, the effective longitudinal modulus E_x can be used for the flexural problem without loss of material characteristics that affect the structural behavior of the member. The values of the effective longitudinal modulus E_x are also listed in Table 1 for various cases of lamination angle ±β.

±β	$\overline{Q}_{11}$	$\overline{Q}_{22}$	$\overline{Q}_{12}$	$\overline{Q}_{66}$	$\overline{Q}_{16}$	$\overline{Q}_{26}$	E_x
0°	48.746	13.507	3.174	5.170	0.000	0.000	48.000
5°	48.213	13.509	3.440	5.436	±3.036	±0.024	47.337
10°	46.653	13.539	4.204	6.200	±5.843	±0.183	45.348
20°	40.985	13.990	6.813	8.808	±9.999	±1.327	37.668
30°	33.332	15.712	9.779	11.775	±11.443	±3.816	27.246
45°	22.320	22.320	11.980	13.976	±8.810	±8.810	15.890

Table 1 : Stiffness components $\overline{Q}_{ij}$ and effective modulus E_x (in GPa) for various lamination angles ±β

3 FINITE ELEMENT FORMULATION

In order to accurately approximate the static and dynamic behavior of the tapered column, a beam finite element is developed for the analysis of tapered members. Consider the tapered element with length L, circular hollow cross-section and uniform thickness t shown in Fig. 2. The radii at the small and the large end are R_1 and R_2, respectively. Since the cross-section is thin-walled, the moment of inertia I can be directly computed as $I=\pi R^3 t$, where the radius R varies linearly over the length L. This implies a cubic variation of the moment of inertia I(x) with respect to the length L. Thus, it is convenient to adopt a coordinate system x-y, see Fig. 2, in which the moment of inertia is expressed as follows:

$$I(x) = I_0 x^3 \tag{5}$$

The shift *a* of the coordinate system origin is defined geometrically since $R_2/R_1 = (L+a)/a$ by:

$$a = \frac{L}{R_2 / R_1 - 1} \tag{6}$$

where, I_0 is a coefficient defined as follows:

$$I_0 = \pi \left(\frac{R_1}{a} \right)^3 t \tag{7}$$

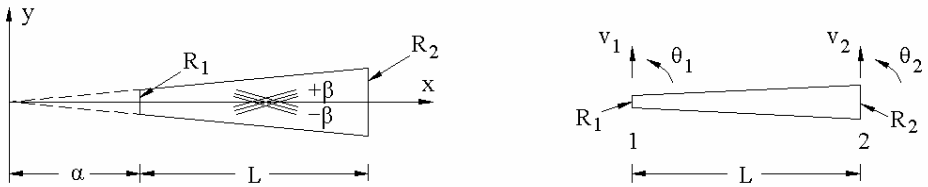

Figure 2. Coordinate system and degrees of freedom of the tapered element

For the bending problem, we will use the shape functions resulting from solution of the static equilibrium equation for bending, which is

$$-\frac{d^2}{dx^2}\left(E_x I(x) \frac{d^2 v}{dx^2} \right) = 0 \tag{8}$$

The general solution of eqn (8) is

$$v(x) = c_1 x + c_2 \ln x + c_3 \frac{1}{x} + c_4 = \{g_f\}^T \{c_f\} \tag{9}$$

where subscript f stands for flexure. The corresponding Vandermode matrix relating coefficients $\{c_f\}$ with the nodal displacements v_i and θ_i (i=1,2) is

$$\{v\} = \begin{Bmatrix} v_1 \\ \theta_1 \\ v_2 \\ \theta_2 \end{Bmatrix} = \begin{bmatrix} a & \ln a & 1/a & 1 \\ 1 & 1/a & -1/a^2 & 0 \\ a+L & \ln(a+L) & 1/(a+L) & 1 \\ 1 & 1/(a+L) & -1/(a+L)^2 & 0 \end{bmatrix} \begin{Bmatrix} c_1 \\ c_2 \\ c_3 \\ c_4 \end{Bmatrix} = [N_f]\{c_f\} \tag{10}$$

Thus, eqn (9) can be written as

$$v(x) = \{g_f\}^T [N_f]^{-1} \{v\} = \{g_f\}^T [B_f] \{v\} \tag{11}$$

from which, by differentiating twice, we directly obtain

$$\frac{d^2v}{dx^2} = \{g_f''\}^T[B_f]\{v\} \tag{12}$$

The strain energy U_f of the element due to bending is

$$U_f = \frac{1}{2}\int_a^{a+L} E_x I(x)\left(\frac{d^2v}{dx^2}\right)^2 dx \tag{13}$$

Substituting eqn (12) into eqn (13) we obtain the element stiffness matrix for bending [4], that is

$$[K_f] = [B_f]^T\left[\int_a^{a+L}\{g_f''\}^T(E_x I_0 x^3)\{g_f''\}dx\right][B_f] = [B_f]^T[k_f][B_f] \tag{14}$$

where

$$[k_f] = EI_0\begin{bmatrix} 0 & 0 & 0 & 0 \\ 0 & \ln(a+L)-\ln a & \dfrac{2}{a+L}-\dfrac{2}{a} & 0 \\ 0 & \dfrac{2}{a+L}-\dfrac{2}{a} & \dfrac{2}{a^2}-\dfrac{2}{(a+L)^2} & 0 \\ 0 & 0 & 0 & 0 \end{bmatrix} \tag{15}$$

The kinetic energy T_f of the element [5] is

$$T_f = \frac{1}{2}\int_a^{a+L}\rho A(x)\left(\frac{dv}{dt}\right)^2 dx \tag{16}$$

and thus, the mass matrix [4] is

$$[M_f] = [B_f]^T\left[\int_a^{a+L}\{g_f\}^T(\rho A_0 x)\{g_f\}dx\right][B_f] = [B_f]^T[m_f][B_f] \tag{17}$$

where the terms of matrix $[m_f]$ are explicitly given as follows

$$\begin{aligned}
m_{f,11} &= \tfrac{1}{4}\rho A_0\{(a+L)^4 - a^4\} \\
m_{f,12} &= \tfrac{1}{9}\rho A_0\{(a+L)^3[3\ln(a+L)-1] - a^3[3\ln a - 1]\} \\
m_{f,13} &= \tfrac{1}{2}\rho A_0\{(a+L)^2 - a^2\} \\
m_{f,14} &= \tfrac{1}{3}\rho A_0\{(a+L)^3 - a^3\} \\
m_{f,22} &= \tfrac{1}{4}\rho A_0\{(a+L)^2[2\ln^2(a+L) - 2\ln(a+L)+1] - a^2[2\ln^2 a - 2\ln a + 1]\} \\
m_{f,23} &= \rho A_0\{(a+L)[\ln(a+L)-1] - a[\ln a - 1]\} \\
m_{f,24} &= \tfrac{1}{4}\rho A_0\{(a+L)^2[2\ln(a+L)-1] - a^2[2\ln a - 1]\} \\
m_{f,33} &= \rho A_0\{\ln(a+L) - \ln a\} \\
m_{f,34} &= \rho A_0 L \\
m_{f,44} &= \tfrac{1}{2}\rho A_0\{(a+L)^2 - a^2\}
\end{aligned} \tag{18}$$

Finally, the equilibrium equation for the tapered element in matrix form can be written as follows

$$[M_f]\{\ddot{\delta}\} + [K_f]\{\delta\} = \{F\} \tag{19}$$

where $\{F\}$ is the nodal force vector and $\{\delta\}$ is the nodal displacement vector, that is

$$\{\delta\}^T = \{v_1 \quad \theta_1 \quad v_2 \quad \theta_2\} \tag{20}$$

4 JOINT FLEXIBILITY MODEL

The transmission pole is constructed by connecting two tapered cylindrical parts using a joint technique that has been developed at the University of Manitoba. The joint is formulated by utilizing an overlapping part of the jointed elements with length ℓ. A thin film with thickness t_j of West System® Epoxy 105 resin with hardener 206 is applied to the interface which, after curing, acts as a glue holding the two parts together. All member forces are transferred through the joint in the form of shear stresses τ acting on the connection surfaces.

In order to model the bending stiffness of the joint, a basic kinematic relation between shear strains γ of the interface resin and joint rotation θ is

$$\delta = t_j\gamma = R_j\theta \tag{21}$$

where R_j is the radius of the interface at the joint position. The infinitesimal force dF due to shear stresses from bending that acts on the joint circumference is given by

$$dF = \tau \ell R_j \cos\varphi \, d\varphi \tag{22}$$

and since the moment arm is $R_j \cos\varphi$, the corresponding moment dM is

$$dM = R_j \cos\varphi \, dF = \tau \ell R_j^2 \cos^2\varphi \, d\varphi \tag{23}$$

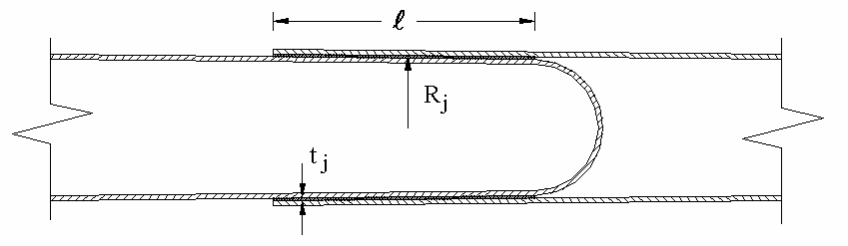

Figure 3. Structural detail at the joint

Figure 4. Joint kinematics and shear stress distribution for bending

Introducing eqn (22) as well as the well-known stress-strain relation $\tau = G\gamma$ (with G being the shear modulus of the applied resin) into eqn (23) and integrating over the circumference, we obtain

$$M = \left(\int_0^{2\pi} G \frac{R_j}{t_j} \ell R_j^2 \cos^2\varphi \, d\varphi \right) \theta \tag{24}$$

where the term in the parenthesis is the rotational spring constant C_f corresponding to the bending stiffness of the joint, that is

$$C_f = G \frac{\pi R_j^3}{t_j} \ell \tag{25}$$

In order to classify the rotational spring constant C_f we introduce the non-dimensional spring stiffness $\overline{C}_f$ as following

$$\overline{C}_f = \frac{C_f}{\frac{E_x \pi R_j^3}{\frac{1}{2} L}} \tag{26}$$

where the denominator in eqn (26) corresponds to the mean bending stiffness of the half-length member.

5 NUMERICAL RESULTS

The tapered beam element developed herein is employed to perform modal analysis of poles with various geometric characteristics. For the cases considered in the analysis, we use material density ρ=1.94 gr/cm^3 and n=50 layers. The total thickness of the column laminate is t=11 mm. The numerical results are first validated through a convergence study. A pole with lamination angle $\beta=\pm10°$, length L=18.0m and taper ratio R_1/R_2 =0.5 is modeled with the tapered element developed herein as well as the classic prismatic beam elements. Moreover, a detailed model of the column is analyzed with 3-D oriented plate elements using the ALGOR finite element program [6]. A rapid convergence is observed for the model with tapered elements, where the fundamental frequency ω=12.064 rad/s is obtained using only three elements with an error of 0.03%, while the convergence is much slower when prismatic elements are employed. The convergence speed is not affected by the ratio R_1/R_2 when the pole is modeled with tapered elements and this is a significant advantage for using the proposed element. The fundamental frequency of the pole modeled with 2400 plate elements is next obtained using ALGOR code and it was found to be ω=12.157 rad/s. The 0.77% difference of ω between the beam and shell models is due to the bending-extension coupling of the antisymmetric laminate that have been ignored in the tapered element formulation. Their effect is proven to be negligible [7].

The natural frequency of the fundamental model is then computed for various cases of the lamination angle β and the taper ratio R_1/R_2 and the results are shown in Fig. 5. The pole under study has total length L=18.0m while the laminate has n=50 layers and total thickness t=11 mm. It is observed that as the taper ratio R_1/R_2 decreases, the fundamental frequency ω increases by almost 9% (see Fig. 5). In addition, the fundamental frequency is directly proportional to the effective modulus E_x and hence, there is a significant drop of the natural frequency for lamination angles greater than 10°. This drop is almost 42% in the case of β=±45°. Given that most of the currently produced poles are constructed with a lamination angle β=±10°, the fundamental period T is expected to be in the range of 0.5-0.6 s. The fundamental frequency is not affected by the thickness t for thin walled sections because the moment of inertia varies linearly with respect to it [see eqn (7)].

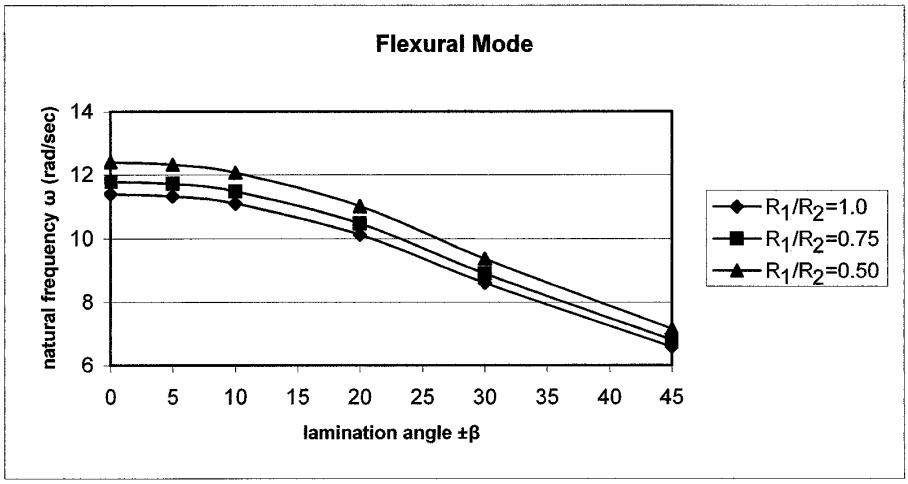

Figure 5. Natural frequency ω for various values of taper ratio R_1/R_2 and lamination angle ±β

Next, the effect of joint flexibility on the dynamic behavior of the pole is studied. A flexible joint is introduced at half-length of the pole and a parametric study is performed for various values of the joint stiffness $\bar{C}_f$. From Fig. 6 one can see the natural frequency of a jointed tapered pole (with R_1/R_2=0.5) for various values of the lamination angle β and the non-dimensional joint stiffness $\bar{C}_f$. It can be easily concluded that for low values of the joint stiffness ($\bar{C}_f \leq 2.0$ that correspond to relatively weak connections) the natural frequency ω reduces with respect to the continuous system (i.e. no jointed pole), while for relatively strong connections ($\bar{C}_f > 5.0$) this reduction is insignificant. Moreover, as the lamination angle β increases the natural frequency ω of the system also decreases (as shown in Fig. 5) and the effect of joint flexibility on the natural frequency ω is limited to almost 50% in the extreme case of ±45°.

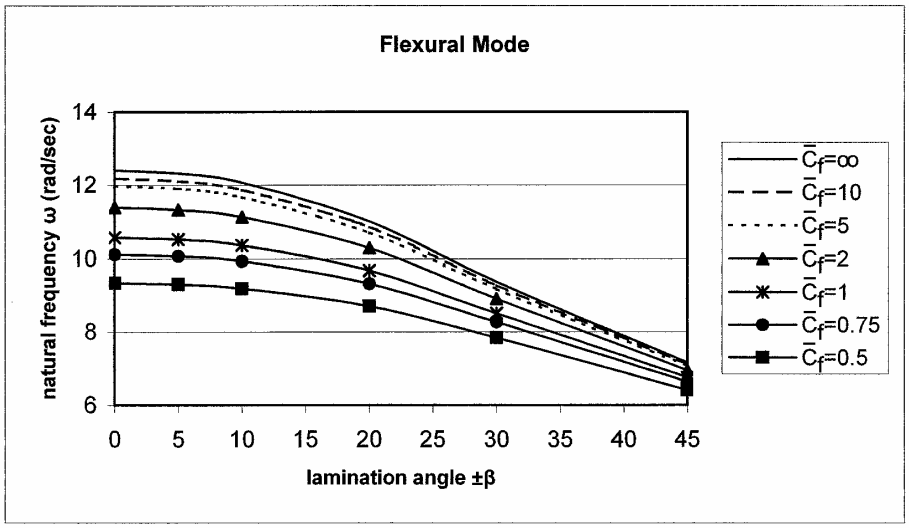

Figure 6. Natural frequency ω for various values of joint stiffness $\bar{C}_f$ and lamination angle ±β

A significant parameter that affects the dynamic behavior of transmission poles is the presence of a cross-arm that is installed at the top to hold the wires as well as possible transformer equipment. These devices are modeled as a concentrated mass M placed at the free end of the pole. A parametric study is performed on the effect of the presence of a mass M at the tip of the column with respect to the mass of the column Mc (=541 kg) (see Fig. 7). In the case of a jointed pole, the fundamental modal shape for flexural vibrations is significantly different than the one corresponding to the continuous system. At the joint position, the continuity of the modal shape function is broken and the slopes of the top and bottom part become different. This effect is more pronounced in the case when a top mass M exists.

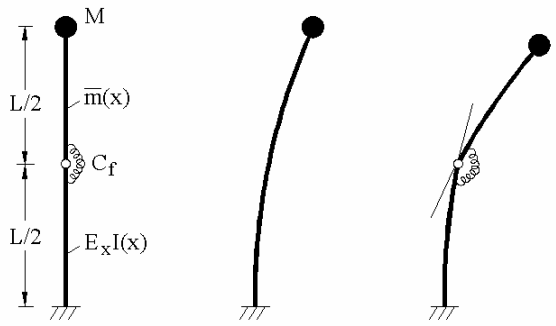

Figure 7. Jointed pole model and fundamental modal shapes for $\overline{C}_f = \infty$ (no joint) and $\overline{C}_f = 1$

The natural frequency and period of the fundamental model of the pole without a joint ($\overline{C}_f = \infty$) is computed for various cases of the mass ratio M/Mc and the results are shown in Fig. 8. It is seen in Fig. 8 that the higher the ratio M/Mc, the lower the fundamental frequency ω. Also, the fundamental frequency in the presence of the top mass M is also proportional to the effective modulus E_x but is greater for small values of the ratio M/Mc. This effect is shown in Fig. 8, where the natural frequency of a pole with $\beta=\pm10°$ and $R_1/R_2=0.5$ is plotted against the ratio M/Mc. One can see the significant reduction of the natural frequency ω due to the presence of the mass Mc at the top of the column.

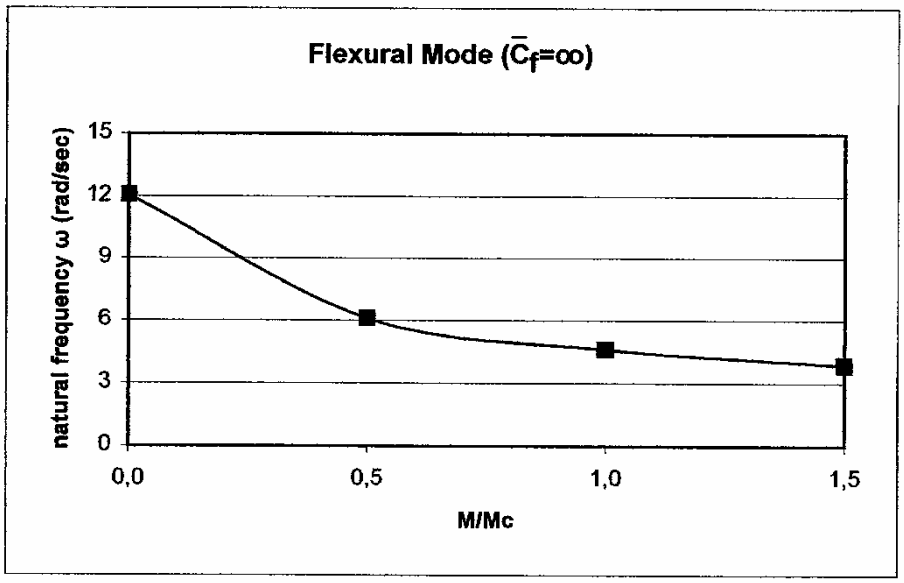

Figure 8. Natural frequency ω of a tapered pole with $R_1/R_2=0.5$, $\overline{C}_f = \infty$ versus mass ratio M/Mc

In Fig. 9, the natural frequency ω of a pole with taper ratio $R_1/R_2=0.5$, lamination angle $\beta=\pm10°$ and various mass ratio M/Mc is plotted for various values of the joint stiffness $\overline{C}_f$. As previously shown (in Fig. 8), the presence of a mass M at the top of the column causes a significant reduction of the natural frequency ω. From the same figure, one can see that for relatively weak connections ($\overline{C}_f \le 2.0$) the natural frequency ω reduces

significantly with respect to the continuous system, while for relatively strong connections ($\bar{C}_f$ > 5.0) the natural frequency ω is negligibly affected.

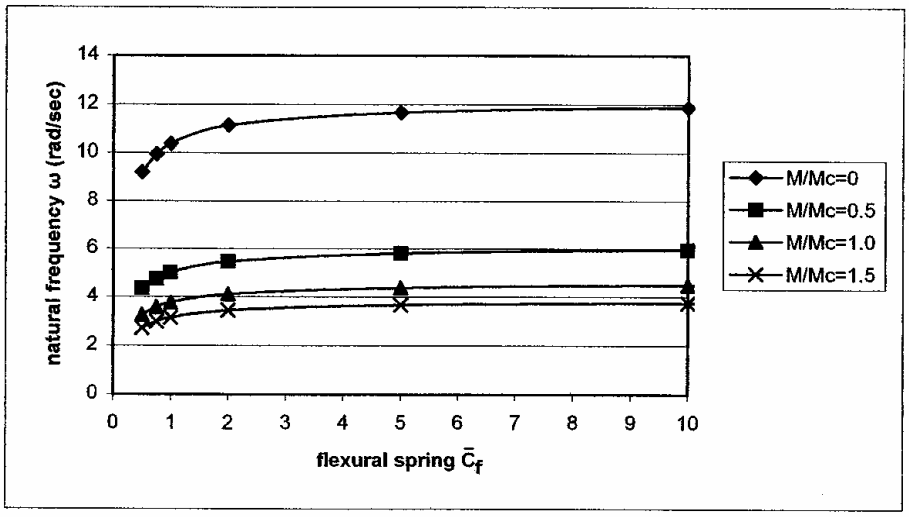

Figure 9. Natural frequency ω for R_1/R_2=0.5, β=±10° and mass ratio M/Mc versus joint stiffness $\bar{C}_f$

6 CONCLUSIONS

The most important conclusions of the present work concerning the dynamic analysis of tapered composite poles with flexible connections can be summarized as follows:

- A simple finite element formulation for the dynamic analysis of tapered composite poles with hollow circular cross-section is presented. The tapered beam presented herein is employed to perform modal analysis of tapered composite poles used in transmission lines.
- A flexible joint model is presented and incorporated into the finite element model. The joint stiffness is affected by the properties of the applied resin, its thickness, as well as the pole diameter at the joint position and the length of the joint. Thus, a joint with suitable stiffness can be formulated.
- The natural frequency of the fundamental flexural vibration mode of the column is computed for various cases of lamination angle, taper ratio, top mass ratio and joint flexibility.
- The joint flexibility affects the dynamic behavior of the pole mainly in the cases of weak connections, while for strong connections this effect becomes insignificant.
- The tapered element presented in this study is valid for a cross-section with any taper ratio as well as cross-section made from conventional materials. It can be easily extended to perform time-history analysis using numerical integration schemes, e.g. Newmark's method.

ACKNOWLEDGEMENTS

The research study reported in this paper was sponsored by ISIS Canada, The Province of Manitoba, and FAROEX Ltd of Gimli, Manitoba.

REFERENCES

[1] Vinson, J.R., and Sierakowski, R.L. (1987), *The behavior of structures composed of composite materials*, Martinus Nijhoff, The Netherlands.

[2] Yuan, R.L., Hasen, Z., Green, A., and Bisarnsin, T. (1991), "Fiber-reinforced plastic composite columns, advanced composite material in civil engineering structures." Eyer SL. Editor, *Proceedings ASCE Specialty Conference*, pp. 205-211.

[3] Tsai, S.W. (1989), *Composites design*, 4th ed., Think Composites, OH.

[4] Warburton, G.B. (1976), *The dynamical behaviour of structures*, Pergamon Press, London.

[5] Timoshenko, S.P., Young, D.H., and Weaver, W. (1974), *Vibration problems in engineering*, 4th ed., McGraw-Hill, New York.

[6] Spyrakos, C.C., and Raftoyiannis, I.G. (1997), *Linear and Nonlinear Finite Element Analysis in Engineering Practice*, Algor Inc. Publ. Div., Pittsburgh, PA.

[7] Polyzois, D., Raftoyiannis, I.G., and Ibrahim, S., (1998), "Finite Elements Method for the Dynamic Analysis of Tapered Composite Poles", *Composite Structures*, vol. 43, pp. 25-34.

INFLUENCE OF EARTHQUAKE-INDUCED POUNDINGS ON THE EFFECTIVENESS OF SEISMIC ISOLATION

Petros I. Komodromos

Department of Civil and Environmental Engineering
University of Cyprus
P.O. BOX 20537, 1678 Nicosia, Cyprus
E-mail: *komodromos@ucy.ac.cy* Web page: *http://www.eng.ucy.ac.cy/petros*

Keywords: seismic isolation, seismic gap, poundings, impact-bumpers.

Abstract. *Seismic isolation introduces flexibility at the isolation level of relatively stiff buildings to avoid resonance with the typical predominant frequencies of earthquakes, in order to reduce the shear forces, interstory deflections, and floor accelerations of a building, and, consequently, prevent damage of its structural and non-structural elements, as well as damage of its contents. However, since the size of the seismic gap, which is provided around a seismically isolated building to facilitate the large relative displacements at the isolation level, is usually finite due to practical limitations, poundings of the building with adjacent structures may occur during strong earthquakes. Therefore, it is important to be aware of how potential poundings of seismically isolated buildings with adjacent structures, due to stronger than expected earthquakes, may affect the effectiveness of seismic isolation. This research work aims to address some aspects of this problem using numerical simulations to investigate how the maximum floor accelerations, story shear forces and interstory deflections of these buildings are affected by poundings and the influence of parameters such as the flexibility of the isolation system, the stiffness and the nonlinearity of the impact, as well as the stiffness of the superstructure.*

1 INTRODUCTION

Although methods of conventional earthquake-resistant design have substantially improved in the last decades, strong earthquakes still result in undesirable damage of buildings and their contents, even in cases of buildings designed according to the most rigorous seismic codes. The latter ensure the required strength and ductility to withstand cycles of inelastic deformations during severe seismic loads, avoiding structural collapse and casualties, but allowing significant structural and non-structural damage as well as damage of the contents of a building. This compromise is unavoidable in high seismicity areas, because it is almost impossible to build a conventionally fixed-supported low- to medium-rise building of reasonable cost to withstand severe seismic loads without inelastic deformations (Fig. 1.a). The fundamental frequencies of such buildings happen to be within the range of the predominant frequencies of common earthquakes, resulting in amplifications of ground accelerations and large interstory deflections (Fig. 1.b). In recent years, there has been an increasing demand to minimize structural and non-structural damage, avoid functionality disruption and protect sensitive and expensive equipment in buildings even under extreme earthquake excitations, which is very difficult to achieve with conventional earthquake-resistant design.

Seismic isolation, an alternative earthquake-resistant design approach [9], [10], [13], [17], introduces flexibility (Fig. 1.c) at the isolation level of relatively stiff buildings to avoid resonance (Fig. 1.b) with predominant frequencies of earthquakes, and, therefore, significantly reduces the induced floor accelerations and the possibility of damaging the contents of the building. Moreover, interstory deflections are considerably reduced due to the almost rigid body motion of the superstructure, since it is relatively very stiff compared to the flexibility of the isolation system, avoiding, or at least minimizing, structural and non-structural damage. The deformations are limited at the isolators, which are specifically designed to withstand several inelastic cycles of deformation and to accommodate the large relative displacements at the isolation level.

However, a practical limitation for the implementation of seismic isolation is the seismic gap (Fig. 1.c) that must be provided around the building to facilitate the expected large relative displacements at the isolation level. Often, there are practical restrictions to the size of the provided seismic gap. Consequently, a reasonable concern is the possibility of poundings of seismically isolated structures with adjacent structures during strong ground motions. Therefore, it is important to investigate that possibility and understand how the maximum floor accelerations and interstory deflections of seismically isolated buildings are affected by the various design parameters and conditions during impacts with adjacent structures.

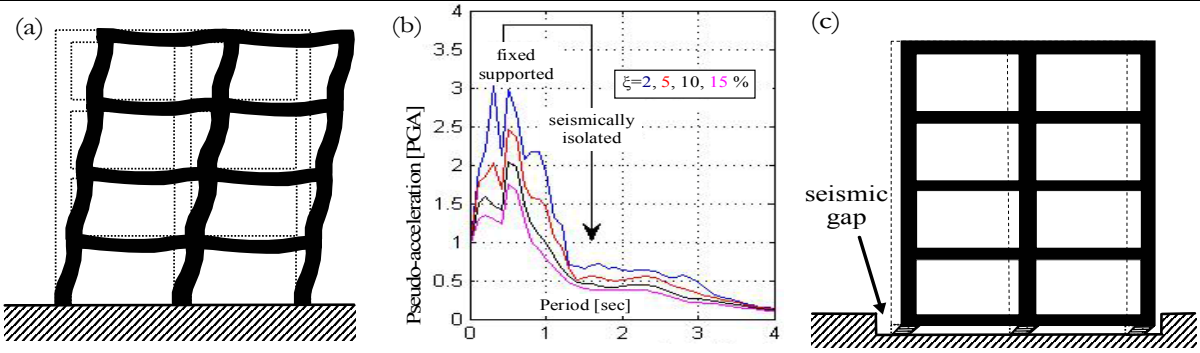

Figure 1. (a) Fixed-supported building (b) response spectrum for El-Centro SE (c) seismically isolated building.

Pounding incidences between fixed-supported buildings during strong earthquakes motivated pertinent research [1], [4], [5], [7], [8], [14], [15], [16], which led to reforms of relevant seismic-code provisions in order to mitigate the risks from poundings of fixed-supported structures. But, limited research studies have been conducted for poundings of seismically isolated buildings [8], [11], [12], [18], which are very flexible and have a sizable seismic gap, although there have been already incidences of seismically isolated structures, such as the Los Angeles FCC building during the 1994 Northridge earthquake [12], that experienced poundings during strong earthquakes.

It is evident that understanding the consequences of potential poundings on the performance of seismically isolated buildings is an important research issue considering that their dynamic characteristics and response are quite different from those of fixed-supported structures. Poundings of seismically isolated buildings happen as a result of large relative displacements at the isolation level, and not due to deformations of the superstructure as in the case of fixed-supported buildings. Furthermore, it is likely to have more rigorous performance requirements and higher expectations for a building that utilizes an innovative earthquake-resistant design approach than for a conventional fixed-supported building. Such demanding requirements for a seismically isolated building, particularly regarding the allowable floor accelerations and story shear forces, may not be satisfied if a stronger than expected earthquake causes poundings.

The goal of this ongoing research work is to investigate how the effectiveness of seismic isolation is affected by poundings that may occur during strong earthquakes using parametric studies. The following section describes the simulation approach and some simplifying assumptions that have been used. Then, a dynamic analysis of a typical seismically isolated 5-floor building under a strong earthquake is used to demonstrate the problem. Next, simulation results are presented for some aspects that have been considered, such as the flexibility of the isolation system, the stiffness and nonlinearity of the impact and the stiffness of the superstructure.

2 SIMULATION APPROACH

The superstructure is modeled as a shear-beam building with lumped masses at the floor levels (Fig 2.a), assuming that it remains elastic during an earthquake excitation, which is a realistic assumption, considering the intention of seismic isolation to avoid inelastic deformations of the superstructure. In this paper the poundings are assumed to happen between the moat wall and the mass at the isolation level, although this is not always the case.

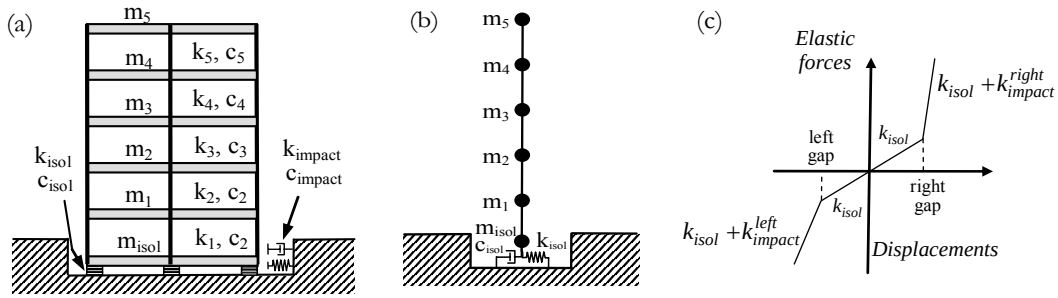

Figure 2. Modeling of a seismically isolated building: (a) building and seismic gap (b) shear beam lumped-mass model (c) bilinear force-displacement relation due to impacts, using linear impact elements.

The inertia, damping and elastic forces depend on total accelerations, relative velocities and relative displacements, respectively. The damping and elastic forces at the isolation level depend on the type and mechanical characteristics of the isolation system, which in this work is modeled using a linearized model with

an effective stiffness, K_{eff} , and damping, C_{eff} .

Nevertheless, when poundings occur, the dynamic response of an isolated building is inherently nonlinear as a result of the sudden applications of impact forces, which correspond to abrupt changes of the stiffness during impacts (Fig 2.c). In this study, a simplified impact model, using equivalent linear contact springs and dashpots, is employed to simulate poundings between a seismically isolated building and the moat wall. A non-linear Hertzian impact spring has also been considered in the last paragraph, where comparisons are made with the linear impact spring and the results that are computed using either of the two models.

The contact spring and dashpot are automatically formed as soon as an impact is detected, kept as long as the building remains in contact with the moat wall and removed as soon as the bodies are detached from each other. The magnitude of the contact forces starts from zero, when the building and the moat wall first come in contact, and increases, either linearly or nonlinearly, as they "interpenetrate" each other up to a maximum value and then start decreasing, and eventually becomes equal to zero when the bodies detach from each other. Some overlapping of the building with the moat wall is allowed, which is justified by local deformability of the wall. Dashpots are used at contact points parallel to the contact springs in order to model the energy dissipated during impact, either in the form of local deformations or stress waves that are dispersed in the surrounding soil.

The governing equations of motion of a seismically isolated building (Fig 2.a), modeled as a shear-beam building (Fig 2.b) with lumped masses and considering potential poundings, have the following general form, where F_I , F_D and F_E are the inertia, damping and elastic forces of the structure, while $F_D{}^C$ and $F_E{}^C$ are the damping and elastic contact forces during impact, respectively:

$$\boxed{\underline{F}_I + \underline{F}_D + \underline{F}_D{}^C + \underline{F}_E + \underline{F}_E{}^C = 0} \tag{1}$$

$$\textit{Inertia forces: } \underline{F}_I = \underline{M}\cdot\ddot{\underline{U}}_{abs} = \underline{M}\cdot\ddot{\underline{U}} + \underline{M}\cdot\underline{1}\cdot\ddot{U}_g(t), \quad \textit{where: } \underline{1} = \begin{bmatrix}1 & \dots & 1\end{bmatrix}^T \tag{2}$$

$$\textit{Damping forces: } = \begin{cases} \underline{F}_D = \underline{C}\cdot\dot{\underline{U}} & \textit{no impact} \\ \underline{F}_D + \underline{F}_D{}^C = \underline{C}\cdot\dot{\underline{U}} + \underline{e}\cdot C_{imp}\cdot\dot{U}_{isol} & \textit{during impact} \end{cases} \tag{3}$$

$$\textit{Elastic forces: } = \begin{cases} \underline{F}_E = \underline{K}\cdot\underline{U} & \textit{no impact} \\ \underline{F}_E + \underline{F}_E{}^C = \underline{K}\cdot\underline{U} + \underline{e}\cdot K_{imp}\cdot(U_{isol} - gap)^p & \textit{during impact} \end{cases} \tag{4}$$

$$\textit{where: } e = \begin{bmatrix}1 & 0 & \dots & 0\end{bmatrix}^T, \quad \underline{C}_{imp} = \underline{e}\cdot C_{imp}, \quad \underline{K}_{imp} = \underline{e}\cdot K_{imp}$$

The contact forces are non-zero whenever the relative displacements at the isolation level exceed the seismic gap leading to poundings with the moat wall, which is assumed to move with the ground during an earthquake. If the impact spring is assumed to be linear, the exponent of the overlap is set to $p = 1.0$, while, for the nonlinear Hertzian impact model it is set to $p = 1.5$.

Using the Central Difference Method [3],[6] for the numerical integration of the equations of motion the displacements at time $(t + \Delta t)$ can be computed from the following equation:

$$\underline{U}(t + \Delta t) = \underline{K}_{eff}^{-1}(t)\cdot\underline{R}_{eff}(t) \tag{5}$$

The effective stiffness $\underline{K}_{eff}$ and load $\underline{R}_{eff}$ are given from equations (6) and (7), without and with impact:

$$\underline{K}_{eff}(t) = \begin{cases} \dfrac{1}{\Delta t^2}\cdot\underline{M} + \dfrac{1}{2\cdot\Delta t}\cdot\underline{C} & \textit{no impact} \\ \dfrac{1}{\Delta t^2}\cdot\underline{M} + \dfrac{1}{2\cdot\Delta t}\cdot(\underline{C} + \underline{C}_{imp})\cdot\dot{\underline{U}} & \textit{during impact} \end{cases} \tag{6}$$

$$\underline{R}_{eff}(t)\begin{cases} = -\underline{M}\cdot\underline{1}\cdot\ddot{\underline{U}}_g(t) - \left(\underline{K} - \dfrac{2}{\Delta t^2}\cdot\underline{M}\right)\cdot\underline{U}(t) - \left(\dfrac{1}{\Delta t^2}\cdot\underline{M} - \dfrac{1}{2\cdot\Delta t}\cdot\underline{C}\right)\cdot\underline{U}(t - \Delta t) & \textit{no impact} \\ = -\underline{M}\cdot\underline{1}\cdot\ddot{\underline{U}}_g(t) - K_{imp}\cdot(U(t) - gap)^p - \left(\underline{K} - \dfrac{2}{\Delta t^2}\cdot\underline{M}\right)\cdot\underline{U}(t) & \\ \qquad - \left(\dfrac{1}{\Delta t^2}\cdot\underline{M} - \dfrac{1}{2\cdot\Delta t}\cdot(\underline{C} + \underline{C}_{imp})\right)\cdot\underline{U}(t - \Delta t) & \textit{during impact} \end{cases} \tag{7}$$

3 EXAMPLE

A 5-story building is considered under the following three different circumstances: (a) as fixed-supported, (b) as seismically isolated without the possibility of impacts, and (c) as seismically isolated with a $0.10\,m$ seismic gap on either side, to illustrate the pounding effects on the response of a seismically isolated building. In particular, the building has 5 floors, each with a $400\ tons$ mass and $1\ GN/m$ stiffness $(T_1 = 0.44\,s)$. In the case of seismically isolated building, it has an additional $500\ tons$ mass at the isolation level and a $30\ MN/m$ effective stiffness $(T_1 = 1.85\,s)$. Rayleigh damping ratio is defined using 5% and 15% damping ratios for the fixed-supported and the seismically isolated buildings, respectively.

A linear impact model is used with impact stiffness equal to $k_{imp}=500\ MN/m$, and damping coefficient $C_{imp}=2\ MN\cdot sec/m$. For each of these three cases, a non-linear dynamic analysis of the building is performed for the El-Centro S00E component scaled to have a $PGA=0.5g$, which is a relatively strong excitation.

Obviously, the maximum relative displacement at the isolation level is reduced when there is a finite seismic gap with size less than the relative displacement at that level. In this case, it is reduced from $U_{max}^{isol} = 155\,mm$, in the no-impact case, to $U_{max}^{isol} = 117\,mm$, in the case of limited seismic gap, which leads to poundings with the moat wall. The excess of the width of the seismic gap by the isolated building is allowed considering the expected deformations of the moat wall. The results confirm that the interstory deflections and, therefore, the story shear forces may significantly increase in the case of a seismically isolated building due to poundings when the seismic gap is exceeded. However, the interstory deflections of a fixed supported building are still much higher than those of the seismically isolated building even when poundings occur.

Comparing the absolute floor accelerations of the building during the same excitation, the influence of poundings in the response of a seismically isolated building are much more pronounced as the peak acceleration at the isolation level (Fig 3.c) is 4 times more than the maximum acceleration at the top floor of the same building without any pounding incidence (Fig 3.b), approaching the magnitude of the top floor acceleration of the fixed-supported building. In addition, due to the poundings at the isolation level the seismically isolated structure may experience maximum floor accelerations at the isolation instead of the top floor of the building. It seems that poundings may change the mode of deformation of a seismically isolated building exciting the higher modes of the building, instead of moving, according to its fundamental mode, as an almost rigid body.

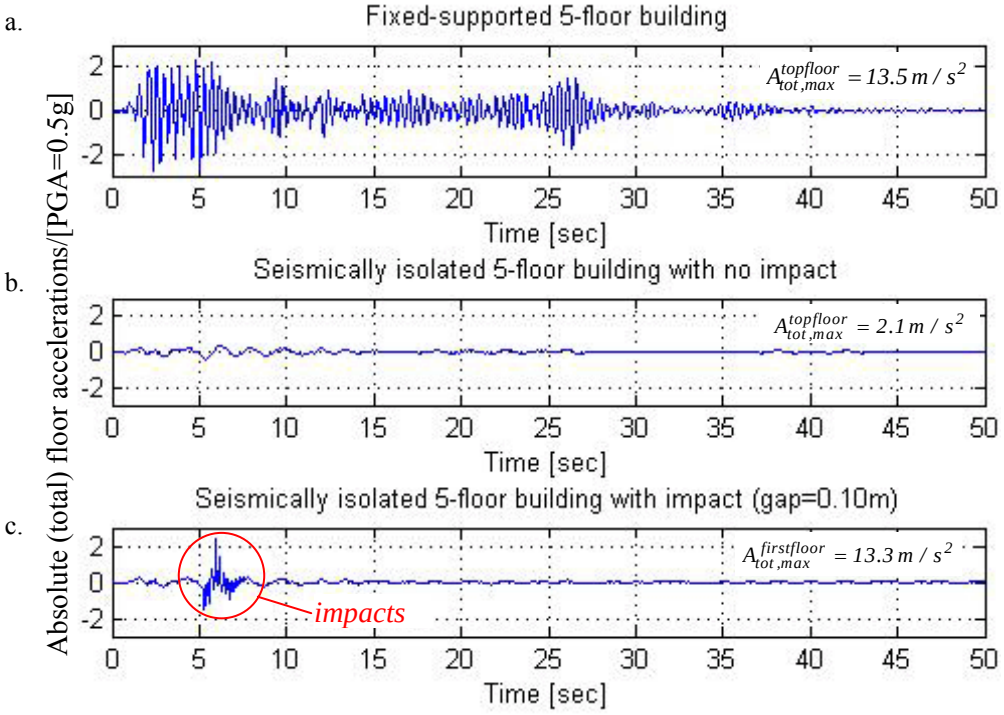

Figure 3. Absolute floor accelerations during the El-Centro S00E scaled to $PGA=0.5g$: (a) top floor of fixed supported building (b) top floor of seismically isolated building without impact (c) isolation-level of seismically isolated building with impact incidences $(gap_{left}=gap_{right}=0.10m)$.

4 PARAMETRIC STUDIES

Based on the above assumptions, specialized software has been developed in order to efficiently perform dynamic simulations of seismically isolated buildings during poundings. The developed software utilizes advances in modern computing and software engineering for rapid object-oriented software development and code reusability. A large number of simulations, of seismically isolated buildings with a variety of characteristics, has been conducted under a range of earthquake excitations in order to systematically investigate the influence of certain parameters and conditions on the maximum floor accelerations, interstory deflections, base shear forces and relative displacements at the isolation level, during poundings.

Simulation results of seismically isolated buildings using single degree of freedom (SDOF) systems with the equivalent stiffness of the isolation system and the total mass of the superstructure are very close to results using more refined models, such as multi degree of freedom (MDOF) systems as long as there are no pounding incidences. This is evident from the response of its fundamental eigenmode and the almost rigid body motion of the superstructure. However, when poundings occur, higher eigenmodes are excited, their contribution can no longer be assumed insignificant, and simulations need to be performed using MDOF systems in order to more accurately capture the consequences of potential impacts. The following paragraphs present results from ongoing research in this area, which concern only few of the many influencing parameters and conditions that should be taken into account and are currently under investigation.

4.1 Effect of the flexibility of the isolation system

The flexibility of the isolation system for a typical 5-story building is varied in order to obtain seismically isolated buildings with fundamental periods in the range from 1.0 to 5.0 seconds. Each of these MDOF systems is simulated for the El-Centro S00E component, scaled to $PGA=0.5g$, considering three different gap sizes: $10\,cm$, $15\,cm$, and ∞, assuming them to be equal on both sides of the building for all three cases. A linear impact model is used, assuming impact stiffness $k_{imp}=500\ MN/m$ and damping coefficient $C_{imp}=2\ MN\cdot sec/m$.

The following graph presents the maximum interstory deflections, maximum absolute floor accelerations and the maximum base shear forces of seismically isolated systems as the flexibility of the isolation system varies, with and without poundings.

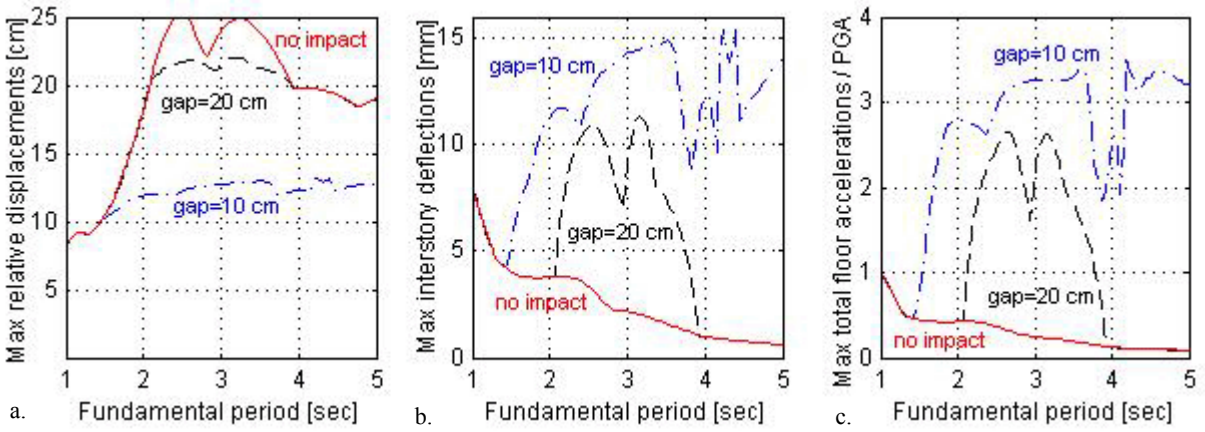

Figure 4. Response of seismically isolated MDOF systems with varying stiffness of the isolation system, with and without impact, for the El-Centro S00E scaled to $PGA=0.5g$.

The interstory deflections and, consequently, the corresponding story shear forces, increase due to poundings. However, they remain relatively low compared to the values of a corresponding fixed-supported building. It is evident that the major consequence of poundings on a seismically isolated building is the substantial increase of the floor accelerations and inertia forces, which can be detrimental for the contents of the building, especially if the latter are sensitive to accelerations. The effect of poundings is more pronounced for seismically isolated buildings with fundamental period in the range of predominant frequencies of the earthquake excitation, where the peak relative displacements occur, which for this specific accelogram is around 3 seconds.

The corresponding fixed-supported building, with a fundamental period of 0.44 *s*, for the same excitation experiences a maximum interstory deflection of 19.7 *mm*, a maximum total acceleration of 13.5 m/s^2 (2.76×PGA), and a maximum base shear force of 19.7 *MN*, which approximates the weight of the structure.

4.2 Effect of the impact stiffness and damping

Considering the 5-story building that has already been defined, the impact stiffness K_{imp} is varied from a small fraction up to 2 times the stiffness of a story of the superstructure. As the impact stiffness varies, the damping coefficient C_{imp} is adjusted in proportion to the square root of the ratio of the change of the impact stiffness according to formulas that express the impact damping coefficient [2] in terms of the impact stiffness. Simulating theses systems for different sizes of the seismic gap, the maximum relative displacements at the isolation level, the maximum total floor accelerations, normalized with the PGA, and the maximum story shear forces, normalized with the total weight, w, of the structure are presented in Fig. 5.

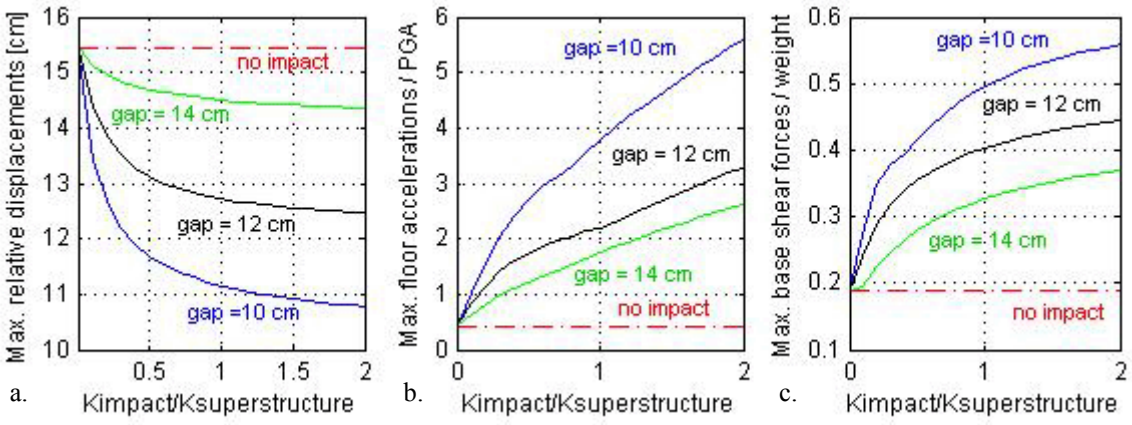

Figure 5. Response of seismically isolated MDOF systems with varying stiffness and damping of the superstructure, for various gap sizes, under the El-Centro S00E scaled to $PGA=0.5g$.

As the impact stiffness increases, the relative displacements at the isolation level (Fig. 5.a) reduce approaching the size of the seismic gap, but at the same time the maximum floor accelerations (Fig. 5.b) and consequently the inertia forces increase substantially due to poundings and may become much higher than what the building would experience without seismic isolation. The maximum interstory deflections and the base shear forces (Fig 5.c) also increase with the impact stiffness, but remain much lower than what a corresponding fixed-supported structure would experience. The substantial increase of the floor accelerations with the impact stiffness indicates that the latter should not be more than a fraction of the stiffness of the superstructure, especially when the contents of the building are very sensitive to large accelerations.

4.3 Effect of the superstructure's stiffness

Varying the stiffness of the superstructure and examining different sizes of the seismic gap, while maintaining other factors constant indicates that by increasing the flexibility of the superstructure the interstory deflections (Fig. 6.a) are significantly increased, the total floor accelerations (Fig. 6.b) are slightly increased, while the story shear forces (Fig. 6.c) are reduced.

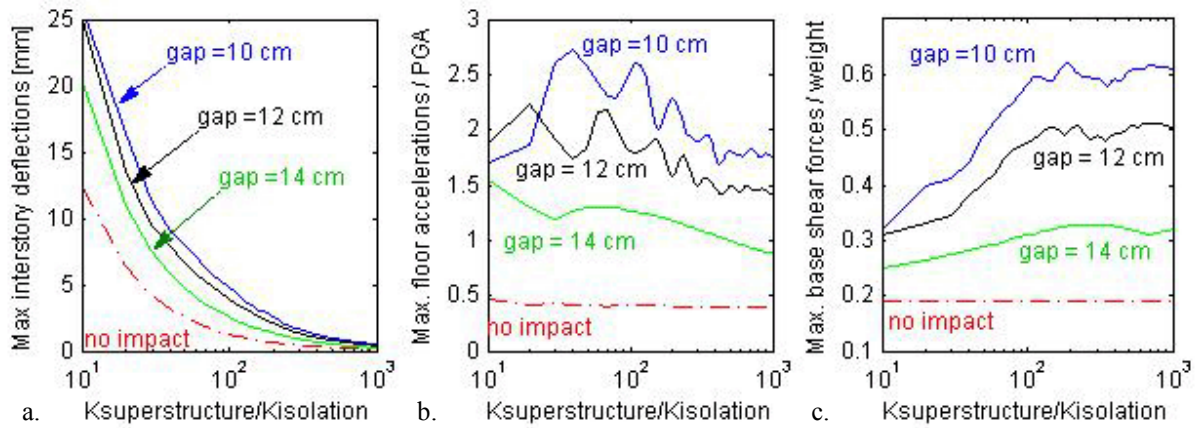

Figure 6. Response of seismically isolated MDOF systems with varying stiffness of the superstructure, for various gap sizes, under the El-Centro S00E scaled to $PGA=0.5g$.

4.4 Effect of the impact nonlinearity

In the previous simulations it has been assumed that the impact spring is linear, i.e. the exponent p in Eq. 7 equals 1.0. However, it has been suggested that a nonlinear contact spring, according to the Hertz theory of impact, i.e. with exponent $p=1.5$, may be more appropriate in simulations of structural poundings. In order to look into the effect of using a nonlinear impact spring to simulate the poundings the 5-story building that has been used as a practical example in the Paragraph 3 is analyzed for the El-Centro S00E component scaled to have two different levels of PGA, $0.4\,g$ and $0.6\,g$, using both a linear and a nonlinear Hertz impact spring (Fig. 6.a).

The stiffness and damping of the nonlinear impact spring is set to $k_{imp}=120\ KN/mm$ and $C_{imp}=3\ MN\cdot sec/m$, while for the linear impact model the $k_{imp}=500\ MN/m$ stiffness and the $C_{imp}=2\ MN\cdot sec/m$ damping coefficient are used. The seismic gap is assumed to be $0.10\,m$ on both sides of the building, which has 5 floors of $400\ tons$ mass and $1\ GN/m$ stiffness each and the isolation has a mass of $500\ tons$ and a $30\ MN/m$ effective stiffness. Rayleigh damping ratio is assumed using 15% damping ratios the minimum and maximum frequencies ω_1 and ω_2.

For the same two levels of PGA, $0.4\,g$ and $0.6\,g$, of the same earthquake excitation, the corresponding fixed-supported building would have $13.9\,mm$ and $20.9\,mm$ maximum interstory deflections, respectively, and $2.76\,PGA$ maximum total floor accelerations.

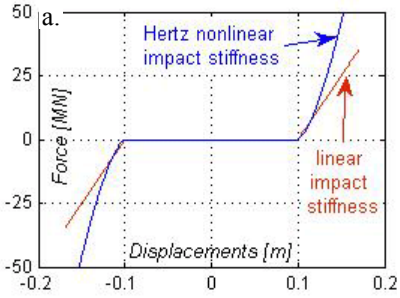

b.

	No impact		Linear impact		Nonlinear impact	
Impact stiffness [KN/mm]	-		500		120	
Impact damping [MN.sec/m]	-		2		3	
PGA [g]:	0.4	0.6	0.4	0.6	0.4	0.6
Max. relative displacements [cm]	12.4	18.6	10.8	12.2	11.0	12.2
Max. interstory deflections [mm]	3	4.5	6.7	13.5	6.4	14.3
Max. floor accelerations [PGA]	0.42	0.42	1.65	2.61	1.46	2.85
Max. inertia force [MN]	0.73	1.10	2.75	6.38	2.29	6.9
Max. elastic force [MN]	3.7	5.56	6.70	13.5	6.37	14.3
Max. impact force [MN]	-	-	4.15	10.9	3.80	12.2

Figure 6. Linear and Hertz nonlinear impact models (a) Displacements vs. impact forces, at the isolation level, with $gap=10\,cm$ (b) peak response for the two systems, under the El-Centro S00E scaled to $PGA=0.5g$.

Considering the uncertainty of various simulation parameters, the results for the two impact models are relatively close, justifying the use of linear impact springs for numerical simulations that aim at qualitative insights on the behavior of seismically isolated buildings during impacts. However, as the exceeding of the seismic gap increases the Hertz impact model seems to be more realistic and conservative, with respect to the impact forces and floor accelerations, than the linear impact model and should be preferred.

In general, the response of a seismically isolated building using the nonlinear impact model exhibits lower floor accelerations and inertia forces for excitations with smaller magnitude, which relatively increase and eventually exceed the corresponding values of the linear impact model as the magnitude of the earthquake increases. This is due to the smoother introduction of the impact forces which increases rapidly with the 1.5 exponent. Even if the beneficial effect of the gradual application of the impact forces is not exactly the case in reality, that can be practically achieved with the attachment of elastomeric material, which can act as shock absorbers, on a seismically isolated building.

5 CONCLUSIONS

The paper discusses the effects of poundings on seismically isolated buildings during strong earthquakes in an effort to gain insight into this complicated problem, considering only some of the many influencing parameters. It is shown that the effectiveness of seismic isolation can be significantly affected, especially when sensitive equipment is housed in a seismically isolated building, due to the substantially increased floor accelerations. In addition, due to poundings other modes of deformations are excited resulting in higher interstory deflections instead of the almost rigid body motion of the superstructure, which is anticipated when using seismic isolation. Understanding the consequences of potential poundings of seismically isolated buildings with adjacent structures is essential in order to rationally take into account the possibility of impact, which realistically should not be excluded, but should be predicted in case the expected earthquake excitation is exceeded.

Numerical simulations demonstrate that poundings may substantially increase floor accelerations, especially as the stiffness of the impact is increased, and, hence, may cause damage to the contents of a seismically isolated building, significantly reducing the effectiveness of seismic isolation. Parametric studies indicate how the effectiveness of seismic isolation is influenced by certain parameters, such as the flexibility of the isolation system, the stiffness and nonlinearity of impact, and the stiffness of the superstructure, when poundings occur during stronger than expected earthquakes. Furthermore, the suitability of the impact model has been briefly discussed, although further research both numerically and experimentally should follow to obtain more realistic models and values for the corresponding parameters. It seems that the most critical consequence is the increase of the floor accelerations, which affects the contents of a seismically isolated building. It seems that the impact stiffness should be limited and preferably kept less than the stiffness of the superstructure, although more research work and validations are necessary to derive definite conclusions for this aspect.

A potential practical measure to alleviate the detrimental effects of poundings could be the installation of flexible material with damping properties, such as elastomeric compounds, that would protrude at certain locations in order to act as collision bumpers. Adding pieces of such material to the moat wall or to the seismically isolated building can work as shock absorbers that smooth the sudden changes of the stiffness during poundings and therefore prevent, to some extent, the acceleration peaks due to impacts. Investigating this possibility is another objective of ongoing research in the area of earthquake-induced poundings of seismically isolated buildings during strong earthquakes.

REFERENCES

[1] Anagnostopoulos A (1988) “Pounding of buildings in series during earthquakes”, Earthquake Engineering and Structural Dynamics, Vol. 16, pp. 443-456.

[2] Anagnostopoulos A (2004) “Equivalent viscous damping for modeling inelastic impacts in earthquake pounding problems”, Earthquake Engineering and Structural Dynamics, Vol. 33, pp. 897-902.

[3] Bathe Klaus-Jurgen (1996) *Finite Element Procedures*, Prentice-Hall Inc., Eaglewood Cliffs, New Jersey.

[4] Chau KT, Wei XX (2001) “Poundings of structures modeled as non-linear impacts of two oscillators”, Earthquake Engineering and Structural Dynamics, Vol. 30, pp. 633-651.

[5] Chau KT, Wei XX Guo X, Shen CY (2003) “Experimental and theoretical simulations of seismic poundings between two adjacent structures”, Earthquake Engineering and Structural Dynamics, Vol. 32, pp. 537-554.

[6] Chopra AK (1995) “*Dynamics of Structures*”, Prentice Hall, pp. 683-702.

[7] Davis RO (1992) “Pounding of buildings modeled by an impact oscillator”, Earthquake Engineering and Structural Dynamics, Vol. 21, pp. 253-274.

[8] Dimova SL (2000) “Numerical problems in modeling of collision in sliding systems subjected to seismic excitations”, Advances in Engineering Software, Vol. 31, pp 467-471.

[9] Kelly JM (1997) *Earthquake Resistant Design with Rubber*, Springer-Verlag, Second Edition.

[10] Komodromos P (2000), “*Seismic Isolation for Earthquake-Resistant Structures*”, WIT Press.

[11] Malhotra PK (1997) “Dynamics of seismic impacts in base-isolated buildings”, Earthquake Engineering and Structural Dynamics, Vol. 26, pp. 797-813.

[12] Nagarajaiah S, Xiaohong S (2001) “Base-Isolated FCC Building: Impact Response in Northridge Earthquake”, Journal of Structural Engineering, ASCE, Vol. 127, No. 9, pp. 1063-1075.

[13] Naeim F, Kelly JM (1999) “Design of Seismic Isolated Structures”, John Wiley & Sons Inc.

[14] Pantelides CP, Ma X (1997) “Linear and nonlinear pounding of structural systems”, Computers and Structures, Vol. 66, No. 1, pp. 79-92.

[15] Papadrakakis M, Apostolopoulou C, Zacharopoulos A, Bitzarakis S, (1996) “Three-dimensional simulation of structural pounding during earthquakes”, Journal of Engineering Mechanics, Vol. 122, No 5, pp. 423-431.

[16] Penzien J (1997) “Evaluation of building separation distance required to prevent pounding during strong earthquakes”, Earthquake Engineering and Structural Dynamics, Vol. 26, pp. 849-858.

[17] Skinner RI, Robinson WH, McVerry GH (1993) “An Introduction to Seismic Isolation”, DSIR Physical Sciences, Wellington, New Zealand, John Wiley & Sons.

[18] Tsai HC (1997) “Dynamic analysis of base-isolated shear beams bumping against stops”, Journal of Earthquake Engineering and Structural Dynamics, Vol. 26, pp. 515-528.

NUMERICAL MODELLING OF STRUCTURAL CONCRETE UNDER IMPACT LOADING

Demetrios M. Cotsovos and Milija N. Pavlović

†Civil Engineering Department, Imperial College, London
email: dkotsovos76@gmail.com

Keywords: finite element nonlinear analysis; impact loading; structural concrete behaviour.

Abstract. The work is concerned with an investigation of the response of structural concrete to high rates of loading. It is based on a finite-element (FE) program capable of carrying out three-dimensional (3D) nonlinear static and dynamic analyses which has been found capable of yielding realistic predictions to the response of plain- and reinforced-concrete structures under arbitrary static and dynamic actions. The FE model incorporates a 3D material model of concrete behaviour which is characterised by both its simplicity and its attention to the actual physical behaviour of concrete in a structure. In the present context of impact loads, the most significant feature of this model is that it is based on the use of static material properties of concrete, in an attempt to elucidate whether or not the effect of loading rate can be attributed primarily to the inertia of the structure's mass and not, as is at present widely considered, to the loading-rate sensitivity of the material properties of concrete. By comparing the ensuing analytical (numerical) results with published experimental data, it is shown that this study validates what constitutes a major departure from current thinking as regards material modelling of concrete under high rates of loading.

1 INTRODUCTION

Over the years a large number of experiments have been carried out on the behaviour of concrete prismatic or cylindrical specimens under high rates of uniaxial compressive loading [5]. The primary objective of such experiments is to investigate the behaviour of concrete under such extreme loading conditions at a material level, since the response exhibited by these specimens during the dynamic tests has been shown to differ from that of their counterparts tested under static conditions. This difference primarily takes the form of an increase in the specimens' load-carrying capacity and maximum sustained axial strain, a difference which becomes more apparent as the loading rate increases. The experimental data obtained from these tests are usually processed in order to derive laws which are incorporated into already existing material models aiming to enhance them by making them sensitive to the rate of loading in an effort to enable them to describe the behaviour of concrete under high loading rates. The majority of these models are then incorporated into various finite-element (FE) packages (e.g. LS-DYNA, ABAQUS, ADINA, etc) aiming at predicting accurately the behaviour of reinforced-concrete (RC) structures under extreme loading conditions such as those encountered in impact and explosion situations.

The formulations of such material models has been based on a variety of theories, including plasticity[15, 21], viscoplasticity[2, 3, 8, 9, 22], continuum damage mechanics[4, 10, 11, 14] or a combination of these theories [6, 7]. Models such as these are referred to as phenomenological since they are based on theories capable of providing a close fit to experimental information without taking into consideration the causes of the observed material behaviour. Regardless of the theory upon which their formulation is based, these models share a number of fundamental assumptions, the validity of which is inherently questioned in the present work: strain softening, stress-path dependency and loading-rate sensitivity are the most common among such assumptions.

The present work follows the opposite approach: it employs the FE model to reproduce the experimental data and, in so doing, also aims to provide a fundamental explanation for the sudden increase in concrete strength and the overall change in the specimen behaviour as a limiting value of loading rate is exceeded. The work is based on a nonlinear FE program, which incorporates a three-dimensional (3D) brittle material model of concrete behaviour and has been shown to be capable of yielding realistic predictions of the response of a wide range of RC structures under static monotonically-increasing loads [12], as well as static load reversals and earthquake loading [5]. The material model presently adopted for describing the behaviour of concrete is fully defined by one parameter only: the uniaxial compressive strength f_c; moreover, it does not account for strain softening, stress-path dependency or loading-rate sensitivity, but places special emphasis on the response of concrete to multiaxial (i.e. triaxial) stress conditions. The aim of the numerical investigation is to demonstrate the reliability of the proposed FE model in realistically predicting the behaviour of structural concrete under extreme loading conditions, such as those encountered during impact and explosion problems, despite its reliance on purely static material properties. This is achieved by comparing the results obtained from the numerical investigation with available experimental data. Such a comparative study allows for the validation of the assumptions upon which the FE model's formulation is based and provides a simple explanation as to the causes of loading-rate effects in high-impact problems.

2 EXPERIMENTAL BACKGROUND

The results obtained from experiments[5] investigating the behaviour of prismatic and cylindrical concrete specimens under high rates of uniaxial compressive loading, presented graphically in figure 1a, clearly indicate that the increase of the loading rate beyond certain levels leads to a substantial increase in the specimen strength. Furthermore, the majority of experimental data depicted in figures 1b and 1c suggest that the maximum axial strain exhibited prior to failure and the axial stiffness of the specimen are also characterized by a significant increase with respect to their counterparts under static loading. However, while it is evident that the concrete specimens under high-rate loading differ significantly from those under static loading, what the experimental data cannot provide are the reasons for these differences.

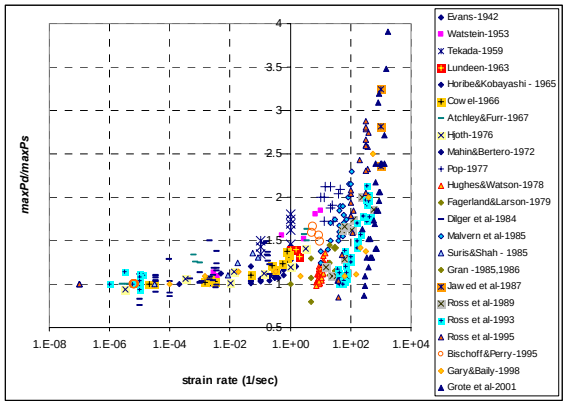

(a)

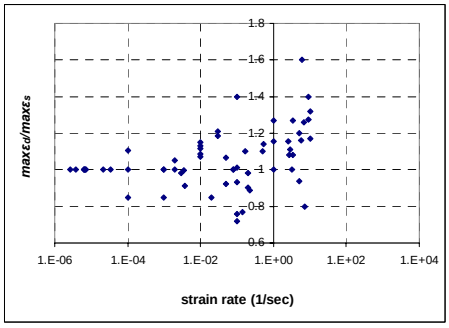

(b)

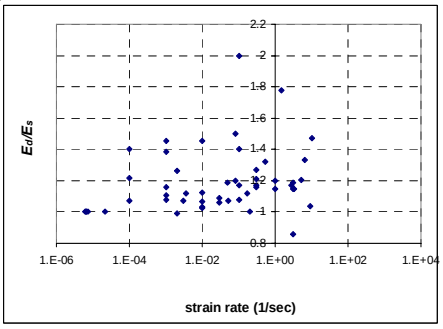

(c)

Figure 1. (a) Variation of load-carrying capacity with strain rate for concrete in uniaxial compression ($maxP_d$=load carrying capacity, $maxP_s$=load-carrying capacity under static loading). (b) Variation of maximum exhibited strain with strain rate for concrete in uniaxial compression (max ε_d = maximum strain, max ε_s = maximum strain under static loading). (c) Variation of specimen axial stiffness with strain rate for concrete in uniaxial compression (E_d= specimen axial stiffness, E_s= specimen axial stiffness under static loading).

By inspecting the experimental data it is clear that they are characterised by considerable scatter and, therefore, it is extremely difficult to derive a law able to describe realistically the change in the specimen strength and its overall behaviour under high rates of loading. Furthermore, the existence of a number of parameters (such as the experimental technique adopted for the tests, the shape, size and moisture content of the specimens, the different types of concrete used, etc), which vary from experiment to experiment, and the absence of laws able to quantify accurately their individual effect on the specimen behaviour add to the uncertainty and difficulty in interpreting the experimental data. Additionally, the difficulty inherent in dynamic tests (in the sense of being able to obtain accurate and meaningful measurements) due to their extremely short duration, combined with the fact that many of these tests were performed before the 1980's when the equipment used was not as advanced as that in use today, are also significant factors which undermine the validity of the data obtained from these tests. Therefore, it is clear that the experimental data can only describe the effect of the loading rate on the specimens' behaviour qualitatively.

3 MODELLING OF CONCRETE BEHAVIOUR

The presently-adopted hypothesis that the material properties of concrete are independent of the rate of loading contrasts with the vast majority of existing constitutive models used for describing the behaviour of concrete under high rates of loading which are based on the assumption that there is a link between the material properties of concrete and the rate at which the loading is imposed ("loading-rate sensitivity"). However, loading-rate sensitivity is based on an uncritical interpretation of the available experimental data, the validity of which is questioned in the present work. By assuming that the material properties of concrete are independent of the loading rate, the effect of the latter on the specimen behaviour is primarily attributed to the inertia effect of the specimen mass: such a simple (and, arguably, obvious – though, at present, unorthodox) postulate will be tested in order to ascertain whether or not it is capable of reproducing the experimental data available from past tests. If correct, the use of such an assumption will then allow the numerical investigation to assess the importance and significance of the role that inertia plays in the specimen's response when subjected to high rates of loading.

Based on available experimental data[12, 24] it is clear that the descending branch does not describe material behaviour but is the result of interaction between specimen and testing device. This implies that concrete is

essentially a brittle material, a view which has recently gained wide acceptance among material specialists – as evidenced in the findings of the report by the relevant RILEM technical committee[23] – but has failed to be implemented by the majority of FE analysts working in the field of nonlinear modelling of concrete. Furthermore, the experimental data (upon which the analytical formulation of all concrete constitutive models, published to date, is based) is characterized by a significant scatter (even when using valid experimental data, this scatter is still substantial): experimental results[12] reveal that any stress-path dependency in concrete behaviour disappears within this scatter of the experimental results. Hence, any effect attributed to stress-path dependency cannot be quantified and it is both realistic and, for practical purposes, accurate to consider that concrete behaviour is stress-path independent.

In view of the above, the present work adopts a material model for concrete which is brittle and independent of both stress-path and loading-rate effects. Its formulation was derived from an analysis of experimental data, the validity of which was verified during an international cooperative project investigating the effect of testing techniques on concrete behaviour under triaxial stress conditions[12]. The brittle nature of the model bypasses the need to introduce extra material parameters associated with the strain-softening assumption. Self-evidently, stress-path and loading-rate independency also result in a radical simplification to many of the material models used hitherto. Thus, the proposed concrete model offers considerable advantages in FE analysis in general and dynamic analysis in particular.

4 NONLINEAR FE SOLUTION PROCEDURE

The FE package adopted in this work was initially restricted to monotonically increasing loading[12] but has recently been expanded so as to encompass cyclic (static) and also generalized dynamic loadings such as those encountered in earthquake and impact problems[5]. In the latter problem types, the inertia of the mass is assumed to have a significant effect on the specimens' overall response, as is evident by the governing equation of motion. Due to the nonlinear behaviour of concrete, this equation is solved numerically through the implicit Newmark integration scheme, with the unconditionally stable average acceleration method[1] being adopted throughout.

The proposed FE package uses 3D nonlinear analysis, employing a 3D material model to account for the triaxial behaviour of concrete and 27-node Lagrangian isoparametric brick elements for the modelling of the concrete medium. The adoption of 3D analysis is dictated by the need to identify and quantify the complex stress field as the imposed load is increased, the allowance of unavoidable triaxiality prior to local failure (i.e. cracking) being reached, and the introduction of non-homogeneity and stress redistribution after cracking is imposed[12]. Additionally, 3D analysis also permits full allowance for the effect of inertia since it enables the more precise modelling of the specimen's mass and its effect on the overall response of the specimen in general as well as on the area surrounding a crack (or a group of cracks) within the concrete medium in particular. The nonlinear analysis is based on an iterative procedure, known as the modified Newton-Raphson method[12] which is used in order to calculate stresses, strains and the residual forces.

5 STRUCTURAL FORM INVESTIGATED

The structural form which provides the basis of this investigation is a concrete prism, similar to the concrete specimens used in various experimental investigations carried out to date on this subject[5]. The prism is assumed to be fixed at its bottom face, and to be subjected to an axial load applied at its upper face through a rigid element with the same cross-section (see figure 2) in order for the external load to be distributed uniformly on the upper face of the concrete prism. It is assumed that concrete and the rigid element on the top are fully bonded at their interface. The prism height is 253mm and its cross-section forms a square with a side of 100mm, whereas the rigid element has a height of 200mm. The uniaxial compressive strength of concrete f_c is assumed to be 30 MPa (a fairly typical value in practice).

In order to explain the behaviour exhibited by the concrete specimen, the dynamic problem must be viewed as a wave-propagation problem. By applying the external load on the upper area of the specimen, the stress wave created is transferred initially from the area where the external load is imposed towards the lower part of the specimen. Because the latter is fixed at the bottom, the stress wave bounces off its bottom surface and moves back upwards. Once the stress wave reaches the top of the specimen, it bounces back down again. The wave is therefore trapped by the boundary conditions imposed on the specimen and moves from top to bottom and vice versa.

6 FE MODELLING OF DYNAMIC PROBLEM

Both the concrete prism and the rigid element (figure 2) are modelled by using the 27-node Lagrangian brick element[1]. Meshes consisting of 3x1x1 and 1x1x1 elements are adopted in order to model the concrete prism and the rigid element respectively (see figures 2a and 2b depicting possible models described below). The use of a sparse FE mesh contrasts with what other investigators have used previously. Usually, a dense FE mesh is preferred in order to model the concrete specimen with several investigations adopting FE's as small as 2-3mm [11, 13, 18, 19, 20, 21]. However, the philosophy upon which the FE model adopted in the present work is based is different and does not employ small FE's [12]. This is because the material model now adopted is based on data obtained from experiments in which concrete cylindrical specimens (subjected to various triaxial loading

conditions) constituted a "material unit" for which average material properties were obtained: thus, the volume of these specimens provides a guideline to the order-of-magnitude of the size of the FE which should be used for the modelling of the concrete structures (in the present instance the structure is a prism specimen). Furthermore, each Gauss point within an FE should correspond to a volume having a size which must be at least 3 times the size of the largest aggregate used in the concrete mix in order to provide a realistic representation of concrete rather than a description of its constituent materials.

The mass of the specimen is modelled as concentrated masses either located on the FE nodes situated along the longitudinal axis of symmetry of the specimen (model A) or distributed to all FE nodes (model B). In the case of model A (case study 1), only mass displacement in the direction of the applied load (i.e. along the axis of symmetry) is allowed and hence it is sufficient to analyse only one quarter of the specimen (see Figure 2). In the case of model B (case study 2), the mass is allowed all three degrees-of-freedom of the nodes and, hence, in order to avoid wave deflection problems on the boundaries of the prism, the whole structure is analysed (see Figure 2). On the other hand, the external load is imposed as a force incrementally at the beginning of each time step. In order to vary the rate of loading, the load increments are kept constant and the time step is varied.

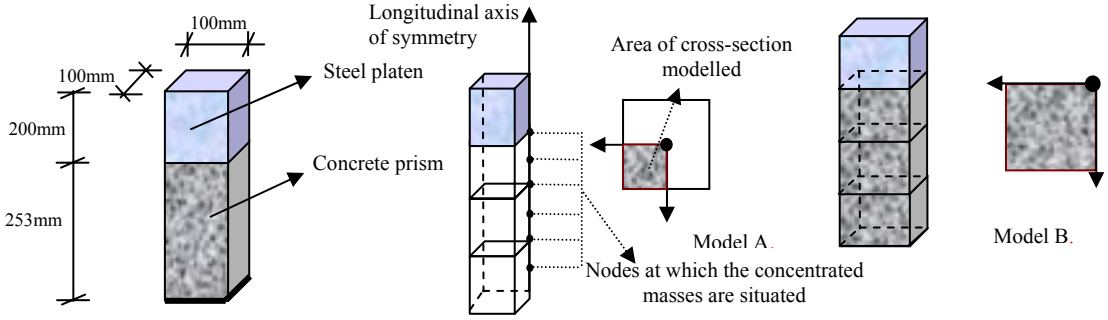

Figure 2. The specimen used for the investigation and FE models of the concrete prism under investigation: (a) Model A; (b) Model B.

At this point, it is important to stress that there is considerable confusion in the literature regarding the way the loading is applied and described, and also how it is measured. For this reason, several possibilities are investigated. To remove any uncertainty, their definitions are as follows:

1. Average strain rate: calculated as the average rate of displacement exhibited by the very top of the specimen divided by the length of the whole specimen.
2. Maximum value of average strain rate: calculated by dividing the specimen into zones by using the nodes along the axis of symmetry and by evaluating which one of these zones exhibits the largest average strain rate.
3. Mid-height strain rate: evaluated at the mid-height region of the specimen.
4. Applied stress rate: defined as the load increment applied in each time step divided by the cross-sectional area of the specimen and the length of the time step used.

7 NUMERICAL PREDICTIONS

A comparison of the numerical results of case studies 1 and 2 reveals significant differences between the two FE models for the concrete prism. The results in figure 3 show that, for stress rates up to about 100,000 MPa/sec, the predictions obtained from the two case studies are similar; however, differences in these predictions begin to occur for stress rates over around 200,000 MPa/sec. In particular, the results obtained from case study 2, which adopts model B for the modelling of the specimen, predict a higher increase in the specimens' load-carrying capacity compared to that predicted by case study 1 (which adopts model A). Moreover, the data in figure 3 reveal that case study 2 predicts an increase of the maximum value of axial strain in the specimen prior to failure ($max\varepsilon_d$) for stress rates above approximately 200,000 MPa/sec, whereas case study 1 predicts that this value remains constant, being practically unaffected by the rate of loading. Such differences in the predictions of case studies 1 and 2 increase as the rate of loading becomes higher. Up to about 100,000 MPa/sec, both models seem to predict approximately the same behaviour. However, as the applied stress rate increases above 200,000 MPa/sec, the response predicted by the two case studies begins to differ, with the specimen in study case 2 exhibiting larger load-carrying capacities and larger axial deformations prior to failure than its counterpart in case study 1 for the same rate of loading.

Based on the predictions obtained from the numerical investigation, it can be concluded that inertia has a significant effect on the specimen behaviour under high rates of loading. However, it is interesting to note the very considerable effect of the modelling of the specimen's mass, as evidenced by the different results stemming from the two case studies (1 and 2). It will be recalled that, in case study 1, the specimen mass was lumped at the mesh nodes situated on the longitudinal axis of symmetry and was allowed one degree of freedom in this longitudinal direction (model A). On the other hand, in case study 2, the mass was equally distributed at all the mesh nodes and was allowed three degrees of freedom (model B). Clearly, the effect of inertia in the lateral

direction has a significant effect on the predicted behaviour of the prisms, especially during the final stages of the loading procedure (i.e. prior to failure). Evidently, case study 2 allows for a more precise modelling of the problem since it is able to account for the effect of inertia in both axial and lateral directions, as well as providing a more refined discretized version of the actual (i.e. continuously distributed) mass of the specimen.

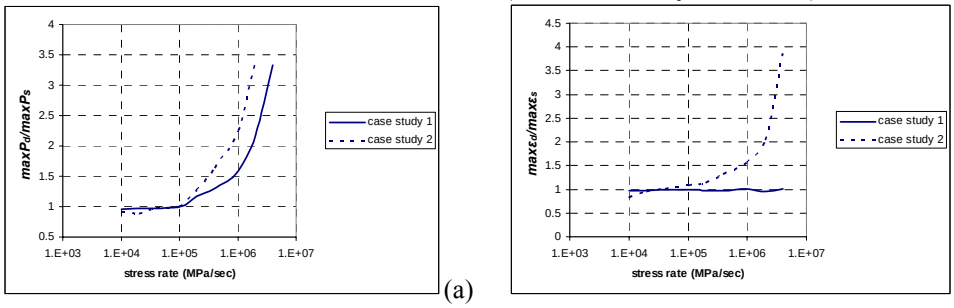

(a) (b)

Figure 3. (a) Variation of load-carrying capacity ($maxP_d$), normalized with respect to its value under static loading ($maxP_s$), with applied stress rate for case studies 1 and 2. (b) Variation of maximum axial strain exhibited by the specimen ($max\varepsilon_d$), normalized with respect to its value under static loading ($max\varepsilon_s$), with applied stress rate for case studies 1 and 2.

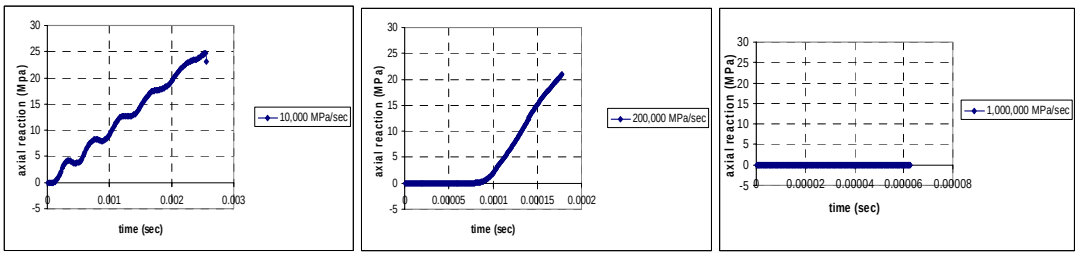

Figure 4. Variation of the axial reaction recorded at the bottom of the specimen with time.

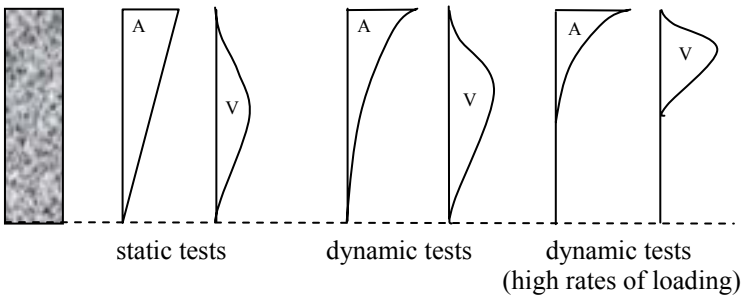

Figure 5. Qualitative distribution of axial displacement (A) and lateral displacement (V) exhibited prior to failure of the specimen along the longitudinal axis.

An interesting observation emerges from the numerical results by reference to the values of the reactions at the bottom of the prism. Thus, for high rates of loading, where the duration of the loading procedure is less than 0.0001 sec (which corresponds approximately to the estimate for the time needed for the stress wave to travel from the top to the bottom of the specimen), the numerical results obtained from case study 2 (presented in figure 4) reveal that the failure of the concrete prism precedes the development of substantial reactions since the stress wave is unable to reach the bottom of the specimen within the time over which the loading procedure lasts. Therefore, it is realistic to assume that, in such cases, the external load does not affect the whole specimen but only a part of it extending to a level which the stress wave is able to reach in the time that the loading procedure lasts. Based on this, it is possible to conclude that higher concentrations of stresses (and strains) develop in the upper part of the specimen whereas, in the bottom part, these concentrations of stresses and strains are much lower. On the other hand, for low rates of loading, where the duration of the loading procedure exceeds 0.0001 sec, the stress wave reaches the bottom of the specimen, bounces off it and starts to travel backwards and forwards along the length of the specimen, trapped by the imposed boundary conditions. Because of this, the stress wave affects the whole of the concrete specimen, adding to the complexity of the stress field which develops within it (except, of course, for static or quasi-static loadings). In such cases, it is difficult to predict where the highest concentrations of stresses (and strains) will develop because of the continuous travelling of the stress wave which causes the internal stress field within the concrete prism to constantly change.

Further analysis of the numerical data obtained from case study 2 indicates that, as the rate of loading increases (over the value of 200,000 MPa/sec), the displacements (both axial and lateral) of the nodes close to the bottom of the specimen gradually decrease. In the case of very high rates of loading, these displacements become very small (even negligible) compared with the displacements exhibited within the upper part of the specimen. It appears, therefore, that the numerical results indicate that the upper part of the specimen deforms far more than its lower part when subjected to high rates of compressive loading, as shown qualitatively in figure 5.

8 VALIDATION OF NUMERICAL PREDICTIONS

In order to establish the validity and accuracy of the predictions obtained from the proposed FE model, the results from case studies 1 and 2 are now compared with published experimental data. Such a comparison reveals good agreement between the two (see figures 6 a to d). However, the scatter that characterises the experimental data does not allow the immediate identification of which of the two case studies provides the closer fit to the experimental data. Both case studies yield results well within the scatter. However, if one accepts that, at high loading rates, the apparent strength of the specimen increases sharply, then it is quite evident from figures 6a to 6d that case study 1 yields a poorer model (as expected) since it does not mimic the sharp strain increase of most experiments (while agreeing with some of the data (likely to be less accurate) which records either no strain increase or even a strain decrease in this range). For extremely high rates of loading, there appears to be some divergence between numerical and experimental data. This divergence may be partly due to the fact that the numerical investigation is carried out by using a specimen with specific dimensions, f_c and method of loading, characteristics which vary in different experimental investigations. However, this deviation is only clearly observed in figure 6a which shows the variation of $maxP_d/maxP_s$ with the applied strain rate, whereas in figures 6b to 6d this deviation is not apparent.

When comparing numerical and experimental results it is important to keep in mind that a high-rate loading test has an extremely short duration, so that it is difficult to obtain accurate measurements. This is particularly relevant for the case of the impact loading tests that were carried out from the early 1940's to the 1980's, which may not have been as accurate as more recent ones benefiting from modern equipment. Furthermore, measuring strains in the mid-height region of the specimen is based on the assumption that the specimen behaves as for the case of static loading. This may explain why many experimental investigations carried out before the 1980's report a significant increase in their specimen strength at low strain rates. Whereas in static tests the specimen has a more uniform distribution of strain along its height, for the case of high-loading rate the lower part of the specimen deforms significantly less than the upper part. Therefore, the strain measured in the mid-height region of the specimen may be considerably less than that which is actually exhibited in the upper part.

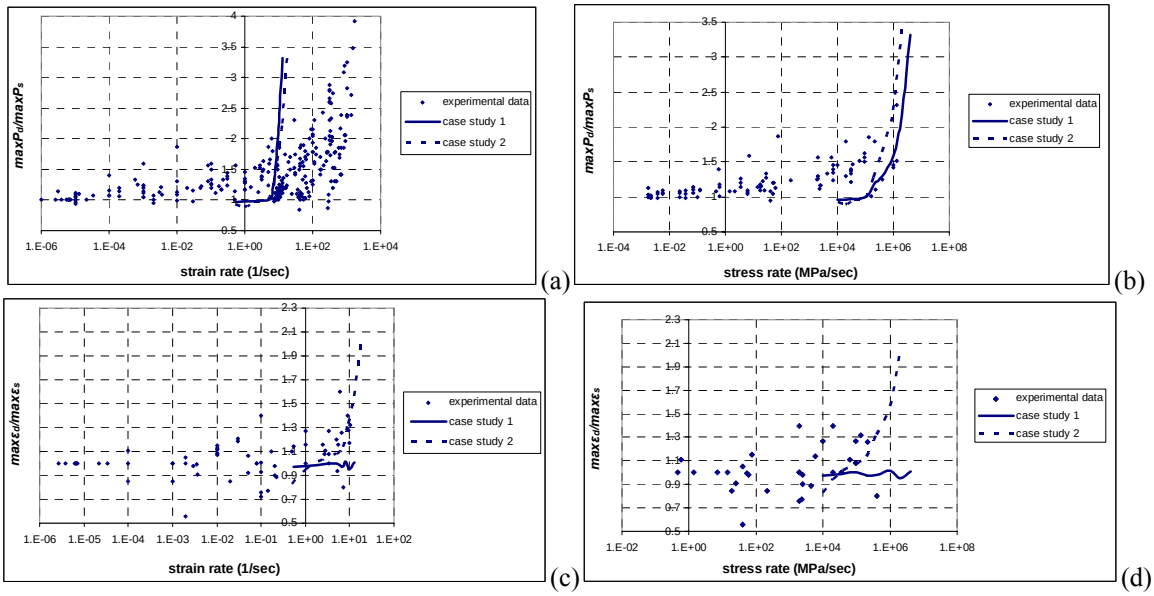

Figure 6. (a) Comparison of numerical and experimental results describing the variation of load-carrying capacity with the applied strain rate. (b) Comparison of numerical and experimental results describing the variation of load-carrying capacity with the applied stress rate. (c) Comparison of numerical (assuming average strain rate) and experimental results describing the variation of maximum exhibited strain with applied strain rate for concrete in uniaxial compression. (c) Comparison of numerical and experimental results describing the variation of maximum exhibited strain with applied stress rate for concrete in uniaxial compression.

In figure 7 a relationship is presented between $maxP_d/maxP_s$ and strain rates evaluated by using different methods (namely average strain rate, maximum value of average strain rate, and mid-height strain rate). By comparing the three resulting relationships (figure 7) it is obvious that they are significantly different. The use of mid-height strain rate calculated in the mid-height region of the specimen may lead to misleading conclusions due to the fact that, for high rates of loading, only the upper part of the prism is affected and, therefore, the mid-height region exhibits less deformation, so that the strain rate calculated in this region is much less than the strain rate exhibited in the upper area of the specimen. Comparing these relationships with the experimental data in figure 7, it is obvious that the relationship between the $maxP_d/maxP_s$ and the maximum value of average strain rate is the relationship which is closest to the experimental data.

9 CAUSES OF THE LOADING-RATE EFFECT ON THE BEHAVIOUR OF THE SPECIMEN

The numerical investigation carried out proves that the change in the behaviour of concrete prismatic elements when subjected to high rates of compressive loading can be attributed primarily to the effect of inertia. Furthermore, it has been proved that the inertia effect in both axial and lateral directions is significant for an accurate description of specimen response. However, in order to understand more comprehensively how inertia affects the behaviour of concrete under high rates of loading, its behaviour must be investigated at a material level so as to fully comprehend the cracking procedure that concrete undergoes and how this is affected by the loading rate.

In a static test, the application of a uniaxial compressive load onto a concrete cubical or cylindrical specimen results in the development of a complex internal stress field. The complexity of the stress field is due to the non-homogeneous nature of the material, characterized by the existence of microcracks[12, 17]. At the tips of the microcracks, high concentrations of tensile stresses form and, once the ultimate tensile strength of concrete is overcome, the cracks extend in the direction of the maximum principal stress[12]. This extension offers relief to concrete, as it is followed by a decrease of the value of the tensile stresses acting at the crack tips. The extension of the cracks continues as the applied load increases until, at some stage, the edges of the microcracks meet and larger cracks (macrocracks) begin to form. Under a high rate of loading the procedure becomes even more complicated since the effect of the inertia forces must also be taken under consideration. The effect of these forces is dual since, on the one hand, they affect the overall response of the concrete specimen and, on the other hand, they have a local effect on the area of the concrete specimen where cracks form.

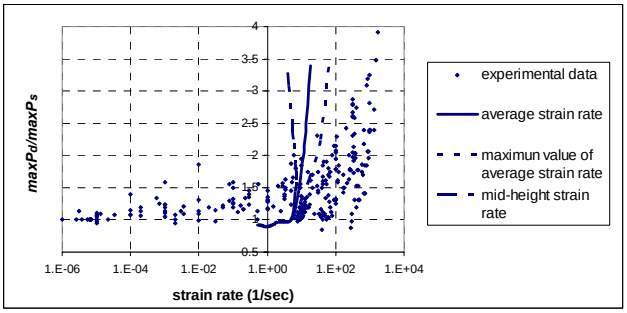

Figure 7. Relationship between $maxP_d/maxP_s$ and differently evaluated strain rates and their comparison with experimental data.

At the final stages of macrocracking the specimen exhibits an increase in lateral strain. In the static tests this lateral deformation is exhibited in the mid-height region of the specimen; however, as already discussed, this is not the case in the dynamic tests, especially when high rates of loading are involved. Because of the high rate of compressive loading imposed on the specimen, the lateral strain rate is also high. In case study 2, because the mass is distributed throughout the FE mesh and is active in all three directions, it reacts to the lateral deformation, trying to restrict it. Hence, the reaction of the mass slows down the cracking process at these final stages and, in doing so, allows the specimen to increase its strength. In case study 1, on the other hand, the mass is not distributed throughout the FE mesh and it is active only in the direction of the external load. Because of this, the mass is unable to respond to the lateral deformation of the specimen and, therefore, failure occurs earlier, the deformation being smaller than that exhibited in case study 2.

10 CONCLUSIONS

The constitutive model used by the FE program in the present study to describe the behaviour of concrete is based on the static properties of the material, which remain constant and independent of the strain rate. The comparative study between numerical and experimental data revealed that the static brittle material model used is capable of providing realistic predictions of the behaviour of concrete at high rates of loading. In view of this, it can be concluded that the effect of loading rate on the specimen's behaviour reflects the effect of the inertia loads that reduce both the rate of cracking of the specimen and its effective height, factors which, in turn, lead to an increase of its load-carrying capacity.

At high rates of loading the numerical results reveal that only the upper region of the concrete specimen deforms whereas the rest remains practically unaffected by the application of the external load. This region is situated under the rigid element used to apply the external load and its height becomes smaller as the rate of loading increases. As a result, its behaviour is also affected by the interaction between the rigid element and the specimen which leads to the conclusion that the experimental and numerical data describe specimen (structural) response, rather than concrete (material) behaviour. On the other hand, for low loading rates, the deflection of the stress waves on the boundary surfaces of the specimen causes a different type of interaction between loading mechanism and concrete specimen. The fact that the stress waves, which arise from the continuous application of the external load during the loading procedure, are trapped by the boundary conditions imposed on the specimen, leads to a non-homogeneous distribution of stress inside the specimen in which it is extremely difficult (if not impossible) to predict where high concentrations of stress and strain will develop. It can, therefore, be concluded that the specimen behaviour cannot be considered to represent the behaviour of concrete as a material but represents its response as a structure.

To this end, concrete specimens under dynamic loading cannot be used to describe concrete behaviour (as usually assumed) since, in contrast with static loading, they do not constitute a material unit from which average material properties may be obtained. Under dynamic tests, concrete specimens must be viewed as structures since their response is directly linked to the inertia effect of their mass (and, of course, boundary conditions). Therefore, the use of experimental data from dynamic tests in order to develop constitutive models of concrete behaviour under dynamic loading is questionable. Moreover, the experimental data suggest that the behaviour of a concrete specimen under impact loading depends on a number of parameters, the effect of which has not been quantified by previous research (but has been considered in the follow-up of the work described presently [5]).

11 REFERENCES

1. Bathe K.-J. (1996) *Finite element procedures*. Prentice-Hall, New Jersey.
2. Barpi F. (2004), "Impact behaviour of concrete: a computational approach", Engineering Fracture Mechanics 71, 2197–2213.
3. Cela J. J. L. (1998), "Analysis of reinforced concrete structures subjected to dynamic loads with a viscoplastic Drucker-Prager model", Appl. Math. Modelling 22, 495-515.
4. Cervera, M., Oliver, J. & Manzoli, O. (1996), "A rate-dependent isotropic damage model for the seismic analysis of concrete dams", Earthquake Eng & Struct. Dynamics 25, 987-1010.
5. Cotsovos D. M. 2004 *Numerical Investigation of Structural Concrete under Dynamic (Earthquake and Impact) Loading*. PhD thesis, University of London, UK.
6. Dube, J.-F., Pijaudier-Cabot, G. & La Borderie, C. (1996), "Rate dependent damage model for concrete in dynamics", J. Eng. Mech. Div. ASCE, 122, 359-380.
7. Faria, R., Olivera, J. & Cevera, M. (1998), "A strain-based plastic viscous-damage model for massive concrete structures", Int. J. Solids & Struct. 35, 1533-1558.
8. Georgin, J. F. & Reynouard, J. M. (2003), "Modeling of structures subjected to impact: concrete behaviour under high strain rate", Cement & Concrete Composites 217, 131-143.
9. Gomes, H. M. & Awruch, A. M. (2001), "Some aspects on three-dimensional numerical modelling of reinforced concrete structures using the finite element method", Advances in Eng. Software 32, 257-277.
10. Hatzigeorgiou, G., Beskos, D., Theodorakopoulos, D. & Sfakianakis, M. (2001), "A simple concrete damage model for dynamic FEM applications", Int. J. Computational Eng. Sci. 2, 267-286.
11. Koh, C. G., Liu, Z. J. & Quek, S. T. (2001), "Numerical and experimental studies of concrete under impact", Mag. Concrete Res. 53, 417-427.
12. Kotsovos, M. D. & Pavlović, M. N. (1995) *Structural Concrete: Finite-element analysis and design*, London, Thomas Telford.
13. Li, Q. M. & Meng, H. (2003), "About the dynamic strength enhancement of concrete-like materials in a split Hopkinson pressure bar test", Int. J. Solids and Struct. 40, 343-360.
14. Lu, Y. & Xu, K. (2004) "Modelling of dynamic behaviour of concrete materials under blast loading", Int. J. Solids and Struct. 41, 131–143.
15. Malvar, L. J., Crawford, J. E, Wesevich, J. W. & Simons, D. (1997), "A plasticity concrete material model for DYNA3D", Int. J. Impact Eng. 19, 847-873.
16. Mander, J.B., Priestley, M. J. N. & Park, R. (1988), "Theoretical stress-strain model for confined concrete", J. Struct. Eng. ASCE 114, 1804-1826.
17. Neville, A. M. (1973) *Properties of concrete* Pitman, London, 2nd edition.
18. Tedesco, J. W., Ross, A. C. & Brunair, R. M. (1989), "Numerical analysis of dynamic split cylinder tests", Computers & Struct. 32, 609-624.
19. Tedesco, J. W., Ross, A. C., McGill, P. B. & O'Neil, B. P. (1991), "Numerical analysis of high strain rate concrete tension tests", Computers & Struct., 40, 313-327.
20. Tedesco, J. W., Powell, J. C., Ross, A. C & Hughes, M. L. (1997), "A strain-rate-dependent concrete material model for ADINA", Computers & Struct. 64, 1053-1067.
21. Thabet, A. & Haldane, D. (2001), "Three-dimensional numerical simulation of the behaviour of standard concrete test specimens when subjected to impact loading", Computers & Struct. 79, 21-31.
22. Winnicki, A., Pearce, C. J. & Bicanic, N. (2001), "Viscoplasic Hoffman consistency model for concrete", Computers & Struct. 79, 7-19.
23. Van Mier, J.G.M, Shah, S. P., Armand, M., Balayssac, J. P., Bascoul, A., Choi, S., Dasenbrock, D., Ferrara, G., French, C., Gobbi, M. E., Karihaloo, B. L., Konig, G., Kotsovos, M. D., Labuz, J., Lange-Korbar, D., Markeset, G., Pavlović, M. N., Simsch, G., Thienel, K-C, Turatsinze, A., Ulmer, M., van Geel, H. J. G. M., van Vliet, M. R. A. & Zissopoulos, D. (1997), "Strain softening of concrete in uniaxial compression", Materials and Structures RILEM 30, 195-209.
24. Zissopoulos, P. M., Kotsovos, M.D. & Pavlović, M. N. (2000), "Deformational behaviour of concrete specimens in uniaxial compression under different boundary conditions", Cement and Concrete Res. 30, 153-159.

EQUIVALENT LINEARIZATION AND FIRST-ORDER EXPANSION IN NON-LINEAR DYNAMICS: A CASE STUDY

Alessandro Palmeri [*] **, Nicos Makris** [†]

[*] Department of Civil Engineering
University of Messina
Vill. S. Agata, I-98166 Messina, Italy
e-mail: alexpalm@ingegneria.unime.it

[†] Department of Civil Engineering
University of Patras
GR-26500 Patras, Greece
e-mail: nmakris@upatras.gr

Keywords: Non-linear Dynamics, Equivalent Linearization, First-Order Expansion, Stability.

Abstract. *When dealing with non-linear dynamic response of structures there are several occasions where an equivalent linear formulation of the non-linear problem reduces considerably the computational effort for the response analysis. In a broader sense, an equivalent linear formulation can be viewed as a first-order expansion of the dynamic equilibrium of the system about a "static" configuration; yet caution should be exercised when identifying the "correct" static configuration. The paper uses as a case study the rocking response of a rigid block stepping on viscoelastic supports, and elaborates on the challenge of identifying the most appropriate static configuration around which a first-order expansion will produce the most dependable results for the rocking response.*

1 INTRODUCTION

This paper elaborates on the problem of selecting the most appropriate center for the first-order expansion in order to linearize a strongly non-linear dynamical system. In some cases equivalent linearization may be attractive since it reduces appreciably the computational effort; however, caution should be exercised when selecting the most appropriate center for the first-order expansion. Our investigation concentrates on a case-study, which is the rocking response of a rigid block stepping on viscoelastic supports.

We consider the rigid block shown in Figure 1, with size R_0 and slenderness α which can pivot about points L and R when it is set to rocking. Once in contact with the vertical supports, points L and R are allowed to move only vertically. When the motion is weak, the body is in continuous contact with both supports at pivot points L and R. When the vertical uplift of the heel of the body exceeds the static deflection of the supporting springs, $\delta_s = M g/(2K) = g/\omega_v^2$, then separation occurs, and the body is supported only at its toe. Accordingly, there are three regimes of motion: (i) full-contact at both points L and R; (ii) contact only at point L (tilting to the left); and (iii) contact only at point R (tilting to the right).

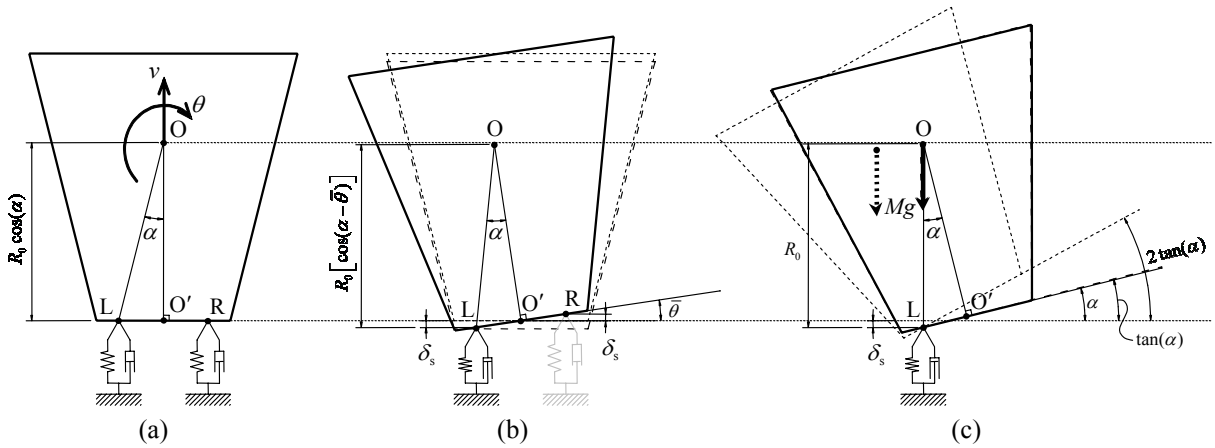

Figure 1. Schematic of a rocking block resting on viscoelastic foundation (a), Separation with right support (b), Rocking about left support (c).

The element that distinguishes the response of rocking structures from other vibrating systems is the energy loss at the impact points. In most practical cases the value of the coefficient of restitution, $e = \dot{\theta}^{\mathrm{a}} / \dot{\theta}^{\mathrm{b}}$ (= ratio of angular velocity after the impact to angular velocity before the impact), is close to the maximum admissible value, $e_{\max}$, which depends on the geometry of the block[1]. Accordingly, the rocking response of a rigid block on a rigid foundation is fully described by two parameters only – its slenderness, α, and the frequency parameter, p, which results from its size, R_0, and the intensity of the surrounding gravitational field, g:

$$p = \sqrt{\frac{\mu}{\mu+1}\frac{g}{R_0}} \tag{1}$$

where $\mu = M R_0^2 / I_0$ is the shape factor of the rigid block. For rectangular blocks, $\mu = 3$ and $p = \sqrt{3g/(4R_0)}$. Accordingly, for a rectangular rigid block rocking on a rigid foundation the response θ depends on the two aforementioned parameters and the excitation:

$$\theta = \mathrm{f}\left(\alpha, p, \text{excitation}\right) \tag{2}$$

In the case of a rigid block with mass M stepping on viscoelastic supports with stiffness $K = \omega_{\mathrm{v}}^2 M/2$ and frequency independent damping $C = \xi_{\mathrm{v}} M \omega_{\mathrm{v}}$ the response depends also on the ratio of the velocity of the pivot point after the impact at the support to the velocity of the imminent pivot point before the impact at the support. This ratio defines an alternative coefficient of restitution, $\varepsilon = \dot{v}_{\mathrm{L}}^{\mathrm{a}}/\dot{v}_{\mathrm{L}}^{\mathrm{b}} = \dot{v}_{\mathrm{R}}^{\mathrm{a}}/\dot{v}_{\mathrm{R}}^{\mathrm{b}}$, which has been introduced by Psycharis and Jennings[2]. Given the abovementioned parameters the response of a rigid block rocking on a two-support viscoelastic foundation is expressed by:

$$\theta = \mathrm{f}\left(\alpha, \mu, p, \varepsilon, \omega_{\mathrm{v}}, \xi_{\mathrm{v}}, \text{excitation}\right) \tag{3}$$

The coefficient of restitution ε introduced by Psycharis and Jennings is related to the coefficient of restitution e introduced by Housner[1], as shown in the report by Palmeri and Makris[3].

Since the rigid block is not allowed to slide, the system has only two degrees of freedom. Among the severable possible choices, we select the vertical displacement of the centre of mass, v, and the rotation of the block, θ (see Figure 1). Using the two degrees of freedom the equations of motion in the full-contact regime are[3]:

$$\begin{cases} \ddot{v} + 2\xi_{\mathrm{v}}\beta p \dot{v} + \beta^2 p^2 v + \dfrac{\mu\beta^2 g}{1+\mu}\cos(\alpha)\left\{1 - \cos(\theta) + \dfrac{2\xi_{\mathrm{v}} p}{\beta}\sin(\theta)\dot{\theta}\right\} + \ddot{v}_{\mathrm{g}}(t) = 0 \\ \left[1 + \mu\cos^2(\alpha)\cos^2(\theta)\right]\ddot{\theta} - \mu\cos^2(\alpha)\cos(\theta)\sin(\theta)\dot{\theta}^2 \\ \quad + \mu\xi_{\mathrm{v}}\beta p\left[1 - \cos(2\alpha)\cos(2\theta)\right]\dot{\theta} \\ \quad + \mu\beta^2 p^2\left[\cos^2(\alpha) - \dfrac{1+\mu}{\mu\beta^2}\cos(\alpha) - \cos(2\alpha)\cos(\theta)\right]\sin(\theta) \\ \quad + \dfrac{(1+\mu)\beta^2 p^2}{g}\cos(\alpha)\sin(\theta)\left[v + \dfrac{2\xi_{\mathrm{v}} p}{\beta}\dot{v}\right] + \dfrac{(1+\mu)p^2}{g}\cos(\alpha)\cos(\theta)\ddot{u}_{\mathrm{g}}(t) = 0 \end{cases} \tag{4}$$

while the equations of motion when the rigid block is in contact with one support are[3]:

$$\begin{cases} \ddot{v} + \xi_{\mathrm{v}}\beta p \dot{v} + \dfrac{\beta^2 p^2}{2} v - \dfrac{g}{2}\left\{\dfrac{\mu\beta^2}{1+\mu}\left[\cos(\alpha \pm \theta) - \cos(\alpha) \mp \dfrac{2\xi_{\mathrm{v}}}{\beta p}\sin(\alpha \pm \theta)\dot{\theta}\right] - 1\right\} + \ddot{v}_{\mathrm{g}}(t) = 0 \\ \left[1 + \mu\cos^2(\alpha \pm \theta)\right]\ddot{\theta} \mp \dfrac{\mu}{2}\sin[2(\alpha \pm \theta)]\dot{\theta}^2 + \mu\xi_{\mathrm{v}}\beta p \sin^2(\alpha \pm \theta)\dot{\theta} \\ \quad \pm \dfrac{\mu\beta^2 p^2}{2}\left[\cos(\alpha) - \dfrac{1+\mu}{\mu\beta^2} - \cos(\alpha \pm \theta)\right]\sin(\alpha \pm \theta) \\ \quad \pm \dfrac{(1+\mu)\beta^2 p^2}{2g}\sin(\alpha \pm \theta)\left[v + \dfrac{2\xi_{\mathrm{v}}}{\beta p}\dot{v}\right] + \dfrac{(1+\mu)p^2}{g}\cos(\alpha \pm \theta)\ddot{u}_{\mathrm{g}}(t) = 0 \end{cases} \tag{5}$$

where in the case of double sign, the upper/lower sign corresponds to the block tilting to the left/right, and $\beta = \omega_{\mathrm{v}}/p$.

2 EQUIVALENT LINEAR ANALYSIS

2.1 Derivation of linear equations

The equations of motion either in the full-contact regime (Eqs. (4)), or when the rigid block is separated from one support (Eqs. (5)) can be rewritten in a compact form as:

$$\mathbf{F}_r\left(\mathbf{x},\dot{\mathbf{x}},\ddot{\mathbf{x}};t\right)=\mathbf{0} \tag{6}$$

where $\mathbf{F}_r=\left[F_{r1}\quad F_{r2}\right]^{\mathrm{T}}$ is a 2×1 vector that consists of the left-hand side of Eqs. (4) or (5). The subscript r denotes the regime of motion, that is $r=0$ during the full-contact regime, $r=-1$ when the block is supported only at the left pivot point, $r=+1$ when the block is supported only at the right pivot point. The vector $\mathbf{x}=\left[v\quad\theta\right]^{\mathrm{T}}$ collects the two degrees of freedom of the system, v and θ.

In order to derive the linearized equations of motion, the vector $\mathbf{F}_r$ can be approximated via a first-order expansion plus a residue:

$$\mathbf{F}_r\left(\mathbf{x},\dot{\mathbf{x}},\ddot{\mathbf{x}};t\right)=\mathbf{K}_r\left(\mathbf{x}-\overline{\mathbf{x}}_r\right)+\mathbf{C}_r\,\dot{\mathbf{x}}+\mathbf{M}_r\,\ddot{\mathbf{x}}+\mathbf{F}_r\left(\overline{\mathbf{x}}_r,\mathbf{0},\mathbf{0};t\right) \tag{7}$$

in which $\mathbf{M}_r$, $\mathbf{C}_r$, and $\mathbf{K}_r$ are mass, damping and stiffness matrices of the system during the regime of motion, r:

$$\mathbf{M}_r=\left[\left.\frac{\partial\mathbf{F}_r}{\partial\ddot{\mathbf{x}}}\right|\mathbf{x}=\overline{\mathbf{x}}_r,\dot{\mathbf{x}}=\mathbf{0},\ddot{\mathbf{x}}=\mathbf{0},\ \ddot{u}_{\mathrm{g}}(t)=0,\ddot{v}_{\mathrm{g}}(t)=0\right],\quad \mathbf{C}_r=\left[\left.\frac{\partial\mathbf{F}_r}{\partial\dot{\mathbf{x}}}\right|\mathbf{x}=\overline{\mathbf{x}}_r,\dot{\mathbf{x}}=\mathbf{0},\ddot{\mathbf{x}}=\mathbf{0},\ \ddot{u}_{\mathrm{g}}(t)=0,\ddot{v}_{\mathrm{g}}(t)=0\right],\quad \mathbf{K}_r=\left[\left.\frac{\partial\mathbf{F}_s}{\partial\mathbf{x}}\right|\mathbf{x}=\overline{\mathbf{x}}_r,\dot{\mathbf{x}}=\mathbf{0},\ddot{\mathbf{x}}=\mathbf{0},\ \ddot{u}_{\mathrm{g}}(t)=0,\ddot{v}_{\mathrm{g}}(t)=0\right] \tag{8}$$

and $\mathbf{x}=\overline{\mathbf{x}}_r$, $\dot{\mathbf{x}}=\mathbf{0}$ and $\ddot{\mathbf{x}}=\mathbf{0}$ define the conditions of motion at the centre of expansion for each regime, r; that is, the rigid block is assumed to be in the static configuration given by the position vector $\overline{\mathbf{x}}_r$.

Substitution of Eq. (7) into Eq. (6) gives the equations of motion in a linear form:

$$\mathbf{M}_r\,\ddot{\mathbf{x}}+\mathbf{C}_r\,\dot{\mathbf{x}}+\mathbf{K}_r\,\mathbf{x}=\mathbf{f}_r(t) \tag{9}$$

in which:

$$\mathbf{f}_r(t)=\mathbf{K}_r\,\overline{\mathbf{x}}_r-\mathbf{F}_r\left(\overline{\mathbf{x}}_r,\mathbf{0},\mathbf{0};t\right) \tag{10}$$

2.2 Eigenvalue analysis

Once the matrices $\mathbf{M}_r$, $\mathbf{C}_r$, and $\mathbf{K}_r$ are evaluated, the complex eigenvalues λ_{ri} can be computed by solving the characteristic equation:

$$\det\left(-\mathbf{M}_r\,\lambda_{ri}^2+\mathrm{j}\mathbf{C}_r\,\lambda_{ri}+\mathbf{K}_r\right)=0 \tag{11}$$

in which $\mathrm{j}=\sqrt{-1}$ is the imaginary unit. Circular frequency and viscous damping ratio of the i-th mode in the r-th regime, then, are given by:

$$\omega_{ri}=\left|\lambda_{ri}\right|\quad,\quad \xi_{ri}=-\frac{\mathrm{Re}\left(\lambda_{ri}\right)}{\omega_{ri}} \tag{12}$$

2.3 Motion in the full-contact regime ($r=0$)

When the rigid block is in the full-contact regime the centre of expansion of the non-linear equatios is merely the static configuration $\overline{\mathbf{x}}_0=[0\quad 0]^{\mathrm{T}}$, corresponding to the rest of the system (Figure 1(a)). Accordingly:

$$\mathbf{M}_0=\begin{bmatrix}1 & 0\\ 0 & 1+\mu\cos^2(\alpha)\end{bmatrix},\quad \mathbf{C}_0=\beta\,p\,\xi_{\mathrm{v}}\begin{bmatrix}2 & 0\\ 0 & 2\mu\sin^2(\alpha)\end{bmatrix},\quad \mathbf{K}_0=p^2\begin{bmatrix}\beta^2 & 0\\ 0 & \mu\beta^2\sin^2(\alpha)-(1+\mu)\cos(\alpha)\end{bmatrix} \tag{13}$$

and:

$$\mathbf{f}_0(t) = \begin{bmatrix} -\ddot{v}_g(t) \\ -(1+\mu)\, p^2 \cos(\alpha) \dfrac{\ddot{u}_g(t)}{g} \end{bmatrix} \tag{14}$$

For instance, in order to derive the first row of the stiffness matrix $\mathbf{K}_0$, the derivatives with respect to v and θ of F_{01} (i.e., the left-hand sides of the first of Eqs. (4)), are:

$$\begin{aligned} &\frac{\partial F_{01}}{\partial v} = \beta^2\, p^2 = K_{011} \\ &\frac{\partial F_{01}}{\partial \theta} = \frac{\mu\, \beta^2\, g}{1+\mu} \cos(\alpha) \left[\sin(\theta) + \frac{2\,\xi_v\, p}{\beta} \cos(\theta)\, \dot{\theta} \right] \;\Rightarrow\; K_{012} = \left[\left. \frac{\partial F_{01}}{\partial \theta} \right|_{\theta=0, \dot{\theta}=0} \right] = 0 \end{aligned} \tag{15}$$

Figure 2 shows the loci of the eigenvalues λ_{0i} in the full-contact regime in the complex plane (shape factor $\mu = 3$). Since the loci of the eigenvalues are symmetric with respect to the real axis, only the half plane of the positive imaginary parts is shown. In the left graph the stiffness of the foundation is constant ($\beta = 20$), and the effect of varying the viscous damping ratio is shown. The larger is ξ_v, the larger are the negative values of the real parts of the eigenvalues and, by virtue of the second of Eqs. (12), the larger is the damping experienced by the vertical and the angular oscillations of the system. In the right graph the viscous damping ratio is constant ($\xi_v = 0.1$), and the effect of varying the stiffness of the foundation is shown. The larger is the parameter β, the larger are the moduli of the eigenvalues and, by virtue of the first of Eqs. (12), the larger are the vibration frequencies of the system.

In both cases the eigenvalues of the system are conjugate pairs, with negative real part (stable modes) and non-zero imaginary part (oscillating modes). The eigenvalues associated with the vertical oscillations are independent of the slenderness α, since the vertical and rocking modes are decoupled. Accordingly, for the entire range $0.15 \le \alpha \le 0.45$ the eigenvalues of the vertical mode occupy the same points. On the other hand, the eigenvalues associated with the angular oscillations are moving along the curved arrows ($0.15 \le \alpha \le 0.45$). The larger is α (stockier blocks), the larger are the moduli and the negative values of the real parts of the eigenvalues; that is, the frequency and damping of the angular oscillations increase with α.

It is worth noting that in the full-contact regime, and in a linear formulation, the matrices $\mathbf{M}_0$, $\mathbf{C}_0$, and $\mathbf{K}_0$ are diagonal. As a consequence, the equations governing the vertical and the angular vibrations in the linearized form are decoupled:

$$\begin{cases} \ddot{v} + 2\,\xi_v\, \omega_v\, \dot{v} + \omega_v^2\, \ddot{v} = -\ddot{v}_g(t) \\ \ddot{\theta} + 2\,\xi_\theta\, \omega_\theta\, \dot{\theta} + \omega_\theta^2\, \theta = -\dfrac{(1+\mu)\, p^2 \cos(\alpha)}{1+\mu\cos^2(\alpha)} \dfrac{\ddot{u}_g(t)}{g} \end{cases} \tag{16}$$

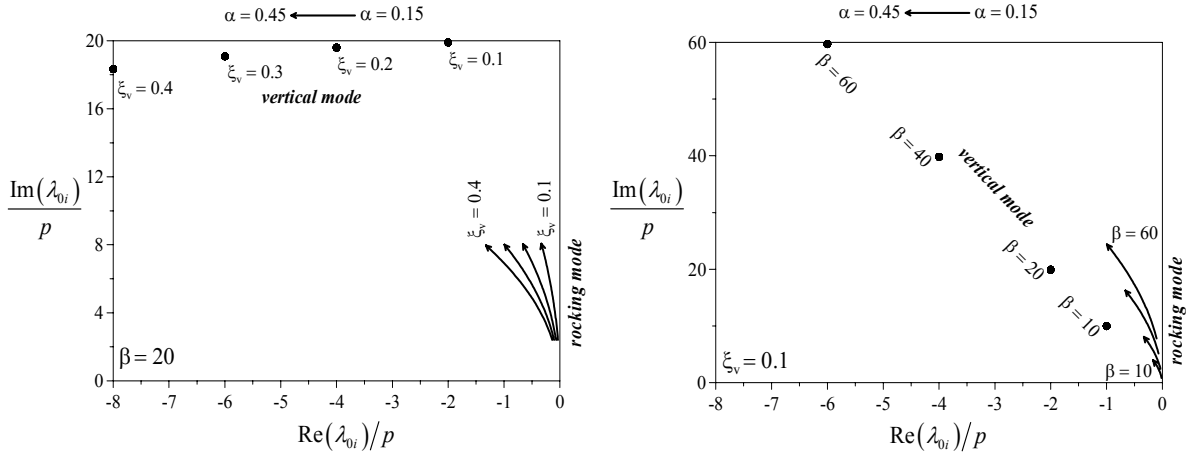

Figure 2. Loci of the eigenvalues in the full-contact regime for different values of vertical damping (left), and different values of vertical stiffness (right)..

The vertical oscillation is characterized by the circular frequency $\omega_{\mathrm{v}} = \beta\, p$ and viscous damping ratio ξ_{v}. These oscillations are independent of the slenderness α. The rocking motion is characterized by the circular frequency, ω_{θ}, and viscous damping ratio, ξ_{θ}, given by:

$$\omega_{\theta} = p\sqrt{\frac{\mu\,\beta^2\sin^2(\alpha) - (1+\mu)\cos(\alpha)}{1+\mu\cos^2(\alpha)}} \quad , \quad \xi_{\theta} = \xi_{\mathrm{v}}\,\frac{\mu\sin^2(\alpha)}{1+\mu\cos^2(\alpha)}\,\frac{\omega_{\mathrm{v}}}{\omega_{\theta}} \tag{17}$$

These expressions have been presented more than twenty years ago by Psycharis and Jennings[2], who investigated the linearized problem with a different formulation, which gives:

$$\omega_{\theta} = \frac{2\,K\,b_0^2 - M\,g\,h_0}{I_0'} \quad , \quad \xi_{\theta} = \frac{C\,b_0^2}{\sqrt{I_0'\left(2\,K\,b_0^2 - M\,g\,h_0\right)}} \tag{18}$$

where $h_0 = R_0\cos(\alpha)$ is the height of the centre of mass from the base, $b_0 = R_0\sin(\alpha)$ is the half-distance between the pivot points L and R, and $I_0' = I_0 + M\,h_0^2$ is the moment of the inertia of the rigid block with respect to the base centre O′ (see Figure 1).

2.4 Motion when the heel separates ($r = \pm 1$)

When the rocking motion is appreciable, separation occurs when the upward displacement of the heel is greater than the static deflection of the support. When this happens the vertical and the rotational mode of vibration are coupled even when the problem is linearized. At the instant when separation is imminent, and assuming that the block is tilting to the left, the deflection in the left support is twice the static one, i.e. $v_{\mathrm{L}} = -\delta_{\mathrm{s}}$ and $N_{\mathrm{L}} = 2\,K\,\delta_{\mathrm{s}} = M\,g$, while the right support is in the unstressed state, $v_{\mathrm{R}} = \delta_{\mathrm{s}}$ and $N_{\mathrm{R}} = 0$. At this configuration the rotation is:

$$\theta = \bar{\theta} \cong \frac{\delta_{\mathrm{s}}}{R_0\sin(\alpha)} \tag{19}$$

and the vertical displacement of the centre of mass is:

$$v = -R_0\cos(\alpha) - \delta_{\mathrm{s}} + R_0\cos(\alpha + \bar{\theta}) \tag{20}$$

Eqs. (19) and (20) define the static configuration for the expansion. Since in most practical applications the angle $\bar{\theta}$ is much less than slenderness α, the static configuration can be approximated as:

$$\bar{\mathbf{x}}_{-1} = \begin{bmatrix} -\delta_{\mathrm{s}} & 0 \end{bmatrix}^{\mathrm{T}} = \begin{bmatrix} -\dfrac{g}{\beta^2\,p^2} & 0 \end{bmatrix}^{\mathrm{T}} \equiv \bar{\mathbf{x}}_{+1} \tag{21}$$

In summary, when the heel separates, the static configuration is different than the one when the block is in full contact. More precisely, when the heel separates the centre of the first-order expansion is obtained by moving the rigid block downward by the static deflection $\delta_{\mathrm{s}} = g\big/\left(\beta^2 p^2\right)$. Accordingly, Eqs. (8) give:

$$\mathbf{M}_{\mp 1} = \begin{bmatrix} 1 & 0 \\ 0 & 1+\mu\cos^2(\alpha) \end{bmatrix} \equiv \mathbf{M}_0 \quad , \quad \mathbf{C}_{\mp 1} = \beta\,p\,\xi_{\mathrm{v}} \begin{bmatrix} 1 & \pm\dfrac{\mu\,g}{(1+\mu)\,p^2}\sin(\alpha) \\ \pm\dfrac{(1+\mu)\,p^2}{g}\sin(\alpha) & \mu\sin^2(\alpha) \end{bmatrix}$$

$$\mathbf{K}_{\mp 1} = \frac{p^2}{2} \begin{bmatrix} \beta^2 & \pm\dfrac{\mu\,\beta^2\,g}{(1+\mu)\,p^2}\sin(\alpha) \\ \pm\dfrac{(1+\mu)\,\beta^2\,p^2}{g}\sin(\alpha) & \mu\,\beta^2\sin^2(\alpha) - 2(1+\mu)\cos(\alpha) \end{bmatrix} \tag{22}$$

and Eq. (10) gives:

$$\mathbf{f}_{\mp 1}(t) = \begin{bmatrix} -\dfrac{g}{2} - \ddot{v}_{\mathrm{g}}(t) \\ \pm\dfrac{1}{2}(1+\mu)\, p^2 \,\sin(\alpha) - (1+\mu)\, p^2 \cos(\alpha)\dfrac{\ddot{u}_{\mathrm{g}}(t)}{g} \end{bmatrix} \tag{23}$$

In this case the damping and stiffness matrices are sparse, therefore, the equations governing vertical and angular oscillations are coupled even in the linearized form.

Figure 3 (left) shows on the complex plane the loci of the eigenvalues $\lambda_{\mp 1i}$ when the heel separates (shape factor $\mu = 3$). The cases considered are the same as for the full-contact regime: $\xi_{\mathrm{v}} = 0.1$ and $\beta = 10,\ 20,\ 40,$ and 60 in the lower graph; and $\beta = 20$ and $\xi_{\mathrm{v}} = 0.1,\ 0.2,\ 0.3,$ and 0.4 in the upper graph. The analysis reveals that the eigenvalues of the system when the heel separates are drastically different from the eigenvalues when the block is in full-contact. Accordingly, even if the response of the system is assumed to be linear during each regime of motion, the overall response is highly non-linear.

The most striking difference between the placement of eigenvalues in the regime when the heel separates and the full-contact regime is that the angular oscillations are associated with a pair of real-valued eigenvalues, symmetrically placed with respect to the imaginary axis; their positions in the graphs are denoted with two circles on the real axis. Consequently, the angular oscillations manifest a stable mode (negative real part) and an unstable mode (positive real part): when the negative eigenvalue prevails, the rigid block reassumes the full contact with the two supports. When the positive eigenvalue prevails, the rigid block overturns. It is worth noting that the eigenvalues associated with the angular oscillations are almost insensitive to the slenderness α of the rigid block, as well as to the dimensionless parameters β and ξ_{v} which characterize the foundation. In all cases considered the values of the eigenvalues are close to $\pm p$. That is, the slenderness of the rigid block and the characteristics of the foundation do not affect the rocking motion once the heel has separated. It is interesting to note that the rots are merely the eigenvalues of the linearized equations of the rocking motion of the block on a rigid foundation.

A second interesting difference between the behaviour of the eigenvalues is that when the heel separates the eigenvalues associated with the vertical mode depend on the slenderness α of the rigid block. The less slender is the block, the vertical mode becomes stiffer with more damping.

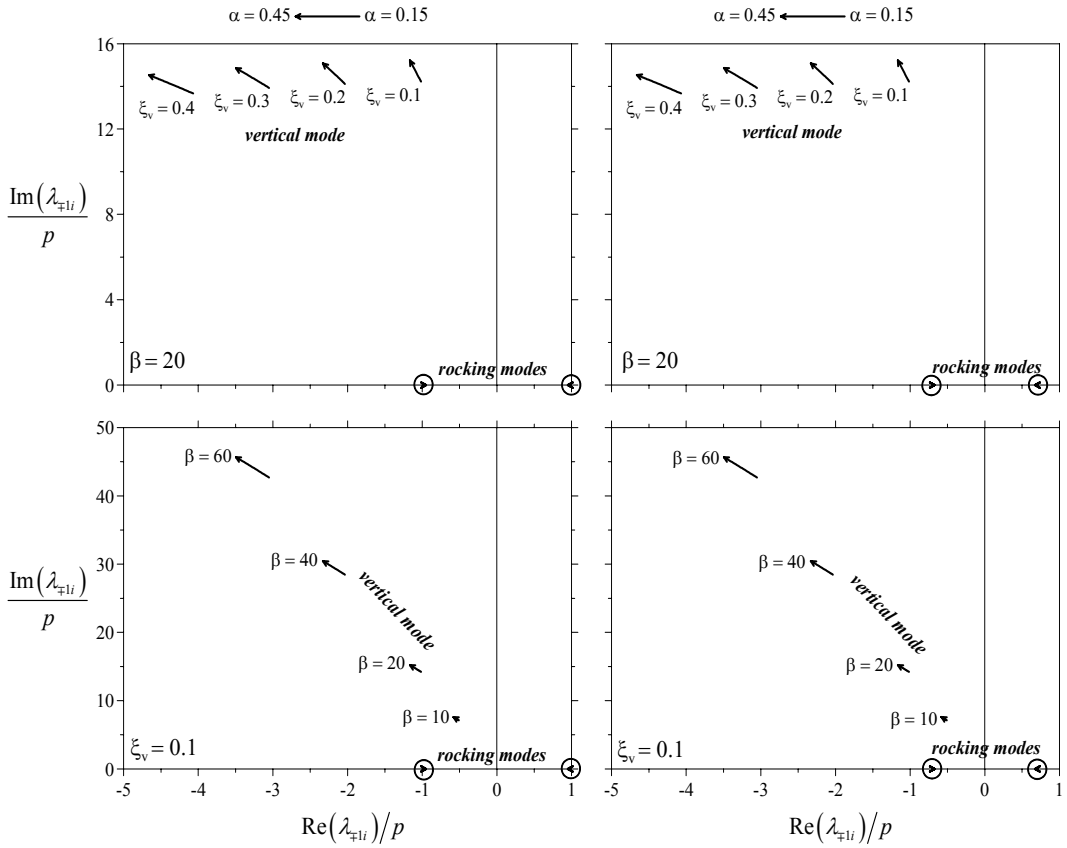

Figure 3. Loci of the eigenvalues when the heel separates according to the linearization presented in this paper (left – dashed line in Figure 1(b)), and according to the linearization proposed by Psycharis and Jennings (right – dotted line in Figure 1(b)))

2.5 Comparison with the work of Psycharis and Jennings (1983)

The response of a rigid block rocking on a viscoelastic foundation when the heel separates was systematically examined in the seminal paper of Psycharis and Jennings[2], which presented the following set of linearized equations after lift-off:

$$\begin{cases} I_0' \ddot{\theta} + C b_0^2 \dot{\theta} \pm C b_0 \dot{v} + \dfrac{1}{2}\left(2 K b_0^2 - M g h_0\right)\theta \pm K b_0 v = -M h_0 \ddot{u}_g(t) \pm M g b_0 \\ M \ddot{v} + C \dot{v} \pm C b_0 \dot{\theta} + K v \pm K b_0 \theta = -\dfrac{1}{2} M g - M \ddot{v}_g(t) \end{cases} \tag{24}$$

These equations were not derived as a first order expansion of the fully non-linear formulation, but rather constructed from dynamics equilibrium after assuming small displacements. Accordingly, at that time (1983) the challenge of selecting the most appropriate centre of linearization to conduct the first-order expansion did not emerge. When the first of Eqs. (24) is divided by I_0 and the second by M, and after using the dimensionless parameters previously introduced, Eqs. (24) become:

$$\begin{cases} \left[1+\mu\cos^2(\alpha)\right]\ddot{\theta} + \mu\beta\, p\, \xi_v \sin^2(\alpha)\dot{\theta} \pm \dfrac{(1+\mu)\beta\, p^3\, \xi_v}{g}\sin(\alpha)\dot{v} \\ \qquad + \dfrac{p^2}{2}\left[\mu\beta^2\sin(\alpha) - (1+\mu)\cos(\alpha)\right]\theta \pm \dfrac{(1+\mu)\beta^2\, p^4}{2g}\sin(\alpha)\, v = \\ \qquad -\dfrac{(1+\mu)\, p^2}{g}\cos(\alpha)\ddot{u}_g(t) \pm \dfrac{(1+\mu)\, p^2}{2}\sin(\alpha) \\ \ddot{v} + \beta\, p\, \xi_v \dot{v} \pm \dfrac{\mu\beta\,\xi_v\, g}{(1+\mu)\, p}\sin(\alpha)\dot{\theta} + \dfrac{\beta^2\, p^2}{2}\ddot{v} \pm \dfrac{\mu\beta^2 g}{2(1+\mu)}\sin(\alpha)\theta = -\dfrac{g}{2} - \ddot{v}_g(t) \end{cases} \tag{25}$$

and after writing Eqs. (25) as a matrix equation with the response vector $\mathbf{x} = \begin{bmatrix} v & \theta \end{bmatrix}^{\mathrm{T}}$, the mass and damping matrices are exactly the matrices $\mathbf{M}_{\mp 1}$ and $\mathbf{C}_{\mp 1}$ of Eqs. (22), while the corresponding stiffness matrix is:

$$\mathbf{K}_{\mp 1} = \frac{p^2}{2}\begin{bmatrix} \beta^2 & \pm\dfrac{\mu\beta^2 g}{(1+\mu)\, p^2}\sin(\alpha) \\ \pm\dfrac{(1+\mu)\beta^2\, p^2}{g}\sin(\alpha) & \mu\beta^2\sin^2(\alpha) - (1+\mu)\cos(\alpha) \end{bmatrix} \tag{26}$$

The only difference in the stiffness matrix given by Eq. (26) and the stiffness matrix that was derived after taking a first order expansion of the equations of motion around the centre $\bar{\mathbf{x}}_{\mp 1} = \begin{bmatrix} -g/\left(\beta^2 p^2\right) & 0 \end{bmatrix}^{\mathrm{T}}$, given by the third of Eqs. (22), is a factor of 2 in the second term of element $(2,2)$. It is easy to show that the stiffness matrix given by Eq. (26) can be obtained after expanding the non-linear equations of motion around the centre $\bar{\mathbf{x}}_{\mp 1} = \begin{bmatrix} 0 & 0 \end{bmatrix}^{\mathrm{T}} = \bar{\mathbf{x}}_0$, which is the configuration at rest (dotted line in Figure 1(b)).

What this analysis reveals is that the linearization presented by Psycharis and Jennings assumes the same centre of the first order expansion $\bar{\mathbf{x}}_0 = \bar{\mathbf{x}}_{\mp 1} = \begin{bmatrix} 0 & 0 \end{bmatrix}^{\mathrm{T}}$ for both the full-contact regime and the regime when the heel separates, while the linearization presented in this work assumes as centre of the first order expansion for the full-contact regime the position at rest, $\bar{\mathbf{x}}_0 = \begin{bmatrix} 0 & 0 \end{bmatrix}^{\mathrm{T}}$, and for the regime when the heel separates, $\bar{\mathbf{x}}_{\mp 1} = \begin{bmatrix} -g/\left(\beta^2 p^2\right) & 0 \end{bmatrix}^{\mathrm{T}}$, which is the configuration of a rigid block that is entering rocking motion.

Obviously the linearization presented by Psycharis and Jennings correspond to a stiffer system that results to an unconservative response at large vibrations. The artificial stiffness/stability to the system that results from the Psycharis and Jennings linearization is also reflected on the eigenvalues analysis. Figure 3 (right) shows the loci of the eigenvalues $\lambda_{\mp 1 i}$ during the regime when the heel separates according to the linearization presented by Psycharis and Jennings. The resulted eigenvalues are close to $\pm p/\sqrt{2} \cong \pm 0.707\, p$, while the eigenvalues resulted from the proposed formulation are close to $\pm p$.

A rectangular block ($\mu = 3$) with frequency parameter p has a size $R = 3g/\left(4p^2\right)$; whereas a block with frequency parameter $p' = p/\sqrt{2}$ has a size $R' = 3g/\left(2p^2\right) = 2R$. Accordingly, the linearization presented by Psycharis and Jennings when the heel separates results to eigenvalues for the rocking mode that corresponds to a block with twice the size, which is a fictitiously more stable configuration.

3 NUMERICAL APPLICATION

In order to investigate the accuracy of the linearized equations of motion derived in the previous sub-sections we compute the rocking motion of a rigid block of slenderness $\alpha = 0.25$, shape factor $\mu = 3$ and frequency parameter $p = 1.5$ rad/s ($R_0 = 3.27$ m) when subjected to a one-sine pulse at the base.

Figure 4 shows the time histories of normalized rotations and angular velocities of the block when the viscoelastic foundation is characterized by the parameters $\beta = 40$ and $\xi_v = 0.4$. The solution of the non-linear equations of motion yield that the minimum amplitude of a one-sine pulse of period $T_p = 0.5$ s to induce overturning is $a_p = 2.3\,g$ (first and second columns). The same value ($a_p = 2.3\,g$) results by the proposed linearized equations. On the other hand, the linearized equations of Psycharis and Jennings[2] yield a minimum overturning acceleration equal to $a_p = 4.3\,g$ (third and fourth columns).

4 CONCLUSIONS

This paper elaborates on the problem of linearizing strongly non-linear problems that involve more than one regime. In a broader sense, an equivalent linear formulation can be viewed as a first-order expansion of the equations of dynamic equilibrium of the system about a "static" configuration.

The paper uses as a case study the dynamic response of a rigid block rocking on a viscoelastic foundation and shows that the static configuration when the block is in full-contact with both supports is different from the static configuration when the heel of the block separates from one support, and the block essentially rocks about its toe. This difference had escape the attention of part investigation, and this paper highlights its importance.

More generally the study concludes that when more than one regimes are involved, the first-order expansion of the equations of motion should be conducted around the new point where the new regime engages.

REFERENCES

[1] Housner G.W. (1963), "The behaviour of inverted pendulum structures during earthquakes," Bulletin of the Seismological Society of America 53, pp. 404-17.

[2] Psycharis I.N., Jennings P.C. (1983), "Rocking of slender rigid bodies allowed to uplift," Earthquake Engineering and Structural Dynamics 11, pp. 57-76.

[3] Palmeri A., Makris N. (2005), *Response Analysis of Rigid Structures Rocking on Viscoelastic and Nonlinear Foundation*, Report No. EEAM 2005-02, Department of Civil Engineering, University of Patras, Greece.

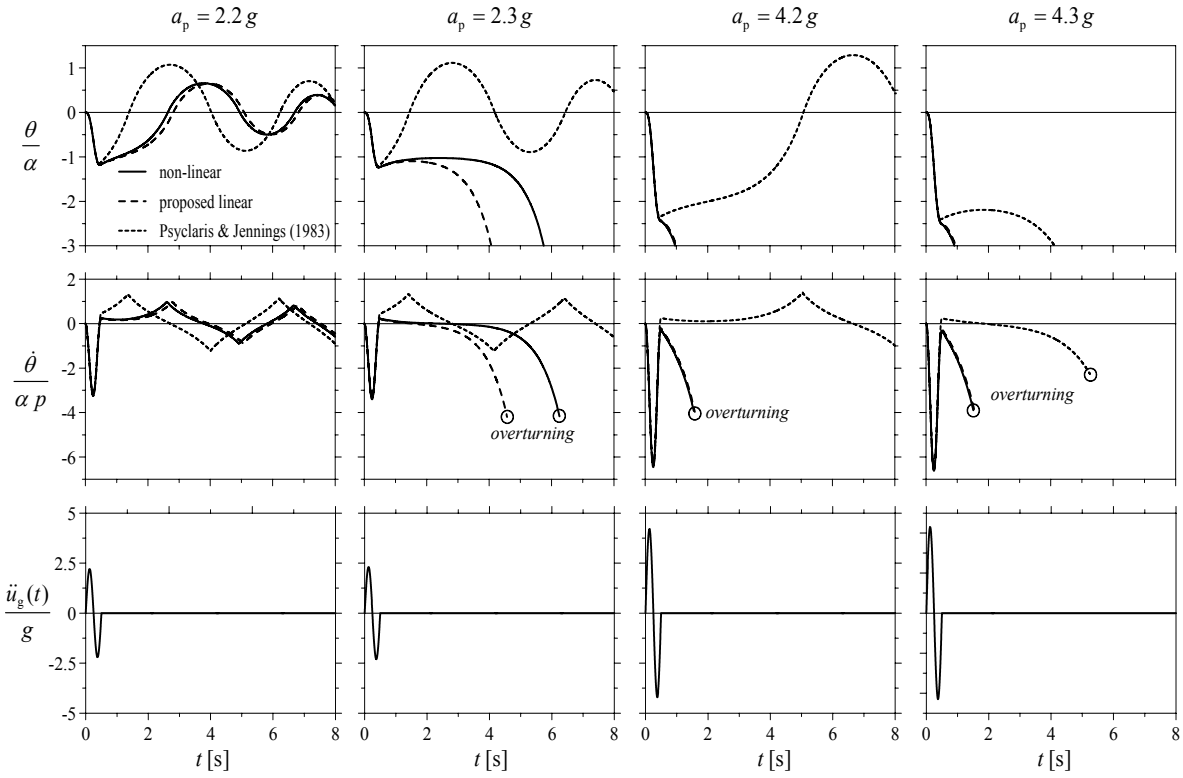

Figure 4. Normalized rotation and angular velocity time histories of a rocking block with $\beta = 40$ and $\xi_v = 0.4$ due to a one-sine pulse with T_p = 0.5 s. The overturning pulse amplitude a_p = 2.3 g predicted with the proposed linearization is in agreement with the results from non-linear time history analysis.

SEISMIC ANALYSIS OF BASE ISOLATED LIQUEFIED NATURAL GAS TANKS

Vassilis P. Gregoriou, Stephanos V. Tsinopoulos and Dimitris L. Karabalis

Department of Civil Engineering
University of Patras
26500, Patras, Greece
e-mail: stsinop@upatras.gr

Keywords: Seismic analysis, high damping rubber bearings, lead core rubber bearings, liquefied natural gas, storage tanks

Abstract. *The time domain seismic response of a representative liquefied natural gas (LNG) tank isolated at its base level by rubber bearings is investigated. The problem is solved numerically by means of a detailed finite element model, taking into account fluid-structure interaction effects. Two types of bearings are investigated: high damping rubber bearings and lead core rubber bearings. The bearings are modeled as non-linear springs with the force-displacement relationships derived by fitting appropriate analytical curves to experimental data obtained from the literature. The seismic excitation considered is an artificial accelerogram compatible with the Eurocode 8 provisions. Results concerning base shear force, sloshing vertical displacement and deflection of the inner steel container are presented. In order to measure the effectiveness of the isolation systems, percentage reductions of the peak response of all mentioned quantities are calculated using the non-isolated tank as reference. The research has been performed in the frameowork of the project INDEPTH (Development of INnovative DEvices for Seismic Protection of PeTrocHemical Facilities), supported by the Environment and Sustainable Development Programme of the European Commission Research Directorate General (Contract EVG1-CT-2002-00065).*

1 INTRODUCTION

Natural gas is a fossil fuel (90% or more methane) that is usually transported at its gaseous state through ducts from the cite of its production to the place of its consumption. Alternatively it is possible to cool the product down to -170 ^{0}C so that it condenses to its liquid state. In that way the density of the product increases by approximately 600 times making it possible to ship it in specially designed vessels and store it in thermally insulated tanks. The stored product can then be re-evaporated in appropriate facilities and piped to the consumption. The facilities related to the unloading, storage and re-vaporisation of the Liquefied Natural Gas (LNG) are located in the same site which is usually called an LNG terminal.

LNG terminals are crucial facilities for a natural gas distribution system because, besides providing a backup in natural gas supply, they balance the difference between the demand, which varies constantly, and the supply from the international ducts, which is essentially constant. Because of the importance of the LNG tanks, but primarily because such a huge amount of stored energy could provoke a major disaster if uncontrollably deliberated, very sever requirements are imposed concerning the ability of LNG tanks to withstand several prescribed accidental actions such as aircraft impact, explosion, fire, major leak and earthquake. Especially for the earthquake action, requirements are that LNG tanks be able to sustain a major seismic event, of a return period of over 5000 years, up to 10000 years, without undergoing catastrophic damage, while being able to remain fully operational during a medium seismic event of return period of 475 years. Design issues for the LNG tanks can be found in several specialized publications, e.g. Bomhard and Stempiniewski [1] and Tajirian [2].

The modern aseismic design of LNG tanks is based on the base isolation technique. The base isolation is a strategy that attempts to isolate the structure at its base, moving the dominant frequency of the isolated tank away from the dominant frequency range of the earthquake acceleration spectrum [3]. The isolators usually implemented in LNG tanks are either rubber-type bearings [4,2], such as the lead core rubber bearings and the high damping rubber bearings, or sliding-type bearings such as the friction pendulum bearings [5,2].

In this work the seismic protection of LNG tanks by implementation of two different base isolation systems is investigated numerically by means of the Finite Element Method (FEM). The two base isolation systems studied are high damping rubber bearings and lead core rubber bearings [6]. Rubber bearings are formed by alternating layers of hot vulcanized elastomer and steel shims. The elastomer layers provide the horizontal flexibility required for the decoupling of the horizontal structural motion from the ground motion, while the steel shims ensure adequate vertical stiffness. In the case of high damping rubber bearings, damping is provided by

the chemical composition of the elastomer, while in the case of lead core rubber bearings absorption of energy is achieved through yielding of a lead prismatic core placed in the center of the bearing. This difference in the energy absorption mechanism is reflected on the shape of the energy absorption loops, which for the first case are nearly viscoelastic while for the second case exhibit an almost bilinear behavior. The seismic excitation considered is an artificial accelerogram compatible with the Eurocode 8 (EC8) provisions [7] for soil type C. Selective results concerning base shear force, sloshing and deflection of the inner steel container are presented. The development of the FEM model and its numerical solution are performed in the environment provided by the ANSYS finite element program [8].

2 DESCRIPTION AND MODELING OF THE TANKS

A storage tank has several functions besides the obvious one of maintaining its content: a) keeping the content from escaping to the environment, b) preventing the atmospheric air from entering the tank, c) defending the content against the effects of external events including accidents such as earthquake, fire and explosion d) maintaining the appropriate conditions in the tank particularly in respect of temperature and pressure (slightly above atmospheric). To achieve these conditions LNG tanks are usually configured as a double shell, as shown in Fig. 1. Thus, they are constituted of an outer prestressed concrete cylindrical shell which is capped by a spherical reinforced concrete dome and an inner steel cylindrical shell open at the top and closed at the bottom by a steel plate. For the more or less typical example studied in this work the outer shell is of constant thickness of (0.8m) along its height, except from a small part near the base which is thicker (1.6m), while the thickness of the inner shell increases from top to bottom from 10.4 to 30.5mm. The space between the two shells is filled with perlite to insure proper thermal insulation of the content. The outer shell seats directly on a circular foundation slab, while between the bottom of the inner container and the foundation slab there is a layer of foam glass (0.8m) for thermal insulation purposes. In addition, the inner tank height is 33.42m, the outer tank height is 37.5m, the inner tank middle radius is 32.5m, the outer tank outer radius is 34.3m, and the maximum height of the liquid volume is 32.601m.

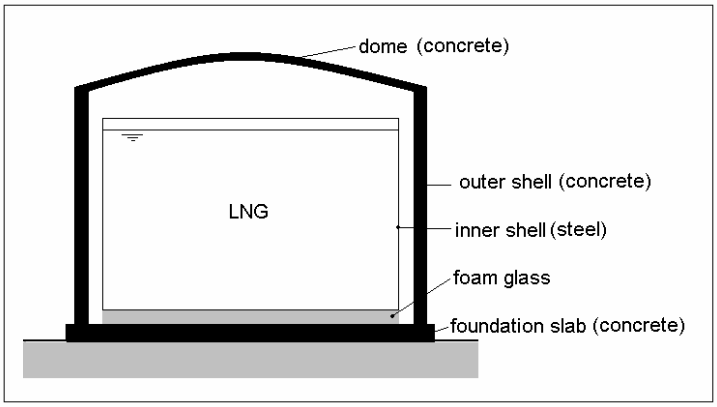

Figure 1: General configuration of an LNG tank with double shell

The seismic analysis of the selected LNG tank is performed by means of the ANSYS finite element program [8]. The outer and the inner shell as well as the dome and the foundation slab are modeled by four-nodded, 24 DOF quadrilateral shell elements. The foam glass layer is modeled by eight-nodded 24 DOF solid elements. The fluid content is modeled by eight-nodded 24 DOF fluid elements. The fluid-structure interaction is approximated by prescribing appropriate coupling equations at the nodal points on the fluid-structure interface.

3 PRELIMINARY DESIGN AND MODELING OF THE ISOLATION SYSTEMS

All the base isolation systems under consideration consist of a number of similar rubber bearings uniformly distributed under the existing foundation slab. However, the total number of required bearings is derived from the assumption that a single bearing supports approximately 10-12 m^2 of foundation slab at maximum. Thus, approximately 340 bearings should be used for the tank under consideration.

Two major assumptions are inherent in the modeling of the base isolation systems analyzed in the present study. The first is that the forces applied from the devices to the existing foundation slab are uniformly distributed on the entire area of the slab. The second is that the in-plane stiffness of the slab is infinite. Following these assumptions, the vertical stiffness of the bearings is simulated using Winckler type plate elements [8,9], with an appropriate foundation coefficient, while the horizontal stiffness of the bearings is

simulated using a single non-linear spring element connected to the centre of the slab. This model for the base isolation system is illustrated in Figure 2

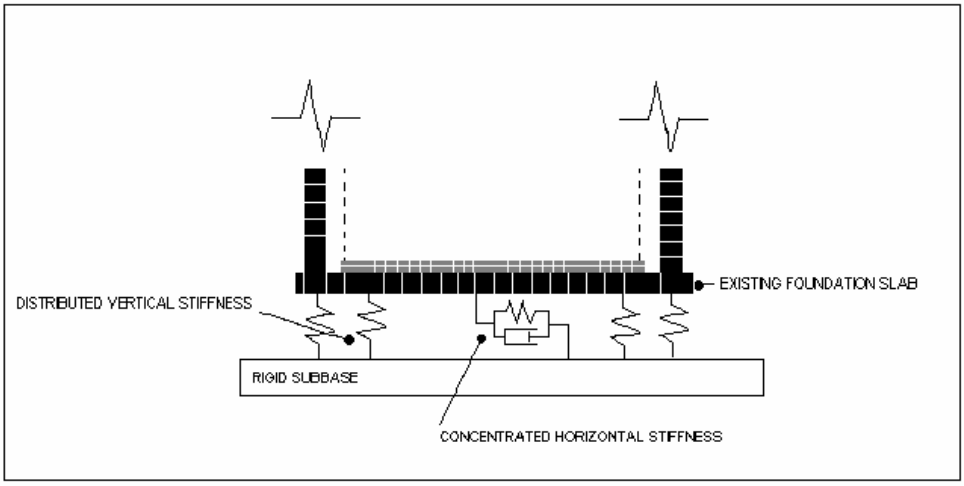

Figure 2: Modeling of the isolation systems

3.1 Vertical stiffness

The Winckler model requires the determination of the elastic foundation stiffness (EFS), which is defined as the pressure required to produce a unit normal deflection of the foundation and is given as

$$EFS = \frac{N * K_v}{A_s} \tag{1}$$

where N is the number of the installed isolators, K_v the vertical stiffness of each isolator and A_s the area of the foundation slab.

3.2 Horizontal stiffness

For isolated structures a fundamental period, i.e. the natural period of the structure moving as an almost rigid body on the isolators, is usually selected in the range of 1.5 to 3 sec. For this study, a fundamental period of 2sec is chosen. Given the total mass M of the structure, the total horizontal stiffness K of an equivalent elastic isolation system that would lead to a fundamental period of 2 sec, can be approximately evaluated, on the assumption of an equivalent single degree of freedom system, from the well known relationship

$$K_{eq} = 4 \cdot \pi^2 \cdot M / T^2 \tag{2}$$

The force-displacement relationship for a set of high damping rubber bearings acting in parallel can be described by the following equations the first of which applies for loading (positive loading) and the second for unloading (negative loading)

$$F_l = \frac{N \cdot t_e}{b}\left[K_0 - K_{\inf} + b\frac{\delta - \delta_{\min}}{t_e} K_{\inf} - \left(K_0 - K_{\inf}\right) e^{\left(b\frac{\delta_{\min}}{t_e} - b\frac{\delta}{t_e}\right)} \right] - a \tag{3a}$$

$$F_u = \frac{N \cdot t_e}{b}\left[\left(K_{\inf} - K_0\right) e^{-b\frac{2\delta_{\max}}{t_e}} + b\frac{\delta + \delta_{\max}}{t_e} K_{\inf} + \left(K_0 - K_{\inf}\right) e^{\left(b\frac{\delta}{t_e} - b\frac{\delta_{\max}}{t_e}\right)} \right] - a \tag{3b}$$

where, F_l is the total force applied to the system during loading, F_u is the total force during unloading, δ is the displacement, $\delta_{\min}$ is the displacement at which loading begins after a change in the direction of the velocity, $\delta_{\max}$ is the displacement at which unloading begins, N is the number of isolators, K_0 is the initial stiffness of the system, $K_{\inf}$ is the stiffness of the system at large displacements, t_e is the total thickness of the elastomer compound, b is a parameter of the model and a is constant defined as

$$a = \frac{N}{b}\left[b\left(\delta_{\max} - \delta_{\min}\right) K_{\inf} + \left(1 - e^{-2b\frac{\delta_{\max}}{t_e}} + e^{-b\frac{\delta_{\max}}{t_e}} + e^{b\frac{\delta_{\min}}{t_e}} \right)\left(K_0 - K_{\inf}\right) t_e \right] \cdot \tag{4}$$

Eqs (3) have been derived by integrating the G-γ relationships presented by Dusi and Rebecchi [10].

For the preliminary design, all the parameters of the model, i.e. K_0, $K_{\inf}$, t_e, and b, should be determined. To this end some assumptions should be made, e.g $\delta_{\min}$(assumed constant for every loop) = $-\delta_{\max}$ = 0.12m, $\lambda = K_0/K_{\inf}$ =2.6, and t_e=0.17m. Additionally two more relationships can be derived from the following considerations: a) The secant stiffness of the isolation system at $\delta_{\max}$ (loading begins at $-\delta_{\max}$) is identical to the stiffness K_{eq} of an equivalent linear system corresponding to the desired fundamental period, as shown in Figure 3. b) The energy dissipated during one full oscillation between $-\delta_{\max}$ and $\delta_{\max}$, equals the energy dissipated during one full oscillation of the same amplitude by an equivalent linear system corresponding to the desired fundamental period and an appropriate percentage of critical damping ξ. The percentage of critical damping that is feasible using high damping rubber bearings varies between 7% and 15% [11]. A value of 10% is considered for the preliminary analysis in this work. On the basis of the above considerations and in view of Eqs (3) the following set of equations is produced

$$\frac{N \cdot t_e}{b}\left((\lambda - 1) K_{\inf} + b\frac{2\delta_{\max}}{t_e} K_{\inf} - (\lambda - 1) K_{\inf} \cdot \exp\left(-b\frac{2\delta_{\max}}{t_e} \right) \right) - 2\delta_{\max} \cdot K_{eq} = 0 \tag{5a}$$

$$\frac{1}{b^2}\left(2 \cdot N \cdot K_{\inf} \cdot t_e \cdot (\lambda - 1)\left(b \cdot \delta_{\max} + t_e + \left(b \cdot \delta_{\max} - t_e\right) \exp\left(2b\frac{\delta_{\max}}{t_e} \right) \right) \exp\left(-2b\frac{\delta_{\max}}{t_e} \right) \right) - 2 \cdot \pi \cdot \xi \cdot K_{eq} \cdot \delta_{\max}^2 = 0 \tag{5b}$$

Once the system of Eqs (5) is solved for the unknown quantities b and $K_{\inf}$, all the parameters of the model of Eqs (3) are determined. Eqs (3) are implemented in the finite element model as the force-displacement relationship of a non-linear spring element connected to the centre of the foundation slab. The energy dissipation loop produced by this force-displacement relationship for maximum displacement equal to $\delta_{\max}$ is plotted in Figure 3.

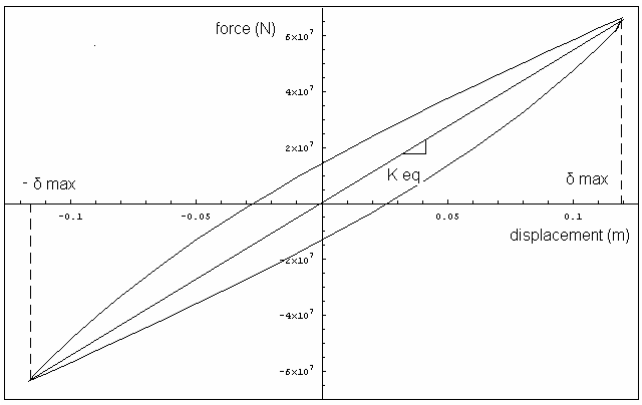

Figure 3: Energy dissipation loop for the high damping rubber bearings

The horizontal stiffness of a set of lead core rubber bearings is simulated by a bilinear elastoplastic model, as shown in Figure 4. Again, some assumptions have to be made for the preliminary design of the isolation system, in order to evaluate the parameters K_{el} K_{pl} and F_y of the model. Thus, $\delta_{\max}$ is assumed equal to 0.18 m, $\lambda = K_{el}/K_{pl}$ is assumed equal to 11, and ξ is assumed equal to 40% which is a reasonable for structures isolated with lead core rubber bearings [11].

The considerations (a) and (b), used in the case of high damping rubber bearings for the determination of the parameters of the applied model, can be also employed in the case of lead core rubber bearings, too. For this case the equations describing the aforementioned considerations are

$$K_{eq} \cdot \delta_{\max} = K_{el} \cdot dp + K_{pl} \cdot dl \tag{6a}$$

$$dp + dl = \delta_{\max} \tag{6b}$$

$$4dp\left(K_{el} - K_{pl}\right)\left(\delta_{\max} - dp\right) - 2 \cdot \pi \cdot \xi \cdot K_{eq} \cdot \delta_{\max}^2 = 0 \tag{6c}$$

$$F_y = K_{el} \cdot dp \tag{6d}$$

After computing the various unknown variables appearing in Eqs (6), the bilinear model of Figure (4) is

implemented in the finite element model as the force-displacement relationship of a non-linear spring element connected to the centre of the foundation slab.

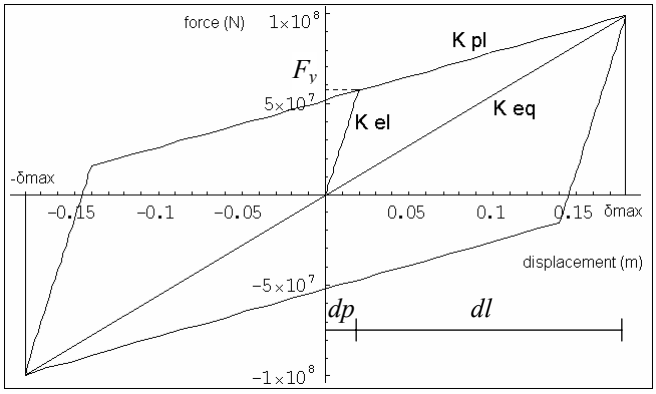

Figure 4: Energy dissipation loop for the set of lead core rubber bearings used in this work

The parameters corresponding to the models of the two isolation systems used in this work, are presented in Table 1

High damping rubber bearings	K_0 (N/m)	K_{inf} (N/m)	b
	$2.86*10^6$	$1.10*10^6$	2.5
Lead core rubber bearings	K_{el} (N/m)	K_{pl} (N/m)	f_y (N)
	$28.6*10^8$	$2.6*10^8$	$0.573*10^8$

Table 1: Parameters for the two isolation systems used in this work

4. NUMERICAL RESULTS AND DISCUSSION

Time domain non-linear dynamic analyses are preformed with non-linearities concentrated at the spring simulating the isolation system. The linear acceleration method is used for the integration of the system of the equations of motion while the full Newton-Raphson method is used for the solution of the non-linear systems of equations. An artificial accelerogram compatible with the EC-8 spectrum for soil type C is used as an input excitation.

In the following, selective results of the analyses are presented. In Figure 5, the base shear force below the foundation slab versus the corresponding base displacement is plotted for each isolation case. In Figure 6, the total base shear force just above the foundation slab is plotted versus time. For comparison purposes the base shear time history for the non-isolated case (fixed base conditions), is also shown. In Figure 7, time histories of base displacement are plotted for each isolation case. The time history of the horizontal displacement, relative to the base, of the inner shell at the fluid free surface level is plotted versus time in Figure 8. For comparison purposes, the horizontal displacement of the inner shell for non-isolated (fixed base conditions) is also shown. Similarly, in Figure 9 the relative displacement at 2/3 of the height of the inner shell, where the maximum deflection is observed, is illustrated. Finally, in Figure 10 the wave height at the intersection of the fluid free surface and the inner shell is plotted versus time for each isolation case and, for comparison purposes, fixed base conditions. For completeness modal analysis has been performed for the fixed base boundary conditions. The eigenfrequencies of the most important modes, based on the mass participation factor (MPF), for horizontal seismic excitation, are listed in Table 2.

Eigenfrequency		1st	2nd	3rd
Outer tank	f (Hz)	7.624	8.65	14.8
	MPF (%)	54.3	19.1	7.13
Inner tank (full)	f (Hz)	0.1136	2.187	
	MPF (%)	48.95	48.7	

Table 2: Eigenfrequencies for fixed base conditions

In view of the results shown in Figures 5-10, a series of conclusions can be made concerning the most prominent design parameters. In terms of base shear force, reductions of the order of 70% are calculated for both isolation systems investigated in this work. Similarly, maximum stresses in the inner shell are reduced by approximately 60%, in comparison to the non-isolated case where fixed base conditions are considered. However, in Figure 10 an increase of the sloshing height, in comparison to the non-isolated tank, is observed, particularly in the high damping rubber bearing isolation case. This is due to the fact that the motion of the liquid free surface can be viewed as a synthesis of the natural sloshing motion (free vibration) and the motion of the base (forced vibration). Concerning the high damping rubber bearing isolation case, the base displacement time history of Figure 7 is characterized by a unique dominant period of 2.04 sec, which is very close to the target isolation period of 2.00 sec. Thus, the wave height time history of Figure 10 appears as the superposition of mainly two harmonic motions, the first one being the sloshing motion itself while the second exhibits the same period as the base motion and a rather large amplitude. In the other hand, for the case of lead core rubber bearings, there is not a unique dominant frequency characterising the base motion of the tank but rather a series of significant frequencies of comparatively small amplitude. The difference in the base motion characteristics between the two cases is explained by the different mechanical behavior of the two bearing types, i.e., while the high damping rubber bearing exhibit a weak nonlinear behavior, the lead core rubber bearings demonstrate a rather strong nonlinear behavior. In conclusion, the use of lead core rubber bearings results for a more effective isolation of liquid storage tanks of the type studied in this work.

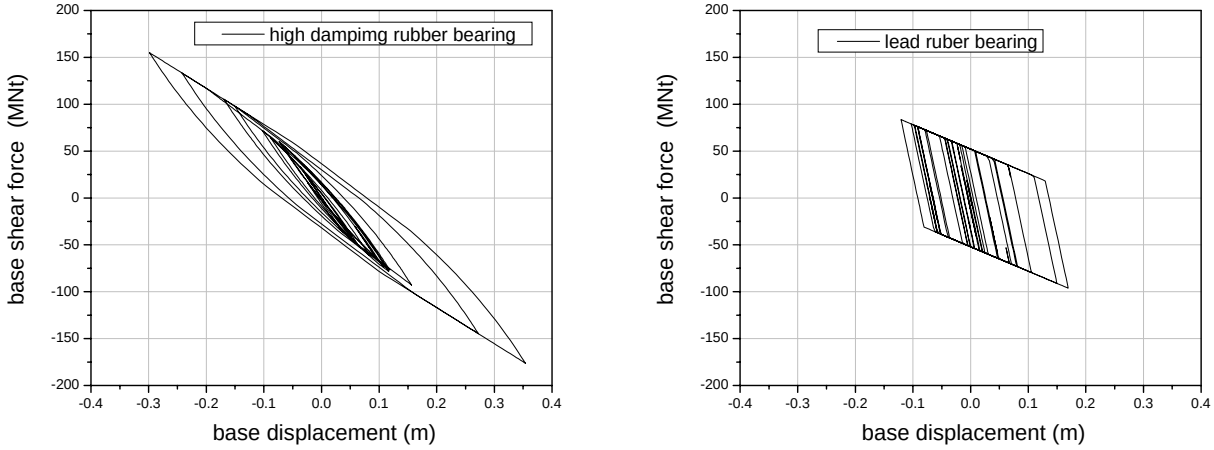

Figure 5: Base shear force below the foundation slab versus base displacement for each isolation case

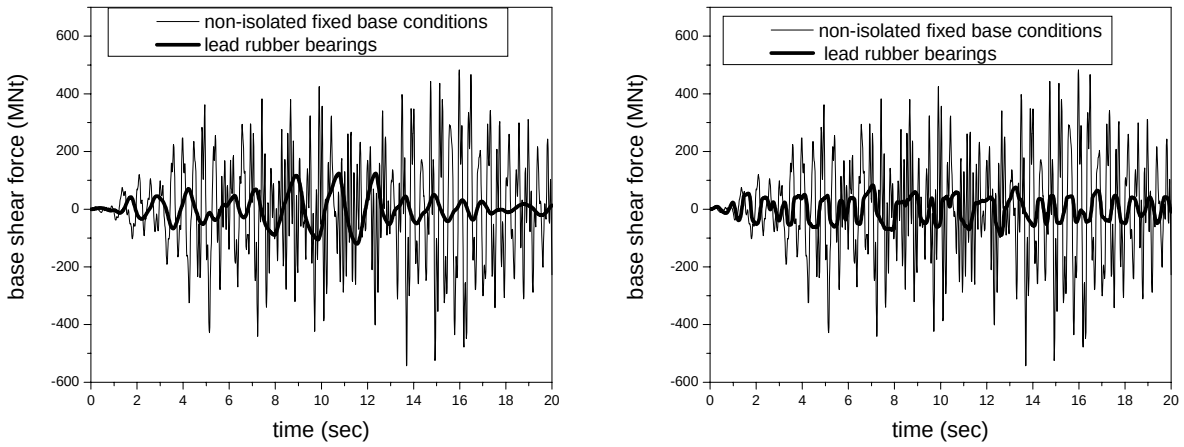

Figure 6: Time histories of total base shear just above the foundation slab for the isolated and the non-isolated (fixed base conditions) cases.

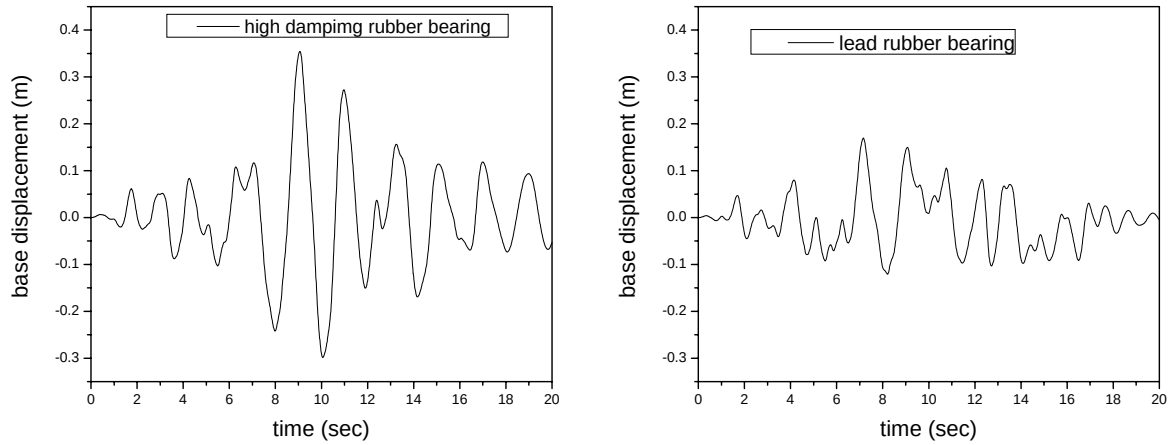

Figure7: Base displacement time histories for each isolation case

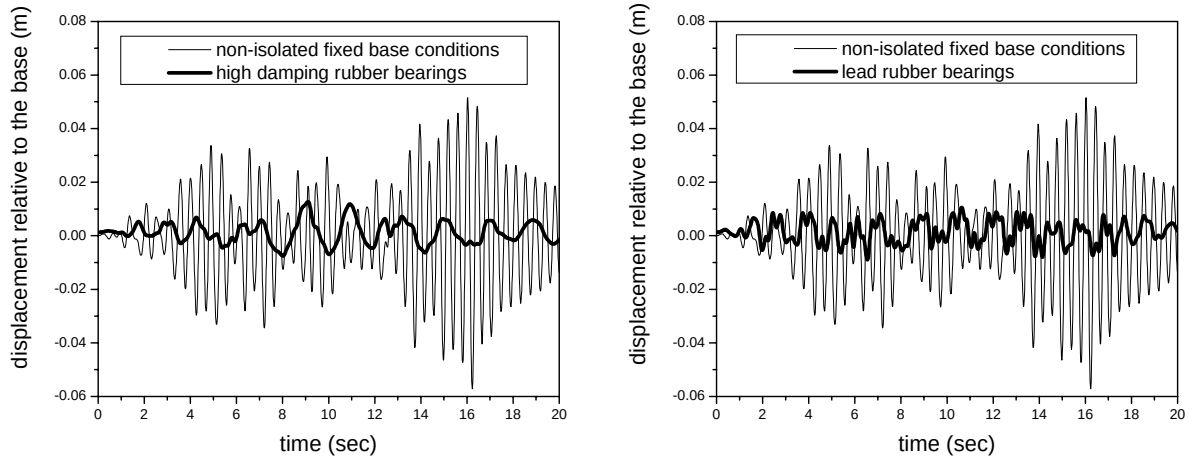

Figure:8 Time histories of the relative to the base displacement of the inner shell at the fluid free surface level

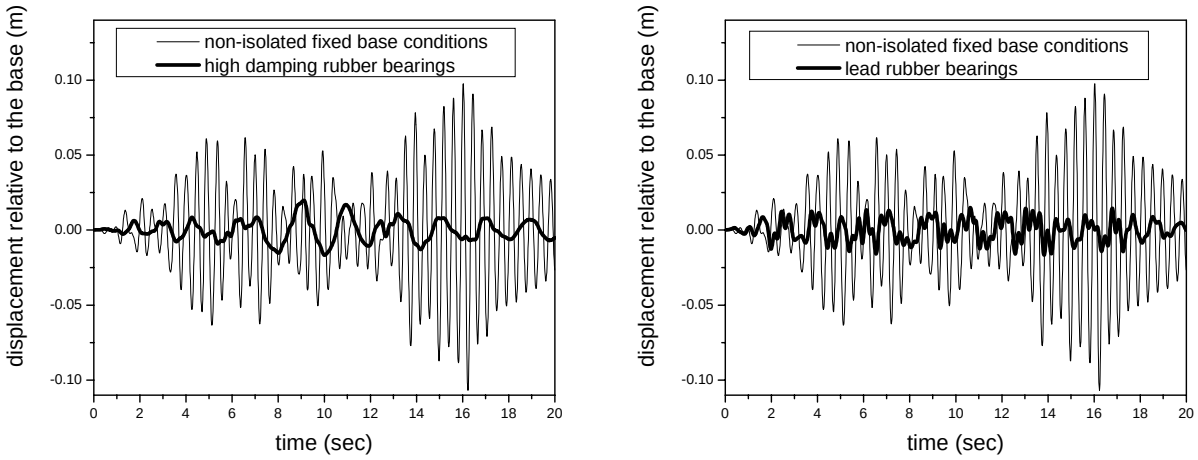

Figure:9 Time histories of the relative to the base displacement of the inner shell at 2/3 of its height

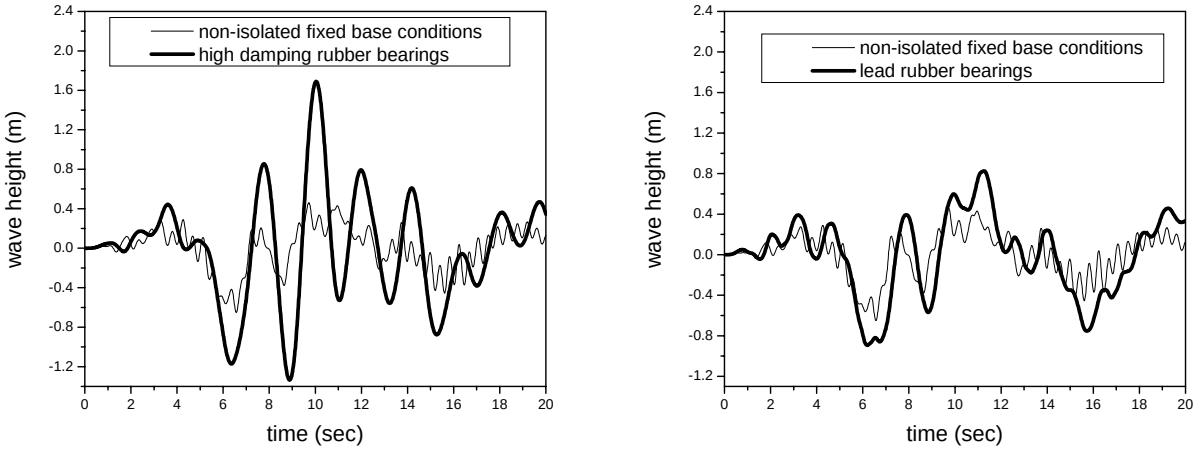

Figure 10 : Wave height time histories at the intersection of the fluid free surface and the inner shell

ACKNOWLEDGMENTS

The authors gratefully acknowledge the financial support by the Environment Programme, Global Change and Natural Disasters of the European Commission, Research Directorate General under Project INDEPTH (EVG1-CT-2002-00065) of the Fifth Framework Program.

REFERENCES

[1] Bomhard, H. and Stempniewski, L (1993) "LNG Tanks for seismically highly affected sites," *Intl. Post-SMiRT Conference Seminar on Isolation, Energy Dissipation and Control of Vibrations of Structures*, Capri, Italy.

[2] Tajirian, F. F. (1998) "Base isolation design for civil components and civil structures," *Proceedings of the Structural Engineers World Conference*, San Francisco, California, July.

[3] Buckle, I. G. and Mayes R. L. (1990) "Seismic Isolation History, Application, and Performance - a World View," Earthquake Spectra 6(2), 161-201.

[4] Tajirian, F. F. (1993) "Seismic isolation of critical components and tanks," *Proceedings of the ATC-17-1 Seminar on Seismic Isolation, Passive Energy Dissipation and Active Control*, San Francisco, California, pp. 233-244.

[5] Zayas, V. A. and Low D.S. (1995) "Application of seismic isolation to industrial tanks," *Proceedings of the ASME/JSME Pressure Vessels and Pipe Conference*, Hawaii, PVP-Vol 319, pp. 273-244.

[6] Soong, T. T. and M. C. Constantinou, eds. (1994), *Passive and Active Structural Control in Civil Engineering, CISM Courses and Lectures No. 345*, Springer-Verlag, Wien-NewYork.

[7] European Committee for Standardisation (2002), *Eurocode 8 European Standard. Design of structures for earthquake resistance, Part 1: General rules, seismic actions and rules for buildings*, ENV1998-1-1.

[8] Swanson Analysis Systems, Inc. ANSYS (1992), *User's Manual for Revision 5.0, Procedures*. Houston, PA.

[9] Anil K. Chopra (1995), *Dynamics of Structures: Theory and Applications to Earthquake Engineering*, Prentice-Hall, New Jersey.

[10] Dusi, A. and Rebecchi, V. (1999), "A Simplified Model for Nonlinear Analysis of Base Isolated Structures: Model Description and Validation," *Seismic Isolation, Passive Energy Dissipation and Active Control of Seismic Vibrations of Structures — Proceedings of the International Post-SMiRT Conference Seminar*, Cheju, Korea, August 23–27.

[11] Naeim, F. and Kelly, J.M. (1999), *Design of seismic isolated structures: From theory to practice*, Wiley, New York.

SEISMIC RESPONSE OF SPHERICAL LIQUID STORAGE TANKS WITH A DISSIPATIVE BRACING SYSTEM

John C. Drosos, Stephanos V. Tsinopoulos and Dimitris L. Karabalis

Department of Civil Engineering
University of Patras
26500, Patras, Greece
e-mail: stsinop@upatras.gr

Keywords: Seismic analysis, viscous dampers, spherical tanks, finite element models, fluid-structure-soil interaction

Abstract. *The seismic response of a typical spherical liquid storage steel tank equipped with a non-linear viscous bracing system is numerically investigated. The numerical analyses are performed by means of a detailed finite element model, taking into account the exact geometry of the steel tank and the fluid-structure-soil interaction effects. The soil-structure-interaction is modeled using discrete mass, spring, and dashpot elements, rigidly connected to the supporting system of the tank. The earthquake motion is in the form of an artificial accelerogram compatible with the Eurocode-8 provisions. Representative results for base shear forces, vertical displacements of the fluid content and displacements at characteristic locations of the spherical tank are presented and compared to those corresponding to a tank with a conventional bracing system. The research has been performed in the frameowork of the project INDEPTH (Development of INnovative DEvices for Seismic Protection of PeTrocHemical Facilities), supported by the Environment and Sustainable Development Programme of the European Commission Research Directorate General (Contract EVG1-CT-2002-00065).*

1 INTRODUCTION

Spherical tanks are usually used in the petro-chemical industry to store pressurized and refrigerated low-density liquids, such as chlorine, suplhur dioxide, carbon dioxide, anhydrous ammonia, polypropylene, etc. The shell of a typical spherical tank is supported by a number of equally spaced columns which are resting on an annular reinforced concrete ring which, for all practical purposes, is considered rigid. The lateral displacement of the structure is restrained by diagonal braces located between adjacent columns, as shown in Figure 1. Conventional bracing systems undertake only uniaxial tension loads since they buckle at low compressive forces.

The seismic behavior of such structures is of great importance since the contained fluids are usually hazardous chemical or flammable fuels, and a possible leak could cause enormous damage such us environmental contamination, fires, explosions, etc., in the broader neighborhood. Therefore, seismic protection systems may prove necessary for new constructions or for retrofitting existing structures, particularly in regions with moderate and high seismicity. The modern anti-seismic techniques can be classified as base isolation and passive energy dissipation techniques. The base isolation approach attempts to isolate the structure at its base by moving dominant frequency of the structure away from the dominant frequency range of the earthquake ground motion. The usual isolators come in the form of rubber–type bearings, such as lead core or high damping rubber bearings, or friction pendulum bearings. On the other hand the passive energy technique uses energy dissipation or damping devices such as viscous dampers, buckling restrained braces, friction devices, etc., in an effort to dissipate a critical portion of the earthquake induced kinetic energy. Although the base isolation technique has been successfully used for the seismic protection of new structures, it may prove ineffective, as far as the associated cost is concerned, in cases where retrofitting is necessary. In these cases the passive energy technique appears to be much more attractive mainly due to its lower cost, compared to the base isolation solution, since merely replaces a conventional bracing system with one that dissipates energy.

Despite intensive research concerning industrial storage tanks in general, only few studies related to spherical storage tanks are available in the literature, Ramaneyulu *et al.* [1], Ciampi and Addessi [2] and Martelli *et al.* [3]. However, the sloshing of liquids in spherical containers has attracted some interest, e.g. Budiansky [4], Abramson, Chu and Garza [5], McIver [6], Evans and Linton [7], Dutta and Laha [8], and Papasryrou *et al.* [9].

In this work the seismic response of a typical spherical storage tank with a conventional or a dissipative bracing system is investigated. The numerical study has been performed on the basis of a detailed finite element model which takes into account the exact geometry of the tank, the fluid-structure interaction effects for an

arbitrary level of filling, the soil-structure interaction using discrete mass-spring-dashpot elements rigidly connected to the supporting system, as well as the non-linearities introduced by either the dissipative bracing system or the tension only behavior of the conventional braces. The dissipative bracing system consists of a series of non-linear viscous fluid dampers. The earthquake motion is assumed to be an artificially created accelerogram compatible with the Eurocode-8 (EC8) provisions. The presented results concern base shear forces, vertical displacements of the fluid content and displacements at characteristic locations of the spherical tank at 50% and 98% fulleness.

2 DESCRIPTION OF STRUCTURE

The structure analyzed in the present study, shown in Fig. 1, is a typical spherical liquid storage tank with a volume of 4200m^3. The contained liquid is assumed to be refrigerated polypropylene with a density of 522Kgr/m^3. The sphere has an inner diameter of 20m, an average shell thickness of 40mm and is constructed from a steel plate with E=2.1GPa, v=0.3 and ρ=7850Kgr/m^3. The equator of the sphere is 12.5m above ground. The sphere is supported by eleven circular columns with an outer diameter of 914.4mm and a wall thickness of 1.7mm. The columns are equally spaced on a circle diameter of 19.63m. The spherical tank is laterally strengthened by pairs of diagonal braces between columns, i.e. 11 pairs in total, as shown in Fig. 1. The braces are made of steel plate 350x30mm the mechanical characteristics of which are the same as those of the spherical container. Each brace is pin-connected to the adjacent columns, at 0.5m and 7.47m above the bottom level of the columns. All braces are considered to be tension-only elements since they buckle at very low compression levels. The damping coefficient of the overall structure has been assumed equal to 2%. The superstructure is supported on a reinforced concrete ring with an outer diameter of 22.12m, a thickness of 2.5m and a height of 2.0m. The foundation is characterized by the following material properties E=30GPa, v=0.29 and ρ=2500Kgr/m^3 and it is considered rigid for all practical purposes. The soil has been chosen, according to EC8 [11] classification, to be of type C (medium soil) with elastic constants E=0.178GPa, v=0.33 and ρ=1834.8Kgr/m^3.

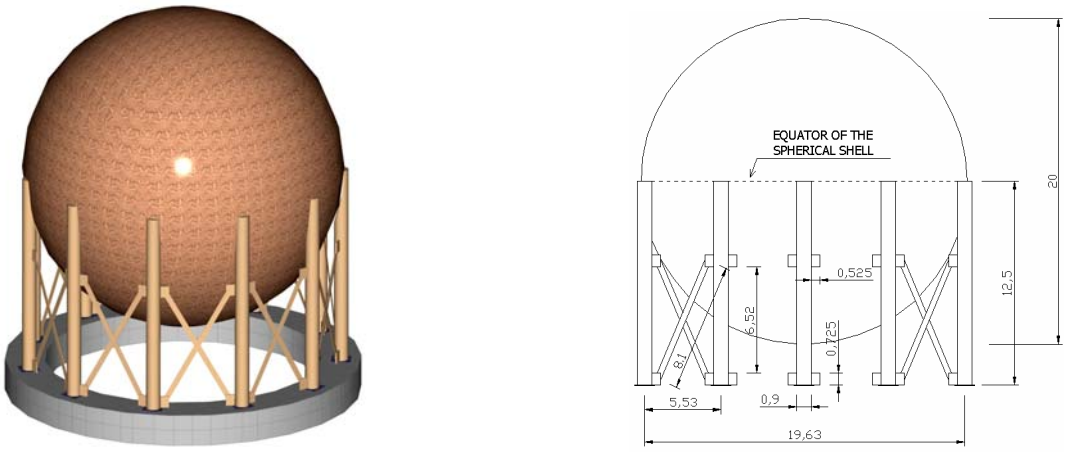

Figure 1. Geometry of spherical liquid storage tank

3 NON LINEAR VISCOUS DAMPER

In the present work, seismic protection for the above-described spherical tank is accomplished by replacing all the braces with viscous fluid damper devices. Viscous fluid dampers are uniaxial, usually non-linear devices whose force is proportional to a power of the velocity, i.e.

$$F = C \cdot V^{a} \tag{1}$$

with C being a constant. For seismic applications the exponent a usually ranges from 0.1 to 1 [10]. In the present study, after some numerical experimentation [11], these constants have been chosen as a =0.15 and C=400 KN/(m/s)$^{0.15}$. However, it should be noted that, opposite to tension-only conventional braces, viscous fluid dampers work both in tension and compression.

4 SEISMIC GROUND EXCITATION

In the present study an artificial seismic ground motion, in accordance to EC8 [11] spectrum for Soil C and soil damping of 5%, is considered [Marti-Crespo-Karabalis]. The ground acceleration has a duration of 20sec and a peak ground acceleration (PGA) of 0.4g. The artificial accelerogram is shown in Fig. 2a, while its compliance to the spectral requirements of EC8 is depicted in Fig. 2b.

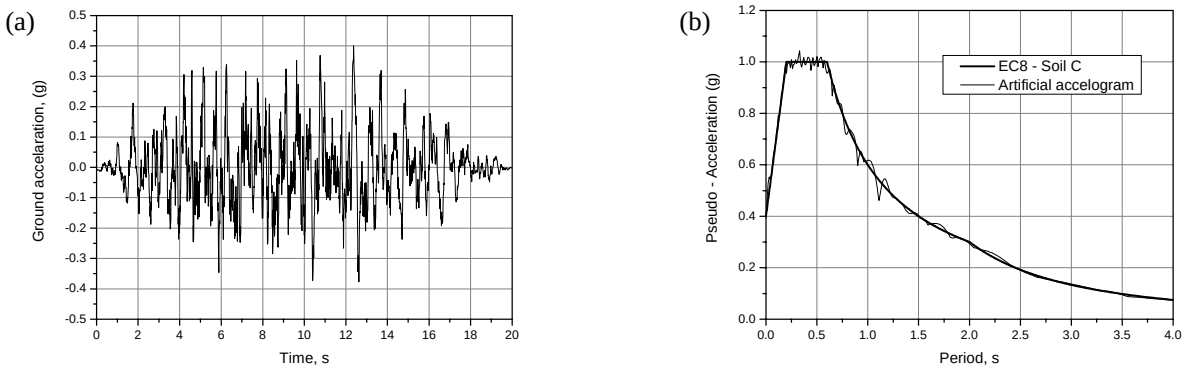

Figure 2: (a) Artificial accelerogram used for the analysis of spherical tank; (b) Compliance of artificial accelerogram to the spectral requirements of the EC8, for soil type C

5 SOIL-STRUCTURE INTERACTION

According to Karavasilis *et al.* [14], the soil-structure interaction (SSI) effects on the dynamic response of a structure supported on a rigid annular foundation can be taken into account by modeling each of the physical degrees-of freedom, i.e. horizontal, vertical, rocking and torsion, of the soil-foundation system as discrete system with two degrees-of-freedom. The discrete 2-mass system considered in the present analysis is shown in Fig. 3, and following the procedures outlined in ref. [14] the constants of all the discrete elements are computed as listed in Table 1. For modeling purposes, the spherical storage tank structure under consideration is connected to the M_1 masses of the discrete systems through rigid connections, as shown in Fig 3.

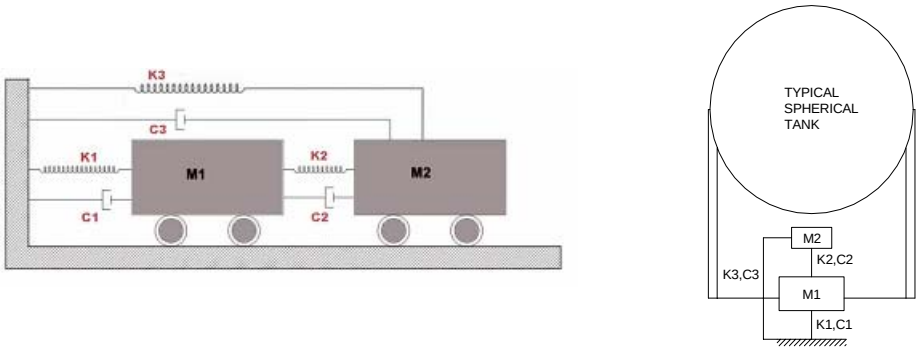

Figure 3: Two degree-of-freedom discrete system for the foundation-soil system modeling

DOF	K_1 [kN/m]	C_1 [kN*s/m]	K_2 [kN/m]	C_2 [kN*s/m]	K_3 [kN/m]	C_3 [kN*s/m]	M_1 [kgr]	M_2 [kgr]
Vertical	4326.8	81.8	3894.1	0	0	61.9	2039	2353
Horizontal	3461.4	37.2	4326.8	0	0	79.3	1725	1098
Torsional	511623.8	1919.3	317559.6	0	0	2626.3	141193	50986
Rocking	370486.2	1414.2	317559.6	0	0	2929.4	117660	58830

Table1: Discrete element constants for the two degree-of-freedom SSI system

6 FEM MODEL

The numerical analysis of the spherical storage tank structure is performed on the basis of detailed FEM model developed with the help of the routines available in the ANSYS Finite Element program [15], as shown in Fig. 4. The spherical shell and the supporting columns are modeled by 10724 four-noded shell elements

(SHELL63) with six DOFs per node. The eight node solid fluid element (FLUID80), with three DOFs per node, has been chosen to model the incompressible fluid content. A total of 3000 or 5300 FLUID80 elements are used, respectively, for the two levels of tank fullness considered in this work, i.e. 50% and 98% fullness. In order to satisfy the continuity conditions between the fluid and solid media at the spherical boundary, the coincident nodes of the fluid and shell elements are constrained to be coupled in the direction normal to the interface, while relative movements are allowed to occur in the tangential directions. The uniaxial "tension only" behavior of the braces is simulated by means of the 3-D spar elements LINK10, which feature a bilinear stiffness matrix, i.e. the stiffness is removed if the element goes into compression. The viscous fluid damper devices are modeled using the 1-D non-linear damper elements COMBIN37. Finally, concentrated mass elements (MASS21) and linear spring-damper elements (COMBIN14) are used to model the discrete elements for the simulation of soil-structure interaction. The motion at the base of the structure is coupled to the motion of the corresponding M_1 masses of the discrete SSI system via a series of rigid body motion constraints.

The above FEM spherical tank model is numerically analyzed by means of a full transient non-linear analysis. The governing equations of motion can be expressed in matrix form as [16]

$$[M]\{\ddot{u}(t)\}+[C(\dot{u})]\{\dot{u}(t)\}+[K(u)]\{u(t)\}=-[M][\ell]\{\ddot{u}_g(t)\} \tag{2}$$

with [*M*], $[C(\dot{u})]$ and $[K(u)]$ being the mass, damping and stiffness matrices of the structure, respectively, $[\ell]$ an influence coefficient matrix, and $\{\ddot{u}_g(t)\}$ the ground acceleration. Eq. (2) is integrated directly in time using the Newmark-β method. The non-linearities, introduced by the "tension-only" behavior of the conventional braces and by the viscous fluid damper devices, require an iterative solution with incremental load steps. In the present study the iterative Newton-Raphson approach is employed [15].

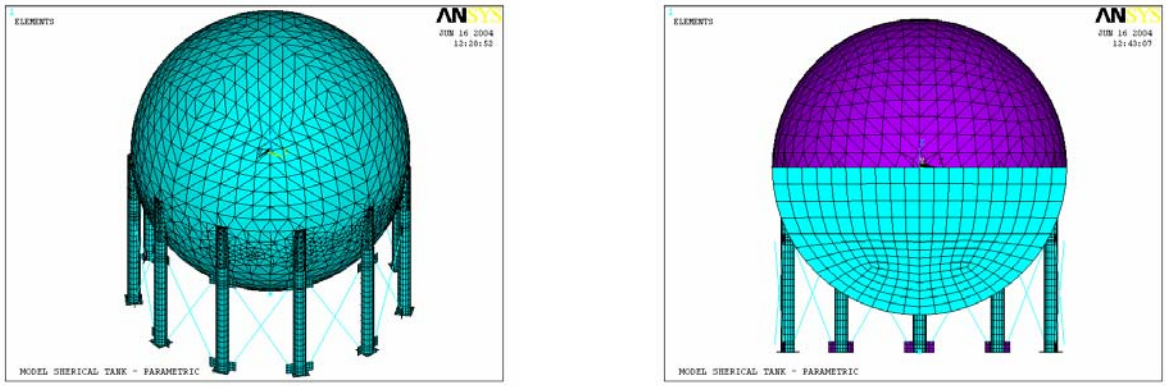

Figure 4: Finite element spherical tank model

7 NUMERICAL STUDY

The seismic response of the spherical liquid storage tank with and without the dissipative bracing system is investigated by performing two types of analyses: (i) modal analysis and (ii) time domain analysis. The problem is solved for two levels of tank fullness, i.e. 50% and 98% fullness. The interested reader can find more detailed analyses in Drosos, Tsinopoulos and Karabalis [17].

7.1 Modal Analysis

Provided that the diagonal braces are virtually non-existent in compression (due to buckling), only one of them, out of each pair of braces, provides stiffness at any given displacement configuration. However, an on-off element is amenable to non-linear analysis only, excluding an eigenfrequency analysis. In order to obtain a sense of the possible modal shapes and corresponding eigenfrequencies, a linear analysis is attempted considering both braces of each pair, but with one-half of their cross section, providing stiffness, in a linear fashion, both in tension and compression. The modal analysis is performed using the reduced method [15], since only lumped mass matrices are produced by the FLUID80 elements. However, the Block Lanzos method

[15] is used to calculate the eigenfrequencies of the empty tank. The eigenfrequencies of the most important modes, based on the mass participation factor (MPF), are listed in Table 2. The results correspond to idealized fixed base boundary conditions, assuming a non-deforming soil subgrade, and SSI conditions as described in section 5.

			1st frequency	2nd frequency
Empty tank	Fixed base	f (Hz)	4.13	44.1
		MPF (%)	97.6	1.16
	SSI	f (Hz)	5.4	3.6
		MPF (%)	61.1	30.5
50% full	Fixed base	f (Hz)	2.82	0.201
		MPF (%)	56.5	38.4
	SSI	f (Hz)	2.55	0.201
		MPF (%)	55.4	35.8
98% full	Fixed base	f (Hz)	1.693	1.691
		MPF (%)	84.00	8.76
	SSI	f (Hz)	1.542	1.541
		MPF (%)	86.4	5.95

Table2: Eigenfrequencies for fixed and SSI boundary conditions and various levels of tank fullness.

7.2 Time Domain Analysis

The seismic response of the spherical tank structure with a dissipative bracing system is compared to that of the tank with conventional bracing in order to investigate the effectiveness of the seismic protection system. The time history analysis corresponds to the artificial earthquake ground motion, described in section 4, applied in horizontal X-direction of the tank.

50% full tank

The time variation of the displacement in the x-direction at the top of the sphere, the total base shear and the vertical fluid displacement at the intersection of the fluid free surface and the tank wall are shown in Figs 5, 6 and 7. Figs 5 and 6 reveal a significant reduction in horizontal movement and base shear of the tank, implying the effectiveness of the seismic protection system. More specifically in Fig 5, the maximum horizontal displacements at the top of the sphere are reduced from 7cm when conventional braces are used to 3.6cm when dissipative ones are employed. Similarly in Fig 6, the total base shear peak responses are reduced from 11586KN to 3560KN. On the other hand, the sloshing vertical displacements of the fluid content, shown in Fig. 7, remain almost the same, as expected, for both bracing systems. This is due to the fact that the natural frequency of sloshing liquid mass (4.975sec) is well apart from the dominant natural frequencies of the structure and corresponds to negligible portion of the seismic excitation, see spectrum of seismic input in Fig. 2(b). In Fig. 8 the hysteretic loop of the viscous damper located almost parallel to the direction of the seismic excitation is plotted.

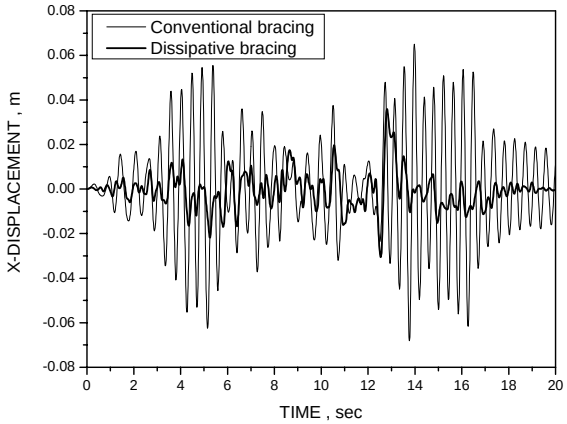

Figure 5: Horizontal displacement at the top of a 50%

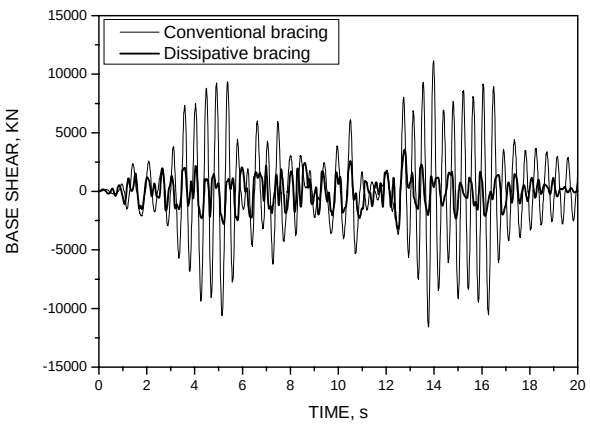

Figure 6: Total base shear force of a 50% full spherical

full spherical tank

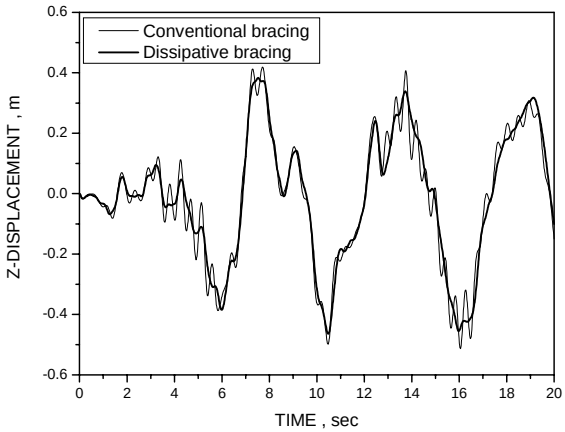

Figure 7:Vertical movement of the fluid free surface for 50% full tank

tank

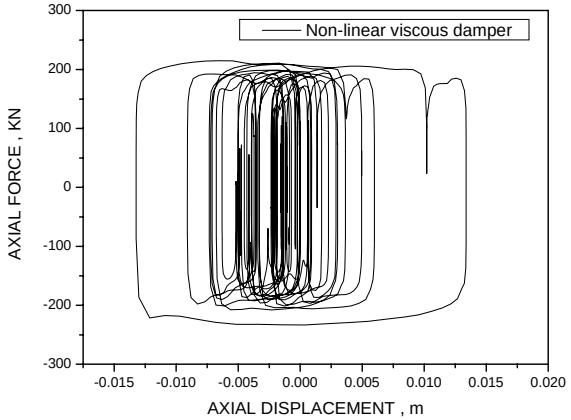

Figure 8: Hysteretic loop of the viscous damper located almost parallel to the excitation for 50% full tank

98% full tank

Similar analyses to the 50% full tank case are performed for an assumed maximum operational level of 98% fullness. Figs 9 and 10 show the time variation of displacement in the x-direction at the top of the sphere and the total base shear, respectively, while in Fig 11 the hysteretic loop of the viscous damper located almost parallel to the direction of the seismic excitation is depicted. In conclusion, percentage reductions in horizontal movement at the top of the sphere and total base shear when dissipative bracing is employed, are in the order of 42% and 74%, respectively.

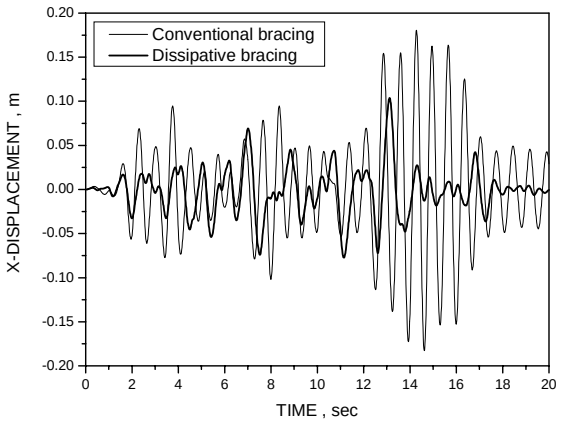

Figure 9: Horizontal displacement at the top of a 98% full spherical tank

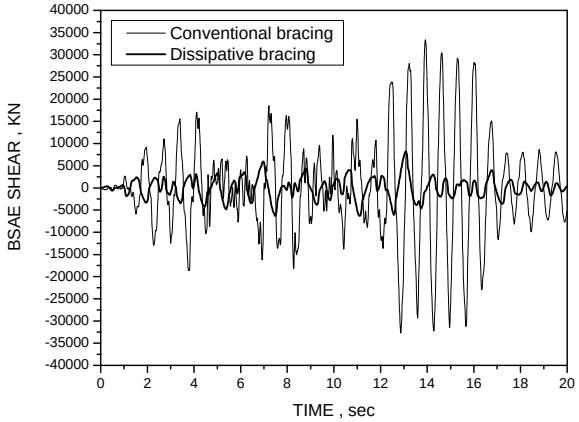

Figure 10: Total base shear force of a 98% full spherical tank

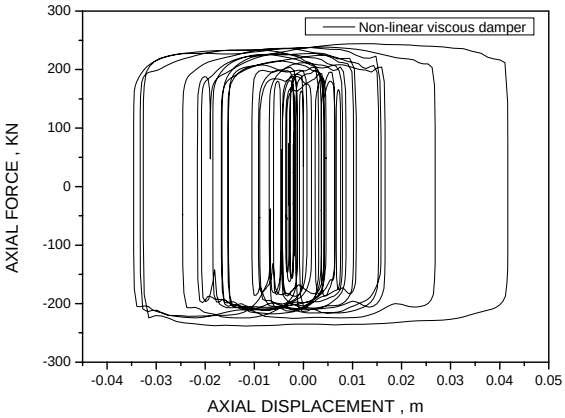

Figure 11: Hysteretic loop of the viscous damper located almost parallel to the excitation, for 98% full tank

ACKNOWLEDGMENTS

The authors gratefully acknowledge the financial support by the Environment Programme, Global Change and Natural Disasters of the European Commission, Research Directorate General under Project INDEPTH (EVG1-CT-2002-00065) of the Fifth Framework Program.

REFERENCES

[1] Ramaneyulu, K., Husain, A., Sehgal, D.K. and Ahmad, S. (2003), "Finite element analysis and reliability assessment of spherical lpg storage tank", IE (I) Journal-MC, 84, pp. 98-103.

[2] Ciampi, V. and Addessi, D. (2001), "Ongoing studies for the application of innovative anti-seismic techniques to chemical plant components in Italy", *Proceedings of 7th International Seminar on Seismic Isolation, Passive Energy Dissipation and Control of Vibration of Structures*, Assisi, Italy, 2-5 October.

[3] Martelli, A., Forni M., Poggianti A. and Spadoni B. (2001), "R&D in progress at ENEA on the innovative anti-seismic techniques, with particular to the industrial plants, *Transactions of SMiRT 16*, Washington DC, USA, August.

[4] Budiansky, B. (1960), ''Sloshing of liquids in circular canals and spherical tanks,'' J. Aerosp. Sci., 27, pp. 161–173.

[5] Abramson, H. N., Chu, W.-H. and Garza, L. R. (1963), ''Liquid sloshing in spherical tanks,'' AIAA J., 1(2), pp. 384–389.

[6] McIver, P. (1989), ''Sloshing frequencies for cylindrical and spherical containers filled to an arbitrary depth,'' J. Fluid Mech., 201, pp. 243–257.

[7] Evans, D. V., and Linton, C. M. (1993), ''Sloshing frequencies,'' Q. J. Mech. Appl. Math., 46, pp.71–87.

[8] Dutta, S. and Laha, M.K (2000), "Analysis of the small amplitude sloshing of a liquid I a rigid container of arbitrary shape using a low-order boundary element method," Int. J. Numer. Meth. Engng, 47, pp. 1633-1648.

[9] Papaspyrou, S., Valougeorgis, D. and Karamanos, S.A. (2003), "Refined solutions of externally induced sloshing in half-full spherical containers," J. Engng Mech., 129, pp. 1369-1379.

[10] Soong, T.T, Dargush, G.F (1997), *Passive energy dissipation systems in structural engineering*, J. Wiley & Sons, New York.

[11] Poggianti, A (2002), "Seismic protection of spherical tanks through the use of dissipative or isolating devices. Numerical analyses on a simplified model", INDEPTH Document IDP-TR-EN-2-02, ENEA, Bologna, Italy.

[12] European Committee for Standardisation (2002), *Eurocode 8 European Standard. Design of structures for earthquake resistance, Part 1: General rules, seismic actions and rules for buildings*, ENV1998-1-1.

[13] Crespo, M, Marti, J and Karabalis, D.L. (2002), "Definition of seismic hazard target facilities and general hazard", INDEPTH Document IDP-IC-PR-1-02, Principia Ingenieros Consultores, S.A., Madrid.

[14] Karavasilis, T.L., Rizos, D.C. and Karabalis, D.L. "A discrete model for foundations with internal openings", Soil Dynamics and Earthquake Engineering (submitted).

[15] Swanson Analysis Systems, Inc. ANSYS (1992), *User's Manual for Revision 5.0, Procedures*. Houston, PA.

[16] Chopra, A.K. (1995), *Dynamics of Structures: Theory and Applications to Earthquake Engineering*, Prentice-Hall, New Jersey.

[17] Drosos, J.C., Tsinopoulos, S.V. and Karabalis, D.L. (2004), "Seismic analysis of isolated spherical tanks", INDEPTH Document IDP-IC-UP-2-07, Dept. of Civil Engng, Univ. of Patras, Patras, Greece.

5th GRACM International Congress on Computational Mechanics
GRACM 05
Limassol, 29 June – 1 July, 2005

SYSTEM IDENTIFICATION OF NON-LINEAR HYSTERETIC SYSTEMS WITH APPLICATION TO FRICTION PENDULUM ISOLATION SYSTEMS

Panos C. Dimizas and Vlasis K. Koumousis

Institute of Structural Analysis and Aseismic Research
National Technical University of Athens
NTUA, Zografou Campus GR-15773, Athens, Greece
e-mail: vkoum@central.ntua.gr, web page: http://users.ntua.gr/vkoum

Keywords: System Identification, Hysteresis, Friction Pendulum Systems, Seismic Isolation.

Abstract. *In this work, the parameter identification of non-linear dynamical systems is presented. More specifically the non-linear hysteretic behavior of seismic isolators modeled by the versatile Bouc-Wen model such as FPS is determined based on given data. The primal objective of this paper is to develop a parametric identification method for the modeling of FPS seismic isolator from periodic vibration experimental data. The estimation of the model parameters based on measured data from periodic experiments is implemented using a time domain method. The Bouc-Wen differential model is adopted to take into account the hysteretic frictional damping of the FPS bearings. Then, the parameter identification problem is solved using nonlinear optimization methods such as the Levenberg-Marquardt algorithm. The identification results, of the proposed method, are verified by numerical simulations and the accuracy of the identified parameters is verified by comparing the experimentally measured and the identified time histories.*

1 INTRODUCTION

In recent years, the Friction Pendulum System (FPS) has become a widely accepted device for seismic isolation of structures. The concept is to isolate the structure from ground shaking during strong earthquake. Seismic isolation systems like the FPS are designed to lengthen the structural period far from the dominant frequency of the ground motion and to dissipate vibration energy during an earthquake. The FPS consists of a spherical stainless steel surface and a slider, covered by a Teflon-based composite material. During severe ground motion, the slider moves on the spherical surface lifting the structure and dissipating energy by friction between the spherical surface and the slider.

Friction Pendulum Systems exhibit nonlinear inelastic behavior under severe dynamic loading such as earthquakes. In the case of cyclic loading the nonlinear restoring force of such isolators exhibits hysteretic loops and is memory-dependent. It depends not only on the instantaneous deformation, but also on the history of deformation. This memory nature makes modeling and analysis more difficult than other non-linear systems. A widely used model that describes hysteretic behavior that belongs to the class of endochronic models is that of Bouc-Wen [1]. This model consists of a system of nonlinear differential equations where the memory-depended nature of hysteresis is taken into account with the use of an extra variable. Different values of the parameters of this model reveal a wide range of different mechanical behavior. This accounts for softening/hardening behavior, stiffness degradation, strength deterioration, pinching etc. An appropriate choice of parameters determined by the identification algorithm on experimental data makes it possible to describe sufficiently the non-linear dynamic behavior of a hysteretic system.

In the past two decades, several researchers have devoted their efforts to identify the parameters of the Bouc-Wen model using experimental data. From a mathematical standpoint, determination of the hysteretic loop parameters by identification is a problem of non-linear multivariate optimization. In this paper, this problem is solved using a popular gradient optimization algorithm called the Levenberg-Marquardt method. In section 2, the versatile Bouc-Wen model is presented to take into account the inelastic behavior of the FPS bearings. The time domain identification algorithm is presented in section 3. The effectiveness and accuracy of the proposed algorithm is addressed in section 4 with the aid of a numerical study. Finally, this paper concludes with the presentation of identification results using the proposed algorithm and a summary of the findings in section 5.

2 HYSTERETIC MODEL

2.1 Bouc-Wen hysteretic model

In the context of a forced single degree of freedom hysteretic oscillator the equation of motion using the Bouc-Wen model is as follows:

$$m\ddot{x} + c\dot{x} + akx + (1-a)kz = f \tag{1}$$

where m, c, k, f and a are the mass, damping coefficient, stiffness, external excitation and plastic to elastic stiffness ratio respectively. The hysteretic auxiliary variable z, according to the Bouc-Wen model is given by:

$$\dot{z} = A\dot{x} - |z|^n \left(\gamma sign(\dot{x}z) + \beta\right)\dot{x} \tag{2}$$

The ultimate value of z is given by:

$$z_{MAX} = \left[\frac{A}{\beta+\gamma}\right]^{\frac{1}{n}} \tag{3}$$

In the case of system identification, apart from the mass m that can be measured, all the other parameters of the model are to be identified resulting in the following unknown parameter vector:

$$p = \begin{bmatrix} a & k & c & A & \beta & \gamma & n \end{bmatrix}^T \tag{4}$$

2.2 Identification issues and model limitations

The Bouc-Wen model parameters A, β, γ are the one that control the hysteretic loop shape, whereas parameter n affects the smoothness of the hysteretic curves. A large variety of complex non-linear hysteretic dynamic behavior can be represented by the Bouc-Wen model through an appropriate choice of these parameters. Wong et al [2, 3] conducted an extensive study of the parameters effect on the response of the Bouc-Wen model. On the other hand, Erlicher and Point [4] proved the constraints that must hold for the Bouc-Wen model parameters so that it is thermodynamically admissible. Therefore, during Bouc-Wen model identification, one must also take into account the restrictions and constraints regarding the Bouc-Wen model parameters.

Another issue that has to do with the identification of the Bouc-Wen model is the non-smoothness of the hysteretic restoring force. The main advantage of the Bouc-Wen model is the ability to capture non-smooth dynamic behavior as the sliding of an FPS seismic isolator using an analytic mathematical formulation. However, the implementation of identification algorithms on rapidly changing dynamical systems, such as the FPS isolators, renders the common identification methodologies unable to track them. As claimed by Ching and Glaser [5], the reason is that all these identification methodologies possess the inherent assumption that the degree of change of the dynamical system studied is uniform in time. So, systems with frictional slip like the FPS are difficult to be identified. Additionally, the problem identification of the Bouc-Wen model becomes harder because of the fact that in certain cases, different combinations of some parameters may produce almost identical hysteretic loops [6].

2.3 Modelling of FPS seismic isolators

As explained in the last section, identification of the seven unknown parameters of equation possesses great difficulties. However, in the case of FPS bearings, the identification problem can be simplified. The natural period of a FPS bearing is only related to the radius of the concave surface R:

$$T = 2\pi\sqrt{\frac{R}{g}} \tag{5}$$

where g is the acceleration of gravity.

With the aid of equation (5), the post yield (sliding) stiffness of the FPS can be calculated by:

$$ak = m\frac{g}{R} \tag{6}$$

It is common among researchers [7] to assume that in the case of FPS bearings, energy is dissipated by means of frictional sliding of the isolator, so one can assume that there is very little or not at all viscous damping:

$$c \approx 0 \tag{7}$$

Finally, the value of parameter a usually, in the case of FPS isolators, is taken equal to:

$$a \approx 0.1 \tag{8}$$

Using equation (7), the equation of motion of the FPS becomes:

$$m\ddot{x} + akx + (1-a)kz = f \tag{9}$$

where the hysteretic auxiliary variable z is given by equation (2).

The post yield stiffness ak can be calculated by equation (6) resulting to the following unknown parameter vector:

$$p = \begin{bmatrix} A & \beta & \gamma & n \end{bmatrix}^T \tag{10}$$

One can see that the unknown parameters were reduced from seven to four and that in the case of a periodic vibration experiment, the hysteretic auxiliary variable can be easily measured.

3 TIME DOMAIN PARAMETER ESTIMATION

In the case of a periodic vibration test of a FPS bearing, both the cyclic excitation f and response x are measured. One can then evaluate the post yield stiffness ak and the evolution of the hysteretic auxiliary variable z using equations (6) and (9) respectively. The evolution of $\dot{z}$ can then be calculated by numerical differentiation of the variable z. Equation (2) can be rewritten as:

$$D(t) = \dot{z} - A\dot{x} + |z|^n \left(\gamma sign(\dot{x}z) + \beta\right)\dot{x} \tag{11}$$

If the actual force-displacement relation conforms completely to the Bouc-Wen model and p are the true model parameters, then equation (11) should be equal to zero regardless of time t. In fact, equation (11) never approaches zero due to model errors and measurement noise. Hence, the identification problem becomes a non-linear optimization one, with equation (11) representing the error residuals. The objective function whose minimum one seeks, in terms of non-linear least squares, becomes:

$$F(p) = \frac{1}{2}\sum_{1}^{t} D_t^2(p) \tag{12}$$

The resulting non-linear least-squares optimization problem can be solved using the Levenberg-Marquardt algorithm [8]. The parameters that minimize the objective function (12) are found by the iteration formula of the algorithm:

$$p^{t+1} = p^t - \left[J^T J + \mu I\right]^{-1} J^T D \tag{13}$$

where J is the Jacobian matrix and μ the Levenberg – Marquardt parameter.

The Jacobian matrix J that is required for the implementation of the algorithm can be derived analytically by the equations:

$$\begin{aligned}
\frac{\partial D(t)}{\partial A} &= -\dot{x} \\
\frac{\partial D(t)}{\partial \beta} &= \dot{x} \mid z \mid^{n} \\
\frac{\partial D(t)}{\partial \gamma} &= \dot{x} \mid z \mid^{n} \; sign(\dot{x}z) \\
\frac{\partial D(t)}{\partial n} &= \dot{x} \mid z \mid^{n} \; \ln(|z|)\left(\gamma\, sign(\dot{x}z) + \beta\right)
\end{aligned} \tag{14}$$

In the time domain implementation of the algorithm, the residuals are calculated at each iteration step with the aid of equation (11) using the time series from the periodic vibration experiment. After that, the Jacobian matrix is calculated analytically using equation (14). Finally, the new parameter values are estimated using the iteration formula shown in equation (13). In the case where there is a range of different periodic vibration tests, the algorithm is implemented in a similar way, but using as an objective function the sum of residuals of each experiment.

The Levenberg-Marquardt algorithm is a popular gradient method for unconstrained optimization. To improve convergence and stability, one can impose constraints on the algorithm by introducing new parameters enforced by logistic transformations as Zhang et al. [9] suggest.

4 APPLICATION TO FRICTION PENDULUM SYSTEMS

The identification method presented in the previous sections was examined through identification of FPS bearings. In order to evaluate the accuracy of the identification algorithm, a set of realistic parameters were used to numerically generate experimental data. The experimental data were obtained by solving numerically the system of non-linear differential equations (9) and (2) using a 4th-5th order Embedded Runge Kutta method under sinusoidal excitation *f*. The Bouc-Wen model parameters used throughout the numerical simulation are summarized in table 1.

m	a	k	c	A	β	γ	n
1	0.1	10	0	1	0.1	0.9	2

Table 1: Bouc-Wen model parameter values used throughout the numerical simulation

This set of parameters yields maximum value for the hysteretic auxiliary parameter $z_{MAX} = 1$ and it was chosen because it is suggested by other researchers [10] for capturing the dynamic behavior of FPS seismic isolators in a sufficient way. According to this set of parameters, the natural period of such a system is $T = 6.3\,\text{sec}$.

To verify the time domain identification algorithm, a numerical experiment was conducted using sinusoidal excitation ($f = 15\sin 0.1t$). The amplitude of the excitation was chosen so that strong nonlinearities and sliding of the isolator was manifested. As claimed by other researchers [11], the identification method gives best results with a few cycles of non-linear response. The hysteretic loops and the evolution of the hysteretic auxiliary variable z are shown in figure 1 and 2 respectively.

The identification method was conducted on the steady state part of the experimental data using a two-period signal. To examine whether the algorithm was sensitive to initial parameter guesses, four sets of initial parameter values were tried. The initial values used are shown in table 2. The results of identification algorithm are summarized on table 3 and it becomes evident that the method behaved very well since it managed to converge to the global minimum of the objective function.

	Initial Parameter Values Sets			
Model Parameters	1st	2nd	3rd	4th
A	0.1	1	5	10
β	0.1	1	5	10
γ	0.1	1	5	10
n	0.1	1	5	10

Table 2: Different initial parameter values sets.

		Identified parameter using different initial sets			
Model Parameters	Real	1st	2nd	3rd	4th
A	1	1.002	1.002	1.002	1.002
β	0.1	0.1076	0.1076	0.1076	0.1076
γ	0.9	0.8944	0.8944	0.8944	0.8944
n	2	1.9962	1.9962	1.9962	1.9962
z_{MAX}	1	1	1	1	1

Table 3: Identification results.

In order to examine the effect of noise on the identification accuracy the numerical experimental data were corrupted with noise:

$$x(t) = x(t) + \varepsilon r \tag{15}$$

where ε represents the signal to noise ratio level and r is a random variable with zero mean and unit variance. The time series of numerically obtained displacement and velocity were corrupted with discrete noise of various levels and the identification method was implemented again using various initial conditions. The results of the identification method using the second set of initial conditions are summarized in table 4.

		Identified parameter using different noise levels			
Model Parameters	Real	e=0.001	e= 0.005	e= 0.01	e=0.02
A	1	1.002	1.0095	1.036	1.1542
β	0.1	0.1078	0.1455	0.2591	0.5572
γ	0.9	0.8941	0.8626	0.7721	0.5839
n	2	1.9888	1.8091	1.3876	0.6507
z_{MAX}	1	1.0001	1.0008	1.0033	1.0176

Table 4: Identification results using noise corrupted data.

It becomes clear from table 4 that the identification accuracy is reduced with the increase of the level of noise. In the case of substantial noise, identified parameter values may be completely different from the real ones. The most sensitive parameter seems to be *n*. The values of the other parameters seem to deviate from the real ones, but in a way such that the ultimate value of the hysteretic variable *z* is very close to the real one.

Zhang et al. [9] propose the use of digital filters in series into the identification algorithm for expanding the capabilities of the optimization algorithm. Following their suggestion, the noisy experimental data were filtered using two digital filters. The first was a median filter and the second was a least-squares lowpass filter also known as the Savitzky-Golay FIR lowpass filter. The algorithm was implemented for various noise levels and the results are summarized in table 5.

		Identified parameter using different noise levels			
Model Parameters	Real	e=0.01	e= 0.02	e= 0.05	e=0.1
A	1	1.004	1.0037	1.0092	0.9623
β	0.1	0.1064	0.1049	0.1482	0.0793
γ	0.9	0.8946	0.8952	0.8576	0.876
n	2	1.9889	1.9644	1.9212	1.8872
z_{MAX}	1	1.0015	1.0019	1.0018	1.0038

Table 5: Identification results using digitally filtered data.

A comparison between table 4 and table 5 shows that noise pre-filtering of the experimental data expands significantly the accuracy and effectiveness of the proposed identification algorithm. A comparison between the hysteretic loops obtained from noisy and noise pre-filtered data is shown in figures 3 and 4.

5 CONCLUSIONS

An identification method is proposed for the estimation of parameters of the Bouc-Wen model based on experimental data. The identification problem is solved using nonlinear optimization methodologies developed in the time domain. Parameter estimation was accomplished using the gradient Levenberg-Marquardt method. It was shown that the identification method was able to capture the inelastic dynamic behavior in the case of reliable experimental data. From the parametric studies conducted, the method was found to be insensitive to the initial guesses of the parameter values.

The effect of noise on the accuracy of the method was studied extensively. It was found that the method is sensitive to noise-corrupted data. As far as the Bouc-Wen model parameters are concerned, the presence of noise seems to play an important role in the final parameter values, especially for the exponential parameter n. It was also shown that a change in this parameter requires a significant change in the other parameter values in order to fit the same hysteretic loops. However, it was shown that by digital filtering the noisy experimental data, one can expand the capabilities and the accuracy of the identification method significantly.

REFERENCES

[1] Wen, Y. K., (1976), "Method of random vibration of hysteretic systems" J. Engineering Mechanics Division 102, pp. 249-263.

[2] Wong, C. W., Ni, Y. Q. and Ko, J. M., (1994), "Steady state oscillation of hysteretic differential model. I: Response analysis" J. Engineering Mechanics, 120, pp. 2271-2298.

[3] Wong, C. W., Ni, Y. Q. and Ko, J. M., (1994), "Steady state oscillation of hysteretic differential model. II: Performance analysis" J. Engineering Mechanics, 120, pp. 2299-2325.

[4] Erlicher, S. and Point, N., (2004), "Thermodynamic admissibility of Bouc-Wen type hysteresis models" Comptes Rendus Mecanique, 332(1), pp. 51-57.

[5] Ching, J. and Glaser, S. D., (2003), "Tracking rapidly changing dynamical systems using a non-parametric statistical method based on Wavelets" Earthquake Engineering & Structural Dynamics, 32, pp. 2377-2406.

[6] Ni, Y. Q., Ko, J. M. and Wong, C. W., (1998), "Identification of non-linear hysteretic isolators from periodic vibration tests." J. Sound and Vibration, 217(4), pp. 737-756.

[7] Nagarajaiah, S. and Constantinou, M. C., (1989), "Nonlinear dynamic analysis of three dimensional base isolated structures (3D-BASIS)" Buffalo, NY, National Center for Earthquake Engineering Research.

[8] Marquardt, D., (1963), "An algorithm for least-squares estimation of nonlinear parameters" SIAM J. Appl. Math., Vol. 11, pp. 431-441.

[9] Zhang, H., Foliente, G. C., Yang, Y. and Ma, F. (2002), "Parameter identification of inelastic structures under dynamic loads." Earthquake Engineering & Structural Dynamics, 31, pp. 1113-1130.

[10] Constantinou, M. C., Mokha, A. and Reinhorn, A. M., (1990), "Teflon bearings in base isolation II: Modelling" J. Struct. Engrg. ASCE, 116(2), pp.455-474

[11] Sues, S. T., Mau, S., T., and Wen, Y. K., (1988), "Identification of Degrading Hysteretic Restoring Forces" J. Engrg. Mech., ASCE, 114, pp.833-846.

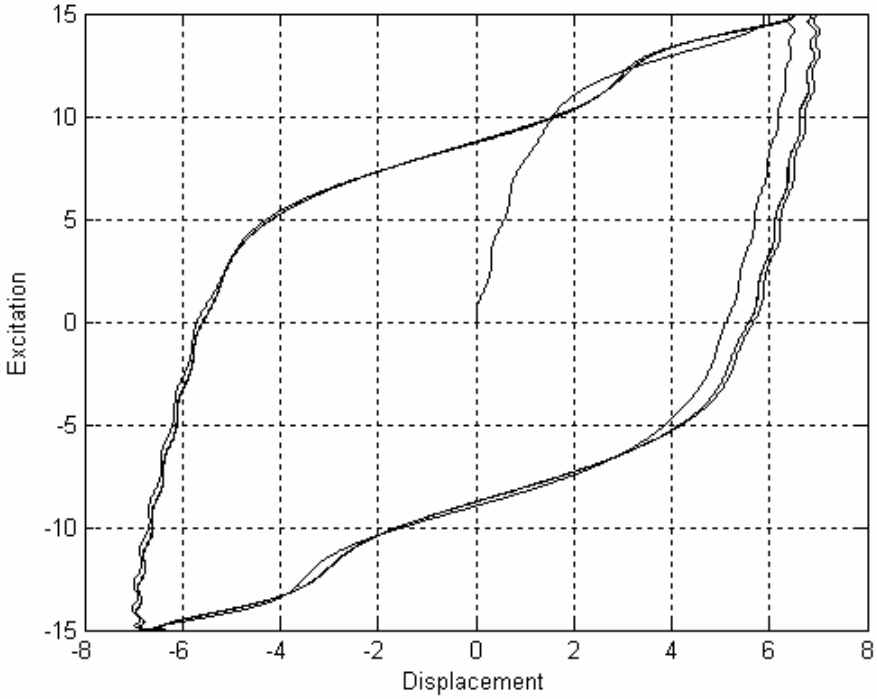

Figure 1. Hysteresis loops obtained by numerical simulation

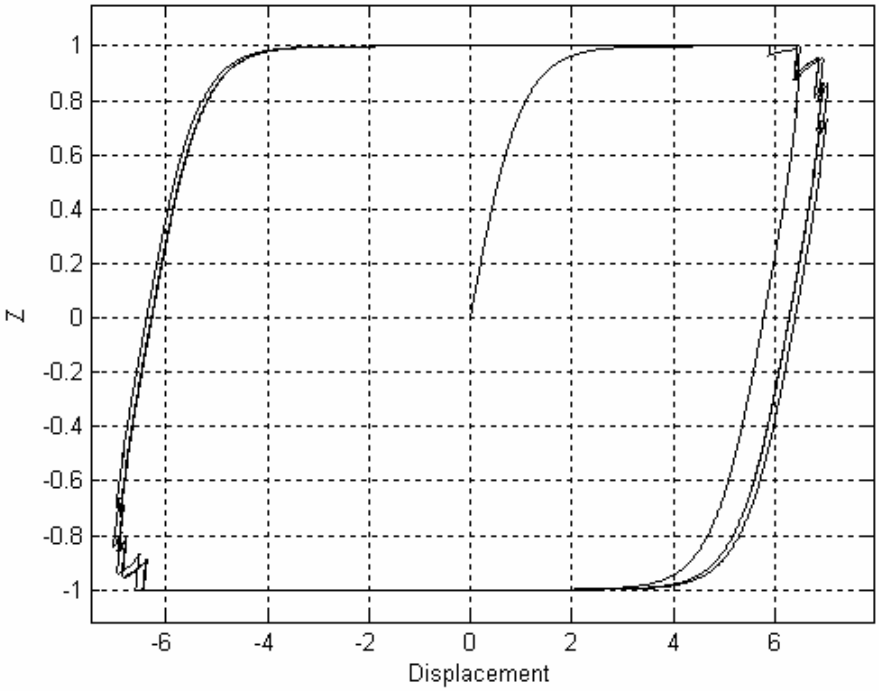

Figure 2. Hysteresis loops obtained by numerical simulation

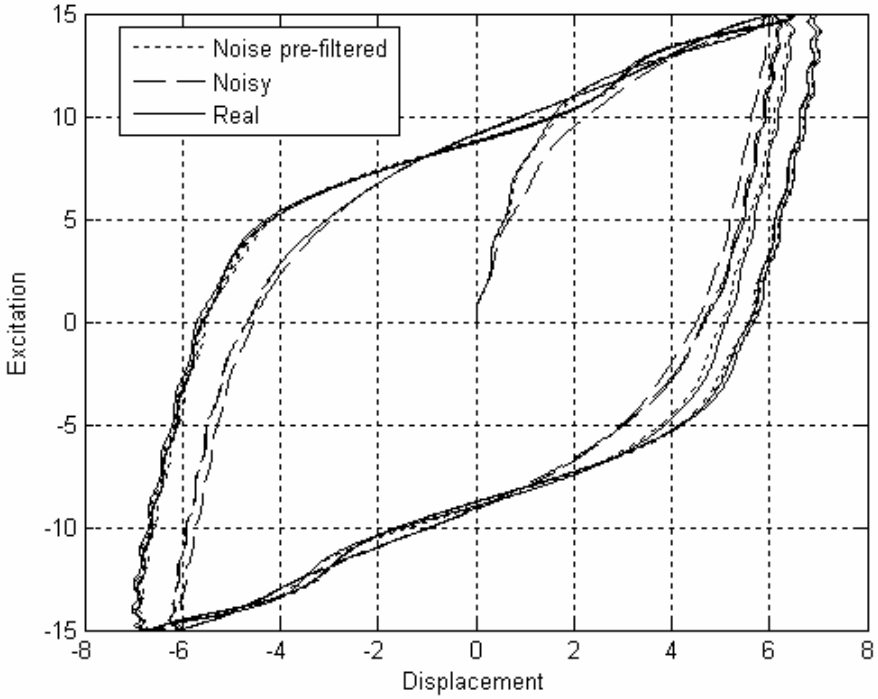

Figure 3. Comparison between hysteresis loops obtained from noisy data and noise pre-filtered data.

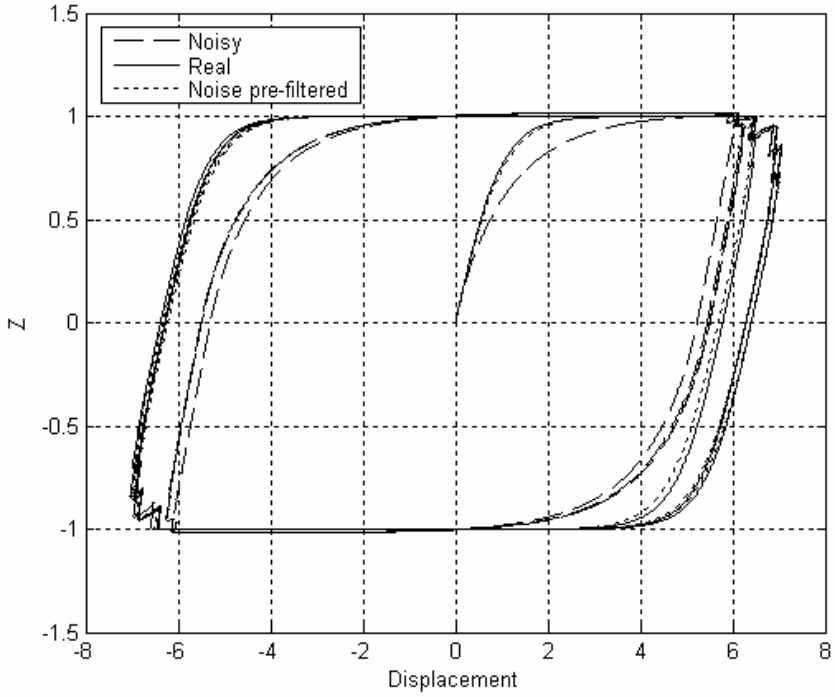

Figure 4. Comparison between hysteresis loops obtained from noisy data and noise pre-filtered data.

A COMPUTER PROGRAM FOR 3D INELASTIC ANALYSIS OF R/ C STRUCTURES

Eleni N. Chatzi, Savvas P. Triantafillou and Vlasis K. Koumousis

Institute of Structural Analysis and Aseismic Research
National Technical University of Athens
NTUA, Zografou Campus GR-15773, Athens, Greece
e-mail:vkoum@central.ntua.gr, web page: http://users.ntua.gr/vkoum

Keywords: inelastic analysis, time history, Bouc-Wen, damage index

Abstract. *A new computer program "Plastique", for the inelastic dynamic analysis of R/C structures is presented. A macro modeling approach is implemented in which structural members are represented by a single nonlinear element. Three different types of 2D-macro elements are formulated namely, beams, columns and shear walls. The mechanical properties of each element are calculated through a flexibility formulation based on both element edge sections and a distributed plasticity law. A fiber model is used to define the monotonic strength envelope at each section. The hysteretic behavior of structural elements is monitored by a smooth hysteretic model of Bouc-Wen type. This model is capable of expressing the stiffness degradation, strength deterioration and pinching phenomena which are observed in R/C elements in cyclic loading. Plane frames consisting of combinations of plane elements are linked at the levels of floors with diaphragms to produce a 3D mathematical model of the structure. Solutions are obtained by direct integration of the equations of motion, while an iterative procedure is implemented to satisfy equilibrium at every time step. Finally, a damage analysis is performed using an appropriate damage model. Numerical examples are presented, revealing the features of the program.*

1 INTRODUCTION

A problem of significant importance in structural engineering deals with the response of R/C structures subjected to dynamic loading. For load factored linear elastic analysis, suggested by the codes, the results are quite satisfactory, but do not reveal the characteristics of the true behaviour of the structure. However, if inelastic response is taken into account, more refined models are needed as to achieve a realistic behaviour. In recent years, significant research has been carried out in order to overcome the difficulties arising in such an analysis. Difficulties emanate not only from the inherent complexity of R/C structures, but also from the uncertainties related to terms such as dynamical loading, material nonlinearity and hysteresis.

The macro-modeling of structures has been one of the main methods introduced to simulate these complex phenomena. In a macro-modeling simulation, the field of knowledge concerning the actual behaviour of reinforced concrete is incorporated in the structure using an element–based approach. In such a way, the well established, from matrix structural analysis, beam element is enriched with a moment curvature envelope describing the behaviour of both end sections, a hysteretic law and a relevant yield penetration rule for the beam. By introducing such an elasto-plastic element, one is able to simulate the gradual shift of the mechanical properties of the element as it passes from the elastic to the inelastic region of its response. The overall behaviour of the structure is assessed using a proper damage index.

An aspect of utmost importance, for a non linear analysis, is the hysteretic rule needed to model the cyclic response of the structure. Over the last twenty years, significant development has occurred in the so-called phenomenological approach of hysteresis. Beginning with Bouc's original formulation (1967, 1969, 1971) of the single degree degrading hysteresis model with pinching, many modifications have been subsequently introduced, such as the Bouc-Wen model (1976, 1980), the Baber-Noori model (1985, 1986) and the Reinhorn model (1996). These hysteresis models –also known as smooth hysteretic models- are capable of simulating a number of different types of loops using a single smooth hysteretic function affected by a set of user-varied parameters. In doing so, one can easily model the three main attributes describing the cyclic response of R/C elements-stiffness degradation, strength deterioration and pinching behaviour due to bond-slip effects.

Following these rules, many computer programs have been developed, capable of performing a non-linear structural analysis such as DRAIN-2D (Kanaan and Powell,1973), SARCF (Chung et al.,1998; Gomez et al.,1990), IDARC (Park et al., 1978;Kunnath et al., 1992) and ANSR (Oughourlian and Powell,1982). "*Plastique"* code presented herein, although it keeps the elastoplastic behaviour within the 2D plane frames works with a 3D stiffness of the entire structure based on diaphragmatic action.

2 MATERIAL PROPERTIES

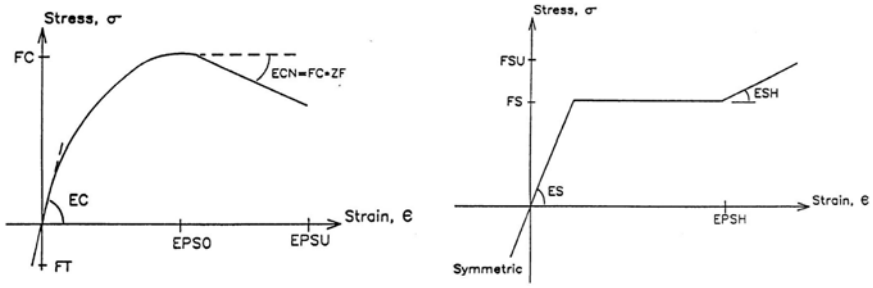

Figure 1. Stress –Strain diagrams a) for unconfined concrete and b) for reinforcing steel

Material properties are defined through certain conventional stress-strain curves both for unconfined concrete and reinforcing steel. In the former a parabolic stress-strain relationship with a softening branch is used, while in the latter a bilinear stress-strain diagram with hardening is implemented. The aforementioned stress – strain curves are depicted in Figure 1.

3 ELEMENT MODELING

Three different types of two dimensional structural elements can be modelled in the present version of the programme, namely beams, columns and shear walls. By combining such elements one assembles multistorey plane frames, which are coupled through rigid diaphragms at the floor levels to create a 3D model of the structure.

3.1 Beam Element

Beam elements are considered as flexural elements with shear deformations taken into account while, axial deformations are neglected as the beams are part of the diaphragm. Beside the flexural part two rigid zones are introduced one at each end to account for the stiffness increase at the joint, if needed. The element stiffness matrix varies throughout the analysis due to plasticity effects. In order to simulate such effects a hysteretic law and a spread plasticity model are used. The hysteretic model acts upon an initial moment-curvature relationship, a skeleton curve. A skeleton curve must be defined for each one of the edge sections of the element. Such a curve can be either user defined or computed by a fiber model given certain properties of the section under consideration such as geometry, concrete and reinforcement properties.

3.2 Column Element

The column element formulation is identical to the one mentioned above. However, in this case axial deformations are taken into account.

3.3 Shear Wall Element

Shear wall elements are modelled combining an axial linear-elastic spring, a nonlinear shear and a nonlinear flexural spring in series. In this case one defines not only a moment-curvature skeleton curve, but a shear force-shear deformation curve as well. These curves can be either user defined, or computed through a fiber model.

4 SPREAD PLASTICITY MODEL

Inelastic deformations vary along the element's length. Consequently an element will also exhibit different flexibility characteristics. In order to formulate the flexibility matrix of such an element a spread plasticity model is incorporated in the programme. This model can formulate the element flexibility matrix taking into account the current stiffness (i.e. flexural stiffness concerning beams and columns and also shear stiffness for walls) at each end section, a corresponding yield penetration length and/or the elastic core stiffness depending on the values of the yield penetration lengths.

5 YIELD PENETRATION MODEL

A yield penetration model is used to compute the yield penetration lengths at the end sections of the element as shown in Figure 2. Yield penetrations parameters α_A and α_B specify the portion of the element where the current moment is greater than the corresponding section's yield moment. For simplicity, a linear moment distribution is assumed even in the case of distributed loads. However one can subdivide each structural element in more elements in order to capture different types of moment variation.

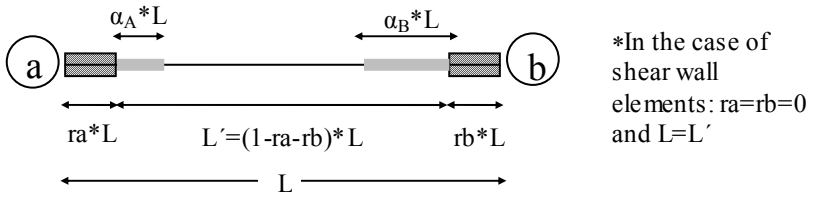

Figure 2. Yield Penetration Parameters

As long as the current moment distribution is defined, a set of geometrical in nature rules is used in order to define both the yield penetration lengths and the core stiffness. The yield penetration parameters are checked with the previous maximum penetration lengths. The plastic state of the element can only move into increasing penetration lengths.

6 THE HYSTERETIC MODEL

The smooth model presented herein is a variation of the model originally proposed by Bouc (1967) and modified by several others (Wen 1976; Baber Noori 1985, Reinhorn 1996). The model was developed in the context of moment-curvature relationships of beam-columns. Therefore, the stress variable is here referred to as "moment" (M) and the strain variable as "curvature" (φ). However, these can be replaced by any other work-conjugate pair.

The use of such a hysteretic constitutive law is necessary for the effective simulation of the behavior of R/C structures under cyclic loading, since often structures that undergo inelastic deformations and cyclic behavior weaken and loose some of their stiffness and strength. Moreover, gaps tend to develop due to cracking causing the material to become discontinuous. The Bouc-Wen Hysteretic Model is capable of simulating stiffness degradation, strength deterioration and progressive pinching effects.

The model can be visualized as a parallel combination of a linear and a nonlinear element, as shown in Figure 3. The relation between generalized moments and curvatures is given by:

$$M(t) = M_y \left[\alpha \frac{\phi(t)}{\phi_y} + (1-\alpha) z(t) \right] \tag{1}$$

where M_y is the yield moment; φ_y is the yield curvature; α is the ratio of the post-yield to the initial elastic stiffness and z(t) is the hysteretic component defined below.

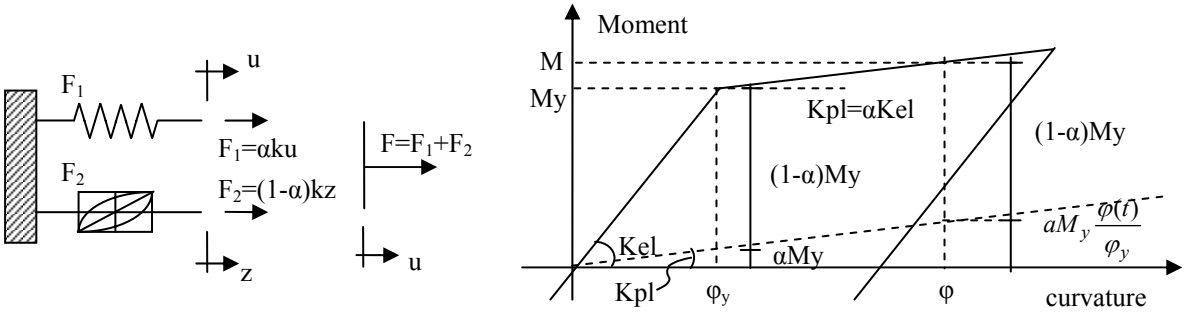

Figure 3. Bouc-Wen Hysteretic Model

The hysteretic function z(t) is obtained from the non-linear differential equation:

$$\dot{z}(t) = f(\dot{\phi}(t), z(t)) \frac{1}{\phi_y} \text{ or alternatively } \frac{dz}{d\phi} = K_z \frac{1}{\phi_y} \text{ where } K_z = \left[A - B \frac{1+sign(d\phi)}{2} \left(\frac{|z(t)|+z(t)}{2} \right)^{n_B} - C \frac{1+sign(d\phi)}{2} \left(\frac{|z(t)|-z(t)}{2} \right)^{n_C} - D \frac{1-sign(d\phi)}{2} \left(\frac{|z(t)|+z(t)}{2} \right)^{n_D} - E \frac{1-sign(d\phi)}{2} \left(\frac{|z(t)|-z(t)}{2} \right)^{n_E} \right] \tag{2}$$

In the above expression A, B, C, D & E are constants which control the shape of the hysteretic loop for each direction of loading, while the exponents n_B, n_C, n_D & n_E govern the transition from the elastic to the plastic state. Small values of n_i lead to a smooth transition, however as n_i increases the transition becomes sharper tending to a perfectly bilinear behavior in the limit ($n \to \infty$).

The program defaults are:

$$A=1,\ \ C=D=0\ \&\ B=\frac{1}{b^{n_B}},\ E=\frac{1}{e^{n_E}}\ \text{ where } e=\frac{-M_y^-}{M_y^+},\ b=1 \text{ and } n_B=n_E=n \tag{3}$$

The parameters C, D control the gradient of the hysteretic loop after unloading occurs. The assignment of null values for both, results to unloading stiffness equal to that of the elastic branch. Also, the model is capable of simulating non symmetrical yielding, so if the positive yield moment is regarded as a reference point, the resulting values for B and E are those presented in equation (3). The hysteretic parameter *Kz* is then limited in the range of 0 to 1, while the hysteretic function *z* varies from $-\left|M_y^- / M_y^+\right|$ to 1.

Finally, the flexural stiffness can be expressed as:

$$K=EI=\frac{dM}{d\phi}=M_y\left[\alpha\frac{1}{\phi_y}+(1-\alpha)\frac{dz}{d\phi}\right]=M_y\left[\alpha\frac{1}{\phi_y}+(1-\alpha)K_z\frac{1}{\phi_y}\right]=EI_0\left[\alpha+(1-\alpha)K_z\right] \tag{4}$$

6.1 Hysteretic behavior with Degradation

a) Stiffness Degradation

The stiffness degradation that occurs due to cyclic loading is taken into account by introducing the parameter η into the differential equation:

$$\frac{dz}{d\phi}=\frac{K_z}{\eta}\frac{1}{\phi_y}\rightarrow K=EI_0\left[\alpha+(1-\alpha)\frac{K_z}{\eta}\right]\ \ where\ \ \eta=1.0+S_k\frac{\mu_{\max}+\mu}{2} \tag{5}$$

The parameter η depends on the current, $\mu=\phi/\phi_y$, and maximum achieved plasticity, $\mu_{\max}=\phi_{\max}/\phi_y$. S_k is a constant which controls the rate of stiffness decay. Common values for S_k are 0.1 and 0.05.

b) Strength Deterioration

The strength deterioration is simulated by multiplying the yield moment M_y with a degrading parameter S_β:

$$M(t)=S_\beta M_y\left[\alpha\frac{\phi(t)}{\phi_y}+(1-\alpha)z(t)\right] \tag{6}$$

The parameter S_β depends on the damage of the section which is quantified by the Damage Index, DI:

$$S_\beta=1-S_d DI\ \text{ where }\ DI=\frac{\mu_{\max}-1}{\mu_c-1}\frac{1}{\left(1-\frac{S_{p1}\int dE_{diss}}{4E_{mon}}\right)^{S_{p2}}} \tag{7}$$

In the above expression S_d, S_{p1}, S_{p2} are constants controlling the amount of strength deterioration; μ_c is the maximum ductility factor that can be reached, $\mu_c=\phi_u/\phi_y$; $\int dE_{diss}$ is the energy dissipated before unloading occurs and finally E_{mon} is the amount of energy absorbed during a monotonic loading until failure as shown in Figure 4.

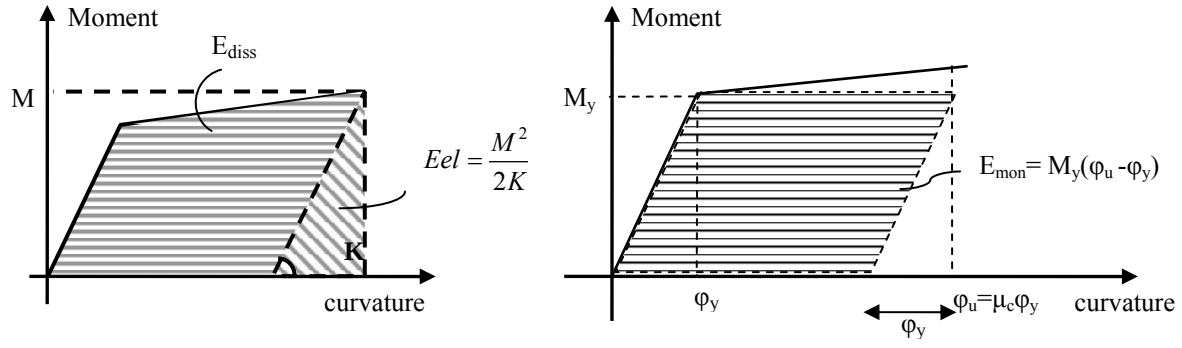

Figure 4. Dissipated Energy (Ediss) and Monotonic Energy (Emon).

c) Pinching or Slip

Pinching of hysteretic loops due to shear cracking and bond slip of the reinforcement is commonly observed in reinforced concrete structures during cyclic loading. This phenomenon is taken into account by introducing the "slip length" parameter a and a function *f (z)* in the expression of *Kz*:

$$K_z^{pin} = \frac{K_z}{1 + \mathrm{a} \cdot f(z) \cdot K_z} \tag{8}$$

In the above equation K_z^{pin} is the hysteretic parameter affected by pinching, K_z is the original expression of the hysteretic parameter obtained from (3) and a, f(z) are given by:

$$\mathrm{a} = A_s(\mu' - 1) \;\; \& \;\; \mathrm{f(z)} = \exp\left[-\frac{(\mathrm{z}-\mathrm{z_m})^2}{z_s^2} \right] \tag{9}$$

where A_s is a control parameter which may be linked to the size of crack opening or reinforcement slip or both; μ' is the normalized curvature attained at the load reversal prior the current loading circle; z_s is the range where slip occurs. A non zero value of the parameter z_m will shift the effective slip region to become symmetric about $z=z_m$.

7 METHOD OF ANALYSIS

The computer program "*Plastique"* which is described herein, is able to perform the following types of analysis:

- Push-over analysis
- Quasi-static analysis
- Eigenvalue analysis
-Non-linear dynamic analysis

The first two analysis types, although significantly simplified, can lead to valuable conclusions concerning the behavior of the structure and the possible collapse mechanism. The applied procedure can be described in brief as follows. In the case of 2-D analysis the structure is assumed to consist of a finite number of nodes interconnected by a finite number of elements. The types of elements have been described in section 3. In the case of 3-D analysis the structure is assumed to consist of the aforementioned 2-D frames, assuming a rigid diaphragm assemblage of their horizontal dof's per floor slab. Loads may be applied to the nodes or to the elements. In both cases though, they are transformed to nodal loads.

After the stiffness matrix has been formulated the equilibrium equations are solved by an efficient algorithm based on the Gaussian elimination method. The structure stiffness is stored in a banded form to optimize the use of core storage and during the elimination process virtually all unnecessary arithmetic operations are avoided. An incremental method is applied for all types of analysis. The specified loads are divided to sufficiently smaller sub-loads, in order to simulate more efficiently the stress redistribution which occurs due to the non linear behaviour of the structure. An iterative process (modified Newton Raphson Method) is incorporated in each load step so that a higher level of accuracy can be achieved, as shown in Figure 5.

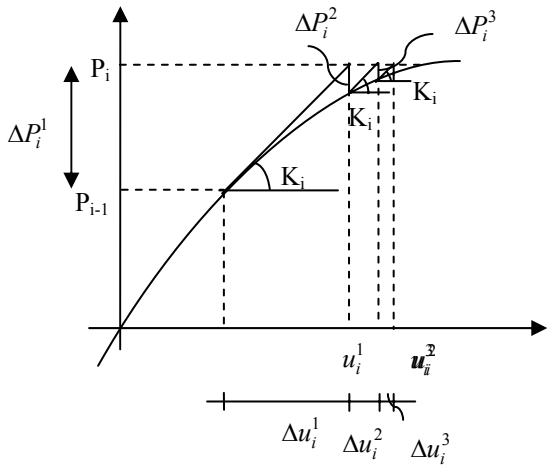

Figure 5. Modified Newton Raphson Method

The member forces are computed for each load increment and the tangent stiffness matrix is updated to account for changes in any of the element stiffnesses. A spread plasticity model is used, as described in section 4, in order to simulate the changes in the flexibility of each element. In the case of the dynamic analysis the Newmark Method is used for the direct integration of the equations of motion.

The equation of motion that is solved at any stage of the analysis is written as:

$$[M]\{\ddot{U}\}+[C]\{\dot{U}\}+\{P_{\text{int}}\}=\{P_{ext}\}=-[M]\{S\}\{\ddot{U}_g\} \tag{10}$$

where [M] is the mass matrix; [C] is the damping matrix; [P_{int}] is the internal load vector of the structure; [P_{ext}] is the external load vector of the structure; [S] is a modal influence vector; [U] is the structure displacement vector and $\{\ddot{U}_g\}$ is the ground acceleration vector.

The above system of equations is solved using the constant acceleration method, according to which equation (10) can be rewritten for time t+Δt and iteration k as:

$$[M]^{t+\Delta t}\cdot\{\ddot{U}\}^{(k)}+[C]^{t+\Delta t}\cdot\left\{\dot{U}^{(k)}\right\}+{}^{t+\Delta t}\{P_{\text{int}}\}^{(k-1)}+{}^{t}[K_t]^{t+\Delta t}\cdot\{\Delta U\}^{(k)}={}^{t+\Delta t}\{P_{ext}\} \tag{11}$$

The hysteretic model applied is the Bouc Wen - Baber Noori model which, as mentioned previously, is able to simulate R/C characteristics such as stiffness degradation, strength deterioration and pinching behaviour. At every step of the analysis, the elements' and the structure's Damage Indices are calculated providing an evaluation not only of the damage occurred, but also of the structure's residual strength and capacity to withstand further loading. The Damage Index for each section is given by (7). The Damage Index for each element is computed as the maximum of its sections' Damage Indices and finally the Damage Index of the whole structure can be obtained from the following expressions:

$$DI=\sum_i \frac{E_{tot,i}}{\sum_i E_{tot,i}}(DI)_i \tag{12}$$

where $(DI)_i$ is the Damage Index for each element and $E_{tot,i}$ is the total amount of absorbed energy per element.

8 EXAMPLES

8.1 Example 1

This example deals with the behavior of structures subjected to dynamical loading of varied frequency content The Tabas (Iran – 0.68g) earthquake was used for this particular analysis and the method of wavelets was applied for the construction of the corresponding time-frequency spectrum. The carried out analysis examines the response of a structure that has a natural frequency close to the primary frequency of the dynamic load, demonstrating the fact that consecutives resonances might occur as the structure proceeds deeply in its plastic deformation region.

The original Tabas accelerogram is presented in Figure7 accompanied by its corresponding time-frequency spectrum Fig. 8.

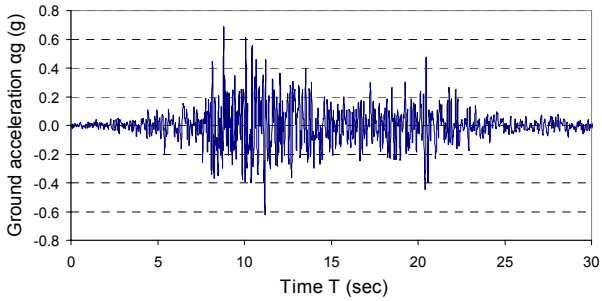

Figure 7. Tabas accelerogram

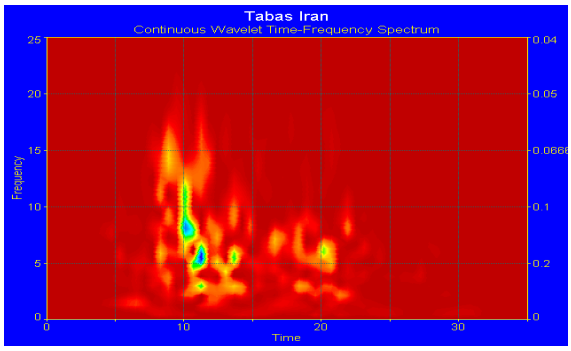

Figure 8. Time-Frequency spectrum

From the time-frequency spectrum one can distinguish the three peaks presented in the first three rows of Table 1. Since Max_2 and Max_3 belong in the same frequency domain and arise in relatively close time periods we can substitute them by an "equivalent" spectral frequency presented in the last row of Table 1.

	Time t (sec)	Frequency F (Hz)
Max_1	11.1	8.12
Max_2	12	5.47
Max_3	14	5.55
$Max_{2,3}$ equivalent	13	5.50

Table 1: Frequency Peaks

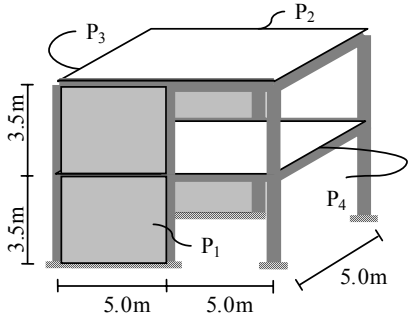

Figure 9. Structural Model

The structure studied in the present example is depicted in Figure 9. A convenient set of geometrical and mechanical properties was used in order to achieve a natural frequency variation for the primary mode which would start from a value of 8.12Hz at around t=11.1 sec and then reach 5.50 Hz at 13sec. The structure's response is presented in Figure 10. The structure shows evidence of primary resonance in the time period from t=10 to t=11sec and finally failure occurs just after t=13sec.

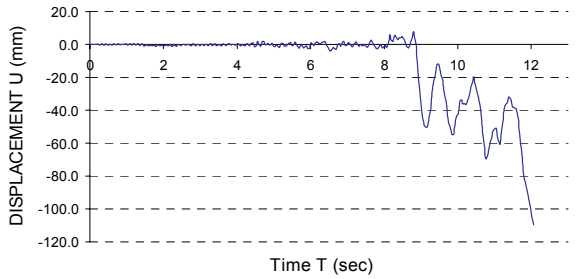

Figure 10. Top story disp. history (failure)

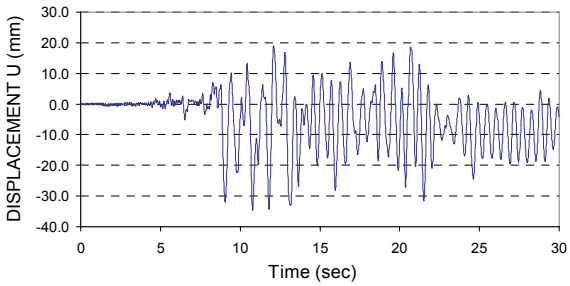

Figure 11. Top story disp. history (no failure)

By filtering out the first primary spectral frequency of the excitation (of approximately 8.12Hz) and carrying out the previous analysis one can get a qualitatively different response with no failure mechanism occurring (Figure 11).

8.2 Example 2

This example demonstrates the use of the different analysis and design options of program "*Plastique"*. The structure used in the particular example is a two column frame shown in Figure 12. A monotonic push-over analysis can provide the possible collapse mechanism of the particular structure as shown in Figure 13.

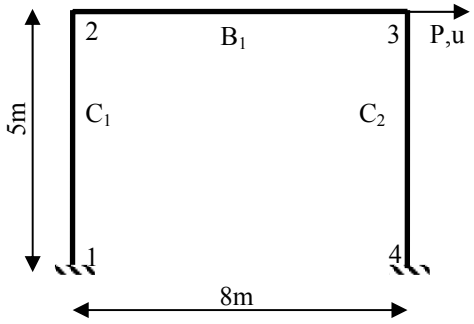

Figure 12. Structure -2 Column Frame

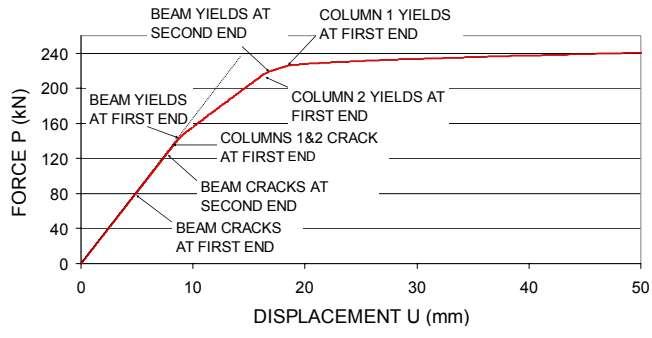

Figure 13. Possible Collapse Mechanism

Next, a dynamic analysis is carried out. The accelerogram of the Northridge earthquake, normalized at 0.50g, was chosen for the particular analysis (Figure 14).

The resulting displacement time history, the force displacement hysteretic loop, as well as the final Damage Indices (DI) and yield penetration lengths are presented in the following figures.

In Figure 16, one can easily notice the gradual shift in the column section's stiffness due to stiffness/strength degradation and pinching effects. A transition factor n=2 has been used in the current example, which accounts for the smooth transition of the section from the elastic to the inelastic region.

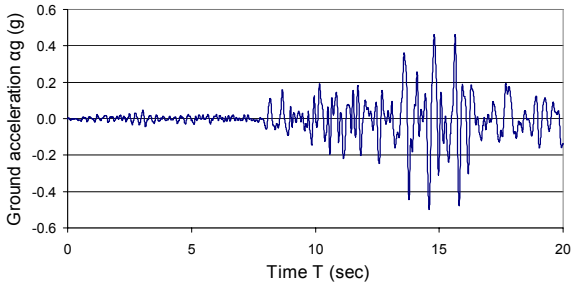

Figure 14. Northridge accelerogram

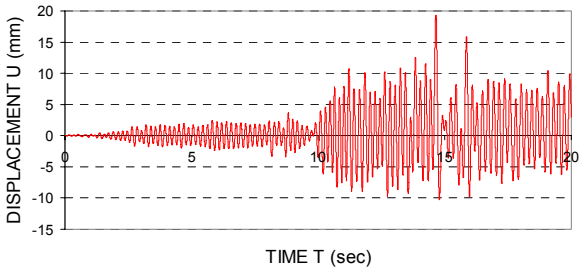

Figure 15. First floor displacement time history

The damaged state of the structure at the end of the analysis is depicted In Figure 17. The reduced sections are a graphical representation of the inelasticity distribution along each member's length.

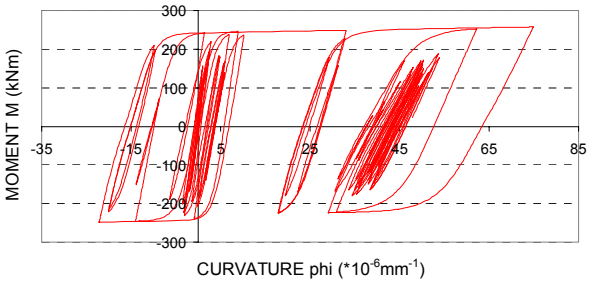

Figure 16. Moment-Curvature Hysteretic loop

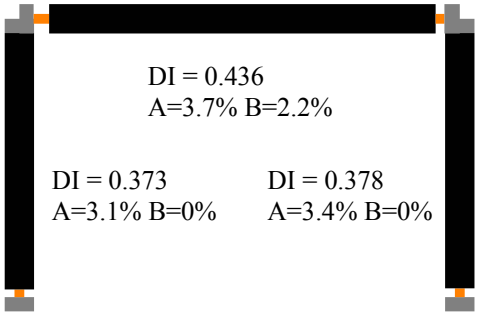

Figure 17. Final DI and yield penetration lengths

9 CONCLUSIONS

A new computer program "*Plastique"* for the inelastic analysis of R/C structures is presented. A macro modeling approach is implemented, combined with spread plasticity and a yield penetration model to account for the impact of inelastic phenomena on structural response. By introducing a smooth Bouc-Wen type hysteretic model, a reliable and automatic simulation of R/C cyclic response is achieved. An iterative procedure is used to solve the equilibrium equations. The program proves to be a versatile tool for different types of static and dynamic analysis.

10 REFERENCES

[1] R. E. Valles, A. M. Reinhorn, S. K. Kunnath, C. Li, and A. Madan (1996), "IDARC 2D Version 4.0 : A Computer Program for the Inelastic Damage Analysis of Buildings", Technical Report NCEER-96-0010, State University of New York at Buffalo.

[2] Young J. Park, Andrei M. Reinhorn, and Sashi K. Kunnath, (1987), "IDARC : Inelastic damage analysis of reinforced concrete frame – shear-wall structures", Technical Report NCEER-87-0008, State University of New York at Buffalo.

[3] Robert D. Cook, David S. Malkus, and Michael E. Plesha, "Concepts and applications of Finite Element Analysis", Third Edition.

[4] Klaus-Jürgen Bathe, "Finite Element Procedures".

[5] Anil K. Chopra, "Dynamics of Structures".

[6] Vlasis K. Koumousis, 1990, "Static & Dynamic Analysis of multistory buildings".

[7] S. Dobson, M. Noori, Z. Hou, M. Dimentberg, and T. Baber, (1997), "Modelling and random vibration analysis of SDOF systems with asymmetric hysteresis".

[8] Sashi K. Kunnath, John B. Mander, and Lee Fang, (1996), "Parameter identification for degrading and pinched hysteretic structural concrete systems".

[9] E. N. Chatzi & S. P. Triantafillou, NTUA Diploma Thesis, (2004), "Inelastic analysis of multistory buildings with a Bouc-Wen type hysteretic model".

[10] T. I. Psycogios, NTUA, Diploma Thesis, (2002), "Inelastic analysis of R/C frames with a Bouc-Wen type hysteretic model ".

[11] P. Kolettas, NTUA, Diploma Thesis, (2004) "Study of the dynamical behavior of buildings using accelerograms of a varied frequency content and wavelet transformation".

SYSTEM RELIABILITY OF STEEL STRUCTURES BASED ON INTERSTORY DRIFT AND DIRECT LOSS DEMANDS

D.G. Lignos[a], E.C. Stergiou[a], and C.J. Gantes[b]

[a,] Stanford University, Civil and Environmental Engineering Department, Stanford,

CA 94305 – 4020, USA

[b] National Technical University of Athens, Civil Engineering School,

GR -15780, Athens, Greece

Keywords: FORM, SORM, story drifts, loss estimation, seismic demands, Incremental Dynamic Analysis.

Abstract. *This paper focuses on the application of system reliability to steel structures, relating story drifts, which is one of the most sensitive engineering demand parameters (EDPs) that cause significant damage to structures, and direct loss demands after an earthquake event. First and second order reliability measures (FORM, SORM) are used to quantify the probability of failure of the system and a sensitivity analysis is performed to identify the importance of the parameters that are used as threshold values for direct loss and story drifts.*

In order to determine representative data for story drifts, rigorous non linear time history analysis is used for 20 ground motions. Incremental Dynamic Analysis is used in order to scale the ground motions to produce mean quantities for 7 levels of intensity. The direct loss of each scenario is also taken into consideration using ATC-13 manual empirical relationships.

It is concluded that direct losses are more critical for lower levels of intensity in comparison with story drifts. The latter is the governing parameter for intermediate levels of intensity. Both parameters contribute the same for higher hazard levels. The reliability index is more sensitive to the threshold value for direct loss based on a sensitivity analysis.

1.0 INTRODUCTION

Until recently, structural reliability was not routinely analyzed or quantified in the design process. Reliability was accounted for tacitly by the factor-of-safety approach to design in most of the engineering codes (ATC [1], Eurocode[10], FEMA[5],[6]). Also practical guidelines and lessons learned helped to improve reliability. The structural designer/analyst did not perform a formal risk analysis on newly designed structure. The complications that reduce the ability to quantify reliability reside in the stochastic nature of design inputs.

The primary purpose for establishing a factor-of-safety for design is to ensure safety. In the field of structural reliability, the performance of a structure is evaluated with respect to a prescribed set of limit states that define acceptable and unacceptable behavior. If the response of a structure violates one or more limit states, its performance is deemed unacceptable. This fact suggests that future design and design processes might benefit greatly by focusing on reliability targets rather than factors-of safety. Many attempts have been made for loss estimation after an earthquake (HAZUS [8], Miranda et al. [9], Rojahn et al. [14]) and also fragility curves have been developed to estimate the probability of failure of different systems as a function of the system characteristics and the frequency content of the ground motions (Krawinkler and Ibarra [11]).

The present paper focuses on the application of system reliability to steel structures, based on story drifts, which is one of the most sensitive EDPs that cause significant damage to structures, and also direct loss. First and second order reliability measures (FORM, SORM) are used to quantify the probability of failure of the system and a sensitivity analysis is performed to identify the importance of the parameters that are used as threshold values for direct loss and story drifts. In the next paragraphs, the basic assumptions, theoretical background and applications are documented.

2.0 CHARACTERISTICS OF THE BUILDILG

The 9-story SAC[1] building in Los Angeles, presented in figure 1a, is used to define the system reliability. The building was designed for the SAC Phase II Steel Project and is 150ft by 150ft and 122ft in plan view and

[1] Joint venture of three non-profit organizations: The Structural Engineers Association of California (SEAOC), the Applied Technology Council (ATC), and California Universities for Research in Earthquake Engineering (CUREE).

elevation, respectively. Furthermore, in both north-south (N-S) and east - west (E-W) directions it consists of five bays, each 30ft long. Floor to floor heights are considered to be 13ft, except the first story, which is 18ft. Concrete foundation walls with 12ft height exist in the building and, together with the surrounding soil, they are assumed to restrain the structure from horizontal displacement at the ground level. The columns of the system are 50ksi steel wide – flange sections. Monolithic column pieces are connected every two levels. Column splices are located on the 1st, 3rd, 5th, and 7th levels at 6ft. More information for the building are presented by Chopra and Goel[2].

The floor system is composed of 36ksi steel wide-flange beams. Each of the frames resists one half of the seismic mass associated with the entire structure. The seismic mass of the structure is 66.0kips.sec^2/ft for the ground level, 69.0kips.sec^2/ft for the first level, 67.7kips.sec^2/ft for the second through the eighth level, and 73.2kips.sec^2/ft for the ninth level. Note that the total weight W of the structure is 10989kips. Also, the predominant period T_1 of the structure is 2.27sec. Based on NEHRP[5] provisions, the base shear V of the building is determined to be 180kips.

The building is modeled in DRAIN-2DX (Prakash et al.[3]) using the standard bilinear model with 3% strain hardening, without deterioration, in order to take into consideration the material nonlinearity. Geometric nonlinearities (P-Δ effects) are included into nonlinear time history analysis and collapse indeed can happen only due to P-Δ effects.

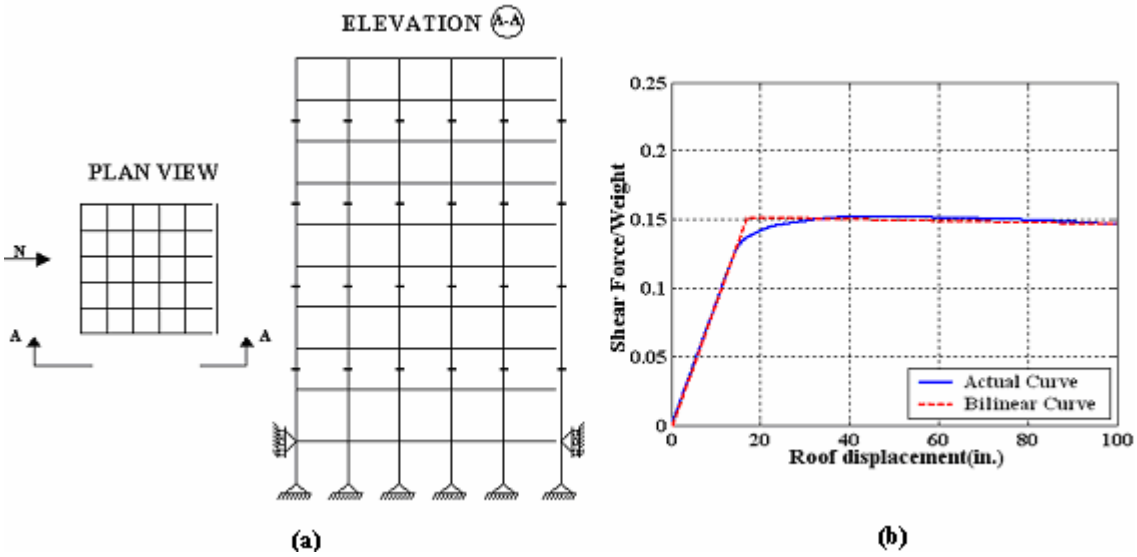

Figure 1: (a) Plan view and elevation of SAC building, (b) normalized actual and bilinear pushover curve

3.0 GROUND MOTIONS AND INCREMENTAL DYNAMIC ANALYSIS

The seismic excitation that is used in the present investigation is defined by a set of 20 large-magnitude small - distance records (LMSR) (6.5 < Mw < 7.0, 13km < R < 30km). The records were selected from the PEER database. Details for the ground motions can be found in Mendina and Krawinkler [12]. In particular, the same ground motions have been used to evaluate seismic demands over a wide range of hazard levels based on the widely used Incremental Dynamic Analysis (IDA) (Vamvatsikos and Cornell [16]).

Seven levels of intensity have been used for this evaluation and the control parameter used to "scale" the ground motion intensity for a given structure strength, or to "scale" the structure strength for a given ground motion intensity, is the parameter $[S_a(T_1)/g]/\gamma$, where $S_a(T_1)$ is the 2% damped spectral acceleration at the fundamental period of the structure (without P-Δ effects), and γ is the base shear coefficient, i.e., $\gamma = V_y/W$, with V_y being the yield base shear. Based on figure 1b, in which the actual and bilinear normalized pushover curves are presented, γ parameter is estimated to be 0.15. The parameter $[S_a(T_1)/g]/\gamma$ represents the ductility dependent strength reduction factor (often denoted as R_μ), which in the context of present codes, is equal to the conventional R factor if no overstrength is present.

4.0 RESPONSE STATISTICS AND STORY DRIFTS

Presented in this paper are the median values, $\bar{x}$, defined as the geometric mean, of n observed values x_i and the dispersion δ defined as the standard deviation of the logarithm of the n observed values,

$$\bar{x} = \exp\left[\frac{\sum_{i=1}^{n} \ln(x_i)}{n}\right] \tag{1}$$

and,

$$\delta = \left[\frac{\sum_{i=1}^{n} \left(\ln\left(x_i\right) - \ln\left(\bar{x}\right)\right)^2}{n-1}\right]^{1/2} \tag{2}$$

Equations (1) and (2) are logical estimators for the median and dispersion, especially if the data are sampled from lognormal distribution, an appropriate distribution for the peak earthquake response of structures (Shome and Cornell [15]). This basic approach is denoted as computed statistics. This approach is used in order to fit lognormal distributions to data that was created using IDA for story drifts.

5.0 DIRECT LOSS ESTIMATION

In order to estimate the direct loss demands for each earthquake, the probability of earthquake damage needs to be related to peak roof drifts. The required input is provided to estimate building damage, using fragility functions. In particular, model building type and seismic design level are selected. The output of fragility curves is an estimate of the cumulative probability of being in, or exceeding, each damage state for the given level of ground shaking. Discrete damage state probabilities are created using cumulative damage probabilities.

The 9-story building that is used is a high-rise steel moment frame S1H, as tabulated in HAZUS [8]. These model building types are based on the classification system of FEMA 178 [13]. In addition, a moderate seismic design level has been selected in order to develop the building damage functions assuming lognormal distribution. Note that the building is located in seismic zone 2B or map area 5 (FEMA [4], [7]).

Fragility functions that are used are characterized by median and lognormal standard deviation. Peak roof displacement has been used as the critical parameter for structural and nonstructural damage. The probability of being in or exceeding a given damage state is modeled as a cumulative lognormal distribution and the probability of being in or exceeding a damage state, d_s, is modeled as,

$$P\left[d_s \middle| \theta_{r,max}\right] = \Phi\left[\frac{1}{\beta_{d_S}} \ln\left(\frac{\theta_{r,max}}{\bar{S}_{d,ds}}\right)\right] \tag{3}$$

in which, $\bar{S}_{d,ds}$ is the median value of spectral displacement at which the building reaches the threshold of the damage state, d_s, β_{ds} is the standard deviation of the natural logarithm of the spectral displacement of damage state, d_s, and Φ is the standard normal cumulative distribution function.

Median values of structural component fragility are based on building drift ratios that describe the threshold of damage states. Damage-state drift ratios are converted to spectral displacement using the relationship,

$$\bar{S}_{d,Sds} = \delta_{R,S_{ds}} \cdot a_2 \cdot h \tag{4}$$

in which, $\delta_{R,Sds}$ is the drift ratio at the threshold of the structural damage state d_s, a_2 is the fraction of the building (roof) height at the location of push-over mode displacement and h is the typical roof height, in inches, of the model building type of interest.

Finally, the loss is determined for each ground motion, based on the relationship,

$$\text{Loss} = P_{slight} \cdot \tilde{L}_{slight} + P_{mod.} \cdot \tilde{L}_{mod} + P_{ext.} \cdot \tilde{L}_{ext} + P_{complete} \cdot \tilde{L}_{complete} \tag{5}$$

in which, P_{slight} , $P_{mod.}$ P_{ext}, and $P_{complete}$ are the probabilities for slight, moderate extensive and complete damage of the building respectively. $\tilde{L}_{slight}$, $\tilde{L}_{mod}$, $\tilde{L}_{ext}$ and $\tilde{L}_{complete}$ are direct losses for moderate extreme and complete damage of the building respectively.

6.0 SYSTEM RELIABILITY AND THRESHOLD VALUES

System reliability for the 9-Story SAC building is defined for a given level of intensity based on a set of 10 limit state functions. 9 of these functions represent the story drift, which is assumed to have a lognormal distribution, and the one left represents the direct loss, which is again assumed to have a lognormal distribution. Each of them is the basic component problem,

$$Z_i = R_i - S_i \tag{6}$$

and they all constitute a series system, due to the fact that the system will fail if any of its components fails. The system function for a given level of intensity $S_a(T_1)/g/\gamma$, for the series problem is,

$$a_s(S_a(T_1)/g/\gamma) = \Psi(a) = \min(a_1, a_2, ...a_{10}) = \prod_{i=1}^{10} a_i \tag{7}$$

In order to create the limit state functions for each story, given the intensity measure, threshold values need to be assumed for drifts and direct loss. The suggested values are 6% for story drifts and 75% of the total cost of the building for loss demands. The 6% story drift is used due to the fact that beyond this point it is assumed that collapse of the system occurs. Also, the amount of drift threshold should be at a comparable level with the loss threshold.

7.0 RESULTS

7.1 Roof displacements

Mean values, the 16% and 84% percentile of roof displacements of the structure are presented in figures 2a and 2b together with individual responses as determined by IDA with rigorous nonlinear time history analysis. A different way of normalization has been used for each figure. In the first case, the intensity measure is plotted versus the roof drift $\theta_{r,max}$ which is the roof displacement over the total height of the building. In the second case, roof drift is normalized with respect to the first mode spectral displacement. Note that the roof drift is used to estimate the direct loss demands for each seismic excitation and level of intensity.

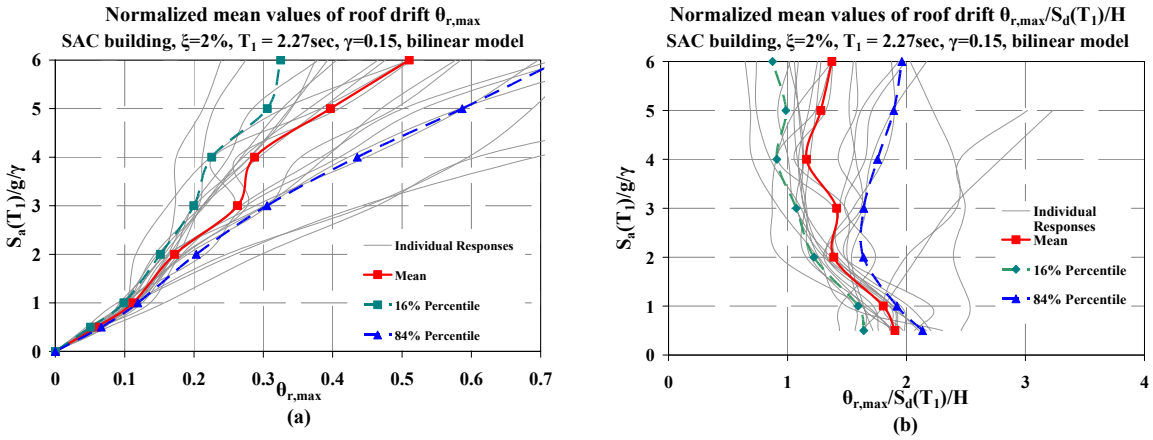

Figure 2: (a) Mean roof drifts $\theta_{r,max}$ and (b) normalized mean roof drifts $\theta_{r,max}/S_d(T_1)/H$ (IDA curves)

7.2 Interstory drifts – fitted distributions

An important response quantity in performance - based engineering, are story drifts. For this particular case story drift ratios $\theta_{s,max}$ are presented in figures 3a and 3b for R = 2 and 5 levels of intensity using computed statistics, as determined by NL-THA. For the sake of brevity, results for the other 5 levels of intensity are not included here. Interstory drift ratios are normalized with respect to the spectral displacement $S_d(T_1)$, corresponding to the predominant period of the structure, over the total height of the building.

A lognormal distribution is assumed to fit the data. The parameters λ and Z of the lognormal distribution for each story are defined. Note that correlation between story drifts was assumed to be zero, due to lack of reference. An attempt to define the correlation directly from the data that were determined by (IDA) was performed but it is concluded that the difficulty was extremely high and results were not reliable. Also, no

correlation was assumed between story drifts and direct loss. Given the level of intensity, using the Bootstrap method to take into consideration the uncertainty of the statistical estimator the final parameters λ and Z are presented in tables 1 and 2, respectively, for each story. The difference between the latter and initially estimated parameters is negligible, so it is concluded that results based on fitted distributions are reliable.

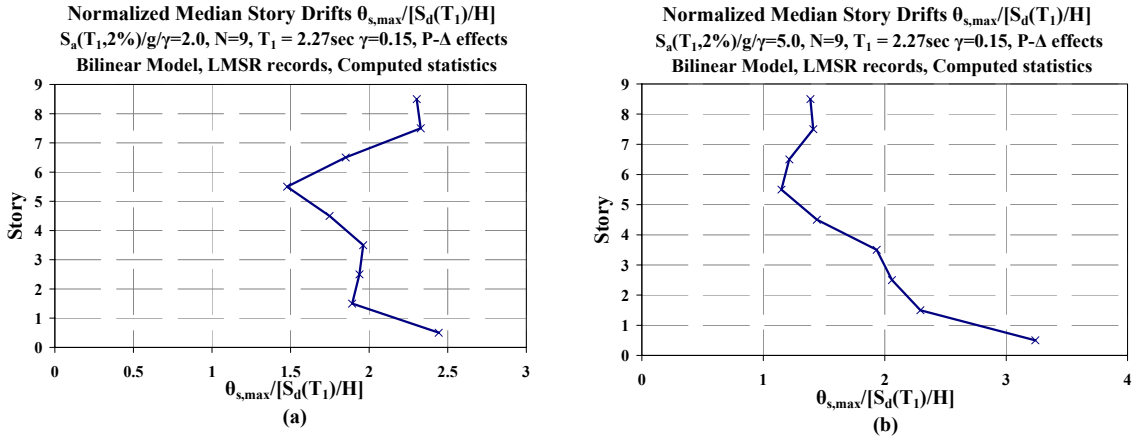

Figure 3: (a) Normalized median story drifts for $S_a(T_1,2\%)/g/\gamma = 2.0$ and (b) $S_a(T_1,2\%)/g/\gamma = 5.0$

	Intensity level $S_a(T_1)/g/\gamma$						
Story	**0.5**	**1**	**2**	**3**	**4**	**5**	**6**
1	1.2383	2.3332	3.9346	4.6275	5.1769	5.9167	6.1843
2	1.3986	2.5542	3.9287	4.7723	5.3629	5.9378	6.2457
3	1.0784	1.9935	3.0673	3.9951	4.5263	5.0307	5.4788
4	0.9457	1.6770	2.4741	3.4443	4.1939	4.8553	5.7337
5	0.9598	1.7250	2.9180	4.1278	4.9553	6.0798	7.0384
6	0.9430	1.7679	3.2903	4.9021	6.2012	8.0120	9.7626
7	0.8458	1.5729	3.2720	5.0905	6.5702	8.7361	10.9198
8	0.8674	1.6390	3.1803	5.3205	7.3795	9.9857	11.9470
9	1.4526	2.5543	4.1376	7.0247	10.0021	13.7407	18.5520

Table 1: Parameters λ of the assumed lognormal distribution for story drifts, for 7 levels of intensity after Bootstrap method

	Intensity level $S_a(T_1)/g/\gamma$						
Story	**0.5**	**1**	**2**	**3**	**4**	**5**	**6**
1	0.5729	0.4505	0.3880	0.2773	0.2798	0.2809	0.2600
2	0.4533	0.3645	0.3186	0.2211	0.2544	0.2956	0.2252
3	0.3444	0.3339	0.3070	0.2746	0.3158	0.3367	0.2587
4	0.2517	0.2088	0.3007	0.2966	0.2363	0.2065	0.1825
5	0.2534	0.2317	0.2773	0.2646	0.2455	0.1708	0.1657
6	0.1747	0.1580	0.2447	0.2391	0.3034	0.2944	0.2756
7	0.1391	0.1169	0.1920	0.2685	0.3445	0.3731	0.3595
8	0.1523	0.0991	0.1942	0.3160	0.4364	0.5239	0.7433
9	0.2118	0.0831	0.2306	0.3974	0.5362	0.6850	1.0587

Table 2: Parameters Z of the assumed lognormal distribution for story drifts, for 7 levels of intensity, after Bootstrap method

7.3 Fragility functions and loss estimation

As it was presented in paragraph 4.0, fragility functions are defined for each damage state, in order to determine direct loss. It is assumed that the latter follows a lognormal distribution, for a given intensity level. Fragility functions that are used are presented in figure 4a. The probability of being at or exceeding a damage state is computed versus the mean peak roof displacement that was obtained from NL-THA. Values that were

used for each of four damage states for mean and standard deviation are presented in table 3 as determined by HAZUS [8]. Loss estimation can be easily computed for each seismic excitation, given the ground motion intensity. Using equation (5), loss is specified and then a lognormal distribution is assumed to fit the data. Mean and standard deviation of each distribution (one for each level of intensity) are presented in table 4 in million dollars.

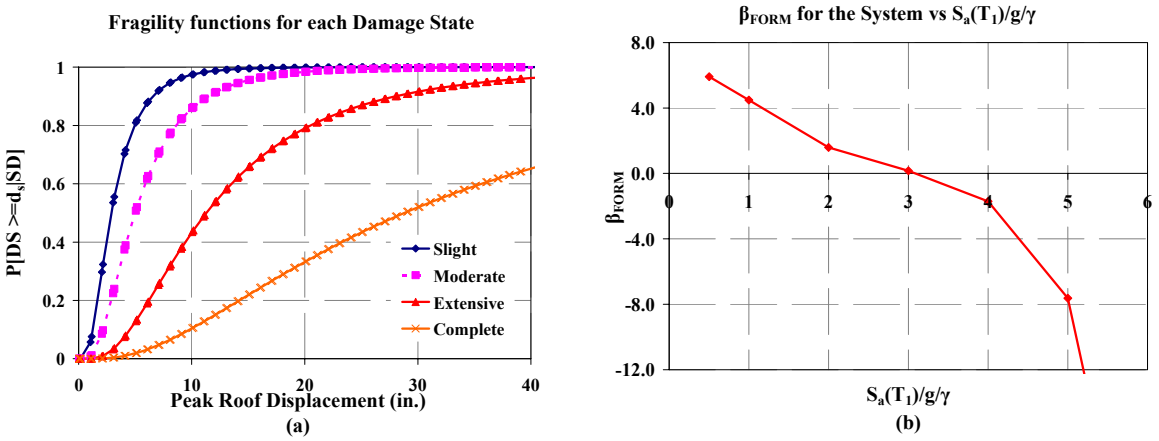

Figure 4: (a) Fragility functions for the 4 damage states, (b) reliability index β as determined using FORM

Slight		Moderate		Extensive		Complete	
$\hat{m}$	β	$\hat{m}$	β	$\hat{m}$	β	$\hat{m}$	β
2.88	0.64	4.99	0.65	11.29	0.70	28.82	0.84

Table 3: Mean value and standard deviation as determined by HAZUS for 4 damage states

Parameters	Intensity level $S_a(T_1)/g/\gamma$						
	0.5	1	2	3	4	5	6
Mean Loss $	0.2058	0.4383	0.6225	0.7412	0.7998	0.8566	0.8944
Standard Deviation $	0.0412	0.0534	0.0762	0.0845	0.0869	0.0741	0.0646

Table 4: Mean and standard deviation of loss in million $ for each level of intensity

7.4 First and second order reliability measure – FORM, SORM

A system reliability analysis is performed using first order reliability measure (FORM) for each level of intensity. As can be seen in figure 4b, for lower levels of intensity $S_a(T_1)/g/\gamma$ the β_{FORM} value is high, compared to values for higher values of $S_a(T_1)/g/\gamma$, and this is something that was expected, since the probability of having failure in a low intensity excitation should not be significant. In figure 5a the probability of failure P_f is plotted versus the intensity measure. Above a level of intensity 5, the system fails since the probability of failure becomes practically 1.

For low levels of intensity the failure due to direct loss is more likely to occur, since the threshold values that are used for drifts are too far from the mean values that were obtained from NL-THA. The opposite is observed for high levels of intensity. The structure is more likely to fail due to drifts, as can be seen from figure 5b, in which the probability of drift failure is plotted versus the probability of loss failure. Note that it is assumed that all random variables are independent.

The same analyses were performed using the second order reliability measure (SORM). The same results with FORM were determined for each level of intensity, since the system consists of 10 simple component problems.

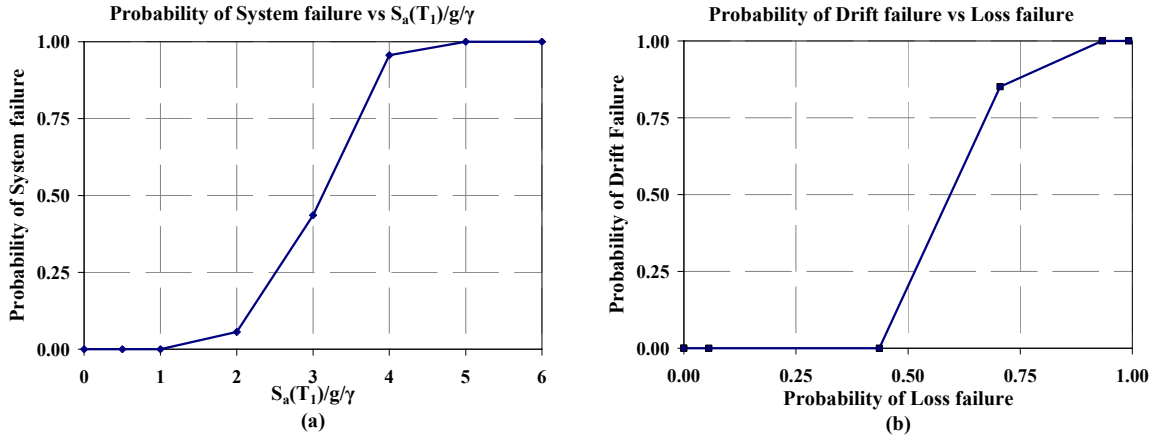

Figure 5: (a) Probability of system failure versus the intensity measure, and (b) probability of drift failure versus probability of Loss failure

7.5 Sensitivity analysis

A sensitivity analysis is performed with respect to the parameters L_o and d_o, threshold values for loss and drift demands, respectively. As shown in figure 6a, there is an increasing tendency of the gradient of b at level of intensity 1. For higher levels of intensity, the sensitivity analysis showed approximately constant gradient with respect to the parameters. On the other hand, the importance of parameter L_o is increasing with increasing level of intensity, as presented in figure 6b.

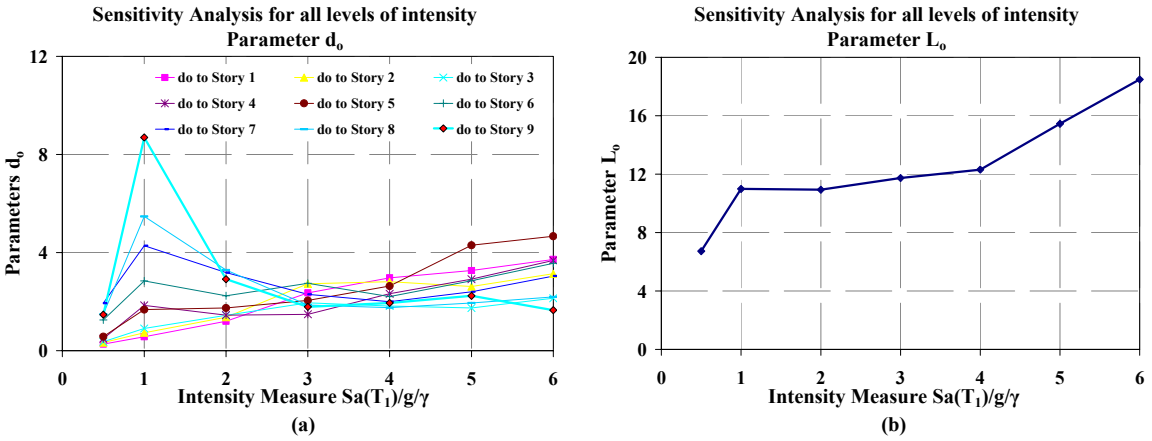

Figure 6: Sensitivity analysis for (a) drift threshold value d_o, and (b) direct loss threshold value, versus the intensity measure

8.0 CONCUSIONS

A system reliability analysis was performed for the 9-story SAC building in Los Angeles, based on story drifts and direct loss. Lognormal distributions were assumed in order to fit data for both story drifts and direct losses after an earthquake. Using FORM it can be seen that system reliability is satisfactory up to levels of intensity of 3. The probability of system failure for higher levels of intensity approaches unity. Checking the individual first order reliability indexes it can be seen that direct loss demands are more critical for low levels of intensity in comparison with drift demands, due to the fact that the threshold value that is used for drifts is far from the mean value of the recorded data. For intermediate levels of intensity, story drifts control the probability of system failure, but for higher levels of intensity, both contribute approximately the same. A SORM analysis has been also used and results were identical with the ones obtained with FORM due to the fact that the limit state functions of the series system are simple component problems.

Finally, a sensitivity analysis was performed, and it is concluded that the reliability index is more sensitive to the threshold value L_o that is used for the direct loss. The gradient of b with respect to the parameter Lo is

increasing with the level of intensity. On the other hand, only for the 2nd level of intensity ($S_a(T_1)/g/\gamma = 1$) there is a tendency of increasing sensitivity for all story drifts. For all the other levels of intensity, the gradient of first order reliability index with respect to d_o is approximately constant.

9.0 ACKNOWLEDGMENTS

Reliability analysis was performed using Cardinal software which was provided by Dr. Chuck Menun, Assistant Professor at Stanford University. His help on critical issues of current research is well appreciated.

10.0 REFERENCES

1. Applied Technology Council. (1996), "Seismic evaluation and retrofit of concrete buildings," Volume 1, California seismic safety commission, report SSC 96-01.
2. Chopra, A.K., Goel, R.K. (2001), "A Modal Pushover Analysis Procedure to Estimating Seismic Demands for Buildings: Theory and Preliminary Evaluation." PEER Report 2001/03, Pacific Earthquake Engineering Research Center, University of California, Berkeley.
3. DRAIN-2DX. (1993), "DRAIN-2DX: basic program description and user guide", Report No. UCB/SEMM-93/17, by Prakash, V., Powell, G. H., and Campbell, S., University of California, Berkeley, CA.
4. Federal Emergency Management Agency. (2003), ''Improvement of inelastic seismic analysis procedures'', Rep. FEMA 440.
5. Federal Emergency Management Agency. (1997a), ''NEHRP guidelines for the seismic rehabilitation of buildings.'' Rep. FEMA 273 (Guidelines) and Rep. 274 (Commentary), Washington, D.C.
6. Federal Emergency Management Agency. (1997b), ''NEHRP recommended provisions for seismic regulations for new buildings and other structures.'' *Rep*. FEMA 302 (Provisions) and Rep. 303 (Commentary), Washington, D.C.
7. Federal Emergency Management Agency. (1998), "NEHRP recommended provisions Chapter 5, structural design criteria".
8. Hazus99 Technical Manual SR-2. (1999), "Loss estimation methodology".
9. Miranda, E., Aslani, H., Taghavi, S. (2004) "Assessment of seismic performance in terms of economic losses" *Proceedings of Bled conference in Slovenia, June '04,* pp. 149-160.
10. Eurocode 8, (2003) "Design provisions for earthquake resistance of structures,".
11. Krawinkler, H., Ibarra, L. (2003), "Collapse probability of frame structures with deteriorating properties", *Proceedings for Otani Symposium, Tokyo '03*.
12. Mendina, R.A., Krawinkler, H. (1999), "Seismic demands for nondeteriorating frame structures and their dependence on ground motions", Final report on PEER project, Seismic demands on performance based design.
13. NEHRP. (1992), "Handbook for the Seismic Evaluation of Existing Buildings" (FEMA).
14. Rojahn, C., King, S.A., Scholl, R.E., Kiremidjian, A. S., Reaveley, L.D., Wilson, R.R. (1997), "Earthquake damage and loss estimation methodology and data for Salt Lake country, Utah (ATC-36)", Earthquake Spectra Vol.13, No.4.
15. Shome, N., and Cornell C.A. (1999), "Probabilistic seismic demand analysis of nonlinear structures", Report No. RMS-35, Department of Civil Engineering, Stanford University.
16. Vamvatsikos, D., and Cornell, C.A. (2002), "Incremental dynamic analysis", Earthquake Engineering & Structural Dynamics, 31, 3, March, pp. 491-514.

Structural Control and Optimization

OPTIMAL TRUSS DESIGN USING ANT COLONY OPTIMIZATION

Symeon Christodoulou

Department of Civil and Environmental Engineers
University of Cyprus
P.O.BOX 20537, 1678 Nicosia, Cyprus
e-mail: schristo@ucy.ac.cy

Keywords: Ant colony optimization, truss design optimization.

Abstract. *The paper presents a methodology to arrive at optimal truss designs using Ant Colony Optimization (ACO) algorithms. Ant Colony Optimization is a population-based, artificial multi-agent, general-search technique for the solution of difficult combinatorial problems with its theoretical roots based on the behavior of real ant colonies and the collective trail-laying and trail-following of its members in searching for optimal solutions in traversing multiple paths. In essence, ACO is inspired by the foraging behavior of natural ant colonies which optimize their path from an origin (ant nest) to a destination (food source) by taking advantage of knowledge acquired by ants that previously traversed the possible paths and the pheromone trail these ants leave behind as the traverse the paths to optimal solution. In computer implementations of the ACO algorithms, artificial ants are agents and solution-construction procedures that stochastically build solutions by considering (1) artificial pheromone trails which change dynamically at run time to reflect the agents' acquired search experience, and (2) heuristic information on the problem/network being solved. The paper outlines the fundamental mathematical background of the ACO method and a suggested possible implementation strategy for solving for optimal truss designs (geometrical configuration and member characteristics).*

1 INTRODUCTION

Truss design optimization is of paramount importance to both designers and owners, since it provides for more efficient (structurally and financially) structures. The goal of truss optimization is to maximally utilize the geometry and material of the proposed design elements to result in the lightest structure while satisfying all the design, manufacturing and other physical constraints. Traditionally, truss optimization is performed using mathematical, or numerical, optimization techniques for a truss with a fixed configuration which, in essence, optimize the members' cross sectional areas given the geometry and topology of the proposed structure.

Truss design is usually originated with a given distance that the desired structure needs to span and the assumed extreme loading conditions. Designers then determine the depth and overall profile of the truss (geometry), the number and arrangement of truss members (topology), and the shape and cross sectional areas of each member (component properties) such that proposed truss design can satisfy both loading/resistance requirements service requirements. The goal of truss optimization is the arrival at optimal truss topology configurations that result in the lightest possible structure while satisfying all design and other constraints.

Traditionally, optimization is performed using mathematical optimization techniques assuming a truss with a fixed configuration (where, given the geometry and topology, the member cross sectional areas are optimized). In the past decade, genetic algorithms (GAs) were employed to solve for optimized designs (selection of members, angles of inclination) given fixed topologies[6],[7] and more recently GAs were employed to optimize the topology as well[2]. The latter is based on an assumed starting topology based on a triangularized shape that then is adjusted to satisfy problem constraints (locations of supports and loads), followed by shape optimization based on stress.

More recently, further adaptations of genetic algorithms were utilized to arrive at complete topology optimizations either by mutations[11], floating-point genetic algorithms[12] or random-cost methods[1]. The random-cost method is of particular interest because of the similarities in the approach, of minimizing an objective function through "random-walks" in the topology.

The following sections present preliminary work on the application of agent-based methods for the optimization of truss topologies. The method of interest is called "Ant Colony Optimization" and originates from the field of agent-based artificial intelligence.

1 ANT COLONY OPTIMIZATION

2.1 Introduction

Ant Colony Optimization (ACO) is a population-based general search technique, proposed by Dorigo (1992, 1996), for the solution of difficult combinatorial problems. The method is inspired by the foraging behavior exhibited by real ant colonies and the essential characteristic of ACO algorithms is "the combination of a priori information about the structure of a promising solution with a posteriori information about the structure of a previously obtained good solution"[10].

Real ant colonies exhibit interesting behaviors, suitable to network traversing and thus optimization. In particular, an ant can find shortest paths between food sources and a nest and in doing so deposit a chemical substance, called "pheromone", forming "pheromone trails" which can then be followed by other ants in the colony. When choosing their way through the possible path routes, ants can smell the deposited pheromone and tend to follow those paths marked by stronger pheromone concentrations. In essence, while an isolated ant moves essentially at random, an ant encountering a previously traversed path and pheromone-laid trail can detect that the path was previously traversed and then decide with high probability to follow this path and subsequently reinforce the trail with its own pheromone.

The collective behavior is therefore characterized by a positive (reinforcing) feedback loop where the probability with which each ant chooses the path to follow increases with the number of ants having chosen the same path in the preceding steps. The final result is the relative quick convergence of the path-traversing to the shortest path.

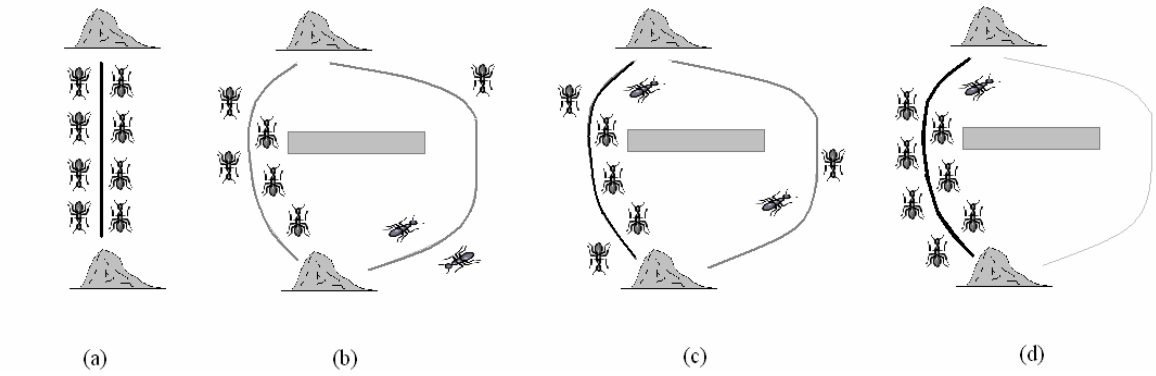

Figure 1: Basic ACO concepts (pheromone laying and shortest path searching)

Figure 1 depicts this behavior for a hypothesized "ant colony" of eight, traversing a path from the nest to the food source (1a) and its behavior when encountering a path obstacle (1b). In this case the population randomly follows possible paths (1b) laying pheromone on the way to the food source and then back to the nest (1b, 1c). The pheromone trail is reinforced with each successive pass until the ant population and path traversing converge to the shortest path between source and destination (1d).

2.2 Theoretical Framework of the ACO Metaheuristic

A number of ACO algorithms, starting from the original work by Dorigo[3],[4], have been developed and proposed over the years, the most known of which are the Ant Colony System (ACS), the Elitist Ant System, the MAX-MIN Ant System, a Rank-based version of Ant System, and the Best-Worst Ant System.

The common framework for ACO applications was proposed posteriori to be the ACO metaheuristic[4], with artificial ants seen as stochastic solution procedures and acting as agents. The solution construction is biased by the pheromone trails which change at run-time, the heuristic information on the problem instance and the ants' private memory.

The generic problem topology is as follows[11]:

- A finite set of components is given, $\mathbf{C} = \{c_1, c_2, c_3, \cdots, c_N\}$.
- The states of the problem, $\mathbf{x} = \{c_i, c_j, \cdots, c_k, \cdots\}$, are defined in terms of sequences (relationships) over the elements of $\mathbf{C}$ and the set of all possible sequences is denoted by $\mathbf{X}$. A

finite set of constraints in the system, Ω, defines the feasible states, $\overline{\mathbf{X}} \subseteq \mathbf{X}$.

- A set of feasible solutions, $\mathbf{S}^*$, is given with $S^* \subseteq \overline{\mathbf{X}}$.
- A cost function $f(s,t)$ is associated with each candidate solution $\mathbf{s} \in \mathbf{S}$, and in some cases a separate cost function is defined and associated to states other than solutions.

The generic behavior of the artificial ants can also be outlined as follows (Stützle et al. 2002):

- Ants build solutions by moving on the construction graph $G = (\mathbf{C}, \mathbf{R})$, where $\mathbf{C}$ is the set of components in the network, and $\mathbf{R}$ is the set of relationships (connections) fully connecting the components. Even though both feasible and infeasible solutions can be built, artificial ants, in general, try to build feasible solutions. The problem constraints, Ω, are implemented during the network traversing and policy followed by the artificial ants.
- The components, $c_i \subseteq \mathbf{C}$, and connections, $r_{ij} \subseteq \mathbf{R}$, can have a pheromone trail, τ, associated with them which allows for the implementation of a long-term memory policy about the ant search process. Similarly, the components, $c_i \subseteq \mathbf{C}$, and connections, $r_{ij} \subseteq \mathbf{R}$, can have a heuristic value, η, which allows incorporation of problem-specific information.
- The path that each artificial ant, k, follows can be stored in the ant's memory M^k.
- Each artificial ant, k, can be assigned a start state, x_s^k, and one or more termination conditions, e^k. The construction procedure of ant k stops when at least one of the termination conditions e^k is satisfied.
- When in state $x_r = (x_{r-1}, i)$ an ant attempts to move to any node j in the feasible solutions subset (immediate successors) N_i^k. If this is not possible, it might be allowed to move to any other node that it is not part of the immediate-successors subset.
- The move to a successor node is determined by a stochastic decision rule and it is subject to a function of the locally pheromone and the connection's heuristic, the ant's memory, and the problem constraints.
- Each addition of a component c_j to the current solution updates the pheromone trail associated with it.
- Once a solution is built the ant retraces the same path backwards and updates the pheromone trails of the used components or connections.

2.1 Ant Colony Optimization Algorithm

The above described topology and ACO metaheuristic form the basis for most ant colony optimization algorithms found in literature. A pseudocode adaptation of such algorithm is shown below.

```
procedure AntColonyOptimization
  Initialize topology_parameters
  ConstructNetwork
  Initialize pheromone_trails
  for each Ant
        while (termination condition not met) do
          ConstructSolutions
          ForwardTraversePath
          ApplyLocalPheromoneUpdate
          BackwardTraversePath
          ApplyLocalPheromoneUpdate
        end
  next ant
end AntColonyOptimization
```

2 ANT COLONY OPTIMIZATION AND TRUSS DESIGN OPTIMIZATION

2.1 Introduction

The concepts and methodology employed by the Ant Colony Optimization metaheuristic can find applications in truss design optimization since the underlying topology and optimal path searching exhibit several similarities. The idea is to treat a proposed truss topology as a maze to be traversed by artificial ants looking for the best way to reach an end (truss supports) from a starting point (nodes where the loads are applied). This "best way" can be a combination of optimization parameters such as the traveling distance (thus the length of truss members traversed), the resistance to movement (stress within such members, thus the interior member forces and corresponding cross sectional areas), the cost of the truss members, etc.

If one makes the simplistic assumption that the optimal design takes advantage of longer distances between truss nodes (to "tone down" internal forces in them as a result of longer spanning distances and increased resistance), and if one substitutes the search for shortest path (ACO) to the search for longest path (truss optimization) and treats ACO ants, states, connections and a cost function to truss optimization's external loads, truss members, connectivity and internal forces respectively then the ACO metaheuristic can be employed in solving for the longest path in connected, acyclic graphs (such as truss topology problems).

The optimization starts with a fully connected graph of truss nodes/members that is successively analyzed for the longest path from the nodes where the loads are applied to the nodes where the truss supports are. The shortest path for each such combination is pruned (corresponding elements are removed) and the resulting topology is analyzed structurally for obtaining the internal forces in each element. The method is iterative and it stops when the necessary conditions are met or when successive optimization designs converge to a proposed topology.

2.1 ACO-Based Algorithm

For a given truss topology defined by a graph $\mathbf{G} = (N, A)$, with N being the set of nodes (truss nodes) and A being the set of arcs (truss elements) connecting the subject nodes, the proposed ACO-based procedure for finding the longest path(s) between chosen nodes N_1 and N_2 can be summarized by the following steps:

1. Initialize all arcs with small amount of pheromone, τ_0. This value can be an inverse line-distance between the nodes N_1 and N_2, or the inverse line-distance of the subject arc.
2. An artificial ant is launched from node N_1 (the start node) pseudo-randomly walking from a node to a successor node via the connecting arcs until it reaches either the end-node (N_2) or a dead end. When at a given node, the artificial ant's selection of an arc to follow is probabilistic, based on a stochastic assignment of each i^{th} arc's likelihood of selection, as defined by

$$p_i = \frac{\tau_i \eta_i^{\beta}}{\sum_i \tau_i \eta_i^{\beta}} \tag{1}$$

   In the above equation, τ_i is the pheromone concentration on the i^{th} arc, η_i is an a priori available heuristic value for the i^{th} arc and β_i is a parameter determining the relative influence of the heuristic information. The value of η_i can be defined either as the inverse of the length of the arc, or the inverse of the length of the plus the line-distance between the subject node and N_2. It should be noted that previously visited arcs are excluded from the selection (to enable complete "tree spanning" and avoid "memorization").
   a. The selection is further assisted by the consideration of a randomly generated number, $0 \le q \le 1$, which is compared to a predefined value, q_0, specific to the network topology. If $q \le q_0$ then the arc with the highest value p_i is selected. Otherwise, a random selection of an arc is used based on the distribution defined by the equation for p_i.
3. Upon crossing each i^{th} arc during the aforementioned solution-constructing phase a local pheromone update rule is applied to update the level of pheromone concentration at the given arc. The updated pheromone level is defined by

$$\tau_i = (1-\rho)\tau_i + \rho\tau_0 \tag{2}$$

where ρ is another network topology parameter ($0 \le \rho \le 1$). As already noted, the goal of the local updating is to enable exploration of more path/route variations by making already traversed arcs less likely to be chosen again during the randomization of the arc selection process.

4. Steps (2) and (3) are repeated for all ants in the ant colony and the most successful ant (i.e. the one whose path defines the solution) is used to globally update the network's pheromone trails. The global update rule is defined by

$$\tau_i = (1-\alpha)\tau_i + \alpha\tau_L \tag{3}$$

where α is yet another network topology parameter ($0 \le \alpha \le 1$) whose value determines the level of evaporation of pheromone concentrations. The factor τ_L is a value inversely proportional to the path length of the best solution in case of an arc visited by the best ant or zero for all other ants.

   a. The global update rule can be applied by either the "global-best" or the "iteration-best" ant. In the first case, the ant to perform the update is the one that obtained the best solution (found the longest path in the network) during the entire optimization process. In the second case the update is performed by the ant reaching the best solution during each iteration of the algorithm.

5. Steps (2) - (4) are repeated for either a fixed number of iterations or until a predefined condition is met, and upon termination of the algorithm the pheromone trail in the graph $\mathbf{G} = (N, A)$ is used to determine the solution (the arcs with highest pheromone concentration form the longest path of the network).

2.1 Sample Application

The ACO algorithms were implemented by means of custom software developed with truss topology optimization in mind, so as to enable integration with structural analysis software. The developed software application can be executed in either "test mode" (randomized network topologies) or "project mode" (actual truss topologies to be solved) and integrated with external database management systems to account for additional common design features such as standard truss members (steel members, cross sectional areas, etc.), material costs, etc.

The sample truss design optimization considered consists of a two-layer truss system (2x5 nodes), simply supported at the bottom edges and loaded with equal loads at the top layer (P = 100 units) as shown in Figure 2. A non-symmetric geometry was chosen on purpose, to serve as a stepping stone for a second-phase research work that will consider allowance of wider spatial modifications (such as adding/pruning nodes, modification of x,y coordinates of existing nodes, resizing of elements/spans, etc.)

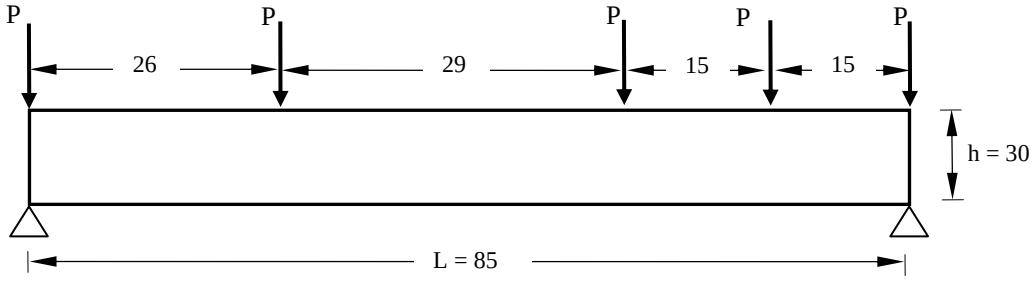

Figure 2: Initial topology of sample truss optimization problem

The optimization process starts with the automatic generation of a fully-connected network of truss nodes and elements as shown in Figure 3a. The ACO algorithm then performs a first-cut path-traversing optimization sequence, based on a population of 50 artificial agents which, after traversing the interconnected nodes, report on the longest paths from a node to any other node. At the end of this first-cut simulation process all elements on each node-to-node shortest path are pruned (deleted from the connection graph) resulting in the topology shown in Figure 3b, based on an imposed constraint that no peripheral elements are deleted during the process.

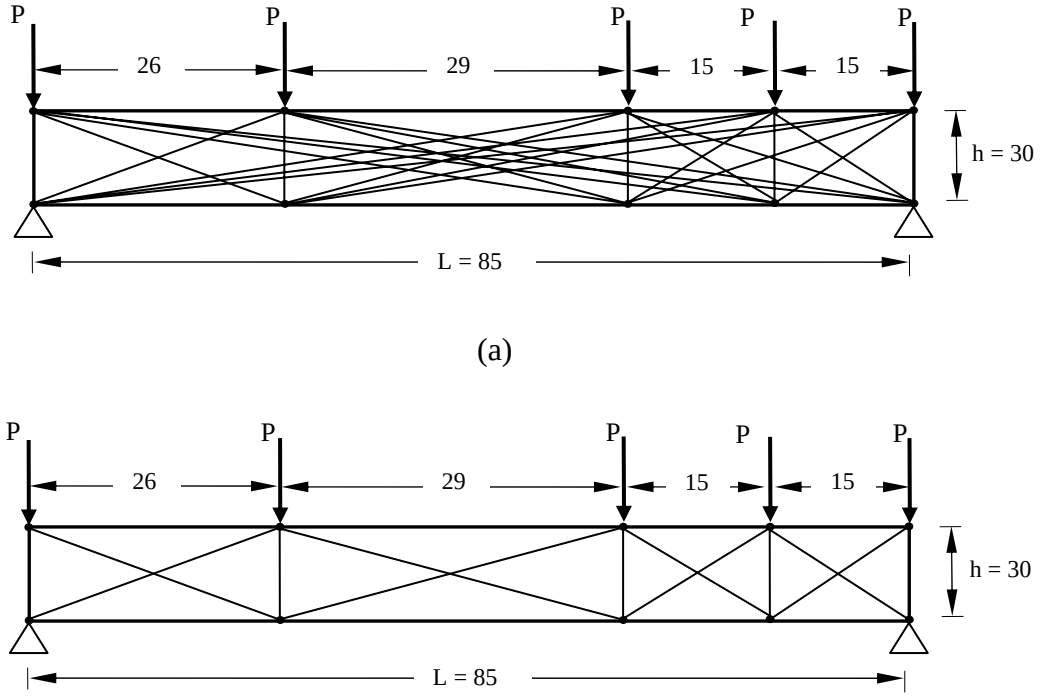

Figure 3: Topology of sample truss optimization problem, (a) at the start of the process (iteration 0) and (b) at the end of the ACO search for shortest node-to-node paths (iteration 50).

The next step in the optimization process involves the integration of the external truss-analysis software and the external database of truss members and their properties. The system calculates the internal element forces at the end of every specified simulation iteration (e.g. every 50 cycles of path traversing by an artificial agent) and upon ranking these forces in descending order it then prunes the element with the smaller internal force, less than a given threshold value (considering such element to be unnecessary). Appropriate members are selected automatically from an electronic database of truss members and the total weight of the structure is calculated. The process continues until the structure becomes indeterminate, or until there is convergence of the resulting total weight of it. Sample resulting truss topologies are shown in Figure 4, with resulting total truss weights tabulated in Table 1. The topologies were optimized with assumed identical truss members (A=1, E, ρ) of variable lengths, as dictated by the generated geometry. The goal at this early stage of the research is the optimization of geometry and not necessarily section types. The selection of section types for the truss elements can be achieved by linking the ACO metaheuristic and software code with a database of readily available truss elements and the corresponding sectional and material properties, from which the program can select the sections with minimum weight satisfying the stress and displacement constraints and tolerances dictated by the user.

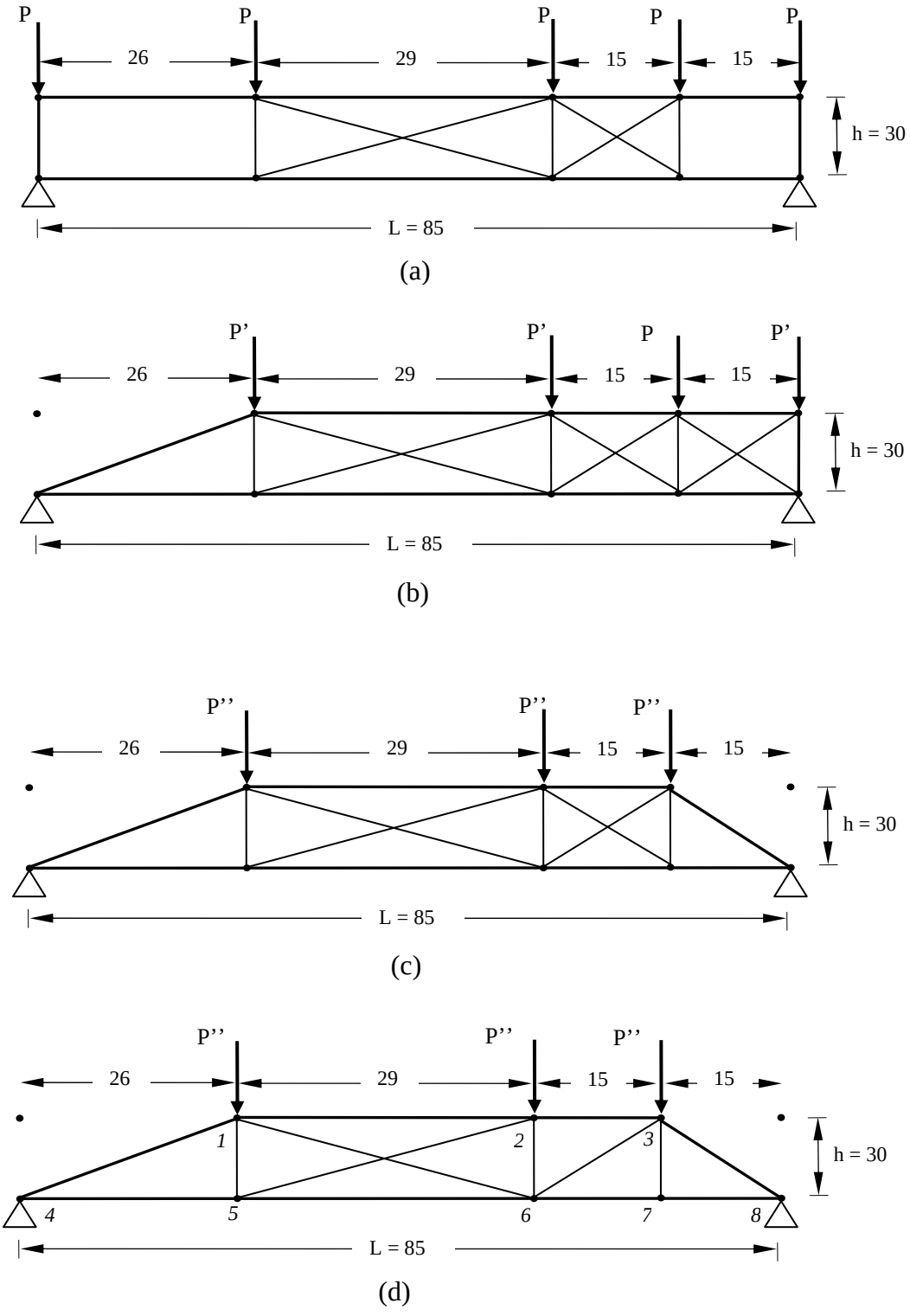

Figure 4: Topology of sample truss optimization problem at the end of various stages of the optimization process.

The results of the ACO topology optimization algorithm for six sample network topologies are shown in Table 1. The ACO topology parameters were kept constant ($q_0 = 0.5$, $\beta = 1.0$, $\rho = 0.5$, $\alpha = 0.5$, $C = 100$) but the other network characteristics varied (the number of nodes and arcs in the network topology, and the number of "ant nests" (i.e. the number of possible start nodes in the network) as a result of adding and pruning elements

during optimization.

Iteration No.	Figure	Truss Topology			
		Nodes	Elements	Total Length	Total Weight
50	3(a)	10	45	2066	2066
100	3(b)	10	29	1144	1144
150	4(a)	10	17	464	464
200	4(b)	9	18	462	462
250	4(c)	8	15	436	436
300	4(d)	8	14	375	375

Table 1 : Best-ant solutions for sample topologies

3 CONCLUSIONS

The ACO seems to be functioning well in searching for optimal truss topology solutions. As Table 1 shows, the ACO metaheuristic was able to improve on the initial topology, in terms of total truss weight and resulted in a modified topology of reduced weight prior to reaching an indeterminate structure. The algorithm stopped at the topology shown in Figure 4(d), while attempting to prune the element '3-7' (its internal force was zero) and causing singularity (indeterminate structure). Attempts to prune elements '5-6' or '1-2' (elements with the smaller internal forces in the network) were also the cause of indeterminacy and their pruning was abandoned.

At this early stage of the research the results are encouraging. Future work will focus on linking the ACO algorithm to external databases of typical truss sections of known sectional and material properties and automating the selection of such elements to optimize truss weights subject to given topologies, and also modifying the algorithm to allow for reconfiguration of the truss topology in terms of locations of truss nodes and therefore element lengths (not just adding and pruning of elements).

REFERENCES

[1] Baumann, B. and Kost, B. (1997). Topology Optimization of Trusses – Random Cost Method Versus Evolutionary Algorithms. Computational Optimization and Applications, 14, pp. 203-218, Netherlands.

[2] Cagan, J. and Mitchell, W. J. (1993). A grammatical approach to network flow synthesis. In Gero, J., editor, Preprints of the IFIP WG 5.2 Workshop on Formal Design Methods for Computer-Aided Design, pp. 153-166, Tallinn, Estonia.

[3] Dorigo, M. (1991). "Ant Colony Optimization, New Optimization Techniques in Engineering", by Onwubolu, G. C., and B. V. Babu, Springer-Verlag Berlin Heidelberg, pp. 101-117.

[4] Dorigo, M., Maniezzo, V., and Colorni, A. (1996). "The Ant System: Optimization by a Colony of Cooperating Agents". IEEE Transactions on Systems, Man, and Cybernetics Part B, vol.26(2), pp. 29-41.

[5] Goldberg, D. E. (1989). Genetic Algorithms in Search, Optimization, and Machine Learning. Addison-Wesley, Reading, MA.

[6] Goldberg, D.E. and Samtani, M.P. (1999). "Engineering Optimization Via Genetic Algorithms ". In *Proceedings of the Ninth Conference on Electronic Computation*, ASCE, New York, NY, pp. 53–60.

[7] Jenkins, W. (1991). Towards structural optimization via the genetic algorithm. Computers and Structures, 40(5):1321-1327.

[8] Louis, S. J. (1993). Genetic Algorithms as a Computational Tool for Design. PhD thesis, Indiana University, Bloomington. Department of Computer Sciences.

[9] Louis, S. J. and Rawlins, G. (1991). Designer genetic algorithms: Genetic algorithms in structure design. In *Proceedings of the Fourth International Conference on Genetic Algorithms*, pages 53–60. Morgan Kauffman, San Mateo, CA.

[10] Maniezzo V, Gambardella L.M., De Luigi F. (2004). "Ant Colony Optimization, New Optimization Techniques in Engineering", by Onwubolu, G. C., and B. V. Babu, Springer-Verlag Berlin Heidelberg, 101-117.

[11] Stützle, T. and Dorigo, M. (2002). "The Ant Colony Optimization Metaheuristic: Algorithms, Applications, and Advances". In F. Glover and G. Kochenberger (editors), Handbook of Metaheuristics, Kluwer Academic Publishers, Norwell, MA.

[12] Turkkan, N. (2003). Discrete Optimization of Structures Using a Floating-Point Genetic Algorithm. Annual Conference of the Canadian Society for Civil Engineering, Moncton, N.B., Canada, June 4-7.

ROBUST CONTROL IN STRUCTURAL DYNAMICS, TAKING INTO ACCOUNT STRUCTURAL UNCERTAINTIES

Georgios E. Stavroulakis*, Daniela G. Marinova†, and Emmanouel C. Zacharenakis††

* Department of Mathematics, Institute of Mechanics, University of Ioannina, GR-45110 Ioannina, Greece and Department of Civil Engineering, Carolo Wilhelmina Technical University, Braunschweig, Germany
e-mail: gestavr@cc.uoi.gr, g.stavroulakis@tu-bs.de web page: http://www.math.uoi.gr/~gestavr

† Faculty of Applied. Mathematics and Informatics, Technical University of Sofia, BG-1756 Sofia, Bulgaria
e-mail: dmarinova@dir.bg

†† Department of Civil Engineering, Technological Educational Institute of Crete, GR-71306 Heraklion, Greece
e-mail:zacharen@stef.teiher.gr

Keywords: Smart structures, Robust control, H_∞ optimal control, structural uncertainty.

Abstract. *This paper considers the problem of active vibrations-suppression of smart structures with structural uncertainties. A linear, discrete dynamical model of the structure is used. Damages or further inaccuracies in the structural system are considered and modeled as uncertainties in the structural parameters of the system using the linear fractional transformation (LFT) technique. The control design is based on the H_∞ optimal control theory. A suboptimal numerical algorithm is used for the numerical solution of the control problem. Numerical examples demonstrate the efficiency of the proposed approach.*

1 INTRODUCTION

Active or passive feedback control of structures provides a number of potentially interesting applications in vibration-suppression for civil engineering, like the design against earthquake or wind loads. The classical theory of optimal control has been extensively used for the study of academic demonstrative examples and for real applications. Besides the technological limitations, a serious problem related to active structural control is related to uncertainties in the structure or/and in the external loads. The case of structural uncertainties arisen in the main parameters (mass, stiffness and damping) of the structure is considered in this paper. They may represent incompleteness or inability of the used structural analysis model and damage- or ageing-related deterioration of the structure. Since the optimal control will be designed with the use of a nominal model, its efficiency on a modified model is not always guaranteed. Robust control methods, which take into account the presence of certain amount of uncertainty during the design, are suitable.

The concept of robust optimal control using the H_∞ approach is suitable for systems with certain classes of structured uncertainties [1, 7]. In fact, since we consider linear structural systems, uncertainties that can be represented in the form of linear fractional transformations (LFT) are introduced [7]. The importance of robust control for real-life applications has been discussed in several recent publications, among others in [2, 4, 5, 6].

The model of the structure is given by means of classical matrix structural analysis or finite element methods. A simple shear-type frame is used for demonstration here. Damages and inaccuracies can be attached to mass, damping and/or stiffness characteristics. Their LFT model can be correlated to damage-induced or other type of uncertainty.

2 MODELING AND PROBLEM STATEMENT

Let us suppose a classical discretized system of structural dynamics with the typical mass, damping, and stiffness matrices, the vector of nodal degrees of freedom, the loading vector and an additional control loading vector. Let us further suppose that the main parameters (mass, damping and stiffness) of the dynamical structure are not known exactly and can be represent as an uncertain system of the following form

$$[M + p_M \Delta_M(t) M]\ddot{x}(t) + [C + p_C \Delta_C(t) C]\dot{x}(t) + [K + p_K \Delta_K K]x(t) = HU(t) + F(t)$$
$$Y(t) = x(t). \tag{1}$$

Here $X(t)$ is the vector with the degrees of freedom (usually, displacements), M, C, K are the nominal parameters of the structure, and Δ_M, Δ_C, Δ_K are normed matrix functions (actually, members of a Hardy space), corresponding to uncertain parameters, that for every t satisfy the conditions

$$\Delta_M^T(t)\Delta_M(t) \le I, \qquad \Delta_C^T(t)\Delta_C(t) \le I, \qquad \Delta_K^T(t)\Delta_K(t) \le I, \tag{2}$$

where I is the unique matrix. The coefficients p_M, p_C, p_K correspond to some parameters of perturbation and F is the external disturbance (usually, loading). The uncertainty in the matrices M^{-1}, C, K can be represented by upper linear fractional transformation (LFT) in the perturbations Δ_M, Δ_C, Δ_K.

To this end, let us denote by Y_M, Y_C, Y_K the inputs to perturbations Δ_M, Δ_C, Δ_K, add the vector $Y_\Delta = [Y_M \quad Y_C \quad Y_K]$ to the outputs of the system, denote by U_M, U_C, U_K the outputs of Δ_M, Δ_C, Δ_K and add the vector $U_\Delta = [U_M \quad U_C \quad U_K]$ to the inputs of the system. After this shaping and by using the canonical form of the equation (1) we receive the state-space matrix form of the dynamical system:

$$\begin{bmatrix} \dot{X} \\ Y_\Delta \\ Y \end{bmatrix} = G \begin{bmatrix} X \\ U_\Delta \\ U \end{bmatrix} \qquad U_\Delta = \Delta(t) Y_\Delta \quad , \tag{3}$$

$$G = \begin{bmatrix} A & B_1 & B_2 \\ C_1 & D_{11} & 0 \\ C_2 & 0 & D_{22} \end{bmatrix}, \quad A = \begin{bmatrix} 0 & I \\ -M^{-1}K & -M^{-1}C \end{bmatrix}, \quad B_1 = \begin{bmatrix} 0 & 0 & 0 \\ -p_M I & -p_C M^{-1} & -p_K M^{-1} \end{bmatrix}$$

$$B_2 = \begin{bmatrix} 0 \\ -M^{-1}H \end{bmatrix}, \; C_1 = \begin{bmatrix} -M^{-1}K & -M^{-1}C \\ 0 & C \\ K & 0 \end{bmatrix}, \; D_{12} = \begin{bmatrix} M^{-1}H \\ 0 \\ 0 \end{bmatrix}, C_2 = \begin{bmatrix} I & 0 \end{bmatrix}, \; D_{21} = \begin{bmatrix} 0 & 0 & 0 \end{bmatrix},$$

where H is control location matrix. Please, note that from relation (3) $X = [x \quad \dot{x}]$ denotes the state-space vector which involves both displacements and velocities of relation (1). The matrix G of the system (3) contains only physical nominal parameters of the system and is known. The uncertainty matrix of the system $\Delta = [\Delta_M \quad \Delta_C \quad \Delta_K]$ is a block-diagonal structural matrix and influences the input/output connection between the control U and the output Y in a way that can be represented as a feedback by the upper LFT

$$Y = F_U(G, \Delta)U \; . \tag{4}$$

The linear system (4) can be described with the structural scheme of Figure 1, where F is the external disturbances and E is a normed error.

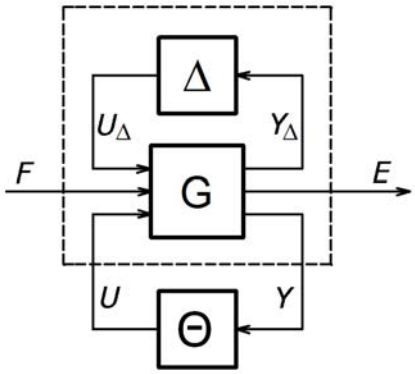

Figure 1. Closed-loop diagram of uncertainty system for robust H_∞ control

Let $W = [U_\Delta \quad F]^T$ denote all external inputs coming to the system and let $Z = [Y_\Delta \quad E]^T$ denote all signals that characterize the system's behaviour. The system (3) can be represented in compact form by the equation

$$\begin{bmatrix} z \\ y \end{bmatrix} = P \begin{bmatrix} w \\ u \end{bmatrix}, \tag{5}$$

The aim of this work is to design a numerical control algorithm in order to suppress the external disturbances of the uncertain system (5). The problem consists in designing of a suboptimal H_∞ control feedback law in the form

$$U = -\Theta X(t), \tag{6}$$

that ensures for any admissible uncertainties:
a) suppression of external excitations in a given ratio

$$\frac{\|Y\|_2}{\|w\|_2} \le \gamma \tag{7}$$

for zero initial conditions and all excitations bounded in L_2 space, where $\|Y\|_2$ denotes the norm of $Y(t)$ in L_2, and
b) the asymptotical stability of the equilibrium state when the system is not excited.
The solution of this problem will be done using a LFT technique. The closed loop transfer matrix of the system (5) from disturbances W to regulated outputs Z is given as a lower LFT in Θ

$$Z = F_L(P, \Theta)W, \tag{8}$$

Then the suboptimal H_∞ control design problem can be formulated by the equation

$$\|F_L(P, \Theta)\|_\infty < \gamma, \tag{9}$$

Since the described problem may have, in general, multiple solutions and local minima, one speaks about a suboptimal solution. The robust H_∞ suboptimal control law is determined in the classical way from the solutions of certain matrix Riccati equations.

3 CONTROL DESIGN

The robust performance and the robust stability for the closed loop system are of paramount importance. The system matrix G describes the set of perturbed models. For the robust stability analysis the controller Θ can be viewed as a known system component that is absorbed into an interconnection structure P together with the plant G. For the robust stability we are interested in finding the smallest admissible perturbation Δ in the sense of the maximal singular value $\overline{\sigma}(\Delta)$ such that destabilizes the closed loop framework. The loop is well-posed and internally stable if and only if

$$\sup_{\omega \in R} \mu_{\Delta}(P(j\omega)) < 1, \tag{10}$$

where μ_{Δ} is the structured singular value.

The parameter perturbations can amplify significantly the effect of the external influences. As a result the performance of the closed loop system can be deteriorated before loosing stability. To arise at a desirable performance it is necessary that, for all frequencies, the following relation is satisfied

$$\left\| W_p (I + G\Theta) \right\|_{\infty} < 1. \tag{11}$$

The weight matrix W_p, reflects the relative importance of different frequency ranges on the performance and controls the system's performance via an iterative process. Let us assume for W_p the diagonal form

$$W_p(s) = w_p(s) I, \tag{12}$$

Thus, the assumption (11) implies that the maximal singular value of the sensitivity transfer matrix must satisfy the following inequality

$$\overline{\sigma}[(I + G\Theta)^{-1}(j\omega)] < \left| \frac{1}{w_p(j\omega)} \right|. \tag{13}$$

The exact values of the parameters in the weighing function w_p depend on the application and were chosen here by trial-and-error. For the numerical simulations the weight function w_p is chosen as

$$w_p = \frac{s^2 + s + 8}{2s^2 + 7s + 0.008} \tag{14}$$

The corresponding H_{∞} suboptimal controller in frequency domain has been obtained by using MATLAB routines and has the following form:

$$\Theta = \frac{239.09s^3 + 915.56s^2 + 2664.07s + 8366.22}{s^4 + 15.84s^3 + 101.23s^2 + 203.19s + 0.23}. \tag{15}$$

The parameter γ achieves the value 19.9966 . For a γ less than this value the matrix Riccati equations have no stable solutions.

4 NUMERICAL RESULTS AND SIMULATIONS

Numerical results are given for two-storey shear-type building. The horizontal displacements are measured and controlled. The mass of every storey is taken 2000 and the stiffness of each storey is taken to be equal to 20.10^6 in compatible units. The damping matrix is considered as linear combination of mass and stiffness matrices (Rayleigh assumption) with coefficients equal to 0.03. The perturbation coefficients p_M, p_C, p_K are taken equal to 0.05. The H_∞ suboptimal controller is designed on the nominal model and takes into account the perturbation coefficients. The intervals for the admissible perturbations of the nominal parameters of the structure in which the controlled system remains stable are related but are not directly equal to p_M, p_C, p_K. They are influenced from the chosen weight function as well. The numerical simulations show that the system remains stable for perturbations higher than two times of the assumed perturbation coefficients.

Two kinds of external load impulsive and random are applied for simulations. The response of uncontrolled and controlled structure is compared. The results for the nominal (not perturbed) system are shown in Figures 2 and 3.

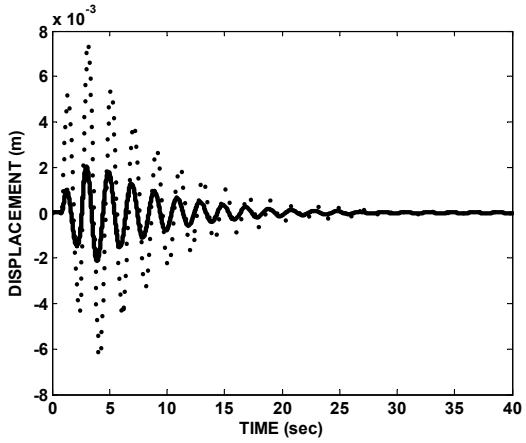

Figure 2. Transient response of the uncontrolled (dot) and controlled (solid) structures due to impulsive load

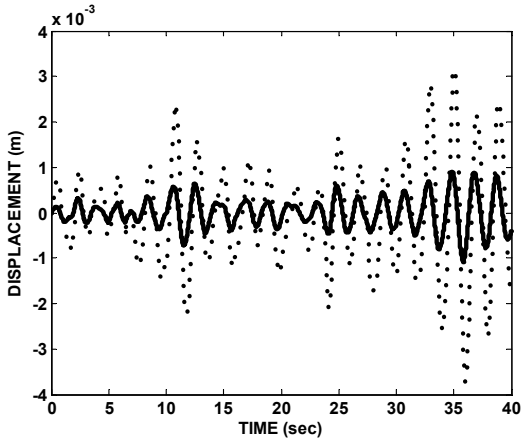

Figure 3. Transient response of the uncontrolled (dot) and controlled (solid) structures due to random load

To demonstrate the good closed loop transient response in tracking we supply the structure system with periodic impulsive command input without external loading. The time response to the reference is shown in Figure 4. Suppressions of redundant vibrations directly reflect to rejections of disturbances. The good closed loop transient response in disturbance rejection due to periodic isolated influences is demonstrated in Figure 5.

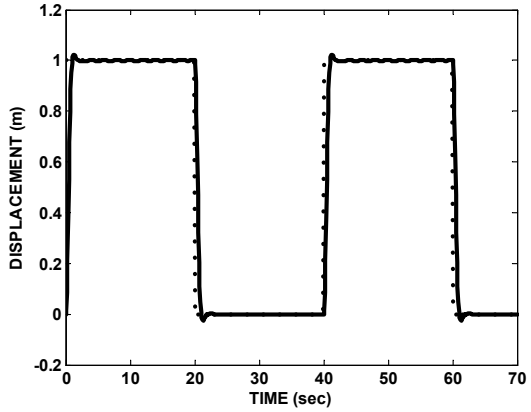

Figure 4. Transient response of the structure (solid) to reference (dot)

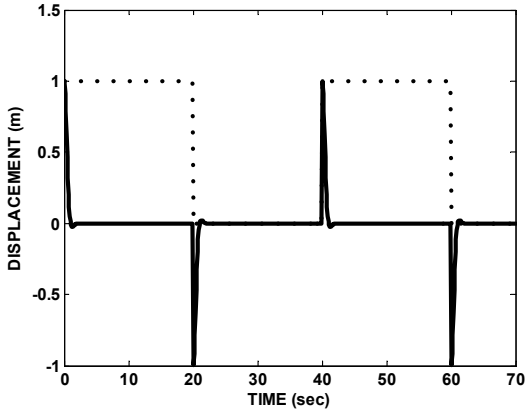

Figure 5. Transient response of the structure (solid) and disturbance (dot)

Comparing the maximal singular value of the closed loop sensitivity transfer matrix with the inverse of the weight matrix we observe that the magnitude of its maximal singular value satisfies the inequality (12) and lies under the inverse of the performance weight matrix for any frequency. These properties indicate good robust performance with good disturbance rejection and transient response. The result is displayed in Figure 6.

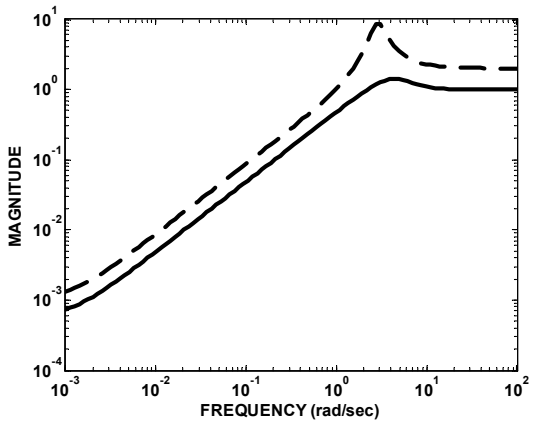

Figure 6. Frequency response of the inverse of the weight function (dashed) and of the sensitivity function (solid)

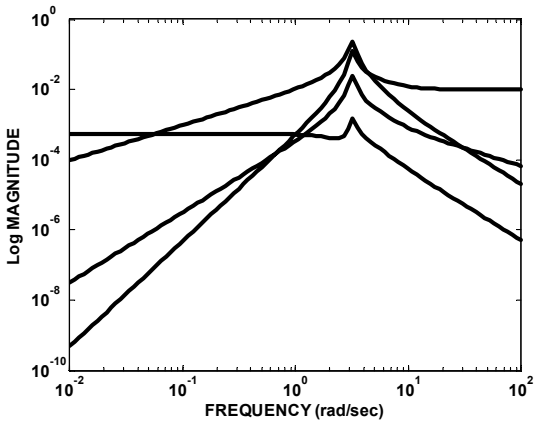

Figure 7. Frequency response of the controlled structure

In the Figure 7 the frequency response of the closed loop structure is shown. Investigation of the robustness of the obtained controller is done in the last set of numerical results. Uncertainty is considered by a change of the mass, stiffness and damping matrix of the structure. Then the performance of the robust H_∞ controller, which has been designed with information taken from the nominal system, is tested on the modified dynamical system. In Figure 8 a comparison of the responses between the nominal system and a system with ten percent higher mass is shown. It can be observed that by virtue of the good sensitivity of the controlled system the magnitude of the suppressed vibrations is slightly increased but the system remains stable. In Figure 9 analogous results are provided for the case of a system with ten percent less stiffness than the nominal one Finally the robustness of the controlled system for the case of a twenty percent higher damping value is demonstrated in Figure 9 is shown the robustness of the controlled system when uncertainty twenty percent occurs in the damping matrix. The response of the controlled system is modified. However, it remains stable. At this point it should be mentioned that when the mass and stiffness matrices are changed significantly, a case which appears after extended deterioration of the system, the controller fails and the system looses its stability.

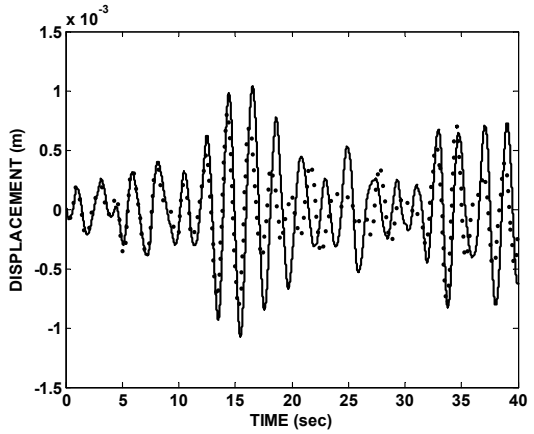

Figure 8. Response of the robust controlled nominal (dot) and mass perturbed (solid) systems

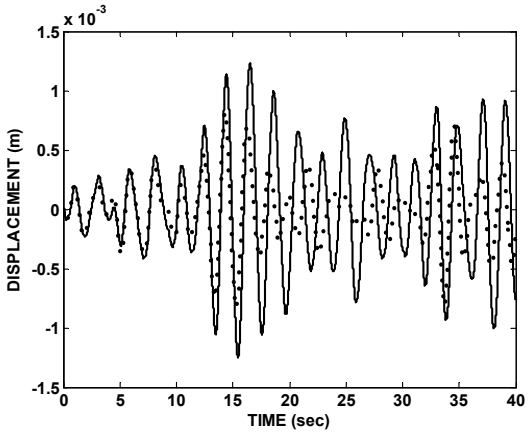

Figure 9. Response of the robust controlled nominal (dot) and stiffness perturbed (solid) systems

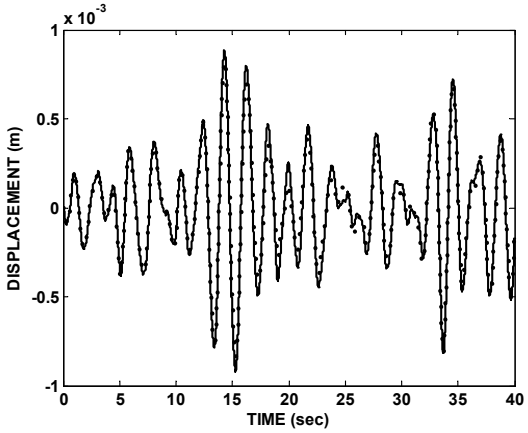

Figure 10. Response of the robust controlled nominal (dot) and damping perturbed (solid) systems

11 CONCLUSIONS

Uncertainty in engineering design is an unavoidable fact of life. Practical methods to account for the worst-case scenario have been developed within the area of optimization in the presence of uncertainty. In optimal control of dynamical systems the corresponding investigations are known under the name of robust control. This paper demonstrates the applicability of the robust control methodology on civil engineering structures with the example of the old-fashioned, well-known shear-type frame of aseismic design. The robust control system, which is designed with the nominal structural data, continues to work, even with some acceptable lower performance, on the modified structure, provided that the modification lies within the assumed uncertainty level. A comparable classical optimization scheme (say, LQR) is, in general, less effective or even fails to work. The extension of this approach to general systems modeled with the finite element method is straightforward. Furthermore the uncertainty levels may be correlated in several ways with damage-, fatigue- or crack-induced modifications of the structure, depending on the application. For example, in the aseismic design of buildings the uncertainty levels may be related with the damage levels predicted from a nonlinear push-over analysis.

From the theoretical point of view it should be mentioned that for higher levels of uncertainty the complexity of the corresponding problems and of their numerical solution increases. In several cases one could identify the source of the higher difficulty: a convex optimization problem becomes nonconvex, therefore multiple solutions and local minima may appear. Currently available numerical tools, like the ones used in this paper, can only guarantee the calculation of a suboptimum. Further investigation on the applicability of global optimization tools in this area seems to be justifiable.

ACKNOWLEDGEMENTS

Financial support of the Greek Secretariat for Research and Technology through an ARCHIMIDES research grant to the TEI of Crete is greatfuly acknowledged.

REFERENCES

[1] Arvanitis, K.G., Zacharenakis, E.C., Soldatos, A.G. and Stavroulakis, G.E. (2003), "New trends in optimal structural control," *Selected Topics in Structronic and Mechatronic Systems,* Editors: Belyaev, A. and Guran, A., World Scientific Publishers, New Jersey, London, Singapore, Hong Kong, Chapter 8, pp. 321-416.

[2] Calise, A.J. and Sweriduk, G.D. (1998), "Active attenuation of building structural response using robust control," ASCE Journal of Engineering Mechanics 124(5), pp. 520-528.

[3] Marinova, D.G. and Stavroulakis, G.E. (2004), "Numerical investigations of optimal control design for building structures subjected to earthquake and wind loadings," Journal of Computer Systems Sciences International 43(4), pp. 574-581.

[4] Schmitendorf, W.E., Jabbari, F. and Yang, J.N. (1994), "Robust control techniques for buildings under earchquake excitation," Earthquake Engineering and Structural Dynamics 23(5), pp. 539-552.

[5] Zacharenakis, E.C. (1997), "On the disturbance attenuation and H infinity-optimization in structural analysis," ZAMM 77(3), pp. 189-195.

[6] Zacharenakis, E.C. and Stavroulakis, G.E. (2000), "On the seismic disturbance rejection of structures," Journal of Global Optimization 17(1-4), pp. 403-410.

[7] Zhou, K. (1998), *Essentials of Robust Control,* Prentice-Hall, Upper Saddle River, New Jersey.

PERFORMANCE-BASED OPTIMUM DESIGN OF STRUCTURES CONSIDERING UNCERTAINTIES

Yiannis Tsompanakis [*,†], **Nikos D. Lagaros** [**,†], **Michalis Fragiadakis** [**] **and Manolis Papadrakakis** [**,†]

[*] Division of Mechanics, Department of Applied Sciences,
Technical University of Crete, University Campus, Chania 73100, Greece
Email: jt@mechanics.tuc.gr, web page: http://www.mechanics.tuc.gr

[**] Institute of Structural Analysis & Seismic Research
National Technical University of Athens, Zografou Campus, Athens 15780, Greece
Email: {nlagaros,mfrag,mpapadra}@central.ntua.gr, web page: http://www.civil.ntua.gr/papadrakakis

[†] Greek Association of Computational Mechanics

Keywords: structural optimization, reliability analysis, Monte Carlo simulation, evolutionary computation, neural networks.

Abstract. *In this paper a robust and efficient methodology is presented for treating large-scale reliability-based, structural optimization problems under seismic loads using the pushover analysis method. The optimization problem is solved with the Evolution Strategies method, while the reliability analysis is carried out with the Monte Carlo simulation method. In order to reduce the excessive computational cost of the reliability-based optimization process the repeated structural analyses that are required during the Monte Carlo simulations are replaced by an efficient neural network approximation scheme.*

1 INTRODUCTION

Reliability analysis methods have been developed significantly over the last decades and have stimulated the interest for the probabilistic optimum design of structures. Despite the theoretical advancements and the improvements in the efficiency of the reliability analysis techniques, they still require disproportionate computational effort for treating practical reliability problems. On the other hand, structural optimization is the only rational procedure to assess whether the design adopted meets the required performance targets. In addition, modern earthquake engineering design philosophy has introduced the concept of performance-based design (PBD)[1-6] for structures subjected to seismic loading conditions. In conjunction with the advancements in the computational tools for earthquake engineering, the shift from design procedures based on conventional static analysis to more realistic non-linear analysis procedures is possible and also necessary.

It is generally accepted that performance-based design has to be reliability-based[7,8]. The most effective way to treat the inherent probabilistic nature of geometry, material properties and loading conditions is to consider them in a framework of a Reliability-Based Optimization (RBO) process[9]. However, the computational cost for the solution of large-scale structural systems under seismic loading is orders of magnitude higher than in the case of a conventional seismic design, especially when, as in the present study, a non-linear analysis method is employed in order to evaluate the inelastic behavior of the structure.

In this paper a robust and efficient methodology is presented for performing RBO of space steel frames under seismic loading. The proposed methodology combines efficient structural optimization and reliability analysis procedures. For the solution of the optimization problem the efficient Evolution Strategies (ES) algorithm is used. The employed reliability analysis procedure requires that a particular structural design satisfies certain displacement-based performance criteria and it is carried out via the Monte Carlo Simulation (MCS) method. Finally, for the structural analysis an efficient pushover scheme is employed using a fiber-type beam element, which has been chosen in order to achieve a more accurate simulation of the inelastic behavior.

In order to reduce the excessive computational cost and make the whole procedure viable for real-life engineering applications the use of Artificial Neural Networks (ANN) is incorporated in the proposed methodology[10]. The use of ANN was motivated by the time-consuming repeated analyses required by the MCS in the reliability analysis phase and by the ES during the optimization process. According to the proposed implementation, the pushover analysis required in every simulation is replaced by a neural network based metamodel. An efficient training algorithm is implemented for training the ANN utilizing available information generated from selected analyses. In the reliability analysis phase the training data for the ANN are derived from

a “coarse” initial Latin hypercube sample. In the sequence the discretization of the sample space becomes finer in order to approximate the probability of failure via fast and accurate metamodel predictions. As far as the optimization phase is concerned, the structural analysis is replaced by a neural network prediction for the computation of the necessary data, i.e. values of the objective and constraint functions, for the ES optimizer. The proposed methodology has been applied in sizing structural optimization of a characteristic 3D steel frame.

2 DESIGN UNDER SEISMIC LOADING

Performance-based design concepts have been introduced over the last ten years by various guidelines (ATC-40 (1996), FEMA-273 (1997), SEAOC (1995)) for the assessment and rehabilitation of existing structures and the analysis and design of new ones. The main objective is to increase the safety against natural hazards and in the case of earthquakes to make them having a predictable and reliable seismic performance. In other words, the structures should be able to resist earthquakes in a quantifiable manner and to present levels of acceptable possible damages. Performance-Based Earthquake Engineering (PBEE) is a multi-level design approach where various levels of structural performance are considered. For example FEMA-273 suggests the following performance levels: operational level, immediate occupancy, life safety and collapse prevention.

The structural performance can be measured either in terms of stresses, or in terms of displacements. Since the latter approach provides a better indicator of damages it is usually preferred, especially when expressed in terms of maximum interstory drift limits. The guidelines suggest various types of analysis methods: linear static, non-linear static, linear dynamic and non-linear dynamic. The most commonly used approach is the non-linear static, or pushover analysis method. Pushover analysis allows for the direct evaluation of the performance of the structure at each limit state as opposed to conventional static analysis based design procedures, such as that of EC3, where the structure is designed for the ultimate limit state while for the serviceability limit state a number of deflection checks are performed at the end of the design process.

The purpose of the present pushover analysis based optimization problem is to obtain optimum designs that satisfy design codes provisions in order to be acceptable in current practice. In the iterative optimization procedure each candidate design is initially checked against the provisions of EC3 and EC8. Two design load combinations are considered

$$S_d = 1.35\sum_j G_{kj} "+" 1.50\sum_i Q_{ki} \tag{1}$$

$$S_d = \sum_j G_{kj} "+" E_d "+" \sum_i \psi_{2i} Q_{ki} \tag{2}$$

where “+” implies “to be combined with”, the summation symbol implies “the combined effect of”, G_{kj} denotes the characteristic value of the permanent action j, E_d is the design value of the seismic action, and Q_{ki} refers to the characteristic value of the variable action i, while ψ_{2i} is the combination coefficient for quasi permanent value of the variable action i, here taken as 0.30. The multi-modal response spectrum analysis procedure is employed for the calculation of the stress resultants of the earthquake action, while the imposed lateral loading scheme is obtained from the elastic design spectrum of EC8 for a peak ground acceleration (PGA) that corresponds to a frequent earthquake, small enough to cause no yielding on the structure.

All EC3 and EC8 checks: axial, flexural (or combined axial-flexural) and shear capacity of each member are considered. Furthermore, the strength ratio of column to beam is calculated and also a check of whether the sections chosen are of class 1, as EC3 suggests, is carried out. The later check is necessary in order ensure that the members have the capacity to develop their full plastic moment and rotational ductility, while the former is necessary in order to have a design consistent with the strong column - weak beam design philosophy. In order to ensure that the structure is not potentially unstable an additional constraint is imposed. Finally, an inter-storey drift ratio limit of 3% is introduced in order to control the seismic damage severity on the structure.

2.1 Pushover analysis

The purpose of pushover analysis is to assess the structural performance in terms of strength and deformation capacity globally as well as in the element level. The structural model is “pushed” using a commonly used lateral load pattern, which is proportional to the fundamental mode of the structure. The method can provide the sequence of the member yielding and identify the regions where inelastic deformations are expected to be high. Pushover analysis is based on the assumption that the response of the structure is related to the response of an equivalent single degree of freedom system.

The pushover analysis step is initiated as soon as the structure has satisfied the initial static analysis step. Gravity loads are present and follow the load combination of Eq. (2). The lateral loads are increased

automatically via the constant arc-length criterion, which has been implemented in order to reduce the number of necessary iterations required and also to increase the robustness of the elasto-plastic analysis algorithm. Geometric nonlinearities were also considered. The analysis is terminated as soon as the target displacement that corresponds to the 2% in 50 (2/50) years earthquake is reached or earlier if the algorithm fails to converge because a collapse mechanism has been formed. The target displacement is obtained from the FEMA-356 formula:

$$\delta_t = C_0 C_1 C_2 C_3 Sa \frac{T_e^2}{4\pi^2} g \tag{3}$$

where C_0, C_1, C_2, C_3, are modification factors: C_0 relates the spectral displacement to the likely building roof displacement; C_1 relates the expected maximum inelastic displacements to the displacements calculated for linear elastic response; C_2 represents the effect of the hysteretic shape on the maximum displacement response; and C_3 accounts for P-Δ effects. In the present study C_1 and C_3 are both set equal to 1.0, while C_2 is equal to 1.0, 1.1 and 1.2 depending on the structural performance level considered. T_e is the effective fundamental period of the building in the direction under consideration. S_a is the response spectrum acceleration at the T_e period. The pushover curve is converted to a bilinear curve with a horizontal post-yield branch using an iterative process that balances the area below and above the curve.

2.2 Finite element analysis

The so-called BEC fiber beam element based on the natural mode method[11] is employed for the FE modeling in order to perform the pushover analysis. This finite element formulation is based on the description of the variation of the displacement field along the beam on quantities with a clear physical meaning known as the natural modes of the beam element. The fiber approach is used to account for material inelasticity. Each structural element is discretized into a number of sections. Each section is further divided into a number of small fibers, which are restrained to beam kinematics and each employs its own constitutive model. The sections are located either at the center of the element or at the Gaussian integration points. The main advantage of the fiber approach is that each fiber has a simple uniaxial material model allowing an easy and efficient implementation of the constitutive model. A bilinear material law was used in this study. For the solution of the system of nonlinear equations an incremental-iterative numerical procedure is engaged using the arc-length method.

3 STRUCTURAL RELIABILITY ANALYSIS

The inherent probabilistic nature of design parameters, material properties and loading conditions involved in structural analysis is an important factor that influences structural safety. Reliability analysis leads to safety measures that a design engineer has to take into account due to the aforementioned uncertainties. Most often a limit state function is defined as G(R,S)=S-R and the probability of structural failure is given by

$$p_f = p[G(R,S) \geq 0] = \int_{G \geq 0} f_R(R)\, f_S(S) dR dS \tag{4}$$

In general, it is practically impossible to evaluate R analytically for complex and/or large-scale structures. In such cases the integral of Eq. (4) can be calculated only approximately using either simulation methods, such as the Monte Carlo Simulation, or approximation methods. Despite the fact that the mathematical formulation of the MCS is relatively simple and the method has the capability of handling practically every possible case regardless of its complexity, this approach has not received an overwhelming acceptance due to the excessive computational effort that is required. Efficient sampling techniques, advanced solution methods and parallel processing have been recently implemented having a beneficial effect on the efficiency of MCS. Expressing the limit state function as $G(x)<0$, where $x=(x_1,x_2,...,x_M)$ is the vector of the random variables, Eq. (4) can be written as

$$p_f = \int_{G(x) \geq 0} f_x(x) dx \tag{5}$$

where $f_x(x)$ denotes the joint probability density function for all random variables. In order to estimate p_f an adequate number of N independent random samples is produced using a specific, usually uniform, probability density function of the vector x. The value of the failure function is computed for each random sample x_j and the MCS estimation of p_f is given in terms of sample mean by

$$p_f \cong \frac{N_H}{N} \tag{6}$$

in which N_H is the number of failure simulations ($G(x)<0$) and N the total number of simulations. In order to reduce the number of simulations and the computational cost of the standard MCS one of the most efficient sampling reduction techniques[12,13]: Latin Hypercube Sampling (LHS) has been used.

4 RELIABILITY-BASED OPTIMIZATION

In reliability-based sizing optimization of large-scale multi-storey 3D frames the main aim, apart from minimizing structural weight, is to minimize the overall probability of failure of the structure. The probabilistic variables are chosen to be the cross-sectional dimensions of structural members and the material properties, modulus of elasticity E and yield stress σ_y. Due to engineering practice demands the members are divided into groups having the same design variables. Due to manufacturing limitations the design variables are not continuous but discrete since cross-sections belong to a certain set provided by the manufacturers. Thus, a discrete RBO problem can be formulated as follows:

$$\begin{aligned} &\min && F(s) \\ &\text{subject to} && g_j(s) \le 0 \quad j=1,...,m \\ &&& s_i \in R^d, \quad i=1,...,n \\ &&& p_f \le p_a \end{aligned} \tag{7}$$

where F(s) is the objective function, s is the vector of design variables, $h_j(s)$ are the deterministic constraints imposed by the design codes, while p_f is the probability of failure of the structure required to remain below a threshold value (p_a) which comprise the probabilistic constraint.

5 ARTIFICIAL NEURAL NETWORKS

The aim of the present study is to train a neural network to provide computationally inexpensive estimates of analysis outputs required during the MCS process. A trained ANN provides a rapid mapping of a given input into the desired output quantities, thereby enhancing the efficiency of the structural analysis process. This major advantage of a trained ANN over the conventional procedure, under the provision that the predicted results fall within acceptable tolerances, is that it leads to results that can be produced in a few clock cycles, representing orders of magnitude less computational effort than the conventional process. In this work a fully connected network with one hidden layer is used. The learning algorithm, which was employed for the training, is the well-known Back Propagation (BP) algorithm.

In the present implementation the objective is to investigate the ability of the ANN to predict the probability of failure for different values of the basic random variables used by the MCS method for reliability analysis. The results of the reliability analyses are used to verify the feasibility or not of the design with respect to the probabilistic constraint function. The ANN training comprises the following tasks: (i) select the proper training set, (ii) find a suitable network architecture and (iii) determine the appropriate values of characteristic parameters such as the learning rate and momentum term; two user defined BP parameters that effect the learning procedure.

6 EVOLUTION STRATEGIES

The two most widely used optimization algorithms belonging to the class of evolutionary computation that imitate nature by using biological methodologies are the Genetic Algorithms (GA) and Evolution Strategies (ES). In this work ES are used as the optimization tool[10]. ES were introduced in the early seventies and have three characteristics that make them differ from other conventional optimization algorithms: (i) in place of the usual deterministic operators, they use randomized operators: mutation, selection, recombination; (ii) instead of a single design point, they work simultaneously with a population of design points; (iii) they can easily handle continuous, discrete and mixed optimization problems.

6.1 Reliability-based structural optimization using ES and ANN

In RBO problems the probabilistic constraints enforce the condition that the probability of a local failure of the system or the global system failure is smaller than a certain value (i.e. 10^{-5} to 10^{-3}). In this work the overall probability of failure of the structure, as a result of pushover analyses, is taken as the global reliability

constraint. The probabilistic variables are chosen to be the cross-sectional dimensions of the structural members and the material properties (E, σ_y). The proposed ES-ANN methodology can be briefly described with the following algorithm:

1. *Parents Initialization.*
2. *Deterministic constraints check*: all parents become feasible.
3. *Monte Carlo Simulation step*:
   3a. Selection of the ANN training set.
   3b. ANN training.
   3c. ANN Monte Carlo Simulations.
4. *Probabilistic constraints check*: all parents become feasible.
5. *Offspring generation.*
6. *Deterministic constraints check*: if satisfied continue, else go to *step 5.*
7. *Monte Carlo Simulation step*:
   7a. Selection of the ANN training set.
   7b. ANN training.
   7c. ANN Monte Carlo Simulations.
8. *Probabilistic constraints check*: if satisfied continue, else go to *step 5.*
9. *Parent selection step.*
10. *Convergence check.*

7 TEST EXAMPLE

A characteristic test example has been considered in order to illustrate the efficiency of the proposed design procedure in structural optimum design problems. The structural elements of the six storey space frame are divided into five groups, each of them having one design variable, i.e. element's cross-section, thus corresponding to 5 independent design variables. The space frame consists of 63 members (6 adaptively distributed BEC elements per member and approximately 100 fibers in each W-shaped member) with 383 beam elements and approximately 2100 d.o.f. The modulus of elasticity is 200 GPa and the yield stress is f_y=250 MPa. The objective function is the weight of the structure. The deterministic constraints are imposed on the inter-storey drifts and stress constraints.

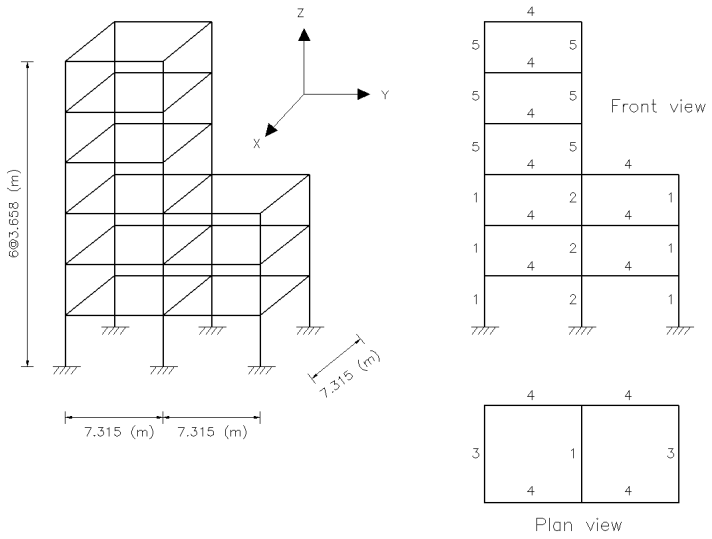

Figure 1. Test example – Geometry and member grouping

The structure is loaded with a 19.16 kPa gravity load on all floor levels and a simplified earthquake load, i.e. the lateral load distribution applied at each node in the front elevation along the x direction follows the fundamental structural mode according to EC8 design spectrum. The constraints of the pushover analysis step concern maximum interstorey drift limits. More specifically, the maximum interstorey drift that corresponds to the displacements of the 2/50 earthquake should be less than 3%. The type of probability density functions, mean values, and variances of the random parameters are presented in Table 1. The mean value for each geometric variable (i.e. the cross-sectional dimensions) is taken as the value the current design step of the

corresponding variable s_i. The probabilistic constraint that is imposed requires p_a to be less or equal than 0.001. The probability of failure caused by uncertainties related to material properties and geometry of the structures is estimated using MCS with the LHS technique.

For the optimization part the $(\mu+\lambda)$-ES approach is used with $\mu=\lambda=5$ following the rule that μ, λ should be in the same order as the number of design variables. For the standard RBO process a sample size of 500 for the MCS employing the LHS procedure is used. As it can be observed from Table 2 the probability of failure for the deterministic optimum (DBO) is unacceptable since it exceeds substantially the allowable value. The same observation can be made for the standard RBO procedure due to relatively small sample size, while in the case of RBO-ANN the sample size is not a problem any more and the target probability of failure is achieved. On the other hand, the optimum weight achieved using RBO is 18% more than the deterministic one.

For the application of the RBO-ANN methodology the number of ANN input units is equal to the number of random variables, whereas one output unit is needed corresponding to the probability of failure. Consequently the ANN configuration results in a 7-7-1 ANN architecture, which is used for all runs. The number of conventional analyses for the training of ANN is taken equal to 60. As it can be observed in Table 2 the proposed RBO-ANN optimization scheme manages to achieve the optimum weight in one third of the CPU time required by the conventional RBO procedure (which in addition violates the probabilistic constraint). As it was previously mentioned, the number of MCS in the case of ANN scheme can be extremely large, thus RBO-ANN increases computational efficiency and accuracy of the whole RBO process, due to the trivial computing time required by the ANN to perform MCS.

Random variable	pdf	Mean value (μ)	St.dev. (σ)
E	N	200	0.10E
σ_y	N	25.0	$0.10\sigma_y$
Design variables	N	s_i	$0.1s_i$

Table 1. Characteristics of the random variables

Optim. Procedure	ES cycles	p_f	Opt. weight (kN)	Time (h)
DBO	40	$0.1\ 10^{-0}$	1126	1.6
RBO (500 siml.)	47	$0.21\ 10^{-1}$	1317	129.2
RBO-ANN*	47	$0.93\ 10^{-3}$	1375	17.7

*For 100,000 ANN simulations

Table 2. Performance of the methods

8 CONCLUSIONS

The solution of realistic RBO problems in structural mechanics is an extremely computationally intensive task. Due to the size and the complexity of seismic RBO problems a stochastic optimization method, such as ES, appears to be the most suitable choice. In the test example considered the conventional RBO procedure was found eighty times more expensive than the corresponding deterministic optimization procedure. The aim of the proposed RBO procedure is to increase the safety margins of the optimized structures under various model uncertainties, while at the same time minimizing the weight of the structure as well as the additional computational cost. This goal was achieved using ANN predictions to replace the pushover analyses involved in the standard RBO process. The implementation of the proposed RBO procedure in a parallel computing environment could further improve its computational efficiency.

REFERENCES

[1] Collins, K.R., Wen, Y.K. and Futch, D.A. (1996), "Dual-level design: A reliability-based methodology", Earthquake Engineering and Structural Dynamics Vol. 25(12):1433-1467.

[2] Beck, J.L., Chan, E., Irfanoglu, A. and Papadimitriou, C. (1999), "Multi-criteria optimal structural design under uncertainty", Earthquake Engineering and Structural Dynamics Vol. 28, pp. 741-761.

[3] Foley, C.M. (2002), Optimized performance-based design for buildings, in Burns S.A. (ed.), *Recent Advances in Optimal Structural Design*, ASCE Publications, pp.169-236.

[4] Ganzerli, S., Pantelides, C.P., and Reaveley, L.D. (2000), "Performance-based design using structural optimization", Earthquake Engineering and Structural Dynamics Vol. 29, pp. 1677-1690.
[5] Hasan, R., Xu, L. and Grierson, D.E. (2002), "Push-over analysis for performance-based seismic design", Computers and Structures Vol. 80, pp. 2483–2493.
[6] Alimoradi, A. (2003), State-of-the-art in performance-based design optimization - Inference to consequence-based engineering optimization, Technical Report, University of Illinois at Urbana-Champaign, USA.
[7] Krawinkler, H. (1999), Challenges and progress in performance-based earthquake engineering, International Seminar on Seismic Engineering for Tomorrow – In Honor of Professor Hiroshi Akiyama, Tokyo, Japan.
[8] Wen, Y.K. (2000), "Reliability and performance-based design", in Haldar, K.A., Spencer, B.F. and Johnson, E.A. (eds) Proceedings of the 8th ASCE Specialty Conference on Probabilistic Mechanics and Structural Reliability, 24–26 July, Notre Dame, IN, USA.
[9] Papadrakakis, M., Tsompanakis, Y., Lagaros, N.D. and Fragiadakis, M. (2004), "Reliability based optimization of steel frames under seismic loading conditions using evolutionary computation", Journal of Theoretical and Applied Mechanics, Vol. 42(3), pp. 585-608.
[10] Papadrakakis, M., Lagaros, N.D. and Tsompanakis, Y. (1998), "Structural optimization using evolution strategies and neural networks", Computer Methods in Applied Mechanics and Engineering Vol. 156, pp. 309-333.
[11] Argyris, J., Tenek, L. and Mattsson, A. (1998), "BEC: A 2-node fast converging shear-deformable isotropic and composite beam element based on 6 rigid-body and 6 straining modes", Computer Methods in Applied Mechanics and Engineering Vol. 152, pp. 281-336.
[12] McKay, M.D., Beckman, R.J. and Conover, W.J. (1979), "A comparison of three methods for selecting values of input variables in the analysis of output from a computer code", Technometrics Vol. 21(2), pp. 239-245.
[13] Stein, M.L. (1987), "Large sample properties of simulations using latin hypercube sampling", Technometrics 29(2), pp. 143-151.

DIGITAL FILTER BASED MAXIMALLY ROBUST AND TIME OPTIMAL VIBRATION FREE MOTION OF STRUCTURES WITH DENSELY PACKED MODES

G. N. Glossiotis **I. A. Antoniadis**
Research Assistant **Associate Professor**

National Technical University of Athens, School of Mechanical Engineering,
Machine Design and Control Systems Section
P.O. Box 64078, Athens 15710, Greece
Email: antogian@central.ntua.gr

Keywords: Flexible Structures, Vibration Suppression, Robust Control, FIR Digital Filters

Abstract. *Due to the inherent flexibility of engineering structures, transient and residual vibrations occur during their motion, raising thus several practical restrictions concerning their fast, accurate and safe motion. Numerous command shaping techniques for the effective suppression of the excited residual vibration in actual applications have been implemented over the years. The dominant tradeoff that these methods have to deal with is between the robustness of the command and the speed of response of the system. Traditional digital filters have been proven to be efficient for vibration suppression in several flexible systems and mechanisms, when they are properly designed. Among them, a special class of Finite Impulse Response (FIR) filters has been shown to present a maximally robust behavior, while simultaneously introducing the minimum possible delay. In this work, the exploitation of this class of filters is considered for structures that present highly complex and vigorous dynamic response, characterized by wide bands of dense clusters of eigenfrequencies. The proposed filtering method is implemented for the generation of the motion profile of a multibay truss. First, the transient responses of the truss at multiple points are computed in order to identify the eigenfrequencies of the system. Then, properly designed Finite Impulse Response (FIR) filters are applied to the motion commands of the system. The resulting filtered motion commands are shown to effectively suppress the truss vibration during and after its motion, covering uniquely all the excited modes of the structure.*

1 INTRODUCTION

Lightweight flexible structures are often encountered in civil engineering, aerospace and several industrial applications. The performance of these systems is straightforwardly affected by the presence of undesirable vibration in their transient responses, due to the inherent excitation of several flexible modes. In practice, these structures are essential components incorporated in larger mechanical systems, which as a direct result influence even more their dynamic response in a rather complex and unpredictable manner.

The dynamic analysis of extended multibay lightweight trusses poses interesting technical challenges. This is because such structures generally posse high modal densities, with clusters of densely packed modes, existing even at relatively low frequencies[1-3]. The problem of moving effectively a flexible structure, such as a multibay truss, cannot be rationally addressed, unless a thorough analysis in terms of system dynamics identification is primarily preceded[4,5]. The described framework explains the particular engineering interest from the optimal motion control aspect.

The traditional approaches to minimize the effect of residual vibrations are focused on either redesigning the structure of the system, in order to obtain acceptable dynamic characteristics, or on using sophisticated closed loop control methods. Each one of them is subjected to a number of disadvantages and drawbacks. An alternative approach for suppressing residual vibrations is the proper design of a pre-specified excitation pattern, *the Guidance*, so that the system moves exactly to the desired end position without any residual vibration[6].

A typical well-known example of such methods is the input shaping approach, based on the convolution of an arbitrary guidance function with a series of impulses[7-8]. While input shaping methods present a good performance in a variety of systems and applications, their robustness is limited in local areas around the system natural frequencies and can be increased only by increasing the total duration of the pulse sequence. This causes undesired delays in the total duration of the system motion.

The existing literature concerning control of flexible structures by utilizing input shaping methods,

although plentiful in applications and examples concerning SDOF systems that justify the time-optimization approach[13,14], lacks characteristically in evaluation to more sophisticated systems. The vast majority of the proposed input shaping methods when implemented to MDOF, or generally multi mode systems[9-12], are most of the times restricted to two mode systems, revealing a limited prospective for further exploitation.

In reality, control of flexible structures becomes an even more complex issue, taking into account the deterministic non-linear behavior that real systems posse. The input shaping techniques can compensate for this, if only a detailed dynamic model of the system is expressed, and a rather strict linearization procedure for the determination of the several natural frequencies and damping ratios is implemented[15,16].

In order to overcome the above problems of limited robustness offered by the existing open loop or "input shaping" methods, a new framework has been proposed, according to which the design of an appropriate guidance function for vibration suppression can be transformed to the proper design of a low-pass digital filter[20]. Based on five requirements, that ensure vibration suppression with minimum residual vibration error, short delays, increased robustness, and proper rigid body motion, a systematic design procedure has been introduced, which is based on the concept of Delay-Error-Order (DEO) curves.

The effectiveness of conventional filters for residual vibration suppression has been extensively examined, both theoretically and experimentally. Experimental demonstrations on a flexible robot[18,20] have shown that the exploitation of both FIR and IIR filter types can effectively suppress the excited vibration. Furthermore, the application of the method to large structures, such as the case of a rotary crane[21], has shown that it can compensate for the highly non-linear characteristics of the system, and drastically diminish the sway excitation phenomena. The main advantage of the method is that it can be applied to any mechanical system by simply digital filtering the guidance input, no matter what pattern does the original force input follows.

The objective of the present work is to demonstrate that the proposed filtering approach in[18] can be effectively applied to precondition the motion profiles of flexible structures, in order to suppress both transient, as well as residual vibration, in the optimal time. The interest is focused in a characteristic case of a rather flexible structure, such as a multibay truss, which comprises plethora of characteristics that form a sophisticated dynamic system. Initially, the exact transient dynamics of the impulsively loaded flexible truss are extracted, by employing a Finite Element based simulation. Then, the time optimal motion profiles for the motion of the truss are proposed, followed by the description of the alternative input preconditioning approach using FIR digital Filters. Finally, the new motion profiles are applied numerically to the system, and the results justify uniquely the usage of the motion command filtering technique. The maximally robust features, introduced by the filtered commands, present also a time optimal behavior, while achieving an almost vibration free motion of the flexible structure.

2 PROBLEM DEFINITION

2.1 Truss description

The truss structure examined (Fig. 1) is exactly the same one considered in [3]. It consists of 18 periodic sets (bays) connected by clamped joints. Each periodic set consists of coupled beams undergoing axial and bending vibrations. The joints connecting the beams of each periodic set transmit longitudinal (axial) and transverse forces, as well as bending moments. The (6×1) vector $u_L^{(i)}$ of generalized displacements at the left boundary of the i^{th} periodic set can be defined as follows:

$$u_L^{(i)} = \left[u_{1,L}^{(i)} \quad u_{2,L}^{(i)} \quad \theta_{1,L}^{(i)} \quad u_{3,L}^{(i)} \quad u_{4,L}^{(i)} \quad \theta_{2,L}^{(i)} \right]^T \tag{1}$$

where $u_{p,L}^{(i)}$ and $\theta_{k,L}^{(i)}$, $p=1-4$, $k=1,2$ represent the horizontal or vertical displacements, and the rotations respectively, of the joints at the left boundary of the set (Figure 1).

During the subsequent analysis, the following assumptions are made:

1. The truss structure is considered to be free (unsupported) in space,
2. The damping effect is neglected, and
3. The influence of gravity is neglected.

2.2 Truss characteristics

The structural members of the truss are considered to be out of aluminum[3]. Indicative values of the material properties and geometric parameters of these elements, employed in the numerical simulations, are:

$EI = 5.587$ Pa m^2, (E: modulus of elasticity, I: moment of inertia of a beam member),

$EA = 2.216 \cdot 10^6$ Pa, (E: modulus of elasticity, A: cross-section of a beam member),

$\bar{m} = 0.0855$ Kg/m, (mass per unit length of a beam member),

$\rho = 2700$ Kg/m^3, (Aluminium density)

$l_y = l_{vert} = 0.903$ m (length of a vertical beam member), and

$l_x = l_{horiz} = 0.903$ m (length of a horizontal beam member).

The computation of the transient responses at a given location on the truss were performed using ANSYS© v8.0, while the FFT and any other necessary numerical operations were conducted using MATLAB© 7.0.

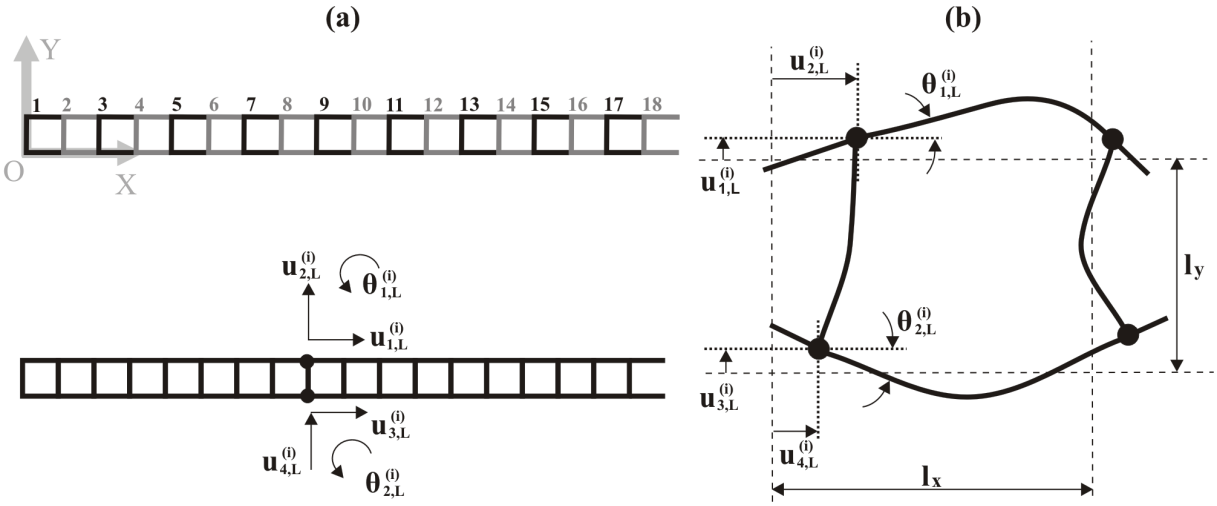

Figure 1. (a) The truss structure consists 18 periodic sets (bays), (b) Generalized displacements as they are defined at an individual truss beam.

3 SIMULATION OF THE TRANSIENT DYNAMICS

3.1 Impulsive excitation

The detailed dynamic response of the truss has been extensively studied before[1,2]. However, in order to rationally proceed to its motion control, a simple numerical experiment will be implemented for the proper identification of fundamental dynamic characteristics of the system. The features extracted by this analysis will define the filter preconditioning approach that will be adopted, as this is described later.

The truss is subjected to a simulated impulsive excitation. The impulse force is applied vertically on the upper joint of the truss's left boundary (Figure 2). The characteristic trapezoidal shape of the force is described by the equation[1]:

$$F(t) = \begin{cases} 10t, & 0 \le t < 0.1 \\ 1, & 0.1 \le t < 0.5 \\ 6 - 10t, & 0.5 \le t < 0.6 \\ 0, & t \ge 0.6 \end{cases} \quad (2)$$

In Figure 3 some representative numerical FFTs for the three degrees of freedom (horizontal/vertical displacement and rotation) of a joint at three individual joints of the truss are presented. We note that resonances in this system occur in dense clusters, which correspond to propagation zones of the various wavemodes of the corresponding truss of infinite spatial extent[4]. These dense clusters of eigenfrequencies are extended in a very wide frequency band (0 Hz – 60 Hz) when referring to the vertical displacement and rotation of a joint. In comparison, the clusters of eigenfrequencies appearing at the FFTs of horizontal displacements are limited to relatively low frequencies (0 Hz – 10 Hz).

The last remarks are better clarified if the respective acceleration time series for horizontal and vertical directions at the three joints of the truss are computed (Figure 4). It is noticeable that the magnitude of the accelerations in the vertical direction is approximately 10 times larger compared to the accelerations in the horizontal direction. This is logically justified because the vertical impulsive load excites a steady vibration,

with predominantly vertical motions of the joints of the truss. Respective results are extracted if a horizontal impulsive load is applied to the truss[1].

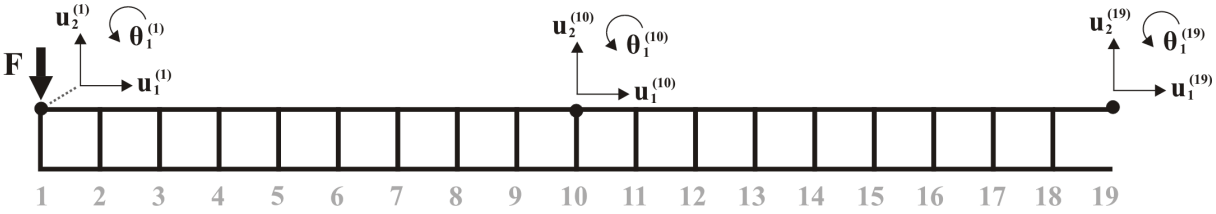

Figure 2. The truss structure is subjected to vertical forcing at the upper joint of the left boundary.

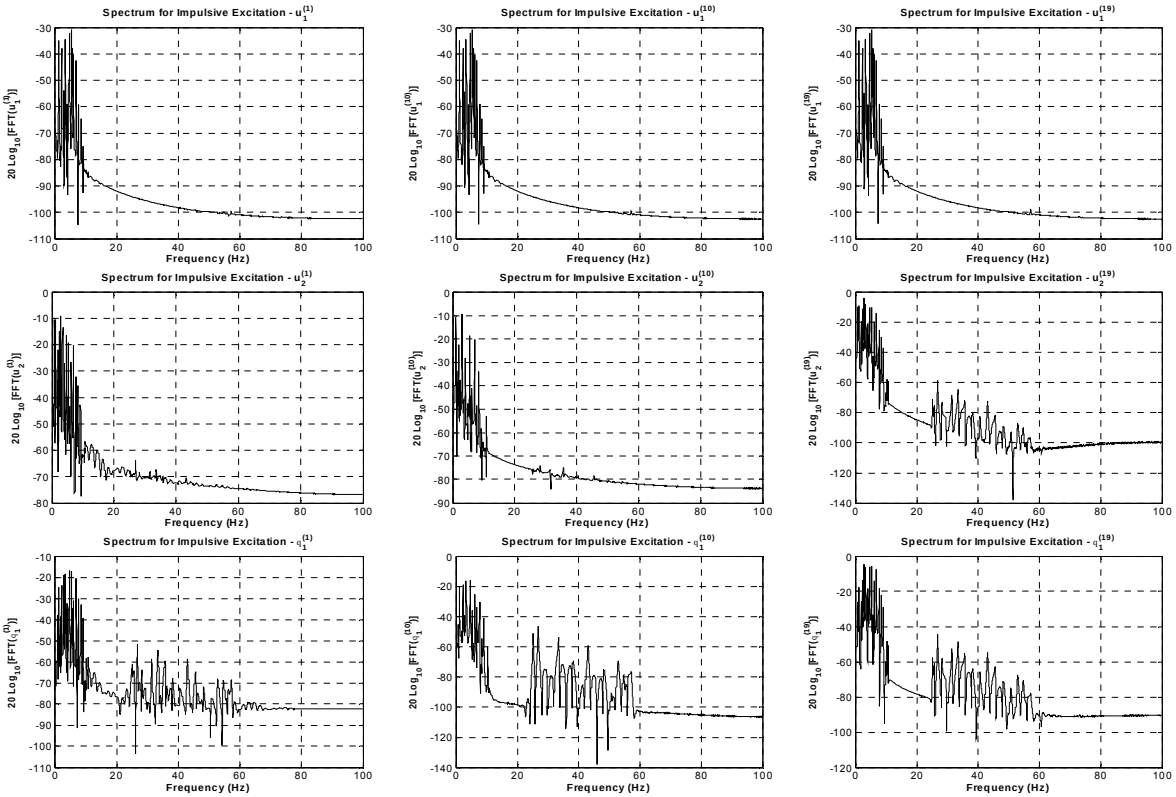

Figure 3. Numerical FFTs for the three degrees of freedom (horizontal/vertical displacement and rotation), at three individual joints on the upper part of the truss (1,10 and 19) for the case of a single vertical forcing.

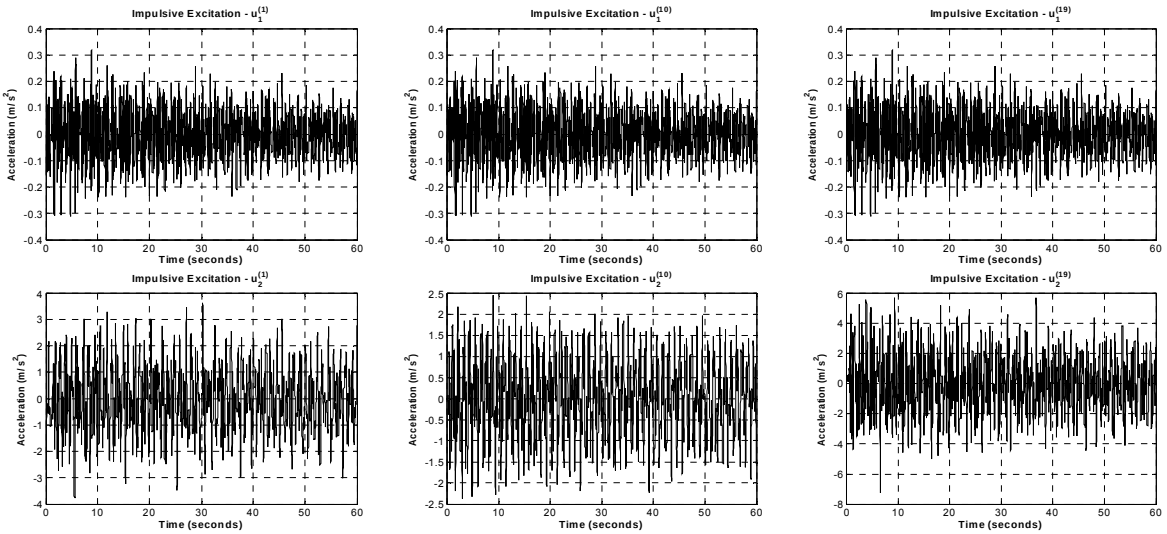

Figure 4. Acceleration time series at the three individual joints on the upper part of the truss (1,10 and 19).

4 TRUSS MOTION PROFILES

4.1 Time optimal profiles

The truss structure can be seen either as an individual system actuated at its right boundary, or as a component attached to a larger mechanical system, through its right joints boundaries. In order to define the appropriate commands for the time optimal point-to-point motion, the truss is temporarily treated as a rigid-body structure. The feedforward control problem is to generate the force required for acceleration of the truss mass, over a desired distance. Conversely, the motion distance should be such that the force is allowable and can be generated by the actuating device.

Taking into account that the current problem is approached by means of numerical implementation, the interest focuses basically on the proper generation of the force. The exact determination of the moving distance is a separate problem and is out of the interest of this study.

It is assumed that the force that determines the exact motion of the truss is applied at the right boundary of it. The geometry of the structure dictates the split of this force to two equal forces of half of the initial amplitude, acting respectively at the two joints of the right boundary (Figure 4). If the maximum acceleration and velocity along the moving direction are defined, then the quickest motion of the truss can be derived using a bang-bang or bang-off-bang force input.

Since no specific values for the maximum acceleration, or velocity, of the truss are available, a representative force profile can be formed if a rough estimation is made based on conservative values of its motion characteristics (acceleration, velocity). Given that the mass of the structure is approximately 4Kgs, a maximum acceleration of approximately 0.5m/s^2 is considered to be rather realistic and safe. The rigid-body approach implies that for a mass of 4Kg to be optimally accelerated with 0.5m/s^2, a minimum force of 2N must be applied. Hence the amplitude of the force acting at each of the two joints at the right boundary will be 1N.

If the estimated maximum force value is adopted, an indicative motion profile can be obtained by the sequential completion of the following tasks: The maximum acceleration (0.5m/s^2) is applied for time duration equal to 5 sec until the assuming maximum velocity of motion is reached (2.5m/s). Then a constant velocity motion is performed for 10s, and finally the maximum deceleration is applied for 5s until the motion stops. When such inputs are applied, the response of the system can be numerically calculated using ANSYS.

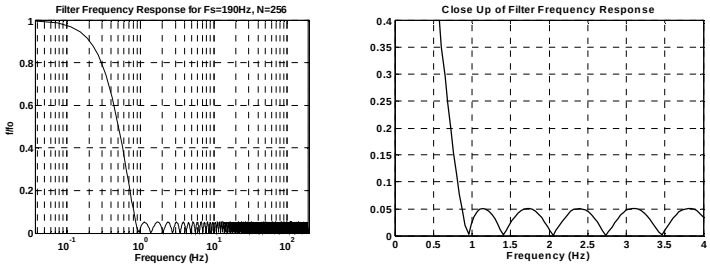

Figure 5. Filter frequency response of a FIR filter and a close up of it, focused at the area of the cutoff frequency

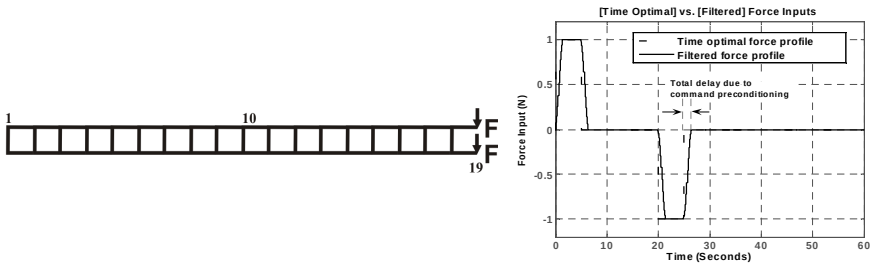

Figure 6. Comparison of Time Optimal vs Filtered Force Inputs, and their placement on the truss.

4.2 Input preconditioning using FIR filters

The objective of the filtering procedure is to move the truss at an end point at the optimal time, while vibration at the truss joints remains minimum. The filtering procedure can compensate for these variations, by forming appropriately a filter frequency response function, which is as close as possible to zero at the frequency bands coinciding with the anticipated natural frequencies of the dynamic system.

According to the proposed preconditioning approach, instead of the direct implementation of the original input force functions F, conditioned guidance functions F_C can be alternatively used, obtained by appropriately digital filtering the original guidance functions.

A FIR filter, designed according to the Parks-McClellan method, is then used for suppressing the truss vibrations. Although several types of filters can be equivalently used, FIR filters of the Parks-McClellan type have been shown[19,21] to belong in the class of the best performing filters. The permissible vibration error is set at 5%. Due to the highly non-linear, time varying nature of the problem considered, the filter order was respectively selected to be N=256. According to [18], the chosen filter order results to a very large relative robustness of almost 99%. The total time delay introduced by the filtering process is equal to approximately 1.37s, which is approximately 1.25 times the highest natural period of the system. The rest of the filter design parameters were retrieved from the DEO curves and the look-up tables corresponding to the specific filter[18].

The filter transfer function is shown in Figure 5. The stop band of the filter covers frequencies from 0.87Hz up to approximately 190Hz. This stop band is significantly wider than that actually needed, in view of the actual bands of the spectrums presented in Figure 3. The size of the stop-band ripples is less than 0.05 while the amplitude of the pass-band is equal to one.

5 NUMERICAL RESULTS

5.1 Original (time optimal) inputs to the system

The profiles for the time optimal bang-bang types of commanded inputs of the truss motion are shown in Figure 6 as they result from the procedure described in paragraph 4.1. Figure 7 presents respectively the velocity and acceleration time series for horizontal and vertical directions, and rotations, at three individual joints of the truss, for the above force input of Figure 6. It can be observed that the vibration is excited as soon as the motion starts.

This excited vibration clearly indicates that although the motion profiles are theoretically designed to be time-optimal, in practice due to the low damping ratio of the structure proved to be ineffective in terms of optimal control in general.

5.2 Effects of the preconditioned inputs

The filter designed in paragraph 4.2 is then used to filter the commanded inputs. The resulting filtered inputs are shown in Figure 6, in comparison to the original inputs.

The resulting velocity and acceleration time series for horizontal and vertical directions, and rotations, at three individual joints of the truss are illustrated in Figure 7, together with the original vibrations. It can be easily observed, that the vibration magnitude remains practically negligible in both cases of the transient and residual state.

It must be underlined that although the filter procedure itself introduces a small delay, this is compensated for by the fact that no vibration is now present. Thus, the long periods of rest-times, due to the low damping ratio of the initial vibration, need not to be encountered in a practical situation.

The results indicate that the application of a filtering method to non-linear time-varying flexible systems, such as the case under consideration, is legalized. Furthermore, taking into account that the vibrations at the joints of the truss are practically negligible during the entire motion, the flexible structure presents an almost rigid body behavior.

This implies that once a specific filter has been designed, it can be applied to all operating conditions of the truss. Moreover, the flexibility offered by the filter design procedure of [18] can meet different design requirements, such as acceptable vibration level, acceptable filter delay, minimization of power consumption etc.

5 CONCLUSIONS

Transient and residual vibrations of flexible structures can be controlled efficiently when appropriate conventional digital filters are used to precondition the motion inputs to the system. As shown by the results presented, the preconditioned inputs reduce significantly both the transient and the residual vibrations of the multibay truss, even under extreme conditions.

The only cost anticipated, is a small time delay for the motion, which is of the order of magnitude of the largest expected natural period of the system. However, this drawback can be also efficiently handled, since the vibration suppression capabilities of the proposed method omit the long rest times introduced by lightly damped systems.

The method is simple to implement in actual configurations, it is efficient and does not require special sensors or other equipment. Although, in this work, this method is presented as an open-loop control approach, it can be also efficiently combined with simple close-loop positioning controllers.

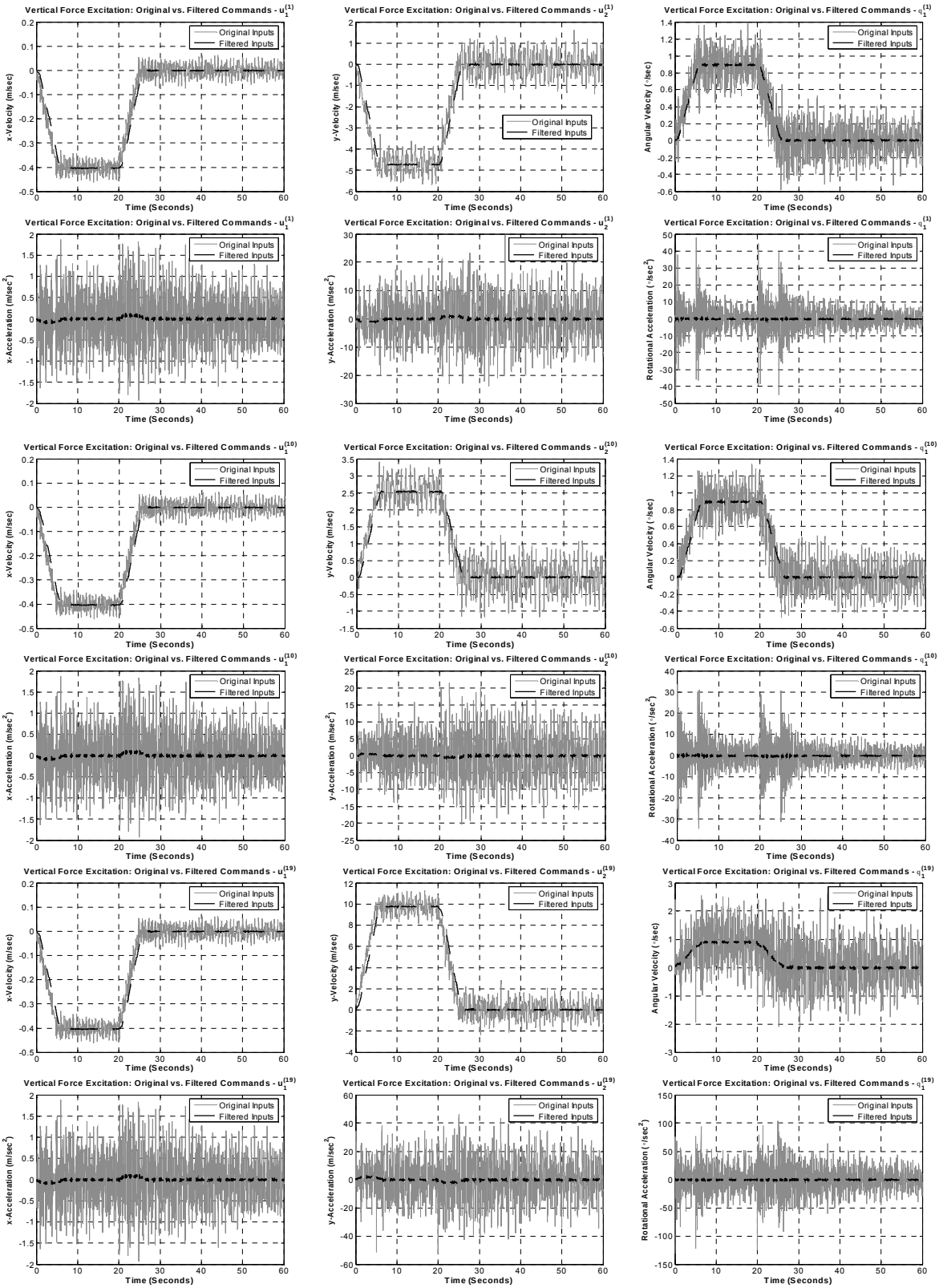

Figure 7. The resulting velocity and acceleration time series for horizontal and vertical directions, and rotations, at three individual joints of the truss (1, 10, 19).

ACKNOWLEDGEMENTS

This work has been supported in part by a grant of the basic research program “Herakleitos”, from the Greek Ministry of Education. The project is co-funded by the European Social Fund (75%) and National Resources (25%).

REFERENCES

[1] Xiaghong M., Vakakis A. F., (1999), “Karhunen-Loeve decomposition of the transient dynamics of a multibay truss”, AIAA Journal 37(8), pp.939-946.

[2] Xiaghong M., Vakakis A. F.,Bergman L. A., (2001), “Karhunen-Loeve modes of a truss: Transienr response reconstruction and experimental verification”, AIAA Journal 39(4), pp.687-696.

[3] Emaci E., Azeez M. A. F., Vakakis A. F., (1998), “Dynamics of Trusses: Numerical and experimental results”, Journal of Sound and Vibration 214(5), pp.953-964.

[4] Mead D.J., (1975), “Wave propagation and natural modes in periodic systems: II. Multi-coupled systems with and without damping”, Journal of Sound and Vibration 40(1), pp.19-39.

[5] Signorelli J., Von Flotow A.H., (1988), “Wave propagation, power flow and resonance in a truss beam”, Journal of Sound and Vibration 126(1), pp.127-144.

[6] Smith O.J.M., (1958), *Feedback Control Systems*, McGraw-Hill, New York.

[7] Singer N.C., Seering W.P., (1990), "Preshaping command inputs to reduce system vibration", ASME Journal of Dynamic Systems, Measurement and Control 112, pp. 76-82.

[8] Singhose W., Seering W., Singer N.C., (1994), “Residual vibration reduction using vector diagrams to generate shaped inputs”, ASME Journal of Dynamic Systems, Measurement and Control 116, pp. 654-659.

[9] Singh T., Heppler G. R., (1993), “Shaped input control of a system with multiple modes”, ASME Journal of Dynamic Systems, Measurement and Control 115, pp. 341-347.

[10] Singh T., Vadali S. R., (1995), “Robust time-delay control of multi-mode systems”, International Journal of Control 62, pp.1319-1339.

[11] Crain E., Singhose W., Seering W., (1996), “Derivation and properties of convolved and simultaneous two-mode input shapers”, *Proceedings of the 1996 IFAC World Congress*, San Fransisco, CA, USA.

[12] Pao L. Y., Cutforth C. F., (2003), “On frequency-domain and time-domain input shaping for multi-mode flexible structures”, ASME Journal of Dynamic Systems, Measurement, and Control 125(3), pp. 494-497.

[13] Singhose W. E., Pao L. Y., (1997), “A comparison of input shaping and time-optimal flexible-body control”, Control Engineering Practice 5(4), pp. 459-467.

[14] Pao L. Y., Singhose W. E., (1998), “Robust minimum time control of flexible structures”, Automatica 34(2), pp. 229-236.

[15] Smith J. Y., Kozak K., Singhose W., (2002), “Input shaping for a simple nonlinear system”, *Proceedings of the 2002 American Controls Conference*, May 8-10, Anchorage, USA.

[16] Kozak K., Ebert-Uphoff I., Singhose W., (2004), “Locally linearized dynamic analysis of parallel manipulators and application of input shaping to reduce vibration”, ASME Journal of Mechanical Design 126(1),pp. 156-168.

[17] Antoniadis I., (1999), "Guidance preconditioning by an impulse sequence for robust residual vibration suppression", Shock And Vibration 6, pp. 133-145.

[18] Economou D., Mavroidis C., Antoniadis I., Lee C., (2002), “Maximally robust input preconditioning for residual vibration suppression using low pass FIR digital filters”, ASME Journal of Dynamic Systems, Measurement and Control 124(1), pp. 85-97.

[19] Economou D., Mavroidis C., Antoniadis I., (2002) “Comparison of filter types used for command preconditioning in vibration suppression applications”, *Proceedings Of The 2002 American Control Conference*, May 8-10, Anchorage, AK, USA.

[20] Antoniadis I., Economou D., (2001), “Robust residual vibration suppression for linear time invariant systems by digital filtering of the guidance function”, Mechanical Systems And Signal Processing, 15(3), 565-580.

[21] Glossiotis G., Antoniadis I., (2003), “Payload sway suppression in rotary cranes by digital filtering the commanded inputs”, Proceedings Of The I Mech E, Part K, Journal Of Multi-Body Dynamics 217(2), pp. 99-109(11).

VULNERABILITY ASSESSMENT AND DESIGN OPTIMIZATION OF STRUCTURES WITH UNCERTAIN MATERIAL PROPERTIES AND EARTHQUAKE LOADING

Dimos C. Charmpis[1,2], Nikolaos D. Lagaros[1†], and Manolis Papadrakakis[1†]

[1]Institute of Structural Analysis & Seismic Research
National Technical University of Athens
Zografou Campus, Athens 15780, Greece

[2]Institute of Engineering Mechanics
Leopold-Franzens University
Technikerstr. 13, A-6020 Innsbruck, Austria

e-mails: Dimos.Charmpis@uibk.ac.at, nlagaros@central.ntua.gr, mpapadra@central.ntua.gr

[†]Greek Association of Computational Mechanics

Keywords: Seismic, Earthquake, Random, Stochastic, Monte Carlo simulation, Optimization.

Abstract. *The present work is concerned with assessing the vulnerability of seismically excited structures using non-deterministic analysis concepts, in order to take uncertainties into account. In this respect, uncertainties in both structural properties and earthquake loads are considered. Hence, the variation characteristics of uncertain material parameters along the length of frame members are modeled using Gaussian stochastic fields. Moreover, non-Gaussian probabilistic earthquake loading is assumed, which is described with the use of random variables based on data obtained from natural ground motion records. The modeling of uncertainties using random variables and fields is implemented in the framework of the direct Monte Carlo Simulation (MCS) method, in order to calculate structural response statistics and estimate the reliability for multi-storey frames with stochastic properties subjected to random seismic excitation. This MCS process can be incorporated into a multi-objective Robust Design Optimization (RDO) formulation, in which the aim is to minimize the response variability and the weight of a structure, in order to obtain the global Pareto front curve.*

1 INTRODUCTION

Uncertainty is inherent in structural mechanics applications, since an imperfect state of knowledge is usually involved in material and geometric properties of engineering structures and systems, as well as in the imposed loading and boundary conditions. Experience shows that several of these uncertainty types – depending each time on the particular structural problem at hand – result in severe variations of structural response and therefore directly affect structural safety and reliability. Therefore, the treatment of such uncertainties has been established as a research area of great importance and interest within the structural mechanics community.

The present work is concerned with assessing the vulnerability of seismically excited structures using non-deterministic analysis concepts, in order to take uncertainties into account. This topic, as well as the broader field of stochastic structural dynamics, has been a subject of investigation for decades[1]. Past research efforts in this scientific field have mainly considered uncertainties involved in seismic loading. In this respect, several procedures have been proposed for evaluating statistical moments of response quantities or for estimating the reliability of deterministic structures subjected to random earthquake excitation[2-5]. A number of studies have also appeared assuming that both the seismic ground motion and the structural resistance are non-deterministic. In these investigations, apart from modeling uncertainties in earthquake loading, selected structural properties are typically treated as simple random variables[6-9]. Thus, it can be generally stated that the area of seismic structural reliability has attracted considerable attention by engineering mechanics researchers. However, despite numerous and important relevant contributions, there is still great need for research work in this area due to the difficulties encountered in effectively modeling and treating parameters and phenomena, which are random in nature.

Seismic vulnerability is assessed in this work by taking into account uncertainties in both structural properties and earthquake loads. In this respect, uncertain material parameters are modeled using Gaussian

stochastic fields. Hence, material randomness is included in the seismic risk analysis process by considering a detailed representation of the variation characteristics of material properties along the length of frame members. Moreover, non-Gaussian probabilistic earthquake loading is assumed, which is described with the use of random variables based on data obtained from natural ground motion records. This modeling of uncertainties using random variables and fields is implemented in the framework of the direct Monte Carlo Simulation (MCS) method, in order to calculate structural response statistics and estimate the reliability for multi-storey frames with stochastic properties subjected to random seismic excitation.

As a result of the importance of the uncertainties mentioned above, stochastic performance measures are increasingly being taken into consideration in many contemporary structural optimization applications. In deterministic-based structural sizing optimization problems the aim is to minimize the weight or the cost of the structure taking into account certain behavioral constraints, mainly on stresses and displacements, as imposed by design codes. To incorporate stochastic performance measures into the structural optimization process, two distinct formulations can be used: the multi-objective Robust Design Optimization (RDO) and the single-objective Reliability-Based Design Optimization (RBDO)[10]. According to the RDO formulation, the aim is to minimize the influence of the stochastic variation of some structural parameters on the design, while the main goal in the RBDO formulation is to achieve optimum design with respect to extreme uncertain events. The present work aims in incorporating uncertainties in structural properties and earthquake loads into the RDO formulation. The aim of minimizing the response variability and the weight of a structure in the context of the multi-objective RDO approach may be handled with a non-dominant cascade evolutionary algorithm-based methodology[11], in order to obtain the global Pareto front curve.

2 STOCHASTIC MODELING OF UNCERTAIN STRUCTURAL PROPERTIES

There are basically two approaches for the modeling of uncertain structural properties: using simple *random variables* or *random fields*. In the simple random variable case, an uncertain property has a constant value across the structural domain at hand; this constant value is then assumed to follow some probability distribution, which describes the random characteristics of the property. In the random field case, the value of the property varies across the structural domain according to some correlation pattern and the resulting structural investigation is called *stochastic analysis*; hence, several random variables are invoked, in order to adequately represent the random field of the property. Under the condition that sufficient information on the spatial variation of the property across the structural domain is available, the stochastic approach allows for more detailed description of the property's uncertain characteristics than the use of a simple random variable.

Following the above discussion, a basic assumption in stochastic formulations is that the variation of an uncertain structural property P across a one-dimensional domain (or a certain region of it) can be represented at each point x as:

$$P(x) = P_0[1 + f(x)], \tag{1}$$

where P_0 is the mean value of P and $f(x)$ is a zero-mean random field, which describes the variation of P about P_0. As an example, Fig. 1 illustrates a random field sample for the stochastic modulus of elasticity of a beam. Stochastically modeled structural properties are utilized in the present work in the framework of the direct MCS method. In this respect, the spectral representation method is used to generate Gaussian stochastic field samples, while the midpoint method is applied to derive discretized random field values.

2.1 Spectral representation of stochastic fields

According to the spectral representation method, the sample required at the ith MCS for a one-dimensional univariate (1D-1V) homogeneous Gaussian stochastic field, which describes an uncertain parameter of the structure at hand, can be digitally generated by the following series of cosines formula as $N \to \infty$ [12]:

$$f^{(i)}(x) = \sqrt{2} \sum_{n=0}^{N-1} [A_n \cos(\kappa_n x + \varphi_n^{(i)})], \tag{2}$$

where $\varphi_n^{(i)}$ (n=0,1,…,N-1) denotes the ith realization of the random phase angle φ_n, which is uniformly distributed in the range [0, 2π]. A_n is given by:

$$A_n = \sqrt{2 S_{ff}(\kappa_n) \Delta\kappa}\,, \tag{3}$$

with:

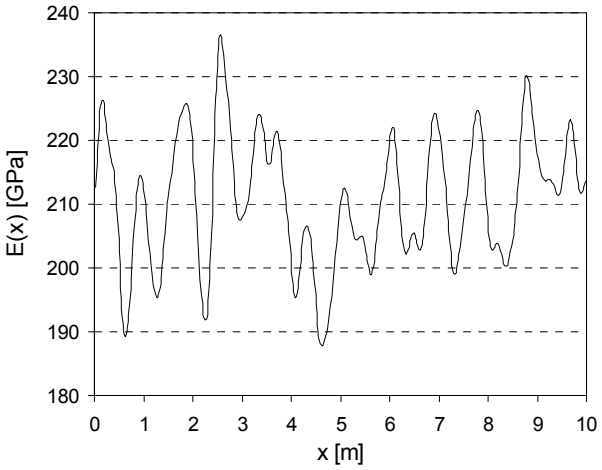

Figure 1. Gaussian random field sample for the stochastic modulus of elasticity E of a beam with length L=10m (mean value of E: E_0=210GPa).

$$\kappa_n = n\Delta\kappa \ , \ \Delta\kappa = \frac{\kappa_u}{N} \ . \tag{4}$$

In the above expressions, the power spectrum S_{ff} of the stochastic field is a real nonnegative function of the wave number κ, while $\Delta\kappa$ is the wave number increment. The upper cut-off wave number κ_u defines the active region of the power spectrum, since $S_{ff}(\kappa)$ is assumed to be zero beyond the value of κ_u. The power spectral density function used in the present work is expressed as:

$$S_{ff}(\kappa) = \frac{1}{4}\sigma^2 b^3 \kappa^2 \mathrm{e}^{-b|\kappa|} , \tag{5}$$

where σ represents the coefficient of variation of the stochastic field, while b is the correlation length parameter. Correlation length b measures the distance of two different stochastic field locations, over which the correlation between the respective random variables approaches zero or a practically very small value. Hence, $b\to\infty$ implies a perfectly correlated stochastic field with all its random variables being linearly dependent, while $b\to 0$ corresponds to white noise yielded by an uncorrelated random field.

The spectral representation method is a widely used technique due to its robustness and straightforward implementation[13,14]. For sufficiently large N-values this method yields stochastic processes, which are Gaussian within engineering accuracy. Hence, using equation (2), a Gaussian random field may be sampled per MCS for each uncertain parameter involved in the stochastic analysis. By considering a large number of simulations n_{sim}, a set of corresponding structural problems is produced. Thus, structural response variability and/or reliability may be evaluated by processing the response statistics obtained by the n_{sim} structural solutions.

2.2 The midpoint method

The midpoint method[15] uses a single random variable per element to delineate a stochastic field, since the field's random characteristics are represented only at the centroid of each element. Thus, given a stochastic field $f(x)$, the midpoint method provides discretized values of f for all n_e elements of the structural model at hand by:

$$\hat{f}(x) = f(\bar{x}_e), \quad x \in \Omega_e , \tag{6}$$

where $\bar{x}_e$ represents the location of the centroid of element e and $\hat{f}(x)$ is an approximation of the original field $f(x)$ over the element's domain Ω_e. Hence, any sample of $\hat{f}$ is piecewise constant and discontinuous at the element boundaries, since the single $\hat{f}$-value considered per element is assumed to be constant over the entire element. Consequently, the random vector

$$\left\{ f(\bar{x}_1), f(\bar{x}_2), \ldots, f(\bar{x}_{n_e}) \right\}, \tag{7}$$

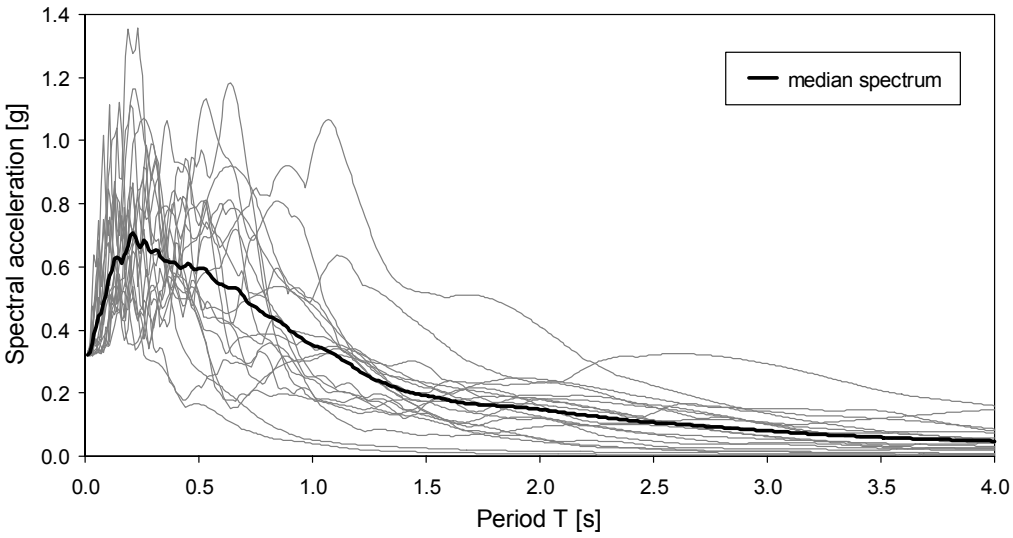

Figure 2. Natural record response spectra and their median.

suffices to define the approximated field $\hat{f}$.

The midpoint method belongs to the point discretization class of methods for stochastic field representation. Alternative representation options are discussed by Matthies et al.[16]

3 MODELING OF UNCERTAIN SEISMIC EXCITATION

The most common approach for the definition of seismic input is the use of design code response spectrum. This approach is general and easy to implement. An alternative option providing seismic input of potentially higher precision is to use spectra derived from natural earthquake records. Since significant dispersion on structural response has been observed due to the use of different natural records, the aforementioned spectra must be scaled to the same desired earthquake intensity. The most commonly applied scaling procedure is based on the Peak Ground Acceleration (PGA).

A set of 20 natural accelerograms is used in the present work to derive probabilistic seismic input. The natural records of this set are given by Papadrakakis et al.[17] and correspond to various earthquake magnitudes, soil properties and PGA-values, i.e. to a wide range of earthquake damage potentials. In order to ensure compatibility between these n_{rec}=20 records, they are scaled to the same PGA-value of 0.31g, which is associated with the hazard level of a rare earthquake with an exceedance probability of 10% in 50 years. The response spectrums corresponding to the 20 scaled records are shown in Fig. 2.

Following the distributional seismic response characteristics justified and used in relevant studies[18-21], spectral acceleration data are assumed to follow the lognormal distribution. Therefore, median values μ_{SA} and standard deviations σ_{SA} are calculated for the aforementioned set of 20 spectra using the following expressions:

$$\mu_{\text{SA}} = \exp\left\{\frac{1}{n_{\text{rec}}}\sum_{i=1}^{n_{\text{rec}}} \ln\left[R_{\text{d},i}(T)\right]\right\}, \tag{8}$$

$$\sigma_{\text{SA}} = \sqrt{\frac{1}{n_{\text{rec}}-1}\sum_{i=1}^{n_{\text{rec}}} \left\{\ln\left[R_{\text{d},i}(T)\right] - \ln \mu_{\text{SA}}\right\}^2}\ , \tag{9}$$

where $R_{\text{d},i}(T)$ is the response spectrum value of the ith record for a period equal to T (i=1,…,n_{rec}). The median spectrum obtained is depicted in Fig. 2. Thus, for a given period value, R_{d} is described by a random variable following the lognormal distribution with mean value μ_{SA} and standard deviation σ_{SA}.

4 FORMULATION OF THE ROBUST DESIGN OPTIMIZATION PROBLEM

In a robust design sizing optimization problem, except of the weight of the structure, an additional objective function is considered which is related to the influence of the random nature of some structural parameters on the response. Thus, the aim is to minimize both the weight and the variance of the response of the structure due to the uncertainty of the random parameters. This problem can be treated as a two-objective optimization

problem using the weighted Tchebycheff metric[11]. The mathematical formulation of the RDO problem may be expressed as:

$$\begin{aligned} &\min && \Phi(s) \\ &\text{subject to} && g_j(s) \le 0, \quad j = 1,...,k, \\ &&& s_i \in \mathrm{R}^{\mathrm{d}}, \quad i = 1,...,n, \end{aligned} \tag{10}$$

where $\Phi(s)$ is the multi-objective function

$$\Phi(s) = \max\left[w_1 \frac{\left|f(s) - z_1^*\right|}{f(s)} + \rho \sum_{i=1}^{m} \frac{\left|f(s) - z_1^*\right|}{f(s)}, \quad w_2 \frac{\left|\sigma_{u_i}(s) - z_2^*\right|}{\sigma_{u_i}(s)} + \rho \sum_{i=1}^{m} \frac{\left|\sigma_{u_i}(s) - z_2^*\right|}{\sigma_{u_i}(s)} \right]. \tag{11}$$

In the above equations s represents the vector of n design variables taking values from the discrete data-set R^{d}, $g_j(s)$ are the k constraint functions, $f(s)$ is the weight of the structure and $\sigma_{u_i}(s)$ is the standard deviation of the response of the structure. Moreover, w_i are m weighting coefficients and z_i^* are utopian objective function values.

5 NUMERICAL EXAMPLE

The seismic vulnerability of a two-dimensional frame is parametrically investigated in this section. Multi-Modal Response Spectrum (MMRS) analysis is used, which is the basic procedure for the performance evaluation of arbitrary frame structures under earthquake loading according to Eurocode 8[22]. MMRS analysis is based on a simplification of the mode superposition approach, in order to avoid time history analyses required by the direct integration and mode superposition approaches. The structure examined is the two-bay, four-storey concrete plane frame shown in Fig. 3, which is supported by assuming zero displacements at its ground nodes. The dimensions of outer and middle columns are 40×40cm^2 and 50×50cm^2, respectively, while the dimensions of all beams are 30×60cm^2. A permanent load of 5kN/m^2 and a variable load of 2kN/m^2 are applied. The frame is considered to be part of a three-dimensional structure with each frame 5m apart.

Uncertainties in both material properties and seismic excitation are taken into account. Hence, the frame is subjected to probabilistic earthquake loading according to the description of section 3. Moreover, the variation of the modulus of elasticity E along the length of the frame members is represented by a 1D-1V homogeneous Gaussian stochastic field with mean value E_0=2.9·109kN/m^2, coefficient of variation σ and correlation length b (see section 2). Although E is the only stochastic variable considered, other material and/or geometric properties of the frame could also be represented by random fields in the same manner.

MMRS analyses are carried out in the framework of the direct MCS method. In any simulation run performed, the aim is to calculate the coefficient of variation of the structure's maximum inter-storey drift $\delta_{\max}$:

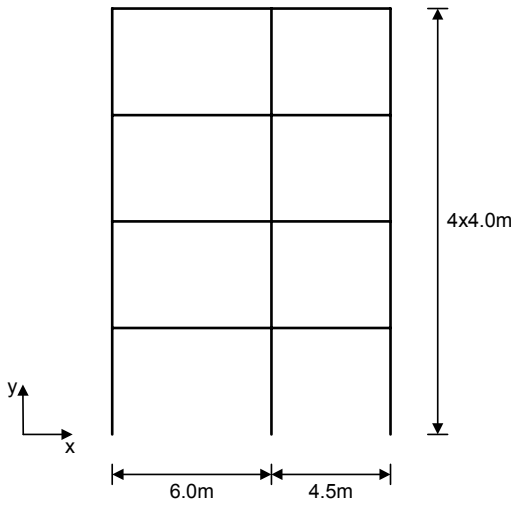

Figure 3. The concrete plane frame test problem.

Correlation length	Mesh	Average element size (m)	$COV(\delta_{max})$	
			σ=10%	σ=20%
b=5m	M_0	4.50	9.9%	22.5%
	M_1	2.05	8.2%	18.0%
	M_2	0.98	8.0%	17.3%
	M_3	0.50	8.0%	17.2%
b=1m	M_1	2.05	6.7%	14.9%
	M_2	0.98	3.9%	9.1%
	M_3	0.50	2.6%	6.1%
	M_4	0.25	2.5%	5.9%
b=0.5m	M_2	0.98	4.7%	10.7%
	M_3	0.50	2.3%	5.7%
	M_4	0.25	1.3%	3.4%
	M_5	0.15	1.3%	3.4%

Table 1. Concrete plane frame test problem: variability of maximum inter-storey drift δ_{max} for various correlation lengths, σ-values and meshes.

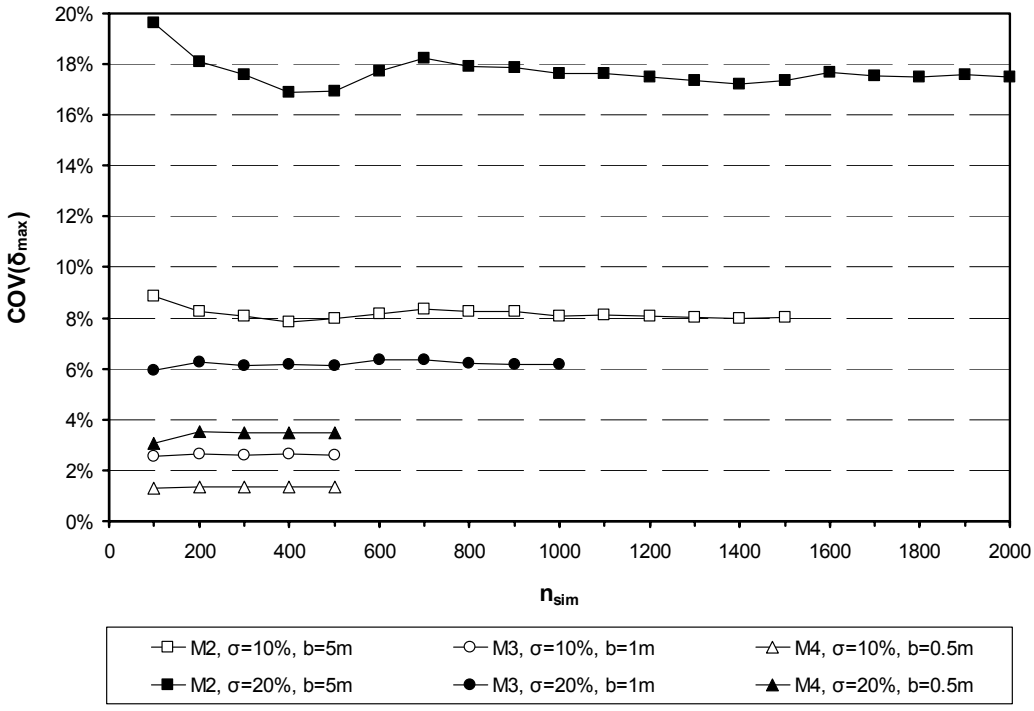

Figure 4. Concrete plane frame test problem: $COV(\delta_{max})$ as a function of the number of simulations for various meshes and values of parameters σ and b.

$$COV(\delta_{max}) = \frac{\sigma(\delta_{max})}{\mu(\delta_{max})}, \tag{12}$$

where $\mu(\delta_{max})$ and $\sigma(\delta_{max})$ are the mean value and standard deviation of δ_{max}, respectively. Drifts are often utilized as vulnerability measures for seismically excited structures. Preliminary results obtained for $COV(\delta_{max})$ are summarized in Table 1. In order to effectively represent the generated random field samples of E using the

midpoint method, various element sizes are used to provide discretizations of various refinement levels for the 20 column and beam members of the concrete frame. Thus, 6 different meshes M_0 (original mesh – each structural member corresponds to one element), M_1, M_2, M_3, M_4 and M_5 are considered with 20, 44, 92, 180, 360 and 604 elements, respectively. As illustrated in Fig. 4, several hundreds or even thousands of simulations are needed to reach converged structural response statistics with the direct MCS approach.

The numerical results reported show the influence of random field parameters on drift variability. Hence, larger random field coefficients of variation σ induce larger drift variability. Moreover, the value given to correlation length b appears to play a decisive role in the evaluation of $COV(\delta_{max})$: drift variability is rather large for larger b-values, but it tends to diminish as smaller b-values are taken. It should also be noticed that converged simulation results are obtained with element sizes equal to ¼ to ½ of the correlation length value. The latter conclusion is in accordance with observations in other stochastic analysis studies[15]. Due to limitations in the length of this paper, results on the application of the MCS process in the RDO framework are not presented.

6 CONCLUDING REMARKS

The aim of the present work is to combine modeling approaches for uncertain structural properties and earthquake loads, in order to accurately represent randomness in seismically excited structures. For this purpose, stochastic fields are utilized to describe the variation of structural properties along the length of frame members, while probabilistic spectral acceleration data are derived from natural ground motion records. The presented modeling and analysis techniques allow the evaluation of structural response statistics and/or the estimation of reliability for seismically excited multi-storey frames.

Although dynamic structural analysis taking uncertainties into account is a computationally very intensive task (especially when the direct MCS method is applied), simulation runs can be drastically accelerated with the use of parallel processing and the implementation of efficient computational techniques[23-25]. The use of such computational approaches is increasingly important as the size of the structural problem or the number of MCS becomes larger. Especially in the case of evolutionary robust optimization, in which the MCS procedure needs to be invoked for each candidate optimum design, the arising computing costs are excessive and the utilization of advanced computational techniques is practically necessary in realistic problems.

REFERENCES

[1] Lin YK, Kozin F, Wen YK, Casciati F, Schuëller GI, Der Kiureghian A, Ditlevsen O, Vanmarcke EH (1986), "Methods of stochastic structural dynamics", Structural Safety, 3:167-194.

[2] Cai GQ, Lin YK (1998), "Reliability of nonlinear structural frame under seismic excitation", Journal of Engineering Mechanics, ASCE, 124(8):852-856.

[3] Chen M-T, Harichandran RS (2001), "Response of an earth dam to spatially varying earthquake ground motion", Journal of Engineering Mechanics, ASCE, 127(9):932-939.

[4] Pradlwarter HJ, Schuëller GI, Schenk CA (2003), "A computational procedure to estimate the stochastic dynamic response of large non-linear FE-models", Computer Methods in Applied Mechanics and Engineering, 192:777-801.

[5] Au SK, Beck JL (2003), "Subset simulation and its application to seismic risk based on dynamic analysis", Journal of Engineering Mechanics, ASCE, 129(8):901-917.

[6] Song J, Ellingwood BR (1999), "Seismic reliability of special moment steel frames with welded connections: II", Journal of Structural Engineering, ASCE, 125(4):372-384.

[7] Huh J, Haldar A (2001), "Stochastic finite-element-based seismic risk of nonlinear structures", Journal of Engineering Mechanics, ASCE, 127(3):323-329.

[8] Ghiocel DM, Ghanem RG (2002), "Stochastic finite-element analysis of seismic soil-structure interaction", Journal of Engineering Mechanics, ASCE, 128(1):66-77.

[9] Franchin P (2004), "Reliability of uncertain inelastic structures under earthquake excitation", Journal of Engineering Mechanics, ASCE, 130(2):180-191.

[10] Frangopol DM, Soares CG, editors (2001), Special issue on reliability-oriented optimal structural design, Reliability Engineering & System Safety, 73(3):195-306.

[11] Lagaros ND, Plevris V, Papadrakakis M (2005), "Multi-objective design optimization using cascade evolutionary computations", Computer Methods in Applied Mechanics and Engineering, in print.

[12] Shinozuka M, Deodatis G (1991), "Simulation of stochastic processes by spectral representation", Applied Mechanics Reviews, ASME, 44(4):191–203.

[13] Schuëller GI, editor (1997), "A state-of-the-art report on computational stochastic mechanics", Probabilistic Engineering Mechanics, 12(4):197-321.

[14] Spanos PD, Zeldin BA (1998), "Monte Carlo treatment of random fields: A broad perspective", Applied Mechanics Reviews, ASME, 51(3):219-237.

[15] Der Kiureghian A, Ke J-B (1988), "The stochastic finite element method in structural reliability", Probabilistic Engineering Mechanics, 3(2):83-91.

[16] Matthies HG, Brenner CE, Bucher CG, Guedes Soares C (1997), "Uncertainties in probabilistic numerical analysis of structures and solids – Stochastic finite elements", Structural Safety, 19(3):283-336.

[17] Papadrakakis M, Tsompanakis Y, Lagaros ND, Fragiadakis M (2004), "Reliability based optimization of steel frames under seismic loading conditions using evolutionary computation", Journal of Theoretical and Applied Mechanics, 42(3):585-608.

[18] Beck JL, Chan E, Irfanoglu A, Papadimitriou C (1999), "Multi-criteria optimal structural design under uncertainty", Earthquake Engineering and Structural Dynamics, 28:741-761.

[19] Chintanapakdee C, Chopra AK (2003), "Evaluation of modal pushover analysis using generic frames", Earthquake Engineering and Structural Dynamics, 32:417-442.

[20] Warn GP, Whittaker AS (2004), "Performance estimates in seismically isolated bridge structures", Engineering Structures, 26:1261-1278.

[21] Liu M, Burns SA, Wen YK (2005), "Multiobjective optimization for performance-based seismic design of steel moment frame structures", Earthquake Engineering and Structural Dynamics, 34(3):289-306.

[22] Eurocode 8 (1994), "Design provisions for earthquake resistance of structures, Part 1-2: General rules – General rules for buildings", CEN, ENV 1998-1-2.

[23] Johnson EA, Proppe C, Spencer Jr BF, Bergman LA, Székely GS, Schuëller GI (2003), "Parallel processing in computational stochastic dynamics", Probabilistic Engineering Mechanics, 18:37-60.

[24] Charmpis DC, Papadrakakis M (2005), "Improving the computational efficiency in finite element analysis of shells with uncertain properties", Computer Methods in Applied Mechanics and Engineering, 194(12-16):1447-1478.

[25] Charmpis DC, Papadrakakis M (2005), "Using parallel processing for large-scale finite element computations in the context of Monte Carlo simulation", In: Proceedings of 9th International Conference on Structural Safety and Reliability (ICOSSAR 2005), Rome, Italy.

STRUCTURAL OPTIMIZATION OF A FIXED-TANK VEHICLE USING COMPLEX METHOD

Dimitris V. Koulocheris, Vasilis K. Dertimanis, and Constantinos N. Spentzas

Vehicles Laboratory
School of Mechanical Engineering
National Technical University of Athens
Iroon Politechniou 9, 15780, Zografou Campus, Athens, Greece
e-mail: dbkoulva@central.ntua.gr

Keywords: Structural optimization, Fixed-tank vehicles, Suspension systems, Lateral stability, Complex method.

Abstract. *This paper aims at optimizing the dynamic behavior of a fixed-tank, two-axle vehicle, with respect to its lateral stability performance. A linear full-car model with ten degrees of freedom is proposed, subject to typical road surface profiles and all the corresponding stiffness and damping characteristics of the model are optimized with respect to design limitations, as well as to any geometrical constraints of the vehicle. For the optimization tasks, the Complex method is implemented.*

1 INTRODUCTION

Fixed tank vehicles are torsionally very rigid, therefore the tank must be fitted in a way that the chassis retains sufficient and gradual torsional flexibility, by avoiding areas of high stress, and the vehicle maintains an acceptable dynamic performance. Considering manufacturer recommendations, ADR Agreement[1] and relative European Regulations, the installation of tanks requires the use of an appropriate auxiliary frame, in which the rigid mounts are installed in a position corresponding to the rear suspension supports and the flexible mounts as near as possible to the rear support of the front suspension. Furthermore, the effect of load on lateral force at a given slip angle is of fundamental importance in problems of handling. As far as the dynamic performance of the vehicle is taken under consideration, several studies have been reported[2-5], regarding the dynamics of heavy vehicles, as well as the optimal shape of the installed tank, with respect to vehicle's rollover stability[6].

This paper aims at optimizing the dynamic behavior of a fixed-tank two-axle vehicle, with respect to its lateral stability performance. For this, a linear full-car model with ten degrees of freedom (DOF's) is proposed, subject to typical road surface irregularities and all the corresponding stiffness and damping characteristics of the model are optimized, with respect to any design limitations and geometrical constraints of the vehicle. The Complex method has been selected for the numerical implementation of the optimization procedure, as it has been shown to be flexible in non convex problems; it's very simple to program, computationally efficient and usually reliable in the search for global optimum.

The rest of the paper is organized as follows: In Section 2 the suspension model is presented and in Section 3 the corresponding optimization problem is formulated and a brief presentation in Complex method is given. Section 4 covers the optimization tasks and in Section 5 the results are concluded and suggestions for further research are given.

2 THE FULL-CAR SUSPENSION MODEL

A typical two-axle truck vehicle, with a two supports' fixed tank installed on the chassis frame, is presented in Fig. 1, while in Fig. 2-3, the corresponding pitch-bounce-roll model is displayed. The tank and the vehicle are modeled as rigid bodies with 3 DOF's, that is bounce $x_T(t)$ & $x_M(t)$, pitch $\varphi_T(t)$ & $\varphi_M(t)$, and roll angle $\theta_T(t)$ & $\theta_M(t)$, respectively. The front and rear supports have been considered as mass-less elements with corresponding stiffness and damping characteristics. Each tyre is modeled as an unsprung mass with a single DOF (bounces $x_{fr}(t)$, $x_{fl}(t)$, $x_{rr}(t)$ and $x_{rl}(t)$) and corresponding stiffness and damping, and it's connected to the vehicle through the relative suspension.

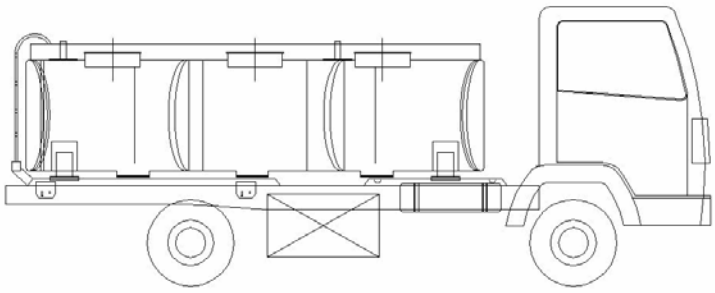

Figure 1. Two axle fixed-tank vehicle.

Despite their simplicity, as suspension nonlinearities or complexities of the sprung masses' motion are not modeled, this kind of models illustrate many critical characteristics of the lateral dynamics of heavy vehicles[7] and may used for design purposes. The part of the model that describes the vehicle is not symmetric with respect to the pitch axis, neither in its centre of mass, nor in its front and rear wheelsets, while the installed tank is generally assumed symmetric in fixed-tank vehicles.

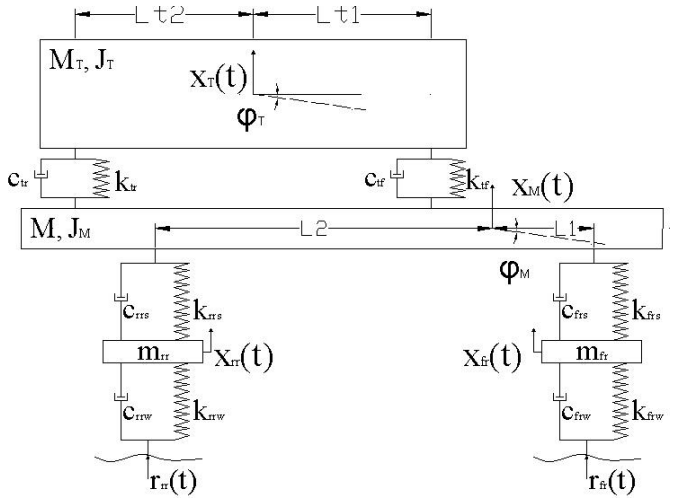

Figure 2. Full-car model, pitch-bounce view.

With respect to the above described model, the equivalent stiffness and damping, which describe the dynamic interconnection between the chassis and the tank, are the structural characteristics that must optimized. Naturally, in the case where there is the availability to further interfere in vehicle's structural components, such as the suspension system, it's of crucial importance to simultaneously optimize their relative stiffness and damping, so that a more complete view of the whole vehicle set up may assessed. As far as concerned the lateral dynamics, it's obvious that the corresponding lateral force is affected by critical factors, such as the vertical load, the roll angle and the tyre construction. Thus, a simple technique to interconnect lateral and vertical dynamics is by optimizing the roll angle relative DOF's and requiring at the same time that the tyres are keeping their contact to the ground.

3 THE OPTIMIZATION PROBLEM

Taking under consideration the required symmetry of the structural characteristics with respect to the roll axis, a total of eight parameters is entered in the optimization vector, corresponding to the stiffness and damping of the suspension and the supports. The objective function for the specific optimization problem can be formulated as,

$$f(\mathbf{p}) = \max\{q(t), t \in [0\ T]\} + M \cdot \sum_i c_i(\mathbf{p}) \tag{1}$$

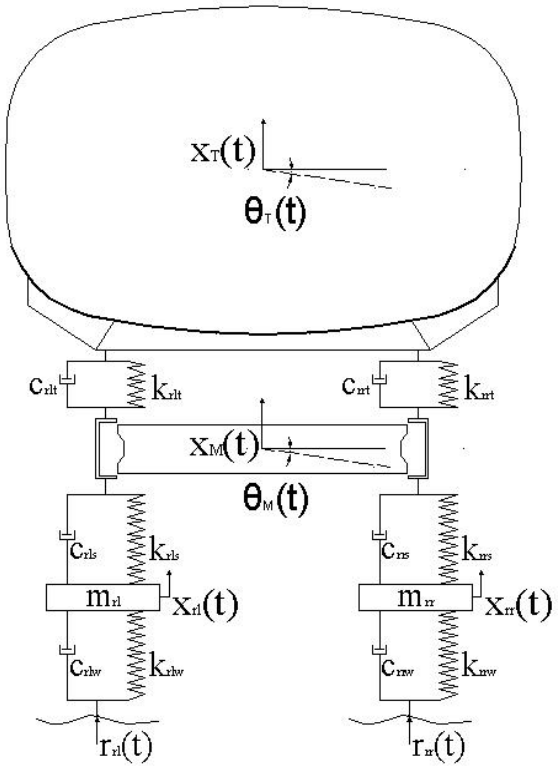

Figure 3. Full-car model, roll-bounce view.

where **p** is the parameter vector, *q(t)* any vibration displacement, velocity or acceleration data, which is available over a *[0 T]* time interval, *M* is a penalty coefficient and $c_i(\mathbf{p})$ are all the required constraints, related to the feasible values of stiffness and damping, as well as to the limited working space of the suspension.

Obviously, the above formulation covers the most general case of the corresponding optimization problem. Referring to the model described in Section 2, the vibration data may be taken either from the vehicle chassis, or from the tank. A more detailed assessment of the specific optimization problem, regarding the selection of the data and the selection of penalty criteria, is given in Section 4, where the numerical implementation is taking place.

3.1 The Complex Method

The Complex optimization method belongs to the family of semi-stochastic algorithms. It was originally given by Spendley, Hext and Himsworth and further developed by Nedler and Mead. According to Complex method, an initial parameter vector p0, which represents any available insight about the problem of interest, is determined and a number of *k* random parameter vectors is consequently generated according to normal distribution, with $\mathbf{p}_0$ their mean value. The basic idea is to compare the values of the objective function at the *k+1* vectors and move the parameter population toward the optimum point. This movement is achieved using three operations, known as reflection, expansion and contraction. The *k+1* vectors are sorted in descending order of their corresponding objective function value. The first (and worst) vector is notated as $\mathbf{p}_H$, while the last (and best) as $\mathbf{p}_L$ and a new vector is generated, known as weight centre according to:

$$\mathbf{p}_A = \frac{1}{k} \cdot \sum_{j=2}^{k+1} \mathbf{p}_j \tag{2}$$

The weight centre vector is used for the search of the reflection vector $\mathbf{p}_R$, in the opposite direction to that of the $\mathbf{p}_H$,

$$\mathbf{p}_R = \mathbf{p}_A + R \cdot (\mathbf{p}_A - \mathbf{p}_H) \tag{3}$$

where R is the reflection factor, taking values in the *[1 1.7]* interval. Depending on the value of objective function at $\mathbf{p}_R$, three cases are considered:

➔ Case 1: $f(\mathbf{p}_L) < f(\mathbf{p}_R) < f(\mathbf{p}_H)$

In this case the algorithm returns to the initial stage, after replacing the worst vector $\mathbf{p}_H$ by the reflection one, $\mathbf{p}_R$.

➔ Case 2: $f(\mathbf{p}_R) < f(\mathbf{p}_L)$

In this case the expansion procedure is executed and a corresponding vector is generated,

$$\mathbf{p}_E = \mathbf{p}_A + E \cdot (\mathbf{p}_R - \mathbf{p}_A) \tag{4}$$

where E is the expansion factor, taking values in the *[1.8 2.2]* interval. If $f(\mathbf{p}_E) < f(\mathbf{p}_R)$, the worst vector $\mathbf{p}_H$ is replaced by $\mathbf{p}_E$, otherwise, if $f(\mathbf{p}_E) > f(\mathbf{p}_R)$, $\mathbf{p}_H$ is replaced by $\mathbf{p}_R$ and the algorithm returns to the initial stage.

➔ Case 3: $f(\mathbf{p}_R) > f(\mathbf{p}_H)$

The contraction procedure is executed in this case and a new vector is formulated as,

$$\mathbf{p}_C = \mathbf{p}_A + C \cdot (\mathbf{p}_H - \mathbf{p}_A) \tag{5}$$

where C is the expansion factor, which belongs to [*0.3 0.8*] interval. If $f(\mathbf{p}_C) < f(\mathbf{p}_H)$, the worst vector $\mathbf{p}_H$ is replaced by $\mathbf{p}_C$, otherwise, if $f(\mathbf{p}_C) > f(\mathbf{p}_H)$, all the vector population is substituted according to:

$$\mathbf{p}_i = \frac{\mathbf{p}_i + \mathbf{p}_L}{2},\ i = 1,...,k+1 \tag{6}$$

It's obvious that the Complex method does not implement any computation of derivatives, thus is computationally very efficient. Additionally, it's easily programmable and does not require large computer storage. The initial vector $\mathbf{p}_0$ may, however, affects the convergence procedure, although is has been reported that this is not a major restriction.

PARAMETERS	CONSTRAINT	UNIT
Suspension Stiffness	10000-100000	N/m
Suspension Damping	1000-10000	N.s/m
Support equivalent Stiffness	100-5000	N/m
Support equivalent Damping	10-500	N.s/m
Suspensions' available working space (from the equilibrium point)	± 0.2	m
Stability of the system	-	-
Road-handling ability	-	-

Table 1 : Constraints of the optimization problem.

4 NUMERICAL IMPLEMENTATION

In order to study and optimize the dynamic performance of the fixed-tank vehicle, it was assumed to travel with a constant velocity of 40 km/h and the vibration data selected as objective function was chassis' roll angle. The required constraints are presented in Tab. 1. As far as concerned the limits of the quantities in the parameter vector, these were a-priori satisfied, using a simple change of variable. More specifically, if lower and upper bounds are specified for a variable as

$$l_{lv}^{i} \leq \mathbf{p}(i) \leq u_{uv}^{i}, \quad i = 1,..,8 \tag{7}$$

they can be satisfied by transforming **p***(i)* as

$$\mathbf{p}(i) = l_{lv}^{i} + (u_{lv}^{i} - l_{lv}^{i}) \cdot \sin^2 \mathbf{h}(i) \tag{8}$$

where h(i) is the new variable, which can take any value, assuring that the original vector satisfies the inequality constraints. This is a very simple and efficient way of avoiding additional penalty functions into the objective function, which disaffect the search space of the optimization problem. It must be noted though that, prior to the change of variable, a rescaling of the quantities in the parameter vector has been applied, with respect to Tab. 1, in order to avoid well-known numerical drawbacks, due to the different ranges of the respective variables.

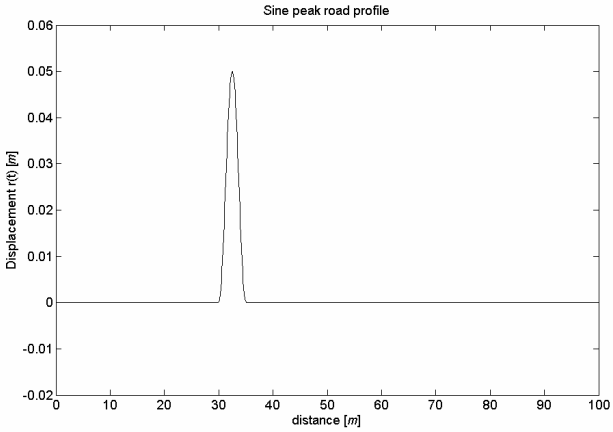

Figure 4. Sine peak road excitation.

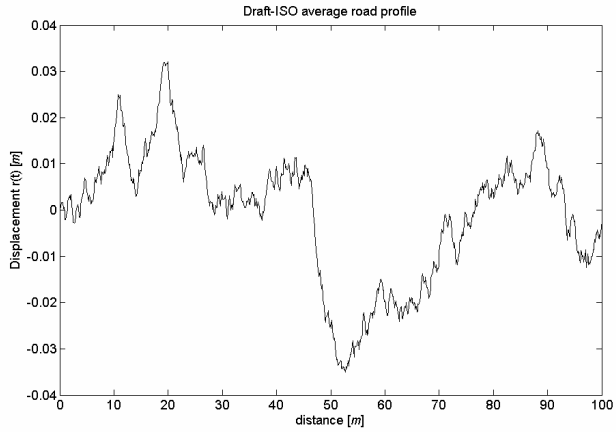

Figure 5. Average quality road profile.

As far as concerned the road excitation profiles, two distinct cases where implemented: in the first, a sine peak (see Fig. 4) was applied to the right path of the vehicle, while in the second, an average quality road profile (see Fig. 5), according to the Draft-ISO formulation[7] , was simultaneously applied on both paths of the vehicle, keeping the same sine peak an the right.

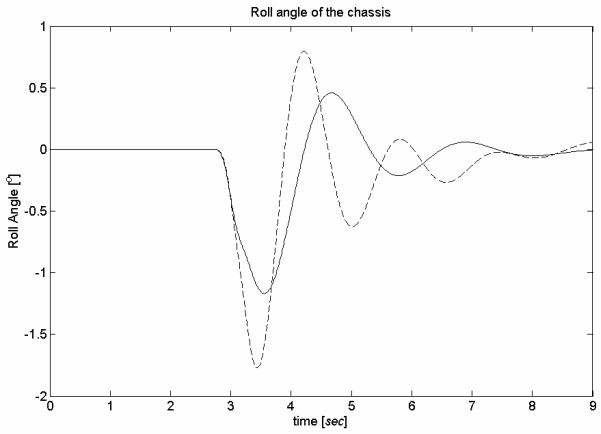

Figure 6. Initial (dashed line) and optimized (continuous line) roll angle of the chassis, 1st case of road excitation.

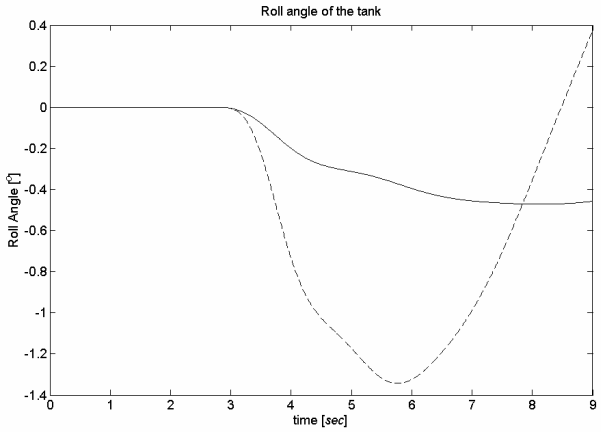

Figure 7. Initial (dashed line) and final (continuous line) roll angle of the tank, 1st case of road excitation.

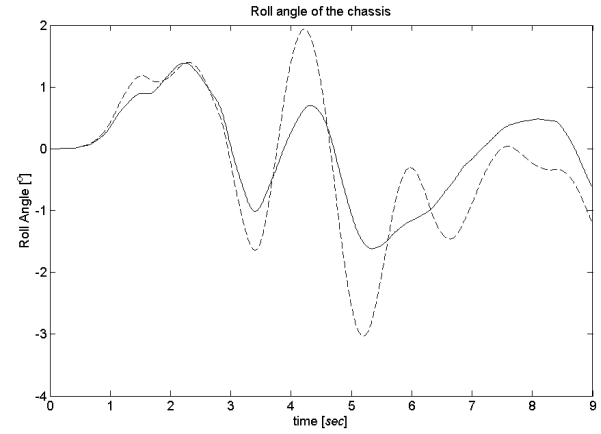

Figure 8. Initial (dashed line) and optimized (continuous line) roll angle of the chassis, 2nd case of road excitation.

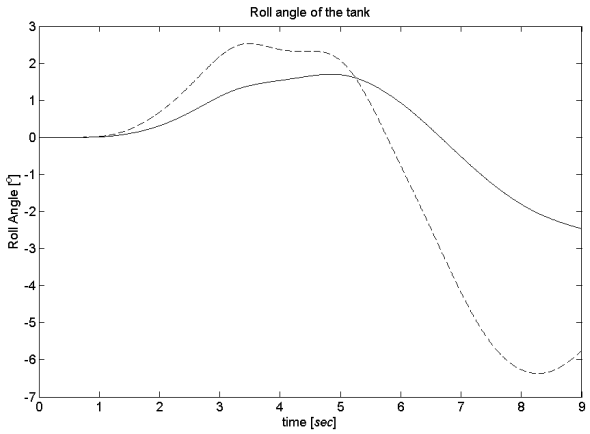

Figure 9. Initial (dashed line) and final (continuous line) roll angle of the tank, 2nd case of road excitation.

In both cases of road excitation, the initial parameter vector was selected in the mid range of the variables' limits. Figures 6 to 9 display the resulted roll angles for the chassis and the tank, where the sufficient decrease in the maximum values of the relative vibration curves is obvious. The Complex method managed to overcome the constraints at a low number of iterations and additionally, returned optimized vibration data for both the chassis and the tank. Table 2 displays the final values for the optimization vector, for the two cases of road excitation. Clearly, the installation of the tank is resulted with elastic front support and rigid rear, followed by contradictious damping setup, for every road profile. A big difference is observed in the rear suspension's stiffness, where in the case of an average road profile, the corresponding installation requires a vehicle with the same stiffness in its front and rear suspensions.

PARAMETERS	1st road excitation	2nd road excitation
Front Suspension stiffness (N/m)	11974	10767
Rear Suspension stiffness (N/m)	38961	12401
Front Suspension damping (N.sec/m)	7563	9604
Rear suspension damping (N.sec/m)	1549	4814
Front support's stiffness (N/m)	398	115
Rear support's stiffness (N/m)	484	319
Front support's damping (N.sec/m)	357	430
Rear support's damping (N.sec/m)	210	189

Table 2 : Results of the optimization procedure.

6 CONCLUSIONS

This paper attempted to optimize the structural characteristics of a two-axle fixed-tank vehicle, with respect to its lateral stability. A 10-DOF full-car suspension model was proposed and all the design and geometric limitations were considered for the optimization tasks, which where implemented using two different kinds of road irregularities. The Complex method managed to perform consistently, producing acceptable results that were, naturally, varied, as far as concerned the suspension system, for every profile. Yet, a useful conclusion which can be extracted is the installation of the tank upon the chassis frame, using an elastic front support and a more rigid rear.

Nowadays, the increased demands for safety in the road transport of dangerous goods force on the understanding of the dynamic performance of a fixed body, which is installed on a chassis' frame, and the mechanisms that may reduce the reliability of the vehicle. Minimization of failure in vehicle's components, as well as of road damage, plays also a vital role. In order to highlight all these important issues in heavy vehicles, more complicated models may be implemented and many of their critical characteristics can be optimized with respect to safety and cost.

REFERENCES

[1] E.C.E./Trans ADR 2003 (2002), *European Agreement, Concerning the International Carriage of Dangerous Goods by Road*, Geneva, United Nations.

[2] Nalcez, A.G. and Genin, J (1984), "*Dynamic Stability of Heavy Articulated Vehicles"*, International Journal of Vehicle Design 5(4), pp. 417-426.

[3] Rakheja, S., Sankar, S. and Ranganatham, R. (1998), *"Roll Plane Analysis of Articulated Tank Vehicles during Steady Turning"*, Vehicle System Dynamics (1-2), pp. 81-104.

[4] Rakheja, S. and Ranganatham, R. (1993), "*Estimation of the Rollover Threshold of Heavy Vehicles Carrying Liquid Cargo: A Simplified Approach"*, Heavy Vehicle Systems, International Journal of Vehicle Design 1 (1), pp. 79-98.

[5] Winkler, C.B., Blower, D. and Ervin, D.R. (2000), "*Rollover of Heavy Commercial Vehicles*", SAE Research Report.

[6] Kang, X., Rakheja, S. and Stiharu, I. (2000), "Tank Shape Optimization for Enhancement of Roll Stability of Partially-filled Tank Vehicles in Steady Turning", *Proceedings ASME IMECE 2000 Conference*, Orlando, Florida, November 2000.

[7] Cebon D. (2000), *Handbook of Vehicle-Road Interaction*, Swets & Zeitlinger, Lisse.

DESIGN OF A HYBRID ALGORITHM FOR ARMA PARAMETER ESTIMATION

Vasilis K. Dertimanis, Dimitris V. Koulocheris, and Constantinos N. Spentzas

Vehicles Laboratory
School of Mechanical Engineering
National Technical University of Athens
Iroon Politechniou 9, 15780, Zografou Campus, Athens, Greece
e-mail: bullit@central.ntua.gr

Keywords: ARMA models, Prediction-error method, hybrid optimization algorithms, parameter estimation.

Abstract. *This paper proposes a new methodology for the estimation of ARMA models, based on the implementation of a hybrid optimization algorithm and a corresponding estimation procedure. The specific algorithm attempts to interconnect the diverse characteristics of two entirely different optimization techniques, deterministic and stochastic, combining high convergence rate with increased reliability in the search for global optimum. The corresponding estimation procedure is split into two parts, due to the mixed linear-nonlinear relationship between the prediction errors and the parameter vector, and assures the stability and invertibility of the resulted models. The parametric identification test case, which is considered in this study, refers to the estimation of an ARMA model for the description of a half-car passive suspension system of a road vehicle, taking into account that the response data consists of a noise-corrupted, at 10% noise to signal ratio, vertical acceleration of the sprung mass.*

1 INTRODUCTION

Parametric identification relies mostly on the Prediction-error method (PEM)[1,2], which formulates the one-step ahead prediction errors sequence, between the actual response and the one computed from the model, and uses a scalar-valued index function (loss function) to evaluate that sequence. Over a set of candidate models, the one which minimizes the loss function is chosen, with respect to the corresponding fitness to data. In the case where a moving average polynomial is present in the model, PEM turns into a mixed linear-nonlinear optimization problem and requires iterative numerical techniques to estimate the parameter vector. Yet, the relative optimization methods that have been implemented for this kind of problems present some well-known drawbacks[3,4] and in the case of noise-corrupted observations are even more dysfunctional.

To overcome this difficulty, an alternative approach, based in the implementation of stochastic optimization algorithms, has been developed in the past decade. Several techniques have been formulated for parameter estimation and model order selection, using mostly Genetic Algorithms (GA). The basic concept of these algorithms is the simulation of natural evolution for the task of global optimization, and they have received considerable interest since the work done by Kristinsson and Dumont[5], who applied them to the identification of both continuous and discrete time systems. Relative studies are reported in the work of Tan and Li[6], Gray *et. al*[7], Billings and Mao[8], Rodriguez *et. al*[9], Kanarachos *et. al*[10]. Fleming and Purshouse[11] have presented an extended survey on these techniques, while Schoenauer and Sebag[12] address the use of Domain knowledge and the choice of fitness functions in Evolutionary System Identification. Yet, the main drawback of these methods is that they are computationally expensive, even for parameter vectors of low dimension, they often fail to converge in real-world, noisy systems[8,11] and their application in identification problems with unobservable excitation is largely unexplored. On the other hand, the implementation of hybrid optimization algorithms in the parameter estimation problem is considerably less reported in the literature[13-15], where they appear to be effective, in the sense that they significantly reduce the computational cost, in comparison to conventional stochastic optimization algorithms, leading in many cases to better results, due to the involvement of a local search procedure.

This study proposes a hybrid optimization algorithm and a corresponding estimation technique, for the estimation of ARMA models, by means of PEM. The algorithm interconnects the advantages of its deterministic and stochastic components, combining high convergence rate together with increased reliability in the search for global optimum. Its stochastic component has been selected to be the (μ+λ)-Evolution Strategy (ES)[16], which uses unaltered recombination and selection operators, while the deterministic counterpart consists of an algorithm especially designed for nonlinear least-squares (NLS), which replaces the original mutation operator of ES. The specific algorithm takes advantage of analytical gradient information and uses a secant

approximation to compute one portion of the Hessian matrix, as well as a mixed trust region / line search technique, in order to obtain global convergence characteristics and to reduce the computational cost. The corresponding estimation procedure takes advantage of the fact that the ARMA parameter estimation problem may considered as a mixed linear-nonlinear one, so it consists of two stages: in the first, the estimation of an AR model is implemented, while in the second stage the resulted vector is mixed with the coefficients of the noise polynomial, which are randomly selected from the normal distribution, to form the initial population of the algorithm. For the practical evaluation of the above, the proposed method is implemented in the parametric identification of a half-car passive suspension system under unobservable excitation, taking into account that the response data consists of a noise-corrupted at 10% noise to signal ratio vertical acceleration of the sprung mass.

The rest of the paper is organized as follows: In Section 2 the ARMA structure is presented and PEM is outlined. In Section 3 the corresponding optimization problem is implemented and the hybrid algorithm is described, while in Section 4 the estimation methodology is presented. Section 5 illustrates the identification experiments. Finally in Section 6 the results are discussed and some final remarks are made.

2 THE ARMA PARAMETER ESTIMATION PROBLEM

ARMA is a notation for the Auto-Regressive (AR), Moving Average (MA) model, and it has the following general form[1,2],

$$A(q)\cdot y_t = C(q)\cdot e_t \tag{1}$$

with $A(q)$ and $C(q)$ polynomials that represent the AR and MA parts respectively, having the following form:

$$A(q) = 1 + a_1\cdot q^{-1} + \ldots + a_{na}\cdot q^{-na} \tag{2}$$

In Eq. 1, y_t is the output time-series, q is the backshift operator, so that $q^{-k}y_t = y_{t-k}$, and e_t white noise with zero expectance and autocorrelation function given by $E\{e_t\cdot e_{t+l}\} = \sigma_e^2\cdot\delta_l$, where $E\{*\}$ denotes expectation, σ_e^2 is the white noise variance , and δ_l Kronecker's delta. For the successful representation of a vibrating system, by means of ARMA models, required conditions are the stability and invertibility of the noise transfer function $C(q)/A(q)$ [1], which means that the roots of the MA and AR polynomials must lie inside the unit circle with zero origin, in the complex plane.

The parametric identification problem focuses on the determination of the ARMA parameters (polynomial orders and coefficients, white noise variance), by means of any available time-series, which yield a corresponding model, capable to describe the dynamics of the system, as well as the presence of noise in the measurements. For a given series over the time $t = 1,...,N$, the one step ahead prediction-errors sequence, between the actual system's response and the one computed by the model, is

$$\hat{e}_t(1/\vec{p}) = y_{t+1} - \hat{y}_t(1/\vec{p}) \tag{3}$$

where $\vec{p} = \left[a_i\ c_i\right]$ is the parameter vector to be estimated, y_{t+1} the measured output, $\hat{y}_t(1/\vec{p})$ the model's predicted output and $\hat{e}_t(1/\vec{p})$ the residuals[i]. PEM uses the loss function to evaluate the residuals, leading to a standard optimization problem, in which the loss function has to be minimized using numerical methods. Yet, PEM combines asymptotic ($N\to\infty$) optimality with statistical consistency[1], compared to other identification methods[2].

[i] The argument $(1/\vec{p})$ denotes conditional probability and the hat indicates estimate.

3 THE HYBRID ALGORITHM

3.1 The optimization problem

Assuming a quadratic loss function of the form

$$f(\vec{p}) = \frac{1}{2 \cdot N} \cdot \sum_{t=1}^{N} \hat{e}_t^2 (1/\vec{p}) \tag{4}$$

the corresponding PEM optimization problem is

$$\min_{\vec{p} \in R^n} f(\vec{p}), n = na + nc \tag{5}$$

subject to

$$\max\left\{\left|roots\{A(q)\}\right|\right\} < 1 \tag{6}$$

$$\max\left\{\left|roots\{C(q)\}\right|\right\} < 1 \tag{7}$$

3.2 Description of the algorithm

The hybrid algorithm is based on the distribution of the local and the global search for the optimum. The method consists of a super-positioned stochastic global search and an independent deterministic procedure, which is activated under conditions in specific members of the involved population. Thus, while every member of the population contributes in the global search, the local search is realized from single individuals. Similar algorithmic structures have been presented in several fully stochastic techniques that simulate biological procedures of insect societies. Such societies are distributed systems that, in spite of the simplicity of their individuals, present a highly structured social organization. As a result, such systems can accomplish complex tasks that in most cases far exceed the individual's capabilities. The corresponding algorithms use a population of individuals, which search for the optimum with simple means. The synthesis, though, of the distributed information enables the overall procedure to solve difficult optimization problems. Such algorithms were initially designed to solve combinatorial problems[17,18], but were soon extended to optimization problems with continuous parameters[19-21].

The algorithm is based on a mechanism that aims at the cooperation between the (μ+λ)-ES and a NLS algorithm. The conventional ES is based on three operators that take on the recombination, mutation and selection tasks. In order to maintain an adequate stochastic character of the new algorithm, the recombination and selection operators are retained without alterations. The improvement is based on the substitution of the stochastic mutation operator by the NLS algorithm. The new deterministic mutation operator acts only on the *v* non-privileged individuals in order to prevent loss of information from the corresponding search space regions, while any other alternatives that were tested led to various types of problematic behavior[22].

3.3 The NLS operator

A NLS algorithm substitutes the original mutation operator of the (μ+λ)-ES. If $\mathrm{r}(\vec{p}) = \left[\hat{e}_1(1/\vec{p}) \ldots \hat{e}_N(1/\vec{p})\right]^T$ is the residual vector and $\mathrm{J}(\vec{p}) \in R^{Nxn}$ the Jacobian matrix of $r(\vec{p})$, the first and second order derivatives of $f(\vec{p})$ are respectively

$$\nabla f(\vec{p}) = \frac{1}{N} \cdot J^T(\vec{p}) \cdot r(\vec{p}) \tag{8}$$

$$\nabla^2 f(\vec{p}) = \frac{1}{N} \cdot \left(J^T(\vec{p}) \cdot J(\vec{p}) + S(\vec{p})\right) \tag{9}$$

where

$$S(\vec{p}) = \sum_{t-1}^{N} \hat{e}_t\left(1/\vec{p}\right) \cdot \nabla^2 \hat{e}_t\left(1/\vec{p}\right) \tag{10}$$

The NLS algorithm utilizes a modified version of the full Newton's method in the optimization problem stated in Eq. 5, using a successful secant approximation of the matrix $S(\vec{p})$, proposed by Dennis *et. al*[23], as well as a mixed trust-region / line search technique, introduced by Nocedal and Yuan[4]. The interesting reader should refer to Koulocheris *et. al*[22] for a thorough description of the operator.

In the original Newton's method the parameter vector is updated using

$$\vec{p}^{\,j+1} = \vec{p}^{\,j} - \left[\nabla^2 f(\vec{p})\right]^{-1} \cdot \nabla f(\vec{p}) \tag{11}$$

The recurrent formula which updates $\mathbf{S}_k$ initiates with zero entries, so that initially the NLS operator coincides with the Newton one. However, due to the stochastic nature of the (μ+λ)-ES, a globally convergent algorithm must implemented as mutation operator. Thus, at each iteration the constrained subproblem

$$\min_{\mathbf{s}_j \in R^n} \left\{ f(\vec{p}) + \mathbf{s}_j^T \cdot \nabla f(\vec{p}) + \mathbf{s}_j^T \cdot \nabla^2 f(\vec{p}) \cdot \mathbf{s}_j \right\} \tag{12}$$

subject to $\left\|\mathbf{s}_j\right\| \le \Delta_j$ is solved, and if the corresponding direction $\mathbf{s}_j$ does not result in a sufficient decrease of the objective function, a line search is performed along to that direction, which assures the required decrease of the objective function[4]. Additionally, at each iteration the corresponding direction of the Gauss-Newton direction is also computed (that is the part of the Hessian without the secant update) and the NLS operator selects the model with the best results. For the computation of the Jacobian matrices, a version of the recursive formulas used in[22] is implemented.

4 THE ESTIMATION PROCEDURE

The estimation of ARMA models is split into two stages. In the first, an AR(na) model of the form

$$A(q) \cdot y_t = e_t \tag{13}$$

is estimated using linear least squares[1,2], based on the fact that the innovations have a linear relationship with the $\left[a_i\right]$ part of the parameter vector $\vec{p}$. In the second stage, the hybrid algorithm is implemented for the estimation of ARMA models using μ parent population and λ offspring. Among the μ parents, only one keeps the AR stage information unaltered, while the others are generated using the normal distribution. The μ parents are recombined to form the λ offspring, according to the original ES operator, and after the evaluation of (μ+λ) vectors, only the ν worst are mutated, according to the NLS algorithm.

As far as the constraints are taken under consideration, it can be proved[22] that if

$$\rho_e = \max\left\{\hat{e}_t(1/\vec{p})\right\} \quad t = 1,\ldots,N \tag{14}$$

then

$$\frac{f(\vec{p})}{\rho_e} + l_{ac} \le 1.5 \tag{15}$$

where

$$l_{ac} = \max\left\{\max\left\{roots(A(q))\right\}, \max\left\{roots(C(q))\right\}\right\} \tag{16}$$

5 IDENTIFICATION EXPERIMENTS

The identification test case considered in this study consists of a half-car, linear, passive suspension model, which is presented in Fig.1. The frequency band of the 4-degrees of freedom system lies in the [1-10] *Hz* interval, with two pairs of closely spaced frequencies being present, that is chassis' bounce and pitch at 1.16 and 1.81 *Hz* respectively, and front and rear wheels' bounces at 9.8 and 10.1 *Hz*. The simulation of the system was implemented for 30 *sec* with sampling period T_s=0.01 *sec*. The resulted vertical acceleration of the sprung mass, noise-corrupted at 10% noise to signal ratio, form the time-series presented in Fig.2.

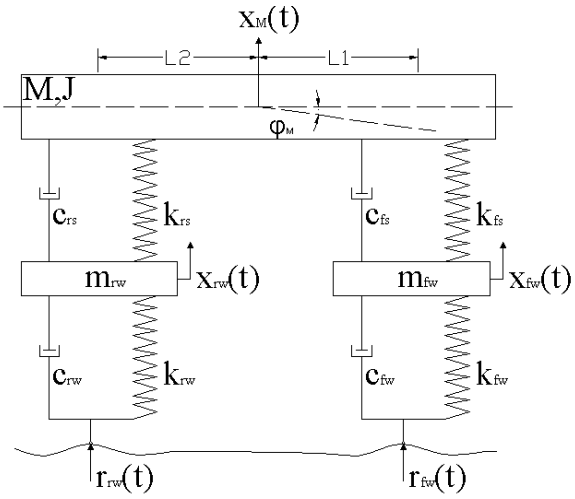

Figure 1. The half-car suspension model.

For the identification experiments the data set was mean-value subtracted and the first 500 data samples were excluded in order to avoid transient dynamics. Two phases were employed, each one for the determination of AR and MA polynomials, respectively. In every phase the corresponding models were compared using the BIC and RSS criteria[1], for the determination of polynomial order (which in the AR estimation phase coincides with the identification of structural degrees of freedom). Regarding the ES-NLS algorithm, a version with 3 parents and 6 offspring was implemented. The statistical properties of the estimated models were validated in every phase. That is, the sample autocorrelation of residuals and the covariance matrix (estimated as $\sigma_e^2\left[J^T(\vec{p})\cdot J(\vec{p})+S(\vec{p})\right]$) of the parameter vector were examined.

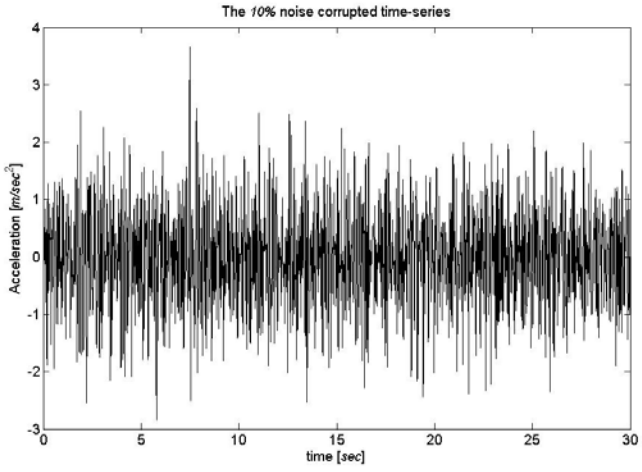

Figure 2. The chassis acceleration time-series.

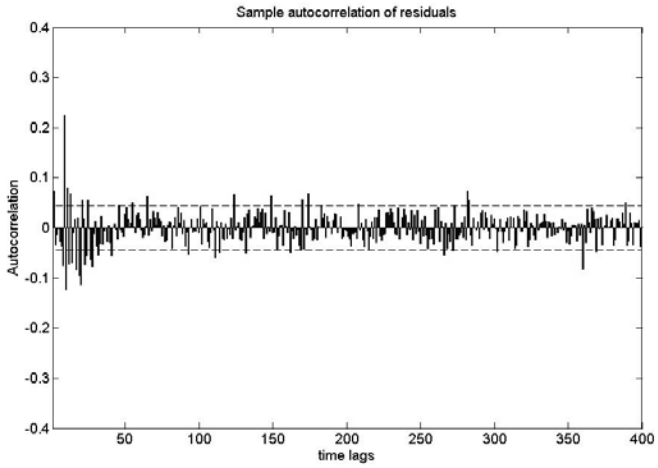

Figure 3. The sample autocorrelation of residuals for the ARMA(12,11) model.

In the first phase, employed for the estimation of AR polynomial order, ARMA(k,k) models were estimated for k=4,...,30. The hybrid algorithm presented satisfying performance and resulted in stable and invertible models in a few number of iterations and objective function evaluations. As expected, the BIC and RSS criteria showed contradictious performance, with the former penalizing the higher orders and the latter decaying up with increasing order. The autocorrelation of residuals was generally kept in the $\pm 1.96/\sqrt{N}$ statistical bounds, but for model order up to 10, prejudging that overdetermination was inevitable.

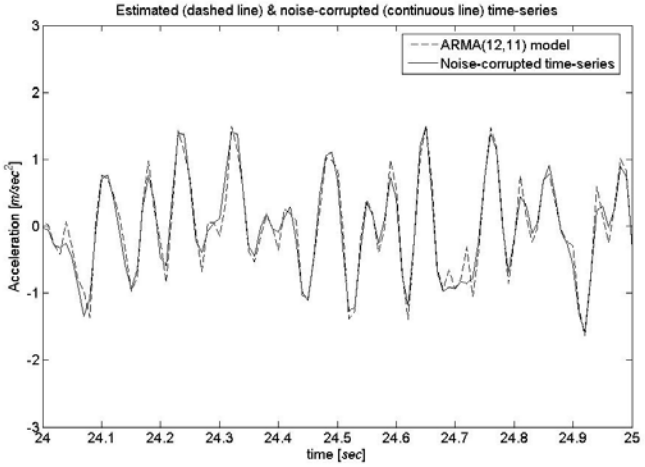

Figure 3. One second portion of estimated (dashed line) and noise-corrupted (continuous line) series.

After the selection of the ARMA(12,12) model, the phase that followed (ARMA(12,k) models , with k=10,..., 30) yielded similar performance to that of the first. Figures 3 and 4 display the autocorrelation of residuals and the time-series for a portion of data, respectively, for the selected model, which was ARMA(12,11). The residuals can be classified as white, while the percentage fitness to the noise-corrupted time-series (at about 81%) is satisfying.

6 CONCLUSIONS

This paper presented a hybrid optimization algorithm and a corresponding estimation procedure for the PEM estimation of ARMA models. The optimization algorithm interconnected the diverse characteristics of its stochastic and deterministic counterparts, combining reliability in the search for minimum with fast local convergence, and the estimation procedure took advantage of the mixed linear-nonlinear dependence between the residuals and the parameter vector. The main characteristics of the above can be summarized as follows:

- ✓ Guaranteed convergence to a stationary point, even in the presence of noise-corrupted data.
- ✓ Guaranteed stability and invertibility, regardless the size of the parameter vector.
- ✓ Sufficiently lower number of iterations and objective function evaluations, compared to conventional Evolutionary Algorithms.
- ✓ Statistical consistency.

The total performance of the proposed methodology throughout the identification experiments was satisfying. Yet, the required overdetermination, as well as the algorithmic complexity of the hybrid algorithm may be viewed as its main drawbacks.

REFERENCES

[1] Petsounis, K.A. and Fassois, S.D. (2001), "Parametric time domain methods for the identification of vibrating structures – A critical comparison and assessment", Mechanical Systems and Signal Processing 15(6), pp. 1031-1060.

[2] Ljung, L. (1999), *System Identification: Theory for the user*, Prentice-Hall PRT, New Jersey.

[3] Dennis, J.E. and Schnabel, R.B. (1996), *Numerical Methods for Unconstrained Optimization and Nonlinear Equations*, SIAM, Philadelphia.

[4] Nocedal, J. and Yuan, Y. (1998), "Combining trust region and line search techniques", Advances in Nonlinear Programming.

[5] Kristinsson, K. and Dumont, G.A. (1992), "System Identification and Control using Genetic Algorithms", IEEE Transactions on Systems, Man, and Cybernetics 22, pp. 1033-1046.

[6] Tan, K.C. and Li, Y. (2002), "Grey-box model identification via evolutionary computing", Control Engineering Practice 10(7), pp. 673-684.

[7] Gray, G.J., Murray-Smith, D.J., Li, Y., Sharman, K.C. and Weinbrenner, T. (1998), "Nonlinear model structure identification using genetic programming", Control Engineering Practice 6, pp. 1341-1352.

[8] Billings, S.A. and Mao, K.Z. (1998), "Structure detection for nonlinear rational models using genetic algorithms", International Journal of Systems Science 29(3), pp. 223--231.

[9] Rodriguez-Vazquez, K., Fonseca, C.M. and Fleming, P.J. (1997), "Multiobjective genetic programming: A nonlinear system identification application", Late breaking papers at the 1997 Genetic Programming Conf., pp. 207-212.

[10] Kanarachos, A., Koulocheris, D., Dertimanis, V. and Vrazopoulos, H. (2002), "Identification of a robotic arm using optimization methods for model estimation", *Proceedings of IBEC 2002*, Paris, France.

[11] Fleming, P.J. and Purshouse, R.C. (2002), "Evolutionary algorithms in control systems engineering: a survey", Control Engineering Practice 10(11), pp. 1223-1241.

[12] Schoenauer, M. and Sebag, M. (2002), "Using Domain knowledge in Evolutionary System Identification", *Evolutionary Methods for Design, Optimization and Control, Proceedings of Eurogen 2001*,Athens, Greece, pp. 35-42.

[13] Dertimanis, V., Koulocheris, D., Vrazopoulos, H. and Kanarachos, A. (2003), "Time-series parametric modeling using Evolution Strategy with deterministic mutation operators", *IFAC International Conference on Intelligent Control Systems and Signal Processing (ICONS 2003)*, Faro, Portugal, pp. 328-333.

[14] Koh, C.G., Chen, Y.F. and Liaw, C.-Y. (2003), "A hybrid computational strategy for identification of structural parameters", Computers & Structures 81, pp. 107-117.

[15] Koulocheris, D., Dertimanis, V. and Vrazopoulos, H. (2004), "Evolutionary parametric identification of dynamic systems", Forschung im Ingenieurwesen 68(4), pp. 173-181.

[16] Baeck, T. (1996), *Evolutionary Algorithms in Theory and Practice*, Oxford University Press, New York.

[17] Dorigo, M., Bonabeau, E. and Theraulaz, G. (2000), "Ant algorithms and stigmergy", Future Generation Computer Systems 16, pp. 851-871.

[18] Colorni, A., Dorigo, M., Maffioli, F., Maniezzo, V., Righini, G. and Trubian, M. (1996), "Heuristics from nature for hard combinatorial optimization problems", International Transactions on Operational Research 3(1), pp. 1-21.

[19] Monmarche, N., Venturini, G. and Slimane, M. (2000), "On how Pachycondyla apicalis ants suggest a new search algorithm", Future Generation Computer Systems 16, pp. 937-946.

[20] Rajesh, J.K., Gupta, S.K., Rangaiah, G.P. and Ray, A.K. (2001), "Multi-objective optimization of industrial hydrogen plants", Chemical Engineering Science 56, pp. 999-1010.

[21] Jayaraman, V.K., Kulkarni, B.D., Karale, S. and Shelokar, P. (2000), "Ant colony framework for optimal design and scheduling of batch plants", Computers and Chemical Engineering 24, pp. 1901-1912.

[22] Koulocheris, D., Dertimanis, V. and Spentzas, C. (2004), "A novel optimization algorithm for the estimation of ARMAX models", *7th Biennial ASME Engineering Systems Design and Analysis*, Manchester, United Kingdom.

[23] Dennis, J.E., Gay, D.M. and Welsch, R.E. (1981), "An adaptive nonlinear least-squares algorithm", ACM Transactions on Mathematical Software 7(3), pp. 348-368.

Fracture Mechanics

HYDRAULIC FRACTURING IN WEAK ROCKS

P. Papanastasiou

Department of Civil and Environmental Engineering
University of Cyprus
P.O.BOX 20537, 1678 Nicosia, Cyprus
e-mail: panospap@ucy.ac.cy, web page: http://www.eng.ucy.ac.cy/CEE/CEEHome.htm

Keywords: hydraulic fracturing, plasticity, finite element analysis, fracture propagation, fracture closure

Abstract. *This paper reviews some of the author's research work on hydraulic fracturing carried out in the research centre of Schlumberger in Cambridge. The work concentrates on the effect of rock plastic behaviour on the pressure needed for propagation, on the dimensions of the created fractures and on the fracture closure. The studies were based on a finite element analysis with a fully coupled elastoplastic hydraulic fracturing code. It was found that plastic yielding provides a shielding mechanism near the tip resulting in an increase of the effective fracture toughness. Higher pressure is needed to propagate an elastoplastic fracture and the created fracture is shorter and wider than an elastic fracture.*

1 INTRODUCTION

Hydraulic fracturing (HF) is a technique used to stimulate oil and gas reservoirs by inducing fractures in the formation and then propagating them by the injection of a high viscosity fluid. HF is also used in Environmental engineering for waste disposal in shallow formations, for cleaning up contaminated sites and in Geotechnical projects such as injection of grout, permeability testing, deep well injection and dam construction. A correct prediction of fracture geometry is vital for a safe design of such a process. Modelling the propagation of hydraulic fractures is usually carried out prior to fracturing in order to optimize the treatment. The fracturing fluid-pressure is the only parameter measured in the field that is available for controlling and evaluating the HF treatment. Classical hydraulic fracturing simulators are based on linear elasticity and often underestimate the down-hole pressures which are measured in field operations[1,2,3]. The differences between model predictions and actual field measurements are higher in weak formations[4].

A particular task of this work was to investigate the effect on non-linear rock behaviour on the hydraulic pressure needed for propagation and on the dimensions of the created fractures. Extension of this study into fracture closure examined the influence of rock plastic deformation on the closure pattern and the redistribution of the geostatic stresses near the fracture faces. The influence of inelastic rock behaviour in hydraulic fracturing was investigated experimentally[4,5,6].

The physical and mathematical modelling of hydraulic fracturing leads to strong non-linearity characterized by full coupling between the viscous flow of the fracturing fluid, the rock deformation and the fracture propagation processes. We solved the problem numerically by developing a fully coupled elastoplastic HF FEM code in which we incorporated a non-linear cohesive type fracture propagation criterion. In the FE code we incorporated a meshing/ remeshing scheme and a special continuation method (arc-length type) based on the volume of the injected fluid for controlling the solution during fracture propagation and closure.

This paper presents an overview of a numerical study on rock plasticity in hydraulic fracturing. In the next section we summarize the essential components of the coupled elastoplastic hydraulic fracturing model. In section 3 we present the main results of fracture propagation and fracture closure. In section 4 we summarize the main findings and we discuss some of the practical implications.

2 A FINITE ELEMENT COUPLED ELASTOPLASTIC HYDRAULIC FRACTURING MODEL

The study was based on fracture propagation and closure of a plane strain (KGD) elastoplastic fracture. The fracture propagates perpendicular to the direction of the minimum insitu stress and parallel to the direction of the maximum insitu stress (Figure 1). The fluid pressure leads to extensile loading of the rock ahead of the fracture tip whereas in the area near the tip intensive shearing takes place resulting in rock plastic yielding. Rock deformation is modelled by Mohr-Coulomb plasticity for a cohesive-frictional dilatant material. A cohesive model based on the softening behaviour of rocks is employed as the propagation criterion. Such a criterion is often used in the modelling of the cracking process in concrete[7]. Fluid flow in the fracture is modelled by lubrication theory and the complete mass conservation equation. Depending on formation properties, insitu

stresses and pumping parameters, the fluid may not necessarily reach the fracture tip thus allowing for the possibility of a dry zone (fluid lag) near the fracture tip. A special continuation method based on the volume of injected fluid in the fracture is used for direct coupling of the fluid-flow with rock deformation and for driving the solution during propagation. A fine mesh was used and a meshing/remeshing scheme was employed in order to carry out longer propagations with fine mesh near the fracture tip. Detailed information on the numerical implementation is provided in reference [8].

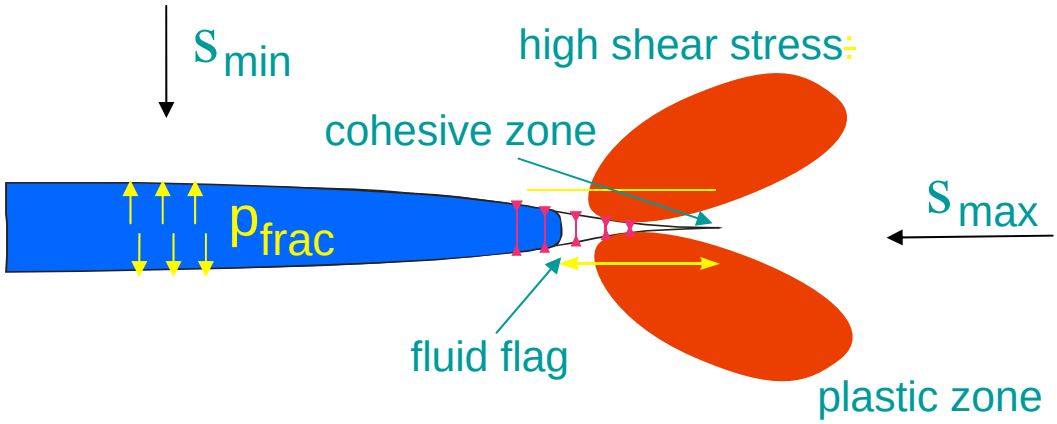

Figure 1: Geometry for a plane strain hydraulic fracture

The parameters upon which the numerical computations were based are given in Table 1. The only extra material parameters required for propagating an elastoplastic fracture are the plastic constants. With the chosen material parameters and in-situ stresses the rock is initially elastic but very close to a yielding state.

Pumping parameters	
Fluid viscocity	$\mu=10^{-7}$ MPa sec=100cp
Flow rate	q = 0.0005 m^3/sec
Insitu stresses	
Vertical	S'_{vert} = 14.49 MPa
Minimum horizontal	S'_{hmax} = 9 MPa
Maximum horizontal	S'_{hmin} = 3.7 MPa
Elastic constants	
Young's modulus	$E_{unloading} = 9E_{loading}$ MPa
Poisson ratio	ν= 0.3
Plastic parameters	
Friction angle	φ= 28°
Dilation angle	ψ= 28°
Loading modulus	$E_{loading}$ = 1785 MPa
Initial UCS	σ_c= 4 MPa
Fracturing parameters	
Fracture toughness	K_{IC} = 1 MPa $m^{1/2}$
Tensile strength	σ_T = 0.5 MPa

Table 1: Input parameters for finite element computations

2 COMPUTATIONAL RESULTS

2.1 Fracture Propagation

Figure 2 shows the profiles of propagating elastic (solid-lines) and elastoplastic (dashed-lines) fractures for the same fracture lengths. The cusping of the crack tips with zero slope is a result of the cohesive model which was incorporated as the propagation criterion.

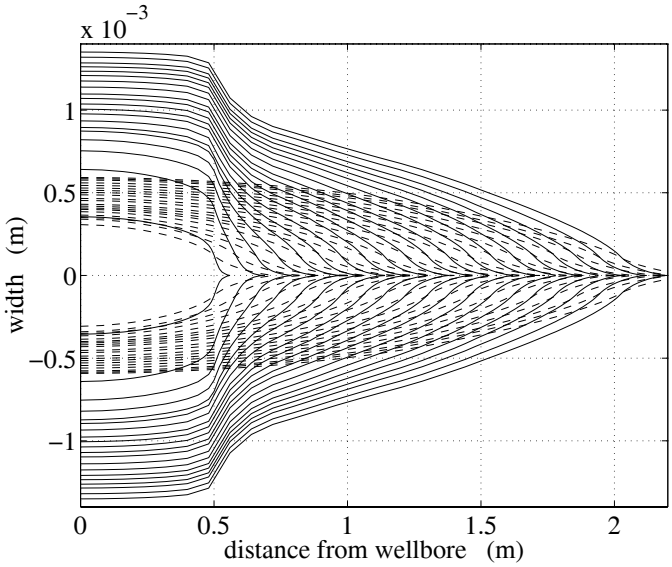

Figure 2: Fracture profiles for elastoplastic (solid lines) and elastic (dashed lines)

As mentioned earlier, the model of the elastoplastic fracture requires an initial fracture length which was set to 0.5 m; the influence of this can be seen in the width profiles in Fig.2. If we compare the fracture openings in the region where the fractures were propagated (i.e., distance from wellbore between 0.5 and 2.2 m) we see that the width profile of the elastoplastic fracture is much wider than the width profile of the elastic fracture.

Figure 3 shows the comparison of the net-pressure (difference between fluid-pressure in the fracture and minimum insitu stress) profiles in the fracture for the same fracture length. The very narrow opening of the elastic fracture results in greater pressure drop near the fracture tip and significant fluid-lag. Higher energy is required for propagating the elastoplastic fracture. Most of this energy is coming from the smaller fluid lag region.

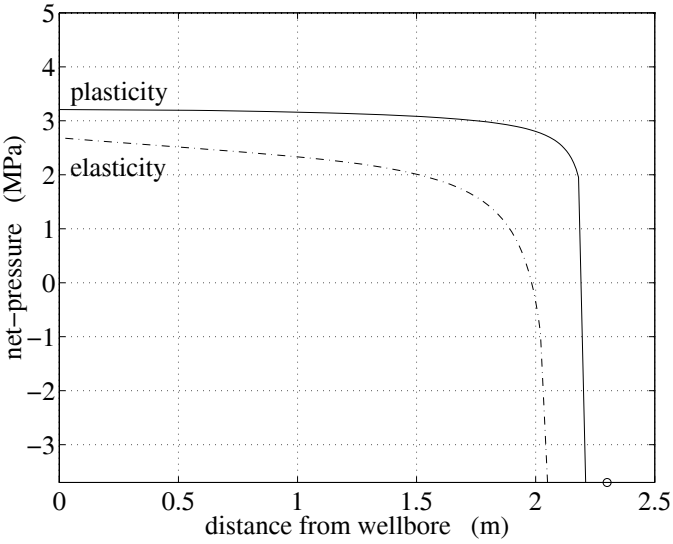

Figure 3: Net-pressure profiles on fractures

Plastic yielding near the tip of a propagating fracture provides an effective shielding, resulting in an increase in the effective rock fracture toughness[9]. This is shown in Fig.4 where we plotted the increase in the effective fracture toughness as a function of the fracture growth. The effective fracture toughness was determined using the calculated, path independent, J-integral[10]. The value of the effective fracture toughness is directly related to the size of the plastic zones. In other series of computations with different parameters much higher values of the fracture toughness were calculated. These results suggest that the field fracture toughness is much higher than

the fracture toughness measured in laboratory experiments on small cores. This discrepancy may partially explain the higher net-pressures accounted in field conditions. Scaling and tables with values of the effective fracture toughness for a representative set of physical parameters were presented in reference[9].

In addition, numerical studies with the elastic model in comparison with the plastic model, showed that for long propagation better results are obtained when the unloading elastic modulus it is used in the elastic model[11]. This is explained by the unloading state near the bulk of the fracture behind the advancing crack whereas the plastic deformation around the tip can be embedded in the increase value of the apparent fracture toughness

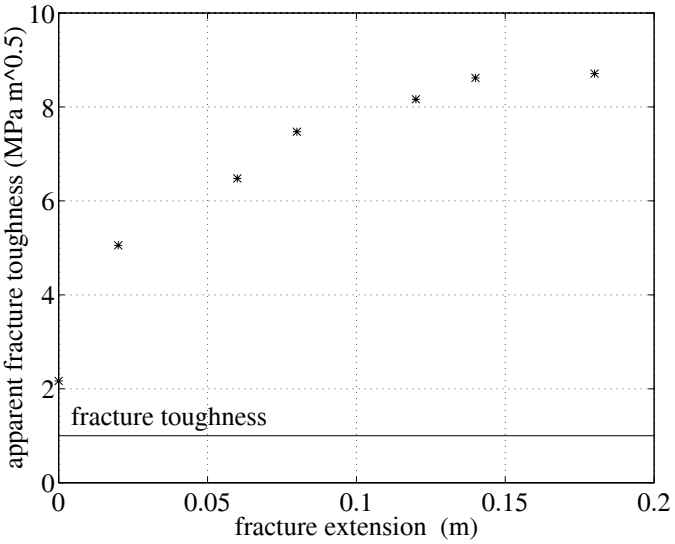

Figure 4: Apparent fracture toughness vs fracture extension

2.2 Fracture Closure

The elastoplastic fracture was propagated further to reach a length of 8 m before examining the closure pattern (Fig.5). Figure 6 shows the width profile of a receding elastoplastic fracture. It was assumed that there was no fluid-flow in the fracture during closure, therefore the pressure acting along the fracture was constant. The elastoplastic fracture makes contact initially near the tip and then the closure moves towards the wellbore[12]. This closure pattern agrees with the experimental results reported on soft rock samples[6].

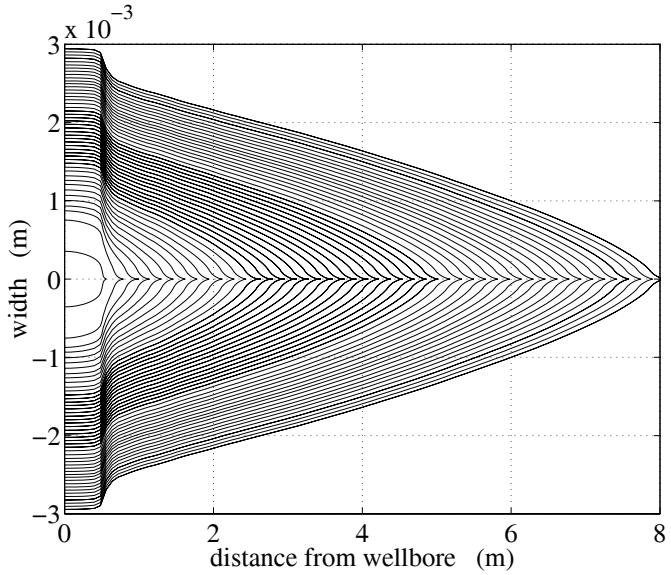

Figure 5: Propagation of elastoplastic fracture

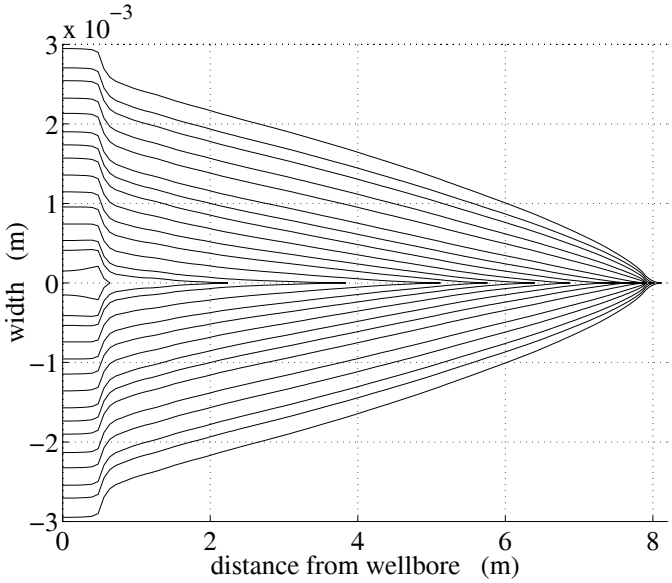

Figure 6: Closure of elastoplastic fracture

Figure 7 shows the corresponding net-pressure at the wellbore vs fracture length during propagation and closure after the fracture has reached a) 5 m and b) 8 m length. These results show that the net-pressure drops to zero while the fracture is still wide-open along a large proportion of the original length. The decrease of the fracture surface during closure will result in the underestimation of the insitu leak-off coefficient at the late stage of the pressure decline analysis. More accurate leak-off predictions can be obtained in the early stage of pressure decline analysis, immediately after shut-off of the pumping stage. The results of Fig.7 suggest that the fracture will close completely at negative net-pressures (fluid pressure less than the far-field stress). Application of classical analysis, which assumes that the fracture closes completely when the fluid-pressure drops to the value of the far-field stress, would lead to the underestimation of the minimum insitu stress. Furthermore, special considerations are necessary to identify the time instant the pressure in the fracture is equal to the far-field confining stress. This has been recognized in reference[13] which introduced diagnostic methods to detect deviations from ideal behaviour in practice.

Figure 8 shows the stress profiles on the propagation plane after the last closure step. The irregularity in the stress distribution in the area near the wellbore is due to the effect of the initial fracture length. As a result of the fracture closing first near the tip, the closure stress $S_{\_hmin}$ is higher than the in-situ stress in this area (5-8 m) and lower near the wellbore. This implies that the closure stress on the proppant will be higher near the fracture tip and lower in the area near the wellbore ($S_{\_hmin}$ in Fig.8). In addition, after fracture closure, due to permanent deformation, the stress state does not return to the original state. The risk of formation failure is significantly reduced after fracturing and closure not only due to increase of minimum insitu stress as a result of the enlarged propped fracture but also due to decrease in the other two insitu stresses[14]. Avoiding rock failure will minimize the risk of sand production which is one of the major problems in petroleum production from weak formations.

Finally the difference in the results obtained with the elastic model and elastoplastic model depend on the contrast of the magnitude of the insitu stresses, on rock strength and elastic modulus and also on the pumping parameters (fluid viscosity and flow rate).

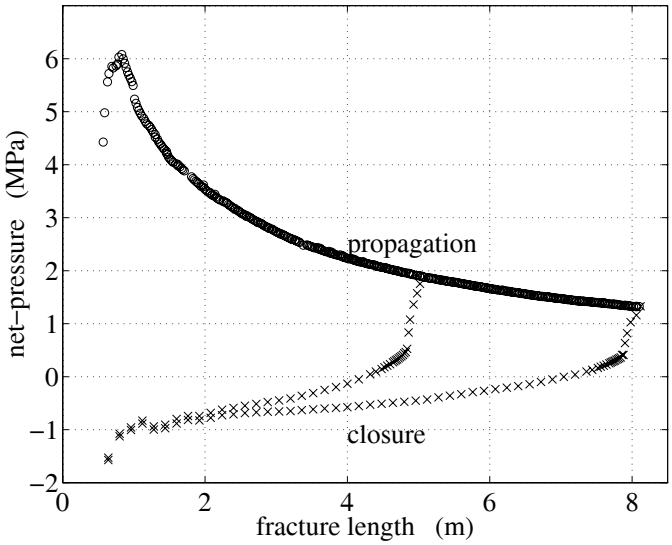

Figure 7: Net-pressure at wellbore vs fracture length

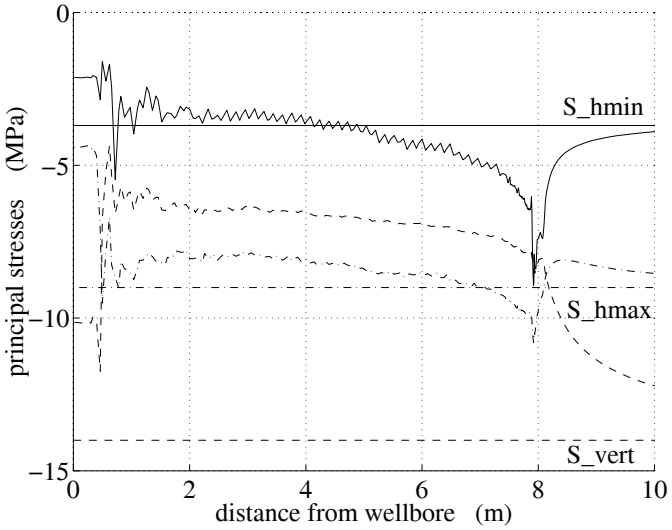

Figure 8: Redistribution of formation stresses on fracture plane after closure

3 CONCLUSION

We reviewed the work on the effect of rock plastic behaviour on the pressure needed for propagation and on the dimensions of the created fractures. We found that plastic yielding provides a shielding mechanism near the tip resulting in an increase of the effective fracture toughness which was determined using the J-integral. Higher pressure is needed to propagate an elastoplastic fracture and the created fracture is shorter and wider than an elastic fracture. The difference in the results obtained with the elastic model and elastoplastic model depend strongly on the contrast of the insitu stresses, on rock strength and elastic modulus but also on the fluid viscosity and flow rate.

We demonstrated that the standard HF simulators, which are all based on elasticity, will yield better results if the unloading modulus is used as the Young's modulus. We have also modelled fracture closure in an elastoplastic formation. In practice, the measured pressure vs time is analyzed during closure for determining the insitu stresses and permeability. It was found that the assumption made that the fracture closes completely once the fluid-pressure in the fracture drops to the value of the far-field stress, is not valid. In addition we showed that the formation will be more stable after it is fractured due to the redistribution of the stresses.

ACKNOWLEDGEMENT

This research work was supported by Schlumberger Cambridge Research.

REFERENCES

[1] Palmer, I.D., Veatch R.W. Jr. (1987), "Abnormally high fracturing pressures in step-rate tests. Proceedings of the 62nd Annual Technical Conference and exhibition of the Society of Petroleum Engineers, Dallas, Texas, USA, SPE 16902.

[2] Shlyapobersky, J., Chudnovski, A. (1994), "Review of recent developments in fracture mechanics with petroleum engineering applications" , *Eurock'94 Symposium, Delft, The Netherlands*, paper SPE 28074.

[3] Shlyapoberski, J., Wong G.K., Walhaug W.W. (1988), "Overpressure calibrated design of hydraulic fracture stimulations", SPE Paper 18194.

[4] Dam, D.B. van, Pater C.J. de, Romijn R. (1997), "Experimental Study of the Impact of Plastic Rock Deformation on Hydraulic Fracture Geometry", International Journal of Rock Mechanics and Mining Science, 34, No. 3-4, Paper No. 318, 439.

[5] Dam, D.B. van, Pater, C.J. de, Romijn, R. (1998), "Analysis of Hydraulic Fracture Closure in Laboratory Experiments", SPE/ISRM Eurock '98 Symposium, Trondheim, Norway, paper SPE 47380,

[6] Dam, D.B. van, (1999), "The Influence of Inelastic Rock behaviour on Hydraulic Fracture Geometry", PhD thesis, Delft University of Technology, The Netherlands.

[7] Hillerborg, A., Modeer, M.,Peterson, P.E. (1976), "Analysis of crack formation and crack growth in concrete by means of fracture mechanics and finite elements", Cement and Concrete Research 6, pp.773-782.

[8] Papanastasiou, P. (1999a), "An efficient algorithm for propagating fluid-driven fractures, Computational Mechanics, 24, pp.258-267.

[9] Papanastasiou, P. (1999b), "The effective fracture toughness approach in hydraulic fracturing", International Journal of Fracture, 96, pp.127-147.

[10] Rice J.R. (1968), "A path independent integral and the approximate analysis of strain concentration by notches and cracks", Journal of Applied Mechanics, 35, pp.379-386.

[11] Papanastasiou, P. (1997), "A coupled elastoplastic hydraulic fracturing model", International Journal of Rock Mechanics and Mining Science, 34: 3-4, paper No. 240.

[12] Papanastasiou, P. (2000), "Hydraulic fracture closure in a pressure-sensitive elastoplastic medium", International Journal of Fracture, 103, pp. 149-161.

[13] Nolte, K.G (1990) "Fracturing pressure analysis: deviations from ideal assumptions", presented at the SPE Annual Technical Conference and Exhibition, New Orleans, LA, paper SPE 20704, pp 23-26.

[14] Papanastasiou, P. (1999c), "Formation stability after hydraulic fracturing", International Journal for Numerical and Analytical Methods in Geomechanics, 23, pp.1927-1944.

THE STRAIN ENERGY RATE DENSITY CONCEPT IN FRACTURE ANALYSIS PROBLEMS OF CREEPING MATERIALS

Costas P. Providakis and Stelios G. Kourtakis

Department of Applied Sciences
Technical University of Crete
GR-73100 Chania, Greece
e-mail: cpprov@mred.tuc.gr, web page: http://www.mechanics.tuc.gr

Keywords: Creep, Fracture, Boundary Elements, Strain Energy Density Rate.

Abstract. *This paper explores the concept of strain energy density rate in relation to the crack initiation in fracture analysis problems arising in creeping cracked structural components. The analysis of the components is performed by using the boundary element methodology in association with the employment of singular boundary elements for the modeling of the crack tip region. The deformation of the material is assumed to be described by an elastic power law creep model. The strain energy density rate theory is applied to determine the direction of the crack initiation for a center cracked plate in tension which is subjected to Mode I loading conditions.*

1 INTRODUCTION

Cracks can degrade the integrity of structural components. This is a particular concern in the design of aircraft engines and steam turbines where the high temperature prevails and failure by creep components deformation is a concern. In these high level of temperatures the time-dependent creep fracture phenomenon can be considered as of multi-scale nature, particularly when physical size is scaled down to the dimensions of the material microstructure. For a dominant crack in metallic components that undergo creep deformation, the creation of macrocrack surface along the main crack (Mode I) path should be distinguished from the creation of microcrack surfaces off to the side of main crack where the creep enclaves are located. In this sense, creep fracture could be also considered as a multiscale process.

More than two decades ago, the strain energy density criterion was proposed[1] as a fracture criterion in contrast to the conventional theory of G and K of the Griffith's energy release rate assumptions in elastic fracture mechanics. This provided an alternative approach to failure prediction for the same stress solution. The distinctions were empasized in the works of Sih[2]. The strain energy density criterion gained momentum and credibility in engineering. A review on the use of this criterion can be found in Ref. 3 and 4.

It is well known that for cases of realistic and practical problems in time-dependent fracture analysis of creeping cracked components the use of numerical solutions such as finite element method (FEM) and boundary element method (BEM) become imperative. For a review on the subject on can consult Beskos[5]. In the search for an accurate, yet generalized, computational method for evaluating singular crack tip stress and strain fields, the singular element approach in conjunction with boundary element method (BEM) has been properly used in various fracture mechanics applications. Several researchers have contributed to this field: Blandford et al[6] was the first who introduced the traction singular quarter-point boundary element approach in combination with a multi-domain formulation to the solution of both symmetrical and non-symmetrical crack problems. Thereafter, this approach has been extensively used in the application of the boundary element method to two- and three-dimensional crack problems. An extension of the quarter-point element technique was used by Hantschel et al[7] who made an attempt to model crack tip fields arising in two-dimensional elastoplastic cracked panels by introducing some special singular boundary elements which took into account the HRR singularity field (Hutchnison[8]; Rice and Rosengren[9]) near the crack tip.

In connection with the boundary element determination of near crack tip stress and strain fields in cracked structural components undergoing two-dimensional inelastic deformation one should mention the works of Professor Mukherjee and his co-workers for Mode I and II[10, 11] and Mode III[12]. A more comprehensive review in BEM solutions of inelastic could be found in the review article of Aliabadi[13].

In the present paper, the strain energy density rate concept is applied as a fracture criterion in association with the use of a previously developed, by the present authors, creep strain-traction singular element (CR-STSE) to determine the crack initiation involved in creeping cracked two-dimensional plates. A numerical example is presented for a shallow edge cracked plate (SENT). The creep constitutive model used in the

numerical calculations is the Norton power law creep model (Nortan[14]) but any other creep constitutive model having similar mathematical structure can be easily implemented in the proposed algorithm.

2 ASYMPTOTIC CRACK TIP FIELDS IN A CREEPING MATERIAL

The material behavior in this paper is described by the elastic-nonlinear viscous constitutive relation according to the Norton power law relation

$$\dot{\varepsilon} = \frac{\dot{\sigma}}{E} + \dot{\varepsilon}_0 \left(\frac{\sigma}{\sigma_0}\right)^m \tag{1}$$

where E is the elasticity modulus, σ_0 is a reference stress, $\dot{\varepsilon}_0$ is a reference creep strain rate and m is the creep exponent. Under the assumption of multiaxial stress states, the extension of equation (1) can be read as

$$\begin{aligned} \dot{\varepsilon}_{ij} &= \dot{\varepsilon}^e_{ij} + \varepsilon^n_{ij} \\ \dot{\varepsilon}^e_{ij} &= \frac{1+\nu}{E}\dot{S}_{ij} + \frac{1-2\nu}{3E}\dot{\sigma}_{kk}\delta_{ij} \\ \dot{\varepsilon}^n_{ij} &= \frac{3}{2}\dot{\varepsilon}_0 \left(\frac{\sigma_e}{\sigma_0}\right)^{m-1} \frac{S_{ij}}{\sigma_0} \end{aligned} \tag{2}$$

where Sij are the components of the deviatoric stress tensor and $S_{ij} = \sigma_{ij} - \sigma_{kk}\delta_{ij}/3$ and σe is the Misses effective stress defined by $\sigma_e = \left((3/2)S_{ij}S_{ij}\right)^{1/2}$. From the inspection of (1) and (2) it could be noted that if there is a singular crack tip field at time t=0 the elastic singularity fields prevail at the crack tip. In subsequent time step and at distances sufficient close to the crack tip the creep strain part of the total strain rate is much larger than the elastic strain rates and it seems to control the crack tip fields (m>1). Thus, the constitutive equations (1) and (2) become power law creep relationships. Using the Hoff analogy[15] to contrast the power-law creep relation with the power-law hardening relation, Riedel and Rice[16] and Ohji et al[17] presented the HRR-type singularity fields for power-law creep material described by the equations

$$\begin{aligned} \sigma_{ij} &= \sigma_0 \left(\frac{C(t)}{\dot{\varepsilon}_0 \sigma_0 I_n r}\right)^{\frac{1}{n+1}} \tilde{\sigma}_{ij}(\theta) \\ \dot{\varepsilon}_{ij} &= \dot{\varepsilon}_0 \left(\frac{C(t)}{\dot{\varepsilon}_0 \sigma_0 I_n r}\right)^{\frac{n}{n+1}} \tilde{\varepsilon}_{ij}(\theta) \\ \dot{u}_i &= \dot{\varepsilon}_0 r \left(\frac{C(t)}{\dot{\varepsilon}_0 \sigma_0 I_n r}\right)^{\frac{n}{n+1}} \tilde{u}_{ij}(\theta) \end{aligned} \tag{3}$$

where the radial distance r from the crack tip and the angle θ in relation to the x axis are shown in Figure 1.

The dimensionless constants In and the θ-variation functions of the suitably normalized functions $\tilde{\sigma}_{ij}$, $\tilde{\varepsilon}_{ij}$ and $\tilde{u}_{ij}$ depend on the creep exponent m and have been tabulated in Shih[18].

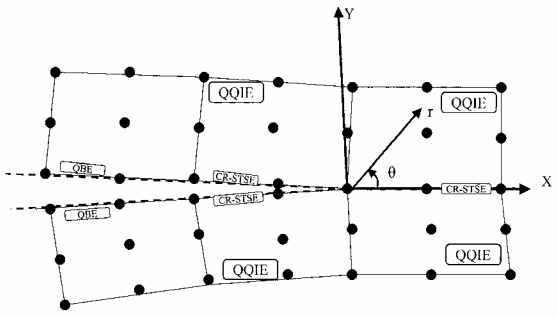

Figure 1. Geometry of the crack tip and CR-STSE element configuration

3 DERIVATION OF BOUNDARY INTEGRAL EQUATIONS

The Navier equation for the displacement rates of a structural component undergoing plane strain deformation

and under the presence of non-elastic strains can be written as

$$\dot{u}_{i,jj} + \frac{1+\nu}{1-\nu}\dot{u}_{k,ki} = -\frac{\dot{F}_i}{G} + 2\dot{\varepsilon}^n_{ij,j} + \\ + \frac{2(1+\nu)}{1-2\nu}(\alpha\dot{T})_{,i} \quad (i,j,k = 1,2) \tag{4}$$

where F_i is the prescribed body force per unit volume, G, ν and α are the shear modulus, Poisson's ratio and coefficient of linear thermal expansion, respectively, u_i is the displacement vector. Suitable traction and displacement rate boundary conditions must be prescribed. The integral representation of the solution of a point P on the boundary of the body (with $\dot{F}_i = 0$) has the following initial strain form

$$\left(\delta_{ij} - C_{ij}\right)\dot{u}_i(P) = \int_\Gamma \left[U_{ij}(P,Q)\dot{\tau}_j(Q) - T_{ij}(P,Q)\dot{u}_j(Q)\right]d\Gamma_q + \\ + \int_\Omega [\Sigma_{jki}(P,q)\dot{\varepsilon}^n_{jk}(q) + + \widetilde{\Sigma}_{jki}(P,q)\delta_{jk}\alpha\dot{T}(q)]d\Omega_q \tag{5}$$

where δ_{ij} is Kronecker delta, P,Q are boundary points, q is an interior point, Γ and Ω are the boundary and the surface of the body, respectively. The kernels $U_{ij}, T_{ij}, \Sigma_{jki}$ and $\widetilde{\Sigma}_{jki}$ are known singular solutions due to a point load in an infinite elastic solid in plane strain (Mukherjee[19]). The traction and displacement rates are denoted by $\dot{\tau}$ and $\dot{u}$, respectively. The coefficients C_{ij} are known functions of the included angle at the boundary corner at P, the angle between the bisector of the corner angle and the x-axis. Equation (5) is a system of integral equations for the unknown traction and displacements rates in terms of their prescribed values on the boundary, and the non-elastic strain rates. The unknown quantities only appear on the boundary of the body and the surface integrals are known at any time through the constitutive equations.

The stress rates can be obtained by direct differentiation of equation (5) resulting in

$$\dot{\sigma}_{ij}(p) = \int_\Gamma \left[\overline{U}_{ijk}(p,Q)\dot{\tau}_k(Q) - - \overline{T}_{ijk}(p,Q)\dot{u}_k(Q)\right]d\Gamma_q - \\ - 2G\dot{\varepsilon}^n_{ij}(p) - 3K\alpha\dot{T}(p)\delta_{ij} + + \int_\Omega [\overline{\Sigma}_{ijkl}(p,q)\dot{\varepsilon}^n_{kl}(q) + \\ + \overline{\widetilde{\Sigma}}_{ijkl}(p,q)\delta_{kl}\alpha\dot{T}(q)]d\Omega_q \qquad (i,j,k,l = 1,2) \tag{6}$$

where G and K are the shear and bulk modulus, respectively; $\overline{\Sigma}_{ijkl}$ and $\overline{\widetilde{\Sigma}}_{ijkl}$ are inelastic and temperature effect kernel functions, respectively, which are also defined in the work of Mukherjee[19].

4 SINGULAR ELEMENT IMPLEMENTATION AND SOLUTION PROCEDURE

The integral equations (5) and (6) are expressed in this paper by discretizing the boundary and the interior into a number of standard three-noded quadratic boundary elements and nine-noded quadratic quadrilateral interior surface elements, respectively, provided that they are not adjacent to the crack tip.

By following the procedure developed in Providakis and Kourtakis[20] to produce a special element which presents the HRR-type singularity of equations (3) at the crack tip (Figure 1), one can obtain the following new set of shape functions N^u_a which depend upon the creep exponent m

$$N_1^u = 2^{\frac{1}{1+m}}[(\frac{r}{l})^{1+\frac{1}{1+m}} - (\frac{r}{l})^{\frac{1}{1+m}}] + (\frac{r}{l})$$
$$N_2^u = 2^{1+\frac{1}{1+m}}[(\frac{r}{l})^{\frac{1}{1+m}} - (\frac{r}{l})^{1+\frac{1}{1+m}}] \quad (7)$$
$$N_3^u = 2^{\frac{1}{1+m}}[(\frac{r}{l})^{1+\frac{1}{1+m}} - (\frac{r}{l})^{\frac{1}{1+m}}] - (\frac{r}{l}) + 1$$

where l is the length of the new special quadratic element, the distance r=l-x and the ratio can be defined in terms of the intrinsic coordinate ζ as (r/l)=(1-ζ)/2. By taking the derivatives of the new shape functions (7) one can observe that these derivatives display a r-m/(m+1) singularity near the crack tip which is the actual situation for the strain rate singularities according to (3).

Since in boundary element methodology displacement and tractions are independently represented the above derived singular element for the simulation of crack tip behavior of displacement rates, fails to model the expected from equations (3) crack tip behavior of tractions which displays an order of –1/(m+1) singularity. Thus, for the proper simulation of the traction rate singularity different shape functions are derived by the use of the derivatives of the shape functions (7) and finally modified to the following separate forms N_a^t in terms of creep exponent m

$$N_1^t = 2^{\frac{m}{1+m}}[(\frac{l}{r})^{\frac{1}{1+m}} - (\frac{r}{l})^{\frac{m}{1+m}}] - 2 + 2(\frac{r}{l})$$
$$N_2^t = 2^{\frac{m}{1+m}}[(\frac{l}{r})^{\frac{1}{1+m}} - (\frac{r}{l})^{\frac{m}{1+m}}] \quad (8)$$
$$N_3^t = 2^{\frac{m}{1+m}}[-(\frac{l}{r})^{\frac{1}{1+m}} + (\frac{r}{l})^{\frac{m}{1+m}}] + 1$$

where now r=x and the ratio (r/l)=(1+ζ)/2. A simultaneous simulation of displacement and traction rate fields, by the use of the shape functions (7) and (8), respectively, yields to the proposed, in the present BEM approach, creep strain-traction singular element (CR-STSE) (Figure 1). Then, by applying a boundary nodal point collocation procedure to the discretized versions of equations (5) and (6) one can obtain the following system of equations in matrix form

$$[A]\{\dot{u}\} = [B]\{\dot{\tau}\} + [E]\{\dot{\varepsilon}^n\} + [T]\{\dot{b}^T\} \quad (9)$$
$$\{\dot{\sigma}\} = [\widetilde{B}]\{\dot{\tau}\} + [\widetilde{E}]\{\dot{\varepsilon}_n\} + [\widetilde{T}]\{\dot{b}^T\} \quad (10)$$

However, the vector $\{\dot{\varepsilon}^n\}$ is known at any time through the constitutive equations and the stress rates of equation (6) while the vector $\{\dot{b}^T\}$ could be easily computed through the known values of temperature profile for the whole structural component. Half of the total number of components of $\{\dot{u}\}$ and $\{\dot{\tau}\}$ are prescribed through the boundary condition while the other half are unknowns.

Then, the initial distribution of the nonelastic strain has to be prescribed. Thus, the only existed strains at time step t=0 are elastic and then, the thermal and initial stresses and displacements can be obtained from the solution of the corresponding elastic problem. By the use of equations (9) and (10) the displacement and stress rates can be obtained at time step t=0 while the rates of change of the nonelastic strains can be computed from constitutive equations. Thus, the initial rates of all the relevant variables are now known and their values at a new time Δt can be obtained by integrating forward in time. The rates are then obtained at time Δt and so on, and finally the time histories of all the variables can be computed. Another important task in this approach is the choice of a suitable time integration scheme. For the purposes of the present paper, an Euler type algorithm with automatic time-step control is employed.

5 THE STRAIN ENERGY RATE

For power law creep materials the strain energy density rate (SEDR) can be analytically determined as

$$\dot{W} = \int_0^{\dot{\varepsilon}^n} \sigma d\dot{\varepsilon}^n = \frac{m}{m+1}\sigma_e \dot{\varepsilon}^n \tag{11}$$

The SEDR was estimated according to the boundary element procedure developed previously by solving in time the system of equations (9) and (10) and then by using the analytic equation (11) for each time step.

6 NUMERICAL RESULTS

Consider a central cracked plate (CCP) specimen with height (h) and width (w) = 16in x 8in made by a power law creeping material (superalloy Inconel 800H at 1200^{o}F) with properties E=22294 Mpsi,, σ_0=60487psi,ν=0.33, creep exponent m=5 and the parameter

$$B = \frac{\dot{\varepsilon}_0}{\sigma_0^m} = 2.1x10^{-27} \quad (psi)^{-5}/h \tag{12}$$

The specimen contains a central crack of depth a= 0.125w. The specimen is subjected to a remote uniform load of 18750 psi which is suddenly applied. The symmetry of the specimen was used and thus a quarter of the plate was analyzed.

The computer software established according to the BEM methodology presented in this paper can provide sufficient data related to stress and strain distribution history. Based on these data and after using equation (11) the strain energy density rate distribution could be predicted at each time step. Typical diagrams of contours of strain energy density rate distributions for a quadrant of the specimen and for two different time steps (t=0.0 and 5.01 hours) are shown in Figures 2 and 3, respectively.

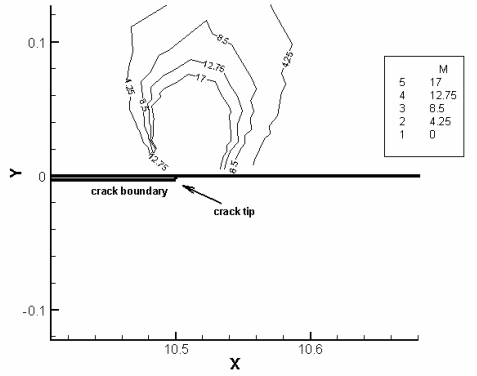

Figure 2. Contours of strain energy density rate for time step t=0.0 hours

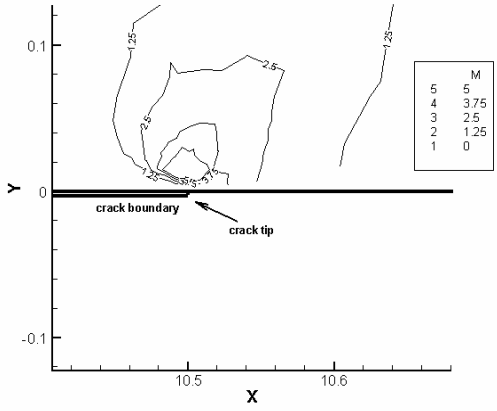

Figure 3. Contours of strain energy density rate for time step t=5.01 hours

Depicted in Figure 4 are the angular variations of the strain energy density rate for different time steps. It could be noted from the inspection of this figure that the strain energy density rate decreases with increasing time. This trend was expected since the applied load remains fixed in time and the crack is assumed to be stationary. It could be also noted that all curves posses a minimum at angle θo=0.

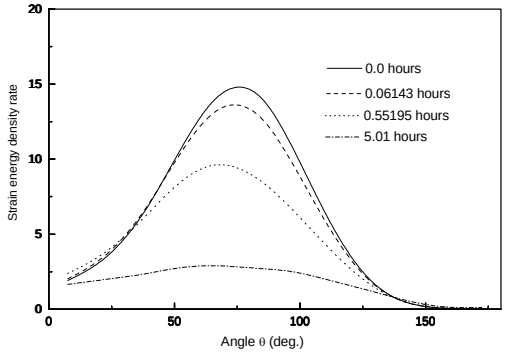

Figure 4. Angular variation of strain energy rate for different time steps.

Taking into account the strain energy density criterion[2] this indicates that crack would initiate at θo=0 and along the axis of symmetry of load symmetry under present crack mode I.

7 CONCLUSIONS

In this paper a new singular boundary element approach based on the implementation of a special singular boundary element is performed for the estimation of the strain energy density rate distribution close to crack tip fields arising in creeping structural components undergoing Mode I deformation under the effect of remote loading condition.

REFERENCES

[1] Sih, G.C. (1973), "Some basic problems in fracture mechanics and new concepts", J. Eng. Fract. Mech., pp. 365-377.

[2] Sih, G.C. (1991), *Mechanics of Fracture Initiation and Propagation*, Kluwer Academic Publishers, Dordrecht.

[3] Gdoutos, E.E. (1984), "Problems of mixed mode crack propagation", In: *Engineering Applications of Fracture Mechanics*, vol. II, Martinus Nijhof, Netherlands.

[4] Carpinteri, A. (1986), "Crack growth and material damage in concrete: plastic collapse and brittle fracture", In: *Engineering Applications of Fracture Mechanics*, vol. V, Martinus Nijhof, Netherlands.

[5] Beskos, D.E. (1987), *Numerical methods in dynamic fracture mechanics*, EUR-11300 EN, Joint Research Center of EC Ispra Establishment, Ispra, Italy.

[6] Blandford, G.E., Ingraffea, A.R. and Ligget, J.A. (1981), "Two dimensional stress intensity factor computations using the boundary element method", Int. J. Num. Meth Engng, 17, pp. 387-404.

[7] Hantschel, T., Busch, M., Kuna M. and Maschke, H.G. (1990), "Solution of elastic-plastic crack problems by an advanced boundary element method". In: *Numerical Methods in Fracture Mechanics*, pp. 29-40, A.R. Luxmoore and D.R.J. Owen (Eds.), Pineridge Press, Swansea.

[8] Hutchinson, J.W. (1968), "Singular behavior at the end of a tensile crack in a hardening material", J. Mech Phys Solids, 16, pp. 13-31.

[9] Rice, J.R. and Rosengren, G.F. (1968), "Plane strain deformation near a crack tip in a power-law hardening material", J. Mech Phys Solids, 16, pp. 1-12.

[10] Mukherjee S. and Morjaria, M. (1981), "A boundary element formulation for planar time-dependent inelastic deformation of plates with cutouts", Int. J. Solids and Structures, 17, pp. 115-126.

[11] Morjaria, M. and Mukherjee, S. (1981), **"**Numerical analysis of planar, time-dependent inelastic deformation of plates with cracks by the boundary element method", Int. J. Solids and Structures, 17, pp. 127-143.

[12] Morjaria, M. and Mukherjee, S. (1982), "Numerical solution of stresses near crack tips in time-dependent inelastic fracture mechanics", Int. J. Fracture, 18 (4), pp. 293-310.

[13] Aliabadi, M.H. (1977), "Boundary element formulations in fracture mechanics", Appl Mech Rev, 50(2), pp. 83-96.

[14] Nortran, F.H. (1929),*The Creep of Steel at High Temperatures*, McGraw-Hill, New York.

[15] Hoff, N.J., (1954), *Quarterly of Applied mechanics*, 12, pp. 49-55.

[16] Riedel, H. and Rice, J.R. (1988), "Tensile cracks in creeping solids and Fracture Mechanics", in *Twelfth Conference*, ASTM STP 700, pp. 112-130.

[17] Ohji, K., Ogura, K., and Kubo, S. (1979), "Stress-strain field and modified J-integral in the vicinity of crack tip under transient creep conditions", Japanese Society of Mechanical Engineer 790(13), pp. 18-20.

[18] Shih, C.F. (1983), Tables of Hutchinson-Rice-Rosengren singular field quantities, MRL E-147, Division of Engineering, Brown University.

[19] Mukherjee, S. (1977), **"**Corrected boundary integral equations in planar thermoelastoplasticity", Int. J. Solids Structures, 13, pp. 331-335.

[20] Providakis, C.P., Kourtakis, S.G., (2002), "Time-dependent creep fracture analysis by the use of singular boundary elements", Compt. Mech, accepted.

STABILITY ASSESSMENT OF SE/E ROCK CORNER SLOPE OF THE ACROPOLIS HILL IN ATHENS

I. Stefanou and I. Vardoulakis

Department of Mechanics
Faculty of Applied Mathematics and Physics
National Technical University of Athens ,
P.O.BOX 15773, 5 Iroon Polytechniou Av., Athens, Greece
e-mail: istefanou@mechan,ntua.gr, web page: http://geolab.mechan.ntua.gr

Keywords: Acropolis Hill, Acropolis Wall, DEM, 3DEC, Key-block method, Rock Mechanics, Stability.

Abstract. *The SE/E rock corner slope of Acropolis Hill in Athens is composed of fractured limestone resting on the Athenian Schist. This slope forms also the base of the SE/E part of the Acropolis Wall, an ancient structure with appreciable fissuration, mainly running in a vertical direction. Here is presented a preliminary analysis that has been made by exploiting the existing topographical and geological data of the site and by applying the key-block method, and the dynamic three dimensional distinct element algorithm 3DEC. The study of the fractured rock mass lead us to the identification of a critical rock block whereas the distinct element simulation of the Wall revealed similar fissuration patterns as the ones superficially observed.*

1 INTRODUCTION

The general hydrogeological conditions that are prevailing in the SE/E part of Acropolis Hill in Athens, the dense network of discontinuities in the rock and the fallen rock blocks (Figure 2) that are observed around the rocky slope are the main reasons that earlier studies[1] characterize the same part of the Acropolis Hill as a zone of significant damage. An additional factor affecting the stability of the rock slope is the negative slope at its base, which can be distinguished in the picture below that was taken in 1880 (Figure 1). Examining photographs that were taken before the restoration and in parts reconstruction of the SE/E part of the Acropolis Wall, like the one below that is dated back to 1920 (Figure 1), we can easily ascertain its sharp vertical fissuration. Moreover some of the fissures are believed to be connected with the traces of the rock discontinuities. Despite the reparations that have been made by filling and covering these fissures, today the wall appears again fissured (Figure **2**).Taking into account the above conditions and observations we could argue that the system rock-wall is evolving.

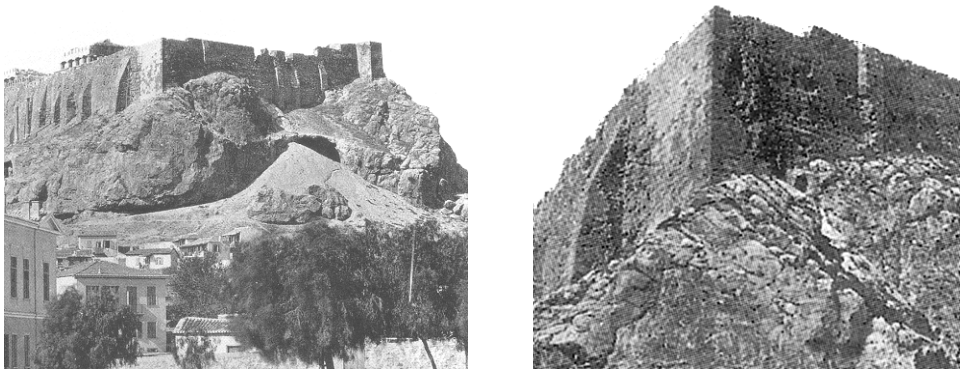

Figure 1. Left: Photo of the SE/E part of the Acropolis Hill in Athens in 1880. The negative slope of the rocky slope is easily distinguishable. Right: Photo of the SE/E part of the Acropolis Hill and Wall in Athens taken in 1920. The Wall is sharply vertically fissured.

Figure 2. Left: Recent photo of the SE side of the SE/E part of the Acropolis Wall in Athens. The fissures on it are apparent. Right: Sizeable detached rock block of the SE/E part of the Acropolis Hill in Athens

2 GEOLOGICAL DATA

According to existing geological studies[1] the region of Athens is covered by the Athenian Schist, which also forms the base of the rock slope we study. It is a flysch formation, which is constituted by argileous schist, sandstone, quartzitic sandstone, marl, limestone and the transitive-combination types of the above rocks (i.e. sandstone marls or argileous schist limestones).The limestone rocks appear mostly to the upper soil layers of the region of Athens and they are related with the presence of the limestone Hills of Athens, which are Acropolis, Filopappou, Lycabetus and others. These massive limestone rocks are dated to the late cretaceous period and as far it concerns the way of their creation many theories exist, the most popular among them wants these limestone masses native and sited over the Athenian schist[1]. As a consequence the possibility of a generalized activation of the tectonic contact, which could lead to significant seismic instabilities, is rejected in the study of B. Andronopoulos and G. Koukis[1]. For the most part the limestone that constitutes the SE/E part of the rock of Acropolis is not laminated. It is not covered by soil and therefore it is susceptible to erosion; it is appearing carsted and hydropermeable. The erosion phenomena are in places very intense and justify the rock cavities, of which the smaller ones have been filled with calcareous and marley material. Finally the limestone rock mass appears intensively fractured. Mostly the discontinuities are filled with soil material, which according to sampling measurements[2] is composed of 64.2% sand, 31.7% silt and 4.1% clay.

3 TECTONIC DATA

At the SE/E part of the Acropolis Hill we observe many smooth surfaces which are considered to be the sliding or detachment surfaces of the rock blocks, some of them are found fallen around the rocky slope. A sizeable fallen rock block is shown at Figure 2. Examining carefully the same picture we perceive that the fallen block leans on the ruins of the Dionysus ancient theater wall, which was built during the Classic period and was functioning until the end of the Roman period. Consequently we infer that the detachment of the rock block from the slope took place in the last two millennia. Looking into the ballistics of this fall we could in principle infer the possible original location of this block.

The determination of the geometrical characteristics of the fractures that intersect the rock mass of the SE/E part of the Acropolis Hill is of great importance as they determine the different possible failure mechanisms and so they influence directly the stability of the rock slope. Exploiting the existing geological studies[1],[2], we detect a total of 24 fractures (Figure 3). At this point it has to be mentioned that a detailed and exact tectonic map of sufficient resolution at the SE/E part of Acropolis Hill is not available. Therefore our analysis and

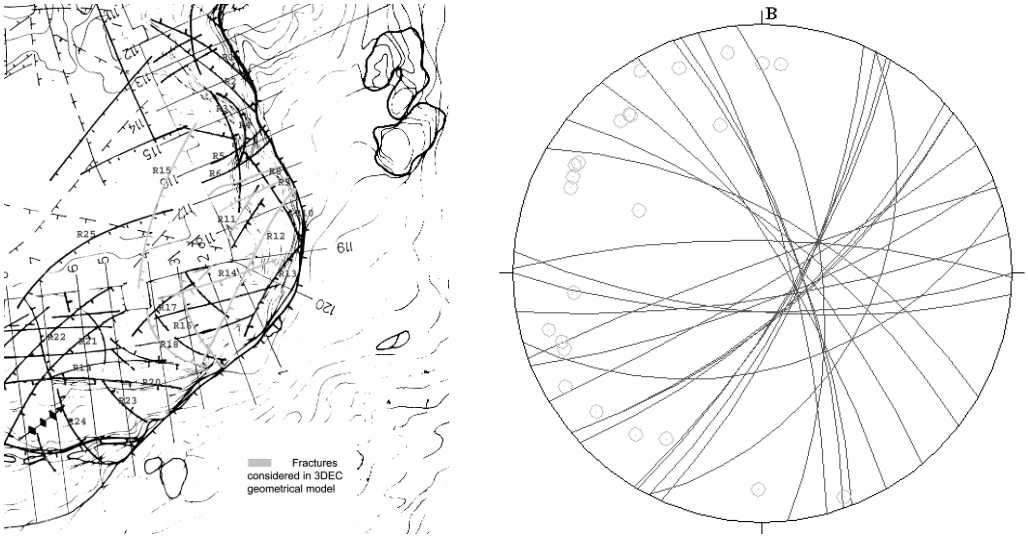

Figure 3. Left: Tectonic Map[2]. With bold lines are depicted the traces of the fractures. Right: Stereographic projection of 24 fractures of the SE/E part of the Acropolis Hill in Athens.
Three families of fractures are distinguished.

the 3D models that were made may not represent the exact topography and tectonics. In spite of the fact that in reality the discontinuities are not necessarily planar, in our analysis they were assumed as planes. Taking into account that the area of interest is of limited geological scale the aforementioned assumption is very close to reality. Notice that this assumption is central to the key-block method[3],[4], which is usually applied to problems of similar geological extend. Moreover, extracting data from the traces of the fractures[2],[5],[6] and from the topography of the slope and applying to these data the least square method (for planes) we calculated a correlation coefficient (R-squared value) very close to unity. At Figure 4 are presented two snapshots of the three dimensional CAD that represents the SE/E rock corner of Acropolis Hill and was developed during our analysis in order to help us in the evaluation of the assessment of the various rock blocks that the fractures form (Figure 3). In this 3D model we show the discontinuities of the rock mass as infinite planes.

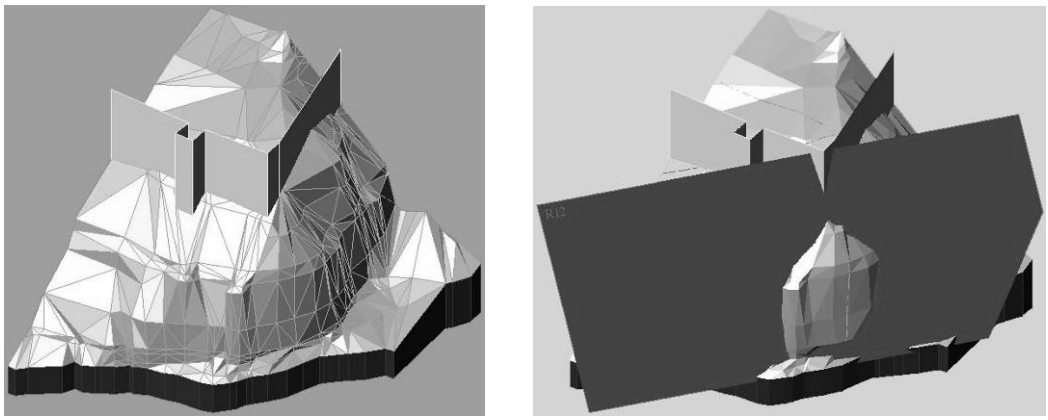

Figure 4. 3D CAD model of the SE/E part of the Acropolis Hill in Athens.

4 ROCK STABILITY

For our analysis we used the Distinct Element Method, applying the three dimensional software 3DEC, which is especially adapted to problems of Rock Mechanics. Significant advantages of this software is the possibility of studying and reproducing complex three dimensional failure mechanisms and the displacement monitoring of the rock blocks. However our analysis with 3DEC did not reveal more complex failure mechanisms except the plane slide of rock block A over the discontinuity plane R12 and the wedge sliding of rock block B over the discontinuity planes R8 and R9 (Figure 5). These results from 3DEC are in agreement with the results of the key-block method.

The application of the key-block method proved two rock blocks that are considered as removable. Failure on the discontinuity interface is considered according to the *Mohr-Coulomb* failure criterion when: $\tau > \tau_{max} = \sigma \tan\varphi + c$, where τ is the applied shear stress , τ_{max} is the maximum shear stress, σ the applied normal stress, φ the friction angle and c the cohesion of the interface. The safety factor of a rock block is defined as the ratio of the moving forces that act on a rock block, including seismic action (pseudo-static approach[7]), to the resisting forces that act on the same rock block. Disregarding the role of the cohesion to the stability of the rocky slope ($c = 0$, $\varphi = 25^{o}$[2]) the value of the safety factor was calculated equal to S.F. = 3,30 > 1 for rock block B and extremely low and equally to S.F. = 0,14 < 1 for rock block A. In other words if we do not take into account the influence of the cohesion of the discontinuity interface to the stability, the rock block A appears potentially instable.

The fact that the rock block A has not failed until day is attributed to the value of the cohesion c of the joint, for which however we do not have reliable experimental data. In most cases the adhesion of the rock and the fill material is assumed to be very low and accordingly the assumed cohesion c of the interface is neglected. Consequently the cohesion of the discontinuity plane R12 should be principally attributed to the interlocking of the rock blocks and to the existence of rock bridges[10]. We should mention however that the experimentally determined cohesion of the filling material equals to c = 48,71 kPa (the standard deviation of the samples was 22% of this value[2]). If we assume this value in our analysis, then the safety factor of rock block A is calculated equal to S.F. = 1,32 > 1. In any case the minimum value of the joint cohesion is c = 40,00 kPa (S.F. = 1). Assuring the aforementioned cohesion value with anchor support, a total force of 16 GN is needed. Currently the rock slope appears to be reinforced by 15 anchors[2] that can totally apply a force of 2,3 GN (15×150 kN) to the rock block A, which corresponds to 15% of the needed force. Here we have to notice that these anchors have been installed before thirty years and we don't know if they should be considered as "permanent" or not. Moreover the length of these anchors is only 12 m and as a result we have doubts on the degree that the aforementioned rock block is sufficiently supported. From our point of view the length of the anchors should be at least 20 m in order to assure that the head of the anchors is being well encastred to the healthy rock mass.

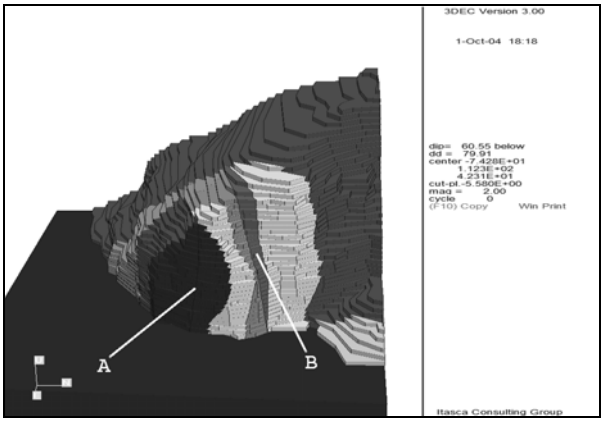

Figure 5. 3DEC Model of the SE/E part of the Acropolis Hill in Athens. A and B are the rock blocks which were characterized as removable during our analysis.

5 WALL FISSURES

Analysing the SE/E part of the Acropolis Hill rock mass we determined the vertical displacements of the various rock blocks at the base of the SE/E part of the Acropolis Wall (Figure 6). As we have already mentioned the Acropolis Hill rests on the Athenian schist. Due to the lack of experimental data for the mechanical properties of the schist at the base of the rock slope we study, we will consider the schist mechanical properties from nearby regions[8]. As far it concerns the joints' mechanical properties we assume that they behave elastically under compression provided that sliding did not occur at the joint interface. Consequently we will use the mechanical properties (Young Modulus) that were specified at previous studies[2].

With the above hypotheses for the mechanical properties of the system we applied at the region of the rock mass that the Wall occupies (Figure 6) a uniformly distributed vertical loading of 0,1 MPa (approximately three times the weight of the wall and the filling material behind it). The application of the aforementioned loading enabled us to determine the vertical displacements at the base of the Wall and the behavior of the Wall structure because of these vertical displacements. At Figure 6 are presented the vertical displacements at the base of the SE/E part of the Acropolis Wall. It should be mentioned that at the Wall corner the vertical displacement of the rock mass is much lesser than the vertical displacements at the two sides of the Wall, resulting to a differential subsidence at the base of it and consequently to its charging.

The building blocks that construct the SE/E part of the Acropolis Wall vary in size and quality. The total non-homogeneity of this part of the Wall is being increased by previous reparations and fillings of the damaged segments of the Wall with building blocks of different size and quality. The thickness of the Wall is approximately 6 m but it varies a lot from place to place. For our analysis with the DEM method we made the following simplifications-assumptions in our model:

- The building blocks of the Wall are considered as orthogonal parallelepipeds of the same dimensions. Their dimensions have been chosen to be equal to the average dimensions of the wall blocks (1,2 m width, 0,7 m height and 0,6 m thick).
- The modeled Wall is being constructed by only one layer of blocks (in cross section). On the contrary the number of the blocks would enormously increase the calculation time.
- The blocks are considered as rigid and unbreakable in our 3DEC model.
- The system Wall-rock mass is considered uncoupled, meaning that the mechanical behavior of the Wall does not influence the mechanical behavior of the rock mass. Consequently we managed to study separately, in a different DEM model, the mechanical behavior of the Wall. The simulation of the Wall was carried out introducing the vertical displacements of the rock mass that we had previously determined to the base of the Wall structure.

As a result of these simplifications-assumptions is the fact that the interlocking of the wall blocks in the vertical direction of the wall length is ignored and that the mechanically weak zones (repaired areas of the Wall) are not taken into account. Thus the analysis is focused on the investigation of the impact of the rock mass displacements on the wall fissures. In Figure 7 we present the results from our simulation with 3DEC. Comparing the results from 3DEC with the fissures superficially observed (Figure 1 and Figure 2) we could easily distinguish the similarities.

6 CONCLUSIONS

In this paper we applied the key-block and distinct element method to investigate the stability of the SE/E part of the Acropolis Hill in Athens. Our analysis revealed one instable rock block (rock block A Figure 5). The type of failure for this rock block is sliding over the discontinuity plane R12. A cohesion of c = 40,00 kPa over the discontinuity plane R12 is needed for the limit equilibrium of this rock bock (including seismic action, pseudo-static approach[7]). This value of the cohesion is believed to be attributed to the interlocking of the rock blocks and to the possible rock bridges that have been probably developed.

The system rock mass-Wall is still evolving. The simulation of the SE/E part of the Acropolis Wall and rock mass with the three dimensional distinct element code 3DEC showed that the mechanical behavior of the wall depends on the mechanical behavior of the rock mass. In other words a possible increase in the loading of the system (rainfall, seismic action, etc.) could lead to similar fissuration patterns as the ones superficially observed.

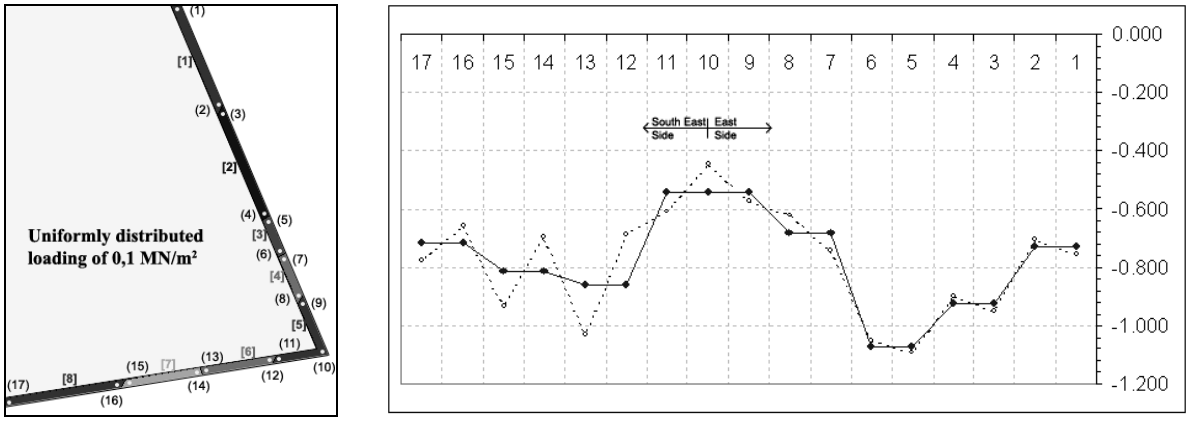

Figure 6. Left: The region that the SE/E part of the Acropolis Wall occupies. The number in the brackets express the different rock blocks of the rock mass that the Wall is based on and the numbers in the parenthesis are the displacement monitoring points in 3DEC.
Right: With dashed line are depicted the vertical displacements in millimeters of the base of the Wall in our 3DEC model after the application of a vertical uniformly distributed loading of 0,1 MN/m^2 to the area that the Wall occupies. The straight line depicts the average values of the results from 3DEC per rock block. From this diagram we conclude also the rotation of the rock blocks.

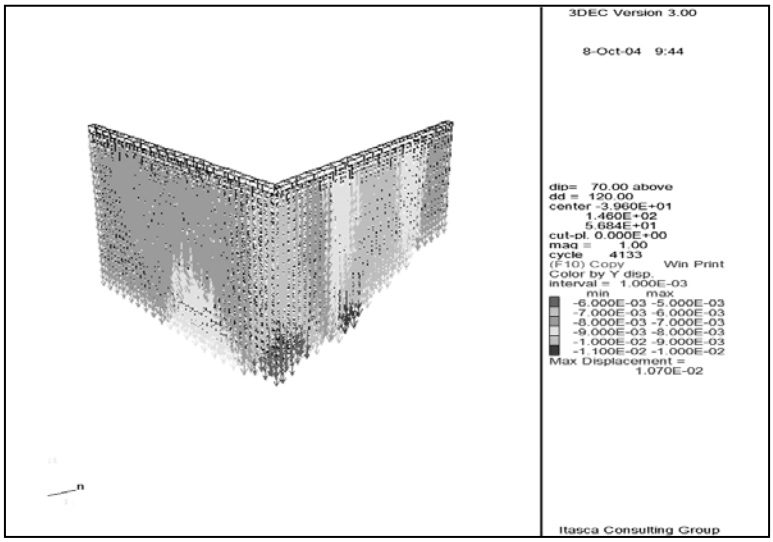

Figure 7. Vertical displacements vectors of the bricks of the SE/E part of the Acropolis Wall because of differential subsidence of the rock mass. The displacements of the rock mass have been multiplied by a factor of ten.

ACKNOWLEDGEMENTS

We would like to express our gratitude to Prof. Felix Darve (INPG) for his collaboration and help during this project, to Prof. Frederic Donze (INPG) for his advise and contribution in the application of the Distinct Element Method and to Prof. Thierry Villemin (LGCA) for his contribution in applying the key-block method. The authors also want to thank Professor Ioannis Psycharis of N.T.U.A. for his valuable advise and support in using 3DEC.

Finally we would like to thank the members of the Committee for the Preservation of Acropolis Monuments and especially the director Mrs. M. Ioannidou and the Achitect Mrs. B. Manidaki for the help they provide us and their permission to access the archives of the site.

REFERENCES

[1] Andronopoulos, B., Koukis, G. (1976), *Geological - Geotechnical Study of the region of Acropolis in Athens* (Greek), Institute of Geology and Mineral Exploration (IGME).

[2] Monokrousos, D. (1995), *Restoration Work of Acropolis Rocks* (Greek), Committee for the preservation of Acropolis Monuments.

[3] Goodman, R.E., Gen-hua Shi (1985), *Block Theory and Its Application to Rock Engineering,* Prentice-Hall Inc.

[4] Goodman, R.E. (1980), *Introduction to Rock Mechanics,* John Wiley & Sons.

[5] Committee for the preservation of Acropolis Monuments (2004), *Photo Archives*.

[6] Institute Geographique Nationale (IGN) de France (1971), *Photo Archives*.

[7] OASP-SPME (2000), *Greek Anti-seismic Regulation* (Greek).

[8] Vardoulakis, I. (2002), "Geotechnical Parameters of the Athenian Schist", Report to EDRASIS Group of Companies.

[9] Stefanou, I., (2004), *Stability Assessment of the SE rock corner of Acropolis Hill with the Distinct Element Method* (Greek), Diploma Thesis in Structural Civil Engineering under the supervision of Professor I. Vardoulakis (National Technical University of Athens).

[10] Scavia, C. (1995), "A Method for the Study of Crack Propagation in Rock Structures", Geotechnique, vol. 45, n^{o}3, p. 447-463.

[11] Itasca Consulting Group Inc (2003), *3DEC 3 Dimensional Distinct Element Code*, Online Manual.

[12] Heyman, J. (1995), *The Stone Skeleton – Structural Engineering of Masonry Architecture*, Cambridge University Press.

WIRE CUTTING OF SOFT SOLIDS

Maria N. Charalambides, Suk Meng Goh, and J. Gordon Williams

Department of Mechanical Engineering
Imperial College London
South Kensington Campus, London SW7 2AZ, UK
e-mail: m.charalambides@imperial.ac.uk, web page: http://www.imperial.ac.uk/mechanicalengineering

Keywords: wire cutting, viscoelastic, fracture toughness, food texture.

Abstract. *The wire cutting process is used in the food industry during the manufacture and testing of products. The cutting process involves fracture as well as large strain deformation and surface friction. This paper investigates the mechanics of the wire cutting process of cheese through a combination of experiments and finite element simulations. The experiments revealed that there was secondary damage on the cut surface, thus a higher fracture energy is consumed than the common assumption of a single crack propagation. The numerical simulations showed that there was a six-fold change in the strain rate when wire diameters of 0.25mm to 2mm are used. The numerical models were also used to predict the cutting forces using two failure criteria: critical strain, which was applied to the initiation of cracking, and a cohesive zone model to simulate crack propagation. Both criteria showed reasonable success in predicting the cutting forces, particularly for cuts made with small wire diameters.*

1 INTRODUCTION

Many food processes, such as shredding and cutting, involve breaking the food into smaller components. Fracture of food also occurs during mastication when the structure of the food is broken down and the flavour and aroma are released. The concern of food technologists is in designing foods that break down in the optimal way. For example, during a separation process, the food must not crumble to reduce wastage. When eaten, the food must fracture in a way which provides the optimal sensorial experience. Few studies in the literature have investigated in detail the fracture behaviour of foods.

The three-point-bend test has been utilised in studies of cheese at low temperatures [1-3]. However, at room temperature, cheese exhibits a high degree of non-linearity, viscoelastic effects and low stiffness. Therefore, conventional fracture tests that are widely used to determine the fracture properties of engineering materials are not suitable. The wire cutting test has been proposed as a simpler alternative to measure the fracture toughness [2,4,5]. The wire cutting test involves pushing wires of known diameters through specimens from an initial indentation to a steady-state cutting stage. The steady state cutting force, F, when divided by the width of the cut, b, gives an apparent value of the fracture toughness, G_c, i.e. the energy released during fracture divided by the new surface (cracked) area. The force-displacement relationship depends on a combination of fracture, plastic/viscous deformation and surface friction effects, but the exact details of the mechanics of cutting are still not understood. The objective of this study was to evaluate the possibility of predicting the steady state cutting forces during wire cutting; for this accurate failure criteria are needed.

2 EXPERIMENTS

Two cheeses, mild Cheddar and Gruyere, were tested at 21°C and 50% relative humidity. Mechanical tests in the form of monotonic uniaxial compression tests were performed at true strain rates, $\dot{\varepsilon}$, of 0.25, 2.5 and 25/min, and stress relaxation tests were performed at a true strain rate of 2.5/min up to a strain of 0.04 [6]. The true stress - true strain curves from the compression tests are shown in figure 1. The stresses increased significantly with increasing strain rate, but the fracture strains remained constant at approximately 0.5 and 0.45 for mild Cheddar and Gruyere respectively.

Wire cutting tests were performed using steel wires of diameter, d, of 0.25, 0.5 and 0.89mm, as well as dowel pins of diameter 1.6 and 2mm. The specimens for the wire cutting tests were rectangular blocks of length 25mm, height 20mm and width 15mm for the three smaller diameters. Blocks of length 30mm, height 30mm,

and widths 20mm and 30mm were used for the 1.6mm and 2mm diameters respectively. Three cutting speeds, v, of 5, 50 and 500mm/min were used. For each case of d and v, three cuts were made on a new specimen each time. The experimental steady-state cutting force, F, divided by the specimen width, b, is shown in figure 6. The cutting forces are seen to increase as the test speed and the wire diameter increase. The dependence on wire diameter is due to the increase in the plastic/viscous and frictional energy dissipations.

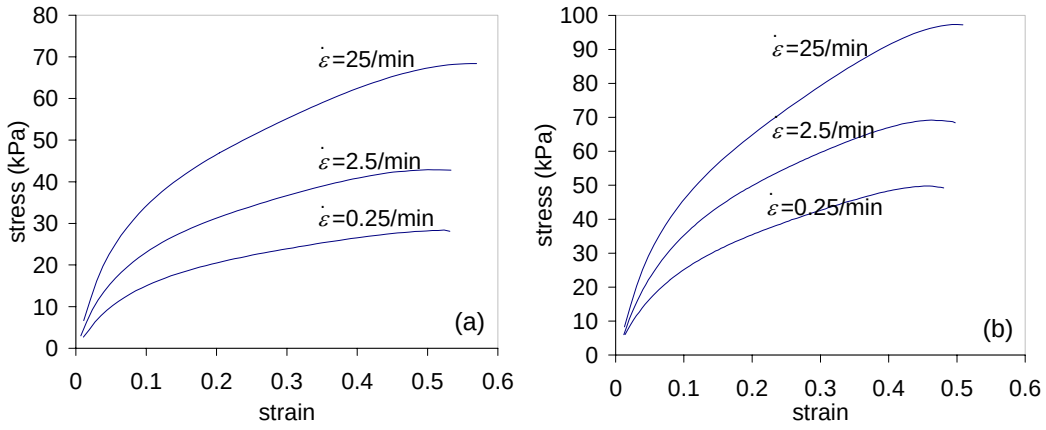

Figure 1. Stress-strain relationships for (a) mild Cheddar and (b) Gruyere.

3 MATERIAL MODEL

The cheese samples were assumed to be incompressible and homogeneous. A non-linear viscoelastic model consisting of separable strain and time dependent functions was chosen to model the constitutive behaviour of the cheese. During a step strain relaxation test, the model characterises the relaxation stress as the product of separable strain ($\sigma_0(\varepsilon)$) and time ($g(t)$) dependent functions, i.e.,

$$\sigma(\varepsilon,t)=\sigma_0(\varepsilon)g(t) \tag{1}$$

where σ is the stress at true strain ε and time t. The strain dependent function has dimensions of stress and the time dependent function is dimensionless.

The strain dependent behaviour was modelled using the Van der Waals hyperelastic potential [7,8]. For this potential, the stress during the uniaxial deformation state is expressed as,

$$\sigma_0(\lambda)=\psi\lambda\left(\lambda-\frac{1}{\lambda^2}\right)\left[\frac{\sqrt{\lambda_m^2-3}}{\sqrt{\lambda_m^2-3}-\sqrt{\lambda^2+2\lambda^{-1}-3}}-a\sqrt{\frac{\lambda^2+2\lambda^{-1}-3}{2}}\right] \tag{2}$$

where ψ is the shear modulus, λ_m and a are dimensionless material constants, and λ is the stretch ratio in the direction of load and is calculated from the strain, i.e. $\lambda=\exp(\varepsilon)$.

The time dependent behaviour was defined by the Prony series:

$$g(t)=g_\infty+\sum_{i=1}^{5}g_i\exp\left(\frac{-t}{\tau_i}\right) \tag{3}$$

where τ_i are time constants with values of 0.1s, 1s, 10s, 100s and 1000s for i =1 to 5 respectively. The dimensionless constants, g_i, are related via:

$$g_\infty+\sum_{i=1}^{5}g_i=1 \tag{4}$$

For any general loading condition, the stress can be calculated via the Leaderman form of the convolution integral [9]:

$$\sigma(\varepsilon,t)=\int_0^t g(t-s)\frac{d\sigma_o(\varepsilon)}{ds}ds \tag{5}$$

The above integral was evaluated numerically as in Goh et al [10] and the result was used to determine the set of material parameters that results in the best fit between the analytical model and the experimental data from the mechanical tests. A summary of the parameters is presented in Table 1.

	ψ(kPa)	λ_m	a	g_1	g_2	g_3	g_4	g_5	g_∞
mild Cheddar	190	2.54	2.19	0.304	0.303	0.114	0.106	0.089	0.084
Gruyere	236	2.64	1.98	0.221	0.333	0.117	0.123	0.097	0.109

Table 1. Material parameters.

4 FRICTION PROPERTIES

The surface friction between the wire and the cheese was assumed to be described by Coulomb friction. The coefficient of friction, μ, was assumed from previous studies of mild Cheddar and Gruyere [11] where cylindrical specimens of various initial height/diameter ratios were compressed between steel platens under nonlubricated conditions. The values of μ were found to be 0.16 and 0.14 for mild Cheddar and Gruyere respectively.

5 NUMERICAL SIMULATIONS AND FAILURE CRITERIA

The numerical simulations were performed using the commercial finite element code ABAQUS [7]. Two separate models were developed, and schematics of the models are shown in figure 2. The first model (figure 2a) was used for the prediction of crack initiation. The second model was used to simulate crack propagation. In all cases, the bulk material was modeled using four noded, plane strain, solid (continuum) elements. Large strain, non-linear, time-dependent analysis was used through the command *VISCO. The wires were defined as rigid surfaces and were prescribed to move at the same speeds as in the experiments. The bottom surface of the models was constrained in the vertical (y) direction but was allowed to move freely in the horizontal (x) direction.

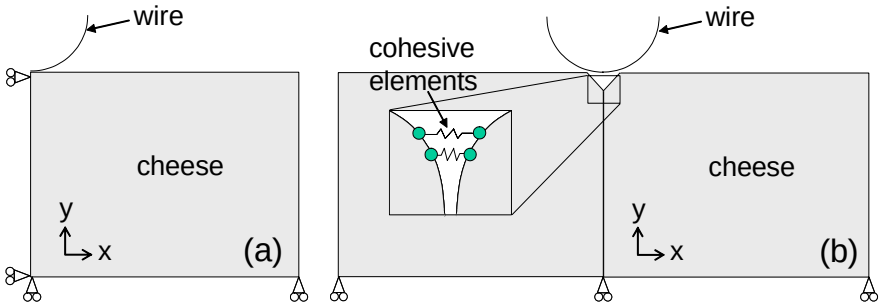

Figure 2. Finite element geometry for (a) crack initiation (b) crack propagation models. Not to scale.

Two fracture criteria were utilised to predict the steady-state cutting force. The first criterion is based on a critical strain to predict crack initiation. The critical strain, ε_{crit}, was assumed to be equal to the fracture strain as measured in the uniaxial compression test (see figure 1). The maximum tensile strain, $\varepsilon_{xx\ max}$, in the model was monitored such that when ε_{crit} was reached, the corresponding reaction force on the wire was assumed to be the steady-state cutting force [6]. For this criterion, the model shown in figure 2a was used.

In the second criterion (see figure 2b), a single crack was assumed to propagate along the line of symmetry. The fracture process was modeled by cohesive elements as used by Chen et al [12]. The traction-separation law of these elements (see Figure 3) is described by a third order polynomial:

$$T=\frac{12G_c}{\delta_{crit}^4}\left(\delta^3-2\delta_{crit}\delta^2+\delta_{crit}^2\delta\right) \tag{6}$$

where T is the traction, δ is the separation, δ_{crit} is the critical separation and G_c , the fracture toughness of the material, is given by the area under the curve. The peak stress, $\hat{\sigma}$, is given by $16G_c/9\delta_{crit}$.

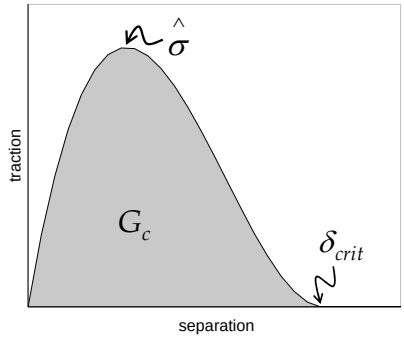

Figure 3. Traction-separation curve of cohesive zone model.

The cohesive elements were implemented using a 'user subroutine' (*UEL) in ABAQUS. The cohesive elements are linear, four noded, and each one connects two solid elements on either side of the line of symmetry. The size of the solid elements along the fracture path was 0.009mm by 0.009mm. For diameters of 1.6mm and 2mm, a longer crack path was necessary to achieve the steady-state cutting phase. Therefore, the solid element size was increased to 0.025mm by 0.025mm to reduce computation costs.

6 RATE EFFECTS ON WIRE CUTTING

The effective strain rate in wire cutting increases as cutting speed increases whereas it decreases as wire diameter increases. Experimentally, the strain distribution is difficult to measure, so it was estimated from the finite element models shown in figure 2a. Since the strain distribution is not uniform, the rate of change of the maximum tensile strain in front of the wire was taken as an indication of $\dot{\varepsilon}$. These estimates are shown in Table 2 for v =5mm/min. For v =50 and 500mm/min, the values of $\dot{\varepsilon}$ are respectively ten and a hundred times the values shown in Table 2 for the same d. It can be seen that $\dot{\varepsilon}$ decreases by about six fold as d increases from 0.25mm to 2mm.

Wire diameter, d (mm)	0.25	0.5	0.89	1.6	2
Strain rate, $\dot{\varepsilon}$ (1/min)	~ 6.0	~ 3.4	~ 2.1	~ 1.2	~ 1.0

Table 2. Approximate rate of change of the maximum tensile strain in the x-direction in front of the wire for v =5mm/min.

The change in strain rate will have an effect on the parameters of the cohesive model, i.e. G_c and $\hat{\sigma}$. There is no independent data to evaluate the strain rate dependence of G_c , but as shown in figure 4, the relationships between F/b and v follow a power law relationship:

$$\frac{F}{b} \propto v^n \Rightarrow \frac{F}{b} \propto t^{-n} \tag{7}$$

where t is time and n is a constant and approximately equal to 0.17 for both cheeses.

In addition, figure 5 shows the stress-strain data from figure 1 re-plotted as isometric curves. The stresses are found to be related to $\dot{\varepsilon}$ via:

$$\sigma \propto \dot{\varepsilon}^m \Rightarrow \sigma \propto t^{-m} \tag{8}$$

where m is a constant and equal to 0.17 for both cheeses. The agreement between m and n suggests that the rate dependency of the constitutive and fracture properties is similar.

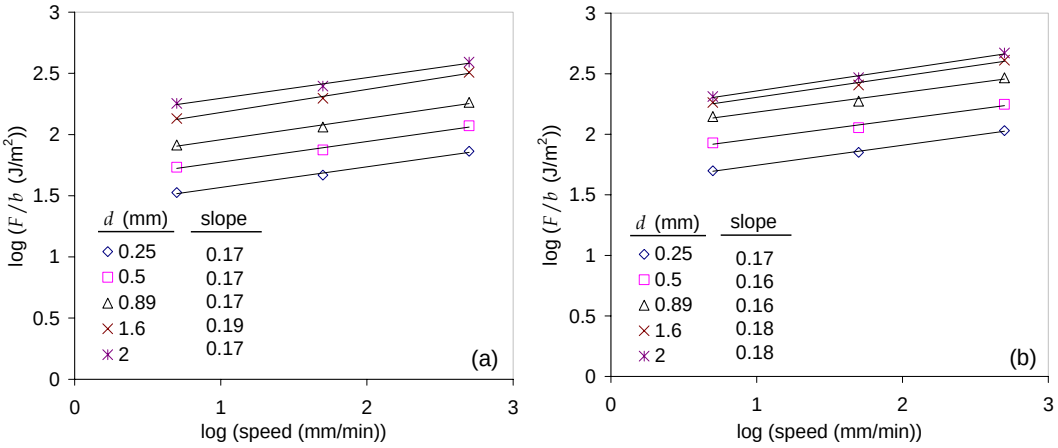

Figure 4. Relationships between *F*/*b* and speed. (a) mild Cheddar (b) Gruyere.

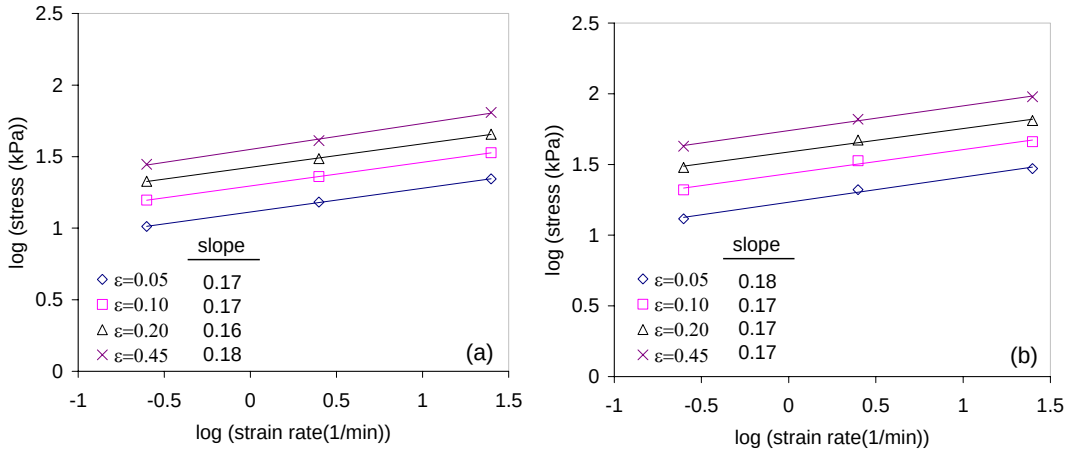

Figure 5. Relationships between stress and strain rate. (a) mild Cheddar (b) Gruyere.

7 RESULTS

The predictions of F/b using the crack initiation model are compared with the average experimental values of F/b in figure 6. The agreement is reasonable for most cases, suggesting that the critical strain criterion can be utilised to predict the steady state cutting force.

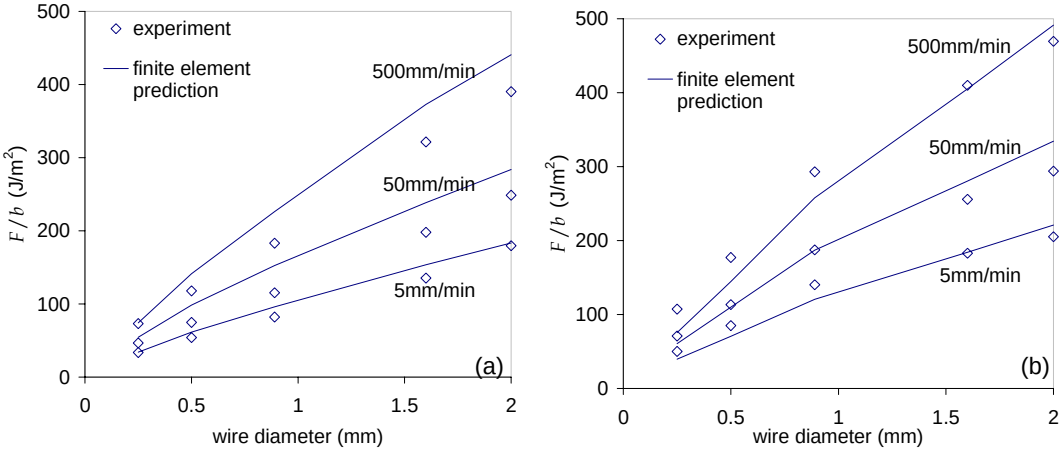

Figure 6. Prediction of wire cutting energies using critical strain fracture criterion. (a) mild Cheddar (b) Gruyere.

In the absence of independent fracture data to calibrate the traction-separation laws, the values of G_c and $\hat{\sigma}$

could only be determined by matching the numerical steady-state energies to the experimental data through a trial and error approach. This was performed for d =0.25mm and v =5mm/min. The validity of the parameters was checked by applying them to the models for the other cases of d and v. The ratio of G_c to $\hat{\sigma}$ was chosen so that δ_{crit} was arbitrarily fixed at 0.22mm and smaller than 0.25mm which was the smallest d used in the experiments.

The estimations of G_c and $\hat{\sigma}$ from the trial and error approach were 15J/m^2 and 120kPa for mild Cheddar and 25J/m^2 and 200kPa for Gruyere. Figure 7 shows the numerical predictions of F/b when the same values of G_c and $\hat{\sigma}$ were applied to all wire diameters for v =5mm/min. There is a reasonable agreement between the numerical predictions and the experimental data for the three smallest wire diameters, but a larger discrepancy is observed for d =1.6 and 2mm. This is probably due to the increase in the amount of secondary cracks as d increases; these were obvious in the fracture surfaces which are shown in figure 8. Secondary cracks imply higher fracture energies and hence higher cutting forces. If the values of G_c and $\hat{\sigma}$ are changed through the power laws of equations (7) and (8) so that the new values reflect the changes in $\dot{\varepsilon}$, the predicted values of F/b will be lower (see figure 7). This is due to the decreasing $\dot{\varepsilon}$ with increasing d which leads to even larger errors in the predictions at larger wire diameters.

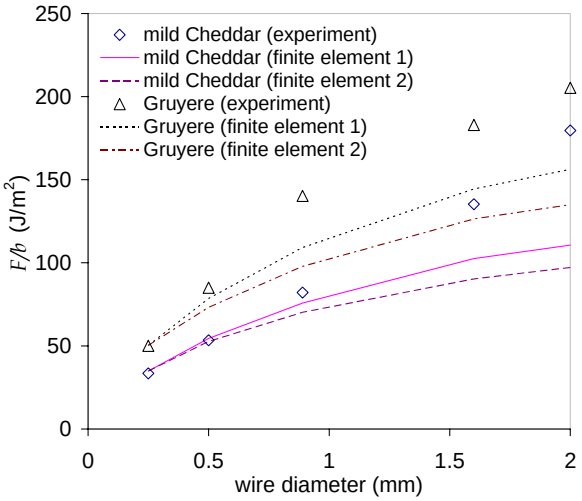

Figure 7. Wire cutting data at v =5mm/min. The numerical results numbered '1' are obtained using the same values of G_c and $\hat{\sigma}$ for all wire diameters. The numerical results numbered '2' are obtained using the values of G_c and $\hat{\sigma}$ adjusted for the change in $\dot{\varepsilon}$.

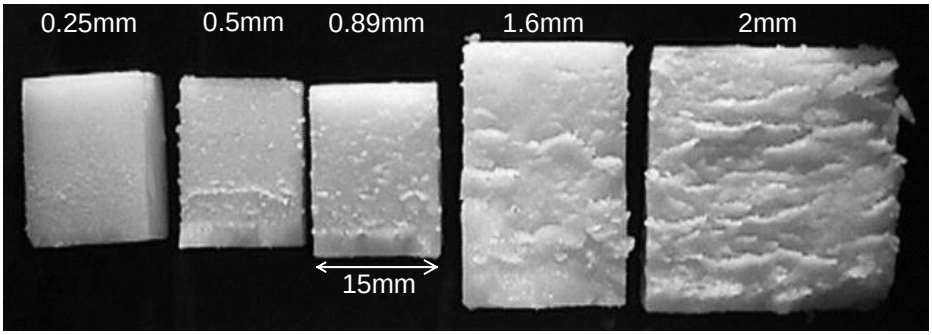

Figure 8. Fracture surface of wire cutting specimens for mild Cheddar(v =5mm/min). Direction of cuts is from top to bottom.

For the simulations of the cutting process at v =50 and 500mm/min, the values of G_c and $\hat{\sigma}$ were increased using the power law approximations. The same values of G_c and $\hat{\sigma}$ were applied to all wire diameters and the results are shown in figures 9 and 10 for v equal to 50mm/min and 500 mm/min respectively. The predictions when v is 50 mm/min are reasonably good for the three smallest wire diameters. However, similar to the trend

seen for v =5mm/min, the finite element results are increasingly lower than the experimental measurements as d increases. The finite element predictions for v =500mm/min are much lower than the experimental data. The erroneous predictions from the finite element model at high speeds are probably due to the inaccurate calibration of the constitutive model. For v =500mm/min, the strain rates in the wire cutting process may reach 100-600/min (see table 2). However, the constitutive models were calibrated using stress-strain data which were measured only up to $\dot{\varepsilon}$ =25/min (see figure 1). Because the same inadequacies apply to Gruyere, the finite element analysis for this cheese at v =500mm/min was not pursued.

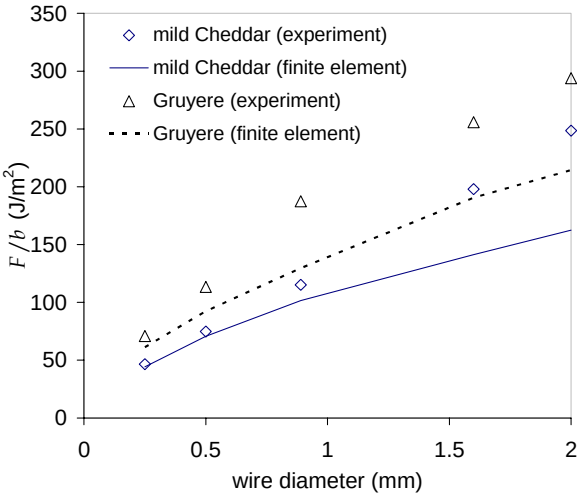

Figure 9. Wire cutting data for v =50mm/min.

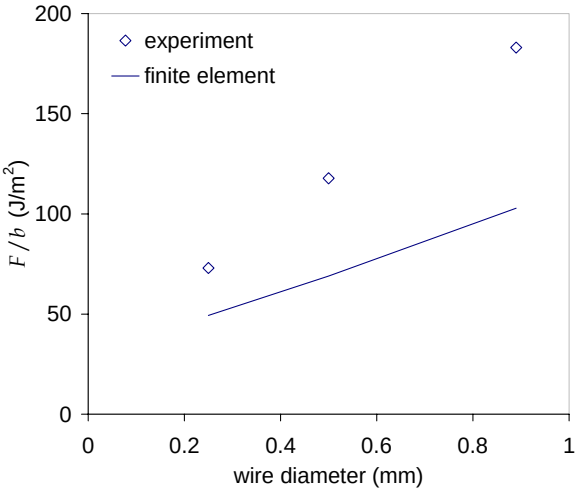

Figure 10. Wire cutting data for mild Cheddar for v =500mm/min.

The discrepancies between the numerical model and the experimental data show that there are still some areas which require further investigation. Although the numerical model predicted the cutting energies for the small wire diameters, it would be necessary to include the effect of the secondary damage for more accurate predictions of the cutting conditions when large wire diameters are used. This can be achieved by incorporating the cohesive elements within the bulk material and not just along a single, predefined, fracture path. Furthermore, the current computer code for the cohesive element does not allow for the element to 'deform' as it comes into contact with the wire. Instead, the cohesive elements overlap the wire for a certain period before the critical separation is reached. This is not a true reflection of reality, where complete decohesion occurs ahead of the wire.

8 CONCLUSIONS

This study has revealed some new information regarding the mechanics of the wire cutting process. For example, the variation in the strain rate when cutting viscoelastic materials with different wire diameters has to

be taken into account when estimating the fracture toughness. The presence of secondary cracks makes the cutting process less predictable since a higher fracture energy is required. The errors due to the secondary damage can be limited by using small wire diameters.

The numerical predictions based on a maximum strain criterion were computationally cheaper to use and more successful in predicting cutting forces. This method however does not allow an estimation of the fracture toughness nor can it be used for the prediction of crack paths. The use of cohesive zone models allows the simulation of crack propagation based on an energy release rate approach and has been shown to successfully predict the cutting energies for small wire diameters at two speeds. Improvements to the cutting models, so that they can predict the crack path as well as the cutting force will be considered in the future.

An understanding of the wire cutting process is important to eliminate the problems relating to distorted cuts and lost yield as currently faced in the food industry. From a more general perspective, a model of the fracture process in food systems is also required in computer simulations of mastication. Such simulations are needed to give a clearer picture of the important interactions between texture, flavour and odour.

ACKNOWLEDGEMENTS

The authors would like to thank the Biotechnology and Biological Sciences Research Council (BBSRC) and the Royal Commission for the 1851 Exhibition Research for their financial support.

REFERENCES

[1] Charalambides M.N., Williams J.G. and Chakrabarti S. (1995), "A study of the influence of ageing on the mechanical properties of Cheddar cheese", *J Mater Sci* 30, pp. 3959-3967.

[2] Kamyab I., Chakrabarti S. and Williams J.G. (1998), "Cutting cheese with wire", *J Mater Sci* 30, pp. 2763-2770.

[3] Imbeni V., Atkins A.G., Jeronimidis J. and Yeo J. (2001), "Rate and temperature dependence of the mechanical properties of Cheddar cheese", Proceedings of 10th International Conference on Fracture, ICF1001101 PR.

[4] Luyten H.(1988), "The rheological and fracture properties of Gouda cheese", PhD thesis, Wageningen Agricultural University.

[5] Green M.L., Lamgley K.R., Marshall R.J., Brooker B.E., Willis A. and Vincent J.F.V. (1986), "Mechanical properties of cheese, cheese analogues and protein gels in relation to composition and microstructure", *Food Microstruc* 5, pp. 169-180.

[6] Goh S.M., Charalambides M.N. and Williams J.G. (2003), "Large strain time dependent behavior of cheese", *J of Rheol* 47, pp. 701-716.

[7] ABAQUS User's Manual (2003), Version 6.4, Hibbit Karlsson and Sorensen, USA.

[8] Killian H.G. (1982), "Thermoelasticity of networks", *Colloid Polym Sci* 260, pp. 895-910.

[9] Williams J.G. (1980), *Stress Analysis of Polymers*, Ellis Horwood, Chichester.

[10] Goh S.M., Charalambides M.N. and Williams J.G. (2004), "Determination of the constitutive constants of non-linear viscoleastic materials", *Mech Time Depend Mat* 8, pp. 255-268.

[11] Charalambides M.N., Goh S.M., Lim S.L. and Williams J.G. (2001), "The analysis of the frictional effect on stress-strain data from uniaxial compression of cheese", *J Mater Sci* 36, pp. 2313-2321.

[12] Chen J., Crisfield M., Kinloch A.J., Busso E., Matthews F.L. and Qiu Y. (1999), "Predicting progressive delamination of composite material specimens via interface elements", *Mech Comp Mater Struc* 6, pp. 1-17.

5th GRACM International Congress on Computational Mechanics
GRACM 05
Limassol, 29 June – 1 July, 2005

A THEORETICAL AND NUMERICAL STUDY OF DISCS WITH FLAT EDGES UNDER DIAMETRAL COMPRESSION (FLAT BRAZILIAN TEST)

K. N. Kaklis, Z. Agioutantis, E. Sarris, and A. Pateli

Department of Mineral Resources Engineering
Technical University of Crete
73 100 Hania, Greece
e-mail : kaklis@mred.tuc.gr

Keywords: Flattened Brazilian test, indirect tensile test, tensile strength, finite element analysis.

Abstract. In this paper the study of the diametral compression of a disc with flat edges (flat Brazilian test) is presented. The test is studied numerically for two different loading cases. The critical value of the loading angle $2a$, which guarantees the crack initiation at the centre of the disc, is investigated according to stress analysis and Griffith's strength criterion. Also the coefficient k is calculated for each loading angle, which is used for the determination of the tensile strength σ_t.

1 INTRODUCTION

The conventional method of measuring the tensile strength of rocks is the direct tension test, which, however, presents experimental difficulties and is not commonly conducted in rock mechanics laboratories. This is due to both the bending stresses or torsion moment (caused by the eccentricity of applied axial loads) and the localized concentrated stresses (caused by improper gripping of specimens)[1, 2].

Because of these experimental difficulties, alternative techniques were developed to determine the tensile strength of rock. The Brazilian test uses a circular solid disc, which is compressed to failure across the loading diameter. In principle, the stress field, which induces tensile failure when the disc is compressed diametrically, can be fully determined, provided that the material maintains a perfect linear elastic behavior up to the point of failure. Hondros[3] has analytically solved the Brazilian test configuration in the case of isotropic rocks, while Pinto[4] extended Hondros' method to anisotropic rocks and checked the validity of his methodology on schisteous rock. Recent investigations have led to a closed form solution for an anisotropic disc[5, 6], a series of charts for the determination of the stress concentration factors at the center of an anisotropic disc[7] and explicit representations of stresses and strains at any point of an anisotropic circular disc compressed diametrically[8].

However, the Brazilian test has the disadvantage that high shear stresses are induced close to the loading platens apart from the tensile stresses, which are developed in the disc. Failure may be attributed not only to the development of a tensile crack at the center, but also to the formation of small wedges at the contact surfaces. So the fundamental question "how to guarantee the centre crack initiation" of the specimen remains unresolved.

For the proposed configuration of the flattened Brazilian test, an exact analytical elasticity solution cannot be obtained, so a Finite Element Analysis program is used to calculate the stresses for various lengths of the two parallel flat ends that are introduced to the disc.

The main objective of this paper is the determination of the critical loading angle $2a$, which corresponds to the flat ends, so as to ensure crack initiation at the centre of the disc. Also a formula for the determination of the tensile strength is provided, based on a coefficient k that is calculated by the finite element analysis.

2 THE FLATTENED BRAZILIAN TEST.

The proposed configuration of the flattened Brazilian test is presented in Fig. 1. The elastic, homogeneous, continuous and isotropic disc of diameter D and thickness t, is subjected to a uniform diametral pressure p acting

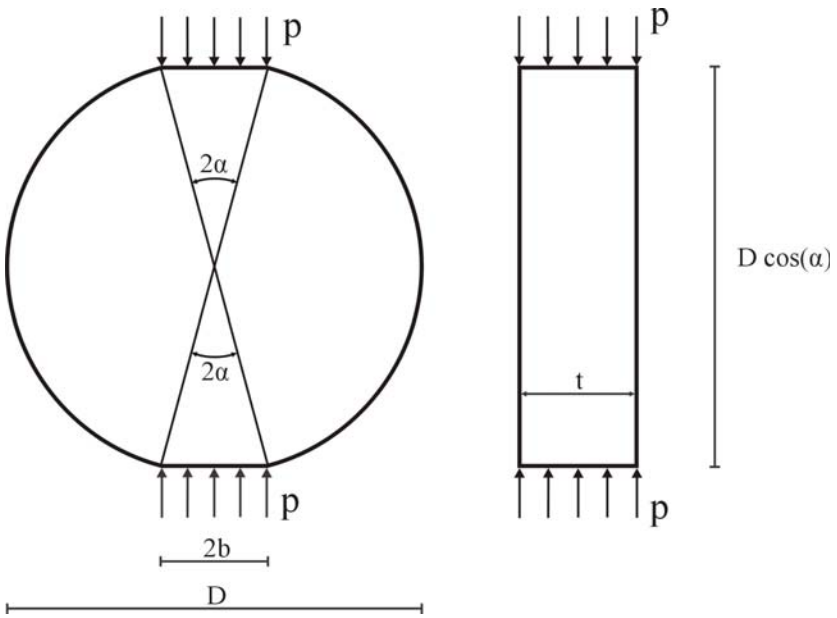

Figure 1. The flattened Brazilian disc specimen under uniform diametral compression.

over two equal-width $(2b)$ parallel ends which correspond to the loading angle $2a$.

Throughout this paper (unless stated otherwise) tensile stresses and strains are considered to be positive quantities and consequently compressive stresses and strains are taken as negative quantities.

3 NUMERICAL ANALYSIS

For the elastic equilibrium of a homogeneous, continuous, isotropic disc with diameter $D = 2R$ and thickness t, subjected to a uniform radial pressure p acting along an arc which corresponds to a loading angle $2a$ (original Brazilian test), the exact stress solution on the loading diameter is given by the following relationships[9]:

$$\sigma_\theta = \frac{2p}{\pi}\left\{\frac{\sin 2\alpha}{1-2\left(\frac{r}{R}\right)^2\cos 2\alpha+\left(\frac{r}{R}\right)^4}\left[1-\left(\frac{r}{R}\right)^2\right]-\arctan\left[\frac{\left(\frac{r}{R}\right)^2\sin 2\alpha}{1-\left(\frac{r}{R}\right)^2\cos 2\alpha}\right]-\alpha\right\}$$

$$\sigma_r = \frac{2p}{\pi}\left\{\frac{\sin 2\alpha}{1-2\left(\frac{r}{R}\right)^2\cos 2\alpha+\left(\frac{r}{R}\right)^4}\left[\left(\frac{r}{R}\right)^2-1\right]-\arctan\left[\frac{\left(\frac{r}{R}\right)^2\sin 2\alpha}{1-\left(\frac{r}{R}\right)^2\cos 2\alpha}\right]-\alpha\right\} \quad (1)$$

At the centre of the disc these stresses become:

$$\sigma_\theta = \frac{2P}{\pi Dt}$$
$$\sigma_r = -\frac{6P}{\pi Dt} \quad (2)$$

where P is the total force.

However, for the flattened Brazilian disc (Fig. 1) a similar closed-form solution cannot be obtained, so a Finite Element Analysis program is used to calculate the tangential (σ_θ) and radial (σ_r) stresses along the loading diameter for different loading angles $2a$.

3.1 Geometry

The test was modeled in 2-D space in the MSC.Mentat front-end program, and it was solved by the MSC.Marc Finite Element Analysis program[10 ,11]. To fully simulate the behavior of the material during diametral compression, both the specimen and the steel platens used to apply the load were modeled. Two sets of seven different models were developed, according to the loading angle $2a$ of the specimens: 5^o, 10^o, 15^o, 20^o, 30^o, 40^o, 50^o and the loading conditions: uniformly distributed traction was applied in the vertical direction and traction free in the horizontal direction on the flat ends of the specimen (Case A) and the same traction in the vertical direction on a platen between the flat end of the specimen with friction coefficient $\mu = 0.4$ in the horizontal direction (Case B) (Fig. 2). Contact elements were used to model the interface between steel platens and specimen. Symmetry across axis *x* was taken into consideration, so the final model was the upper half of each specimen category. Dimensions of each model matched the actual dimensions for future experimental investigation. The diameter of the discs was 54 mm.

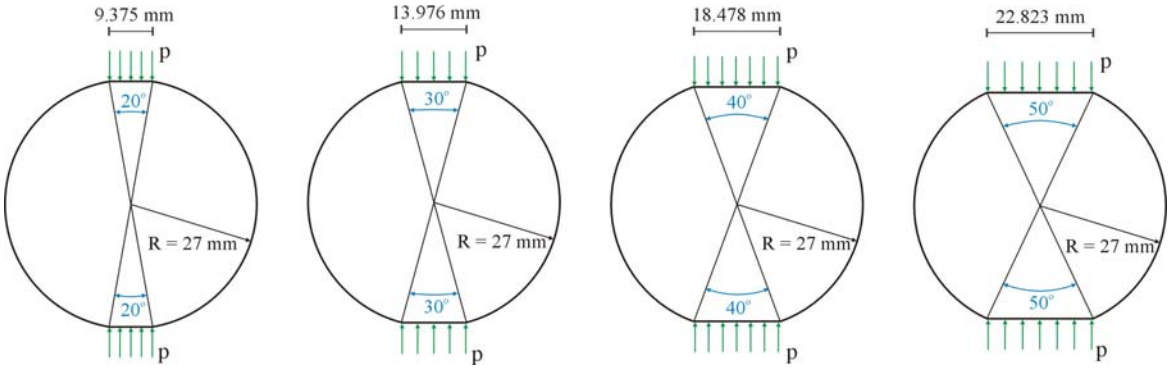

(a): Case A

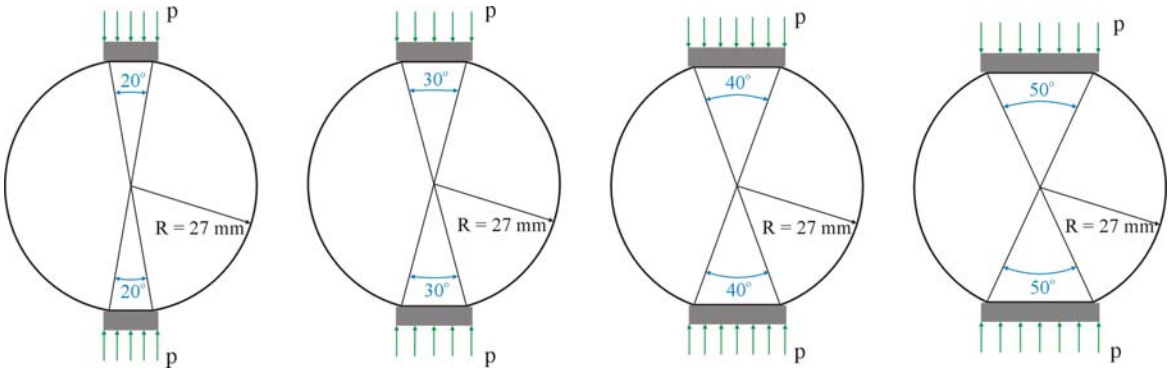

(b): Case B

Figure 2. A series of specimens for both Cases A (a) and B (b) with diameter $D = 54\ mm$ and four different loading angles $2a$.

Two typical models for each case are shown in Fig. 3. The number of elements and nodes used for the discretization of each model is presented in Table 1.

3.2 Material models and boundary conditions

The steel platens and the specimen were modeled as linearly elastic isotropic materials with elastic constants $E = 210\,GPa$, $\nu = 0.3$ and $E = 80\,GPa$, $\nu = 0.25$, respectively. Boundary conditions were as follows:

a. A maximum pressure of 39.51 MPa was applied on the upper flat edge of the specimen (Case A) and 33.07 MPa on the upper horizontal edge of the steel platen (Case B), in twenty linear loading steps.
b. The central vertical line of nodes for each model was fixed for vertical displacement $(dx = 0)$. Simulations were run using a plain stress assumption.
c. The nodes along the horizontal diameter of the disc were fixed for horizontal displacement $(dy = 0)$. No other boundary condition was required (Fig. 4).

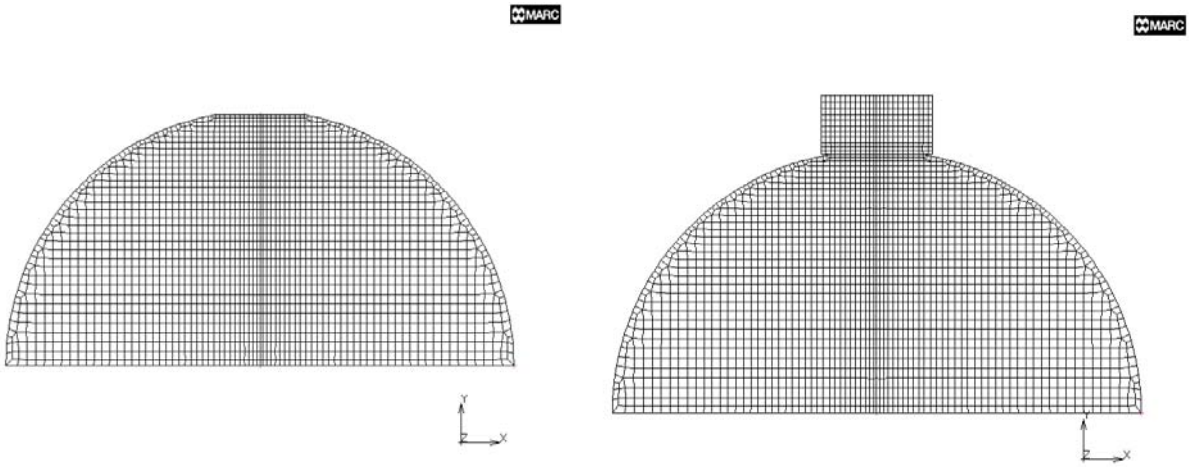

(a) (b)

Figure 3. Discretization of the model with loading angle $2a = 20^o$ for Case A (a) and Case B (b).

Case A							
Loading Angle $2a$	**5**	**10**	**15**	**20**	**30**	**40**	**50**
Elements	2980	1792	2928	2124	1896	2046	2052
Nodes	3103	1886	3050	2229	1988	2147	2158
Case B							
Loading Angle $2a$	**5**	**10**	**15**	**20**	**30**	**40**	**50**
Elements	3092	1912	3198	2388	2050	2430	2514
Nodes	3238	2029	3354	2529	2172	2574	2670

Table 1: Mesh generation parameters for each model

4 THEORETICAL ANALYSIS AND RESULTS

Fig. 5 presents a typical distribution of horizontal stress contours for a flattened Brazilian specimen with $2a = 20^o$. Similar results were obtained for all models.

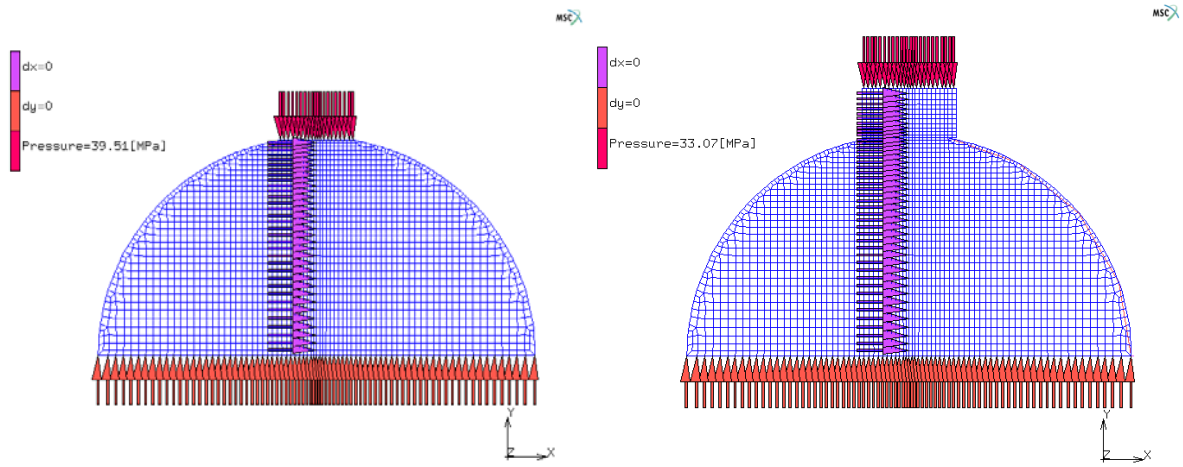

(a) (b)

Figure 4. Typical boundary conditions for all models. Model with loading angle $2a = 20^o$ for Case A (a) and Case B (b).

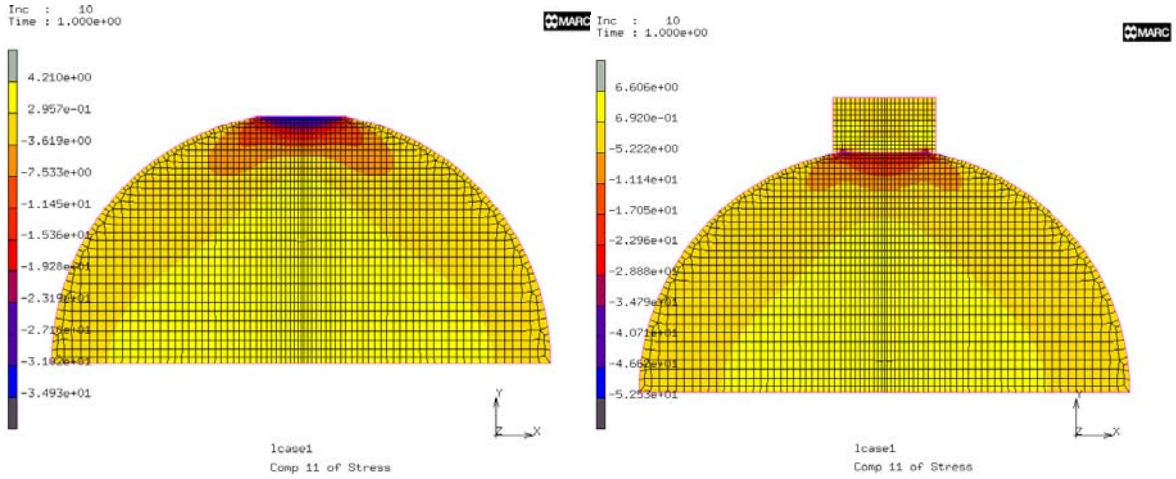

(a) (b)

Figure 5. Distribution of horizontal stress on flattened Brazilian specimen ($2a = 20^o$) for Case A (a) and B (b).

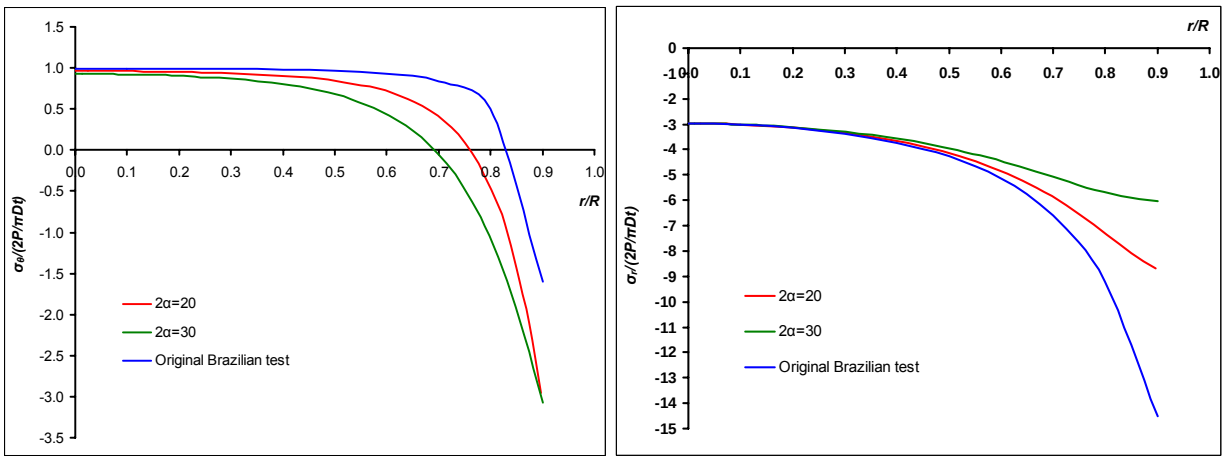

(a) (b)

Figure 6. Variation of the calculated dimensionless σ_θ (a) and σ_r (b) at the vertical diameter, for Case A.

Figure 6 presents the variation of the dimensionless $\frac{\sigma_\theta}{2P/\pi Dt}$ and $\frac{\sigma_r}{2P/\pi Dt}$ along the loading diameter for the models with $2a = 20^o$, 30^o and the case of the original Brazilian test.

The Griffith strength criterion[12] is considered suitable for these stress conditions. If the tensile stress is considered positive and $\sigma_1 \geq \sigma_2 \geq \sigma_3$, the equivalent stress σ_G is calculated as follows:

$$\text{when } 3\sigma_1 + \sigma_3 \geq 0, \quad \sigma_G = \sigma_1 \tag{3}$$

$$\text{when } 3\sigma_1 + \sigma_3 < 0, \quad \sigma_G = -\frac{(\sigma_1 - \sigma_3)^2}{8(\sigma_1 + \sigma_3)} \tag{4}$$

In the case of the original Brazilian test, eq (3) becomes $3\sigma_1 + \sigma_3 = 0$ at the disc center, which yields $\sigma_G = \frac{2P}{\pi Dt}$. The latter represents the basic formula for the determination of the tensile strength using the Brazilian test, either by σ_G or σ_θ. As a result, it follows that central crack initiation is fundamental for a Brazilian test.

For the flattened Brazilian test $\sigma_1 = \sigma_\theta$, $\sigma_3 = \sigma_r$ and $3\sigma_\theta + \sigma_r < 0$ for all studied loading angles $2a$, so the equivalent stress σ_G can be calculated using equation (5).

$$\sigma_G = -\frac{(\sigma_\theta - \sigma_r)^2}{8(\sigma_\theta + \sigma_r)} \tag{5}$$

Fig. 7 presents the variation of the dimensionless quantity $\frac{\sigma_G}{2P/\pi Dt}$ with $\frac{r}{R}$ along the loading diameter for different values of the loading angle $2a$ for both cases A and B.

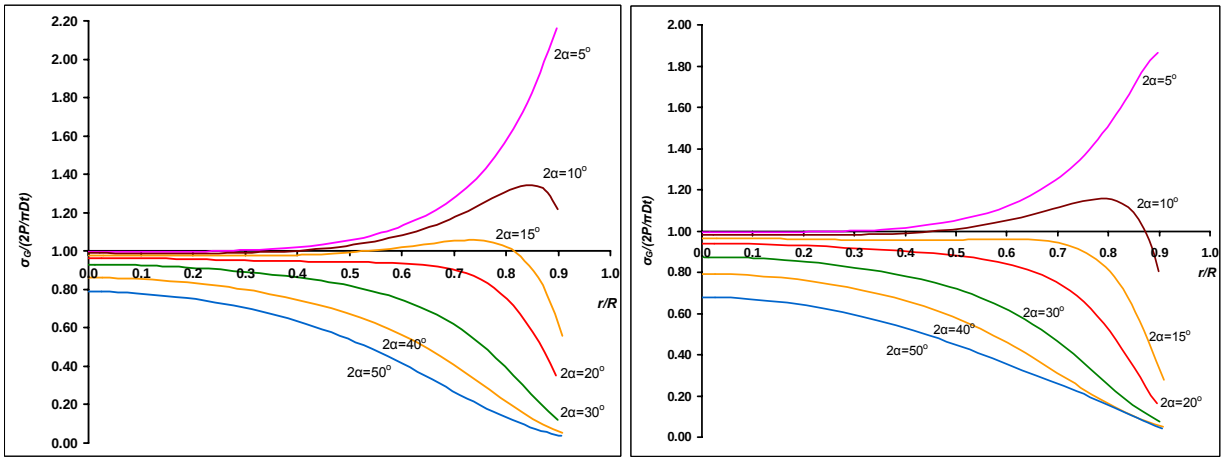

(a) (b)

Figure 7. Variation of the dimensionless calculated σ_G at the vertical diameter, for both Cases A and B.

It is evident that only when $2a \geq 20^o$ for Case A and $2a \geq 15^o$ for Case B the disc centre has a larger value of σ_G than any point elsewhere at the loading diameter, so the crack is most likely to initiate at the centre of the disc. These loading angles are the conditions for a valid test using the flattened Brazilian configuration. In this case, the tensile strength can be determined using the following equation:

$$\sigma_t = k\frac{2P_f}{\pi Dt} \tag{6}$$

where P_f is the failure load and k is a coefficient related to the loading angle (when $2a = 0^o$, coefficient becomes $k = 1$ - original Brazilian test). For a given value of $2a$, k can be determined by finite element analysis using the following formula:

$$k = \frac{\sigma_G}{2P/\pi Dt} \tag{7}$$

The values of coefficient k for different loading angles $2a$ and for both Cases A and B are presented in Table 2. It can be noted that the values of the coefficients k for the loading angles 20^o and 30^o in Case A are in full agreement with the corresponding values presented by Wang et al.[13].

		Case A			
Loading Angle $2a$		**20**	**30**	**40**	**50**
Coefficient k		0.9646	0.9299	0.8600	0.7878
		Case B			
Loading Angle $2a$	**15**	**20**	**30**	**40**	**50**
Coefficient k	0.9660	0.9401	0.8737	0.7923	0.6789

Table 2: The coefficient k for each model.

5 CONCLUSIONS

Two series of 2D numerical models were created to simulate the Flattened Brazilian test. The numerical results obtained for Case A are in full agreement with the corresponding values presented by Wang et al.[13]. The

models for Case B, however, represent a more realistic simulation of the experiment. As a result it is proposed that the loading angle for centre crack initiation should be at least $2a = 15^o$.

It should be noted that the designing and manufacturing of the two parallel flat ends demands additional time with respect to the original Brazilian test, but it is essential for the centre crack initiation of the specimen.

Finally, based on the numerical results for the coefficient k for each loading angle $2a$ and equation (6), the indirect tensile strength can be calculated.

REFERENCES

[1] Barla, G. & Goffi, L. (1974), "Direct tensile testing of anisotropic rocks", *Proceedings of the Third International Congress of Rock Mechanics*, Denver, Vol. 2, Part A, pp.93-98.

[2] Nova, R. & Zaninetti, A. (1990), "An investigation into the tensile behavior of a schistose rock", Int. J. Rock Mech. Min. Sci and Geomech. Abstr., 27, 231-242.

[3] Hondros, G. (1959), "The evaluation of Poisson's ratio and the modulus of materials of a low tensile resistance by the Brazilian (indirect tensile) test with particular reference to concrete", Aust. J. Appl. Sci., 10, 243-264.

[4] Pinto, J.L. (1979), "Determination of the elastic constants of anisotropic bodies by diametral compression tests", *Proceedings of the Fourth ISRM Congress*, Montreux, Vol. 2, 359-363.

[5] Amadei, B., Rogers, J.D. & Goodman, R.E. (1983), "Elastic constants and tensile strength of anisotropic rocks", *Proceedings of the Fifth ISRM Congress*, Melbourne, A189-A196.

[6] Amadei, B. (1996), "Importance of anisotropy when estimating and measuring in situ stresses in rock", Int. J. Rock Mech. Min. Sci and Geomech. Abstr., 33, 293-325.

[7] Chen, C.S., Pan, E. & Amadei, B. (1998), "Determination of deformability and tensile strength of anisotropic rock using Brazilian tests", Int. J. Rock Mech. Min. Sci and Geomech. Abstr., 35, 43-61.

[8] Exadaktylos, G.E. Kaklis, K.N. (2001), "Applications of an explicit solution for the transversely isotropic circular disc compressed diametrically", Int. J. Rock Mech. Min. Sci and Geomech. Abstr., 38, 227-343.

[9] Kaklis K.N. (2003), "Characterization of rock anisotropy and tensile strength using the Brazilian test", PhD thesis, Technical University of Crete, Hania, Greece.

[10] Mentat 2 (1996), User's guide.

[11] MARC Analysis Research Corporation (1995-1998), User's manual.

[12] Griffith A.A. (1924), "Theory of rupture", *Proceedings of the First International Congress on Applied Mechanics*, pp. 55-63.

[13] Wang Q.Z., Jia X.M., Kou S.Q., Zhang Z.X. & Lindqvist P.A. (2004), "The flattened Brazilian disc specimen used for testing elastic modulus, tensile strength and fracture toughness of brittle rocks: analytical and numerical results", Int. J. Rock Mech. Min. Sci and Geomech. Abstr., 41, 245-253.

5th GRACM International Congress on Computational Mechanics
Limassol, 29 June-1July 2005

NUMERICAL ANALYSIS OF THE DYNAMIC PHASE OF ROCK BLASTING UNDER THE INFLUENCE OF PRE-EXISTING DISCONTINUITIES

E. Sarris and Z. Agioutantis

Department of Mineral Resources Engineering
Technical University of Crete
73 100 Hania, Greece
E-mail: esarris@mred.tuc.gr, zach@mred.tuc.gr

Keywords: Dynamic Rock blasting, discontinuities, wave propagation, jointed medium, finite element analysis.

Abstract: *The propagation of stress waves due to rock blasting is responsible for rock fragmentation. This work presents a two-dimensional simulation of stress wave propagation in anisotropic rock. The influence of rock discontinuities such as joint planes is also investigated. Six models were developed using 2D finite element methodology. Results concerning the magnitude of the stress wave in various locations along the stress path are presented and critically evaluated.*

1. INTRODUCTION

For efficient blasting, it is necessary to understand the fragmentation mechanism under the influence of stress waves propagating from the blast hole to the free surface. Although this is a complicated mechanism, it can be assumed to take place in two discrete phases. The first phase is created by the stress waves imparted to the rock by the rapid release of energy, during the detonation of the explosive in the blast hole (dynamic phase). The second phase is created immediately following the first phase due to the gases released by the chemical reaction. The pressure developed is responsible for creating a quasi-static stress field around the blast hole, which helps separate and displace the broken rock. Both phases can be treated as parts of the same function of pressure versus time [1, 2]. However, in the present work, only the first phase is investigated.

When studying the fragmentation, due to stress wave propagation, the rock mass weakness, local inhomogeneities, fractures, beddings and/or joints should be taken into account. Due to the complexity of the dynamic problem, most researchers focus on isotropic – weakness free media. However, rock formations are by nature not homogeneous and isotropic. Variations can occur due to difference in the origin of the formations, current and previous tectonic regime, etc. Furthermore, it is the interaction between the features of the rock mass and the stresses generated due to an explosive detonation, which may cause favorable or unfavorable blasting results. For example, when the propagating transient waves encounter discontinuities positioned in a favorable direction, then the performance of the particular blast design is enhanced, whereas adversely oriented discontinuities may not achieve the desired fragmentation [2].

Many researchers have studied the damage in the media (i.e., rock) caused by the stress waves induced by blasting. Some have proposed a simple dynamic damage model based on the equivalence theory between the damaged media and the non damaged media [3]. Others presented a non local analysis of the dynamic damage accumulation processes in brittle solids as well as a transient dynamic finite element computer code based on the same work [3]. However the damping properties induced by the opening and closing of the joints are ignored by such theories.

The main objective of this paper is to study the effect of a joint, which is transversely positioned across the path of a propagating wave. Since rock break easier in tension than in compression, it is evident that the reflected compressive waves returning as tensile waves may cause more damage than the original waves. This analysis is performed in both isotropic and anisotropic rock. The basic mechanism of waves propagating through jointed media is given below.

A rock media with a straight joint is shown in Figure 1. The joint, having a width of d, is assumed to be empty inside and can be closed under pressure waves. An incident wave P_i with incident angle a_1, strikes the joint surface A-A'. There are only two cases possible. A) The wave can propagate to the other side B-B' and B) the wave is not strong enough to pass through the joint. In Case A, the wave passes through the joint after the joint is closed. Two stages can be observed. Initially, before the joint is closed, only reflected waves are generated when the incident waves propagate to the joint face (a free boundary). If the magnitude of the stress pulse is strong enough, the face A-

A' moves against face B-B'. Thus the stress wave causes the joint to close and consequently part of the incident wave can be transmitted through the joint, making the face A-A' and B-B' to move together as an elastic body [4].

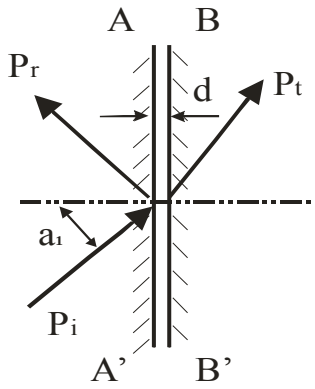

Figure 1. Transmitted (P_t) and reflected (P_r) waves at the joint face

2. NUMERICAL ANALYSIS

2.1 Geometry

The simulation was carried out in 2-D space utilizing MSC.Mentat/MSC.Marc suite of programs. Mesh design and generation was accomplished in MSC.Mentat and the models were solved by MSC.Marc, a nonlinear finite element standard code [5]. Two basic geometric schemes were designed as shown in Figure 2 utilizing repetitive symmetry (i.e. symmetry on both sides). These schemes correspond to single row blasting considering plain strain conditions. For a single row blasting the spacing (S) may be taken as twice the burden (B) (Figure 2) to maximize the output of the fragmented rock. Note that if fragmentation conditions are not good, then the ratio S/B may be reduced to 1:1.5 or lower. The borehole is located at the center back of the models and the ratio between the borehole radius (r) and the burden (B) is 2.5:100 (i.e. for a 10 cm diameter blast hole the burden is 2 m). The joint has an aperture width (d) of 0.05 cm and is located exactly in the middle of the burden (50% B) with the tips forming an angle of 90^0 with the borehole (Figure 2). The number of elements and nodes used for the discretization are presented in Table 1.

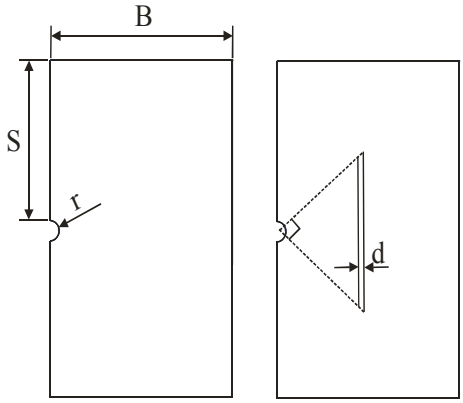

Figure 2. Geometry of the models

2.2 Material Properties

Three material models where generated for the geometries shown in Figure 2. The rock was modeled at first as linear elastic and isotropic. Then it was also modeled as linear elastic orthotropic with a) the strong material direction in the X axis (OrthoX) and b) the strong material direction in the Y axis (OrthoY). The material properties for the

three material models are presented in Table 1. In order to achieve realistic conditions during the explosion, Rayleigh damping was also considered. A percentage of 5% damping in the rock is the most common in many rocks, so the Rayleigh damping coefficients were the same in all simulations and are as follows: a = 0.001, b = 0.01.

	Isotropic	**Orthotropic A (xx is strong direction)**	**Orthotropic B (yy is strong direction)**
Elements	3200	3200	3200
Nodes	3321	3356	3356
E_{xx} (GPa)	20	20	10
E_{yy} (GPa)	20	10	20
E_{zz} (GPa)	20	20	10
v_{xy}	0.30	0.30	0.11
v_{yz}	0.30	0.11	0.30
v_{zx}	0.30	0.30	0.11
G_{xy} (GPa)	7.69	7.69	4.50
G_{yz} (GPa)	7.69	4.50	7.69
G_{zx} (GPa)	7.69	7.69	4.50

Table 1. Mesh generation parameters and material properties for both geometry schemes

2.3 Boundary Conditions

The boundary conditions which were applied on the models are presented in Figure 3 and were as follows:

a. The pressure applied to the borehole walls corresponds to a typical value for a decoupled charge. A maximum pressure of 6000 MPa was considered.
b. The nodes on the upper and lower boundary (i.e. in the horizontal direction) were fixed for vertical displacement (dy=0), satisfying the condition of repetitive symmetry in the media (i.e. a row a blast holes against a free surface)
c. The nodes on the left boundary (i.e. in the vertical direction) were fixed for horizontal displacement (dx=0). This condition also implies a symmetry on the Y axis, (i.e. that there is a free surface to the left, in symmetry to the one on the right). Previous investigations have shown that this model yields similar results with models where the left boundary is 10B to the left of the borehole[6]. Hence, the simpler model is utilized.
d. Contact elements are used around the boundaries of the discontinuity with a friction angle of about 22 degrees.

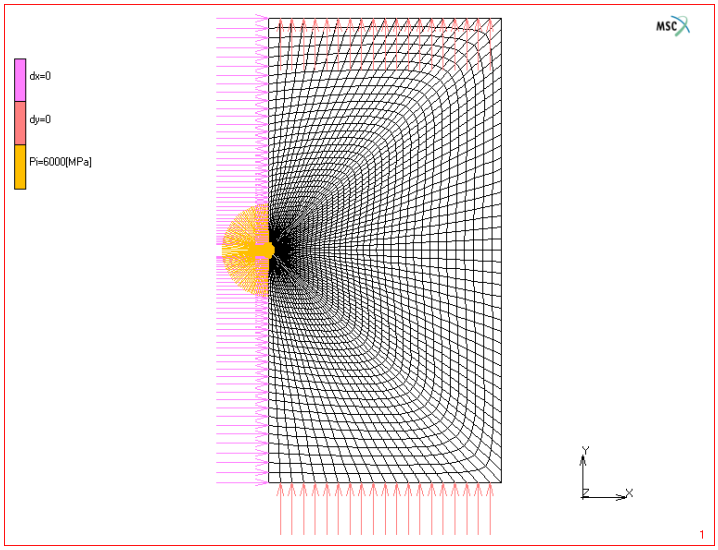

Figure 3. Discretization and boundary conditions of the models

2.4 Loading Conditions and Time Integration Scheme

To fully simulate the dynamic phase of the explosion, the actual time duration of the phenomenon must be taken into account. The time duration is 30-50 msec depending mainly on the type of the explosive and the type of the media (i.e. rock). The time of the dynamic phase begins from the moment of the explosion and finishes when the wave reflects on the free surface and returns back to the borehole. In Figure 4, the pressure profile versus time for a total time of 0.05 second is presented.
provided

In dynamic transient wave analysis, the number of elements, which are used, is bound with the time step of the time integration. Furthermore, the size of the elements must be calculated (and thus specified) so that the stress wave propagation does not surpass two elements in each propagation step, otherwise an error called numerical dispersion is introduced in the solution. The time step used for the analysis was $\Delta t = 0.00033$ sec [5]. Thus for a total time duration of 50msec, 150 iteration steps were needed for each model. Note that in this type of analysis, the total time should include the necessary time space for the transient phenomenon to be completed. In this case, the pulse is applied in 15msec, but 50msec are allowed to study the stress wave propagation.

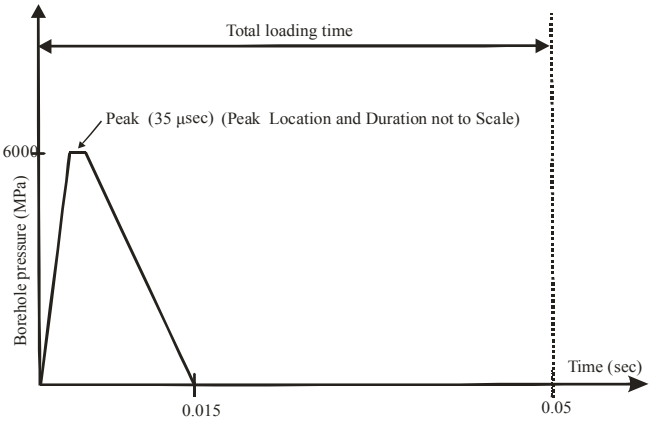

Figure 4. Loading conditions of the models

For the dynamic analysis, the Newmark time integration scheme was used. The relationships for Newmark's method are as follows [7]:

$$u^{n+1} = u^n + \Delta t v^n + (\frac{1}{2} - \beta)\Delta t^2 \alpha^n + \beta \Delta t^2 \alpha^{n+1} \text{ (Displacements)} \quad (1)$$

$$v^{n+1} = v^n + (1-\gamma)\Delta t a^n + \gamma \Delta t a^{n+1} \quad \text{(Velocities)} \quad (2)$$

Where n is the number of the time step. For the method to be unconditionally stable when this type of dynamic equations are used (which correspond to the trapezoidal integration rule), the values for the constants β,γ should be β=0.25 and γ=0.5. The classic equation of motion of the system takes the form:

$$\left(\frac{4}{\Delta t^2} M + \frac{2}{\Delta t} C + K\right)\Delta u = F^{n+1} - R^n + M\left(a^n + \frac{4}{\Delta t} v^n\right) + C v^n \quad (3)$$

where the external forces are given by the relationship:

$$R = \int_V \beta^T \sigma dv \quad (4)$$

Substituting R from equation (4) in (3) the implicit solution of the system is obtained:

$$u^{n+1} = u^n + \Delta u \quad (5)$$

3. ANALYSIS AND RESULTS

In total six models were developed and solved. Three pertain to the first geometry scheme (without discontinuity) and three are for the second geometry scheme. The stresses were studied by taking history plots in three discrete nodes. These nodes were located a) on the borehole perimeter, b) at 50% of the burden, c) on the free surface and are shown in Figure 5a. In the models with the pre-existing discontinuity, the node in the middle of the burden (b) was selected to the right of the discontinuity so that an estimation of the magnitude of the transmitted stress waves through the joint could be obtained (Figure 5b).

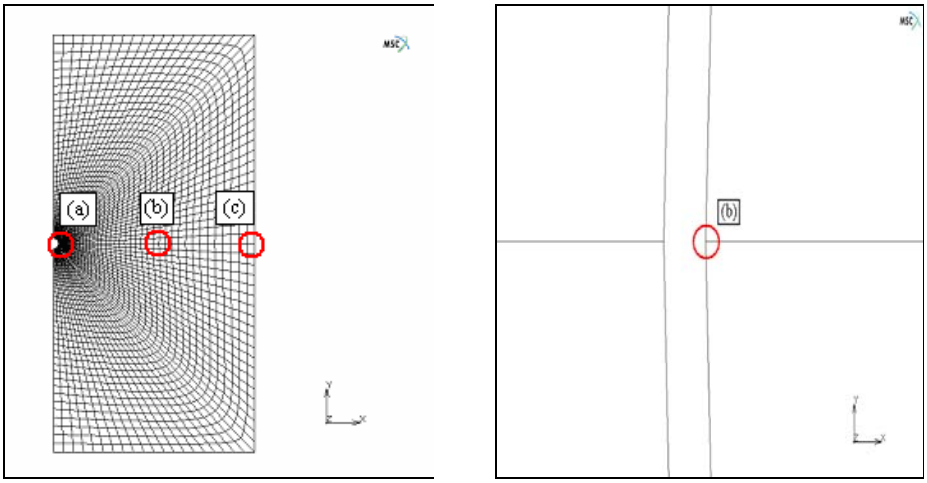

Figure 5. (a) Location of the studied nodes (b) Detail of center node

Figure 6 presents a typical distribution of the horizontal stress contours for the isotropic models with and without the pre-existing discontinuity respectively. Similar results were obtained for all models.

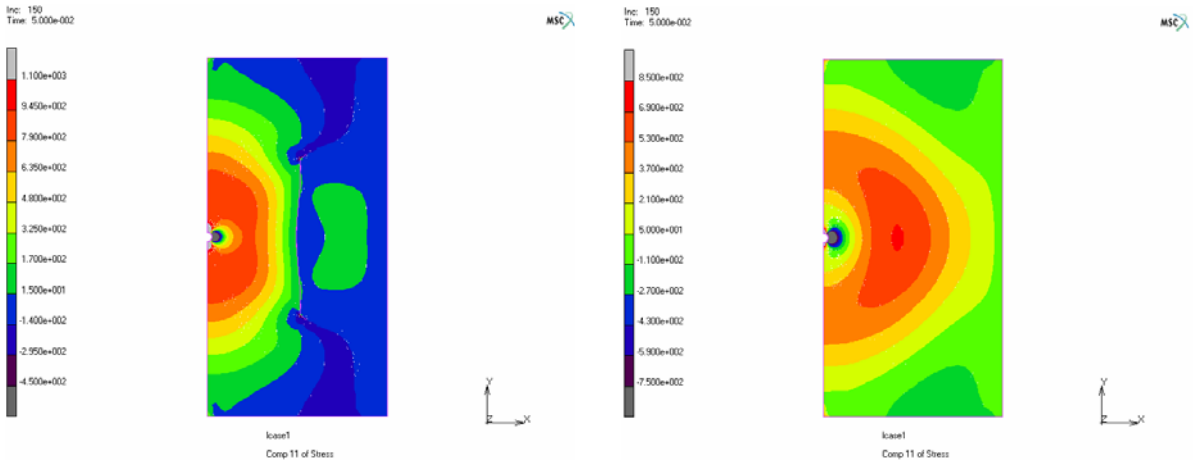

(a) (b)

Figure 6. Distribution of horizontal stress (σ_{11}) of the models without and with pre-existing discontinuity

Figure 7a presents the horizontal stress (σ_{11}) while Figure 7b presents the vertical stress (σ_{22}) versus time respectively for the nodes on the borehole. Positive values correspond to tension and negative values to compression. Figures 8ab and 9a,b present the horizontal stress (σ_{11}) and the vertical stress (σ_{22}) versus time respectively for the nodes at the middle of the burden and on the free surface for the case without any discontinuity for all three material models.

More specifically, Figure 7 presents the stress history of the explosive excitation. It is evident that the excitation profile is different for the cases of orthotropic media. Also, the stresses in the X direction remain compressive throughout the duration of the simulation, while the stresses in the transverse direction remain tensile. In Figure 8a the stress regime is compressive at the beginning of the event, but as time progresses, stresses become tensile. This is due to the tensile wave created by the reflection of the compressive stress at the free surface, which passes through the center node traveling towards the blasthole. Similarly in Figure 8b, the stress regime is compressive but becomes tensile at the end of the event duration. In the case where the X direction coincides with the weak material direction (Ortho Y) the stresses remain compressive at the end of the simulation. This suggests that more time is needed for such stresses to become tensile.

The transverse stress history depicted in Figures 9a,b shows that tensile stresses are predominant throughout the event at magnitudes capable of breaking the rock under tension. Again in the case of model Ortho Y (Figure 9b), it seems that tensile stresses are developed later in time during the event.

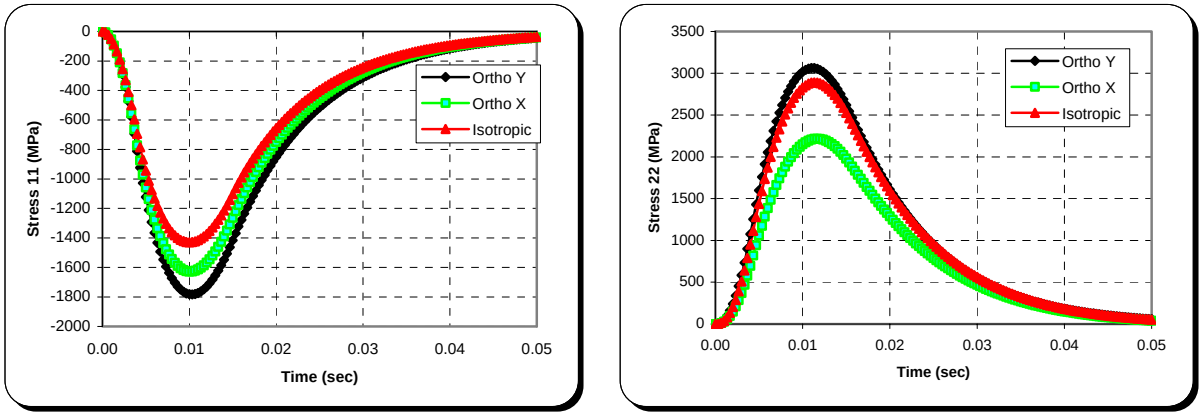

(a) (b)

Figure 7. Stress history of the nodes on the borehole for the stresses (σ_{11}) and (σ_{22}) respectively

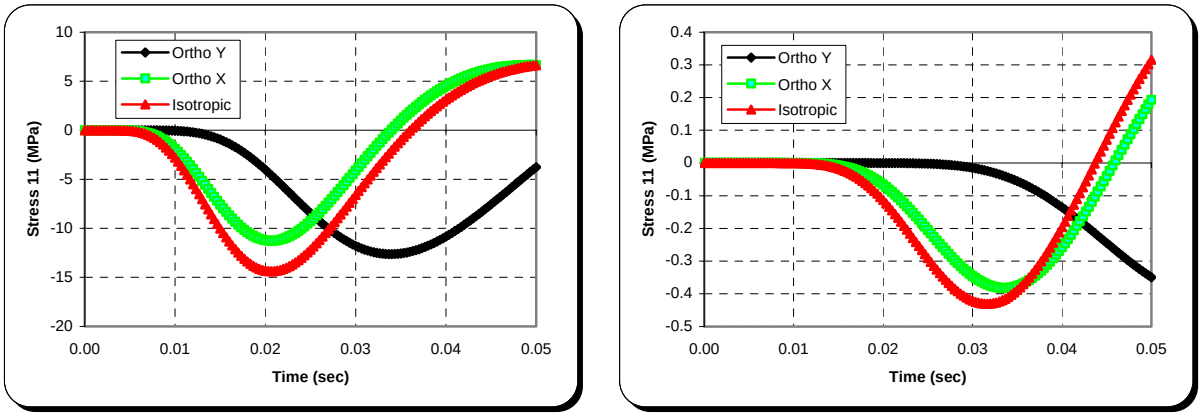

(a) (b)

Figure 8. Stress history (σ_{11}) of the nodes at a) 50% of the burden and b) on the free surface (no discontinuity)

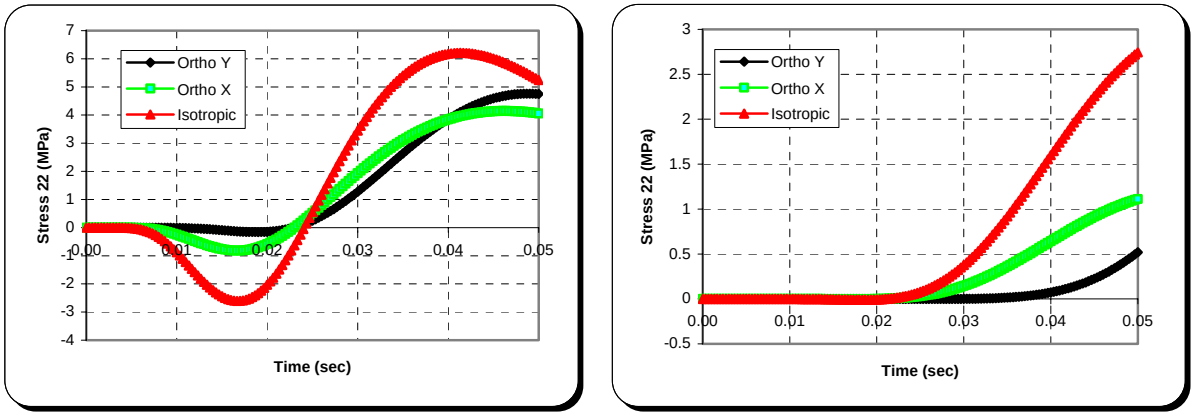

(a) (b)

Figure 9. Stress history (σ_{22}) of the nodes at a) the 50% of the burden and b) on the free surface (no discontinuity)

Figures 10a,b, present the horizontal stress history of the nodes (a) at the middle of the burden and (b) on the free surface, for the case which includes a pre-existing discontinuity (Figure 2) for all three material models. It should be noted that the horizontal and vertical stress history on the nodes on the borehole (excitation profiles) are exactly the same as those presented in Figure 7 for the models without discontinuity.

More specifically, Figure 10a presents the magnitude of the horizontal compressive stress wave that passes through the discontinuity. The stress magnitude is in the same order of magnitude as in the previous case but it is lower in value, which shows that for the specific discontinuity geometry, the crack has closed and has allowed enough energy through. Figure 10b presents the magnitude of the stress wave as it hits the free surface. Again it can be observed that the stress values are in the same order of magnitude after passing through the discontinuity (but are diminished compared to the intact media)

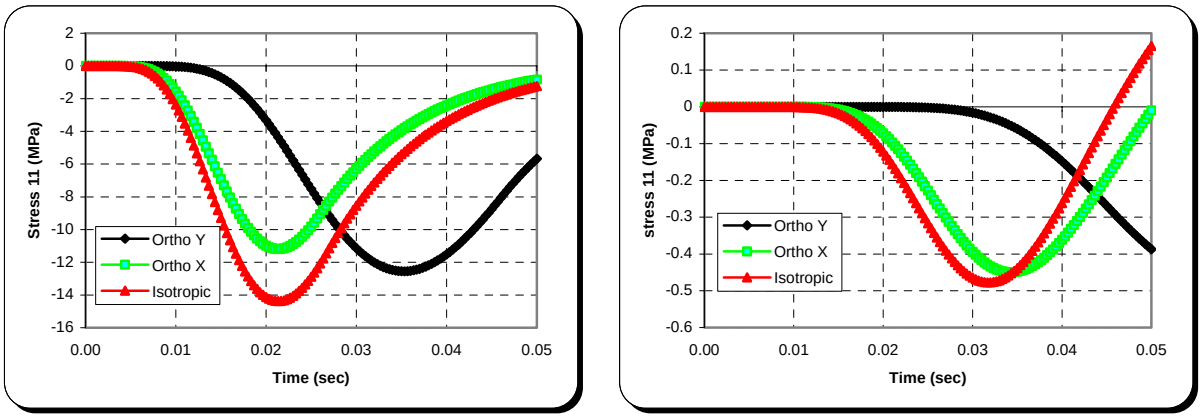

(a) (b)

Figure 10. Stress history (σ_{11}) of the nodes at a) the 50% of the burden and b) on the free surface (with discontinuity)

Similarly, Figure 11a presents the magnitude of the vertical stress wave that passes through the discontinuity, while Figure 11b presents the magnitude of the vertical stresses that are generated at free surface. In this case, the presense of the discontinuity alters the shape of the profiles (no compression is evident at the center node, and no tension at the free surface node). Again, this can be interpreted in the sense that opposite stresses will be developed at a much later time and of less magnitude.

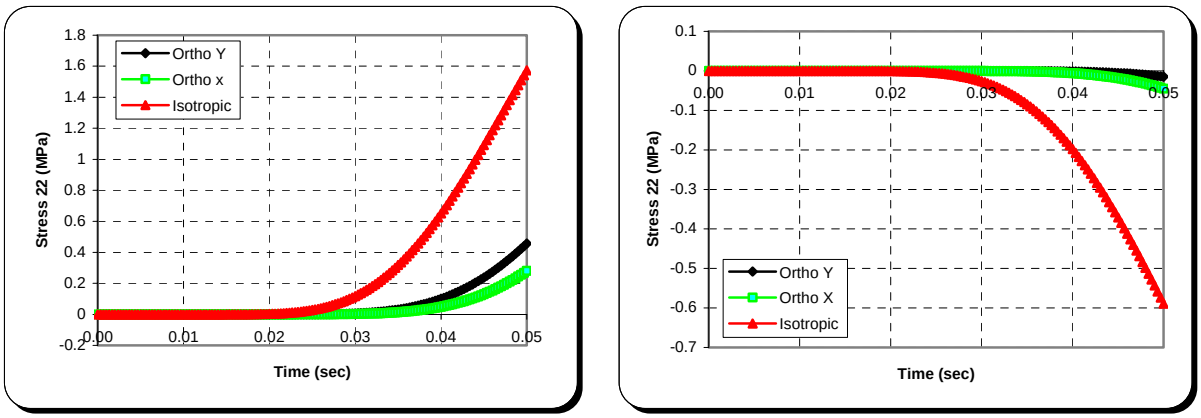

(a) (b)

Figure 11. Stress history (σ_{22}) of the nodes a) at the 50% of the burden and b) on the free surface (with discontinuity)

4. CONCLUSIONS

Three series of numerical models were created in order to simulate the dynamic phase of rock blasting under the influence of pre-existing discontinuities in isotropic and orthotropic media. Parameters include the duration of the dynamic phase and the profile of the initial pulse, the damping coefficients, the rock properties, the discontinuity properties, etc.

According to the simulation results regarding longitudinal and transverse stresses generated as the pulse propagates to the free surface, structure characteristics (e.g. joints) affect the properties of wave propagation in the jointed media. This is manifested either in the form of a) reduction of stress magnitudes and b) delay of the development of tensile or compressive stresses due to symmetry or reflection. In addition, it is shown than a single discontinuity is not capable of inhibiting the generation of tensile stresses that result in rock fragmentation.

Furthermore, additional work is needed to establish a discontinuity density and/or orientation at can adversely affect blasting fragmentation. Also, given the multitude of unknowns in a real life blasting operation, a parametric analysis as well as a sensitivity analysis can be very useful in establishing the critical parameters that affect this event.

5. REFERENCES

[1] Jimeno C.L., E.L. Jimeno, and F.J.A. Cardeco. (1995), "*Drilling and Blasting of Rocks*", Balkema, Netherlands.

[2] Bhandari, S. (1997), "*Engineering Rock Blasting Operations",* Balkema, Netherlands.

[3] Chen, E.P. (1989), "*A Constitutive Model for Jointed Rock Mass with Orthogonal Sets of Joints*", 56, pp. 25-32.

[4] Ning Li., Z. Ping, D. Qingwei, and G. Swobota. (2003), "*Dynamic Damage Model of the Rock Mass Medium with Microjoints*", International journal of damage mechanics, 12, pp. 163-172.

[5] Cook R., D. Malkus and M. Plesha. (1989), "*Concepts and Applications of Finite Element Analysis*", John Wiley and sons, New York.

[6] Sarris, E. and Z. Agioutantis, (2004), Numerical simulation of the dynamic phase during rock blasting, Mineral Wealth, 2004, vol. 133, pp. 9-18 (in Greek).

[7] Msc Engineering Group. (2000), "*Theory and User Information*", Marc-Mentat, Manuals.

5th GRACM International Congress on Computational Mechanics
Limassol, 29 June — 1 July, 2005

PINWHEEL MESHES FOR DYNAMIC FRACTURE SIMULATION

Katerina D. Papoulia[1], **Stephen A. Vavasis**[2] **and Pritam Ganguly**[3]

[1]School of Civil & Environmental Engineering
Cornell University
Ithaca, NY 14853, USA
kp58@cornell.edu

[2]Department of Computer Science
Cornell University
Ithaca, NY 14853, USA
vavasis@cs.cornell.edu

[3]Department of Theoretical & Applied Mechanics
Cornell University
Ithaca, NY 14853, USA
pg45@cornell.edu

Keywords: Pinwheel, mesh dependence, cohesive fracture, convergence, crack path, explicit dynamics

Abstract. *We consider the use of initially rigid cohesive interface models in a dynamic finite element solution of a fracture process. Our focus is on convergence of finite element solutions using rigid cohesive interfaces to a continuum solution as the mesh spacing Δx (and therefore time step Δt) tends to zero. We present pinwheel meshes, which possess the "isoperimetric property" that for any curve C in the computational domain, there is an approximation to C using mesh-cell edges that tends to C including a correct representation of its length, as the grid size tends to zero. We suggest that the isoperimetric property is a necessary condition for any possible spatial convergence proof in cohesive zone modeling in the general case that the crack path is not known in advance. Conversely we establish that if the pinwheel mesh is used, the discrete interface first activated in the finite element model will converge (as the mesh size tends to zero) to the continuum initial crack. We carry out mesh refinement experiments to check convergence of both nucleation and propagation. Our results indicate that the crack path computed in the pinwheel mesh is more stable as the mesh is refined compared to other types of meshes.*

1. RIGID COHESIVE MODELS

Cohesive zone modeling, which was originally proposed by Dugdale [3] and Barenblatt [1], and which was generalized and put in modern form by Rice [13], postulates that the separation of bulk material is resisted by cohesive forces governed by a constitutive model relating opening displacement to traction. Cohesive zone models are well suited for finite element analysis. The usual approach combines a volume mesh of bulk elements (to model the elastic or inelastic behavior of the undamaged material) with a network of cohesive elements that lie on some of the interfaces between the bulk elements. It is particularly natural to apply cohesive modeling to problems where defined interfaces exist. In such analyses, the fracture path is assumed *a priori* and can usually be justified by the nature of the problem (e.g., physical weak interfaces in delamination problems) or by experience gained from experiments (e.g., observations that fracture occurs frequently along inter-granular polycrystal boundaries). The interface elements are placed along the fracture path.

In applications where the crack pattern is not known in advance, notably in dynamic applications in the absence of bimaterial interfaces, interface elements cannot be prepositioned along the crack path. Instead, every edge of the bulk elements must be considered as a potential fracture surface, and the crack propagation path must be resolved as part of the solution of the governing equations. In this setting, an adaptive approach [2, 8] is often followed, in which cohesive surfaces are inserted as needed. The surface therefore is inactive prior to insertion and upon insertion is governed by the cohesive constitutive model. We call this type of model initially rigid or simply rigid (also called extrinsic [6]).

The crack path in this finite element model is composed of activated interfaces all of which lie on boundaries of cells in the initial mesh. A continuum crack path, on the other hand, has no such constraint. Allowing the crack to grow along element interfaces only, introduces obvious mesh dependence, which, if not addressed, may preclude convergence of the method as the mesh is refined. In what follows, the issue of the discrepancy between the true crack path and the discretized crack path of bulk element interfaces is considered, and a solution is proposed, namely, the pinwheel mesh. A theoretical convergence result is presented, and the paper concludes with a computational experiment.

2. REPRESENTING THE CRACK PATH IN THE MESH

To analyze the impact of mesh dependence, we must first consider the sense in which a discrete sequence of crack representations can converge to a continuum path. Note that a sequence P_i can converge to a path P in the Hausdorff sense, whereas $\mathrm{length}(P_i)$ converges to a quantity strictly greater than $\mathrm{length}(P)$. The Hausdorff distance between P_i and P is the maximum over all points $a \in P_i$ of the distance from point a to the closest point $b \in P$.An example like this is not pathological; indeed, failure of length to converge is the typical behavior for any family of structured meshes.

The length of the discrete versus continuum crack path is significant physically because the energy needed to create a crack is proportional to its length. This leads us to conjecture that a necessary condition for spatial convergence in cohesive modeling is that the sequence of meshes $\mathcal{M}_1, \mathcal{M}_2, \ldots$ must contain a sequence of paths $P_1, P_2, \ldots$ such that $P_i \rightarrow P$ in the Hausdorff sense and such that $\mathrm{length}(P_i) \rightarrow \mathrm{length}(P)$, where P is the continuum crack solution.

To provide some evidence for this conjecture, we carried out a computational simulation of the experiment used by Kalthoff and Winkler [5] to study failure mode transition. In the setup shown in Fig. 1 a plate of high strength steel with two edge notches was impacted by a steel projectile with speed v_o. Two different modes of failure were observed as v_o was varied. At low impact speeds, the plate failed in a brittle manner with a crack propagating at an angle of about 70° counterclockwise with respect to the original notch. Ductile failure in the form of an adiabatic shear band occurred at high impact speeds, with the shear band forming ahead of the notch at an angle of about 10° clockwise. We only simulated the brittle fracture mode.

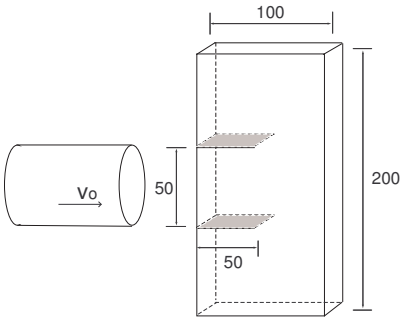

Figure 1: Schematic of the double edge-cracked specimen. Dimensions in mm.

To investigate the effect of mesh angles on the computed crack path, a 4mm $\times$ 8mm region ahead of the initial crack tip was discretized by a structured mesh consisting of rectangular cells, each subdivided into four triangles; the rest of the domain was covered with a gradually coarsened unstructured mesh to reduce computational time. The corresponding cells' height-to-width aspect ratios are 1.67, 1 and 0.6 respectively. A complete unstructured mesh was also used for comparison. Fig. 2 shows the fracture paths obtained with the four meshes. It is obvious that the results depend on the layout of the mesh. In particular, the 100×120 mesh and the unstructured mesh seem to best match the experiment, and these also are the meshes that have the best approximation to a 70° crack path.

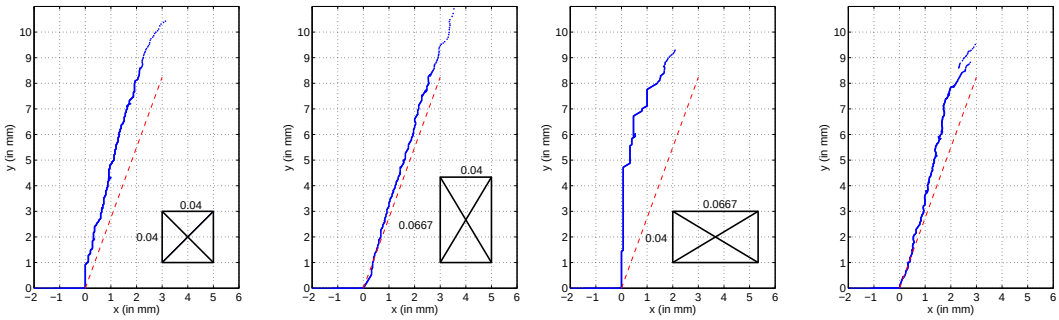

(a) 100×200 (b) 100×120 (c) 60×200 (d) unstructured

Figure 2: Fracture paths obtained with meshes having different aspect ratios. The dashed reference line is 70° counterclockwise from the origin.

3. PINWHEEL MESHES

As mentioned earlier, the goal of rigid cohesive modeling is often to solve problems in which the crack path is not known in advance but is an outcome of the simulation. Based on the results in the previous section, we conclude that if spatial convergence is desired, the family of meshes must represent every possible crack path both in the Hausdorff sense and in the sense of length. There is one family of meshes known to have this property, namely, pinwheel meshes in two dimensions. The pinwheel mesh is derived from Radin and Conway's [11] pinwheel tiling, which we now describe. The pinwheel tiling starts with a $1 : 2 : \sqrt{5}$ right triangle T_0 and subdivides it into five $1 : 2 : \sqrt{5}$ subtriangles that are similar to each other. See Fig. 3. This subdivision process may be repeated indefinitely, yielding a tiling of the original triangle with an arbitrary level of refinement. The distinction between a tiling and a mesh is that the triangles in a tiling are not required to meet edge-to-edge and therefore may have hanging nodes.

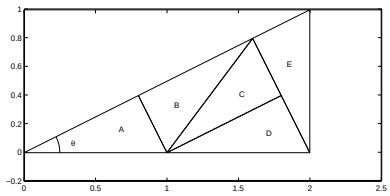

Figure 3: The basic pinwheel subdivision of a $1 : 2 : \sqrt{5}$ right triangle.

Radin and Sadun [12] have proved that the pinwheel tiling has the following isoperimetric property. Let $\mathcal{M}_1, \mathcal{M}_2, \ldots$ be the sequence of pinwheel tilings such that $\mathcal{M}_i$ repeats the construction in the previous paragraph to the ith level (and thus contains 5^i tiles). Let L be an arbitrary line segment in the initial triangle T_0. Then $\mathcal{M}_i$ contains a path L_i such that the L_i's converge to L in the Hausdorff and length sense. Their theorem extends easily to arbitrary curves, since any curve can be approximated in the two senses by a path of line segments, and then the line segments can be approximated by the mesh.

In recent work [4], we generalized the pinwheel tiling to arbitrary triangles (not only $1 : 2 : \sqrt{5}$) and showed how to use this generalization to create a mesh generator that possesses the isoperimetric property for arbitrary two-dimensional polygonal domains.

4. SPATIAL CONVERGENCE THEOREM

Rigid cohesive models defined on pinwheel meshes satisfy what we believe to be the necessary condition for spatial convergence, so we can now consider whether spatial convergence is indeed attained on these meshes. This question is far from trivial, since the presence of a path that approximates the continuum solution does not imply that a cohesive finite element model will find that path.

In this section we present a convergence result that is a first step toward a complete theory of spatial convergence. Our theorem covers only nucleation, i.e., the initial formation of a crack. Our setting for the continuum problem is as follows. We consider a two-dimensional body whose motion is governed by linear elastodynamics. We hypothesize that a crack nucleates in this body whenever the stress tensor first attains a principal value of σ_c, where $\sigma_c > 0$ is called the critical stress. We assume that the crack nucleates at the point where σ_c is first achieved. We hypothesize that its orientation is orthogonal to the dominant principal axis of the stress tensor at that point.

Our finite element model is the usual discretization of linear elasticity on triangles. We assume initially rigid cohesive interfaces at all element boundaries with an activation criterion that the normal traction on the interface reaches σ_c.

We also hypothesize that the sequence of meshes $\mathcal{M}_1, \mathcal{M}_2, \ldots$ has grid size tending to zero and is quasi-uniform. The sequence also has the following property. For every point x in the computational domain, for every angle θ, and for every $\epsilon > 0$, there is an $I > 0$ such that every mesh M_I, $M_{I+1}, \ldots$ contains an interface whose distance from x is at most ϵ and whose orientation is at most ϵ away from θ. Our pinwheel family of meshes have these properties. Note that these properties are different from, but apparently closely related to, the isoperimetric property.

Under all these assumptions plus a few more technical assumptions about smoothness, we prove that the first interface to activate in the discrete model converges to the continuum nucleation point in three senses: the location of the interface converges to the location of the continuum point, the orientation of the interface converges to the continuum nucleation orientation, and the time of nucleation converges to the continuum time. Our proof [10] is not difficult but is technical in the sense that it relies heavily on compactness arguments. Our theory does not extend to crack propagation. It would extend to three dimensions if a three-dimensional analog of pinwheel meshes could be constructed.

5. A MESH REFINEMENT STUDY

The setup of the study is of the compression compact specimen (CCS) impact-experiment used by Rittel et. el. [14, 7]. The schematic of the experiment is shown in Figure 4. The PMMA specimen is fractured by impacting with a Hopkinson bar, and the load at the bar-specimen interface can be measured and subsequently used for the boundary condition of our simulations. We investigate, through a series of simulations, the effects of different mesh layouts on the crack path. This setup is more suitable for a convergence study than the Kalthoff-Winkler experiment because the crack path is not a straight line segment, and therefore there is no structured mesh that exactly represents it.

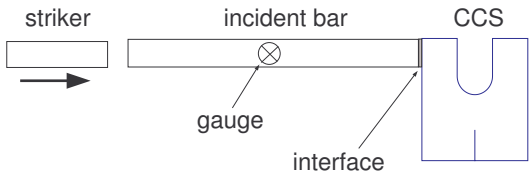

Figure 4: Schematic of compression compact specimen impact-experiment. The dimensions of the specimen are 51mm high 46mm wide, 11mm deep. The notch at the bottom is 12 mm long, and the U-shaped notch is 15mm wide and 27.5mm high.

Three mesh types—structured, unstructured, and pinwheel—are considered with several different levels of refinement repeated for each. Since this problem has no known analytic solution, a comparison of crack paths from different levels of refinement of the mesh seems to be the best approach for checking convergence.

The meshes in the crack-path zone are generated by mapping a mesh of a rectangle (either structured, unstructured, or pinwheel) via a curvilinear coordinate transformation. The three families of meshes of the crack-path zone are shown in Fig. 5. In each mesh family, there is a second parameter (besides degree of refinement) that can be varied, namely, the aspect ratio of the rectangle used as the domain of the coordinate transformation. In order to study mesh dependence, we consider variation of this second parameter. If a family of meshes leads to a convergent solution, then one expects that variation in this second parameter should matter less and less as the mesh is refined. On the other hand, if the solutions exhibit mesh-dependence (nonconvergence), then varying this parameter will continue to affect the solution to the same degree as the mesh is refined.

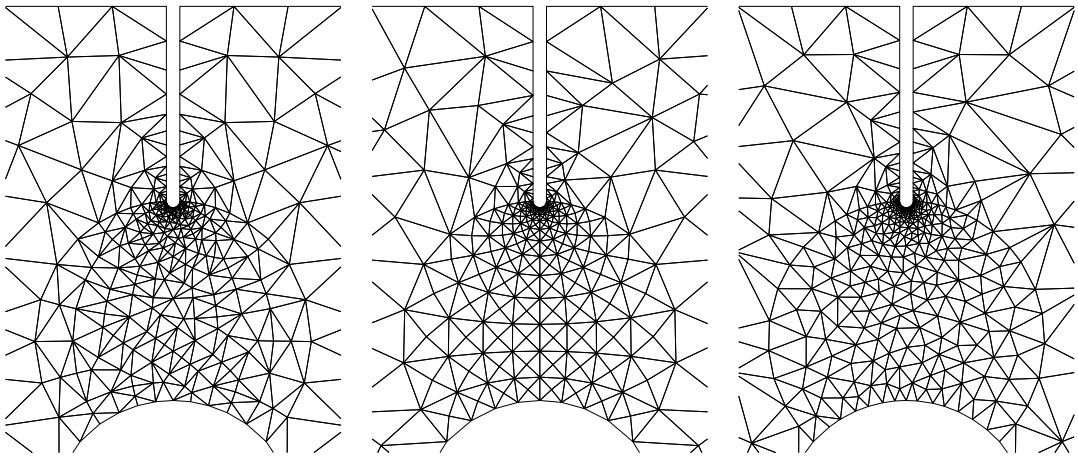

Figure 5: Diagrams of the crack-path zone meshes: (a) pinwheel, (b) structured, (c) unstructured. The portion of the mesh shown corresponds to the portion of the domain starting at the tip of the slit and connecting to the large U-shaped hole in the CCS specimen. These meshes were generated by mapping a pinwheel, structured and unstructured mesh of a rectangular region via a curvilinear coordinate transformation.

The cohesive model is the initially rigid model of [15] with $\sigma_c = 105$MPa, $G_c = .0048$MPa-m, $\beta = 1$. This model is time continuous, a property that leads to better behaved numerical solutions [9]. In Fig. 6, we observe that the crack paths in the fine mesh appear to be closer to each other than in the coarse mesh as desired. In contrast, the crack paths in the structured mesh shown in Fig. 7 and in Fig. 8 do not appear to be any closer in the fine mesh than they were in the coarse mesh, indicating a lack of spatial convergence.

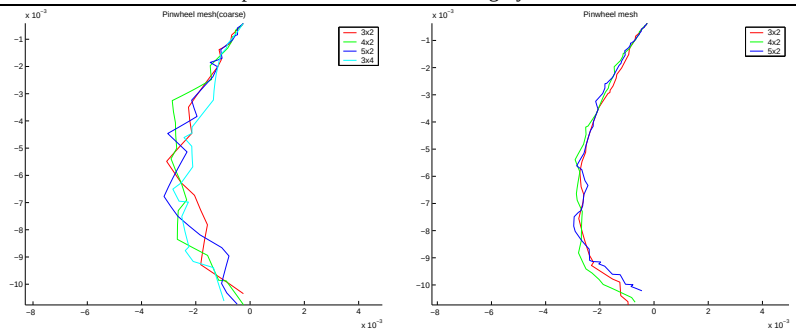

Figure 6: Crack path results for the pinwheel mesh: (a) coarse mesh and (b) fine mesh. The various paths illustrated in each plot correspond to different values for the aspect-ratio parameter of the mesh described in the text. The fine mesh shows less sensitivity to this parameter in the crack path than the coarse mesh.

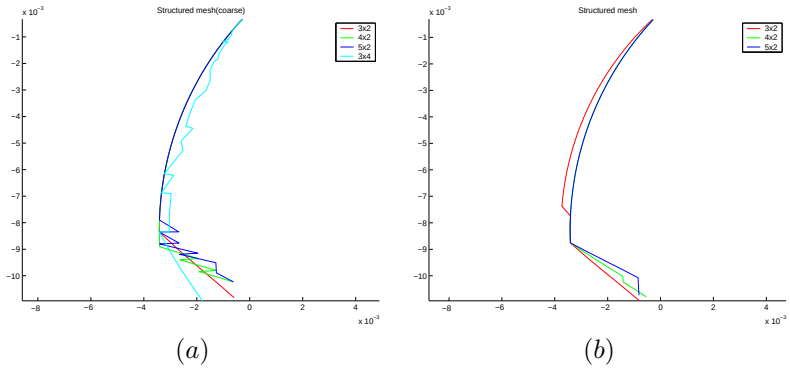

Figure 7: Crack path results for the structured mesh: (a) coarse mesh and (b) fine mesh. The various paths illustrated in each plot correspond to different values for the aspect-ratio parameter of the mesh described in the text. The coarse and fine meshes shows equal sensitivity to this parameter particularly in the lower part of the crack, indicating lack of convergence.

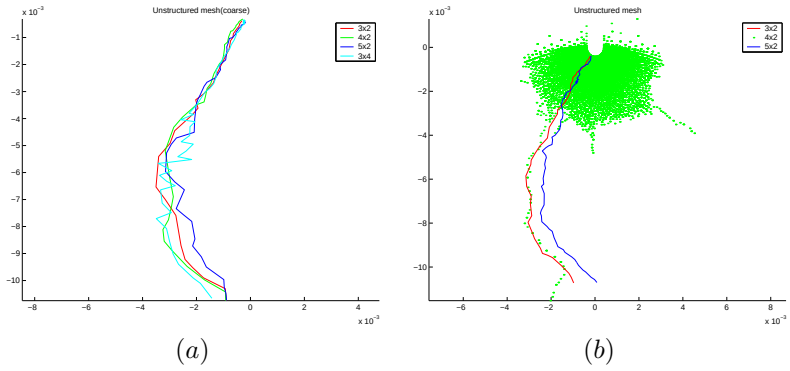

Figure 8: Crack path results for the unstructured mesh: (a) coarse mesh and (b) fine mesh. The various paths illustrated in each plot correspond to different values for the aspect-ratio parameter of the mesh described in the text. The coarse and fine meshes shows equal sensitivity to this parameter indicating lack of convergence. In the fine mesh, one of the choices of the parameter caused activation of many interfaces in a widespread zone of the material; this activation pattern is illustrated by the cloud of dots in (b).

Since our theoretical result applies only to the first active interface of the crack, we have also provided close-up pictures of the initial portion of the crack path for each of the three families of meshes. These zoomed-in views are shown in Figs. 9, 10, and 11. The initial portion of the crack shows convergent behavior for both the pinwheel and structured meshes. The latter result is not surprising since the initial part of the crack path in this case follows a mapped vertical grid line that is preserved in all the meshes. Therefore, the appearance of convergence in the

structured case is probably misleading. The unstructured figures seem to show no convergence of the initial portion of the path.

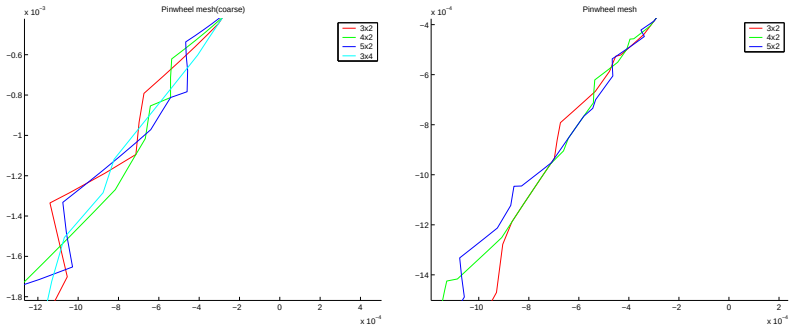

(a) (b)

Figure 9: Close-up view of crack path results for the pinwheel mesh: (a) coarse mesh and (b) fine mesh. The various paths illustrated in each plot correspond to different values for the aspect-ratio parameter of the mesh described in the text. The fine mesh shows less sensitivity to this parameter in the crack path than the coarse mesh.

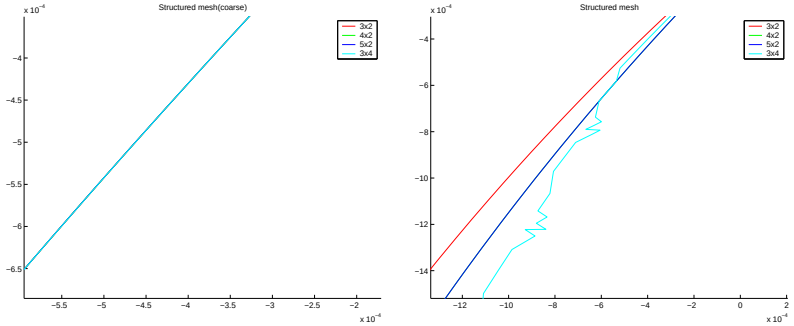

(a) (b)

Figure 10: Close-up view of crack path results for the structured mesh: (a) coarse mesh and (b) fine mesh. The various paths illustrated in each plot correspond to different values for the aspect-ratio parameter of the mesh described in the text. These meshes show complete agreement of the initial portion of the crack path, but this agreement is an artifact of the mesh generation procedure: the vertical gridlines in the structured mesh of the rectangle are preserved in all meshes shown.

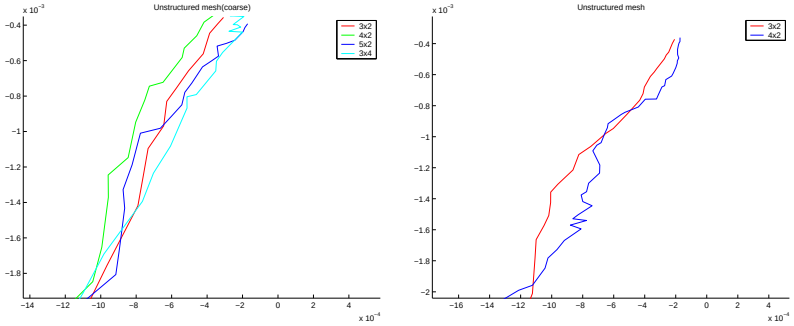

(a) (b)

Figure 11: Close-up view of crack path results for the unstructured mesh: (a) coarse mesh and (b) fine mesh. The various paths illustrated in each plot correspond to different values for the aspect-ratio parameter of the mesh described in the text. The coarse and fine meshes shows equal sensitivity to this parameter indicating lack of convergence. In the fine mesh, one of the choices of the parameter caused activation of many interfaces in a widespread zone of the material; this activation pattern is illustrated by the cloud of dots in (b).

References

[1] G. I. Barenblatt. The mathematical theory of equilibrium of cracks in brittle fracture. *Advances in Applied Mechanics*, 7:55–129, 1962.

[2] G. T. Camacho and M. Ortiz. Computatonal modeling of impact damage in brittle materials. *International Journal of Solids and Structures*, 33(29-22):2899–2938, 1996.

[3] D. S. Dugdale. Yielding of steel sheets containing slits. *Journal of the Mechanics and Physics of Solids*, 8:100–104, 1960.

[4] P. Ganguly, S. A. Vavasis, and K. D. Papoulia. An algorithm for two-dimensional mesh generation based on the pinwheel tiling. Submitted to SIAM J. Scientific Computing, 2004.

[5] J. F. Kalthoff and S. Winkler. Failure mode transition at high rates of shear loading. *International Conference on Impact Loading and Dynamic Behavior of Materials*, 1:185–195, 1987.

[6] D. V. Kubair and P. H. Geubelle. Comparative analysis of extrinsic and intrinsic cohesive models of dynamic fracture. *International Journal of Solids and Structures*, 40(15):3853–3868, 2003.

[7] H. Maigre and D. Rittel. Mixed-mode quantification for dynamic fracture initiation: application to the compact compression specimen. *International Journal of Solids and Structures*, 30(23):3233–3244, 1993.

[8] A. Pandolfi, P. Krysl, and M. Ortiz. Finite element simulation of ring expansion and fragmentation. *International Journal of Fracture*, 95:279–297, 1999.

[9] K. D. Papoulia, C.-H.Sam, and S. A. Vavasis. Time continuity in cohesive finite element modeling. *International Journal for Numerical Methods in Engineering*, 58(5):679–701, 2003.

[10] K. D. Papoulia, S. A. Vavasis, and P. Ganguly. Spatial convergence of crack nucleation using a cohesive finite element model on a pinwheel-based mesh. In preparation, 2005.

[11] C. Radin. The pinwheel tilings of the plane. *The Annals of Mathematics*, 139(3):661–702, 1994.

[12] C. Radin and L. Sadun. The isoperimetric problem for pinwheel tilings. *Communications in Mathematical Physics*, 177:255–263, 1996.

[13] J. R. Rice. Mathematical analysis in the mechanics of fracture. In H. Liebowitz, editor, *Fracture: An Advanced Treatise*. Academic Press, New York, 1968.

[14] D. Rittel and H. Maigre. A study of mixed-mode dynamic crack initiation in PMMA. *Mechanics Research Communications*, 23(5):475–481, 1996.

[15] C.-H. Sam and K. D. Papoulia. Obtaining initially rigid cohesive finite element models that are temporally convergent. To appear in Engineering Fracture Mechanics, 2005.

Mechanics of Materials

AN ANISOTROPIC HYPERELASTIC-VISCOPLASTIC DAMAGE MODEL FOR ASPHALT CONCRETE MATERIALS AND ITS NUMERICAL IMPLEMENTATION

Vassilis P. Panoskaltsis[1], Dinesh Panneerselvam[2]

[1] Department of Civil Engineering
Case Western Reserve University
10900, Euclid Ave. Cleveland, Ohio, 44106, USA
e-mail: vpp@nestor.cwru.edu,

[2]ABAQUS Great Lakes Inc, Plymouth, Michigan, USA.

Keywords: Hyperelasticity, anisotropy, viscoplasticity, damage, asphalt concrete, predictor-corrector algorithm, finite element analysis.

Abstract. *In this paper, numerical implementation and algorithmic aspects of a new multi-dimensional anisotropic hyperelastic-viscoplastic damage model, introduced by the authors, are presented. Anisotropy has been introduced into the model through a fabric tensor formulation. In the beginning, the governing equations of the model are developed. The paper then concentrates on the numerical and computational aspects of the complete anisotropic model. A robust integration algorithm for the nonlinear differential equations is described; also the algorithmic (consistent) tangent moduli are derived. The model is implemented into the finite element environment ABAQUS to study boundary value problems. The implementation is done through user subroutines UHYPER and UMAT. Triaxial and shear tests at constant height are studied as boundary value problems and model's predictions are compared to these experiments. Finally, a section of a pavement is studied as a boundary value problem to assess the capability of the model to predict accumulation of permanent deformations in the pavement.*

1 INTRODUCTION

Rutting, fatigue cracking and thermal cracking are the three most prominent distress mechanisms in asphalt concrete. In an industry wide survey, conducted by researchers at the University of Maryland, rutting was rated the most significant distress type regarding damage in pavements (Witczak[1], Christensen[2], Witczak[3]). A thorough understanding of the rutting phenomenon is required in order to improve pavement design and performance. Rutting is defined in ASTM Standard E 867 as "a contiguous longitudinal depression deviating from a surface plane defined by transverse cross slope and longitudinal profile". The longitudinal depressions (sometimes referred to as "ruts") are accompanied by upheavals to the side. In the asphalt – concrete layer, the rutting is caused by a combination of densification (compaction) and shear flow. The initial rut is caused by densification of the pavement under the path of the wheel. However, the subsequent rut is a result of shear flow of the mix. In properly compacted pavements, it has been found that shear flow in asphalt – concrete layer is the primary rutting mechanism, see e.g. Eisenmann and Hilmer[4]. A great need for a constitutive model for asphalt – concrete exists in order to analyze and predict the rutting caused by this layer of the pavement. In this paper, a multi-dimensional constitutive model to describe the reversible and rate dependent permanent deformations in asphalt concrete is developed and also the numerical implementation of the model is presented.

2 CONSTITUTIVE MODEL

The proposed constitutive model is a hyperelastic viscoplastic model. Damage is also introduced into the model through effective stress theories as shown later in the paper. Asphalt mix exhibits volumetric/deviatoric coupling when subjected to shear loading. This coupling behavior is modeled using elasticity since the evolution of normal stresses is apparent from the very first cycles, see e.g. Sousa[5]. A second order hyperelastic model is chosen over first order linear elastic model as first order model would not capture the characteristic volumetric/deviatoric coupling in asphalt concrete. The viscoplastic component describes the rate dependent behavior and is based on Perzyna's theory of viscoplasticity.

2.1 Hyperelastic model

Materials whose elastic response function is restricted by the existence of strain energy functions are called hyperelastic materials. Eq. (1) describes a general hyperelastic constitutive law,

$$\sigma_{ij} = \frac{\partial W}{\partial \varepsilon_{ij}}, \tag{1}$$

where W is the elastic strain energy function and is a function of strain given as follows:

$$W = b_0 + b_1 I_1 + b_2 I_1^2 + b_3 I_1^3 + b_4 I_1 I_2 + b_5 I_2 + b_6 I_3, \tag{2}$$

where b_0, b_1, b_2, b_3, b_4, b_5, and b_6 are material constants and I_1, I_2, I_3 are the strain invariants. The model should be able to represent the material at its natural state. In other words, at zero strain state, the stress is equal to zero. This condition requires that the parameters b_0 and b_1 be equal to zero. From Eqs. (1) and (2), the stress tensor is given as

$$\sigma_{ij} = \frac{\partial W}{\partial I_1}\frac{\partial I_1}{\partial \varepsilon_{ij}} + \frac{\partial W}{\partial I_2}\frac{\partial I_2}{\partial \varepsilon_{ij}} + \frac{\partial W}{\partial I_3}\frac{\partial I_3}{\partial \varepsilon_{ij}} \tag{3}$$

$$\text{or } \sigma_{ij} = \left(2b_2 I_1 + 3b_3 I_1^2 + b_4 I_1\right)\delta_{ij} + \left(b_5 + b_4 I_1\right)\varepsilon_{ij} + b_6 \varepsilon_{im}\varepsilon_{mj}. \tag{4}$$

Eq. (4) represents a second order hyperelastic stress strain relation. To determine the material parameters in the second order hyperelastic model, the tests conducted by Sousa et al.[6] at the University of California, Berkeley are used. The following three experiments: simple shear test, volumetric test and uniaxial strain compression test were conducted in the elastic range. In other words, the experiments were conducted at low strain levels to minimize the permanent strain effects and at low temperature (4^{o}C) to minimize the viscous effects. The model was made to fit simultaneously to all three experimental data obtained from the above mentioned experiments and parameters were evaluated based on a nonlinear optimization scheme. The objective function for the optimization procedure is the least square function constructed using the model predictions and experimental results. The optimization procedure is carried out using the optimization toolbox of the mathematical software MATLAB®, developed by Mathworks Inc. The model fit to experimental data is shown below in Figures 1, 2 and 3. With the values of parameters obtained from the optimization procedure the model's predictions of dilatancy are compared to experimental results. Figure 4 shows model's predictions of the axial force developed during the simple shear test. As the figure shows the model has the ability to predict dilatancy.

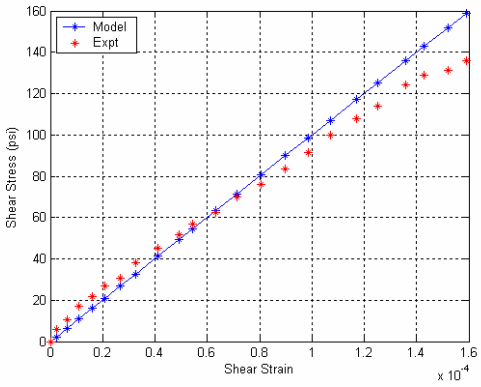

Figure 1. Shear Stress vs. Shear Strain.

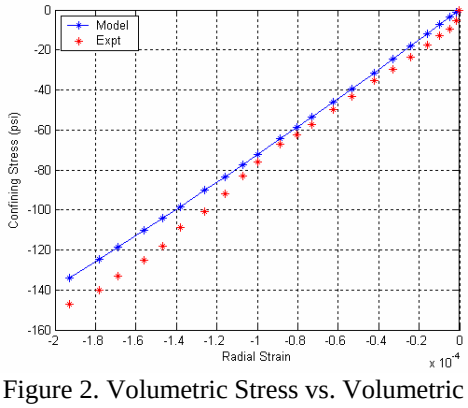

Figure 2. Volumetric Stress vs. Volumetric Strain.

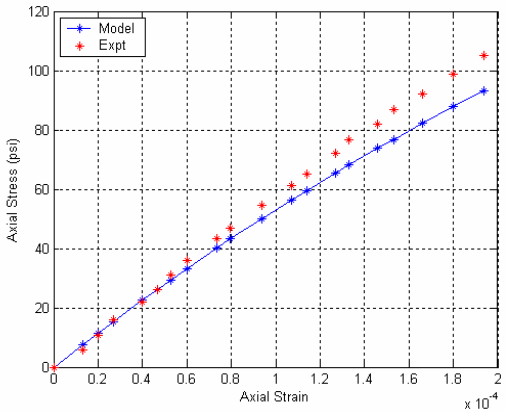

Figure 3. Axial Stress vs. Axial Strain.

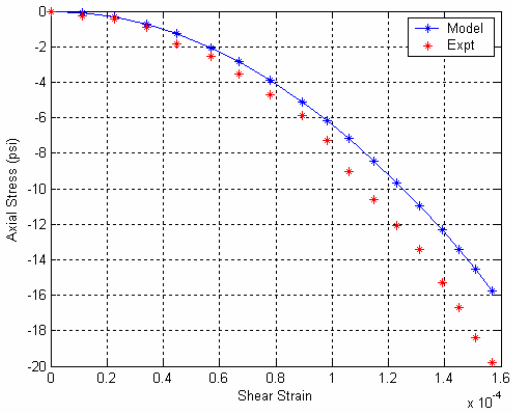

Figure 4. Axial Stress vs. Shear Strain.

2.2 Viscoplastic model

In this section, a viscoplastic model based on loading surface is proposed to describe the time dependent permanent deformations in asphalt concrete. The model is then appropriately modified to account for damage, in order to characterize the softening behavior of asphalt concrete, as well as for anisotropy. In a recent work by Bahuguna et al.[7] the evolution of permanent strains of asphalt concrete has been successfully modeled, but without taking into account rate effects. The basic aspects of the viscoplastic model are given below. The primary requirements in such models are the loading surface, the hardening law and the flow rule. The loading surface considered for the viscoplastic model is similar to the Vermeer type and is given by Eq. (5)

$$f = I_1 I_2 + \alpha I_3 - H\kappa, \tag{5}$$

where H is the hardening parameter, κ is the isotropic hardening variable and I_1, I_2 and I_3 are the invariants of the stress tensor. Flow rule, which represents the evolution of plastic strain in a deformation process is given by

$$\dot{\boldsymbol{\varepsilon}}^{vp} = \left(\frac{\langle f \rangle}{\eta}\right)^m \frac{1}{\left(x+\kappa^l\right)} \boldsymbol{\nu}, \tag{6}$$

where $\boldsymbol{\nu}$ is the normal to the viscoplastic potential, η is the temperature dependent viscosity parameter, κ is the hardening variable and x, l, and m are parameters. The normal to the viscoplastic potential, denoted by Ω, is given by

$$\boldsymbol{\nu} = \frac{\partial \Omega}{\partial \boldsymbol{\sigma}}. \tag{7}$$

In an associative flow rule the viscoplastic potential Ω is same as the loading function and the plastic flow is normal to the loading surface. Associative flow rule predicts excessive plastic dilatancy and to avoid this, a non-associative flow rule is assumed. The viscoplastic potential chosen here is of Drucker-Prager form and it is expressed as

$$\Omega = \sqrt{J_2} + \gamma I_1, \tag{8}$$

where J_2 is the second invariant of the deviatoric stress tensor and γ is a material parameter. History is taken into account through hardening. The evolution equation of the hardening variable is given by

$$\dot{\kappa} = \left(\frac{\langle f \rangle}{\eta}\right)^m \frac{1}{\left(x+\kappa^l\right)}. \tag{9}$$

The anisotropy which is due to the preferred orientation of aggregate particles, is included in the model through the so called fabric tensor ***F,*** which was first introduced by Oda and Nakayama[8]. The three dimensional fabric tensor is written in terms of a vector magnitude Δ as

$$\boldsymbol{F}=\begin{pmatrix}(1-\Delta)/(3+\Delta) & 0 & 0\\ 0 & (1+\Delta)/(3+\Delta) & 0\\ 0 & 0 & (1+\Delta)/(3+\Delta)\end{pmatrix}. \tag{10}$$

The vector magnitude Δ is an index measure to show the intensity of the preferred orientation of particles, it was first introduced by Curray[9] in 1956 and is defined as

$$\Delta=\frac{1}{M}\left[\sum_{k=1}^{M}\left(\cos 2\theta^{k}\right)^{2}+\sum_{k=1}^{M}\left(\sin 2\theta^{k}\right)^{2}\right]^{\frac{1}{2}}, \tag{11}$$

where θ^{k} is the inclination angle of a unit vector m^{k} corresponding to a k^{th} particle on a two dimensional section of the material and ranges between $\frac{-\pi}{2}$ and $\frac{\pi}{2}$ and *M* is total number of measurements. Anisotropy is incorporated into the model by appropriately modifying the loading function by introducing the fabric tensor in it. First, the stress invariants are modified as follows:

$$\overline{I_1}=a_1\sigma_{ii}+a_2F_{ij}\sigma_{ij}=a_1tr\left(\boldsymbol{\sigma}\right)+a_2tr\left(\boldsymbol{F}^{T}\boldsymbol{\sigma}\right) \tag{11}$$

$$\overline{I_2}=2b_6\sigma_{ik}\sigma_{jk}+4b_7F_{ik}\sigma_{kj}\sigma_{ij}=2b_6tr\left(\boldsymbol{\sigma}^{T}\boldsymbol{\sigma}\right)+4b_7tr\left(\left(\boldsymbol{F}^{T}\boldsymbol{\sigma}\right)^{T}\boldsymbol{\sigma}\right) \tag{12}$$

$$\begin{aligned}\overline{I_3}&=\left(c_1\sigma_{lj}\sigma_{nl}\sigma_{jn}+c_2F_{il}\sigma_{ij}\sigma_{nl}\sigma_{jn}\right)\\&=c_1tr\left(\boldsymbol{\sigma}^{3}\right)+c_2tr\left(\left(\boldsymbol{F}^{T}\boldsymbol{\sigma}\right)^{T}\left(\boldsymbol{\sigma}^{T}\boldsymbol{\sigma}\right)\right),\end{aligned} \tag{13}$$

where the operator *tr* denotes the trace of a tensor. Accordingly, the modified loading function is given by Eq. (15).

$$\overline{f}=\overline{I}_1\overline{I}_2+\alpha\overline{I}_3-Hk\,. \tag{14}$$

Damage is included in the model to capture the softening behavior exhibited by asphalt mixes. Effective stress theory, proposed by Kachanov, forms the basis for the damage model developed in this paper. The damage variable is a scalar denoted by ω and defined as

$$\omega=\frac{A}{A_0};\ 0\le\omega\le 1, \tag{15}$$

where A is the damaged area and A_0 is the undamaged original area. The damage variable is a positive, monotonically increasing function i.e. $\dot{\omega}>0$; in other words, the damage is irreversible. Effective stress given by σ_a is defined as

$$\sigma_a=\frac{\sigma}{1-\omega}, \tag{16}$$

where σ is the nominal stress. Following this principle, damage is incorporated in the model and stress invariants are modified accordingly as

$$I_1^{e}=\frac{\overline{I}_1}{1-\omega},\ I_2^{e}=\frac{\overline{I}_2}{\left(1-\omega\right)^{2}},\ I_3^{e}=\frac{\overline{I}_3}{\left(1-\omega\right)^{3}}\,. \tag{17}$$

Then the updated loading surface is given by

$$f^{e}=I_1^{e}I_2^{e}+\alpha I_3^{e}-Hk\,. \tag{18}$$

The damage variable is assumed to be a function of total plastic strain as follows,

$$\omega=d_1+d_2(\varepsilon^{p})^{d_3}, \tag{19}$$

where d_1, d_2, d_3 are parameters.

3 NUMERICAL IMPLEMENTATION OF THE MODEL

The complete model can be thought of as a model in series and accordingly, the total strain is additively decomposed into elastic and viscoplastic parts, i.e.

$$\boldsymbol{\varepsilon} = \boldsymbol{\varepsilon}^{e} + \boldsymbol{\varepsilon}^{vp} .$$

This decomposition is valid since the strains involved are small.

Let $[0,T] \subset R$ be the time interval of interest. At time $t_n \in [0,T]$ it is assumed that the total strain and viscoplastic strain fields, as well as internal variables are known, that is

$\boldsymbol{\varepsilon}_n$: *total strain tensor*

$\boldsymbol{\varepsilon}_n^{vp}$: *viscoplastic strain tensor*

κ_n : *isotropic hardening variable*

are given at time t_n. The elastic strain is then obtained by Eq. (21) as

$$\boldsymbol{\varepsilon}_n^{e} = \boldsymbol{\varepsilon}_n - \boldsymbol{\varepsilon}_n^{p} , \tag{20}$$

and the stress tensor is obtained using the elastic stress strain relationships,

$$\boldsymbol{\sigma} = \frac{\partial W(\boldsymbol{\varepsilon}^{e})}{\partial \boldsymbol{\varepsilon}^{e}}, \tag{21}$$

where *W* is the strain energy function introduced for the hyperelastic model. The stress components can be calculated using Eq. (21).

Let $\Delta \boldsymbol{u}_{n+1}^{i}$ be the incremental displacement field, which is assumed to be resulting from the i^{th} iteration of the global equilibrium equations at time step t_{n+1}. The basic problem is to update the field variables to $t_{n+1} \in [0,T]$ in a manner consistent with the elasto-viscoplastic constitutive equations developed previously. The problem is strain driven in the sense that the total strain tensor is updated according to

$$\boldsymbol{\varepsilon}_{n+1} = \boldsymbol{\varepsilon}_n + \nabla^{s}\left(\Delta \boldsymbol{u}_{n+1}^{i}\right). \tag{22}$$

where $\nabla^{s}(\bullet)$ denotes the symmetric gradient operator. The evolution equations for the continuum problem are transformed into discrete, algebraic equations by applying an implicit backward –Euler difference scheme, which is first order accurate and unconditionally stable. Applying the backward-Euler difference scheme and using initial conditions, a system of coupled nonlinear equations is obtained, which is given below.

$$\boldsymbol{\varepsilon}_{n+1}^{vp} = \boldsymbol{\varepsilon}_n^{vp} + \left(\frac{\left\langle f_{n+1}^{e} \right\rangle}{\eta}\right)^{m} \frac{\boldsymbol{\nu}_{n+1}}{x + \kappa_{n+1}^{l}} \Delta t , \tag{23}$$

$$\kappa_{n+1} = \kappa_n + \left(\frac{\left\langle f_{n+1}^{e} \right\rangle}{\eta}\right)^{m} \frac{1}{x + \kappa_{n+1}^{l}} \Delta t , \tag{24}$$

where Δt is the time step increment, i.e. $\Delta t = t_{n+1} - t_n$. These equations are supplemented by Eq. (21) and Eq. (22). This system of nonlinear coupled equations is solved under the general framework of predictor-corrector algorithm. The predictor phase consists of an elastic problem and the internal variables are assumed to be frozen. In the corrector phase, the internal variables evolve, and the total plastic strain and hardening parameter are updated to time step t_{n+1}. This is obtained as a solution of the evolution equations Eq. (23) and Eq. (24) by a Newton scheme (in multi dimension). See, Panneerselvam[10] for more details on the numerical implementation of the model. To complete the global procedure, the algorithmic tangent moduli, which are defined as the derivative of the stress tensor with respect to (total) strain tensor at time step t_{n+1} after convergence at the local level has been obtained, are calculated. See, e.g. Simo and Taylor[11], Simo and Hughes[12] and Panoskaltsis and Lubliner[13]. The algorithmic tangent moduli for the complete model are derived as follows:

$$\boldsymbol{C}_{alg}^{-1} = \frac{d\boldsymbol{\varepsilon}_{n+1}}{d\boldsymbol{\sigma}_{n+1}} = \frac{d\boldsymbol{\varepsilon}_{n+1}^{e}}{d\boldsymbol{\sigma}_{n+1}} + \frac{d\boldsymbol{\varepsilon}_{n+1}^{vp}}{d\boldsymbol{\sigma}_{n+1}} = \boldsymbol{D}^{-1} + \frac{d\boldsymbol{\varepsilon}_{n+1}^{vp}}{d\boldsymbol{\sigma}_{n+1}} \ , \tag{25}$$

where $\boldsymbol{D}$ is the Hessian matrix obtained from the hyperelastic model. Therefore, the algorithmic tangent moduli can be written as:

$$\boldsymbol{C}_{alg} = \left(\boldsymbol{D}^{-1} + \frac{d\boldsymbol{\varepsilon}_{n+1}^{vp}}{d\boldsymbol{\sigma}_{n+1}} \right)^{-1} . \tag{27}$$

The second term in the expression for $\boldsymbol{C}_{\text{alg}}$ is determined from Eqs. (24) and (25) as follows.

$$\frac{d\boldsymbol{\varepsilon}_{n+1}^{vp}}{d\boldsymbol{\sigma}_{n+1}} = \left(\frac{\left\langle f_{n+1}^{e} \right\rangle}{\eta} \right)^{m} \frac{1}{\left(x + \kappa_{n+1}^{l} \right)} \frac{d\boldsymbol{\nu}_{n+1}}{d\boldsymbol{\sigma}_{n+1}} \Delta t + \frac{m \left(\frac{\left\langle f_{n+1}^{e} \right\rangle}{\eta} \right)^{m-1} \frac{\boldsymbol{\nu}_{n+1} \Delta t}{\left(x + \kappa_{n+1}^{l} \right)} \frac{df_{n+1}^{e}}{d\boldsymbol{\sigma}_{n+1}}}{1 + \left(\frac{\left\langle f_{n+1}^{e} \right\rangle}{\eta} \right)^{m} \frac{\Delta t l \kappa_{n+1}^{l-1}}{\left(x + \kappa_{n+1}^{l} \right)^{2}} \Delta t} . \tag{28}$$

3.1 Results from finite element analysis

The numerical integration algorithm described so far can be implemented into a finite element environment in order to study boundary value problems. In our case the combined hyperelastic-viscoplastic-damage anisotropic model is implemented into the finite element program ABAQUS®, which is a commercial finite element code developed and marketed by ABAQUS Inc. The implementation is done through user subroutine modules UHYPER and UMAT. The repeated simple shear tests under constant height (RSST-CH) and triaxial experiments are modeled as boundary value problems and the results obtained from finite element analysis are compared to experimental results. In the triaxial experiments, performed by Tashman et al.[14] at Texas A&M University, cylindrical specimens of 4 in diameter and 6 in height are subjected to uniaxial stresses at different rates and different confining pressures. The specimens were loaded at three rates, namely at 46.42%/min, 8.03%/min, and 1.6%/min and at two confining pressures of 0 psi and 15 psi. The base of the cylinder is fixed and the top of the cylinder has displacement boundary conditions in the axial direction. The uniaxial compression tests are performed using displacement control in the axial direction. The results from the finite element analysis are compared to the experimental data and this is shown in Figure 5 and Figure 6 for 0 and 15 psi confining pressures respectively.

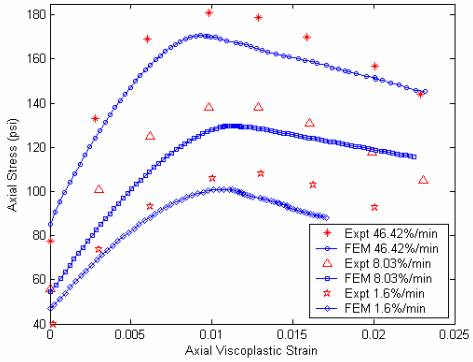

Figure 5. Axial stress vs. axial viscoplastic strain. Comparison of finite element results to experimental data at 0 psi confining pressure.

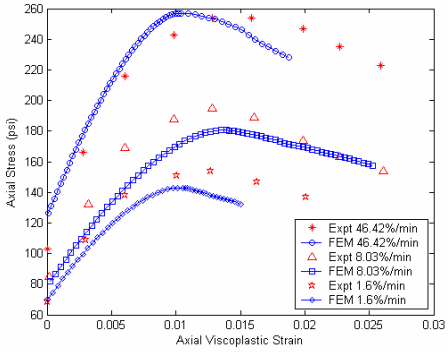

Figure 6. Axial stress vs. axial viscoplastic strain. Comparison of finite element results to experimental data at 15 psi confining pressure.

Next, the repeated simple shear test at constant height (RSST-CH) developed by Sousa et al. at the University of California, Berkeley, see e.g Sousa[6], is modeled and solved as a boundary value problem. In the RSST-CH experiment a cylindrical specimen of asphalt concrete is subjected to repeated shear loading, while the height of the specimen is kept constant. A haversine load of 0.05 s loading and 0.05 s unloading time is applied on a 0.2 in thick steel plate, which is glued to the cylindrical specimen of asphalt concrete of dimensions

6 in diameter and 2 in height. The asphalt specimen is subjected to cyclic shear loading at two different loading amplitudes, namely 8 psi and 10 psi. A striking characteristic of these experiments is that the accumulation of permanent strain with increasing number of cycles is a straight line on a log-log scale. The evolution of permanent shear strain with number of cycles predicted by the model is compared with the experimental data for the two loading amplitudes and the results are shown in Figure 7 in a log-log plot.

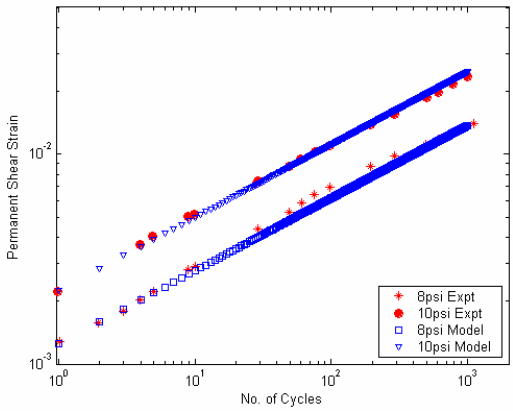

Figure 7. Evolution of permanent shear strain with number of cycles.

Next, a section of a pavement, subjected to repeated tire pressure loading, is studied as a boundary value problem under plane strain conditions. This is a two dimensional model in which the two wheel pressure loads have been simulated as continuous loading strips, consistent with the plane strain assumption. The boundary conditions used in the model are consistent with physical conditions of the pavement and also the symmetry in the road section has been used effectively; this results in more efficient computational time. The asphalt concrete layer is taken to be 15 in deep and rests on a 40 in deep subgrade. The bottom edge and also the sides of the subgrade are fixed. The width of the half pavement is 80 in and the width of the subgrade is 160 in. The outer edge of asphalt pavement is assumed to be unsupported and is free to deform. Traffic load is applied as two tire pressure loads of magnitude 100 psi; the wheel loads are 10 in wide and they have a distance equal to 12 in. The plane strain conditions, under which the complete model of the pavement section is studied, is a good assumption for a section of a highway where the traffic does not stop or start. A more complicated three dimensional pavement model could be used to represent pavement sections such as intersections, where traffic accelerates, decelerates or stands still. The asphalt concrete pavement is modeled using the anisotropic hyperelastic-viscoplastic-damage model developed in this work. The subgrade in reality is a granular material and a nonlinear material model would best represent its behavior. However, for simplicity and to keep the computational time down, the subgrade is modeled as a linear elastic material with elasticity modulus of 20000 psi and Poisson's ratio of 0.3; see Sousa et al[6]. Figure 8 shows the deformed shape of the pavement at the end of 15 cycles, magnified 100 times, and also the stress distribution in the pavement section. The figure shows permanently deformed shape and also shows the upheavals to the sides due to shear flow and dilation and is similar to those observed in rutted pavement sections. This simulation of rutting pattern illustrates the capability of the model to study boundary value problems representing pavement sections as well as model's potential for rational analysis and design of pavements.

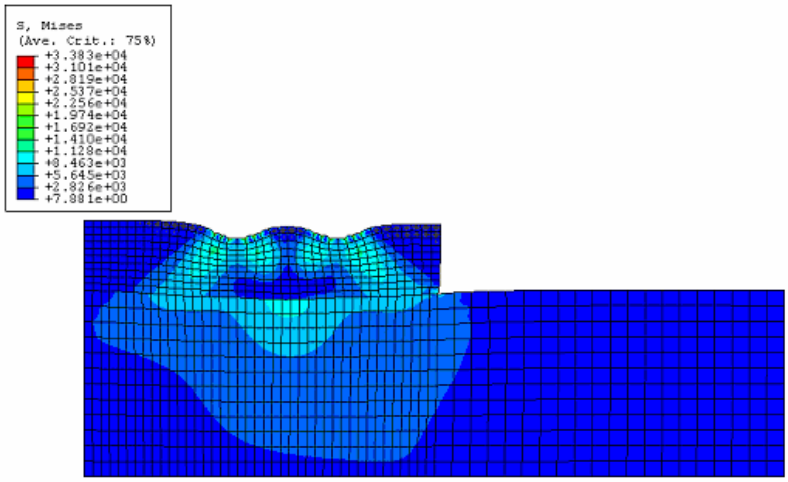

Figure 8. Stress distribution in the deformed pavement.

4 CONCLUSIONS

A new multi-dimensional anisotropic hyperelastic-viscoplastic-damage model has been developed in order to describe the permanent deformations and coupling behavior of asphalt concrete. The reversible component of the asphalt concrete response is modeled by a second order hyperelastic model, which captures the coupling behavior. Predictions of the hyperelastic model show good agreement with experimental results. The viscoplastic component depicts the rate-dependent behavior of the material and is based on Perzyna's theory of viscoplasticity. The constitutive model developed in this work also takes into account the anisotropy exhibited by the material and in addition it can describe damage. The model is implemented into the finite element environment ABAQUS® to study boundary value problems. The model predictions show good agreement with triaxial and RSST-CH experimental results modeled as boundary value problems. In addition, the model is capable of representing the pavement's rutting behavior.

REFERENCES

[1] Witczak, M.W., Bonaquist, R., Von Quintus, H. and Kaloush, K. (2000), "Specimen Geometry and Aggregate Size Effects in Uniaxial Compression and Constant Height Shear Tests", Journal, Association of Asphalt Paving Technologists, **69**, pp. 733 - 793.

[2] Christensen, D.W., Bonaquist, R., and Jack, D.P. (2000), "Evaluation of Triaxial Strength as a Simple Test for Asphalt Concrete Rut Resistance", Final Report prepared for Pennsylvania Department of Transportation, The Pennsylvania Transportation Institute, The Pennsylvania State University, University Park, PA.

[3] Witczak, M.W., Kaloush, K., Pellinen, T., El-Basyouny, M., and Von Quintus, H. (2002), "Simple Performance Test for Superpave Mix Design", NCHRP Report 465, Transportation Research Board, Washington, D.C.

[4] Eisenmann, J., and Hilmer, A. (1987), "Influence of Wheel Load and Inflation Pressure on the Rutting Effect at Asphalt Pavements – Experiments and Theoretical Investigations", *Proceedings of the Sixth International Conference, on Structural Design of Asphalt Pavements*, July, pp. 392-403.

[5] Sousa, J. (1994), "Experiments on Asphalt Concrete Mixes", Internal Report, SHRP Corporation, Walnut Creek, California.

[6] Sousa, J.B., Weissman, S.L., Sackman, J.L., and Monismith, C.L. (1993), "A Nonlinear Elastic Viscous with Damage Model to Predict Permanent Deformation of Asphalt Concrete Mixes", Transportation Research Record, 1384, pp. 80- 93.

[7] Bahuguna, S., Panoskaltsis, V.P., and Papoulia, K.D. (2005), "Identification and Modeling of Permanent Deformations of Asphalt Concrete", Journal of Engineering Mechanics, to appear.

[8] Oda, M., and Nakayama, H. (1989), "Yield Function for Soil with Anisotropic Fabric," Journal of Engineering Mechanics, 115(1), pp. 89-104.

[9] Curray, J.R. (1956), "Analysis of Two Dimensional Orientation Data", Journal of Geology, 64, pp. 117-131.

[10] Panneerselvam, D., *"Mechanics of Asphalt Concrete: Analytical and Computational Aspects"*, Ph.D. Dissertation, Department of Civil Engineering, Case Western Reserve University, Cleveland, Ohio.

[11] Simo, J.C., and Taylor, R.L. (1985), "Consistent Tangent Operators for Rate Independent Elastoplasticity," Computer Methods in Applied Mechanics and Engineering, 48, pp. 101-119.

[12] Simo, J.C., and Hughes, T.J.R. (1998), *Computational Inelasticity*, Springer-Verlag, New York.

[13] Panoskaltsis, V.P. and Lubliner J. (1991), "Integration Algorithm for Frictional Materials Including Plasticity, Damage and Rate Effects", in *Anisotropy and Localization of Plastic Deformation*, J.-P. Boehler and A.S. Khan eds., Elsevier, London, pp. 651-654.

[14] Tashman, L., Masad, E., Little, D., and Zbib, H. (2004), "Identification of Hot Mix Asphalt Permanent Deformation Parameters Using Triaxial Strength Tests and a Microstructure-Based Viscoplastic Continuum Model," Transportation Research Board, 83rd Annual Meeting, January 11-15, Washington, D.C.

ELASTODYNAMIC FUNDAMENTAL SOLUTIONS FOR 2D INHOMOGENEOUS ANISOTROPIC DOMAINS

G.D. Manolis, T.V. Rangelov†, and P.S. Dineva†

Department of Civil Engineering, Aristotle University, GR-54006 Thessaloniki, Greece
e-mail: gdm@civil.auth.gr, web page: http://www.civil.auth.gr

† Bulgarian Academy of Sciences, 1113 Sofia, Bulgaria

Keywords: Anisotropy, Elastic Waves, Fundamental Solutions, Inhomogeneous Media, Radon Transformation

Abstract. *The existence of frequency-dependent fundamental solutions for anisotropic, inhomogeneous continua under plane strain conditions is a necessary pre-requisite for studying wave motion in geological formations with both depth and direction-dependent material parameters. The path followed herein for recovering these solutions is to (a) use a simple algebraic transformation for the displacement vector so as to bring about a governing partial differential equation of motion with constant coefficients, albeit at the cost of introducing a series of constraints on the types of material profiles; (b) carefully examine the constraints, which reveals a rather rich range of possible variations of the elastic modulii in both vertical and lateral directions; and (c) use the Radon transformation for handling material anisotropy. Depending on the type of constraints that have been introduced, two basic classes of materials are identified, namely 'Class A', where further restrictions are placed on the elasticity tensor and 'Class B', where further restrictions are placed on the material profile. The present methodology is quite general and the homogeneous isotropic medium can be recovered as a special case.*

1 INTRODUCTION

The ability to model anisotropic, inhomogeneous materials is of paramount importance in many engineering fields such as acoustics, fluid and solid mechanics, electromagnetism, geophysics and seismology[1]. In general, there has been a surge of work in the last two decades regarding numerical work on elastodynamics of various types of man-made and naturally occurring media. A review of the literature can be found in some of the earlier papers by the present authors[2, 3, 4]. Specifically, there is relatively little work dealing with the combined inhomogeneous-anisotropic material. We mention here Ref. [5], where the dual-reciprocity BEM for elastostatic non-homogeneous problems was employed. Also, Refs. [6,7], investigated mode I crack problems in an inhomogeneous orthotropic medium, with the former work assuming static and the latter transient conditions. Finally, fracture of a plane FGM orthotropic strip containing an edge crack, as well as an internal crack perpendicular to the boundaries, was studied in Ref. [8]. To the author's best knowledge, in-plane elastic wave propagation problems involving inhomogeneous and anisotropic materials have not been treated so far.

The mathematical background behind wave motion in non-homogeneous media involves solution of partial differential equations with variable coefficients. In general, these equations do not possess explicit and easy to calculate fundamental solutions (or Green's functions), which prevents reduction of the physical boundary-value problem (BVP) to a system of boundary-integral equations (BIE) that is processed by standard numerical quadrature techniques. The key role played by the fundamental solution in a BEM formulation is to reduce a given BVP into a system of BIE through use of reciprocal theorems[9]. It is for this reason that the recovery of fundamental solutions in analytical form, or at least in an easy to calculate numerical form, is so important.

Thus, the aim of this work is to derive fundamental solutions for a point force in a domain whose material properties are dependent on both direction and position. Briefly, the main points are: (a) An algebraic transformation is applied to the displacement vector and the governing equations of motion now posses constant coefficients; (b) the Radon transformation reduces the system of coupled partial differential equations to a system of coupled ordinary differential equations; and (c) subsequent application of the inverse Radon transform yields the displacement fundamental solution in terms of an integral over the unit circle.

2 PROBLEM STATEMENT

Consider a Cartesian coordinate system Ox_1x_2 in R^2 and let Ω be an inhomogeneous anisotropic domain. This domain has mass density $\rho(x)$ and its mechanical behavior is defined through elastic tensor $C_{ijkl}(x)$, which is symmetric and positive definite:

$$C_{ijkl} = C_{jikl} = C_{klij} \tag{1}$$

Furthermore, $C_{ijkl} g_{ij} g_{kl} > 0$ for every nonzero, real and symmetric tensor g_{ij}. Assume now that all material parameters vary in the same fashion with coordinate $x = (x_1, x_2)$ as follows

$$C_{ijkl}(x) = C^0_{ijkl}\, h(x) \;,\; \rho(x) = \rho_0\, h(x) \tag{2}$$

where

$$h \in C^2(\Omega) \;,\; h(x) \geq h_0 > 0 \quad , \quad x \in \Omega \,. \tag{3}$$

The governing equations of motion for this domain, written in terms of displacement vector u_i, in the absence of body forces and under time-harmonic conditions, are as follows:

$$\sigma_{ij,j}(x,\omega) + \rho(x)\omega^2 u_i(x,\omega) = 0 \tag{4}$$

The stress tensor is defined here as $\sigma_{ij}(x,\omega) = C_{ijkl}(x)\;\; u_{k,l}(x,\omega)$, while $\sigma_{ij,j}$ are its spatial derivatives and ω is the frequency of vibration.

If eqn (4) is to be treated by BIE formulations, then a special BVP for a point load needs to be solved first in order to obtain a fundamental solution. These types of solutions, which besides being useful on their own right, form the basic ingredient (i.e., the kernel functions) of BEM formulations that have been most successful in dealing with problems involving semi-infinite domains. In general, if the coefficients of eqn (4), which is of the elliptic type, are analytical functions, then a fundamental solution exists. The corresponding BVP that yields the fundamental displacement tensor solution denoted by (*) is therefore

$$\sigma^*_{jki,i} + \rho\omega^2 u^*_{kj} = -e_{kj}\;\; \delta(x-\xi) \tag{5}$$

where $\sigma^*_{jki} = C_{jkpq}\, u^*_{ip,q}$, δ is Dirac's generalized function and e_{kj} is the unit tensor. Our aim is to identify a class of functions h and a range of values for constants $C^0_{ijkl}, \rho_0, \omega$ for which fundamental solutions $u^* = \{u^*_{kj}\}$ can be derived in closed form, suitable for numerical implementation within the BEM.

3. TRANSFORMATION OF THE GOVERNING EQUATIONS

We will employ the algebraic transformation used for isotropic materials in Ref. [10]. Specifically, eqn (4) transforms into an equation with constant coefficients, under some additional restrictions besides those given in eqn (3) for function $h(x)$. The key step is to introduce a smooth transformation of u_i in Ω as

$$u_i = h^{-1/2}(x) U_i \tag{6}$$

so that the homogeneous part of eqn (4) can be written in terms of the transformed displacement U_i as

$$C_{ijkl}(x)\left[U_{k,jl} + h^{-1/2}\left(h^{1/2}_{,j} U_{k,l} - h^{1/2}_{,l} U_{k,j} - U_k h^{1/2}_{,jl}\right)\right] + \rho(x)\omega^2 U_i = 0 \tag{7}$$

By reducing common factor $h(x)$ in both $C_{ijkl}(x)$ and $\rho(x)$, and using eqs (2)-(3), we obtain

$$C^0_{ijkl}\left[U_{k,jl} + h^{-1/2}\left(h^{1/2}_{,j} U_{k,l} - h^{1/2}_{,l} U_{k,j}\right) - h^{-1/2} h^{1/2}_{,jl} U_k\right] + \rho_0\omega^2 U_i = 0 \tag{8}$$

We will now specify additional constraints on h and C^0_{ijkl} under which eqn (8) has constant coefficients. Suppose there exist constants p_{ik}, q_i such that

$$C^0_{ijkl} h^{1/2}_{,jl} = p_{ik} h^{1/2} \quad \text{and} \quad \left(C^0_{i1k2} - C^0_{i2k1}\right)\; h^{1/2}_{,k} = q_i h^{1/2} \tag{9}$$

Then, expression $\left(-C^0_{ijkl} h^{-1/2} h^{1/2}_{,jl} U_k + \rho_0\omega^2 U_i\right)$ has constant coefficients with respect to U_i if

(a) $\quad C^0_{ijkl} h^{-1/2} h^{1/2}_{,jl} = p_{ik}$.

Also note that $C^0_{ijkl} h^{-1/2}\left(h^{1/2}_{,j} U_{k,l} - h^{1/2}_{,l} U_{k,j}\right) = C^0_{i1k2} h^{-1/2}\left(h^{1/2}_{,1} U_{k,2} - h^{1/2}_{,2} U_{k,1}\right) - C^0_{i2k1} h^{-1/2}\left(h^{1/2}_{,2} U_{k,1} - h^{1/2}_{,1} U_{k,2}\right) =$
$= C^0_{ik} h^{-1/2}\left(\nabla h \times \nabla U_k\right)$, where $C^0_{ik} = C^0_{i1k2} - C^0_{i2k1}$ and $(\times)$ denotes the vector product. This last expression has constant coefficients with respect to the gradient of transformed displacement ∇U_k if either

(b) $\quad C^0_{ik} = 0$, without additional constraints on h, or

(c) $\quad h^{-1/2}\nabla h^{1/2} = d$, where d is a constant vector, without additional constraints on C^0_{ijkl}.

In sum, eqn (9) is fulfilled either under combinations (a)&(b) or (a)&(c), in which case eqn (8) becomes a partial differential equation with constant coefficients.

We note here that combination (a)&(b) with $p_{ik} = 0$ was used in Ref. [11] for the elastostatic case. For the isotropic case, the first condition translates as $\lambda_0 = \mu_0$ for the Lame constants. Furthermore, condition (b) simply imposes additional symmetry on the elastic tensor, while condition (c) is essentially a restriction on the class of available functions h and on the domain Ω. For the orthotropic case and with the principal elastic axes parallel to the coordinate axes, $C_{16} = C_{26} = 0$ and the independent material constants are now four: $C_{11}, C_{12}, C_{22}, C_{66}$.

3.1 Material Profiles

Combination (a)&(b), labeled as '*Class A*', yields the following inhomogeneous material profiles:

(1) $h(x) = e^{2(\langle a,x\rangle + b)}$, where $\langle a,\ x\rangle = a_1x_1 + a_2x_2$ is the scalar product, in $\Omega = R^2$

(2) $h(x) = \sinh^2(\langle a,x\rangle + b)$, in the half-plane $\Omega_\delta = \{x,\ \langle a,x\rangle + b \ge \delta > 0\}$

(3) $h(x) = \cosh^2(\langle a,x\rangle + b)$, in $\Omega = R^2$

(4) $h(x) = \sin^2(\langle a,x\rangle + b)$, in the strip $\Omega_{\delta_1,\delta_2} = \{x, 0 < \delta_1 \le \langle a,x\rangle + b \le \delta_2 < \pi\}$

(5) $h(x) = \cos^2(\langle a,x\rangle + b)$, in the strip $\Omega_{\delta_1,\delta_2} = \left\{x, -\frac{\pi}{2} < \delta_1 \le \langle a,x\rangle + b \le \delta_2 < \frac{\pi}{2}\right\}$

(6) $h(x) = (\langle a,x\rangle + b)^2$, in the half-plane $\Omega_\delta = \{x,\ \langle a,x\rangle + b \ge \delta > 0\}$

For combination (a)&(c), labeled '*Class B*', the only possible example is again (1) $h(x) = e^{2(\langle a,x\rangle + b)}$ in $\Omega = R^2$.

3.2 Transformed Equations

By algebraically transforming eqn (5) using eqn (6) and conditions (9), we recover the following governing equation in lieu of eqn (8):

$$h^{1/2}(x)\left[M_{ik}(\partial^2) + N_{ik}(\partial) + \Gamma_{ik}\right]U^*_{ks} = -\delta_{is}\delta(x,\xi),\ \ (x,\xi) \in \Omega\times\Omega \tag{10}$$

where $M_{ik}(\partial^2) = C^0_{ijkl}\partial_j\partial_l$, $N_{ik}(\partial) = C^0_{ik}(q_1\partial_2 - q_2\partial_1)$ are differential operators and $\Gamma_{ik} = \delta_{ik}\rho_0\omega^2 - p_{ik} = \rho_0\omega^2 I_2 - P(q)$. Dividing eqn (10) by $h^{1/2}(x)$ and keeping in mind that $h^{-1/2}(x)\delta(x,\xi) = h^{-1/2}(\xi)\delta(x,\xi)$, since the support of $\delta(x,\xi)$ is on $\{x = \xi\}$, we obtain

$$\left[M_{ik}(\partial^2) + N_{ik}(\partial) + \Gamma_{ik}\right]U^*_{ks} = -\delta_{is}h^{-1/2}(\xi)\delta(x,\xi),\ \ (x,\ \xi) \in \Omega\times\Omega \tag{11}$$

The above is a system of two coupled linear partial differential equations of second order with constant coefficients, whose solution will be recovered by use of the Radon transformation.

4 RADON TRANSFORM

The Radon transform is a powered tool for deriving fundamental solutions of elastodynamics. As examples, see Ref. [12] for inclusion problems in 3D elastostatics, Ref. [13] for a steadily traveling point load on the surface of the half-space, and Ref. [14] for anisotropic homogeneous media. For completeness, we define the Radon transform[15], which is defined in R^2 for $f \in \Im$, the set of rapidly decreasing C^∞ functions, as follows:

$R(f) = \hat{f}(s,m) = \int\limits_{\langle x,m\rangle = s} f(x)dS = \int f(x)\delta\left(s - \langle x,m\rangle\right)dx$, $s \in R^1$, $m \in S^1$ is the direct transform and

$f(x) = R^{-1}(\hat{f}(s,m)) = R^*(K(\hat{f})) = R^*(\tilde{f}) = \frac{1}{4\pi^2}\int\limits_{|m|=1} K(\hat{f})(s,m)\Big|_{s=\langle m,x\rangle} dm$ is the inverse transform, where

$K(\hat{f}) = \int\limits_{-\infty}^{\infty} \frac{\partial_\sigma \hat{f}(\sigma,m)}{s-\sigma}d\sigma$. The transform is linear, and if $L(\partial)$ is a homogeneous differential operator of degree k with constant coefficients, then $R(L(\partial)f(x)) = L(m)\frac{\partial^k}{\partial s^k}\hat{f}(s,m)$. The Radon transform is defined on the space of distributions and $R(\delta(x,\xi)) = \delta(s - \langle m,\xi\rangle)$. Applying the Radon transform to both sides of eqn (11) yields

$$\left[M(m)\partial_s^2 + N(m)\partial_s + \Gamma\right]\ \hat{U}^*(s,m,\omega) = -h^{-1/2}(\xi)\delta(s - \langle m,\xi\rangle)\ \ I_2 \tag{12}$$

where I_2 is the unit matrix in R^2, $M = \{M_{ik}(m)\}$, $M_{ik}(m) = C^0_{ijkl}m_jm_l$, $N = \{N_{ik}(m)\}$, $N_{ik}(m) = C^0_{ik}(d\times m)$,

$\Gamma = \{\Gamma_{ik}(\omega)\}$, $\Gamma_{ik}(\omega) = \delta_{ik}\rho_0\omega^2 - p_{ik}$, and variable $m \in R^2$, $|m| = 1$ is the unit circle.

The above is a system of two second-order, ordinary differential equations with constant coefficients. Under the conditions specified in eqn (1), matrix M is symmetric and positive definite, matrix N is skew-symmetric and matrix Γ is symmetric. In order to solve eqn (12), we recover its canonical form by diagonalizing matrices M and Γ. Specifically, we start with the eigenvalues $\alpha_{1,2}(m) = \frac{1}{2}\left(\mathrm{Tr}M \pm \sqrt{(\mathrm{Tr}M)^2 - 4\det M}\right)$ of M, where Tr is the trace and det is the determinant. For an isotropic material, $\alpha_1 = \lambda + 2\mu$, $\alpha_2 = \mu$, while for the anisotropic material, $\alpha_{1,2}$ depend on m, $|m| = 1$. Next, let g_1, g_2 be the two corresponding normalized eigenvectors of M so that orthogonal matrix $G = \begin{pmatrix} g_1^1 & g_2^1 \\ g_1^2 & g_2^2 \end{pmatrix}$ transforms the basis to canonical form as $G^{-1}MG = A = \begin{pmatrix} \alpha_1 & 0 \\ 0 & \alpha_2 \end{pmatrix}$. Now define $\hat{U}^* = G\hat{V}$, in which case the transformed displacement vector $\hat{V}$ satisfies equation

$$\left[MG\partial_s^2 + NG\partial_s + \Gamma G\right]\hat{V} = -h^{-1/2}(\xi)\delta(s - \langle m, \xi\rangle)I_2 \tag{13}$$

Left-hand side multiplication of eqn (13) by G^{-1} gives

$$\left[A\partial_s^2 + N\partial_s + \Gamma_1\right]\ \hat{V} = -h^{-1/2}(\xi)\delta(s - \langle m, \xi\rangle)\ \ G^{-1} \tag{14}$$

where the commutative property of skew-symmetric matrix N and of orthogonal matrix G has been used to give $NG = GN$, along with the fact that $\Gamma_1 = G^{-1}\Gamma G$. Matrix A is strictly positive for every m, $|m| = 1$, so $A^{1/2}$ exists. A subsequent displacement vector transformation, denoted by $\hat{W} = A^{1/2}\hat{V}$, is introduced in eqn (13) yielding

$$\left[A^{1/2}\partial_s^2 + NA^{-1/2}\partial_s + \Gamma_1 A^{-1/2}\right]\ \hat{W} = -h^{-1/2}(\xi)\delta(s - \langle m, \xi\rangle)\ \ G^{-1} \tag{15}$$

An additional left-hand side multiplication of eqn (15) by $A^{-1/2}$ results in

$$\left[\partial_s^2 I_2 + Q\partial_s + \Gamma_2\right]\ \hat{W} = -h^{-1/2}(\xi)\delta(s - \langle m, \xi\rangle)\ \ A^{-1/2}G^{-1} \tag{16}$$

Observe $Q = A^{-1/2}NA^{-1/2}$ is skew-symmetric. Also, matrix $\Gamma_2 = A^{-1/2}\Gamma_1 A^{-1/2}$ is symmetric, has two real eigenvalues $\eta_{1,2}(m) = \frac{1}{2}\left(\mathrm{Tr}\Gamma_2 \pm \sqrt{(\mathrm{Tr}\Gamma_2)^2 - 4\det\Gamma_2}\right)$ and the corresponding normalized eigenvectors are e_1, e_2. Use of the orthogonal matrix $E = \begin{pmatrix} e_1^1 & e_2^1 \\ e_1^2 & e_2^2 \end{pmatrix}$ transforms the basis to canonical form as $E^{-1}\Gamma_2 E = R = \begin{pmatrix} \eta_1 & 0 \\ 0 & \eta_2 \end{pmatrix}$. A third (and final) displacement vector transformation, defined as $\hat{Z} = E^{-1}\hat{W}$, is introduced in eqn (16) resulting in

$$\left[\partial_s^2 E + QE\partial_s + \Gamma_2 E\right]\hat{Z} = -h^{-1/2}(\xi)\delta(s - \langle m, \xi\rangle)A^{-1/2}G^{-1} \tag{17}$$

As before, pre-multiplication of the above equation by E^{-1} yields

$$\left[\partial_s^2 I_2 + Q\partial_s + R\right]\hat{Z} = \delta(s - \tau)F \tag{18}$$

where $F = -h^{-1/2}(\xi)E^{-1}A^{-1/2}G^{-1}$, and $\tau = \langle m, \xi\rangle$. At this point, it is important to note that matrices $\Gamma_0 = M^{-1/2}\Gamma M^{-1/2}$ and Γ_2 have the same eigenvalues, namely η_1, η_2, since the characteristic polynomials of Γ_0 and Γ_2 are the same.

5 FUNDAMENTAL SOLUTION FOR *'CLASS A'* MATERIAL

With matrix $Q = 0$, eqn (18) assumes the form given below

$$\left[\partial_s^2 I_2 + R\right]\hat{Z} = F\delta(s - \tau)\ \ . \tag{19}$$

and because matrix R is diagonal, eqn (19) is uncoupled. As previously noted, since the elements η_j of matrix R are invariants, the eigenvalues of matrix $M^{-1/2}\Gamma M^{-1/2}$ depend on ρ_0, ω, p_{ik} and on m, $|m| = 1$. Using

Silvester's theorem and compactness arguments with respect to m, we ascertain that the number of positive, negative and zero eigenvalues is preserved. Therefore, the following five different sub-cases can be identified:

$$\text{(i) } \eta_1 \geq \eta_2 > 0 \text{ (ii) } \eta_1 > 0,\ \ \eta_2 = 0 \text{ (iii) } \eta_1 > 0,\ \ \eta_2 < 0 \text{ (iv) } \eta_1 = 0,\ \ \eta_2 < 0 \text{ (v) } 0 > \eta_1 \geq \eta_2 \tag{20}$$

The fundamental solutions corresponding to these five sub-cases behave differently. For instance, we note the possibility of double eigenvalues for arbitrary values of m for sub-cases (ii) and (iv). Which sub-case is actually realized depends on the elasticity constants (through matrix M), on the degree of inhomogeneity (through function h), on the density and on the frequency (through matrix Γ). For example, if matrix $P = \{p_{ik}\}$ is negative, only sub-case (i) materializes; if P is positive, then all five sub-cases can occur, with (i) corresponding to large values of frequency ω, (v) to small values of ω, and (ii)-(iv) to intermediate values of ω. In the quasi-homogeneous case, matrix $P = 0$ and only sub-case (i) can be realized[3]. In the purely homogeneous case, it is also true that $P = 0$ and two wave numbers are recovered as $k_j = \sqrt{\eta_j} = \sqrt{\dfrac{\rho_0}{\alpha_j(m)}}\omega$.

Finally, wave numbers k_j are independent of variable m in the isotropic case only.

Therefore, in view of the above, eqn (19) can be re-written as

$$\left[\partial_s^2 + \eta\right]\ \hat{v} = f\,\delta(s-\tau)\ \ ,\ \ f = h^{-1/2}(\xi)\, f_0(m,\omega) \tag{21}$$

where parameter η can be positive, zero or negative. In order to find the fundamental solution of eqn (11), which is one step away from the final form, we start by solving eqn (21) to recover $\hat{v}$ for different values of η. Next, we compute the first component of the inverse Radon transform as $\tilde{u} = K(\hat{v})$, which is subsequently integrated with respect to m, $|m| = 1$. This step completes the inverse Radon transformation and yields U^* in terms of the original basis functions $\tilde{u}$. It is also possible to compute the spatial derivatives of U^*. Finally, the simple algebraic transformation specified in eqn (6) produces u^*, the fundamental solution of the original equation of motion.

Using calculus of distributions, we recover $\hat{v}$ and $\tilde{u} = K(\hat{v})$ for the following three possibilities regarding parameter η:

(a) Possibility η is positive (superscript +):

Let $\eta > 0$, or $\eta = k^2$. Then, $\hat{v}^+ = \alpha e^{ik|s-\tau|}$, $\alpha = -\dfrac{if}{2k}$ and let $\gamma^+ = -\dfrac{f}{2}$. We compute

$$\left.\begin{aligned} \tilde{v}^+(s) &= K(\hat{v}^+) = \gamma^+\left[\cos kz - 2\left(ci(kz)\cos(kz) + si(kz)\sin(kz)\right)\right]\Big|_{z=|s-\tau|} \\ \partial_s\tilde{v}^+ &= \gamma^+\left[-k\cos kz - \frac{2}{z} + 2k\left(ci(kz)\sin(kz) - si(kz)\cos(kz)\right)\right]\Big|_{z=|s-\tau|}\ \operatorname{sgn}(s-\tau) \end{aligned}\right\} \tag{22}$$

where $\operatorname{ci}(p) = -\int_p^\infty \dfrac{\cos t}{t}dt$, $\operatorname{si}(p) = -\int_p^\infty \dfrac{\sin t}{t}dt$ are the cosine and sine integral functions, respectively.

(b) Possibility η is zero (superscript 0):

Let $\eta = 0$, and then $\hat{v}^0 = \dfrac{f}{2}|s-\tau|$, with

$$\left.\begin{aligned} \tilde{v}^0 &= K(\hat{v}^0) = f\,\ln z\big|_{z=|s-\tau|} \\ \partial_s\tilde{v}^0 &= -\frac{f}{z}\Big|_{z=|s-\tau|}\ \operatorname{sgn}(s-\tau) \end{aligned}\right\} \tag{23}$$

(c) Possibility η is negative (superscript -):

Let $\eta < 0$, $\eta = -k^2$, $k > 0$. Then $\hat{v}^- = \alpha e^{-k|s-\tau|}$, $\alpha = -\dfrac{f}{2k}$ and $\gamma^- = \dfrac{f}{2}$. We compute

$$\left.\begin{aligned} \tilde{v}^-(s) &= K(\hat{v}^-) = \gamma^-\left[ch(kz) + 2\left(chi(kz)ch(kz) - shi(kz)sh(kz)\right)\right]\Big|_{z=|s-\tau|} \\ \partial_s\tilde{v}^- &= \gamma^-\left[k\ \ sh(kz) + \frac{2}{z} + 2k\left(chi(kz)sh(kz) - shi(kz)ch(kz)\right)\right]\Big|_{z=|s-\tau|}\ \operatorname{sgn}(s-\tau) \end{aligned}\right\} \tag{24}$$

with $\mathrm{chi}(z)=\int_0^z \frac{ch\ \ t-1}{t}dt+\ln z,\quad z>0,\quad \mathrm{shi}(z)=\int_0^z \frac{sh\ \ t}{t}dt$ the hyperbolic cosine and sine integrals.

5.1 Inverse Radon Transform

Details regarding this procedure is given in Ref. [4]. The inverse Radon transform is

$$U^*=R^{-1}(\hat{U}^*)=\frac{1}{4\pi^2}\int_{|m|=1}\tilde{U}^*(z)\Big|_{z=|\langle m,x-\xi\rangle|}\ \ dm \tag{25}$$

By denoting $K(\hat{Z})=\begin{pmatrix} f_1^1\tilde{u}_1 & f_1^2\tilde{u}_1 \\ f_2^1\tilde{u}_2 & f_2^2\tilde{u}_2 \end{pmatrix}$ and $GA^{-1/2}E=\begin{pmatrix} t_1^1 & t_1^2 \\ t_2^1 & t_2^2 \end{pmatrix}$, eqn (25) for the fundamental solution and its spatial derivative assumes the form

$$\left.\begin{aligned} U^*(x,\xi)&=\frac{1}{4\pi^2}\int_{|m|=1}\begin{pmatrix} t_1^1 & t_1^2 \\ t_2^1 & t_2^2 \end{pmatrix}\begin{pmatrix} f_1^1\tilde{u}_1 & f_1^2\tilde{u}_1 \\ f_2^1\tilde{u}_2 & f_2^2\tilde{u}_2 \end{pmatrix}\Big|_{z=|\langle m,x-\xi\rangle|}\ dm \\ U^*_{,k}(x,\xi)&=\frac{1}{4\pi^2}\int_{|m|=1}\begin{pmatrix} t_1^1 & t_1^2 \\ t_2^1 & t_2^2 \end{pmatrix}\begin{pmatrix} f_1^1\partial_z\tilde{u}_1 & f_1^2\partial_z\tilde{u}_1 \\ f_2^1\partial_z\tilde{u}_2 & f_2^2\partial_z\tilde{u}_2 \end{pmatrix}\Big|_{z=|\langle m,x-\xi\rangle|}\ m_k\ \mathrm{sgn}(\langle m,x-\xi\rangle)\ dm \end{aligned}\right\} \tag{26}$$

where

$$\tilde{u}_j(s,m,\xi)=h^{-1/2}(\xi)\begin{cases} \tilde{u}_j^+ & ,\ \eta_j>0 \\ \tilde{u}_j^0 & ,\ \eta_j=0 \\ \tilde{u}_j^- & ,\ \eta_j<0 \end{cases}\quad\text{and}\quad \partial_s\tilde{u}_j(s,m,\xi)=h^{-1/2}(\xi)\begin{cases} \partial_s\tilde{u}_j^+ & ,\ \eta_j>0 \\ \partial_s\tilde{u}_j^0 & ,\ \eta_j=0 \\ \partial_s\tilde{u}_j^- & ,\ \eta_j<0 \end{cases}$$

The aforementioned five sub-cases are now

(i) $\tilde{u}_j=\tilde{u}_j^+$ (ii) $\tilde{u}_1=\tilde{u}_1^+,\ \tilde{u}_2=\tilde{u}_2^0$ (iii) $\tilde{u}_1=\tilde{u}_1^+,\tilde{u}_2=\tilde{u}_2^-$ (iv) $\tilde{u}_1=\tilde{u}_1^0,\ \tilde{u}_2=\tilde{u}_2^-$ (v) $\tilde{u}_j=\tilde{u}_j^-$

Following Ref. [3] and combining eqs (6) and (26), we obtain the two fundamental solutions for the original equation of motion, along with the necessary expressions for the spatial derivatives as follows:

$$\left.\begin{aligned} u_{ij}^*(x,\xi)&=h^{-1/2}(x)h^{-1/2}(\xi)U_{ij}^*(x,\xi) \\ \sigma_{ijk}^{*z}(x,\xi)&=h(z)C_{ijml}^0u_{mk,l}^{*z}(x,\xi),\ z=x\quad\text{or}\quad\xi \end{aligned}\right\} \tag{27}$$

where

$$\left.\begin{aligned} u_{mk,l}^{*x}(x,\xi)&=(h^{-1/2}(x))_{,l}h^{-1/2}(\xi)U_{mk}^*+h^{-1/2}(x)h^{-1/2}(\xi)U_{mk,l}^{*x} \\ u_{mk,l}^{*\xi}(x,\xi)&=(h^{-1/2}(\xi))_{,l}h^{-1/2}(x)U_{mk}^*+h^{-1/2}(x)h^{-1/2}(\xi)U_{mk,l}^{*\xi} \end{aligned}\right\} \tag{28}$$

6 INHOMOGENEOUS ISOTROPIC MATERIAL

We will illustrate the '*Class A*' material by considering a specific example involving the isotropic case, where inhomogeneity is of the form $h(x)=e^{2\langle q,x\rangle+q_0}$ (see section 3.1) with $q_1>0$, $q_2=q_0=0$. More details can be found in Ref. [4], along with an additional example addressing the '*Class B*' material.

All matrices involved in eqs (12)–(18) are given below for this specific type of material as

$$M(m)=\begin{pmatrix} (\lambda_0+2\mu_0)m_1^2+\mu_0m_2^2 & (\lambda_0+\mu_0)m_1m_2 \\ (\lambda_0+\mu_0)m_1m_2 & \mu_0m_1^2+(\lambda_0+2\mu_0)m_2^2 \end{pmatrix},\ P(q)=\begin{pmatrix} -(\lambda_0+2\mu_0)q_1^2 & 0 \\ 0 & -\mu_0q_1^2 \end{pmatrix}=-M(q),$$

$$N(m)=\begin{pmatrix} 0 & (\lambda_0-\mu_0)q_1m_2 \\ -(\lambda_0-\mu_0)q_1m_2 & 0 \end{pmatrix},$$

$$\Gamma(q,\omega)=\begin{pmatrix} \rho_0\omega^2-(\lambda_0+2\mu_0)q_1^2 & 0 \\ 0 & \rho_0\omega^2-\mu_0q_1^2 \end{pmatrix},\qquad A=\begin{pmatrix} \lambda_0+2\mu_0 & 0 \\ 0 & \mu_0 \end{pmatrix},\qquad G=\begin{pmatrix} m_1 & m_2 \\ -m_2 & m_1 \end{pmatrix},$$

$$Q(q,m)=\begin{pmatrix} 0 & \dfrac{(\lambda_0-\mu_0)}{\sqrt{\mu_0(\lambda_0+2\mu_0)}}q_1m_2 \\ -\dfrac{(\lambda_0-\mu_0)}{\sqrt{\mu_0(\lambda_0+2\mu_0)}}q_1m_2 & 0 \end{pmatrix}, \qquad R(m,\omega)=\begin{pmatrix} \dfrac{\rho_0\omega^2}{\lambda_0+2\mu_0}-q_1^2 & 0 \\ 0 & \dfrac{\rho_0\omega^2}{\mu_0}-q_1^2 \end{pmatrix} \text{ and}$$

$$F=-e^{-q_1\xi_1}\begin{pmatrix} \dfrac{1}{\sqrt{\lambda_0+2\mu_0}} & 0 \\ 0 & \dfrac{1}{\sqrt{\mu_0}} \end{pmatrix}\begin{pmatrix} m_1 & -m_2 \\ m_2 & m_1 \end{pmatrix}=-e^{-q_1\xi_1}\begin{pmatrix} \dfrac{m_1}{\sqrt{\lambda_0+2\mu_0}} & -\dfrac{m_2}{\sqrt{\lambda_0+2\mu_0}} \\ \dfrac{m_2}{\sqrt{\mu_0}} & \dfrac{m_1}{\sqrt{\mu_0}} \end{pmatrix}.$$

6.1 Analytical Results for '*Class A*' Material and Sub-cases

For this case, $\lambda_0=\mu_0$, $E=\begin{pmatrix}1&0\\0&1\end{pmatrix}$ and system of eqs (21) becomes

$$\begin{pmatrix} \partial_s^2+\dfrac{\rho_0\omega^2}{3\mu_0}-q_1^2 & 0 \\ 0 & \partial_s^2+\dfrac{\rho_0\omega^2}{\mu_0}-q_1^2 \end{pmatrix}\begin{pmatrix} \hat{v}_{11} & \hat{v}_{12} \\ \hat{v}_{21} & \hat{v}_{22} \end{pmatrix}=-e^{q_1\xi_1}\delta(s-\langle m,\xi\rangle)\begin{pmatrix} \dfrac{m_1}{\sqrt{3\mu_0}} & -\dfrac{m_2}{\sqrt{3\mu_0}} \\ \dfrac{m_2}{\sqrt{\mu_0}} & \dfrac{m_1}{\sqrt{\mu_0}} \end{pmatrix}.$$

All sub-cases (i)–(v) listed in eqn (20) can now be realized, depending on the actual values of material parameters μ_0, ρ_0, ω, q_1:

Sub-case (i): If $\dfrac{\rho_0\omega^2}{3\mu_0}-q_1^2>0$ and $\dfrac{\rho_0\omega^2}{\mu_0}-q_1^2>0$, then all four solutions of eqn (21) are as in case (+) (see eqn (20)).

Sub-Case (ii): If $\dfrac{\rho_0\omega^2}{3\mu_0}-q_1^2=0$, i.e., $q_1^2=\dfrac{\rho_0\omega^2}{3\mu_0}$, then $\dfrac{\rho_0\omega^2}{\mu_0}-\dfrac{\rho_0\omega^2}{3\mu_0}=\dfrac{2\rho_0\omega^2}{3\mu_0}>0$ and two solutions of eqn (21) are as in case (+), and two more are as in case (0) .

Sub-case (iii): If $\dfrac{\rho_0\omega^2}{3\mu_0}-q_1^2<0$, but $\dfrac{\rho_0\omega^2}{\mu_0}-q_1^2>0$, then two solutions of eqn (21) are as in case (-), and two more are as in case (+).

Sub-case (iv): If $\dfrac{\rho_0\omega^2}{3\mu_0}-q_1^2<0$, but $\dfrac{\rho_0\omega^2}{\mu_0}-q_1^2=0$, then two solutions of eqn (21) are as in case (-), and two more are as in case (0).

Sub-case (v): If $\dfrac{\rho_0\omega^2}{3\mu_0}-q_1^2<0$ and $\dfrac{\rho_0\omega^2}{\mu_0}-q_1^2<0$, then all four solutions of eqn (21) are as in case (-).

It is seen that we can control (theoretcally at least) the type of the fundamental solution we wish to recover by changing the value of the frequency ω.

7 CONCLUSIONS

In this work, the combined algebraic plus Radon transforms were applied to the governing time-harmonic equations of motion for the general anisotropic, inhomogeneous material under plane strain conditions for recovering fundamental solutions. The former transform addresses material inhomogeneity and yielded a finite number of material profiles that were compatible with the transform itself. The latter transform was then used to treat the equations of motion, which now posses constant coefficients, for a rather wide range of direction-dependent elastic parameters. Analytical results were derived for the type of material that was labeled as '*Class A*', while Ref. [4] gives additional information for materials belonging to '*Class B*'. Finally, numerical results will be communicated in a future publication. In closing, the aforementioned fundamental solutions may be used within the context of integral equation formulations as kernel functions for the solution of boundary-value problems involving realistic material profiles for geological as well as other types of continua.

Acknowledgement: The authors acknowledge the financial support from NATO Grant EST.CLG.980303.

REFERENCES

[1] De Hoop AT (1995) Handbook of Radiation and Scattering of Waves: Acoustic Waves in Fluids, Elastic Waves in Solids, Electromagnetic Waves, Academic Press, San Diego.
[2] Manolis GD, Rangelov TV, Shaw RP (2002) Conformal mapping methods for variable parameter elastodynamics, Wave Motion 36(2): 185-202.
[3] Manolis GD, Dineva PS, Rangelov TV (2004) Wave scattering by cracks in inhomogeneous continua using BIEM, International Journal Solids Structures 41(14): 3905-3927.
[4] Rangelov TV, Manolis GD, Dineva PS (2005) Elastodynamic fundamental solutions for 2D inhomogeneous anisotropic domains: Basic derivations, European Journal of Mechanics, submitted.
[5] Ang WT, Clements DL, Vahdati N (2001) A dual-reciprocity boundary element method for a class of elliptic boundary value problems for non-homogeneous anisotropic media, Engineering Analysis Boundary Elements 27: 49-55.
[6] Ozturk M, Erdogan F (1997) Mode I crack problem in inhomogeneous orthotropic medium, International Journal Engineering Sciences 35: 406-413.
[7] Chen J, Liu ZX, Zhou ZZ (2002) Transient internal crack problem for a nonhomogeneous orthotropic strip (mode I), International Journal Engineering Sciences 40: 1761-1774.
[8] Guo LC, Wu LZ, Zeng T, Ma L (2004) Mode I crack problem for a functionally graded orthotropic strip, European Journal of Mechanics A/Solids 23: 219-234.
[9] Beskos DE (1997) Boundary element methods in dynamic analysis: Part II, 1986-1996, Applied Mechanics Reviews 50(3): 149-197.
[10] Manolis GD, Shaw RP (1996) Green's function for a vector wave equation in a mildly heterogeneous continuum, Wave Motion 24: 59-83.
[11] Azis M, Clements D (2001) A boundary element method for anisotropic inhomogeneous elasticity, International Journal Solids Structures 38: 5747-5763.
[12] Franciosi P, Lormand G (2004) Using the Radon transform to solve inclusion problems in elasticity, International Journal Solids Structures 41: 585-606.
[13] Georgiadis HG, Lycotrafitis G (2001) A method based on the Radon transform for three-dimensional elastodynamic problems of moving loads, Journal of Elasticity 65: 87-129.
[14] Rangelov TV (2003) Scattering from cracks in an elasto-anisotropic plane, Journal Theoretical Applied Mechanics 33(2): 55-72.
[15] Zayed A (1996) Handbook of Function and Generalized Function Transforms, CRC Press, Boca Raton.

ELASTODYNAMIC F.E. ANALYSIS OF PILE RESPONSE FOR COMBINED HORIZONTAL AND VERTICAL SOIL HETEROGENEITY

George Mylonakis[*], Costis Syngros [†], and Thomas E. Price[††]

[*] University of Patras
Department of Civil Engineering
Patras, 26500, Greece
e-mail: mylo@upatras.gr

[†] Langan Engineering & Environmental Services, U.S.A.

[††] The City University of New York, New York, U.S.A.

Keywords: Finite Elements, Dynamics, Piles, Inhomogeneity, Damping

Abstract. *Most studies of dynamic pile response are restricted to homogeneous or horizontally-layered soil. This work considers a soil medium, which is inhomogeneous both vertically (with depth) as well as in the horizontal (radial) direction. Vertical inhomogeneity typically arises from sedimentation of soil particles forming layers and from overburden effects. On the other hand, radial inhomogeneity may arise from soil disturbance due to pile installation as well as from material nonlinearity due to pile loading. In this study, the problem is treated in the realm of linear elastodynamic theory by means of a rigorous finite-element formulation developed by the Authors. The study is concerned with the effect of this double soil inhomogeneity on: (1) pile head stiffness, (2) pile radiation damping, (3) modulus of equivalent Winkler springs and dashpots along the pile shaft. Swaying, rocking, and vertical oscillations are considered, arising from concentrated harmonic forces and moments imposed at the pile head. It is shown that ignoring soil inhomogeneity may substantially underestimate pile head stiffness and overestimate damping. On the other hand, modeling a vertically inhomogeneous deposit as a stiffness-equivalent homogeneous layer may grossly overestimate radiation damping leading to un-conservative predictions of dynamic pile movements. Implications of radiation damping effects in design are discussed.*

1 INTRODUCTION

The problem of determining the elastic settlement of a pile has been investigated extensively over the past decades, starting from the simple case of a single pile in homogeneous soil under static loading, and progressing to the more complicated cases of dynamic loading, inhomogeneous soil, and pile groups (Poulos, H. G. and Davis, E. H.[1]; Roesset, J. M.[2]; Novak, M.[3]; Mylonakis, G. and Gazetas, G.[4]; Randolph, M. F.[5], among others). Most early studies consider the static case for determining pile head settlement for design against gravity loads. More recently, the dynamic case has been analyzed for designing piles to support vibrating machines and/or resist earthquake and blast loads. To this end, a variety of theoretical methods has been developed (Kaynia, A. M. and Kausel, E.[6]; Novak, M.[3]). In most studies the supporting soil has been treated as homogeneous or horizontally layered with constant material properties within each layer. A more realistic assumption is perhaps that of combined vertical and horizontal inhomogeneity to account for the weakening of the soil in the vicinity of a pile due to installation and/or loading effects. Only a handful of studies on the effect of radial inhomogeneity are available today. Most of these efforts adopt simplified plane-strain models which cannot adequately capture salient features of the problem, such as static stiffness and cut-off frequencies (e.g., Novak, M. and Sheta, M.[7]; Veletsos, A. S. and Dotson, K. W.[8]; Han, Y. C. and Sabin, G. C. W.[9]; Michaelides, O. et al.[10]). Regarding combined vertical-horizontal inhomogeneity, no systematic investigations of its effect on dynamic pile response are available to date.

The available solutions indicate that radiation damping in the soil generally decreases as a result of inhomogeneity, leading to increased response at the pile head for a given dynamic load. These effects are expected to be stronger under combined vertical and horizontal inhomogeneity, having significant implications in design (Poulos, H. G.[11]; Novak, M.[3]; Syngros, C.[12]).

2 PROBLEM DEFINITION AND MODEL DEVELOPMENT

The system considered is depicted in Figure 1: A solid cylindrical pile of length L and diameter d embedded in a viscoelastic soil layer of thickness H over rigid or elastic bedrock, is subjected to an axial or lateral harmonic head force or bending moment. For the simulation of the pile and the surrounding soil, quadratic isoparametric triangular elements are used in axisymmetric mode. The mesh is designed to be finer close to the pile (where large stress gradients are anticipated), and coarser towards the boundaries. The change in element size is done accordingly.

A finite-element computer code named K-PAX has been developed (Syngros, C.[12]) to produce numerical results. In developing the code special modelling options have been incorporated, such as variable soil modulus within the elements, special transmitting boundaries to minimize wave reflections at the boundaries of the mesh, and a novel integration scheme to properly evaluate element stiffness close to the axis of symmetry.

Linear variation in Young's modulus within the elements is considered, by linearly interpolating the value of the modulus at the corner nodes. This is to better describe soil inhomogeneity and minimize potential wave reflections due to stiffness discontinuities at the interfaces between neighbouring elements. Since voids ratio and water content vary spatially much less than stiffness, mass density is considered constant within the elements.

The transmitting boundary developed by Kellezi, L.[13]) is adopted in this work. For the static case special infinite elements which exhibit superior accuracy over dynamic transmitting boundaries, were implemented following Marques, J. M. M. C. and Owen, D. R. J.[14]).

Concerning the integration of stiffness matrices close to the axis of symmetry, the Rational-Gauss stencil developed by Price, T. E.[15]) for the evaluation of the associated singular integrals is adopted. For more information the Reader is referred to the above study.

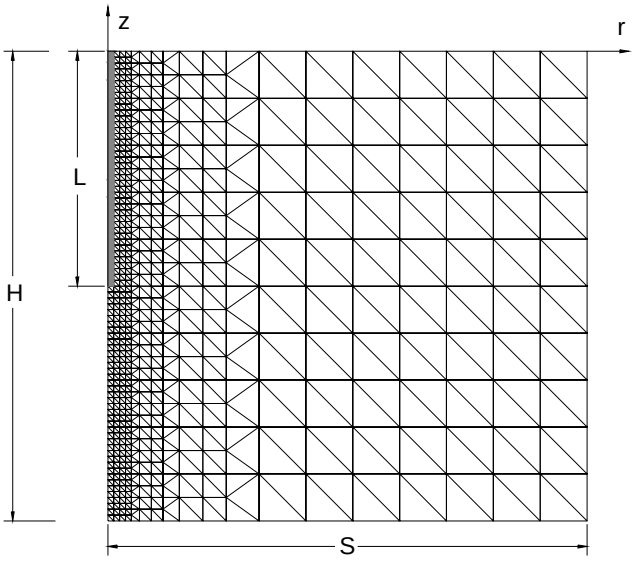

Figure 1. Typical F.E. mesh used in this study

3 FORMULATION OF RADIAL INHOMOGENEITY

3.1 Treatment of radial soil inhomogeneity

In their pioneering work, Novak, M. and Sheta, M.[7] model a radially inhomogeneous soil around an oscillating pile with a toroidal inner zone ("near-field") of reduced elastic properties, and an outer zone ("far-field") of constant properties using an axisymmetric plane-strain model. This formulation introduces a discontinuity in stiffness at the boundary of the two zones, thus making the results sensitive to both frequency and ring radius. In subsequent studies, Veletsos, A. S. and Dotson, K. W.[8] and Kim, Y.-S.[16] introduce a smooth transition of soil properties to the far-field by adopting concentric soil rings of increasing elastic properties. More recently, Han, Y. C. and Sabin, G. C. W.[9] Michaelides, O. et al.[10] and El-Naggar, M. H.[17] considered continuous variation of elastic soil properties with radial distance from the pile and derived solutions for the plane-strain axisymmetric oscillation mode.

Following Michaelides, O. et al.[10], the following simplified expression is adopted in this study:

$$E(r)/E_{\infty} = 1 - \{A\, d/2r\}^{3/4} \tag{1}$$

where E(r) = soil Young's modulus at distance r from the axis of symmetry and E_∞ = soil Young's modulus at infinity. A is a "load intensity factor" or, equivalently, a "radial inhomogeneity factor", encompassing the combined effects of soil plasticity, inertia, and interface action. In the parametric studies the values A = 0.1, 0.5 and 0.8 were used, corresponding to soil moduli at the pile-soil interface equal to approximately 80, 40 and 15 percent of the far-field modulus, respectively.

Four different profiles are utilized, as shown in Figure 2:

a) A homogeneous soil profile characterized by a constant soil modulus E_s

$$E_s\,(r,z) = E_s \tag{2}$$

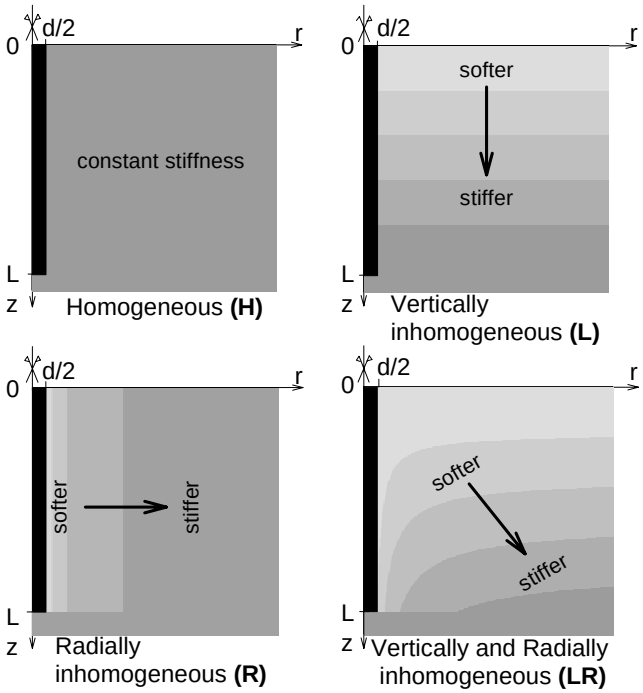

Figure 2. Soil profiles considered. In all profiles the soil stiffness under the pile tip is constant with depth.

b) A soil profile whose modulus increases proportionally with depth, z, up to a depth of one pile length (z = L) and remains constant for z > L

$$E_s(r, z) = E_{sL}\, z/L \tag{3}$$

c) A soil profile whose elastic modulus is constant with depth, but varies with radial distance from the pile, starting from a near-field value E_s and increasing to a limiting far-field value $E_{s\infty}$. The rate of modulus change with radial distance is given by eqs. (1) and (4). As in the case of the linear profile, soil modulus is constant underneath the pile tip, equal to $E_{s\infty}$.

$$E_s(r, z) = E_{s\infty}\,[1 - \{A\, d/2r\}^{3/4}] \tag{4}$$

d) A doubly inhomogeneous soil profile in which soil modulus varies linearly with depth, up to the depth of the pile tip (z = L), and with radial distance from the pile according to eq. (4). This is essentially a combination of the two previous cases and is characterized by a soil modulus $E_{sL\infty}$ taken at a depth of one pile length and infinite radial distance from the pile. Underneath the tip, soil has constant Young's modulus equal to $E_{sL\infty}$.

$$E_s(r, z) = E_{sL\infty}\,[1 - \{A\, d/2r\}^{3/4}] \tag{5}$$

The following dimensionless parameters are adopted in the simulations: a) pile slenderness ratio (L /d); b) pile-to-soil stiffness contrast (E_p /E_s). For a vertically inhomogeneous profile, the value of soil modulus at the pile tip E_{sL} is used for E_s. For the radially inhomogeneous profile, the far-field modulus $E_{s\infty}$ is used. For the

doubly inhomogeneous profile, the normalization is performed using the far-field value $E_{sL\infty}$ c) Pile-soil mass density contrast (ρ_p / ρ_s); d) material damping ratio β. Hysteretic damping $\beta_s = 0.05$ and $\beta_p = 0.01$ are considered in all analyses for the soil and the pile, respectively.

4 RESULTS

4.1 Dynamic pile-head stiffness

In the herein-reported analyses, pile-head stiffness is represented by a complex number $\mathbf{K}$ composed of a real and an imaginary part. Two alternative forms are used to this end:

$$\mathbf{K}_z = Re(\mathbf{K}_z) + Im(\mathbf{K}_z) = \mathbf{K}_z + i\,\omega C_z = \mathbf{K}_z (1+2i\beta) \tag{5}$$

in which K_z denotes the real part of the complex stiffness, ω is the oscillation frequency, C_z the pile-head damping and β an equivalent frequency-independent damping ratio. The above equation corresponds to the vertical oscillation mode. Analogous expressions can be written for the other modes. For details the reader is referred to Gazetas, G.[18] or Mylonakis, G. et al.[19]. In Figure 3 the real and imaginary part of dynamic pile stiffness are plotted against dimensionless frequency a_0 (= ω d/ V_s). Note that all soil profiles have the same properties at the far field. It is evident how radial inhomogeneity affects static and dynamic stiffness and damping – especially at high frequencies.

4.2 Stiffness equivalent soil profiles

To better understand the effect of soil inhomogeneity on radiation damping and pile displacement, the concept of stiffness-equivalent soil profiles is introduced. By this notion, two soil profiles may have different elastic properties at the far field, but provide common static pile-head stiffness. This concept is introduced to shed light on certain aspects of dynamic pile response, as influenced by soil inhomogeneity. In the following graphs, soil profiles having same static pile-head stiffness are referred to as *stiffness-equivalent*.

4.3 Effect of radial inhomogeneity on damping

Energy dissipation in an unbounded medium arises from two main sources: Material damping which describes energy consumed mainly through hysteretic action in the soil (such as friction between soil particles) and radiation damping which stands for energy radiated to infinity, as waves are emitted from the foundation and propagate in the unbounded medium. The latter effect has no counterpart in media of finite size.

From Eq. (5), the damping ratio apparent at the pile head can be cast in the following form:

$$\beta = \frac{Im(\mathbf{K}_z)}{2\,Re(\mathbf{K}_z)} = \beta_{(radiation)} + \beta_{(hysteresis)} \tag{6}$$

In Figure 4, pile-head damping is examined with reference to four stiffness-equivalent soil profiles. Dimensionless frequency a_0 is normalized with the shear wave velocity of the stiffness-equivalent homogeneous profile. The role of inhomogeneity in reducing radiation damping becomes evident in this plot. Note that increased inhomogeneity is associated with an increase in cut-off frequency. This yields substantial differences in radiation damping at low frequencies as compared to a homogeneous halfspace. Figure 4 shows that radiation damping is typically much less than damping estimated considering a homogeneous unbounded layer. This has important implications in design, since an actual profile is never perfectly homogeneous.

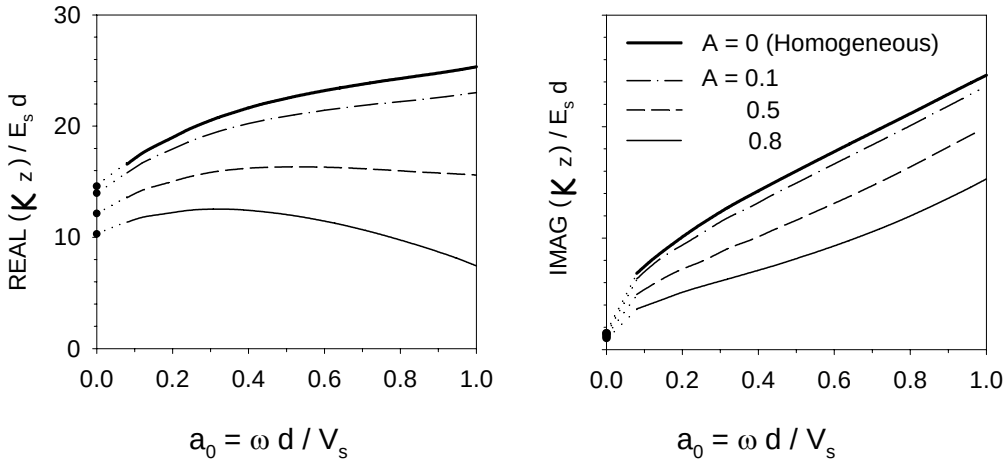

Figure 3. Normalized vertical dynamic stiffness of a floating single pile in a radially inhomogeneous halfspace; L / D = 40, E_p / E_s = 1000.

4.4 Equivalent Winkler springs along the pile shaft

It is of interest to investigate how soil stiffness and damping vary along the pile shaft. As mentioned earlier, a simple method for modelling the dynamic response of a pile is by replacing the soil by equivalent Winkler springs and solving the corresponding one-dimensional beam or rod on a dynamic elastic foundation problem. The associated Winkler modulus can be expressed as function of the near-pile elastic modulus of the soil material at the same depth

$$k(z) = \delta(z)\, Es(z) \tag{7}$$

where δ(z) is a dimensionless parameter.

Using K-PAX to determine the soil reactions and corresponding displacements at the pile-soil interface, the corresponding springs are calculated as force per unit pile length over displacement. Soil reaction is estimated by evaluating the normal stresses at the soil pile interface and integrating them over the pile surface. In Figure 5, normalized pile displacements, soil reactions and normalized Winkler moduli are plotted versus depth, for laterally-loaded fixed-head piles in four stiffness-equivalent profiles. The following are worthy of note:

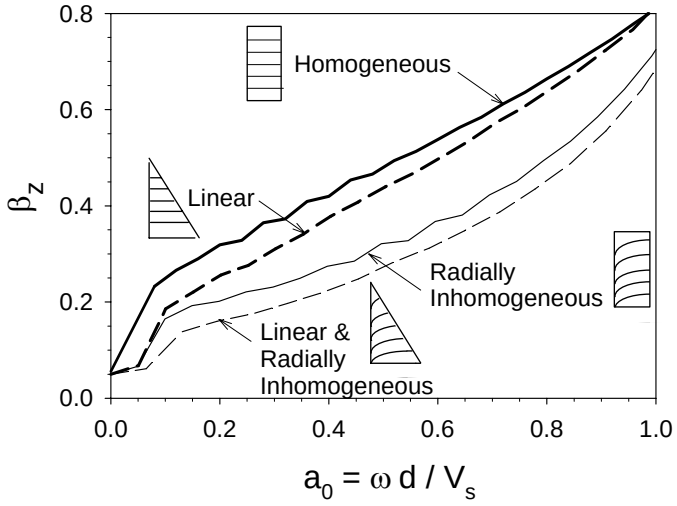

Figure 4. Damping ratio of a pile in four soil profiles. All piles have equal static stiffness; L / D = 20

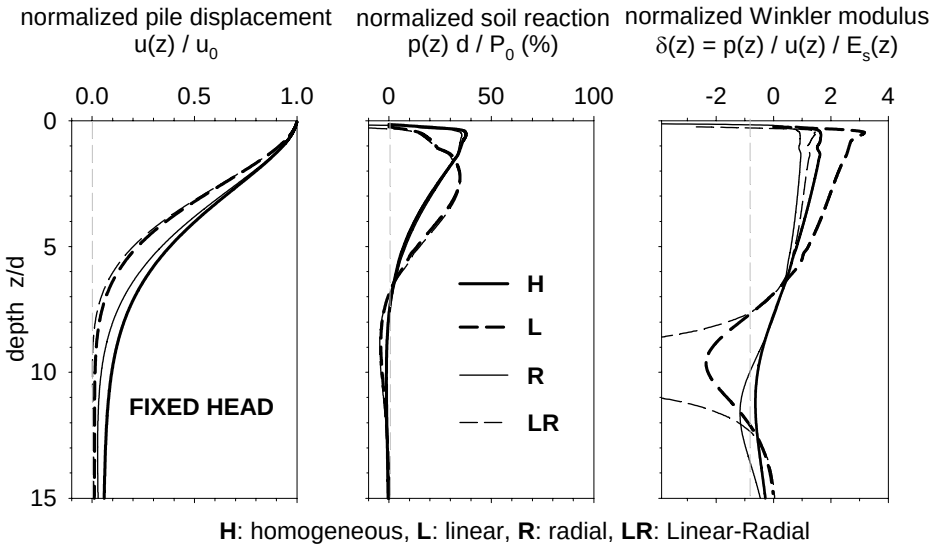

Figure 5. Deflected shape, soil reaction and normalized Winkler modulus for laterally loaded fixed-head piles of equal swaying stiffness in four different soil profiles.

Comparing homogeneous (H) and linear profile (L), it is evident that pile displacement dies out much faster with depth in the linear profile. In radially inhomogeneous (R, LR) profiles, displacements attenuate faster than in the corresponding radially homogeneous (H and L) cases. These trends are anticipated because the more inhomogeneous a soil layer (e.g., L, LR), the smaller its modulus becomes at the surface. Accordingly, to match the static stiffness of a homogeneous layer (H), soil modulus has to increase very fast with depth resulting in faster attenuation of pile displacement with depth. The trend is more or less the same for fixed and free-head piles.

Soil reaction in a homogeneous halfspace (H) attains its peak at a shallower elevation compared to a linear soil profile (L). This is reasonable, since the linear profile has very small Young's modulus at the surface, thus making it unable to produce significant reaction to pile movement.

On the other hand, it is observed that the homogeneous profile (H) has similar soil reactions as the radially inhomogeneous (R) profile, and the linear (L) profile similar reactions as the linear-radial (LR) profile. This is counter-intuitive, since one might have anticipated different reactions for same displacements in inhomogeneous soil.

Plotting the variation of Winkler modulus with depth, it can be seen, for the case of fixed head piles and (LR) soil, that normalized Winkler modulus δ (= k / E_s) becomes infinite at a certain depth. This implies that soil reaction is finite at regions of small pile displacement. It is also apparent that beyond that depth δ takes negative values. It is seen, however, that this depth is higher than the active pile length ($\approx$ 10 to 15 pile diameters) and thus has negligible influence on the response.

The difference between dynamic and static p-y curves is that now, in addition to force and displacement, excitation frequency is involved. In Figure 6, the real parts of deflection, soil reaction and $\delta(z)$ are plotted for a single excitation frequency and four different stiffness-equivalent profiles. Both fixed and free-head piles are considered. It can be seen that, unlike Figure 5, which applies to the static case, displacements now seem to be smaller for the radially inhomogeneous profiles. Soil reactions continue to be very close to each other and Winkler modulus does not become infinite at the points of zero displacement. Soil reactions are practically unaffected by frequency (a_o = 0.25)

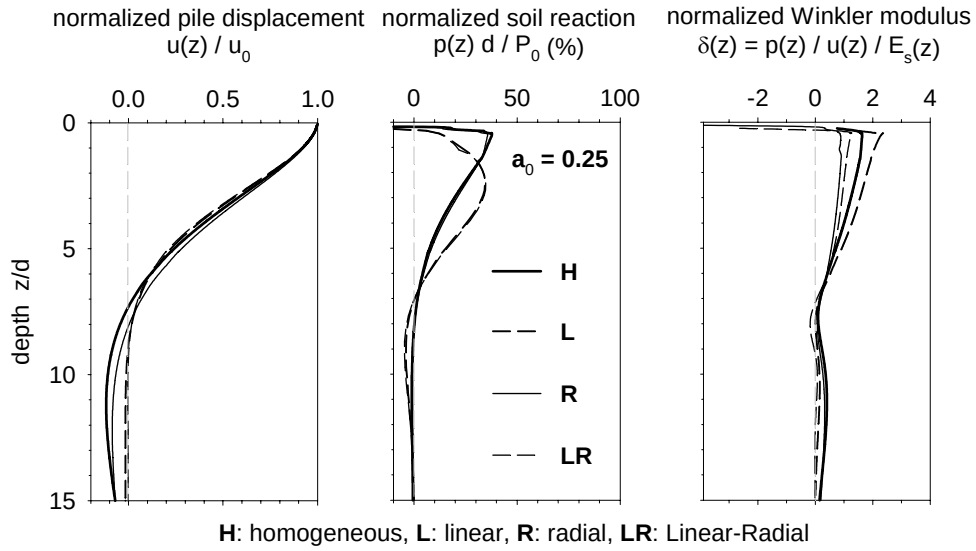

Figure 6. Dynamic deflected shape, soil reaction and normalized Winkler modulus for laterally loaded fixed-head piles of equal swaying stiffness in four different soil profiles; $a_0 = 0.25$

5 MAIN CONCLUSIONS

It was shown that radiation damping in stiffness-equivalent soil profiles is significantly reduced with increased levels of inhomogeneity in the soil. This implies that using a homogeneous profile in a dynamic analysis will result to lower response due to high radiation damping. This reduction may exceed 100% - particularly at high frequencies.

It was also demonstrated that for stiffness-equivalent soil profiles, attenuation of pile displacement with depth varies depending on the characteristics of the profile, starting from the same value at the pile-head. In addition, soil reaction along the pile shaft is independent of radial inhomogeneity for statically-equivalent profiles. The above results are valid for both axially- and laterally-loaded piles.

ACKNOWLEDGEMENTS

This project was partially sponsored by the Caratheodory Program (#B.388), University of Patras. The Authors are thankful for this support.

REFERENCES

[1] Poulos, H. G. and Davis, E. H. (1980), *Pile foundation analysis and design*, Jonh Wiley & Sons
[2] Roesset, J. M. (1980), "Stiffness and damping coefficients of foundations", *Proceedings of ASCE Geotechnical Engineering Division National Convention*, Oct. 30, 1980, 1-30.
[3] Novak, M. (1991), "Piles under dynamic loads: State of the art", *Proceedings, 2nd International Conference on Recent Advances in Geotechnical Earthquake Engineering and Soil Dynamics*, St. Louis, 3, 2433-2456.
[4] Mylonakis, G. and Gazetas, G. (1998),"Vertical vibrations and additional distress of grouped piles in layered soil", Soils and Foundations, 38, 1, 1-14
[5] Randolph, M. F. (2003),"Science and Empiricism in Pile Foundation Design", Geotechnique, 54, 1, 43rd Rankine Lecture
[6] Kaynia, A. M. and Kausel, E. (1982). *Dynamic stiffness and seismic response of pile groups*, Massachusetts Institute of Technology, Research Report R82-03.
[7] Novak, M. and Sheta, M. (1980), "Approximate approach to contact effects of piles", *Proceedings of a Session sponsored by Engineering Division at the ASCE National Convention*, Oct. 30 1980
[8] Veletsos, A. S. and Dotson, K. W. (1986),"Impedances of soil layer with disturbed boundary zone", Journal of Geotechnical Engineering, ASCE, 112, 3
[9] Han, Y. C. and Sabin, G. C. W. (1995),"Impedances for radially inhomogeneous viscoelastic soil media", Journal of Engineering Mechanics Division, ASCE, 121, 9, 939-947
[10] Michaelides, O., Gazetas, G., Bouckovalas, G. and Chrysikou, E. (1998),"Approximate non-linear dynamic

axial response of piles", Geotechnique, 48, 1, 33-53
[11] Poulos, H. G. (1988),"Modified Calculation of Pile-Group Settlement Interaction", Journal of Geotechnical Engineering, ASCE, 114, 6, 697-706
[12] Syngros, C. (2004). *Seismic response of piles and pile-supported bridge piers evaluated through case histories,* Ph.D. Dissertation, The City College and the Graduate Center of the City University of New York, New York.
[13] Kellezi, L. (2000),"Local transmitting boundaries for transient elastic analysis", Soil Dynamics and Earthquake Engineering, 19, 533-547
[14] Marques, J. M. M. C. and Owen, D. R. J. (1984),"Infinite elements in Quasi-Static Materially Nonlinear Problems", Computers and structures, 18, 4, 739-751
[15] Price, T. E. (2003),"Numerically exact integration of a family of axisymmetric finite elements", Communications in Numerical Methods in Engineering, 19, 4, 253-274
[16] Kim, Y.-S. (1987). *Dynamic response of structures on pile foundations,* Ph.D. Dissertation, The University of Texas at Austin
[17] El-Naggar, M. H. (2000),"Vertical and torsional soil reactions for radially inhomogeneous soil layer", Structural Engineering and Mechanics, 10, 4, 299-312
[18] Mylonakis, G., Gazetas, G. and Nikolaou, S. (2005),"Footings under Dynamics Loads: Analysis and Design Issues with Emphasis on Bridge Foundations", Soil Dynamics and Earthquake Engineering, (in press 2005),

WAVE DISPERSION IN DRY SAND BY EXPERIMENTAL, ANALYTICAL AND NUMERICAL METHODS

T. Wichtmann[a], E. I. Sellountos[b], S. V. Tsinopoulos[c], A. Niemunis[a], S. Papargyri-Beskou[d], D. Polyzos[b], T. Triantafyllidis[a] and D. E. Beskos[c]

[a]Institute of Soil Mechanics and Foundation Engineering
Ruhr-University Bochum
D-44801 Bochum, Germany
[b]Department of Mechanical and Aeronautical Engineering
University of Patras
GR-26500 Patras, Greece
[c]Department of Civil Engineering
University of Patras
GR-26500 Patras, Greece
e-mail: d.e.beskos@upatras.gr (D. E. Beskos)
[d]Mechanics Division, General Department, School of Technology
Aristotle University of Thessaloniki
GR-54006 Thessaloniki, Greece

Keywords: Wave dispersion, Granular medium, Dry sand, Experimental method, Gradient elasticity, Porous elasticity, Boundary element method.

Abstract. *The dispersion of longitudinal and shear elastic waves propagating in dry sand cylindrical specimens is studied by experimental, analytical and numerical methods. Wave propagation in the specimen is studied experimentally with the aid of a triaxial cell system equipped with pairs of piezoelectric ceramic elements for the generation and reception of longitudinal and shear waves. Two different models taking into account the microstructural properties of dry sand, a gradient elastic and an elastic porous model, are also employed to study wave dispersion analytically. The same problem is also studied by the boundary element method in the frequency domain in conjunction with the iterative effective medium approximation on the assumption that dry sand is a porous medium with equally sized spherical pores. The results of all methods are critically compared and discussed.*

1 INTRODUCTION

Wave propagation in granular materials, such as sands, sandstones, grains, ceramics, porous bones and pressed powders is an important field of study in geotechnical engineering, geophysics, bioengineering and material science and engineering. Wave propagation studies in these materials aim at the understanding of their internal microstructure, determining their mechanical properties and establishing accurate and efficient methods for the evaluation of their response to dynamic loading.

Among the many published works on elastic wave propagation in granular media, one can mention experimental studies[1-5], analytical studies[6-13] and numerical studies[14-17]. To the authors' best knowledge, with the exception of references[4, 15] where there is a comparison between experimental and analytical results, no comparisons between the results of the above three kinds of methods have been reported in the recent literature.

The present work represents a moderate effort towards a comparison of experimental, analytical and numerical methods as applied to the study of wave propagation in granular media. More specifically, this work studies dispersion of longitudinal (P) and shear (S) waves in dry sand assuming small-amplitude harmonic waves. Experimental dispersion curves are obtained with the aid of a triaxial cell system with pairs of piezoelectric transducers for the generation and reception of waves at the bottom and top, respectively, of a cylindrical dry sand specimen pre-pressured uniformly. The dispersion curves of the specimen are also obtained on the basis of two different microstructural elasticity theories: the linear elasticity with pores (voids) due to Cowin and Nunziato[7] and the linear dipolar gradient elasticity due to Mindlin[18]. Finally, dispersion is also studied by a numerical method that combines the iterative effective medium approximation technique[14, 15] used for the elastic porous medium of the sand specimen with the frequency domain boundary element method used

for the wave scattering analysis. All the methods are in agreement for the cases of high frequencies for which there are essentially no dispersional waves. However, for the cases of low frequencies there is disagreement between the methods, which is clearly pointed out.

2 EXPERIMENTAL METHOD

The phase velocities of longitudinal (P) and shear (S) waves propagating in dry sand cylindrical specimens have been measured with the aid of a triaxial cell test device instrumented with pairs of piezoelectric elements. These elements (three types of them) are placed at the specimen end plates and serve to generate and receive P and S waves. The experimental technique for measuring wave velocities is shown schematically in Fig. 1. A single sine voltage is generated by a function genarator, then is amplified and finally is conducted towards an oscilloscope and towards the selected piezoelectric transducer placed at the lower specimen end plate. The electrical impulse causes a deformation of the piezoelectric element and thus the emission of a wave. Conversely, the wave arrival at the upper specimen end plate has as a result the generation of an eclectric output to the corresponding receiver. Finally, the received signal after amplification is transferred to a computer for post-processing purposes. The wave velocity is then calculated as the quotient of the travel length (length of the specimen) and travel time (time difference between the start of the transmitted signal and the first arrival of the received signal). Since every generated sine signal is associated with a specific frequency, every measured wave velocity becomes a function of frequency, thereby creating a phase velocity versus frequency relation, i.e., a dispersion curve.

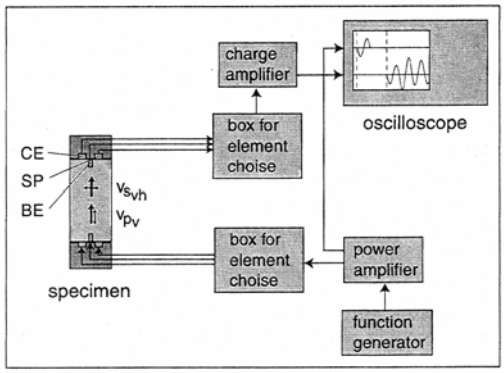

Figure 1. Scheme of the test device

In the present work, cylindrical triaxial specimens 10cm in diameter and 5cm in height were used. The small specimen height was chosen in order to reduce the influence of material damping and the reflections of the waves at the specimen boundaries. A medium coarse dry sand with mean diameter $d = 0.55\text{mm}$ and maximum and minimum void ratios $e_{\max} = 0.874$ and $e_{\min} = 0.577$, respectively, was used. The specimens were prepared by pluviating dry sand out of a funnel through air into half cylinder moulds. Having placed the specimen top cap, sealed the membrane and applied a vacuum of 50 kPa to the grain skeleton, the half-cylinder moulds were removed. The geometry of the specimen was measured and the plexiglass cylinder of the pressure cell was mounted. The vacuum in the grain skeleton was gradually replaced by the pressure in the cell keeping the effective isotropic stress $\sigma_1 = \sigma_3$=50 kPa, where the indices 1 and 3 stand for the axial and the radial component, respectively.

The experimental measurements were performed on sand specimens having three different void ratio values (e = 0.797, 0.667, 0.571) under four effective isotropic stress values $\left(\sigma_1 = \sigma_3 = 50, 100, 200, 400\ \text{kPa}\right)$ in order to study the influence of the relative density of the soil as well as the surrounding pressure on the wave propagation velocities. The frequencies of the transmitted waves were varied from 5 kHz up to 200 kHz in steps of 5 kHz.

3 ANALYTICAL METHODS

According to the theory of linear elastic materials with voids due to Cowin and Nunziato[7], the void volume in elastic porous materials changes with the deformation. Thus, the governing equations of motion for such materials has the form

$$\mu u_{i,jj} + (\lambda + \mu) u_{j,ji} + \beta \phi_{,i} = \rho \ddot{u}_i \tag{1}$$

$$\alpha \phi_{,ii} - \gamma \dot{\phi} - \xi \phi - \beta u_{\kappa,\kappa} = \rho \delta \ddot{\phi} \tag{2}$$

where u_i is the displacement vector, ϕ the change in void volume fraction, ρ the mass density, λ and μ the Lamè constants, $\alpha, \beta, \gamma, \xi$ and δ material constants, indicial notation holds, commas indicate spatial differentiation and overdots differentiation with respect to time t. Assuming harmonic waves of the form

$$u_i(x_i,t) = \bar{u}\, d_i\, e^{-i[(\omega/V) m_i x_i + \omega t]}, \qquad \phi(x_i,t) = \bar{\phi}\, e^{-i[(\omega/V) m_i x_i + \omega t]} \tag{3}$$

where d_i and m_i are unit vectors indicating the directions of displacement and propagation, respectively, V the phase velocity, ω the circular frequency and $\bar{u}$ and $\bar{\phi}$ amplitudes, one can prove that, while shear waves propagate with $V_s = c_s = \sqrt{\mu/\rho}$ (no dispersion), longitudinal waves propagate with a velocity V_p, which depends on frequency $\omega = 2\pi f$, where f is the frequency in Hz. This V_p versus f dispersion relation for the special case of $\xi = \gamma = 0$ takes the form

$$V_p^2 = \left\{ \left[\alpha/\delta + (\lambda + 2\mu) \right] \pm \sqrt{\left[\alpha/\delta - (\lambda + 2\mu) \right]^2 + \beta^2/\pi^2 \delta f^2} \right\} / 2\rho \tag{4}$$

According to the dipolar gradient theory of elasticity due to Mindlin[18], as simplified in [13, 4, 16], one can have the governing equation of motion of an elastic body with microstructure in the form

$$\mu u_{i,jj} + (\lambda + \mu) u_{j,ji} + g^2 \left(\mu u_{i,jj} + (\lambda + \mu) u_{j,ji} \right)_{,\kappa\kappa} = \rho \ddot{u}_i - \rho h^2 \ddot{u}_{i,\kappa\kappa} \tag{5}$$

where g and h are the gradient coefficients of volumetric strain energy and velocity, respectively.

Assuming harmonic waves of the form

$$\begin{aligned} \mathbf{u} &= \nabla \phi + \nabla \times \mathbf{A} \\ \nabla \phi &= \mathbf{m}\, e^{-i\left[(\omega/c_p)\mathbf{m}\cdot\mathbf{x} + \omega t\right]} \\ \nabla \times \mathbf{A} &= \mathbf{d}\, e^{-i[(\omega/c_s)\mathbf{m}\cdot\mathbf{x} + \omega t]} \end{aligned} \tag{6}$$

where $c_p^2 = (\lambda + 2\mu)/\rho$ and $c_s = \mu/\rho$ stand for the longitudinal and shear wave velocities of classical wave propagation, one can prove that both longitudinal and shear waves are here dispersive and the $V_{p,s}$ versus $f = \omega/2\pi$ relation takes the form

$$V_{p,s}^2 = 8\pi^2 c_{p,s}\, g^2 f^2 \Big/ \left[-\left(c_{p,s}^2 - 4\pi^2 h^2 f^2 \right) + \sqrt{\left(c_{p,s}^2 - 4\pi^2 h^2 f^2 \right)^2 + 16\pi^2 c_{p,s}^2\, g^2 f^2} \right] \tag{7}$$

4 NUMERICAL METHOD

The numerical method used here to study wave dispersion in dry sand is based on the iterative effective medium approximation [14, 15] applied with the aid of an advanced frequency domain boundary element method for axisymmetric problems [19].

An elastic wave propagating in a soil medium, which is strongly inhomogeneous, can be considered as the sum of a mean wave and a number of fluctuating waves. The mean wave exists in a homogeneous effective medium with equivalent properties, while the fluctuating waves are the result of the multiple scattering of the mean wave by the randomly distributed material variations with respect to those of the effective medium. Under this consideration, the average of fluctuating fields should be vanishing at any direction within the effective medium. This self-consistent condition, for the case of a material consisting of grains and voids (dry sand) can take the simplified form [14, 15]

$$n g^{(1)}\left(\hat{\mathbf{k}}, \hat{\mathbf{k}} \right) + (1-n)\, g^{(2)}\left(\hat{\mathbf{k}}, \hat{\mathbf{k}} \right) = 0 \tag{8}$$

where n represents the volume fraction of the sand grains and $g^{(1)}(\hat{\mathbf{k}}, \hat{\mathbf{k}})$ and $g^{(2)}(\hat{\mathbf{k}}, \hat{\mathbf{k}})$ are the forward

scattering amplitudes taken by the solution of the two single wave scattering problems illustrated in Fig. 2.

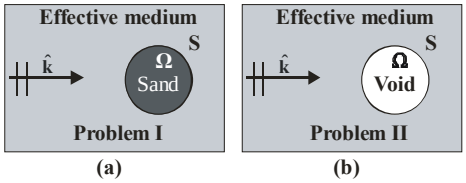

Figure 2: Single wave scattering problems of a mean wave propagating in the effective medium; a) the scatterer is the sand grain (problem I) and b) the scatterer is a void inclusion with identical to the sand grain geometrical properties (problem II).

In the present work, the self-consistent condition (8) is satisfied numerically by following an iterative procedure. This iterative effective medium approximation (IEMA) procedure can be summarized as follows: Consider a soil medium consisting of identical spherical sand grains with density, shear and Young's moduli, ρ, μ and *E*, respectively in a volume fraction equal to *n*. A harmonic elastic wave either longitudinal (P) or shear (S) is propagated through the soil. Due to the inhomogeneity, multiple scattering occurs which makes the mean wave both dispersive and attenuated. Thus, its complex wavenumber $k_d^{eff}(\omega)$ can be written as

$$k_d^{eff}(\omega) = \frac{\omega}{V_d^{eff}(\omega)} + i\alpha_d^{eff}(\omega) \tag{9}$$

where $V_d^{eff}(\omega)$ and $\alpha_d^{eff}(\omega)$ are the frequency dependent phase velocity and attenuation coefficient, respectively, of the mean plane wave, while the subscript d denotes either longitudinal $(d \equiv \mathrm{P})$ or shear $(d \equiv \mathrm{S})$ waves. Next, the soil medium is replaced by an elastic homogeneous and isotropic medium with effective shear and Young moduli μ^{eff} and E^{eff}, respectively, given by the simple mixture rule

$$\mu^{eff} = n\mu \text{ and } E^{eff} = nE \tag{10}$$

At the first step of the IEMA method, the effective density is assumed to be

$$\left(\rho^{eff}\right)_{step1} = n\rho \tag{11}$$

Then, the real effective wave number $(k_d^{eff})_{step1}$ is straightforwardly evaluated through (9), using the material properties (10) and (11). At the second step of the IEMA, by utilizing the material properties obtained from the first step, the two single wave scattering problems, illustrated in Fig. 1, are solved. The solution of the scattering problems is accomplished numerically by means of an advanced 3-D axisymmetric boundary element code [19]. Combining relation (8) with a dispersion relation due to Foldy [20], one can arrive at the new effective wave number of the mean wave, given by

$$\left[\left(k_d^{eff}\right)_{step2}\right]^2 = \left[\left(k_d^{eff}\right)_{step1}\right]^2 + \frac{3n_1}{r^3} g_d\left(\hat{\mathbf{k}}, \hat{\mathbf{k}}\right) \tag{12}$$

where r is the radius of the sand grain. The new, complex now, density $(\rho^{eff})_{step2}$ is evaluated from the $(k_d^{eff})_{step2}$ and relations (10). Then the second step is repeated with the material properties (10) and the new density $(\rho^{eff})_{step2}$ until the self consistent condition (8) is satisfied. Finally, from the relation (9), the frequency dependent effective phase velocity $V_d^{eff}(\omega)$ and the attenuation coefficient $\alpha_d^{eff}(\omega)$, are computed.

5 COMPARISON OF RESULTS

Due to space limitations only a few results are presented herein. They correspond to the case of dry sand with E=338 MPa, G=137 MPa, ρ_g=1580 kg/m^3 for the grain matter and volume fraction of grains V_g=0.6 or void ratio e = 0.667. Thus, one has $\rho = \rho_g V_g = 948\,\mathrm{kg/m^3}$. Figures 3 and 4 show the dispersion curves for P and S waves, respectively, as obtained by the four methods considered in this work, i.e., the experimental, the two analytical and the numerical method. The analytical method of porous elasticity [7] was used with material

coefficient ratios $\alpha/\delta = 24\times10^{7}\ \mathrm{N/m^2}$ and $\beta^2/\delta = 92\times10^{26}\ \mathrm{N/m^4s^2}$, while that one of gradient elasticity[18] with material constants $g = 55\times10^{-5}\mathrm{m}$ and $h = g/1.034\,\mathrm{m}$ as well as $g = 16.5\times10^{-5}\mathrm{m}$ and $h = \mathrm{g}/1.030\,\mathrm{m}$.

One can observe that for both types of waves (P and S) all the methods are in agreement for high frequencies for which no dispersion is essentially observed. However, for low frequencies, there is disagreement between the methods. Here the experimental method again indicates zero dispersion, while the analytical method of gradient elasticity [18] indicates an almost zero dispersion, which however, shows a slight increase for high frequencies. On the other hand, the analytical method of porous elasticity [7] and the numerical method IEMA/BEM indicate a rapid increase of phase velocity with decreasing values of frequency in the low frequency range. More specifically, the analytical method approaches infinite values of velocity for frequencies approaching zero, while the numerical method does the same for finite values of frequency $(f \le 80\,\mathrm{KHz})$. The similar behavior of the last two methods can be attributed to the fact that both model dry sand as a porous elastic solid. The gradient elasticity method [18] has a different behavior because it incorporates microstructural effects in a continuum setting. However, it approaches experimental results better than the other methods, eventhough exhibits almost zero dispersion contrary to expectations in view of its internal microstructure. However, a slight dispersion increase for high frequencies is noticeable, especially for S waves. Experimental results show zero dispersion. However, measurements near very small frequencies $(f \le 5\,\mathrm{kHz})$ cannot be considered as reliable, leaving a question whether or not there is really dispersion in that range.

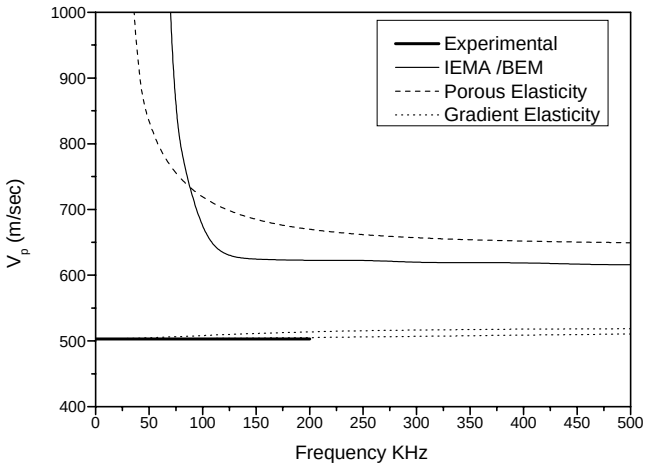

Figure 3. Dispersion curves for P waves

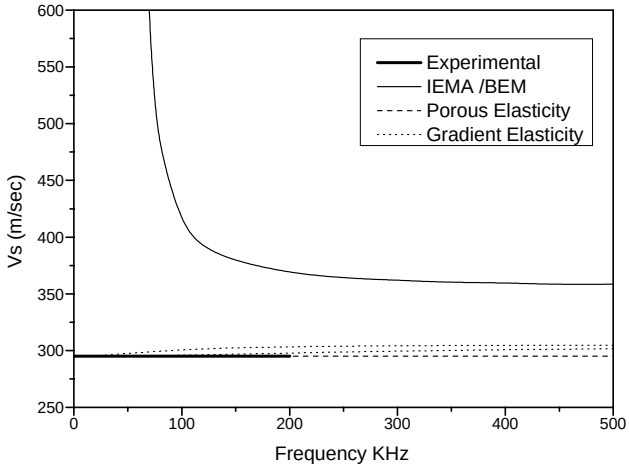

Figure 4. Dispersion curves for S waves

6 CONCLUSIONS

On the basis of the preceding analysis and discussion the following conclusions can be stated:

1) Experimental results exhibit zero dispersion for all frequencies, eventhough measurements for very low frequencies cannot be considered as very reliable.
2) The analytical method of dipolar gradient elasticity due to Mindlin [18] shows results very close to the experimental results, eventhough the values of velocities are always above the experimental ones.
3) The analytical method of porous elasticity due to Cowin and Nunziato [7] and the numerical method of IEMA/BEM [14, 15] agree with the experimental results only for high frequencies and exhibit values of velocity approaching infinity for low frequencies.
4) It is apparent that more in depth investigations are needed in order to more clearly understand the dynamic behavior of dry sand and assess the performance of the various analytical and numerical models in connection not only with wave dispersion, but in addition, with wave attenuation and the solution of wave propagation boundary value problems in dry sand.

ACKNOWLEDGEMENTS

The authors acknowledge with thanks the support provided to them through the IKYDA-DAAD programs in the framework of the Greek – German Scientific Co-operation. Thanks are also due to Miss M. Dimitriadi for her excellent typing of the manuscript.

REFERENCES

[1] Bathia, S., Blaney, G., Editors (1991), "Recent Advances in Instrumentation, Data Acquisition and Testing in Soil Dynamics", ASCE Geotechnical Special Publication No 29, ASCE, New York.
[2] Brignoli, E. G. M., Gotti, M., Stokoe, K. H. II (1996), "Measurement of shear waves in laboratory specimens by means of piezoelectric transducers", Geotechnical Testing Journal 19, pp. 384-397.
[3] Wichtmann, T., Triantafyllidis, T. (2004), "Influence of a cyclic and dynamic loading history on dynamic properties of dry sand, Part II: cyclic axial preloading", Soil Dynamics and Earthquake Engineering 24, pp. 789-803.
[4] Aggelis, D. G., Philippidis, T. P., Tsinopoulos, S. V., Polyzos, D. (2004), "Wave dispersion in concrete due to microstructure", *CD-ROM Proceedings of the 2004 Int. Conference on Computational & Experimental Engineering & Sciences*, Madeira, Portugal, 26-29 July.
[5] Donald, J. A., Butt, S. D. (2005), Experimental technique for measuring phase velocities during triaxial compression tests", International Journal of Rock Mechanics and Mining Sciences 42, pp. 307-314.
[6] Nunziato, J. W., Walsh, E. K. (1977), "Small-amplitude wave behavior in one-dimensional granular solids", Journal of Applied Mechanics (ASME) 44, pp. 559-564.
[7] Cowin, S. C., Nunziato, J. W. (1983), "Linear elastic materials with voids", Journal of Elasticity 13, pp. 125-147.
[8] Walton, K. (1988), "Wave propagation within random packing of spheres", Geophysical Journal 92, pp. 89-97.
[9] Chang, C. S., Gao, J. (1995), "Non-linear dispersion of plane wave in granular media", International Journal of Non-Linear Mechanics 30, pp. 111-128.
[10] Chang, C. S., Gao, J. (1997), "Wave propagation in granular rod using high-gradient theory", Journal of Engineering Mechanics (ASCE) 123, pp. 52-59.
[11] Tsepoura, K. G., Papargyri-Beskou, S., Polyzos, D., Beskos, D. E. (2002), "Static and dynamic analysis of gradient elastic bars in tension", Archive of Applied Mechanics 72, pp. 483-497.
[12] Papargyri-Beskou, S., Polyzos, D., Beskos, D. E. (2003), "Dynamic analysis of gradient elastic flexural beams", Structural Engineering and Mechanics 15, pp. 705-716.
[13] Georgiadis, H. G., Vardoulakis, I., Velgaki, E. G. (2004), "Dispersive Rayleigh-wave propagation in microstructured solids characterized by dipolar gradient elasticity", Journal of Elasticity 74, pp. 17-45.
[14] Verbis, J. T., Tsinopoulos, S. V., Polyzos, D. (2002), "Elastic wave propagation in fiber reinforced composite materials with non-uniform distribution of fibers", Computer Modeling in Engineering and Sciences (CMES) 3, pp. 803-814.
[15] Aggelis, D., Tsinopoulos, S. V., Polyzos, D. (2004), "A practical IEMA for predicting wave dispersion in particulate composites and suspensions", Journal of the Acoustical Society of America 116, pp. 3443-3452.
[16] Polyzos, D. (2005), "3D frequency domain BEM for solving dipolar gradient elastic problems", Computational Mechanics 35, pp. 292-304.
[17] Polyzos, D., Tsepoura, K. G., Beskos, D. E. (2005), "Transient dynamic analysis of 3-D gradient elastic solids by BEM", Computers and Structures 83, pp. 783-792.

[18] Mindlin, R. D. (1964), “Microstructure in linear elasticity”, Archive of Rational Mechanics and Analysis 16, pp. 51-78.
[19] Tsinopoulos, S. V., Kattis, S. E., Polyzos, D., Beskos, D. E. (1999), “An advanced boundary element method for axisymmetric elastodynamic analysis”, Computer Methods in Applied Mechanics and Engineering 175, pp. 53-70.
[20] Foldy, L. L. (1945), “The multiple scattering of waves”, Physical Review 67, pp. 107-119.

A CONTRIBUTION TO THE STUDY OF THE SIZE EFFECT FOR NATURAL BUILDING STONES

S.K. Kourkoulis*, C. Caroni, E. Ganniari-Papageorgiou***

* Department of Mechanics, Laboratory of Testing and Materials, National Technical University of Athens, Theocaris Building, 157 73 Zografou, Campus, Athens, HELLAS, stakkour@central.ntua.gr
** Department of Mathematics, National Technical University of Athens, 157 73 Zografou Campus, Athens, HELLAS, ccar@math.ntua.gr

Keywords: Porous stones, Size effect, Mechanical properties, Statistical analysis

Abstract. *The dependence of the mechanical properties of rock-like materials on the specimens size is presented together with a statistical analysis of the parameters governing the phenomenon. The phenomenon, known as size effect, is studied for the case of the porous stone of Cefallonia, a natural building stone considered as a candidate substitute of the porous stone of Kenchreae, the material used by ancient Greeks for the erection of the Asklepieion of Epidauros. Uniaxial compression tests were carried out using both cubic and cylindrical specimens of various sizes and the basic mechanical properties were determined by appropriate analysis of the test data. The results exhibited clearly the dependence of the mechanical properties on the dimensions of the specimens and also indicated that the dependence is not the same for the cylindrical and the cubic specimens. A statistical analysis of the data followed using appropriate dummy variables for the factors describing the specimens. Interesting conclusions, concerning the mutual dependence of the mechanical properties of the material, were drawn from the correlations between the variables. Finally it was found that the most appropriate distribution for describing the experimental data is the Lognormal rather than the Normal one.*

1 INTRODUCTION

Restoring and conserving an ancient monument is a complicated multidisciplinary scientific task. A series of problems are to be considered and solved before decisions are made. These problems vary from elementary ones, such as the strength and deformability of the materials, to rather complex ones, such as the preservation of the structural system, the determination of the minimum interventions, their reversibility and of course their durability. Archaeologists, architects and civil engineers collaborate in order to meet the final target, the extension of life of the monument. The decisions are usually a compromise between various, and often contradictory, points of view.

The structural stability of the monument is, of course, the most important among the problems of the experts working for the restoration; however it is outweighed in public perception by the aesthetics of the surface of the stone. The later is particularly acute in the case of temples made of limestone, since this material has softer and harder areas weathering differently. The problem is exacerbated in case large fragments of structural elements, or whole elements of the structure, are missing and have to be replaced. The ideal solution is to have access to the source of the authentic material. Unfortunately this is the exception rather than the rule. In most cases there are no known functioning quarries of the desired material or the areas of the ancient quarries have been built over. In such a case a new stone has to be chosen as a substitution material. The substitution stone and the authentic one should react similarly to environmental influences, mechanical loading and natural wear and weathering.

This paper focuses on the behaviour of the porous stone of Cefallonia, a stone considered as a candidate substitute for the Kenchreae porous stone, used by ancient Greeks for building the Epidaurean Asklepieion, the most celebrated healing centre of the ancient world. The authority and radiance of Asklepios, as the most important healer god of antiquity, brought to the sanctuary financial prosperity, which in the 4th and the 3rd centuries BC enabled the implementation of an ambitious building program aimed at housing the worship in monumental buildings. The extensive remains of the site have been brought to light during excavations conducted on behalf of the Archaeological Society at Athens since the late nineteenth century to the present day. The responsibility for the site preservation lies since 1984 with the "Committee for the Preservation of the Epidauros Monuments".

The study of the Cefallonia porous stone is associated with the restoration of three monuments of the Asklepieion, namely the circular building of Tholos (the healing god's assumed subterranean dwelling place), the Avaton or Enkoimeterion (a large stoa used for the incubation and cure of the sick) and the Propylon of the

Gymnasium (a building complex used for the sacred meals). All three follow the same construction principles regarding the choice of material. Their foundations are built of the locally available weak calcareous conglomerate, known as foundation porous stone. The main part of their upper structure is built of the Kenchreae porous stone. Other stones have been used depending on the particular design and functional requirements of each monument; for example local hard limestone, both red and grey, as well as white marble were used where sculptures are involved.

2 THE SIZE EFFECT

The fact that the nominal strength of structures changes by scaling their size is long ago well known in the engineering community under the term "size-effect". Indeed the dependence of the strength of ropes with constant cross sectional area on their length was studied by Leonardo da Vinci who concluded that "*if two ropes have the same thickness the longest is the weaker*" [1]. However, it was only at the beginning of the twentieth century that the first quantitative results concerning the dependence of the nominal strength of glass fibers on their diameter were published by Griffith [2]. In fact this dependence is caused by the dimensional inhomogeneity between the stress σ ($[F][L]^{-2}$) and the stress intensity factor K_I ($[F][L]^{-3/2}$), which leads to a -1/2 constant slope of the dependence of the nominal strength versus the structural size in a bilogarithmic diagram [3].

From this point on and for almost half a century the size effect was attributed to the statistical nature of the distribution of flaws within a structure and it was described by the "weakest-link" concept introduced by Fisher and Tippett [4] and developed by Weibull [5]. A non-statistical approach did not appear during this period and it was only at the beginning of 1970's when Walsh [6] published results for the fracture of concrete that could not be described by the purely statistical approach of the size fact. This discrepancy, and similar ones observed experimentally for other materials, placed serious limitations on the use of the statistical approach. The main point of scepticism was the fact that the power law form of the Weibull theory for the nominal strength implies the absence of any characteristic length. Such a conclusion is unacceptable for the materials characterized as quasi-brittle which exhibit a finite fracture process zone. Thus the development of new theories for the description of the size-effect was motivated. Today two basic approaches are identified, beyond the classical statistical theory: the deterministic energetic theory [7]; and the theory of crack fractality [8].

The first one, introduced by Bažant is based on the observation that the failure of quasibrittle materials is characterized by both energy and stress quantities, i.e. the fracture energy, G_f, and the tensile strength, f_t. Dimensional analysis indicates that such a material possess a characteristic length, ℓ_o, depending on the size of the fracture process zone [7]. The theory has been applied in a variety of problems (structures with pre-existing notches, structures failing at crack initiation right after the Fracture Process Zone has formed) and types of structures (with positive geometry having no notches and pre-existing large cracks or with positive geometry with initial notches) [9,10]. Following Bažant [10] the nominal strength for structures with preexisting notches, σ_N, is given as:

$$\sigma_N = Bf_t'\left(1+\frac{D}{D_0}\right)^{1/2},\quad Bf' = \left[\frac{EG_f}{g'(\alpha_o)c_f}\right]^{1/2},\quad D_0 = c_f\left[\frac{g'(\alpha_0)}{g(\alpha_0)}\right]$$

In this equation B is a dimensionless parameter depending on the geometry, D is the characteristic size of the specimen, D_o is a geometry dependent parameter, E is the modulus of elasticity, α_o is the initial crack length, $2c_f$ is the length of the fracture process zone and $g(\alpha_o)$ the dimensionless energy release rate according to the LEFM.

The second theory, introduced by Carpinteri [8], relates the size effect to the fractal nature of crack surfaces. According to this approach the scaling law of the nominal tensile strength reads as [11]:

$$\sigma_N = f_t\left(1+\frac{\ell_0}{D}\right)^{1/2}$$

The dimensionless term (ℓ_0/D) in the above equation is controlled by the characteristic length of the material, l_0, and represents the variable influence of disorder on the mechanical behavior.

Both theories were introduced for tensile loading of structures with preexisting cracks or notches, for which the failure is caused by the localization of the strain, which in turn results in a finite size fracture process zone. However, it is believed today that the strain localization is the cause of failure also for structures under uniaxial compression, the difference being that the damage zone is of larger extent. For the case of concrete structures under uniaxial compression Kim and Yi [12] proposed a modification of Bažant's law for the dependence of the compressive strength, f_o, on the dimensions of the specimen, assuming a ratio of height-to-diameter equal to 2:

$$f_0 = \frac{Bf_c'}{\left[1+\frac{d}{\lambda_1(f_c')d_a^m}\right]^{1/2}} + \alpha(f_c')f_c'$$

In this equation d_a stands for the maximum aggregate size, B, m, λ_1 are constants, f_c' is the compressive strength of the standard cylinder, d is the diameter of the specimen and α is the crack band length.

Understanding the size effect is of paramount importance for the engineering community since the vast majority of laboratory tests (~85%) are carried out using specimens with characteristic dimension of the order of 10 cm to 40 cm [9]. These results are then extrapolated in order for conclusions to be drawn for structures with dimensions of much larger size, of the order of a few meters (Fig.1). Taking into account the unavoidable scattering of the experimental results for quasi brittle materials, it becomes obvious that for the design of large structures to be safe both reliable experimental results as well as a sound theoretical interpretation of the size effect are necessary. Unfortunately up to now, and despite intensive scientific research, definite conclusions concerning the laws governing the transition region from the size of the specimens used in the laboratory to the size of the real structures have not been reached and as a result the design codes are still based on empirical or semi-empirical formulas obtained from curve fitting to the experimental results [9].

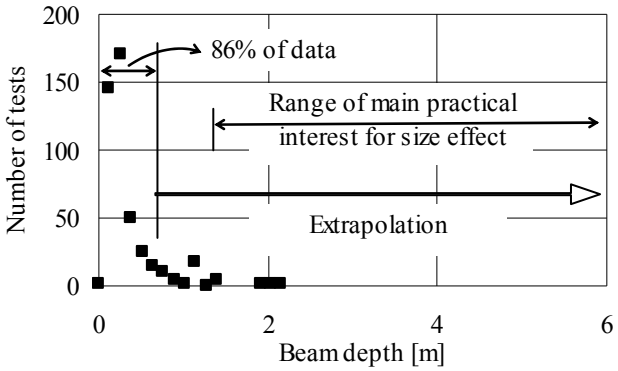

Figure 1: Number of laboratory tests versus the characteristic dimension of the specimens.

For obvious reasons the phenomenon has been studied extensively, both theoretically and experimentally, for the case of concrete, since it is the material most widely used in modern structures. The experimental data available for other structural materials and natural building stones are rather limited. In this direction data concerning the size effect for a widely used natural building stone, the porous stone of Cefallonia, are presented in the following paragraphs, together with some additional data for marble, in an effort to establish the dependence of some mechanical constants and parameters on the size of the specimens used in the experiments.

3 THE MATERIAL

The Cefallonia porous stone is a relatively soft stone from the island of Cefallonia, in the Ionian sea, with clearly layered structure. It is characterized by high porosity (~ 38%) and nets of internal pores and surface vents (Fig. 2a). It contains about 55% CaO and 0.3% MgO. Its bulk density is equal to about 1.47 g/cm^3, its absolute density is 2.38 g/cm^3 and the void ratio is 0.61. The texture is relatively massive and its color is usually whitish-beige.

(a) (b) (c)

Figure 2: A close view of the surface of the material just after it was quarried (a), and typical cylindrical and cubic specimens after being tested (b), (c).

4 EXPERIMENTAL PROCEDURE AND RESULTS

Long series of uniaxial compression tests were executed with cubic (Code: KCCu0DN) and cylindrical (Code: KCCy0DN) specimens of three different sizes (small, medium and large). For the characterization of the spe-

cimens the symbols used were K for Cefallonia, C for compression, Cu for cubes and Cy for cylinders, L for the lubrication conditions of the end platens (0 for dry and 1 for lubricated conditions), D for the dimension (S for small, M for medium and L for large specimens) and N for the number of the specimen (01, 02,...). The tests were carried out with the aid of a very stiff hydraulic Amsler loading frame of capacity 1 MN, equipped with an electronic data acquisition and storage system. The stiffness of the frame was considered infinite since the maximum load recorded did not exceed 1/5 of the capacity of the frame. This is very important in case the post-peak behaviour of the material is to be studied. The load was applied statically and perpendicular to the material layers.

Special care was taken during the preparation of the specimens to ensure that the bases of the specimens were parallel to each other and perpendicular to the load direction. In addition a special semi-spherical head interposed between the loading plate and the moving piston ensured further the coaxiality between the load and the axis of the specimen. For the measurement of axial displacements three LVDT's (Linear Voltage Displacement Transducers) of sensitivity equal to 10^{-6} m were used, placed at 120^{o} to each other in order to check the symmetry of the loading. The detected rotation of the end platens was negligible for the vast majority of tests.

Characteristic axial stress - axial strain curves are plotted in Fig. 3. It can be seen that for the majority of the experiments, after an almost linearly elastic portion a rather abrupt drop of the stress level was observed. Then the stress increased again exceeding, in some cases, even the level of the initial peak value. From this point on, the stress-strain curves become almost horizontal or slightly inclined with a very small negative slope up to the final disintegration of the specimen. By appropriate analysis of the raw experimental data the basic mechanical properties of the material were determined. The quantities calculated are the peak stress, σ_{peak}, the peak strain, ε_{peak}, the modulus of elasticity, E, the stress drop after the peak load, $\delta\sigma$, the elastic strain energy density absorbed by the material up to the peak load or the first visible crack (E_{el}) and the respective energy absorbed after the peak load (E_{pl}). The mean values of these properties are summarized in Table 1 for all classes of tests.

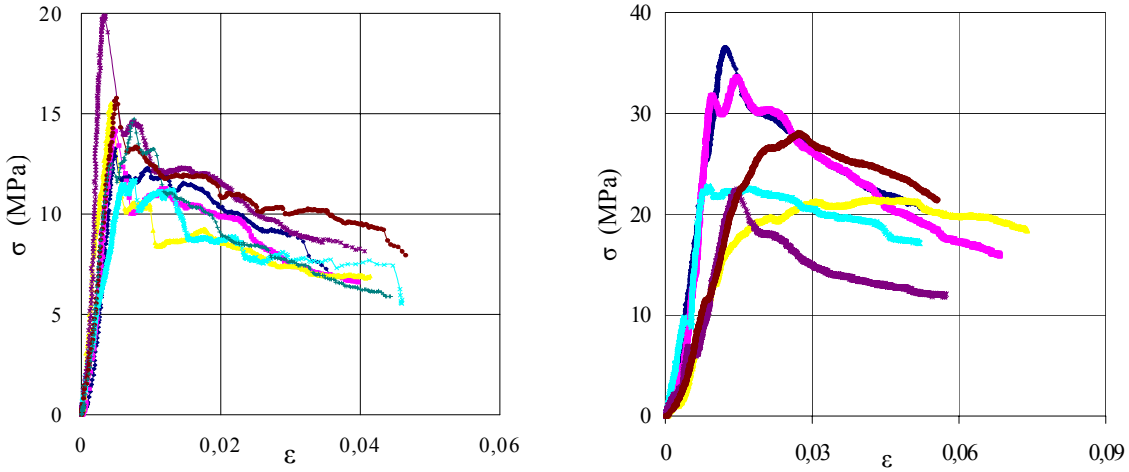

(a) (b)

Figure 3: Axial stress versus axial strain for characteristic tests:
(a) Small cubes (KCCu0S1-6) and (b) Small cylinders (KCCy0S1-6).

Specimens' Class	**σ_{peak} (MPa)**	**ε_{peak} (-)**	**E (MPa)**	**$\delta\sigma$ (MPa)**	**E_{el} (MPa)**	**E_{pl} (MPa)**
KCCu0SN	14.668	0.0046	3738.29	3.052	0.032	0.370
KCCu0MN	27.858	0.0061	8199.77	4.152	0.067	0.478
KCCu0LN	24.716	0.0061	9270.9	1.746	0.053	0.367
KCCy0SN	24.966	0.0150	3278.71	0.810	0.214	0.949
KCCy0MN	24.942	0.0050	7303.48	2.290	0.054	0.334
KCCy0LN	19.619	0.0036	8534.62	10.60	0.028	0.126

Table 1: Mean values of the mechanical properties of the porous stone of Cefallonia.

In order to study the size effect the mean values of the above determined mechanical properties were plotted versus the size of the specimen. A comparative presentation of the results between cubic and cylindrical speci-

mens is shown in Figure 4 for the peak stress and the elastic strain energy density. The results clearly exhibited the dependence of these mechanical properties on the dimensions of the specimens as well as on the shape of the specimens. The most striking conclusion, however, is that the dependence is of different nature for the case of cylinders (monotonic dependence) in comparison with that for cubic specimens (non-monotonic dependence). It is obvious that neither of the above mentioned theoretical approaches, i.e. the energetic-deterministic and the fractal one can describe both types of the size effect characterizing the specific material (at least in their present form), suggesting that the phenomenon should be studied further, both theoretically and experimentally. The dependence of the other mechanical properties on the size of the specimen is of similar nature.

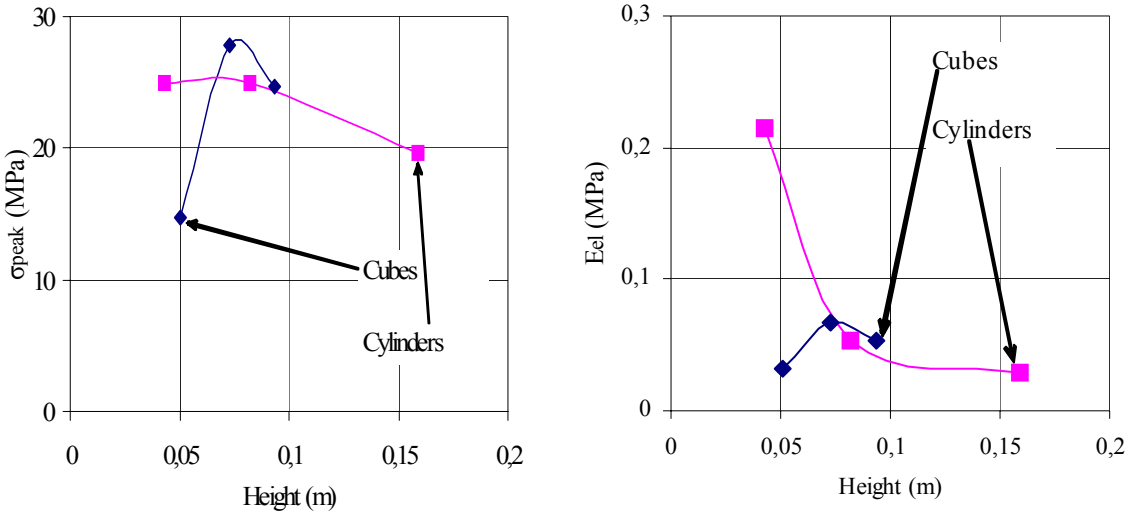

(a) (b)

Figure 4: The dependence of (a) the peak stress and (b) the elastic strain energy density on the size of the specimens.

5 STATISTICAL ANALYSIS

The statistical analysis of the experimental data was conducted with the aid of the statistical program MINITAB. Graphical tests were carried out for all dependent variables (peak stress, peak strain, modulus of elasticity, drop in stress, elastic and inelastic energy) in order to detect the distribution best fitting the experimental data. The sample values were plotted versus the expected values of the hypothetical distribution (Weibull, Normal, Exponential, Gumbel, Lognormal, Logistic, Log-logistic), as seen in the probability plots shown in Figures 5 and 6. It was concluded from this analysis that the most appropriate distribution for the description of the present set of experimental data is the Log-normal distribution, since all plots for this distribution formed an almost straight line for all variables. Consequently, all values were transformed logarithmically in order to apply the standard statistical procedures that assume the Normal distribution.

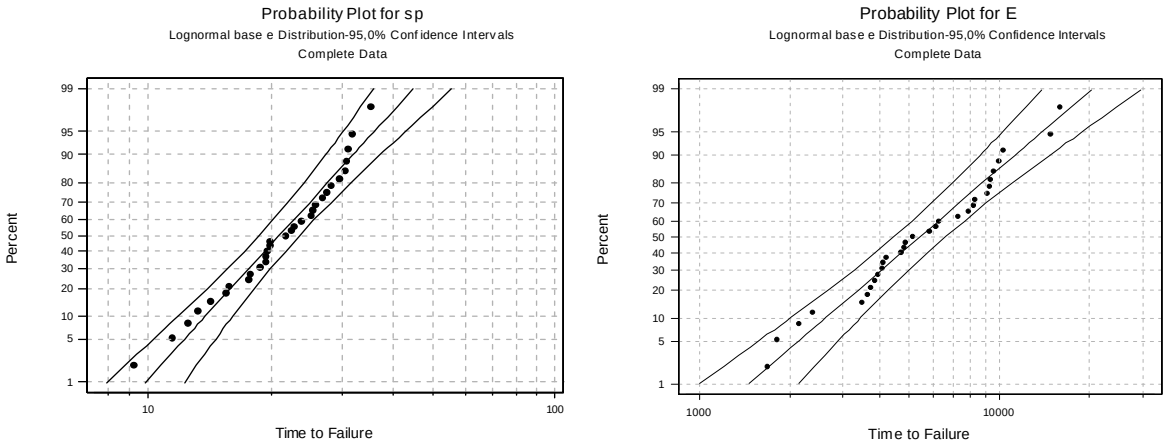

(a) (b)

Figure 5: Probability plot for the Log-normal distribution for (a) The peak stress and (b) The modulus of elasticity.

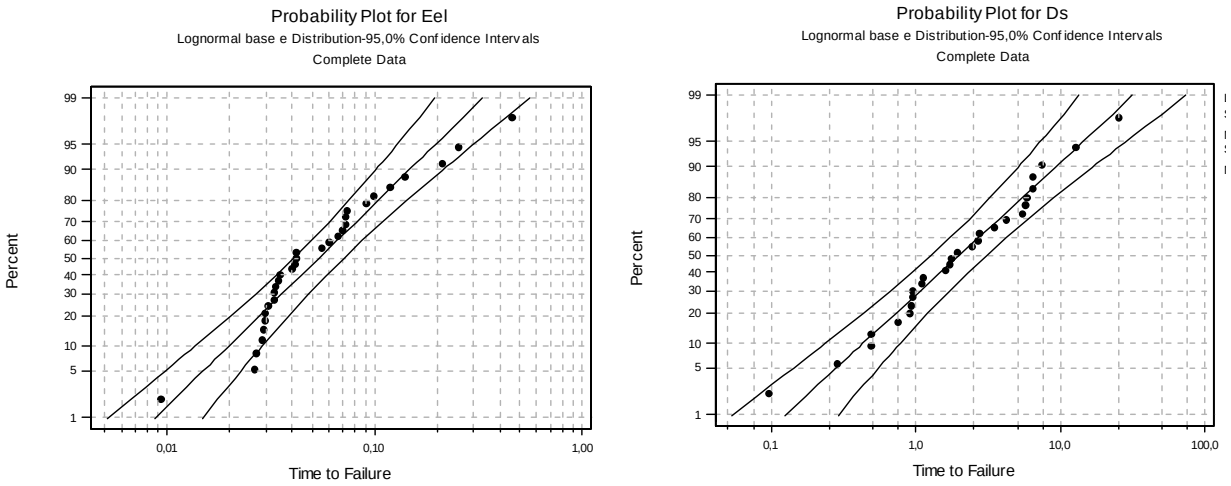

(a) (b)

Figure 6: Probability plot for the Log-normal distribution for (a) The elastic energy and (b) The drop in stress.

As a second step the correlation coefficients between every pair of variables were estimated as:

$$r_{xy} = \frac{\sum_i (x_i - \bar{x})(y_i - \bar{y})}{\sqrt{\sum_i (x_i - \bar{x})^2 \sum_i (y_i - \bar{y})^2}}$$

High correlations were detected between specific mechanical properties for most classes of specimen, even though the number of specimens in each class was rather small. A summary of these conclusions is presented in Table 2. Descriptive statistics (mean ± standard deviation on the logarithmic scale) are summarized in Table 3.

Specimen class	**n**	**Significant correlations**
KCCu0SN	7	σ_{peak}- $\delta\sigma$: 0.86; σ_{peak}- ε_{peak}: -0.81; ε_{peak}- $\delta\sigma$: -0.73; E- $\delta\sigma$: 0.71
KCCu0MN	3	None
KCCu0LN	5	ε_{peak}-Eel: 0.92; ε_{peak}-E: -0.85
KCCy0SN	6	None
KCCy0MN	5	E-Epl: 0.87
KCCy0LN	5	σ_{peak}- $\delta\sigma$: 0.97; ε_{peak}-$\delta\varsigma$: 0.90; σ_{peak}- ε_{peak}: 0.94; E- $\delta\sigma$: 0.91; σ_{peak}-E: 0.92; ε_{peak}-E: 0.88; Eel- $\delta\varsigma$: 0.88; Eel- σ_{peak}: 0.95; ε_{peak}-Eel: 0.99; Eel-E: 0.86

Table 2: Significant correlations (P≤0.05) between the mechanical properties for each class of specimens.

Specimen class	**ln(σ_{peak}) (MPa)**	**ln(ε_{peak}) (-)**	**lnE (MPa)**	**ln($\delta\sigma$) (MPa)**	**ln(E_{el}) (MPa)**	**ln(E_{pl}) (MPa)**
KCCu0SN	2.67 ± 0.18	5.39 ± 0.19	8.20 ± 0.27	0.81 ± 0.94	3.46 ± 0.14	1.00 ± 0.15
KCCu0MN	3.29 ± 0.36	5.11 ± 0.14	8.96 ± 0.42	0.95 ± 1.49	2.71 ± 0.16	0.75 ± 0.18
KCCu0LN	3.19 ± 0.21	5.19 ± 0.50	9.04 ± 0.50	0.38 ± 0.66	3.01 ± 0.47	1.00 ± 0.11
KCCy0SN	3.20 ± 0.17	4.31 ± 0.51	7.99 ± 0.50	0.73 ± 1.33	1.68 ± 1.57	0.09 ± 0.31
KCCy0MN	3.20 ± 0.18	5.35 ± 0.34	8.86 ± 0.31	0.49 ± 0.95	2.98 ± 0.38	1.14 ± 0.31
KCCy0LN	2.91 ± 0.43	5.64 ± 0.22	8.98 ± 0.41	2.03 ± 0.96	3.67 ± 0.59	2.15 ± 0.46

Table 3: Descriptive statistics of the tests.

As a final step regression analysis was carried out in order to examine to what extent the mechanical properties of the specific stone are influenced by the shape and size of the specimens. It was assumed that the

values of each property (dependent variable Y) are affected by two factors, A and B, which interact mutually. Factor A is related to the specimen's shape and has two levels (cubes and cylinders). Factor B is related to the specimen's size and has three levels (small, medium and large). Appropriate dummy variables (X_1, Z_1, Z_2, W_1, W_2) were introduced for the factors describing the specimens defined as follows:

For factor A: $X_1 = \begin{cases} 0, & \text{cylinders} \\ 1, & \text{cubes} \end{cases}$

For factor B: $(z_1, z_2) = \begin{cases} (0,1) & \text{small specimens} \\ (1,0) & \text{medium specimens} \\ (0,0) & \text{large specimens} \end{cases}$

For the interaction between the factors, AB: $W_1 = X_1 Z_1$ and $W_2 = X_1 Z_2$
The linear model fitted to the data had finally the form:

$$Y = \beta_0 + \beta_1 X_1 + \gamma_1 Z_1 + \gamma_2 Z_2 + \delta_1 W_1 + \delta_2 W_2 + \varepsilon$$

Interesting conclusions were drawn from this analysis concerning the statistical significance of the dependence of each mechanical property on the size and shape of the specimens. In particular, in most of the analyses one or more of the interaction terms is significant, showing dependence on size-shape combinations rather than on size and on shape independently. A summary of the regression results is shown in Table 4.

Factors		σ_{peak} (MPa)	E (MPa)	E_{el} (MPa)	ε_{peak} (-)	E_{pl} (MPa)	$\delta\sigma$ (MPa)
Constant		2.91 (0.12)	8.98 (0.18)	-3.67 (0.19)	-5.64 (0.16)	-2.15 (0.13)	2.03 (0.45)
Size	X_1	0.28 (0.16)	0.06 (0.26)	***0.66 (0.27)***	***0.45 (0.22)***	***1.14 (0.18)***	***-1.65 (0.63)***
Shape	Z_1	0.30 (0.16)	-0.12 (0.26)	***0.69 (0.27)***	0.29 (0.23)	***1.01 (0.18)***	***-1.54 (0.63)***
	Z_2	0.29 (0.16)	***-0.99 (0.24)***	***1.99 (0.26)***	***1.32 (0.22)***	***2.05 (0.17)***	***-2.77 (0.67)***
Interaction	W_1	-0.20 (0.240	0.04 (0.39)	-0.38 (0.42)	-0.20 (0.35)	***-0.76 (0.27)***	***2.11 (1.05)***
	W_2	***-0.81 (0.22)***	0.15 (0.34)	***-2.43 (0.36)***	***-1.52 (0.30)***	***-2.05 (0.24)***	***3.19 (0.89)***
R^2 (%)		49.6	58.6	75.4	65.0	85.8	45.2

Table 4: Summary of the results of regression analyses: Estimated regression coefficients for each factor with standard errors in parentheses. Statistically significant (P≤0.05) coefficients are in italics.

6 DISCUSSION AND CONCLUSIONS

The mechanical behavior and failure of the Cefallonia porous stone as well as the dependence of its mechanical constants on the size and the shape of the specimens were studied. The most striking conclusion of the study is that the size effect for this material appears to be irregular, at least for some of the parameters studied.

Indeed, both the compressive strength (expressed in terms of the peak stress recorded just before the first stress drop or the formation of the first visible crack on the lateral surface of the specimen) of this material as well as the strain energy density absorbed up to the peak load depend on the size of the specimens according to a non-monotonic law in the case of cubic specimens. Such behaviour is in accordance with the predictions of the fractal theory of size effect [11]. Similar non-monotonic behaviour for the compressive strength has been also observed by Vardoulakis and Kourkoulis [13] for specimens made of Dionysos marble, the material used for the restoration of the Parthenon Temple (Fig.7a), by Kourkoulis, Ninis and Bakolas [14] for specimens made of conchyliates shell stone, the material used for the erection of the Zeus Temple at Olympia and by Thuro et al. [15] for a number of commercial building stones (Fig. 7b).

On the other hand, for the cylindrical specimens the size effect appears to be monotonic in accordance with the predictions of the energetic-statistical theory [7] for the nominal strength at failure for specimens of different

height/diameter ratio. It should be mentioned, however, that the sample of the present series of tests was rather limited. Additional tests are required with specimens of different dimensions cut from the same material (and the

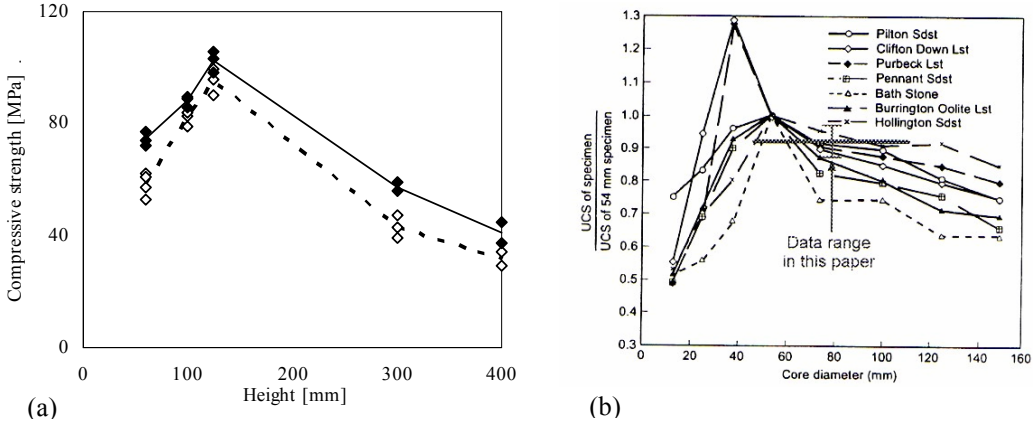

(a) (b)

Figure 7: Size effect irregularities (a) for marble [13] and (b) a number of commercial building

same block) in order for safer conclusions to be drawn and for a clearer understanding of the size effect.

The statistical analysis revealed a number of very interesting conclusions for the size effect which can be summarized as follows: a) The Log-normal distribution rather than the Normal should be used for describing the distributions of the relevant variables, b) Various significant correlations were found for the different mechanical properties for each specimen class, c) All the mechanical properties were found to depend statistically significantly on both the size and shape of the specimens except that the modulus of elasticity did not depend on shape.

REFERENCES

[1] Carpinteri, A. and Chiaia, B. (2002), "Embrittlement and decrease of apparent strength in large-sized structures", Sādhanā, 27(4), pp. 425-448.

[2] Griffith, A. A. (1921), "The phenomenon of rupture and flow in solids", Philos. Transactions of the Royal Society of London, A221, pp.163-198.

[3] Carpinteri, A. (1989), "Decrease of apparent tensile and bending strength with specimen size: two different explanations based on fracture mechanics", Int. J. Solids and Structures, 25, 407-429.

[4] Fisher, R. A. and Tippett, L. H. C. (1928), "Limiting forms of the frequency distribution of the largest and smallest member of a sample", Proc. of the Cambridge Phil. Soc., 24, 180-190.

[5] Weibull, W. (1939), "The phenomenon of rupture in solids", Proc. R. Swed. Inst. Engng. Res, 153, pp. 1-55.

[6] Walsh, P. F. (1972), "Fracture of plain concrete", Indian Concrete J., 46, pp. 469-476.

[7] Bažant, Z. P. (1984), "Size effect in blunt fracture: concrete, rock, metal", J. of Engng. Mech, 110, pp. 518-535.

[8] Carpinteri, A. (1994), "Fractal nature of material microstructure and size effects on apparent mechanical properties", Mechanics of Materials, 18, pp. 89-101.

[9] Bažant, Z.P. and Yavari, A. (2005), "Is the cause of size effect on structural strength fractal or energetic-statistical?", Engng. Fract. Mech., 72, pp. 1-31.

[10] Bažant, Z.P. (2004), "Probability distribution of energetic-statistical size effect in quasibrittle fracture", Probabilistic Engineering Mechanics, 19, pp. 307-319.

[11] Carpinteri A., Chiaia, B. and Cornetti, P. (2003), "On the mechanics of quasi-brittle materials with a fractal microstructure", Engng. Fract. Mech., 70, pp. 2321-2349.

[12] Kim, J.-K. and Yi, S.-T. (2002), "Application of size effect to compressive strength of concrete members", Sādhanā, 27, pp. 467-484.

[13] Vardoulakis, I. and Kourkoulis, S.K. (1997), "Mechanical properties of Dionysos marble", *Final Report of the Environment Project EV5V - CT93 - 0300*, Dept. of Mechanics, Nat. Techn. Univ. of Athens, Athens.

[14] Kourkoulis, S. K, Ninis, N. L. and Bakolas, V. (2004), "The mechanical behaviour of Conchyliates shell-stone – The size effect", *Proc. Int. Conf. on Influence of Traditional Mathematics and Mechanics on Modern Science and Technology*, Messini, Greece, pp. 307-315.

[15] Thuro, K., Plinningr, R.J., Zäh, S., Schütz, S. (2001), "Scale effects in rock strength properties", *Eurock 2001: Rock Mechanics a challenge for society*, Espoo, Finland, June 2001, pp. 169-174.

MULTI-FREQUENCY PASSIVE NONLINEAR TARGETED ENERGY TRANSFERS IN SYSTEMS OF COUPLED OSCILLATORS

Stylianos Tsakirtzis ([1]), Panagiotis N. Panagopoulos ([1]), Gaetan Kerschen ([2]), Oleg Gendelman ([3]), Alexander F. Vakakis ([4,†]), Lawrence A. Bergman ([5])

([1]) School of Applied Mathematical and Physical Sciences,
National Technical University of Athens,
tsakstel@central.ntua.gr, panago58@central.ntua.gr
([2]) Département d'Aérospatiale, Mécanique et Matériaux (ASMA),
Université de Liège, g.kerschen@ulg.ac.be;
currently, postdoctoral fellow, National Technical University of Athens
and University of Illinois at Urbana – Champaign
([3]) Faculty of Mechanical Engineering,
Technion – Israel Institute of Technology, ovgend@techunix.technion.ac.il
([4]) School of Applied Mathematical and Physical Sciences,
National Technical University of Athens, vakakis@central.ntua.gr;
and
Department of Mechanical and Industrial Engineering (adjunct),
Department of Aerospace Engineering (adjunct),
University of Illinois at Urbana-Champaign, avakakis@uiuc.edu
([5]) Department of Aerospace Engineering,
University of Illinois at Urbana-Champaign, lbergman@uiuc.edu

Keywords: Nonlinear coupled oscillators, passive energy transfer

Abstract. *We study the dynamics of a system of coupled linear oscillators with a multi-DOF end attachment with essential (nonlinearizable) stiffness nonlinearities. We show numerically that the multi-DOF attachment with damping can passively absorb broadband energy from the linear system in a one-way, irreversible fashion, acting in essence as nonlinear energy sink (NES). Strong passive targeted energy transfer from the linear to the nonlinear subsystem is possible, over wide frequency and energy ranges. We numerically demonstrate that the topological structure of the periodic orbits in the frequency – energy plane of the underlying hamiltonian system greatly influences the strength of targeted energy transfer in the damped system, and governs to a great extent the overall transient damped dynamics. This work may be regarded as a contribution towards proving the efficacy the utilizing essentially nonlinear attachments as passive broadband boundary controllers.*

1 INTRODUCTION

We study the dynamics of a two-degree-of-freedom (DOF) linear system coupled to a multi-DOF essentially nonlinear attachment. Interesting energy exchange phenomena can occur in this type of coupled oscillators, including numerous coexisting branches of subharmonic periodic solutions, and one-way, irreversible transfer of energy from the linear oscillator to the nonlinear attachment, termed *targeted nonlinear energy pumping*. Such energy exchanges are often associated with transient or sustained *resonance captures* [1,2], whereby the nonlinearizable, nonlinear attachment engages in transient resonance with the linear oscillator, before the dynamics 'escape' to a different regime of the motion. In cases where the nonlinear attachment acts as passive recipient of vibration energy from the linear oscillator, it essentially acts as *nonlinear energy sink (NES).*

In this work we show that multi-DOF NESs are capable of passively absorbing broadband energy from the primary linear systems to which they are attached. Moreover, this targeted energy transfer is more profound compared to analogous transfers in single-DOF NESs. Alternative configurations of single-DOF NESs were considered in previous works [3,4], whereas alternative mechanisms of targeted energy transfer were studied by other authors [5-8].

2 NUMERICAL EVIDENCE OF PASSIVE ENERGY TRANSFER

The system considered is depicted in Figure 1. It consists of a two-degree-of-freedom (DOF) linear primary oscillator connected through a weak linear stiffness of constant ε (which is the small parameter of the problem,

$0 < \varepsilon << 1$) to a three-DOF nonlinear attachment possessing essential stiffness nonlinearities. Each mass of the primary system is normalized to unity, and the stiffnesses of the nonlinear attachment obey cubic laws with constants C_1 and C_2, and have no linear terms; thus they are essentially nonlinear (nonlinearizable); each mass of the nonlinear attachment is equal to μ, and both linear and nonlinear subsystems possess linear viscous dampers with small constants $\varepsilon\lambda$. Assuming that impulsive excitations $F_1(t)$ and $F_2(t)$ are applied to the primary system no direct forcing excites the nonlinear attachment, the equations of motion are,

$$\begin{aligned}
&\ddot{u}_1 + (\omega_0^2 + \alpha)u_1 - \alpha u_2 + \varepsilon\lambda\dot{u}_1 = F_1(t)\\
&\ddot{u}_2 + (\omega_0^2 + \alpha + \varepsilon)u_2 - \alpha u_1 - \varepsilon v_1 + \varepsilon\lambda\dot{u}_2 = F_2(t)\\
&\mu\ddot{v}_1 + C_1(v_1 - v_2)^3 + \varepsilon(v_1 - u_2) + \varepsilon\lambda\left(\dot{v}_1 - \dot{v}_2\right) = 0\\
&\mu\ddot{v}_2 + C_1(v_2 - v_1)^3 + C_2(v_2 - v_3)^3 + \varepsilon\lambda\left(2\dot{v}_2 - \dot{v}_1 - \dot{v}_3\right) = 0\\
&\mu\ddot{v}_3 + C_2(v_3 - v_2)^3 + \varepsilon\lambda\left(\dot{v}_3 - \dot{v}_2\right) = 0
\end{aligned} \tag{1}$$

In the limit $\varepsilon \to 0$ the system decomposes into two uncoupled oscillators: a two-DOF linear primary system with natural frequencies $\omega_1 = \sqrt{\omega_0^2 + 2\alpha}$ and $\omega_2 = \omega_0 < \omega_1$, corresponding to out-of-phase and in-phase linear modes, respectively; and a three-DOF essentially nonlinear oscillator with a rigid body mode, and two flexible nonlinear normal modes – NNMs.

The aim of this work is to study the dynamics of this system, and to show that it is possible to achieve passive and irreversible *targeted energy transfer (energy pumping)* from the directly forced primary system to the nonlinear attachment; in that context, the nonlinear attachment will act as *nonlinear energy sink (NES).* This work differs from previous works on targeted energy transfer in two basic aspects: first, it considers the possibility of *multi-frequency targeted energy transfer* from multiple modes of the primary system to multiple (nonlinear) modes of the NES; in addition, it shows that complex transitions in the damped dynamics can be related to the topological structure of the periodic orbits of the corresponding undamped system.

The study of the damped dynamics is performed initially through direct numerical simulations of the equations of motion and post processing of the transient results. An extensive series of numerical simulations was performed over different regions of the parameter space of the system, in order to establish the system parameters for which optimal passive energy transfer from the primary system to the NES occurs. Moreover, by varying the linear coupling stiffness α of the primary system we studied the influence of the closeness of the natural frequencies ω_1 and ω_2 of the two linear ('uncoupled') modes of the primary system on this targeted energy transfer. The numerical simulations were carried out by assigning different sets of initial conditions of the primary system, and always considering the NES to be initially at rest. To assess the degree of passive targeted energy transfer to the NES, the following energy measure was numerically computed,

$$E(t) = \frac{\varepsilon\lambda}{E_{in}}\int_0^t \left[\left(\dot{v}_1(\tau) - \dot{v}_2(\tau)\right)^2 + \left(\dot{v}_2(\tau) - \dot{v}_3(\tau)\right)^2\right]d\tau \tag{2}$$

where E_{in} is the input energy provided to the system by the initial conditions. This nondimensional energy measure represents the instantaneous portion of input energy dissipated by the NES up to time instant t. Clearly, for transient excitation of the passive system (1) this instantaneous energy measure is expected to reach a definite asymptotic limit:

$$E_{NES} = \lim_{t>>1} E(t) \tag{3}$$

This asymptotic energy measure represents the portion of input energy *eventually* dissipated by the NES. In what follows, we use the asymptotic evaluation (3) as a measure of the efficiency of targeted energy transfer from the primary system to the NES.

The numerical simulations indicated that, for small values of the perturbation parameter ε, *enhanced passive targeted energy transfer from the primary system to the NES could be achieved for small values of the mass parameter* μ *and nonlinear characteristic* C_2 *of the NES, with all other parameters being quantities of O(1).* This combination of system parameters led to large relative internal displacements in the NES, which, in turn, produced large values of the dissipated energy measures (2) and (3). Accordingly, in the following numerical simulations the system parameters were assigned the values:

$$\varepsilon = 0.2,\ \alpha = 1.0,\ C_1 = 4.0,\ C_2 = 0.05,\ \varepsilon\lambda = 0.01,\ \mu \to \varepsilon^2\mu = 0.08,\ \omega_0^2 = 1.0$$

The results presented in this work demonstrate the potential of system (1) to passively channel energy from the directly excited primary system to the nonlinear attachment, in a one-way, irreversible fashion.

In the following numerical simulations three types of impulsive forcing conditions - IFCs (or, equivalently, initial conditions) for the primary system are considered:

I1: Single impulse forcing, $F_1(t) = Y\delta(t)$ (or, equivalently, $\dot{u}_1(0) = Y$), and all other initial

conditions zero.

I2: In-phase impulsive forcing, $F_1(t) = F_2(t) = Y\delta(t)$ and all other initial conditions zero.

I3: Out-of-phase impulsive forcing, $F_1(t) = -F_2(t) = Y\delta(t)$ and all other initial conditions zero.

In Figures 2-4 we depict the energy measure E_{NES} as function of the magnitude of the impulse Y and the linear coupling stiffness of the primary system α, for the above types of IFCs. The following conclusions are drawn from these results.

In all cases, a significant portion (reaching as high as 86% for IFC I1; 92% for IFC I2; and 90% for IFC I3) of the input energy gets passively absorbed and dissipated by the NES. This significant passive targeted energy transfer occurs in spite of the fact that the (directly forced) primary linear system and the NES have identical dashpots. Moreover, the energy transfer is *broadband*.

Whereas the portion of energy eventually dissipated at the NES, E_{NES}, depends on the level of energy input and the closeness of the natural frequencies of the primary system, this dependence is less pronounced compared to single-DOF NES. This is concluded by comparing the plots of Figures 2-4 with results reported in earlier works where grounded single-DOF NESs were considered [4]. The enhanced targeted energy transfer achieved through the use of multi-DOF NESs is concluded from the comparative plots of Figure 5, where the energy measure E_{NES} is depicted for a system with $\alpha = 0.2$, and IFCs I1 and I3. The system with single-DOF NES whose response is depicted in that plot is identical to that of Figure 1, but with the multi-NES replaced by a single mass $3\varepsilon\mu$ grounded by means of a cubic stiffness nonlinearity with characteristic Cv^3, $C = 1.0$, and a weak viscous damper $\varepsilon\lambda$. We note the significant improvement of targeted energy transfer achieved by using the multi-DOF NES, and the less pronounced dependence on the magnitude of the input impulse Y in that case.

Particularly notable is the capacity of the multi-DOF NES to absorb a significant portion of the input energy even at low values of the applied impulse. Such low-energy targeted energy transfer is markedly different from the performance of single-DOF NESs, which, as reported in previous works [4,8], is 'activated' only when the magnitude of input energy exceeds a certain critical threshold; for the case of multi-DOF NES such a critical energy threshold can only be detected in the energy plot for $\alpha = 4$ of Figure 4, i.e., only in the case when the primary system possesses well separated natural frequencies and is excited through out-of-phase initial conditions. In all other cases (Figures 2-4) no such critical input energy threshold is identified, for the multi-DOF NES. This interesting feature of the dynamics will be reconsidered in more detail in a later section.

Of particular interest is the plot of E_{NES} in Figure 4 corresponding to $\alpha = 1$ (corresponding to natural frequencies of the uncoupled primary system $\omega_1 = 1.7321$, $\omega_2 = 1.0$ rad/sec) and out-of-phase impulse excitations. For small impulse magnitudes, the portion of energy dissipated at the NES develops a local minimum before reaching higher values. To get some insight into the dynamics of targeted energy transfer in that region, in Figures 6 and 7 we depict the numerical Cauchy wavelet transforms (WTs) of the internal relative NES displacements $[v_2(t) - v_1(t)]$ and $[v_3(t) - v_2(t)]$ at points labeled A and B in Figure 4; point A is a case where no rigorous energy transfer to the NES, in contrast to point B where nearly 90% of the input energy gets absorbed and dissipated by the NES. The WT can be viewed as a basis for functional representation but is at the same time a relevant technique for time-frequency analysis. In contrast to the Fast Fourier Transform (FFT) which assumes signal stationarity, the WT involves a windowing technique with variable-sized regions. Small time intervals are considered for high frequency components whereas the size of the interval is increased for lower frequency components, thereby giving better time and frequency resolutions than the FFT. The plots shown represent the amplitude of the WT as a function of frequency (vertical axis) and time (horizontal axis). Heavy shaded areas correspond to regions where the amplitude of the WT is high whereas lightly shaded regions correspond to low amplitudes. Such plots enable one to deduce the temporal evolutions of the dominant frequency components of the signals analyzed. Comparing the two responses of Figures 6 (point A) and 7 (point B), it is clear that the enhanced energy transfer in the later case is due mainly to the large-amplitude transient relative response $[v_3(t) - v_2(t)]$; judging from the corresponding WT, this time series consists of a 'fast' oscillation with frequency close to ω_1, modulated by a large-amplitude 'slow' modulation. Moreover, this modulated response is not sustained over all times; rather, it takes place only at the initial phase of the motion, and escapes this regime of the motion at approximately $t = 50$. Similar behavior is observed for the time series of the other relative response, $[v_2(t) - v_1(t)]$, in Figure 7. It is well established [4,13,14] that this represents a *transient resonance capture (TRC)* of the NES dynamics on a resonance manifold near the out-of-phase linear mode of the uncoupled primary system, which results in enhanced and irreversible energy transfer from the primary system to the NES. Comparing to the responses of Figure 6 (where less significant energy transfer occurs), we note that the transient responses are dominated by sustained frequency components, indicating excitation of nonlinear modes, rather than occurrence of TRCs; the frequencies of some of the nonlinear modes

that are excited differ from the linearized natural frequencies ω_1 and ω_2, indicating the presence in the response of essentially nonlinear modes with no linear analogs.

3 DAMPED TRANSITIONS IN THE FREQUENCY – ENERGY PLANE

We wish to study in more detail the damped transitions associated with the peculiar behavior of the targeted energy transfer plot for $\alpha = 1.0$ and impulsive forcing conditions I3 (depicted in Figure 4). More specifically, it was numerically found that when the linear system is excited by a pair of anti-phase impulses of magnitude Y, strong targeted energy transfer to the NES occurs at low values of the impulse (as much as 90% for Y=0.1); for increasing magnitude of the impulse the eventual energy transfer to the NES first decreases (reaching nearly 50% for Y=1.0), before increasing again to high levels (up to nearly 90% for Y=1.5). Further increase of Y decreases the portion of input energy that is eventually dissipated at the NES. The damped transitions leading to this peculiar behavior of the energy transfer capacity of the NES are depicted and analyzed in Figures 8-10. We will superimpose the wavelet transforms of the NES relative displacements to the frequency energy plot of the periodic orbits of the underlying hamiltonian system with no damping (these were computed in [15]).

In Figure 8 the damped response of the system is depicted for impulsive forcing conditions I3 and Y=0.1 (i.e., impulses $F_1(t) = -F_2(t) = Y\delta(t)$ and zero ICs). In this case both internal NES displacements $[v_1(t) - v_2(t)]$ and $[v_2(t) - v_3(t)]$ follow regular backbone branches. The relative displacement $[v_1(t) - v_2(t)]$ has a dominant frequency component that approaches a linearized natural frequency with decreasing energy; by contrast, $[v_2(t) - v_3(t)]$ has two strong harmonic components that approach two other linearized natural frequencies for decreasing energy, indicating *multi-frequency transfer of energy simultaneously from two modes of the linear limiting system (5)*. Moreover, the same backbone branches are tracked by the response throughout the motion, and strong energy transfer occurs right from the early stage of the response. This explains the strong eventual energy transfer to the NES (~90%) that occurs for this low impulse excitation.

By increasing the magnitude of the impulse to Y=1.0 the overall energy transfer from the linear to the nonlinear subsystem significantly decreases. The damped response in this case is depicted in Figure 9, were some major qualitative differences are observed compared to the previous simulation. Judging from the partition of the instantaneous energy among the linear and nonlinear subsystems, it is concluded that in the energy transfer is significantly delayed, which explains the weak eventual energy transfer to the NES (~50%). This delay is explained when one studies the wavelet transforms of the NES responses in the frequency – energy plot of Figure 9a. At the initial stage of the motion there occurs strong resonance capture of the damped motion by the out-of-phase mode of the linear subsystem; this results in a motion mainly localized to the (directly excited) linear subsystem, with a small portion of energy 'spreading out' to the NES. As energy decreases due to damping dissipation, the damped motion 'escapes' from out-of-phase resonance capture, and follows regular backbone branches; this results in strong energy transfer develops (as in the simulations of Figure 8), which, however, is delayed at a stage where the overall level of energy of the system is already small. Hence, no significant overall targeted energy transfer from the linear subsystem to the NES occurs in this case.

Increasing the magnitude of the impulse to Y=1.5 enables the system to escape from the strong initial out-of-phase resonance capture, leading to resumed strong targeted energy transfer. This is depicted in Figure 10, showing that the NES relative responses possess multiple strong frequency components, indicating that strong targeted energy transfer occurs at multiple frequencies. Note in this case the early strong energy transfer from the linear subsystem to the NES that results in an eventual targeted energy transfer of nearly 90%.

4 CONCLUDING REMARKS

The dynamical system considered in this work possesses complicated dynamics due to its degenerate structure. The system has strong passive targeted energy transfer capacity, leading, in some cases, to as much as 90% of input energy in the linear subsystem being irreversibly transferred to, and dissipated at the nonlinear attachment; then the attachment acts in essence as nonlinear energy sink. The capacity of the attachment to irreversibly absorb broadband vibration energy was demonstrated numerically in this work, but it can also be analytically studied by reduction and local slow/fast partition of the damped dynamics. It was shown that multi-DOF essentially nonlinear attachments may be more efficient energy absorbers than single-DOF ones, since they are capable of absorbing energy simultaneously from multiple modes of the linear subsystem, and over wider frequency and energy ranges. Passive targeted energy transfer can be related to transient resonance captures (TRCs) in the damped dynamics, whereby orbits of the system in phase space are captured transiently in neighborhoods of resonance manifolds.

ACKNOWLEDGMENTS

This work was supported in part by a grant for basic research 'HRAKLEITOS' funded by the European

Commission and the General Secretariat for Research and Technology, Hellenic Ministry of Development; by AFOSR grant FA9550-04-1-0073; by the Taub and Shalom Foundadtions (Horev fellowship); and by grants from the Belgian National Fund for Scientific Research - FNRS, the Belgian Rotary District 1630, and the Fulbright and Duesberg Foundations.

REFERENCES

[1] Arnold V.I. (ed.), 1988, *Dynamical Systems III*, Encyclopaedia of Mathematical Sciences, Springer Verlag, Berlin and New York.

[2] Quinn, D., 1997, 'Resonance Capture in a Three Degree of Freedom Mechanical System,' *Nonlinear Dynamics* 14, 309-333.

[3] Vakakis A.F., Gendelman O., 2001, 'Energy Pumping in Nonlinear Mechanical Oscillators II: Resonance Capture', *Journal of Applied Mechanics* 68(1), 42-48.

[4] Vakakis A.F., McFarland D.M., Bergman L.A., Manevitch L.I., Gendelman O., 2004, 'Isolated Resonance Captures and Resonance Capture Cascades Leading to Single- or Multi-Mode Passive Energy Pumping in Damped Coupled Oscillators,' *Journal of Vibration and Acoustics*, 126 (2), 235-244.

[5] Kopidakis G., Aubry S., Tsironis G.P., 2001, 'Targeted Energy Transfer Through Discrete Breathers in Nonlinear Systems,' *Physical Review Letters*, 87 (16), paper 165501-1.

[6] Aubry S., Kopidakis S., Morgante A.M., Tsironis G.P., 2001, 'Analytic Conditions for Targeted Energy Transfer Between Nonlinear Oscillators or Discrete Breathers,' *Physica B* 296, 222-236.

[7] Gendelman O.V., Vakakis A.F., Manevitch L.I. and McCloskey R., 2001, 'Energy Pumping in Nonlinear Mechanical Oscillators I: Dynamics of the Underlying Hamiltonian System,' *Journal of Applied Mechanics* 68(1), 34-41.

[8] Panagopoulos P.N., Vakakis A.F., Tsakirtzis S., 2004, 'Transient Resonant Interactions of Linear Chains with Essentially Nonlinear End Attachments Leading to Passive Energy Pumping,' *International Journal of Solids and Structures*, 41 (22-23), 6505-6528.

[9] S. Tsakirtzis, P.N. Panagopoulos, G. Kerschen, O. Gendelman, A.F. Vakakis, L.A. Bergman, 2005, 'Complex Dynamics and Targeted Energy Transfer in Systems of Linear Oscillators Coupled to Multi-degree-of-freedom Essentially Nonlinear Attachments,' Physical Review E (submitted).

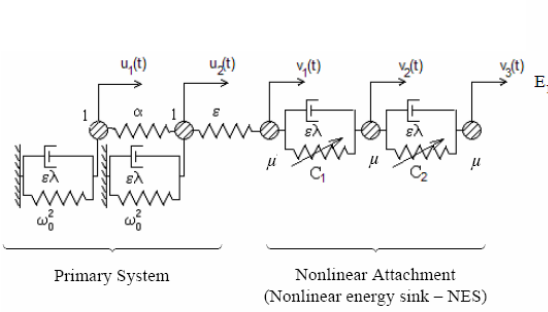

Figure 1. Primary (linear) system with multi-degree-of-freedom (MDOF) nonlinear attachment

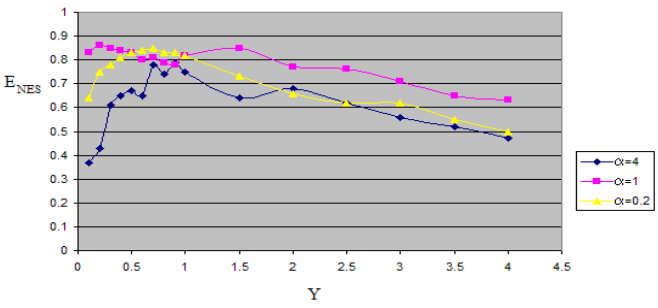

Figure 2. Portion of energy eventually dissipated at the nes for varying values of single impulse Y (impulsive forcing condition I1), and coupling stiffness α of the primary system

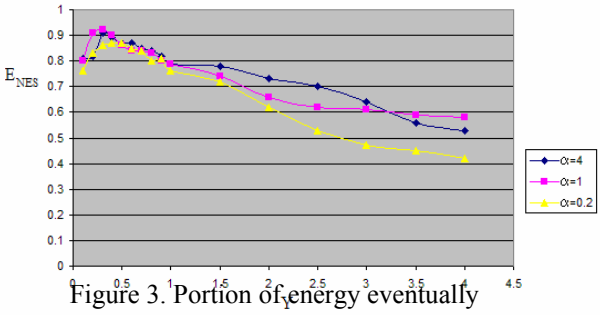

Figure 3. Portion of energy eventually dissipated at the nes for varying values of single impulse Y (impulsive forcing condition I2), and coupling stiffness α of the primary system

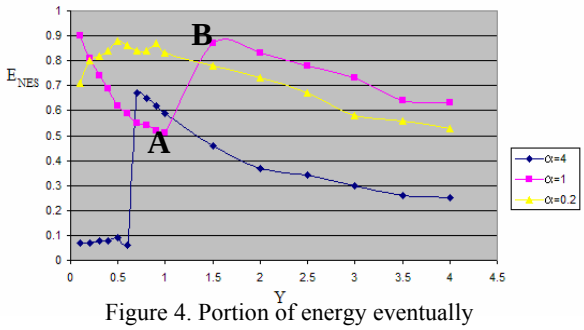

Figure 4. Portion of energy eventually dissipated at the nes for varying values of single impulse Y (impulsive forcing condition I3), and coupling stiffness α of the primary system; the letters A and B at the plot for $\alpha = 1$ refer to the results depicted in figures 6 and 7.

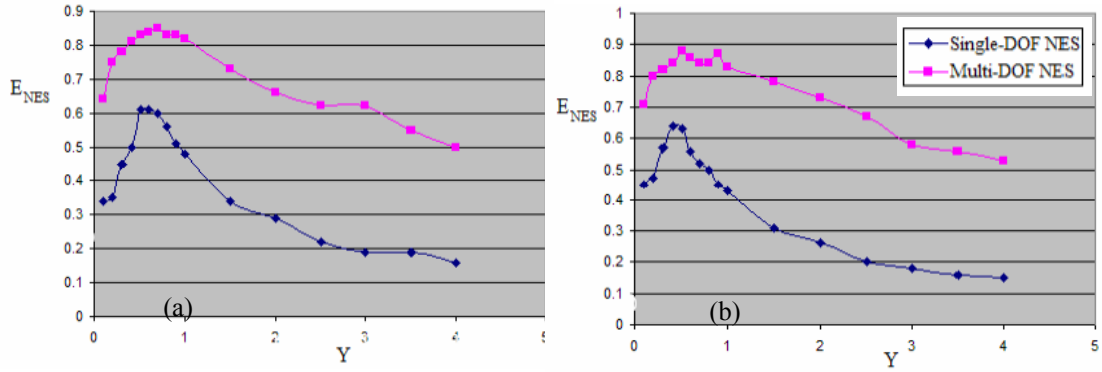

Figure 5. Energy measures E_{NES} for primary systems with single- and multi-DOF NESs, and impulsive forcing conditions, (a) I1, and (b) I3

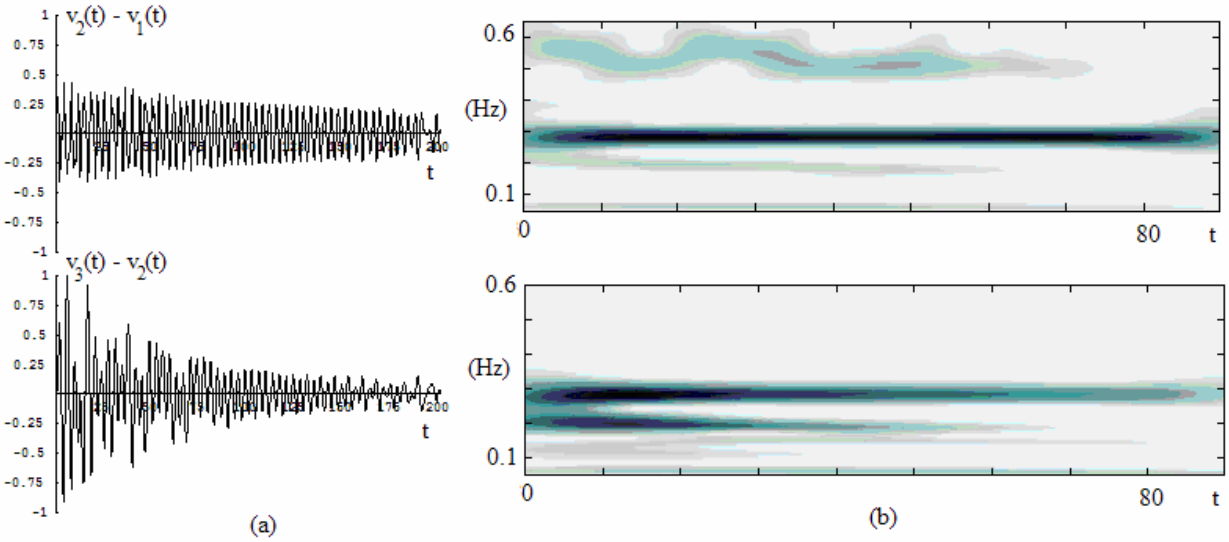

Figure 6. Internal NES relative displacements for out-of-phase impulses (I3) with $Y = 1$ and $\alpha = 1$ (point A in figure 4): (a) time series,
(b) Cauchy wavelet transforms

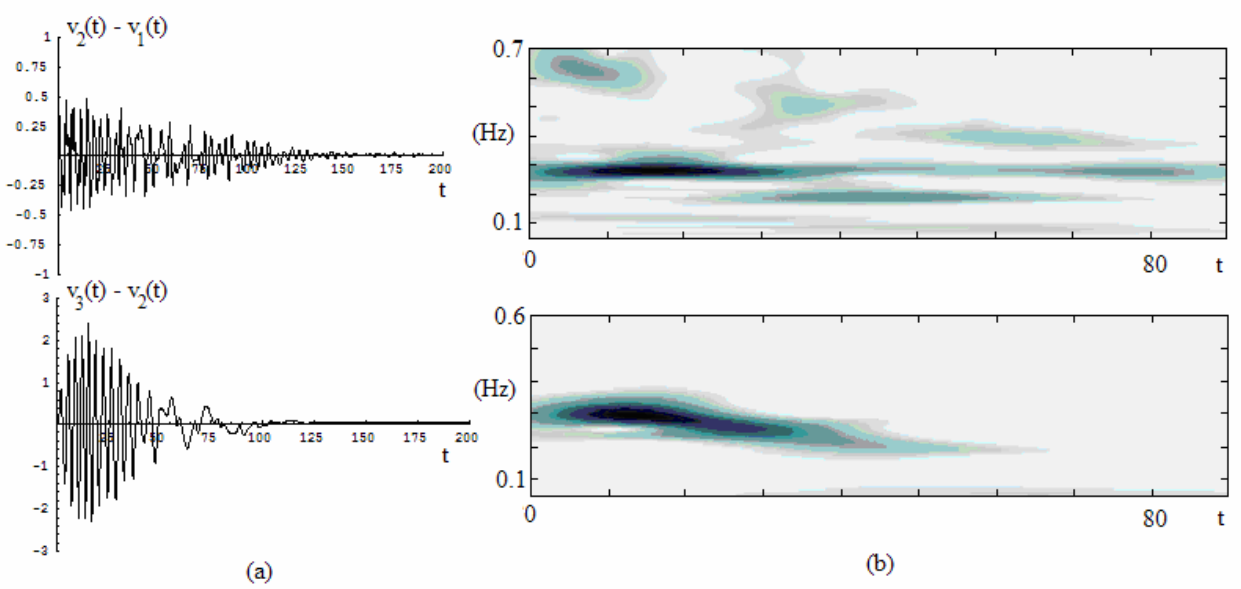

Figure 7: Internal NES relative displacements for out-of-phase implulses (I3) with $\Upsilon = 1.5$ and $\alpha = 1$ (point B in figure 4): (a) time series, (b) Cauchy wavelet transforms

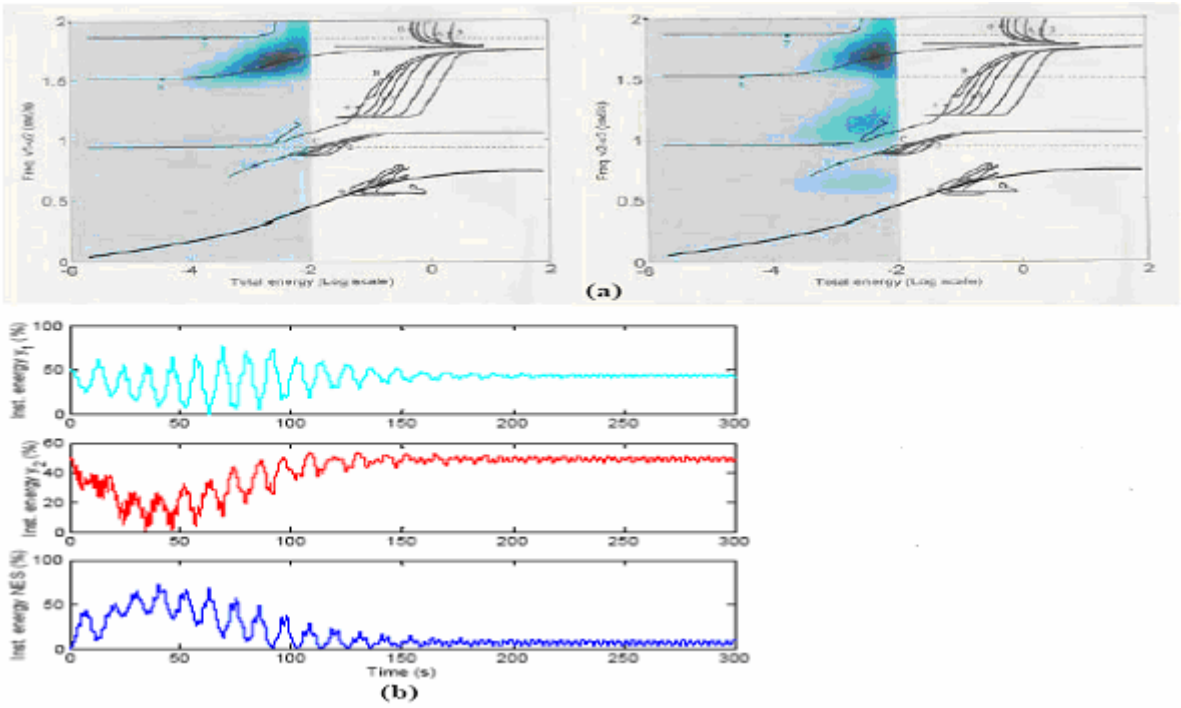

Figure 8: Damped responses for out-of-phase impulses Y=0.1 (impulsive forcing condition I3); (a) Cauchy wavelet transforms superimposed to the frequency – energy plot of the periodic orbits of the underlying hamiltonian system [9], (b) partition of instantaneous energy of the system.

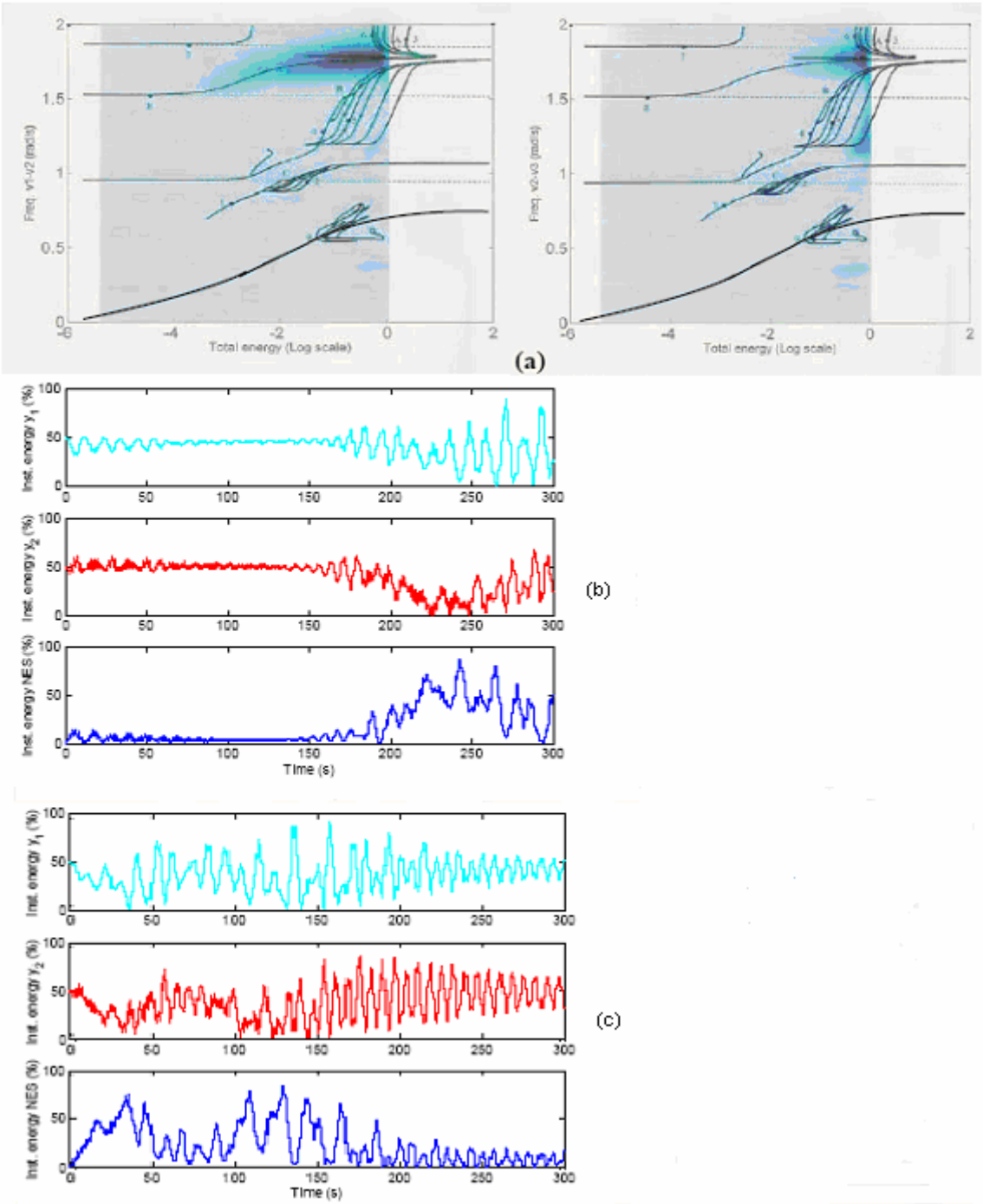

Figure 9: (a) Cauchy wavelet transforms superimposed to the frequency – energy plot of the periodic orbits of the underlying hamiltonian system [9], (b) Damped responses for out-of-phase impulses Y=1.0 (impulsive forcing condition I3partition of instantaneous energy of the system, (c) Damped responses for out-of-phase impulses Y=1.5 (impulsive forcing condition I3partition of instantaneous energy of the system

CLASSICAL LIMITS OF A MICROPOLAR PLASTICITY MODEL

P. Grammenoudis and Ch. Tsakmakis

Department of Mechanics
Darmstadt University of Technology
D-64289 Darmstadt, Germany
e-mail: pascha@mechanik.tu-darmstadt.de, tsakmakis@mechanik.tu-darmstadt.de
web page: http://ag1.mechanik.tu-darmstadt.de/

Keywords: Micropolar Plasticity, Finite Deformations, Kinematic hardening rules, Torsional loadings.

Abstract. *We focus attention on finite deformation micropolar plasticity theories developed previously, which deal with a second-order non-symmetric micropolar strain tensor and a second-order curvature tensor. The aim of the paper is to investigate the classical limiting plasticity models, which may be approached by these theories. The differences compared with a standard classical plasticity model consists in the constitutive equations governing kinematic hardening. With reference to torsional loading, this causes different responses essentially only in the so-called second-order effects.*

1 INTRODUCTION

Micropolar models indicate the property that the Cauchy stress tensor is no longer symmetric and that so-called couple stress tensors are present, which are thermodynamically conjugate to curvature tensors (see e.g. Mindlin[1], Eringen[2], de Borst[3], Steinmann[4]). Latter are expressed in terms of the spatial gradient of a micropolar rotation tensor, which is invoked to capture the effect of the underlying substructure of the overall material body. Phenomenological and crystal plasticity micropolar models have been proposed and investigated among others by Lippmann[5], Diopolder et al. [6] and Forest[7]. Generally, such models may be employed to capture size effects in the material response or to study strain softening material response and related localization phenomena in the framework of rate-independent plasticity (see e.g. Grammenoudis & Tsakmakis[8,9,10], de Borst & Mühlhaus[11], Mühlhaus & Vardoulakis[12], Steinmann & Willam[13]).

The present paper is concerned with the micropolar plasticity theory developed in Grammenoudis & Tsakmakis[8,9,10]. This constitutive theory is formulated for finite deformations and incorporates nonlinear isotropic and nonlinear kinematic hardening. A limiting classical plasticity model, i.e. a resulting particular model with symmetric Cauchy stress tensor and vanishing couple stress tensors, is established in Grammenoudis & Tsakmakis[14,15]. The characteristic feature of the limiting classical model, compared with standard classical plasticity models, is the law for kinematic hardening. In fact, the back stress tensor is non-symmetric, even in the case of isotropic specific free energy functions, and the evolution equation governing kinematic hardening involves objective time derivatives of mixed Oldroyd type. With reference to torsional loading, this causes different responses essentially only in the so-called second-order effects.

2 THE MICROPOLAR PLASTICITY MODELS

Micropolar theories use as independent kinematical variables the deformation gradient tensor $\mathbf{F}$ and the so-called micropolar rotation tensor $\overline{\mathbf{R}}$. For formulating plasticity models, Steinmann[4] postulated the multiplicative decompositions of $\mathbf{F}$ and $\overline{\mathbf{R}}$ into elastic and plastic parts, respectively:

$$\mathbf{F} = \mathbf{F}_e\mathbf{F}_p \quad , \quad \overline{\mathbf{R}} = \overline{\mathbf{R}}_e\overline{\mathbf{R}}_p \quad . \tag{1}$$

(For classical plasticity, the multiplicative decomposition of $\mathbf{F}$ goes back to Lee (see e.g.[16])) Geometrically, $\mathbf{F}_p$ and $\overline{\mathbf{R}}_p$ introduce a so-called plastic intermediate configuration. Based on Equations (1), a thermodynamically consistent theory for micropolar plasticity, exhibiting isotropic and kinematic hardening effects, has been proposed in Grammenoudis & Tsakmakis[8,9,10]. Using the notation introduced in Grammenoudis & Tsakmakis[8,9], the most relevant constitutive relations of that theory, relative to the plastic intermediate configuration, are given as follows.

Kinematics:

$$\mathbf{F}=\mathbf{R}\mathbf{U}=\mathbf{V}\mathbf{R} \quad , \quad \mathbf{F}_e=\mathbf{R}_e\mathbf{U}_e=\mathbf{V}_e\mathbf{R}_e \quad , \quad \mathbf{F}_p=\mathbf{R}_p\mathbf{U}_p=\mathbf{V}_p\mathbf{R}_p\,, \tag{2}$$

$$\mathbf{F}=\overline{\mathbf{R}\,\mathbf{U}}=\overline{\mathbf{V}\,\mathbf{R}} \quad , \quad \mathbf{F}_e=\overline{\mathbf{R}}_e\overline{\mathbf{U}}_e=\overline{\mathbf{V}}_e\overline{\mathbf{R}}_e \quad , \quad \mathbf{F}_p=\overline{\mathbf{R}}_p\overline{\mathbf{U}}_p=\overline{\mathbf{V}}_p\overline{\mathbf{R}}_p\,, \tag{3}$$

$$\hat{\mathbf{L}}_p=\dot{\mathbf{F}}_p\mathbf{F}_p^{-1} \quad , \quad \hat{\mathbf{D}}_p=\frac{1}{2}(\hat{\mathbf{L}}_p+\hat{\mathbf{L}}_p^T) \quad , \quad \hat{\mathbf{W}}=\frac{1}{2}(\hat{\mathbf{L}}_p-\hat{\mathbf{L}}_p^T) \quad , \quad \hat{\mathbf{\Omega}}_p=\dot{\overline{\mathbf{R}}}_p\overline{\mathbf{R}}_p^T, \tag{4}$$

$$\hat{\boldsymbol{\varepsilon}}=\hat{\boldsymbol{\varepsilon}}_e+\hat{\boldsymbol{\varepsilon}}_p \quad , \quad \hat{\boldsymbol{\varepsilon}}_e=\overline{\mathbf{U}}_e-1 \quad , \quad \hat{\boldsymbol{\varepsilon}}_p=1-\overline{\mathbf{V}}_p^{-1}, \tag{5}$$

$$\hat{\mathbf{K}}=\hat{\mathbf{K}}_e+\hat{\mathbf{K}}_p=\overline{\mathbf{R}}_p\tilde{\mathbf{K}}\overline{\mathbf{R}}_p^T \quad , \quad \tilde{\mathbf{K}}=\left\{axl\left(\overline{\mathbf{R}}^T\frac{\partial\overline{\mathbf{R}}}{\partial X_k}\right)\right\}\otimes\mathbf{E}_k\,. \tag{6}$$

Stress and couple stress tensors:

$$\mathbf{S}=(\det\mathbf{F})\mathbf{T}=\overline{\mathbf{R}}_e\hat{\mathbf{T}}\mathbf{F}_e^T=\mathbf{F}_e\hat{\mathbf{S}}\mathbf{F}_e^T \quad , \quad \hat{\mathbf{P}}=(\mathbf{1}+\hat{\boldsymbol{\varepsilon}}_e^T)\hat{\mathbf{T}}=(\mathbf{F}_e^T\mathbf{F}_e)\hat{\mathbf{S}}\,, \tag{7}$$

$$\mathbf{S}_c=(\det\overline{\mathbf{V}})\mathbf{T}_c\overline{\mathbf{V}}^{T-1}=\overline{\mathbf{R}}_e\hat{\mathbf{T}}_c\overline{\mathbf{R}}_e^T \quad , \quad \hat{\mathbf{P}}_c\equiv\hat{\mathbf{T}}_c\,. \tag{8}$$

Specific free energy:

$$\psi(t)=\psi_e(t)+\psi_p(t) \quad , \quad \psi_p(t)=\psi_p^{(iso)}(t)+\psi_p^{(kin)}(t)\,. \tag{9}$$

Elasticity laws:

$$\psi_e=\hat{\psi}_e\left(\hat{\boldsymbol{\varepsilon}}_e,\hat{\mathbf{K}}_e\right) \quad , \quad \hat{\mathbf{T}}=\rho_R\frac{\partial\hat{\psi}_e}{\partial\hat{\boldsymbol{\varepsilon}}_e} \quad , \quad \hat{\mathbf{T}}_c=\rho_R\frac{\partial\hat{\psi}_e}{\partial\hat{\mathbf{K}}_e}\,. \tag{10}$$

Yield function:

$$\begin{aligned} f=\{&(\alpha_1+\alpha_2)\left(\hat{\mathbf{P}}-\hat{\boldsymbol{\xi}}\right)^D\cdot\left(\hat{\mathbf{P}}-\hat{\boldsymbol{\xi}}\right)^D+(\alpha_1-\alpha_2)\left(\hat{\mathbf{P}}-\hat{\boldsymbol{\xi}}\right)^D\cdot\left(\hat{\mathbf{P}}^T-\hat{\boldsymbol{\xi}}^T\right)^D\\ &+(\alpha_3+\alpha_4)\left(\hat{\mathbf{P}}_c-\hat{\boldsymbol{\xi}}_c\right)^D\cdot\left(\hat{\mathbf{P}}_c-\hat{\boldsymbol{\xi}}_c\right)^D+(\alpha_3-\alpha_4)\left(\hat{\mathbf{P}}_c-\hat{\boldsymbol{\xi}}_c\right)^D\cdot\left(\hat{\mathbf{P}}_c^T-\hat{\boldsymbol{\xi}}_c^T\right)^D\}^{\frac{1}{2}}-k, \end{aligned} \tag{11}$$

$$k=h+R \quad , \quad h=const. \quad R \text{ : isotropic hardening variable.} \tag{12}$$

Flow rules:

$$\overset{\diamond}{\hat{\boldsymbol{\varepsilon}}}_p=\dot{\hat{\boldsymbol{\varepsilon}}}_p-\hat{\mathbf{\Omega}}_p\hat{\boldsymbol{\varepsilon}}_p+\hat{\boldsymbol{\varepsilon}}_p\hat{\mathbf{L}}_p\equiv\hat{\mathbf{L}}_p-\hat{\mathbf{\Omega}}_p=\frac{\dot{s}}{\chi}\frac{\partial f}{\partial\hat{\mathbf{P}}}, \tag{13}$$

$$\overset{\diamond}{\hat{\mathbf{K}}}_p=\dot{\hat{\mathbf{K}}}_p-\hat{\mathbf{\Omega}}_p\hat{\mathbf{K}}_p-\hat{\mathbf{K}}_p\hat{\mathbf{\Omega}}_p=\frac{\dot{s}}{\chi}\frac{\partial f}{\partial\hat{\mathbf{P}}_c}, \tag{14}$$

$$\dot{s}:=\sqrt{\hat{\boldsymbol{\varepsilon}}_p\cdot\hat{\boldsymbol{\varepsilon}}_p+\hat{\mathbf{K}}_p\cdot\hat{\mathbf{K}}_p} \quad , \quad \chi:=\sqrt{\frac{\partial f}{\partial\hat{\mathbf{P}}}\cdot\frac{\partial f}{\partial\hat{\mathbf{P}}}+\frac{\partial f}{\partial\hat{\mathbf{P}}_c}\cdot\frac{\partial f}{\partial\hat{\mathbf{P}}_c}}\,. \tag{15}$$

Isotropic hardening:

$$\psi_p^{(is)}=\hat{\psi}_p^{(is)}(r)=\frac{1}{\rho_R}\left(\frac{1}{2}\gamma^{(is)}r^2+R_0r\right), \tag{16}$$

$$R:=\rho_R\frac{\partial\hat{\psi}_p^{(is)}}{\partial r}=\gamma^{(is)}r^2+R_0 \quad , \quad R_0=R(s=0) \quad , \quad k_0:=k(s=0)=R_0+h\,, \tag{17}$$

$$\dot{r}=\left(1-\beta^{(is)}r\right)\frac{\dot{s}}{\chi} \quad , \quad r(s=0)=0 \quad \Leftrightarrow \tag{18}$$

$$\dot{R}=\left[\gamma^{(is)}-\beta^{(is)}(R-R_0)\right]\frac{\dot{s}}{\chi} \quad \Leftrightarrow \quad \dot{k}=\left[\gamma^{(is)}-\beta^{(is)}(k-k_0)\right]\frac{\dot{s}}{\chi}\,. \tag{19}$$

Kinematic hardening:

$$\psi_p^{(kin)} = \hat{\psi}_p^{(kin)}(\hat{\mathbf{Y}}, \hat{\mathbf{Y}}_c), \tag{20}$$

$$\hat{\mathbf{Z}} := \rho_R \frac{\partial \hat{\psi}_p^{(kin)}}{\partial \hat{\mathbf{Y}}} \quad , \quad \hat{\mathbf{Z}}_c := \rho_R \frac{\partial \hat{\psi}_p^{(kin)}}{\partial \hat{\mathbf{Y}}_c}, \tag{21}$$

$$\hat{\boldsymbol{\xi}} := (\mathbf{1} - \hat{\mathbf{Y}}^T)\hat{\mathbf{Z}} \quad , \quad \hat{\boldsymbol{\xi}}_c \equiv \hat{\mathbf{Z}}_c, \tag{22}$$

$$\overset{\diamond}{\hat{\mathbf{Y}}} = \dot{\hat{\mathbf{Y}}} - \hat{\boldsymbol{\Omega}}_p \hat{\mathbf{Y}} + \hat{\mathbf{Y}}\hat{\mathbf{L}}_p = \overset{\diamond}{\hat{\boldsymbol{\varepsilon}}}_p - \dot{s}\left\{(b_1 + b_2)\hat{\mathbf{Z}} + (b_1 - b_2)\hat{\mathbf{Z}}^T\right\}, \tag{23}$$

$$\overset{\diamond}{\hat{\mathbf{Y}}}_c = \dot{\hat{\mathbf{Y}}}_c - \hat{\boldsymbol{\Omega}}_p \hat{\mathbf{Y}}_c - \hat{\mathbf{Y}}_c \hat{\boldsymbol{\Omega}}_p = \overset{\diamond}{\hat{\mathbf{K}}}_p - \dot{s}\left\{(b_{c1} + b_{c2})\hat{\mathbf{Z}}_c + (b_{c1} - b_{c2})\hat{\mathbf{Z}}_c^T\right\}. \tag{24}$$

In these relations, the specific free energy is supposed to be an isotropic tensor function of its arguments and plastic incompressibility is assumed to apply, so that $\det \mathbf{F}_p = 1$ or $tr\hat{\mathbf{L}}_p = 0$. While Equations (2) represent polar decompositions, this is not the case for Equations (3). It is important to notice that the second-order tensors $\overline{\mathbf{U}}, \overline{\mathbf{V}}, \overline{\mathbf{U}}_e, \overline{\mathbf{V}}_e, \overline{\mathbf{U}}_p, \overline{\mathbf{V}}_p$ do not represent symmetric tensors generally. The micropolar strains $\hat{\boldsymbol{\varepsilon}}, \hat{\boldsymbol{\varepsilon}}_e, \hat{\boldsymbol{\varepsilon}}_p$ and the so-called curvatures $\hat{\mathbf{K}}, \hat{\mathbf{K}}_e, \hat{\mathbf{K}}_p$ are second-order tensors, which are generally non-symmetric. $\mathbf{T}$ and $\mathbf{T}_c$ are the Cauchy stress tensor and the Eulerian couple stress tensor, respectively. These stresses enter into the balance laws of momentum and moment of momentum, not considered here. $\hat{\mathbf{P}}$ and $\hat{\mathbf{P}}_c$ denote so-called Mandel stress and couple stress tensors, respectively. The yield function in Equation (10) represents a counterpart for finite deformations of a yield function for small deformations proposed by de Borst[3]. Equations governing isotropic hardening are summarized in (16)-(19). Such forms of isotropic hardening rules are intensively investigated for classical plasticity by Chaboche[17]. It is pointed out that this isotropic hardening model captures effects of micropolar strains and curvatures in a unified manner. Of course, one may regard isotropic hardening rules which are additively decomposed into two parts, accounting for micropolar strains and curvatures, respectively. However, such possibilities will not effect the goals of the paper essentially. Kinematic hardening is modeled by Equations (20)-(24), with $\hat{\boldsymbol{\xi}}$ and $\hat{\boldsymbol{\xi}}_c$ being back-stress and back-couple stress tensors of Mandel type, respectively. The evolution equations (23), (24) correspond to the well-known Armstrong-Frederick kinematic hardening rule in classical plasticity. Finally, the quantities $\alpha_1, \alpha_2, \alpha_3, \alpha_4, h, \beta^{(is)}, \gamma^{(is)}, R_0, b_1, b_2, b_{c1}, b_{c2}$ are material parameters, which have to be chosen appropriately.

3 THE LIMITING CLASSICAL MODEL (LCM)

Grammenoudis & Tsakmakis[14,15] worked out the conditions, under which the micropolar constitutive theory of Section 2 approaches to a classical limit, i.e. a plasticity theory with symmetric Cauchy stress tensor and vanishing couple stress tensors. It turned out, according to the assumptions made, that $\overline{\mathbf{R}}_e = \mathbf{R}_e$ and $\hat{\boldsymbol{\Omega}}_p = \hat{\mathbf{W}}_p$. The resulting limiting classical model may be summarized, relative to the plastic intermediate configuration, as follows.

$$\hat{\boldsymbol{\Gamma}} = \hat{\boldsymbol{\Gamma}}_e + \hat{\boldsymbol{\Gamma}}_p \quad , \quad \hat{\boldsymbol{\Gamma}}_e = \frac{1}{2}(\mathbf{F}_e^T \mathbf{F}_e - \mathbf{1}) \quad , \quad \hat{\boldsymbol{\Gamma}}_p = \frac{1}{2}(\mathbf{1} - \mathbf{F}_p^{T-1}\mathbf{F}_p^{-1}), \tag{25}$$

$$\mathbf{S} = (\det \mathbf{F})\mathbf{T} = \mathbf{F}_e \hat{\mathbf{S}} \mathbf{F}_e^T, \tag{26}$$

$$\psi = \psi_e + \psi_p^{(iso)} + \psi_p^{(kin)}, \tag{27}$$

$$\psi_e = \psi_e(\hat{\boldsymbol{\Gamma}}_e) \quad , \quad \hat{\mathbf{S}} = \rho_R \frac{\partial \psi_e}{\partial \hat{\boldsymbol{\Gamma}}_e} \quad , \quad \hat{\mathbf{P}} = (\mathbf{1} + 2\hat{\boldsymbol{\Gamma}}_e)\hat{\mathbf{S}}, \tag{28}$$

$$f = \sqrt{\frac{3}{2}(\hat{\mathbf{P}} - \hat{\boldsymbol{\xi}})_S^D \cdot (\hat{\mathbf{P}} - \hat{\boldsymbol{\xi}})_S^D} - k \quad , \quad k = h + R \quad , \quad h = const., \tag{29}$$

$$\hat{\mathbf{D}}_p = \overset{\Delta}{\hat{\mathbf{\Gamma}}}_p := \dot{\hat{\mathbf{\Gamma}}}_p + \hat{\mathbf{L}}_p^T \hat{\mathbf{\Gamma}}_p + \hat{\mathbf{\Gamma}}_p \hat{\mathbf{L}}_p = \dot{s} \frac{\partial f}{\partial \hat{\mathbf{P}}} \quad , \quad \dot{s} = \sqrt{\frac{3}{2} \hat{\mathbf{D}}_p \cdot \hat{\mathbf{D}}_p} \, , \tag{30}$$

$$\hat{\boldsymbol{\xi}} = (\mathbf{1} - \hat{\mathbf{Y}}^T)\hat{\mathbf{Z}} , \tag{31}$$

$$\psi_p^{(kin)} = \psi_p^{(kin)}(\hat{\mathbf{Y}}) , \tag{32}$$

$$\hat{\mathbf{Z}} = \rho_R \frac{\partial \psi_p^{(kin)}}{\partial \hat{\mathbf{Y}}} = c_1 (tr\hat{\mathbf{Y}})\mathbf{1} + (c_2 + c_3)\hat{\mathbf{Y}} + (c_2 - c_3)\hat{\mathbf{Y}}^T , \tag{33}$$

$$\overset{\diamond}{\hat{\mathbf{Y}}} = \dot{\hat{\mathbf{Y}}} - \hat{\mathbf{L}}_p \hat{\mathbf{Y}} + \hat{\mathbf{Y}} \hat{\mathbf{L}}_p = \hat{\mathbf{D}}_p (\mathbf{1} - \hat{\mathbf{Y}}) - \dot{s} \left\{ (b_1 + b_2)\hat{\mathbf{Z}} + (b_1 - b_2)\hat{\mathbf{Z}}^T \right\}. \tag{34}$$

The isotropic hardening rule is identical to that one in Section 2 and is no further discussed here. The peculiarity of this model consists in the kinematic hardening rule. The back-stress tensor and the associated internal strain $\hat{\mathbf{Y}}$ are always non-symmetric. Additionally, a mixed Oldroyd objective time derivative $\overset{\diamond}{\hat{\mathbf{Y}}}$ is involved in the evolution equation (34), which is usually not the case for standard classical plasticity models.

In the following we shall investigate typical properties of the limiting classical model with reference to torsional loading. For this end, it is convenient to compare predicted responses with that ones obtained for standard classical plasticity models. Such a classical model is presented in the next section.

4 A STANDARD CLASSICAL MODEL (SCM)

Standard classical plasticity models for finite deformations are characterized by a symmetric internal strain tensor $\hat{\mathbf{Y}}$ responsible for kinematic hardening effects. For the case of isotropic specific free energy function, we deal with here, the conjugate internal stress tensor $\hat{\mathbf{Z}} = \rho_R \dfrac{\partial \psi_p^{(kin)}(\hat{\mathbf{Y}})}{\partial \hat{\mathbf{Y}}}$ is also symmetric, and additionally $\hat{\mathbf{Z}}$ is given as an isotropic function of $\hat{\mathbf{Y}}$. This implies that the back-stress tensor $\hat{\boldsymbol{\xi}}$ will always be symmetric, whenever $\hat{\boldsymbol{\xi}}$ is represented as an isotropic function of $\hat{\mathbf{Y}}$ and $\hat{\mathbf{Z}}$. The latter is the case when $\hat{\boldsymbol{\xi}}$ is postulated to obey the mathematical structure of a Mandel stress tensor (cf. Tsakmakis & Willuweit[18]).

Some standard classical models exhibiting non-linear kinematic hardening rules of Armstrong-Frederick type have been intensively discussed by Tsakmakis et al. (see e.g.[18,19,20]). All constitutive equations are identical to those in Section 3, except of the kinematic hardening rule. As a typical example, and for reasons of comparison, we refer to the kinematic hardening rule proposed in[18,20].

$$\hat{\boldsymbol{\xi}} = (\mathbf{1} + 2\hat{\mathbf{Y}})\hat{\mathbf{Z}} \text{ : back-stress tensor,} \tag{11}$$

$$\psi_p^{(kin)} = \psi_p^{(kin)}(\hat{\mathbf{Y}}) = \frac{1}{2\rho_R}\left(c_1 (tr\hat{\mathbf{Y}})^2 + c_2 \hat{\mathbf{Y}} \cdot \hat{\mathbf{Y}}\right), \tag{12}$$

$$\hat{\mathbf{Z}} = \rho_R \frac{\partial \psi_p^{(kin)}}{\partial \hat{\mathbf{Y}}} = c_1 (tr\hat{\mathbf{Y}})\mathbf{1} + c_2 \hat{\mathbf{Y}} , \tag{13}$$

$$\overset{\triangledown}{\hat{\mathbf{Y}}} = \dot{\hat{\mathbf{Y}}} - \hat{\mathbf{L}}_p \hat{\mathbf{Y}} - \hat{\mathbf{Y}} \hat{\mathbf{L}}_p^T = \hat{\mathbf{D}}_p - \dot{s} b \hat{\mathbf{Z}} . \tag{14}$$

5 TORSIONAL LOADING

We shall discuss the properties of the limiting classical model, compared with the standard classical model presented in Section 4, by concentrating ourselves on torsional loading of a circular cylinder with fixed ends. Small elastic deformations are assumed to apply, with Youngs modulus E=200000MPa and Poisson ratio $\nu = 0{,}3$. Since the equations governing isotropic hardening are identical for both models, we focus attention on kinematic hardening only, the yield stress being k=const.=200 MPa. The remaining material parameters read as follows.

Classical Limiting Model:

$b_1 = b_2 = 0{,}00125(MPa)^{-1}$,

$c_1 = 0, \quad c_2 = c_3 = 10000MPa$.

Standard Classical Model:

$b = 0{,}0025(MPa)^{-1}$,

$c_1 = 0, \quad c_2 = 20000MPa$.

For uniaxial homogeneous tension-compression loading, the predicted responses according to both models are displayed in Figure 1. It can be recognized that there exist quantitative differences only. However, the amout of the differences is so small that the predicted behaviors may be regarded to be identical for such loadings.

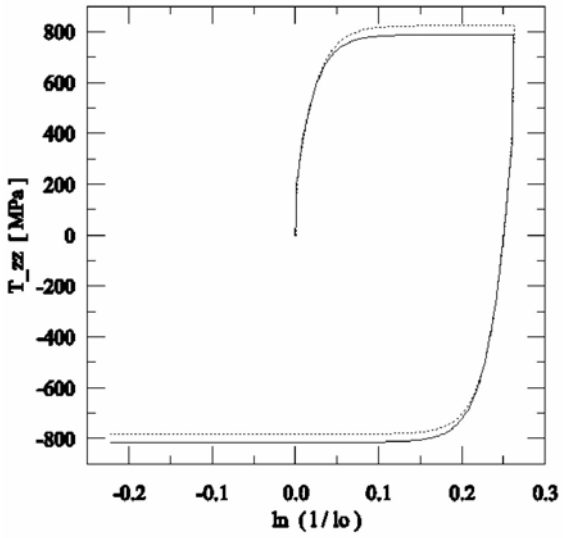

Figure 1. Uniaxial tension compression loadings of a bar in zz-direction. (l: length of the bar at time t, l_0: length of the bar at time t=0, ———: CLM, ...: SCM)

The two models have been implemented into the UMAT subroutine of the finite element code ABAQUS, as described in[20]. For torsional loading, the finite element discretization consists of 75 8-node axisymmetric elements (ABAQUS type CGAX8) and 266 nodes. The outer radius r_0 and the length l of the cylinder are chosen to be equal to 0,85mm. All radial distributions of stress components except of the axial stress component T_{zz} are essentially identical. Consequently, we concentrate ourselves on the predicted $r - T_{zz}$-responses $(0 \le r \le r_0)$ displayed in Figures 2-4, which represent so-called second-order effects. In these figures, $\gamma_0 = \Theta r_0$ is the global shear of the cylinder (shear at the outer radius), where Θ is the twist per unit length. It can be seen that at the beginning of the loading process (see Figure 2) there exist only quantitative differences of small amount between the predicted responses according to both models. However, with increasing load, the quantitative differences become larger and convert to significant qualitative differences. Thus, at sufficient large amount of shear the maxima of the graphs are at $r = 0$ for LCM and at $r = r_0$ for SCM. It is worth remarking that as the shear load increases, the minimum of the $r - T_{zz}$-graphs according to SCM approaches the point $r = 0$. Moreover, at the neighborhood of the minimum the stress distributions for SCM indicate large amounts of gradients.

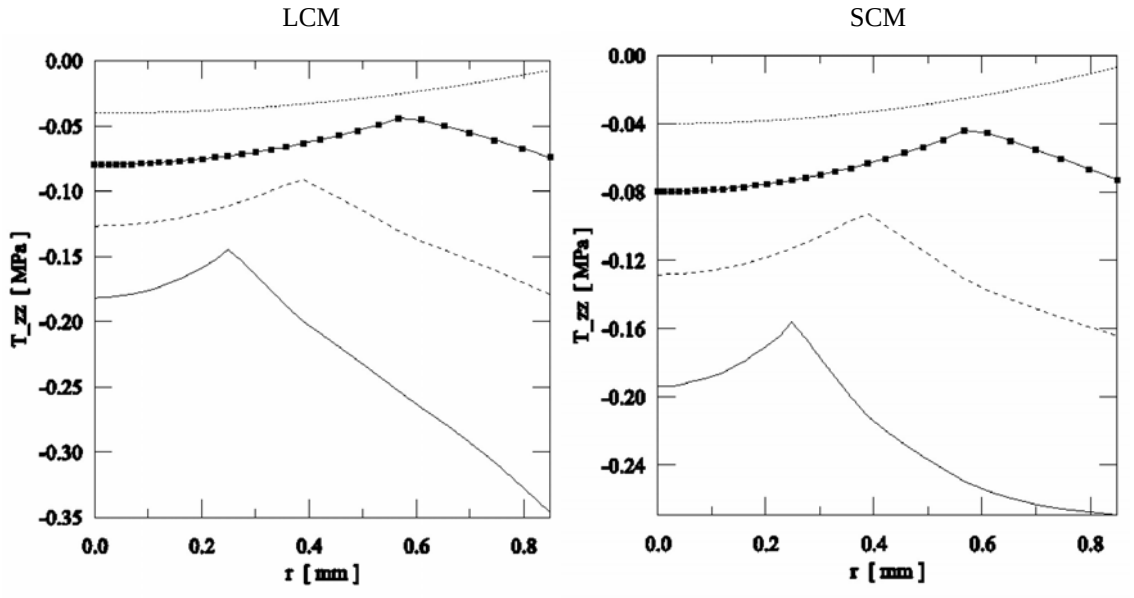

Figure 2. Radial distribution of the axial stress component T_{zz}. (·····: $\gamma_0 = 0{,}00142$, ■——■: $\gamma_0 = 0{,}0022$, - - - - - - - - -: $\gamma_0 = 0{,}0033$, ——: $\gamma_0 = 0{,}005$)

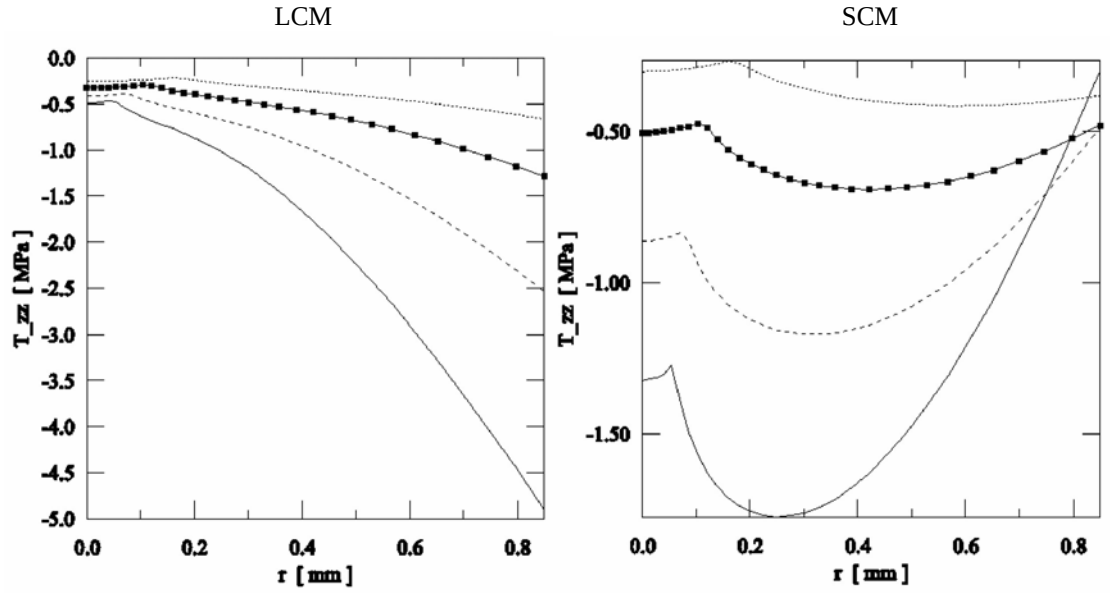

Figure 3. Radial distribution of the axial stress component T_{zz}. (·····: $\gamma_0 = 0{,}0076$, ■——■: $\gamma_0 = 0{,}011$, - - - - - - - - -: $\gamma_0 = 0{,}0172$, ——: $\gamma_0 = 0{,}021$)

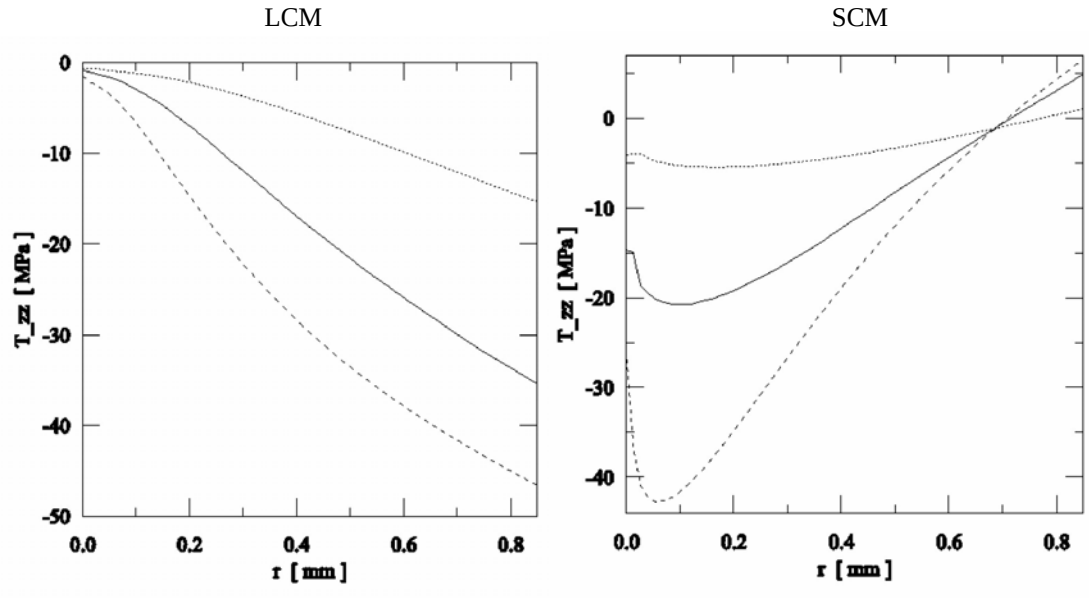

Figure 4. Radial distribution of the axial stress component T_{zz}. (·····: $\gamma_0 = 0{,}04$, ——: $\gamma_0 = 0{,}1$, – – – –: $\gamma_0 = 0{,}2$)

6 CONCLUSIONS

The limiting classical model is characterized by a kinematic hardening law, which is expressed in terms of non-symmetric internal strain and stress tensors. In particular, a mixed Oldroyd time derivative is involved. As mentioned above, standard classical models deal with symmetric internal strain tensors responsible for kinematic hardening. For such models evolution equations involving both, the upper und the lower Oldroyd time derivatives, in connection with back-stress tensors of Mandel type, have already been investigated (see e.g.[18,19]). It has been recognized, that the main differences occur in the predicted second-order effects. Therefore, it is natural to except that for different kinematic hardening models, including the limiting classical model considered, the most important differences in predicted responses will be present in second-order effects. Indeed, the investigations here confirm this supposition. To complete the investigation of kinematic hardening rules on the basis of Oldroyd time derivatives, it remains still to discuss the other mixed Oldroyd time derivative. Also, it is of interest to find the corresponding micropolar plasticity model. However, the answer of such questions is beyond of the scope of the present paper and will be tackled in future work.

Acknowledgement – The authors thank Dipl.-Ing. Ch. Sator for providing some finite element calculations.

REFERENCES

[1] Mindlin, R.D. (1964), "Micro-structure in Linear Elasticity", Archs. Ration. Mech. Anal. 10, pp. 51-78.

[2] Eringen, A.C. (1999), "*Microcontinuum Field Theories, I Foundations and Solids*", Springer, New York.

[3] de Borst, R. (1993), "A generalization of J_2 – flow theory for polar continua" , Computer Methods in Applied Mechanics and Engeneering 103, pp. 347-362.

[4] Steinmann, P. (1994),"A micropolar theory of finite deformation and finite rotation multiplicative elastoplasticity", Intern. J. Solids. Struct. 31, pp. 1063-1084.

[5] Lippmann, H. (1969), "Eine Cosserat-Theorie des plastischen Fließens", Acta Mechanica 8, pp. 255-284.

[6] Diepolder, W., Mannl, V., Lippmann, H. (1991), " The Cosserat continuum, a model for grain rotations in metals?", International Journal of Plasticity 7, pp. 313-328.

[7] Forest, S. (1998), "Modelling slip, kink and shear banding in classical and generalized single crystal plasticity", Acta mater. 9, pp. 3265-3281.

[8] Grammenoudis, P., Tsakmakis, Ch. (2001), "Hardening rules for finite deformation micropolar plasticity: Restrictions imposed by the second law of thermodynamics and the postulate of Il'iushin", Continuum Mechanics and Thermodynamics 13, pp. 325-363.

[9] Grammenoudis, P., Tsakmakis, Ch. (2005), "Finite element implementation of large deformation micropolar plasticity exhibiting isotropic and kinematic hardening effects", International Journal for Numerical Methods in Engineering 62, pp. 1691-1720.

[10] Grammenoudis, P., Tsakmakis, Ch. (2005), "Predictions of microtorsional experiments by micropolar plasticity", Proc. R. Soc. A 461, pp. 189-205.

[11] de Borst, R., Mühlhaus, H.-B., (1992), "Finite Deformation Analysis of Inelastic Materials with Micro--Structure," *Finite Inelastic Deformations --- Theory and Applications, IUTAM Symposium* , Hannover, Germany, pp. 313-322.

[12] Mühlhaus, H.-B., Vardoulakis, I., (1987), "The thickness of shear bands in granular materials", Gèotechnique 37, pp. 271-283.

[13] Steinmann, P., Willam, K., (1991), "Localization within the framework of micropolar elasto—plasticity", *Advances in Continuum Mechanics*, pp. 296-313.

[14] Grammenoudis, P., Tsakmakis, Ch. (2005), "Micropolar plasticity. Part I: The classical limiting model", submitted for publication.

[15] Grammenoudis, P., Tsakmakis, Ch. (2005), "Micropolar plasticity. Part II: Comparison of responses predicted by the limiting and standard classical models", submitted for publication.

[16] Lee, E.H., (1969), "Elastic plastic deformation at finite strains", ASME Trans. J. Appl. Mech. 36, pp. 1-6.

[17] Chaboche, J.-L., (1993), "Cyclic viscoplastic constitutive equations. Part I: A thermodynamically consistent formulation", Journal of Applied Mechanics 60, pp. 813-821.

[18] Tsakmakis, Ch., Willuweit, A., (2004), "A comparative study of kinematic hardening rules at finite deformations", Int. J. Nonl. Mech. 39, pp. 539-554.

[19] Tsakmakis, Ch., (1996), "Kinematic hardening rules in finite plasticity. Part I: A constitutive approach", Continuum Mech. Thermodyn. 8, 215-231.

[20] Tsakmakis, Ch., Willuweit, A., (2003), "Use of the Elastic Predictor-Plastic Corrector Method for Integrating Finite Deformation Plasticity Laws", *Deformation and Failure of Metallic Materials*, pp. 1-36.

Author index

E

F

G

H

I

J

K

L

M

N

P

R

S

T

U

V

W

X

Y

Z